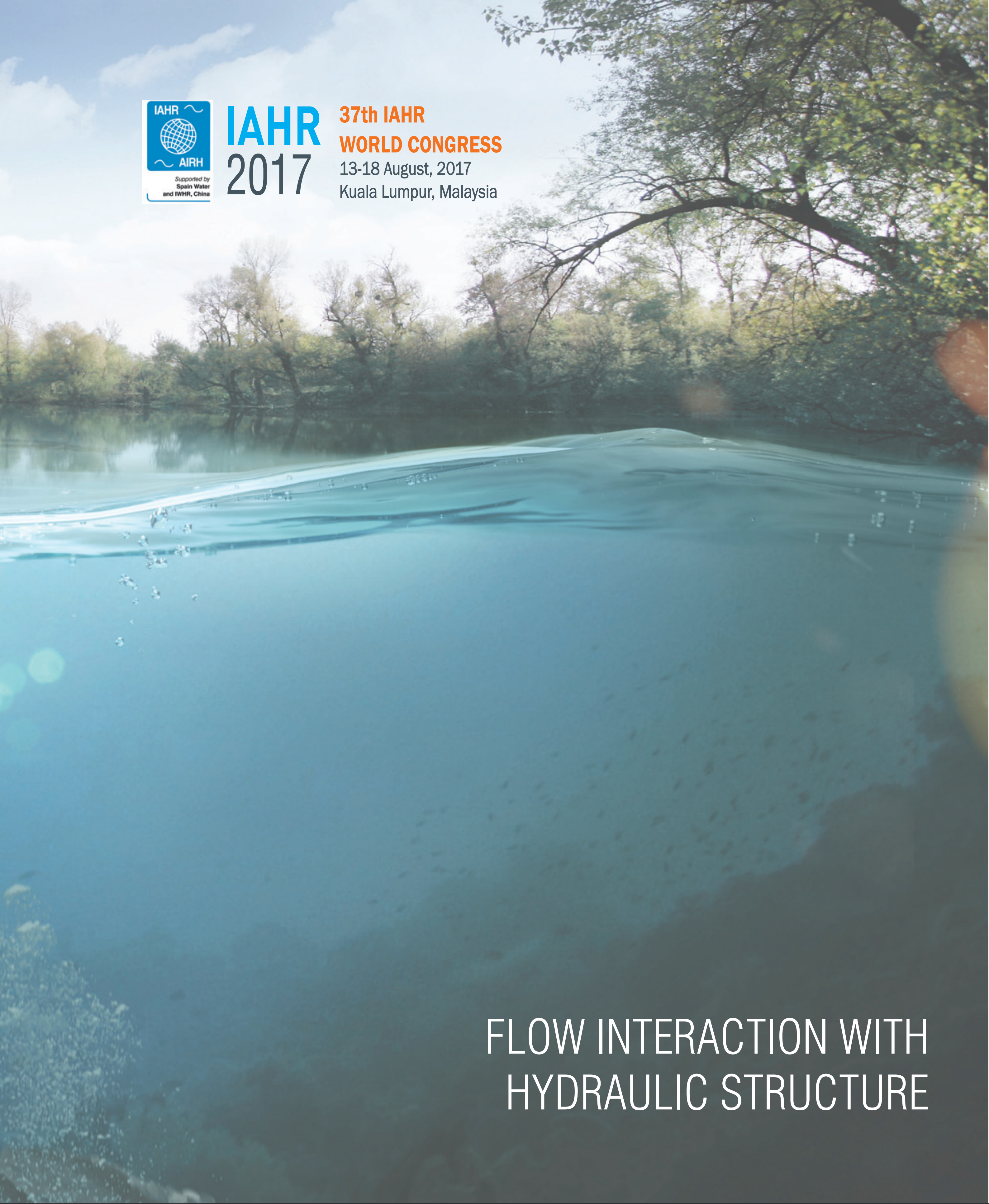

IAHR 2017

Supported by Spain Water and IWHR, China

37th IAHR WORLD CONGRESS

13-18 August, 2017

Kuala Lumpur, Malaysia

FLOW INTERACTION WITH HYDRAULIC STRUCTURE

SCOUR MORPHOLOGY DUE TO VERTICAL CROSSING JETS WITH DIFFERENT DIAMETERS

MICHELE PALERMO(1) & STEFANO PAGLIARA(2)

(1,2) DESTEC-Department of Energy, Systems, Territory and Construction Engineering, University of Pisa, Pisa, Italy,
michele.palermo@ing.unipi.it; s.pagliara@ing.unipi.it

ABSTRACT

The scour hole due to the plunging jets can be characterized by significant geometric dimensions which can undermine dam foundations. Therefore, a correct assessment of the main parameters influencing the erosive process is fundamental. In general, the equilibrium scour morphology mainly depends on the following parameters: jet impact angle into the stilling basin; jet densimetric Froude number; granulometric characteristics of the stilling basin material and tailwater level. In particular, the effect of these parameters can be different if scour hole morphology is either 2D or 3D. Furthermore, successive studies analyzed the erosive process due to multiple jets. The analysis of the scour process was conducted in the presence of both vertical and symmetric crossing jets. It has been experimentally proven that these two geometric configurations, in most of hydraulic conditions, determine a reduction of the scour hole lengths. Nevertheless, the scour process due to crossing jets is a complex phenomenon, as it depends on many parameters, including the crossing angles and the distance of the jet crossing point from the stilling basin water surface. To the authors' knowledge, no studies are present in literature dealing with vertical crossing jets of different diameters. Therefore, a dedicated experimental apparatus is built in order to simulate two vertical crossing jets with different diameters. Experimental tests are conducted for different tailwater levels with different jet diameter ratios. The resulting morphology is compared with that due to a single plunging jet. This last configuration is obtained simply removing the pipe with smaller diameter from the experimental apparatus. The comparison is conducted in order to understand for which geometric configurations the presence of the smaller diameter jet becomes negligible in terms of scour hole characteristics.

Keywords: Plunge pool, scour; spillway; tailwater; vertical crossing jet.

1 INTRODUCTION

Plunge pool scour is a phenomenon which should be carefully analyzed and predicted in order to minimize structural risks. It assumes a particular importance in correspondence with dams. The scour phenomenon due to plunging isolated jets has been extensively studied. There are many studies in literature dealing with this topic, furnishing useful empirical relationships to evaluate the maximum scour depth and length of the scour hole. Namely, the analysis of the scour process involved both the jet characteristics and the configurations. In particular, the analysis of the jet characteristics and their effects on the scour process were deepened by several author (among others, Rajaratnam and Berry, 1977; Rajaratnam, 1981; Mih and Kabir, 1983; Aderibigbe and Rajaratnam, 1996; Chiew and Lim, 1996; Ade and Rajaratnam, 1998; Pagliara et al., 2006; Dey and Sarkar, 2006; Faruque et al., 2006; Sarkar and Dey, 2007; Pagliara et al., 2008; Pagliara et al., 2015; Pagliara et al., 2016). Nevertheless, due to the complexity of the erosive mechanism, most of the cited studies lack generality, i.e., the results and the analyses proposed can be considered valid for relatively limited ranges of parameters and configurations. This occurrence is mainly due to the fact that most of the studies are related to peculiar configuration and, at the same time, they are mainly based on experimental evidences. Despite of this limitation, it appears that there is a clear difference in jet scour behavior in the case in which the scour process results either bi- or three-dimensional. Namely, one of the first analyses allowing for a derivation of a clear parameter by which the phenomenon can be classified either 2D or 3D was due to Pagliara et al. (2008). Based on the study of Pagliara et al. (2006), authors developed a quantitative criterion to distinguish the different scour processes. In particular, Pagliara et al. (2006) analyzed the scour mechanism due to plane plunging jets, resulting in a two-dimensional scour hole geometry. They experimentally showed that the scour process in the case of 2D resulting equilibrium morphology is characterized by a substantial 2D flow structure and the equilibrium geometry mainly depends on both the geometric configuration of the jet (inclination) and on its flow characteristics (discharge, air entrainment, etc.). In addition, they showed that the tailwater level plays a fundamental role, resulting in an increase of the jet diffusion length in the stilling basin. This occurrence was also confirmed by Hoffmans (1998). He conducted a theoretical analysis of the erosive process, proposing an innovative approach based on Newton's law by which he was able to derive a predictive relationship valid for a large range of hydraulic conditions. Nevertheless, even if it is mainly based on theoretical derivations, the approach proposed by Hoffmans is affected by several limitations. In particular, Hoffmans (1998) did not take into account the effect of air entrainment in jets and, at the same time, he assumed that the jet impinging angle into the stilling basin is generally bigger than 60°. In addition, he limited his analysis to a single jet and did not take into consideration multiple jets configurations. Finally, he analyzed the scour process due to an isolated jet, without considering eventual protection structures located in the stilling basin in order to reduce the scour geometry. These limitations led researchers to further investigate the scour phenomenon due to plunging jets both in the presence of protections structures and for different jet configurations. In particular, the first aspect (effect of protection structures in the stilling basin) was deepened by Rajaratnam and Aderibigbe (1993), Pagliara and Palermo (2008) and Pagliara et al. (2010b). Namely, Rajaratnam and Aderibigbe (1993) analyzed the possibility to use horizontal screens in order to limit scour evolution. The use of permeable and impermeable screens (vertical) allowing for a reduction of the scour hole geometries was further investigated by both Pagliara and Palermo (2008) an Pagliara et al. (2010b), who analyzed the effects of both screen spatial positions and their permeability on the scour characteristics, concluding that, if opportunely located, protection structures can lead to a 40% scour depth reduction. Another important aspect which has been analyzed only recently is the influence of jet configuration on the scour features. Namely, the possibility to use multiple jets was investigated by several authors, and it appeared very useful in terms of scour reduction. In particular, Li et al. (2006) analyzed multiple crossing jets and applied their findings for a real dam. Nevertheless, their analysis was limited to the prototype characteristics whereas, only very recently, many studies have been conducted at the University of Pisa (Pagliara et al., 2010a; Pagliara et al., 2011; Pagliara et al., 2012a; and Pagliara and Palermo, 2013). These last studies proposed a systematical investigation on the scour features due both multiple vertical and horizontal crossing jets, also involving the air entrainment effect. Namely, the investigation of the scour characteristics due to multiple vertical crossing jets was conducted by Pagliara et al. (2012a). Authors proposed a set of useful equations in order to estimate the main geometric characteristics. In addition, they found that the scour geometry can be significantly less if compared to that due to an equivalent single jets for same conditions, mainly depending on the crossing angle and on the tailwater level. A similar analysis for horizontal crossing jets was conducted by Pagliara et al. (2011), Pagliara et al. (2012b) and Pagliara and Palermo (2013), involving also the effect of air discharge. They experimentally showed that the there is a significant reduction of the scour depth when the air discharge in the jets increases. Furthermore, they analyzed the scour typologies, proposing useful practical criteria to distinguish them. For both multiple vertical and horizontal crossing jets, a prominent role is played by the distance of the jet crossing point from the water surface. This is mostly due to the fact that by increasing this distance the resulting impinging jet could be more spread, resulting, generally, in a reduction of the forces exerted on the stilling basin material. Nevertheless, to the authors' knowledge, there are no studies relative to the scour process due to multiple vertical crossing jets with different diameters. This reason led authors to systematically investigate this aspect, focusing on the scour geometry characteristics. This paper aims to analyze the variations due to multiple crossing jets made of different diameters on the equilibrium scour morphology, by comparing them with those due to the single jet, located in the same position of that characterized by the bigger diameter in the crossing jet configuration. The preliminary results allowed to establish that the increase of the crossing jet diameters ratio can result in slight differences in the scour morphology under selected hydraulic conditions. Therefore, it can be concluded that a bigger flow discharge can be discharged using crossing jets of different diameters, without causing a significant increase of the equilibrium morphology characteristics. This paper will show the preliminary results based on the analysis of two different crossing jet ratios. In particular, the analysis will focus on the similarities and differences in the resulting equilibrium morphology. Nevertheless, further investigations are required in order to generalize the proposed results, which can be very useful for practical applications. In particular, they will allow to derive useful relationships to evaluate the main geometric parameters of the scour hole and the downstream ridge.

2 EXPERIMENTAL SET-UP

Tests were conducted in a channel whose geometric characteristics are: 6 m long, 0.8 m wide and 0.9 deep. The granulometric characteristics of the channel bed material were: d_{90}=10.26 mm, d_{84}= 10.02 mm, d_{16}=7.49 mm and $\sigma=(d_{84}/d_{16})^{0.5}=1.17$, where d_{xx} is the characteristic diameter, for which xx% of the material is finer. The two vertical crossing jets were simulated using two pipes characterized by different inclination with respect to the horizontal and different diameters. Namely, experimental tests were conducted for different jet angles combinations, i.e. for α_1=30° and α_2=60, α_1=30° and α_2=85, α_1=45° and α_2=60, α_1=45° and α_2=85, and α_1=60° and α_2=85, where α_1 and α_2 are the inclinations with respect to the horizontal of the lower and upper jet, respectively (see Figure 1b). In addition, different diameters were adopted, i.e., tests were conducted varying the jet diameters of both lower and upper jets. Namely, for the lower jet two pipe diameters were used, i.e., D_1=1.67 cm and D_1=2.2 cm, whereas, for the upper jet, the tested diameters were D_2=3.11 cm and D_2=4.25 cm. It means that the ratio between the cross section areas $A_1=\pi D_1^2/4$ and $A_2=\pi D_2^2/4$ of the upper and lower jets ranged between 2 and 6.47. Namely, two jet diameter ratios and five crossing angle combinations were tested. The total discharge was divided in such a way that both the jets were characterized by the same densimetric Froude number. In addition, the diameter of the equivalent single jet $D_{eq}=(D_1^2+D_2^2)^{0.5}$

(i.e., the diameter of the single jet characterized by the same densimetric Froude number, same flow velocity and same total discharge) varied between 3.81 cm and 4.57 cm. Selected tests were conducted for different tailwaters and densimetric Froude numbers $F_{d90}=V_{eq}/[g\cdot(\rho_s/\rho-1)\cdot d_{90}]^{0.5}$, where g is the acceleration due to gravity, ρ_s and ρ sediment and water densities, respectively, d_{xx} is the material size for which xx% is finer, and $V_{eq}=V_1=V_2$ is the equivalent jet velocity, with V_1 and V_2 jet velocities in the lower and upper pipe, respectively. For this paper, experimental tests were conducted for F_{d90} varying between 8.61 and 10, whereas the non-dimensional tailwater $T_w=h_0/D_{eq}$ ranged between 0.71 and 7.07, where h_0 is the water depth above the original channel bed level. In addition, tests were conducted by varying the distance S between the jet crossing point form the water surface. Namely, the non-dimensional distance $\delta=S/D_{eq}$ ranged between 0 and 5.25. Note that $\delta=0$ means that the two jets cross in correspondence with the water surface in the stilling basin. The duration of each test was one hour, i.e., a time sufficient to reach the dynamic equilibrium configuration. During the tests, the scour hole profile was measured with a particular point gauge (see Pagliara et al., 2008) at different instants, i.e., 5, 10, 20 40 and 60 minutes after the beginning of the test. In addition, when the equilibrium configuration had been achieved, all the main geometric characteristics of both the scour hole and downstream ridge were measured, i.e. the maximum scour hole depth z_{mc}, the scour hole length, l_c and the ridge height z_{Mc} (see Figure 1c). Figure 2 and Figure 3 report pictures of some tests conducted in the presence of crossing jets characterized by different diameters. Namely, Figure 2 shows both frontal and side views of an experimental test in which $A_2/A_1=2$, whereas Figure 3 shows the same for a test in which $A_2/A_1=6.47$.

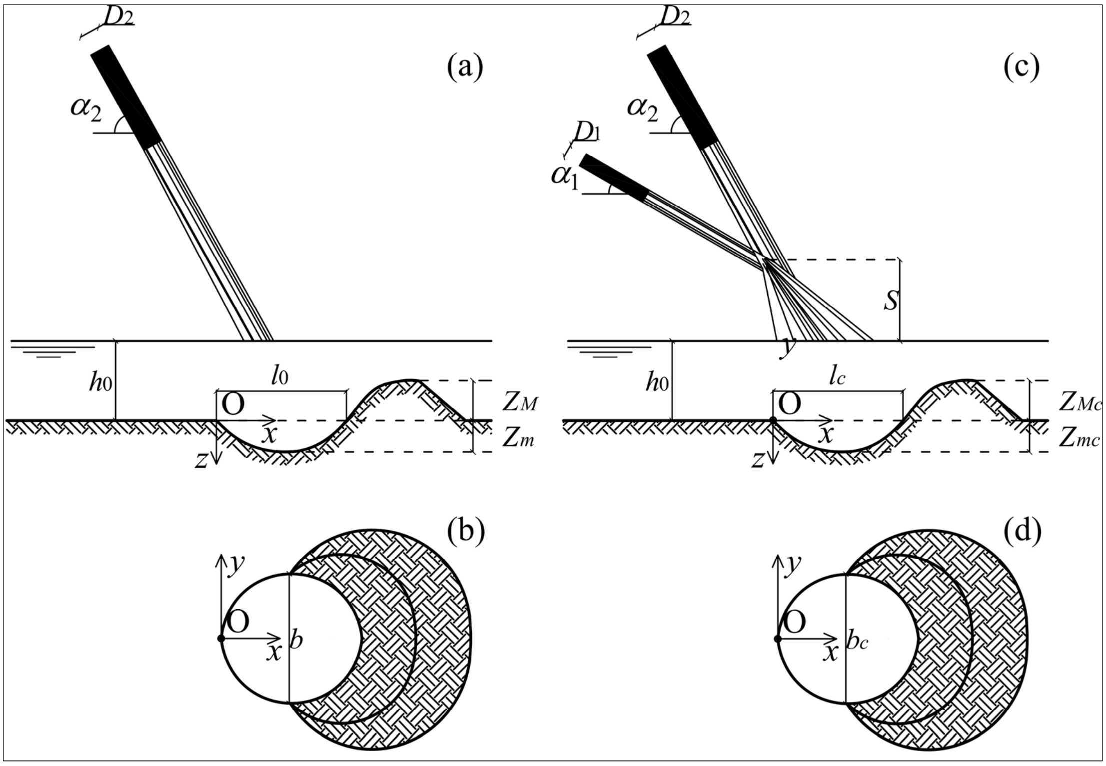

Figure 1. Diagram sketch of the experimental apparatus, along with the main geometric parameters: (a) side and (b) planar view for single plunging jet; (c) side and (d) planar view for two crossing jets with different diameters.

The same experimental tests were repeated using only one jet located in the same position of the upper jet and characterized by the same discharge Q_2, same diameter D_2 and same non-dimensional tailwater level $T_w=h_0/D_2$. These last tests were conducted in order to compare the effect of the lower jet presence (characterized by a discharge Q_1 and diameter D_1) on the erosive process. Namely, the aim of the tests conducted with single jets was to establish the effect of the lower jet on the erosive process. In other words, these last tests were conducted in order to verify which jet cross section area ratio above which the effect of the lower jet can be considered negligible. Therefore, also in this case, the scour profile readings were taken at different instants and the dynamic equilibrium configuration was carefully surveyed, deriving the values of the maximum scour depth z_m, the scour hole length l_0 and the ridge height z_M (see Figure 1a). This last aspect can have a huge practical relevance. In fact, it implies that bigger discharge can be discharged using two jets without causing significant modifications in terms of maximum scour depth and length. Therefore, all the tests with single jets were conducted in the same non-dimensional conditions of the multiple crossing jets.

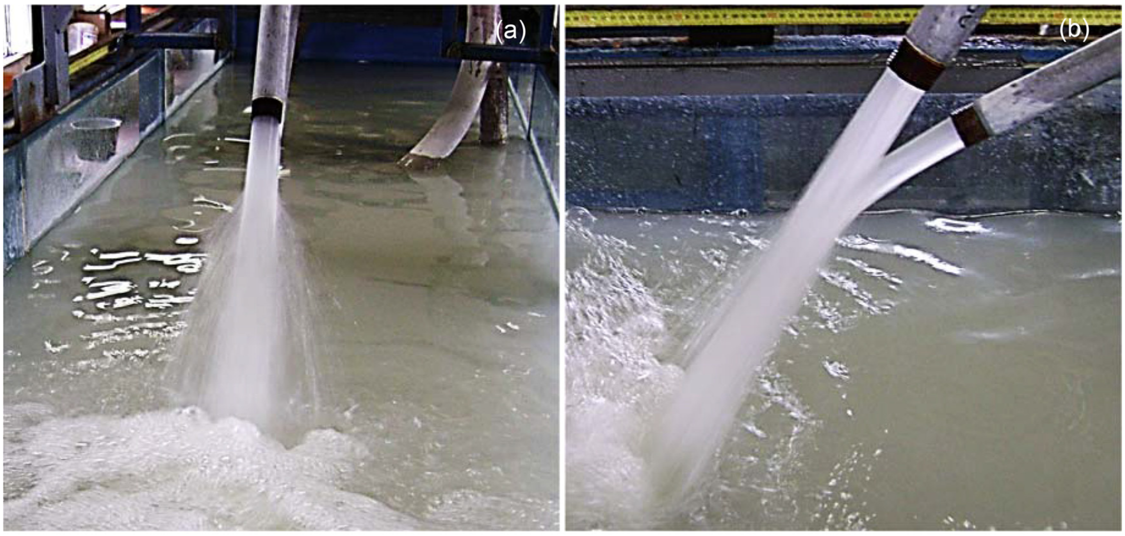

Figure 2. Experimental test for A_2/A_1=2, α_1=30°, α_2=60°, δ=5.25, F_{d90}=8.61, T_w=7.07: (a) frontal view; (b) side view.

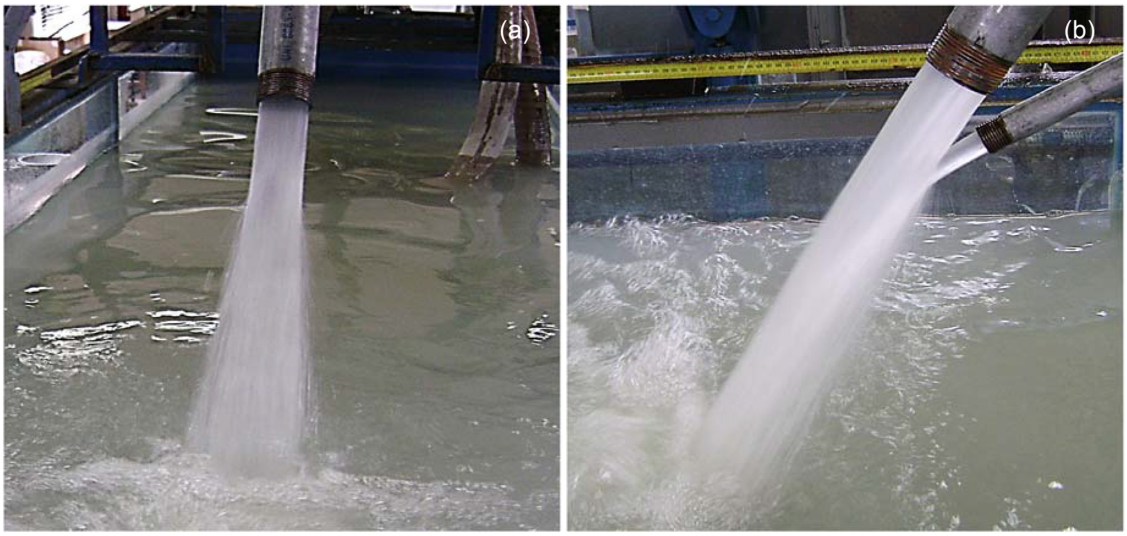

Figure 3. Experimental test for A_2/A_1=6.47, α_1=30°, α_2=60°, δ=4.16, F_{d90}=8.61, T_w=7.07: (a) frontal view; (b) side view.

3 LITERATURE BACKGROUND

3.1 Single jet

In order to discuss the findings of the present paper, it is worthy to synthetize the main results of Pagliara et al. (2008) relative to a single jet. Namely, in this section we will briefly report the main results obtained by Pagliara et al. (2008) for 3D equilibrium scour morphologies due to a single plunging jet. In particular, Pagliara et al. (2008) experimentally showed that the maximum non-dimensional scour depth $Z_m=z_m/D_2$ depends on serval parameters, i.e., the non-dimensional tailwater T_w, the jet inclination α_2, the densimetric Froude number F_{d90} and the three-dimensionality parameter μ (i.e., a parameter which takes into account if the scour morphology is either 2D or 3D). Based on experimental evidences, Pagliara et al. (2008) derived the following relationship to estimate Z_m:

$$Z_m = f_1(F_{d90}) \cdot f_2(\alpha_2) \cdot f_3(T_w) \cdot f_4(\mu) \quad [1]$$

where,

$$f_1(F_{d90}) = F_{d90} \quad [2]$$

  / ISSN 1562-6865 (Online) - ISSN 1063-7710 (Print)

$$f_2(\alpha_2) = [-0.38\sin(\alpha_2 + 22.5°)](1.360 - 0.012\alpha_2) \quad [3]$$

$$f_3(T_w) = (1/0.30)[0.12\ln(1/T_w) + 0.45](4 + T_w) \quad [4]$$

$$f_4(\mu) = 0.140 \quad [5]$$

In synthesis, Pagliara et al. (2008) showed that the combined effects of the influencing parameters determine both the scour hole and ridge shape. Namely, they stated that the maximum scour depth occurs in correspondence with high tailwater and low jet inclination. In this case, the scour hole appears longitudinally extended and well confined by a prominent ridge. By increasing both the jet angle and the tailwater, the scour hole appears more symmetric and semi-spherical. The flow is mostly directed radially and the ridge tends to surround the scour hole. In terms of non-dimensional longitudinal and transverse scour hole profiles, Pagliara et al. (2012a) proved that there is a substantial similitude, resulting in a not significant dependence of the non-dimensional shape of the scour hole on the independent variables. Namely, they proposed the following equations to predict both the non-dimensional longitudinal and transversal scour hole profiles, respectively:

$$Z = -2.852X^4 + 0.433X^3 + 0.818X^2 + 1.607X \quad [6]$$

$$Z = 15.430Y^4 - 30.463Y^3 + 14.680Y^2 + 0.340Y \quad [7]$$

where $Z=z/z_m$, $X=x/l_0$ and $Y=(y+b/2)/b$, with b scour width, x, y and z longitudinal, vertical and transversal coordinates, respectively, and O axes origin (see Figure 1a,b).

3.2 Vertical crossing jets

The analysis of vertical crossing jets with same diameter was conducted by Pagliara et al. (2012a). Namely, authors analyzed the effects of several parameters on the scour morphology, including the tailwater, several combinations of jet inclinations, and different non-dimensional distances of the jet crossing point from the water surface. Namely, the ranges of the tested parameters include those tested in the present study with different diameters, therefore the results proposed by Pagliara et al. (2012a) are useful to understand the similarities and differences for crossing jets with $A_2/A_1>1$. In particular, Pagliara et al. (2012a) showed that the maximum scour depth $Z_{mc}=z_{mc}/D_{eq}$ mainly depends on T_w, δ, F_{d90} and on jet inclinations, which can be equivalently represented by the inclination of the lower jet and the difference $\Delta\alpha=\alpha_2-\alpha_1$ and proposed the following equation to estimate Z_{mc}:

$$Z_{mc} = f_1(F_{d90}, \Delta\alpha) \cdot f_2(\delta, T_w) \cdot f_3(\alpha_1, T_w) \quad [8]$$

where,

$$f_1(F_{d90}, \Delta\alpha) = [0.500F_{d90} + (-0.002\Delta\alpha^2 + 0.134\Delta\alpha - 3.800)] \quad [9]$$

$$f_2(\delta, T_w) = (-0.017T_w + 0.022)\delta + 1 \quad [10]$$

$$f_3(T_w, \alpha_1) = (0.003T_w - 0.010)(\alpha_1 - 30°) + 1 \quad [11]$$

In addition, they conducted further experimental tests to compare the maximum scour depth due to a single equivalent jet whose inclination was $\alpha_v=0.5(\alpha_2+\alpha_1)$, i.e., located in a symmetric position respect the two crossing jets and characterized by the same F_{d90}. They proved that the scour morphology depends on the combined effects of tested parameters. In synthesis, they showed that, generally, the scour depth decreases with $\Delta\alpha$ because of the spread of the resulting jet due to high $\Delta\alpha$ values. Furthermore, a reduction was also observed for higher Tw and δ values, mainly because of the increase of the diffusion length and of the huge air entrainment due to the increase of the distance from the water surface. Finally, it was also shown that, in terms of non-dimensional transversal and longitudinal profiles, substantial similitudes with those due to an equivalent single jet can be detected. Therefore, Eq. (6) and Eq. (7) also apply for crossing jets with same diameters, for which $Z=z/z_{mc}$, $X=x/l_c$ and $Y=(y+b_c/2)/b_c$, where the subscript c refers to crossing jets.

4 RESULTS AND DISCUSSION

Experimental data were compared with those predicted by empirical relationships derived by both Pagliara et al. (2008) and Pagliara et al. (2012a), in order to understand the dynamics of the erosive process in the case in which two crossing jets are present with two different diameters. Namely, in Figure 4a, the measured data of the non-dimensional variable Z_{mc}, relative to the configuration in which the ratio between upper jet cross section area and lower jet cross section area A_2/A_1 is 4.67, were compared with those predicted by Eq. (1) valid for the single jet, characterized by the same F_{d90} and T_w=0.71. Figure 4b shows the same comparison for Tw=7.07, whereas Figure 4c compares Z_{mc} measured in the experimental tests with those predicted by Eq. (8) valid for crossing jets with same diameter (i.e., same cross section area, A_2/A_1=1). Figures 4d-f shows the same for A_2/A_1=2. The proposed comparison allowed to understand the behavior of the tested configuration with respect to the single equivalent jet and two crossing jets with same diameters. It can be easily observed (Figure 4a) that for low tailwaters and δ=0, the crossing angle combinations α_1=30°-α_2=60° and α_1=45°-α_2=60° cause a scour hole whose depth is comparable with that due to a single jet. It implies that for $\alpha_2 \leq 60°$ the effect of the lower jet is not significant for the equilibrium scour configuration. From a practical point of view, this is a very significant result. In fact, being the single jet F_{d90} the same of the crossing jets, it means that its discharge is less than the sum of those of the crossing jet, i.e., more water can be discharged without causing relevant effects on the scour depth. This observation is also confirmed for higher tailwater and different δ values as shown by Figure 4b. The reasons of this behavior are essentially due to: 1) the high A_2/A_1 value, which, generally, implies a reduced effect of the lower jet; 2) the inclination of the upper jet (α_2=60°, i.e., $\alpha_1 \leq 45°$).

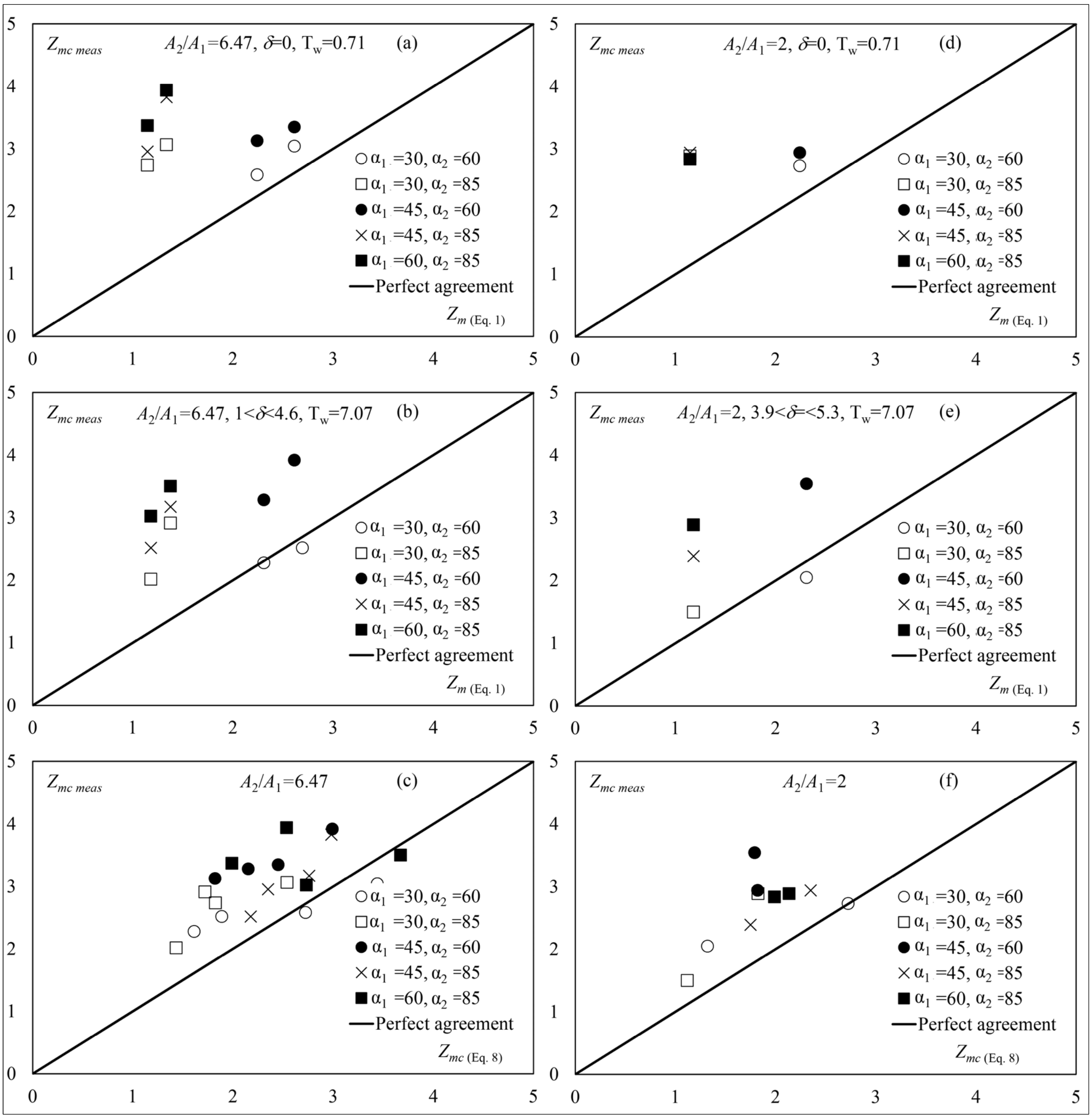

Figure 4. Comparison of measured Z_{mc} values with (a) Z_m values computed with Eq. (1) for δ=0, T_w=0.71 and A_2/A_1=6.47; (b) Z_m values computed with Eq. (1) for 1<δ=4.6, T_w=7.07 and A_2/A_1=6.47; (c) Z_{mc} values computed with Eq. (8) for A_2/A_1=6.47. Comparison of measured Z_{mc} values with (d) Z_m values computed with Eq. (1) for δ=0, T_w=0.71 and A_2/A_1=2; (e) Z_m values computed with Eq. (1) for 3.9<δ=5.3, T_w=7.07 and A_2/A_1=2; (f) Z_{mc} values computed with Eq. (8) for A_2/A_1=2.

This last occurrence can be explained by considering that for lower single jet inclinations, the scour depth increases. In fact, as shown by Pagliara et al. (2008), this peculiar behavior depends on the modified ridge geometry, with respect to both the 2D case and the case in which the upper jut inclination is higher. In particular, the downstream ridge is longitudinally extended and partially surrounds the scour hole, therefore less suspended granular material is retained in the scour hole, contributing to increase its depth. This occurrence is clearly evident by observing the non-dimensional profiles reported in Figure 5. Namely, Figure 5 shows the non-dimensional profiles of selected experimental tests with crossing jets and the corresponding tests with equivalent single jet. In this figure Z_{mc} and Z_m represent the non-dimensional scour depth for crossing jets and equivalent single jet, respectively and X is the non-dimensional longitudinal coordinate, i.e., $X=x/l_0$ for single jet and $X=x/l_c$ for crossing jets. It is clear that for $\alpha_2 \leq 60°$ (Figure 5a-b-d), the scour hole profile, along with the dune profile, show substantial similitudes, including the maximum scour depth. Furthermore, the scour hole is not longitudinally symmetric for both single jet and crossing jet. This is due to the fact that for lower jet angles, there is a significant component of the momentum quantity directed horizontally, which contributes to transport sediment downstream.

For higher α_2 values (see Figure 5c), the behavior of a single jet is essentially different. Namely, for single jet, the scour hole is quite symmetric and it is confined by a less extended longitudinal dune. In the case of crossing jets, the maximum scour depth occurs further downstream and the presence of a lower inclined jet contributes to transport sediment of the scour hole downstream, resulting in a more longitudinally extended dune.

The description of the scour dynamics reported above apply also for $A_2/A_1=2$. Namely, slight differences can be detected. Nevertheless, it is worth mentioning that, in this last case, the role of the lower jet is more prominent, therefore more differences in terms of equilibrium configuration can be detected respect to the previous case.

In synthesis, it can be noted that, by increasing the A_2/A_1 ratio and for lower α_2, the equilibrium morphology due to crossing jets with different diameters does not differ significantly from that due to an equivalent single jet. This result appears particularly important and requires further investigations because of the evident advantage to discharge a bigger amount of water, avoiding substantial modifications of the scour morphology, i.e., avoiding to increase the maximum scour depth.

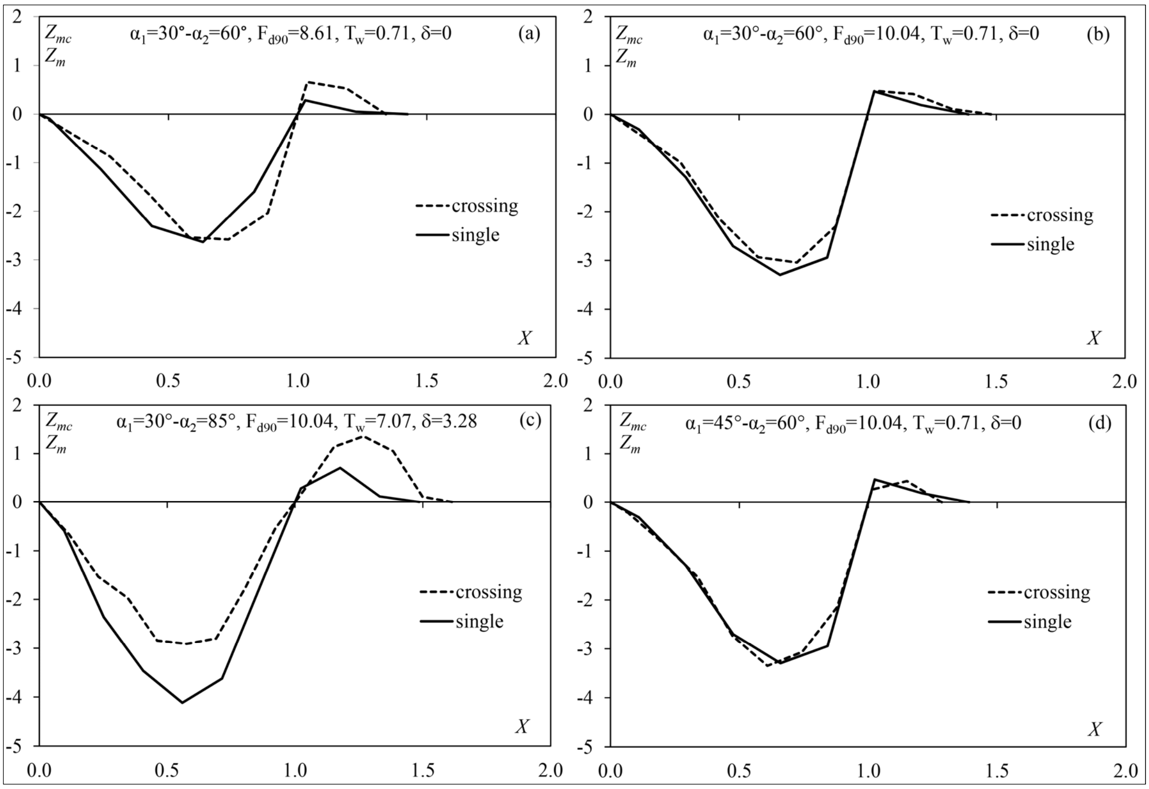

Figure 5. Comparison between non-dimensional profiles due to crossing jets for $A_2/A_1=6.47$ and the corresponding single jet for the same hydraulic and geometric conditions reported in figure captions.

Finally, the maximum scour depths due to crossing jets with different diameters were also compared with those due to crossing jets with same diameters, for both $A_2/A_1=6.47$ and $A_2/A_1=2$ (see Figure 4c and 4f, respectively). It can be noted that, for the same jet inclinations and hydraulic conditions, the maximum scour depths in the case of crossing jets with different diameters is generally bigger if compared with that due to crossing jets with same diameters. This occurrence is due to the fact that if crossing jets have the same diameter, the momentum quantities of the two jets are identical, resulting in a huger jet splash and in a reduction of the erosive action.

5 CONCLUSIONS

In the present paper a preliminary analysis of the scour process due to crossing jets characterized by different diameters is reported. A dedicated experimental apparatus was built and several experimental tests were conducted for different hydraulic conditions and jets configurations. Namely, two different crossing jet section area ratios were tested. In addition, tests were repeated by using a single jet characterized by the same upper crossing jet inclination, in order to compare the scour mechanism. It was experimentally shown that for lower inclination of the upper crossing jet, the equilibrium scour morphology is essentially the same of that due to the equivalent single jet. Furthermore, also the non-dimensional profiles show substantial similitudes. Whereas for higher values of the upper crossing jet inclination, the scour mechanism and the resulting morphology exhibit substantial differences. This occurrence allows to state that, in terms of practical applications, it is possible to increase the water discharge by using two crossing jets with different diameters without causing a substantial modification of the equilibrium morphology. Furthermore, it was also shown that in terms of maximum scour depth reduction, it is more appropriate to adopt crossing jets with the same diameter. The preliminary results proposed in the present paper are very promising. Further investigations are going on, aiming to furnish quantitative criteria to optimize the crossing jet configurations which can both reduce the scour depth and increase the water discharge.

REFERENCES

Ade, F. & Rajaratnam, N. (1998). Generalized Study of Erosion by Circular Horizontal Turbulent Jets. *Journal of Hydraulic Research*, 36(4), 613-635.

Aderibigbe, O.O. & Rajaratnam, N. (1996). Erosion of Lose Beds by Submerged Circular Impinging Vertical Turbulent Jets. *Journal of Hydraulic Research*, 34(1), 19-33.

Chiew, Y.M. & Lim, S.Y. (1996). Local Scour: By a Deeply Submerged Horizontal Circular Jet. *Journal of Hydraulic Engineering*, 122(9), 529-532.

Dey, S. & Sarkar, A. (2006). Scour Downstream of an Apron due to Submerged Horizontal Jets. *Journal of Hydraulic Engineering*, 132(3), 246-257.

Faruque, M.A.A., Sarathi, P. & Balachandar, R. (2006). Clear Water Local Scour by Submerged Three-Dimensional Wall Jets: Effect of Tailwater Depth. *Journal of Hydraulic Engineering*, 132(6), 575-580.

Hoffmans, G.J.C.M. (1998). Jet Scour in Equilibrium Phase. *Journal of Hydraulic Engineering*, 124(4), 430-437.

Li, L.-X., Liao, H.-S. & Li, T.-X. (2006). A Hybrid Model for Simulating Velocity Field of a River with Complex Geometry Plunged by Multiple Jets. *Journal of Hydrodynamics*, 18(6), 752–759.

Mih, W.C. & Kabir, J. (1983). Impingement of Water Jets on Nonuniform Streambeds. *Journal of Hydraulic Engineering*, 109(4), 536-548.

Pagliara, S. & Palermo, M. (2008). Plane Plunge Pool Scour with Protection Structures. *Journal of Hydro-Environment Research*, 2(3), 182-191.

Pagliara, S. & Palermo, M. (2013). Analysis of Scour Characteristics in Presence of Aerated Crossing Jets. *Australian Journal of Water Resources*, 16(2), 163-172.

Pagliara, S., Hager, W.H. & Minor, H.-E. (2006). Hydraulics of Plane Plunge Pool Scour. *Journal of Hydraulic Engineering*, 132(5), 450-461.

Pagliara, S., Amidei, M. & Hager, W.H. (2008). Hydraulics of 3D Plunge Pool Scour. *Journal of Hydraulic Engineering*, 134(9), 1275-1284.

Pagliara, S., Hassanabadi, L. & Kurdistani, S.M. (2015). Clear Water Scour Downstream of Log Deflectors in Horizontal Channels. *Journal of Irrigation and Drainage Engineering*, 141(9),1-8.

Pagliara, S., Mahmoudi Kurdistani, S, Palermo, M. & Simoni, D. (2016). Scour due to Rock Sills in Straight and Curved Horizontal Channels. *Journal of Hydro-Environment Research*, 10, 12-20.

Pagliara, S., Roy, D. & Palermo, M. (2010a). Scour due to Crossing Jets at Fixed Vertical Angle. *Journal of Irrigation and Drainage Engineering*, 137(1), 49-55.

Pagliara, S., Roy, D. & Palermo, M. (2010b). 3D Plunge Pool Scour with Protection Measures. *Journal of Hydro-Environment Research*, 4(3), 225-233.

Pagliara, S., Palermo, M. & Carnacina, I. (2011). Scour Process due to Symmetric Dam Spillways Crossing Jets. *International Journal of River Basin Management*, 9(1), 31-42.

Pagliara, S., Palermo, M. & Roy, D. (2012a). Stilling Basin Erosion due to Vertical Crossing Jets. *Journal of Hydraulic Research*, 50(3), 290-297.

Pagliara, S., Roy, D., & Palermo, M. (2010). Scour due to Crossing Jets at Fixed Vertical Angle. *Journal of Irrigation and Drainage Engineering*, 137(1), 49-55.

Rajaratnam, N. (1981). Erosion by Plane Turbulent Jets. *Journal of Hydraulic Research*, 19(4), 339-358.

Rajaratnam, N. & Aderibigbe, O. (1993). A Method for Reducing Scour Below Vertical Gates. *Proceedings of the Institution of Civil Engineers – Water and Maritime Engineering*, 101, 73-83.
Rajaratnam, N. & Berry, B. (1977). Erosion by Circular Turbulent Wall Jets. *Journal of Hydraulic Research*, 15(3), 277-289.
Sarkar, A. & Dey, S. (2007). Effect of Seepage on Scour due to Submerged Jets Resulting Flow Field. *Journal of Hydraulic Research*, 45(3), 357-364.

Proceedings of the 37th IAHR World Congress
August 13 – 18, 2017, Kuala Lumpur, Malaysia

FLOW BEHAVIOR OVER OGEE AND STEPPED SPILLWAY UNDER DIFFERENT FLOW CONDITIONS: AN EMPIRICAL APPROACH

SUMIT GANDHI(1), KIRTIKA SACHDEVA(2), MUDIT KHANDELWAL(3), RAJESH RAI(4), VIKRAM SINGH(5), SUDEEP SRIVASTAVA(6) & SURYA PRATAP MEENA(7)

(1, 2, 3, 4, 5, 6, 7) Department of Civil Engineering,
Jaypee University of Engineering & Technology, Guna, India
sumitgandhi1@rediffmail.com

ABSTRACT

An elaborate experimental study is carried out to develop the understanding of energy dissipation phenomenon in both ogee as well as stepped spillway in open channel under varying flow conditions. Non-dimensional discharge (Q/Q_d), Energy loss ratio (E_L/E_1) and Relative length of roller (L_r/Y_1) for ogee spillway and Energy loss ratio (E_L/E_1), Critical depth ratio (Y_c/S_H) and Relative length of roller (L_r/Y_2) for stepped spillway are studied and empirical models are proposed for considered conditions. Baffle blocks are also considered to find the effectiveness in amount of energy dissipation. Due importance is given to effective head ratio (H_e/H_d) in case of ogee spillway and baffle blocks dimensions (2:4, 2:5 and 3:4) (rise and tread) in case of stepped spillway. Results were also compared and validated with other analytical and computational models by other authors.

Keywords: Spillway; Dimensional analysis; Non-dimensional discharge; Critical depth ratio; Effective head ratio.

1 INTRODUCTION

It is an important task for a hydraulic engineer to design safe energy dissipation structure for reservoir storage and discharge. The purpose of such structure is not only to dissipate the kinetic energy of the flowing stream in order to have safe flow in downstream but also to eliminate the requirement for stilling basin at the toe or considerably reduces the size of stilling basin. Besides this, it not only results in low sequent depth combined with high energy dissipation but also provides safety against cavitational erosion and environmental aspects. Recent advancement led to construction of compacted concrete dams and necessitated the advantages of more energy dissipation. Safe dissipation at downstream of flow is achieved by either providing ogee spillway or providing steps in the spillway as per Tozzi (1994) as monolithic structure.

According to Savage and Johnson (2001), ogee spillways which have a control weir with an S-shape in profile have been preferred substantially. It comes out to be the most commonly used spillways due to their function, ability to control floodwater and high safety factor. Horton (1907) and Bazin (1888) presented an extensive laboratory investigation which was the first study to determine the ogee shape on the basis of flow behavior. Although much is understood about general ogee shape and its flow characteristics, however these modifications in the standard shape require engineers to evaluate its performance. On the other hand, stepped spillways have been used for centuries (Murillo, 2006). It either eliminates the requirement for stilling basin at the toe or considerably reduces the size of stilling basin as Das et al., (2016) suggested. Among the other benefits as per Chanson and Gonzalez (2005) of using stepped spillway compared with equivalent smooth spillway are compatibility with reinforced concrete placement, a significant increase in the rate of energy dissipation takes place on the spillway face, reduction in risks of scouring and cavitations, increase in the discharge capacity.

2 THEORY

Savage and Johnson (2001) compared flow parameters for an ogee spillway using a physical and numerical model with existing literature and discussed about the discharge due to aerated sharp-crested spillway with negative crest suctions pressure. Kim and Park (2005) gave special attention to study the flow structure in consideration of scale and roughness effects. Rageh (2001) considered the effect of baffle block and sill on a radial hydraulic jump to investigate and analyze the limiting design parameters. Comparative studies have been made by Ellayn and Sun (2012) about the hydraulic jump properties for an artificially roughened bed with wedge-shaped baffle blocks; experiments were conducted for both smooth and rough beds with a Froude number in the range of $3.06 \le F_{r1} \le 10.95$ and a relative bed roughness ranging $0.22 \le K_R \le 1.4$. Morales et al., (2012) discussed about the different concepts introduced in hydraulic engineering to ensure energy dissipation in stilling basins to fix the transition of supercritical into subcritical flow in a controllable area and to avoid objectionable downstream scour.

According to Carlos and Chanson (2004) energy dissipation mainly depends on frictional loss and momentum exchange in stepped spillway. They varied bed slope from 11° to 30°, Y_C/S_H ratio between 1 to 3.2, flow velocity and step height and concluded that having moderate slope (16° and 22°) high amount of aeration and high turbulence of flow occur. Nayak and Nagesh (1998) used continuous steps from crest to toe as stepped spillway to check its effectiveness. At lowest discharge there is air entrainment on each step, afterwards as the discharge is increasing air entrainment is reducing, also at designed discharge, energy loss is 80.89 %. Salmasi et al., (2011) extensively studied the overflow and through flow in stepped spillways with different porosities. Approximately eight physical models of stepped spillways with three different porosities (38%, 40% and 42%) and two slopes (1.1 and 1.2) (V: H) were made with permeable and impermeable faces. Rajaratnam (1990) classified the flow by considering submerged flows with baffle blocks and observed the variation in flow characteristics. However, Habibzadeh et al. (2012) conducted a preliminary study of the flow properties of submerged jumps with baffle blocks.

Keeping above fact in view, the present experimental study is made and oriented towards the development of empirical models of different flow characteristics for flow over both the spillway under different flow conditions.

3 EXPERIMENTATION

As such experiments were conducted in the hydraulics laboratory of JUET Guna, India. Ogee and stepped spillway model were tested in 4 m long, 0.2 m wide open channel with flow rates ranging from 0.35–3.83 m^3/s and 0.91-2.14 m^3/s respectively. A closed re-circulated controlled water supply from a large tank of 1.5 X 6.8 X 4.8 m^3 with adjustable frequency motor is provided with spillway arrangement followed by an open channel and a dissipation tank. The effect of surface roughness 'ε' is ignored in the present study due to experimental limitations. Work is explored to study the variation of various characteristics namely Q/Q_d, E_L/E_1 and L_r/Y_1 for ogee spillway and E_L/E_1, Y_c/S_H and L_r/Y_2 for stepped spillway varying the discharge under different conditions of baffle blocks (Table 1 and Table 2 respectively). Rise and tread of baffle blocks are kept in the ratio of 2:4, 2:5 and 3:4 (Run 2). Run 1 was made without baffle blocks in stepped spillway. Results were also compared and validated with other analytical and computational models.

4 DIMENSIONAL ANALYSIS: DEVELOPMENT OF EMPIRICAL EQUATION

4.1 Ogee Spillway

Ogee spillway is a modified form of drop spillway. Hence the downstream profile of the spillway is made to coincide with the shape of the lower nappe of the free falling water jet from a sharp crested weir. If the spillway runs with the maximum head, overflowing water just follows the curved profile of the spillway whereas the lower nappe does not follow the ogee profile and gets separated from the spillway surface. Horton (1907) and Bazin (1888) had given an extensive laboratory investigation which was projected to determine the ogee shape and these experiments have served as the basis of many designs. Bhajantri et al., (2006) studied hydrodynamic modeling and hydrodynamics were obtained through physical and numerical modeling.

The important variables affecting the jump pattern and energy dissipation can be expressed as a function:

$$f(Y_1, Y_2, H_e, H_d, V_1, V_2, L_r, E_L, g, \varepsilon) = 0 \qquad [1]$$

The effect of surface roughness 'ε' is ignored in the present work due to experimental limitations. Using linear fitting of the experimental data (Table 1) following empirical model for Q/Q_d, E_L/E_1 and L_r/Y_1 were developed and expressed. Dimensionless groups and hydraulic jump characteristics are the function of incoming Froude number, which can be represented as:

Table 1. Range of experimental values for ogee spillway with baffle blocks.

Y_1 (m)	Y_2 (m)	V (m/s)	Q (m^3/s)	F_{r1}	H_e/H_d	Q/Q_d	E_L/E_1	L_r/Y_1
0.012-0.025	0.08-0.15	0.40-1.04	0.35–3.83	1.0-5.40	1.53-14.04	1.24-3.65	1.37-27.60	4.19-46.53

$$\frac{Q}{Q_d} = 0.012\left(\frac{H_e}{H_d}\right)^2 - 0.066\left(\frac{H_e}{H_d}\right) + 0.08 \qquad R^2 = 0.97 \qquad [2]$$

$$\frac{E_L}{E_1} = 1.53F_{r1}^2 - 1.45F_{r1} + 1.33 \qquad R^2 = 0.95 \qquad [3]$$

$$\frac{L_r}{Y_1} = 35.88 \ln(F_{r1}) - 24.09 \qquad R^2 = 0.93 \qquad [4]$$

4.2 Stepped Spillway

Energy dissipation in stepped spillway is estimated by the indirect method through hydraulic jump formation and measuring the sequent depths in a channel. The flow over the stepped spillway is classified into two regimes: nappe flow and skimming flow. In the nappe flow regime, the water proceeds in a series of plunges from one step to another. According to Rajaratnam (1990), transition from nappe flow to the skimming flow occurs when critical depth to step height ratio 'Y_c/S_H' is approximately equal to 0.8. Christodoulou (1993) found that the energy loss due to the steps depends primarily on the ratio of critical depth to step height 'Y_c/S_H' as well as on the number of steps. For stepped spillway E_L/E_1, Y_C/S_H, L_r/Y_2 are modeled and verified with the existing results.

The important variables affecting the jump pattern and energy dissipation can be expressed as a function:

$$f(Y_1, Y_2, Y_c, S_w, S_H, V_1, V_2, L_r, E_L, g, \varepsilon) = 0 \qquad [5]$$

Using Buckinham's π-theorem and assuming repeating variables, the various dimensionless groups are developed. Using linear fitting of the experimental data (Table 2) following empirical model for E_L/E_1, Y_C/S_H and L_r/Y_2 were developed and expressed. Dimensionless groups and hydraulic jump characteristics are the function of incoming Froude number, which can be represented as:

Table 2. Range of experimental values for stepped spillway with baffle blocks.

Y_1 (m)	Y_2 (m)	V (m/s)	Q (m^3/s)	F_{r1}	Y_c (m)	E_L/E_1	Y_c/S_H	L_r/Y_2
0.16-0.19	0.48-1.54	0.94-6.94	0.903-2.142	1.0-5.5	0.27-2.27	0.97-0.79	0.14-1.13	3.10-9.20

$$\frac{E_L}{E_1} = 0.011\left(F_{r1}\frac{Y_c}{S_H}\right)^2 - 0.18\left(F_{r1}\frac{Y_c}{S_H}\right) + 0.98 \qquad R^2 = 0.98 \qquad [6]$$

$$\frac{Y_c}{S_H} = \frac{0.132F_{r1}^2 - 0.023F_{r1} + 0.045}{\left(\frac{S_H}{S_w}\right)^{1.67}} \qquad R^2 = 0.99 \qquad [7]$$

$$\frac{L_r}{Y_2} = \frac{0.788\,F_{r1}^{1.76}}{\left(\frac{Y_c}{S_w}\right)^{0.5}} \qquad R^2 = 0.99 \qquad [8]$$

5 RESULTS AND DISCUSSION

5.1 Ogee Spillway

Figure 1 shows a non-linear variation of non-dimensional discharge with effective head ratio for considered condition. There is similar trend obtained for experimental observed values and for other author's model for non-dimensional discharge and effective head ratio. Result has been compared to Savage and Johnson (2001) who have obtained similar graph with only exception of lower values of head taken. The crest of the model made by these researchers is slightly different; there model was operated at 10 different reservoir elevations 'H_e/H_d' ranging from 0.07 - 1.2 as compared to presented model which is designed for 'H_e/H_d' ratio varying from 1.5 - 14. Also, results produced by Savage and Johnson (2001) is based on their numerical and physical model in which they applied few boundary conditions like turbulence, aeration, etc. which are neglected in the present study. Similarly, Alhashimi (2013) has proposed computational model for flow rate using numerical model, which was found to be greater than those obtained in their experimental study. Reason is attributed to the inappropriate matching of physical condition of flow with boundary conditions provided in numerical analysis. As a result, the data shows small deviation but follows similar pattern in Fig. 1. It is also clear that discharge over the spillway increases as the head over the spillway increases.

Figure 2 shows a nonlinear increasing trend for energy loss ratio against Froude number due to formation of hydraulic jump over ogee spillway. Similar trend being also observed by Ranga Raju (1993) except with the range of energy loss ratio as it was plotted for different experimental and flow conditions of low head.

Figure 3 shows similar result when compared to that given by Rageh (2001) except that the tests conducted are with different dimensions of baffle blocks in horizontal expanding channel. However pattern obtained being the same. The relative length of roller is non-linearly varying with Froude number. Slight deviation in results is attributed to the baffle blocks distances from the toe of spillway and tail gate. Again, due to expansion of channel, flow conditions changes and air entrapment takes place and hence the energy loss. Rageh (2001) studied the effect of baffle block on hydraulic jump to investigate and analyze the limiting design parameters under such flow condition. The limiting design conditions refer to the radial hydraulic jump, when it occurs entirely on the horizontal bed.

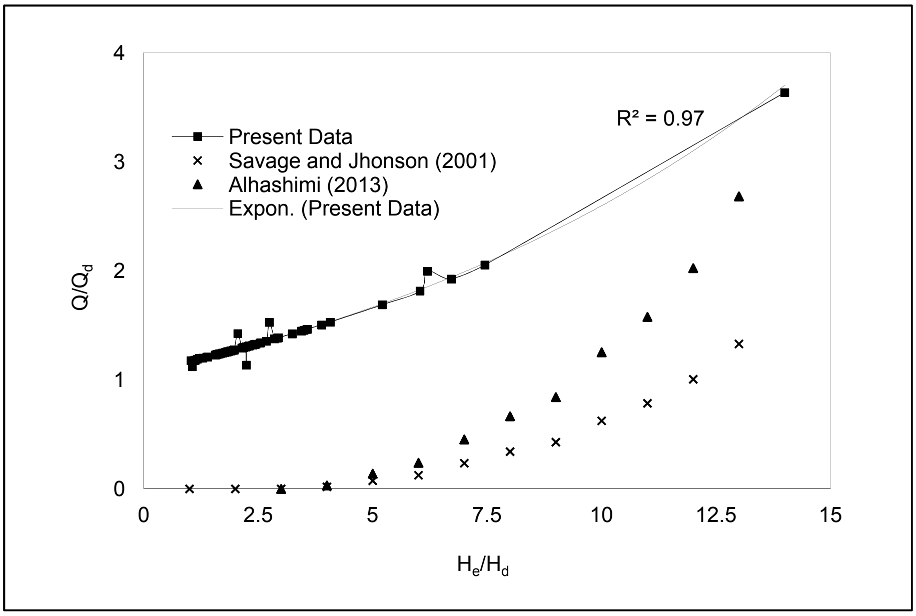

Figure 1. Variation of non-dimensional discharge with effective head ratio.

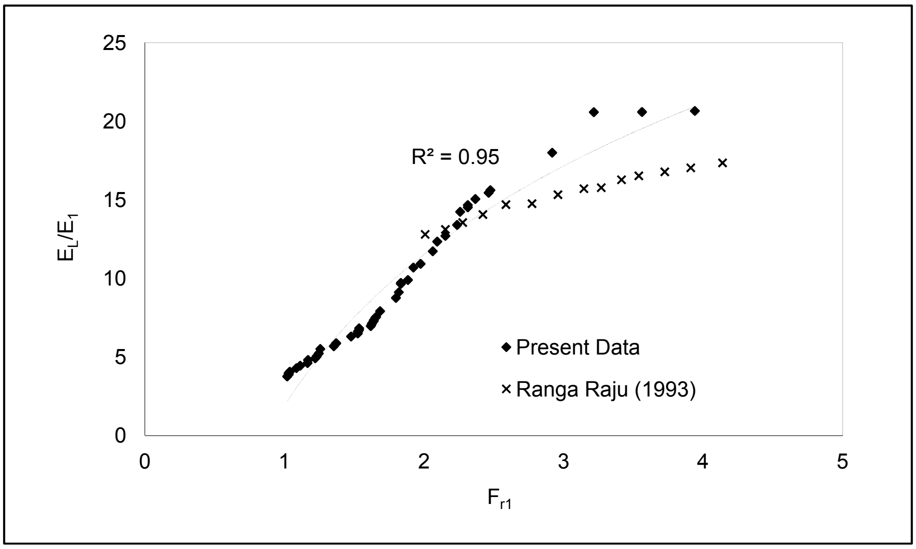

Figure 2. Variation of energy loss ratio with Froude number.

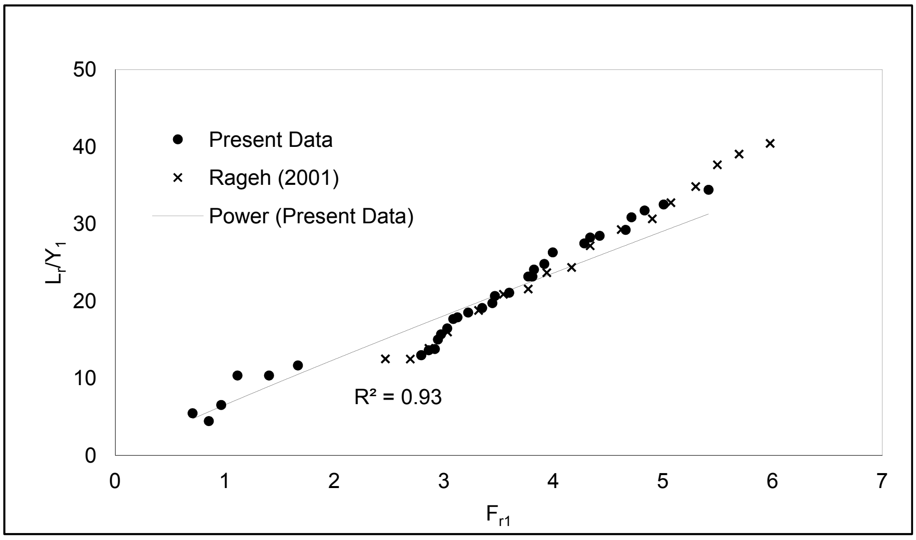

Figure 3. Variation of relative length of roller with Froude number.

5.2 Stepped Spillway

The curves obtained as in Figure 4 shows that the baffles are slightly enhancing the energy dissipation with stepped spillway. The curves are almost same in both the Runs (Run 1 and Run 2) indicating the baffles have not significant effect on energy dissipation for the considered range of critical depth ratio. Few data points are deviating at higher Froude number due to some turbulence and side wave's generation. Results were also compared with the experimental data of Salmasi et al., (2011) and Christodoulou (1993), showing a similar decreasing pattern. The Christodoulou (1993) data shows large deviation in graph due to higher range of critical depth ratio and considered experimental conditions.

Figure 5 shows a similar pattern in all conditions whether it is a stepped spillway model or a combination of stepped spillway and baffles. The curves are almost same in both the Run (Run 1 and Run 2) indicating the baffles have not much effect on critical width ratio. Same is also verified by the study of Salmasi et al., (2011) and Christodoulou (1993) which shows similar increasing pattern, were as deviation is attributed to the same reason as mentioned above.

Figure 6 shows the representation of relative length of roller against Froude number. Results of Ranga Raju (1993), Chow (1973) and Mohan (2008) is also verified with the present data and found to be satisfactory. Other author's data are seen deviating from the best fit line may be due to inaccurate measurement of length of roller as stated by Ranga Raju (1993). It is difficult to locate exactly the roller position during the jump formation. However, the trend in all the cases are similar.

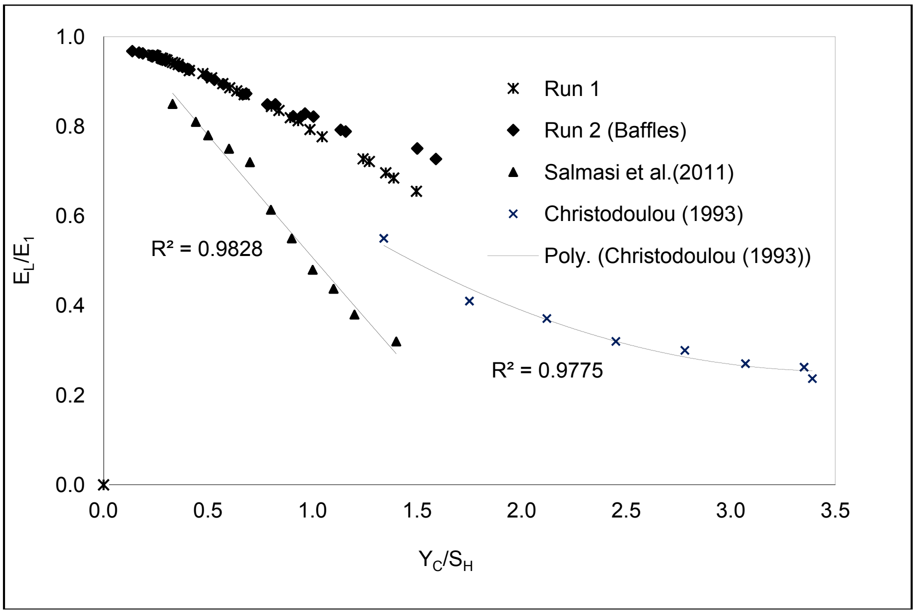

Figure 4. Variation of energy loss ratio with critical depth ratio.

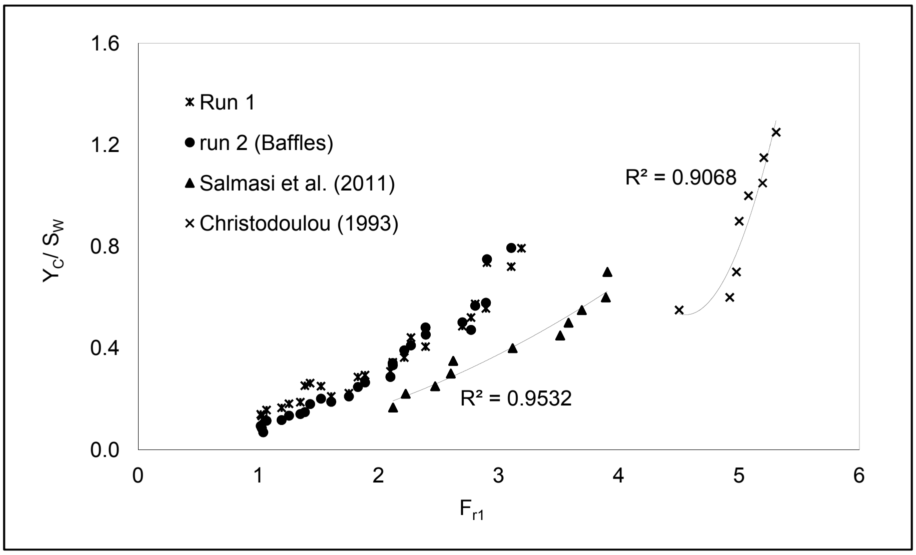

Figure 5. Variation of critical depth ratio with Froude number.

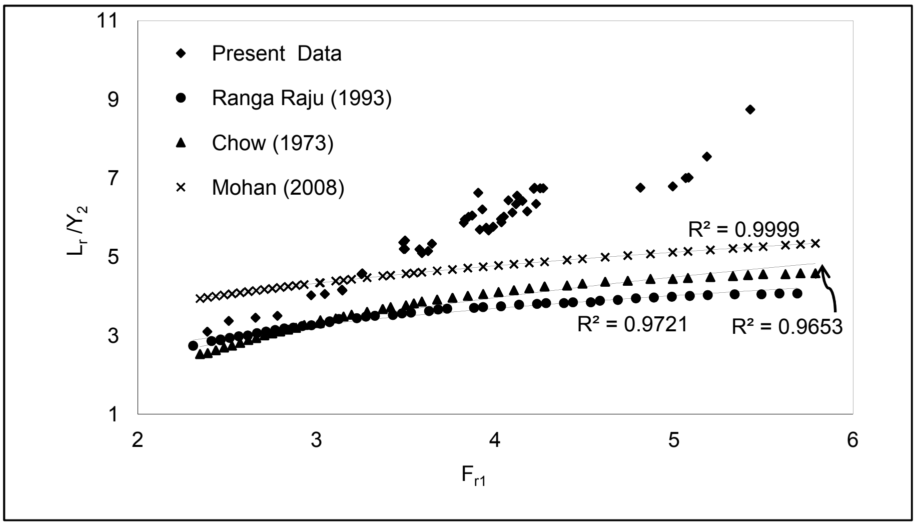

Figure 6. Variation of relative length of roller with Froude number.

6 CONCLUSION

It is observed that non-dimensional discharge shows similar variation against effective head ratio with Savage and Jhonson (2001) and Alhashimi (2013) for their numerical and computational models respectively for ogee spillway; energy dissipation takes place similar to the Ranga Raju's (1993) results; also the relative length of roller shows the similar pattern to Rageh (2001) for ogee spillway. For stepped spillway, effect of baffle blocks can be observed through reduced relative length of roller and increased energy loss; same is also in agreement with Ranga Raju (1993), Chow (1973) and Mohan (2008) results. Salmasi et al., (2011) result for energy loss also depicts satisfactory performance of provided baffle blocks. Model shown by eqn. [2]-[4] for ogee spillway and eqn. [6]-[8] for stepped spillway is therefore used for further application and study.

NOTATIONS

E_1	=	Energy before the jump
E_2	=	Energy after the jump
E_L	=	Energy loss (E_1 - E_2)
E_L/E_1	=	Energy loss ratio
F_{r1}	=	Froude number
H_e	=	Total head
H_d	=	Design head
H_e/H_d	=	Effective head ratio
K_R	=	Relative bed roughness
L_r	=	Length of roller
L_r/Y_1 or L_r/Y_2	=	Relative length of roller
Q	=	Discharge

Q_d	=	Design discharge
Q/ Q_d	=	Non-dimensional discharge
S_w	=	Spillway width
S_H	=	Spillway height
V	=	Velocity of flow
V_1	=	Velocity of flow at section 1
V_2	=	Velocity of flow at section 2
Y_1	=	Depth before jump
Y_2	=	Depth after jump
Y_c	=	Critical depth
Y_c/S_H or Y_c/S_w	=	Critical depth ratio

ACKNOWLEDGEMENTS

Authors would like to thank Hydraulics Laboratory and its staff, Department of Civil Engineering, Jaypee University of Engineering & Technology, Guna (M.P.), India to carry out the experimental work.

REFERENCES

Alhashimi, S.A. (2013). CFD Modeling of Flow over Ogee Spillway by using Different Turbulence Models. *International Journal of Scientific Engineering and Technology Research*, 2(15), 1682-1687.

Bazin, H. (1888). Recent Experiments on the Flow of Water over Weir (Experiences nouvelles sur1'Ecoulement par Deversoir). *Memoires et Documents, Annales des Ponts et Chaussees*, Paris, France, 6(16), 393-448. (in French)

Bhajantri, M.R., Eldho, T.I. & Deolalikar, P.B. (2006). Hydrodynamic Modelling of Fow over a Spillway using a Two-Dimensional Finite Volume-based Numerical Model. *Sadhana*, 31(6), 743–754.

Carlos, A.G. & Chanson, H. (2004). Hydraulic Design of Stepped Spillways and Downstream Energy Dissipators for Embankment Dams. *Dam Engineering*, XVVII, 4, 223-243.

Christodoulou, G.C. (1993). Energy Dissipation on Stepped Spillways. *Journal of Hydraulic Engineering*, 119(5), 644-650.

Chanson, H. (2006). Hydraulics of Skimming Flows on Stepped Chutes: The Effect of Inflow Conditions. *Journal of Hydraulic Research*, IAHR, 44(1), 51-60.

Chanson, H. & Gonzalez, C.A. (2005). An Experimental Study of Free-Surface Aeration on Embankment Stepped Chutes, *PhD thesis.* The University of Queensland, Australia.

Chow, V.T. (1973). *Open Channel Hydraulics*. McGraw- Hill International, New York USA, 525-609.

Das, S., Jahad, U.A., Al-Ameri, R., Lloyd HC. & Chua, H.C.L (2016). Energy Dissipation and Geometry Effects over Stepped Spillways. *International Journal of Civil Engineering and Technology (IJCIET)*, 7(4), 188–198.

Ellayn, A.F. & Sun, Z.L. (2012). Hydraulic Jump Basins with Wedge-Shaped Baffles. *Journal of Zhejiang University SCIENCE A*, 13(7), 519-525.

Habibzadeh, A., Loewen, M.R. & Rajaratnam, N. (2012). Performance of Baffle Blocks in Submerged Hydraulic Jumps. *Journal of Hydraulic Engineering*, 138(10), 902-908.

Horton, R.W. (1907). *Weir Experiments, Coefficients and Formulas*. U.S. Geological Survey Water Supply and Irrigation, Paper 200, Series M, General Hydrographic Investigations, 1-235.

Kim, D.G. & Park, J.H. (2005). Analysis of Flow Structure over Ogee-Spillway in Consideration of Scale and Roughness Effects by Using CFD Model. *KSCE Journal of Civil Engineering*, 9(2), 161-169.

Mohan M., Das (2008). *Open Channel Flow*. *PHI Learning Pvt. Ltd.*, 1-360.

Morales, V., Tokyay, T.E. & Garcia, M. (2012). Numerical Modeling of Ogee Crest Spillway and Tainter Gate Structure of a Diversion Dam on Canar River, Ecuador. *XIX International Conference on Water Resources* CMWR, 19, 1-9.

Murillo, R.E. (2006). Experimental Study of the Development Flow Region on Stepped Chutes, *PhD thesis*. University of Manitoba. Canada.

Nayak, P.C. & Nagesh Kumar, D. (1998). *Stepped Spillway of Jambhira Earth Dam*, Subarnarekha Project Report, Orissa, 295-300.

Rageh, O.S. (2001). Effect of baffle blocks on the performance of radial hydraulic jump. *Fourth International Water Technology Conference IWTC 99*.

Ranga Raju, K.G., Kitaal, M.K., Verma, M.S. & Ganeshan, V.R. (1980). Analysis of Flow over Baffle Blocks and End Sills. *Journal of Hydraulic Research*, 18(3), 227-241.

Ranga Raju, K.G. (1993). Flow through Open Channels. *McGraw-Hill International, New Delhi.*

Rajaratnam, N. (1990). Skimming Flow in Stepped Spillways. *Journal of Hydraulic Engineering*, 116(4), 587-591.

Salmasi, F., Chamani, M.R. & Zadeh, D.F. (2012). Experimental Study of Energy Dissipation over Stepped Gabion Spillways with Low Heights. *Iranian Journal of Science and Technology. Transactions of Civil Engineering*, 36(C2), 253.

Savage, B.M. & Johnson, M.C. (2001). Flow over Ogee Spillway: Physical and Numerical Model Case Study. *Journal of Hydraulic Engineering*, 127(8), 640-649.

Tozzi, M.J. (1994). Residual Energy in Stepped Spillways. *International waterpower & dam construction*, 46(5), 32-34.

Proceedings of the 37th IAHR World Congress
August 13 – 18, 2017, Kuala Lumpur, Malaysia

SCOUR AROUND BRIDGE ABUTMENTS UNDER UNSTEADY FLOWS

JIAN-HAO HONG[1], RAJKUMAR V. RAIKAR[2], ANAND R. DESHMUKH[3] & WEN-DAR GUO[4]

[1, 4] Taiwan Typhoon and Flood Research Institute, Taichung, Taiwan
dinohong@narlabs.org.tw
[2] Department of Civil Engineering, KLE Dr. M. S. Sheshgiri College of Engineering and technology, Belgaum, India,
rvraikar@gmail.com
[3] Department of Civil Engineering, Rajarshi Shahu College of Engineering, Tathwade, India,
anand21desh@gmail.com

ABSTRACT

A semi-empirical model is proposed to compute the time-dependent scour depth at rectangular/vertical wall abutments under unsteady clear-water flow conditions. The parameters used in this model include flow shallowness, flow intensity, sediment coarseness, and time factor. The experiments were conducted only for time-dependent scour depth under unsteady flows at three types of abutments, namely rectangular/vertical wall, semi-circular and trapezoidal/450 wing-wall abutments in uniform sediments under unsteady clear-water conditions. Based on the superimpose concept and the correction of shape factor for different types of abutments, the proposed model is adopted to compute the temporal variations of rectangular/vertical wall, semi-circular and trapezoidal/450 wing-wall abutments scour depth under clear-water with unsteady flow conditions. It was found that the proposed model corresponds well with the data of time-dependent scour depth in uniform sediments obtained from the present experiments (unsteady flows) and reported by different investigators (steady flows).

Keywords: Bridge; abutments; scour; sediment transport; unsteady flows.

1 INTRODUCTION

In the land transportation system, crossing-river bridge is important to connect the people and commodities from each side of rivers. Bridge foundations consisting of bridge piers and abutments are founded into mobile riverbeds, and their interaction with the approach flow and bed materials cause the scour hole around the bridge pier and abutment. The phenomenon of bridge pier and abutment scour and equilibrium scour depth under steady flow conditions have been intensively studied for a long time (Laursen, 1963, Gill, 1972, Sturm and Janjua, 1993, Melville, 1997). The temporal variation of abutment-scour depth has been carried out by Tey (1984), Cardoso and Bettess (1999), Ballio and Oris (2000), Oliveto and Hager (2002), Coleman et al. (2003), Dey and Barnhuiya (2005), and Yanmaz and Kose (2009). Also, the study on time-dependent of pier-scour depth under unsteady flow conditions has been carried out by Kothyari et al. (1992), Briaud et al. (2001), Chang et al. (2004), Oliveto and Hager (2005). However, only limited study of abutment-scour under unsteady flows has been reported.

Therefore, the main objective of the present investigation is aimed to study the evolution of local abutment-scour depth under unsteady clear-water scour conditions. An attempt of this study is to develop a semi-empirical calculation scheme for the temporal variation of abutment-scour depth under unsteady flows at short abutments (rectangular/vertical wall, semi-circular, and trapezoidal/450 wing-wall abutments). Experiments were conducted for time variation of abutment-scour depth in uniform sediments under unsteady flows with clear-water conditions to validate the proposed model.

2 EXPERIMENTAL SETUP AND PROCEDURE

The experiments were conducted in the Department of Civil Engineering at Rajarshi Shahu College of Engineering Pune. The tests were carried out in a glass-sided and stainless steel bottom open-channel tilting flume 8 m long, 0.3 m wide, and 0.3 m deep. The details of the flume are as shown in Figure 1. Three types of Perspex made abutment models, namely rectangular/vertical wall, semi-circular, and trapezoidal/45^0 wing-wall abutment, were employed in the study. The streamwise length (b) and the transverse length (L) of abutments are detailed in Figure 2. Two uniform sediments with median grain size (d_{50}) =0.52 and 0.712 mm were used for the experiments. All the experiments were run under clear-water scour (V/V_c < 1, where V = average approach flow velocity, V_c = critical velocity) with unsteady flow conditions. Three types of hydrographs are having the same base period (t_d = 7 hours) and the same peak flow but different shapes, as shown in Figure 3, were considered in this study. The peak flow occurs at the 3rd, 4th and 5th hour for the Type I, Type II and Type III hydrographs, respectively. Type I has a steep rising limb and flat recession limb while Type III is reverse of Type I. Unsteady uniform flow was developed by regulating the inlet orifice and the tailgate simultaneously, and the desired stepwise hydrographs were attained. In addition, the range of flow intensity (V/V_c) for all runs under each step was maintained between 0.7 and 0.85 so that the flow was always at clear-water condition (V/V_c < 1). Total eighteen experiments were conducted and the details are furnished in Table 1. As listed in Table 1, y = approach flow depth, $d_{sf,\,m}$ and $d_{sf,\,c}$ are the measured and calculated final scour depth after the hydrograph, respectively.

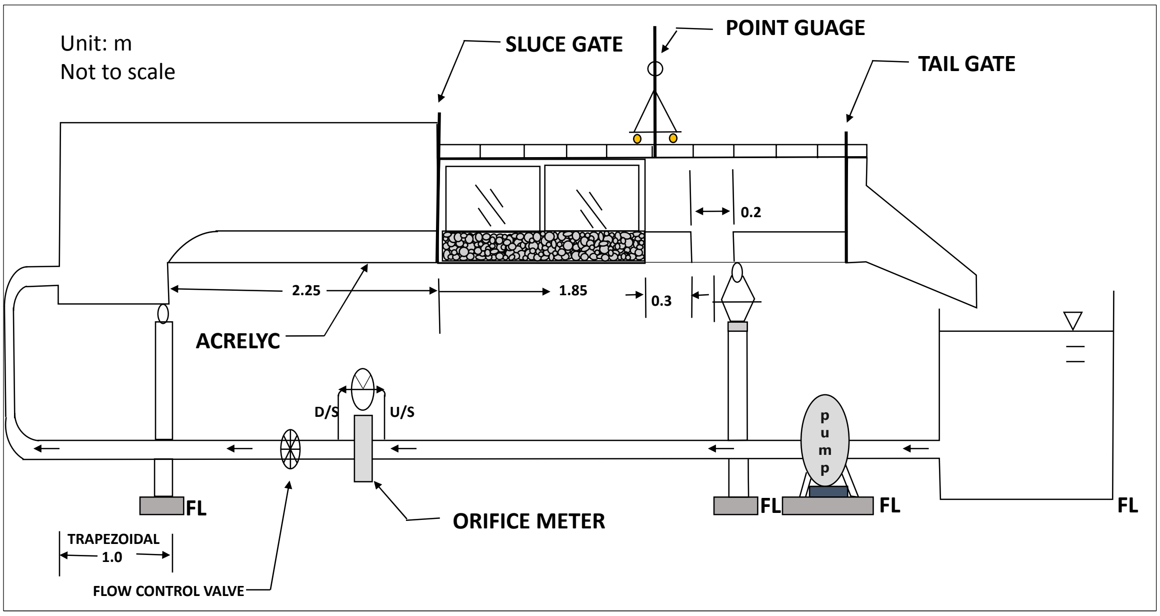

Figure 1. Sketch of experimental flume system.

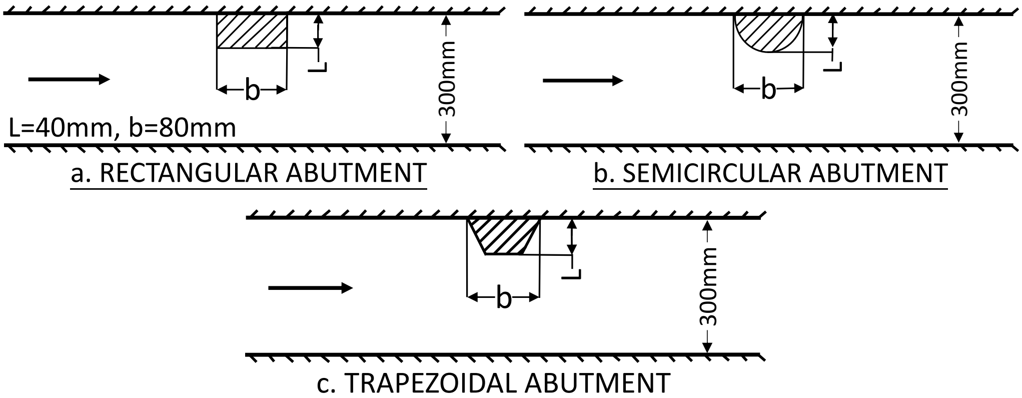

Figure 2. Top view of abutment models.

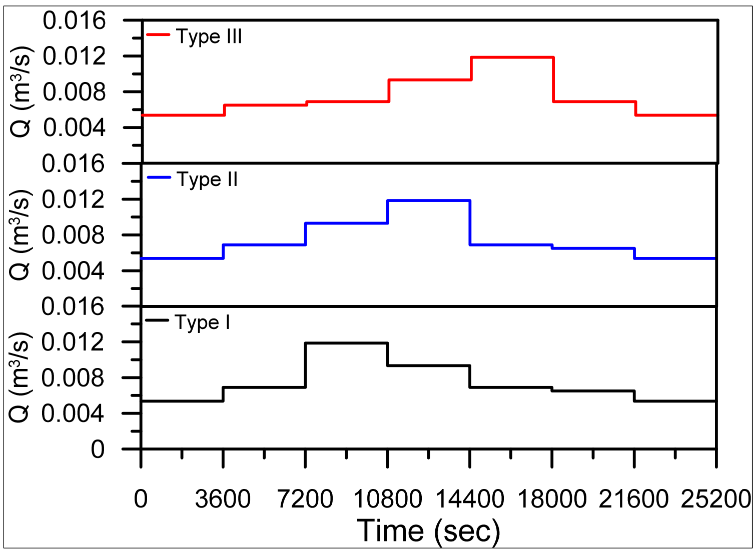

Figure 3. Three types of hydrographs used in this study.

Table 1. Summary of test conditions under clear-water with unsteady flow.

Hydrograph type	Abutment type	d_{50} *(mm)*	V (m/s)	y (m)	Observed $d_{sf,m}$ (m)	Computed $d_{sf,c}$ (m)
Type I	Rectangular	0.520	0.20, 0.19, 0.22	0.09, 0.12, 0.18	0.0265	0.0312
		0.712			0.0240	0.0264
	Semicircular	0.520			0.0210	0.0234
		0.712			0.0210	0.0196
	Trapezoidal	0.520			0.0250	0.0265
		0.712			0.0220	0.0223
Type II	Rectangular	0.520	0.20, 0.19, 0.21, 0.22	0.09, 0.12, 0.15, 0.18	0.0295	0.0332
		0.712			0.0265	0.0278
	Semicircular	0.520			0.0235	0.0249
		0.712			0.0225	0.0209
	Trapezoidal	0.520			0.0270	0.0282
		0.712			0.0245	0.0237
Type III	Rectangular	0.520	0.20, 0.22, 0.19, 0.21, 0.22	0.09, 0.10, 0.12, 0.15, 0.18	0.0295	0.0339
		0.712			0.0265	0.0281
	Semicircular	0.520			0.0235	0.0255
		0.712			0.0220	0.0213
	Trapezoidal	0.520			0.0260	0.0289
		0.712			0.0240	0.0241

3 EVOLUTION OF ABUTMENT-SCOUR DEPTH

The proposed abutment-scour model is similar to that presented pier-scour model by Hong et al. (2014). The data of rectangular/vertical-wall abutment-scour depth under clear-water with steady flow conditions collected from literatures are furnished in Table 2. Uniform sediment particles were used in each study, with sediment coarseness (L/d_{50}) ranging from 26 to 844. Flow intensity (V/V_c) ranges from 0.59 to 0.99, while the flow shallowness ranges (y/L) from 0.07 to 4.0. Based on the parameter analysis, a regression formula is established to compute the abutment-scour depth under steady flow conditions:

$$\frac{d_{st}}{L} = a_0\left(\frac{y}{L}\right)^{a_1}\left(\frac{L}{d_{50}}\right)^{a_2}\left(F_d\right)^{a_3}\left[\log_{10} T_R\right]^{a_4} \qquad [1]$$

where d_{st}= temporal variation of abutment-scour depth, L = transverse length of abutment, y = flow depth, d_{50} = median grain size, F_d = densimetric particle Froude number = $V/(g'd_{50})^{0.5}$, with V = approach velocity, g' = the relative gravitational acceleration = $[(\rho_s-\rho)/\rho]g$, ρ_s = density of sediment particle, ρ = density of fluid, g = gravitational acceleration, T_R = t/t_R = relative time, t = time, t_R = reference time scale = $L_R/[(g'd_{50})^{0.5}]$, L_R = $L^{(2/3)}y^{(1/3)}$ and a_0 to a_4 = regression constants.

A schematic figure for the scour evolution under an unsteady flow condition with the method of superposition is plotted in Figure 4, and the corresponding calculating steps are as follows:

(1) For the first flow discharge (Q_1) of duration t_1, the scour-depth evolution follows the red line (*OA* curve) under the steady flow condition. The final scour depth at t_1 is denoted as d_{s1}.

When the flow discharge increases from Q_1 to Q_2, the scour-depth evolution changes to follow the blue line (*AB* curve) under the steady flow condition, and point *C* is the virtual origin for the scouring process. Because the scouring process can memorize the previous scour depth and because $Q_2 > Q_1$, the time ($t_{*,1}$) required for the scour depth to reach d_{s1} is less than t_1. The corresponding scour-depth evolution from t_1 to t_2 is represented by the *AB* curve. To solve $t_{*,1}$, one can use the intersection point *A* of *OA* curve and *CB* curve, and let $d_{st1}/L=k_1[log_{10}(T_{R1}=t/t_{R1})]^{a_4} = d_{st2}/L= k_2[log_{10}(t_{*,1}/t_{R2})]^{a_4}$, then $t_{*,1}$ can be obtained as

$$t_{*,1} = t_{R2}[t/t_{R1} - 10^{(k_2/k_1)^{(1/a_4)}}].$$

(2) Similar to the computing procedure mentioned in step 2, when the flow rate increases from Q_2 to Q_3 ($>Q_2$), the scour-depth evolution follows the green line under steady flow condition, and point *E* is the virtual origin for the scouring process. Because $Q_3 > Q_2$, the time ($t_{*,2}$) required for the scour depth to reach d_{st2} is less than $t_{*,1} + (t_2 - t_1)$. The corresponding scour-depth evolution from t_2 to t_3 is

shown by the *BD* curve.$t_{*,2}$ can be solved by using the same method as mentioned in step (2),

$$t_{*,2} = t_{R3}[\left(t_{*,1} + t_2 - t_1\right) \Big/ t_{R2} + 10^{(k_2/k_3)^{(1/a_4)}}]$$

(3) Repeat the procedure until all of the subdivisions are completed.
(4) Obtain the temporal variation of scour depth under unsteady flow conditions.

Table 2. Summary of vertical-wall abutment scour under clear-water with steady flow conditions.

Expt. Number	L (cm)	d_{50} (mm)	V/V_c	y (cm)	$d_{sf,m}$ (m)	$d_{sf,c}$ (m)	t_m (min)
KW-1	71.7	0.85	0.936	5	0.231	0.183	6944
KW-2	31.4	0.85	0.936	5	0.157	0.138	3095
KW-3	16.4	0.85	0.936	5	0.084	0.124	4904
KW-4	16.4	0.85	0.864	10	0.171	0.135	1430
CO-1	30	0.82	0.742	20	0.272	0.186	4740
CO-3	30	0.82	0.742	20	0.112	0.172	2277
CO-8	60	0.82	0.599	12	0.140	0.112	3711
CO-14	60	0.82	0.557	20	0.274	0.128	4760
CO-17	60	0.82	0.742	20	0.367	0.223	5571
CO-23	30	0.82	0.848	20	0.266	0.239	4868
CO-25	5	1.02	0.588	20	0.064	0.059	3698
CO-30	5	1.02	0.731	10	0.079	0.076	4096
CO-34	30	0.8	0.949	10	0.270	0.209	5285
CO-37	5	0.85	0.989	20	0.182	0.180	5429
CO-40	5	0.85	0.980	10	0.148	0.125	3713
DB-1	8	0.26	0.950	20	0.127	0.136	6795
DB-2	10	0.26	0.950	20	0.141	0.159	4164
DB-3	10	0.52	0.950	20	0.176	0.147	3542
DB-4	8	0.91	0.950	20	0.170	0.136	4205
DB-5	6	1.86	0.950	20	0.188	0.206	3083
DB-6	8	3.1	0.950	20	0.250	0.256	3976
YK-1	12.5	1.8	0.777	8.9	0.126	0.133	360
YK-2	12.5	1.8	0.777	8.3	0.123	0.128	360
YK-3	12.5	1.8	0.741	7.5	0.118	0.106	360
YK-4	12.5	1.8	0.713	6.8	0.116	0.097	360
YK-5	12.5	1.8	0.682	6.1	0.105	0.084	360
YK-6	12.5	1.8	0.640	5.3	0.074	0.069	360
YK-7	10	1.8	0.777	8.9	0.120	0.125	360
YK-8	10	1.8	0.751	8.3	0.115	0.114	360
YK-9	10	1.8	0.741	7.5	0.110	0.105	360
YK-10	10	1.8	0.713	6.8	0.097	0.092	360
YK-11	10	1.8	0.682	6.1	0.078	0.080	360
YK-12	10	1.8	0.640	5.3	0.050	0.065	360
YK-13	5	1.8	0.777	8.9	0.083	0.089	360
YK-14	5	1.8	0.751	8.3	0.073	0.079	360
YK-15	5	1.8	0.741	7.5	0.062	0.070	360
YK-16	5	1.8	0.713	6.8	0.053	0.060	360
YK-17	12.5	0.9	0.985	5.2	0.095	0.100	360
YK-18	12.5	0.9	0.899	4.4	0.066	0.077	360
YK-19	10	0.9	0.985	5.2	0.089	0.094	360
YK-20	10	0.9	0.899	4.4	0.063	0.073	360
YK-21	5	0.9	0.985	5.2	0.062	0.059	360

Note: References; KW-Kwan(1984), CO-Coleman et al. (2003), DB-Dey and Barbhuiya (2005), YK-Yanmaz and Kose (2009).

Coleman et al. (2003) reported that the flow shallowness (y/L) has the significant effect on the evolution of abutment scour depth, for obtaining the best regression result, the data shown in Table 2 were classified into three groups as: (1) $y/L < 1$, (2) $1 \leq y/L < 2$, and (3) $2 \leq y/L$. The coefficients of Eq. (1) based on the range of flow shallowness are listed in Table 3. In general, the R^2-values for all range of flow shallowness are very good.

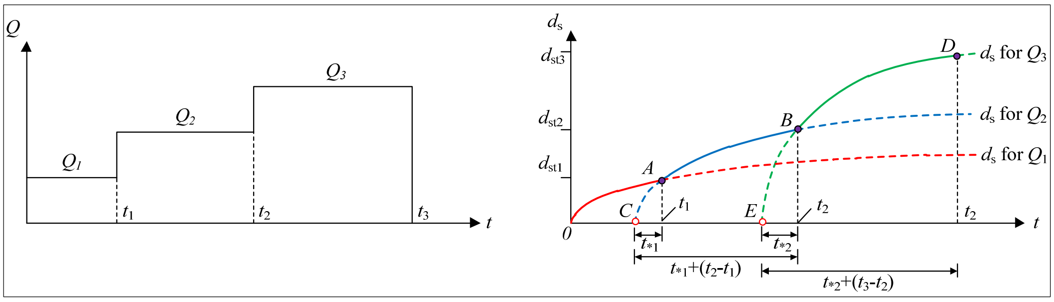

Figure 4. Method of superposition for computing the abutment-scour evolution under a stepwise hydrograph.

Table 3. Summary of coefficients used in Eq. [1].

Coefficients	$y/L \le 1$	$1 < y/L \le 2$	$2 < y/L$
a_0	0.209	0.100	0.022
a_1	0.263	0.424	0.700
a_2	-0.427	-0.523	-0.469
a_3	1.857	2.168	2.274
a_4	1.269	1.594	1.938
R-square	0.892	0.916	0.935

4 RESULTS

4.1 Comparison using data of steady flow

Figures 5-8 compare the experimental data of Kwan (1984), Coleman et al. (2003), Dey and Barbhuiya (2005), and Yanmaz and Kose (2009), respectively. The data were collected to include a wide range of approach flow depths, approach flow intensities, abutment length (only rectangular/vertical-wall abutment), and sediment sizes. The computed normalized temporal variations of abutment-scour depths (d_{st}/L) with (t/t_m) were plotted along with the corresponding measured normalized abutment-scour depths for comparison. In general, the agreement is not as good with the data of Kwan (1984). However, a good agreement was found between the observed and computed abutment-scour depths using the proposed model for the data of other investigators. In addition, in the initial period of scouring process (t/t_m < 0.05), the proposed model gives very good agreements with the experimental data. This result is very useful for the calculation of scour depth under unsteady flow conditions. In general, for a certain unsteady flow, each flow discharge would not persist for a long period. If one would like to apply the concept of superposition method (see section 3), a good prediction for the initial period of scouring process is very important. Figure 9 compares the final abutment-scour depth under clear-water with steady flow conditions between the measured data and the calculated results using the proposed model. The dotted lines show the ± 25 % error boundaries, while the solid diagonal line shows the line of perfect agreement. For the data of Coleman et al. (2000), the proposed model underestimates the final scour depth ($d_{sf,m}/L$ < 1). However, for the data of Yanmaz and Kose (2009), the proposed model gives a comparatively good agreement as compared to the other data. In general, the proposed model fits well to the measured final scour depths. Hence, the accuracy of calculated result by the proposed model is considered to be reasonably good.

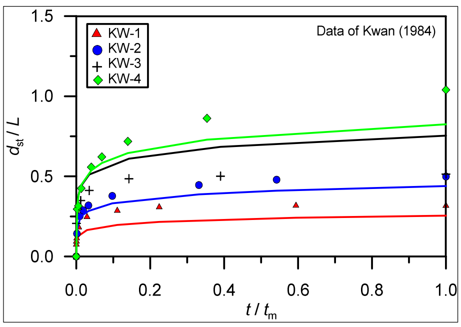

Figure 5. Comparison of temporal variation of scour depth between the proposed model and the experimental data of Kwan (1984).

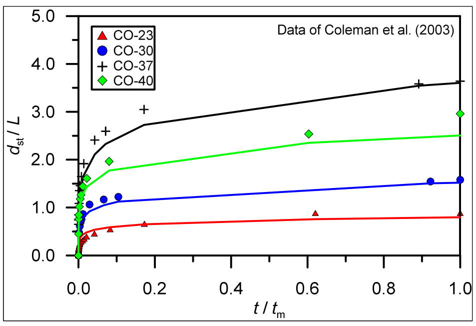

Figure 6. Comparison of temporal variation of scour depth between the proposed model and the experimental data of Coleman et al. (2003).

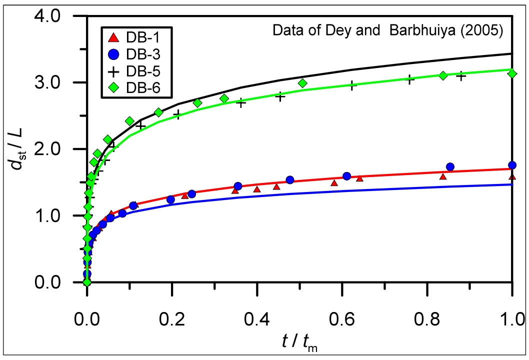

Figure 7. Comparison of temporal variation of scour depth between the proposed model and the experimental data of Dey and Barbhuiya (2005).

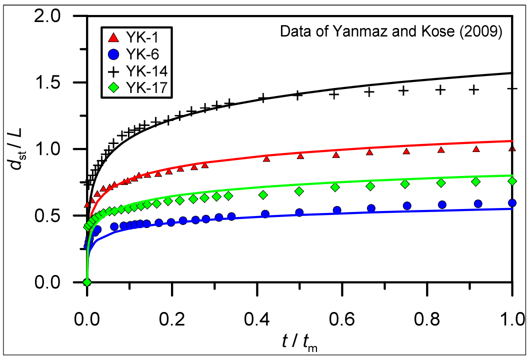

Figure 8. Comparison of temporal variation of scour depth between the proposed model and the experimental data of Yanmaz and Kose (2009).

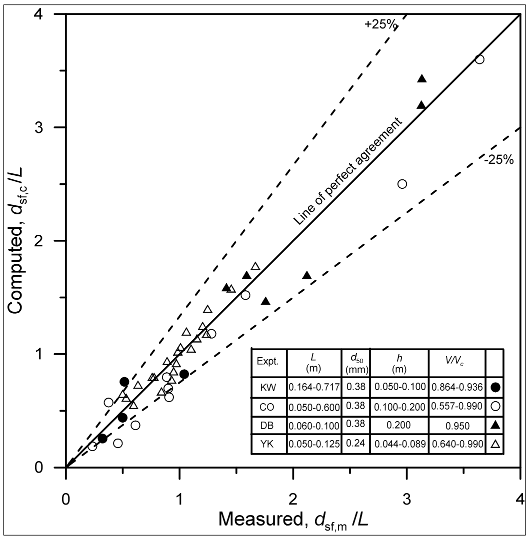

Figure 9. Comparison of final scour depth between the proposed model and the experimental data of KW (Kwan, 1984), CO (Coleman et al., 2003), DB (Dey and Barbhuiya, 2005), and YK (Yanmaz and Kose, 2009).

The shape of an abutment plays an important role on the equilibrium scour depth (Melville and Coleman, 2000; Barbhuiya and Dey, 2004). For streamline abutments, such as semi-circular and 45^0 wing-wall abutments, induce weak vortices; while blunt bodies, such as vertical-wall abutment, generate strong vortices causing deeper scour depth, according to the experimental data of Laursen and Toch (1956), Liu et al. (1961), Garde et al. (1961), and Wong (1982). Melville and Coleman (2000) used shape factor to account for the effect of the shape of abutments on equilibrium scour depth. The vertical-wall is the simplest shape of an abutment and used as reference (shape factor = 1). Melville and Coleman (2000) gave the suggested shape factors for 45^0 wing-wall and other type of abutments (shape factors ranges from 0.45 - 0.75). However, the shape factor for different types of abutments on the temporal variation of scour depth has not been discussed.

Figures 10-13 compare the experimental data of Ballio and Oris (2000), Dey and Barbhuiya (2005) and Tey (1984), respectively. The data includes the temporal variations of scour depths at vertical-wall (rectangular), semicircular, and 45^0 wing-wall abutments. The data were not included in the regression analysis, as discussed in previous discussion.

The coefficients used in Eq. [1], listed in Table 3 were not changed, except for trapezoidal and semicircular abutments. For trapezoidal abutment (45^0 wing-wall abutment), the coefficient $a_{o,\ rec}$ is adjusted as $a_{0,\ trap} = 0.85a_{o,\ rec}$, while for semicircular abutment, the coefficient $a_{o,\ semi}$ is adjusted as $a_{0,\ semi} = 0.75a_{o,\ rec}$.This is similar to the result as reported by Melville and Coleman (2000) and Dey and Barbhuiya (2005). For the same transverse, abutment length (L) approaches flow (y, V) and bed sediment (d_{50}) conditions, the abutment scour depth in sequential order is $d_{s,rec} > d_{s,trap} > d_{s,semi}$, this result is the same as Melville and Coleman (2000). It is because the abutment scour depth is mainly depended on shape of the abutment. As shown in Figures 10-13, in general, the comparison shows a good agreement between computed and experimental data. The accuracy of the calculated result is reasonably good. The proposed model for the temporal variation of abutment-scour depth under clear-water with steady flow conditions thus allow a wide range of flow intensity, flow shallowness, sediment coarseness, and abutment dimensions related to the evolution of abutment scour. In the next section, for the comparison of abutment scour depth under unsteady flows, the coefficients were kept the same as previous mentioned, details will also be discussed.

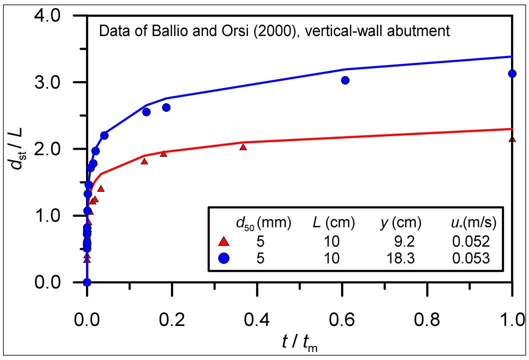

Figure 10. Comparison of scour evolution at a vertical-wall abutment between the proposed model and the experimental data of Ballio and Oris (2000).

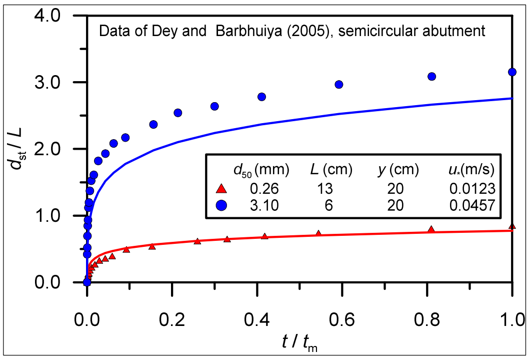

Figure 11. Comparison of scour evolution at a semicircular abutment between the proposed model and the experimental data of Dey and Barbhuiya (2005).

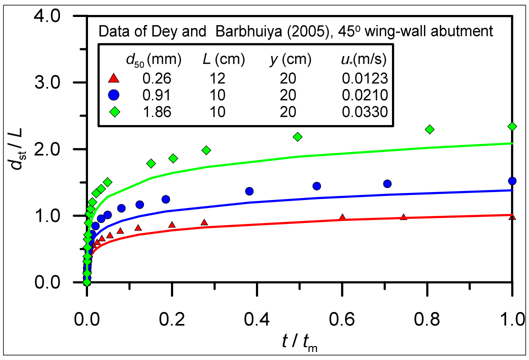

Figure 12. Comparison of scour evolution at a 45^0 wing-wall abutment between the proposed model and the experimental data of Dey and Barbhuiya (2005).

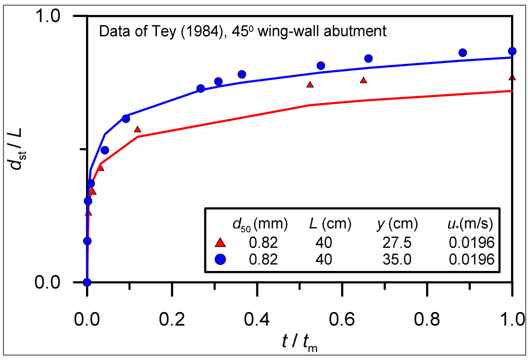

Figure 13. Comparison of scour evolution at a 45^0 wing-wall abutment between the proposed model and the experimental data of Tey (1984).

4.2 Comparison using data of unsteady flow

From the observation of the unsteady flow experiments, it was found that the abutment-scour depth increases steadily during the rising limb of the hydrograph, and reaches the maximum at peak flow and then remains unchanged during the recession period. Furthermore, for the same hydraulic and sediment properties, the abutment-scour depth varies with the shape of abutment. The magnitude of the abutment-scour depth is in the order of vertical-wall (rectangular) abutment, 45^0 wing-wall (trapezoidal) abutment, and semicircular abutment, as shown in Figure 14.The experimental results really make sense. The blunt obstruction produces feeble-strength vortices, causing shallow scour depth as compared with the scour depth caused by the vortices induced by sharp-wall obstacles.

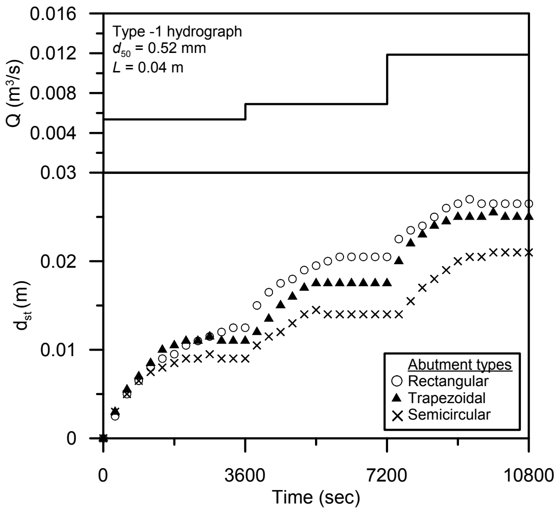

Figure 14. Comparison of the scour evolution for different shape of abutment under Type I stepwise hydrograph.

  / ISSN 1562-6865 (Online) - ISSN 1063-7710 (Print)

The simulations of abutment-scour evolution under stepwise hydrographs are carried out using the method described in section 3. The computed results are shown in Figures 15-17 for Type-I, Type-II, and Type-III hydrographs, respectively, together with the experimental data. For each type of hydrograph, three types of abutments, namely vertical-wall (rectangular), semi-circular, and 45^0 wing-wall (trapezoidal) abutments are used. As seen from these figures, reasonably good agreements between the computed results and the experimental data indicate that the proposed method can be applied to the calculation of abutment scour under unsteady flows. For the practical purpose, the final scour depth for a given hydrograph is also important. Figure 18 shows the comparison between the computed and measured final scour depth for different type of hydrographs, indicating acceptable agreement of the proposed model results with the experimental data. All computed final scour depths under unsteady flows fall within $\pm$ 25 % error boundaries. Hence, the proposed model can predict the abutment scour depth remarkably well under unsteady clear-water flow conditions.

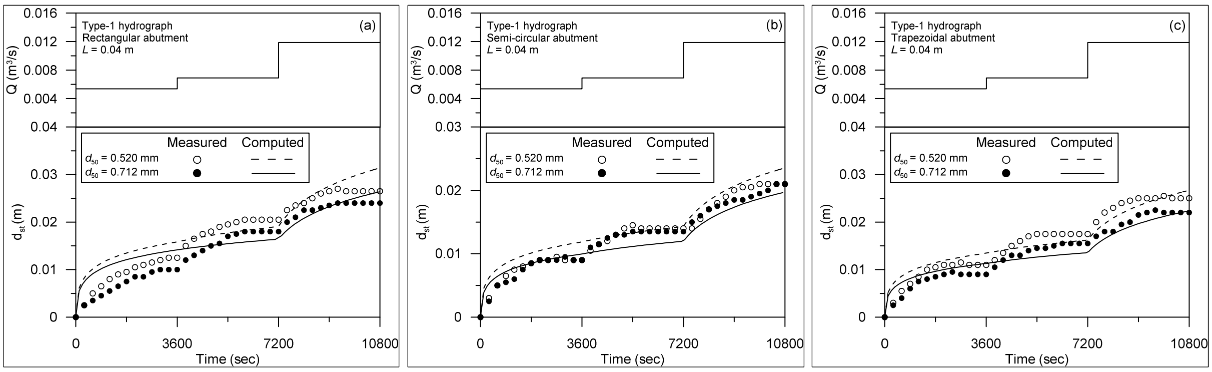

Figure 15. Comparison of computed and measured abutment-scour evolution under Type-I stepwise hydrograph.

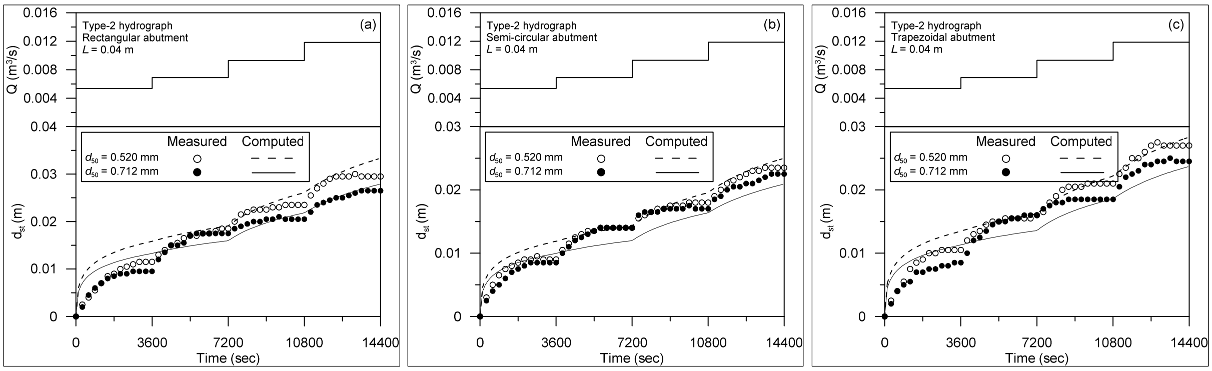

Figure 16. Comparison of computed and measured abutment-scour evolution under Type-II stepwise hydrograph.

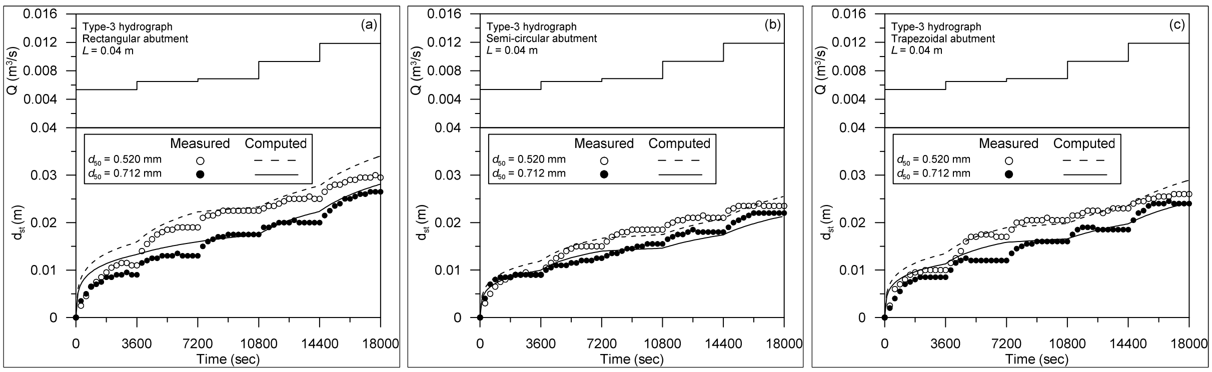

Figure 17. Comparison of computed and measured abutment-scour evolution under Type-III stepwise hydrograph.

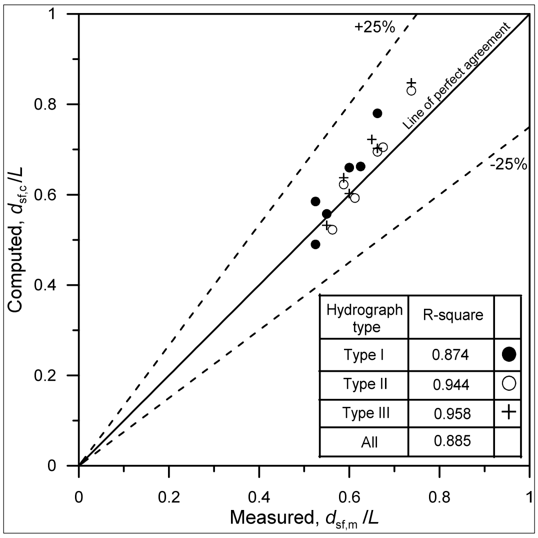

Figure 18. Comparison of final scour depth under unsteady flow conditions between the proposed model and the present-experimental data.

5 CONCLUSIONS

A semi-empirical model was proposed for estimating the temporal variation of abutment scour at three types of abutments, namely rectangular/vertical wall, semi-circular and trapezoidal/450 wing-wall abutments in uniform sediments under clear-water conditions with steady and unsteady flows. The development of proposed model only uses the data of rectangular/vertical wall abutment scour under steady flow conditions. After adopting the shape correction factor, the proposed model on the time-dependent scour depth can be employed to semi-circular and trapezoidal/450 wing-wall abutments. Furthermore, on the basis of the superimpose concept, the proposed model was applied to compute the temporal variation of abutment scour depth at three types of abutments under unsteady flows. The comparisons between the experimental data and the calculated results are reasonably acceptable. It was demonstrated that the proposed model is accurate, practical and suitable for computing time-dependent scour depth at rectangular/vertical wall abutments and thus may be used in the bridge closure for practical purpose.

ACKNOWLEDGMENTS

The financial support from the Ministry of Science and Technology, Taiwan, under Grants MOST 105-2625-M-492-014 and All India Council for Technical Education (AICTE), New Delhi, India are highly appreciated.

REFERENCES

Ballio, F. & Oris, E. (2000). Time Evolution of Scour around Bridge Abutments. *Water Engineering Research,* 2(4), 243-259.

Barbhuiya, A.K. & Dey, S. (2004). Local Scour at Abutments: A Review. *Sadhana*, 29(5), 449-476.

Briaud, J.L., Chen, H.C., Kwak, K.W., Han, S.W. & Ting, F.C.K. (2001). Mutiflood and Multilayer Method for Scour Rate Prediction at Bridge Piers. *Journal of Geotechnical and Geoenvironmental Engineering,* 127(2), 114-125.

Cardoso, A.H. & Bettess, R. (1999). Effects of Time and Channel Geometry on Scour at Bridge Abutments. *Journal of Hydraulics Engineering*, A.S.C.E., 125(4), 388-399.

Chang, W.Y., Lai, J.S. & Yen, C.L. (2004). Evolution of Scour Depth at Circular Bridge Piers. *Journal of Hydraulics Engineering,* A.S.C.E., 130(9), 905-913.

Coleman S.E., Lauchlan C.S. & Melville B.W. (2003).Clear-Water Scour Development at Bridge Abutments. *Journal of Hydraulics Research,* 41(5), 521-531.

Dey, S. & Barbhuiya, A.K. (2005). Time Variation of Scour at Abutments. *Journal of Hydraulics Engineering,* A.S.C.E., 131(1), 11-23.

Garde, R.J., Subramanya, K. & Nambudripad, K.D. (1961). Closure of 'Study of Scour around Spur-Dikes'. *Journal of Hydraulic Div.*, A.S.C.E., 98, 1587-602.

Gill, M.A. (1972). Erosion of Sand Beds around Spur Dikes. *Journal of Hydraulics Div.,* A.S.C.E., 98(9), 1587-1602.

Hong, J.H., Chiew, Y.M. & Yeh, P.H. (2014.) Comparisons of Time-Dependent Pier-Scour Models under Unsteady Flow Conditions, *7th International Conference on Scour and Erosion*, Perth, Australia, 473-481.

Laursen, E.M. (1963). Analysis of Relief Bridge Scour. *Journal of Hydraulics Div*., A.S.C.E., 89(3), 93-118.

Laursen, E.M. & Toch, A. (1956). *Scour around Bridge Piers and Abutments,* Iowa Highways Research Board, 4.
Liu, S.Y., Chang, F.M. & Skinner, M.M. (1961). *Effect of Bridge Construction on Scour and Backwater,* CER 60 HKL 22, Colorado State University, Civil Engineering Section, Fort Collins, Colorado.
Kothyari, U.C., Garde, R.J. & Ranga Raju, K.G. (1992). Temporal Variation of Scour around Circular Bridge Piers. *Journal of Hydraulics Engineering,* 118(8), 1091-1106.
Kwan, T.F. (1984). *Study of Abutment Scour,* Report No. 328, School of Engineering, The University of Auckland, New Zealand.
Melville, B.W. (1997). Pier and Abutment Scour - An Integrated Approach. *Journal of Hydraulic Engineering,* A. S. C. E., 123(2), 125-136.
Melville, B.W. & Coleman, S.E. (2000). *Bridge Scour.* Water Resources Publication, LLC. Colorado, U.S.A., 550.
Oliveto, G. & Hager, W.H. (2002). Temporal Evolution of Clear Water Pier and Abutment Scour. *Journal of Hydraulics Engineering*, A.S.C.E., 128(9), 811-820.
Oliveto, G. & Hager, W.H. (2005). Further Results to Time-Dependent Local Scour at Bridge Elements. *Journal of Hydraulics Eng*ineering, A.S.C.E., 131(2), 97-105.
Sturm, T.W. & Janjua, N.S. (1993). Bridge Abutment Scour in a Flood Plain. *Proceeding of National Conference on Hydraulic Engineering*, A.S.C.E., San Francisco, California, U.S.A., 767-772.
Tey, C.B. (1984). *Local Scour at Bridge Abutments,* Report No. 329, School Of Engineering, University of Auckland, New Zealand.
Yanmaz, A.M. & Kose, O. (2009). A Semi-Empirical Model for Clear-Water Scour Evolution at Bridge Abutments. *Journal of Hydraulic Res*earch, 47(1), 110-118.
Wong, W.H. (1982). *Scour at Bridge Abutments,* Report No. 275, School Of Engineering, University Of Auckland, New Zealand.

NUMERICAL INVESTIGATION OF STEP DIMENSIONS IMPACT OVER GABION STEPPED SPILLWAYS

ALI ADEL ZUHAIRA [(1)], HARSHINIE KARUNARATHNA[(2)] & DOMINIC E. REEVE[(3)]

[(1, 2 3)] Energy & Environment Research Group, College of Engineering, Swansea University, Swansea, United Kingdom
e-mail:801288@swansea.ac.uk; h.u.karunarathna@swansea.ac.uk; d.e.reeve@swansea.ac.uk

ABSTRACT

Energy dissipation is one of the most important issues in spillway design as the downstream water flow can be highly energetic, which may lead to the creation of a scour hole in the downstream region. As a means of dissipating energy, stepped spillways can be used. The presence of steps can generate greater flow turbulence dissipating more energy than other types of spillway such as ogee spillways. Gabion stepped spillways are one type of stepped spillway which can offer low construction costs, flexibility, porosity and noise reduction. A 2D numerical model, NEWFLUME, is implemented in this study to simulate flow over different types of gabion spillways. The model is an open source code that solves the Reynolds-Averaged Navier-Stokes equations using a Volume of Fluid technique. A validation of the model is conducted against the experimental data, and good agreement has been found. The model is then set up to investigate a wider range of spillway conditions. Flows over gabion spillways with three different step heights (0.06m, 0.09m and 0.12m) and three different slopes for each step size (1V:2H, 1V:2.5H and 1V:3H) are investigated. All spillway types are tested with same initial conditions to evaluate the energy dissipation over the gabion steps. The initial results showed that energy dissipation varies with spillway slope and this quantity will play a vital role in the effective design of gabion stepped spillways.

Keywords: Stepped spillways; gabion; energy dissipation; numerical simulation.

1 INTRODUCTION

Spillways are the structures located in dams to release any excess water during rainy seasons. During the last few decades, there has been a noticeable increase in flooding frequency around the world. Andre (2004) claimed that about 40% of embankment dams around the world, not including China, with heights less than 30 m are damaged due to overtopping. Therefore, it is crucial to reduce the impact of flooding on dam safety and releasing flood waters via spillways is one way to achieve this. Spillways must be designed to be able to discharge the excess water which accumulates during the flooding season (Kositgittiwong, 2012). Many existing embankment dams experience overtopping because they were built at a time when computational modelling and measuring techniques of hydrological data were limited (Andre, 2004). Moreover, changes in land use and rainfall patterns have altered catchment hydrology.

A gabion is a basket that may be filled with gravel, cobbles, stones or rocks depending on the purpose of construction. Gabions have been used in China and Egypt since the middle of the 1800s, if not before. Gabions have been used for various purposes such as river bed protection, bank stabilization and retaining walls. Depending on the water discharge, three types of flow can occur over a gabion stepped spillway: nappe flow when the discharge of water is low; skimming flow when the discharge is high; and transition flow which might be observed when the discharge is between the nappe flow and skimming flow (Chanson, 1994). The nappe flow regime can be recognized by three features: firstly, free falling nappe at each step (series of free falling flows); secondly, air bubbles can appear in the pool step when the water are recirculating (Andre, 2004); finally, a partial or full hydraulic jump may be noticed in some cases at the downstream of the impacting point of the jet on each step. The free surface appearance of transition flow is different from the skimming flow and nappe flow because the water splashing is greater than the step height by 3-8 times and that could be clearly seen at the downstream of the inception point (Andre, 2004). Skimming flow can be identified when the water flows down over stepped spillway and all of the cavities are filled with water. Thus, the water flow looks like a coherent stream above the pseudo-bottom (a line formed by hitting the external edge of the steps). There are two flow regimes over the gabion stepped spillways; the first regime is called the non-aerated regime where cavitation damage might be observed because of the absence of air entrainment. The second regime is called the aerated regime, where the air entrainment can be observed, (Andre, 2004; Chanson, 1994), and the potential for cavitation damage is greatly reduced.

2 BACKGROUND

Many studies have been conducted to investigate the energy dissipation over stepped spillways; some of these studies were done experimentally through the construction of physical models of stepped spillways such as Sorensen (1985), Chanson (1994), Boes (1999), Matos (2000), Fratino and Piccinni (2000), Chanson (2002), Andre (2004), Barani et al. (2005) and Hunt and Kadavy (2010). Different instruments to measure the velocity have been used in those studies. It is important to mention that all of them were conducted without gabions; however, some of these studies were under nappe flow conditions and some of them under skimming flow conditions. Important conclusions arising from these studies include:

- Energy dissipation is dependent on the chute length and type of flow; for instance, the amount of energy dissipation under nappe flow conditions for a short chute is greater than for skimming flow, whereas a long chute can dissipate more energy under skimming flow conditions;
- Increasing the discharge for a certain configuration will decrease the energy dissipation;
- The number of steps, step height and spillway slope can affect the energy dissipation.

Many numerical studies have been conducted on the energy dissipation over stepped spillways such as Tabbara et al. (2005) who studied the energy dissipation by using ADINAA software which uses finite element technique to discretise the equation and a K-ε turbulence sub-model. Abbasi and Kamanbedast (2012) produced a new numerical model which is based on the turbulent Navier-Stokes equation to investigate the sensitivity of the step dimension on the energy dissipation. They solved the governing equation using the Finite Volume method (3D) and a k-ε turbulence sub-model on a structured grid with a volume of fluid technique (VOF) to capture the free surface.

Regarding gabion stepped spillways (Figure 1), published results have all been conducted experimentally. For example, Stephenson (1979) performed a study on the energy dissipation over stepped gabion of two to four steps with four different slopes 1/1, 1/2, 1/3 and 2/3. Peyras et al. (1992) conducted an experimental study to investigate the energy dissipation over stepped gabion weirs. Kells (1994) studied experimentally the energy dissipation over a stepped gabion weir when the critical depth of the discharge is increasing or decreasing over the crest. Shafai-Bajestan and Kazemi-Nasaban (2011) investigated the energy dissipation over gabion stepped spillways and its influence on the dimensions of the scour hole at the end of spillway. Wüthrich and Chanson (2014) carried out a laboratory study to investigate the characteristics of flow and Zhang and Chanson (2014) reported on results of a study of the effect of air entrainment on gabion stepped spillways.

In contrast to the case of stepped spillways, there is a dearth of numerical studies of flow over porous gabion stepped spillways. As such there is little scientific understanding of the effect of gabion step dimensions and the presence of porous media on energy dissipation; and this provides the motivation for this paper.

Figure 1. Gabion stepped weir at Robina (Wüthrich and Chanson, 2014).

3 NUMERICAL MODEL

As the flow in this study contains elements that are sub-critical, supercritical and highly turbulent, a code that solves the Reynolds-Averaged Navier-Stokes equations with a turbulence sub-model was selected. The NEWFLUME code, (Lin & Xu, 2006), is used because it solves the Reynolds-averaged Navier-Stokes equations in two dimensions, (2DV), on a fixed grid employing a volume of fluid method to capture the free surface. The model also permits areas of porous media to be defined and solves the appropriate flow equations in these areas. The reader is referred to Lin & Liu, (1998a) and Lin & Xu, (2006) for further details of the numerical implementation. The Reynolds equations for an incompressible fluid are used as the governing equation of the mean motion of a turbulent flow (Lin and Xu, 2006):

$$\frac{\partial\langle u_i\rangle}{\partial x_i}=0 \qquad [1]$$

$$\frac{\partial\langle u_i\rangle}{\partial t}+\langle u_j\rangle\frac{\partial\langle u_i\rangle}{\partial x_j}=-\frac{1}{\rho}\frac{\partial\langle p\rangle}{\partial x_i}+g_i+\frac{1}{\rho}\frac{\partial}{\partial x_j}\left(\mu\frac{\partial\langle u_i\rangle}{\partial x_j}-\rho\langle\tilde{u}_i\tilde{u}_j\rangle\right) \qquad [2]$$

where,
$\langle u_i\rangle$ the mean velocity in the i directions (ms^{-1})
$\langle P\rangle$ mean pressure (KNm^{-2})
$\boldsymbol{\rho}$ fluid density (Kgm^{-3})
g_i gravitational acceleration in the i direction (ms^{-2})
$\boldsymbol{\mu}$ molecular viscosity (m^2s^{-1})
$\langle\tilde{u}_i\tilde{u}_j\rangle$ Reynolds stress (KNm^{-2})

Reynolds stress has been calculated by using a nonlinear viscosity model. This model uses mean velocity, turbulence kinematic energy (k) and dissipation rate of turbulence (ε). The k- ε transport equation is used to calculate the last two parameters k and ε, (Lin and Xu, 2006), as follows:

$$\frac{\partial k}{\partial t}+\langle u_j\rangle\frac{\partial k}{\partial x_j}=\frac{\partial}{\partial x_j}\left[\left(\frac{v_t}{\sigma_k}+v\right)\frac{\partial k}{\partial x_j}\right]-\langle\tilde{u}_i\tilde{u}_j\rangle\frac{\partial\langle u_i\rangle}{\partial x_j}-\varepsilon\frac{\partial\varepsilon}{\partial t}+\langle u_j\rangle\frac{\partial\varepsilon}{\partial x_j} \qquad [3]$$

$$\frac{\partial\varepsilon}{\partial t}+\langle u_j\rangle\frac{\partial\varepsilon}{\partial x_j}=\frac{\partial}{\partial x_j}\left[\left(\frac{v_t}{\sigma_\varepsilon}+v\right)\frac{\partial\varepsilon}{\partial x_j}\right]-c_{1\varepsilon}\frac{\varepsilon}{k}\langle\tilde{u}_i\tilde{u}_j\rangle\frac{\partial\langle u_i\rangle}{\partial x_j}-c_{2\varepsilon}\frac{\varepsilon^2}{k} \qquad [4]$$

where,
σ_k, σ_ε,$c_{1\varepsilon}$ and $c_{2\varepsilon}$ are empirical coefficients (unitless)
v_t and $v=\frac{c_d{*}\,k^2}{\varepsilon}$ are kinematic and eddy viscosity m^2s^{-1}
and c_d is a coefficient.

For free surface tracking, the NEWFLUME model uses the volume of fluid method. The VOF equation for incompressible flow is

$$\frac{\partial F}{\partial t}+\langle u_j\rangle\frac{\partial F}{\partial x_j}=0 \qquad [5]$$

where,
F is volume of fluid function and refers to the fraction fluid in the cell. For instance,
F=1 means that the cell is completely full,
F=0 means that the cell is empty,
F between 1 and 0 means that the fluid surface lies within the cell.

The mean flow in porous media is governed by

$$\frac{\partial\overline{u}_i}{\partial x_i}=0 \qquad [6]$$

$$\frac{1+c_A}{n}\frac{\partial\overline{u}_i}{\partial t}+\frac{\overline{u}_j}{n^2}\frac{\partial\overline{u}_i}{\partial x_j}=-\frac{1}{\rho}\frac{\partial\overline{p}_i}{\partial x_i}+g_i+\frac{\upsilon}{n}\frac{\partial^2\overline{u}_i}{\partial x_j\partial x_i}-ga_p\overline{u}_i-gb_p\sqrt{\overline{u}_k\overline{u}_k}\,\overline{u}_i \qquad [7]$$

where,
n porosity of the porous medium,
C_A, a_p and b_p are coefficients of the porous medium, and the subscript K refers to the summation of velocities in two directions.

4 VALIDATION

Since the main purpose of this work is to simulate flow over gabion stepped spillways, numerical model validation was conducted against the experimental work of Wüthrich and Chanson (2014). Their test section consists of a broad crested weir with length 1.01m and height 1.0m, followed by ten identical impervious steps with height 0.1m and length 0.2m. Gabion steps were installed over the impervious steps, which are made from marine plywood, with 0.1m height and 0.3m length. The gravel inside the gabions had a D_{50} of 0.01m. The porosity ranged from 0.35 to 0.4.

The same experimental details were established in the numerical model and the mesh size was set to 0.01m and 0.005m in the x-direction and y-direction respectively. The depth of the initial water was set to 1.4 m in order to achieve the required discharge. The discharge has been calculated by determining the critical section over the broad crested weir from an estimation of the Froude number. To ensure numerical stability, the initial time step was set to 0.001s and the total time for the simulation was 24s. As in the experimental works, all of the boundaries were closed except the right boundary which was open. Finally, the porosity of the gravel particles was fixed to 0.375 representing the average value used in the experimental study.

The fluid was initially at rest. The barrier at x = 9m was removed instantaneously and the resulting flow computed. The time needed to achieve the skimming flow was 2.848s (Figure 2). Four different discharges were used for comparison. The discharge value was calculated by multiplying the water depth at the critical section over the broad crested weir by the velocity at that point, (Chow, 1959). To determine the critical section, the Froude Number was calculated and it should be equal to 1 at the critical section. The Froude Number is defined as:

$$Fr = \frac{V}{\sqrt{g * Y}} \qquad [8]$$

where,
V: velocity (ms^{-1})
Y: water depth (m)
g: gravitational acceleration (ms^{-2})

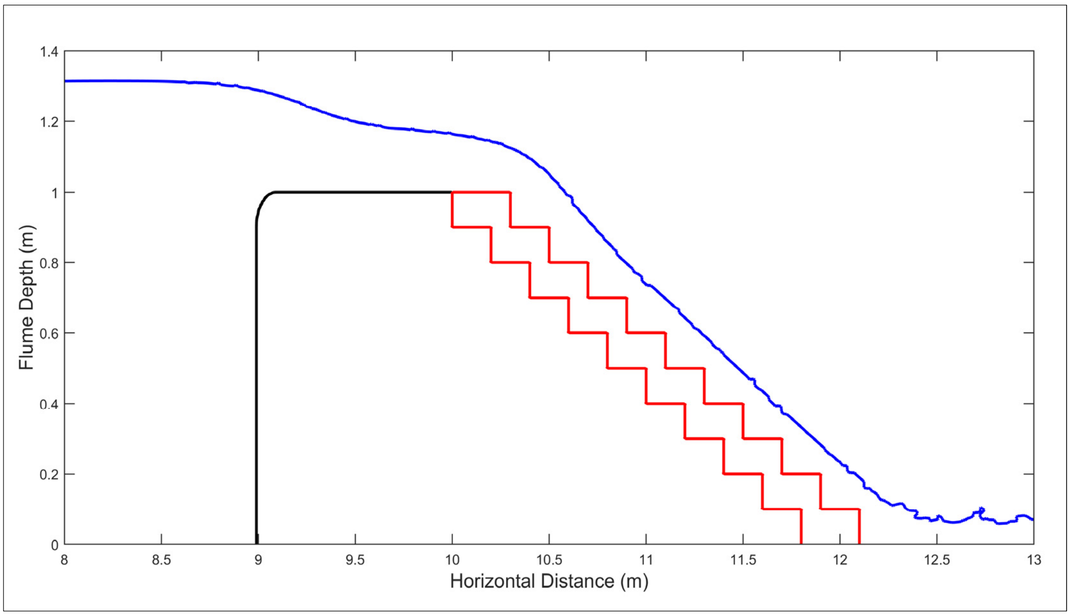

Figure 2. Free surface of skimming flow at 2.848s**.**

According to Husain et al. (2014), the location of the inception point may be estimated from the assumption that the inception point represents the intersection point between the free surface water and the point where the velocity equal to 99% of the maximum velocity over the pseudo-bottom (Figure 3). Also, it can be defined by that point where the depth of the turbulent boundary layer equals to the water depth. Therefore, inception point represents the point where the turbulent velocity near the flow surface is high enough to eject water slugs into air (Andre, 2004).

Chanson (2002) report that the length of the non-aerated zone might be affected by three important factors: discharge, step height and chute slope. Andre (2004) claimed that one of the important benefits of using steps to increase the roughness of the spillway which consequently will accelerate the growth of the turbulent boundary layer. This will increase the opportunity to have the inception point closer to the upstream weir. Minimising the length of the non-aerated zone is significantly important as that will reduce the probability to achieve cavitation damage which might be observed due to the absence of air entrainment. Results from the four experiments are summarised in Table (1); the results reveal good agreement between the numerical and experimental work.

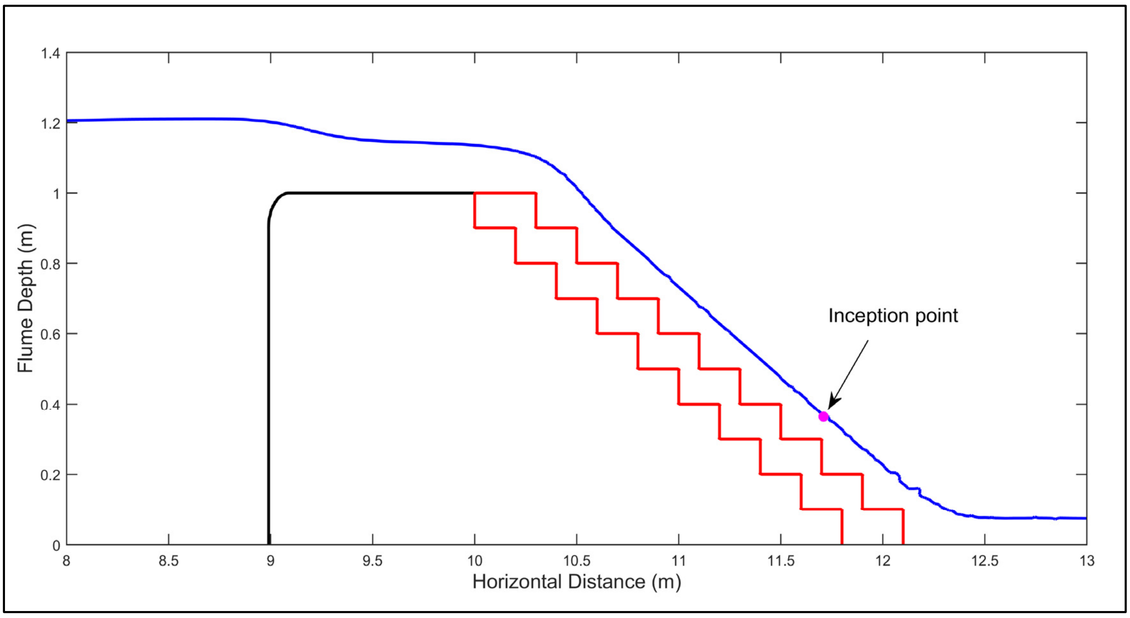

Figure 3. Inception point location for the second experiment at 5.936s.

A comparison of the measured and computed velocity profiles is shown in Figure 4 for the third experiment. This show the velocity profiles on steps 8 to 10, all the values of velocity profiles were divided by Vc and Yc to present them in dimensionless form, Vc and Yc represent the velocity and the depth of the water at the critical section. There are differences in the velocity values near the gabion surface, however, the results agree closely towards the top of the velocity profile where the maximum velocity is achieved. The average value for the root mean square error and the correlation coefficient of the three profiles was 0.32 and 0.991 respectively.

It should be noted that due to the absence of measurements of velocity profiles in the non-aerated zone, the comparison with the numerical results was conducted against velocity profiles in the aerated zone. Therefore, discrepancies are expected in the profile as the numerical model simulates single phase flow in which air entrainment is not considered while the velocity profiles were measured where air entrainment is present.

Overall, the discrepancies at the bottom of the profile are not entirely unexpected. They could arise from the intrinsic limitation of the measurement methods and equipment and also from the limitations of the computational model which simulates single phase flow and in two-dimensions (2D). Work by Kalal et al. (2014) states that the k-ε model underestimates the turbulent quantities, which results in underestimation of the power number computed from the integral of the turbulent dissipation rate. However, current design uses the peak value of the velocity, normally located near the top of velocity profiles, and the numerical results reproduce the observed maximum velocities with a relative error of less than 5%, (Figure 4). The numerical code has given an acceptable level of accuracy considering all the points mentioned earlier, and in particular has reproduced the observed location of the inception point very well.

Table 1. Comparison between the inception point location in the experiment and numerical results.

Experiment Number	Time(s)	Discharge (m^2s^{-1})	Inception point location (Wüthrich & Chanson 2014)	Inception point location (Computed)
1	5.568	0.114	Step 8 to step 9	At the end of step 8
2	5.984	0.095	Step 7 to step 8	At the end of step 7
3	6.432	0.076	Step 5 to step 6	At the end of step 5
4	7.008	0.059	Step 5	At the middle of step 5

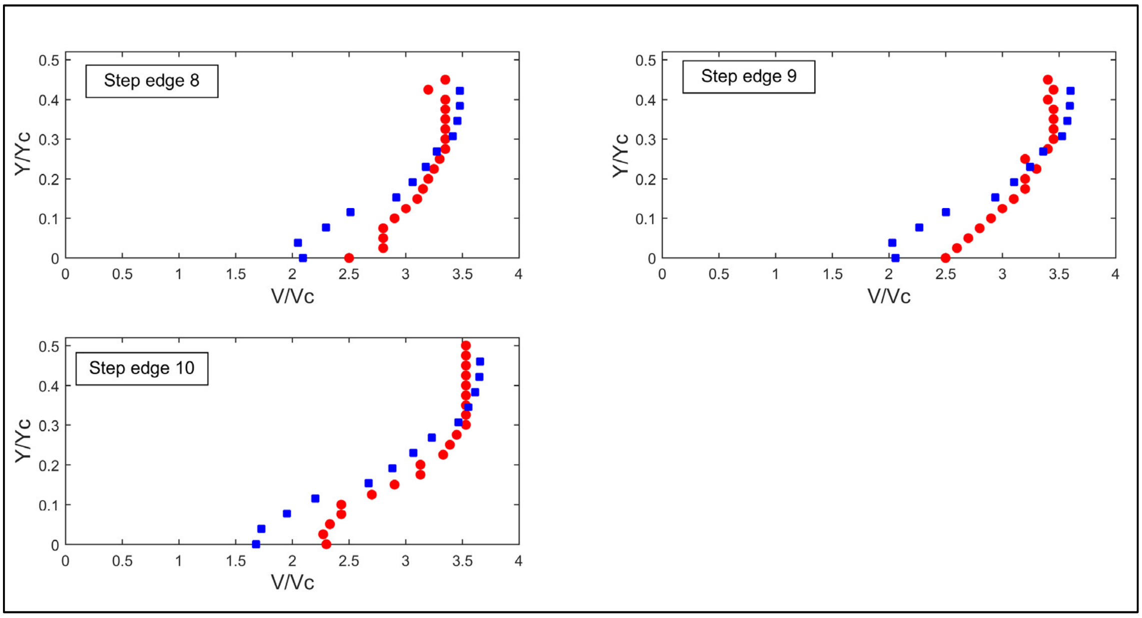

Figure 4. Comparison between the velocity profiles of the experimental results (red circles) and numerical results (blue squares) of the second discharge.

5 STEP CONFIGURATION IMPACT

Three different step heights and different widths were tested with the numerical code to investigate how the step configuration can affect the energy dissipation over gabion stepped spillways. Step widths were set to give spillway slopes of 1:2, 1:2.5 and 1:3. The porosity and the grain size for the gabions were fixed to the values p=0.35 and D_{50}=0.005 as the purpose of this study was investigated the effect of slope on the energy dissipation.

In the numerical model, stepped spillways with 0.06 m step height were located at 7.5 m while the weir was placed at 6.9 m with length 0.6 m, (Figure 5). Stepped spillways with 0.12 m and 0.09 m step height were positioned at distance 8 m from the boundary edge, while the weir of 0.6 m length was placed at a distance of 7.4 m, (Figure 6 and 7).

The initial water depth was 1.58 m, 1.7 m and 1.8 m for 0.12 m, 0.06 m and 0.09 m step height respectively; so that the contents of the upstream tank was sufficient to achieve the required discharge and to allow transients to dissipate. As mentioned above that the gabion stepped spillways were located in different positions and also with different values of initial water depths, this is because the numerical tests have established in dam break conditions; therefore, it is important to set both of them in a way to achieve all the required discharge and to diminish the wavy free surface in the upstream tank.

The total simulation time was set to 15s for 0.12m step height, 16.5s for 0.09m step height and 18s for 0.06m step height. The time step was taken as 0.0001s to satisfy the stability criterion in all cases. The mesh sizes in the x- and y-directions were 0.01m and 0.005m respectively for 0.09m and 0.12m step height, however, for 0.06m step height, it was chosen as 0.0075m in the x-direction and 0.003m in the y-direction in order to maintain numerical stability. The model domain has closed boundaries except the right-hand boundary which was set as an open boundary to let the water exit the flume.

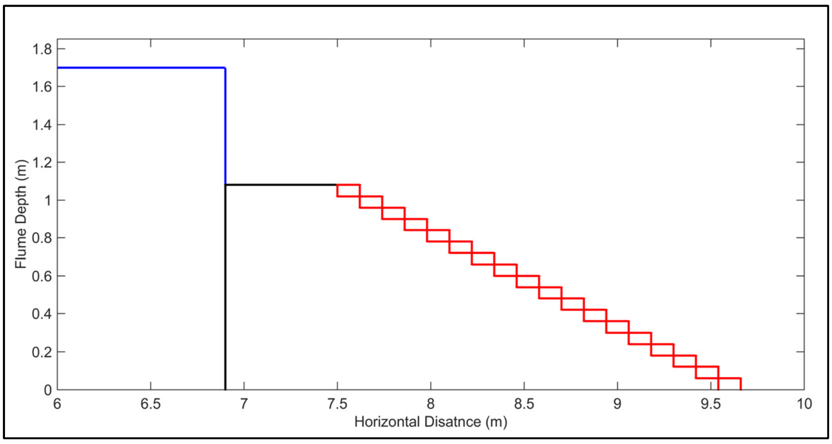

Figure 5. Gabion stepped spillway with 0.06 m step height.

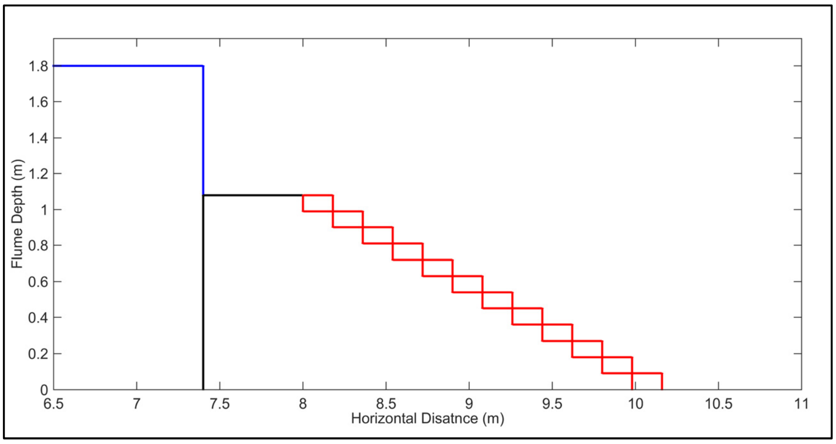

Figure 6. Gabion stepped spillway with 0.09 m step height.

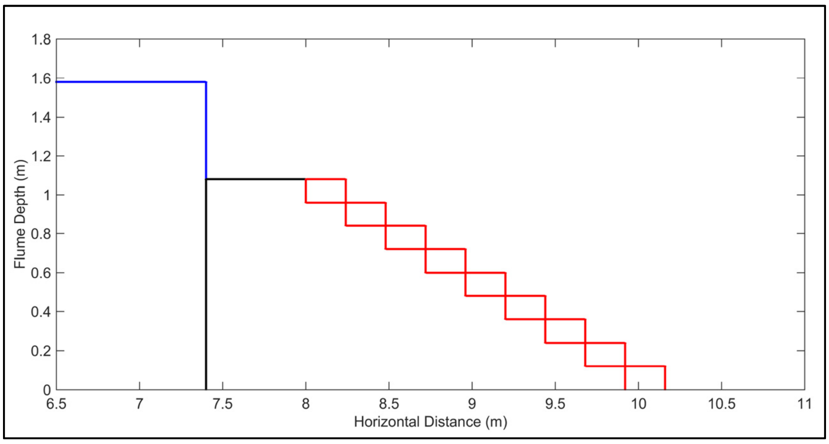

Figure 7. Gabion stepped spillway with 0.12 m step height.

As mentioned earlier, energy dissipation represents the most important parameter over gabion stepped spillways as the energy gained through loss of head can lead to severe scouring downstream of the spillway. Turbulent kinetic energy (TKE) is associated with eddies in the turbulent flow so there is a direct relation between the energy dissipation and TKE. For instance, when the eddy energy increases in turbulent flow due to one of the effective parameters such as fluid shear or friction, high values of TKE are expected and that could lead to an increase in the energy dissipation. The turbulent kinetic energy was computed directly from the instantaneous velocities over the whole domain. Figures 8, 9 and 10 show the variation of the turbulent kinetic energy over the whole domain as a function of time and slope for each of the three different step heights.

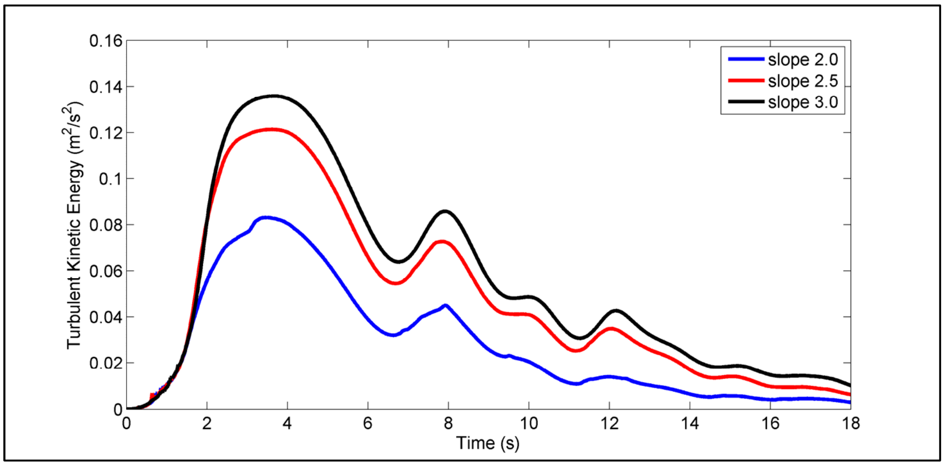

Figure 8. TKE of gabion stepped spillway with 0.06 m step height for three different slopes.

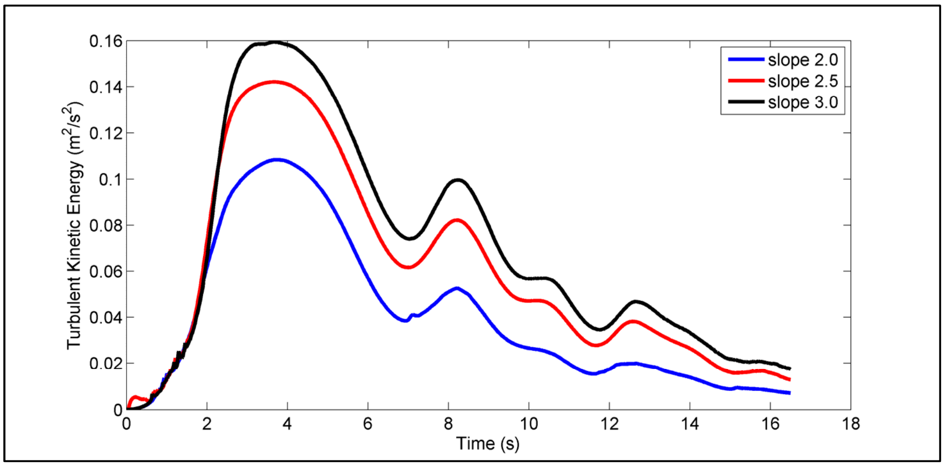

Figure 9. TKE of gabion stepped spillway with 0.09m step height for three different slopes.

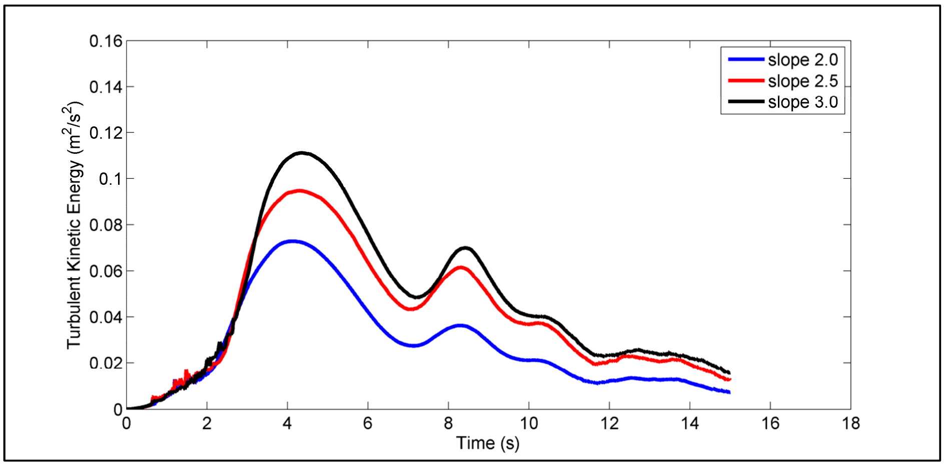

Figure 10. TKE of gabion stepped spillway with 0.12 m step height for three different slopes.

All plots show a similar morphology: from being initially at rest the fluid gradually accelerates down the spillway resulting in a rise in the TKE (Turbulent Kinetic Energy). There are some fluctuations in TKE as skimming flow establishes and it gradually reduces as the head in the upstream tank falls towards the level of the weir. In all the step heights, slope 3.0 always gives the best results in comparison with slope 2 and slope 2.5. In Figure 9, TKE value of slope 3.0 is around 0.16 and it's around 0.14 and 0.12 for slopes 2.5 and 2 respectively, considering the same initial conditions these differences in TKE values are quite high, thus slope can consider as one of the crucial parameters which can affect the energy dissipation. The same differences are captured for step heights 0.06m and 0.12m and reinforce the conclusion above.

Comparisons were conducted for each individual step height as slope impact represents the main interest in the present work. However, it is important to highlight that the peak values for the step heights are different, as can be seen from Figures 8, 9 and 10; the maximum values for TKE are around 0.139, 0.16 and 0.117 for 0.06m, 0.09m and 0.12m respectively. The reason for that is due to the differences in the initial conditions such as the initial water depth and the location of the spillway. The time at which the peak value of TKE occurs is also connected to the initial water depth; therefore, 0.09m step height has reached the peak value earlier than 0.12m step height due to differences in the initial water depth.

6 CONCLUSIONS

The hydraulic performances in terms of energy dissipation of different heights and slopes of gabion stepped spillways have been investigated using an advanced computational model. High energy flow can cause many problems in the downstream area of spillways, such as erosion and scour. As a result, it is important for design to promote energy dissipation to mitigate these effects. Gabion stepped spillways offer one potential solution. The computational model was used to simulate the flow over gabion stepped spillways. The model has been successfully validated against the experimental results of Wüthrich and Chanson (2014).

The validated model was used to test the impact of slope on turbulent kinetic energy levels. The results showed that the energy dissipation over gabion stepped spillways is sensitive to the slope. The reason for this is postulated to be that the contact area with rough horizontal part of the steps increases as the slope of the spillway becomes shallower, and this has an impact on turbulence generation.

We can conclude that the energy dissipation of gabion stepped spillways has a similar behaviour to normal stepped spillways in that it is sensitive to step dimension in both cases. A comparison study between the performance of normal stepped spillways and gabion stepped spillways is currently underway by the authors to investigate the impact of gabions on energy dissipation.

ACKNOWLEDGEMENTS

The first author would like to thank the Higher Committee for Education Development in Iraq (HCED) for supporting his PhD research.

REFERENCES

Abbasi, S. & Kamanbedast, A. (2012). Investigation of Effect of Changes in Dimension and Hydraulic of Stepped Spillways for Maximization Energy Dissipation. *World Applied Sciences Journal*, 18(2), 261-267.

Andre, S. (2004). *High Velocity Aerated Flows on Stepped-Chutes with Macro-Roughness Elements*, Laboratorie de Constructions Hydrauliques Ecole Polytechnique Federale de Lausanne, Switzerland, 1661–1179.

Barani, G.A., Rahnama, M.B. & Sohrabipoor, N. (2005). Investigation of Flow Energy Dissipation over Different Stepped Spillways. *American Journal of Applied Sciences*, 2(6) 1101-1105.

Boes, R.M. (1999). Physical Model Study on Two-Phase Cascade Flow. *Proceeding of the 28th IAHR Congress*. Graz, Austria.

Chanson, H. (1994). Hydraulics of Skimming Flows over Stepped Channels and Spillways. *Journal of Hydraulic Research*, 32(3), 445–60.

Chanson, H. (2002). *The Hydraulics of Stepped Chutes and Spillways*. Lisse: A.A.Balkema Publishers, 1-350.

Chow, V.T. (1959). *Open Channel Hydraulics*. McGraw-Hill, New York, USA, 1-680.

Fratino, U. & Piccinni, A. (2000). Dissipation Efficiency of Stepped Spillways, in H.-E. Minor and W. Hager, *Proceeding of the International Workshop on Hydraulics of Stepped Spillways*, IAHR,A.A. Balkema/Rottersam/Brookfield, Zurich, Switzerland.

Hunt, S.L. & Kadavy, K.C. (2010). Energy Dissipation on Flat-Sloped Stepped Spillways: Part 2. Downstream of the Inception Point. *Transactions of the ASAE (American Society of Agricultural Engineers),* 53(1), 111-118.

Husain, S.M., Muhammed, J.R., Karunarathna, H.U. & Reeve, D.E. (2014). Investigation of Pressure Variation over Stepped Spillways using Smooth Particle Hydrodynamic. *Advances in Water Resources*, (66), 52-69.

Kálal, Z., Jahoda, M. & Fořt, I. (2014). CFD Prediction of Gas-Liquid Flow in an Aerated Stirred Vessel using the Population Balance Model. *Chemical and Process Engineering*, 35(1), 55-73.

Kells, J.A. (1994). Energy Dissipation at a Gabion Weir with Throughflow and Overflow. *Canadian Society for Civil Engineering*, *Annual Conference*, Winnipeg, MB.

Kositgittiwong, D. (2012). Validation of Numerical Model of the Flow Behaviour through Smooth and Stepped Spillways using Large-scale Physical Model, *Degree of Doctor of Philosophy*. King Mongkut's University of Technology Thonburi.

Lin, P. & Liu, P.L.-F. (1998a). A Numerical Study of Breaking Waves in the Surf Zone. *Journal of Fluid Mechanics.* 359(1), 239–264.

Lin, P. & Xu, W. (2006). NEWFLUME: A Numerical Water Flume for Two Two-Dimensional Turbulent Free Surface Flow. *Journal of Hydraulic Research*, 44(1), 60-64.

Matos, J. (2000). Hydraulic Design of Stepped Spillways over RCC Dams. *Proceeding of International Workshop on Hydraulics of stepped spillways*, Zurich, Ed. Balkema, Rotterdam: 187-194.

Peyras, L. Royet, P. & Degoutte, G. (1992). Flow and Energy Dissipation over Stepped Gabion Weirs. *Journal of Hydraulic Engineering*, 118(5), 707-717.

Shafai-Bejestan, M. & Kazemi-Nasaban, G. (2011). Experimental Study on Gabion Stepped Spillway. In *Experimental Methods in Hydraulic Research,* 1, 267-274. Springer Berlin Heidelberg.

Sorensen, R.M. (1985). Stepped Spillway Hydraulic Model Investigation. *Journal of Hydraulic Engineering*, ASCE, 111(12), 1461–72.

Stephenson, D. (1979). Gabion Energy Dissipators. *13th International Congress on Large Dams*, New Delhi, India, Q. 50(3), 33-43.

Tabbara, M., Chatila, J. & Awwad, R. (2005). Computational Simulation of Flow over Stepped Spillways. *Computers & Structures*, 83(27), 2215-2224.

Wüthrich, D., and Chanson, H. (2014). Hydraulics, Air Entrainment, and Energy Dissipation on a Gabion Stepped Weir. *Journal Of Hydraulic Engineering*, 140(9), 1-10.

Zhang, G. & Chanson, H. (2014). Step Cavity and Gabion Aeration on a Gabion Stepped Spillway. In *5th International Symposium on Hydraulic Structures*. Brisbane, Australia: Hydraulic Structures and Society: Engineering Challenges and Extremes.

APPLICATION OF RNG *k–ε* TURBULENCE MODEL TO SUPERCRITICAL BEND FLOW

BO WANG[1], YUNLIANG CHEN[2], CHAO WU[3], XIAO MA[4], JIAJUN SONG[5] & ZHONG TIAN[6]

[1,2,3,4,5,6] State Key Laboratory of Hydraulics and Mountain River Engineering, Sichuan University, Chengdu, China.
e-mail: wangbo@scu.edu.cn

ABSTRACT

This work deals with a brief evaluation of the performance of the computational fluid dynamics (CFD) model, shallow water equations (SWE) model and analytical solution for predicting the water surface profiles of supercritical bend flows and the demonstration of the 3D characteristics of the velocity field and wall shear stress along a bend. Numerical simulations on supercritical bend flow are performed in this study using a 3D CFD model that solves the three-dimensional Reynolds-averaged Navier-Stokes equations using the finite-volume method. The volume of fluid (VOF) method is used to track the free water surface. The obtained outer and inner wall wave profiles, maximum and minimum depths and first wave crest and trough locations using the CFD model are successfully validated against laboratory measurements. A good agreement is also found between the CFD predictions and the analytical solutions for the free surface profiles. The CFD model appears to be more robust than the SWE one in reproducing the flow field for large approach Froude numbers. Velocity characteristics along the bend are captured by the CFD model, which are consistent with observations in physical model. The CFD simulation shows zones of high shear stress along the outer wall responding to each wave crest and ones on the bed located between two wave crests.

Keywords: Supercritical bend flow; RNG k–ε model; free surface profile; velocity field; shear stress.

1 INTRODUCTION

The study of free-surface flow in bends is a relevant topic in engineering practice. A bend is an important element in chutes, whose presence is unavoidable in open channel designs. For channels with a considerable curvature, the selection of wall height depends on the maximum flow depth and its location. The supercritical flow pattern around a curve is complex because cross waves are generated at changes of channel alignment, size or shape (Hager et al. 1994). The streamlines of supercritical flows are curvilinear and interwoven along a bend, resulting in cross waves. Furthermore, the centrifugal force acting on the flow around a bend produces a unique feature known as super-elevation (Chow 1986). Since flows in channel bends were first analyzed by Ippen and Knapp (1936), it has been extensively studied theoretically, experimentally and numerically in recent decades.

Analytical relationships for the extremum wave heights and locations of shock wave that is produced along a bend were proposed by Knapp and Ippen (1938) and by Ghaeini-Hashemi and Tahershamsi (2009). Supercritical flow in bends has also been studied experimentally (Poggi 1956, Marchi 1988, Reinauer and Hager 1997, Beltrami et al. 2007). Due to the cost and time requirements of laboratory studies, investigators attempt to apply the numerical models to the analyses of the features of supercritical bend flow.

The classical, widely used shallow water equations (SWE), which are based on the restrictive hypotheses of hydrostatic pressure distribution along each vertical and negligibility of the acceleration along the vertical direction (Liggett 1994), was adopted by Valiani and Caleffi (2005), Ghaeini-Hashemi et al. (2011) and Jaefarzadeh et al. (2012). The limits of the SWE formulation was observed by Valiani and Caleffi (2005), such as systematic underestimation of computed maximum water depths with respect to measured values and systematic increasing of the same underestimation with an increasing relative curvature and undisturbed Froude number of the flow. Fully three-dimensional (3D) models are required to accurately represent the flow field in bends. 3D simulation on the turbulent flow in S-shaped chutes was conducted by Ye et al. (2006) using a k–ε turbulence model. Montazeri-Namin et al. (2012) used the FLUENT software package to simulate the water surface profiles along a bend. The aforementioned numerical simulations on supercritical bend flow focus on water surface profiles. However, velocity field and wall shear stress are seldom involved, which are important as the same as water surface profiles in bend designs.

Herein, numerical simulations on supercritical bend flow were performed using a 3D computational fluid dynamics (CFD) model. The aims of the present work are to: (1) briefly evaluate the performance of the CFD model, SWE model and analytical solution for predicting the water surface profiles of supercritical bend flows; and (2) demonstrate the 3D characteristics of the velocity field and wall shear stress along a bend.

2 SELECTED EXPERIMENTAL DATA SETS

A significant experimental study on three horizontal, smooth and rectangular channel bends was conducted by Reinauer and Hager (1997). The experimental data obtained in channel I was selected for comparison with numerical simulations, because the main experiments were conducted in this channel. The geometrical characteristics of channel I was: bend radius = 3.607 m, bend angle = 51° and channel width = 0.25 m. The flow depth at the inlet of channel I was 0.05 m, and the approach Froude numbers were between 1.42 and 4.84.

3 MODEL DESCRIPTION

The CFD solver ANSYS FLUENT version 6.3.26, a commercial computational fluid dynamics package used to simulate the supercritical bend flow in the present study, solves the three-dimensional Reynolds-averaged Navier-Stokes (RANS) equations for incompressible flow. The governing equations are solved in FLUENT using the control volume method; and they are integrated over each control volume to construct discretized algebraic equations for the dependent variables. These discretized equations are linearized using an implicit method.

3.1 Governing Equations

The Reynolds-averaged conservation equations for mass and momentum for an incompressible fluid can be expressed respectively as (Ferziger and Peric 2002)

Continuity equation:

$$\frac{\partial \overline{u}_i}{\partial x_i} = 0 \qquad [1]$$

Momentum equation:

$$\frac{\partial \rho \overline{u}_i}{\partial t} + \frac{\partial}{\partial x_j}(\rho \overline{u}_i \overline{u}_j) = -\frac{\partial \overline{p}}{\partial x_i} + \frac{\partial}{\partial x_j}[\mu(\frac{\partial \overline{u}_i}{\partial x_j} + \frac{\partial \overline{u}_j}{\partial x_i})] + \frac{\partial \tau_{ij}}{\partial x_j} \qquad [2]$$

where $\overline{u}_i$ and $\overline{u}_j$ are the Reynolds-averaged velocities, x_i and x_j are the Cartesian coordinate axes; ρ is the fluid density; t is the time; and μ is the molecular viscosity. The variable $\overline{p}$ represents the Reynolds-averaged pressure and $\tau_{ij} = -\rho\left(\overline{u_i u_j} - \overline{u}_i \overline{u}_j\right)$ denotes the Reynolds stress or sub-grid-scale Reynolds stress components.

3.2 Turbulence model

In the present work, the RNG-based k–ε model, which is derived from the Navier-Stokes equations using a mathematical technique called "renormalization group" theory (Yakhot and Orszag, 1986), is utilized for turbulence closure. It consists of the following two transport equations for an incompressible fluid: one for the turbulent kinetic energy k and the other for its dissipation rate ε:

$$\frac{\partial(\rho k)}{\partial t} + \frac{\partial(\rho u_i k)}{\partial x_i} = \frac{\partial}{\partial x_i}\left[\alpha_k \mu_{eff} \frac{\partial k}{\partial x_i}\right] + G_k - \rho\varepsilon \qquad [3]$$

$$\frac{\partial(\rho \varepsilon)}{\partial t} + \frac{\partial(\rho u_i \varepsilon)}{\partial x_i} = \frac{\partial}{\partial x_i}\left[\alpha_\varepsilon \mu_{eff} \frac{\partial \varepsilon}{\partial x_i}\right] + C^*_{\varepsilon 1}\frac{\varepsilon}{k} G_k - C_{\varepsilon 2}\rho\frac{\varepsilon^2}{k} \qquad [4]$$

where μ_{eff} is the effective viscosity and G_k is the generation of turbulent kinetic energy (Orszag et al. 1993, for more comprehensive description).

3.3 VOF method

The partial volume of fluid (PVOF) approach is used to track the free surface, which is partly based on the VOF method outlined by Hirt and Nichols (1981). In the VOF method a special advection technique is used that gives a sharp definition of the free surface, whereas in Fluent the combined air–water flow is solved (Bombardelli et al. 2001).

3.4 Domain and Grid

For sake of comparison, the computational domain having upstream- and downstream-bend channel trenches and the bend adopted in the simulations by Valiani and Caleffi (2005) was used in the present study as shown in Figure 1(a). Both the upstream- and downstream-bend channel trenches are 0.4 m long. The height of the bend wall is 0.35 m. Grids were created using GAMBIT version 2.4.6, a mesh generation package. Structured 3D hexahedral mesh elements were used to discretize the geometry for simulation, as shown in Figure 1(b). The average grid size in the radial and tangential directions of the bend is about 0.01 m, which was used in the 2D simulation conducted by Valiani and Caleffi (2005). The size of the vertical side is also 0.01 m. A total of 369,250 cells were used for discretizing the equations. A post processing check on mesh quality in GAMBIT based on assessing the skewness of the generated cells indicated that the mesh is of high quality and would not compromise solution stability. To test for grid independence, the F_o = 8 case was repeated using a finer mesh with 738,500 cells, i.e. the size of the vertical side was 0.005 m. The finer mesh gave the same results as the coarser mesh so the remaining simulations were conducted with 369,250 cells.

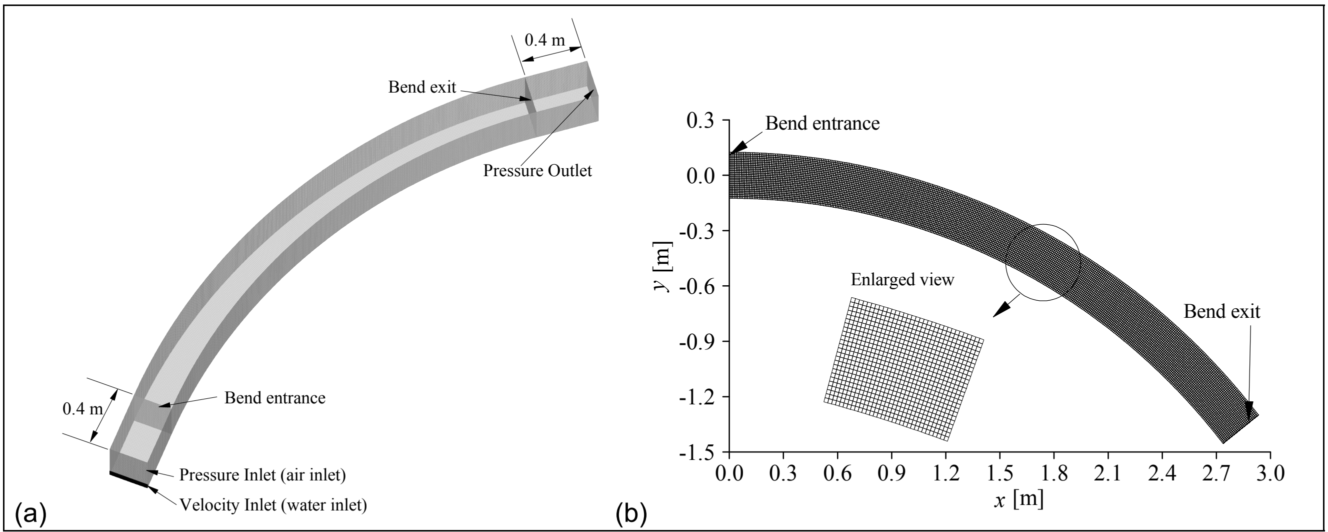

Figure 1. Computational domain and mesh used for modelling the Channel I of Reinauer and Hager (1997).

3.5 Boundary Conditions

The inlet boundary includes a water inlet and an air inlet. The velocity inlet boundary was adopted as the water inlet. As the water depth at the inlet was measured in the experiments and the approach Froude number was given by Reinauer and Hager (1997), the average velocity of the water inlet could be calculated. All the air boundaries were defined as pressure boundaries. A pressure outlet boundary condition was used at the channel exit to allow free-air flow. Both the side and bottom walls were defined as wall boundaries with no slip.

3.6 Solution Procedures

A small initial time step is required in the unsteady free surface calculations. A time step equal to 0.001 s was selected, which was based on the Courant-Friedrichs-Lewy (CFL) condition. During the calculations, solution convergence and the discharges of both at the inlet and outlet of channel were monitored. Convergence was reached when the normalized residual of each variable was on the order of 1×10^{-3}. The free surface was defined by a value of VOF=0.5, which is a common practice for volume fraction results (Fluent 2006).

4 RESULTS AND DISCUSSIONS

4.1 Maximum Wave Height and the Location

Knapp and Ippen (1938) proposed a model for predicting the location and the crest height of the first wave at the outer wall for small relative curvature

$$\tan\theta_M = \frac{2b}{\left(2R_a + b\right)\tan\beta} \quad [5]$$

$$\beta = \arcsin\left(1/\mathsf{F}_o\right) \quad [6]$$

$$Y_M = \mathsf{F}_o^2 \sin^2\left(\beta + \theta_M/2\right) \quad [7]$$

where θ_M = angular location of first wave crest, b = channel width, R_a = bend radius, β = wave front angle, Y_M = ratio of the maximum flow depth h_M to the approach flow depth h_o, F_o = approach Froude number, $F_o = V_o/(gh_o)^{1/2}$, V_o = approach velocity, g = gravitational acceleration.

Based on the experiments, Reinauer and Hager (1997) developed empirical expressions for the maximum wave height and its location at the outer wall as well as the minimum wave height and its location at the inner wall as follows:

$$Y_M = \begin{cases} \left(1 + 0.40\mathbf{B}^2\right)^2 & \mathbf{B} \le 1.5 \\ \left(1 + 0.60\mathbf{B}\right)^2 & \mathbf{B} > 1.5 \end{cases} \quad [8]$$

$$\tan\theta_M = \begin{cases} \mathsf{F}_o\, b/R_a & \mathsf{F}_o\, b/R_a \le 0.35 \\ 0.60\sqrt{\mathsf{F}_o\, b/R_a} & \mathsf{F}_o\, b/R_a > 0.35 \end{cases} \quad [9]$$

$$Y_m = \left(1 - 0.50\mathbf{B}^2\right)^2 \quad [10]$$

$$\tan\theta_m = \sqrt{2}\mathsf{F}_o\, b/R_a \quad [11]$$

where **B** = bend numbers = $F_o(b/R_a)^{1/2}$, Y_m = ratio of the minimum flow depth h_m to the approach flow depth h_o, θ_m = angular location of the minimum flow depth.

The flow profile along the upstream-bend channel trench is a backwater curve due to the contributions of the horizontal bottom and skins friction. Thus the water depth at the bend entrance is larger than 0.05 m; and the consequent Froude number F_o is lower than the one in the experiment of Reinauer and Hager (1997). The water depth at the domain inlet, denoted by h_i, and the water depth at the bend entrance h_o, in the present simulations are given in Table 1, where the corresponding Froude numbers F_i and F_o are contained.

Table 1. Values of h_i and F_i at the domain inlet and h_o and F_o at the bend entrance.

Domain inlet		Bend entrance	
h_i (m)	F_i	h_o (m)	F_o
0.05	2.5	0.05163	2.383
0.05	3.0	0.05153	2.867
0.05	4.0	0.05145	3.832
0.05	5.0	0.05141	4.796
0.05	6.0	0.05139	5.758
0.05	7.0	0.05138	6.719
0.05	8.0	0.05137	7.681

The maximum dimensionless depth Y_M obtained from the analytical solutions of Eqs. [7] and [8], the SWE simulations by Valiani and Caleffi (2005) and Jaefarzadeh et al. (2012), the CFD predictions and the experiments of Reinauer and Hager (1997), are plotted against F_o, as shown in Fig. 2(a). The solution of Eq. [7] compares well to the experimental results up to F_o = 4, whereas an increasing deviation is found as the value of F_o is larger. The maximum depth is predicted well using Eq. [8] except a notable discrepancy in the vicinity of the inflection point, i.e. **B** = 1.5. The CFD results are in close agreement with the experimental data. The SWE results are nearly identical, although the Roe solver used by Jaefarzadeh et al. (2012) is different from the HLL solver used by Valiani and Caleffi (2005). For F_o > 4.5, the maximum depth is underestimated using the SWE model.

The minimum dimensionless depth Y_m produced from CFD and the experiments of Reinauer and Hager (1997), are plotted against F_o, as shown in Fig. 2(b), where the data points relating to a dry inner bend bottom (i.e., F_i = 6, 7, 8) are not shown. Both the CFD predictions and the solution of Eq. [10] compare well with the experimental data.

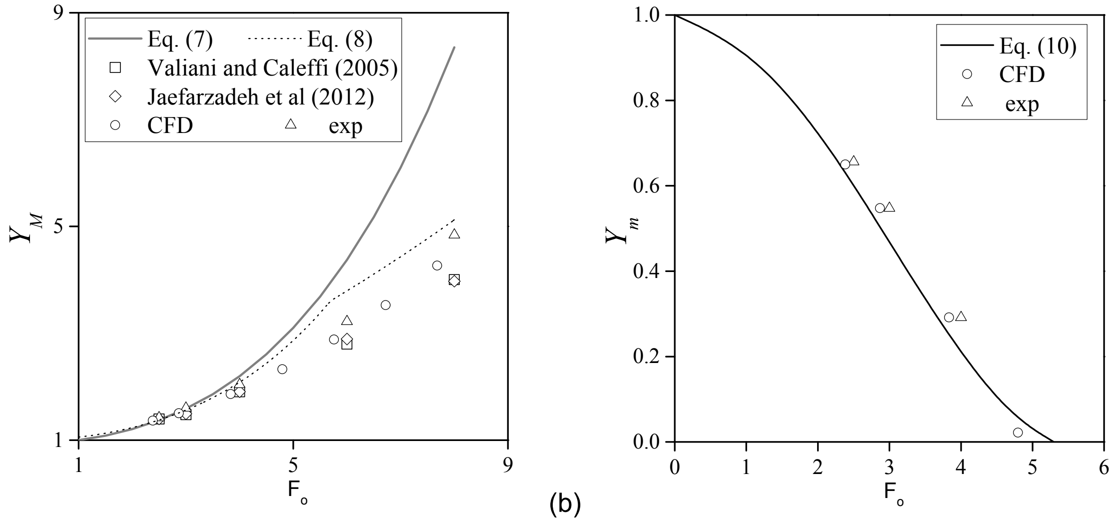

(a) (b)

Figure 2. Maximum dimensionless depth $Y_M(\mathrm{F_o})$ and minimum dimensionless depth $Y_m(\mathrm{F_o})$.

Fig. 3(a) shows the crest location $\tan\theta_M$ versus $\mathrm{F_o}b/R_a$, in which the solution of Eq. [9], the SWE simulations by Jaefarzadeh et al. (2012), the CFD predictions and the experiments of Reinauer and Hager (1997) are included. The increasing tendency of $\tan\theta_M$ with $\mathrm{F_o}b/R_a$ is captured using Eq. [9]. The SWE model under-predicts the crest location and the discrepancies between SWE predictions and experimental data increase when the value of $\mathrm{F_o}b/R_a$ is larger. The crest location estimate provided using the CFD model is in the vicinity of the measured data.

The solution of Eq. [11], CFD predictions and the experiments of Reinauer and Hager (1997) for the crest trough location $\tan\theta_m$ are plotted against F_ob/R_a in Figure 3(b). Good agreement is found between the predictions and the experimental data.

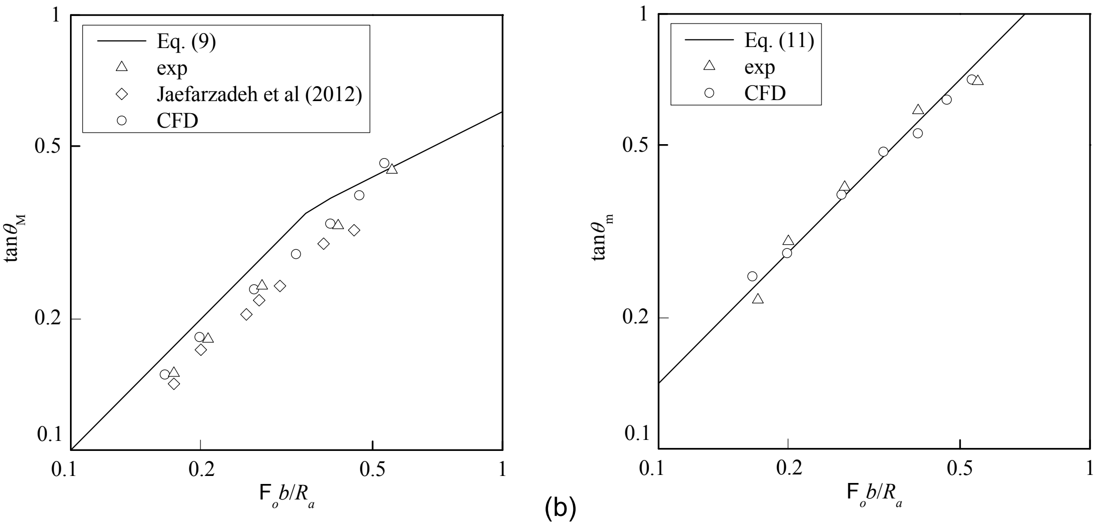

(a) (b)

Figure 3. Crest location $\tan\theta_M$ and trough location $\tan\theta_m$ versus $\mathrm{F_o}b/R_a$.

4.2 Wall Surface Profile

The surface profiles along the outer and inner bend wall were normalized as follows:

$$\tau_M = (h - h_o)/(h_M - h_o) \qquad [12]$$

$$\tau_m = (h - h_o)/(h_m - h_o) \qquad [13]$$

An empirical expression for the outer wall wave configuration was proposed by Reinauer and Hager (1997) based on the experiments:

$$\tau_M = \left[\sin\left(\frac{\pi}{2}\frac{\theta}{\theta_M}\right)\right]^{3/2} \qquad [14]$$

where τ_M = normalized outer wall profile.

Beltrami et al. (2007) suggested an alternative surface profile along the outer wall as

$$\tau_M = \frac{1 - J_0\left(3.8\theta/\theta_M\right)}{1.4} \qquad [15]$$

where J_0 = Bessel function of the first kind and of order zero.

The numerical results for τ_M are shown in Fig. 4(a), where the analytical solutions of Eqs. [14] and [15], the SWE simulations by Jaefarzadeh et al. (2012), the CFD predictions and the experiments of Reinauer and Hager (1997) are plotted. The wall profile is repeated well using Eq. [14] when $\theta/\theta_M \leq 1.25$. Equation [15] is close to Eq. [14] if $0.75 \leq \theta/\theta_M \leq 1.25$ and catches the tendency of the observed profiles if $1.25 < \theta/\theta_M \leq 2.00$. The CFD model provides good estimates of water surface profiles for different F_o when $\theta/\theta_M \leq 1.6$. Discrepancies between CFD predictions and experimental data are found when $1.6 < \theta/\theta_M \leq 2.0$. The SWE results are lower than the experimental data for $0.5 < \theta/\theta_M < 0.8$. The SWE model appears not robust for $1.5 < \theta/\theta_M \leq 2.0$.

Figure 4(b) shows the CFD predictions and the experiments of Reinauer and Hager (1997) for τ_m. The numerical results compare well to the experimental data when $\theta/\theta_M \leq 1.2$. Substantial discrepancy occurs in the range $1.2 < \theta/\theta_M \leq 2.0$, due to the possible occurrence of wave breaking.

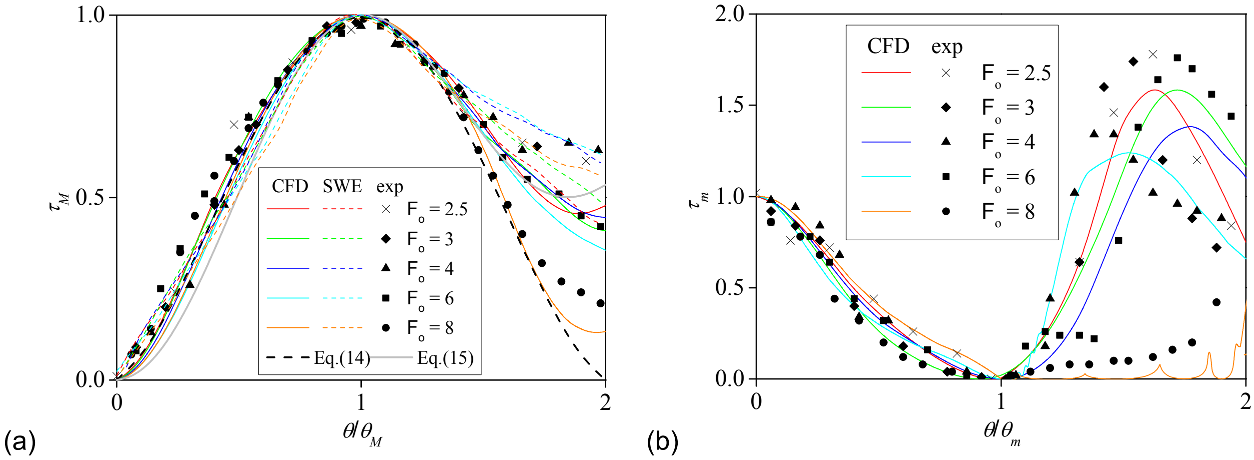

Figure 4. Normalized outer and inner wall profiles.

4.3 Velocity field

Velocity fields were studied in various horizontal layers, *z*, above the channel bottom. For length limit, the velocity field of only one selected run with approach Froude numbers F_o = 3.832, as shown in Fig. 5. The data points of flow velocity were reduced by half for visual observations.

It is seen that the tangential velocity in the streamwise and radial directions decays slowly. Furthermore, the decay of velocity in the vertical direction is negligible. The velocity direction is almost tangential throughout the flow field. A notable decay of velocity may be found in the radial direction towards the centre of curvature. These characteristics of velocity decay captured by the CFD model were observed in the experiment by Reinauer and Hager (1997). For F_o = 5.758 similar findings apply, as shown in Figure 6.

  / ISSN 1562-6865 (Online) - ISSN 1063-7710 (Print)

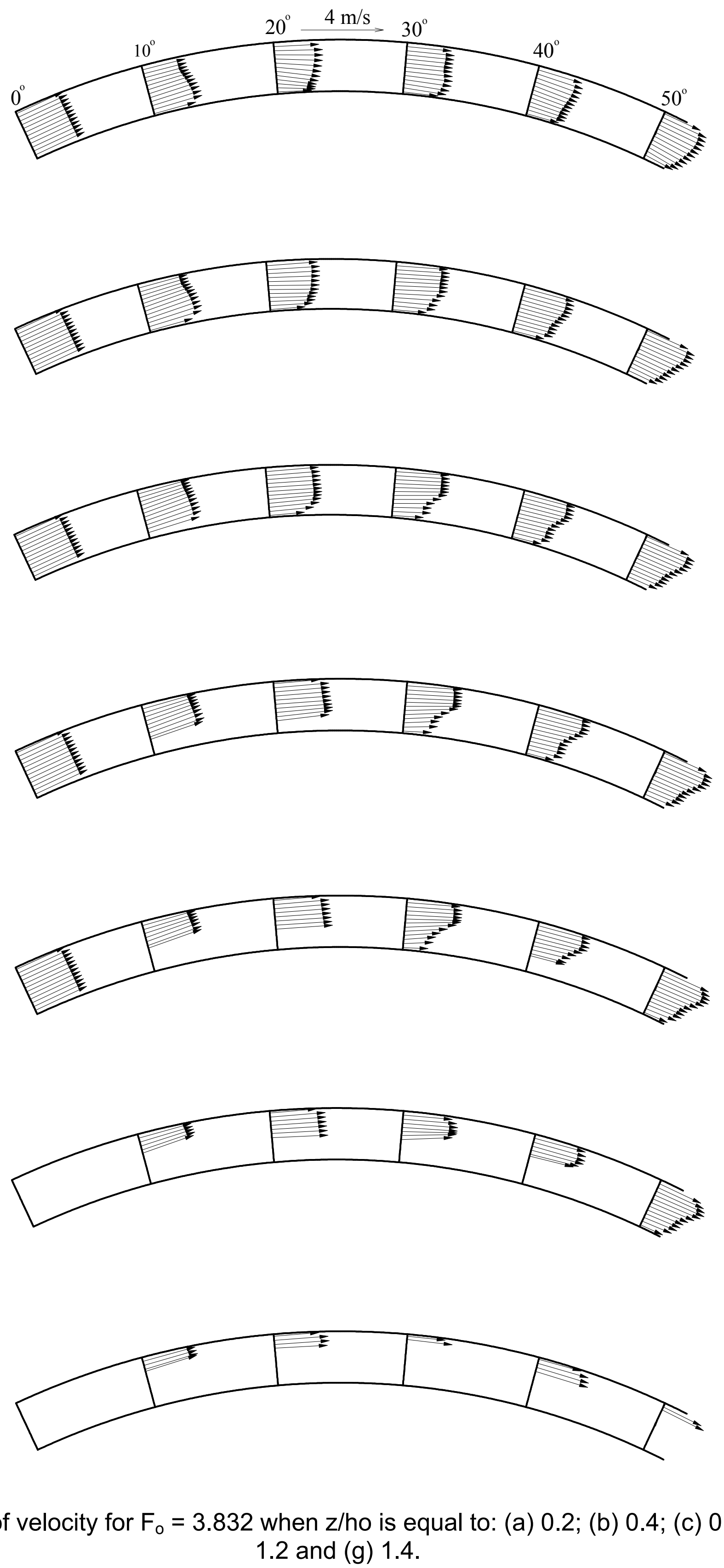

(a) (b) (c) (d) (e) (f) (g)

Figure 5. Vector plots of velocity for F_o = 3.832 when z/ho is equal to: (a) 0.2; (b) 0.4; (c) 0.6; (d) 0.8; € 1.0; (f) 1.2 and (g) 1.4.

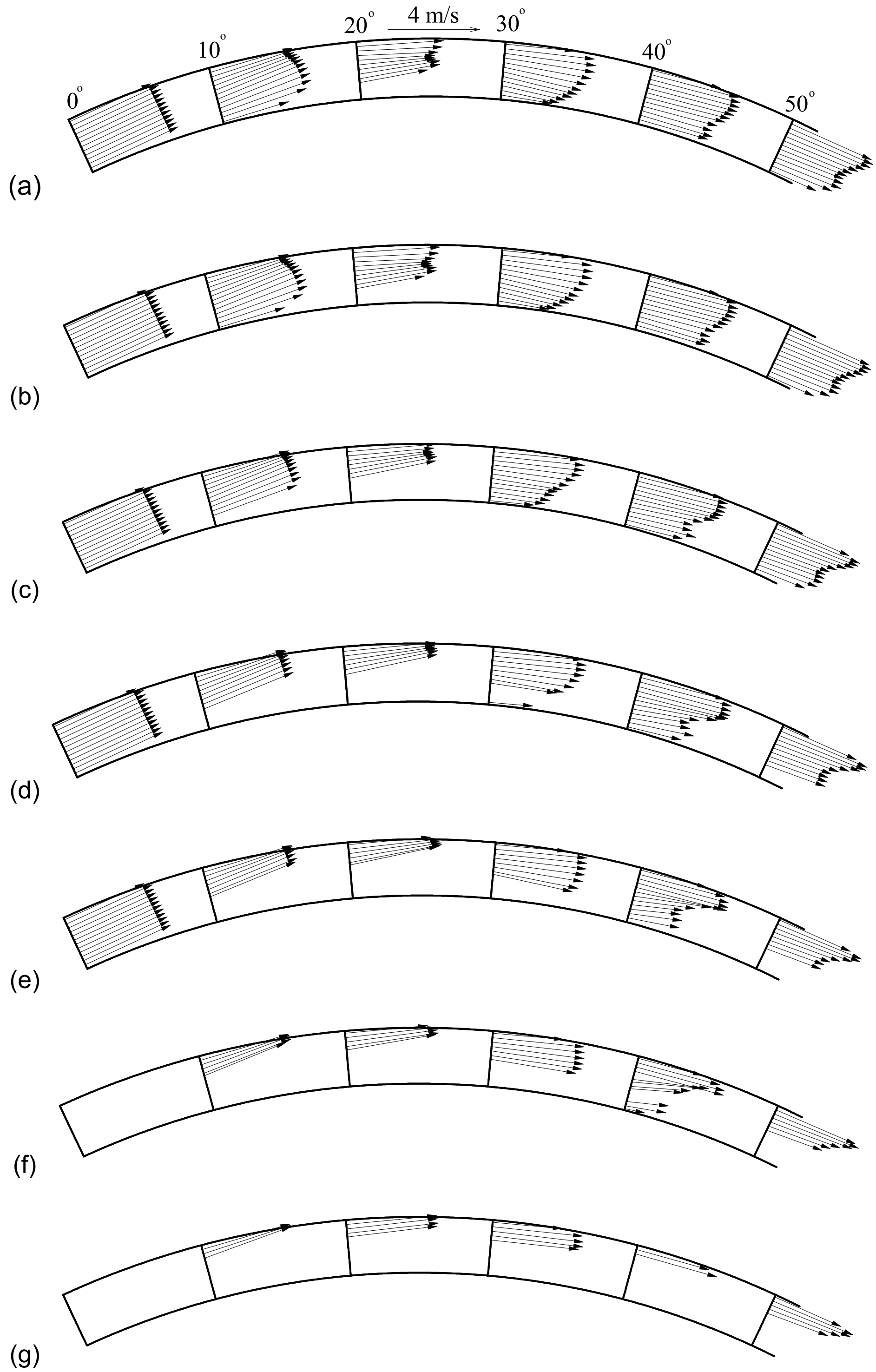

Figure 6. Vector plots of velocity for F_o = 5.758 when z/h_o is equal to: (a) 0.2; (b) 0.4; (c) 0.6; (d) 0.8; (e) 1.0; (f) 1.2 and (g) 1.4.

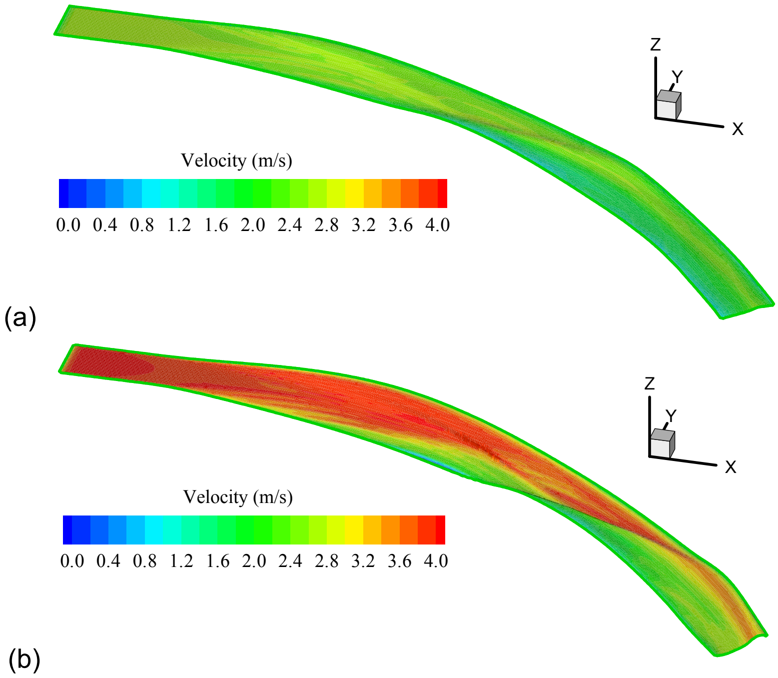

Figure 7. Contours of velocity near water surface for (a) $F_o = 3.832$ and (b) $F_o = 5.758$.

Contours of velocity near water surface for $F_o = 3.832$ and 5.758 are shown in Figure 7. In the upstream-bend channel trench, the velocity in the radial direction is uniform. When the flow enters the bend, the decay of velocity in the range of first wave is small along the outer wall; whereas a minimum value of velocity is found in the vicinity of wave trough along the inner wall.

4.4 Shear stress

Figure 8 shows the distribution of shear stress τ_w on the bed and outer wall for $F_o = 3.832$ and 5.758. The approach flow value of τ_w is high because the velocity gradient in the near-wall zones is great due to an average velocity defined at the inlet. τ_w decreases along the bend because of the readjustment of velocity. This phenomenon may be considered as an exception produced by the inlet boundary definition. Emphases should be placed on the zones of high shear stress, excluding the effect of the inlet boundary definition. Zones of high shear stress along the outer wall respond to each wave crest; and the ones on the bed are located between two wave crests. In the zones, the channel is prone to erosion damage.

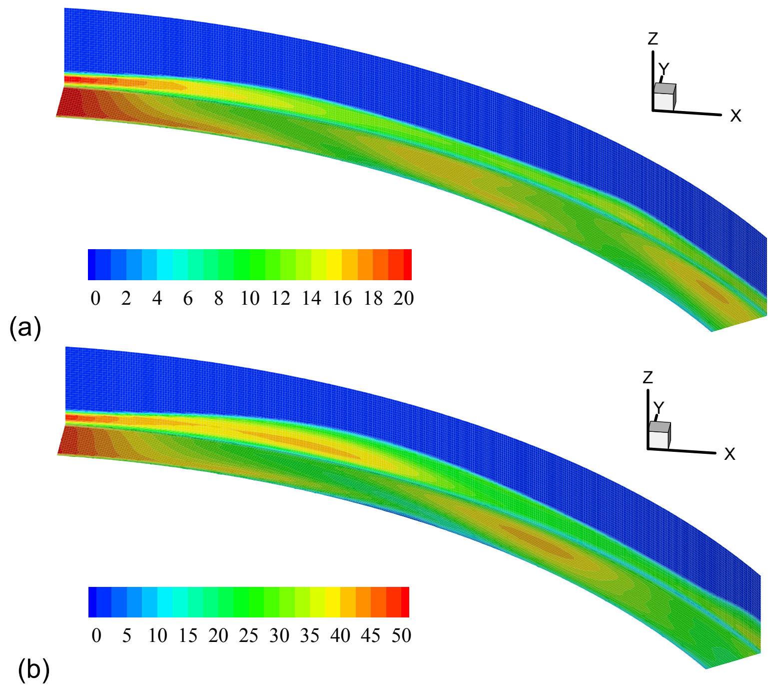

Figure 8. Contours of bed and wall shear stress for (a) $F_o = 3.832$ and (b) $F_o = 5.758$.

5 CONCLUSIONS

The RNG k–ε turbulence model was applied to simulate supercritical flows in bends. The CFD simulations were compared with the selected experimental data, analytical solutions and the SWE predictions. Specific conclusions are summarized as follows:

1. The maximum and minimum depths, and first wave crest and trough locations produced by the CFD model show good agreement with laboratory measurements. The solutions by Knapp and Ippen (1938) and Reinauer and Hager (1997) have their own limitations for calculating the maximum depth. The SWE model under-predicts both the maximum depth and crest location for F_o > 4.5.2. The CFD model provides good estimates of the outer wall surface profiles for different F_o when $\theta/\theta_M \leq 1.6$, but discrepancies between CFD predictions and experimental data are found when $1.6 < \theta/\theta_M \leq 2.0$. The CFD predictions for the inner wall surface profiles compare well to the experimental data when $\theta/\theta_M \leq 1.2$, however substantial discrepancy occurs in the range $1.2 < \theta/\theta_M \leq 2.0$. The SWE model underestimates the outer wall surface profiles for $0.5 < \theta/\theta_M < 0.8$ and appears not robust for $1.5 < \theta/\theta_M \leq 2.0$.
3. The CFD simulations show that the tangential velocity in the streamwise and radial directions decays slowly; and the velocity direction is almost tangential throughout the flow field. These velocity characteristics are consistent with observations in the experiment by Reinauer and Hager (1997).
4. It is observed from the CFD simulation that there are zones of high shear stress along the outer wall responding to each wave crest and ones on the bed located between two wave crests. In these zones, the channel is prone to erosion damage.
5. It is demonstrated from this study that the CFD model is an alternative or effective supplement for experiments and is superior to the SWE model in reproducing the bend flow field.

ACKNOWLEDGEMENTS

The financial supports of the National Natural Science Foundation of China (Grant No. 51209155) and the National Key Research and Development Program of China (2016YFC0401707) are greatly acknowledged.

REFERENCES

Beltrami, G.M., Repetto, R. & Guzzo, A.D. (2007). A Simple Method to Regularize Supercritical Flow Profiles in Bends. *Journal of Hydraulic Research*, 45(6), 773-786.

Bombardelli, F.A., Hirt, C.W. & García, M.H. (2001). Discussion of “Computations of Curved Free Surface Water Flow on Spiral Concentrators”. *Journal of Hydraulic Engineering*, 127(7), 629-631.

Chow, V.T. (1986). *Open Channel Hydraulics*, McGraw-Hill, New York, 728.

Ferziger, J. & Peric, M. (2002). *Computational Methods for Fluid Dynamics,* 3rd Ed., Springer, Berlin, 423.

Fluent Inc. (2006). *FLUENT 6.3* User’s guide. Lebanon NH.

Ghaeini-Hashemi, M. & Tahershamsi, A. (2009). Analytical Model of Supercritical Flow in Rectangular Chute Bends. *Journal of Hydraulic Research*, 47(7), 566-773.

Ghaeini-Hashemi, M, Tahershamsi A. & Montazeri-Namin, M. (2011). Numerical modelling of supercritical flow in rectangular chute bends. *Journal of Hydraulic Research*, 49(5), 685-688.

Hager, W.H., Schwalt, M., Jimenez, O. & Chaudhry, M.H. (1994). Supercritical Flow near an Abrupt Wall Deflection. *Journal of Hydraulic Research*, 32(1), 103-118.

Hirt, C.W. & Nichols, B.D. (1981). Volume of Fluid (VOF) Method for Dynamics of Free Boundaries. *Journal of Computer and Physics*, 39(1), 201-225.

Ippen, A.T. & Knapp, R.T. (1936). A Study of High-Velocity Flow in Curved Channels of Rectangular Cross-Section. *Transaction of American Geophysical Union*, 17, 516-521.

Jaefarzadeh, M.R., Shamkhalchian, A.R. & Jomehzadeh, M. (2012). Supercritical Flow Profile Improvement by Means of a Convex Corner at a Bend Inlet. *Journal of Hydraulic Research*, 50(6), 623-630.

Knapp, R.T. & Ippen, A.T. (1938). Curvilinear Flow of Liquids with Free Surfaces at Velocities above that of Wave Propagation. *Proceeding of 5th International Congress of Applied Mechanics*, Cambridge University Press, New York, 531-536.

Liggett, J.A. (1994). *Fluid Mechanics*, McGraw-Hill, New York, 495.

Marchi, E. (1988). Correnti veloci in curve a 90° molto strette. *Idrotecnica*, 6, 439-455. (in Italian)

Montazeri-Namin, M., Ghazanfari-Hashemi, R. & Ghaeini-Hessaroeyeh, M. (2012). 3D Numerical Simulation of Supercritical Flow in Bends of Channel. *International Conference on Mechanical, Automotive and Materials Engineering (ICMAME’ 2012)*, January, Dubai, 167-171.

Orszag, S.A., Yakhot, V., Flannery, W.S., Boysan, F., Choudhury, D., Maruzewski, J. & Patel, B. (1993). Group Modeling and Turbulence Simulations. *International Conference on Near-wall Turbulent Flows*, Tempe, AZ.

Poggi, B. (1956). Correnti veloci nei canali in curva. *L’energia Elettrica*, 33(5), 465-480. (in Italian)

Reinauer, R. & Hager, W.H. (1997). Supercritical Bend Flow. *Journal of Hydraulic Engineering*, 123(3), 208-218.

Yakhot, V. & Orszag, S.A. (1986). Renormalization Group Analysis of Turbulence: I. Basic Theory. *Journal of Scientific Computing*, 1(1), 1-51.

Ye, M., Wu, C., Chen, Y.L. & Zhou, Q. (2006). Case Study of an S-Shaped Spillway using Physical and Numerical Models. *Journal of Hydraulic Engineering*, 132(9), 892-898.

Valiani, A. & Caleffi, V. (2005). Brief Analysis of Shallow Water Equations Suitability to Numerically Simulate Supercritical Flow in Sharp Bends. *Journal of Hydraulic Engineering*, 131(10), 912-916.

CRITICAL SUBMERGENCE FOR WATER INTAKES

MUHAMMAD HASHID[(1)] & ZULFEQUAR AHMAD[(2)]

[(1,2)] IIT Roorkee, India
mhashid@gmail.com, zulififce@gmail.com

ABSTRACT

The issue of critical submergence of water intakes under flow near the intake has been studied through experimental considerations. The depth or submergence at which air-entrainment occurs with tip of air-cone of the vortex just reaches the intake is called as critical submergence. Formation of air-entraining surface vortices at the intakes can cause operational difficulties and affect efficient functioning of the water intakes. The present work has been carried out on a laterally placed horizontal circular intake with bellmouth transitions under uniform channel flow. The parameters affecting the critical submergence has been identified and thoroughly studied experimentally. Formulas for computing the critical submergence of intakes are presented based on the experimental data, which gives an error of less than 15%.

Keywords: Critical submergence; circular water intakes; Bellmouth transitions.

1 INTRODUCTION

Formation of air-entraining surface vortices at the intakes can be considered as the most serious threat to the efficient functioning of the water intakes. These air-entraining vortices cause operational difficulties including loss of efficiency, vibrations and cavitation in the conveyance system and mechanical damages to the associated machineries like turbines, pumps. Vortex formations are reported in so many installations like Nimbus Dam in California, USA, Harspranget Dam in Sweden, Hirfanli Dam in Turkey and Kariba Dam in Zambia. The best solution for avoiding air-entraining vortices is to provide sufficient submergence of water above the intake. The depth or submergence at which air-entrainment occurs with tip of air-cone of the vortex just reaches the intake is called critical submergence. Figure 1 shows an air entraining vortex formed at the experimental study of present work.

Figure 1. Air-entraining vortex formation

Several experimental and analytical studies have been conducted for the estimation of critical submergence (S_c) for water intakes (Gordon, 1970; Anwar et al., 1977; Jain et al., 1978; Gulliver and Rindels, 1987; Hite and Mih, 1994; Eroglu and Bahadirli, 2007; Ahmad et al., 2008; Yildrim and Kocabas, 1995; Yildrim and Kocabas, 2002; Yildrim and Kocabas, 2003; Yildrim, 2004; Yildrim, 2012; Wang et al., 2011). These studies reveals that critical submergence depends on approach flow Froude number (Fr), intake Froude number (Fri), bottom clearance (c), channel width (B), circulation (Γ), shape of intake and size of intake (diameter in case of circular intake D_i), flow characteristics in the front of the intake, orientation of the intake etc. Most of the earlier studies have been conducted for water intakes having almost stagnant water in the front of the intakes. However, in the diversion type of the hydropower projects, velocity of flow in the front of water intake cannot be ignored. Many of these studies also considered the effects of flow and boundaries on critical submergence. Most of the studies indicate that Froude number is the predominant factor which affects critical submergence. Odgaard (1986) found that the Froude number and circulation number are the major controlling parameters of the critical submergence. The vortex core is considered to be controlled by both kinematic and eddy viscosity, which is a function of the imposed circulation. Yildrim and Kocabas (2002) reported that the occurrence of air core vortex and critical submergence are very sensitive to circulation imposed on the flow. Hai-Feng and Hong-Xun (2008) conducted both experimental and numerical studies of air-core vortex and also determined the relation between the critical submergence and the Froude number and compared with other empirical formulas. Yildrim et al. (2011; 2012) also studied the effect of critical submergence on multiple intakes. This paper studies the critical submergence of horizontal intakes both analytically and experimentally using the concept of potential flow theory by a combined point sink and uniform flow condition. Hashid et al. (2015) studied the flow characteristics of an intake with bellmouth under uniform flow conditions.

This paper addresses the issue of critical submergence of water intakes under flow near the horizontally placed circular bellmouth intake through experimental considerations. Experiments were conducted in the Hydraulics Laboratory of I.I.T. Roorkee, India. Water intake having bellmouth inlet was designed and fabricated in the laboratory and installed in an open channel keeping intake perpendicular to the flow direction in horizontal plane. The discharging capacity of bellmouth intake is high as compared to intake without bellmouth opening. Experiments were performed for intakes of varying sizes, different flow conditions in front of the intake. Various parameters affecting the critical submergence have been identified and an empirical equation has been proposed for computing the critical submergence of a horizontal side intake under uniform approach flow condition.

2 DIMENSIONAL ANALYSIS

Dimensional analysis of different parameters has been conducted for finding the functional relationship of critical submergence. These parameters includes intake size (D_i), main channel velocity (V_1), intake velocity (V_i), bottom clearance (c), channel width (B), head of water at the intake (Y_m), circulation (Γ), density (ρ), viscosity (μ), surface tension (σ), and acceleration due to gravity (g). Treating the critical submergence (S_c) as the dependent variable, the functional relationship may be written as follow

$$S_c = f\left(D_i, B, V_i, V_1, c, Y_m, \rho, \mu, \sigma, g, \Gamma\right) \qquad [1]$$

Taking ρ, V_1 and D_i as the repeating variables, Eq. (1) can be expressed in non-dimensional groups using PI theorem of dimensional analysis as

$$\frac{S_c}{D_i} = f\left(\frac{B}{D_i}, \frac{c}{D_i}, \frac{Y_m}{D_i}, \frac{V_i}{V_1}, \frac{\rho V_1 D_i}{\mu}, \frac{V_1}{\sqrt{gD_i}}, \frac{\Gamma}{D_i V_1}, \frac{\rho D_i V_i^2}{\sigma}\right) \qquad [2]$$

Rearranging the terms, Eq. (2) may, alternatively, be written as

$$\frac{S_c}{D_i} = f\left(\frac{B}{D_i}, \frac{c}{D_i}, \mathrm{Re} = \frac{\rho V_1 D_i}{\mu}, \mathrm{Fr} = \frac{V_1}{\sqrt{gY_m}}, \mathrm{Fri} = \frac{V_i}{\sqrt{gD_i}}, \frac{\Gamma}{D_i V_1}, We = \frac{\rho D_i V_i^2}{\sigma}\right) \qquad [3]$$

Yildirim and Jain (1981) and Padmanabhan and Hecker (1984) have reported that surface tension may be important for vortices with low circulation only. Based on the experimental results on a horizontal intake, Ahmad et al. (2008) neglected the effect of circulation on critical submergence. Previous studies reveal that the critical submergence mainly depends on the intake Froude number (Gordon, 1970; Reddy and Pickford, 1972; Gulliver et al., 1986 and Swaroop, 1973). Based on the experimental study, Jain et al. (1978) concluded that there is no influence of surface tension on the critical submergence when Weber number (We) > 120. Padmanabhan and Hecker (1984) suggested We > 600 and Reynolds number (Re) > 7.7 X 10^4 for neglecting the effects of surface tension and viscosity. Odgaard (1986) studied about vertical gravity intake and showed that in the case of air entraining vortices in a still water body, for We > 720, Re > 1.1 x 105, the effects of surface tension and viscosity can be neglected. In the present experiments, the Reynolds and Weber numbers are generally larger than these thresholds; therefore, these terms have been dropped out from Eq. (3). Bottom clearance, c has been kept constant throughout the experimentation. Hence the term c/D_i can also be omitted. Considering the effect of various parameters as discussed above, Eq. (3) may be written as

$$\frac{S_c}{D_i} = f\left(\mathrm{Fr}, \mathrm{Fri}, \frac{B}{D_i}\right) \qquad [4]$$

The data collected in the experimental program have been analyzed for obtaining the relationship for S_c/D_i. Effect of the parameters in Eq. (3) on the critical submergence has also been discussed.

3 EXPERIMENTAL PROGRAMME

Experiments were conducted at the Hydraulic Engineering laboratory of IIT Roorkee. An open channel of length of 9.47 m, width of 0.495 m and height of 0.65 m is used for this study which is shown in Figure 2. Discharge was provided through a valve into the approach channel from where it flows to the main channel. Splitter plates and flow wave suppressors were used to get a uniform flow at the bellmouth intake. Approach channel length upstream of the intake was sufficient to form a developed flow at the intake section. The intake was placed at a distance of 3.47 m from the downstream end. Intake pipes of three diameters, 0.0675 m, 0.106 m and 0.131 m were used for this study. Each pipe was positioned at a clearance with $c = D_i$. Bell mouth transitions were designed as per IS: 9761 for each intake pipes and placed in flush with the left wall of the flume. A sluice gate was provided at the end of channel in order to maintain the desired depth of water in the channel by adjusting the gate. The intake pipe was of length 1m and attached to an outlet pipe which was connected to a 30HP centrifugal pump. A magnetic flow meter was placed on the outlet pipe as shown in the Figure 2. Discharge in the inlet pipe was controlled using a valve fitted in the inlet pipe. The water drawn from the intake was discharged into the sump. Water discharging from the tail gate was passed over a sharp crested weir to measure the discharge. This discharge was also passed to the sump. The water from the sump was recirculated into the test system for further experimentation. Photographic view of the experimental setup is shown in Figure 3.

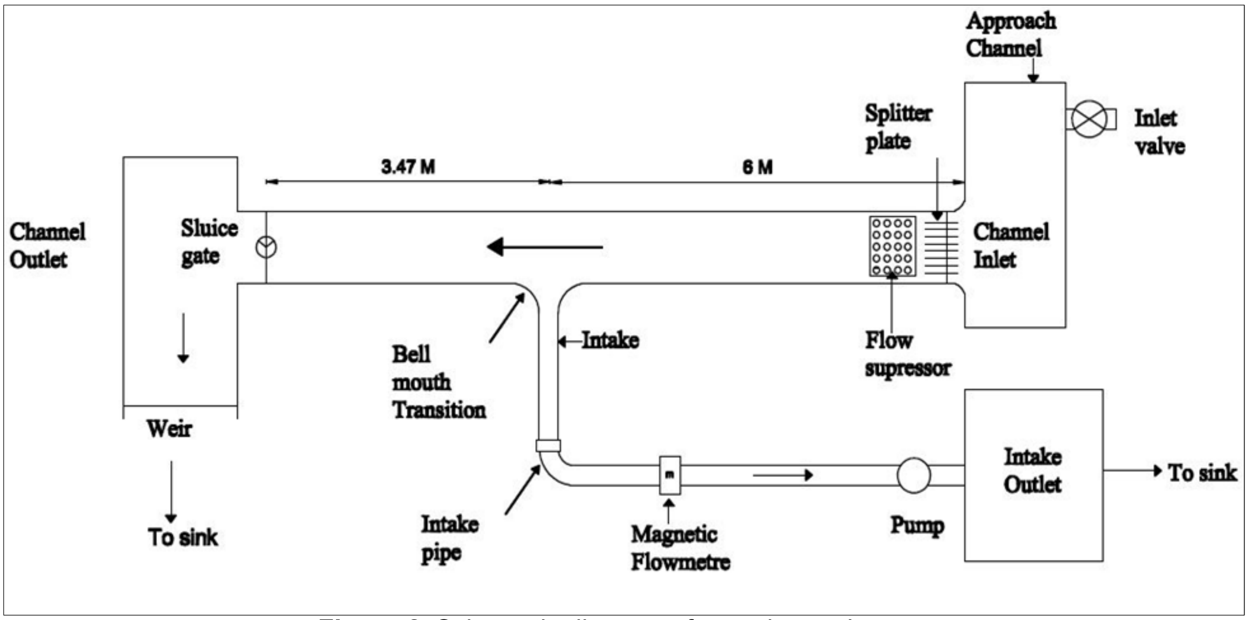

Figure 2. Schematic diagram of experimental setup

Figure 3. Photographic view of experimental setup

After placing one of the intake pipes (Figure 3) and passing the required discharge to the main channel, observations were taken. All the observations were made under stable and uniform flow conditions. Observation for 1-2 h was made to see whether or not any free vortex develops. If no air entrainment vortex occurred during this time, the downstream sluice gate was lifted for some very small amount (submergence was decreased). These steps were repeated until the air-entraining free vortex developed. When the air entraining vortex developed, the measurements related to channel discharge Q_o, intake discharge Q_i, critical submergence S_c, and uniform flow depth Y_m were measured after stabilizing the flow in the main channel. The experiments were conducted for 6 - 8 different discharges through intake keeping the discharge in the main channel constant. The experiments were also conducted for constant discharge through intake and varying the discharge in the main channel. The intake discharge was adjusted through a valve fitted at the end of the intake pipe just after the pump end. The above steps were repeated for all intake pipes. All experiments were conducted for the subcritical flow. Range of data collected in the present study is given in Table 1.

Table 1. Range of data collected in the experimental study

Parameter	Unit	Range of data	
		Min.	Max.
Q_i	m^3/s	0.0124	0.027
D_i	m	0.0675	0.131
H	m	0.1973	0.4462
Fr	Dimensionless	0.081	0.435
Fr_i	Dimensionless	1.06	7.21
Re	Dimensionless	56157	2991355
Q_m	m^3/s	0.021	0.068

4 RESULTS AND DISCUSSION

Data obtained from the experimentation was analyzed thoroughly to understand the effect of different parameters on the problem of critical submergence. Observations are made during the experimentation showed that the formation of air-entraining vortex is a gradual process. Critical submergence was noted when the tail of air core vortex enters into the bellmouth intake and sometimes producing sharp noise indicating the size of vortex. Larger turbulence caused by the higher channel flow velocity created bigger air entraining vortices.

Figure 4 shows the variation of the S_c/D_i with channel Froude number (Fr) for different intake sizes. It shows that critical submergence of the circular intake decreases with increase of the Fr of channel flow when other parameters such as size of the intake and bottom clearance are kept constant. As the velocity in the channel increases Fr also increases since it is a function of velocity in the channel and hence only those streamlines which are nearer to the intake can enter into the intake while the rest pass without entering into the intake. Hence, with the increase of Fr, S_c/D_i decreases.

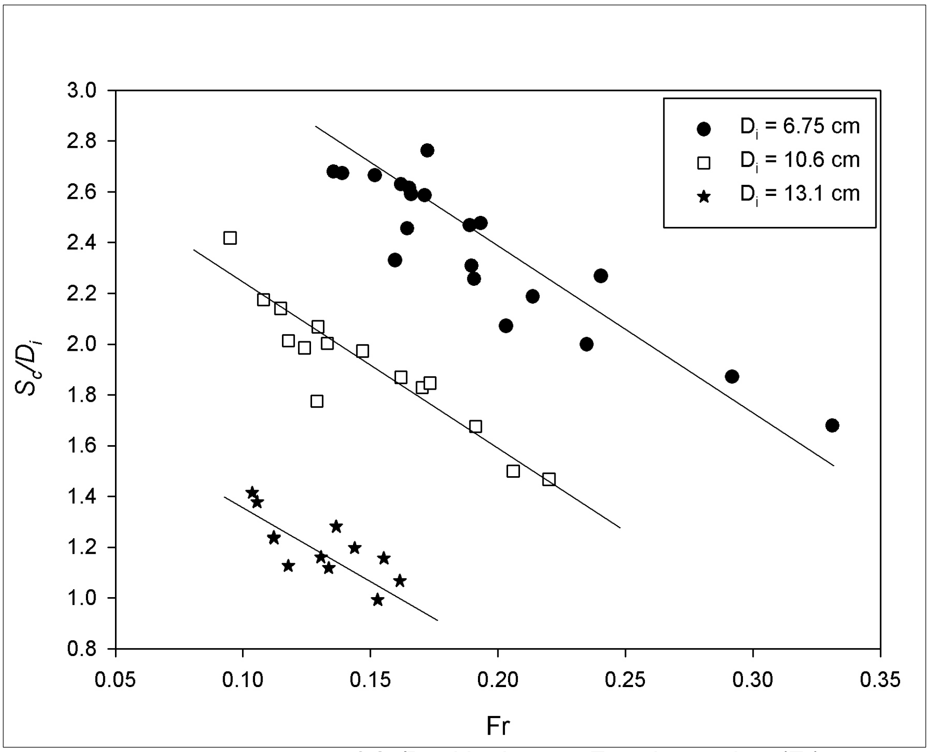

Figure 4. Variation of S_c/D_i with channel Froude number (Fr)

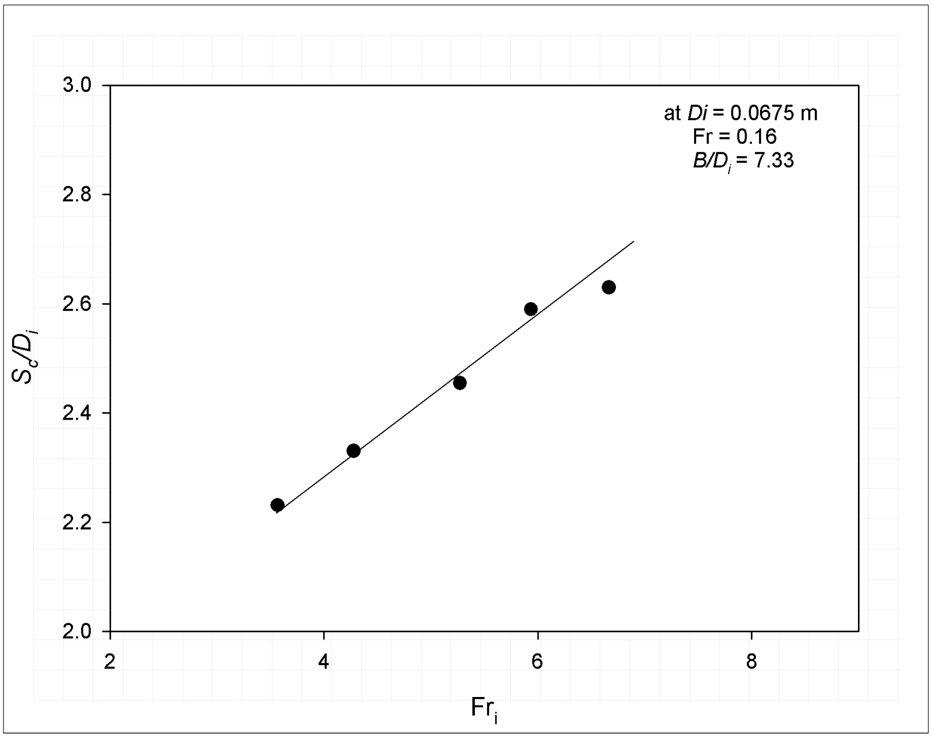

Figure 5. Variation of S_c/D_i with intake Froude number (Fr_i)

Figure 5 shows the effect of Fr_i on the S_c/D_i. This graph shows an increasing trend of S_c/D_i with Fri when other parameters are kept constant like D_i, Fr and B/D_i. The same behavior was observed for each size of the intake. The intake Froude number increases with increase of discharge in the intake. Such increase in intake Froude number results in increase in surface area of the Critical Spherical Sink Surface (CSSS), which is an imaginary body created in front of the intake where the intake suction acts as explained in the theory of potential flow (Yuan 1967) and stream lines from higher level approaches towards intake which result in an increase of S_c/D_i.

The data from the experiments were used to validate the available equations from the literature. Figure 6 shows the validation of accuracy of Reddy & Pickford (1972) and Swaroop (1973) equations using present data for $c = D_i$. Reddy and Pickford (1972) studied the vortices at intakes in conventional sump and Swaroop (1973) worked on the vortex formation at intake structures. Ahmad et al. (2008) studied the critical submergence in a horizontal circular intake without bellmouth transition. The available equations did not give satisfactory results with the present data. This may be due to effect of bottom clearance as the present study neglected the boundary effect from bottom clearance by keeping the intake sufficiently high.ie. $c = D_i$. .

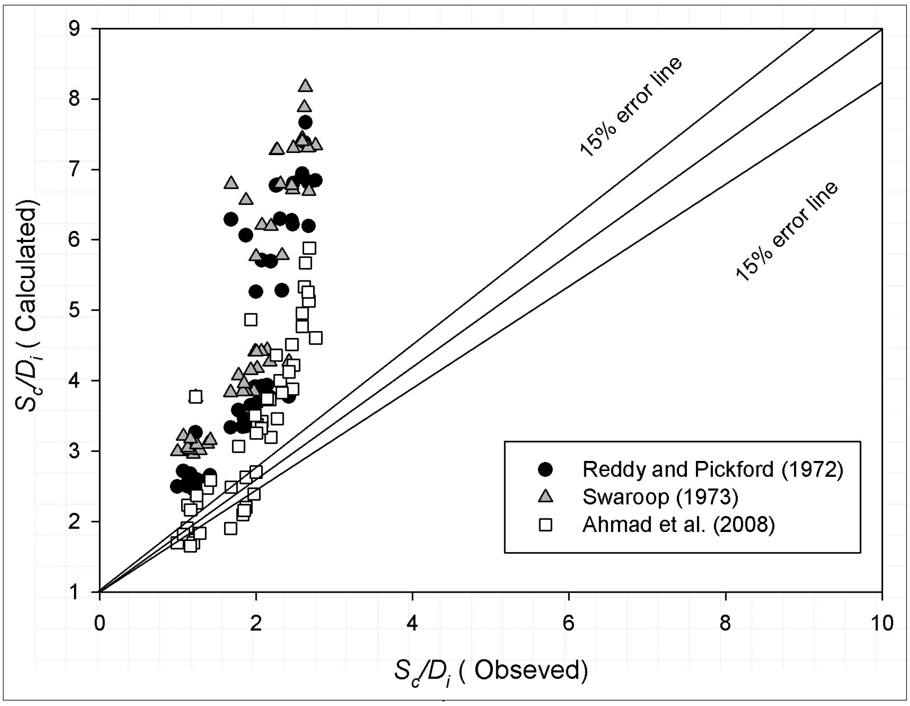

Figure 6. Validation of accuracy of Reddy & Pickford (1972) and Swaroop (1973) equations using present data for $c = D_i$

In the light of the above, it is difficult to comment on the accuracy of the available equations for critical submergence and also the reliability of the available data. Therefore, it is proposed to develop new equations for critical submergence using the data collected in this study. The total data sets collected is used to evolve relationship for S_c/D_i for the different positioning of the intake pipes. In literature many researchers have used the method of least square (Hammerstrom, 1993; Hussain et al., 2011; Hashid et al., 2015) for proposing an equation. Following equations are proposed for S_c/D_i for $c = D_i$, using the least squares technique,

$$\frac{S_c}{D_i} = 1.12\text{-}4.54\mathrm{Fr} + 0.175\mathrm{Fri} + 0.169\frac{B}{D_i} \qquad [5]$$

Graphical comparison of the observed and computed values of S_c/D_i for the side bellmouth intake is carried out as shown in Figure 7. It is found that most of the data for computed S_c/D_i lie within ±15% of the observed ones, which is a satisfactory prediction of S_c/D_i for side bellmouth intake. This error in the computation of S_c/D_i remains even which may be due to neglecting the parameters like circulation, surface tension and boundary effects in the practical equation. Even though the bellmouth transition at the intake increase the efficiency of the intake and decreases the critical submergence when compared to those without bell mouth, the hindrance of flow created due to the boundaries affects the critical submergence adversely.

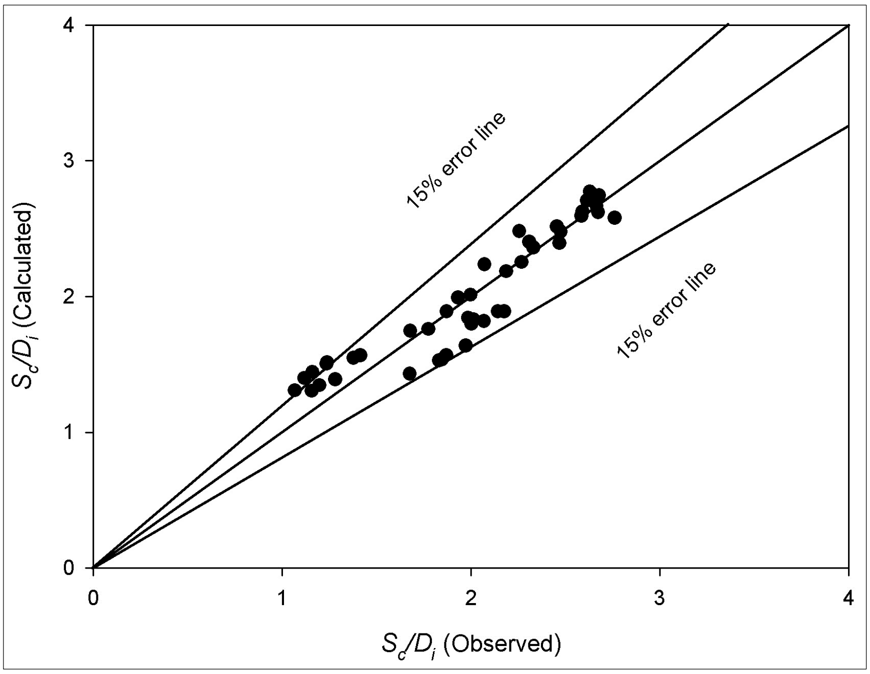

Figure 7. Validation of Eq. 5 for finding critical submergence at $c = D_i$

5 CONCLUSION

A detailed study on the critical submergence for the side intake with bellmouth transition in an open channel under uniform flow has been done experimentally at the hydraulics laboratory of IIT Roorkee. Based on the experimentation done in the present work, it can be concluded that the proposed equation for critical submergence gives satisfactory results with an error less than 15%. In the case of critical submergence, 15% error is obvious as it is difficult to obtain error free observations. Analysis of data reveals that S_c/D_i increases with an increase in intake Froude number, but decrease with an increase in channel Froude number.

REFERENCES

Ahmad, Z., Rao, K.V. & Mittal, M.K. (2008). Critical Submergence for Horizontal Intakes in Open Channel Flows. *Dam Engineering*, 19(2), 71-90.

Anwar, H.O., Weller, J.A. & Amphlett, M.B. (1978). Similarity of Free Vortex at Horizontal Intake. *Journal of Hydraulic Research*, 2, 95-105.

Durai, E.S.R., Ahmad, Z. & Mittal, M.K. (2007). Critical Submergence at Vertical Pipe Intakes. *Dam Engineering*, 18(1), 17-33.

Eroglu, N. & Bahadirli, T. (2007). Prediction of Critical Submergence for Rectangular Intake. *Journal of Energy Engineering*, 133(2), 91-103.

Gordon, J.L. (1970). Vortices at Intake Structures. *International Water Power & Dam Construction*, 4, 137-138.

Gulliver, J.S. & Arndt, R.E.A. (1993*). Hydropower Engineering Handbook*. McGraw-Hill Inc, New York, NY, US.

Hai-feng, L.I., Hong-Xun, C., Zheng, M.A. & Zhou, Y. (2008). Experimental and Numerical Investigation of Free Surface Vortex, *Journal of Hydrodynamics*, 20(4), 485-491.

Hammerstrom, D. (1993). Working with Neural Networks. *IEEE Spectrum*, 30(7), 46-53.

Hashid, M., Hussain, A. & Ahmad, Z. (2015). Discharge Characteristics of Lateral Circular Intakes in Open Channel Flow. *Flow Measurements and Instrumentation*, 46, 87–92.

Hussain, A., Ahmad, Z. & Asawa, G.L. (2011). Flow through Side Square Orifices in Open Channels. *ISH Journal of Hydraulic Engineering*, 17, 1.

Indian Standard Code IS 9761 (1995). *Hydropower intakes - criteria for hydraulic design*, Indian Standard Code IS 9761.

Jain, A.K. (1977). Vortex Formation at Vertical Pipe Intakes, *Ph.D. Thesis*. University of Roorkee (now IIT Roorkee), Roorkee, India.

Khodashenas, S.R., Roshan, R., Sarkardeh, H. & Azamathulla, H.M. (2010). Vortex Study at Orifice Spillways of Karun III Dam. *Dam Engineering*, 21(2), 1-12.

Kocabas F & Yildrim N. (2002). Effect of Circulation on Critical Submergence for an Intake. *IAHR Journal of Hydraulic Research*, 40(6), 741-752.

Marghazar, S.H., Montazerin, N. & Rahimzadeh, H. (1993). Flow Field, Turbulence and Critical Condition at a Horizontal Water Intake. *Journal of Power and Energy,* 217, part A.

Odgaard, A.J. (1986). Free Surface Air Core Vortex. *ASCE Journal of Hydraulic Engineering*, 112(7), 610-620.
Padmanabhan, M. & Hecker, G.E. (1984). Scale Effects in Pump Sump Models. *ASCE Journal of Hydraulic Engineering*, 110(11), 1540-1556.
Reddy, Y.R. & Pickford, J.A. (1972). Vortices at Intakes in Conventional Sump. *International Water Power & Dam Construction*, 24(3).
Sarkardeh, H., Zarrati, A.R. & Roshan, R. (2010). Effect of Intake Head Wall and Trash Rack on Vortices. *Journal of Hydraulic Research*, 48(1), 108-112.
Swaroop, R. (1973). Vortex Formation at Intakes, *M.E. Thesis*. University of Roorkee (now IIT Roorkee), Roorkee, India.
Wang, Y.K., Jiang, C.B. & Liang, D.F. (2011). Study on the Critical Submergence of Surface Vortices and the Design of Anti-Vortex Intakes. *Science China Technological Sciences*, 54(4), 799–804.
Yildirim, N. & Kocabas, F. (1995). Critical Submergence for Intakes in Open Channel Flow. *ASCE Journal of Hydraulic Engineering*, 121(12), 900-905.
Yildirim, N. & Kocabas, F. (1998). Critical Submergence for Intakes in Still Water Reservoir. *ASCE Journal of Hydraulic Engineering*, 124(1), 103-104.
Yildirim, N. Kocabas, F. & Gulcan, S.C. (2000). Flow Boundary Effects on Critical Submergence of an Intake Pipe. *ASCE Journal of Hydraulic Engineering,* 126(4), 288-297.
Yildirim, N. & Kocabas, F. (2002). Prediction of Critical Submergence for an Intake Pipe. *IAHR Journal of Hydraulic Research*, 40(4), 507-518.
Yildirim, N. (2004). Critical Submergence for a Rectangular Intake. *ASCE Journal of Engineering Mechanics*, 130(10), 1195-1210.
Yildirim N & Tastan K. (2009). Critical Submergence for Multiple Pipe Intakes. *ASCE, Journal of Hydraulic Engineering*, 135(12), 1052-1062.
Yildirim, N. Akay, H. & Karem, T. (2011). Critical Submergence for Multiple Pipe Intakes by the Potential Flow Solution. *IAHR Journal of Hydraulic Research*, 49(1), 117-121.
Yuan, S.W. (1967). *Fundamentals of Fluid Mechanics*. Prentice-Hall Inc., Englewood Cliffs. N.J.

Proceedings of the 37th IAHR World Congress
August 13 – 18, 2017, Kuala Lumpur, Malaysia

VELOCITY PROFILE IN A SEDIMENT-LADEN FLOW THROUGH MIXING LENGTH APPROACH

KOELI GHOSHAL[1] & MANOTOSH KUMBHAKAR[2]

[1,2] Department of Mathematics, Indian Institute of Technology Kharagpur, Kharagpur 721302, India
koeli@maths.iitkgp.ernet.in; manotosh.kumbhakar@gmail.com

ABSTRACT

The vertical distribution of stream wise velocity of fluid in an open channel turbulent flow laden with sediment is of primary interest and a long standing topic of research. Generally, the velocity comes through the Reynolds-Averaged Navier-Stokes equation (RANS eqn.) where the unknown Reynolds stresses are modeled by Prandtl's mixing length hypothesis. However, researchers pointed out that the mixing length model introduced by Prandtl is not really correct close to the bed. Present work makes use of a modified mixing length model that considers velocity fluctuations parallel and normal to the mean flow directions in different ways. On the other hand, in clear water turbulent flows the mean velocity profile is described in near bed region by the well-known logarithmic law whose shape is characterized by the von Karman parameter κ having a universal value 0.41 for clear water flows. Further research suggests that κ is different from 0.41 in the presence of sediment particles. Furthermore, previous study shows that the von Karman parameter in sediment-laden flow depends on a function called as damping factor. The damping factor is a function of the distance to the channel bed and depends on the velocity and concentration profiles as well as their gradients. Therefore, this study derives the mean velocity profile of turbulent flow starting from the RANS equation for a two-dimensional steady-uniform turbulent flow by taking into account the aforementioned important key factors of sediment-laden turbulent flow. The derived model is a first order non-linear differential equation which has been solved numerically and validated by comparing it with available experimental measurements. Present model shows good prediction accuracy throughout the water depth especially in the region close to the channel bed.

Keywords: Turbulent flow; RANS eqn.; mixing length; von karman constant; mean velocity.

1 INTRODUCTION

Understanding the mechanism of sediment transport in natural rivers and laboratory channels is a topic of primary interest and this needs essentially the knowledge of vertical distribution of stream wise velocity of fluid carrying sediments. Prandtl (1925) was the pioneer in this field to study the vertical velocity distribution in an open channel and after that numerous models on velocity (Guo and Julien, 2001; Mazumder and Ghoshal, 2006; Kundu and Ghoshal, 2012; Pal and Ghoshal, 2016) have been developed on the basis of his model which is widely known as 'log-law'. The model is based on two fundamental assumptions: (i) the mixing length is proportional to the vertical distance from the channel bed, and (ii) velocity fluctuations, normal and parallel to the channel bed behave similarly. But further research revealed that the Prandtl's mixing length model is not very much correct near the channel bed. The RANS equation contains both the gradient of mean velocity profile and the Reynolds stresses and difficulties arise due to the fact that close to the wall the gradient of mean velocity is very large compared to the Reynolds stresses and at the center of the flow the Reynolds stresses are very large compared to the gradient of velocity. Therefore small errors in modeling stresses may affect the mean velocity seriously which may result into the poor prediction accuracy of the time averaged velocity profile starting from the channel bed to the center of the channel. To overcome these discrepancies, researches have been carried out since long. Different models on mixing length were developed by researchers (van Driest, 1956; Eckelmann, 1974; Umeyama and Gerittsen, 1992) some of which is well applicable for sediment-laden flow also. But all these models are based on modified mixing length which is same for both u' fluctuations in the mean flow direction and v' fluctuations normal to the mean flow direction. Such modeling for Reynold stresses present in the RANS equation may lead to errors which will affect the determination of the vertical profile of mean velocity. Obermeier (2006) was the first to modify the Prandtl's model based on differently modified mixing lengths l_u for u' fluctuations and l_v for v' fluctuations. His velocity model derived from RANS equation for fully developed turbulent flow applying the two different mixing lengths l_u and l_v lead to satisfactory result. But it lacks in showing how good the model is when compared to laboratory channel data. Also that, it is yet to be known from the study that if the model works to study velocity in a flow field where sediments are present.

  / ISSN 1562-6865 (Online) - ISSN 1063-7710 (Print)

Castro-Orgaz et al. (2012) showed that the so called von-Karman constant is not a constant in a sediment-laden flow and it is influenced by quite a number of factors. Taking into account the effect of the added mass force on a particle in a sediment-fluid mixture together with the density stratification effect, they proposed a correction factor ψwhich relates the von-Karman constant κ_m in sediment-mixed fluid and the von Karman constant κ in clear fluid by the relation $\kappa_m=\kappa\psi$. Apart from the added mass & stratification effects, their ψ factor includes the concentration gradient and velocity gradient.

The main objective of the present study is to derive vertical distribution of mean velocity in a sediment mixed fluid starting from RANS equation for a two-dimensional steady-uniform turbulent flow by taking into account velocity fluctuations normal and parallel to the bed differently and by including the effects of sediments present in the flow through a modified von-Karman constant. The equation developed for stream wise normalized velocity gradient is a first order non-linear differential equation which is solved numerically. Unlike log-law, it is able to predict the velocity well in the near-bed region also. Validation of the model has been done by comparing it with experimental data available in literature.

2 MATHEMATICAL MODEL

Let us consider a steady-uniform flow (i.e. zero-pressure gradient in the stream wise direction). It is assumed that the channel bed makes an angle θ with the x-direction. For two-dimensional steady flow, the well-known Reynolds-Averaged Navier-Stokes (RANS) equations reduce to x-component (along the channel bed) and y-component (normal to the channel bed) (Dey, 2014)

$$\bar{u}\frac{\partial \bar{u}}{\partial x}+\bar{v}\frac{\partial \bar{u}}{\partial y}=g_x-\frac{1}{\rho}\frac{\partial \bar{p}}{\partial x}+v\left(\frac{\partial^2 \bar{u}}{\partial x^2}+\frac{\partial^2 \bar{u}}{\partial y^2}\right)-\left(\frac{\partial \overline{u'u'}}{\partial x}+\frac{\partial \overline{u'v'}}{\partial y}\right) \tag{1a}$$

$$\bar{u}\frac{\partial \bar{v}}{\partial x}+\bar{v}\frac{\partial \bar{v}}{\partial y}=g_y-\frac{1}{\rho}\frac{\partial \bar{p}}{\partial y}+v\left(\frac{\partial^2 \bar{v}}{\partial x^2}+\frac{\partial^2 \bar{v}}{\partial y^2}\right)-\left(\frac{\partial \overline{v'u'}}{\partial x}+\frac{\partial \overline{v'v'}}{\partial y}\right) \tag{1b}$$

where $\bar{u}$, $\bar{v}$ are the time-averaged velocity in x and y directions respectively and u', v' are the corresponding fluctuations, $\bar{p}$ is the time-averaged pressure,ν is the kinematic viscosity of fluid, ρ is the density of fluid,g_x and g_y are the gravitational acceleration components in x and y directions respectively.

Furthermore, if $\bar{u}=\bar{u}(y)$, $\bar{v}=0$, $g_x=g\sin\theta$ and the flow parameters are invariant along the stream wise direction (x-direction) due to uniform flow, then Eq. (1a) reduces to the following equation

$$-\frac{d}{dy}\left[\mu\frac{d\bar{u}}{dy}-\rho\overline{u'v'}\right]=\frac{\tau_0}{h} \tag{2}$$

Here $\tau_0=\rho g h S_0$and $\sin\theta\approx S_0$, μ is the coefficient of dynamic viscosity of fluid ($=\rho v$), τ_0 is the bed shear stress, S_0 is the bed slope and h is the maximum flow depth. Integration of Eq. (2) yields the equation

$$\mu\frac{d\bar{u}}{dy}-\rho\overline{u'v'}=\tau_0\left(1-\frac{y}{h}\right)=\rho u_*^2\left(1-\frac{y}{h}\right) \tag{3}$$

The non-dimensionalization of Eq. (3) gives

$$\frac{du^+}{dy^+}-\overline{u'v'}^+=1-\frac{y^+}{h^+} \tag{4}$$

where the non-dimensionalization is done as the following:

$u^+=\frac{u}{u_*}$,$y^+=\frac{yu_*}{v}$, $\overline{u'v'}^+=\frac{\overline{u'v'}}{u_*^2}$ and $h^+=\frac{hu_*}{v}=Re_\tau$; u_* is the shear or friction velocity which is defined as $u_*=\sqrt{\tau_0/\rho}$, Re_τ is the Reynolds number based on the shear velocity.

To obtain the mean velocity profile from Eq. (4), Reynolds stress needs to be known. The most popular model for the Reynolds stresses was given by Prandtl based on the mixing length hypothesis is given as:

$$-\overline{u'v'}^+=l^{+2}\left|\frac{du^+}{dy^+}\right|\frac{du^+}{dy^+} \tag{5}$$

where normalized mixing-length $l^{+} = \kappa y^{+}$, κ being the von Karman constant. However, the model of Prandtl is based on two assumptions (i) mixing length l is linearly proportional to the distance y from the channel bed, and (ii) velocity fluctuations u' and v' behave similarly. But these assumptions are not totally correct in near-bed region (Obermeier, 2006). To overcome these discrepancies, following modifications are used according to Obermeier (2006):

$$u'^{+} \sim l_u^{+} \frac{du^{+}}{dy^{+}} \text{ where } l_u^{+} = \frac{\kappa y^{+}}{1+\beta}\left\{1+\beta.\frac{2}{\pi}\arctan\left(\frac{y^{+}}{\delta}\right)^{2}\right\} \quad (6)$$

and

$$v'^{+} \sim l_v^{+} \frac{du^{+}}{dy^{+}} \text{ where } l_v^{+} = l_u^{+}\left\{1-\exp(-y^{+}/A^{+})\right\} \quad (7)$$

The parameter β accounts for the deviation for the linear behavior of u'^{+}, δ determines the location of maximum of $\overline{u'^{+2}}$ and A^{+} characterizes the distance from the wall where l_u and l_v behave similarly. The values of these parameters were obtained by fitting the model to experimental data (Obermeier, 2006) and the values obtained are β=3, δ=7.5 and A^{+}=43. Using the modified mixing lengths, Reynolds stress can be written as follows:

$$-\overline{u'v'}^{+} = l_u^{+} l_v^{+} \left|\frac{du^{+}}{dy^{+}}\right| \frac{du^{+}}{dy^{+}} \quad (8)$$

All the above mentioned models have been derived for clear-water flows. However, the present study deals with sediment-laden open channel flows. Castro-Orgaz et al. (2012) discussed the effects of sediment suspension on κ. They proposed the parameter for sediment-laden flows in analogy with the clear-water flows as follows:

$$\kappa_m = \kappa\psi \quad (9)$$

This equation suggests that κ_m which varies with the vertical distance y depends on the function ψ=ψ(y). The function ψ can be interpreted as a correction factor to the universal value of $\kappa = 0.41$ for clear water flows. Furthermore, it includes the effect of velocity and concentration gradients in suspension flows, as can be seen in the following. The function ψ can be written as follows:

$$\psi = 1+2u^{+}\left(\frac{R+1-\beta_1}{1+RC}\right)\frac{dC}{dy^{+}}\left(\frac{du^{+}}{dy^{+}}\right)^{-1} \quad (10)$$

where R is the submerged specific gravity, C is the volumetric concentration of sediment and $\beta_1 = 1 - K, K$ being the added-mass coefficient. Using Eqs. (6), (7), (8), along with the von-Karman parameter of sediment-laden flow Eq. (9), in Eq. (4) the result:

$$\left(\frac{du^{+}}{dy^{+}}\right)^{2} + \left\{4u^{+}T_1 + \frac{1}{T_2}\right\}\frac{du^{+}}{dy^{+}} + 4u^{+2}T_1^{2} - \frac{1-\frac{y^{+}}{D^{+}}}{T_2} = 0 \quad (11)$$

From Eq. (8), gradient of stream wise normalized velocity can be obtained as follows:

$$\frac{du^{+}}{dy^{+}} = \frac{-4u^{+}T_1 - \frac{1}{T_2} + \sqrt{\left[\frac{1}{T_2}\left\{4u^{+}T_1 + \frac{1}{T_2} + 4\left(1-\frac{y^{+}}{D^{+}}\right)\right\}\right]}}{2} \quad (12)$$

where $T_1 = \left(\frac{R+1-\beta_1}{1+RC}\right)\frac{dC}{dy^{+}}$ and $T_2 = \frac{\kappa^2 y^{+2}}{(1+\beta)^2}\left\{1+\beta.\frac{2}{\pi}\arctan\left(\frac{y^{+}}{\delta}\right)^{2}\right\}^{2}\left\{1-\exp(-y^{+}/A^{+})\right\}$.

It can be seen that to obtain the mean velocity profile from Eq. (12), a concentration profile of sediment is needed as can be observed from the expression of T_1. For that purpose, an exponential-type concentration profile proposed by Montes (1973) is used here:

$$C = C_b \exp\left(-\frac{A}{h}y\right)\left\{\frac{1+\exp\left(-\frac{2D}{h}y\right)}{2}\right\}^{-A/D} \quad (13)$$

where C_b is the maximum concentration, A and D are empirical coefficients. According to Montes (1973), D can be taken approximately as 30 and the value of A depends on the ratio of settling velocity of sediment particle ω_s to the shear velocity u_*.

Figure 1 plots the mean velocity profile obtained numerically from Eq. (12) with the use of concentration profile Eq. (13). Also, the well-known logarithmic velocity profile (von Karman, 1930) is compared with the present model. It can be observed that for the very large Reynolds number, log-law model agrees very well with the proposed model. But significant differences are found in the figures for smaller Reynolds number. The differences increase for decreasing Reynolds number simply because log-law is not satisfactory near the water surface in sediment-laden flow.

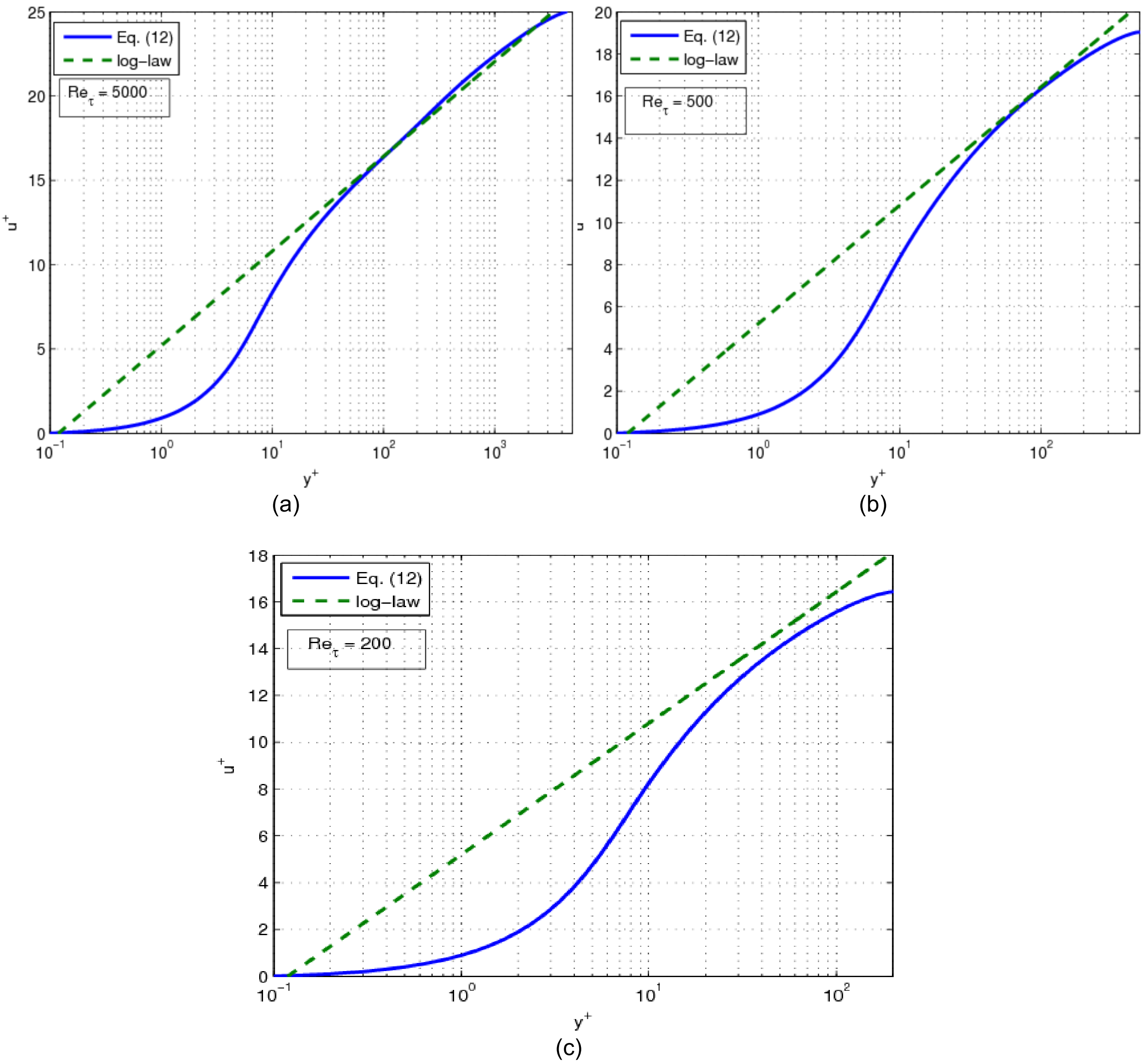

Figure 1. Comparison between the mean velocity profile (Eq. 12) and log-law profile (von Karman 1930) for different shear Reynolds number (a) $Re_\tau = 5000$, (b) $Re_\tau = 500$ and (c) $Re_\tau = 200$.

3 VALIDATION OF THE MODEL

Present model is validated with the experimental data set of Einstein and Chien (1955) and Wang and Qian (1989). For that purpose, Run S4, S8 and S11 from Einstein and Chien (1955) and Run 7, 14 and 21 from Wang and Qian (1989) are used. Figure 2 plots the present velocity profile in comparison with the three different sets of data from Einstein and Chien (1955) with two different particle diameters starting from medium sand (d_{50}=0.94 mm) to coarse sand (d_{50}=1.3 mm). It can be observed from the figures that the present model can predict the mean velocity profile near the channel bed with some slight deviations in the upper region. Figure 3 shows the comparison between the proposed model and the three different sets of data of Wang and Qian (1989) having particle diameters 0.268, 0.960 and 1.420 mm. It can be seen from the figure that the derived model agreed with the observed values well throughout the water depth.

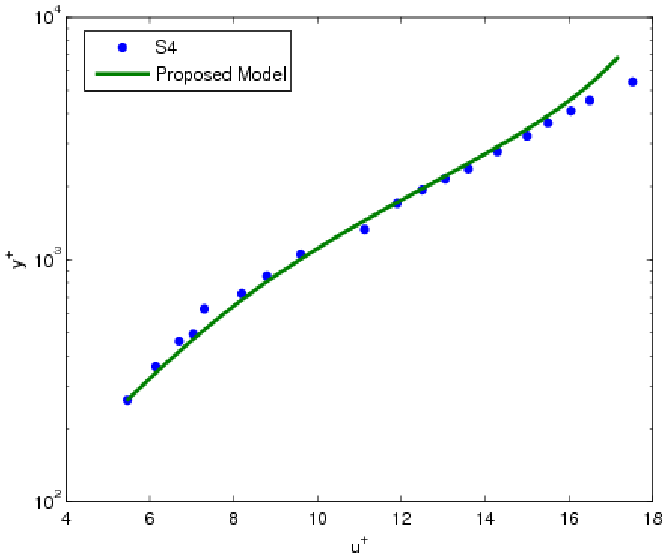

(b)

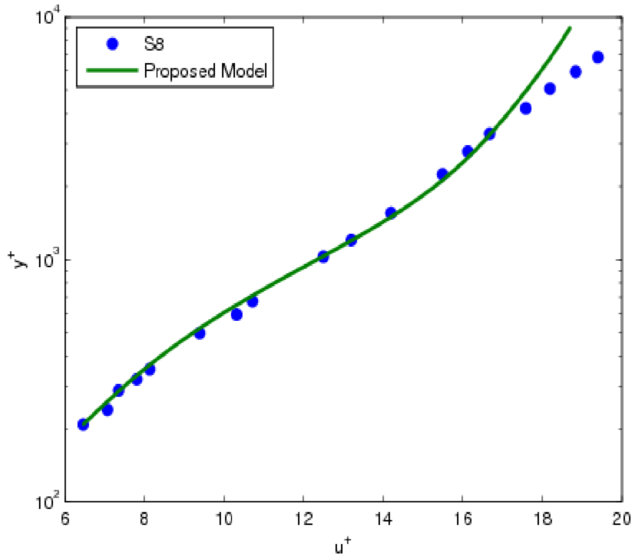

(c)

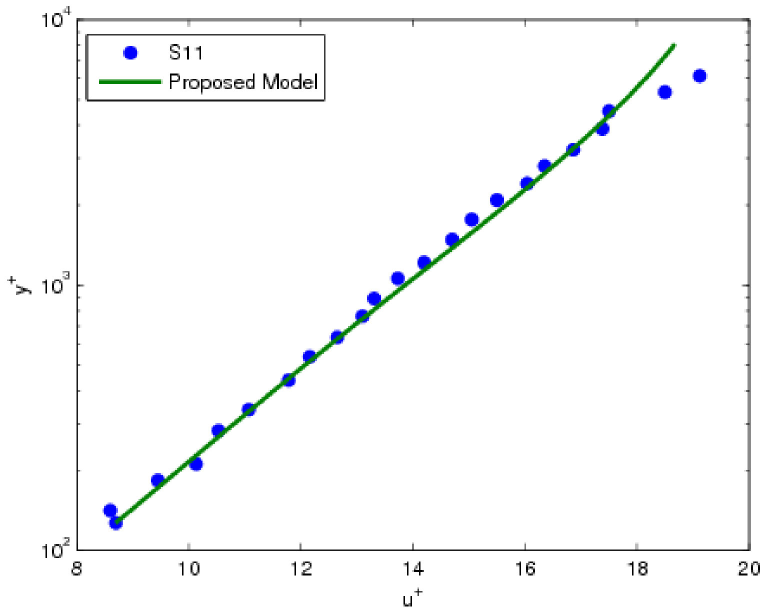

(c)

Figure 2. Comparison between the mean velocity profile (Eq. 12) and three data set of Einstein and Chien (1955) (a) S4, (b) S8 and (c) S11.

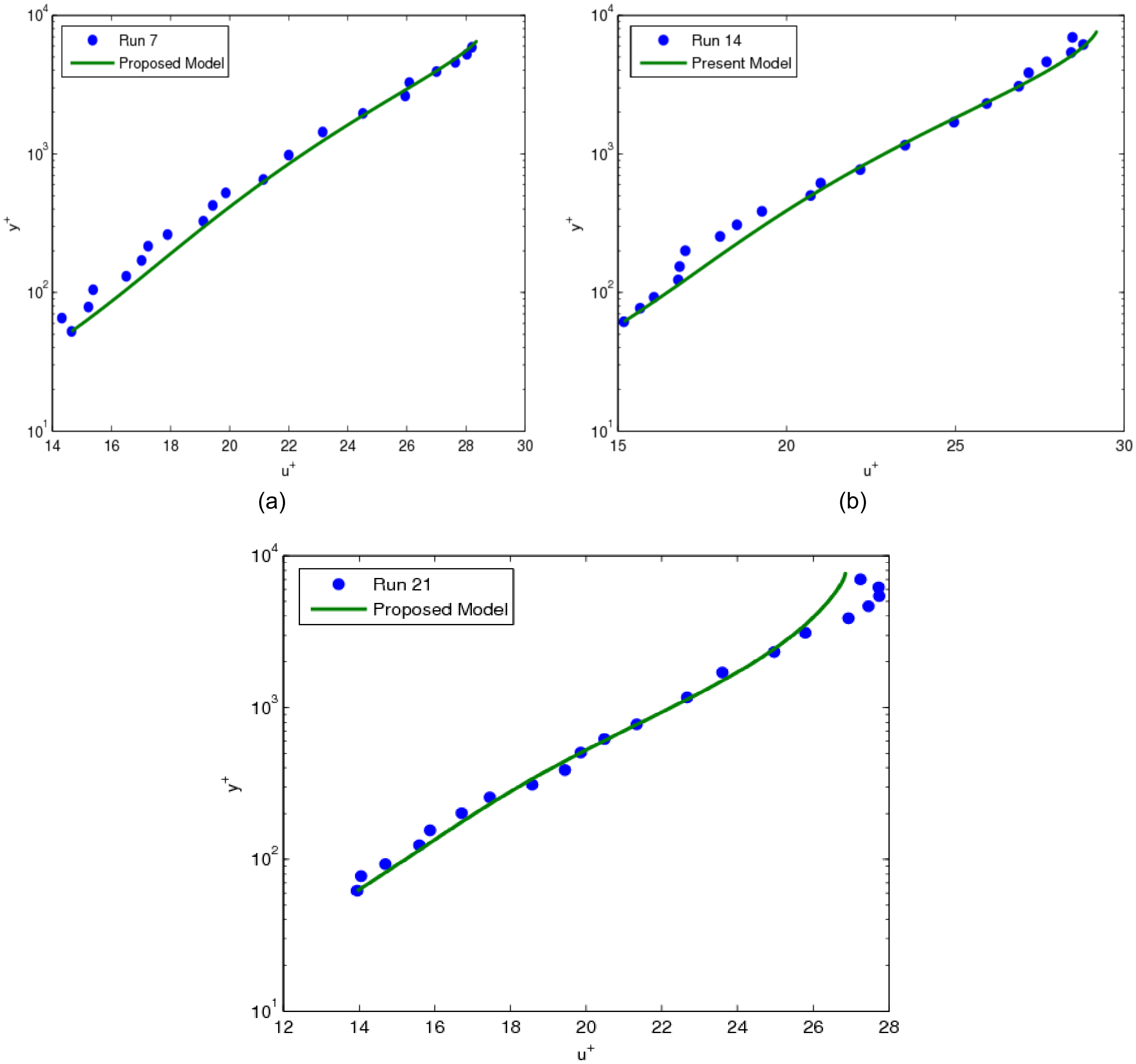

(a) (b) (c)

Figure 3. Comparison between the mean velocity profile (Eq. 12) and three data set of Wang197 and Qian (1989) (a) Run 7, (b) Run 14 and (c) Run 21.

4 CONCLUSIONS

Present study derives the mean stream-wise velocity profile vertically in a sediment-laden flow starting from the Reynolds-Averaged Navier-Stokes (RANS) equation. Derivation of the present model uses modified mixing lengths by addressing the discrepancies associated with the well-known Prandtl's mixing length model.

The model is compared with the classical logarithmic velocity profile. Also, the proposed model is validated with the experimental observations and a good agreement is found between the observed and measured values.

REFERENCES

Castro-Orgaz, O., Giráldez, J.V., Mateos, L. & Dey, S. (2012). Is the Von Karman Constant Affected by Sediment Suspension?, *Journal of Geophysical Research: Earth Surface*, 117(F4), 1-16.

Dey, S. (2014). *Fluvial Hydrodynamics*. Springer–Verlag, Berlin, Germany.

Eckelmann, H. (1974). The Structure of the Viscous Sublayer and the Adjacent Wall Region in a Turbulent Channel Flow, *Journal of Fluid Mechanics*, 65(03), 439-459.

Einstein, H.A. & Chien, N. (1955). *Effects of Heavy Sediment Concentration near the Bed on the Velocity and Sediment Distribution*. University of California, Institute of Engineering Research.

Guo, J. & Julien, P.Y. (2001). Turbulent Velocity Profiles in Sediment-Laden Flows. *Journal of Hydraulic Research*. 39, 11–23.

Kundu, S. & Ghoshal, K. (2012). An Analytical Model for Velocity Distribution and Dip-Phenomenon in Uniform Open Channel Flows, *International Journal of Fluid Mechanics Research,* 39, 381–95.

Mazumder, B.S. & Ghoshal, K. (2006). Velocity and Concentration Profiles in Uniform Sediment-Laden Flow, *Applied Mathematic Modelling,* 30, 164–17.

Montes, J.S. (1973). Interaction of Two Dimensional Turbulent Flow with Suspended Particles, *PhD Dissertation*. Mass. Inst. of Technol., Cambridge, Mass.

Obermeier, F. (2006). Prandtl's Mixing Length Model-Revisited. *PAMM*, 6(1), 577-578.

Pal, D. & Ghoshal, K. (2016). Vertical Distribution of Fluid Velocity and Suspended Sediment in Open Channel Turbulent Flow, *Fluid Dynamics Research*, 48(3), 1-27.

Prandtl, L. (1925). Bericht über Untersuchungen zur ausgebildeten Turbulenz. Zeitschrift für angewandte. *Mathematik und Mechanik*, *5*(2), 136-139.

Umeyama, M. & Gerritsen, F. (1992). Velocity Distribution in Uniform Sediment-Laden Flow. *Journal of Hydraulic Eng*ineering, 118, 229–45.

Van Driest, E.R. (1956). On Turbulent Flow near a Wall. *Journal of the Aeronautical Sciences*, 23(11), 1007-1011.

Von Kármán, T. (1930). Mechanische Ähnlichkeit und Turbulenz. Nachr. Ges. Wiss. Göttingen, *Mathematics Physics*, 611, 58-76.

Wang, X. & Qian, N. (1989). Turbulence Characteristics of Sediment-Laden Flows, *Journal of Hydraulic Engineering,*115(6), 781–799.

Proceedings of the 37th IAHR World Congress
August 13 – 18, 2017, Kuala Lumpur, Malaysia

EFFECT OF ADJUSTABLE FLAPS ON RIVER SURF WAVES AT ABRUPT DROPS

HELGE FUCHS (1)

(1) Laboratory of Hydraulics, Hydrology and Glaciology (VAW), ETH Zurich, Zurich, Switzerland
fuchs@vaw.baug.ethz.ch

ABSTRACT

Surfing is a popular water sport in regions with ocean access. In countries without ocean access, standing river waves occurring in flood situations are often employed for surfing. The hydraulic conditions involving high flow velocities and large recirculation zones impose a risk of injury to the surfers. As an alternative, artificial surf wave conditions are provided at a number of river locations in Europe and worldwide. In most locations, a wave-type hydraulic jump is generated at a bottom drop. Based on the experiences with those engineered surf waves, adjustable installations demonstrate a positive effect on the surf wave characteristics. Physical laboratory experiments were conducted to quantify the effect of adjustable flaps on the generated wave characteristics at abrupt bottom drops. Whereas the wave-jump at a plain bottom drop without flap is very sensitive to the tailwater flow depth, adjustable flaps prevent the change of flow type from the favored wave-jump to non-surfable conditions for a wider range of downstream flow depths. Depending on the approach flow conditions, flaps significantly increase the wave height. However, adjustable flaps may also implicate additional limitations to the parameter range. Flaps with a small angle led to a wave height reduction, as compared to the plain bottom drop without flap. This paper details the above descriptions, and selected wave-type flow features are discussed. The research thus contributes to the general process understanding of surfable river waves and safer surf conditions, as compared to the common use of standing waves in rivers at flood situations.

Keywords: Flow separation zone; physical modelling; river surfing; wave type flow; wave-jump.

1 INTRODUCTION

Surfing is a popular water sport in regions with ocean access. Windsurfers use a sail to convert kinetic wind energy into board motion on the water, for which favorable wind conditions are necessary. For wave riding, the local sea bathymetry is important in addition to wind conditions. The incoming ocean waves, usually generated in a distant wind region, propagate to the shore and are subject to shoaling, as the still water depth continuously reduces. The wavelength then decreases, whereas the wave height increases. The wave steepness as the ratio between the wave heights to the wavelength therefore increases, leading to wave breaking at the shore. Particularly, spilling and plunging type breakers are favorable for ocean surfing. The optimum wave riding conditions depend on the combination of favorable incoming wave characteristics, and the local sea bottom features, such that worldwide surf spots are limited.

In landlocked countries without ocean access, surfers commonly use standing waves in rivers mostly during flood events. Due to the then high flow velocities and additional floating debris, this might be risky, especially for untrained beginners. Downstream of sills or drops, a dangerous plunging jet can establish, also known as a so-called ‘drowning machine’. The recirculation zone is difficult to detect by eye, can have a large expansion, and may drag objects and persons back toward the structure and thus into the plunging jet zone. Surfers may be trapped at the jet, as they are hardly able to rescue themselves by own effort. In addition, the strong air entrainment decreases the water buoyancy, thereby complicating the situation for victims. In June 2008, such a drowning machine caused a rubber boat to capsize at Kander River in Switzerland during a military exercise, thereby leading to five fatalities (Swiss Army, 2008).

At Eisbach River in Munich, Germany, a standing wave at a bottom drop is used intensively for river surfing since the 1980s (Figure 1a). The standing wave occurs coincidentally due to the combination of given upstream and downstream flow characteristics, and the riverbed geometry. The wave properties were further optimized by installing a flow deflector on the riverbed. Based on the successful surf wave at Eisbach River, a number of river surfing initiatives were established for other locations. In Switzerland, these initiatives concentrate on the Reuss River near Lucerne, the Limmat River near Zurich, the Aare River in Berne, or the Aare River in Bremgarten (Dietsche, 2015). Installations to the riverbed aim to create controlled surfable river waves available throughout the entire year without any risk for wave riders. Some projects such as the surf waves at Almkanal (Figure 1b and c) in Salzburg, Austria, or at Cunovo, Slovakia, were successful. Their adjustable installations to control upstream flow conditions proved advantageous. In contrast, the surf wave planned at the river mouth of Sill River in Innsbruck, Austria, does not develop satisfying surf wave properties.

The river mouth discharging into the Inn River in Innsbruck, Austria, was reconstructed in 2012 to generate a surf wave. The channel is divided into an ecologically valuable block ramp, and a concrete sill without flap or flow deflector, at which the surfable hydraulic jump was planned. At this location, the tailwater flow depth is directly controlled by the Inn River with natural flow depth fluctuations and fluctuations caused by downstream hydropower plant operation. For decreasing downstream flow depth, the designed wave-type hydraulic jump becomes unstable and collapses, thereby changing into a not-surfable plunging jet. The site access is restricted by local authorities due to dangerous hydraulic conditions.

In 2013, 2014, and 2016, the Bayerische Ingenieurekammer-Bau ("Bavarian Chamber of Civil Engineers") together with Workshop Wellentechnik ("Workshop wave engineering") organized a forum for ≈ 100 participants. With presentations and exhibitions, these events served as a platform for both responsible authorities and river wave initiatives to discuss various perspectives of planned European river surf waves.

In contrast to river surfing during flood events, artificial river waves can be utilized throughout the entire year and without particular risk for surfers. However, a number of hydraulic, ecologic, and legal constraints need to be respected. Due to the often vague legal situation, local authorities or owners of hydropower plants disclaim liability. In addition, usage restrictions may arise during fish migration periods, given the wave project is located in the main channel of a fish habitat. Transverse structures including sills or weirs may lead to sediment discontinuity with upstream deposition and downstream erosion. Changes in the sediment continuum may have negative effects on the hydraulics of river surf waves.

Figure 1. Surf wave at (a) Eisbach River in Munich, Germany (photo by author), (b) and (c) Almkanal in Salzburg; arrow indicates flow direction (photo by Ingenieurbüro Gostner & Aigner, Wals, Austria).

Surfable river waves are generated by four different basic hydraulic principles: (1) *sheet-flow* on a wave-like bathymetry, (2) generation of a spatial *wave-tube*, (3) plain hydraulic jump at bottom drops, and (4) plain hydraulic jump at bottom drops with additional adjustable installations. A sheet-flow on a wave-like bottom topography (1) is often used in water parks (e.g. Alpamare Pfäffikon, Switzerland), to offer mainly children surfing possibilities using small surfboards without fins on shallow flows (flow depth $h \approx 10$ cm). The Cunovo surf wave at the Danube River close to Bratislava, Slovakia, is based on this principle, but with larger flow depths of $h \approx 40$ cm, thereby compensating variations of the upstream and downstream flow conditions (Bauer, 2015). The location is commercially used and a surfing day-pass is offered for ≈10 EUR. Surfers partially reported damaged surfboard fins caused by the small flow depth.

Spatial wave tubes (2) are similar to the collapsing free surface profile of a pronounced plunging wave breaker. They can be generated by relatively large flow deflectors installed at the channel bottom (Hornung and Killen, 1976; Oertel et al., 2012). Due to the increased injury risk and the relatively high installation effort, this wave type is not favored for river surf projects.

  / ISSN 1562-6865 (Online) - ISSN 1063-7710 (Print)

The plain hydraulic jump at bottom drops (3) is one of the classic hydraulic phenomena and was therefore widely investigated in the past (e.g. Moore and Morgan, 1957, Rajaratnam and Ortiz, 1977, Hager and Bretz, 1986, Kawagoshi and Hager, 1990, Ohtsu and Yasuda, 1991, Mossa et al., 2003). However, these studies mainly focus on fixing the hydraulic jump within a stilling basin, and to increase energy dissipation. As classified by Moore and Morgan (1957), an A-jump (jump upstream of bottom drop), wave-jump (pronounced wave crest directly downstream of bottom drop) or B-jump (jump downstream of bottom drop) occurs depending on both approach flow Froude number and tailwater flow depth. The wave jump, which is favorable for surf projects, occurs only for a specific combination of approach and tailwater flow conditions and transforms rapidly into a non-surfable A- or B-jump as the downstream flow depth changes.

A plain hydraulic jump involving adjustable installations (4) is a promising method to generate surfable river waves for a wide range of flow parameters. The above described wave characteristics are positively affected by regulating the approach flow conditions. For the surf wave at Almkanal in Salzburg, Austria, a l_k = 0.6 m long flap is installed, which can be adjusted to angles between 0 – 30° to the horizontal. The approach flow depth is $h_o \approx$ 0.4 m, and the drop height s = 0.725 m (Figure 1b, c and 2). Similar to regulated gates, e.g. at spillways, the operating personnel needs to be responsible. The wave regulation mechanism can be combined with an adjustable upstream weir to further improve the approach flow conditions (Aufleger et al., 2015).

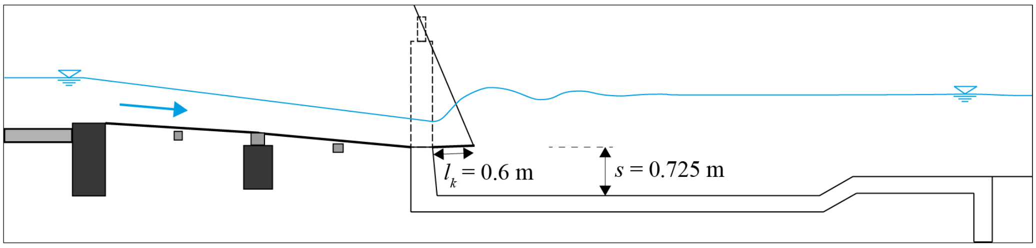

Figure 2. Cross-section of Almkanal surf wave in Salzburg, Austria (adapted from Gostner et al., 2010).

Adjustable flaps at abrupt drops appear promising to optimize existing structures with minimum structural adaptations to obtain surf wave conditions. The generated hydraulic jump is stabilized for varied tailwater flow conditions, thereby leading to safer surf conditions, as compared to the common use of standing waves in rivers at flood situations. Since literature on this configuration does not exist, hydraulic model tests were conducted, investigating the effect of flaps on the wave properties for various downstream and upstream flow conditions. Selected experimental results are presented and discussed below.

2 EXPERIMENTAL SETUP

Physical model experiments were conducted in a 6 m long, 0.3 m wide and 0.5 m deep flow channel at the Laboratory of Hydraulics, Hydrology and Glaciology (VAW) of ETH Zurich. Whereas the back wall is made of steel, the channel bottom and front wall are made of glass to enable optical access. Figure 3 shows a definition sketch with the governing parameters, namely approach flow depth (h_o), approach flow velocity (V_o), drop height (s), flap length (l_k), flap angle (κ), downstream flow depth (h_u), wave height (h_w), as well as wave crest height (h_{wb}), and wave crest length (L_{wb}). The origin of the horizontal and vertical coordinates (x ,z) is set at the drop toe.

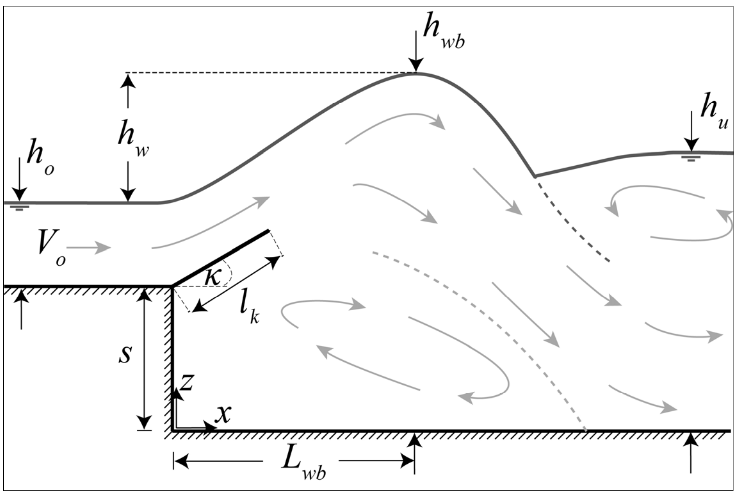

Figure 3. Definition sketch of surf wave at abrupt bottom drop with adjustable flap.

The investigated parameter range is specified in Table 1. A jetbox (Schwalt and Hager, 1992) was used to control the inflow conditions with approach flow Froude numbers $F_o = V_o/(gh_o)^{1/2}$ = 2.0 - 4.0, involving g as the gravity acceleration. The downstream flow depth was regulated with a weir at the channel end. Free surface profiles were measured to ± 1 mm with a point gauge mounted on a traverse system. For selected parameter combinations, the wave-type flow field was recorded using Particle Image Velocimetry (PIV).

Table 1. Investigated parameter range.

Parameter	Range
Q	20 - 40 l/s
h_o	3.3 - 7.7 cm
F	2.0 - 4.0
s	5 cm, 10 cm
l_k	1.0, 2.5, 5.0 cm
κ	10°, 20°, 30°

3 RESULTS

Favorable surf wave properties are shown in Figure 4 for Q = 30 l/s, F_o = 3.0, l_k = 2.5 cm, and κ = 30°. Flow features are separated into four reaches: (1) supercritical approach flow, (2) surf wave, (3) recirculation zone, and (4) subcritical tailwater. If air is entrained by a surface roller, the water buoyancy reduces, thereby complicating surf maneuvers. Waves with a smooth surface are therefore easier to surf. Based on existing river surf waves, a favorable prototype wave height is h_w = 0.5 - 1.2 m. The subsequent recirculation zone should be separated from the surf wave, and possibly short to diminish the risk of injury. Particularly for long recirculation zones, fallen surfers may be unable to rescue themselves. Again, aeration may lead to decreased buoyancy, and thus a complicated situation for victims to emerge from the water. In the subcritical tailwater region, the turbulence reduces, leading to air detrainment.

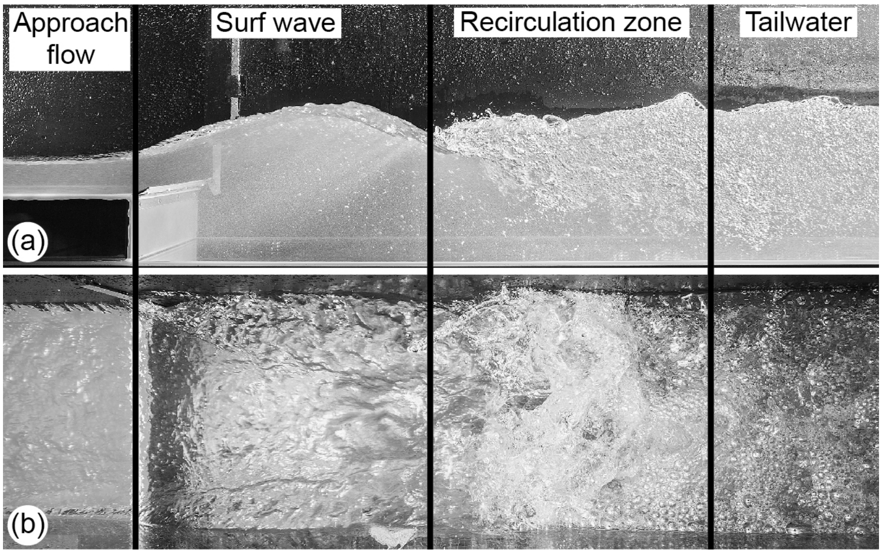

Figure 4. Favored surf wave properties for Q = 30 l/s, F_o = 3.0, l_k = 2.5 cm, with four characteristic reaches in (a) side view and (b) top view.

The maximum wave height occurred for Q = 40 l/s, F_o = 4.0, l_k = 5.0 cm, and κ = 30° (Figure 5). This wave-type flow condition is considered unfavorable due to the strong air entrainment caused by high turbulence, and the large extension of the recirculation zone.

As a major benefit, adjustable flaps demonstrated a stabilizing effect on the surf wave for decreasing tailwater flow depths. Given a reference configuration of a bottom drop without flap and F = 2.5, the wave-type flow changes into a (non-surfable) undulating jump for a reduction of the downstream water depth by only 2.5%. In contrast, an installed flap of l_k = 2.5 cm and κ = 20° maintains a surfable wave-type flow.

Figure 5. Maximum wave height with $h_w \approx$ 23 cm for Q = 40 l/s, F_o = 4.0, l_k = 5.0 cm, and κ = 30°.

The free surface profiles of surf waves for Q = 30 l/s, F_o = 3.0, l_k = 5.0 cm are shown in Figure 6 for different flap angles κ = 30°, 20°, 10°, and the reference geometry without a flap. The maximum wave height h_w = 0.18 m is generated if κ = 30°, and reduces to h_w = 0.15 m (κ = 20°), h_w = 0.126 m (κ = 10°), and h_w = 0.14 m (no flap), respectively. A long flap with a high angle therefore increases h_w by ≈ 29 %, whereas for a flat angle the flow attaches to the flap and deflects downward, leading to wave height reduction by ≈ −10%.

The effect of the flap length on the free surface profiles of the surf wave is shown in Figure 7 for Q = 30 l/s, F_o = 3.0, and both κ = 10° and 30°. Given a flat angle of κ = 10°, the flap length has no significant effect on the free surface profile. However, the wave heights generated at the drop with flap are smaller as compared to a simple drop without flap (Figure 7a). Given a large flap angle of κ = 30°, h_w increases by ≈ 29 % (l_k = 5.0 cm, h_w = 0.18 m) and ≈ 16 % (l_k = 2.5 cm, h_w = 0.162 m) as compared to the plain drop without a flap. Note that the free surface profile generated for l_k = 1 cm is identical to those generated by the drop without a flap.

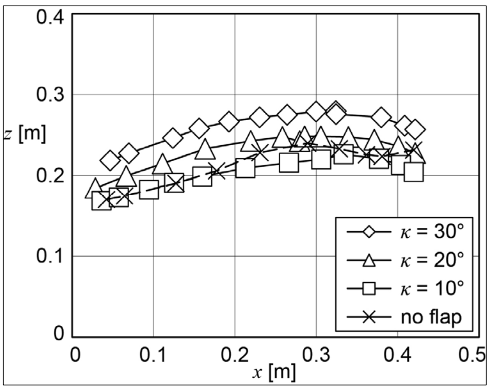

Figure 6. Free surface profiles $z(x)$ of surf wave for Q = 30 l/s, F_o = 3.0, and l_k = 5.0 cm.

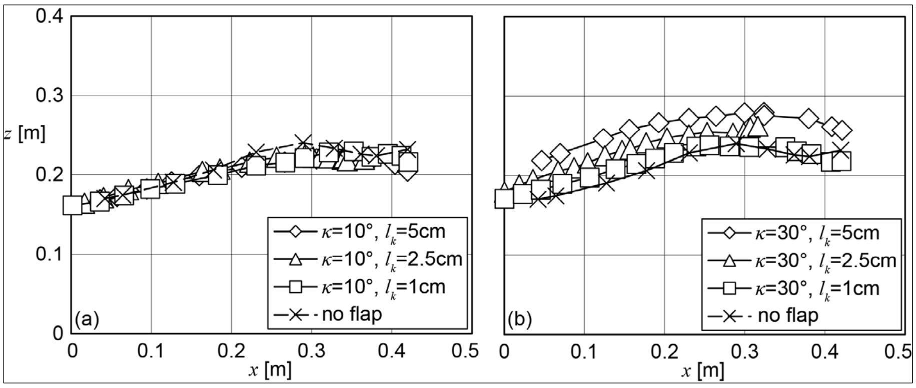

Figure 7. Free surface profiles $z(x)$ of surf wave for Q = 30 l/s, F_o = 3.0 with (a) κ = 10° and (b) κ = 30°.

4 PIV MEASUREMENTS

The flow field downstream of the bottom drop was recorded using Particle Image Velocimetry (PIV) for selected test conditions. Polyamide particles of 1.03 g/cm^3 density and a mean diameter of 5 – 35 µm were used as seeding material. The particles were illuminated using a Litron-DualPower 200-15 with a pulse rate of 15 Hz at a wavelength of 532 nm, and an energy per pulse of 2 x 200 mJ. The laser beam was coupled into a laser-guiding arm and led underneath the channel bottom. A cylinder lens was used to create the vertical light sheet along the flume axis. Images were captured using a Dantec 2 MP FlowSense camera of 1200 x 1600 pixels (V:H) resolution. The corresponding field of view was ≈ 300 mm x 400 mm (V:H). The correlation grid size of 32 x 32 pixels resulted in a spatial vector resolution of ≈ 4.15 mm x 4.15 mm.

The hydraulic jump generated at an abrupt bottom drop was characterized by strong turbulence and pronounced vortex formation, resulting in a continuously changing flow field. For a meaningful comparison of the flow field for different parameter combinations, the temporal average was created from 75 double frames, corresponding to 5 s of flow. The flow field at an abrupt bottom drop is shown in Figure 8 for $F_o = 3.0$, $h_o = 4.8$ cm, and $l_k = 5$ cm with different flap angles (a) $\kappa = 30°$, (b) $\kappa = 20°$, (c) $\kappa = 10°$ as well as (d) without flap. The main approach flow (dark grey) aligns to the flap and is deflected with the flap angle. For a large flap angle $\kappa = 30°$, the approach flow is significantly deflected upwards at $x \approx 50$ mm, but orientates back downward to the channel bottom for $x \approx 250$ mm (Figure 8a). Given a small flap angle (Figure 8c), the approach flow is deflected almost horizontally, resulting in a smaller wave height as compared to the plain bottom drop without flap (Figure 8d). The corresponding free surface profile is therefore flat and not suitable for surfing.

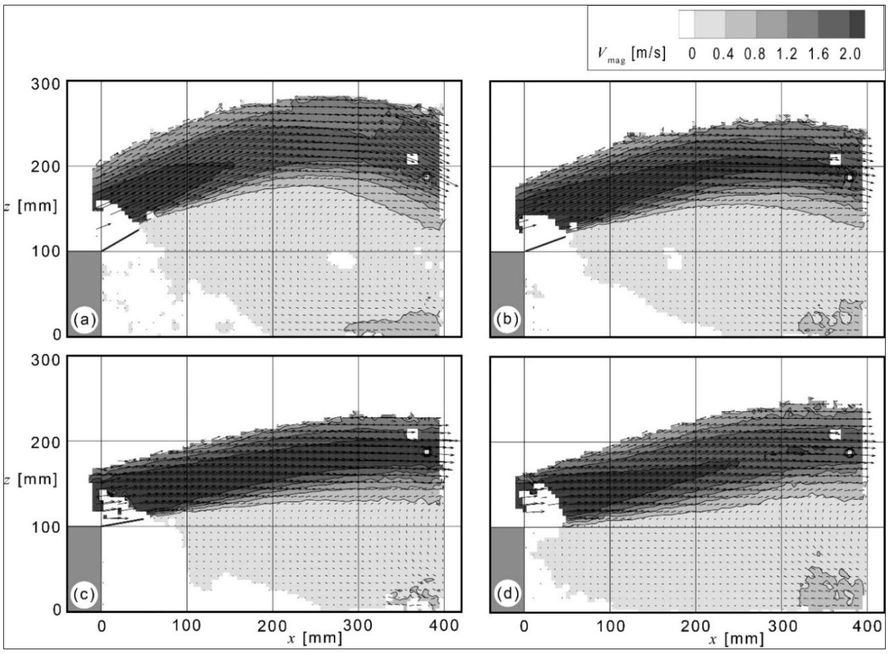

Figure 8. Flow field at abrupt bottom drop for $F_o = 3.0$, $h_o = 4.8$ cm, and $l_k = 5$ cm with (a) $\kappa = 30°$, (b) $\kappa = 20°$, (c) $\kappa = 10°$, and (d) without flap.

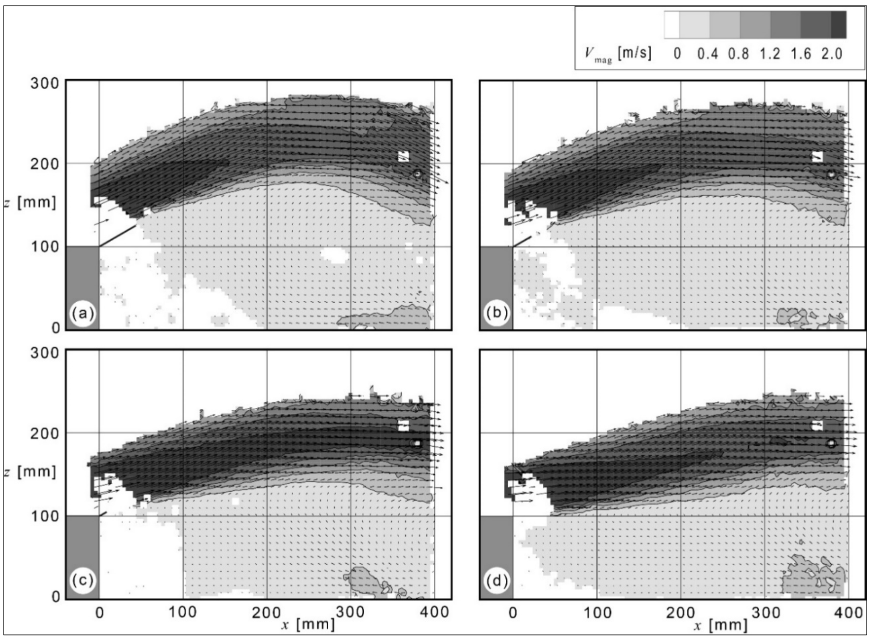

Figure 9. Flow field at abrupt bottom drop for $F_o = 3.0$, $h_o = 4.8$ cm, and $\kappa = 30°$ with (a) $l_k = 5$ cm, (b) $l_k = 2.5$ cm, (c) $l_k = 1$ cm, and (d) without flap.

Figure 9 shows the flow field at an abrupt bottom drop for F_o = 3.0, h_o = 4.8 cm, and κ = 30° with different flap lengths (a) l_k = 5 cm, (b) l_k = 2.5 cm, (c) l_k = 1 cm as well as (d) without flap. For all three configurations involving a flap, the main approach flow is deflected upwards at $x \approx$ 50 mm. As described above, the flow orientates back downward to the channel bottom at $x \approx$ 250 mm. Longer flap lengths thereby result in stronger flow deflection. A short flap with a large flap angle (l_k = 1 cm, κ = 30°) therefore generates a flatter free surface profile as compared to the plain bottom drop without flap (Figure 9c and d).

5 CONCLUSIONS

Only sparse literature exists on the hydraulics of river surf waves at abrupt drops. However, experiences at existing river surf wave locations demonstrate a positive effect of adjustable installations on the generated wave characteristics. Physical model tests conducted at VAW laboratory confirmed that both wave height and steepness, as the important surf wave characteristics, are affected by a flap. Given an approach flow Froude Number of F_o = 3.0, the wave height can be increased by ≈ 30 % using a long flap with a large flap angle (κ = 30°), as compared to a plain bottom drop without a flap.

Longer flaps have their potentially positive effect on the surf wave characteristics for a wider range of approach flow and tailwater conditions. However, adjustable flaps also implicate potential limitations. On the one hand, a hydraulic jump can be generated upstream of the bottom drop (A-jump) given the approach flow Froude number is small. Meanwhile, flaps with a small angle can deflect the main approach flow downwards, thereby decreasing the targeted wave height as compared to a plain bottom drop without flap. Given large approach flow Froude numbers, the long flaps with a large flap angle may have similarities to a ski-jump, leading to a pronounced wave-jump with large air entrainment, and thus an irregular surface profile. The wave is then difficult to surf and can be dangerous for fallen surfers due to the large recirculation zone.

Additional model tests are necessary to extensively quantify the effect of adjustable flaps on the surf wave characteristics. The effect of the bottom geometry is considered important, but not yet investigated. Therefore, in future experiments, the bottom drop height will be varied in a wider range, and a sloped bottom ramp will be involved instead of the abrupt vertical drop.

ACKNOWLEDGEMENTS

J. Trachsel, R. von Wyl and C. Koch are acknowledged for having contributed with their student theses (Trachsel, 2013, von Wyl, 2015, and Koch, 2016) to an improved general process understanding of river surf waves at abrupt drops.

REFERENCES

Aufleger, M., Neisch, V., Hautzel, U. & O'Neill, D. (2015). Stationary Standing Surf Waves. *Proceeding of 36th IAHR World Congress*, The Hague, the Netherlands.

Bauer, J. (2015). *Von Cunovo lernen (Lessons from Cunovo).* TEC21, 141(1-2), 34-36. (In German)

Dietsche, D. (2015). *Surfbare Wechselsprünge (Surfable hydraulic jumps).* TEC21, 141 (1-2), 29-31. (In German).

Gostner, R., Griessner, G. & Fingerlos, W. (2010). *Surfwelle am Almkanal (Surf wave at Almkanal).* Technical Report. (In German, unpublished)

Hager, W.H. & Bretz, N.V. (1986). Hydraulic Jumps at Positive and Negative Steps. *Journal of Hydraulic Research*, 24(4), 237-253.

Hornung, H.G. & Killen, P. (1976). A stationary Oblique Breaking Wave for Laboratory Testing of Surfboards. *Journal of Fluid Mechanics*, 78(3), 459-480.

Kawagoshi, N. & Hager, W.H. (1990). Wave Type Flow at Abrupt Drops. *Journal of Hydraulic Research*, 28(2), 235-252.

Koch, C. (2016). Einfluss einer Klappe auf die Surfbarkeit stehender Wellen (Effect of a Flap on the Surf Properties of Standing Waves). *MSc-Thesis*, ETH Zürich. (In German, unpublished)

Moore, W.L. & Morgan, C.W. (1957). The Hydraulic Jump at an Abrupt Drop. *Journal of the Hydraulics Division ASCE*, 83(HY6), 1-21.

Mossa, M., Petrillo, A. & Chanson, H. (2003). Tailwater Level Effects on Flow Conditions at an Abrupt Drop. *Journal of Hydraulic Research*, 41(1), 39-51.

Oertel, M., Mönkemöller, J. & Schlenkhoff, A. (2012). Artificial Stationary Breaking Surf Waves in a Physical and Numerical Model. *Journal of Hydraulic Research*, 50(3), 338-343.

Ohtsu, I. & Yasuda, Y. (1991). Transition from Supercritical to Subcritical Flow at an Abrupt Drop. *Journal of Hydraulic Research*, 29(3), 309-328.

Rajaratnam, N. & Ortiz, N.V. (1977). Hydraulic Jumps and Waves at Abrupt Drops. *Journal of the Hydraulics Division ASCE*, 103(HY4), 381-394.

Schwalt, M. & Hager, W.H. (1992). Die Strahlbox (The Jetbox). *Schweizer Ingenieur und Architekt*, 110(27/28), 547-549. (In German)

Swiss Army (2008). Communication on 27.06.2008 at (www.vtg.admin.ch/internet/vtg/de/home/dokumentation/news/newsdetail.19730.nsb.html).

Trachsel, J. (2013). Surfbare Wellen (Surfable waves). *Project Thesis*, ETH Zürich (In German, unpublished).

von Wyl, R. (2015). Einfluss einer Klappe auf die Surfbarkeit stehender Wellen (Effect of a Flap on The Surf Properties of Standing Waves). *Msc-Thesis*, ETH Zürich. (In German, Unpublished)

NUMERICAL MODELING OF THE FLOW ON A DAMAGED WEIR APPLICATION TO THE CAVAILLON RIVER, HAITI

OLIVIER CARLIER D'ODEIGNE[1], YVES ZECH[2] & SANDRA SOARES-FRAZÃO[3]

[1,2,3] Institute of Mechanics, Materials and Civil Engineering, Université catholique de Louvain, Louvain-la-Neuve, Belgium
olivier.carlier@uclouvain.be, yves.zech@uclouvain.be, sandra.soares-frazão@uclouvain.be

ABSTRACT

Haiti is one of the most vulnerable countries to floods and inundations. The development of infrastructures enabling systematic river monitoring is quite inexistent and consequently hydrologic and hydrographic data are really scarce. In the frame of an academic cooperation project aiming at enhancing the local capabilities to manage Haitian rivers, the Dory weir is studied because it will be used as upstream boundary condition for further flow simulations. However, due to past severe flow conditions, the weir is seriously damaged and is no more working in standard conditions. So, three different approaches are used to re-build a stage-discharge relation. Recent floods in May 2016 have recorded a set of water level and river discharge measurements. Added to previous field campaigns, these form a first estimate of stage-discharge relation. Then, detailed numerical simulations using OpenFoam are used to generate several flow scenarios on the weir, considering its exact damaged geometry, in order to rebuild a local stage-discharge. The added value of this detailed numerical approach is discussed by comparing a simple approach in defining an equivalent standard profile from which the stage-discharge relation. The objective of establishing a proposition for a stage-discharge relation from numerical approach is completed. Even if some of this approach could be further improved, the OpenFoam model can be easily adapted to other similar applications and researches including the integration of a specific shape or topographic surface. The most important benefit of the present work is therefore the establishment of a numerical-based reproducible method to generate stage discharge relations from real topographies that could, as in Dory's case, be deteriorated and differ from standard shapes.

Keywords: Damaged weir; stage-discharge relation; CFD simulation; Haitian River.

1 INTRODUCTION

Haiti is probably one of the most exposed countries to dramatic floods and inundations due, among other, to intense deforestation. Haiti is also extremely poor in hydrologic and hydrographic data, as this is not considered as a priority in a context numerous social and economic emergencies. The present work is done in the frame of a cooperation program funded by the Belgian Cooperation Administration (ARES-CCD) that aims to develop, through an exemplary watershed and river reach along the Cavaillon River (Figure 1a), a simple and repeatable methodology for enhancing hydrologic data and designing flood protection procedures.

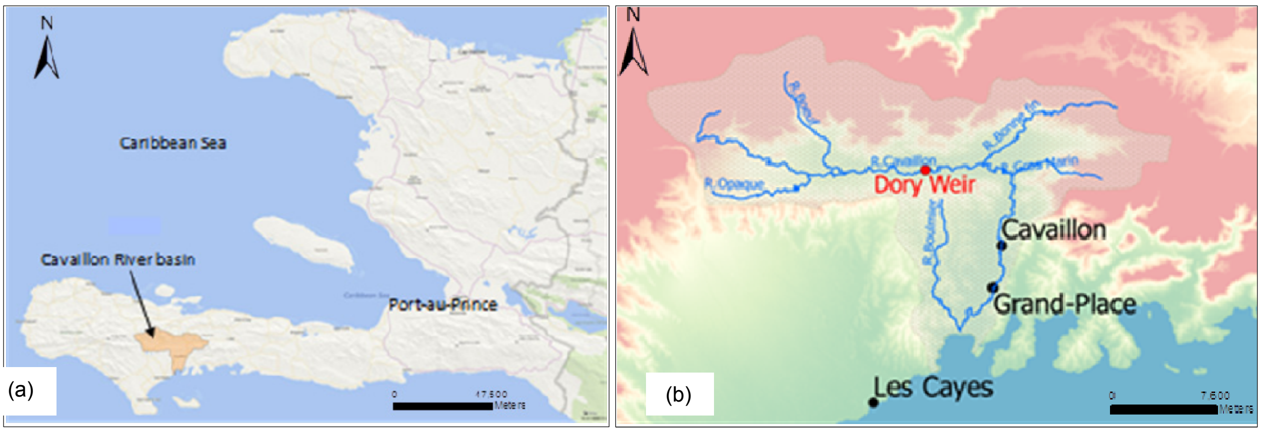

Figure 1. Localization of the studied river reach: (a) general map of Haiti and indication of the Cavaillon river basin, (b) Details of the Cavaillon River and tributaries.

Within this project, the discharge in the river is one of the important required data. The Dory weir, built for irrigation purpose, represents the upstream limit of the studied reach (Figure 1b). It provides a possibility to evaluate the river discharge from a continuous water level measurement at a station located 50 m upstream of the weir. Unfortunately, the infrastructure is in a very bad condition as time and recurrent floods have considerably degraded the initial weir profile (Figure 2). The weir crest is no longer horizontal (see Figures 2a and 2c), the upstream approach is partly invaded by sediments (Figures 2b and 2d) and the concrete apron downstream is partly destroyed by uplift pressures (Figure 2a and 2d).

Figure 2. (a) Damaged concrete slab on the downstream face of the weir (b) general view of the Dory weir (c) aerial view of the crest and the downstream slab d) damaged crest and upstream sedimentation.

The aim of the present work is to build a stage-discharge relation for the Dory weir, considering that no data are available about the design and the construction of this weir and that the damages have the consequence that it is certainly not working in standard conditions. So, in order to obtain a usable stage-discharge relation for this damaged weir, three complementary approaches are used: (1) in situ surveys, (2) numerical simulations using the free Open foam software, and (3) tentative application of the classical theory of weir flows, in order to extrapolate the stage-discharge relation beyond the limits of observations.

2 FIELD SURVEY

In 2015 and 2016, dense topographical surveys were conducted manually (*i.e.* using a portable total station) in Dory, leading to detailed bathymetric data of the weir and surroundings. Form this data, a three-dimensional model of the weir could be constructed (Figure 3). These measurements highlighted the main defects of the weir. First, the crest is no longer horizontal, and presents a difference of 0.23 m between the left and right bank, a difference of 0.29 m between the highest and lowest point with severe irregularities along the crest. Secondly, significant sediment deposits upstream reduced the weir crest level to only 0.32 m above the upstream bottom, while it is about 0.79 m at its maximum. Finally, as illustrated in Figures 2, the concrete apron and the downstream face of the weir were seriously damaged during past flood events, resulting in a complex downstream bathymetry along all the cross-section.

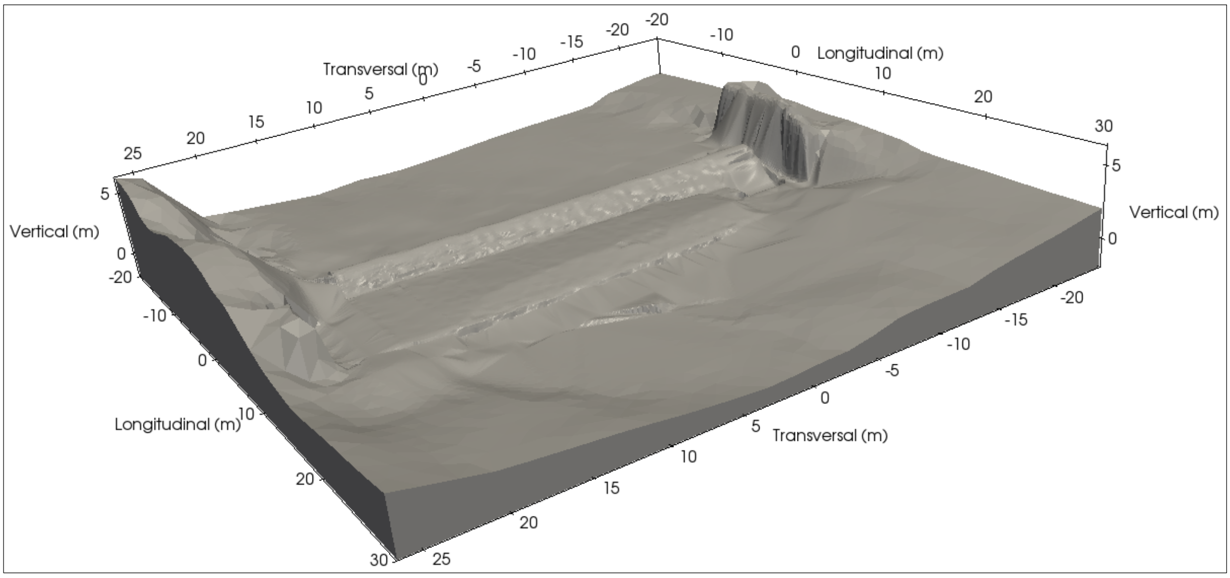

Figure 3. Three-dimensional model of the weir obtained from the topographical survey.

The three-dimensional model of Figure 3 is less accurate near sharp geometry changes, especially near the banks. Moreover, as shown in Figure 4b, a radial gate presents on the left bank to guarantee a minimum flow in the river even if the upstream water level does not reach the weir crest. This radial gate is not included in the topographical model. Due to these considerations, the useful section of the weir on which we can perform further calculations and simulations is limited to a 28 m width section (represented by the blue box in Figure 4a).

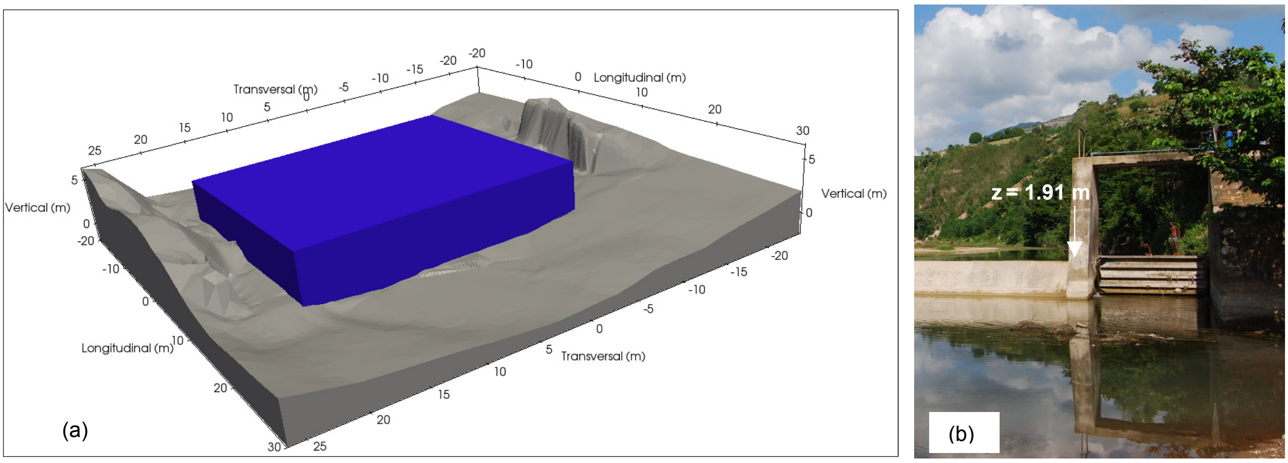

Figure 4. (a) Useful section of the weir on which reflection is performed (b) Picture of the right bank located gate.

The field campaign also included stage-discharge measurements. The water level was measured 50 m upstream from the weir, while velocity measurements by propellers, in a cross-section located 66 m downstream of the weir, were used for estimating the discharge by integration on the cross-section area. Unfortunately, conditions to obtain regular, good quality measurement covering a broad spectrum of values are not fulfilled. First, the whole region mainly suffered from drought during the last five years, reducing the frequency and intensity of precipitation events. Moreover, as the region is difficult to access (without paved road, tributaries to be crossed by fording), any climatic event makes transport to the Dory area even more difficult. Due to technical difficulties and lack of maintenance capabilities, the installation of automated measurement stations is impossible. In consequence, only low discharges could be observed, up to 27.94 m^3/s, even if we know, after Hurricane Matthew, much larger discharges can occur in the river. The scarce available measured points, measured from a common reference point at the base of the right bank, z = 1.91 m (Figure 4b), are listed in Table 1.

Table 1. Available water level and discharge measurements.

Upstream water level (m)	2.16	2.22	2.25	2.3	2.36	2.36
Discharge (m^3/s)	12.01	15.66	16.56	21.53	24.29	27.94

In conclusion, even if intuitively, the field approach seems to be the most appropriate to reconstruct a stage-discharge relation for the weir, the conditions in which any field campaign has to be conducted make it necessary to use a combined approach with theoretical reflection and numerical simulation as proposed in this work.

3 NUMERICAL APPROACH

3.1 Open foam model

The Open Foam software was used to simulate the flow over the Dory weir for several discharge conditions. This software solves the Navier-Stokes equations by a Volume of Fluid method (Hirt and Nichols, 1979), and, for the present application, the inter Foam solver was applied, which consists in a solver for two incompressible and immiscible fluids. So, the water flow and a layer of air above it are represented, the interface between these two phases being captured by a phase-fraction based interface capturing approach. In other words, in each computational cell, the fluid state is described by the value of a variable, α representing the relative volume of water (or air) in the cell, with $\alpha = 1$ corresponds to a cell occupied by fluid only, and $\alpha = 0$ corresponds to a cell with air only. The free-surface then located in cells with an α value between 0 and 1.

In order to select the best appropriate parameters of the simulation, *i.e.* mesh size, local refinement, and turbulence closure model that allow for accurate results and reasonable computational time, a convergence analysis was performed (Roelandt and Verschoore, 2016). As a result, the Dory weir and the surrounding bathymetry were discretized with finer refinement close to the weir. As regards the turbulence closure, the k- ω SST model was selected for providing the more stable results, as it combines the robustness of the k-w model near the walls and the performances of the k-ε model away from the walls.

During the first study, only 2D-V simulations were run on a limited number of vertical slices in the complete 3D model of the weir, in order to limit the computational time and to obtain a first series of results that will, in a later study, be compared to full 3D simulations.

3.2 Applied method

The weir is divided into five representative slices (Figure 5). For each slice a stage-discharge relation is established from the numerical simulations. These five relations are then merged in order to obtain a global relation for the whole structure.

Since the effective part of the structure is located between the transversal coordinates -11 m and 17 m (Figure 4) measured along the crest axis, each slice has a width of 5.6 m. For each slice, the central cross section is chosen to represent the flow.

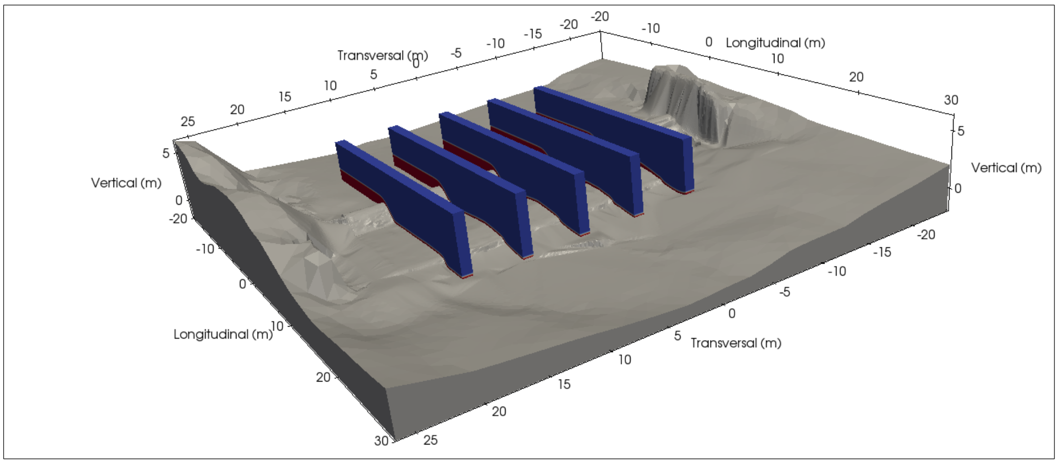

Figure 5. Five simulation slices representing each a 5.6 m wide portion of the weir.

In order to obtain a relation between the upstream water level and the discharge over the slice, simulations are achieved for several inlet flow conditions, since this is the variable that can be easily modified in the solver. The selected flow conditions span over the range of observed discharges (Table 1). Figure 6 shows the steady-state flow observed for four different discharges, and the corresponding upstream water level (according to a common reference explained above) that can be deduced from the simulations.

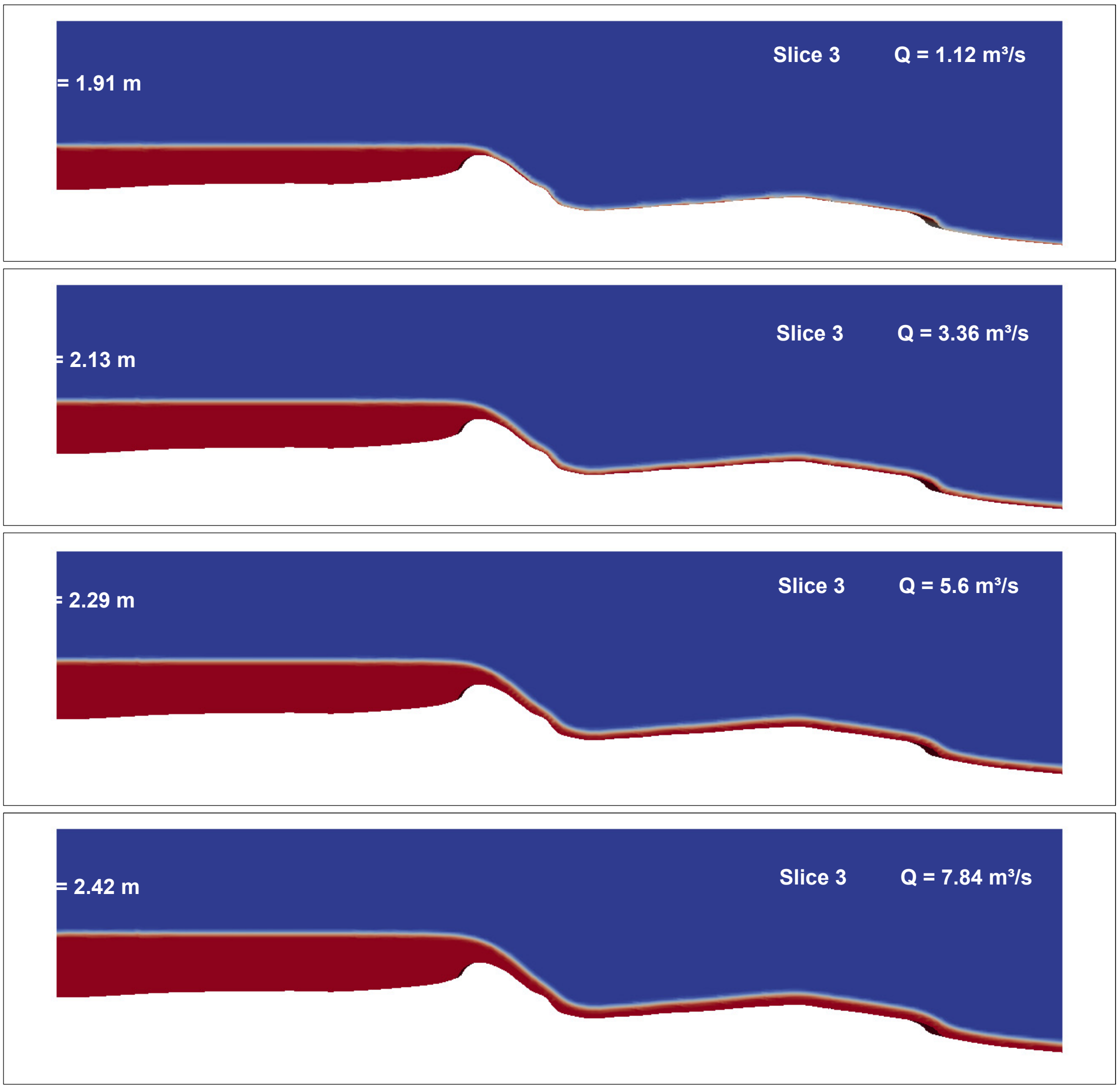

Figure 6. Simulation results on slice 3 with four discharges (1.12 m^3/s, 3.36 m^3/s, 5.6 m^3/s, 7.84 m^3/s) – Red is water, Blue is air, transition is clearer.

The free-surface is found as the location where the α variable representing the water/air ratio of an element is equal to 0.5. Using this condition, the free surface can be extracted as illustrated in Figure 7.

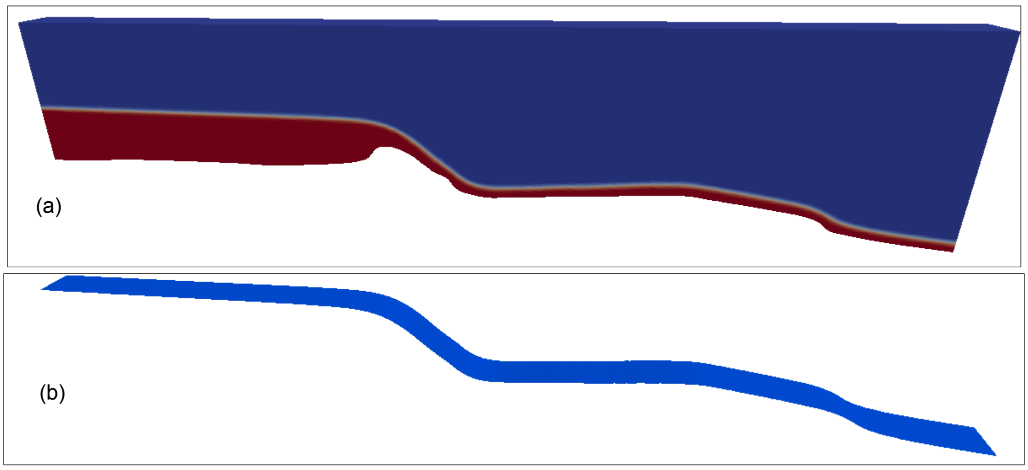

Figure 7. (a) Simulation of the slice 3, Q = 5, 6 m^3/s, and (b) limit layer between water and air (α = 0.5).

Couples of point ($z_{upstream}$, Q) were calculated for each slice in order to build a specific relation between the discharge and the upstream water level. The resulting relations are illustrated in Figures 8a-b-c-d-e. These relations are then combined to establish a single relation considered as representative for the complete weir (Figure 8f). This latter relation is expressed in terms of the upstream water level measured from the common reference system, and not in terms of the head, and the actual head cannot be defined with respect to the crest level because the crest is not horizontal.

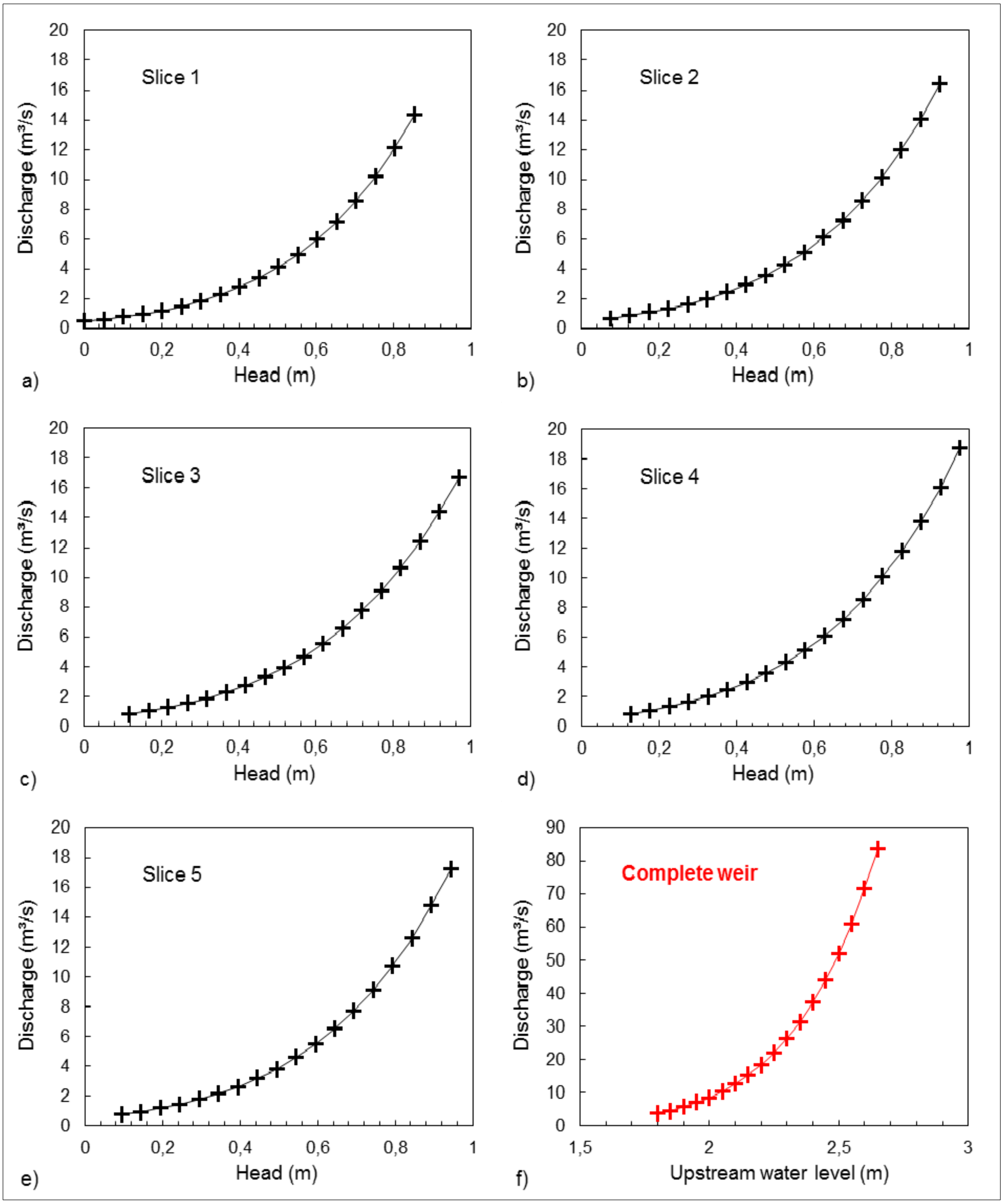

Figure 8. Stage discharge relations calculated for (a) slice 1, (b) slice 2, (c) slice 3, (d) slice 4, (e) slice 5, and (f) the complete weir.

4 THEORICAL APPROACH

If the use of sophisticated approaches seems to be promising, it could be instructive to observe an added value this work has in comparison with a basic idea, replacing the actual damaged Dory weir by an equivalent simple standard profile for which the stage-discharge relation could be extrapolated beyond the range of measurements. In the present work, the exercise is only done for the basic assumptions, *i.e.* limitless upstream approach depth, vertical upstream face, no influence from downstream flow and negligible inlet velocity.

To build a standard profile, a design stage (H_0) has to be defined. This design stage is indeed an unknown, because there is no information available about the design and construction of the weir. Two methodologies to find the design conditions are developed hereunder. The first idea was to fit the profile of a slice directly with a standard profile through the Eq. [1]. By adjustment of H_0, minimizing the least mean square error, it is possible to obtain a curve fitting with the theoretical standard bathymetry (Figure 9a). The normal stage found is $H_0 = 0.065$ m. Two elements are however questionable: (1) how to choose the representative slice along the crest to define a “mean” standard profile? (2) Does the geometrical similitude ensure hydraulic similitude? To answer the second question, an alternative way to build an “equivalent” standard profile was developed. Based on numerical simulation results, the stage discharge relation obtained from the OpenFoam model and Eq. [2] with $\mu_0 = 0.492$ were compared. By adjusting the stage-discharge relation to the one obtained from the OpenFoam model and minimizing the least mean square error, as shown on a log-log graph in Figure 9b, another estimation of the normal stage H_0 could be obtained. The value found is H_0 = 0.635 m.

$$\frac{y}{H_0} = 0.47 \left(\frac{x}{H_0}\right)^{1.8} \qquad [1]$$

$$Q = \mu\, L \sqrt{2g}\, H^{1.5} = \mu_0 \left(\frac{H}{H_0}\right)^{0.17} L \sqrt{2g}\, H^{1.5} = \frac{\mu_0\, L \sqrt{2g}}{H_0^{\;0.17}}\; H^{1.67} \qquad [2]$$

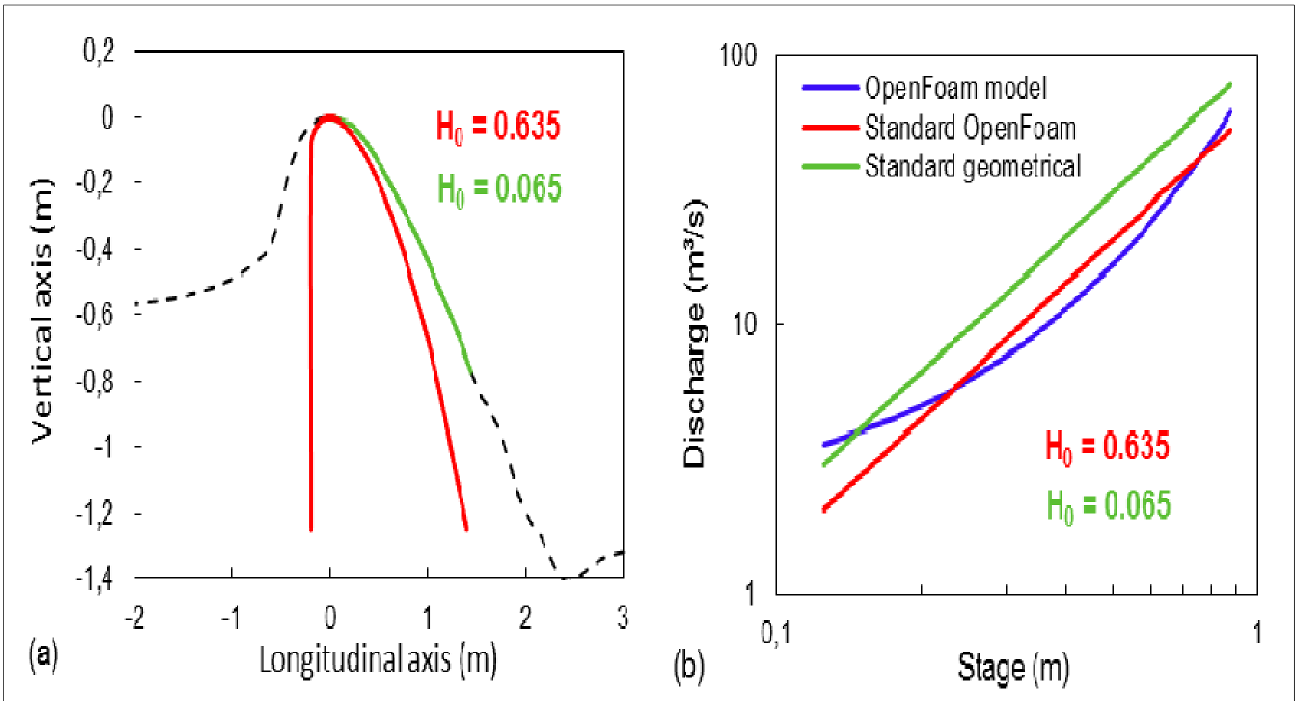

Figure 9. (a) Standard profiles (geometrical and OpenFoam) for their respective nominal head with background central slice profile (dotted line) (b) Comparison Stage-Discharge relations built by OpenFoam model and two equivalent standard profile fitted to geometrical shape and to OpenFoam model results.

5 COMPARAISON BETWEEN THE DIFFERENT APPROACHES

Figure 10 shows the stage-discharge relation for each of the approaches developed in this paper. The poor availability of field data encouraged to use alternatives methods to represent the flow over the Dory weir. First, it is interesting to notice that the best approximation of the measured field data is the one based on the OpenFoam numerical results (blue curve in Figure 10). Moreover, it can be observed that there are two ways of fitting an equivalent standard profile for the Dory weir, based on geometry or numerical results, which give significantly different results. So, it seems more appropriate to consider in terms of hydraulic convergence than pure bathymetric data fitting.

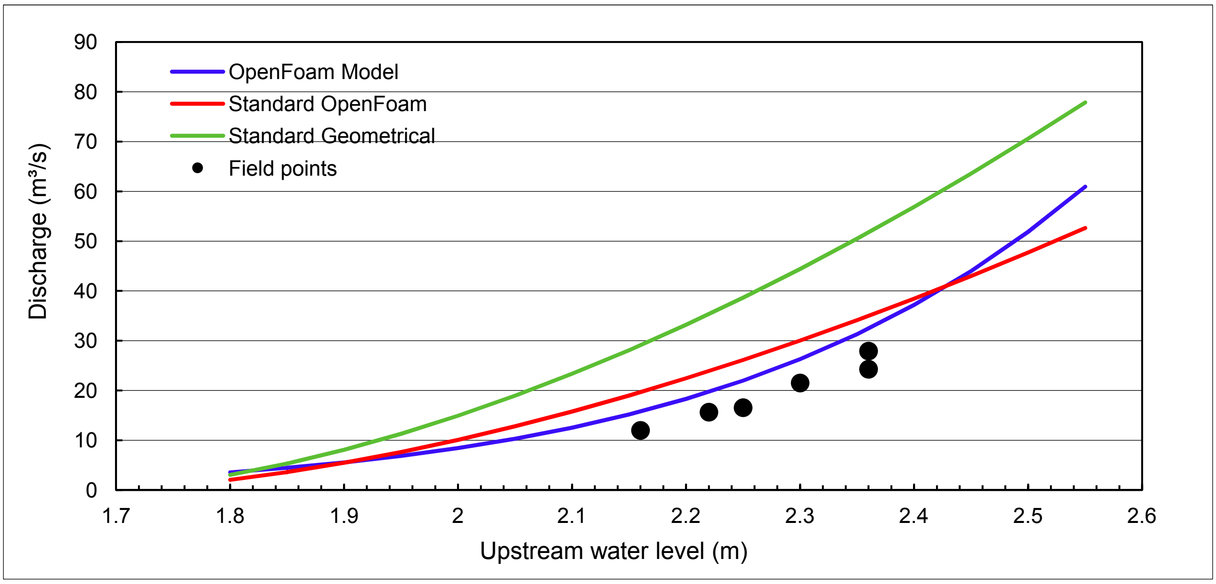

Figure 10. Stage-discharge curves obtained from the different methods.

6 CONCLUSIONS

The damaged weir of Dory on the Cavaillon River in Haïti will be used as an upstream boundary condition of a flow model developed in frame of a scientific cooperation project. Therefore, a reliable stage-discharge relation is required. Unfortunately, no information was available about the design of this weir. So, using scarce measured field data, the classical weir theory and detailed numerical simulations, a new stage-discharge relation was constructed. The results showed that the numerical simulations, even if achieved in a simplified way using only five representative slices of the weir, provided interesting results. These appear to be close to the field measurements, giving some confidence to use such models.

Nevertheless, even if this work demonstrates the merits of the combined approach, it also brings up some questions. In view of the divergence between the standard Open foam equivalent weir (red line in Figure 10) and the detailed Open foam model (blue line in Figure 10) for higher discharges, the question of the reliability of the curves arises, especially if it is to be used for extreme cases.

Further work will be carried out to obtain more information from the Open foam simulations. In particular, a new topographical survey was conducted and the data will be treated in order to improve the accuracy of the Open foam model close to the banks. Also, the radial gate located on the left bank will have to be included in the model in order to represent the overflow in cases of very high discharges. Finally, the full 3D simulations with this detailed model will be carried out to compare to the current five-slice model.

REFERENCES

Bureau of Reclamation (1960). *Design of Small Dams.* A Water Resources Technical Publication. First Edition, 1960. Second Edition, 1973. Revised Reprint 1974.

Hirt, C. W. & Nichols, B. D. (1981) Volume of Fluid (VOF) Method for the Dynamics of Free Boundaries. *Journal of Computational Physics*, 39, 201-205.

Joseph A., Carlier d'Odeigne O., Zech Y., Gonomy N. & Soares-Frazão S. (2015). Construction of One-Dimensional Model for The Cavaillon River, Haiti, from an In-Situ Survey of The Bathymetry, *E-Proceedings of the 36th IAHR World Congress*, The Hague, The Netherlands.

Roelandt O. & Verschoore T (2016). Numerical Modeling of a Flow on a Deteriorated Weir: Application to the Dory Weir, Cavaillon River, Haïti, *Msc Thesis* Work, Université Catholique de Louvain.

A SPH SEDIMENT MODEL FOR SCOURING

ALEX GHAITANELLIS(1), DAMIEN VIOLEAU(2), AGNES LEROY(3), MARTIN FERRAND(4), ANTOINE JOLY(5) & KAMAL EL KADI ABDERREZZAK(6)

(1,2,3,4,5,6) EDF R&D / LNHE and Saint-Venant Laboratory for Hydraulics, Chatou, FRANCE
alex.ghaitanellis@edf.fr
(2) EDF R&D / MFEE, Chatou, FRANCE

ABSTRACT

A multi-fluid SPH formulation combined to an elastic-viscoplastic stress model is applied to the modelling of non-cohesive sediment transport. The multi-fluid formulation is based on Hu and Adam's (2006) model using a modified continuity equation proposed by Vila (1999) so that the model is able to handle free-surface flows. The boundary conditions are imposed using the unified semi-analytical wall (USAW) boundary conditions model that has proved its efficiency in simulating flows that both require an accurate pressure and shear stress treatment at the wall, and present complex boundary geometries (Ferrand et al., 2013). The sediment is assumed to be either dry or fully saturated and the water-sediment mixture is modelled using a continuous description. Regarding the deviatoric stresses, the soil is assumed to behave as an elastic material when the strain rates are low, similarly to Ulrich (2013). Otherwise, it behaves as a viscoplastic fluid for non-negligible strain rates. Hence, the material has a yield stress under which no significant deformation occurs. When it is exceeded, the soil starts to flow following a shear thinning rheological law. The transition between solid and liquid state is made using a blending function driven by the magnitude of strain rate. A new liquid-solid transition threshold based on the granular material properties is proposed, making the model free of numerical parameter. A particular attention is paid to the computation of the yield stress that has a key role in the solid-liquid transition as well as in the rheological behaviour of the non-Newtonian fluid state. The model is tested on 2D soil collapse test case and a dam break over mobile bed where the rapid transient flow involves erosion of sediment and bed-load transport. Results are compared with experimental data (Bui et al., 2008; Spinewine and Zech, 2007) and a good agreement is obtained.

Keywords: Sediment transport; scouring; non-newtonian; smoothed particle hydrodynamics (SPH).

1 INTRODUCTION

The study of sediment transport is a major concern for many industrial and environmental stakeholders. In addition to experimental studies, the simulation of sediment transport has become an essential tool for the design and the maintenance of hydraulic structures. Simulations are used to evaluate the effect of the sedimentation on their functioning and efficiency, to measure the effect of such structures on the natural sediment transport and the resulting impact on the environment. The simulation of these phenomena allows to anticipate the resulting costs, but also to test sediment management strategies.

The Smoothed Particle Hydrodynamics (SPH) is particularly adapted for modelling sediment transport at a local scale. To do so, the main idea is to represent the sediment as a fluid with its proper physical properties (density, viscosity, and so on). Then, rheological laws, erosion criteria and suspended-transport model can be used to improve the modelling of physical phenomena involved in sediment transport.

In SPH literature, these problems have been mainly addressed using a rheological approach. The sediment is usually treated as a viscoplastic fluid. Thus, under a critical shear-stress, referred to as yield stress, the sediment is supposed to behave like a solid and there is no significant deformation. When the yield stress is exceeded, the fluid starts to flow and its viscosity decreases as the strain rate grows. For practical reasons, the solid state is usually approached using a highly viscous state. Ulrich (2013) proposed a more complex formulation modelling the solid state with a linear solid-elastic model.

In the present work, an improvement of Ulrich's model is proposed. The solid stresses are calculated from SPH particles displacement instead of integrating the rate-of-strain tensor. Moreover, a liquid-solid transition threshold based on the granular material properties is developed, making the model free of numerical parameter. The model is combined to a multi-fluid formulation derived from a definition of density proposed by Hu and Adams (2006). The continuity equation proposed by Vila (1999) is used so that the model can handle free-surface flows, and the boundary conditions are imposed using the unified semi-analytical wall (USAW) boundary conditions model (Ferrand et al., 2013). The model is validated on an experimental two-dimensional case of soil collapse (Bui et al., 2008) and applied to a case of dam-break over a mobile bed.

In this paper, the governing equations and the elastic-viscoplastic model are presented is section 2. Then, the multi-fluid SPH model and discretized equations are summarized in section 3 while the simulations results are exposed in section 4.

2 GOVERNING EQUATIONS

2.1 Lagrangian form of weakly-compressible Navier-Stokes equations

In this work suspended load transport is neglected. Therefore, the problem is reduced to the modelling of bed load transport. To do so, a two-fluid approach was adopted where the water and the soil are treated as two non-miscible homogeneous fluids, having their own physical properties. The same set of equations is used for both of them but the deviatoric stresses are calculated with different behaviour laws. In the framework of weakly-compressible flows, the Lagrangian form of continuity equation reads:

$$\frac{d\rho}{dt}=-\rho \text{ div } \mathbf{u} \quad [1]$$

with ρ the fluid density, t the time and $\boldsymbol{u}$ the velocity. Then, the momentum equation reads:

$$\frac{d\mathbf{u}}{dt}=-\frac{1}{\rho}\mathbf{grad}\ p+\frac{1}{\rho}\ \mathbf{div}\ \boldsymbol{\tau}+\mathbf{g} \quad [2]$$

with p the pressure, $\boldsymbol{g}$ the gravity and $\boldsymbol{\tau}$ the deviatoric component of the stress tensor. The pressure is calculated from density using the following state equation:

$$p=\frac{\rho_0 c_0^2}{\zeta}\left[\left(\frac{\rho}{\rho_0}\right)^{\zeta}-1\right] \quad [3]$$

with ρ_0 the reference density, c_0 the numerical speed of sound and ζ the isentropic coefficient. The same state equation is used for soil and water, with suitable values of ρ_0. To satisfy the weakly compressible condition, the numerical speed of sound has to be 10 times greater than the flow maximum velocity. The isentropic coefficient is set to 7 for both water and soil. Finally, water being treated as a Newtonian fluid, the deviatoric stress is nothing but the viscous stress tensor:

$$\mathbf{div}\ \boldsymbol{\tau}=\text{div}\left(\eta\left[\mathbf{grad}\ \mathbf{u}+(\mathbf{grad}\ \mathbf{u})^T\right]\right) \quad [4]$$

where η represents the sum of dynamic and turbulent viscosity obtained from the $k-\epsilon$ model developed in Leroy et al. (2014).

2.2 Soil Model

2.2.1 Homogeneous mixture model

The bed of sediment is composed of grains having a density ρ_g, and it has a porosity ϕ that is assumed to be constant and homogenous. The soil can be either dry or saturated with water. Therefore, an equivalent density of the bed in both cases could be defined:

$$\begin{cases}\rho_{eq}^{DRY}=(1-\phi)\rho_g+\phi\rho_w \\ \rho_{eq}^{SAT}=(1-\phi)\rho_g+\phi\rho_w\end{cases} \quad [5]$$

where ρ_w is the density of water.

2.2.2 Definitions and generalities about rheological approach for the modelling of soil

Adopting a rheological approach, the soil is usually treated as a viscoplastic material. As a consequence, below a yield stress τ_y, there is no deformation and the material behaves like a rigid body. When the yield stress is exceeded, the material starts to flow. In such a model, the yield stress has to be compared to an invariant measure of the deviatoric stress tensor τ. In this work, the tensor second invariant is used according to von Mises (1913) criterion:

$$\tau=\sqrt{\frac{1}{2}\sum_{i,j}\tau_{ij}\tau_{ij}} \quad [6]$$

Many viscoplastic materials can be described using the ideal Bingham model that reads:

$$\begin{cases} \dot{\boldsymbol{\gamma}}=\mathbf{0} & \text{if } \tau<\tau_y \\ \boldsymbol{\tau}=2\left(\eta_\infty+\frac{\tau_y}{\dot{\gamma}}\right)\dot{\boldsymbol{\gamma}} & \text{if } \tau>\tau_y \end{cases} \quad [7]$$

with η_∞ the plastic viscosity, $\dot{\boldsymbol{\gamma}}$ the strain rate tensor and $\dot{\gamma}$ its second invariant defined as:

$$\dot{\gamma}=\sqrt{2\sum_{i,j}\dot{\gamma}_{ij}\dot{\gamma}_{ij}} \quad [8]$$

where $\dot{\gamma}_{ij}$ are components of the strain rate tensor:

$$\dot{\boldsymbol{\gamma}}=\frac{1}{2}\left(\mathbf{grad\ u}+(\mathbf{grad\ u})^{\mathbf{T}}\right) \quad [9]$$

Note that the Bingham model is discontinuous and requires to track down beforehand the yielded and unyielded regions to know which equation should be applied. Indeed, the liquid-solid transitions are not explicitly given by the model. This can be verified calculating the second invariant of the deviatoric stress tensor corresponding to liquid state:

$$\tau=\eta_\infty\dot{\gamma}+\tau_y \quad [10]$$

Thus when the strain rate $\dot{\gamma}$ vanishes, the deviatoric stress tends to the yield stress and never goes below. As a consequence, this model is not suitable for numerical simulation. To circumvent this issue, viscoplastic materials are usually approximated as uniformly liquid materials, exhibiting an infinite viscosity in the limit of low strain rates. Numerically, this is achieved using shear thinning rheological law and limiting the viscosity to a huge but finite maximum value. This method is straightforward and has been widely applied to the simulation of sediment transport with finite volumes (Morichon et al., 2013), Moving Particle Semi-implicit method (Nabian et al., 2016) and Smoothed Particles Hydrodynamics method (Capone et al., 2010).

This approach is particularly adapted for highly dynamic scenarios but exhibits severe drawbacks regarding small strain-rates and deformations. Indeed, the maximum viscosity has to be large enough to guarantee that no significant motion occurs in unyielded regions, and to ensure that results would not be affected by a new increase of this parameter. But in practice, the maximum value of viscosity is actually limited for explicit time integration scheme, because of computational cost.

In the present paper, following the work of Ulrich (2013), the soil is treated as a linear-elastic solid in unyielded regions, and as a shear thinning fluid in yielded regions. A continuous transition between the two states is ensured by a blending function driven by the strain rate magnitude.

2.2.3 Yield stress

The yield stress is calculated according to Mohr-Coulomb's yield criterion. For non-cohesive material, it reads:

$$\tau_y=p_{eff}\tan\psi \quad [11]$$

with p_{eff} the effective pressure and ψ the internal friction angle which is a constant physical property of the granular material.

The effective pressure is the normal stress that actually applies between the grains. It takes into account the pressure due to the weight of sediment above the point of interest, partially compensated by buoyancy forces when the soil is saturated with water. Effective pressure can be calculated with Terzaghi's expression:

$$p_{eff}=p_{tot}-p_{pw} \quad [12]$$

where is p_{tot} is the total pressure due to the weight of overlaying sediment and water, and p_{pw} is the pressure of water inside the pores, referred to as pore water pressure. Usually, p_{pw} is assumed to be close to hydrostatic pressure. Thus, the effective pressure can be calculated from the vertical position of the point of interest z, and the position of soil-water interface z_I:

$$p_{\text{eff}}=g(z_I-z)(\rho_{eq}^{SAT}-\rho_w) \qquad [13]$$

Note that p_{eff} doesn't depend on the weight of water overlaying the soil. Obviously, for dry sediment, the effective pressure is equal to the total pressure. Furthermore, by combining equations [10] and [12], the result was the yield stress is zero in z_I, as expected for non-cohesive sediment.

2.2.4 Solid deviatoric stress tensor

In unyielded regions, the soil is treated as a linear elastic solid. Following Hook's law for an isotropic material, the Jaumann derivative of the solid deviatoric stress tensor $\boldsymbol{\tau}^s$ reads:

$$\dot{\boldsymbol{\tau}}^s = \frac{E}{(1+\nu)}\dot{\boldsymbol{\gamma}} + \dot{\boldsymbol{J}} \qquad [14]$$

with E the Young's modulus, ν the Poisson's coefficient and $\dot{J}$ the rate of Jaumann tensor:

$$\dot{\boldsymbol{J}} = \boldsymbol{\tau}^s\dot{\boldsymbol{\omega}} - \dot{\boldsymbol{\omega}}\boldsymbol{\tau}^s \qquad [15]$$

where $\dot{\boldsymbol{\omega}}$ is the rotation rate tensor, that is to say the anti-symmetric part of the velocity gradient tensor:

$$\dot{\boldsymbol{\omega}} = \frac{1}{2}(\mathbf{grad}\,\boldsymbol{u} - (\mathbf{grad}\,\boldsymbol{u})^T) \qquad [16]$$

Note that the Jaumann derivative is used so that the time derivative of stress does not depend on the frame of reference. To compute the deviatoric stress, equation [14] is integrated in two steps. Regarding the Jaumann tensor, equation [15] is integrated using an explicit time integration scheme. Then, regarding the first term in equation [14], referring to the Lagrangian property of SPH, that is by computing the shear strain from the displacement of particle X instead of integrating the strain rate:

$$\boldsymbol{\gamma} = \frac{1}{2}(\mathbf{grad}\,\boldsymbol{X} + (\mathbf{grad}\,\boldsymbol{X})^T) \qquad [17]$$

with the displacement $\boldsymbol{X}$ defined by:

$$\boldsymbol{X}(t) = \boldsymbol{r}(t) - \boldsymbol{r}(0) \qquad [18]$$

where is $\boldsymbol{r}$ the SPH particle position. The following expression was obtained:

$$\boldsymbol{\tau}^s = \frac{E}{(1+\nu)}\boldsymbol{\gamma} + \boldsymbol{J} \qquad [19]$$

Furthermore, the material is supposed to yield when the stress magnitude reaches the yield stress. Thus, the solid deviatoric stress tensor $\boldsymbol{\tau}^s$ should be rescaled when its invariant τ^s measure exceeds the yield stress τ_y:

$$\begin{cases} \boldsymbol{\tau}^{ss} = \boldsymbol{\tau}^s & \text{if} \quad \tau^s \le \tau_y \\ \boldsymbol{\tau}^{ss} = \frac{\tau_y}{\tau^s}\boldsymbol{\tau}^s & \text{if} \quad \tau^s > \tau_y \end{cases} \qquad [20]$$

where $\boldsymbol{\tau}^{ss}$ denotes the rescaled deviatoric stress tensor.

2.2.5 Fluid deviatoric stress tensor

In yielded regions, the soil is in a fluid state and exhibits a non-Newtonian behaviour. Thus the fluid deviatoric stress tensor $\boldsymbol{\tau}^f$ is calculated according to the following constitutive equation:

$$\boldsymbol{\tau}^f = 2\eta_{\text{eff}}\,\dot{\boldsymbol{\gamma}} \qquad [21]$$

with η_{eff} the effective viscosity defined as:

$$\eta_{\text{eff}} = \frac{\tau_y}{\dot{\gamma}} \quad [22]$$

With this model, the magnitude of fluid deviatoric stress is always equal to the yield stress.

2.2.6 Solid/fluid transition

A continuous transition between solid and liquid state is ensured by a blending function ξ driven by the magnitude of strain rate. Since the physical threshold delimiting yielded and unyielded regions is expressed is terms of stress (*i.e.* the yield stress τ_y), a new one expressed in terms of strain rate was built, denoted $\dot{\gamma}_y$. To do so a yield viscosity η_y was defined as the maximum possible viscosity for the material in fluid state. Thus the result:

$$\dot{\gamma}_y = \frac{\tau_y}{\eta_y} \quad [23]$$

Similarly to the simple rheological approach, Ulrich chose the value of η_y in a trial and error approach, increasing incrementally its value until obtaining the expected result. Here to find a value based on the physical properties of the material the Deborah number De was used which characterize the fluidity of a material under the flow conditions of a specific experiment:

$$De = \frac{t_R}{t_C} \quad [24]$$

where t_C is the characteristic time scale of the experiment and t_R the stress relaxation time. For a granular material, Sun and Wang (2013) proposed to use the characteristic time of Rayleigh waves propagating along a grain surface:

$$t_R^G = \frac{\pi R}{0.163\ v + 0.877}\sqrt{\frac{\rho}{G}} \quad [25]$$

with R the grain radius and G the shear modulus defined by:

$$G = \frac{E}{2(1+v)} \quad [26]$$

On the other hand, in the plastic regime, the soil can be seen as viscoelastic material. In that case, the Deborah number is calculated with a relaxation time defined as:

$$t_R^{VE} = \frac{\eta_y}{G} \quad [27]$$

Therefore, combining equations [26] and [27] and assuming that the two characteristic times are equal a definition of the yield viscosity was found:

$$\eta_y = \frac{\pi R \sqrt{G\rho}}{0.163\ v + 0.877} \quad [28]$$

Therefore the blending function ξ proposed by Ulrich (2013) was defined:

$$\xi(\dot{\gamma}) = \begin{cases} 3\left(\frac{\dot{\gamma}}{\dot{\gamma}_y}\right)^2 - 2\left(\frac{\dot{\gamma}}{\dot{\gamma}_y}\right)^3 & \text{if} \quad \dot{\gamma} < \dot{\gamma}_y \\ 1 & \text{if} \quad \dot{\gamma} > \dot{\gamma}_y \end{cases} \quad [29]$$

It is important to note that the solid stresses in the soil should vanish when the fluid state is reached. Therefore, the displacement is reinitialized when $\xi \geq 0.8$. Finally, the fluid/solid deviatoric stress tensor is given by:

$$\boldsymbol{\tau} = \xi\ \boldsymbol{\tau}^{f} + (1-\xi)\ \boldsymbol{\tau}^{ss} \quad [30]$$

3 NUMERICAL MODELLING

3.1 SPH method

Within SPH framework, the fluid is discretized in a set of macroscopic volumes, thereafter referenced as particles. The SPH particles move at fluid velocity, and carry physical quantities such as the mass m, the position $\boldsymbol{r}$, the velocity $\boldsymbol{u}$, and so on. The fluid governing equations are discretized using a discrete interpolation of fields and differential operators. For a particle a, the contribution of a neighbour b to the SPH interpolation functions is weighted by a kernel function w that only depends on inter-particle distance $r_{ab}=|r_a\text{-}r_b|$.

3.2 USAW boundary conditions

The USAW boundary conditions model is a semi-analytical approach that allows to impose accurately the boundary conditions, even for flows involving complex boundary geometry. In this model, boundaries are discretized using a mesh composed of boundary elements (S) (see Figure 1a). Truncated fluid particles are placed at the vertices of the mesh, they move at wall velocity and are referred to as vertex particles (V). Contrary to boundary elements, they carry a mass m and should be taken into account in the continuity equation. Their volume V depends on the local geometry of the boundary and is calculated as a fraction θ of a reference volume $\bar{V}$: $V=\theta\bar{V}$ (see Figure 1b). In two dimensions, θ is defined as the angle between two connected segments, divided by 2π. Thus, the vertex particles identified as $\theta \in [0;1]$. In order to have a general formulation, the definitions are $\theta=1$ for free particles (F) and $\theta=1/2$ for boundary elements. In three dimensions, θ is calculated in a similar way using solid angles. Moreover, for a particle of fluid close to the walls, the interpolation functions are under-estimated because of the lack of particles beyond the boundary. Therefore, a renormalization factor Γ_a was used and defined by:

$$\Gamma_a=\int_{\Omega\cap\Omega_a} w(|r'\text{-}r|)d^nr' \qquad [31]$$

where Ω is the simulation domain, Ω_a the kernel support centered on particle a and n the space dimension.

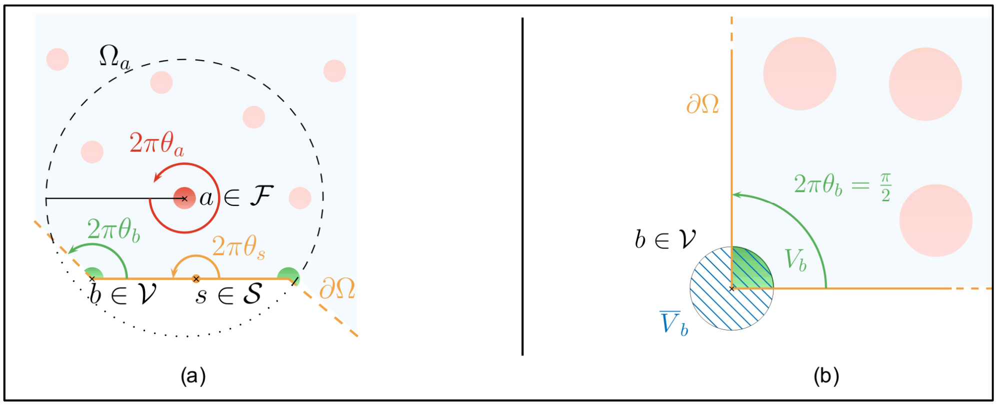

Figure 1. (a) Sketch of a boundary with: a vertex particle $b \in V$; a segment $s \in S$ $(\theta_s = 1/2)$; a fluid particle $a \in F$ $(\theta_a = 1)$. (b) Sketch of a vertex particle in a right-angled corner.

3.3 SPH Multi-Fluid Model

Hu and Adam's SPH density definition adapted to USAW boundary condition (Ghaïtanellis et al., 2015) is given by:

$$\rho_a=\frac{m_a}{\theta_a\Gamma_a}\sum_{b\in F\cup V}\theta_b w_{ab} \qquad [32]$$

denoting $w_{ab}=w(|\boldsymbol{r}_a-\boldsymbol{r}_b|)$. In this framework, the gradient of a scalar field A reads:

$$\mathbf{G}_a\{A_b\}=\frac{1}{V_a\Gamma_a}\sum_{b\in F\cup V}\left(A_aV_a^2\frac{\theta_b}{\theta_a}+A_bV_b^2\frac{\theta_a}{\theta_b}\right)\nabla w_{ab}-\frac{1}{V_a\Gamma_a}\sum_{s\in S}V_s\left(A_aV_a^2\frac{\theta_b}{\theta_a}+A_sV_s^2\frac{\theta_a}{\theta_s}\right)\nabla\Gamma_{as}\approx\langle\mathbf{grad}\,A\rangle_a \qquad [33]$$

where $\nabla\Gamma_{as}$ is the contribution of boundary element s to the gradient of Γ_a. For a boundary element s, delimited by two vertex particles (v_1, v_2), $\nabla\Gamma_{as}$ is defined by:

$$\nabla\Gamma_{as}=\left(\int_{v_1}^{v_2} w(r)\,dl\right)\mathbf{n}_s \qquad [34]$$

where $\boldsymbol{n}_s$ is the inward normal of the boundary element s. The divergence of vector field $\boldsymbol{A}$ was defined as:

$$D_a\{\mathbf{A}_b\}=-\frac{V_a}{\Gamma_a}\sum_{b\in F\cup V}\frac{\theta_b}{\theta_a}(\mathbf{A}_a\text{-}\mathbf{A}_b)\cdot\nabla w_{ab}+\frac{V_a}{\Gamma_a}\sum_{s\in S}\frac{\theta_s}{\theta_a V_s}(\mathbf{A}_a\text{-}\mathbf{A}_s)\cdot\nabla\gamma_{as}\approx\langle\text{div }\mathbf{A}\rangle_a \qquad [35]$$

Finally, a discrete form of the following second order operator is needed:

$$\langle\mathbf{div}\left[B\left(\mathbf{grad\ A}+(\mathbf{grad\ A})^T\right)\right]\rangle_a\approx\mathbf{L}_a\{B_b,\mathbf{A}_b\} \qquad [36]$$

where B and $\boldsymbol{A}$ are respectively a scalar and a vector field. Extending Espanol and Revenga's (2003) formula to USAW framework (Ghaïtanellis et al., 2016), the formula obtained:

$$\mathbf{L}_a\{B_b,\mathbf{A}_b\}=\frac{1}{\Gamma_a}\sum_{b\in F\cup V}V_b\frac{2\,B_aB_b}{B_a+B_b}\left[(n+2)(\mathbf{A}_{ab}\cdot\mathbf{e}_{ab})\cdot\mathbf{e}_{ab}+\mathbf{A}_{ab}\right]\frac{\nabla w_{ab}\cdot\mathbf{e}_{ab}}{r_{ab}}-\frac{1}{\Gamma_a}\sum_{s\in S}2\,B_a\frac{\mathbf{A}_{ab}}{r_{ab}}\nabla\gamma_{as} \qquad [37]$$

Time integration is done with a full explicit symplectic method that leads to the following scheme:

$$\begin{cases}\rho_a^n\mathbf{u}_a^{n+1}=\rho_a^n\mathbf{u}_a^n-\delta t\left[\mathbf{G}_a\{p_b\}+\rho_a\mathbf{g}+\xi\,\mathbf{L}_a\left\{\eta_{eff,b},\mathbf{u}_b\right\}+(1-\xi)(\mathbf{L}_a\{G,\mathbf{X}_b\}+\mathbf{D}_a\{\mathbf{J}_b\})\right]\\ \mathbf{r}_a^{n+1}=\mathbf{r}_a^n+\delta t\ \mathbf{u}_a^{n+1}\\ (\Gamma_a\rho_a)^{n+1}=(\Gamma_a\rho_a)^n+\frac{m_a}{\theta_a}\sum_{b\in F\cup V}\theta_b\left(w_{ab}^{n+1}-w_{ab}^n\right)\\ p_a^{n+1}=\frac{\rho_0c_0^2}{\zeta}\left[\left(\frac{\rho_a^{n+1}}{\rho_0}\right)^{\zeta}-1\right]\end{cases} \qquad [38]$$

Note that in water the blending function ξ is always equal to 1 and η_{eff} is just the sum of dynamic and turbulent viscosity.

4 SIMULATION RESULTS

4.1 Simulation of 2D Soil Collapse

To validate the present model, a simulation of an experimental two-dimensional collapse of dry soil is carried out. The experiment was conducted by Bui et al. (2008) the experimental set-up is illustrated in Figure 2a. The material is composed of aluminium bars of diameter 1 mm and 1.5 mm, length 50 mm and density 2650 kg/m3. The material porosity is not specified by the authors so it is approximated by using the highest compact binary circle packing, leading to $\phi\approx0.1$. All other physical parameters were determined experimentally by Bui et al. (2008) and are summarized in Table 1.

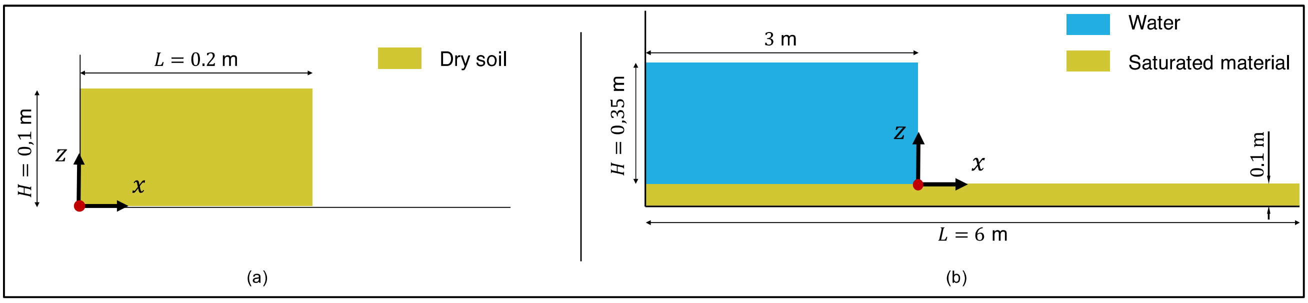

Figure 2. Experimental setups – (a) 2D soil collapse. (b) Dam-break flow on movable bed.

The simulations were performed using approximately 20,000 particles of soil and 1,400 vertex and boundary particles, with an initial particle spacing of $\delta r = 0.001$ m. In all simulations, the ratio between δr and the smoothing length h is $\delta r/h = 2$. The numerical speed of sound was set to $c_0 = 10$ m/s.

Table 1. Physical properties of the material.

	$\rho_g\ [kg.m^{-3}]$	$d_g\ [m]$	ϕ [1]	$E\ [Pa]$	ν [1]	ψ [°]
Aluminium bars	2650	$1.25 \cdot 10^{-3}$	0.10	$8.4 \cdot 10^5$	0.3	19.6

Figure 3 shows the simulation result after 5 seconds of physical time. Note that the model is able to represent the solid state even after a large time compared to the characteristic time of the experiment $t_C = \sqrt{H/g} = 0.1$s. In Figure 4, the surface configuration at the end of the experiment is compared with numerical results obtained after 5 and 10s showing a very good agreement even after $100t_C$.

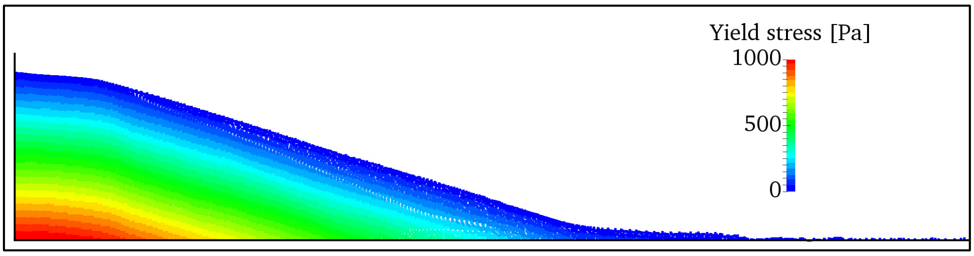

Figure 3. SPH simulation result at $t = 5$ s.

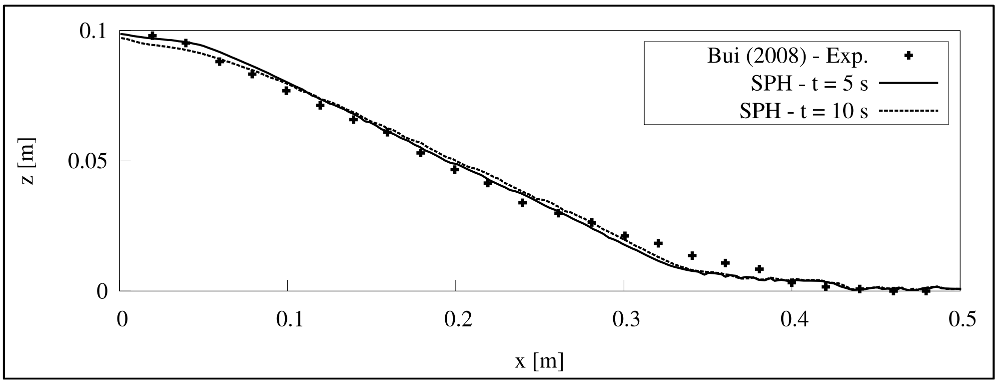

Figure 4. Surface configuration at times 5 and 10 seconds. Solid state is well represented even after $100t_C$.

4.2 Simulation of 2D Dam-break over a mobile bed

The model was also tested on a case of dam-break wave propagating over a saturated granular bed. The study is based on the small-scale experiments carried out by Spinewine and Zech (2007). The experiments were performed in a flume being 25 cm wide and 6 m long. The initial configuration of the experiment is illustrated in Figure 2b. The dam-break is initiated by the sudden lowering of a gate that is not taken into account in the simulation. Two materials are tested to investigate the capability of the model to exhibit different behaviours with respect to different materials. The physical parameters of the materials are summarized in table 2. Note that experimental Young's modulus and Poisson's coefficient were not given for these materials. Consequently, for similar cases the generic values from Ulrich (2013) was used. The simulations were carried out setting a particle spacing of $\delta r = 0.002$ m, resulting in 525,000 particles of water, 150,000 particles of saturated soil and 13,000 particles vertex and boundary particles. The same numerical speed of sound and isentropic coefficient are set for the two fluids, that is $c_0 = 37$ m/s and $\zeta = 7$.

Figure 5 shows a comparison of the experiment and the SPH simulation carried out for the sand. It could be seen that the dynamics of the flow is qualitatively well reproduced by the model. Figure 6 shows the interface between moving and motionless sediment (black), the water-sediment interface (blue) and the water free-surface (red) for the two materials. Continuous lines represent the numerical results while experimental data are represented as dotted lines. A good agreement is obtained for sand and PVC and the differences between the two experiments are well captured as well. Furthermore, comparing the total mass of sediments that have reached the downstream flume outlet the good order of magnitude, with a slightly underestimated value was found. For sand, the result was 1.5 kg while the experimental value is 3.0 kg (48% of error). For the PVC, the finding was 5 kg instead of 7.7 kg (36% of error). Nevertheless, the total mass eroded is very different for sand and PVC, demonstrating the capability if the model to take the material properties into account. To improve this result, other turbulence models could be tested. Indeed, the force exerted by water on the sediment is strongly related to the turbulent viscosity of water near the soil-water interface. The modelling of suspended load transport and seepage forces inside the soil could also help improve the results.

Table 2. Physical properties of the material.

	$\rho_g\ [kg.m^{-3}]$	$d_g\ [m]$	$\phi\ [1]$	$E\ [Pa]$	$\nu\ [1]$	$\psi\ [°]$
Sand	2683	$1.89 \cdot 10^{-3}$	0.47	$8.0 \cdot 10^{5}$	0.3	30
PVC	1580	$3.90 \cdot 10^{-3}$	0.42	$8.0 \cdot 10^{5}$	0.3	38

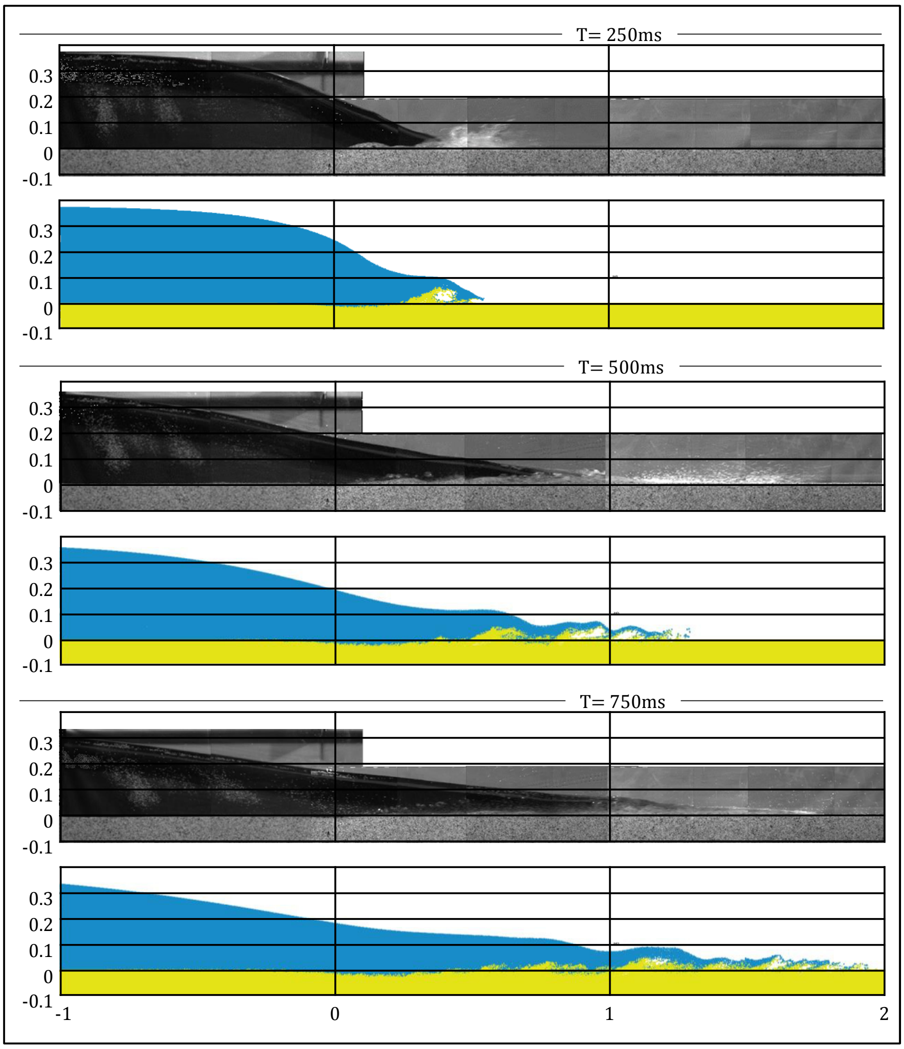

Figure 5. Comparison of experimental and numerical results, with sand, at time t = 250 ms, 500 ms and 750 ms. Graduations in meters.

5 CONCLUSIONS

In this paper, a new formulation of Ulrich's (2013) elastic-viscoplastic model is proposed and applied to the modelling of granular flows and bed load transport. The solid stresses are now calculated taking advantage of the Lagrangian character of SPH, using the displacement of SPH particles, and Espanol & vRevenga's second order operator, instead of integrating the rate-of-strain tensor. Furthermore, liquid-solid transition threshold is now calculated with physical properties of the material, leading to a model totally free of numerical parameters. The model is developed in the frame a multi-fluid SPH formulation with semi-analytical boundary conditions and a $k-\epsilon$ turbulence model.

A validation test case of a two-dimensional collapse of soil was conducted, giving a very good agreement with the experiment. The model was also tested on a case of dam-break wave propagating on a movable bed of saturated soil. Comparisons were made for two materials that are sand and PVC pullets. The general dynamic of the flow as well as the flow interfaces are well predicted by the model for both materials. The total mass of sediments that have reach the flume outlet is satisfactorily predicted, giving the good order of magnitude but an underestimated value. To circumvent this issue, several options are considered. First, another turbulence model could be tested to improve the calculation of the forces exerted by water on sediment. The modelling of suspended load transport could also improve the results, as well as the modelling of seepage forces inside the soil to take into account the effect of the water flow in the pores of the saturated sediment.

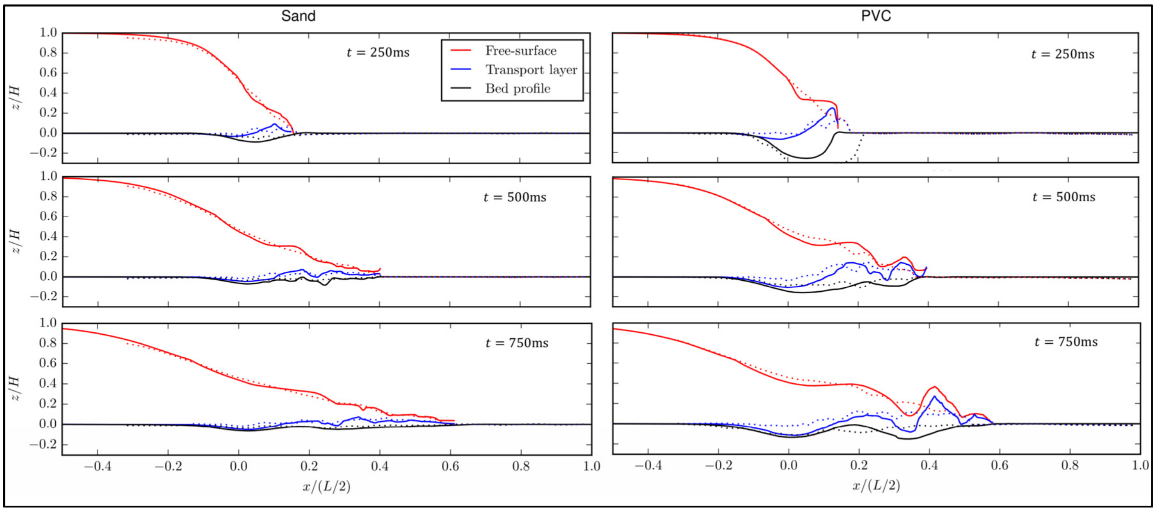

Figure 6. Comparison of experimental (dotted lines) and numerical (continuous lines) results at time t = 250 ms, 500 ms and 750 ms. Flow interfaces with experimental results as circles and SPH results as continuous lines.

REFERENCES

Bui, H.H., Fukagawa, R., Sako, K. & Ohno, S. (2008). Lagrangian Meshfree Particles Method (SPH) for Large Deformation and Failure Flows of Geomaterial using Elastic-Plastic Soil Constitutive Model. *International Journal for Numerical and Analytical Methods in Geomechanics*, 32(12), 1537-1570.

Capone, T., Panizzo, A. & Monaghan, J.J. (2010). SPH Modelling of Water Waves Generated by Submarine Landslides. *Journal of Hydraulic Research*, 48(1), 80–84.

Espanol, P. & Revenga, M. (2003). Smoothed Dissipative Particle Dynamics. *Physical Review E*, 67(2), 1-12.

Ferrand, M., Laurence, D.R., Rogers, B.D., Violeau, D. & Kassiotis, C. (2013). Unified Semi-Analytical Wall Boundary Conditions for Inviscid, Laminar or Turbulent Flows in the Meshless SPH Method. *International Journal for Numerical Methods in Fluids*, 71(4), 446-472.

Ghaïtanellis, A., Violeau, D., Leroy, A., Joly, A. & Ferrand, M. (2016). Improved Shields Criterion for SPH Simulations of Bed-Load Transport and Scouring. *In Proc. 11th international SPHERIC workshop*, 85–92.

Ghaïtanellis, A., Violeau, D., Leroy, A., Joly, A. & Ferrand, M. (2015). Application of the Unified Semi-Analytical Wall Boundary Conditions to Multi-Phase SPH. *In Proc. 10th international SPHERIC workshop*, 333–340.

Hu, X.Y. & Adams, N.A. (2006). A Multi-Phase SPH Method for Macroscopic and Mesoscopic Flows. *Journal of Computational Physics*, 213(2), 844-861.

Leroy, A., Violeau, D., Ferrand, M. & Kassiotis, C. (2014). Unified Semi-Analytical Wall Boundary Conditions Applied to 2-D Incompressible SPH. *Journal of Computational Physics*, 261, 106-129.

Mises, R.V. (1913). Mechanik der festen Körper im plastisch-deformablen Zustand. Nachrichten von der Gesellschaft der Wissenschaften zu Göttingen, *Mathematisch-Physikalische Klasse*, 1913, 582-592.

Morichon, D., Desombre, J. & Simian, B. (2013). VOF Simulation of Sediment Transport under High Velocity Flow Case of a Dam Break Over a Mobile Bed. *Coastal Dynamics* 2013, 1241-1250.

Nabian, M.A. & Farhadi, L. (2016). Multiphase Mesh-Free Particle Method for Simulating Granular Flows and Sediment Transport. *Journal of Hydraulic Engineering*, 143(4), 1-11.

Spinewine, B., & Zech, Y. (2007). Small-Scale Laboratory Dam-Break Waves on Movable Beds. *Journal of Hydraulic Research*, 45(1), 73-86.

Sun, Q. & Wang, G. (2013). *Mechanics of Granular Matter.* WIT Press, Tsinghua University, China.

Ulrich, C. (2013). Smoothed-Particle-Hydrodynamics Simulation of Port Hydrodynamic Problems. *PhD thesis,* Hamburg University of Technology.

Vila, J.P. (1999). On Particle Weighted Methods and Smooth Particle Hydrodynamics. *Mathematical models and methods in applied sciences*, 9(02), 161-209.

EXPERIMENTAL INVESTIGATION OF FREE SURFACE DYNAMICS AND PRESSURE FLUCTUATIONS IN A CLOSED-CONDUIT HYDRAULIC JUMP

YEE-MENG CHIEW [1] & ADEL EMADZADEH [2]

[1,2] School of Civil and Environmental Engineering, Nanyang Technological University, Singapore.
cymchiew@ntu.edu.sg; aemadzadeg@ntu.edu.sg

ABSTRACT

A hydraulic jump may occur in a closed conduit such as shaft spillways, culverts, etc. when the upstream super-critical flow meets a downstream sub-critical flow. If the sub-critical conjugate depth is less than the height of the conduit, a free surface will be present, causing the formation of a hydraulic jump, similar to those formed in open-channel flows. However, if the downstream sub-critical conjugate depth exceeds the closed conduit height, the flow may fill the conduit completely resulting in a pressurized hydraulic jump known as a closed-conduit jump. These jumps are characterized by large vertical surges and low frequency pressure fluctuations that lead to significant vibrations and transient hydraulic loads, resulting in the destabilization of hydraulic structures. While hydraulic jumps in open-channel flows have received extensive attention in the research fraternity, comparatively less information is available on the characteristics of turbulence, pressure fluctuations and energy dissipation in closed-conduit jumps. Consequently, this paper aims to present new experimental data on the flow field and pressure fluctuations associated with such hydraulic jumps in view of their relevance on the stability of hydraulic structures. The present experiments are concerned with closed-conduit jumps in a regular rectangular duct. Free surface fluctuations, if present, are measured using a high speed camera synchronized with a series of pressure transducers mounted on the conduit bed. Water surface dynamics and pressure fluctuations are investigated as a matter of concern in the design of stilling basins and other hydraulic structures. The experimental results show that high pressure fluctuations persist at the downstream end of closed-conduit jumps. Moreover, the mean depth calculated from pressure measurements is smaller than that deduced from the water surface profile obtained using high-speed images, probably due to the presence of air in the flow.

Keywords: Hydraulic jump; closed conduit; water surface profile; pressure fluctuation.

1 INTRODUCTION

A hydraulic jump is categorized by a rapid transition from super-critical to sub-critical flows in natural rivers or man-made hydraulic structures. It exhibits sharp discontinuity in the water surface generating recirculating rollers that entrain a mixture of water and air. It has a strong energy dissipative mechanism due to the formation of high intensity turbulence in a shear zone layer that forms between the roller and the under-flowing jet. Interactions between the mean velocity gradients and high-level turbulence produce high pressure fluctuations and forces at the boundary of the hydraulic structures (Schiebe, 1971). Neglecting the dynamic pressure fluctuations at the bed can lead to catastrophic structural failures through different mechanisms such as vibrations, structural resonance and fatigue. In addition, damages due to cavitation also are important in cases where the minimum local pressure fall below the saturation vapor pressure.

Except for the air model study of Rouse et al. (1959), experimental investigation of pressure fluctuations and turbulence in hydraulic jumps have been nearly absent until about 1965. Attempts in the measurement of turbulent velocity fields has encountered many difficulties in the presence of bubbles because bubbles adversely affect the hot-film and optical and acoustic methods of flow measurements. In addition pressure measurements at high Froude number hydraulic jumps were not feasible due to the absence of pressure transducers with a high sampling rate and data acquisition systems capable of recording and analyzing large amount of fluctuating pressure with high accuracy in the pre-mid 1960's era.

Vasiliev and Bukreyev (1967) could be the first study that attempted measurement of pressure fluctuations by using strain gauge-type transducers within the hydraulic jump in an open-channel flow. They found that the frequency distribution significantly differs from the Gaussian distribution in the initial part of the jump but they are close to each other at the downstream end of the jump. Schiebe (1971) studied the statistical characteristics of the fluctuating pressures exerted on the channel bed under the hydraulic jump. His measurements showed that the pressure distribution is highly skewed and peaked near the toe; and follows the Gaussian distribution in the remaining part of the jump. His results further showed that the maximum root mean square (rms) of pressure fluctuations on the bed occurred at approximately the middle part of the jump and the large pressure fluctuations diminished near its end.

While statistical analyses of the pressure fluctuations in open channel hydraulic jumps have been the subject of numerous researches (Fiorotto and Rinaldo, 1992; Toso and Bowers, 1988; Vasiliev and Bukreyev, 1967), very few studies were conducted to investigate the pressure distribution in closed-conduit hydraulic jumps. These jumps occur when the sub-critical conjugate depth exceeds the height of the closed conduit and the free surface flow changes to a pressurized flow downstream of the jump. In a closed-conduit hydraulic jump, higher bed pressure fluctuations are observed (Smith and Chen, 1989) and the air bubbles entrained by the jump rise to the conduit ceiling to form air pockets that may cause possible oscillations and structural damage (Ervine and Himmo, 1984).

Lane and Kindsvater (1938) may be the first to study closed-conduit hydraulic jumps. Later Kalinske and Robertson (1943) and Fassò (1956) studied air entrainment in closed-conduit hydraulic jumps and Haindl (1957) showed that the energy loss in closed-conduit hydraulic jumps are smaller and at most equal to the Borda-Carnot loss in hydraulic jumps with a free surface at identical Froude numbers. Rajaratnam (1965) and Smith and Chen (1989) also formulated the hydraulic jump conjugate depth in horizontal and sloped closed-conduit flows (Eqs. [2-3]). Although information on air entrainment and conjugate depth are comparatively more abundant in the literature, there is yet little information on the flow surface dynamics (Mouaze et al., 2005) and its association with pressure fluctuations on the bed.

Hitherto, most researches in this topic have been conducted with the aim of determining the conjugate depth ratio, energy dissipation and jump length. However none of these studies are concerned with the pressure fluctuations in closed-conduit jumps and how it is linked to the water surface profile. Therefore the current study aims to investigate these issues with simultaneous measurements of the water surface profile and pressure distribution on the bottom of the hydraulic jump. This is very important because closed-conduit jumps can entrain air into the flow under pressure while in open channel hydraulic jumps; the air is released in the roller section (Haindl, 1957).

2 EXPERIMENTAL SETUP

The present experiments were performed in a horizontal rectangular closed conduit that is 5 m long, 0.15 m deep and 20 cm wide. The conduit had glass-sided walls and the bed was half steel and half glass to accommodate flush mounting of the pressure transducers along the centerline of the channel and to provide optical access for the laser sheet. Water was supplied to the head tank from a sump via a centrifugal pump and the discharge was measured by using a magnetic flow meter. In an effort to provide a smooth and uniform inflow, a sluice gate was positioned 1m downstream of the conduit entrance. The intensity and location of the jump were controlled with the sluice and tail gates, with the latter located at the downstream end of the flume. The sluice gate had a machined streamline lip so that a supercritical stream with a thickness equal to the gate opening was produced.

The test area was located at a distance of 1 m from the sluice gate. Ten pressure transducers were mounted along the centerline of the conduit on the steel portion of the bed. The distance between two successive pressure transducers was 0.1 m (Fig. 1). The location of the toe of the jump was controlled by using the tail gate to ensure that the jump always formed within the test section. The gate opening was constant (3 cm) in all the experiments and the toe of the jump was located more than 1 m from the sluice gate to ensure that the flow is fully developed in the test section. This distance exceeds 50 times the gate opening.

Free surface elevations were measured by using a monochrome high speed camera with a 50-mm lens. Image distortion is kept to a minimum and the entire hydraulic jump from its toe to the end of the jump is kept within view of the camera in the experiment. Four LED lamps were used to illuminate the flow in the background and a thin translucent acrylic sheet was placed between the lamps and glass wall to evenly distribute the light in the background. The test section of the conduit and the camera were surrounded by opaque curtains mounted on a structure; this arrangement ensures that only the desired light is allowed for flow field illumination.

Since the high speed camera and pressure transducers were connected to the same data acquisition and triggering system, data measurement could commence at the same time. Consequently, simultaneous measurements of the pressure and water surface profiles were carried out for all experiments. The sampling rate of both the high speed camera and pressure transducers was 100 Hz with a frame size of 1920×504 pixels and the measurement duration was 20 seconds. Each monochrome frame of the recorded video was processed in the image processing toolbox in Matlab for extraction of the water surface profile. The image was first subtracted from a reference image taken from the empty conduit. Then, by using the threshold value, the water surface was identified, digitized and scaled from the image. This digitized water surface profile was used for further analyses. Figure 2 shows the adopted procedure in a sample image.

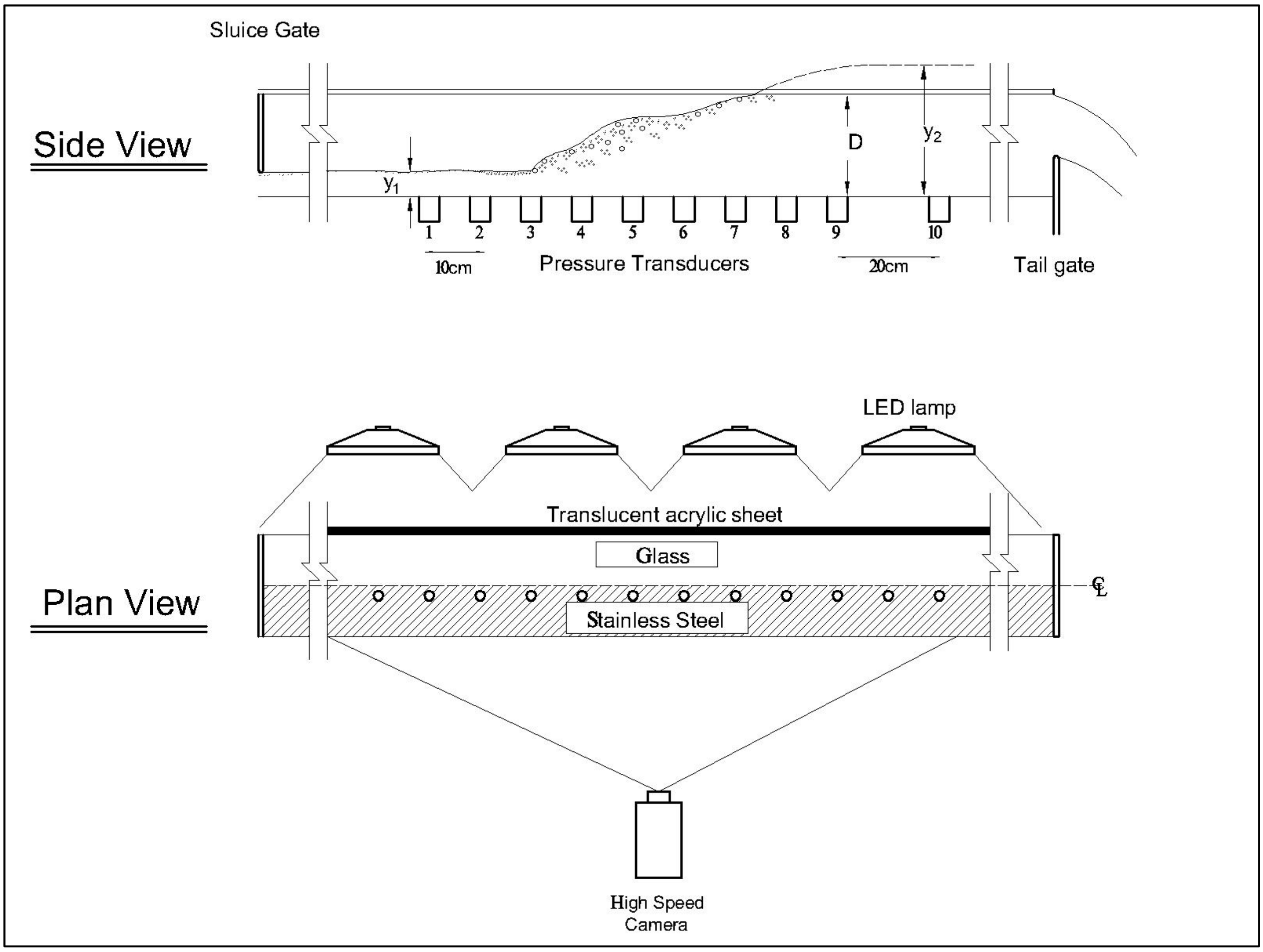

Figure 1. Sketch of the experimental setup (not to scale).

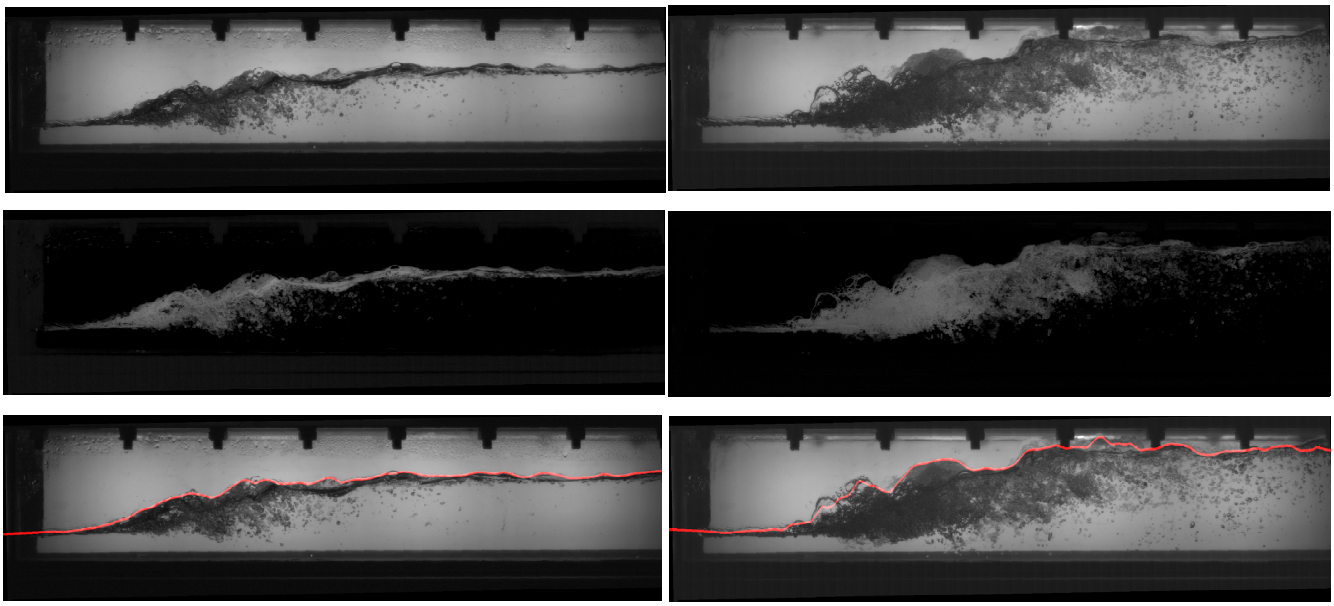

Figure 2. Extraction of water surface profile for Run 2 (Fr_1 = 2.42) on the left and Run 6 (Fr_1 = 3.14) on the right columns (Flow from left to right).

Table 1 shows the experimental data obtained in this study. The data comprise 16 runs with the same sluice gate opening, resulting in a constant inflow depth of around 0.03 m and conjugate depths varying from 0.06-0.184 m. Both the open-channel (Runs 1-10) and closed-conduit (Runs 11-16) hydraulic jumps were formed in the tests. The super-critical Froude number varies from 1.77-4.59, indicating the formation of both weak and oscillating jumps (Te Chow, 1959). It must be stated that the flow depths in Table 1 are extracted from pressure measurements on the bed. The conjugate depths for Runs 11-16 are therefore computed using the measured pressure by assuming a hydrostatic pressure distribution. Figure 3 shows the measured profiles for all 16 test runs.

Table 1. Experimental conditions.

Run	Q(m^3/s)	y_1	V_1	Fr_1	y_2
1	0.0060	0.031	0.97	1.77	0.055
2	0.0080	0.030	1.32	2.42	0.089
3	0.0071	0.033	1.08	1.91	0.075
4	0.0097	0.032	1.51	2.70	0.102
5	0.0100	0.031	1.62	2.96	0.117
6	0.0106	0.031	1.72	3.14	0.115
7	0.0112	0.031	1.81	3.29	0.124
8	0.0119	0.032	1.85	3.31	0.139
9	0.0126	0.034	1.85	3.20	0.139
10	0.0134	0.034	1.96	3.41	0.143
11	0.0139	0.032	2.17	3.88	0.157
12	0.0146	0.032	2.28	4.07	0.167
13	0.0151	0.034	2.21	3.82	0.165
14	0.0159	0.032	2.48	4.44	0.177
15	0.0164	0.032	2.57	4.59	0.184
16	0.0170	0.033	2.57	4.53	0.183

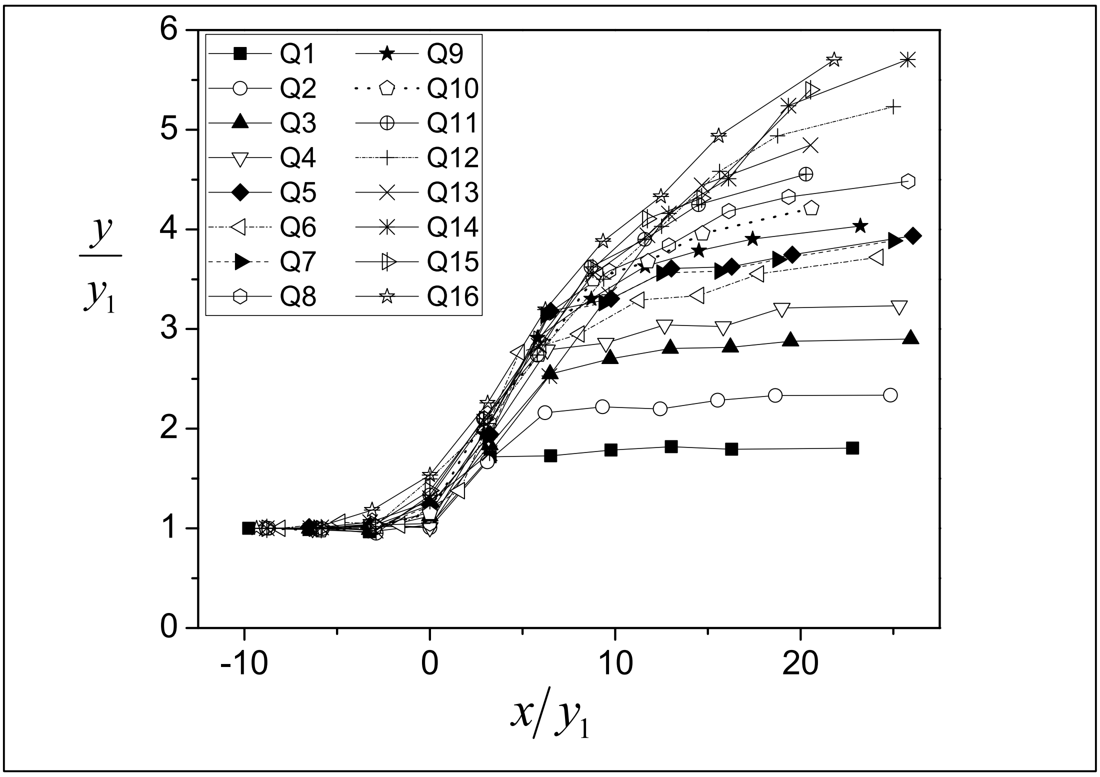

Figure 3. Dimensionless longitudinal mean pressure distribution in the streamwise direction.

Each of the y-values in Fig. 3 represents the mean flow depths computed from the time-averaged pressure measurements. It must be noted that all the pressure transducers were first calibrated in a stagnant water tank before the test to ensure accuracy. The horizontal axis in this figure shows the horizontal distance x from the toe of the jump, thus making the toe to be the reference position. Moreover, the data in both axes are rendered dimensionless by using the super-critical flow depth, y_1. The conjugate depth y_2 in Table 1 is taken from the most downstream pressure transducer where the water surface showed minimum changes in the streamwise direction.

3 Results

Using the momentum equation and assuming hydrostatic pressure and uniform velocity, Bélanger (1938) derived the well-known *simple hydraulic jump* equation to compute the conjugate depth ratio for steady open-channel flows in a horizontal rectangular conduit.

$$\frac{y_2}{y_1} = \frac{1}{2}\left[\sqrt{1+8Fr_1^2} - 1\right] \qquad [1]$$

where $Fr_1 = V_1/\sqrt{gy_1}$ is the upstream Froude number, g is the gravitational acceleration and y_1, y_2 and D are previously defined in Fig. 1. Subsequent researchers have proposed equations for the computation of the conjugate depth ratio for closed-conduit hydraulic jumps as follows:

Rajaratnam (1965)

$$\frac{y_2}{y_1} = \frac{\left(\frac{D}{y_1}\right)^n + n\left(\frac{D}{y_1}\right)^{2n+1} - \frac{n+1}{n}Fr_1^2\left(1+\theta-\left(\frac{D}{y_1}\right)^n\right)}{(1+n)\left(\frac{D}{y_1}\right)^{2n}}, \theta = 0.0066(Fr_1 - 1)^{1.4}, n = 2 \qquad [2]$$

Smith and Chen (1989)

$$\frac{y_2 - y_1}{D} = Fr_1^2\left(\frac{y_1}{D}\right)^2\left(1 - \frac{y_1}{D}\right) + \frac{1}{2}\frac{y_1}{D}\left(\frac{y_1}{D} + \frac{D}{y_1} - 2\right) \qquad [3]$$

Lowe et al. (2011)

$$\frac{y_2}{D} = \frac{1}{2} + \left(Fr_1^2 + \frac{1}{2}\right)\left(\frac{y_1}{D}\right)^2 - Fr_1^2\left(\frac{y_1}{D}\right)^3 \qquad [4]$$

Figure 4 shows the comparison between the measured and computed conjugate depths from the current experiments and those computed using Eqs. [1]-[4]. The figure shows that the results computed using the Bélanger equation compare generally well with the experimental data, not only in open-channel but also closed-conduit jumps within the range of Fr_1 numbers of the study. The results computed from Rajaratnam (1965), Smith and Chen (1989) and Lowe et al. (2011) show some deviations from the measured data.

Energy dissipation in terms of head loss across a simple hydraulic jump can be expressed by

$$\Delta H = \frac{(y_2 - y_1)^3}{4y_1y_2} \qquad [5]$$

Figure 5 shows the comparison of the computed results and measured data. The figure clearly reveals that deviations of the computed head loss using Eq. (5) from the measured data for closed-conduit jumps are more significant compared to the conjugate depths. More specifically, the results show that energy dissipation associated with a closed-conduit jump is less than that with an open-channel jump with the same Froude number.

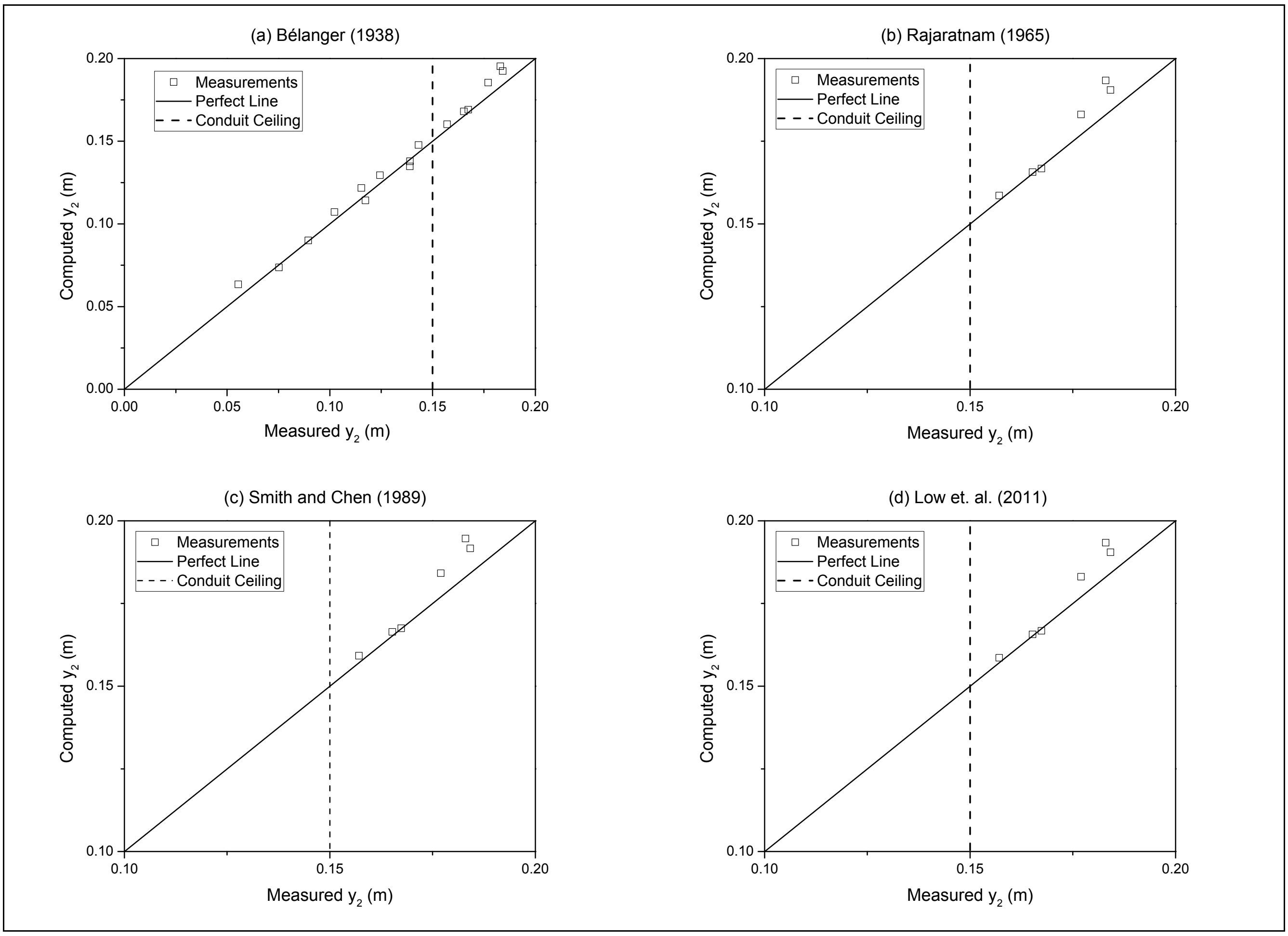

Figure 4. Comparison of measured and computed conjugate depths.

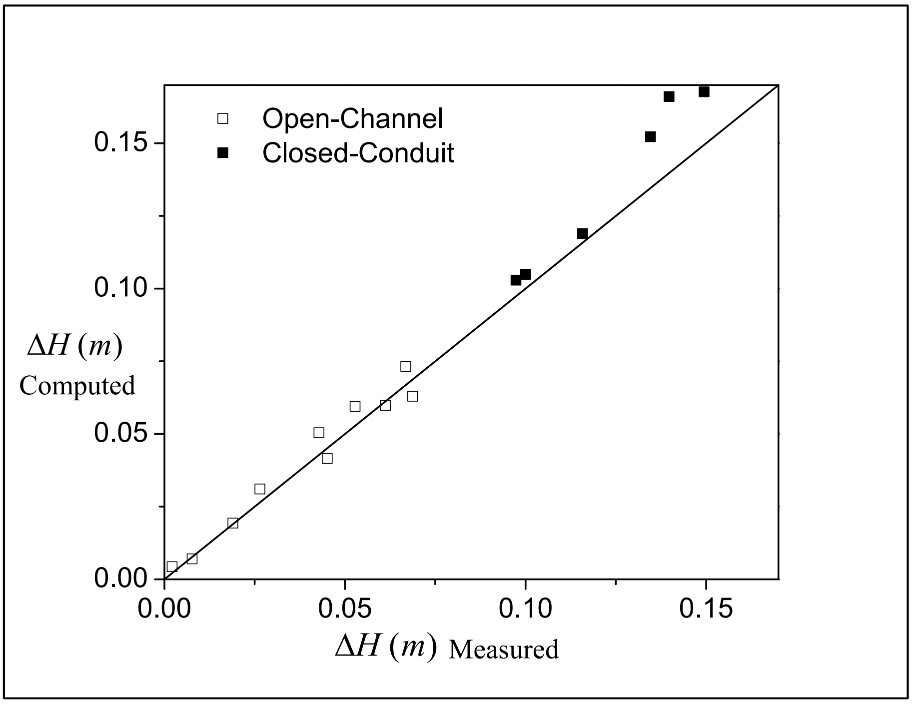

Figure 5. Comparison of measured and computed head loss using Eq. [5].

3.1 Pressure

Figure 6 shows the longitudinal distribution of pressure from three hydraulic jumps with Froude numbers, $Fr_1 = 1.77, 3.29$ and 4.53. The maximum and minimum curves, which envelope the mean values, represent, respectively, the highest or lowest pressure deviations from the mean value. The data show that such deviations generally increase with Froude number. Another noteworthy observation is that negative pressure on the bed is only present in jumps with higher Froude numbers (Runs 7-16). Moreover, the magnitude of the negative pressure increases with Fr, an occurrence that may encourage boundary layer separation beneath the jump, as was hypothesized by (Schiebe, 1971).

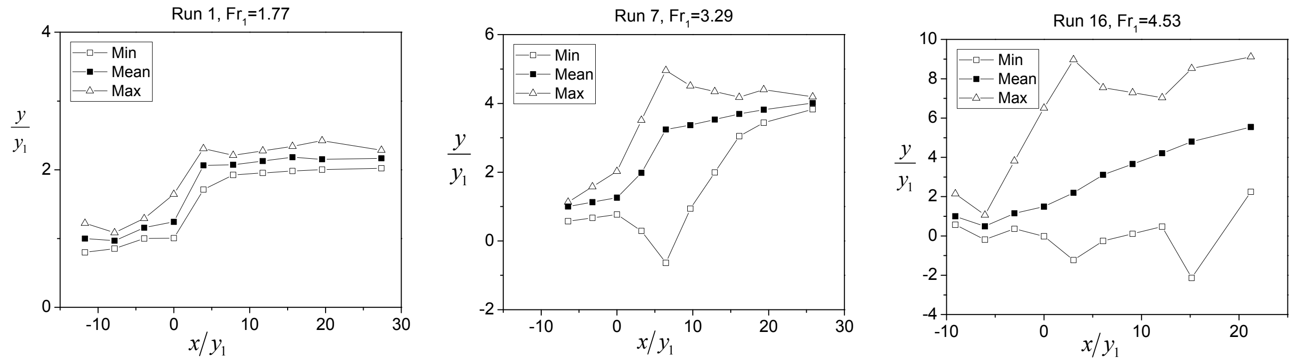

Figure 6. Comparison of maximum, mean and minimum values of pressure measured underneath open channel (Runs 1 and 7) and closed-conduit (Run 16) hydraulic jumps.

Figure 7 shows variations of the standard deviation σ of the pressure signal beneath the hydraulic jump normalized by a reference value σ_0 measured in still water in the streamwise direction. In open-channel (Runs 1-10) and weak closed-conduit hydraulic jumps (Run 11), the standard deviation and hence pressure fluctuations are observed to decrease from its peak value at the middle part to the end of the jump. At the downstream end of the jump, the pressure fluctuation is very small. On the other hand, the data in Fig. 7 reveal that the standard deviation of the pressure associated with closed-conduit jumps (Runs 12-16) diminishes much slower towards the downstream end of the jump and the persistence of large pressure fluctuations likely will have a strong implication on the design and linings of hydraulic structures in that region. To-date, there has been no study to determine to what extent these pressure fluctuations continue to exist beyond a closed-conduit jump.

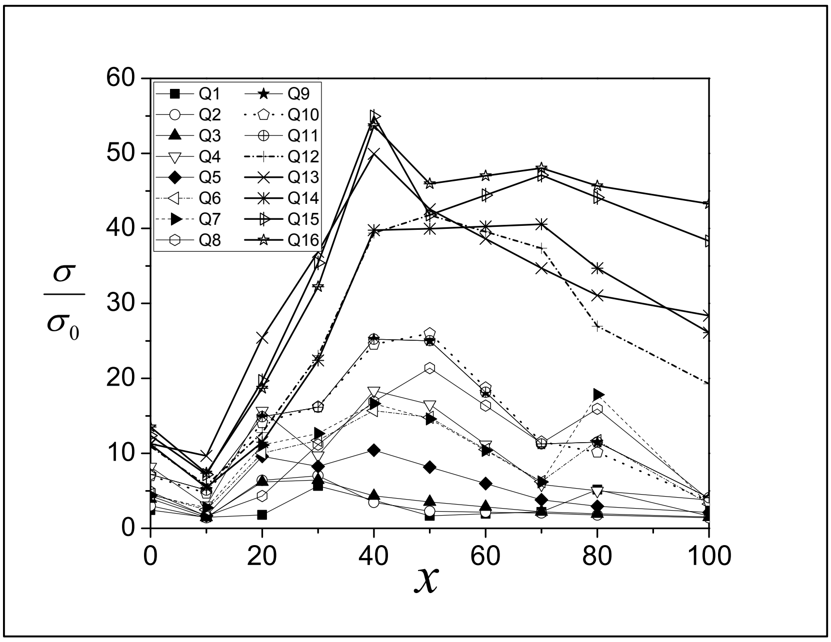

Figure 7. Variation of normalized standard deviation of pressure in the stream wise direction.

3.2 Water surface profile and pressure distribution

Figure 8 shows the comparison between the maximum, mean and minimum values of flow depths y at the same locations obtained from using the pressure transducers and high speed camera recordings in Runs 7 and 16. The mean depths obtained from the two methods are close to each other, with values from the pressure measurements being, arguably, slightly smaller than those deduced from the images. A possible reason for the deviation could be the reduced water density due to air entrainment at the water surface.

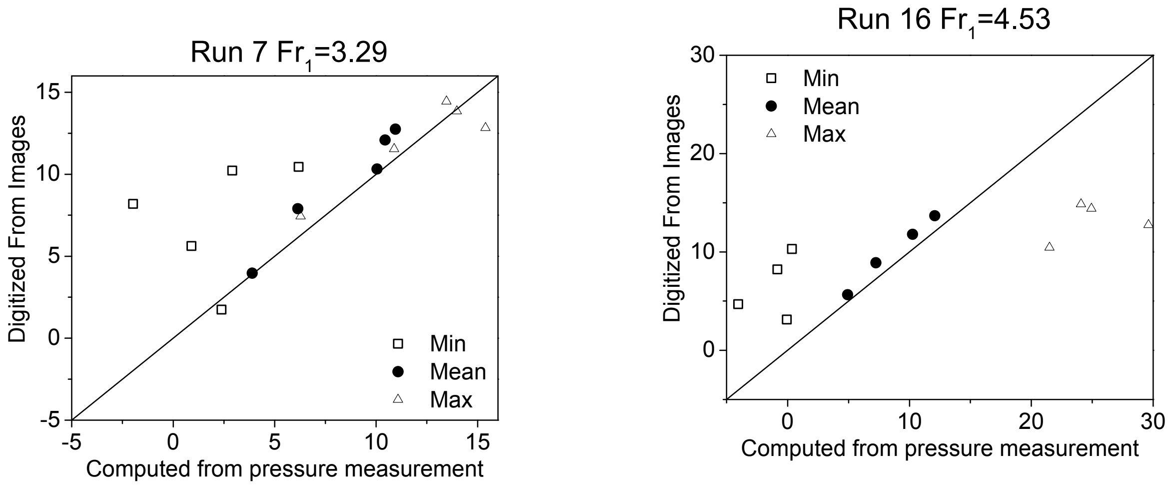

Figure 8. Comparison between flow depths measured by using high-speed camera and pressure transducers in open channel (Run 7) and closed-conduit (Run 16) hydraulic jumps.

In the open channel hydraulic jump (Run 7), the minimum and maximum values of flow depth are similar to each other at locations upstream of the toe and at the end of the hydraulic jump, but they deviate significantly in the mid-section of the jump.

In the closed-conduit hydraulic jump (Run 16), the free surface exists in a short distance in the upstream section before pressurized flow fills the whole conduit and flow depths can only be compared in 4 stations. The flow depths deduced from the pressure transducers show negative values on the minimum curve. Additionally, the magnitude of peak maximum pressures is more than two times larger than that extracted from the images in this run.

The water surface profiles and pressure distributions in a hydraulic jump are generally considered to be identical to each other if the hydrostatic pressure distribution persists. In this study, although the mean values of pressure and water depth are comparable to each other at relatively small Froude numbers, their fluctuations are not and it is postulated that this phenomenon should be thoroughly investigated in hydraulic jump studies. This is because the occurrence of pressure fluctuations is a result of turbulence and the water surface fluctuations appear to be due to the formation of small waves observed at the jump surface.

4 CONCLUSIONS

The pressure fluctuations and water surface profiles were simultaneously measured in both open channel and closed-conduit hydraulic jumps in a horizontal flume. The comparison of the experimentally measured conjugate depths and energy loss with those computed using published equations reveal small deviations in closed-conduit hydraulic jumps. An examination of the streamwise variation of the standard deviation of pressure shows that the pressure fluctuations with closed-conduit jumps remain high even at the downstream end of the jump. This is in contrast to open-channel hydraulic jumps in which the pressure fluctuations generally would have reduced to a small amount. Simultaneous measurements of the water surface profile and pressure fluctuations showed that the mean depth computed from the pressure transducers is smaller than that deduced from the images. This is likely due to the less-dense aerated flow region at the surface of the hydraulic jump. In addition, larger pressure fluctuations were observed in comparison to water surface fluctuations. The result of this study shows that values of the water surface and pressure may not be simply considered identical and should be studied separately in the context of a hydraulic jump, particularly in a closed-conduit hydraulic jump.

ACKNOWLEDGEMENTS

This material is based on research/work supported by the Singapore Ministry of National Development under the Land and Livability National Innovation Challenge (L2NIC) award number [L2NICCFP1-2013-3]. Any opinions, findings, and conclusions or recommendations expressed in this material are those of the authors and do not necessarily reflect the views of the Singapore Ministry of National Development and National Research Foundation.

REFERENCES

Ervine, D.A. & Himmo, S.K. (1984). Modelling the Behaviour of Air Pockets in Closed Conduit Hydraulic Systems. In *Proceeding of the Symposiums on Scale effects in modeling hydraulic structures,* 4, 1-11.

Fassò, C. (1956). *Experimental Research on Air Entrainment in Gated Outlet Works*, Politecnico di Milano.

Fiorotto, V. & Rinaldo, A. (1992). Fluctuating Uplift and Lining Design in Spillway Stilling Basins. *Journal of hydraulic engineering*, 118(4), 578-596.

Haindl, K. (1957). Hydraulic Jump in Closed Conduits. *Proceeding of the International Association of Hydraulic Research, Lisbon*, *2*, D32.

Kalinske, A. & Robertson, J.M. (1943). Entrainment of Air in Flowing Water: A Symposium: Closed Conduit Flow. *Transactions of the American Society of Civil Engineers,* 108(1), 1435-1447.

Lane, E. & Kindsvater, C. (1938). Hydraulic Jump in Enclosed Conduits. *Engineering News-Records,* 121(26), 1938.

Lowe, N., Hotchkiss, R. & Nelson, E. (2011). Theoretical Determination of Sequent Depths in Closed Conduits. *Journal of Irrigation and Drainage Engineering,* 137(12), 801-810.

Mouaze, D., Murzyn, F. & Chaplin, J.R. (2005). Free Surface Length Scale Estimation in Hydraulic Jumps. *Journal of Fluids Engineering,* 127(6), 1191-1193.

Rajaratnam, N. (1965). Hydraulic Jump in Horizontal Conduits. *Water Power,* 17(2), 80-83.

Rouse, H., Siao, T.T. & Nagaratnam, S. (1959). Turbulence Characteristics of the Hydraulic Jump. *Transaction of the ASCE,* 124(1), 926-950.

Schiebe, F. (1971). The Stochastic Characteristics of Pressure Fluctuations on a Channel Bed due to the Turbulence in a Hydraulic Jump*, PhD thesis*. The University of Minnesota, Minneapolis, US.

Smith, C.D. & Chen, W. (1989). The Hydraulic Jump in a Steeply Sloping Square Conduit. *Journal of Hydraulic Research,* 27(3), 385-399.

Te Chow, V. (1959). *Open Channel Hydraulics*: McGraw-Hill Book Company, Inc; New York, 1-728.

Toso, J. & Bowers, C. (1988). Extreme Pressures in Hydraulic Jump Stilling Basins. *Journal of Hydraulic Engineering,* 114(8), 829-843.

Vasiliev, O. & Bukreyev, V. (1967). Statistical Characteristics of Pressure Fluctuations in the Region of Hydraulic Jump. *Journal of Applied Mechanics and Technical Physics*, 7(5), 97–99.

Proceedings of the 37th IAHR World Congress
August 13 – 18, 2017, Kuala Lumpur, Malaysia

FREE SURFACE PROFILE MEASUREMENTS OF FLOW OVER SQUARE BARS USING AN IMAGE PROCESSING APPROACH

SAAD MULAHASAN[(1)], THORSTEN STOESSER[(2)] & SAFAA KH. AL-JUMAILI[(3)]

[(1)]Al-Mustenseryah University,College of Engineering,Civil EngineeringDepartment, Baghdad, Iraq
irrigation_2010@yahoo.com
[(2)]Cardiff University, Cardiff School of Engineering, Hydro-environmental Research Centre, Cardiff, UK
stoesser@cardiff.ac.uk
[(3)]Basrah University, College of Engineering, Materials Engineering Department, Basrah, Iraq
safaakh@gmail.com

ABSTRACT

This paper describes a method for the estimation of the time-averaged free surface profile measured directly from particle image velocimetry (PIV) images of a laboratory open channel flow over a transverse square bars of normalized spacings λ/k = 5.2 and λ/k = 10.4 representing transitional and k-type roughness geometries, respectively. Three different relative submergence ratios of H/k = 2.4, 2.7 and 3.3 for the transitional geometry and H/k = 2.5, 3.0 and 3.5 for the k-type geometry are investigated. 1500 images of the free surface have been recorded using a Baumer TXG14F CCD camera in conjunction with a Polytec BUS-11 Wotan Flash stroboscope and a halogen lamp. Seeding particles are used in capturing the water surface profile. The large spacing is characterized with dynamic free surface profile in which the H/k = 3.5 case is characterized by an extremely dynamic free surface with significant spanwise wandering motion of the hydraulic jumps, while the small spacing showed of less free surface dynamics. The mean longitudinal free surface profile is determined using an image processing approach by the Matlab software. The results by this method is a well-defined water surface profile showing visible hydraulic jumps the bars for all the large spacing and low submergence case of the small spacing. The PIV determined free surface profiles are compared with the point gauge measurements and showed good agreement. In addition to the mean free surface profile the standard deviation of the longitudinal free surface profiles are calculated for the six relative submergences. Small free-surface fluctuations are observed in the case of the small roughness spacing. A significant increase in free surface fluctuation is observed in the small-scale roughness at low submergence, and the free-surface fluctuations reached a maximum value for the large-scale roughness spacing.

Keywords: Hydraulic jumps; open channel flows; square bars; image processing; water surface profiles.

1 INTRODUCTION

Determination of air-liquid interface is important in many engineering and geophysical applications such as the biological, micro fluidic processes and gas transfer mechanism in natural rivers. Open channel free surface profiles, such as natural rivers are influenced by not just the mean stream flow velocity and the water depth but also by the bed configuration such as gravel, boulders and vegetation. The turbulence generated at the bed play a significant role of the free surface dynamics due to generation at the trailing edge of the roughness elements 2-D hairpin vortices “coherent structures” and transferring towards the free surface (Nezu and Nakagawa, 1993; Polatel, 2006; Albayrak and Lemmin, 2007; Djenidi et al., 2008; Chickadel et al., 2009). These coherent structures are responsible for free surface renewal by ejection and sweep events. To gauge water profiles at numerous focuses or to watch the spatial state of the water surface, various accumulations of sensors are required. As of late, measuring procedures, for example, CCD cams, radar and satellite pictures, have been produced and connected to watch the variety of the water surface in the imaging range. Particle-image measurements require that the water be seeded with tracer particles; a light source is used to illuminate the seeded tracer particles; a video camera is used to capture images of the air–water interface from above or below the water surface, and an-processing algorithm is used to detect the location of the air–water interface or wave profile. A number of researches have been carried out experimentally to monitor the water surface profile. Siddiqui et al. (2001) used the particle image velocimetry (PIV) image, and permeated the seed particles as the tracer, to segment the images and detect the wave profiles by applying a constant threshold value which was computed based on the average grey-scale value below the water surface. They used a video camera looking down at an angle of 34° that captured digital images. The uncertainty in the detected wave profiles was estimated to be 0.3 mm. Jensen et al. (2003) extracted water surface profiles using PIV and compared with theory which appealed with a good agreement. Yao and Wu (2005) measured surface wave motions near the air–water interface using Digital Particle Image Velocimetry (DPIV). The camera was pointed

  / ISSN 1562-6865 (Online) - ISSN 1063-7710 (Print)

downwards at an angle of about 6° so that there is no optical blocking would occur in the view of the illuminated free surface. A highly reflective panel whose thickness was approximately 1 mm was attached onto the back sidewall. Therefore, the whole thickness was approximately 1 mm was attached onto the back sidewall. Therefore, the reflective panel can serve as a back-lighting source for the water column. Misra et al. (2006; 2008) estimated instantaneous air-water interface using particle image velocimetry (PIV) images of a laboratory generated air entraining turbulent hydraulic jump. Image processing methods were used to extract the free surface profiles. Mukto et al. (2007) used digital CCD camera to capture the wave profile with varied angles of overhead posture. Simulated and real wind wave profiles and real still water profiles were used to assess the accuracy of the measurement technique. They used the threshold method to correct non-uniform illumination and the non-uniform distribution of near surface seed particles. Errors were estimated to be (±0.05 mm). Hwung et al. (2009) investigated wave profiles experimentally using a digital CCD camera with different overhead posture angles. They considered the space and time impact on the intensity of the wave profile image. The results showed the mean error of wave height increased from 1.5% to 2.7% as the angle changes from 15° to 45°. De Vries et al. (2011) experimentally determined water surface elevations using remote sensing applying stereo photogrammetry with excellent spatial coverage and spatial and temporal resolution. The most commonly measured parameters are wave period and wave height. Sanchis and Jensen (2011) captured an air-water interface free surface flow using PIV. The original PIV image has to be decomposed into a number of segments where the local interface position and inclination is found. Interpolation between adjacent segments permits the reconstruction of the interface across the whole image with an accuracy of ±0.67 pixels. Sanjou et al. (2014) investigated experimentally the hydrodynamic effects of ribs roughness (λ/k =3.0, 5.0, 8.0, and 16.0) on the water surface velocity divergence using PIV to breakthrough a physical model of gas transfer mechanism in natural rivers.

There still remain uncertainties about relation of the water surface profile divergence and rough elements spacing, λ/k, and submergence ratio, H/k. The present study focused on laboratory measurements of a 2-Dimensional water surface profile in rough open channel flow using PIV. PIV was used by seeding particles as the tracer to segment the images and detect two-dimensional profiles of the water surface profile from one side of flume sidewall. Most of the measurements were viewed near horizontally or slightly from above with a very small angle. Distortion of the free surface may occur due to refraction and reflection effects at the free surface. This can be examined from the loss of some information near the water surface. However these are small from the large number of images that tested. All experiments were carried out using discharge ranges of (1.7-4.0 l/sec) with bed slope of 1/50. PIV measurements of free surface profiles were achieved from a small distance from the sidewall to capture an area showing 2 bars and 4 bars of large-scale roughness for spacing between any two successive bars of 12.5 cm and 6.25 cm respectively. Captured video images were carried at a range of 1500 images for each case. The video images were transformed into the binary images to detect the water surface profiles.

Section 2 outlines the experimental set-up; Section 3 presents and discusses the results. Finally, some conclusions are drawn in Section 4.

2 EXPERIMENTAL SET-UP

Experiments were carried out in a 10 m long, 30 cm wide glass-walled recirculating flume in the Hyder Hydraulics Laboratory at Cardiff University. A series of plastic square bars of width 30 cm and cross-section 12 mm × 12 mm were installed along the length of the flume, perpendicular to the direction of mean flow (Figure 1). The roughness height, k, was therefore 12 mm. Two different bar spacings were investigated, λ = 62.5 mm and λ = 125 mm, corresponding to normalized spacings λ/k = 5.2 and λ/k = 10.4, respectively. According to Coleman et al. (2007), the λ/k = 5.2 case should be classified as transitional roughness as it is very close to the boundary between d- and k-type roughnesses, while the λ/k = 10.4 case constitutes k-type roughness. Bed slope was fixed at 1:50 for all experiments and three flow rates were tested for each bar spacing (Q = 1.7, 2.5, 4.0 l s^{-1}), giving a total of six experimental cases. Each case had a different relative submergence, H/k, where H is the double-averaged height of the free surface above the channel bed and the double-averaged bulk velocity, U_b, ranged from 0.20 m s^{-1} to 0.36 m s^{-1}. Table 1 provides a summary of the flow conditions for each case.

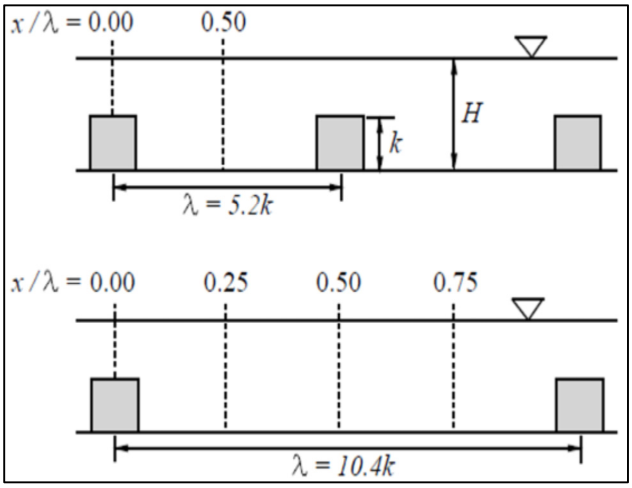

Figure 1. Experimental water surface profile over roughed bed with transverse square bars.

Table 1. Flow conditions.

Case	λ/k	H/k	U_b (m/sec)	Re	Fr
C1	5.2	2.4	0.22	5.7×10^3	0.43
C2	5.2	2.7	0.28	8.3×10^3	0.51
C3	5.2	3.3	0.36	13.3×10^3	0.59
C4	10.4	2.5	0.2	5.7×10^3	0.38
C5	10.4	3	0.24	8.3×10^3	0.42
C6	10.4	3.5	0.32	13.3×10^3	0.51

Measurements of instantaneous free surface position were taken in a section of the flume where the flow was considered to be uniform and fully-developed. The flow was also considered to be spatially periodic with wavelength λ in the streamwise direction, that is to say the temporal mean values of all flow variables in successive cavities between bars were considered to be the same. The bulk Reynolds number was in the range 5700 ≤ Re ≤ 13000 and the friction Reynolds number $Re\tau$(=u_*H/ν) where u_* is the global friction velocity based on the bed shear stress, was in the range 1.8 x 103 ≤ $Re\tau$ ≤ 3.7 x 103. The global Froude number of the flows, Fr = ($U_b/\sqrt{gH}$), was in the range 0.38 ≤ Fr ≤ 0.59; local values based on local depths and velocities can be much higher.

Water surface position was measured using particle image velocimetry (PIV). A Baumer TXG14F CCD camera was used in conjunction with a Polytec BUS-11 Wotan Flash stroboscope and a halogen lamp to capture the dynamic free surface (See Figure 2). Seeding particles that had the same approximate density of water, making them neutrally buoyant, were used. The camera recorded images during 50 seconds for each flow case, at a rate of 30 frames per second.

In addition to the PIV measurements a point gauge was used to measure free surface elevation at the channel centerline. Measurements were taken over a length spanning two or more cavities, at streamwise intervals of between 2.5 mm and 10 mm. Point gauge measurements were taken for all flow cases except C6, which was characterized by an extremely dynamic free surface with a significant spanwise wandering motion of the hydraulic jump, and was therefore impossible to measure with a point gauge.

Figure 2. An instantaneous water surface profile over square bars.

3 RESULTS AND DISCUSSIONS

The free surface fluctuations properties are presented including the mean and fluctuating profiles. The longitudinal free surface profiles were recorded for six experiments. A significant increase in free surface fluctuation was observed in the small scale roughness at low submergence, and the free-surface fluctuations reached a maximum value for the large-scale roughness spacing.

The mean free surface in all three small spacing cases is relatively flat, although some undulation is noticeable in the lowest submergence case as shown in Figure 3(a) and explained in Chua et al. (2016). In fact two unsteady undular jumps are present in this flow case, slightly upstream of the bars. These jumps establish and disestablish periodically. In the large spacing cases well defined hydraulic jumps are visible between the bars, where the local Froude number approaches unity and the flow becomes critical.

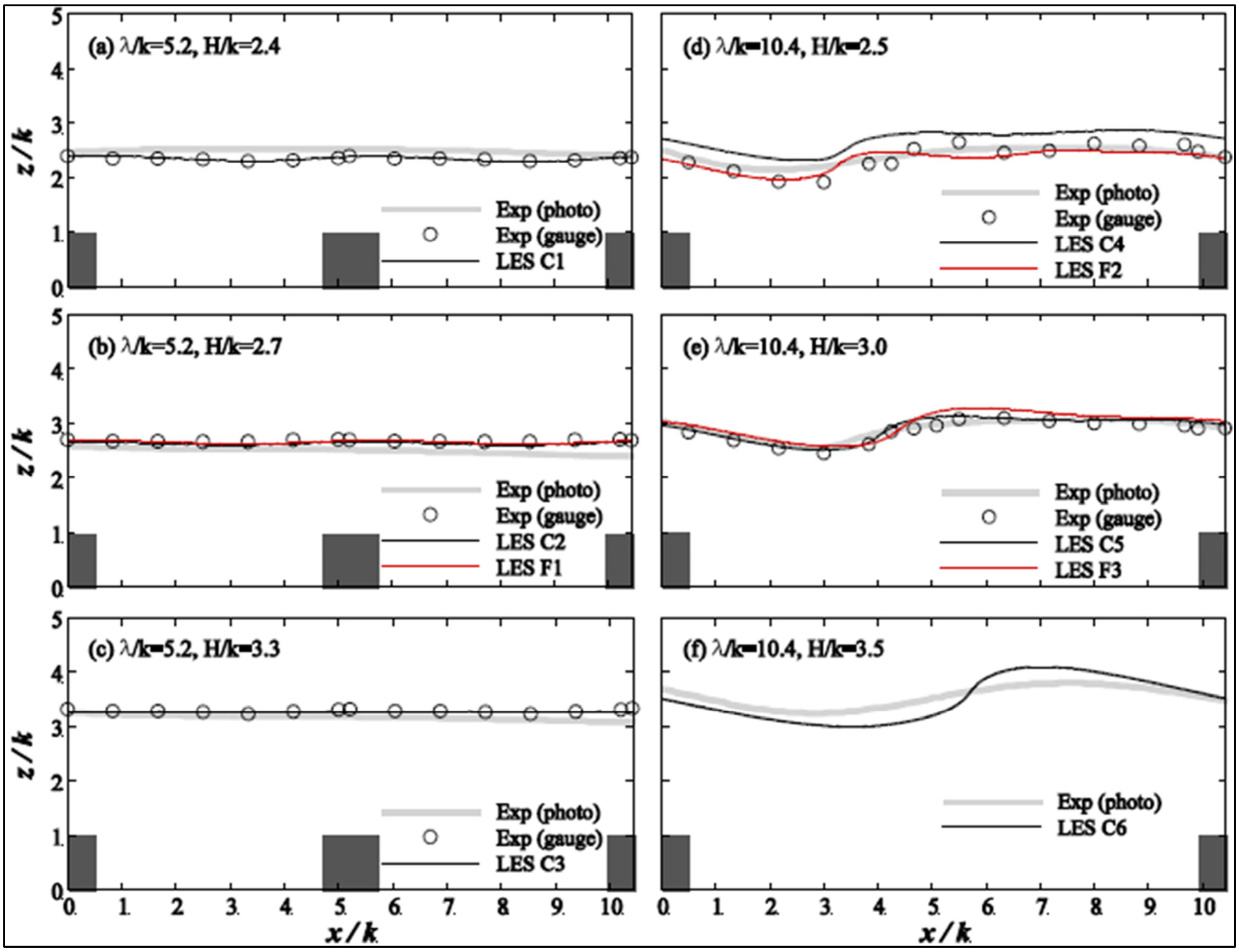

Figure 3. Longitudinal profiles of temporal and spanwise mean free surface elevation for three approaches (experimental using PIV, experimental using point gauges and numerical using LES). (Chua et al., 2016)

Statistical analysis of the experimental data for the longitudinal profiles was examined. The standard deviation of the longitudinal free surface profiles were calculated for the six relative submergences. Small free-surface fluctuations were observed and recorded in the case of the small roughness spacing.

A significant increase in free surface fluctuation was observed in the small scale roughness at low submergence, and the free-surface fluctuations reached a maximum value for the large-scale roughness spacing. This maximum value increased with increasing relative submergence, for which large standard deviations in free-surface elevations were linked. The drawings of the standard deviation hrms/H were explained as a non-dimensionalized relative to the uniform flow depth versus x/k. Standard deviation results of the free surface elevations were explained in Figures (4 to 9). For small spacing, the mean free surface in all three small spacing cases is relatively flat and standard deviation values increased with decreasing the submergence ratio and some undulation was observed. Upstream the bars large magnitudes of the standard deviation were shown (see Figures 4 to 6). For large spacing, the standard deviation values are increased and coincide with the observed strong hydraulic jumps for all the submergence ratios (see Figures 7 to 9).

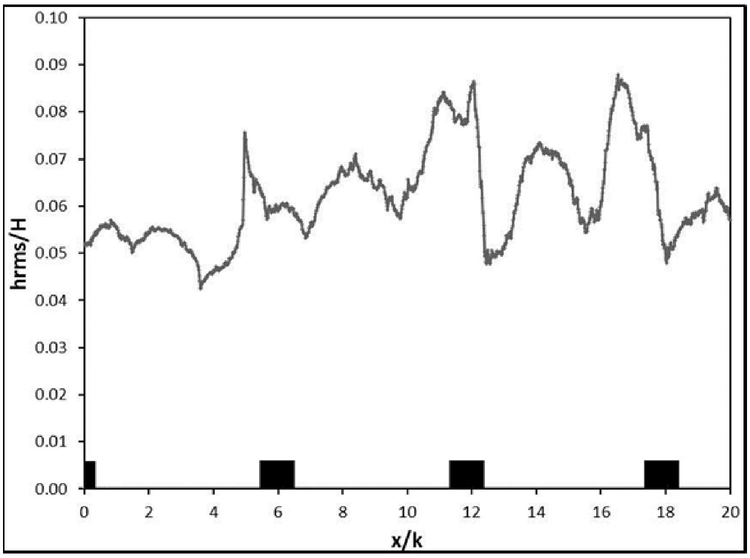

Figure 4. Dimensionless longitudinal profiles of free surface fluctuations hrms/H for Q = 1.7 l/s, H = 2.53 cm and λ/k = 5.2.

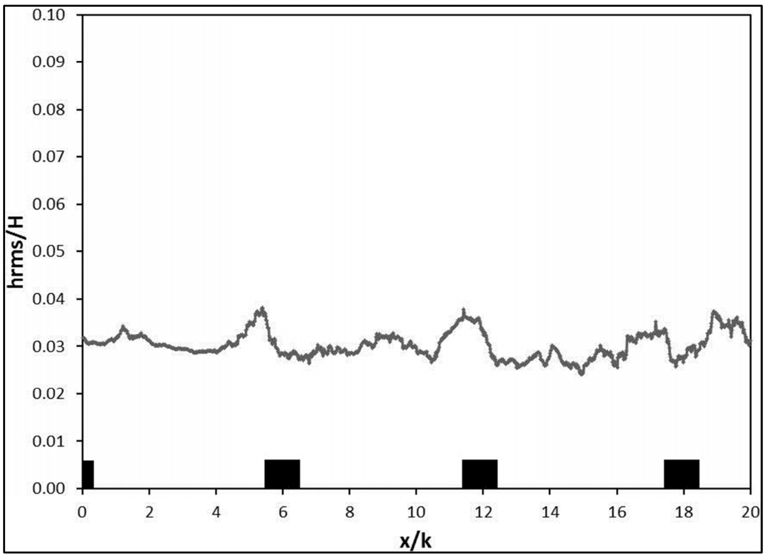

Figure 5. Dimensionless longitudinal profiles of free surface fluctuations hrms/H for Q = 2.5 l/s, H = 2.93 cm and λ/k = 5.2.

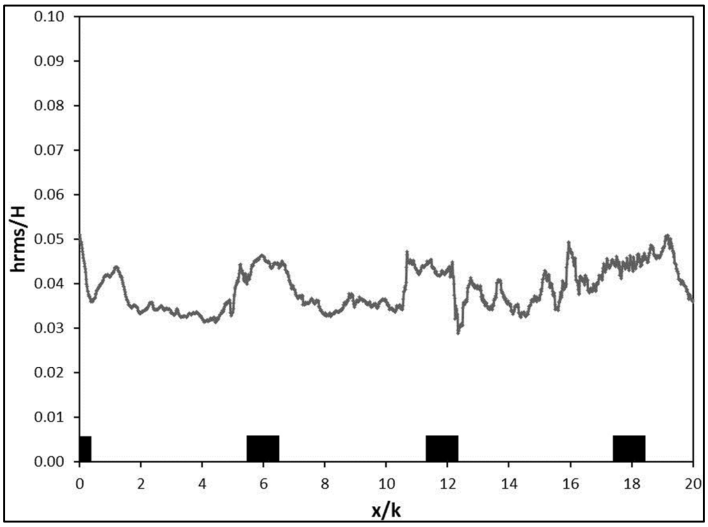

Figure 6. Dimensionless longitudinal profiles of free surface fluctuations hrms/H for Q = 4.0 l/s, H = 3.52 cm and λ/k = 5.2.

  / ISSN 1562-6865 (Online) - ISSN 1063-7710 (Print)

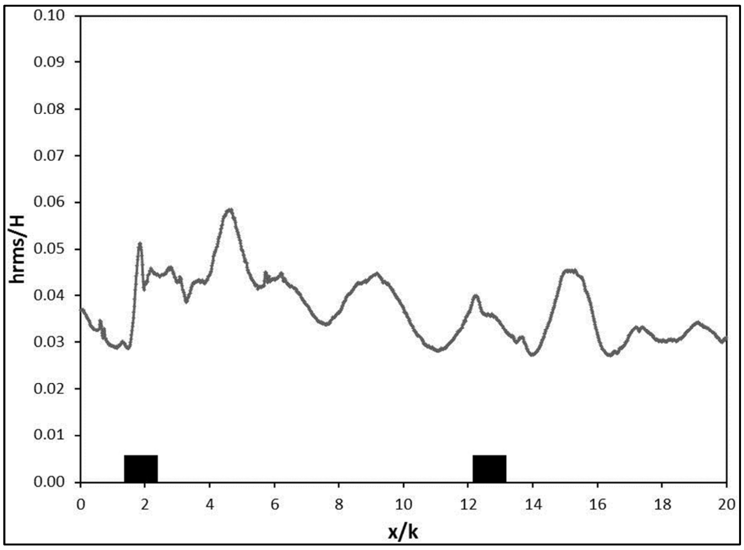

Figure 7. Dimensionless longitudinal profiles of free surface fluctuations hrms/H for Q = 1.7 l/s, H = 2.96 cm and λ/k = 10.4.

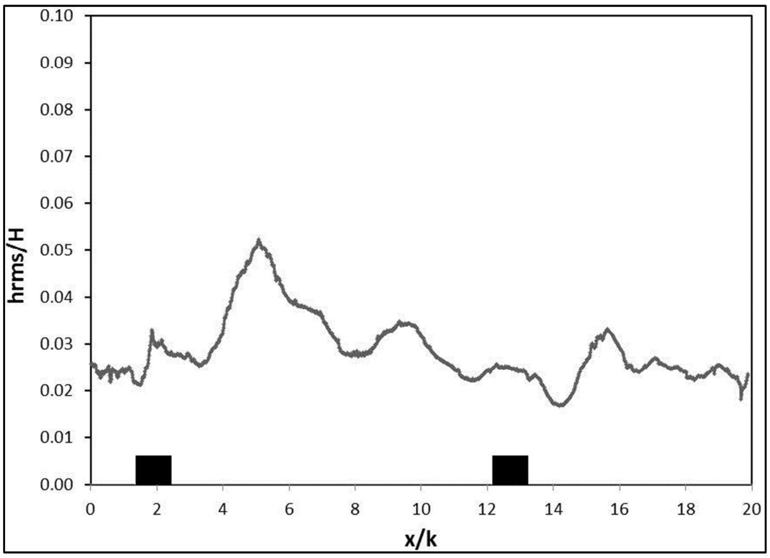

Figure 8. Dimensionless longitudinal profiles of free surface fluctuations hrms/H for Q = 2.5 l/s, H = 3.54 cm and λ/k = 10.4.

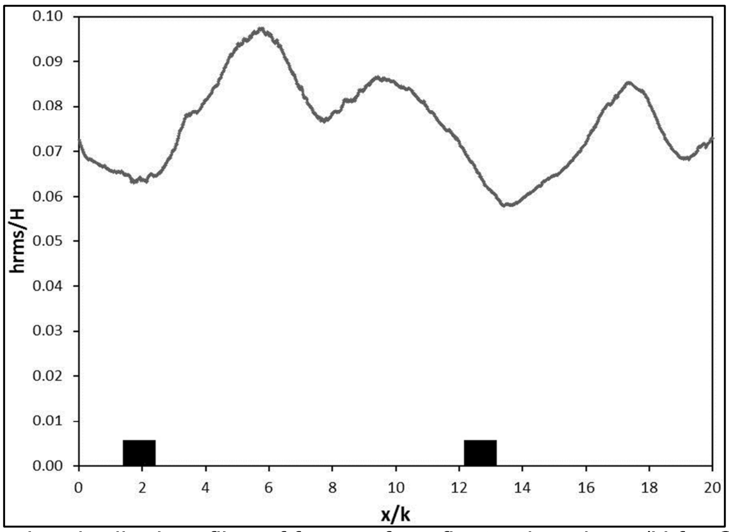

Figure 9. Dimensionless longitudinal profiles of free surface fluctuations hrms/H for Q = 4.0 l/s, H = 4.24 cm and λ/k = 10.4.

4 CONCLUSIONS

This paper described a method for the estimation of the time-averaged free surface profile measured directly from particle image velocimetry (PIV) images of a laboratory open channel flow over a transverse square bars. The mean longitudinal free surface profile was determined using an image processing approach by the Matlab software. Significant errors to the captured profile images by the PIV may occur for a variety of reasons due to the non-uniform illumination, which quantified using an average of 1500 images and compared to point gauge measurements accounting by the image processing technique. The results by this method is a well-defined water surface profile showing visible hydraulic jumps the bars for all the large spacing and low submergence case of the small spacing. The PIV determined free surface profiles were compared with the point gauge measurements and showed good agreement. In addition to the mean free surface profile the standard deviation of the longitudinal free surface profiles were calculated. Small free-surface fluctuations were observed in the case of the small roughness spacing. A significant increase in free surface fluctuation was observed in the small scale roughness at low submergence, and the free-surface fluctuations reached a maximum value for the large-scale roughness spacing. This maximum value increased with increasing relative submergence, for which large standard deviations in free-surface elevations were found.

ACKNOWLEDGEMENTS

The authors would like to thank the Iraqi Ministry of Higher Education and Scientific Research for funding to support this research and the technical staff of Cardiff University-School of Engineering for their kind assistance.

REFERENCES

Albayrak, I. & Lemmin, U. (2007). Large Scale PIV-Measurements on the Water Surface of Turbulent Open-Channel Flow. *18ème CongrèsFrançais de Mécanique* (Grenoble 2007).

Chickadel, C.C., Horner-Devine, A.R., Talke, S.A. & Jessup, A.T. (2009). Vertical Boil Propagation from a Submerged Estuarine Sill. *Geophysical Research Letters*, 36(10), 1-6.

Chua, K., Mcsherry, R., Mulahasan, S. & Stoesser, T. (2016). Large Eddy Simulation of Free Surface Flow over Square Bars with Low Relative Submergence. *Submitted to Journal of Hydraulic Research*.

De Vries, S., Hill, D.F., De Schipper, M.A. & Stive, M.J.F. (2011). Remote Sensing of Surf Zone Waves using Stereo Imaging. *Coastal Engineering*, 58(3), 239-250.

Djenidi, L., Antonia, R.A., Amielh, M. & Anselmet, F. (2008). A Turbulent Boundary Layer over a Two-Dimensional Rough Wall. *Experiments in Fluids*, 44(1), 37-47.

Hwung, H.H., Kuo, C.A. & Chien, C.H. (2009). Water Surface Level Profile Estimation by Image Analysis with Varying Overhead Camera Posture Angle. *Measurement Science and Technology*, 20(7), 075104.

Jensen, A., Pedersen, G.K. & Wood, D.J. (2003). An Experimental Study of Wave Run-Up at a Steep Beach. *Journal of Fluid Mechanics*, 486, 161-188.

Misra, S.K., Thomas, M., Kambhamettu, C., Kirby, J.T., Veron, F. & Brocchini, M. (2006). Estimation of Complex Air–Water Interfaces from Particle Image Velocimetry Images. *Experiments in fluids*, 40(5), 764.

Misra, S.K., Kirby, J.T., Brocchini, M., Veron, F., Thomas, M. & Kambhamettu, C. (2008). The Mean and Turbulent Flow Structure of a Weak Hydraulic Jump. *Physics of Fluids*, 20(3), 035106.

Mukto, M.A., Atmane, M.A. & Loewen, M.R. (2007). A Particle-Image based Wave Profile Measurement Technique. *Experiments in fluids*, 42(1), 131-142.

Nezu, I. & Nakagawa, H. (1993). Turbulence in Open Channel Flows*. International Association for Hydraulic Research*, Monograph Series, A.A Balkema Publishers, Rotterdam.

Polatel, C. (2006). Large-Scale Roughness Effect on Free-Surface and Bulk Flow Characteristics in Open-Channel Flows, Doctor of Philosophy degree. Civil and Environmental Engineering, University of Iowa.

Sanchis, A. & Jensen, A. (2011). Dynamic Masking of PIV Images using the Radon Transform in Free Surface Flows. *Experiments in fluids*, 51(4), 871-880.

Sanjou, M., Okamoto, T., Tanaka, Y. & Toda, K. (2015). Surface Velocity Divergence in Open-Channel Flows with Strip Roughness. In Informatics,Networking and Intelligent Computing, *Proceedings of the 2014 International Conference on Informatics, Networking and Intelligent Computing*, 16-17 November 2014, Shenzhen, China, CRC Press, 71.

Siddiqui, M.K., Loewen, M.R., Richardson, C., Asher, W.E. & Jessup, A.T. (2001). Simultaneous Particle Image Velocimetry and Infrared Imagery of Microscale Breaking Waves. *Physics of Fluids*, 13(7), 1891-1903.

Yao, A. & Wu, C.H. (2005). An Automated Image-based Technique for Tracking Sequential Surface Wave Profiles. *Ocean engineering*, 32(2), 157-173.

WATER SURFACE PROFILES AND ENERGY HEAD IN NONAERATED SKIMMING FLOWS ON STEPPED SPILLWAYS

MASAYUKI TAKAHASHI(1), YUKI YAMAMOTO(2) & IWAO OHTSU(3)

(1,3) College of Science and Technology, Nihon Univ., Tokyo, Japan
e-mail masayuki@civil.cst.nihon-u.ac.jp
(2) Graduate Course of Nihon Univ., Tokyo, Japan

ABSTRACT

For a large discharge and/or small dam height, the nonaerated flow region occupies a large portion of the skimming flow in stepped spillways. For the hydraulic design of stepped channels, it is important to know the depth and the velocity in nonaerated skimming flows to estimate the specific energy. However, most experimental studies for stepped channels have focused on aerated skimming flows, and characteristics of nonaerated skimming flows have not yet been clarified. This study presents reasonable equations for estimating the boundary layer development and the water surface profile along the spillways for nonaerated skimming flows. The energy head along the channel is obtained, indicating that the energy dissipation for the stepped spillway becomes larger than that for the smooth spillway.

Keywords: Stepped spillway; nonaerated skimming flow; surface profile; boundary layer development; energy dissipation.

1 INTRODUCTION

For a skimming flow in stepped spillways, the upstream flow is nonaerated, and the free-water surface appears smooth and glass-like up to the inception point of free-surface aeration. In this nonaerated skimming flow region, a turbulent boundary layer develops from the crest and reaches the water surface (Figure 1), after which the flow becomes fully developed, and the free surface air entrainment starts at the inception point (I.P.); then, the air begins to be entrained in the flow. Downstream of the inception point, the skimming flow can be divided into two regions, a gradually varied aerated skimming flow and a quasi-uniform aerated skimming flow. The quasi-uniform aerated skimming flow is formed at a certain location if the spillway length is sufficiently long. The characteristics of uniform-aerated skimming flows, such as void fraction, velocity profile, and energy head, were investigated for a wide range of spillway angles θ and relative step heights S/d_c (S = step height, d_c = critical flow depth = $(q^2/g)^{1/3}$, g = acceleration of gravity, q = water discharge per unit width) (e.g. Takahashi and Ohtsu 2012). For the gradually varied aerated skimming flow, Takahashi and Ohtsu (2014) developed an analytical equation for the calculation of the aerated flow depth together with the continuity equation for the air phase.

For a large discharge or/and a small dam height, nonaerated skimming flows may occupy a large portion of the flow in stepped spillways. For the hydraulic design of stepped spillways under a large unit discharge or a small dam height, it is important to know the flow characteristics of nonaerated skimming flows, such as the flow depth, flow velocity, and energy head. For an accurate estimation of the energy head, it is necessary to know the boundary layer development and water surface profile in the nonaerated skimming flows.

Recently, Meireles and Matos (2009) obtained the energy head of the nonaerated flow region for a spillway angle θ = 26°. Additionally, for θ = 53°, Meireles et al. (2012) obtained the velocity profile and the energy head. However, the effects of the spillway angles and step heights on the energy head were not clarified.

This paper developed reasonable equations for estimating the boundary layer development and water surface profile along the spillway for nonaerated skimming flows. Flow characteristics of nonaerated skimming flows were investigated for a wide range of spillway angles θ from 19° to 55° and relative step heights S/d_c from 0.03 to 0.9. The boundary layer development is reasonably formulated, and the water surface profile is analytically obtained. The effect of θ and S/d_c on the specific energy of nonaerated skimming flows E is elucidated, and the specific energy for nonaerated skimming flows has been compared with that for flows in smooth spillways, showing the effectiveness of stepped spillways on energy dissipation.

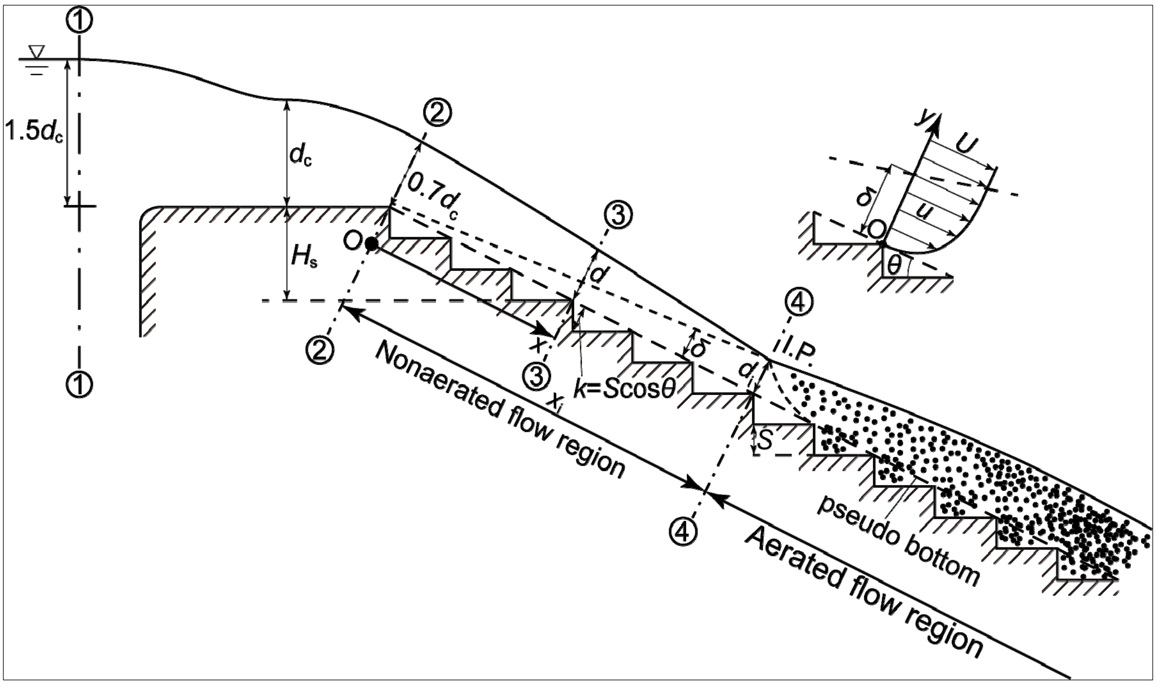

Figure 1. Flow regions of skimming flow.

2 EXPERIMENTS

The experiments were conducted in stepped chutes of constant slope and uniform step height having a broad crested weir. The water depth (d) and the velocity (u) within the nonaerated skimming flow region were measured at an edge section under the conditions shown in Table 1. The velocities (u) in the nonaerated skimming flow region were measured using the Pitot tube. The water depths (d) were obtained using a point gage with a least count of 0.1 mm.

To know the hydraulic characteristics at the inception point, the air concentration, C [= volume of air / (volume of air + volume of water)] and velocity, u were obtained under the conditions shown in Table 2. The air concentration (C) and the aerated flow velocity (u) at the inception point were measured using a double-tip conductivity void probe with leading and trailing tips of 25 μm in diameter at a sampling frequency of 20 kHz and a sampling time of 20 s along the chute axis.

Table 1. Experimental conditions for measurements of the water depth and the velocity.

θ(deg.)	S/d_c (–)	H_{dam} (cm)	R×10^{-4}(–)
19	0.2 – 0.9	60	4 – 6
30	0.2 – 0.9	60	4 – 6
55	0.03 – 0.3	60	9

Note: H_{dam} = total drop height, R = Reynolds number = q/v, v = kinematic viscosity

Table 2. Experimental conditions for measurements of the air concentration and the velocity at the inception point.

θ(deg.)	S/d_c (–)	H_{dam} (cm)	R×10^{-4}(–)
19	0.4 – 0.8	60	6
30	0.4 – 0.8	60	6

3 INCEPTION POINTS

The distance from the upstream end of the stepped chute to the inception point x_i is shown as (Chanson 2005):

$$\frac{x_i}{k} = \text{func}(F_*) \qquad [1]$$

where k = Scosθ, and F_* [= $q/(gk^3\sin\theta)^{1/2}$] is the roughness Froude number. The roughness Froude number, F_* can be presented as F_* = $[(S/d_c)^3 \sin\theta \cos^3\theta]^{-1/2}$, indicating that the effects of S/d_c and θ are included. Figure 2 results by arranging the experimental data based on Eq. [1]. The relative distance x_i/k can be expressed as:

 / ISSN 1562-6865 (Online) - ISSN 1063-7710 (Print)

$$\frac{x_{\mathrm{i}}}{k} = 5.0\mathrm{F}_*^{0.97} \qquad \left(18° \le \theta \le 53°, R^2 = 0.99\right) \tag{2}$$

with R^2 as a coefficient of determination.

The depth averaged air concentration C_{m} is defined by:

$$C_{\mathrm{m}} = \frac{1}{y_{0.9}} \int_0^{y_{0.9}} C \mathrm{d}y \tag{3}$$

where $y_{0.9}$ = the aerated flow depth defined as y at C = 0.9, and y = the normal coordinate from the pseudo-bottom. The experimental results of C_{mi} show that $C_{\mathrm{mi}} \approx 0.2$ in the range of 19° ≤ θ ≤ 55°, which agrees with the results of other researchers (Bung 2011, Matos 2000).

For R ≥ 3×10^4, the time-averaged velocity u at the inception point follows (Takahashi and Ohtsu 2012):

$$\frac{u}{u_{0.9}} = \left(\frac{y}{y_{0.9}}, \theta, \frac{S}{d_c}\right) \tag{4}$$

where $u_{0.9}$ is the time-averaged velocity at $y = y_{0.9}$. If the experimental data at the edge section are arranged in accordance with Eq. [4], the velocity profiles for $0 \le y/y_{0.9} \le 1$ follow the power-law velocity profile as:

$$\frac{u}{u_{0.9}} = \left(\frac{y}{y_{0.9}}\right)^{\frac{1}{N}} \tag{5}$$

Takahashi and Ohtsu (2012) proposed the values of N in the quasi-uniform-aerated flow region as:

$$N = 14\theta^{-0.65} \frac{S}{d_c}\left(\frac{100}{\theta}\frac{S}{d_c} - 1\right) - 0.041\theta + 6.27 \quad (\theta \text{ in deg.}) \tag{6}$$

For a given θ and S/d_c, the velocity profiles at the edge section can be approximated by Eq. [5] with Eq. [6] as shown in Figure 3. Note that the velocity profiles at the inception point follow Eq. [5] with Eq. [6].

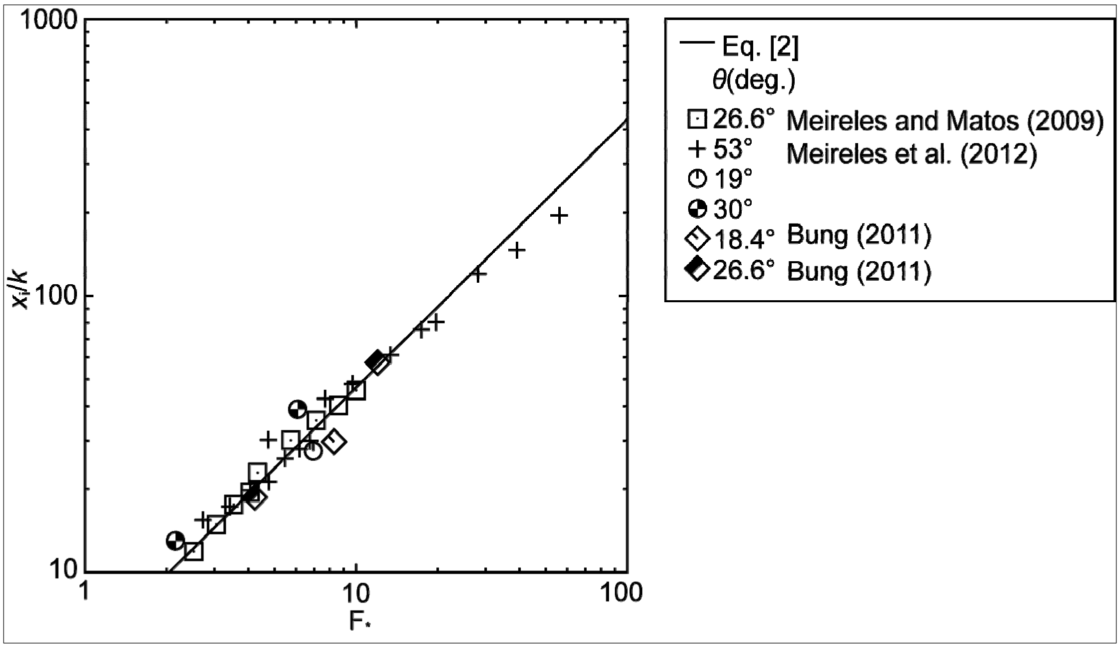

Figure 2. The relative length (x_i/k) from the upstream end of the stepped channel to the inception point.

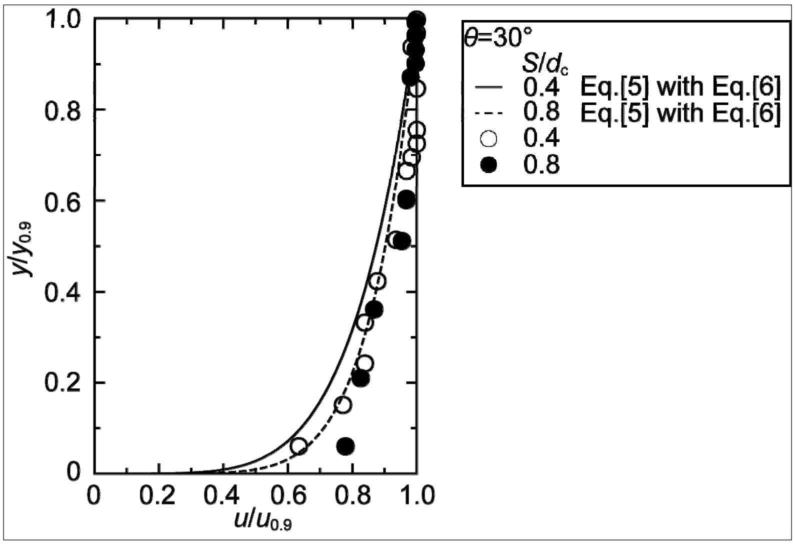

Figure 3. Velocity profiles at the inception point.

4 VELOCITY PROFILES IN NONAERATED SKIMMING FLOWS

In the turbulent boundary layer of the nonaerated skimming flow region, the time-averaged velocity for R ≥ 3.0×10^4 may follow:

$$\frac{u}{U} = \mathrm{f}\left(\frac{y}{\delta}, \frac{S}{d_c}, \frac{x}{d_c}\right). \qquad [7]$$

where U = the velocity outside the boundary layer, and δ = the boundary layer thickness defined as the perpendicular distance from the pseudo-bottom to the point y where $u = 0.99U$. If the experimental data at the edge section are arranged according to Eq. [7], an example of the velocity profiles is shown in Figure 4. Note that the velocity profiles in the boundary layer ($0 \le y/\delta \le 1$) follow the power-law velocity profiles as:

$$\frac{u}{U} = \left(\frac{y}{\delta}\right)^{\frac{1}{N}} \qquad [8]$$

and the value of u/U for the flow outside the boundary layer ($y/\delta > 1$) = 1. Figure 4 shows that the velocity profiles under a given θ and S/d_c are almost independent of x/d_c, indicating that the values of N are independent of x/d_c. The velocity profiles in the nonaerated skimming flow follow Eq. [8] with Eq. [6]. As shown in Figure 4, the difference between the experimental value of u/U and the value of u/U obtained from Eq. [8] with Eq. [6] is within ± 0.1.

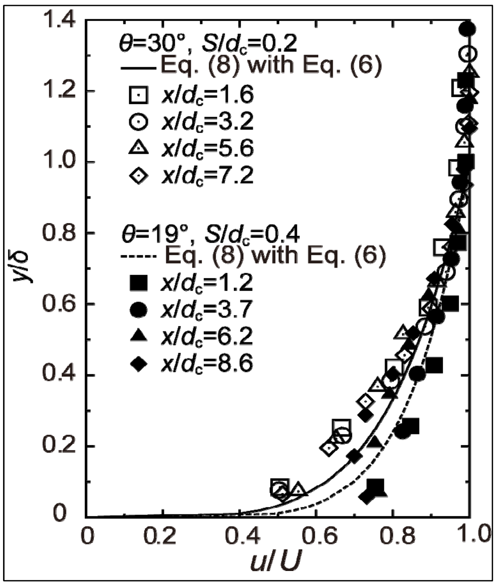

Figure 4. Velocity profiles in nonaerated skimming flows.

5 TURBULENT BOUNDARY LAYER DEVELOPMENT

For a smooth spillway, the thickness of the boundary layer δ is expressed by (Bauer 1954):

$$\frac{\delta}{k} = a\left(\frac{x}{k}\right)^{-b} \qquad [9]$$

where a and b = constant values, and k = roughness. For stepped spillways, the value of k may be represented by $k = S\cos\theta$.

The discharge per unit width, q of the central plane is obtained by:

$$q = \int_0^d u\mathrm{d}y = U(d - \delta_*) \qquad [10]$$

where δ_* = displacement thickness defined as:

$$\delta_* = \int_0^\delta (1 - u/U)\mathrm{d}y\ . \qquad [11]$$

Using Eq. [11] with Eq. [8], δ_* is written as:

$$\delta_* = \frac{\delta}{1+N}\ . \qquad [12]$$

Combining Eqs. [10] and [12] gives:

$$U = \frac{q}{d-\delta_*} = \frac{q}{d - \delta/(1+N)} \qquad [13]$$

At the inception point $x = x_i$, if the water depth and the velocity outside the boundary layer are defined by d_i and U_i, respectively, Eqs. [9] and [13] give:

$$d_i = a\frac{x_i^{-b+1}}{k^{-b}}\ , \qquad [14]$$

and

$$U_i = \frac{1+N}{N}\frac{q}{d_i} \qquad [15]$$

because $\delta = d_i$ is required at the inception point.

Outside the boundary layer, if Bernoulli's principle is applied along the free stream line between section 1 and the inception point ($x = x_i$), the free stream velocity is given by:

$$U_i = \sqrt{2g\left(x_i\sin\theta + \frac{3}{2}d_c - d_i\cos\theta\right)}\ . \qquad [16]$$

Using $x_i\sin\theta >> 1.5d_c - d_i\cos\theta$, Eq. [16] can be represented by:

$$U_i = \sqrt{2gx_i\sin\theta} \qquad [17]$$

From Eq. [15], with Eqs. [14] and [17], the relative distance x_i/k can be expressed by (Chanson 2005):

$$\frac{x_i}{k} = \left(\frac{1+N}{N}\frac{1}{a\sqrt{2}}\right)^{\frac{1}{1.5-b}} F_*^{\frac{1}{1.5-b}}\ . \qquad [18]$$

A comparison between Eqs. [18] and [2] gives:

$$a = 0.135\frac{1+N}{N} \qquad [19]$$

and

$$b = 0.469\ . \qquad [20]$$

Substituting Eqs. [19] and [20] into Eq. [9], the empirical equation of the boundary layer thickness is given by:

$$\frac{\delta}{x} = 0.135\frac{1+N}{N}\left(\frac{x}{k}\right)^{-0.469} \qquad \left(19^\circ \le \theta \le 55^\circ, R^2 = 0.63\right). \qquad [21]$$

Combining Eqs. [21] and [6], the following relation can be represented as:

$$\frac{\delta}{x} = \mathrm{f}\left(\frac{x}{k}, \theta, \frac{S}{d_\mathrm{c}}\right). \qquad [22]$$

The experimental data of the turbulent boundary layer thickness, δ are arranged in accordance with Eq. [22]; as shown in Figure 5, the calculated lines by Eq. [21] agree with the experimental data for 19° ≤ θ ≤ 55°.

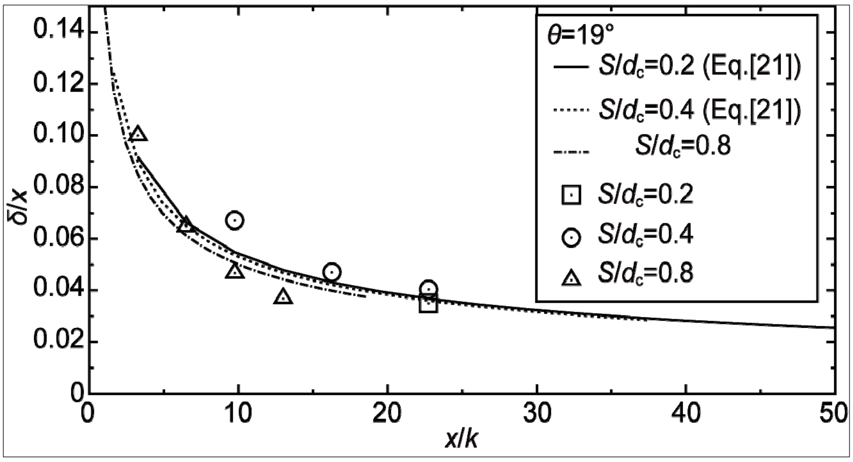

Figure 5. Boundary layer thickness in nonaerated skimming flows.

To know the effect of x/d_c, S/d_c, and θ on δ/d_c, Eq. [21] may be rewritten as:

$$\frac{\delta}{d_\mathrm{c}} = 0.135\frac{1+N}{N}\left(\frac{S}{d_\mathrm{c}}\cos\theta\right)^{0.469}\left(\frac{x}{d_\mathrm{c}}\right)^{0.531}. \qquad [23]$$

The value of δ/d_c for a given x/d_c, S/d_c, and θ follows from Eq. [23] with Eq. [6], as shown in Figures 6 and 7. Note that the values of δ/d_c for a given S/d_c and θ increase with x/d_c. Figure 6 shows that the values of δ/d_c for a given θ and x/d_c increase with increasing S/d_c. Additionally, Figure 7 indicates that the values of θ have little effect on those of δ/d_c for a given x/d_c and S/d_c.

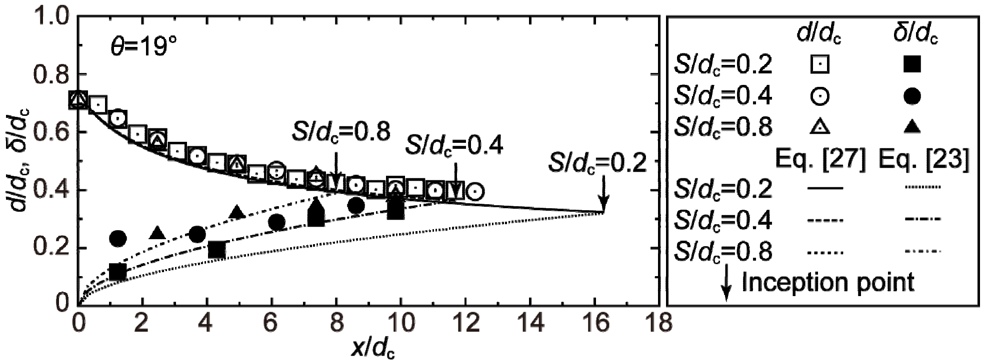

Figure 6. Effects of relative step heights (S/d_c) on the relative water depth (d/d_c) and the relative boundary layer thickness (δ/d_c).

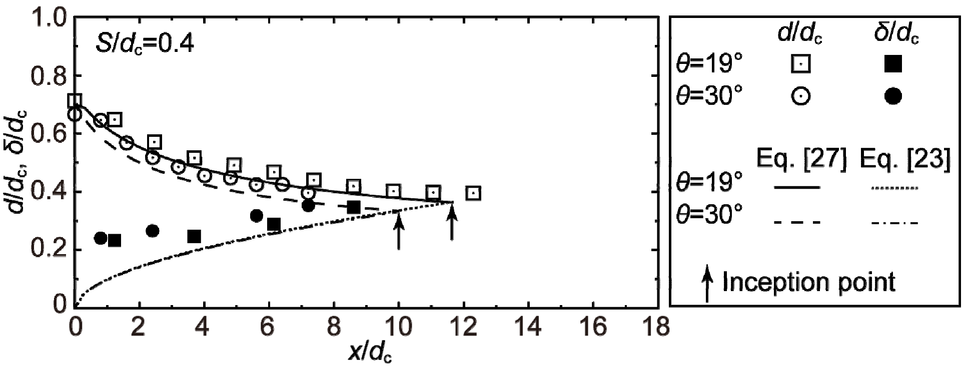

Figure 7. Effects of angle of channel slope (θ) on the relative water depth (d/d_c) and the relative boundary layer thickness (δ/d_c).

6 WATER SURFACE PROFILES

Along the free stream line between section 2 (x = 0) and the section 3 (x = x), Bernoulli's principles gives

$$\frac{3}{2}d_c + x\sin\theta = d\cos\theta + \frac{U^2}{2g}. \qquad [24]$$

From Eq. [13], the velocity head is obtained by

$$\frac{U^2}{2g} = \frac{d_c{}^3}{2(d-\delta_*)^2}. \qquad [25]$$

From Eq. [24] and Eq. [25], the generalized water surface equation for stepped spillways is

$$\frac{\mathrm{d}d}{\mathrm{d}x} = \frac{\sin\theta - \dfrac{d_c{}^3}{(d-\delta_*)^3}\dfrac{\mathrm{d}\delta_*}{\mathrm{d}x}}{\cos\theta - \dfrac{d_c{}^3}{(d-\delta_*)^3}}. \qquad [26]$$

Equation [26] is integrated with respect to x under the boundary condition $d = 0.7d_c$ and $\delta_* \approx 0$ at x = 0, and substituting Eq. [12] into the integrated equation yields

$$\frac{d}{d_c} = \frac{1}{1+N}\frac{\delta}{d_c} + \left[0.7^{-2} + 2\left\{\frac{x}{d_c}\sin\theta - \left(\frac{d}{d_c} - 0.7\right)\cos\theta\right\}\right]^{-\frac{1}{2}} \quad \left(19^\circ \le \theta \le 55^\circ, R^2 = 0.97\right). [27]$$

Using Eq. [27] with Eqs. [23] and [6], the value of the relative water depth d/d_c can be obtained for a given θ, S/d_c, and x/d_c. Figures 6 and 7 show some examples of the calculated values of d/d_c. The lines agree with the experimental data for 19° ≤ θ ≤ 55° and 0.2 ≤ S/d_c ≤ 0.9, and the predicted lines demonstrate the effect of x/d_c on d/d_c for a given S/d_c and θ.

Figure 6 shows the effect of S/d_c on d/d_c for a given x/d_c and θ. Note that the values of S/d_c have little effect on those of d/d_c. Figure 7 shows the effect of θ on d/d_c, indicating that the values of d/d_c decrease as θ increases for a given S/d_c and x/d_c.

7 SPECIFIC ENERGY

The step edge section is selected as the reference section to estimate the specific energy E. If the pressure at the edge section is assumed to be hydrostatic, the specific energy E is given by

$$E = d\cos\theta + \alpha\frac{V^2}{2g} \qquad [28]$$

where V = the depth averaged velocity, which is shown as

$$V = \frac{1}{d}\int_0^d u\mathrm{d}y = \frac{U}{d}\left[d - \frac{\delta}{N+1}\right], \qquad [29]$$

and α = the energy correction coefficient. Using Eq. [29] with Eq. [8] for 0 < y/δ ≤ 1 and u/U = 1 for y/δ > 1 gives

$$\alpha = \frac{1}{d}\int_0^d\left(\frac{u}{V}\right)^3\mathrm{d}y = \left(1 - \frac{3}{N+3}\frac{\delta}{d}\right)\Bigg/\left(1 - \frac{1}{N+1}\frac{\delta}{d}\right)^3. \qquad [30]$$

From Eq. [30], the value of α is 1 for the undeveloped boundary layer (δ = 0). For a given θ, S/d_c, and x/d_c, the values of α can be obtained by Eqs. [6], [23], [27], and [30] and are represented as

$$\alpha = f\left(\frac{x}{d_c}, \theta, \frac{S}{d_c}\right). \qquad [31]$$

To know the effects of θ, S/d_c, and x/d_c on α, some calculated values of α are shown in Fig. 8. Note that the calculated values of α increase with increasing x/d_c for a given θ and S/d_c. For a given θ and x/d_c, Fig. 8 (a) shows that the values of α decrease as S/d_c increases. For a given S/d_c and x/d_c, Fig. 8(b) shows that the values of α decrease with decreasing θ.

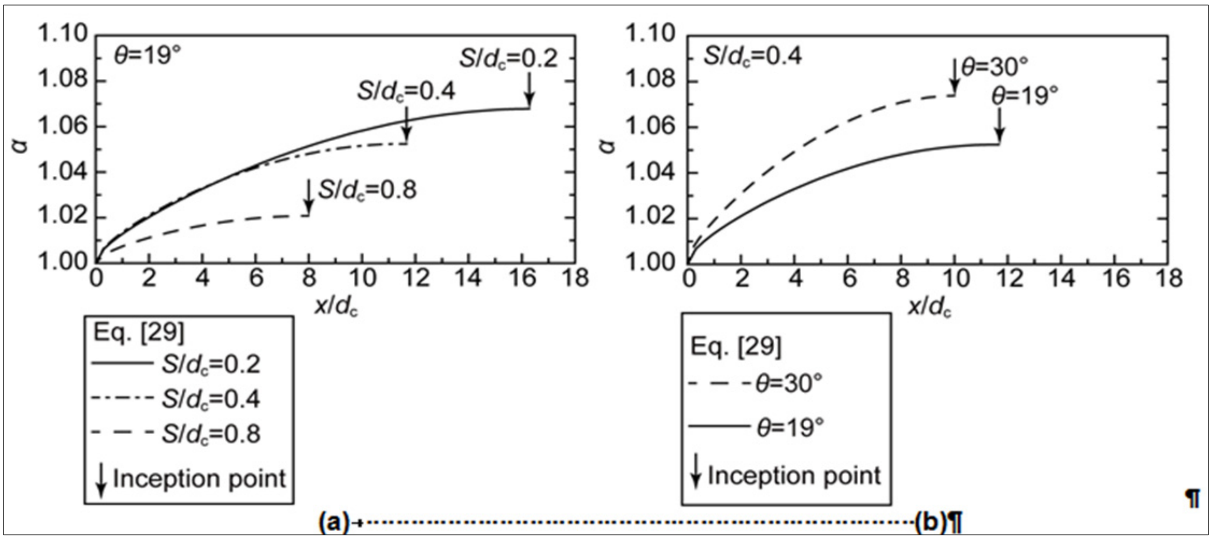

Figure 8. Effects of angle of channel slope (θ) and relative step height (S/d_c) on the energy coefficient, α for (a) θ =19° and (b) S/d_c = 0.4.

From Eq. [28] and $V = q/d$, the relative specific energy E/d_c is given by:

$$\frac{E}{d_c} = \frac{d}{d_c}\cos\theta + \frac{\alpha}{2}\left(\frac{d}{d_c}\right)^{-2}. \qquad [32]$$

For given θ, S, x, and d_c (or q), the predicted E/d_c lines in Figure 9 follow Eq. [32], in which d/d_c and α are given by Eqs. [6], [23], [27], and [30]. If the loss of head is negligible between section 2 (x = 0) and section 3 ($x = x$), the relative specific energy for the potential flow $(E/d_c)_{non\_loss}$ is given by:

$$\left(\frac{E}{d_c}\right)_{non\_loss} = \frac{3}{2} + \frac{x}{d_c}\sin\theta. \qquad [33]$$

Figure 9a shows the effect of S/d_c on E/d_c. For a smooth spillway (S/d_c = 0), the values of E/d_c are nearly equal to those of $(E/d_c)_{non\_loss}$ in the range of $x/d_c \le 3 – 6$, indicating that the loss of head is nearly equal to 0. This is because the boundary layer thickness is thin, and the potential flow occupies a large portion of the flow. For $x/d_c > 4 – 6$, the loss of head increases with increasing x/d_c, so the value of δ/d is in the range of $\delta/d \gtrsim 0.4$. Figure 9a compares the loss of head for stepped spillways with that for smooth spillways (S/d_c = 0), demonstrating that the energy dissipation of stepped spillways is larger than that of smooth spillways for the range of $x/d_c \gtrsim 5$.

Figure 9b indicates the effect of θ on E/d_c, showing that the values of E/d_c for a given x/d_c and S/d_c increase with increasing θ.

  / ISSN 1562-6865 (Online) - ISSN 1063-7710 (Print)

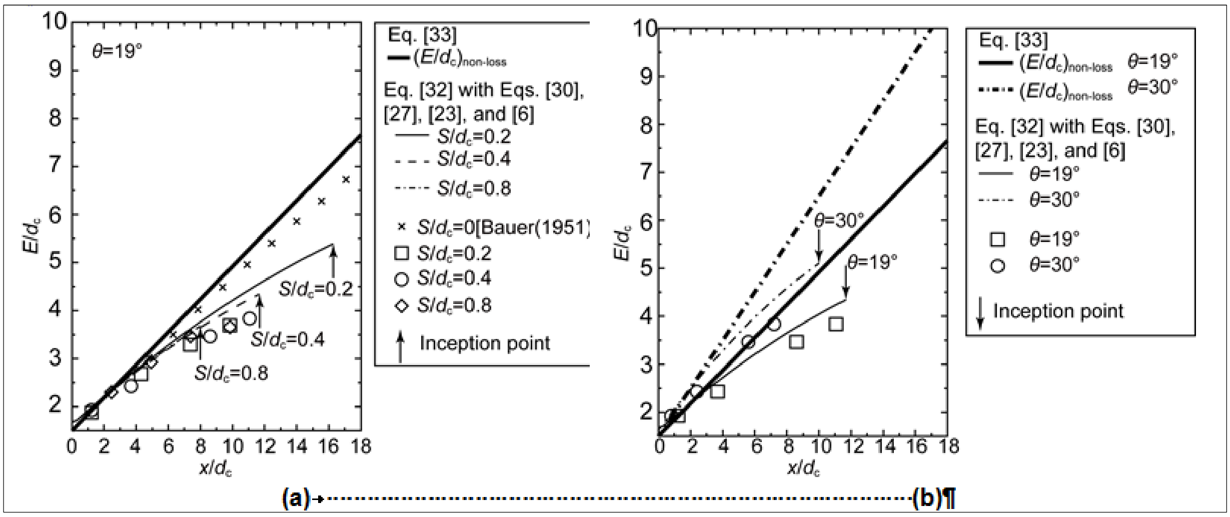

Figure 9. Effects of the angle of channel slope (θ) and relative step height (S/d_c) on the specific energy, E/d_c for (a) θ =19° and (b) S/d_c = 0.4.

8 CONCLUSIONS

The nonaerated flow characteristics of skimming flows were systematically investigated for a wide range of spillway angles (θ) and relative step heights (S/d_c). The results are summarized as follows:

- Velocity profiles in the turbulent boundary layer at the edge section follow the $1/N$ power-law velocity profile. The value of N is independent of x/d_c, and the exponent N is given by Eq. [6].
- The thickness of the boundary layer δ can be obtained by Eq. [23] with Eq. [6] for a given θ, S/d_c, and x/d_c.
- The gradually varied flow equation Eq. [27] is developed for the water depth (d) in the nonaerated skimming flow region. Using Eqs. [27], [23], and [6] gives the water depth (d) under a given x, θ, q (or d_c), and S.
- The relative specific energy E/d_c is calculated using Eq. [32] with the energy coefficients Eq. [30] considering the development of the boundary layer, indicating that the energy dissipation of stepped spillways in the range of $x/d_c \gtrsim 5$ is larger than that of smooth spillways.

ACKNOWLEDGEMENTS

The first author was financially supported by the Japan Society for the Promotion of Science (JSPS), Grant No. 16K06518.

REFERENCES

Bauer, W. J. (1954). Turbulent Boundary Layer on Steep Slopes. *Transactions of the American Society of Civil Engineers,* 119, 1212–1233.

Bung, D. B. (2011). Developing Flow in Skimming Flow Regime on Embankment Stepped Spillways. *Journal of Hydraulic Research*, 49(5), 639–648.

Chanson, H. (2005). Discussion of Two-Phase Flow Characteristics of Stepped Spillways. *Journal of Hydraulic Engineering*, 131(5), 419–421.

Matos, J. (2000). *Hydraulic Design of Stepped Spillways over Rcc Dams.* Ed. H.-E. Minor and W. H. Hager. *Hydraulics of Stepped Spillways*, Rotterdam, Balkema, 187–194.

Meireles, I. & Matos, J. (2009). Skimming Flow in the Non-Aerated Skimming Region of Stepped Spillways over Embankment Dams. *Journal of Hydraulic Engineering*, 135(8), 685-689.

Meireles, I. Renna, F. & Matos, J. (2012). Skimming, Nonaerated Flow on Stepped Spillways over Roller Compacted Concrete Dams. *Journal of Hydraulic Engineering*, 138(10), 870–877.

Takahashi, M. & Ohtsu, I. (2012). Aerated Flow Characteristics of Skimming Flow over Stepped Chutes. *Journal of Hydraulic Research*, 50(4), 427–434.

EFFECT OF BRIDGE PIER DIAMETER ON COLLAR EFFICIENCY

MOJTABA KARIMAEI TABARESTANI (1), AMIR REZA ZARRATI (2) & SEYED AMIN SALAMATIAN (3)

(1)Department of Civil Engineering, Shahid Rajaee Teacher Training University, Tehran, Iran.
Karimaei@srttu.edu
(2)Department of Civil and Environmental Engineering, Amirkabir University of Technology, Tehran, Iran.
Zarrati@aut.ac.ir
(3)Department of Civil Engineering, Shahab danesh Univeristy, Qom, Iran.
Salamatian@aut.ac.ir

ABSTRACT

Collars as an effective scour countermeasure are plates, which are attached to a pier and act as a barrier to the downflow, thereby prevent its direct impingement into the streambed. Experiments show that collar cause considerable delay in scouring at the pier. There is no information can be found in the literature on how this time delay can be calculated or what its relationship with the flow and pier characteristics are. Also, no enough information is available on the scale of time for scouring development in physical models. In the present study, experiments were conducted for collar efficiency in a horizontal flume. Two different hollow Perspex circular pipes with diameter of D = 5 cm and 7 cm were used as the pier model. In addition, a round collar made from 2 mm thick Perspex sheets with an effective width, "W" equals to three times of the pier diameter was installed around the pier at the stream bed level. In each experiment, the temporal variation of scouring around the collar was recorded. In addition to the present data, experimental data from previous study for D = 4 cm were used in the analysis. Formation of scour hole around collar was monitored and different stages for scour hole development was recognized. Experimental results showed that by increasing the pier diameter, the time that the collar is undermined T_t, increases significantly. For example, in flow intensity u_*/u_{*c} = 0.91, by increasing pier width from 4 cm to 7 cm, T_t increases for about 4.4 times. In addition, experimental results showed that the effect of pier diameter on T_t is larger for lower flow intensities. Finally, from dimensional analysis and available experimental data, a new relationship is developed to calculate T_t for different diameters of bridge pier based on different important parameters affecting scour depth development.

Keywords: Bridge pier; scour hole; scour countermeasure; collar efficiency; time for undermining collar.

1 INTRODUCTION

Local scour around bridge piers occurs due to a complex flow field with large-scale structures, such as horseshoe and wake vortices generated by the flow around the pier. Based on the report of Hydraulic Engineering Circular No. 18, the formation of scour hole around bridge pier is recognized as the root cause of bridge failure.

Due to the danger of bridge failure when piers are undermined, many methods have been presented for the prevention of scouring. Collars as an effective scour countermeasure are plates, which are attached to a pier and act as a barrier to the down flow, thereby prevent its direct impingement into the streambed (Figure 1).

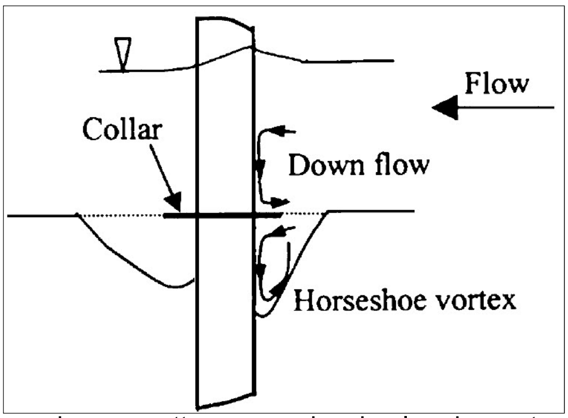

Figure 1. Flow and scour pattern around a circular pier protected by a collar (Zarrati et al. 2004)

A collar at any level above the bed divides the flow into two regions, above and below the collar. For the region above the collar, it acts as an obstacle against the downflow and the downflow loses its strength on impingement at the collar. For the region below the collar, the strength of downflow and therefore the horseshoe vortex is reduced (Tabarestani and Zarrati, 2012). Due to the reduced strength of horseshoe vortex, the scour hole depth reduces when a collar is used. In addition, a collar considerably postpones scour development at the pier face (Chiew, 1992, Zarrati et al., 2004, Allabi, 2006, Tafarojnorouz et al, 2012). Literature review shows that with a collar in place, no scour hole is observed at the pier perimeter in the beginning of experiment (Alabi, 2006, Mashahir et al., 2007, Tabarestani and Zarrati, 2012). However, a scour hole is formed downstream of the collar, which slowly develops towards upstream. When collar is undermined, the flow penetrates below the collar and scouring rate increases. Experimental data from Zarrati et al. (2006) showed that for pier with D = 4 cm and a collar with W/D = 3 installed at stream bed under flow condition of u_*/u_{*c} = 0.91, where u_* is shear velocity and u_{*c} is critical shear velocity for bed sediment movement, scouring reached the upstream face of the pier after 4 hours and after about 30 hours 30 % of final scouring occurred. Mashahir et al. (2007) conducted similar experiments with u_*/u_{*c} = 0.86 and showed that the beginning of scouring at the pier face occurred after 11 hours from the beginning of the experiment. In addition, they reported that, after 30 hours the collar was completely undermined but only 25 % of the maximum scouring was developed at the front face of the pier. They also reported that reduction of the scour depth in this test was 27 % as compared to the unprotected pier. Finally, similar experiments by Tabarestani and Zarrati, (2012) showed that for flow intensity u_*/u_{*c} = 0.8, scouring reached the upstream face of the pier after 15 hours. In this way, collars can be very effective in reducing the risk of bridge failure when duration of the flood flow is not long (Tabarestani and Zarrati, 2016).

The efficiency of a collar basically depends on its size and location with respect to the stream bed and shear stress. The effect of collar in reducing scour depth is previously studied on cylindrical and rectangular piers. These studies showed that with increasing the width of the collar and lowering its elevation, depth of the scour hole is reduced (Chiew, 1992, Kumar et al., 1999, Zarrati et al., 2006). In addition, Mashahir et al., (2007) showed that the development of scour hole around and below a collar depends considerably on bed shear stress. As shear stress on bed increases, area of higher shear stress around the collar and consequently scouring and its rate increases, or in other words, the efficiency of collar decreases.

From the literature, it can be inferred that no information is available about the effect of pier diameter on the time that a collar is undermined. Time development of scouring certainly depends on scale of the model corresponding to the prototype size. However, the time scale of scouring is not given in the literature clearly. In the present work, the effect of pier diameter on efficiency of a collar in various bed shear stresses is examined experimentally. This work helps in understanding better the effect of various parameters and scale of the model on time of scour development in physical models.

2 EXPERIMENTAL SETUP

Experiments were conducted in a horizontal flume with erodible bed 14 m long, 0.75 m wide and 0.6 m deep. Water was circulated in the channel by a centrifugal pump with maximum capacity of 100 (L/s). The flow rate in the flume was controlled and preset by a speed control unit attached to the pump system. An electrical flow meter was installed in the supply conduit to measure the discharge passing through the channel. The channel's rigid bed was overlaid with about 20 cm thick, uniform sand, with median size of 0.00067 m and density of 2650 (kg/m^3). The geometric standard deviation of sediment grading $\sigma_g = \sqrt{d_{84}/d_{16}}$ was 1.2, where d_a is the size of sediment for which a percent of material by weight are finer implying that the sample is uniform. Two different hollow Perspex circular pipes with diameter of D = 5 and 7 cm where used as pier models in the present study. Therefore, the minimum amount of parameter D/d_{50} was about 75. Based on Chiew and Melville (1987), the effect of D/d_{50} on local scour depth around bridge pier is negligible when D/d_{50} > 50.

In order to reduce the flow disturbance and producing a nearly uniform approaching flow, a honeycomb (flow straightener) was used at the upstream section of the channel. Each pier model was installed at about 8 m from flume entrance in boundary layer fully developed region. Collar was made from 2 mm thick Perspex sheets with an effective width, 'W' equal to three times of the pier diameter, 'D' were installed around the pier at stream bed level (Figure 1). Flow depth in the channel was measured with a point gauge with 0.1 mm accuracy. The threshold of bed material motion was found by experiment when the pier was not installed. Threshold of material motion was defined as a condition for which finer materials may move, but the elevation of the bed would not lower more than 2 to 3 mm during the period of the experiment.

Table 1 shows the details of the present experiments. As shown in the table, the range of the flow intensity was 0.8 ≤ u_*/u_{*c} ≤ 0.96. Experiments were continued till the scour hole grooves around the collar reached the upstream face of the pier, or in other words, the collar was undermined and scouring started at the pier. Time of experiment (T_t), which is the time for undermining the collar was very long especially with lower flow intensity (e.g. more than 5 days for u_*/u_{*c} = 0.8 and D = 7cm). The range of T_t in present study was $180 \le T_t \le 7605$ minutes.

Mechanism of sediment movement around collar and pier in different flow intensities was studied carefully. The temporal variation of scouring around the collar was recorded by using two high quality cameras. Figure 2 shows the experimental setup and the positions of cameras. Camera #1 was placed in the hollow Perspex pier to record time development of scouring at the pier nose. In addition, Camera #2 was placed upstream of the pier outside of water to monitor sediment movement around the collar.

Table 1. Details of present experiments for steady flow condition.

Test No.	Test Code	Pier diameter D (cm)	u_*/u_{*c}	T_t (min)
1	S-C7-1	7	0.99	301
2	S-C7-2	7	0.96	550
3	S-C7-3	7	0.91	1060
4	S-C7-4	7	0.86	2760
5	S-C7-5	7	0.80	7605
6	SC-C5-1	5	0.99	180
7	SC-C5-2	5	0.91	600
8	SC-C5-3	5	0.8	3900

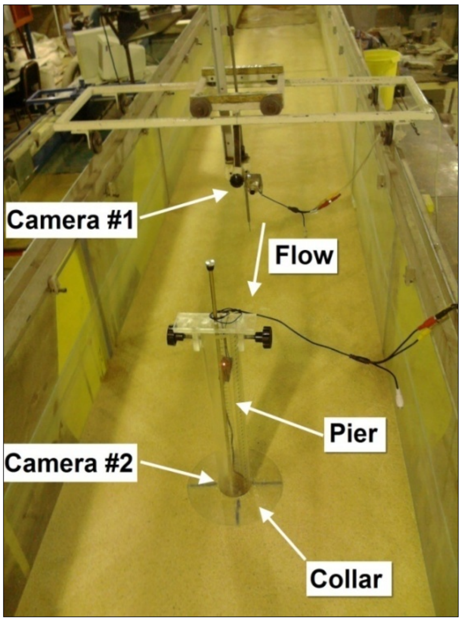

Figure 2. Experimental setup in present study.

3 FORMATION OF SCOUR HOLE AROUND BRIDGE

Figure 3 shows different steps for formation of the scour hole around a circular bridge pier protected by a collar. In these experiments, scouring was first started downstream of the collar due to action of wake vortices (Figure 3a). Simultaneously, two grooves were formed at the downstream of the collar with sediment movement in a spiral path towards the center of channel. Over the time, the grooves gradually grew larger and deeper as they approach the rear edge of the collar (Figure 3b). After that, the sediment beneath the collar was gradually washed away and the scour hole was extended faster due to penetration of flow beneath the collar. Finally, the scour hole reached the collar side edge at point 1 as shown in Figure 3b. With a sudden acceleration in scour hole development, the grooves at both sides of the collar extended to the upstream side of it, around its rim and joint at point 2 as can be seen in Figure 3c. As scouring develops at the downstream of the collar, the bed topography and therefore the flow force distribution on the streambed changes and this can be one of the reasons for the development of the grooves towards the upstream and beneath the collar. Finally, the scour hole reached the upstream face of the pier (point 3 in Figure 3d). As shown in Figure 3d, although at this stage scour hole was developed below the collar and reached the pier face, the downstream of the pier the collar was still attached to the bed. Finally, the scour hole extended in the plan and collar was fully detached from the streambed (Figure 3e).

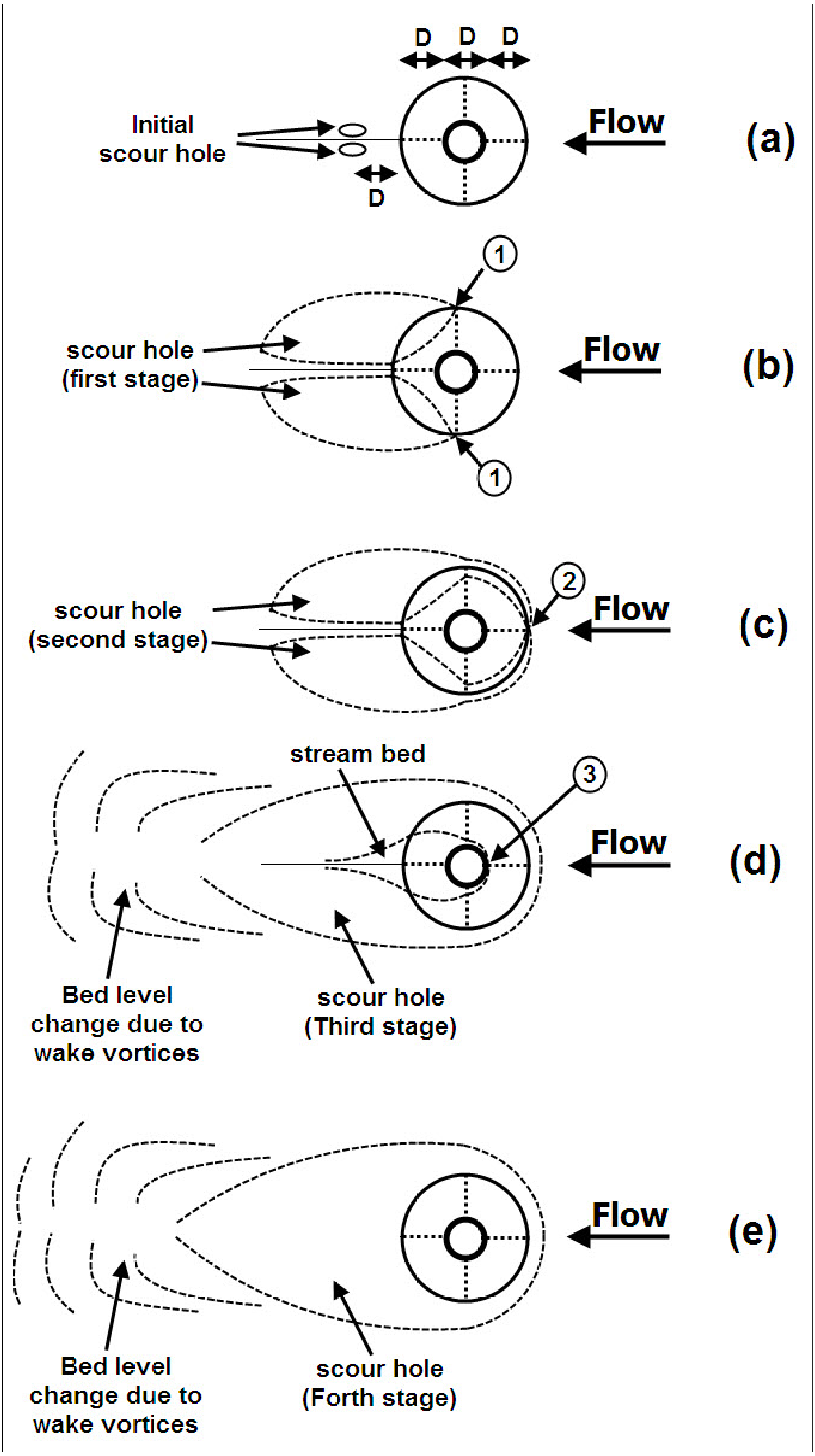

Figure 3. Time development of scour hole around circular bridge pier.

4 EFFECT OF PIER DIAMETER ON COLLAR PERFORMANCE

Table 2 shows the experimental results. In addition to the present data, the experimental data reported by other research works are also presented in this table and used in analysis. Figure 4 shows the effect of pier width on T_t. As shown in this figure, by increasing the pier diameter, T_t increases significantly. For example, in u_*/u_{*c} = 0.91, by increasing the pier width from 4 cm to 7 cm (about 75 %), parameter T_t increases for about 4.4 times. This is due to a larger amount of sediment beneath the collar must be transported, which needs a longer time. In addition, from Table 3, it can also be concluded that with u_*/u_{*c} = 0.80, by increasing pier diameter from 4 cm to 7 cm, parameter T_t increases for about 8.5 times, which is about 2 times larger than u_*/u_{*c} = 0.91. Therefore, the effect of pier diameter on T_t is more obvious in lower flow intensities. From these data, it can be concluded that for size of pier diameter in nature, the time for undermining collar will be much larger. Alabi, (2006) conducted experiments in u_*/u_{*c} = 0.7 for 11 cm pier with W/B = 3 collar at the stream bed level and found that the collar did not undermined after 1000 hours (more than 40 days). From the aspects of dimensional analysis, a new relationship is developed for T_t in the available range of experimental data and based on different important parameters that affecting scour depth:

$$\frac{T_t}{T_{cp}} = 1.7 \times 10^{-5} \times \left(\frac{u_*}{u_{*c}}\right)^{-15.3} \times \left(Re_d\right)^{2.23} \qquad [1]$$

where, T_{cp} is a time scale parameter calculated as T_{cp} = D/U, where U is the upstream undisturbed flow velocity. Different researchers, such as Franzetti et al. (1982) and Melville and Chiew (1999), have also used this parameter to evaluate the rate of scouring around bridge piers. Re_d is the pier Reynolds number, which is defined as:

$$Re_d = \frac{U \cdot D}{\nu} \qquad [2]$$

where v is the water dynamic viscosity. Pier Reynolds number is used by different investigators, such as Shen et al. (1969), as one of the important parameter on the scour depth calculation and strength of horse shoe vortex around bridge piers. In addition, Wei et al, (1997) showed that the maximum stress around the pier is a function of Re_d in a numerical study.

Figure (5) shows the acceptable accuracy of Eq. [2] with coefficient of variation of R^2 = 0.96 in predicting experimental data.

Table 2. Experimental result for determining collar efficiency in different pier diameters.

Test No.	Test Code	Pier diameter (Cm)	u_*/u_{*c}	T_t (hr)	Reference
1	S-C7-1	7	0.99	5.02	Present study
2	S-C7-2	7	0.96	9.17	
3	S-C7-3	7	0.91	17.67	
4	S-C7-4	7	0.86	46.00	
5	S-C7-5	7	0.80	126.75	
6	SC-C5-1	5	0.99	2.54	
7	SC-C5-2	5	0.91	8.75	
8	SC-C5-3	5	0.8	48.12	
9	Test #1	4	0.96	2	Mokalaf, (2007)
10	Test #2	4	0.91	4	Zarrati et al. (2006)
11	Test #3	4	0.86	11	Mashahir et al. (2007)
12	Test No. 1	4	0.8	15	Tabarestani and Zarrati (2012)

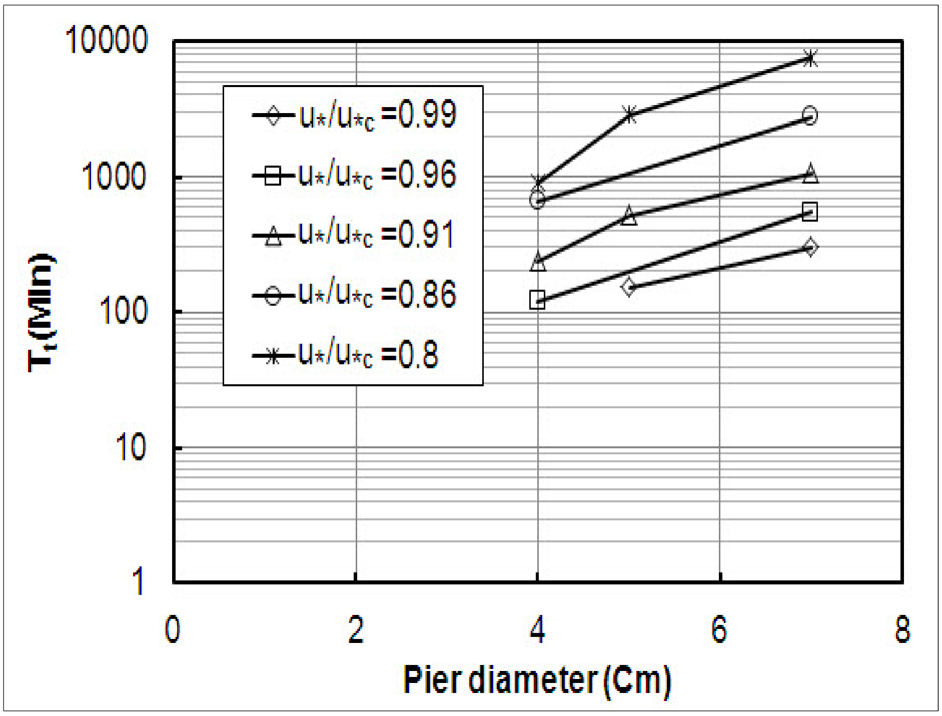

Figure 4. Effect of pier diameter on time for undermining collar in different flow intensity.

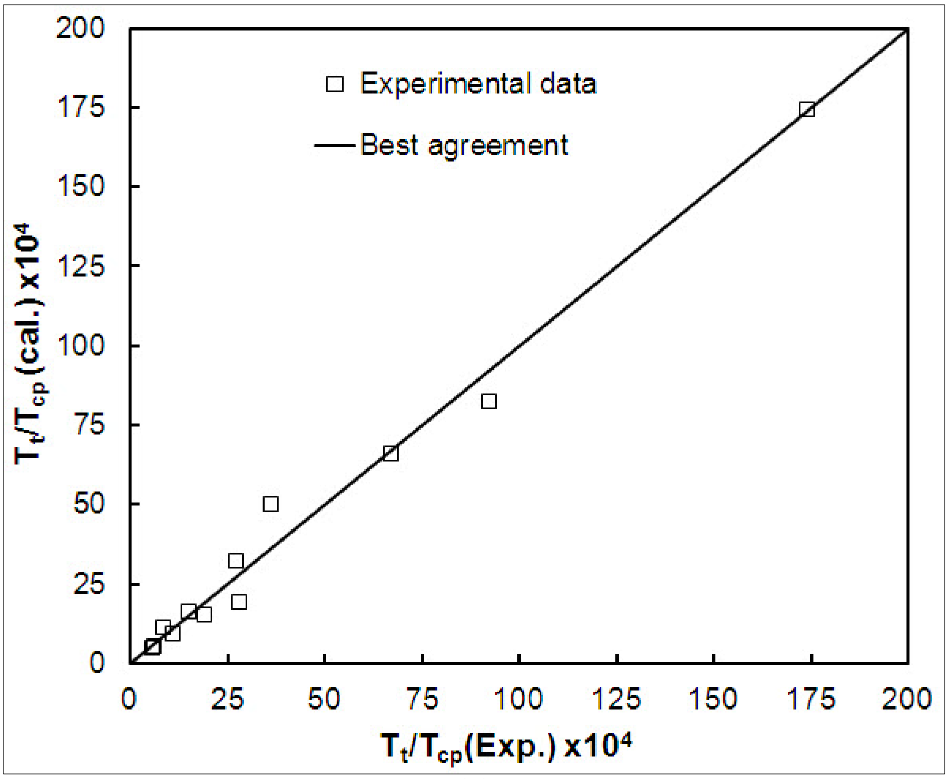

Figure 5. Accuracy of Equation (1) in predicting experimental data.

5 CONCLUSIONS

When a collar is installed on a pier, the development of the scour hole is postponed considerably. Though the efficiency of collars on reducing the depth of scour hole around piers is studied before, there is no enough information available about the time that a collar is undermined. In the present work, experiments were conducted to study the effect of pier diameter on the time that a collar is undermined and the scour hole is reached at the upstream face of the pier. Two different pier model with diameter of D = 5 cm and 7 cm were used. Results of previous studies with D = 4 cm were also used in the analysis. In all the tests, a collar with an effective width, “W” equal to three times of the pier diameter was installed around the pier at the stream bed level. Experiments were conducted in various flow intensities. In each experiment, the temporal variation of scouring around the collar was recorded.

Analysis of experimental data showed that by increasing the pier diameter, the time that the collar is undermined, T_t increases significantly. For example, when u_*/u_{*c} = 0.91, by increasing the pier diameter from 4 cm to 7 cm (about 75 %), T_t increases for about 4.4 times. This is due to a larger amount of sediment beneath the collar must be transported, when the pier diameter increases (and therefore the collar diameter), which needs a longer time. In addition, the experimental results showed that the effect of pier diameter on T_t is larger for lower flow intensities. According to these experimental results, it can be concluded that for larger pier diameters in the nature, much longer time is expected for collar to be undermined and scouring near the pier starts. Finally, from dimensional analysis and available experimental data, a new relationship is developed to calculate T_t for different diameters of bridge pier based on different important parameters affecting scour depth development. Further research is necessary to find a relationship for time scale in scouring development in physical models.

REFERENCES

Alabi P. (2006). Time Development of Local Scour at a Bridge Pier Fitted With a Collar, *MSc. Thesis*. University of Saskatchewan Saskatoon, Saskatchewan, Canada.

Chiew, Y. M. & Melville, B. M. (1987). Local Scour around Bridge Piers. *Journal of Hydraulic Research*, 25(1), 15-26.

Chiew, Y.M. (1992). Scour Protection at Bridge Piers. *Journal of Hydraulic Engineering*, 118(9), 1260-1269.

Fanzetti, S., Larcan, E. & Mignosa, P. (1982). Influence of Tests Duration on the Evaluation of Ultimate Scour around Circular Piers. *International Conference on the Hydraulic Modelling of Civil Engineering Structures,* University of Warwick, Coventry, England, 16 p.

Kumar, V., Ranga Raju, K.G. & Vittal, N. (1999). Reduction of Local Scour around Bridge Piers Using Slots and Collars. *Journal of Hydraulic Engineering*, ASCE, 125(12), 1302-1305.

Melville B.W. & Chiew Y.M. (1999). Time Scale for Local Scour Depth at Bridge Piers. *Journal Hydraulic Engineering*, 125 (1), 59-65.

Mokalaf E. (2007). Time Development of Scouring Around Rectangular Bridge Piers, *MSc. Thesis*. Amirkabir University of Technology, Tehran, Iran. (In Persian)

Mashahir M., Zarrati, A. & Mokallaf E. (2007). Effect of Bed Shear Stress on Development of Scouring Around Bridge Piers Protected by a Collar. *International congress of IAHR*, Veniz, Italy. 32(2), 601.

Shen, H.W. & Schneider, V.R. (1969). Local Scour around Bridge Piers. *Journal of the Hydraulics Division*, *Proceedings of the American Society of Civil Engineers*, 95(6), 1919-1941.

Tabarestani M. K. & Zarrati A.R. (2012). “Effect of Collar on Time Development and Extent of Scour Hole Around Cylindrical Bridge Piers.” *International Journal of Engineering*, Transactions C, 25(1), 11-16.

Tabarestani M. K. & Zarrati A.R. (2016), Local Scour Calculation around Bridge Pier during Flood Event. KSCE *Journal of Civil Engineering*, 21(4), 1462–1472.

Tafarojnorouz, A., Gaudio, R. & Calomino, F. (2012). Evaluation of Flow-Altering Countermeasures against Bridge Pier Scour, *Journal of Hydraulic Engineering*, 138(3), 297-305.

Wei, G., Chen, C., Ting, F., Briaud, L., Gudavalli, R. & Perugu, S. (1997). *Numerical Simulation to Study Scour Rate in Cohesive Soils*, Res. Rep. to the Texas Dep. of Trans., Dep. of Civil Engineering, Texas A&M University, College Station, TX.

Zarrati A.R., Gholami H.& Mashahir, M.B. (2004). Application of Collar to Control Scouring Around Rectangular Bridge Piers. *Journal Hydraulic Research,* 42(1), 97-103.

Zarrati A. R., Nazariha, M. & Mashahir, M. B. (2006). Reduction of Local Scour in the Vicinity of Bridge Pier Groups Using Collars and Riprap. *Journal Hydraulic Engineering*, 132(2), 154-162.

EFFECT OF INTERMITTENT TURBULENT BURSTS ON SEDIMENT RESUSPENSION IN LARGE SHALLOW LAKES

YIPING LI(1), CHUNYAN TANG(2), KUMUD ACHARYA(3) ,WEI DU(4) & JIN WEI(5)

(1,4,5) Key Laboratory of Integrated Regulation and Resource Development on Shallow Lakes, Ministry of Education, Hohai University, Nanjing, 210098, China; College of Environment, Hohai University, Nanjing, 210098, China
liyiping@hhu.edu.cn; 798645315@qq.com; 599194015@qq.com
(2) DHI-NTU Centre, Nanyang Environment and Water Research Institute, Nanyang Technological University, 50 Nanyang Avenue, 639798, Singapore
chyt_06141208@126.com
(3) Division of Hydrologic Sciences, Desert Research Institute, Las Vegas, NV 89119, USA
Kumud.Acharya@dri.edu

ABSTRACT

Sediment resuspended by wind-driven currents and waves releases nutrients that play a critical role in the nutrient cycling of large shallow lakes. Previous studies explain sediment resuspension either in a time-averaged manner based on the laboratory/field experiments or as an instantaneous small-scale turbulence process related to coherent structures in the coastal or estuarial areas. However, few studies have been conducted in large shallow lakes because it is difficult to measure the instantaneous turbulence fluctuation and high-frequency sediment concentration near the lake bottom at the same time, especially because of the complex characteristics of wind-induced wave and current interactions. This study examines the effects of intermittent turbulent bursts on sediment resuspension at the bottom boundary layer of a large, shallow lake by taking high-frequency, synchronous in-situ measurements to monitor fluctuations in velocities and sediment concentrations in Lake Taihu, the third largest freshwater lake in China. To identify the relevant sediment resuspension processes, the near-bed, three-dimensional velocity; Reynolds shear stress; the instantaneous sediment flux (c'w'); and turbulent kinetic energy (TKE) are calculated based on the data collected from Acoustic Doppler Velocimeter (ADV) and Optical Backscatter Sensor (OBS) instruments placed close to the lakebed. The results suggest that the sediment resuspension process is closely connected with the coherent structure in the bottom boundary layers of the lake. The intermittent bursts of coherent structures (dominated by ejection and sweep) are the main energy sources and driving forces for sediment resuspension and nutrient release in large, shallow lakes. The bulk of the sediment flux is accomplished by ejection (57.52%), sweep events (31.49%), and outward interactions (11.17%), whereas the contribution coming from the inward interactions is negligible (-0.18%). Large-amplitude events (6.84%) contribute greatly to sediment resuspension and vertical transportation (40%), which affect internal nutrient release. The results demonstrate the mechanism of sediment resuspension, which are critical for evaluating internal nutrient release.

Keywords: Acoustic inversion; sediment resuspension; suspended sediment concentration; turbulent structure; Lake Taihu.

1 INTRODUCTION

Excessive nutrient loading can induce severe blooms of harmful algae, which are a serious problem in many shallow lakes, reservoirs, and other freshwater bodies (Paerl and Huisman, 2008; Qin et al., 2010). Among the various nutrient sources, internal loading caused by sediment resuspension is the most difficult to quantify. For example, the internal phosphorus (P) load from resuspension is estimated to be 5 to 10 times that of the external load in Lake Taihu, which is the third largest freshwater lake in China and is often plagued by harmful algal blooms (Qin, 2009; Qin et al., 2006). Sediments frequently disturbed and resuspended by wind-driven waves and currents affect the water-sediment interface. However, because of the lack of effective measurement techniques and sound simulation methods, it still remains unclear how the sediments resuspend under the effects of waves and currents.

Waves and currents are the primary driving mechanisms of sediment dynamics in shallow lakes. The combined effects of waves and currents are often stronger than the two forces individually on sediment erosion, suspension, and deposition processes in the bottom boundary layer (Jepsen et al., 2004). Prior studies have focused on the effects of currents and waves on sediment resuspension process using field monitoring and laboratory experiments (flumes and oscillators) (Chung et al., 2009; Hu et al., 2011; Li et al., 2004; Mian and Yanful, 2004; Reardon et al., 2014; Sheng and Lick, 1979; Wu et al., 2013; Zhu et al., 2005). Most of these studies explain sediment dynamics using a time-averaged critical shear stress or velocity and pay less attention to the instantaneous driving force on sediment resuspension. It is believed that once the shear stress or velocity exceeds the critical value, sediments in the boundary layer are eroded and resuspended into water column. However, the time-averaged shear stress or velocity may level peak values of water turbulence in the bottom boundary layers and exclude the instantaneous sediment suspension, which results in an underestimation of the sediment resuspension fluxes and internal nutrient release.

Previous studies show that turbulence near the bottom boundary layers of flumes, estuaries and coastal areas controls instantaneous sediment suspension (Bonnin et al., 2006; Cellino and Lemmin, 2004; Williams et al., 2003; Yuan et al., 2009). Laboratory studies also show that sediment particles are affected by coherent structures, which are a series of large-scale, intermittent motions (Clarkeet al., 1982; Corino and Brodkey, 1969; Fosteret al., 2006; Gordon, 1974). Coherent turbulent structure, which is also known as “bursting phenomenon” is made up of a powerful, well-organized series of events that take place near the boundary layer and are ejections, sweeps, and outward and inward interactions. Ejections and sweeps contribute more to the positive Reynolds stress than outward and inward interactions (Heathershaw, 1974; Heathershaw and Thorne, 1985). Based on a field monitoring study in the south coast of England, Heathershaw and Thorne (1985) found that suspended load and bedload transport are dominated by ejection and sweep events. Cellino and Lemmin (2004) confirmed the sediment entrainment patterns in an open channel study thereafter. Similar bursting phenomena near the boundary layer were also found in the main channel of the Yangtze River and western Yellow Sea, in China (Yuan et al., 2009). Overall, these previous studies explain the sediment dynamics either in a time-averaged manner in the laboratory/field or as an instantaneous, small-scale turbulence process related to coherent structures in the coastal or estuarial areas. However, few studies have been conducted in large shallow lakes because it is difficult to simultaneously measure the instantaneous turbulence fluctuation and high-frequency sediment concentration near the lake bottom, especially because of the complex characteristics of wind-induced wave and current actions. Therefore, how sediment particles respond to turbulence in large, shallow lakes and whether the bursting phenomenon applies to a highly-variable lake environment remain unclear.

For this study, continuous and high-frequency field-observation data are collected using Acoustic Doppler Velocimeter (ADV) and Optical Backscatter Sensor (OBS) instruments placed close to the bottom of the lakebed. The objectives of this study are to: (1) invert the ADV backscatter signal into high-frequency suspended solid concentration (SSC) data; (2) understand the characteristic of turbulent bursts based on the analyses of horizontal and vertical velocity and SSC; (3) verify the hypothesis that sediment and intermittent bursts of coherent structures are the main driving mechanism of sediment resuspension in large, shallow lakes; and (4) elucidate the relationship between turbulence and sediment concentration fluctuations that create sediment resuspension.

2 METHODS AND MATERIALS

2.1 Study area

Lake Taihu, which is the third largest freshwater lake in China, is located in the lower Yangtze River delta between 30°56′-31°33′ N and 119°53′-120°36′ E and has a surface area of 2,338 km^2 and a mean depth of 1.9 m (Qin et al., 2010). Lake Taihu is suffering from nutrient over-enrichment and severe algal blooms. Internal nutrient release caused by sediment resuspension is one of the key driving factors for providing excessive nutrients for algal growth.

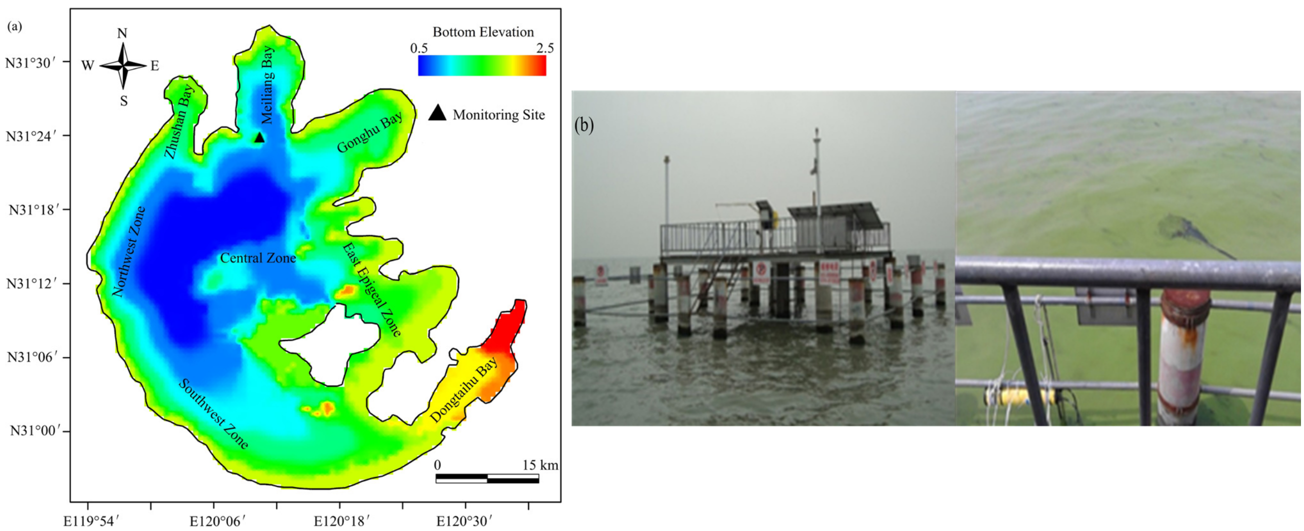

Figure 1. Location and observation platform at which observations of bottom turbulence have been made in Lake Taihu in the year of 2014.

Data were collected in-situ from May 20 to 29, 2014, at the field observation platform located at Tuoshan (N31.38233°- E120.16065°), which is at the mouth of the east coast of the Meiliang Bay (Figure 1). The Meiliang Bay is a semi-enclosed bay located in the northern part of Lake Taihu that has a water surface area of 129.3 km^2 and mean water depth of 1.9 m (Dong et al., 2014; Huang et al., 2004). The observation period covered the early algal bloom duration (Figure 1). The water depth of the sampling site varied from 2.62 to 2.88m and the mean value was approximately 2.7 m during the observation period, which represents high-water-level conditions in Lake Taihu. In the study site, the sediment mainly consists of silt sand that has an average particle size of 12 μm, a bulk density of 1.45 g/cm^3, and an average water content of 48.93%. Wind-induced currents and waves caused some hydrodynamic disturbance in the water column at the data collection site. The main wind directions were southeast, east-southeast, and east during the observation period. Wind speeds mostly ranged from 2 to 5 m/s which were measured at 10m above the water surface.

2.2 Layout of instruments

High-frequency and synchronous measurements of wind, waves, currents, and suspended sediment concentration (SSC) were carried out. The measurement instruments included a bottom-mounted holder equipped with an ADV Ocean Sontek (5MHz) and OBS-3A (Campbell Scientific Companies). The instruments were placed near the bottom layer of the lake, approximately 5 cm above the lake bed. The ADV Ocean (with a sampling frequency of 10 Hz) was used to record turbulent velocities and echo intensity simultaneously. The OBS (with a burst interval of 5 min) was used to record turbidity. Additionally, water samples were collected manually to verify sediment concentrations, which were then used by the Taihu Laboratory for Lake Ecosystem Research, Chinese Academy of Sciences (TLLER, CAS), to verify turbidity in the water column.

2.3 Data analysis methods

2.3.1 Calibration of turbidity with SSC

The OBS can be used to monitor the turbidity over a wide range, from 0 to 1,000 NTU, which makes these sensors useful for many applications (Hanes and Huntley, 1986; Sutherlandet al., 2000). In order to convert the turbidity data into concentration data, the turbidity (NTU) measured by the OBS was calibrated with manually collected SSC (mg/L) data. At every three hours, 150 mL water samples were collected manually at the same time and location as the OBS, filtered using a 0.35 um aperture membrane, and dried in the drying oven at 105 ^{o}C. The SSC values were calculated as follow:

$$c = \left(m_2 - m_1\right) / L \qquad [1]$$

where c is SSC (mg/L), m_1 is the weight of the membrane before filtration and after drying (mg), m_2 is the total weight of the membrane and suspended solids after filtration and drying (mg), and L is the volume of the water samples collected in the field (L).

2.3.2 Calibration of ADV signal strength with SSC

The advantage of the ADV is that it quickly and simultaneously measures flow velocity and SSC in the same sampling volume (Fugate and Friedrichs, 2002; Nikora and Goring, 2002; Trevethan et al., 2007). The ADV emits a burst of sound waves with known durations and frequencies from a source transducer, and then the transducers receive the backscatter. The backscatter wave frequency is shifted by moving the available particles in the target areas. The magnitude of this frequency shift (or "Doppler shift") is proportional to the flow velocities. The signal (in count) received by the ADV is proportional to the logarithm of the acoustic strength (1 count = 0.43 dB; Notes, 1997). The high-resolution signal at 10 Hz provided by the ADV is meant to provide a near-bed SSC time series at turbulent scales. The SSC profiles based on the logarithmic relation between echo intensity (EI) and mass concentration were determined as follow:

$$EI = a \log_{10} SSC + b \qquad [2]$$

where a and b are slopes and the interception point is obtained using linear regression. The echo intensity recorded by the ADV is block-averaged over a three-minute period and beam spreading is compensated for, and then calibrated using the OBS mounted at the same elevation, which is precalibrated using the water samples. The ADV data require pre-processing and the detected outliers are replaced by linear interpolation using neighboring points. Two stages are used in post-processing: an initial signal check and the detection, removal, and replacement of fake large fluctuation. Each stage involves two steps: data error detection and data replacement (Chanson et al., 2008).

2.3.3 Turbulent kinetic energy calculation

Most of the turbulence generation and dissipation in shallow lakes take place near the bed. To describe the roles of near-bed turbulent eddies on sediment suspension, spectral scaling is used for both the turbulent velocities and sediment concentration at different conditions. In regions where the mean flow is considered to be constant in the order of minutes, the turbulent fluctuations (*u'*, *v'*,and *w'*) can be defined as deviations from the mean or the Reynolds decomposition (Tennekes and Lumley, 1972):

$$u'(t)= u(t)-u,\ \ v'(t)= v(t)-v,\ \ w'(t)= w(t)-w \qquad [3]$$

Eq. [3] was used to obtain turbulence measurements from a single instrument in irregular and strongly nonlinear wave conditions. Then, turbulent kinetic energy (TKE) was calculated as follows:

$$TKE = (\overline{u'^2} + \overline{v'^2} + \overline{w'^2}) / 2 \qquad [4]$$

where *u'*, *v'*, and *w'* are velocity fluctuations in the east, north, and vertical directions; and "—" means time averaged.

Turbulent Reynolds stress values were estimated by (Kularatne and Pattiaratchi, 2008):

$$\tau_{Re} = \rho u'w' \qquad [5]$$

where *ρ* is the water density. Because no quantitative analysis of the Reynolds stress was undertaken, the term *u'w'* represented the turbulent Reynolds stress. The Reynolds stress values measured by the ADV were underestimated only by 1%, which suggests that the ADV measures Reynolds stress accurately near the bottom of the lake (Voulgaris and Trowbridge, 1998). The data were used to study relationships between TKE on suspension events and sediment suspension.

2.3.4 Quadrant analysis for turbulence bursting events

Occurrence of the Reynolds stress is highly intermittent and connected with a well-organized sequence of large-scale movements, and these movements are commonly classified into four quadrants in *U'-w'* space (Klineet al., 1967; Heathershaw, 1974) as shown below:

(1) *U'* <0, *w'*>0, *U'w'* <0: an ejection of low-speed fluid away from the boundary
(2) *U'* >0, *w'*<0, *U'w'* <0: a sweep or inrush of high-speed fluid toward the boundary
(3) *U'* >0, *w'*>0, *U'w'* >0: a weak outward interaction of fluid away from the boundary (high-speed fluid reflected by the wall)
(4) *U'* <0, *w'*<0, *U'w'*>0: a weak inward interaction of fluid toward the boundary (low-speed fluid being pushed back)

where *w'* is the vertical component of turbulent velocity, and *U'* is the horizontal component. Because there are no stable flow directions in the lake, *U* presents the combined flow velocity of *u* and *v* in northern and eastern directions, respectively. The relationships are shown below:

$$U = (u^2 + v^2)^{1/2}, \qquad [6]$$

The quadrant method requires simultaneous *U'* and *w'* data. The ADV can achieve this because it can measure the three-dimensional simultaneous velocity.

3 RESULTS AND DISCUSSIONS

3.1 Near-bed sediment concentration measurement

3.1.1 Calibration of OBS concentration to SSC

The SSC measurement based on the laboratory analysis of the bottle samples (34 water samples) was considered to be the actual SSC at the same time and height of the near-bottom OBS. There was a good linear relationship between the turbidity measured by the OBS and the sediment concentration in the water near the lakebed. The correlation coefficient was 0.94, with a 95% confidence level (Figure 2). Prior studies have shown that when there is a large range of suspended particle sizes, the correlation between the OBS recorded turbidity and the "true value" of the sediment concentration drops significantly (Fugate and Friedrichs, 2002). According to the particle-size distribution of the sediment in different areas of Lake Taihu, the particle sizes are relatively stable within the top 10 cm of the surface sediment compared with the particle sizes in the deep sediment. Qin et al. (2003) found that mass exchange in the water-sediment interface occurs mainly within the top 5~10 cm based on field observations and that medium-sized sediment particles were around 16~17 μm. Because of the stable particle size in the surface sediment, the correlation did not show any reduction, which proved the reliability of the SSC measured by the OBS at the near-bottom layer.

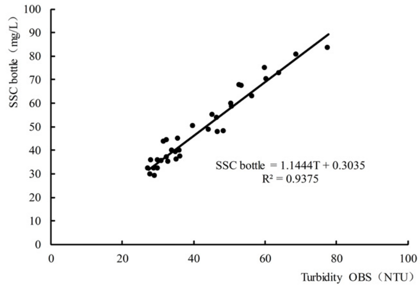

Figure 2. Calibration of OBS turbidity (NTU) at 5 cm above the lakebed with bottle samples at the same height (mg/L).

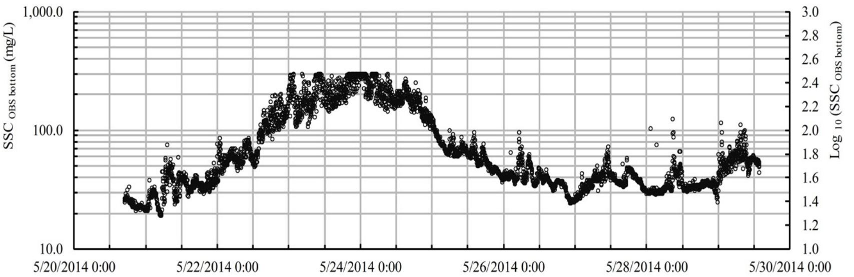

Figure 3. Changing trend of suspended sediment concentrations from OBS at 5cm above the lakebed between May 20, 2014 and May 30, 2014.

Based on calibrated OBS turbidity and SSC, the near-bottom SSC was in the range of 20 to 310 mg/L. The temporal fluctuation is shown in Figure 3 and is consistent with the changing trends of wind speed. Based on the statistical analysis of SSC frequency, the near-bottom values exhibited a partial normal distribution (Figure 4). The highest frequency was 27.2% and the range of corresponding SSC was 30 to 40mg/L. The following several frequencies in sequence were 13.5%, 9.8%, 9.6% for the ranges of 40 to 50mg/L, 20 to 30mg/L, and 50 to 60 mg/L, respectively. Overall, the frequency of SSC ranging from 20 to 60 mg/L accounted for 60.07% during the observation period, which suggests that the near-bottom SSC was in the range of 20 to 60 mg/L in most situations and the probability of a large-scale suspended-sediment event is relatively small.

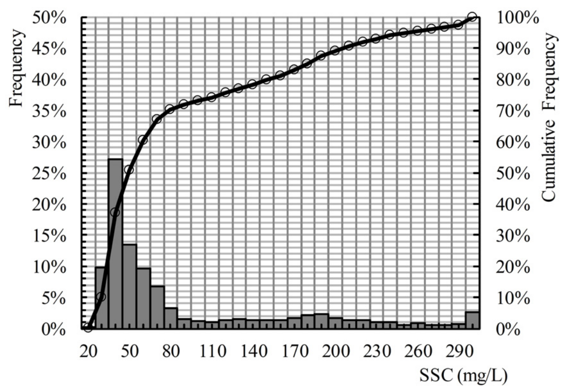

Figure 4. Suspended sediment concentration from OBS in the bottom layer frequency and cumulative frequency analyses.

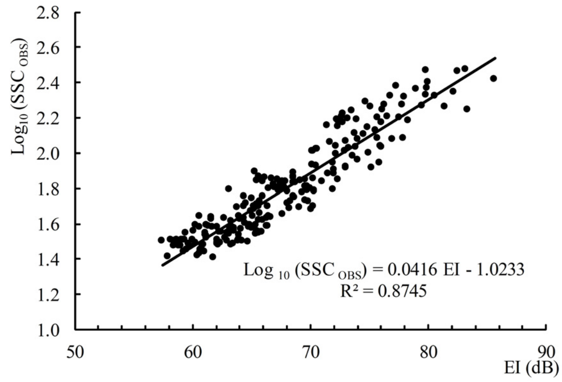

Figure 5. Calibration of ADV backscatter EI (dB) with OBS mass concentration (mg/L).

3.1.2 Calibration of ADV signal to SSC

To analyze intermittent turbulent bursts, a set of high-frequency three-dimensional velocity and sediment concentrations is required. The frequency of turbidity measured by the OBS was 1/180 Hz (data collected every three minutes), and therefore there were not enough data to analyze the bursting phenomenon. In this paper, a high-frequency ADV signal with 10 Hz (data collected every 0.1 second) was used to reflect the corresponding turbidity by precalibrating a curve between them, and then transferring the turbidity to SSC using the relation obtained in Figure 2.

Previous research indicated that there was a simple logarithmic relationship between near-bed mass concentration and EI recorded by the ADV (Fugate and Friedrichs, 2002; Voulgaris and Meyers, 2004). Beam spreading was compensated for the EI. The OBS was mounted at the same height (5cm above the bed) and was used to calibrate the acoustic backscatter (Figure 5). The correlation coefficient between $\log_{10}$ (SSC) and acoustic backscatter EI was 0.87, which confirmed the calibration with EI to SSC reliably. Therefore, this calibration procedure could obtain the near-bed, high-frequency sediment concentration time series with a temporal resolution of 10Hz, which is sufficient for the turbulence burst analysis in this study.

3.2 Direct comparisons of the time series of fluctuating velocity and SSC

To further investigate the effect of the turbulence burst events on the sediment resuspension process, the fluctuations of horizontal and vertical velocities and the sediment concentrations (U', w', c') were compared in

Figure 6. The U', w', and c' fluctuated around their burst-averaged values without large excursions. A dataset of 512s duration (Yuan, 2009) was used to analyze turbulence burst. Figure 6(a) shows that there are 13 waveforms that have an average horizontal velocity (U) of 4.2 cm/s. The horizontal velocity fluctuation (U') ranged from -0.03cm/s to 0.06cm/s. The averaged vertical velocity was 0.37cm/s and the vertical velocity fluctuation (w') ranged from -0.04cm/s to 0.02cm/s (Figure 6(b)). The average SSC was 40.99mg/L (Figure 6(d)). The suspended sediment concentration fluctuation (c') varied from -18.92mg/L to 38.15mg/L.

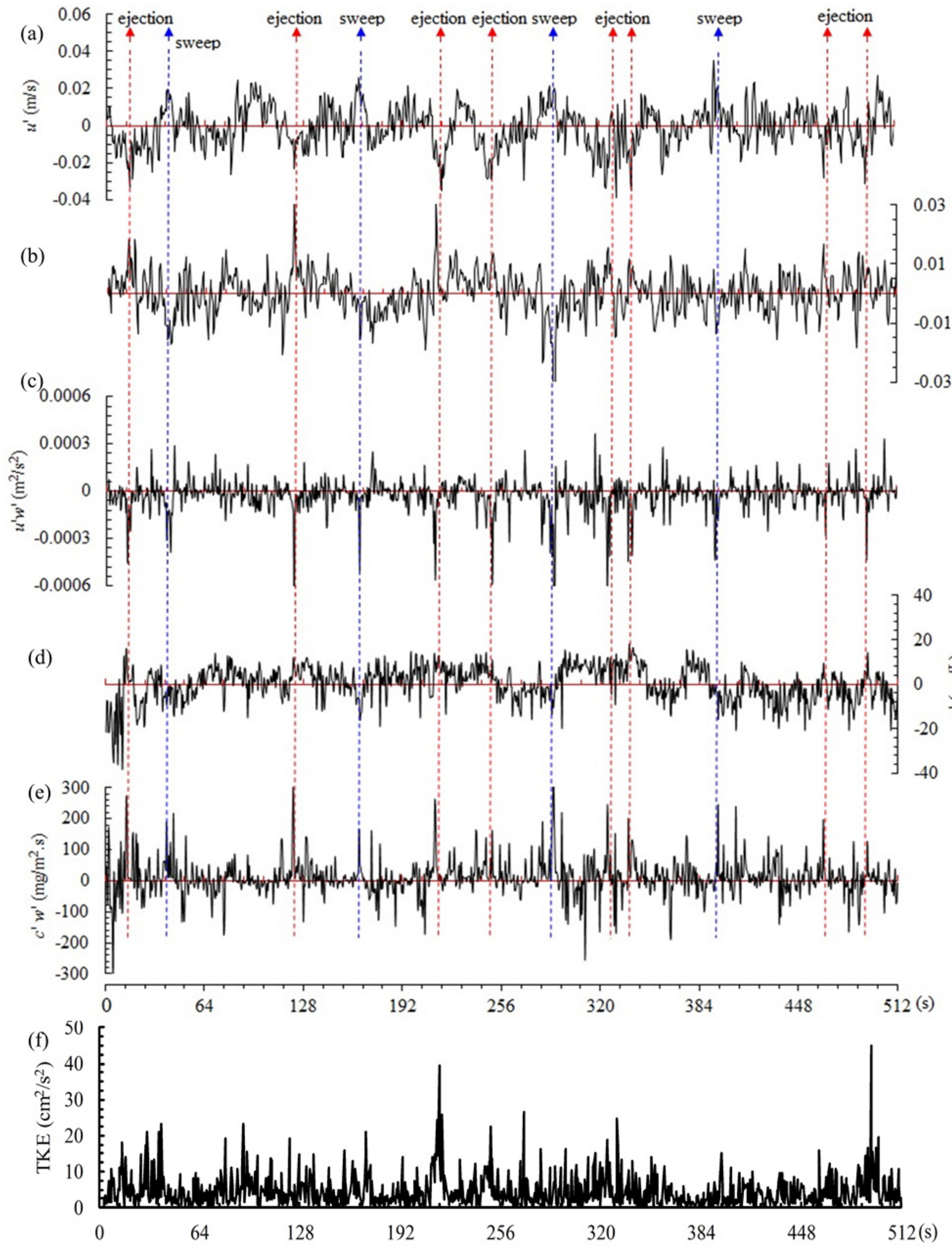

Figure 6. Time series of records of: (a) horizontal velocity fluctuations (U'), (b) vertical velocity fluctuations (w'), (c) the turbulent Reynolds stress ($U'w'$), (d) suspended sediment concentration fluctuations (c'), (e) instantaneous sediment turbulent diffusion flux ($c'w'$), and (f) turbulent kinetic energy (TKE). The red and blue arrows show the ejection and sweep motions, respectively.

The two time series of U' and w' mostly varied in the opposite way, with the U' peak value coinciding with w' at large amplitude events. The time series of w' and c' showed the high SSC fluctuation events occurred with the high vertical velocity fluctuation events at large amplitude events. It was found that high c' events happened in low-speed fluid away from the boundary (ejection) rather than sweep events. The red and blue dashed lines in Figure 6 show the ejection events (low-speed upward movement) and sweep events (high-speed downward washing), respectively. The sweep events loosened the sediment particles they were moved into the water column by the low-speed upward movement of ejection events. Large fluctuation values of U' and w' were mostly opposite at large amplitude events, which is consistent with our result, but high SSC

  / ISSN 1562-6865 (Online) - ISSN 1063-7710 (Print)

events occurred with maximum in ejection in Jiaozhou Bay (Yuan, 2009). Gordon (1974) reported that the high fluctuations in vertical velocity reversed to the one in horizontal velocity in the Irish Sea. Heathershaw (1985) reported that the load transport of finer sediments was dominated by ejection events. It is possible that high SSC events mainly occurred in sweep events in the sea but ejection in the lake maybe because the vertical and horizontal velocities in the sea are faster than in lakes, and the waves contribution on the hydrodynamic in the sea are less than that in the lake.

3.3 Quadrant analysis for turbulence burst

The *U'*, *w'*, and *c'* fluctuated around their burst-averaged values within a small range, simultaneously their instantaneous products *U'w'* and *c'w'* revealed a high degree of variability and intermittency (Figure 6(c) and Figure 6€). The instantaneous momentum flux (*U'w'*) and instantaneous sediment turbulent diffusion flux (*c'w'*) were characterized by irregular fluctuations and interrupted by sudden and salient excursions that were an order of magnitude larger than the average values. The time series of the *U'w'* events were interrupted by the peak value 0.0003 or the valley value -0.0006 m^2/s^2. The time series of *c'w'* events were interrupted by peak value 300 or valley value -260 mg/(m^2s). Additionally, large amplitude events of *U'w'* and *c'w'* were consistent with large fluctuations of *U'* and *w'*, which indicates intermittent sediment resuspension. Yuan (2009) also reported that *u'w'* and *c'w'* coincide with each other without exception in Jiaozhou Bay. This suggests that the *U'w'* time series did not always cause high SSC events in Figure6c and Figure6d, which may indicate that the horizontal flow velocity fluctuations *U'* has greater dynamical effect on sediments movement than *U'w'* (Heathershaw, 1985). Additionally, the large amplitude events of *U'w'* were usually observed under burst and sweep events.

Comparing *U'w'* and *c'w'* time series, the ejection and sweep events often correspond with the turbulent kinetic energy and turbulent diffusion fluxes of sediment large amplitude. It also appeared that ejection motions occur more frequently than sweep motions, which results in a larger contribution to the momentum and sediment fluxes. The high TKE events not only occurred under wave crests, but also under wave troughs. When at peaks and valleys, shear velocity generated strong turbulence that caused particles to move horizontally in the boundary layer. Similar results have been found for tidal environments and costal wave period. Kularatne (2008) suggested that high TKE events usually associated with a wave crest or trough. Generally, the two main forms of sediment suspension are ejection in high-concentration fluid parcels, and sweep in low-concentration fluid parcels. Ejection and sweep are bursting events that correspond to negative momentum flux, which is caused by high concentrations of sediment spreading upward and low concentrations of sediment spreading downward. The large amplitude ejection and sweep events revealed a net upward transport of sediment, which were the main energy sources of sediment resuspension process. In this process, the stationary particles were loosened by high-speed downward flow, and then deposited on the lake bottom at low-speed.

3.4 Contribution of turbulence burst on sediment resuspension

Contributions of large *U'w'* and *c'w'* events to the mean sediment flux ($\overline{U'w'}$ and $\overline{c'w'}$) are summarized statistically in Figure 7. We took out the two, three, and four standard deviations as large amplitude events. The large *c'w'* events that occurred outside the four standard deviations contributed as much as 12.98% to the mean sediment flux $\overline{c'w'}$ in only 0.88% of the time period. The large *c'w'* events outside the two and three standard deviations contributed 49.85% and 32.68% in 7.32% and 2.05% of the time to the mean sediment flux, respectively. The results suggest that sediment transport primarily occurred in short bursts of high amplitude, which was similar to the mean sediment flux analyses.

The large *U'w'* events occurring outside the two, three, and four standard deviations contributed as much as 54.79%, 41.82%, and 37.64% to $\overline{U'w'}$ in 6.84%, 2.83%, and 1.66% of the time, respectively. According to the large *U'w'* events contributing to $\overline{c'w'}$, 40% of the upward sediment flux was caused by large events during only 6.84% of the total time. However, the contributions of large *U'w'* and *c'w'* events compared with the $\overline{U'w'}$ and $\overline{c'w'}$, showed that the ejection-sweep burst cycle transport momentum was more effective than sediment flux. For example, large *U'w'* events that occurred outside two standard deviations contributed 54.79% of the momentum flux, which was higher than that of sediment flux. The analysis suggested that the efficiency of vertical transfer momentum was more than sediment transfer, because the heavy sediments fall more easily to the lakebed.

The instantaneous *U'w'* signals and the contributions of different intermittency burst events to the Reynolds stress were quantitatively evaluated using quadrant analysis (Figure 8 and 9). The occurrences of these four types of bursting motions (ejection, sweep, inward interaction, and outward interaction) were 33.2%, 27.15%, 20.12% and 19.53%, respectively (Figure 8). The ejection motions occurred more frequently than the sweep motions, and contributed more to the $\overline{U'w'}$ and $\overline{c'w'}$, which was consistent with the raw time series comparisons (Figure 6). The results generally agreed with early experiments by Wallace (1972) and Willmarth (1972). Wallace (1972) reported that ejection and sweep were the two main motions and that they had significantly larger timescales than outward and inward interactions. Willmarth (1972) revealed that ejection made the largest contributions to the Reynolds stress and turbulent energy in the bursting process. Both ejections and sweeps were the dominant sources of the Reynolds stress generation and the time occupied by ejections was more than sweeps. The ejection-sweep cycles may dominate the upward transfer of sediment because contributions of ejections and sweeps to the net Reynolds stress are 98.54% and 79.76%, respectively (Figure 9). The histograms (Figure 8 and Figure 9) showed that 57.5% of the upward sediment flux happened during ejection motions of only 33.2% of the time, which suggested that an upwelling of low-speed fluid parcels containing high sediment concentrations were the main factors of $\overline{c'w'}$. Sweeps also contributed significantly to $\overline{U'w'}$ (31.49%), which loosened stationary particles. By contrast, inward and outward motion contributed slightly to transport sediment -0.18% and 11.17%, respectively, which means inward motions turn sediments toward the bed. This phenomenon was also observed by Heathershaw (1985) and Yuan (2008). Heathershaw (1985) suggested that only sweeps were able to support appreciable sediment movement because sweep and outward interactions contribute approximately 46% of the overall stress in the West Solent seabed. Yuan (2008) found that outward contribution was small (approximately 4%) because his observation position was 0.45 meter above the bottom, where few particles arrived at low TKE. Therefore, 99.2% of turbulent sediment flux was accomplished by ejection and sweep events, whereas the contributions of the inward and outward interactions were small.

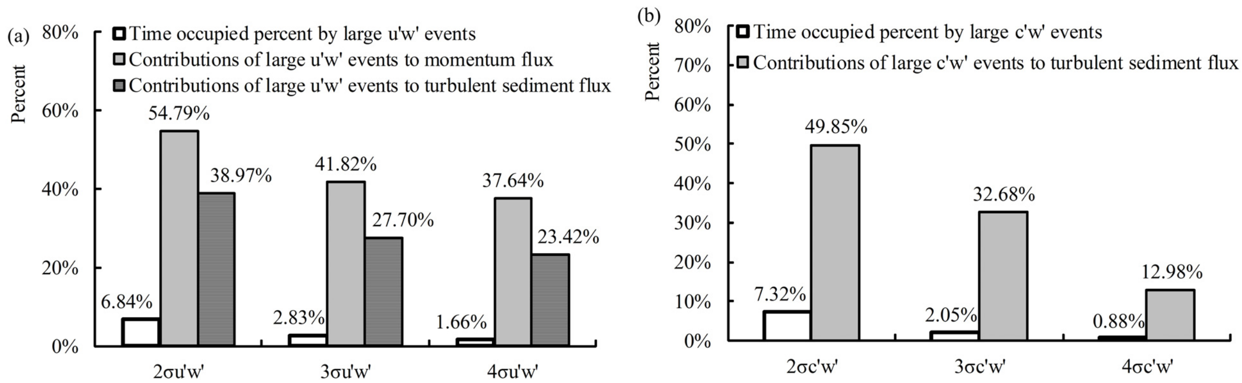

Figure 7. Percentage contributions of large-amplitude events to momentum and sediment fluxes ($\overline{U'w'}$ and $\overline{c'w'}$) are summarized, respectively. (a) the white legends represent time occupied percent by large *U'w'* events, the gray legends represent contributions to large *U'w'* events to momentum flux and the dark gray legends represent contributions to large *U'w'* events to turbulent sediment flux; (b) the white legends represent time occupied percent by large *c'w'* events and the gray legends represent contributions to large *c'w'* events to turbulent sediment flux.

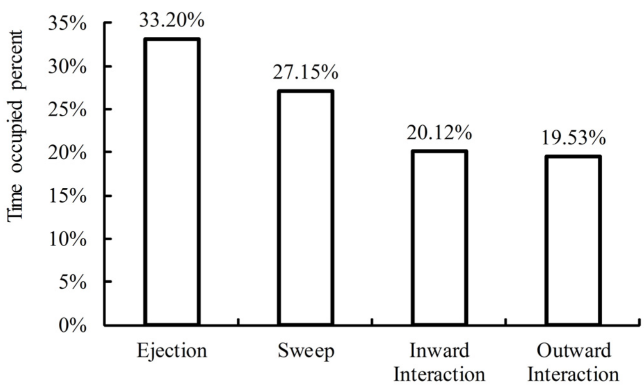

Figure 8. Time occupied by four types of events (ejection, sweep, inward and outward interaction).

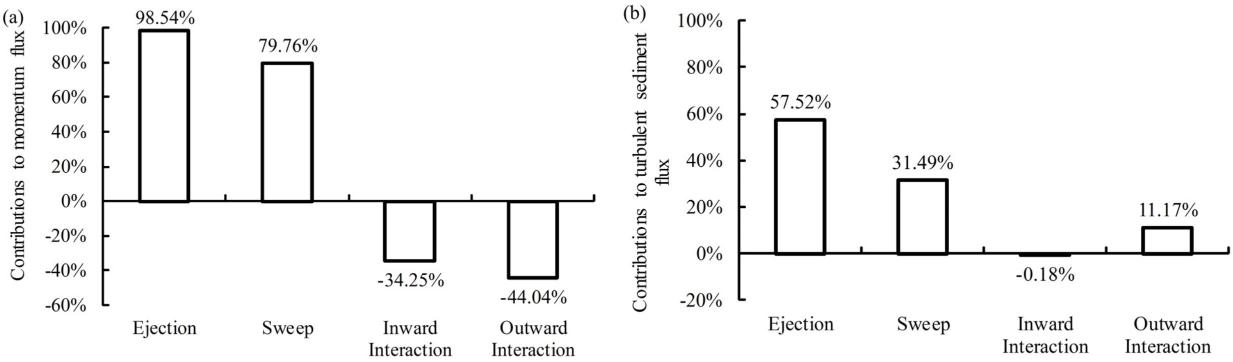

Figure 9. Quadrant analyses of coherent structures: (a) contributions to momentum flux, and (b) contributions to turbulent sediment flux.

4 CONCLUSIONS

This study uses high-frequency and synchronous in-suit observation to analyze the effects of intermittent turbulent bursts on sediment resuspension in the bottom boundary layer of the lake. The results suggest that the sediment resuspension dynamic process has a clear relationship with the coherent structure in the bottom boundary layers. The intermittent burst events (dominant ejection and sweep) are the main energy sources for sediment resuspension processes. 99.2% of turbulent sediment fluxes are triggered by ejection and sweep events and outward interactions, whereas the contributions coming from the inward interactions are negligible. The large-amplitude burst events in the coherent structure dominate the influence on the sediment diffusion. This study provides a better understanding of sediment processes in large shallow lakes.

ACKNOWLEDGEMENTS

The research is supported by Chinese National Science Foundation (51579071, 51379061, 41323001, 51539003), and National Science Funds for Creative Research Groups of China (No. 51421006); the program of Dual Innovative Talents Plan and Innovative Research Team in Jiangsu Province; the Priority Academic Program Development of Jiangsu Higher Education Institutions, and the Fundamental Research Funds for the Central Universities. The author gratefully acknowledges the support of K. C. Wong Education Foundation, Hong Kong.

REFERENCES

Bonnin, J., Van Haren, H., Hosegood, P. & Brummer, G.A. (2006). Burst Resuspension of Seabed Material at the Foot of the Continental Slope in the Rockall Channel. *Marine Geology,* 226, 167-184.

Cellino, M. & Lemmin, U. (2004). Influence of Coherent Flow Structures on the Dynamics of Suspended Sediment Transport in Open-Channel Flow. *Journal of Hydraulic Engineering,* 130, 1077-1088.

Chanson, H., Trevethan, M. & Aoki, S. (2008). Acoustic Doppler Velocimetry (ADV) in Small Estuary: Field Experience and Signal Post-Processing. *Flow Measurement and Instrumentation,* 19, 307-313.

Chung, E.G., Bombardelli, F.A. & Schladow, S.G. (2009). Sediment Resuspension in a Shallow Lake. *Water Resources Research,* 45, W05422.

Clarke, T.L., Lesht, B., Young, R.A., Swift, D. & Freeland, G.L. (1982). Sediment Resuspension by Surface-Wave Action: An Examination of Possible Mechanisms. *Marine Geology,* 49, 43-59.

Corino, E.R. & Brodkey, R.S. (1969). A Visual Investigation of the Wall Region in Turbulent Flow. *Journal of Fluid Mechanic,* 37, 1-30.

Dong, B., Qin, B., Gao, G. & Cai, X. (2014). Submerged Macrophyte Communities and the Controlling Factors in Large, Shallow Lake Taihu (China): Sediment Distribution and Water Depth. *Journal of Great Lakes Research,* 40, 646-655.

Foster, D.L., Beach, R.A. & Holman, R.A. (2006). Turbulence Observations of the Nearshore Wave Bottom Boundary Layer. *Journal of Geophysical Research,* 111(C4), 1-11.

Fugate, D.C. & Friedrichs, C.T. (2002). Determining Concentration and Fall Velocity of Estuarine Particle Populations using ADV, OBS and LISST. *Continental Shelf Research,* 22, 1867-1886.

Gordon, C.M. (1974). Intermittent Momentum Transport in a Geophysical Boundary Layer. *Nature*, 248, 392 - 394.

Hanes, D.M. & Huntley, D.A. (1986). Continuous Measurements of Suspended Sand Concentration in a Wave Dominated Nearshore Environment. *Continental Shelf Research,* 6, 585-596.

Heathershaw, A.D. (1974). "Bursting" Phenomena in the Sea. *Nature*, 248, 394-395.

Heathershaw, A.D. & Thorne, P.D. (1985). Sea-Bed Noises Reveal Role of Turbulent Bursting Phenomenon in Sediment Transport by Tidal Currents. *Nature*, 316, 339-342.

Hu, K., Pang, Y., Wang, H., Wang, X., Wu, X., Bao, K. & Liu, Q. (2011). Simulation Study on Water Quality based on Sediment Release Flume Experiment in Lake Taihu, China. *Ecological Engineering,* 37, 607-615.

Huang, Q., Wang, D., Wang, C., Ma, M. & Wang, Z. (2004). Vertical Variation of the Phosphorus Form in the Sediments of Meiliang Bay and Wuli Lake of Taihu Lake. *China Environmental Science,* 24(2), 147-150. (In Chinese)

Jepsen, R., Roberts, J. & Gailani, J. (2004). Erosion Measurements in Linear, Oscillatory and Combined Oscillatory and Linear Flow Regimes. *Journal of Coastal Research,* 20(4), 1096-1101.

Kline, S.J., Reynolds, W.C., Schraub, F.A. & Runstadler, P.W. (1967). The Structure of Turbulent Boundary Layers. *Journal of Fluid Mechanic,* 30, 741-773.

Kularatne, S. & Pattiaratchi, C. (2008). Turbulent Kinetic Energy and Sediment Resuspension due to Wave Groups. *Continental Shelf Research,* 28, 726-736.

Li, Y.P., Pang, Y., Chen, K.S., Peng, J.P., Ding, L. & Jin, Y. (2004). Study on the Starting Principles of Sediment by Water Force in Taihu Lake. *Advances in Water Science,* 15, 770-774. (In Chinese)

Mian, M.H. & Yanful, E.K. (2004). Analysis of Wind-Driven Resuspension of Metal Mine Sludge in a Tailings Pond. *Journal of Environmental Engineering Science,* 3,119-135.

Nikora, V.I. & Goring, D.G. (2002). Fluctuations of Suspended Sediment Concentration and Turbulent Sediment Fluxes in an Open-Channel Flow. *Journal of Hydraulic Engineering,* 128, 214-224.

Notes, S.A. (1997). *Sontek Doppler current Meters. Using Signal Strength Data to monitor suspended sediment concentrations,* Sontek Application Notes, San Diego, USA, September, 7.

Paerl, H.W. & Huisman, J. (2008). Blooms Like it Hot. *Science,* 320, 57.

Qin, B. (2009). Lake Eutrophication: Control Countermeasures and Recycling Exploitation. *Ecological Engineering,* 35, 1569-1573.

Qin, B., Zhu, G., Gao, G., Zhang, Y., Li, W., Paerl, H.W. & Carmichael, W.W. (2010). A Drinking Water Crisis in Lake Taihu, China: Linkage to Climatic Variability and Lake Management. *Environmental Management,* 45, 105-112.

Qin, B., Zhu, G., Zhang, L., Luo, L., Gao, G. & Gu, B. (2006). Estimation of Internal Nutrient Release in Large Shallow Lake Taihu, China. *Science in China Series D,* 49, 38-50.

Qin, B., Hu, W., Gao, G., Luo, L. & Zhang, J. (2003). Dynamic Mechanism of Sediment Resuspension and Conceptual Model of Internal Nutrient Release in Lake Taihu, China. *Chinese Science Bulletin* 48(17), 1822-1831. (In Chinese)

Reardon, K.E., Bombardelli, F.A., Moreno-Casas, P.A., Rueda, F.J. & Schladow, S.G. (2014). Wind-Driven Nearshore Sediment Resuspension in a Deep Lake during Winter. *Water Resources Research,* 50(11), 8826-8844.

Sheng, Y.P. & Lick, W. (1979). The Transport and Resuspension of Sediments in a Shallow Lake. *Journal of Geophysical Research,* 84(NC4), 1809-1826.

Sutherland, T.F., Lane, P.M., Amos, C.L. & Downing, J. (2000). The Calibration of Optical Backscatter Sensors for Suspended Sediment of Varying Darkness Levels. *Marine Geology,* 162, 587-597.

Tennekes, H. & Lumley, J.L. (1972). *A First Course in Turbulence.* MIT Press, 1-11.

Trevethan, M., Chanson, H. & Takeuchi, M. (2007). Continuous High-Frequency Turbulence and Suspended Sediment Concentration Measurements in an Upper Estuary. *Estuarine, Coastal and Shelf Science,* 73, 341-350.

Voulgaris, G. & Meyers, S.T. (2004). Temporal Variability of Hydrodynamics, Sediment Concentration and Sediment Settling Velocity in a Tidal Creek. *Continental Shelf Research,* 24, 1659-1683.

Voulgaris, G. & Trowbridge, J.H. (1998). Evaluation of the Acoustic Doppler Velocimeter (ADV) for Turbulence Measurements. *Journal of Atmospheric and Oceanic Technology,* 15(1), 272-289.

Wallace, J.M., Eckelmann, H. & Brodkey, R.S. (1972). The Wall Region in Turbulent Shear Flow. *Journal of Fluid Mechanic,* 54, 39-48.

Williams, J.J., Bell, P.S. & Thorne, P.D. (2003). Field Measurements of Flow Fields and Sediment Transport above Mobile Bed Forms. *Journal of Geophysical Research,* 108(C4), 3109.

Willmarth, W.W. & Lu, S.S. (1972). Structure of the Reynolds Stress near the Wall. *Journal of Fluid Mechanic,* 55, 65-92.

Wu, T.F., Qin, B.Q., Zhu, G.W., Zhu, M.Y., Wei, L.I. & Luan, C.M. (2013). Modeling of Turbidity Dynamics caused by Wind-Induced Waves and current in the Taihu Lake. *International Journal of Sediment Research,* 28(2), 139-148.

Yuan, Y., Wei, H., Zhao, L. & Cao, Y. (2009). Implications of Intermittent Turbulent Bursts for Sediment Resuspension in a Coastal Bottom Boundary Layer: A Field Study in the Western Yellow Sea, China. *Marine Geology,* 263, 87-96.

Yuan, Y., Wei, H., Zhao, L. & Jiang, W. (2008). Observations of Sediment Resuspension and Settling off the Mouth of Jiaozhou Bay, Yellow Sea. *Continental Shelf Research,* 28, 2630-2643.

Zhu, G., Qin, B. & Gao, G. (2005). Direct Evidence of Phosphorus Outbreak Release from Sediment to Overlying Water in a Large Shallow Lake caused by Strong Wind Wave Disturbance. *Chinese Science Bulletin,* 50, 577-582.

BUBBLE DYNAMICS AND PIV MEASUREMENTS IN A HYDRAULIC JUMP

ADEL EMADZADEH [1] & YEE-MENG CHIEW [2]

[1,2] School of Civil and Environmental Engineering, Nanyang Technological University, Singapore.
aemadzadeh@ntu.edu.sg; cymchiew@ntu.edu.sg

ABSTRACT

This laboratory study investigates the void fraction (or local air concentration), flow filed and bubble velocity in a simple hydraulic jump. The experimental data are obtained by using a dual-tip optical fiber probe in conjunction with the particle and bubble image velocimetry techniques. This paper aims to provide a full picture of the turbulent flow field in a simple hydraulic jump as no single instrument is capable of measurement in both aerated and non-aerated flow regions. Point and image-based measurements are used as complementary techniques to study the turbulent flow field in the hydraulic jump. The result from each measuring technique is compared in both aerated and non-aerated regions with discussions of the drawbacks and sources of error related to each measuring technique.

Keywords: Hydraulic jump; bubble image velocimetry (BIV); particle image velocimetry (PIV); optical fiber probe; void fraction.

1 INTRODUCTION

A hydraulic jump is frequently observed in open-channel flows, rivers and spillways as a transition from shallow, high-speed supercritical flows to deep, tranquil subcritical flows. It is characterized by intense turbulence, substantial flow aeration, free surface oscillations and considerable energy loss. Large quantities of air bubbles are entrained at the free surface of the jump, thus contributing to the complexity of the turbulent air-water multiphase flow.

Little is known about the turbulence structure of hydraulic jumps because the results obtained by using typical experimental instruments such as Pitot tubes, Acoustic Doppler Velocimeters (ADV), Laser Doppler Anemometers (LDA) and Particle Image Velocimetry (PIV) are adversely affected in two-phase air-water flows (Chanson, 2013). Hitherto, two measurement techniques, in the form of point measuring and image based measuring techniques, have been used to study the flow field, including the air concentration and bubble velocity in hydraulic jumps. The former technique is carried out by using either hot-film anemometry (Rajaratnam, 1962), phase-detection conductivity probes (Felder and Chanson, 2015; Murzyn and Chanson, 2009; Wang and Chanson, 2015) or optical fiber probes (Murzyn et al., 2005; Murzyn et al., 2007; Zhang et al., 2014). The latter or image based measuring technique, on the other hand, is used to study the air concentration (Leandro et al., 2012; Mossa and Tolve, 1998) and air bubble velocity (Lin et al., 2012) in hydraulic jumps. Compared to the point measurement method, flow visualization provides more information on the overall flow field with minimum intrusion. However, flow visualization techniques suffer from absorption of the penetrating laser light sheet through scattering on the surface of the bubbles (Bröder and Sommerfeld, 2007), limiting information from the visible side view of the flow only.

Velocity measurements with double fiber optic/conductivity probe are based on phase detection in the presence of bubbles. Therefore, in areas close to the bed and at low Froude numbers where the bubbles are mainly distributed in the roller section of the hydraulic jump, these point measuring instruments become ineffective. Therefore, several instruments/techniques should be used together to get a complete understanding of the flow turbulence and bubble dynamics in a hydraulic jump.

The current study aims to apply both point measurement and flow visualization techniques together to study an open channel hydraulic jump over a flat bed. The flow visualization techniques include Particle and Bubble Image Velocimetry (PIV and BIV), which are accompanied by phase detecting optical fiber point measurements in the roller section of the jump.

2 EXPERIMENTAL SETUP AND PROCEDURES

The experiments were carried out in a rectangular flume in the laboratory with length of 5 m, height of 0.15 m and width of 0.2 m on a horizontal bed. The flume had glass walls and the bed was half steel and half glass to facilitate experimental observations and flow illumination by the laser. The hydrodynamic condition of the flow at the beginning of the jump was controlled by a sluice gate upstream, while the position of the jump was dictated by a tail gate located at the downstream end of the flume (Figure. 1).

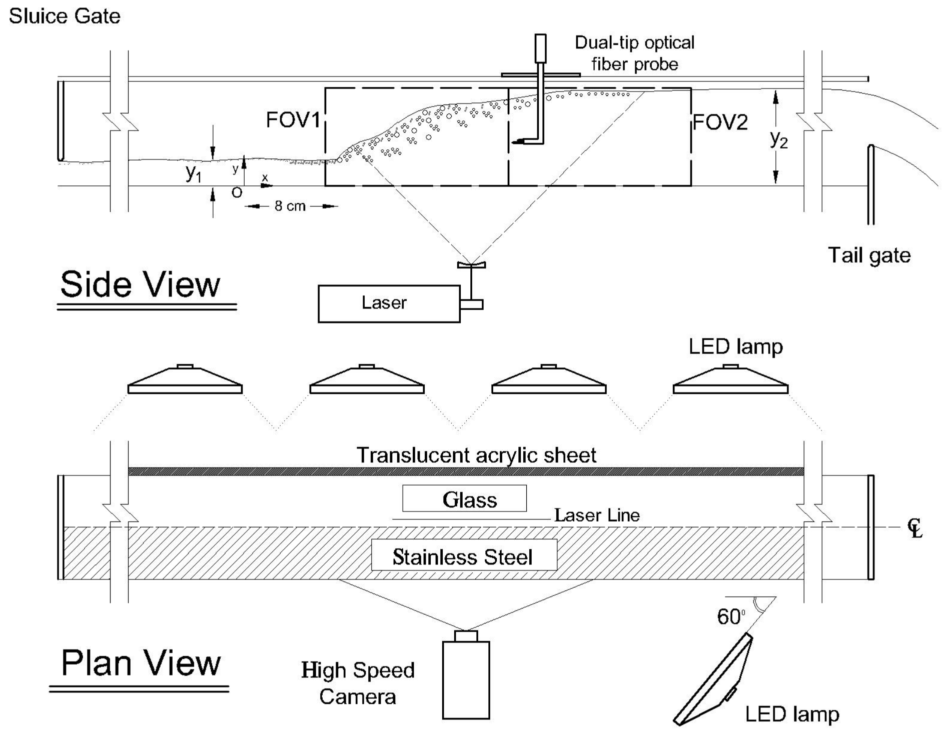

Figure 1. Sketch of the experimental setup (the origin, *O* is located at the position 8 cm upstream of the toe).

A dual-tip optical fiber probe (manufactured by RBI) was used to measure the bubble size, frequency and velocity, as well as the void fraction in the water column. The void fraction, which is defined as the volume of air per unit volume of the air and water mixture, essentially is synonymous to the local air concentration, C. The probe was mounted on a traversing mechanism that was affixed to the ceiling of the flume; this arrangement allows the probe to be positioned at any location along the centerline of the flume. The measurement principle of the optical fiber probe is based on variation of the refraction index of the medium surrounding the tip. The probe consists of two sensitive tips with an external diameter of 30μm, and separated by a distance of 0.2 mm. The data from each fiber was sampled at a rate up to 1MHz to provide measurements on the void fractions and bubble velocities.

Measurements of the mean and turbulent flow fields were carried out using the Particle Image Velocimetry (PIV) technique in the planar cross section of the flow near the bed where a minimum number of bubbles were present. A laser beam, which was generated by a 5W Diode Pump Solid State (DPSS) laser, was expanded into a laser sheet by using a combination of cylindrical and spherical lenses. A digital camera (Phantom Miro M120, 2Mpx resolution) was used to record the light scattered by the seeding particles (Polyamide particles with size = 50 μm; and density = 1.2 g/cm^3). The field of view (FOV) for the PIV was 350 x 100 mm in the x-y plane and PIV measurements were carried out at a sampling rate of 1,500 frames per second. The processing procedure included two passes, starting with a grid size of 64x64 pixels, stepping down to 32x32 pixels overlappedby 50%, and displacement of the particle images in the each interrogation region was measured by using cross-correlation analysis to determine the displacement that gives the maximum correlation.

As the PIV technique is restricted to the region outside the aerated area, Bubble Image Velocimetry (BIV) technique was used to measure the bubble velocities. The technique is similar to PIV except that it uses bubbles as the tracer particles and background illumination instead of a laser light sheet, which renders the bubbles to appear as shadows in the images, is used. In this study, four LED lamps were used in the background for illumination and a translucent acrylic sheet was attached to the back-side of the flume to distribute the light uniformly throughout the test section. Following the technique of Yonguk et al. (2005), another light sheet was placed in the front side with a 60^0 angle with the flume wall (see Figure. 1) to improve the bubble edge detection in regions with a high bubble concentration.

In the captured images using the above technique, bubbles appeared dark. Therefore, the images were inverted so that the high intensity (bright) parts of the image represent the bubbles before correlation for velocity is performed. The maximum intensity of each image was used as the value for inversion of the source images. In order to eliminate the background noise from the instantaneous light reflections, a time filter was applied to subtract the minimum intensity from the source images. Bubble detection was carried out in the Lavision software by defining an intensity threshold before the 2-dimensional Particle Tracking Velocimetry

(2D-PTV) technique was used to extract the bubble velocities in the series of images recorded by the high-speed camera.

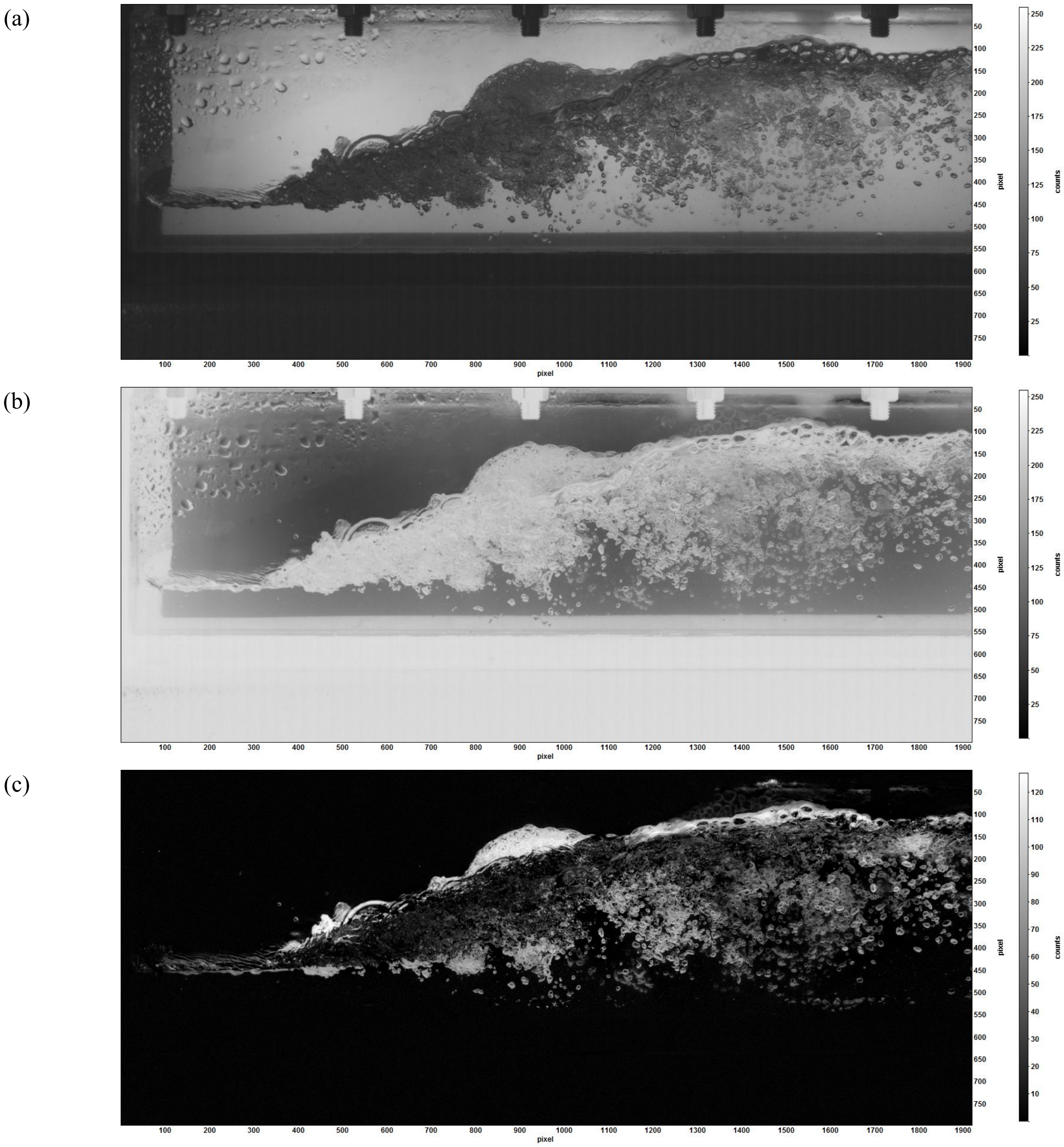

Figure 2. Extracting bubble velocity from the images: (a) original image with flow from left to right; (b) inverted image; and (c) image after application of the time filter.

Table 1 lists the detailed experimental conditions of the hydraulic jump tested in this study, with Q as the flow discharge; y_1 and y_2 as the conjugate depths of the hydraulic jump defined in Figure. 1; V_1 as the mean velocity; Fr_1 as the dimensionless Froude number in the upstream, ($Fr_1 = V_1/\sqrt{gy_1}$); and g as the gravitational acceleration. The subscripts 1 and 2 refer to the section just upstream and downstream of the simple hydraulic jump, respectively.

Table 1. Experimental conditions of the hydraulic jump.

Q (l/s)	$y_1 (cm)$	V_1 (cm/s)	Fr_1	$y_2 (cm)$
9.7	3.2	151	2.7	10.7

3 RESULTS

3.1 Air-water flow properties

Air-water flow properties such as the distribution of void fraction, bubbles size distributions and velocities were measured by using the dual-tip optical fiber probe. The vertical distributions of the void fraction and bubble size are shown in Figure. 3. In the figure, the origin is located 8 cm upstream of the jump toe (Figure. 1).

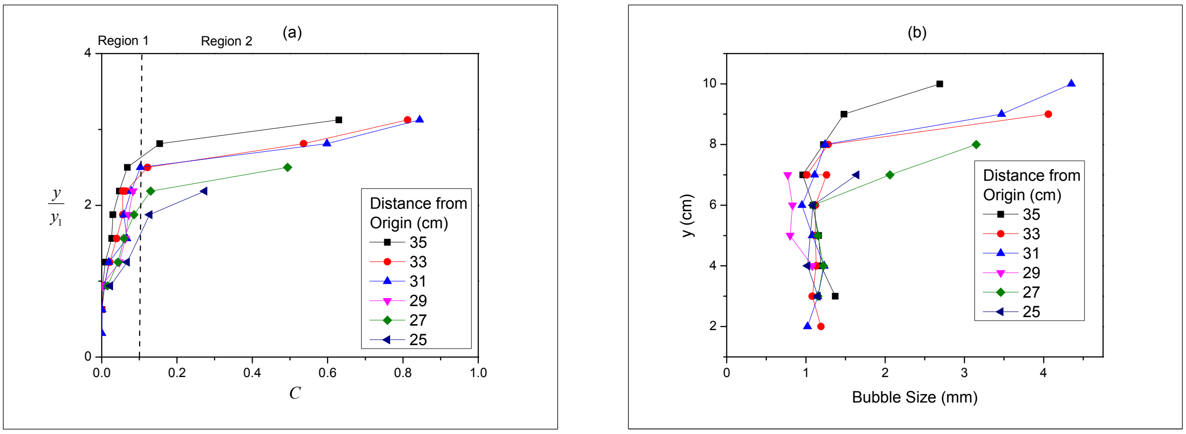

Figure 3. (a) Void fraction distribution (b) Bubble size distribution in the jump (toe location occurs at 8 cm from the origin).

Figure 3(a) shows that the void fraction distribution comprised two distinct regions. The first region, started from the bottom of the flume with a zero void fraction or air concentration (no bubbles, all water). The void fraction or air concentration in this region (Region 1) increased linearly until $y/y_1 \approx 2$. In this region, the void fraction could be fitted to the diffusion equation (Chanson, 1997; Wood, 1991). In the upper part or Region 2, the measured distribution exhibited a different trend and the void fraction increased at a significantly lower rate towards the flow surface. The experimental data clearly showed the two different rates of increase of C with y in this region. Brattberg et al. (1998) and Murzyn et al. (2005) suggested that the distribution in Region 2 follows an error function.

3.2 Particle image velocimetry

The velocity field in the region of the hydraulic jump with limited bubble formation (non-aerated region) was measured using the PIV technique; Figure. 4 shows a typical PIV image. The velocity in locations downstream of the toe of a fully developed hydraulic jump resembles that of an impinging wall jet with the maximum velocity occurring near the bed (Rajaratnam, 1965). Figure 4 shows that no reverse flow with negative streamwise velocities was observed in the PIV measurements and the velocity decreased in the streamwise direction. A zero upward velocity, which was observed at the location upstream of the jump toe, indicates a uniform flow (with streamlines parallel to the bed). However, an upward motion of the flow was observed in the rest of the hydraulic jump.

It must be stated that velocity measurements with the PIV technique is limited to the near-bed region in weak hydraulic jumps. This is because when the supercritical Froude number becomes higher, the bubbles entrained in the roller section occupy the whole water column downstream of the toe. This phenomenon renders PIV measurements ineffective due to the (adverse) reflections from the bubble surfaces that compromise the quality of the image. Under this condition, the Bubble Image velocimetry technique should be applied instead.

  / ISSN 1562-6865 (Online) - ISSN 1063-7710 (Print)

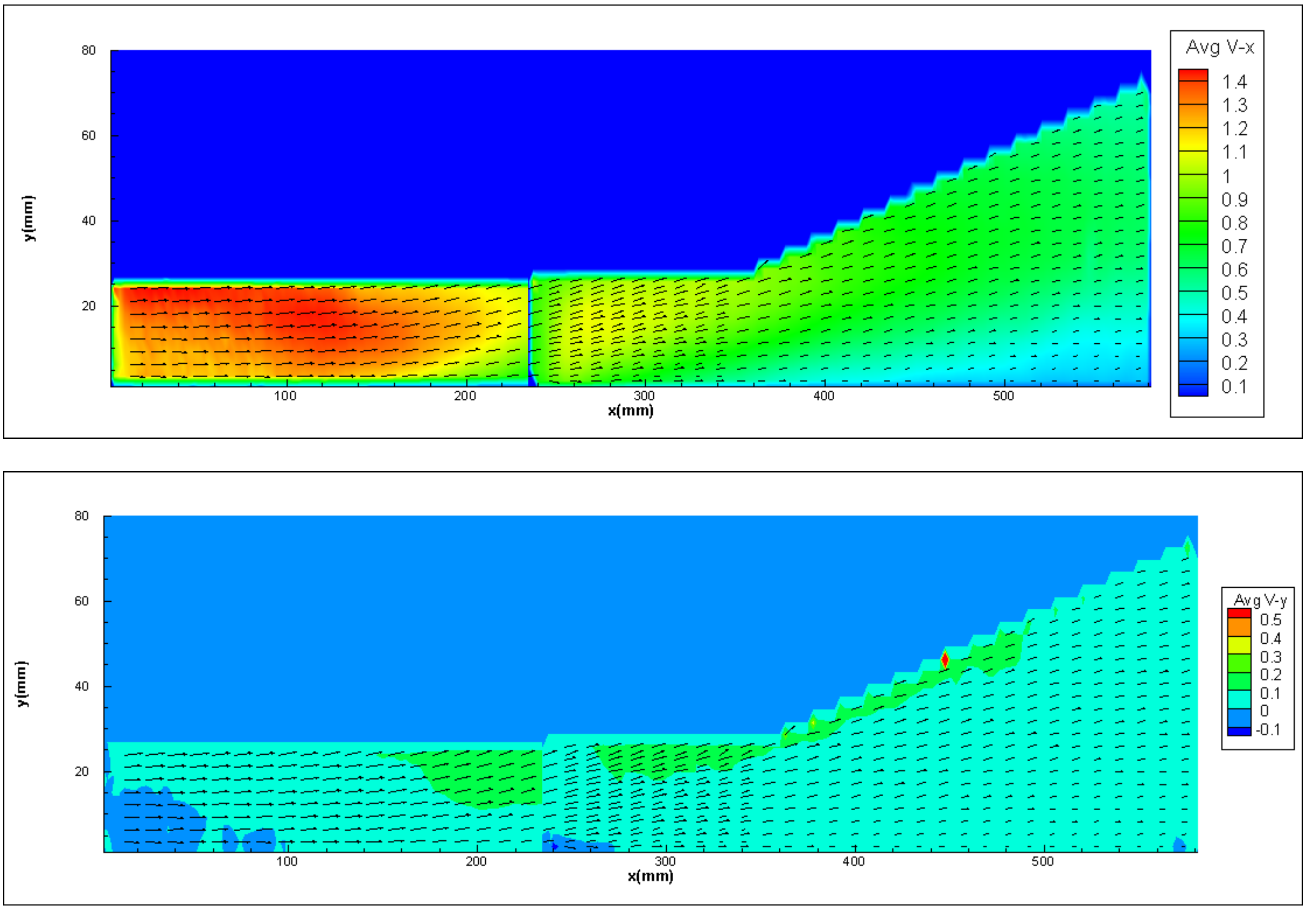

Figure 4. Flow velocity measured by Particle Image Velocimetry (PIV).

3.3 Bubble image velocimetry

Figure 5 shows the bubble velocity vectors superimposed over the raw image. Each arrow in this figure represents the magnitude of the bubble velocity measured within 10 frames captured by the high speed camera. Velocity measurements from the raw images were carried out by using the cross correlation analysis similar to that associated with the PIV analyses. It must, however, be stated that the BIV technique, which is based on detection of the bubble movement, becomes useless in the near-bed region of a weak hydraulic jump because of the absence of bubbles. In addition, as bubbles are only detected near to the side wall of the flume, the bubble velocities may not be the same as those measured in the center of the flume with the dual-tip optical fiber probe. In three-dimensional hydraulic jumps, this variation could be important.

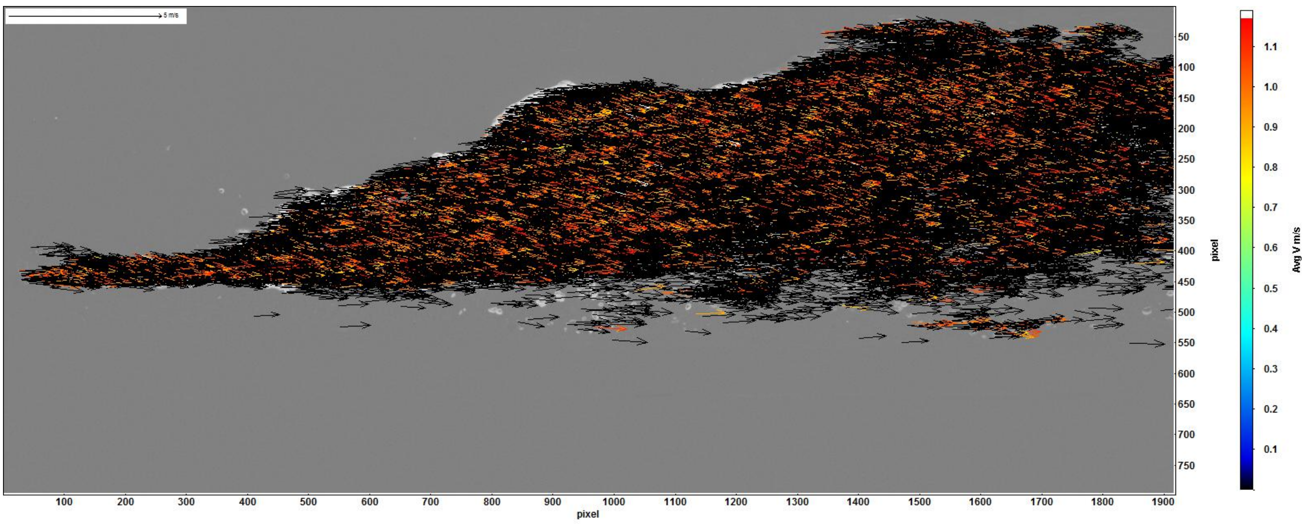

Figure 5. Bubble velocities measured using Bubble Image Velocimetry (BIV)

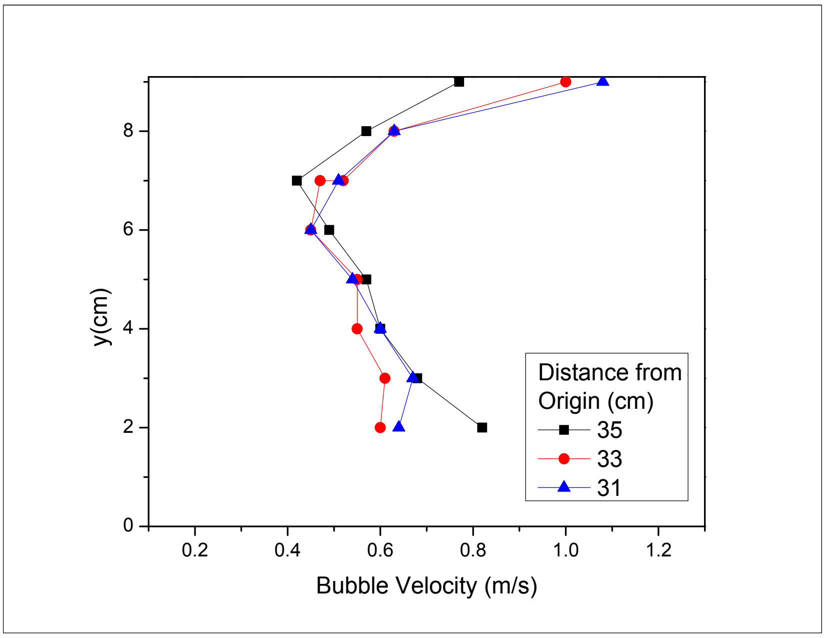

Figure 6. Bubble velocities measured by the dual-tip optical fiber probe.

Figure 6 shows the bubble velocities measured by using the dual-tip optical fiber probe in the aerated region of the hydraulic jump. The probe has an L-shaped with its tip facing upstream (see Figure. 1). The measurement accuracy of the probe relies on the air concentration inside the flow and the flow direction. In his study, Wang (2014) stated that in the recirculating region where the flow velocity is mostly negative, the probe has to be reversed in order to measure the negative flow in the roller section with the tip of the probe pointing downstream. However, since the probe is immersed, its shaft will invariably interfere with the flow. Therefore, meaningful data are difficult to obtain when the probe is facing downstream in the roller region.

4 CONCLUSIONS

The flow associated with a simple hydraulic jump in an open channel is filled with bubbles and velocity measurements using conventional measuring devices are swarmed with difficulties in such two-phase flows. Point velocity measuring instruments such as the dual-tip optical fiber probe or image based velocity measurement techniques such as PIV and BIV are not capable of measuring the velocity and turbulence in the entire 3-dimensional flow field of a hydraulic jump. This study aims at providing a holistic view of the turbulent field in the hydraulic jump by showing the advantages and disadvantages of the dual-tip fiber optic probe and Particle/Bubble Image Velocimetry.

The results demonstrate that the optical fiber probe shows difficulty in measuring the velocity in the recirculating flow region in which the flow changes its direction and the velocity changes from a positive to negative value intermittently. The results show that Bubble Image Velocimetry is a preferred image based measuring technique that should be used in the aerated flow region, although this technique can only show the velocities at the visible side of the flow. Finally, the Particle Image Velocimetry can only be used in regions with very few or no bubbles, e.g., in regions close to the bed, because the presence of bubbles will adversely affect its results.

ACKNOWLEDGEMENTS

This material is based on research/work supported by the Land and Liveability National Innovation Challenge under L2 NIC Award No. [L2NICCFP1-2013-3]. Any opinions, findings, and conclusions or recommendations expressed in this material are those of the author(s) and do not necessarily reflect the views of the L2 NIC.

REFERENCES

Brattberg, T., Toombes, L. & Chanson, H. (1998). *Developing Air-Water Shear Layers of Two-Dimensional Water Jets Discharging into Air,* American Society of Mechanical Engineers, Fluids Engineering Division (Publication) FED.

Bröder, D. & Sommerfeld, M. (2007). Planar Shadow Image Velocimetry for the Analysis of the Hydrodynamics in Bubbly Flows. *Measurement Science and Technology,* 18(8), 2513.

Chanson, H. (1997). Air Bubble Entrainment in Open Channels: Flow Structure and Bubble Size Distributions. *International Journal of Multiphase Flow,* 23(1), 193-203.

Chanson, H. (2013). Hydraulics of Aerated Flows: Qui Pro Quo? *Journal of Hydraulic Research,* 51(3), 223-243.

Felder, S. & Chanson, H. (2015). Phase-Detection Probe Measurements in High-Velocity Free-Surface Flows including a Discussion of Key Sampling Parameters. *Experimental Thermal and Fluid Science,* 61, 66-78.

Leandro, J., Carvalho, R., Chachereau, Y. & Chanson, H. (2012). Estimating Void Fraction in a Hydraulic Jump by Measurements of Pixel Intensity. *Experiments in Fluids,* 52(5), 1307-1318.

Lin, C., Hsieh, S.-C., Lin, I.J., Chang, K.-A. & Raikar, R. (2012). Flow Property and Self-Similarity in Steady Hydraulic Jumps. *Experiments in Fluids,* 53(5), 1591-1616.

Mossa, M. & Tolve, U. (1998). Flow Visualization in Bubbly Two-Phase Hydraulic Jump. *Journal of Fluids Engineering,* 120(1), 160-165.

Murzyn, F. & Chanson, H. (2009). Experimental Investigation of Bubbly Flow and Turbulence in Hydraulic Jumps. *Environmental Fluid Mechanics,* 9(2), 143-159.

Murzyn, F., Mouaze, D. & Chaplin, J.R. (2005). Optical Fibre Probe Measurements of Bubbly Flow in Hydraulic Jumps. *International Journal of Multiphase Flow,* 31(1), 141-154.

Murzyn, F., Mouazé, D. & Chaplin, J.R. (2007). Air–water Interface Dynamic and Free Surface features in Hydraulic Jumps. *Journal of Hydraulic Research,* 45(5), 679-685.

Rajaratnam, N. (1962). An Experimental Study of Air Entrainment Characteristics of the Hydraulic Jump. *Journal of The Institution of Engineers (India),* 42(7), 247-273.

Rajaratnam, N. (1965). Hydraulic Jump in Horizontal Conduits. *Water Power,* 17(2), 80-83.

Wang, H. (2014). *Turbulence and Air Entrainment in Hydraulic Jumps,* PhD Thesis. The University of Queensland, Brisbane, Australia.

Wang, H. & Chanson, H. (2015). Experimental Study of Turbulent Fluctuations in Hydraulic Jumps. *Journal of Hydraulic Engineering,* 141(7), 1-27.

Wood, I. (1991). Air Entrainment in Free-Surface Flows. *IAHR Hydraulic Structures Design Manual No. 4, Hydraulic Design Considerations,* Balkema, Rotterdam, 149.

Yonguk, R., Kuang-An, C. & Ho-Joon, L. (2005). Use of Bubble Image Velocimetry for Measurement of Plunging Wave Impinging on Structure and Associated Greenwater. *Measurement Science and Technology,* 16(10), 1945.

Zhang, W., Liu, M., Zhu, D.Z. & Rajaratnam, N. (2014). Mean and Turbulent Bubble Velocities in Free Hydraulic Jumps for Small to Intermediate Froude Numbers. *Journal of Hydraulic Engineering,* 140(11), 1-9.

HYDRAULIC STUDY FOR BELIBIS RIVER PUMP SUMP THROUGH PHYSICAL MODELLING

MOHD KAMARUL HUDA SAMION[1], MOHD FAUZI MOHAMAD[2] & KHAIROL AZUAN ADAM[3]

[1,2,3] National Hydraulic Research Institute of Malaysia, Selangor, Malaysia,
kamarul@nahrim.gov.my

ABSTRACT

A new flood mitigation project was implemented by Malaysian Government at Pekan, Pahang due to frequent flooding causing various losses of property and lives. A pump station is stationed just downstream of the Belibis river for diverting the discharge to reduce the impact of the flooding. Hydraulic model studies are necessary for the pump sumps intake due to the operational requirements of the pumps in a limited space environment which can leads to hydraulic problems. The purposes of this hydraulic model study is to identify undesirable flow conditions in the pump sump model such as vortices, pre-rotation of flow and uneven distribution of flow and propose improvements to the pump sump prototype based on model testing results. Based on the optimum model discharge, an undistorted scale model of 1:10 is adopted. The model features four pumps (7.91 l/s for pump 1 and 2, and 4.74 l/s for pump 3 and 4) with different values of water depth in total of 4 cases of study. Pump flow rate measurements are obtained by ultrasonic flow meter and swirl angle in the suction intakes are measured by a vortimeter. No vortices occurred near the suction intake for all cases but an uneven flow through the suction intake has been detected in some cases. A minor modification is required by installation of buffer block directly under the pump intake column. During detail testing and analysis, the installation of the buffer shows a better flow distribution in all cases.

Keywords: Hydraulic; physical model; pre-rotation flow; pump sump; vortices.

1 INTRODUCTION

Pekan city in the state of Pahang, Malaysia and its adjacent areas, have experienced frequent flooding causing hardship to the local population and significant damages to the economy. To reduce the impact, a new Pekan Flood Mitigation Project was implemented by Malaysian Government whereby pump station was established just downstream of the Belibis river for diverting excess flows. Hydraulic model studies are necessary for the pump sumps intake due to the operational requirements of the pumps in a limited space environment which can lead to hydraulic problems such as attached surface vortices; submerged vortices; air entrainment from inflow; swirl and undulating flow; and dead flow regions.

Physical modelling is commonly used during design stages to optimize a structure and to ensure a safe operation of the structure (Chanson, 1999). When used in tandem with numerical modelling, this approach leads to great success for fluid-structure interaction studies and discharge capacity evaluation (Archembau et al., 2001; Pirotton et al., 2001; Pirotton et al., 2003). Physical model testing is recommended for pumping stations in which the geometry differs from recommended standards, particularly if previous experience with them is not available. Model testing can also be employed to seek solutions to problems in existing installations. If the source of a problem is unknown, it can be less expensive to determine the cause and find remedies by model studies rather than by trial and error at full scale. In this pump sump model test, the pumping station will house 2 nos. of submersible pumps (main pump) and 2 nos. of submersible pumps (jokey pump).

The objectives for this hydraulic studies of pump sump model are to identify undesirable flow conditions in the pump sump model such as vortices and pre-rotation flow and also to propose improvements to the pump sump prototype based on model testing results. The scope of work for the studies are design and construct the physical model of the pump sump; Carry out hydraulic studies on the pump sump model to confirm the suitability of the designed pump sump; Recommendation on modification of pump sump design based on the outcomes of the initial hydraulic studies on the pump sump model; And also carry out subsequent testing on modified pump sump model to confirm the performance of the modified pump sump design.

2 HYDRAULIC MODEL SIMULATION

Froude number modelling is typically used when friction losses are small and the flow is highly turbulent (Chanson, 1999). As the flows studied were mainly controlled by gravity and as the friction losses could be negligible, studies were adopted with the same ratio between inertia and gravity forces as with the prototype.

  / ISSN 1562-6865 (Online) - ISSN 1063-7710 (Print)

This similarity results in the conservation between model and prototype of the non-dimensional number of Froude (Erpicum et al., 2008). After thorough considerations for the most optimum configuration, an undistorted model scale of 1:10 ratio was decided. Thus, in compliance with the Froude Law the corresponding model and prototype relationships was summarised in Figure 1.

Property	Scale Relationship	Model Value
Geometric	$S = L_m/L_p$	1/10
Velocity	$V_m = V_pS^{0.5}$	1/3.16
Flow	$Q_m = Q_pS^{2.5}$	1/316
Time	$T_m = T_pS^{0.5}$	1/3.16

Figure 1. The relationship between prototype and model values.

A geometrically pump sump model with a scale ratio of 1:10 similar to the prototype was constructed for this study. Figure 2 and 2 below shows the layout plan and side view of the study area.

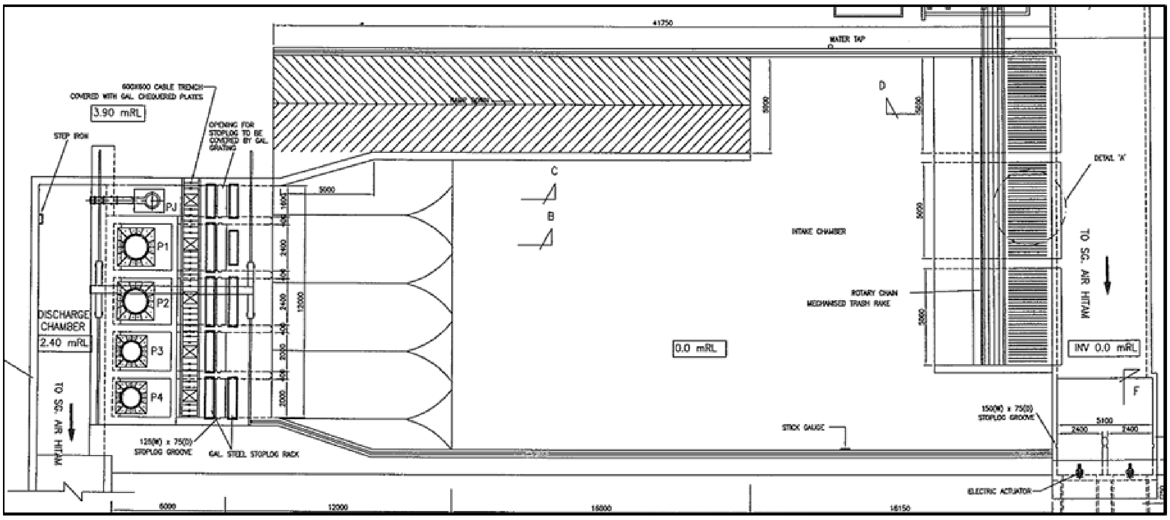

Figure 2. Detail plan view of the pump sump.

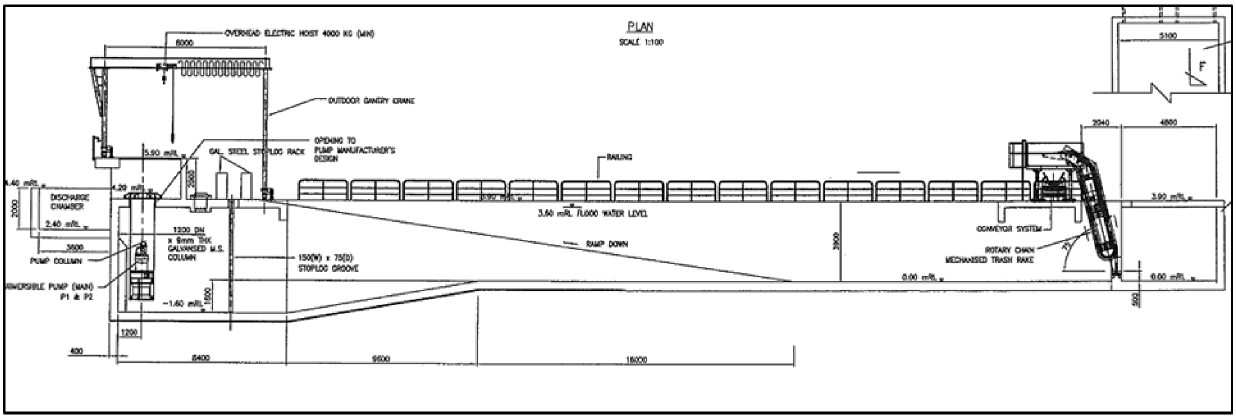

Figure 3. Overall side view of the pump sump.

In order for the pump sump model to maintain the water level at a constant value during observation, a closed loop system using a circulating pump was built (please refer to Figure 4). This system also enables the regulation of water level in the pump sump model by changing the volume of water contained. In the closed loop of flow system, the flow will be drawn through the pump sump model to the suction side of the external circulating pumps and then into the intake structure of the pump sump model. All the flow for the model testing is measured using the ultrasonic flow meter. In order to control the regulation of flow and the delivery head, a butterfly valve is incorporated in each of the external circulating pumps as a control valves.

Figure 4. Water circulation system and scale model of the pump sump.

The assessment of the pump sump model test involved observing the approach flow pattern towards each operating pump intake with the aid of a blue dye tracer. This gave a good insight as to how the pumps would respond since any flow that departs significantly from the one of the steady flow is undesirable. This uneven distribution of flow approaching the pumps can cause swirl and vortex formation at the pump intake.

2.1 Test scenarios

Tests were undertaken under steady conditions with each duty pump operating at the specified design flow rate and water levels provided by client. Using Froude Number similarity, the model flow capacity for each major pump (P1 & P2) is 7.9 l/s and the capacity for minor pump (P3 & P4) is 4.74 l/s. The test scenarios (please referred Table 1) in this study are as follows:

- A single pump, the P4 (minor pump) in operation at MSL +0.40 which is equivalent to 260 mm from the bottom of the sump (minor pump)
- Two pumps, P4 (minor pump) and P1 (major pump) in operation at MSL +0.90 which is 310 mm from the bottom of the sump (minor and major pumps)
- Three pumps, P4 (minor pump), P1 (major pump) and P2 (major pump) in operation at MSL +1.50 which is 370 mm from the bottom of the sump (minor and major pumps)
- All pumps in operation at MSL +1.80 which is equivalent to 400 mm from the bottom of the sump

Table 1. The relationship between prototype and model values.

Test	**Water Level MSL**	**Major Pump 1**	**Major Pump 2**	**Minor Pump 3**	**Minor Pump 4**
Run 1	+1.80	√	√	√	√
Run 2	+1.50	√	√		√
Run 3	+0.90	√			√
Run 4	+0.40 (Min level)				√

3 RESULT AND DISCUSSION

3.1 Vortices

Ideally, the flow of water into a pump should be uniform, steady, without swirl and without air, either entrained from a free surface or released from local low pressure regions. Lack of uniformity can lead to reduction of efficiency. Unsteady flow will result in fluctuating loading of the propeller, leading to noise and vibration. Swirl in the intake can cause a change in flow, reduction in the pump efficiency and power. It may result in vortices leading from the free surface or from a bounding solid surface into the pump. These vortices can become strong enough for the cores to form air bubbles or cavitation. Vortices from the water surface can draw air continuously into the pump while solid surface vortices, often called submerged vortices, provide discontinuities in the flow around the propeller blades.

The free vortices are generated by rotation and separation combined with the effects of accelerated flow at the pump intake. Coherent subsurface swirl is often apparent, sometimes penetrates into the intake but again, since only gravitational and inertial forces are involved, Froude Number similarity accurately predicts the magnitude of such effects. In the extreme, air core vortices will be generated which may have serious consequences. Such vortices, with air core extending near to a model intake, will be subjected to scale effects. In a full-size installation, due to the absence of scale effects, the transition from a surface dimple and coherent subsurface swirl to an air core will occur more readily than in the model.

In order to achieve the objectives, it is necessary to investigate the performance of the pump sump as designed and to make modifications to overcome any encountered problems. The assessment of the pump sump involved observing the approach flow pattern towards each operating pump intake with the aid of dye tracer. The tests were undertaken under steady conditions with each duty pump operating at the specified design flow rate and water levels. When a single pump in operation it was conducted at lower water level of 260 mm (from the bottom sump) and at 400 mm water level when all major and minor pumps are in operation. Observations were made from the dosing of the blue dye at the entrance and immediately downstream of the slope intake showed that the dye had a tendency to flow towards the centre of the suction column for all test scenarios as in Figures 4. Thus, this indicates that the proposed pump sump design work well during all pumps operation cases.

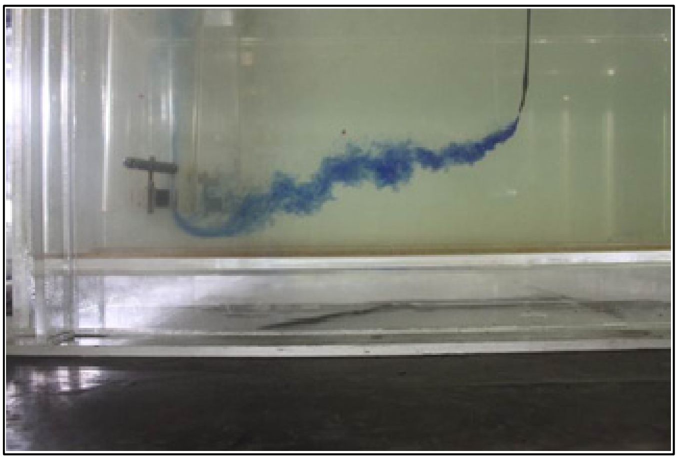

Figure 5. The approach flow pattern towards pump intake with the aid of dye tracer.

3.2 Pre-rotation and swirl at pump intake

Swirl is a general term for any flow condition where there is a tangential velocity component in addition to a usually predominating axial flow component. Pre-rotation is a specific term to denote a cross sectional average swirl in suction line of a pump or, in case of a vertical wet pit pump, upstream of the impeller. Pre-rotation will influence the pump performance since the flow approaching the impeller already has a rotational flow field which may oppose or add to the impeller rotation, depending on direction. The design of the pump impeller vanes i.e. shape and angle assumes no pre-rotation and the existence of pre-rotation implies flow separation along one side of the impeller vanes. The degree that should be of concern is dependent on the type of pump and may not always be known. Pre-rotation should be quantified in a model by an average cross sectional swirl angle, determined by detailed velocity measurement or by reading on a swirl meter. Since swirl decays along a pipe as a result of wall friction, internal fluid shear and turbulence, the swirl meter in the model suction pipe should be located near the impeller.

The method to determine the degree of vortices is by a vortimeter (please refer to Figure 6) developed by Aden Research Laboratory. The vortimeter was constructed and mounted in each of pump column intake suction for swirl angle measurement. The swirl angle was determined using the following relationship:

$$\tan\theta = \left(\frac{V_R}{V_A}\right) \qquad [1]$$

Where: V_R is the rotational velocity of the swirl meter vanes, and V_A is the axial velocity in the pump intake.

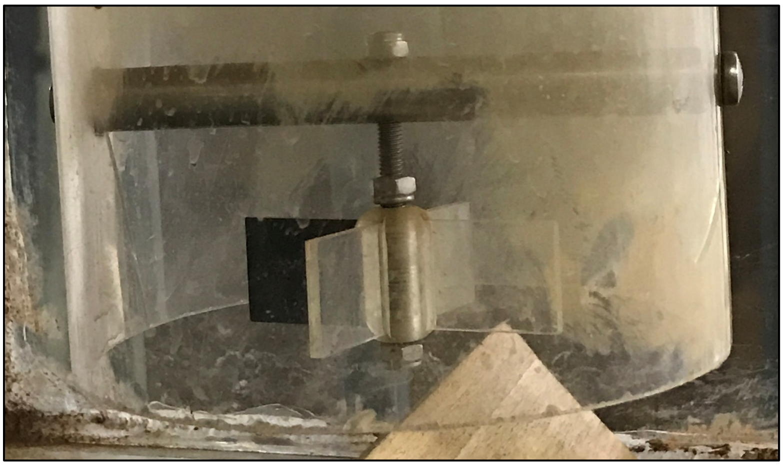

Figure 6. Vortimeter used to detect swirl or rotational flow at the pump intake.

The counting swirl angles are indicated that the results are within the acceptable limit with the installation of the proposed anti-swirl device on the bottom of intake column. As recommended by Ansar (1997), if the swirl angles are less than 5°, the model indicated that the incoming swirl is at a minimum and insignificant. In summary, these results could be considered within the acceptable limit.

From Table 2 through 5, it was found that 3 cases do not meet the requirement of the vortimeter angle. Pump 1 and pump 2 for the Case 1 (all pumps in operation), pump 2 for the Case 2 (3 pumps in operation) and finally for pump 4 in the Case 4. These mean that distributions velocity entered the inlet column with relative larger angle (more than 5°) that the limit suggested by Ansar (1997). There is a possibility for the inflow angle leading to unbalanced pump impellers. Thus, it is recommended to install a triangle buffer block directly under the intake column.

Table 2. Pump configuration and swirl angle degree for case 1.

Test 1	PI	P2	P3	P4	Remark
swirl angle (°)	4.8	0.0	0.9	0.4	cw
swirl angle (°)	0	15.2	2.8	2.1	acw

Table 3. Pump configuration and swirl angle degree for case 2.

Test 2	PI	P2	P3	P4	Remark
swirl angle (°)	4.0	5.3		3.0	cw
swirl angle (°)	0	1.2		1.6	acw

Table 4. Pump configuration and swirl angle degree for case 3.

Test 3	PI	P2	P3	P4	Remark
swirl angle (°)	0.6			0.1	cw
swirl angle (°)	0.2			0.6	acw

Table 5. Pump configuration and swirl angle degree for case 4.

Test 4	PI	P2	P3	P4	Remark
swirl angle (°)				9.1	cw
swirl angle (°)				0.0	acw

3.3 Modification and improvement at pump intake

Since the initial proposed design indicated the existence of some degree of uneven flow distribution in the intake column sections, modification tests are required. The retests were conducted with a triangle buffer blocks directly under all of the pump intake column.

The detail modifications of a triangle buffer block directly under the pump intake column are shown Figure 7. The buffers divide the under current flow on the pump sump and direct them straight to the intake column. These buffers prevent from the occurrences of cross current directly under the intake column. Therefore, these could lead to a better flow distribution.

Figure 7. Modification of a triangle buffer block directly under intake column at all pumps.

The reading and the calculated angle values of vortimeter with a triangle buffer block are shown in Table 6 through 9. The modification minimize the angle of flow and provide a better flow distribution straight to the pump intake column. These buffers also prevent under current to cross each other. Further, the 45° face of the buffer provide a smooth transition of incoming front flows.

Table 6. Swirl angle degree with a triangle buffer block for case 1.

Test 1	PI	P2	P3	P4	Remark
swirl angle (°)	0.9	0.4	0.3	0.0	cw
swirl angle (°)	0.0	0.6	3.3	1.9	acw

Table 7. Swirl angle degree with a triangle buffer block for case 2.

Test 2	PI	P2	P3	P4	Remark
swirl angle (°)	0.9	1.4		0.7	cw
swirl angle (°)	0	0.8		1.0	acw

Table 8. Swirl angle degree with a triangle buffer block for case 3.

Test 3	PI	P2	P3	P4	Remark
swirl angle (°)	0.6			0.3	cw
swirl angle (°)	0.0			0.2	acw

Table 9. Swirl angle degree with a triangle buffer block for case 4.

Test 4	PI	P2	P3	P4	Remark
swirl angle (°)				3.0	cw
swirl angle (°)				0.0	acw

4 CONCLUSION

The results from the initial testing conclude that the proposed design for the Belibis River Pump Sump are not acceptable at three pump protocols. First when all 4 pumps in operations (Case 1 - 2 major and 2 minor). The occurrences of uneven flow distribution into the pump intake columns that are indicated by the entrance degree of vortimeter greater than 5°. Second when 3 pumps in operations (Case 2 - 2 major and 1 minor). The occurrences of uneven flow distribution into the pump intake columns that indicated by the entrance degree of vortimeter greater than 5°. And the last one when only 1 pump in operation (Case 4 – 1 minor). The occurrence of uneven flow distribution into the pump intake column that indicated by the entrance degree of vortimeter greater than 5°. Thus, a minor modification is required by installation a triangle buffer block directly under all of the pump intake column as shown in Figure 7. During detail testing and analysis, the installation of the buffer has shown a better flow distribution on all cases.

REFERENCES

Ansar, M. (1997). Experimental and Theoretical Studies of Pump Approach Flow Distributions at Water Intakes, *PhD Thesis*. University of Lowa, U.S.A.

Archambeau, P., Erpicum, S., Mouzelard, T. & Pirotton, M. (2001). Experimental - Numerical Model Interaction: Example of a Large Dam Project in Laos. *Water Resources Management Management, Progress in Water Resources*, 4, 365-374.

Chanson, H. (1999). *The Hydraulics of Open Channel Flow*. Arnold, London, U.K, 261-283.

Erpicum, S., Dewals, B., Archambeau, P., Detrembleur, S., Fraikin, C. & Pirotton, M. (2008). Scale Modelling and Similarity Laws for the Study of an Under Pressure Settling Structure. *9th International Symposium on River Sedimentation*, Tsinghua University Press, China.

Pirotton, M., Archambeau, P., Erpicum, S. & Mouzelard, T. (2001). Water Management of Large Dams. *International Symposium on Environmental Hydraulics*, Arizona State University, U.S.A.

Pirotton, M., Lejeune, A., Archambeau, P., Erpicum, S. & Dewals, B. (2003). Numerical Experimental Interaction in Hydrodynamics: An Integrated Approach for the Optimal Management of Hydraulic Structures and Hydrographic Basins. *9th International Conference on Enhancement and Promotion of Computational Methods in Engineering and Science*, University of Macau, Hong Kong.

ON PERMEABILITY AND ROUGHNESS EFFECTS IN FLOW PAST A ROW OF CIRCULAR CYLINDERS ARRANGED ALONG THE CENTERLINE OF A STRAIGHT FLUME

SATOSHI YOKOJIMA[1], RYOSUKE ASAOKA[2], KOUDAI YOSHINO[3], HIROSHI NODA[4] & TAKASHI MIYAHARA[5]

[1,2,3,5] Department of Mathematical and Systems Engineering, Shizuoka University, Hamamatsu, Japan.
e-mail: yokojima@shizuoka.ac.jp
[4] Department of Architecture, Kindai University, Higashi-Osaka, Japan.

ABSTRACT

The presence of a row of circular cylinders along the centerline in a flume gives a significant drag to the flow. The row can be seen macroscopically as a porous flat plate having both permeability and roughness effects, and the flow over semiannular stripe roughness elements is the system obtained by removing only the permeability from the flow past the cylinders. In the present study, these flows have been studied comparatively by a two-dimensional high-fidelity numerical experiment to elucidate the impacts of the permeability and roughness on the flow resistance. The drag on the row of cylinders is found to be roughly one order of magnitude higher than that over the roughness elements. In other words, the permeability causes much more resistance to the flow than the roughness. The importance of the former tends to be decreased with the decrease in the number of cylinders (*i.e.* increase in the plate porosity). Visualization of the instantaneous flow fields reveals the presence of large scale vortices in both types of the flows, and the intensity of the vortices is significantly enhanced by the boundary permeability. This then promotes fluid mixing and associated momentum exchange over the whole cross section, and increases the resistance to the flow.

Keywords: Permeability effect; roughness effect; a row of circular cylinders; drag; two-dimensional high-fidelity numerical experiment.

1 INTRODUCTION

It is well known that adding permeability to a body immersed in a fluid flow can increase the resistance to the flow. For example, Noymer et al. (1998) reported that, in a flow past an isolated porous circular cylinder, the drag becomes about 30 – 50 percent higher than that of the corresponding solid cylinder when the porosity is only about a few percent, at the stem Reynolds numbers of 100 and 1000. The drag increases due to permeability was also found in flows parallel to a permeable wall (e.g. Jimenez et al., 2001, Yokojima, 2011). Since porous bodies and permeable boundaries are quite ubiquitous in hydraulic and geophysical flows, it is of substantial importance to gain a greater understanding of the mechanism of the drag enhancement.

In the present study, an attention is paid to a flow past a row of monodisperse circular cylinders of diameter, D arranged along the centerline of a straight flume of width 2δ, as shown in Figure 1a. It can be a simple model for flows around vegetative canopies (Yokojima et al., 2015). The row can be seen macroscopically as a porous flat plate of thickness, D and hence has both the permeable and roughness effects. While the presence of such cylinders may bring a substantial resistance to the flow, it is unclear how much the permeability and roughness contribute to the drag. To elucidate the impacts of these basic properties of solid boundaries encountered in practical applications on the flow resistance, a flow over semiannular stripe roughness elements (Figure 1b), which can be obtained by inserting a flat plate through the centers of the cylinders, is introduced. The introduction of the plate removes the permeability from the row of cylinders but leaves the roughness element unchanged. These flows are studied comparatively by two-dimensional high-fidelity direct simulations.

2 PHYSICAL AND NUMERICAL DETAILS

The details of the flows to be examined, *i.e.* the flow past a row of circular cylinders (Figure 1a) and the flow over semiannular stripe roughness elements (Figure 1b), are described here. The former is established in a straight channel of width 2δ, and a row of circular cylinders of diameter, D is arranged along the centerline of the flume with uniform surface-to-surface spacing, S.

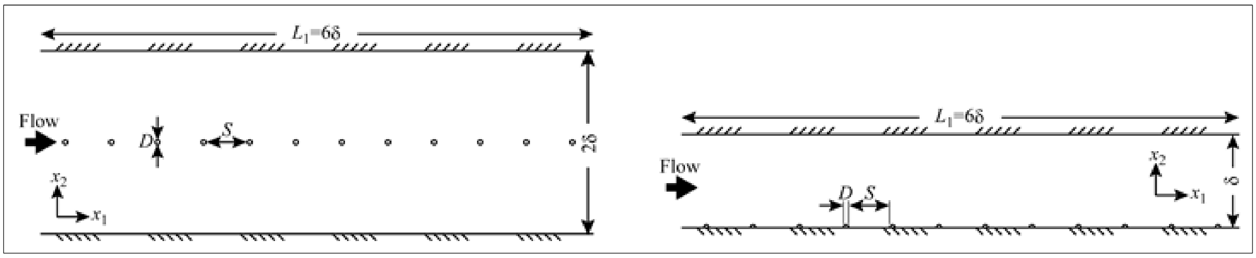

(a) permeable case. (b) impermeable case.

Figure 1. The panel (a) shows a flow past a row of circular cylinders and (b) presents a flow over semiannular stripe roughness elements, which can be obtained by inserting a flat plate to the centers of the cylinders of (a).

The latter is obtained by installing a no-slip impermeable plate along the flume centerline so that the flow domain size is halved in the transverse direction. The no-slip and impermeable constraints are imposed also on the surface of the cylinders/roughness elements as well as at the side walls of the flume. Here periodicity of length $L_1 = 6\delta$ is assumed in the streamwise direction. It has been confirmed that the size L_1 does not affect the drag property of the flows significantly.

In all the cases considered, the driving force of the flow (the mean pressure gradient) is adjusted dynamically so that the bulk mean velocity, U_b is kept constant. The total resistance to the flow is therefore found by the magnitude of the driving force. After the statistically steady state is reached in each case, the time series of the flow driving force are sampled.

The flows are characterized by three parameters: the stem Reynolds number based on the diameter of the cylinders/semiannular roughness elements $Re_D = U_bD/\nu$, the bulk Reynolds number based on the channel half-width $Re_b = U_b\delta/\nu$, and the porosity of the row of circular cylinders/the stripe roughness pattern $\phi = (L_1 - n_cD)/L_1$. Here, ν denotes the kinematic viscosity of the fluid and n_c is the number of the cylinders/roughness elements arranged over the periodic length, L_1. Hence, the porosity (ϕ) shows the fraction of the fluid occupied on the flume centerline. In the present study, the stem and bulk Reynolds numbers are fixed to be 720 and 14400 respectively, and the porosity is changed systematically as ϕ = 0.3, 0.4, 0.5, 0.6, 0.7, 0.75, 0.8, 0.85 and 0.9. The number of the cylinders/roughness elements (n_c) in the abovementioned nine cases are 84, 72, 60, 48, 36, 30, 24, 18 and 12, respectively. Note that Re_D = 720 and Re_b = 14400 are typical values found in laboratory experiments of flows past arrays of circular cylinders (e.g. Yokojima et al., 2015).

The flows are reproduced by a high-resolution numerical experiment based on an immersed boundary method (Uhlmann, 2005, Kempe and Frohlich, 2012). The grid spacing Δ around each cylinder/roughness element is set to be D/20 in the present study. It enables to reproduce the details of the fluid flows around the immersed bodies and the hydrodynamic forces acting on each infinitesimal surface element of the bodies accurately. The code used in the present study has been verified in a flow past an isolated circular cylinder against experimental and numerical results obtained from past studies. The drag and lift coefficients and the Strohal number are found to be well reproduced with the spatial resolution of $\Delta = D/20$.

3 SIMULATION RESULTS

In the following, all the variables are normalized by the bulk-mean velocity (U_b) and the cylinder diameter (D) unless otherwise stated.

3.1 Macroscopic drag property

Figure 2a shows the statistics of the flow driving force required to keep the mass flow rate constant in each case of the flow past a row of circular cylinders/the flow over semiannular stripe roughness elements. Note that n_c = 0 denotes the case with no cylinders, and that $n_c = \infty$ is the case with infinite number of cylinders, which means the presence of a no-slip and impermeable plate of width D along the flume centerline. It is clearly shown that the presence of a row of cylinder increases the flow resistance significantly and that the influence of the friction drag due to the side walls is negligible. The simulation results with $\Delta = D/30$ as well as with $\Delta = D/20$ are presented for the case of ϕ = 0.5 of the flow past the cylinders, where the drag due to the row of cylinders is maximized. No significant difference is found between the results from the two computations, demonstrating that $\Delta = D/20$ is fine enough to reproduce the drag property of the flow accurately.

The flow resistance is maximized at ϕ = 0.5 in the flow past a row of cylinders. The same conclusion was obtained also on other conditions such as Re_D = 180, Re_b = 3600 and Re_D = 270, Re_b = 5400. Figure 2a indicates that the drag acting on the flow over semiannular stripe roughness elements is roughly one order of magnitude lower than that on the flow past the cylinders.

  / ISSN 1562-6865 (Online) - ISSN 1063-7710 (Print)

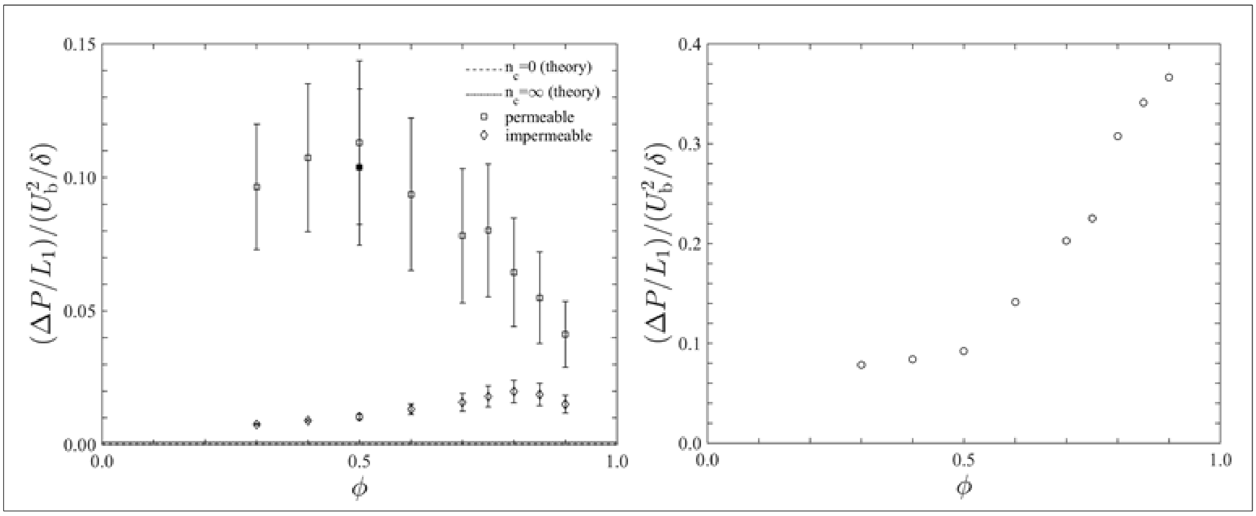

(a) (b)

Figure 2. (a) Driving force required to keep the mass flow rate constant as a function of the porosity (ϕ). The symbols denote the time averaged values and the error bars are the standard deviations. The filled symbol at ϕ = 0.5 presents the results with the spatial resolution of Δ = D/30. (b) Ratio of the driving force required in the impermeable case to that in the permeable case.

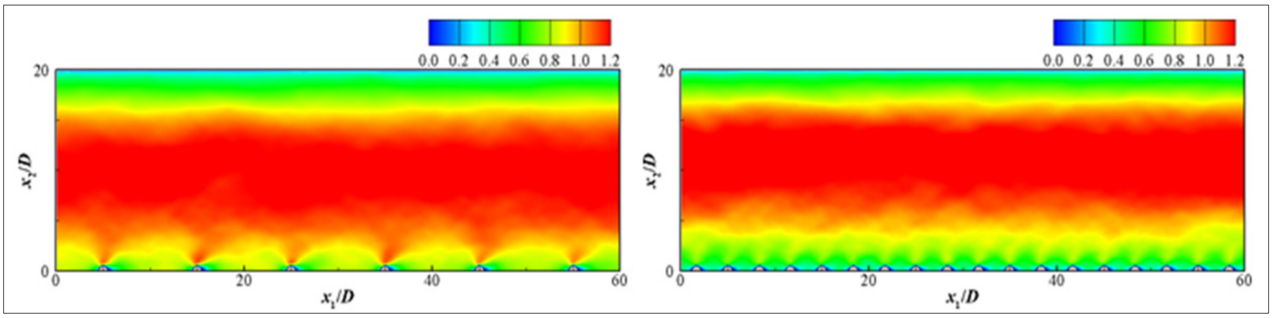

(a) ϕ = 0.9. (b) ϕ = 0.7.

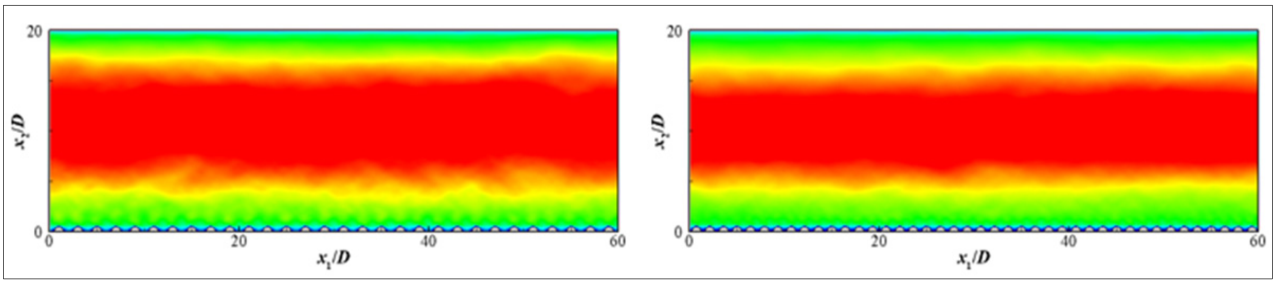

(c) ϕ = 0.5. (d) ϕ = 0.3.

Figure 3. Time-averaged streamwise velocity distributions in the flow past a row of circular cylinders. The region of $0 \le x_1/D \le 60$, $x_2 \ge 0$ is enlarged.

In other words, permeability causes much more resistance to the flow than roughness. In the flow over the roughness elements, the drag is maximized at ϕ = 0.8. It is in good agreement with the findings from past studies on turbulent flows over stripe roughness. To gain an insight into the impacts of the permeability and roughness on the flow resistance, the time-averaged driving force required in the flow over the roughness elements normalized by that in the flow past the cylinders is plotted in Figure 2b. It is just around 10 percent when the porosity is low, but it reaches up to 30 percent or larger at ϕ = 0.8 – 0.9.

3.2 Time-averaged velocity and pressure fields

The time-averaged streamwise velocity profiles for some representative cases are presented in Figures 3 and 4. In the flow past a row of circular cylinders of Figure 3, the flow is strongly accelerated for ϕ = 0.9 in the vicinity of the side edges of the cylinders, and the fluid between the cylinders has a relatively high velocity of $O(U_b)$. As the porosity (ϕ) is decreased, the row of the cylinders is being immersed in the boundary layer.

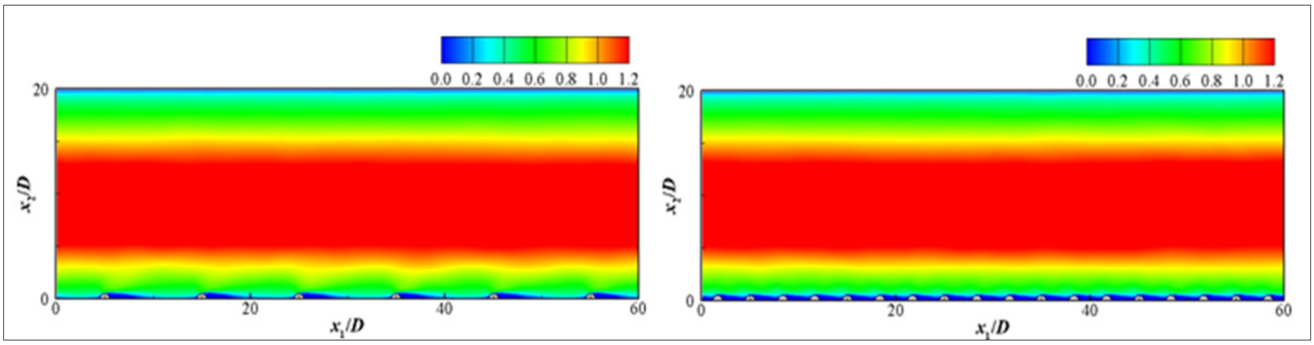

(a) ϕ=0.9. (b) ϕ=0.7.

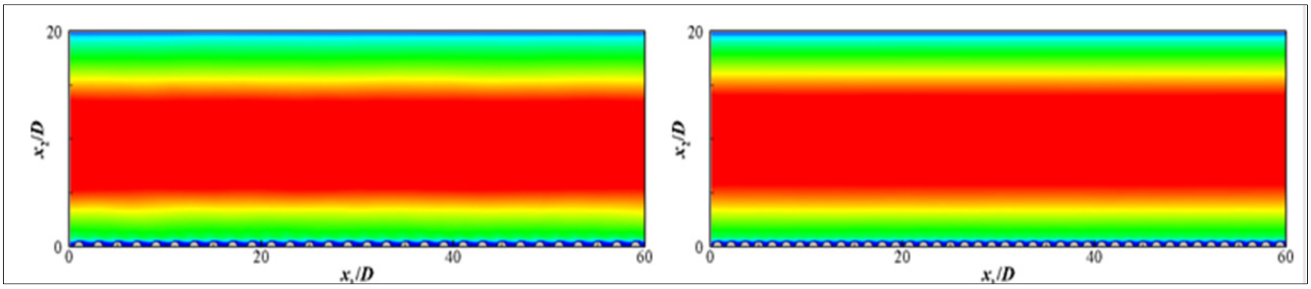

(c) ϕ=0.5. (d) ϕ=0.3.

Figure 4. Time-averaged streamwise velocity distributions in the flow over semiannular stripe roughness elements. The region of $0 \le x_1/D \le 60$ is enlarged.

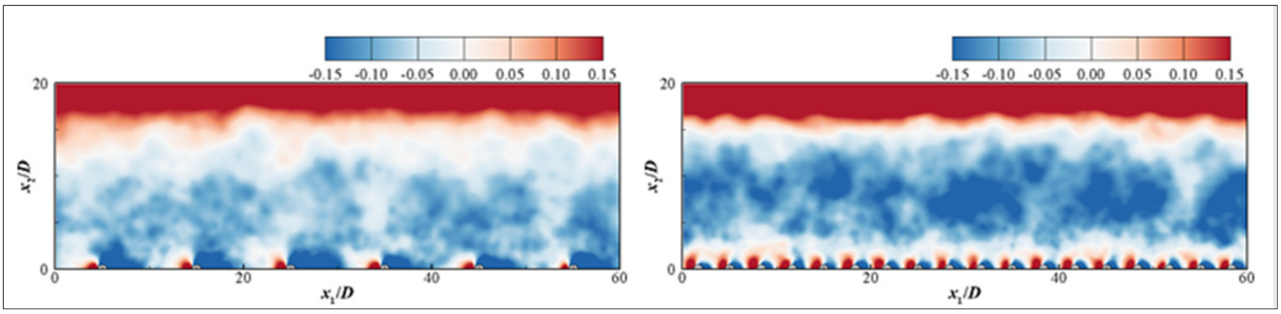

(a) ϕ=0.9. (b) ϕ=0.7.

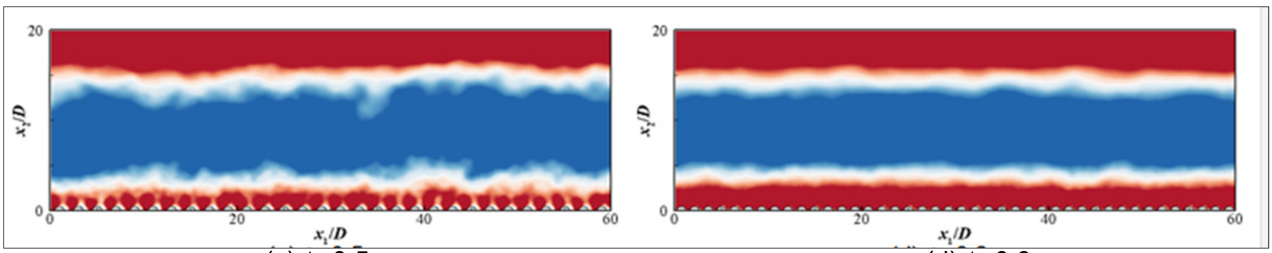

(c) ϕ=0.5. (d) ϕ=0.3.

Figure 5. Time-averaged pressure distributions in the flow past a row of circular cylinders. The region of $0 \le x_1/D \le 60$, $x_2 \ge 0$ is enlarged.

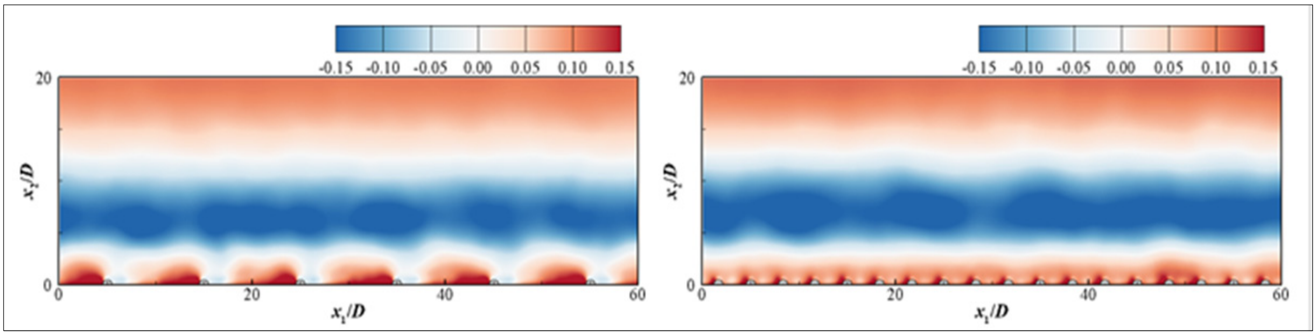

(a) □□= 0.9. (b) □□= 0.7.

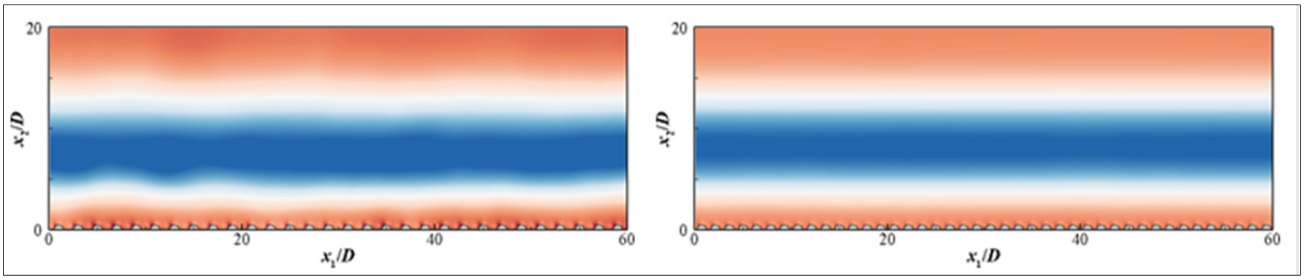

(c) ϕ = 0.5. (d) ϕ = 0.3.

Figure 6. Time-averaged pressure distributions in the flow over semiannular stripe roughness elements. The region of $0 \le x_1/D \le 60$ is enlarged.

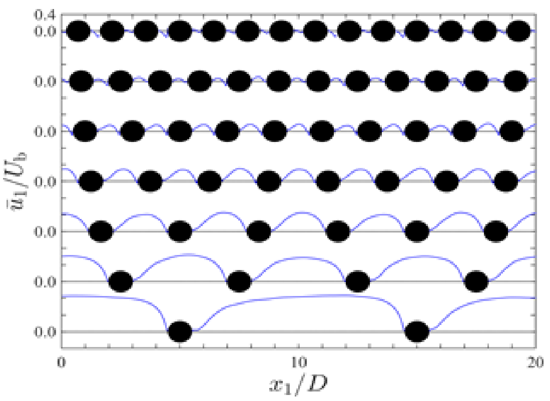

(a) streamwise velocity, permeable case.

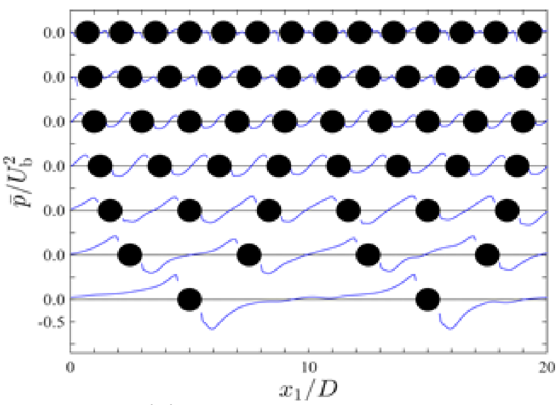

(b) pressure, permeable case.

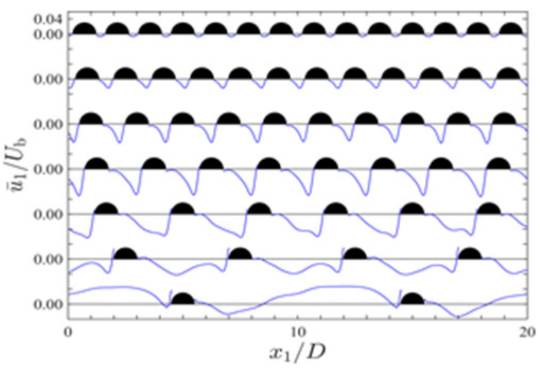

(c) streamwise velocity, impermeable case.

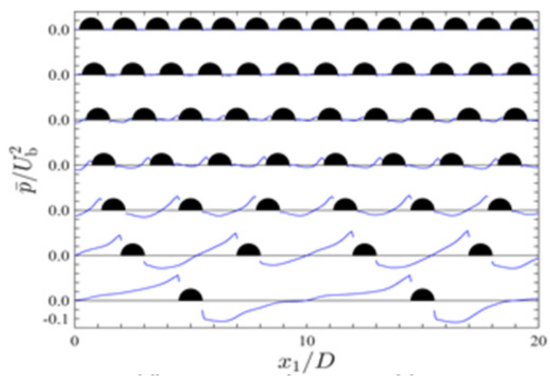

(d) pressure, impermeable case.

Figure 7. Time-averaged streamwise velocity and pressure profiles at $x_2 = D/40$ (immediate vicinity of $x_2 = 0$). In each panel, the data from ϕ = 0.9, 0.8, 0.7, 0.6, 0.5, 0.4, and 0.3 are presented from bottom to top.

On the other hand, the roughness elements are found to be involved in the low-speed layer of $O(0.1U_b)$ in all the cases. Comparison between Figures 2 and 3 indicates that an active momentum exchange in the transverse direction due to the boundary permeability increases the fluid velocity near the cylinders and the resistance to the flow also.

Figures 5 and 6 show the time-averaged pressure distributions. While a pressure difference between the fore and aft of each circular cylinder can be observed clearly for $\phi \geq 0.5$ in the flow past a row of circular cylinders, the pressure difference is not substantial in the flow over semiannular stripe roughness elements even for $\phi = 0.7$. The mean pressure becomes low in the flume core region for both types of the flows. It will be presented in section 3.3 that this pressure depression is due to the presence of large-scale vortices at the instantaneous flow level. The extent of the pressure depression for the flow past the cylinders is deeper than that for the flow over the roughness elements. It suggests that the presence of more intense vortices in the former case. To examine more details of the flow structures around the cylinders/roughness elements, one-dimensional streamwise profiles of the time-averaged streamwise velocity and pressure at $x_2 = D/40$, *i.e.* in the immediate vicinity of the boundaries, are presented in Figure 7.

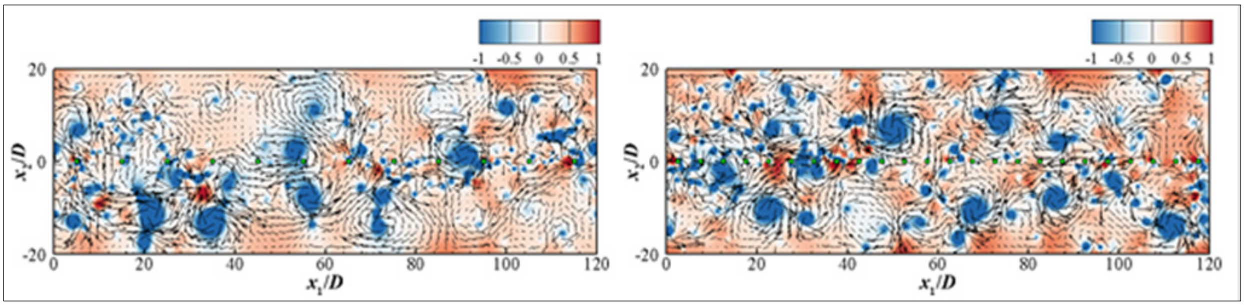

(a) $\phi = 0.9$. (b) $\phi = 0.8$.

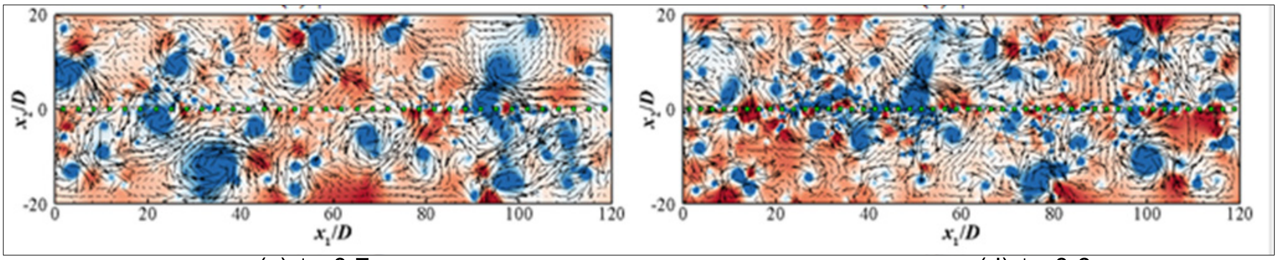

(c) $\phi = 0.7$. (d) $\phi = 0.6$.

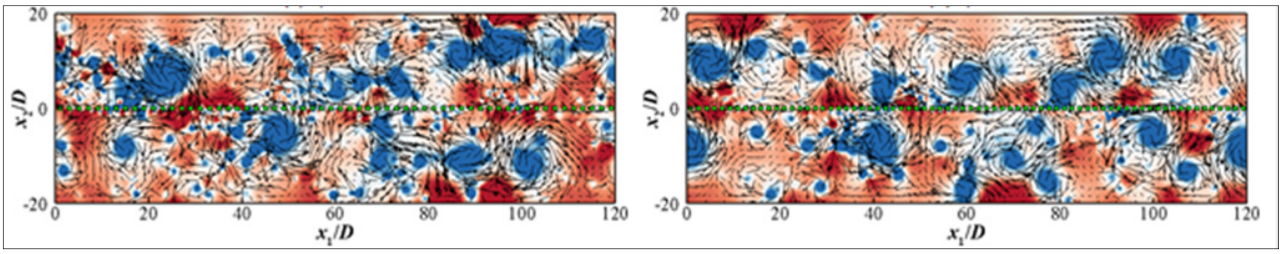

(e) $\phi = 0.5$. (f) $\phi = 0.4$.

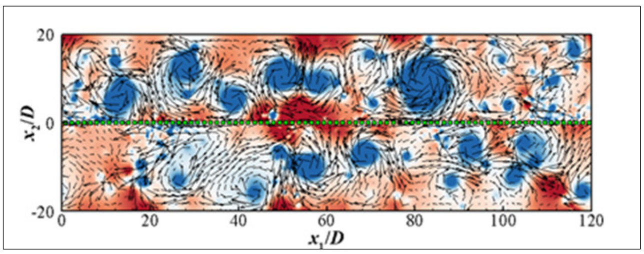

(g) $\phi = 0.3$.

Figure 8. An instantaneous snapshot of the flow past a row of circular cylinders, where the pressure (color contours) and the fluctuating velocity (vector, obtained by subtracting the bulk-mean velocity, U_b) are depicted.

A recirculation region is observed behind of each semiannular roughness element. For ϕ= 0.9, where the surface-to-surface distance between the elements is4.5*D*, the separated streamline is reattached before the fluid encounters the next element. At ϕ= 0.8 or lower, however, the reattachment is absent, and a roughness element is involved in the separation/ recirculation region developed behind the immediate upstream neighbor. The pressure difference between the fore and aft of each element is therefore substantially decreased with decrease in ϕ. For the flow past a row of cylinders, on the other hand, such a reverse flow does not occur even at ϕ= 0.5, where the surface-to-surface distance is 1.0*D* and the fluid encounters the next cylinder with a fairly high velocity. The drag acting on the roughness elements is therefore decreased more substantially than that on the row of cylinders with decrease in the porosity ϕ. It should be borne in mind that the pressure range covered in Figure 7b is five times wider than that in Figure 7d. The difference in the macroscopic drag property between the flow past the cylinders and the flow over the roughness elements presented in Figure 2a can be attributed to the differences in the time-averaged streamwise velocity profiles and also in the associated shape drag between the cylinders and the roughness elements.

3.3 Instantaneous flow property

Figure 8 shows an instantaneous snap shot of the pressure and velocity fields obtained from the flow past a row of cylinders. The low pressure regions indicate the presence of large-scale vortices. More intense vortices are observed in the cases with higher drag to the flow such as ϕ = 0.3 – 0.6. The presence of such vortices whose size is $O(\delta)$ enhances fluid mixing and associated momentum exchange over the whole cross section.

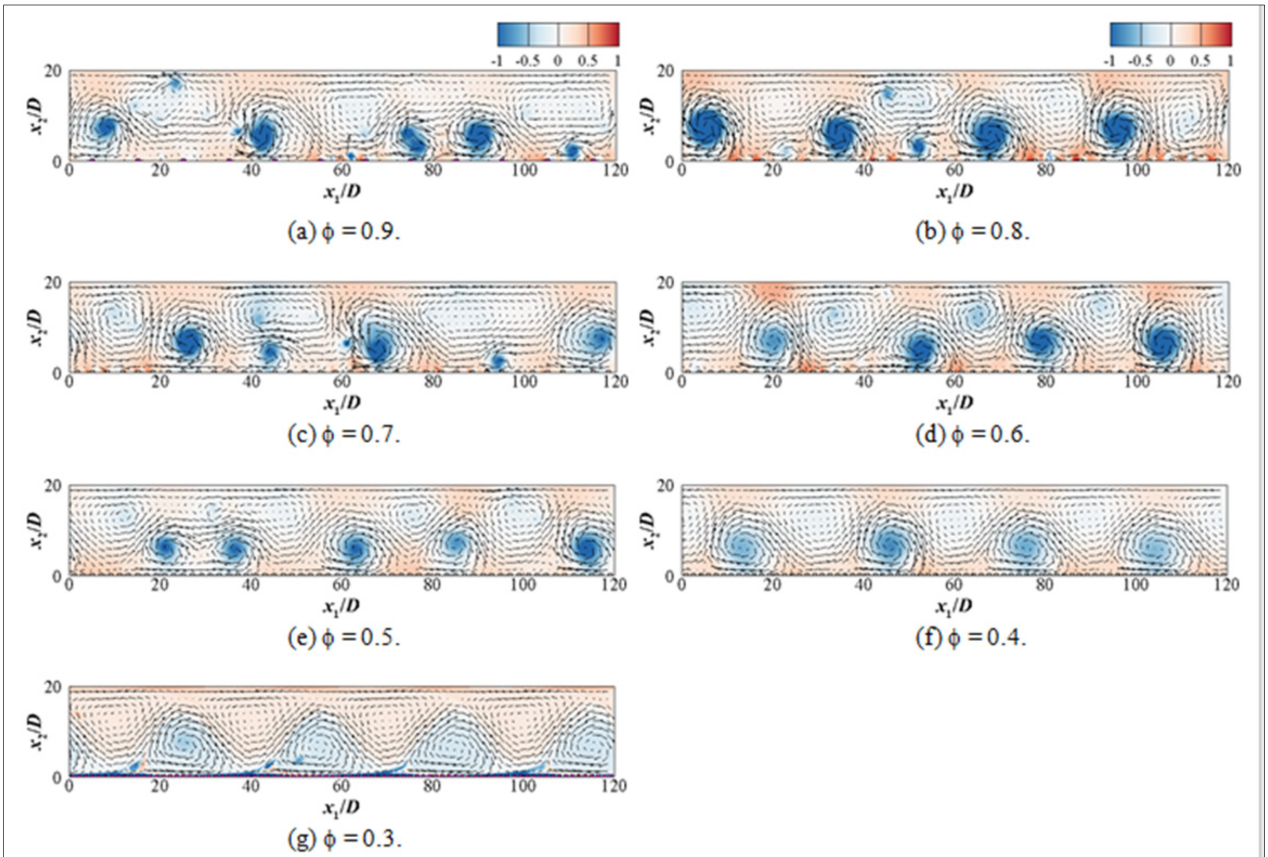

Figure 9. An instantaneous snapshot of the flow over semiannular stripe roughness elements, where the pressure (color contours) and the fluctuating velocity (vector, obtained by subtracting the bulk-mean velocity, U_b) are depicted.

Figure 9 is the counterpart of Figure 8 obtained from the flow over stripe roughness elements. Note that the range of the colorbar for the instantaneous pressure is the same employed in Figure 8. While vortices with various sizes interact actively with each other in the flow past the cylinders, it is not in the flow over the roughness elements. The vortices are found to be simply advected at almost a constant speed without any deformation for ϕ =0.4, and 0.3. Merging and splitting of the vortices are observed at ϕ = 0.5 or larger, but the irregularity of the flow is not as high as in the flow past the cylinders. Comparison between Figures 8 and 9 clearly shows that the pressure depression at the central core of each vortex is more substantial in the flow past the cylinders. It is in accordance with the properties of the time-averaged pressure field depicted in Figures 5 and 6.

4 SUMMARY AND CONCLUSIONS

To deepen the understanding of the macroscopic drag of the flow past a row of cylinders, another flow over semiannular stripe roughness elements, which can be obtained by inserting a flat plate through the centers of the cylinders, is introduced. These flows are studied comparatively by two-dimensional high-fidelity direct simulations based on an immersed boundary method, and the impacts of the permeability and roughness, the basic properties of solid boundaries encountered in practical applications, on the flow resistance are critically examined.

The numerical experiment where the porosity (ϕ) is systematically changed between 0.3 and 0.9, has revealed that the drag on the row of cylinders is roughly one order of magnitude higher than that over the roughness elements. In other words, permeability causes much more resistance to the flow than roughness. While the drag on the row of cylinders is maximized at ϕ = 0.5, the drag over the roughness elements has the largest value at ϕ = 0.8. The impact of the permeability on the flow resistance is therefore decreased with increase in ϕ.

In the flow over semiannular stripe roughness elements, an element is involved in the separation/ recirculation region developed behind the immediate upstream neighbor at ϕ = 0.8 or lower. The shape drag acting on the element is therefore substantially decreased. For the flow past a row of circular cylinders, on the other hand, such a reverse flow does not occur even at ϕ = 0.5 and the fluid encounters the next cylinder with a fairly high velocity. It causes a high resistance to the flow.

Vortices whose sizes are comparable to the flume width are frequently observed in both types of the flows. The vortices are found to have various sizes and interact actively with each other in the flow past the cylinders. In the flow over the roughness element, on the other hand, there exist some cases where the vortices are simply advected at almost a constant speed without any deformation. The presence of intense vortices in the flow past the cylinders enhances fluid mixing and associated momentum exchange over the whole cross section, and increases the resistance to the flow.

REFERENCES

Jimenez, J., Uhlmann, M., Pinelli, A. & Kawahara, G. (2001). Turbulent Shear Flow Over Active and Passive Porous Surfaces. *Journal Fluid Mech*anics, 442, 89-117.

Kempe, T. & Frohlich, J. (2012). An Improved Immersed Boundary Method with Direct Forcing for the Simulation of Particle Laden Flows. *Journal of Computational Physics,* 231(9), 3663–3684.

Noymer, P.D., Glicksman, L.R. & Devendran, A. (1998). Drag on a Permeable Cylinder in Steady Flow at Moderate Reynolds Numbers. *Chemical Engineering and Science*, 53(16), 2859-2869.

Uhlmann, M. (2005). An Immersed Boundary Method with Direct Forcing for the Simulation of Particulate Flows. *Journal of Computational Physics*, 209(2), 448-476.

Yokojima, S. (2011). Effect of Wall Permeability on Wall-Bounded Turbulent Flows. *Journal of the Physical Society of Japan,* 80(3),1-4.

Yokojima, S., Kawahara, Y. & Yamamoto, T. (2015). Impacts of Vegetation Configuration on Flow Structure and Resistance in a Rectangular Open Channel. *Journal of Hydro-environment Research*, 9(2), 295-303.

Proceedings of the 37th IAHR World Congress
August 13 – 18, 2017, Kuala Lumpur, Malaysia

THREE DIMENSIONAL NUMERICAL MODELLING OF FULL-SCALE HYDRAULIC STRUCTURES

CATERINA TORRES[(1)], DUNCAN BORMAN[(2)], ANDY SLEIGH[(3)] & DAVID NEEVE[(4)]

[(1,2,3)] School of Civil Engineering, University of Leeds, Leeds UK
cnctmo@leeds.ac.uk; d.j.borman@leeds.ac.uk; p.a.sleigh@leeds.ac.uk
[(4)] Arup, Leeds, UK
david.neeve@arup.com

ABSTRACT

This study presents the three-dimensional (3D) hydraulic modelling of free surface flows over complex full-scale hydraulic structures. The work outlined therein forms part of a larger ongoing project which focuses on the assessment of the capabilities of different 3D computational fluid dynamics (CFD) techniques to reproduce hydraulic flows over real scale spillway structures and on the comparison with physical scale models. The aim of the first part of the study, presented in this work, is to evaluate a range of 3D free surface methods with a particular focus on the Eulerian mesh-based Volume of Fluid (VOF) technique. A range of 2D and 3D free surface approaches are initially investigated and validated using an experimental case with a simple geometry. The commercial solver Ansys Fluent and the CFD open source platform OpenFOAM are used to implement the VOF model and the DualSPHysics code is used to conduct simulations using the Lagrangian meshless particle-based Smoothed Particle Hydrodynamics (SPH) method. The hydraulic flow over a real hydraulic structure is subsequently modelled, applying the evaluated model implementations. The scheme consists of a newly constructed flood storage reservoir with a labyrinth weir and extended spillway. Different hydraulic conditions is modelled using a 1:25 physical scale hydraulic model of the prototype which is used to validate the numerical models. In order to remove numerical model uncertainties and provide insight into scale effects, numerical simulations are applied first to the physical scale hydraulic model and then to the full-scale prototype. Results show the model is capable of accurately predicting the interface features as well as the velocity and water depths measured in the physical model. It is observed that full-scale predictions present approximately a 17% increase in velocity and a 20% decrease in water depth compared to the equivalent scaled predictions.

Keywords: Computational fluids dynamics (CFD); free-surface models; volume-of-fluid (VOF); physical scale model.

1 INTRODUCTION

With increasing water demand and higher occurrence of extreme flooding events, the design and upgrade of hydraulic infrastructure like dams, weirs and spillways is critical for human safety and development. The current industry practice of hydraulic modelling for the design of this type of hydraulic structures is physical scale hydraulic modelling. Physical scale models are scaled representations of the prototype and are well trusted since they have for long been the conventional means to evaluate hydraulic designs. To achieve similarity between the prototype and the physical scale model, geometric, kinematic and dynamic similitudes need to be satisfied. That is, equal ratios of all length dimensions, velocities, accelerations and forces between prototype and model. However, because hydraulic models are not capable of satisfying the ratios of all forces between prototype and model simultaneously, the dominant forces affecting the flow for the type of problem (gravity, pressure, viscosity, etc.) are matched. For free surface flows the gravity effects are the most important and the Froude similarity is typically implemented. Therefore, scale effects in hydraulic models are inevitable since full dynamic similitude cannot be satisfied. When simulating free surface flows over hydraulic structures using the Froude similarity, the turbulence levels in the scale model are significantly lower, while the viscosity and surface tension effects are overestimated (Chanson, 2009). This causes the predictions of air entrainment in the physical model to be lower than in the full-scale. Scale effect challenges have been investigated in detail in some studies such as Erpicum et al. (2013) or Pfister and Chanson (2012) and limits on model upstream head, Reynolds number and Weber number have been established in order to minimise the effects of scaling.

Advances in computer processing power enabled dramatic improvements over the recent decades and a range of numerical approaches have been proposed to model free surface flows over complex structures. Such numerical models can provide detailed continuous data predictions of the relevant field quantities across the entire domain, which from a design perspective is very attractive. The additional information provided by CFD models provides richer understanding of the problem as well as the ability to simulate the full-scale prototype flow conditions which cannot be achieved by the physical scale models. However, these models have been validated only in a limited number of cases and flow conditions to model free surface flows over full-scale complex structures like weirs and spillways. 3D CFD models have a strong potential to provide accurate and flexible solutions with high prospects of time and cost savings in the design process. Further evidence of accurate numerical modelling of free surface flows over weirs and spillways is needed to demonstrate the reliability of such numerical approaches for specific applications. Developing a range of exemplar validated cases along with guidance on numerical aspects will provide a resource for those working in this area. One of the most well-known CFD models to simulate hydraulic free surface flows is the Eulerian grid-based Volume of Fluid (VOF) model by Hirt and Nichols (1981). The VOF employs the volume fraction function with values between zero and one to distinguish between the two fluids. The exact position of the interface is determined by solving an advection equation for the volume fraction function. This equation is solved using interface capturing schemes. Numerous formulations of the VOF model along with a range of discretisation schemes have been proposed. The VOF method has been successfully applied to model free surface flows in many problems, some examples are Oertel and Bung (2012) where the VOF model captured different types of flows generated in breaking waves; Biscarini et al. (2010) where the VOF model was used to reproduce several dam break flows, Hieu and Tanimoto (2006) who applied the VOF model to model wave-structure interactions and Borman et al. (2014) who found that VOF model could reliably predict shape and position of complex hydraulic jumps using validation data from a novel measurement approach. Flow over simple hydraulic structures has also been accurately simulated and validated with experimental data in studies like Sarker and Rhodes (2004)

In the present work, the capabilities of the VOF method to reproduce a real hydraulic structure are evaluated and utilised to provide insight into scale effects. In order to be able to validate a numerical technique, full dynamic similarity between the numerical model and the physical process modelled should be present. Therefore the physical model of a hydraulic structure is first simulated and the models are validated. Subsequently, modelling of the full-scale prototype is undertaken. Section 2 describes the validation study conducted to test the 2D and 3D VOF and SPH models for a simplified experimental geometry. Section 3 shows the application of the VOF model to simulate the flow over a large labyrinth weir and an extended spillway.

2 CFD VALIDATION STUDY

Initially the VOF and the SPH methods were investigated using a relatively simple dam break geometry, using data available in Biscarini et al. (2010). This is based on an experimental dam break case over a triangular obstacle set up in the laboratory. Figure 1 shows the experimental and numerical results at 3 seconds after the dam break.

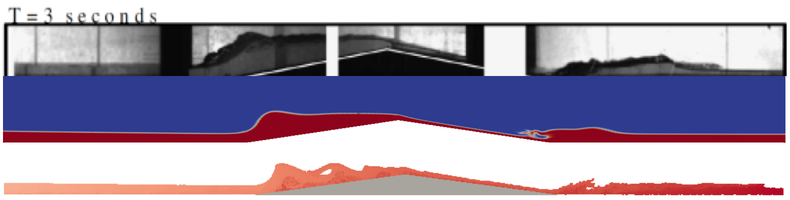

Figure 1. Experimental measurements from Biscarini et al. (2010), 2D VOF water volume fraction and 2D SPH predictions 3 seconds after the dam break.

The experiment involves the release of water which is able to flow over the top of the triangular obstacle. Part of the water reflects back upstream and the other part flows over the top of the obstacle and discharges into the second pool. 2D and 3D VOF simulations were conducted of the model set up using 6 meshes with different cell sizes ranging from 2×10^{-2} m to 1.5×10^{-3} m on the horizontal directions (x,y) and from 5×10^{-3} m to 4×10^{-4} m in the vertical direction (z). In the VOF simulations, the Reynolds-Averaged Navier Stokes (RANS) equations were adopted to solve the effect of turbulence using the standard k-ε model with a standard wall function. The water free surface was resolved using an explicit VOF multiphase model available in Fluent and OpenFOAM to solve the transient free surface flow. The interface capturing scheme implemented was geometric reconstruction using a PLIC (Piecewise Linear Interface Construction) approach in Fluent and the multi-dimensional limiter for explicit solution (MULES) algorithm in OpenFOAM (which incorporates a compressive term in the transport equation of the volume fraction similarly to the Compressive Interface Capturing Scheme for Arbitrary Meshes (CICSAM) method). The pressure-velocity algorithm used was PISO. 2D and 3D SPH simulations were performed with particle spacing ranging from 2.5×10^{-3} m to 5×10^{-4} m using the Symplectic time step algorithm, laminar + SPS viscosity treatment and Cubic Splines. Sensitivity analyses in respect to different Fluent model implementations were performed in order to decide optimal model settings. These included sensitivity to turbulence model, different multiphase model and interface tracking scheme in the VOF model. Sensitivity analyses were also conducted for the SPH simulations in respect to the time step algorithm, the viscosity treatment and the Kernel definition. The main conclusions of this CFD validation study can be summarised as follows:

- The 2D and 3D VOF predictions using Fluent and OpenFOAM (with fixed time stepping) accurately reproduce the flow features and the free surface depths measured in the experiment. The use of adaptive time stepping in the 2D and 3D VOF models provides accurate results in OpenFOAM;
- A mesh with cell size 1×10^{-2} m (x, y) by 2.5×10^{-3} m (z) with a fixed time step size of 1×10^{-3} s is considered to be appropriate for the dam break case modelled and the dimensions of the domain (5.6 x 0.5 x 0.1 m);
- The sensitivity analyses show no significant changes in the free surface predictions when using the SST k-ω and the standard k-ε turbulence models;
- The model shows comparable results with the implementation of two different interface capturing schemes (PLIC and CICSAM);
- The use of the Fluent Eulerian-Eulerian multiphase model significantly improved the slight flow delay observed in Fluent when using adaptive time stepping and also presents an accurate capture of the flow behavior;
- 2D SPH model using a particle spacing value (dp) of 1×10^{-3} m provides an acceptable estimation of the flow characteristics and free surface. Numerical predictions were not found to be sensitive to viscosity treatment or kernel definition but they were strongly dependent on the time step algorithm. The Symplectic algorithm is recommended for this type of problem. 3D results present satisfactory representation of the interface and flow features for a particle spacing value of 5×10^{-3} m.

3 CFD MODELLING OF A REAL HYDRAULIC STRUCTURE

3.1 Methodology

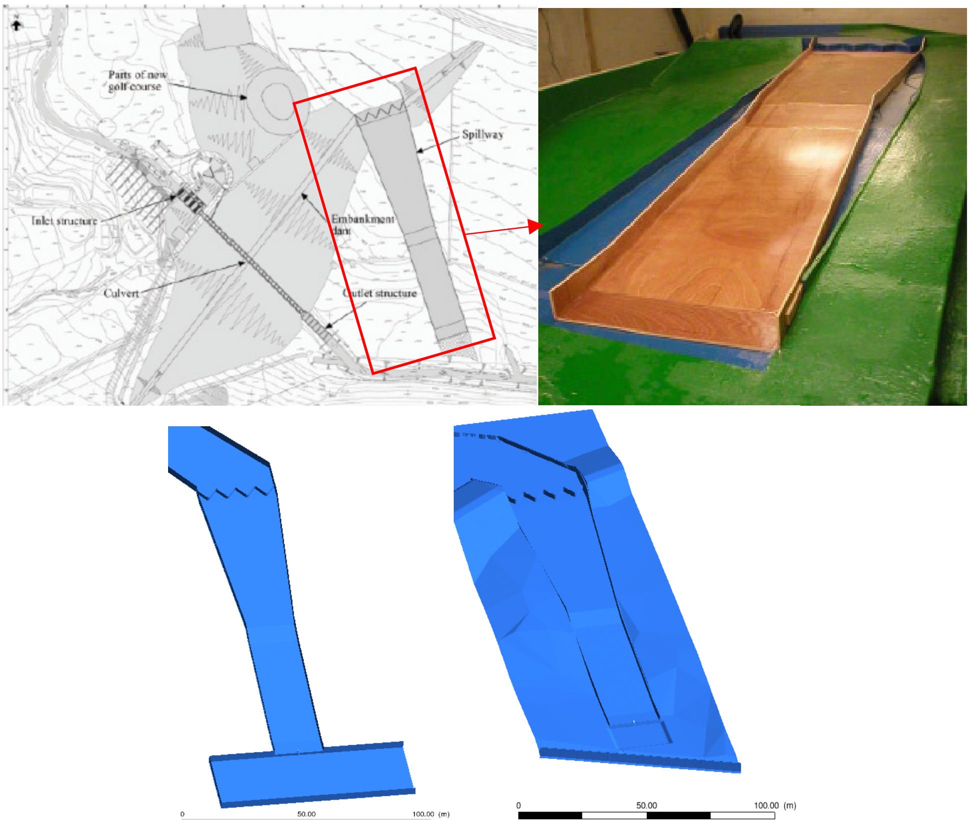

Figure 2. Layout of the flood storage reservoir with labyrinth weir and spillway (top left) from Brinded (2014) and model of the weir and spillway including surrounding terrain (top right). Intermediate and comprehensive geometries of spillway (bottom left and right).

Using the numerical implementations from the initial validation study, VOF simulations of a real hydraulic structure were undertaken. The scheme is composed of an embankment dam with a labyrinth weir and extended spillway to allow controlled discharge. The spillway channel has a length of approximately 150 m. The width of the labyrinth weir is 32 m which is the widest part of the spillway. 75 m downstream the weir the spillway channel narrows down to 20 m and increases in gradient. There are approximately 9 m of steep channel and then there is a further change in gradient to become gentler and constant until the end sill. Thus, the spillway has three different gradients along the channel which together with the complexity of the labyrinth weir makes it a challenging geometry to mesh and conduct CFD simulations on. In addition, the existence of a road embankment immediately downstream of the spillway creates an impoundment for the discharged water which will reflect in different levels of tail water created behind the road embankment. A hydraulic jump is expected at each of the different water levels. In order to confirm the structure design and inspect the hydraulic characteristics, hydraulic modelling is undertaken. A 1:25 physical scale hydraulic model was built based on Froude similarity. The experiments included 8 different flow rates with three different levels of tail water each. The layout of the scheme and a photograph of the physical scale hydraulic model of the spillway and surrounding terrain are shown on Figure 2.

The creation of the modelling geometry was possible given the availability of the full CAD drawings which include the detailed topography of the surrounding terrain. The approach taken to model this complex case is to first extract an intermediate geometry comprising the spillway and labyrinth weir only. The model is implemented and refined using the intermediate geometry with measurements of water depths and velocities in the spillway from the physical scale model. Decisions are then made on design cell size which will inform the meshing of the more comprehensive geometry. Modelling the comprehensive geometry allows the simulation of different tail water level conditions and an assessment of the capability of the model to predict the characteristics of the hydraulic jump. The creation of the modelling geometries is done using the Civil 3D toolbox in AutoCAD and the hexahedral meshing of the geometry is performed with the Ansys Workbench meshing application. Figure 2 shows the intermediate and the comprehensive geometries created for the CFD study. In order to capture impacts of scaling and appropriately validate the model, numerical modelling is first applied to the laboratory scale model and then to the full-scale prototype. CFD simulations are conducted in both Ansys Fluent and OpenFOAM to allow for solver comparison. Numerical results presented are primarily from the intermediate geometry and therefore the validation of the model is based on the flow behaviour within the spillway.

3.2 Scaled Intermediate Geometry

The physical scale hydraulic model was scaled using Froude number similarity, where the Froude number of the physical scale model and that of the prototype are the same. The model scale is 1:25 and by geometric similitude, the length ratio is equal to the model scale as shown in Eq. [1], where L_m is the characteristic lenght in the model and L_p the characteristic length in the prototype. Eq. [2] shows the velocity equivalence, where v_m is the water velocity in the model and v_p is the flow velocity in the prototype. Eq. [3] shows the flow rate correlation, where Q_m is the flow rate in the model and Q_p is the flow rate in the prototype. The time equivalence is shown in Eq. [4] where T_m is the time in the model and T_p is the real time.

$$S = \frac{L_p}{L_m} \qquad [1]$$

$$v_p = v_m\sqrt{S} \qquad [2]$$

$$Q_p = Q_m S^{5/2} \qquad [3]$$

$$T_p = T_m\sqrt{S} \qquad [4]$$

The intermediate geometry (originally constructed to be full-scale) was scaled down to the physical model dimensions (i.e. 25 times smaller), to run scaled CFD simulations. Numerical simulations for the scaled model have complete dynamic similitude and hence all the force ratios in the numerical model coincide with those in the hydraulic physical model. Mesh independence was investigated with the creation of three hexahedral meshes of average cell size 0.02 m, 0.008 m and 0.004 m with base inflation. These meshes had 645,397, 3.3 million and 6.7 million elements respectively. The mesh with cell size 0.008 m with base inflation (0.2 m with inflation in full-scale) was found to be of appropriate resolution for this case and numerical predictions did not present substantial changes with further refinement. VOF simulations were conducted in both Ansys Fluent version 14.5.7 and in OpenFOAM version 3.0.0. The RANS equations were solved using the k-ε turbulence model using a standard wall function and the PISO algorithm was employed to solve velocity-pressure coupling in both solvers. The volume fraction function was solved using the MULES scheme in OpenFOAM and the PLIC approach in Fluent. Time step was fixed in Fluent and equal to 0.001 s and adaptive in OpenFOAM with a restriction of the CFL number to 0.1.

The flow rate of 40 m^3/s was scaled accordingly and simulations were run using the design mesh (0.008 m with base inflation) in both solvers. A constant flow rate was implemented and run until an effective steady state was achieved. The same approach was implemented in the physical scale model experiments.

  / ISSN 1562-6865 (Online) - ISSN 1063-7710 (Print)

Figure 3 shows the experimental free surface and the numerically predicted free surface once the models reached steady state. Numerical results present accurate capturing of the complex configuration of cross waves generated by the labyrinth weir in both solvers.

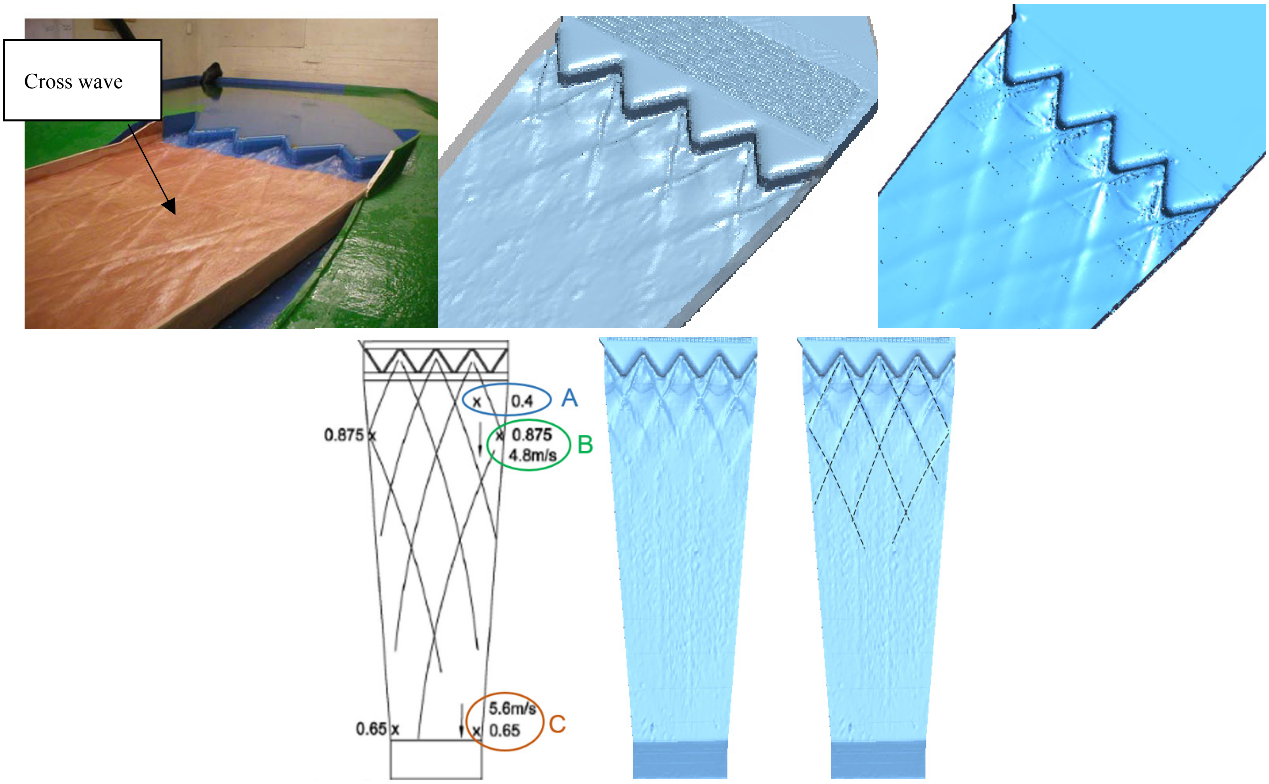

Figure 3. Free surface cross waves pattern in the experiment (top left), numerically predicted with OpenFOAM (top centre) and Fluent (top right). Measurement locations (bottom left) and free surface predictions with the drawing of the cross waves observed in the experiment and predicted by the model for a scaled flow rate of 40 m^3/s.

Point measurements of velocity and depth are available at several locations outlined in Figure 3. Experimental measurements presented are the highest values of depth and velocity measured in the experiment and have an error of ±0.025 m and ±0.05 m/s in the prototype respectively.

A full time history of the simulation is presented in Figure 4 which shows that the steady state is reached after around 90 s. Figure 4 shows the plot of experimental values of water depth along with OpenFOAM and Fluent predictions at location A and velocity magnitude predictions at locations B and C. The contours of volume fraction of the water phase are plotted on a plane perpendicular to the flow at the same coordinate point as where the numerical results are plotted. These are presented at the three locations with a line indicating the point where the numerical predictions were extracted and plotted on the time series graphs. Point A is located in between cross wave crests (as shown in Figure 3) immediately downstream of the labyrinth weir. There is good agreement between the numerical results predicted using OpenFOAM and the experimental measurements. Fluent results present slightly lower values of water depth to those from OpenFOAM and are also in reasonable agreement with values recorded in the experiment. It should also be noted that the maximum water depth was recorded in the experiments.

Location of experimental points B and C is shown in Figure 3. Point B coincides with the crest of one of the cross waves and point C is located just before the first change in gradient. Overall numerical predictions at the interface appear acceptably close to the maximum values of velocity measured in the experiment. In addition, the water volume fraction contours show a very accurate capturing of the flow features. The water depth and velocity predictions from Fluent and OpenFOAM are overall comparable.

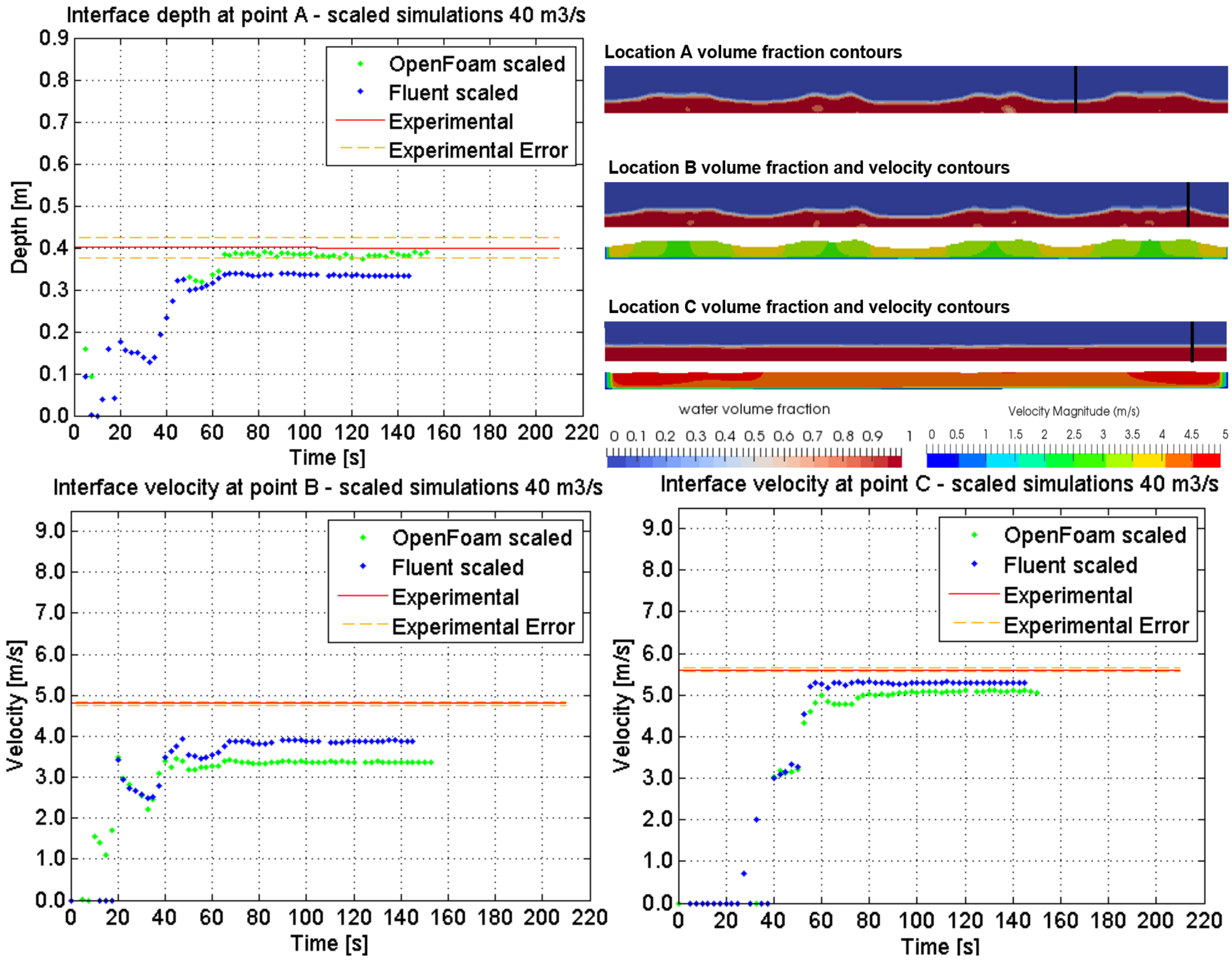

Figure 4. Experimental measurements and numerical predictions of water depth at location A (top left) and velocity magnitude at locations B and C (bottom) against time for a flow rate of $40m^3/s$. Cross sectional profile of water volume fraction and velocity contours at a plane passing through the three locations across the width of the channel (top right).

Point C is located next to the spillway wall at a point where there is a change in gradient. At this location the cross waves have settled and the water free surface profile shows a constant depth across the spillway. This situation is consistent in the numerical and the physical models as shown in the velocity graphs and in the volume fraction contour plots

Numerical results of depth and velocity at location C calculated with both solvers are slightly lower than the maximum values of experimental measurements. The presence of flat free surface allows a simple calculation of a mass balance at location C to check the reliability of the numerical predictions. Eq. 5 can be employed to determine the flow rate at location C:

$$Q = A \cdot v \qquad [5]$$

Where Q is the flow rate, A is the flow area and v is the average velocity. Using the OpenFOAM numerical predictions at location C, for a width of the channel of 20 m at point C, the flow rate is calculated as per Eq. 6:

$$Q = 0.4m \cdot 20m \cdot 5\frac{m}{s} = 40\frac{m^3}{s} \qquad [6]$$

Which is equal to the flow rate established in the inlet and hence conservation of mass is obeyed. Therefore, this calculation highlights the value of conducting numerical simulations to aid structure design and the need to inspect scale and measurement effects of the physical scale hydraulic models.

  / ISSN 1562-6865 (Online) - ISSN 1063-7710 (Print)

3.3 Full-Scale Intermediate Geometry

In the full-scale analysis, the exact same three meshes previously used in the scaled 7odeling were employed to model the real size structure. These had 0.5 m, 0.2 m and 0.1 m average cell size with a base inflation layer, which generated cell sizes of 0.1 m, 0.06 m and 0.04m on the z direction for each mesh respectively. Simulations using mesh with cell size 0.1 m indicate that there are only very minor differences to those using mesh with cell size 0.2 m which was therefore chosen as design mesh. The same simulations conducted in the scaled geometry using a flow rate of 40 m^3/s were conducted in full-scale using Fluent and OpenFOAM. It should be noted that the mesh used, for each solver, at the different scales has the same total number of cells when run at the two scales (it is a scaled version of the same mesh). Figure 5 shows the OpenFOAM and Fluent scaled and full-scale predictions of interface features and interface velocity contours once the model reached steady state using the design mesh. The free surface patterns appear to be different for the scaled and the full-scale simulations, presenting differences in shape and length. The crossing point of the cross waves is located at approximately 1 m further downstream in the full-scale cases compared to the scaled ones. This is shown in both solvers and indicated with an arrow on the free surface plots in Figure 5. Also, the full-scale waves structures are wider than the scaled ones. Figure 5 also shows the velocities are higher in the full-scale than in the scaled simulations, and this situation occurs in the results computed using the two CFD packages although is more pronounced in OpenFOAM.

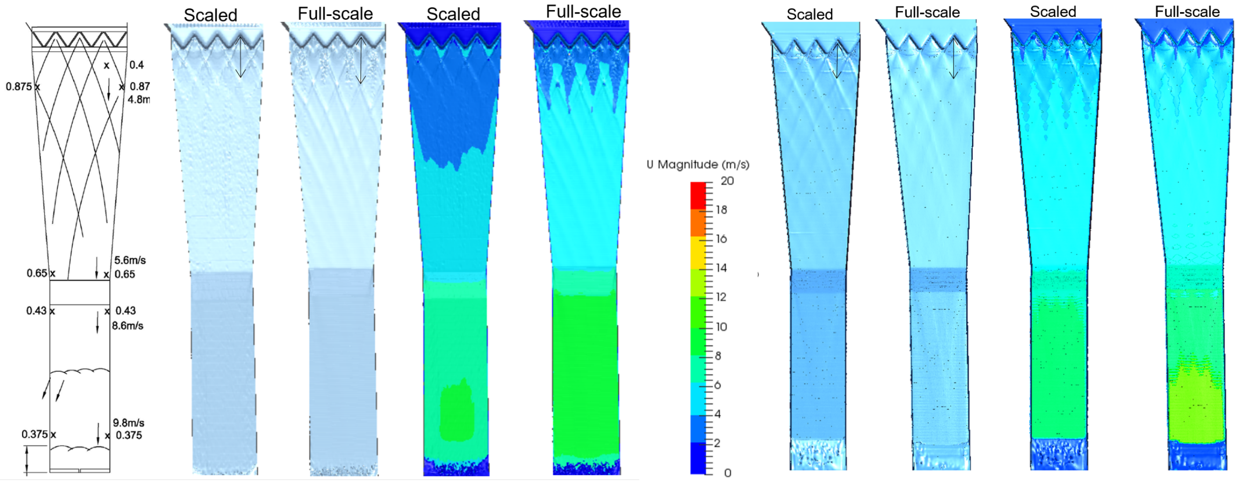

Figure 5. Physical scale model results (left), OpenFOAM (left of the legend) and Fluent (right of legend) predictions of the wave profiles and velocity contours at the water surface for a scaled and full-scale flow rate of 40 m^3/s.

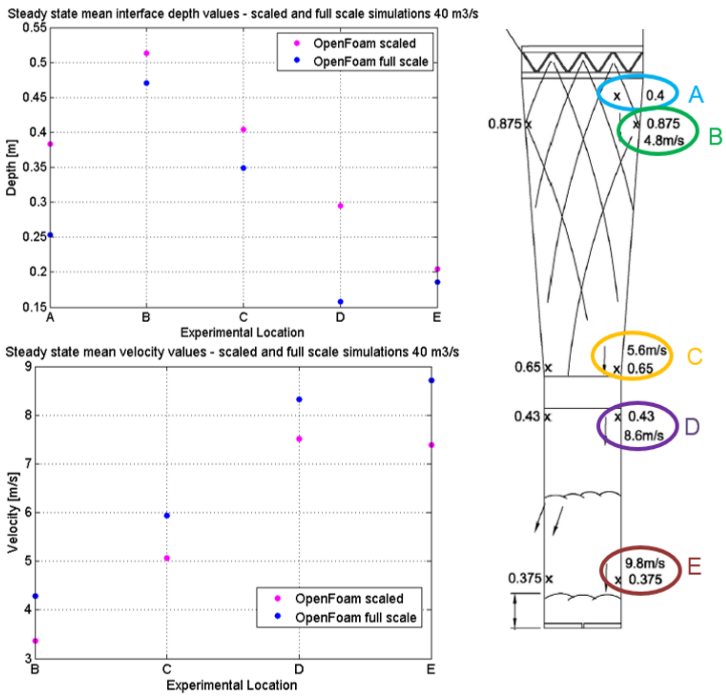

Figure 6. Scaled and full-scale OpenFOAM predictions of water depth (top) and velocity (bottom) and experimental loacations on the spillway for a flow rate of 40m^3/s.

Data from the full-scale simulations were plotted at the same locations as previously outlined with the scaled simulations and also at locations D and E, as shown in Figure 6. A graph showing the steady-state values of interface depth and velocity of the scaled and full-scale OpenFOAM simulations at the different measurement locations is shown in Figure 6. It is observed that scaled results present higher water depth and lower velocities than their full-scale equivalent. This implies the full-scale flow expected in the prototype is shallower and faster than that predicted in the physical scale model in all locations.

The scaled-down results present higher water depths and lower velocities than their equivalent full-scale results. It is calculated that full-scale results present an increase in velocity of approximately 17% and the decrease in water depth is estimated to be around 20% compared to the scaled results. This provides an indication as to the likely inaccuracies that could arise when using the physical model to estimate the full-scale flow behaviour.

3.4 Full-Scale Comprehensive Geometry

Preliminary VOF simulations with a relatively coarse mesh were conducted on the full-scale comprehensive geometry of the domain in Fluent and OpenFOAM. The main purpose of these initial simulations was to confirm the extracted geometry could be successfully meshed with acceptable quality for the VOF model to run in the two CFD codes (given the irregularity of the surrounding terrain and associate complexity of the geometry). A second purpose in conducting the initial VOF simulations using a preliminary coarse mesh was to be able to extract depth measurements to inform the process of establishing realistic downstream boundary conditions such that tail water levels could be maintained as in the experiments. Initial results (using a mesh with no inflation of 0.4 m cell size) show very realistic estimates of flow characteristics as well as reasonable agreement between Fluent and OpenFOAM predictions. Figure 7 shows the physical scale model in operation for a flow of 159.5 m^3/s with low tail water level and the equivalent simulation results of free surface characteristics and velocity contours predicted using OpenFOAM. Results with higher resolution of the comprehensive domain will be discussed in detail in the IAHR World Congress as will results from a full range of flow rates.

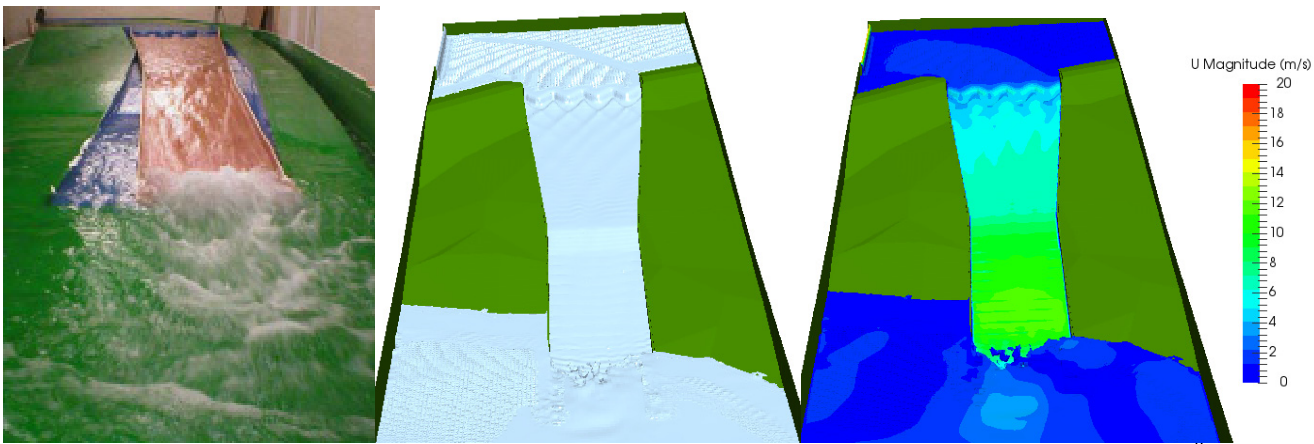

Figure 7. Photograph of the physical scale hydraulic model for a probable maximum flow of 159.5 m^3/s with a low tail water level and equivalent preliminary simulation results of free surface characteristics and velocity contours.

4 INITIAL CONCLUSIONS

This study forms part of a larger on-going work which is being conducted at the present time on evaluating the ability of VOF-CFD approaches to be used effectively for design of large-scale hydraulic infrastructure to identify best-practice and to better understand the limitations. A summary of key findings with the work conducted to-date can be outlined as follows:

- OpenFOAM and Fluent VOF-CFD simulations applied to a scaled spillway geometry using a mesh of cell size 0.008 m show overall accurate predictions for water velocity, depth and wave patterns observed in experiments. The complex configuration of the cross waves generated by the labyrinth weir is well reproduced even in the mesh of the lowest resolution both in scaled and full-scale simulations. The interface features become very well defined when using the meshes of intermediate resolution (0.008 m scaled and 0.2 m full-scale) and are in strong agreement with the experiments;
- In a comparison between full-scale and scaled simulations it is observed that for the same mesh the scaled simulations predict higher depths and lower velocities than the equivalent full-scale simulation. The increase in velocity when modelling full-scale is estimated to be around 17% and the decrease in water depth is approximately 20% for a flow rate of 40m^3/s. In addition, the free surface profile

between these present significant differences in shape and size (when comparing the full-scale simulations and scaled ones). This study highlights the importance and value in conducting CFD simulations to help understand any scaling differences that may be observed in a full-scale design compared with that observed in the physical scale hydraulic model. A detailed analysis investigating the scale effects of the hydraulic model is currently being performed and will be presented in the near future. However, results to date demonstrate that unlike the physical scale models, full-scale CFD simulations allow the prediction of many full-scale flow conditions which will be occurring at the prototype scale;

- A successful workflow and methodology has been developed to obtain the complex comprehensive modelling domain. An appropriate meshing strategy for the geometry has also been determined and successfully evaluated. Simulations using a reduced resolution mesh on a geometry that include the entire modelling domain have been undertaken in Fluent and OpenFOAM with the currently available results appearing promising. Results from a fully refined comprehensive mesh will be presented at the conference.

REFERENCES

Biscarini, C., Di Francesco, S. & Manciola, P. (2010). CFD Modelling Approach for Dam Break Flow Studies. *Hydrology and Earth System Sciences*, 14, 705-718.

Borman, D., Sleigh, A., Coughtrie, A. & Horton, L. (2014). Hydraulic Free Surface Modelling with a Novel Validation Approach. *9th South African Conference on Computational and Applied Mechanics*. Somerset West.

Brinded, P., Gilbert, R., Kelham, P. & Peters, A. (2014). Eller Beck Flood Storage Reservoir – The Challenges of Low Impact Flood Storage Design. *18th Biennial Conference of the British Dam Society* at Queen's University, 2014 Belfast, 348-360, ICE Publishing.

Chanson, H. (2009). Current Knowledge in Hydraulic Jumps and Related Phenomena. A Survey of Experimental Results. *European Journal of Mechanics* - B/Fluids, 28, 191-210.

Erpicum, S., Silvestri, A., Dewals, B., Archambeau, P., Pirotton, M., Colombié, M. & Faramond, L. (2013). Escouloubre Piano Key weir: Prototype Versus Scale Models. *Labyrinth and Piano Key Weirs II*, 65, Chatou, Paris, France.

Hieu, P.D. & Tanimoto, K. (2006). Verification of a VOF-based Two-Phase Flow Model for Wave Breaking and Wave–Structure Interactions. *Ocean Engineering*, 33, 1565-1588.

Hirt, C.W. & Nichols, B.D. (1981). VOF Method for the Dynamics of Free Boundaries. *Journal of Computational Physics*, 39, 201-225.

Oertel, M. & Bung, D.B. (2012). Initial Stage of Two-Dimensional Dam-Break Waves: Laboratory Versus VOF. *Journal of Hydraulic Research*, 50, 89-97.

Pfister, M. & Chanson, H. (2012). Scale Effects in Physical Hydraulic Engineering Models. *Journal of Hydraulic Research*, 50, 244-246.

Sarker, M.A. & Rhodes, D.G. (2004). Calculation of Free-Surface Profile over a Rectangular Broad-Crested Weir. *Flow Measurement and Instrumentation*, 15, 215-219.

Proceedings of the 37th IAHR World Congress
August 13 – 18, 2017, Kuala Lumpur, Malaysia

CHARACTERISTICS OF TOTAL PHOSPHORUS TRANSPORT IN MIDDLE REACHES OF YARLUNG ZANGBO RIVER

SHUQING NAN[1], JIA LI[2] and LINLEI ZHANG[3]

[1,2,3]State Key Laboratory of Hydraulics and Mountain River Engineering, College of Water Resource & Hydropower, Sichuan University, Chengdu 610065, PR China
647872662@qq.com; lijia@scu.edu.cn; zhanglinglei@hotmail.com

ABSTRACT

Phosphorus is one of the necessary nutrition elements for biological growth, and its transport and variation properties can reflect the evolution process of aquatic ecological environment. With the special geographic climate characteristics of the plateau river, Yarlung Zangbo River (YZR) is unique in rainfall, runoff, sediment transport, water temperature variation, etc., which facilitate the formation of the special dynamic process of total phosphorus (TP) transport. The results show that the TP concentration of single measurement for years in the main stream of YZR is within ND-0.32 mg/L, and the annual average value of various points is between 0.015 mg/L and 0.13 mg/L. In the time scale, the TP concentration curve has the unimodal shape in a year. The variation process is synchronous with the runoff and sediment. That is to say, the peak value appears in wet season and the valley value appears in dry season, and the maximum peak-to-valley ratio is 64, which is different from Huaihe River and other inland rivers. In the space scale, the TP concentration along the main stream of YZR mostly reaches to the maximum value with the confluence of Lhasa River. From the point of view of the transport flux level, the average monthly TP flux at different points varies from 0.036 to 0.143 kg/s. The Pearson correlation analysis shows that the TP concentration has a higher degree of correlation with other factors, and the correlation coefficient varies from 0.509 to 0.959. The correlation degree with suspended sediment discharge is the largest, and with flow rate is the second. The distributions of TP in particle state and dissolved state show that the TP in the main stream of YZR is mainly from the non-point source, and runoff and sediment are the main controlling factors of its transport.

Keywords: Yarlung Zangbo River, Hydrological parameter, TP, transport.

1 INTRODUCTION

Yarlung Zangbo River (YZR) is the longest plateau river in China and one of the rivers with the highest altitude in the world. As an important international river, YZR is originated from Jiemayangzong glacier, flows through India, Nangladesh, Bhutan, and other countries, and then flows into the Bay of Bengal in the Indian Ocean. According to the data in 2014, the total water resources of YZR account for 42.4% of that of Tibet. It is not only the major source of fresh water and the water vapor channel in Tibet (Zhang et al., 2009), but also the hydropower and water resources reserve of China (Zhang, 2011). YZR watershed gives birth to abundant and extremely special species, and is the important environmental background value area and the biodiversity conservation area of China and even the world (Zhang, 2000). However, the arctic-alpine natural environment leads to poor stability of the ecological environment and weak self-recover ability (Zhong et al., 2005). As the biogenic substance, P is one of the much-needed elements in the primary production of the ecological system. The concentration change of P can lead to the variation of the ecological environment. In recent years, the rising of TP concentration in YZR watershed is emerging (some scholars have started to study the P concentration in YZR): in tributaries, the P concentration in Nyang River varies from 0.005 mg/L to 0.010 mg/L, in Lhasa River and surface water in wetlands in the watershed from 0.0275 mg/L to 0.0781 mg/L (Zhou et al.,2014), and the TP concentration in the surface water of growing area in the small watershed of Lhasa River varies from 0.0149 mg/L to 0.127 mg/L (He et al., 2015), and the water quality can meet or is better than the class II standard of the *Environmental Quality Standards for Surface Water* (GB3838-2002); in main stream, the TP concentration is the highest among the inorganic nutrient salts, especially in the middle reach, the largest TP concentration reaches to 0.197mg/L, which is close to the class III water quality limit in GB 3838-2002 (Li et al.,2010). As an international river, the water resources development of YZR concerns the interests of many countries, the security and stability of border areas. So the development of YZR has a very important strategic position. The particularity of regional ecological system and geological location requires the in-depth study and explore of the environment effect in the water resources development of YZR watershed. Providing guiding principles and optimization modes for the adaptive utilization of water resources has practical significance for the development strategy of water resources development and protection in China.

Hydrological parameters have great influence on the P transport in water (Li et al., 2003). After surveying the TP distribution and hydrological characteristics of YZR watershed, the TP transport properties are studied, and these can provide bases for the water resources development, economic development and ecological environment protection.

2 STUDY AREA AND DATA

2.1 Study Area

YZR (shown in Figure 1) originates in the north of the middle of Himalayas in Tibet. Its total length in China is 2057 km. The river source is named as Jiemayangzongqu, the stretch at the downstream of Lizi is called Yarlung Zangbo River, and the stretch in India is called the Brahmaputra. The stretch from Jiemayangzong glacier to Lizi is the upper reach (268km), the stretch from Lizi to Pai Town is the middle reach (1340km), and the stretch at the downstream of Pai Town is the lower reach (496km). In the middle reach, five tributaries Dogxung Zangbo River, Nyangqu River, Lhasa River, Nyang River and Parlung Zangbo River feed into YZR. The densely populated and economically developed Xigazê Prefecture, Lhasa area and Nyingchi Prefecture are located at the intersections of YZR with Nyangqu River, Lhasa River and Nyang River.

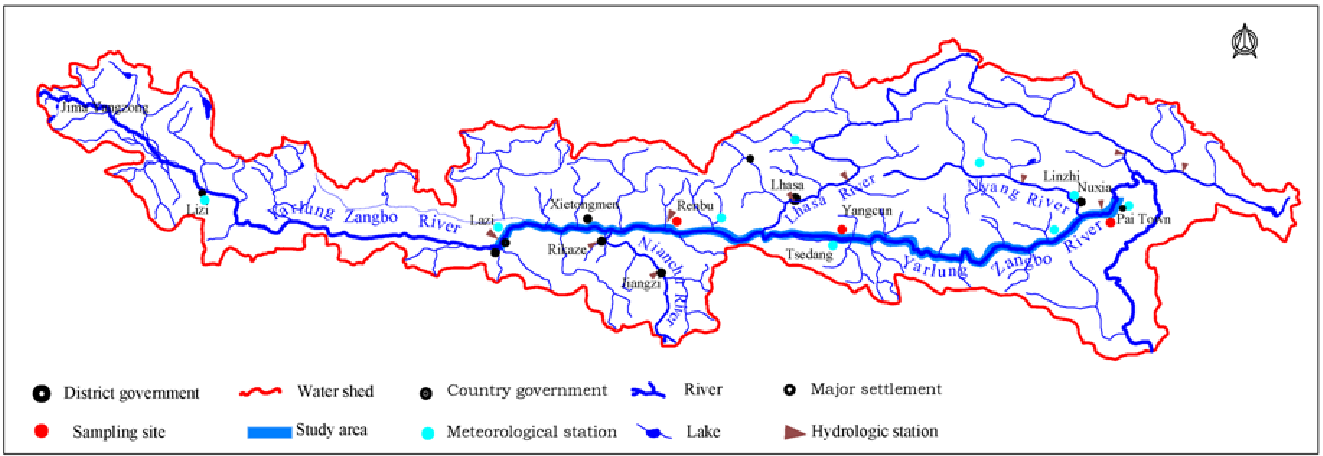

Figure 1. River system of YZR watershed

2.2 Data Source

The 1380 hydrology and TP concentration data within 2003-2016 were gathered from Changjiang Water Resources Commission of the Ministry of Water Resources. Correlation analysis was used.

3 RESULTS AND ANALYSES

3.1 Main Hydrological Parameters

Flow rate, sediment, water temperature and other hydrological parameters are the carrier and driving force of TP transport in water. It is of great important to study the influences of hydrological parameters to TP transport (Tian et al., 2016; Wang et al., 2009; Ernstberger, H. et al., 2004). The average monthly flow rate, water level, suspended sediment discharge, sediment concentration, water temperature and rainfall of Renbu Town, Tsedang Town and Pai Town from 2009 to 2013 (Renbu town does not have the condition to monitor the suspended sediment discharge and sediment concentration from October to the next April, so these data are lacking) were used to study the characteristics of hydrological parameters in the main stream of YZR, as shown in Figure 2 to Figure 4.

In the study section, the flow rate, water level, suspended sediment discharge, sediment concentration, water temperature, rainfall, and other hydrological parameters showed inter-annual cyclical change and annual phase change characteristics. The distribution within the year was uneven with a unimodal shape. The peak value appeared in wet season (June to September) and the valley value appeared in dry season (October to the next May). The distributions of hydrological parameters along the main stream were not consistent.

3.1.1 Flow Rate and Water Level

The valley of the research section on the main stream of YZR is narrow and wide alternatively like a string of beads. Due to the uneven uplift and extrusion by Himalayas, the wide valleys were formed in Shigatse, Qushui-Naidong, Gyaca and Mainling, and deep valleys were formed in Tuoxia-Yongda, Sangri, Lang County, and the big turn of YZR. Renbu Town, Tsedang Town and Pai Town are located at the first, second and fourth wide valleys. The largest widths of these valleys are 10 km, 3 km and 3 km, which lead to the inconsistency of the flow rate and water level distribution patterns (Chou, 1987; Wang et al., 2014).

In the space scale, the flow rate increased from upstream to downstream, and the water level increased first and then dropped. The five-year average flow rates of Renbu Town, Tsedang Town and Pai Town were 486 m^3/s, 912 m^3/s and 1806m^3/s, separately; and the five-year average water levels were 10.50 m, 13.61 m and 3.59 m, separately.

In the time scale, the changes of flow rates and water levels in different years were small. The maximum annual average flow rates of Renbu Town, Tsedang Town and Pai Town were 1.88 times, 1.63 times and 1.53 times of the corresponding minimum flow rates; the largest annual average water levels were 1.06 times, 1.03 times and 1.13 times of the corresponding lowest water levels; within one year, the maximum monthly average flow rates were 7.79 - 23.18 times, 7.11 - 14.75 times and 8.73 - 14.21 times of the minimum values; and the largest monthly average water levels were 1.05 - 1.45 times, 1.25 - 1.39 times and 3.31 - 5.31 times of the lowest values.

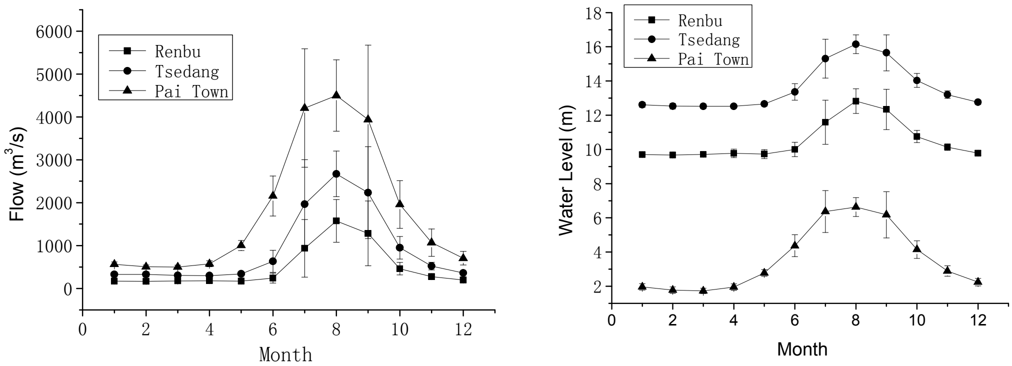

Figure 2. Hydrological parameters of YZR

3.1.2Suspended Sediment Discharge and Sediment Concentration

The soil erosion research of Tibet shows that the soil erosion area in the middle reach of YZR accounts for 69.9% of the total area. The sediment on the river bed mainly comes from gravitational erosion (debris flow and landslide), freeze-thaw erosion, water erosion and wind erosion (Wen et al., 2002; Jin et al., 2000). The water erosion and freeze-thaw erosion account for 45.57% and 47.19% of the total erosion area, respectively. The beaded valley in the middle reach on the main stream of YZR allows the sediment to deposit for a long time in the wide valleys. The largest thickness of the silt sediment in the wide valleys of Shigatse, Qushui-Naidong and Mainling were 800 m, 600 m and 400 m, separately. The paleomagnetic study shows that the age of sediment at the bottom of Xietongmen valley is about 800kaB.P. (Yu et al., 2012).

In the space scale, the suspended sediment discharge and sediment concentration decreased from upstream to downstream. The five-year average suspended sediment discharges of Renbu Town, Tsedang Town and Pai Town were / kg/s, 440 kg/s and 278 kg/s, separately; the five-year average suspended sediment discharges from May to October were 1959 kg/s, 858 kg/s and 540 kg/s; the five-year average sediment concentrations were / kg/m^3, 0.211 kg/m^3 and 0.084 kg/m^3; and the five-year average sediment concentrations from May to October were 1.69 kg/m^3, 0.36 kg/m^3 and 0.14 kg/m^3.

In the time scale, the suspended sediment discharges and the sediment concentrations varied greatly between different years and with one year: the minimum values of suspended sediment discharge and sediment content of Rendong County were 3.37 kg/s - 145 kg/s and 0.031 kg/m^3- 0.138 kg/m^3, separately, and the maximum values were 660 kg/s - 21100 kg/s and 0.623 kg/m^3 - 12.9 kg/m^3; the minimum values of Tsedang Town were 4.3 kg/s - 12.6 kg/s and 0.014 kg/m^3-0.034 kg/m^3, and the maximum values were 1190 kg/s-4240 kg/s and 0.538 kg/m^3-1.31 kg/m^3; the minimum values of Pai Town were 5.49 kg/s-8.92 kg/s and 0.006 kg/m^3-0.016 kg/m^3, and the maximum values were 482 kg/s-3270 kg/s and 0.121 kg/m^3-0.570 kg/m^3.

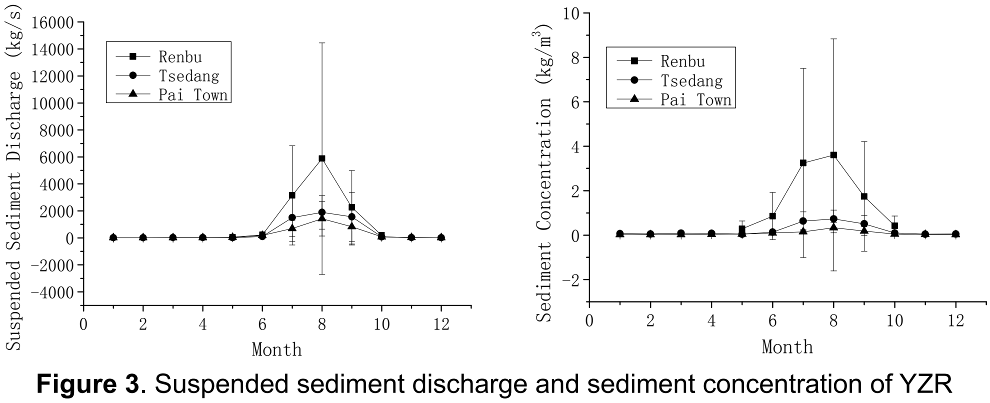

Figure 3. Suspended sediment discharge and sediment concentration of YZR

3.1.3Water Temperature and Rainfall

In the space scale, the water temperature in winter increased from upstream to downstream on the main stream of YZR and in summer increased first and then dropped. The five-year average temperature of Renbu Town, Tsedang Town and Pai Town were 9.00 °C, 10.0 °C and 10.1 °C, separately, and the temperature differences within a year are 15.4 °C, 16.8 °C and 11.7 °C. The altitudes of Renbu Town-Tsedang Town-Pai Town were 3950 m-3560 m-3000 m, the annual average temperatures were 6.8 °C-8.5 °C-9.6 °C, and the ratios of glacial melt water recharge to the river water recharge modes (precipitation recharge, groundwater recharge and glacial melt water recharge) were increasing from 18 % to 38 % (Liu, 1999), which made Pai Town river reach with the lowest water temperature in summer and the highest water temperature in winter.

In the space scale, the rainfall capacity reduced first and then increased; and in the time scale, the rainfall distribution in different months of the year was scattered. The five-year average rainfalls of Renbu Town-Tsedang Town-Pai Town were 374.5 mm, 329.7 mm and 493.3 mm, and the rainfalls from June to August accounted for 73.9%, 67.1% and 49.6% of the annual rainfall (five-year average). The distribution pattern of rainfall within the year was similar to that of the flow rate, water level, suspended sediment discharge, sediment concentration and water temperature.

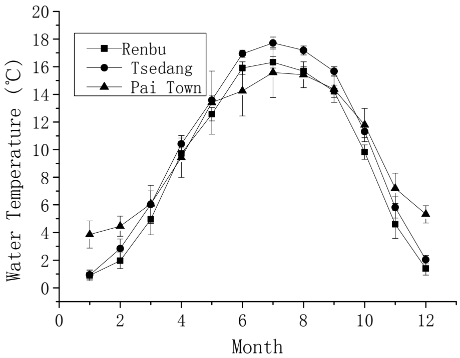

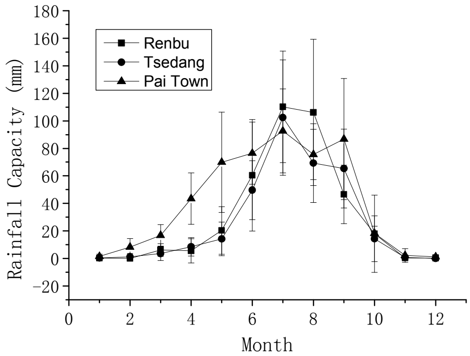

Figure 4. Water temperature and Rainfall capacity of YZR

3.1.4Correlation of Hydrological Parameters

The Pearson correlation analyses of flow rate, water level, suspended sediment discharge, sediment concentration, water temperature and rainfall showed that all parameters had significant correlations at 0.01 or 0.05, and the correlation coefficient varied from 0.562 to 0.994. The correlation coefficient of rainfall with flow rate, water level and suspended sediment discharge in Renbu Town-Tsedang Town-Pai Town were 0.794-0.860-0.785, 0.791-0.863-0.787 and 0.826-0.879-0.681, separately, which increased first and then reduced; and the correlation coefficient of rainfall with sediment concentration was 0.943-0.907-0.705, which increased. The correlation coefficients of rainfall with other hydrological parameters along the main stream of YZR were basically consistent with the distribution pattern of hydrological parameters, which indicated that rainfall was the main driving force for the distribution of flow rate, water level, suspended sediment discharge, sediment concentration, and other hydrological parameters.

3.2 Distribution of TP

The distribution of TP in YZR watershed in 2015 is listed in Table 1. In 12 months, the TP concentrations in 2.6% of the point locations within the watershed exceeded the water quality goal. The TP concentrations in the main stream of YZR, Parlung Zangbo River, Lhasa River and Nyang River were stable in the whole year, and reached to the class II water quality requirement in GB 3838-2002. The TP concentration in Nyangqu River was high, and 8.3% of the point locations cannot reach the water quality goal.

Table 1. TQ water quality status of the research area in 2015

River	Area represented by the point location	Water quality goal	Water quality status											
			Jan.	Feb.	Mar.	Apr.	May	Jun.	Jul.	Aug.	Sep.	Oct.	Nov.	Dec.
Nyangqu River	Water source reserve	II	II	ND	II	ND	II	ND	III	ND	II	II	II	ND
	Reserve zone	III	II	II	II	III	ND	III	III	III	V	II	II	II
	Shigatse City	III	II	II	II	III	II	III	III	III	V	II	II	II
	Downstream of Shigatse	III	II	II	II	III	III	III	III	III	IV	III	II	III
Lhasa River	Water source reserve	II	II	ND	II	ND	II	ND	II	ND	I	ND	I	ND
	Upstream reserve zone	II	II	II	II	II	II	II	II	II	II	II	II	II
	Upstream of Lhasa	III	II	II	II	II	II	II	II	II	II	II	I	II
	Lhasa City	II	II	II	II	II	II	II	II	II	II	II	II	I
Nyang River	Water source reserve	II	II	ND	I	ND	I	ND	II	ND	II	ND	I	ND
	Upstream of Nyingchi	II	ND	II	ND	II	ND	II	ND	II	ND	II	ND	III
	Upstream of Bayi Town	II	II	ND	II	ND	II	ND	II	ND	II	ND	II	ND
	Bayi Town	II	II	II	I	II	I	II	II	II	II	I	I	I
	Downstream of Bayi Town	III	II	II	II	II	I	II	III	III	II	II	I	I
Parlung Zangbo River	Natural reserve	II	ND	ND	ND	II	ND	II	ND	ND	ND	ND	ND	II
main stream of YZR	Upstream	II	ND	II	ND	II	ND	II	ND	II	ND	II	ND	II
	Middle and downstream	II	II	II	II	II	II	II	II	II	II	II	II	II

3.2.1Time Distribution Pattern of TP

From the point of view of distribution within a year, the TP concentrations of the main stream of YZR, Parlung Zangbo River, Lhasa River and Nyang River were low and barely changed, and mostly reached to the class II water quality requirements in GB 3838-2002, and some sections in Nyang River and Lhasa River even reached to the class I water quality requirements; the TP concentration in Nyangqu River changed greatly with low concentration from October to the next March, high concentration from April to September, and highest concentration from July and September, which were consistent with the distributions of rainfall and sediment concentration of YZR watershed. However, from the point of view of many years distribution, the extreme values of daily precipitation within a year were random from June to September, which overlapped with the high concentration time of TP, which was also similar to the yearly distribution pattern of Little Arkansas River, Hudson River (Qin et al., 2014; G, G. Lampman et al., 1999). However, it was different with low altitude rivers in China, such as Yangtze River and Huaihe River: the sections exceeding the water quality goal in Yangtze River and Huaihe River in January and September of 2015 accounted for 31.1% and 12%, 50% and 0 (Yangtze River Water Resources Protection Bureau, 2015; Huai Water Resources Protection Bureau, 2015).

The peak value of TP concentration in YZR watershed was in Nyangqu River, which also had the largest change of TP concentrations in the small watershed of Nyangqu River. The distribution of TP concentrations in different months in the section of Shigatse on Nyangqu River over the years (2003-2016) was studied to find out the variation pattern and the cause of formation. According to GB 3838-2002, the monthly TP concentration was used to classify the water quality, and Fig 5. (a) shows the frequencies of different water qualities in different months; and by selecting the data from July to September from 2003 to 2016, Fig 5.(b) shows the water quality in different years (the water quality of III, IV, V and V- are represented by 3, 4, 5 and 6, while 0 represents the missing of data). It can be seen from Fig 5.(a) that the time that TP water quality meeting the class II and class III water quality standard was mainly from October to the next February, and from March to July, and the occurring frequencies were 0.62-0.73 and 0.54-0.75, separately; while the time meeting the class IV, class V and class V- was in August and September, and the occurring frequencies were 0.09-0.25, 0.09 and 0.25-0.27, which were consistent with the distribution patterns of rainfall, flow rate and other hydrological parameters of the small watershed of Nyangqu River in 2015. This indicated that rainfall, flow rate and other hydrological parameters play a key role in the variation of TP. It can be seen from Fig 5.(b) that the TP did not have obvious lasting water quality changes from July to September over the years, which was caused by the lack of obvious changes of the ecological environment, water loss and soil erosion of Nyangqu River watershed over the years.

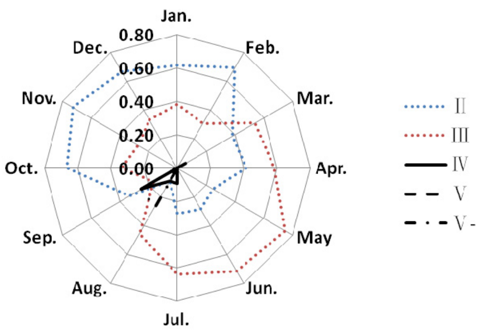

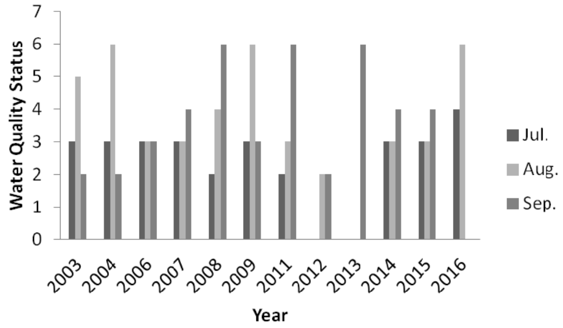

(a) (b)

Figure 5. Distribution of TP water qualities in the section of Shigatse on Nyangqu River

3.2.2Spatial Distribution Pattern of TP

In the space scale, the TP concentrations in the main stream of YZR, Parlung Zangbo River, Lhasa River and Nyang River were basically stable and can reach to the class II water quality in GB 3838-2002; the TP concentration in Nyangqu River was high; the TP concentrations varied in different functional areas in the small watersheds of Nyangqu River, Lhasa River and Nyang River, and the TP concentrations in the water source reserve in the densely populated Shigatse and Bayi Town were relatively high. The spatial distribution pattern of TP in YZR watershed depends on the topography, economic structure, and other situations of YZR watershed: the soil erosion area in the midstream area of YZR accounted for 69.9% of the total area, and the water erosion area accounted for 46% of the total eroded area; Shigatse and Lhasa are the main agricultural areas of Tibet, more than 60% of the fertilizers is used in these areas, and the proportion of compound fertilizers is increasing and has been more than 35% (Hou et al.,2010); The small watershed of Nyangqu River has the highest altitude and the worst soil loss and water erosion, but it is the most developed area of husbandry. The small flow rate and small environmental capacity of TP makes the small watershed of Nyangqu River the most affected one.

The Pearson correlation analysis showed that the TP concentration had high correlation degree with other factors, and the correlation coefficient varied from 0.509 to 0.959. The correlation degree with the suspended sediment discharge was the highest, and flow rate took the second place. The research results of “Variation of water temperature and sediment in YZR under runoff regulation and the response of P transport” show that the TP is mainly in particle state and dissolved state in wet and dry seasons, the TP concentration in wet season is 20 times of that of dry season, and the TP concentration in soils at both banks of the watercourse is much higher than that in the sediment, which indicates that the source of TP in the water of YZR basin is mainly non-point source (non-point source in wet season and point source in dry season) (Pu et al., 2017; Mao et al., 2015).

3.3 Transport Flux of TP in the Main Stream of YZR

The TP concentration of single measurement for years in the middle reach of the main stream of YZR was within ND-0.32 mg/L, and the annual average value of various points was between 0.015 mg/L and 0.13 mg/L. In the time scale, the TP concentration curve had the yearly unimodal shape in Renbu Town and Tsedang Town. The variation process was synchronous with the rainfall, runoff and sediment. That is to say, the peak value appeared in wet season and the valley value appeared in dry season, and the maximum peak-to-valley ratio was 64, while the distribution pattern in Pai Town requires further study. In the space scale, the TP concentration along the main stream of YZR reached to the maximum value with the confluence of Lhasa River.

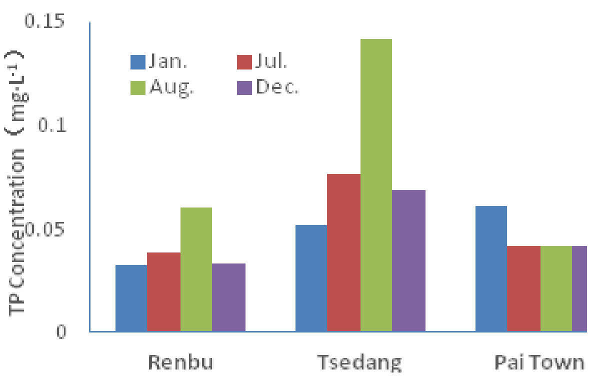

Figure 6. TP Concentration in YZR

The transport flux of TP can be calculated by the following equation:

$$F=10^{-3}\cdot C\cdot Q \quad [1]$$

where F is the transport flux of TP (kg/s), C is the concentration of TP at various sections (mg/L), and Q is the runoff of that section with the corresponding TP concentration (m^3/s).

The transport fluxes of TP in Renbu Town, Tsedang Town and Pai Town were 0.036 kg/s, 0.143 kg/s and 0.107 kg/s, separately, which were much lower than other rivers (Qin et al., 2014; Hou et al., 2010).

4 CONCLUSIONS

The research results show that the hydrological parameters in the research area on the main stream of YZR are affected by the special geographical climate and other factors. In the time scale, the flow rate, water level, suspended sediment discharge; sediment concentration; water temperature and rainfall couple with each other and show some specificity. The annual and inter-annual distributions are uneven, but the pattern is consistent: high value in July to September and low value in October to the next April. In the space scale, the flow rate and rainfall increase, the water level and water temperature increase first and drop later, while the suspended sediment discharge and sediment concentration reduce. Except the rising of TP concentration in the middle and lower reaches of Nyangqu River in wet season, the TP concentration in YZR watershed maintains at the class II water quality GB 3838-2002. In the time scale, the TP concentration in YZR watershed is consistent with the distribution patterns of flow rate, sediment concentration, rainfall and other hydrological indicators in a year; in the space scale of the watershed, it is closely related to the land use type, and the peak value in the watershed appears at Nyangqu River watershed with the most developed agrarian economy; from the point of view of small watershed in tributaries, the TP concentration in the water source reserve is lower than other areas, and the peak value appears in the densely populated and economically developed areas, which indicates that the distribution of TP is related to the population density, economic development level, and other factors. The distribution of peak values of TP concentration in the section of Shigatse in Nyangqu River over the years shows that there are no obvious and lasting water quality changes, which is caused by the lack of obvious changes of the ecological environment, water loss and soil erosion of Nyangqu River watershed over the years. The transport flux of TP in the main stream of YZR is 0.095kg/s, which is much lower than rivers in low altitude. The TP concentration and the distribution of P in particle state and dissolved state show that the TP in the main stream of YZR is mainly from non-point source, and runoff and sediment are the main controlling factors of TP transport.

This research is based on the distribution and transport properties of TP in space scale and time scale in YZR watershed over the years. The cause of formation is analyzed in the aspects of ecological environment and social economy. It can assist further theoretical study and practical exploration of the environment effect by water resource development in YZR watershed, and it can also provide technical support for the economic development, water resources development and ecological environment protection of YZR watershed.

ACKNOWLEDGMENTS

This work is funded by the National Natural Science Foundation of China (No. 91547211) and the National Key R&D Program of China (No. 2016YFC0502200).

REFERENCES

Changjiang River Water Resource Bulletin (January to December in 2015). Yangtze River Water Resources Protection Bureau.

Chou, C.J. (1987). A Discussion on the Middle Yarlung Zangbo River Paternoster Characteristics. Journal of Central China Normal University, 21(4), 611-618.

Ernstberger, H., Edwards, A. and Balls, P. (2004). The distribution of phosphorus between soluble and particulate phases for seven Scottish East Coast rivers. Biogeochemistry, 67(1), 93-111.

He, J.F., Liu, Q.H., Qiu, C. and Da, W. (2015). Research of Nutrient and Heavy Metal Change in Lhasa Typical Agricultural Basin. Tibet Journal of Agricultural Sciences, 37(1), 42-44, 36.

Hou, Y.H., Dawa, Z.M. and Chen G.H. (2010). The Situation and Countermeasure of Using Chemical Fertilizer in Tibet. Tibet Journal of Agricultural Sciences, 32 (4), 43-46.

Huai River Water Resource Bulletin (January to December in 2015). Huai Water Resources Protection Bureau.

Jin, H.L., Dong, G.R. and Zhang, C.L. (2000). Deposition Features and Causes of Loess in Yarlung Zangbo River Valley Area. *Journal of Desert Research*, 20(1), 14-19.

Lampman, G.G., Carazo, N.F. and Cole, J.J (1999). Spatial and temporal patterns of nutrient concentration and export in the tidal Hudson River [J]. *Estuaries*, 22, 285-296.

Li, H.J., Zhang, N. and Lin, X.T. (2010). Spatio-Temporal Characteristics of Yarlung Zangbo River in Tibet. *Journal of Henan Normal University (Natural Science)*, 38(2), 126-130.

Li, Y.T., Zhang, S.G. and Li, S.Z. (2003). Influence of Yellow River Sediment on Water Quality Parameters. *Advances in Science and Technology of Water Resources*, 23(1), 11-13, 34.

Liu, T.C. (1999). Hydrological Characteristics of Yalungzangbo River. *Acta Geographica Sinica*, 54 (supplement), 157- 164.

Pu, X.C., Yang, Y.J., An, R.D., Huang, W.D. and Li, J. (2017). The Spatial-temporal distribution of different species of phosphorus in the Yarlung Zangbo (Brahmaputra) River [C]// Proceedings of World Environmental & Water Resources Congress 2017. Wuhan, [poster].

Qin, J., Lou P., Lu W., Yang F. and Sun X.L. (2014). Spatiotemporal Distribution of Agricultural Non-point Source Pollutants in the Little Arkansas River Watershed in the United States. Chinese Agricultural Science Bulletin, 30(5), 235-241.

Mao, Z.P., Yang, S.Z., Wang, L. and Cheng, D.S. (2015). A review of phosphorus retention in river ecosystems. Journal of Hydraulic Engineering, 64(5), 515-524.

Shen, Z.L. (2006). Phosphorus and Silicate Fluxes in the Yangtze River. Acta Geographica Sinica. 61(7), 741-751.

Tian, Q., Li, L.Q., Ou, F.P., Lu, S.Y., Wang, C.M. and Zhang, Y. (2016). Temporal-spatial Distribution and Speciation of Nitrogen and Phosphorus in Dongting Lake. Journal of Hydro ecology, 37(3), 19-25.

Wang, W.L., Chen, J.F., Jin, H.Y., Liu, J.D., Jin, M.M., Lu, Y., Xue, B., Li, H.L. and Wang, K.(2009). The distribution Characteristics and Influence Factors of Some Species Phosphorus in Waters of the Changjiang River Estuary in summer. Journal of Marine Sciences, 27(2), 32-41.

Wang, Z.Y., Yu, G.A., Wang, X.Z. and Liu, L. (2014). Impact of Techtonic Motion on Sediment Storage and Morphology of Yalu Tsangpo Valley. Journal of Sediment Research, 2,1-7.

Wei, J.F., Chen, H.T., Liu, Y.L., Shan, K., Yao, Q.Z., He, H.J. and Yu, Z.G. (2011). Phosphorus Forms of the Suspended Particulate Matter in the Yellow River Downstream During Water and Sediment Regulation 2008. Environmental Science, 32(2), 368-374.

Wen, A.B., Liu, S.Z., Fan, J.R. and Zhu, P.Y. (2002). Current Change on Sedimentation and Control Its Method in Middle Yalungtsangpo River. Journal of Soil and Water Conservation, 2002,16(6), 148-150.

Yu, G.A., Wang, Z.Y., Liu, L., Hang, H.W. and Gong, T.L. (2012). Drainage network and fluvial morphology features of Yarlung Tsangpo River under the Impact of Neotectonic Movement. Advance in Water Science,23(2), 163-169.

Zhang, T.H. (2000). Emphasis of Tibet Environmental Protection with Features of Plateau Environment. *Local Environment*, 1, 27-29.

Zhang, T.Y., Xing, Y.Q., Zhang, Z., Zhao, H.Y., Cao, X.Q. (2009). The Effect Analysis of Yalu Tsangpu River Water Vapor Channel and Its Development Assumption. Areal Research and Development, 28(1), 120-123.

Zhang, X.X. (2011). Spatial-Temporal Evolutional Laws of the Key Hydrological Elements in Yarlung Zangbo River Basin. Beijing Forestry University.

Zhong, C., He, Z.Y. and Liu, S.Z. (2005). Evaluation of Eco-environmental Stability in Tibet. Scientia Geographica Sinica, 25(5), 573-578.

Zhou, C.N. and Pang, G.(2014). Analysis and Evaluation of water Quality of Plateau Wetlands in Lhasa River Basin. Guizhou Agricultural Sciences, 42(9), 249-252.

STEREO-PARTICLE IMAGE VELOCIMETRY (S-PIV) STUDY OF FLOW AROUND A COMPLEX BRIDGE PIER (CBP)

PRIYANKA GAUTAM(1), THEKKILAKKATTU IYPE ELDHO (2), BIJOY SINGHA MAZUMDER (3) & MANASA RANJAN BEHERA (4)

(1,2,3,4) Department of Civil Engineering, Indian Institute of Technology Bombay, Mumbai, Maharashtra, India
priyankagautam@iitb.ac.in, priyankagautam.ce@gmail.com

ABSTRACT

The objective of this paper is to study the velocity field around a Complex Bridge Pier (CBP) with elliptical shape of pile cap, through experimental research using Stereo-Particle Image Velocimetry (S-PIV). The complex bridge pier model consisted of three different components, viz. a cylindrical column resting on an elliptical shaped pile cap covering a 2x2 array of cylindrical piles. The three components of CBP are exposed to the flow in such a way that the contribution of each component could be obtained in generating the vortex system. Time averaged flow velocity U, V and W in the x-, y- and z- direction respectively are obtained from the PIV images and analyzed to understand the flow hydrodynamics around a CBP. Results shows that each of the three components of a CBP have individual effects on the flow pattern. The flow structure is vortical on the upstream of the CBP (below the pile cap) and downstream of the CBP (at the tail of pile cap) due to interfaces of different intensity velocity layers separating from the 3 pier components. On the upstream of CBP, the effect of pile cap can easily be seen in the form of a low velocity region around the nose of the pile cap. The effect of each component of CBP on the flow field is studied to identify the high gradient regions around the pier which leads to scour.

Keywords: Particle image velocimetry (PIV); complex bridge pier (CBP); hydrodynamics; mean velocity; 3-D flow field.

1 INTRODUCTION

A complex bridge pier is an assembly of different structural components, i.e. a pier column built on a pile-cap or footing, supported by a number of piles (Coleman, 2005), also known as pile foundation. Because of the geotechnical, structural and economic considerations, they are preferred over uniform piers to be constructed in rivers these days. Over its lifetime, the different components of a complex pier gets revealed to the flow because of varying amount of sand aggradation or degradation around the pier assembly, posing a challenge to hydraulic engineers to calculate maximum scour depth around such pier. The extreme situations occurs when all the three components of the complex pier gets exposed to the flow. In such cases, a comprehensive understanding of the flow field aids in the accurate prediction of the scour magnitude. Hence, it is particularly crucial to evaluate the vortex pattern as a result of the interaction of flow with the different components of a complex pier.

The complications in the local scouring process at complex bridge pier locations are because of the interaction of flow structures (i.e., down flow and horseshoe vortex) with the three components of the complex pier, generating new vortex structures, as witnessed by Beheshti and Ataie-Ashtiani (2010). This augments to the difficulty in predicting local scour depth at these complex pier structures. Research on scouring at complex bridge piers is comparatively newer than on single uniform piers, with lesser number of studies present in the literature and thus demanding additional research on the flow changes occurring around complex bridge piers (HEC-18, 2001). Identification of extreme turbulence zones around a complex pier may aid in better design of the pier and also reduction in scour.

To the best of author's knowledge, few studies have examined the flow and turbulence field around CBPs and PIV studies are only done for simple circular cylinder mostly. Some studies have been done for the calculation of local scour-depth (e.g. Gautam et al., 2016; Akib et al., 2014; Melville et al., 2006) around rectangle shaped pier and pile-cap or rectangle with round ends and fewer for investigating the flow patterns around a complex bridge pier structure (e.g., Beheshti and Ashtiani, 2016; 2010). Oruc et al. (2015) investigated the passive control of water flow downstream of a circular cylinder with 50 mm diameter, experimentally using particle image velocimetry (PIV) technique. Johnson and Ting (2003) studied flow around a circular pier on a smooth bed using Stereo PIV. Melville et al. (2006) gave a methodology to predict local scour depth around a CP to identify the relative scouring capacity of the various elements of CP and the evolution of scouring phenomenon occurring for variable pile-cap elevations. Over its lifetime, the different elements of a CP get revealed to the flow because of varying amount of sand aggradation or degradation

  / ISSN 1562-6865 (Online) - ISSN 1063-7710 (Print)

around the pier, and it is a challenge for hydraulic engineers to calculate maximum scour depth around such pier. The extreme situation occurs when all the three elements of CP gets exposed to the flow. Comprehensive understanding of the turbulent flow aids in the accurate prediction of the scour magnitude. Hence, it is particularly crucial to evaluate the complex flow pattern as a result of the interaction of flow with the different elements of a CP. Through experiments, Beheshti and Ashtiani (2010) investigated the three-dimensional turbulent flow field around a rectangular complex bridge pier (with rectangular pile-cap) placed on a fixed rough bed with the aid of an Acoustic Doppler Velocimeter (ADV). In their setup, they exposed all the components of the pier (column, pile-cap and piles) to the incoming flow. They found out the governing features of the flow around the pier which are responsible for the scouring process around a complex pier. The main reasons being the constricted flow below the pile-cap and towards the piles, a strong downward flow along the sides of the pile-cap in the upstream region of the pier and a vortex flow behind the pile-cap. Few researchers have conducted experiments to study scour around complex bridge piers, with varying shape of the pier structure, flow conditions as well as at different pile-cap elevations.

The primary objective of the present study is to analyze the mean flow field around a complex pier with elliptical shape of pile cap using whole flow field measuring technique known as Particle Image Velocimetry (PIV). Unlike ADV which takes point velocity measurements, PIV is capable of taking velocity measurements in the defined flow field all at the same time.

2 EXPERIMENTAL SETUP & PROCEDURE

2.1 Flume

All the experiments were carried out in the Hydraulics Laboratory in Department of Civil Engineering at Indian Institute of Technology (IIT) Bombay, India. The experimental flume was 8.4 m long, 0.31 m wide and 0.6 m deep horizontal, non-tilting flume (Figure 1).

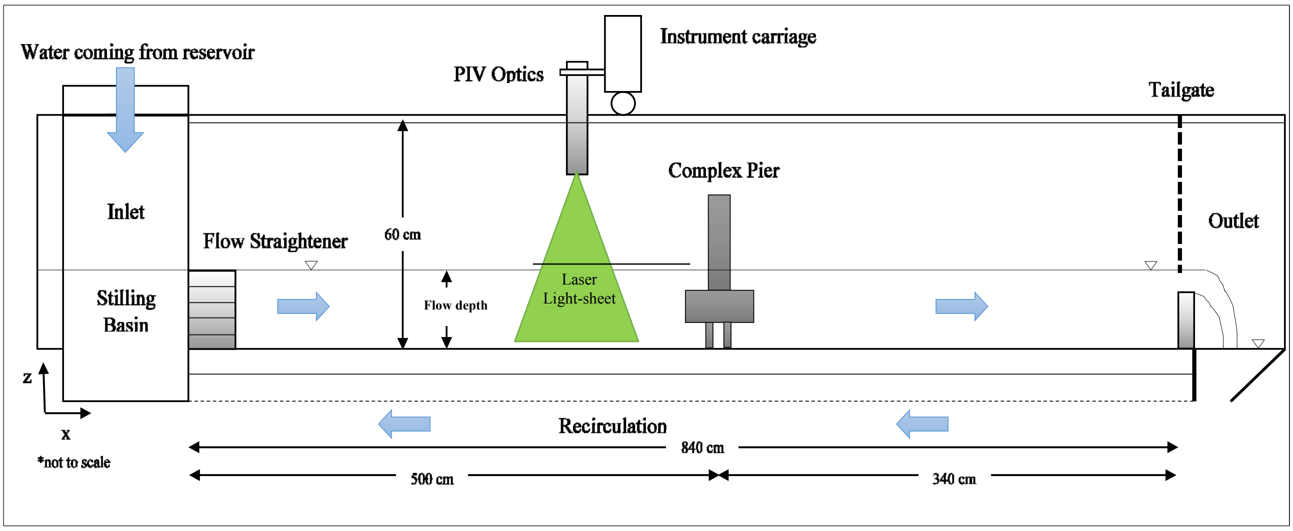

Figure 1. Schematic diagram of the experimental setup.

The sidewalls and bottom of the flume were made of transparent Perspex glasses to facilitate visual observation of the flow. The water was lifted from the main reservoir to a constant head reservoir (inlet tank) by a centrifugal pump and recirculated in the flume. In the entry zone of the flume, stilling grids and a flow straightener was provided for damping the flow disturbances leading to vortex free uniform flow distribution in the flume. The pier was placed on the flat bed at a distance of 5.0 m away from the flume inlet, to assure fully developed flow in the test section. Desirable normal flow depth over the bed was obtained by an adjustable tailgate located at the downstream end of the flume. A variable frequency driver (VFD) was used to control the rpm of the pump motor and obtain the desired discharge accurately. The flow rate was monitored using an Ultrasonic Flow-meter (UFM) attached to the pump. A movable carriage was provided on the rails of the flume to clamp the PIV sheet optics over the test section.

2.2 Complex Pier Model

The complex pier model used in this study was an assembly of various components, consisting of a column, a pile cap and a group of piles, as constructed in field. It was specifically designed as a cylinder resting on an elliptical pile cap supported on a 2x2 pile group (all built in Perspex). The details and dimensions of CBP are given in Figure 2 and Table 1.

The purpose of studying an ellipse shaped pile cap was to study its' contribution in streamlining the flow and hence reducing the scour around it. Till date, various researchers (Moreno et al., 2015; Akib et al., 2014; Ferraro et al., 2013; Melville et al. 2006) have studied rectangular, circular and oblong shapes of pile caps to evaluate their scouring potentials. Till date, only Ashtiani and Beheshti (2016; 2010) have attempted to study the hydrodynamics of flow around a complex bridge pier with rectangular pile cap.

The longitudinal axis of the complex pier (with respect to the pile cap length) was aligned with the flow direction and all the components of the pier were exposed to the flow. The pier model was carefully installed (vertically and centrally) in the test section of the flume at 5.0 m distance from the flume inlet. The approach flow depth was adjusted using a tail gate installed at the end of the flume. The experiments were performed for various discharges ranging between 0.006 m^3/s to 0.021 m^3/s, Reynolds number (Re, based on flow depth) ranging between 19,000 to 67,000.

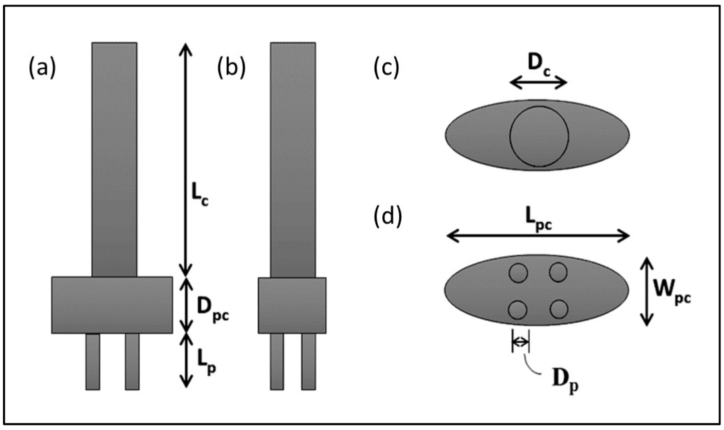

Figure 2. Schematic diagram of complex pier: (a) side view; (b) front view; (c) top view; (d) bottom view.

Table 1. Complex pier definition and dimensions.

Parameter	Definition	Dimension (*cm*)
L_c	Height of cylindrical column	15
D_{pc}	Height of pile-cap	5
L_p	Height of pile	5
D_c	Diameter of column	3
D_p	Diameter of piles	1
L_{pc}	Length of pile-cap	12
W_{pc}	Width of pile-cap	4

2.3 PIV System

A Stereoscopic PIV system from *Dantec Dynamics* was used to capture the images in a plane for three-dimensional velocity derivation (*http://www.dantecdynamics.com/particle-image-velocimetry). The system included a double pulsed Nd:YAG laser (1200 mJ/pulse) with minimum pulse duration of 4 ns, laser light sheet optic, two Nikon CCD (Charged Coupled Device) cameras (resolution 2048 x 2048 pixels), a laser pulse synchronizer, an Intel (R) Xeon (R) CPU E5-1680 V3@3.20GHz Computer, PIV software (Dantec Dynamics), and a three-dimensional computer operated traversing system (1000 mm travel along each axis). The seeding of the flow was done using 10 µm diameter Silver coated hollow glass spheres (S-HGS).

2.4 Experimental Procedure

The experiments were conducted for different discharges ranging from 0.006 m^3/s to 0.021 m^3/s. The results are presented here only for moderate Reynolds number (discharge= 0.012 m^3/s; Re= 39,000). The velocity vector fields around the pier were measured at 3 different vertical planes (1 on the upstream of pier, 1 with pier in the middle of the plane and 1 on the downstream of pier). For illuminating the planes of measurement, the Laser light sheet was emitted perpendicular to the flow from the top of the flume and adjusted over the mid-plane of the flume. To make sure that the laser light sheet coincided perfectly with the calibration plane, a transparent Graph sheet was pasted below the bottom of flume. The CCD cameras were set at a distance from the plane, set at an angle of 30^o, such that the required plane is uniformly visible through both the cameras. Though the plane of measurement was about 450 mm X 450 mm, the images were post processed to identify only the region of interest according to the flow depth. The Laser light sheet optic was manually positioned on the flume rails.

For stereoscopic PIV, the calibration was done using a grid of size 450 mm X 450 mm. Figure 3 (a) shows the calibration tile with a Camera (second camera not in the picture) in the foreground. The black markers on the grid were identified by the acquisition software and the pixels were converted to true physical distance generating a scale factor. After the calibration, desired flow conditions were established in the flume. The PIV system was synchronised using a Timer Box. The laser power output was regulated using Laser system control. The pulse duration between the lasers was adjusted to optimize the Laser intensity and uniform illumination of flow plane in both the frames. PIV images were captured by the two cameras which continuously transferred the data to the computer at a frame rate of 15 Hz, denoting 15 instantaneous (double frame) vector fields per second. The raw data was then saved to the main database for post-processing and analysis using *Dantec Dynamics* software.

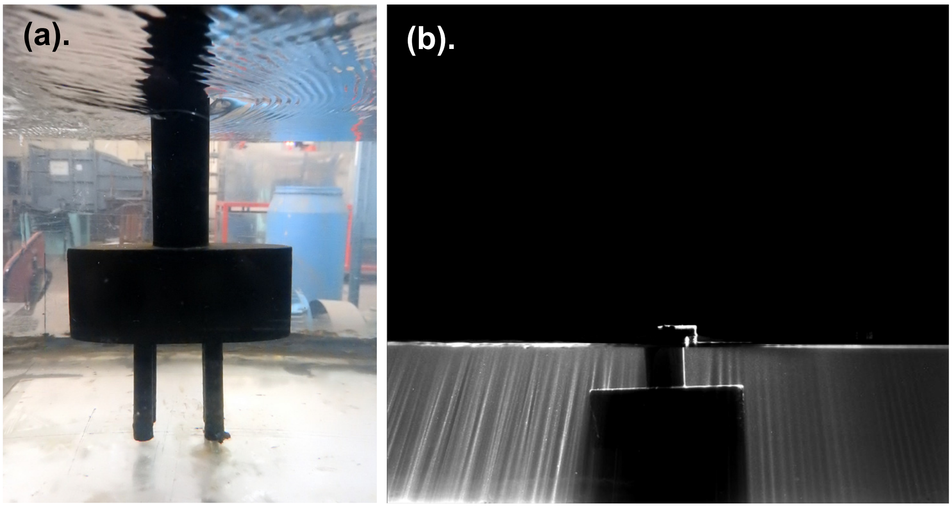

Figure 3. Photographs showing: (a) complex bridge pier placed in the flume; (b) flow plane illuminated by Laser with CBP in the plane center.

Figure 3 (a) show the complex bridge pier placed in the flume and 3 (b) shows the vertical flow plane on the centreline of the same pier and flume illuminated by the Laser light sheet introduced from the top of the plane. The illuminated portion in Figure 3 (b) is the water flowing around the CBP and only that portion is processed for velocity data. In each test run, a pair of 350 instantaneous velocity vector maps were captured by each Camera for every location. A cross-correlation based adaptive method of image processing was utilized to process the images into vector fields. A low pass Gaussian filter was used to remove spiked vectors and were replaced with neighbourhood mean values. The validated velocity fields were averaged to produce an ensemble-averaged velocity field.

3 RESULTS & DISCUSSIONS

In the following section, mean velocity vector fields obtained from processing the PIV images are shown and discussed. The results are shown only for discharge 0.012 m^3/s with moderate Reynolds number (other flow parameters shown in Table 2).

Table 2. Flow parameters,

Discharge (Q, m^3/s)	**Average flow depth (z, *m*)**	**Average flow velocity (U, *m/s*)**	**Reynolds number (Re)**	**Froude number (Fr)**
0.012	0.145	0.267	39,000	0.22

The measurements were done at 3 different vertical planes in the centreline of the flume (along the flow); one on the upstream of the pier; one with pier in the middle of the section and one on the downstream of the pier. The length of the plane of measurement was 45 cm in every case and the depth was 0.145 m for 0.012 m^3/s. In the following section, streamwise mean velocity profiles on the centreline of the flume as well as the pier are shown. Two- dimensional velocity vector field, streamlines and contours are also presented for better understanding of the mean flow around a Complex pier.

3.1 Streamwise Mean Velocity Profiles

Figure 4 presents the time averaged mean velocity in the flow direction (U = streamwise velocity; in x-direction) where (a) shows the velocity profiles on the upstream of the pier and (b) shows the velocity profiles on the downstream of the pier. The profiles are shown for various locations (the distance is from the pier center) using different symbols and colors as mentioned below (the origin is considered at the pier center):

Upstream	**A**	16.5 cm	**B**	14.5 cm	**C**	12.5 cm	**D**	10.5 cm	**E**	8.5 cm	**F**	6.5 cm
Downstream	**G**	6.5 cm	**H**	8.5 cm	**I**	10.5 cm	**J**	12.5 cm	**K**	14.5 cm	**L**	16.5 cm

The flow depth is divided into three distinct zones, viz, **I**, **II** and **III**. These zones correspond to the location of the complex pier component with respect to the flow depth. Zone **I** represents the column region, zone **II** represents the pile cap region and zone **III** represents the pile group region. All the profiles are extracted from the PIV data only.

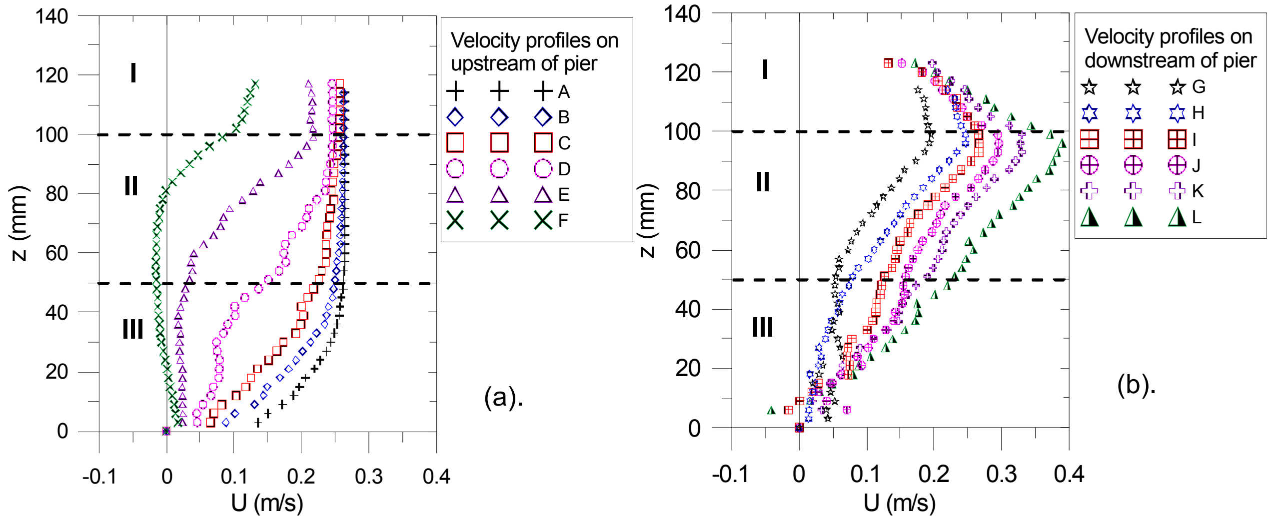

Figure 4. Comparison of Streamwise velocity profiles measured at different locations, (a) on the upstream of the pier (locations A-F); (b) on the downstream of the pier (locations G-L).

Figure 4 (a) shows that the velocity profile at location A gives a non-disturbed profile following logarithmic law (Nezu and Rodi, 1986), but as the flow progresses towards the pier, a decrease in the velocity is observed which is dominant in zone **III** indicating the effect of pile group in shielding the downflow. In between zone **II** and **III** at location F, the velocity attained negative magnitude indicating back flow on the upstream of the pile cap. In zone **I**, a decrease in velocity is observed too but the magnitude didn't change its sign indicating a deceleration in the flow in front of the column but no backflow.

Figure 4 (b) shows an increase in the magnitude of the velocity in zone **II** and then a decrease in zone **I**. All the three zones show different flow velocity patterns signifying the importance of studying all the components of a complex pier. The variations in the velocity in each zone are attributed to the non-homogeneity of the complex pier structure.

3.2 Two- Dimensional Mean Velocity vectors and streamlines

Figure 5 shows the vectors of U and V velocity in x- and z- directions respectively (U is the streamwise velocity in x- direction and V is the vertical velocity in z- direction). The vector field is shown for the section at the mid plane of the flume with the complex pier in the middle of the measurement plane.

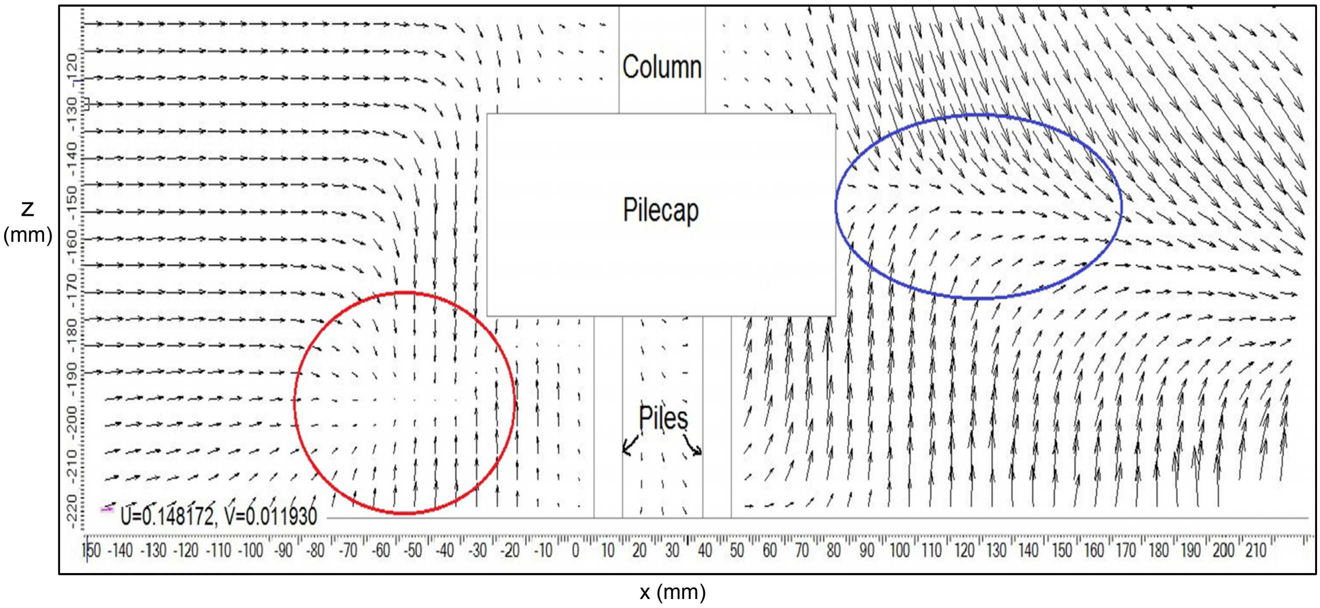

Figure 5. Two- dimensional (U, V) velocity vector representation on the centerline of the flume (y=0) with complex pier in the middle of the measurement plane.

The vectors shown in Figure 5 gives a clear picture of presence of vortex in the flow. Far upstream of the complex pier, the vectors show no two- dimensionality, but as they reach the vicinity of the pier, the vectors near the water surface start to move downward. The downward flow meets the upward flow near the bed surface and causes a vortex below the pile cap region. On the upstream of the complex pier, the vectors shown inside the red boundary show a rotational behavior. On the downstream of the pier, a downward flow is observed near the flow surface and an upward flow near the bed surface. Being deflected by the presence of the pile cap, the downward and the upward flow join together in the vicinity of the pile cap as shown inside the blue boundary.

Figure 6 shows streamlines in the x-z direction on the centerline of the flume with complex pier in the middle of the measurement plane. The converging and diverging streamlines can be clearly observed in the figure. The streamlines seemingly emerging from the bed are the upward flow (wakes).

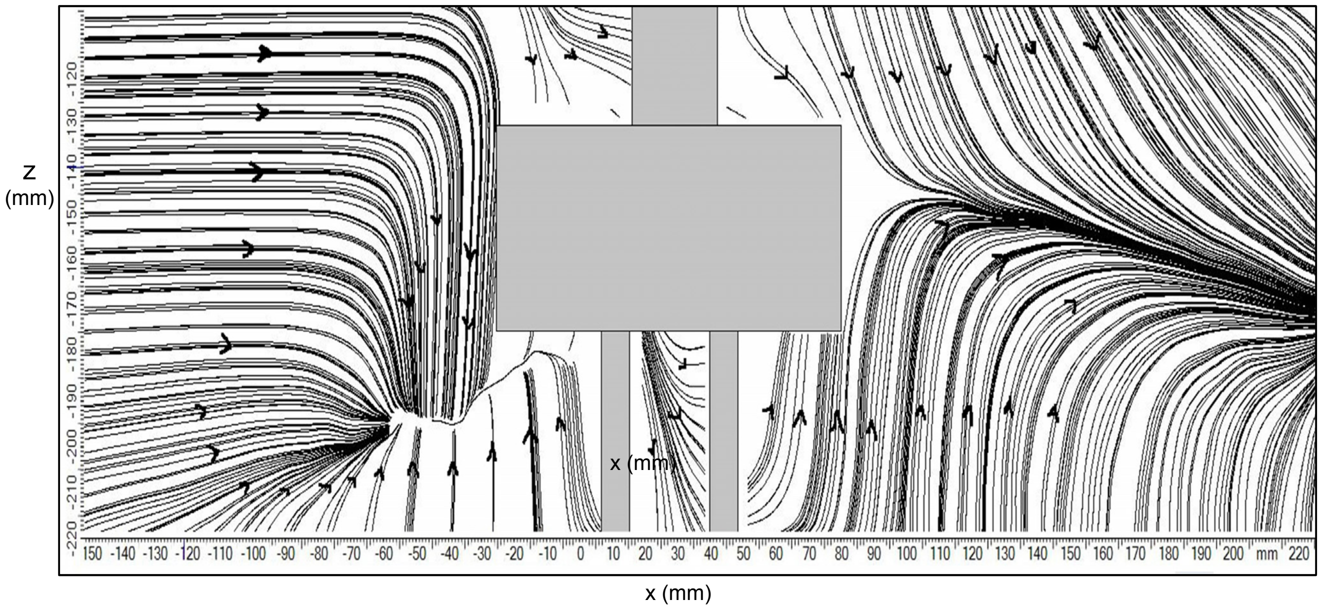

Figure 6. Two- dimensional (U, V) velocity vector representation on the centerline of the flume (y=0) with complex pier in the middle of the measurement plane.

3.3 Three- Dimensional Mean Velocity contours

Figure 7 shows colored mean velocity contours obtained from PIV image processing with two dimensional (UV) velocity vectors imposed on them. Figure 7 (a) represents the time averaged streamwise velocity, (b) represents the time averaged vertical velocity and (c) represents the time averaged transverse velocity.

The magnitude of the velocities are shown clearly through the contours. In figure 7 (a), streamwise velocity show a decrease in its magnitude in the pile cap and piles region, whereas on the downstream of the pier, comparatively higher velocities are observed. Although, the velocities are in the nominal range just in the downstream of the pile cap.

In figure 7(b), vertical velocities indicate downflow in front of the pier and an upward flow on the downstream of the pier. Highest magnitude of vertical velocity attained just below the pile cap and on its downstream. This high vertical velocity in the pile group zone may contribute significantly in the scouring of sand around the pile group.

In figure 7 (c), the transverse velocity contours are shown. Presence of low transverse velocity region dominantly on the upstream of the pile cap indicates slow and smooth bifurcation of flow leading to lower level of turbulence.

4 CONCLUSIONS

In this paper, flow field around a complex pier was recorded using Particle Image Velocimetry and analyzed using a cross-correlation based algorithm to understand the flow hydrodynamics. For clear understanding, moderate Reynolds number flow was presented here. Following are the main findings from the study:

1. All the three zones showed different flow velocity patterns signifying the importance of studying all the components of a complex pier. The variations in the velocity in each zone are attributed to the non-homogeneity of the complex pier structure.
2. As the flow progressed towards the complex pier, a decrease in the velocity was observed which was dominant in zone below the pile cap indicating the effect of pile group. Just in front of the pile cap, backward flow was observed. In zone above the pile cap, a decrease in velocity was observed but the magnitude didn't change its sign indicating a deceleration in the flow in front of the column but no backflow.
3. Far upstream of the complex pier, the vectors showed no two- dimensionality, but as they reached the vicinity of the pier, a vorticular structure was observed. On the downstream of the pier, both upward and downward moving flow fields were identified.
4. Streamwise velocity contour showed a decrease in magnitude in the pile cap and piles region, whereas on the downstream of the pier, comparatively higher velocities were observed. Although, the velocities were in the nominal range just in the downstream of the pile cap.
5. Vertical velocity contour indicated downflow in front of the pier and an upward flow on the downstream of the pier. Highest magnitude of vertical velocity was observed just below the pile cap and on its downstream. This high vertical velocity in the pile group zone may contribute significantly in the scouring of sand around the pile group.
6. Transverse velocity contours showed presence of low velocity region dominantly on the upstream of the pile cap indicating slow and smooth bifurcation of flow leading to lower level of turbulence.
7. This study would be very useful to identify the high velocity and pressure gradient regions around a complex pier in order to identify the maximum or minimum scouring regions around the pier.

ACKNOWLEDGEMENTS

The PIV system discussed in this paper was procured was procured under a Grant from FIST program and Department of Science and Technology (DST), New Delhi, India. The authors would like to acknowledge DST for the grant and sincerely express gratitude to the staff of Hydraulics laboratory of Department of Civil Engineering, IIT Bombay for their continuous help in this project.

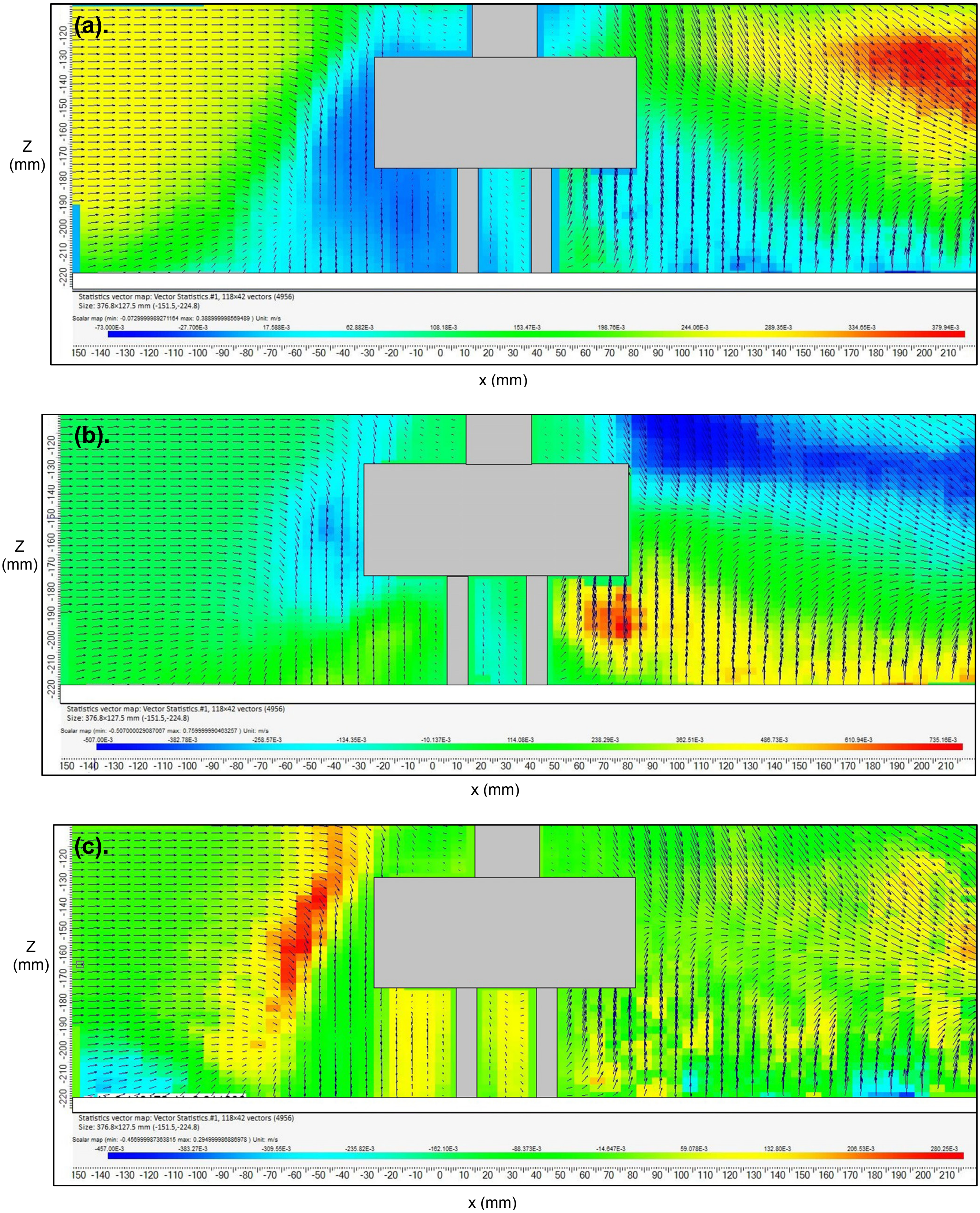

Figure 7. Contours showing (a) streamwise velocity; (b) vertical velocity; (c) transverse velocity, with 2-D vectors imposed on them.

REFERENCES

Akib, S. & Jahangirzadeh, A. (2014). Local Scour around Complex Pier Groups and Combined Piles at Semi-Integral Bridge. *Journal of Hydrology and Hydromechanics,* 62(2), 108-116.

Beheshti, A.A. & Ataie-Ashtiani, B. (2016). Scour Hole Influence on Turbulent Floe Field around Complex Bridge Piers. *Flow Turbulence and Combustion*, 97(2), 451-474.

Beheshti, A.A. & Ataie-Ashtiani, B. (2010). Experimental Study of Three-Dimensional Flow Field around a Complex Bridge Pier. *Journal of Engineering Mechanics*, 136(2), 143-154.

Coleman, S.E. (2005). Clearwater Scour at Complex Piers. *Journal of Hydraulic Engineering*, 4, 330-334.

Ferraro, D., Tafarojnoruz, A., Gaudio, R. & Cardoso, A.H. (2013). Effects of Pile Cap Thickness on the Maximum Scour Depth at a Complex Pier. *Journal of Hydraulic Engineering*, 139(5), 482-491.

Gautam, P., Eldho T.I. & Behera M.R. (2016). Experimental Study of Scour around a Complex Pier with Elliptical Pile-Cap. *International Conference on Scour and Erosion* (Vol. 8), Oxford, United Kingdom.

Hydraulic Eng. Circular (HEC-18) manual. (2001). *Evaluating Scour at Bridges*, Federal Highway Administration (FHWA), USA.

Johnson K.R. & Ting F.C.K. (2003). Measurements of Water Surface Profile and Velocity Filed at a Circular Pier. *Journal of Engineering Mechanics*, 129(5), 502-513.

Meliville, B.W., Coleman, S.E. & Priestley, S. (2006). Local Scour at Complex Piers*. World Environmental and Water Resource Congress*, ASCE, 1-9.

Moreno, M., Maia, R. & Couto, L. (2015). Effects of Relative Column Width and Pile-Cap Elevation on Local Scour Depth around Complex Piers. *Journal of Hydraulic Engineering*. ASCE, 142(2), 1-9.

Nezu, I. & Rodi, W. (1986). Open-Channel Measurement with a Laser Doppler Anemometer. *Journal of Hydraulic Engineering*, 112(5), 335–355.

Oruc, V., Akill, H. & Sahin, B. (2015). PIV Measurements on the Passive Control of Flow Past a Circular Cylinder. *Experimental Thermal and fluid Science*, 70, 283-291.

STUDY ON EFFECT OF RADIUS OF CURVATURE ON LATERAL OVERFLOW IN CURVED CHANNEL

KOJI ASAI[1] & NOBUYUKI KAWAMOTO[2]

[1] Department of Civil and Environmental Engineering, Graduate School of Science and Technology for Innovation,
Yamaguchi University, Ube, Japan,
kido@yamaguchi-u.ac.jp
[2] Faulty of Engineering, Yamaguchi University, Ube, Japan,
mozart@yamaguchi-u.ac.jp

ABSTRACT

In this study, we investigated the accuracy of the lateral overflow discharge formulations for the curved channel of which the radius of curvature is constant. From the experimental results, we found that the lateral overflow discharges are in proportion to the power of 3/2 to the overflow depth, so we can use the same formulation as Honma formulation for the front overflow discharge. The Froude number, the ratio of the channel width to the lateral weir width, the ratio of the weir height to the weir width, and the ratio of channel width to the radius of curvature, were used as the parameters of the discharge coefficient. We assumed that the discharge coefficient is the simple product of these parameters and having the power. The powers of these parameters were determined from the experimental data. It was confirmed that the accuracy of the proposed formulation is good.

Keywords: Lateral overflow; discharge formulation; curved channel; discharge coefficient; radius of curvature.

1 INTRODUCTION

Lateral overflow weirs are often used for water depth adjustment of a main channel or irrigation. Recently, as one of the flood control methods, the lateral over flow weir has been used to supply flood water to the plain dam. Generally, these lateral overflow weirs are installed in the straight channels. There are many studies for the lateral overflow weir in the straight channel and many lateral overflow formulations have been proposed, for example, De Marchi. (1934), Ranga. et al (1979), Murota A. et al (1985) Hager (1987), Onitsuka et al (2005, 2007), Vatankhah (2013), Yilmaz (2001).

As well known, a flood hazard map is very useful non-structural measures. The flood hazard map shows a predicted inundation area. This area is estimated by using a numerical flood simulation. The breaching point of a river dike is assumed and a lateral overflow formulation for a straight channel or a front overflow formulation is applied to estimate the discharge from this point, and then the flood simulation is conducted with the estimated discharge.

In real rivers, however, a braking point of a river dike is not always at straight portion of the river but meandering portion. It is anticipated that the lateral overflow discharge cannot be predicted by using the conventional lateral overflow formulations because of the centrifugal force effect.

The final objective of our study is to develop the lateral overflow formulation for meandering open channels or rivers. In this study, as first step of the final objective we investigated the accuracy of the lateral overflow discharge formulations for the curved channel of which the radius of curvature is constant.

2 EXPERIMENT

Figure 1 shows the schematic view of the experimental channels. One is the straight channel and the other is the curved channel. The width, B of the both channels is 0.20 m. The length, L of the lateral side weir is also 0.20 m for both channels. The length of the straight channel is 2.40 m and the lateral side weir is installed at 1.10 m from the upstream edge. The curved channel consists of two straight channel parts and the bend channel part. R is the radius of curvature. □ is the angular measured from the entrance of the bend part as shown in figure 1. Both channels are made of the acryl grass. The specification of this channel is shown in Table 1. The center of the lateral side weir is located at θ = 90 degree. The straight channel can be interpreted as the curved channel of which the radius of curvature is infinity.

Figure 2 shows the schematic view of the lateral side weir. This is the sharp-crested weir. Q_{IN} is the inflow discharge, Q_{OUT} is the outflow discharge and Q_{MEA} is the lateral overflow discharge, W is the weir height, L is the length of the lateral weir, h is the water depth measured at the center of the channel, h_1 is the overflow depth measured at the center of the channel, H is the water level measured from the bed. The bed slope of both channels is set to be 0, so the water level (H) is identical to the water depth (h).

The width of our channel is narrow, so the aspect ratio B/h of our experiments is very much smaller than that of real rivers. A wide space is needed to set the curved channel. We had to make our experimental channels compact because of the space of our experimental room. This is why the width of the channel was narrow.

The experimental conditions are shown in Table 2. L is fixed at 0.20 m, which is the same as B. The parameters of our experiments are W and Q_{IN}. h, Q_{OUT}, Q_{MEA} were measured and the water depths at the inner and the outer side wall were also measured in order to check the centrifugal force effect.

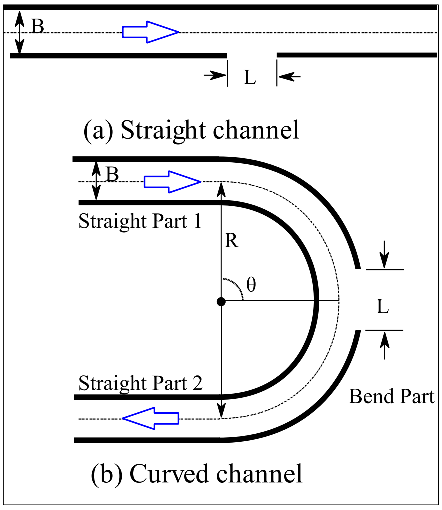

Figure 1. Over view of open channels.

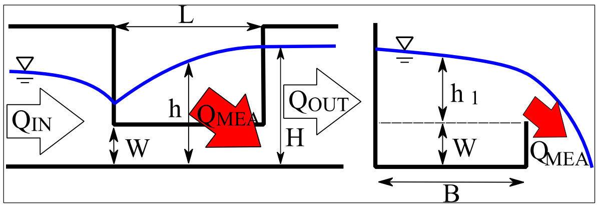

Figure 2. Schematic view of lateral side weir.

Table 1. Specification of curved channel.

R (m)	Straight Part 1 (m)	Bend Part (m)	Straight Part 2 (m)
0.50	1.40	1.57	1.10
0.70	1.40	2.20	1.10
0.90	1.00	2.83	1.10

Table 2. Experimental condition.

Dimension of Weir		**Inflow Discharge Q_{IN} (m^3/s)**
L(m)	W(m)	
0.20	0∼0.045	0.0043, 0.003, 0.002, 0.001

3 EXPERIMENT RESULT

3.1 Result of straight channel

Figure 3 shows the water depth profile in the straight channel for Q_{IN} = 0.003 m^3/s. The vertical axis indicates the water depth (h) and the horizontal axis indicates the distance in the flow direction of x. The origin of x is taken at the center of the lateral weir. The broken line shown in the figure indicates the position of the lateral weir.

In the case of no lateral discharge (W = Full), the water depth (h) is almost uniform in x direction. It is widely known that the water depth profile increases in the overflow region. These profiles also show the same tendency. The clearer this tendency is, the smaller the W is.

The overflow discharge is in proportion to the power of 3/2 to the overflow depth, h_1, if the cross section of the weir is rectangular for the front overflow. We check and our experimental results had this property. Figure 4 shows the relationship between the lateral overflow discharge (Q_{MEA}) and the overflow depth (h_1). It is found that the lateral overflow is almost in proportion to the power of 3/2 to h_1.

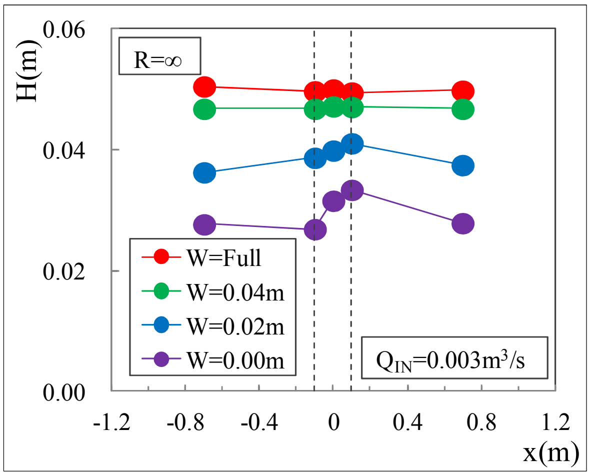

Figure 3. Water depth profile in straight channel.

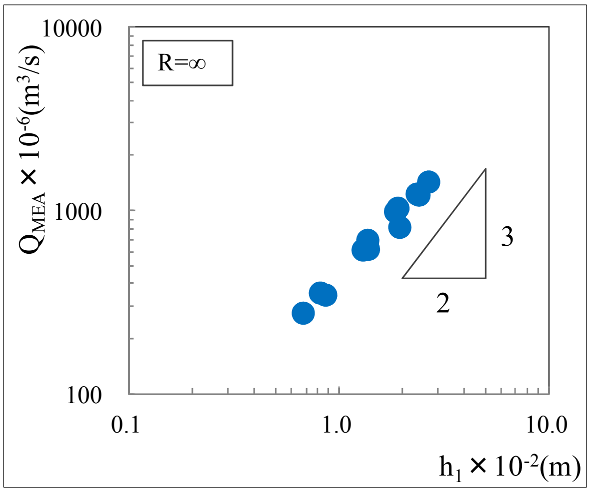

Figure 4. Relationship between h_1 and Q_{MEA}.

In this study, we conducted the experiments for both the straight channel and the curved channel with the same cross section from the weir and the same inflow discharge conditions. The relationship between the lateral overflow discharge and the overflow depth is discussed. Moreover, the simple lateral overflow discharge formulation considers the centrifugal force effect. For the comparison, we will use the following lateral overflow discharge formulation. This formulation is Honma formulation for the front overflow modified to apply in the lateral overflow (MLIT (2005)).

$$Q_{CAL} = \alpha \cdot \cos\theta \cdot C \cdot h_1 \cdot \sqrt{2gh_1} \cdot L \qquad [1]$$

Where g is the gravity acceleration, α, θ and C are the model parameters as follow:

C = 0.35

If the bed slope, I is less than 1/1580,

$$\alpha = 0.14 + 0.19 \times \log_{10}\frac{1}{I}, \quad \theta = 48^\circ - 15^\circ \times \log_{10}\frac{1}{I}$$

If the bed slope, I is greater than or equal to 1/1580,

$$\alpha = 1, \quad \theta = 0^\circ$$

Figure 5 shows the fitness of Eq. (1) to the experimental data. The vertical and the horizontal axis indicate the experimental lateral overflow discharge (Q_{MEA}) and the lateral overflow discharge (Q_{CAL}) estimated by Eq. (1). Eq. (1) can predict the lateral overflow discharge well, but the maximum relative error is up to 17 %

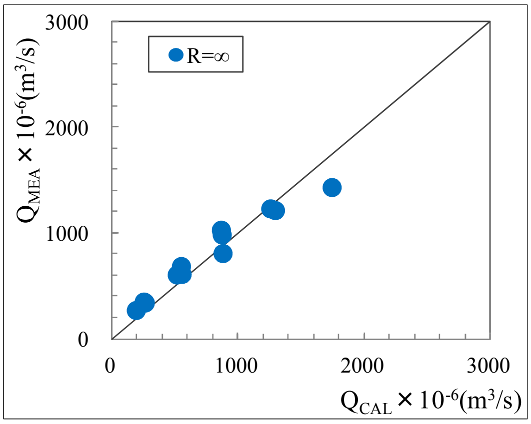

Figure 5. Comparison between Q_{CAL} and Q_{MEA}.

3.2 Result of curved channel

Figure 6 shows the water depth profile in the curved channel for R = 0.50 m and Q_{IN} = 0.003 m^3/s. The meanings of both axes are the same as figure 3. The broken line indicates the position of the lateral weir similar in Figure 3. It can be confirmed that the water depth profiles increase in the region of the lateral weir similar in Figure 3.

Figure 7 shows the difference of the water depth between the inner and the outer side walls, ΔH. The solid lines shown in this figure are the theoretical lines obtained by Eq. (2).

$$\Delta H = Bu^2 / (gR) \quad [2]$$

Where u is the cross sectional averaged velocity. The color of the lines corresponds to R of the same color.

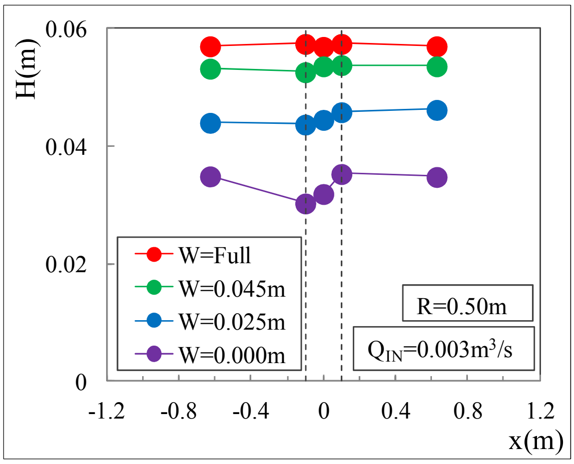

Figure 6. Water depth profile in curved channel.

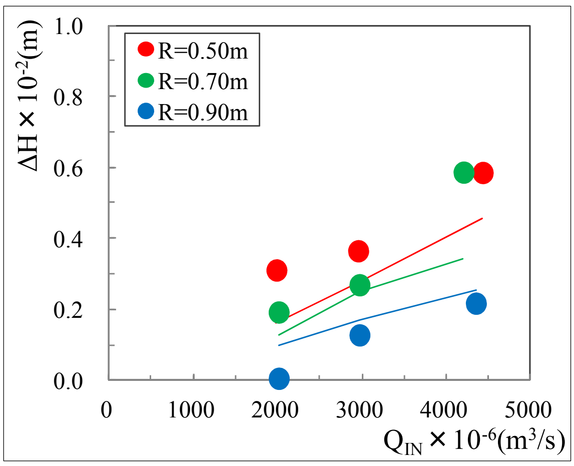

Figure 7. Difference of water depth between inner and outer side walls.

The experimental results agree with the theoretical lines qualitatively. It is confirmed from this figure that the bigger ΔH is, the smaller the radius of curvature R is, and ΔH increases with the inflow discharge Q_{IN}.

Figure 8 shows the relationship between the lateral overflow discharge and the radius of curvature. The vertical axis indicates the ratio of Q_{MEA} to Q_{IN}, here we call it the inflow-overflow ratio, and the horizontal axis indicates the radius of curvature, R. The solid vertical lines in Figure 8 indicate the values of the straight channel. Here, the experiments with the straight channel of Q_{IN} = 0.0043 m^3/s were not conducted. It is found from Figure 8(a) that when W = 0.025 m, W = 0.020 m for the straight channel, the inflow-overflow ratios are taken 0.3 - 0.5 for both the straight channel and the curved channel, no matter what R and Q_{IN} are. On the other hand, Figure 8(b) shows that the inflow-overflow ratios of the curved channel are larger than that of the straight channel. In addition, the ratios of the curved channel become smaller as the radius of curvature increases.

As shown in Figure 7, the water depth at the outer side wall is larger than that of the inner side wall because of the centrifugal force. In other words, there is velocity component towards the outer side wall. It could be said that this velocity component makes the lateral overflow larger than that of the straight channel, especially in the whole water depth when W = 0.00 m.

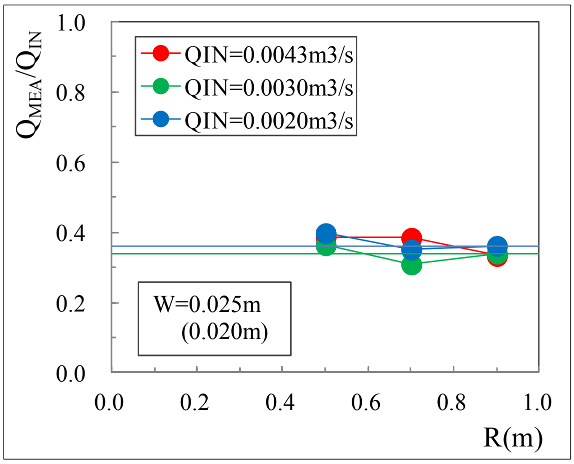

(a) W = 0.025 m for curved channel and W = 0.020 m for straight channel.

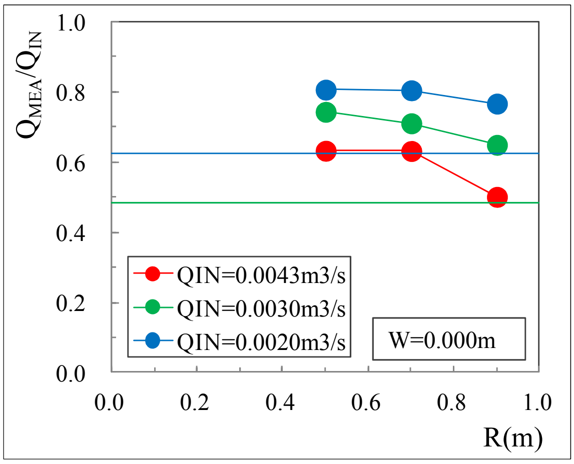

(b) W=0.00m

Figure 8. Relationship between inflow-overflow ratio and the radius of curvature.

Figure 9 shows the relationship between the lateral overflow discharge and the overflow depth. Similar to Figure 4, the lateral overflow discharge is in proportion to the power of 3/2 to the overflow depth. Therefore, Eq. (1) could be used for the lateral overflow discharge formulation.

Figure 10 shows the comparison between the measured lateral overflow discharge and the discharge estimated by Eq. (1). It can be seen that the measured discharges are larger than the estimated discharges. In other words, Eq. (1) underestimates the lateral overflow discharge. The table shown in Figure 10 shows the averaged values, which are the division of the measured discharges by the estimated discharges. It is found from these values that the measured discharges are 20 to 30 % more than the estimated discharges, and this value increases as the radius of curvature, R decreases.

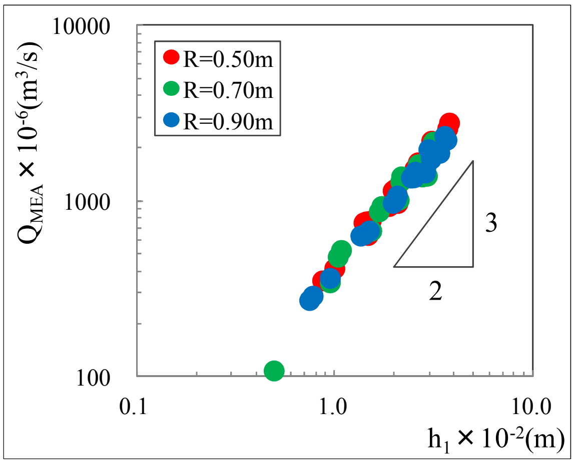

Figure 9. Relationship between h_1 and Q_{MEA}.

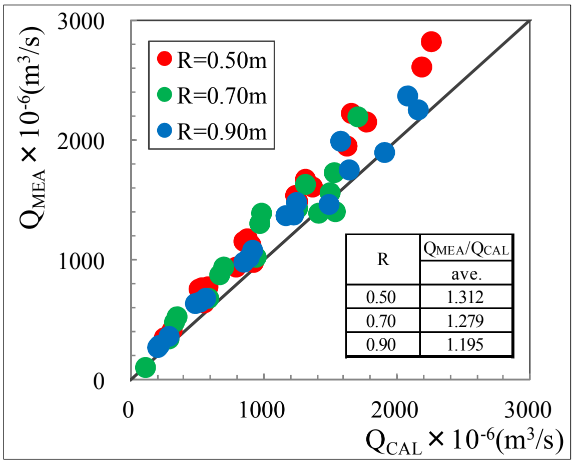

R	QMEA/QCAL ave.
0.50	1.312
0.70	1.279
0.90	1.195

Figure 10. Comparison between Q_{CAL} and Q_{MEA}.

4 LATERAL OVERFLOW FORMULATION CONSIDERING RADIUS OF CURVATURE

Here, we try to develop a simple lateral overflow discharge formulation by considering the radius of curvature. From the experimental results, we found that the lateral overflow discharges are in proportion to the power of 3/2 to the overflow depth, so we can use the same formulation as Eq. (1):

$$Q_{CAL} = C_a \cdot 0.35 \cdot h_1 \cdot \sqrt{2gh_1} \cdot L \qquad [3]$$

Where C_a is a new correction coefficient. The effect of the shape of the weir, hydraulic conditions and the radius of curvature are introduced to this coefficient. C_a is assumed to be a function of the non-dimensional parameters made of the geometrical quantities of the channel and the weir, and non-dimensional hydraulic parameters. There are so many formations of the function of C_a. Here, we use the production of the non-dimensional parameters, which is the simplest formation as shown in Eq. (4):

$$C_a = C_0 \cdot \left(\frac{L}{B}\right)^{\alpha} \cdot \left(1-\frac{W}{L}\right)^{\beta} \cdot Fr^{\gamma} \cdot \left(1-\frac{B}{R}\right)^{\omega} \qquad [4]$$

Where C_0, α, β, ω are the model constants, which are determined by the experiments. F_r is the Froude number and is defined using the cross sectional averaged velocity and the water depth at the center of the channel in front of the side weir.

Figure 11 shows the determination of each model coefficients. The horizontal axes in Figure 11(a), (b) and (c) indicate non-dimensional parameters, 1-W/L, F_r, 1-B/R, respectively. The vertical axis indicates the measured lateral overflow discharge normalized by $L \cdot \sqrt{2gh_1^3}$. In other words, the vertical axis represents the discharge coefficient. In these figures, the fitting curve is shown.

The power of this fitting curve is the model constant. .*L*/*B* is the non-dimensional parameter defined by the length of the lateral weir and the width of the channel. *L*/*B* is fixed at 1.0 in this study, so we cannot discuss the influence of L/B to the lateral overflow. Therefore, the power of this parameter, α is set as 0.

1-*W*/*L* is the non-dimensional parameter concerning the shape of the weir. This parameter approaches 1 as W decreases to 0. As shown in Figure 11 (b), the discharge coefficient becomes smaller as this parameter increases. The power of this parameter, □ is -0.828.

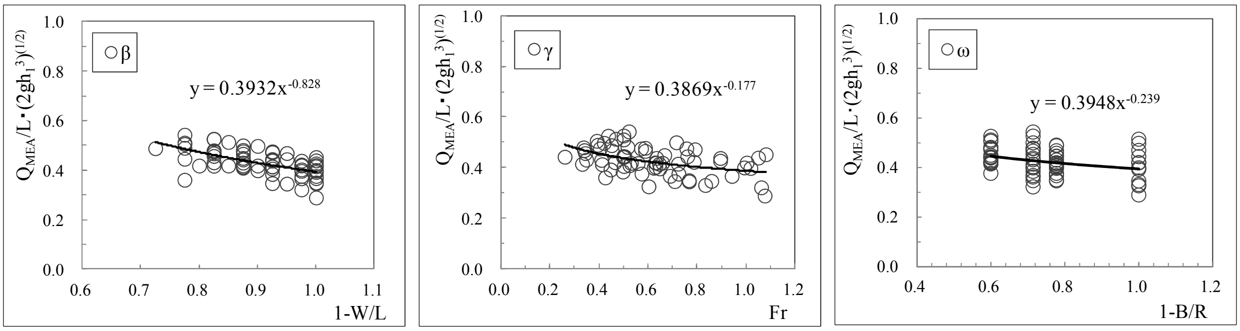

(a) Determination of β (b) Determination of γ (c) Determination of ω

Figure 11. Determination of model constants.

F_r is the well-known non-dimensional parameter and means the ratio of the inertial force to the gravity force. In our experiments, the range of F_r is 0.2 - 1.08. The power of the Froude number, γ is - 0.177. The discharge coefficient decreases as F_r increases.

1-B/R is the non-dimensional parameter concerning the radius of curvature. The straight channel can be considered as the curved channel of which the radius of curvature is infinity, so 1-B/R is 1 for the straight channel. We used the experimental data of the straight channel to determine the power of this parameter. The discharge coefficient decreases as this parameter increases. In other words, the discharge coefficient of the straight channel is smaller than that of the curved channel, as shown in Figure 8. The power of this parameter, ω is -0.239. Based on the results of Figure 11, C_0 is determined to fit the measured lateral overflow discharges. Finally, C_a is given as follows:

$$C_a = 0.944 \cdot \left(\frac{L}{B}\right)^0 \cdot \left(1-\frac{W}{L}\right)^{-0.828} \cdot Fr^{-0.177} \cdot \left(1-\frac{B}{R}\right)^{-0.239} \qquad [5]$$

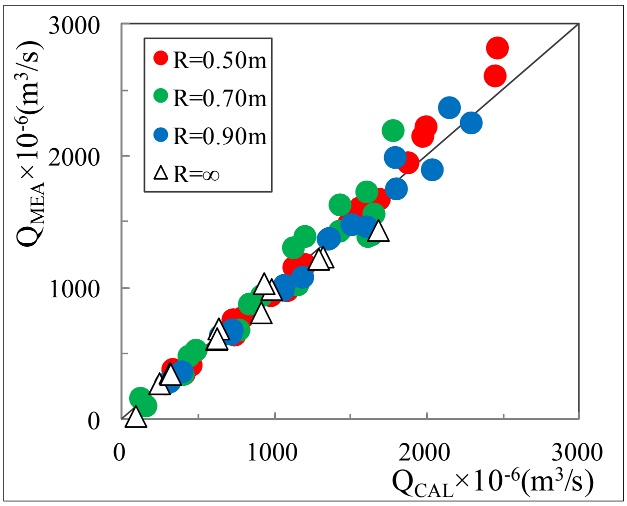

Figure 12. Comparison between Q_{CAL} and Q_{MEA}.

Figure 12 shows the fitness of the proposed formulations, which are Eq. (3) and Eq. (5), to the experimental data. The vertical axis indicates the experimental lateral overflow discharge (Q_{MEA}) and the horizontal axis indicates the lateral overflow discharge estimated by the proposed formulation (Q_{CAL}). It can be seen that the proposed formulation can predict the lateral overflow discharge well in comparison with Eq. (1).

Figure 13 shows the estimation of the accuracy of the proposed formulation with the radius of curvature. The vertical axis indicates the ratio of the measured lateral overflow discharge to the estimated lateral overflow discharge, Q_{MEA}/Q_{CAL}. The horizontal axis indicates the non-dimensional parameter, 1-B/R. The error bars are also indicated in Figure 13. Q_{CAL} in the upper figure is obtained by Eq. (1) and that in the lower figure is obtained by the proposed formulation. All the center values of Q_{MEA}/Q_{CAL} in the upper figure are over 1.0. This means that Eq. (1) underestimates the lateral overflow discharge. On the other hand, in the lower figure these values are nearly 1.0, no matter what the radius of curvature is. The scattering in the lower figure is smaller than that of the upper figure. It is also found that Q_{CAL} estimated by the proposed formulation for the straight channel, 1-B/R = 1.0, is good in comparison with Q_{CAL} estimated by Eq. (1).

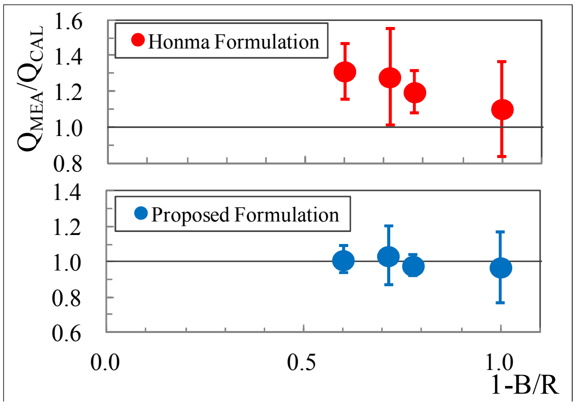

Figure 13. Q_{CAL}/Q_{MEA} vs 1-B/R.

5 CONCLUSIONS

In this study, we investigated the characteristics of the lateral overflow in the curved channel of which the radius of curvature is constant as the first step to develop the lateral overflow formulation for meandering open channels or rivers. We also proposed a simple lateral overflow in the curved channel. The main conclusions in this study are as follows:

i. The lateral overflow discharge in the curved channel is in proportion to the power of 3/2 to the overflow depth.
ii. The Honma formulation underestimates the lateral overflow discharge in the curved channel.
iii. Based on the experimental data, the lateral overflow discharge formulation for the curved channel is proposed.

The proposed formulation can predict the lateral overflow discharge for both straight and the curved channels. However, the proposed formulation is the empirical formulation, which is effective under the experimental conditions in this study. As a future task, we will develop the formulation that is more accurate and applicable for wide hydraulic conditions.

ACKNOWLEDGMENTS

We would like to express our deepest gratitude to Mr. Hironori Babazono, Mr. Masahiro Mizui, Mr. Yuta Nakatani and Mr. Ryoji Hashimoto for conducting the experiments.

REFERENCES

De Marchi, G. (1934). Essay on the Performance of Lateral Weirs. *L' Energia Elettrica*, Milan, Italy, 11, 840-860.

Hager, W.H. (1987). Lateral Outflow over Side Weirs. *Journal of Hydraulic Engineering,* 9, 491-504.

Murota A., Fukuhara T. & Sukita Y. (1985). Study on Evaluation of Discharge over Side Weirs. *Proceeding of JSCE*, 363(II-4), 249-252. (In Japanese)

Onitsuka K., Akiyama J., Tsunematsu T. & Mataga M. (2005). Discharge Coefficients of Side-Weirs in Subcritical Open-Channel Flows. *Journal of Hydraulic Coast Environment Engineering,* JSCE, 803(II-73), 81-89. (In Japanese)

Onitsuka K., Akiyama J., Mataga M. & Ida C. (2007). Discharge Coefficients of Side-Weirs in Supercritical Open-Channel Flows. Doboku Gakkai Ronbunshu B, 63(2), 134-143 (In Japanese)

Ranga Raju, K.G., Prasad, B. & Gupta, S.K. (1979). Side Weir in Rectangular Channel. *Journal of Hydraulics Division,* ASCE, 105(5), 547-554.

Vatankhah A.R. (2013). Water Surface Profiles along a Rectangular Side Weir in a U-Shaped Channel (Analytical Findings). *Journal of Hydrologic Engineering,* 18(5), 593-602.

Yilmaz Muslu (2001). Numerical Analysis for Lateral Weir Flow. *Journal of Irrigation Drain Engineering,* 127(4), 246-253.

Proceedings of the 37th IAHR World Congress
August 13 – 18, 2017, Kuala Lumpur, Malaysia

CONTROL OF LOCAL SCOUR AT VICINITY OF BRIDGE PIERS USING FLOW DIVERSION STRUCTURE

MOHSEN RANJBAR ZAHEDANI[1], ALIREZA KESHAVARZI[2] & HADI KHABBAZ[3]

[1, 3] School of Civil and Environmental Engineering, University of Technology Sydney, Sydney, Australia,
mohsen.ranjbar80@gmail.com
Hadi.Khabbaz@uts.edu.au
[2] Water Department, Shiraz University, Shiraz, Iran
arzkeshavarzi@gmail.com

ABSTRACT

Previous studies have shown that most waterway bridge failures are due to local scour, which is the result of flow structures and bridge piers interactions. In order to control and reduce the impact of the problem around the piers, armoring countermeasures, such as riprap and gabion are commonly used. In this study, to find the possibility of reducing local scour around the piers, a flow diversion structure is introduced and used as a countermeasure. This triangular prismatic structure with dimensions much smaller than the pier, was installed at different spacing upstream of the pier. After achieving equilibrium condition, the bed profile was measured and the volume of the scour hole was determined for each experimental test. The above results were compared to a test case with no flow diversion structure at the upstream. The results revealed that the optimum distance between the pier and flow diversion structure to achieve the maximum reduction of local scour, was approximately 1.5 times of the pier diameter. In this situation, the volume of scour hole and the maximum of scour depth reduced 61 % and 38 %, respectively. Furthermore, in the control test and the best performing test regarding the local scour reduction, three dimensional velocity components were measured at 35 grid points using an Acoustic Doppler Velocimeter (ADV). The velocity analysis indicated that the proposed flow diversion structure could change both the magnitude and the direction of velocity component at the upstream of pier, and consequently, reduced the local scour around pier.

Keywords: Local scour; bridge piers; flow diversion structure; piers - flow interaction; velocity components.

1 INTRODUCTION

Bridges on waterways are important structures for transportation. Local scouring around piers is a significant cause of bridges failure. According to a report by Clopper et al. (2007), bridge pier scouring results 60 % of bridge failures in the United States. The above problem interrupts transport system and then produces high financial losses. Therefore, the prediction of local scouring around bridge piers is very important. Furthermore, finding a way to control and reduce the local scouring can be very essential and it is the focus of this study. The local scouring mechanism around a bridge pier is complex due to the interactions of three dimensional flow structures and bridge pier. Many researchers such as Melville (1975), Ettema (1980), Qadar (1981), Chiew (1984), Hamill (1999), Melville and Coleman (2000), Richardson and Davis (2001), Sheppard (2004), and FODT (2010) have declared that the basic mechanism of local scouring is a system of vortices developed around the bridge piers. Figure 1 demonstrates the different components of flow contributing to the scour around the bridge piers. As reported by Melville and Coleman (2000), the principal features of the flow structure at a bridge pier are down-flow at upstream side of the pier, the horseshoe vortex at the base of the pier, the surface roller at upstream side of the pier and wake vortices downstream of the pier.

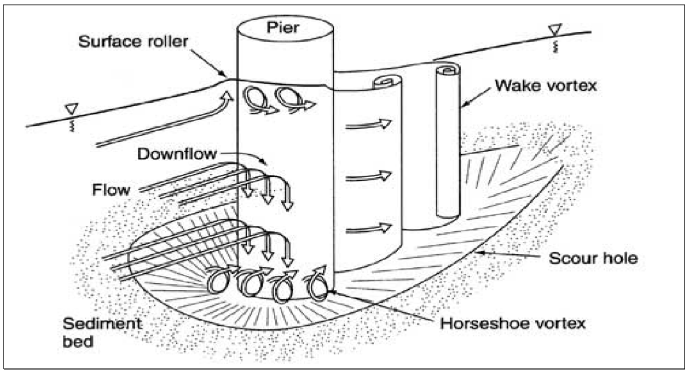

Figure 1. Main features of flow around a bridge pier (Hamill, 1999).

A number of studies (e.g. Kirkegaard et al. 1998; Ozdemir 2004; Clopper et al. 2007; Park et al. 2007; Yanmaz and Gris 2010) have been conducted to control the local scour around bridge piers. Chiew (1992) used a slot in and a collar around the pier, as devices for controlling the depth of scour. He concluded that the slot alone (with a width equal to one-fourth of the pier diameter) can reduce equilibrium scour depth by 20 %, while a combination of slot and collar can further reduce the scouring depth. Melville and Hadfield (1999) studied sacrificial piles as a pier scour countermeasure. Sacrificial piles are piles placed upstream of a bridge pier for the purpose of protecting it from local scour. They reported that sacrificial piles are recommended, when the flow remains aligned and the flow intensity is small.

To control and reduce local scouring of sediment, riprap is commonly used as an armoring countermeasure. Lauchlan and Melville (2001) studied the effects of bed degradation on riprap protection at bridge piers and reported that riprap protection is not effective for bed scouring when the channel bed degrades. In this situation, the riprap layer disintegrates and cannot protect the pier from local scour. In another study carried out by Lauchlan and Melville (2002), riprap failure mechanisms were investigated; and it was found that under clear-water conditions, riprap was subject to shear, winnowing, and edge failure; and under live-bed conditions, destabilization by bed-form progression, became important as a fourth failure mechanism. Furthermore, lowering the placement level of riprap provided a better protection against local scour.

Bridge pier scour protection by sack gabions was studied experimentally, in a clear water condition by Yoon and Kim (2001). They found that the stability of riprap scour countermeasures can be improved in a collective body rather than an individual riprap. In addition, sack gabions become much more stable by increasing its length. Experimental formulas sizing sack gabion were derived in terms of length and thickness of gabion, critical velocity, approach flow depth and pier width. Chiew (2004) investigated local scour and riprap stability at bridge piers in a degrading channel and reported that riprap around a pier would eventually develop into a stable mound, when the bed shear stresses reduced with bed degradation. However, the mound is very vulnerable to another designed flood flow accompanied by large dunes and this type of riprap instability may be called bed-degradation induced failure.

Dey et al. (2006) found that splitter plate attached to the pile along the vertical plane of symmetry and threaded pile (helical wires or cables wrapped spirally on the pile to form threads) were effective to reduce the scour depth. They declared that splitter plate divides the flow by two sides of the pile and disrupts the vortex shedding from its usual frequency, whereas for threaded piles, the helical wires disturbs the vortex shedding.

Grimaldi et al. (2009) conducted a series of laboratory experiments to investigate the effectiveness of bed sill as a countermeasure against local scouring at a smooth circular bridge pier. Their results showed that a bed sill placed at a short distance downstream of the pier reduced scouring depth, area, and volume. In particular, smaller distance between two structures has larger effectiveness of the countermeasure. They declared that the bed sill seems to be not effective at the beginning of the test and when the scour hole develops sufficiently and interacts with the countermeasure, the bed sill is more effective. In another study by Grimaldi et al. (2009), the combination of bed sill and slot to reduce local scouring at bridge piers were tested. Results of their study showed that best combination of slot and bed sill causes 45 % average reduction in scour depth at the upstream of pier.

Gogus and Dogan (2010) experimentally studied the effects of collars on scour reduction at bridge abutments. They noticed that when the collar width increased and it was placed at or below the bed level, the reduction in the maximum local scour depth increased considerably. Moreover changing of the sediment size did not affect the optimum location of the collar at the abutment, which yielded the maximum scour reduction around the abutment.

Nouri Imamzadehei et al. (2016) investigated the effect of geotextile layer in decreasing local scour of a cylindrical pier and showed that by using geotextile with an appropriate cover, the scour location moved downstream and the scour depth is decreased.

A review of previously published studies on the local scour countermeasures around the bridge piers indicates that the emphasize of most of them is to armor bed sediment as a countermeasure and just a few studies have been conducted to change the flow structure for controlling and reducing the local scour. This paper suggests applying a flow diversion structure at the upstream of the bridge pier in order to change the flow structure around the pier in order to decrease the local scour. The flow diversion structure suggested in this study has a triangular prismatic shape with dimensions much smaller than the bridge piers.

2 EXPERIMENTAL SETUP AND PROCEDURE

Experiments were carried out using a rectangular laboratory flume with dimensions of 15.0 m long, 0.7 m wide, and 0.6 m deep. The flow discharge was supplied from a constant head tank and measured using an electromagnetic Danfos flow-meter of 1 % accuracy. This flume has also been equipped with a digital point gage of 0.1 mm accuracy to measure the scour hole topography, a micro Acoustic Doppler Velocimeter (ADV) to measure the flow velocity component, and a downstream sluice gate to regulate the water depth.

The pier diameter was carefully chosen to have no contraction effect on the depth of scour. According to Melville and Coleman (2000), to avoid the contraction effect, the flume width should be at least 10 times greater than the pier diameter. In this study, a pier with a diameter of 50 mm was adopted for the tests. The flume width to the pier diameter ratio (W/D) was 14, satisfying the condition recommended by Melville and Coleman (2000). The flow diversion structure, employed in this study, was built in the shape of a prismatic of isosceles triangle with dimensions with a base of 10, and height of 25 mm that was located at the six different spacing from the pier (*i.e.* L/D = 0.5, 1, 1.5, 2, 2.5 and 3.5, where L is the clear distance between the pier and the flow diversion structure). Figure 2 shows the experimental test set up schematically.

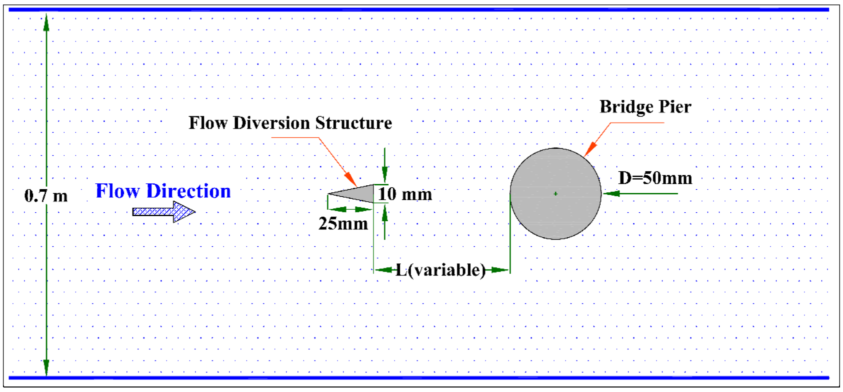

Figure 2. Schematic diagram of the experimental setup (plan view).

The working section in the flume comprised a sediment recess, which was 3.0 m long and 0.12 m deep, and was located at the downstream, 9 m from the flume inlet section. The experimental tests were conducted using 120 mm thick uniformly graded non cohesive sand with median grain size, d_{50} = 0.8 mm. According to Melville and Coleman (2000), the maximum possible local scour depth for an aligned circular pier is equal to 2.4D. In this study, sand thickness was selected equal to 120 mm to satisfy the aforementioned criterion. Once the diameter of the model pier was determined, the mean grain size of bed material was verified as the design criteria developed by Ettema (1980), according to which, the grain size does not affect the depth of scour if the pier width to the grain size ratio exceeds a value of about 50. Based on these design criteria, the mean grain size of the bed material was checked with the adopted bed material. For this study, the ratio was 62.5, satisfying the criterion suggested by Ettema (1980).

At first step of the experiment, the bed material was placed in the sand recess and after levelling the sand bed, the pier and the flow diversion structure were carefully installed at the centre line of the flume along the longitudinal direction. The flume was initially filled with water using a very small flow rate in such a way that the sand bed was not disturbed by the flow of water. As the depth of water approached the target depth of flow (0.1 m), flow rate was then gradually increased with extra care up to the designed rate (Q = 21 L/s). The tail gate, provided at the downstream end of the flume, was moved up and down to maintain the required depth of flow. At the end of the test (after 24 hours), the flow was stopped and all water was drained out from the flume. Measurements of the final bed level were carried out using a digital point gage. The experimental tests were repeated at different distances between the pier and the flow diversion structure. In addition, a control test was conducted without the flow diversion structure, in order to recognise the effects of this structure on the amount of local scouring. Furthermore, in the control test and the tests with L/D = 1.5, the flow velocity components were measured at 35 grid points on XZ plane of Y = 0 by a micro ADV. The positions of grid points and axis coordinates are shown in Figure 3.

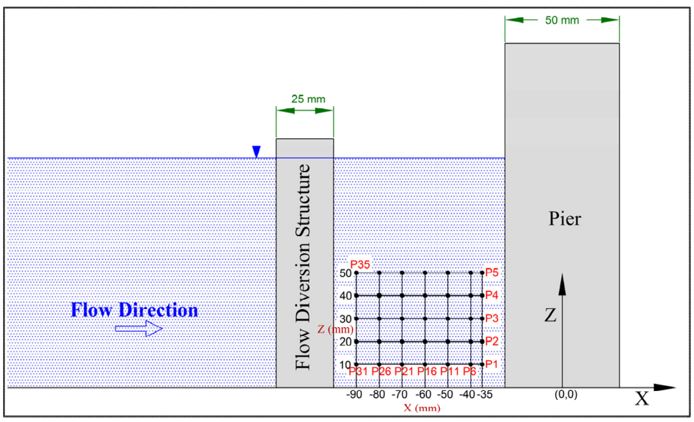

Figure 3. Schematic diagram of grid points positions for measuring velocity components (longitudinal view).

3 RESULTS AND DISCUSSION

The effect of flow diversion structure on local scouring around the pier was investigated. Seven tests were carried out with a single pier as well as the single pier and the flow diversion structure with L/D = 0.5, 1, 1.5, 2, 2.5 and 3.5. The duration of each experiment was 24 hours, because no sediment movement around piers was noticed after this duration. Melville and Coleman (2000) introduced a time factor (k_t), defined as the ratio of the local scour depth at a particular time, to the equilibrium scour depth at the time to reach equilibrium scour depth. For this study, the time factor K_t (24 hours) was calculated as 0.96, *i.e.* 96 % of the equilibrium scour depth. All tests were conducted under clear water scour conditions. The critical flow velocity, V_c, for sediment entrainment, was predicted using the expression given by Melville and Coleman (2000). General tests conditions are presented in Table 1.

Table 1. Characteristics of Tests.

Test No.	L/D	Test time (hour)	Q (L/s)	Water Depth (m)	Mean Flow Velocity (m/s)	V/Vc
1	0 (Single Column)	24	21	0.1	0.3	0.96
2	0.5	24	21	0.1	0.3	0.96
3	1.0	24	21	0.1	0.3	0.96
4	1.5	24	21	0.1	0.3	0.96
5	2.0	24	21	0.1	0.3	0.96
6	2.5	24	21	0.1	0.3	0.96
7	3.5	24	21	0.1	0.3	0.96

3.1 Determination of the Maximum Scour Depth and the Scour Hole Volume

Table 2 presents the maximum scour depth, the scour hole volume and the reduction percentage of these parameters after installing the flow diversion structure. Figures 4 and 5 indicate the maximum scour depth and scour volume for each test, respectively.

Table 2. Scour Depth Characteristics.

Test No.	L/D	Maximum Scour Depth (mm)	Scour hole volume (mm^3)	Percentage of Max. scour depth reduction with comparison to the control test	Percentage of scour hole volume reduction with comparison to the control test 1
1	0	77	4,866,977	0	0
2	0.5	61	3,310,937	21	32
3	1.0	51	2,272,134	33	53
4	1.5	48	1,895,839	38	61
5	2.0	54	2,050,803	31	58
6	2.5	68	2,750,639	11	43
7	3.5	73	3,229,726	5	34

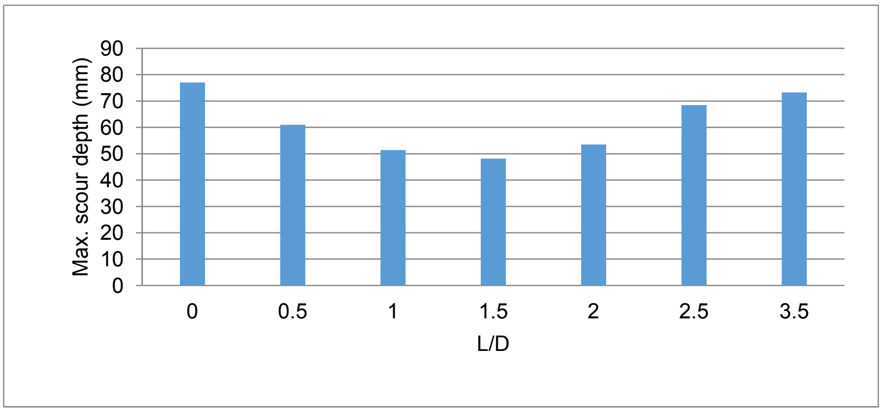

Figure 4. Max. scour depth with consideration of L/D.

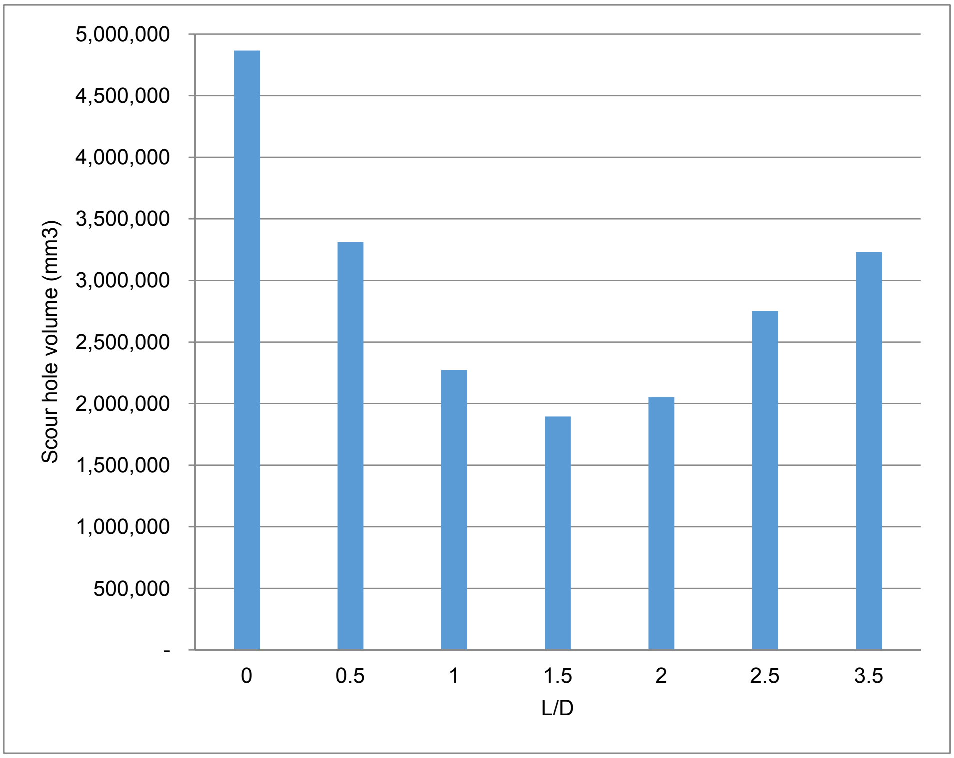

Figure 5. Scour hole volume with consideration of L/D.

Referring to Table 2 and Figure 4, the maximum scour depth occurred in a single pier case. The scour depth decreased when the flow diversion structure was installed at the upstream of the pier. Referring to Figure 4, the maximum scour depth reduced with an increase in the spacing between the pier and the flow diversion structure up to 1.5D, and then began to increase with an increase in L/D. The maximum reduction of scour depth was 38 % and occurred when L/D = 1.5. Similarly, these results were achieved for the scour hole volume. As illustrated in Table 2 and Figure 5, when L/D was equal to 0.5, 32 % of scour hole volume was reduced. With increasing L/D up to 1.5, the trend of reducing the scour hole volume increased. The maximum decline of scour hole volume was obtained to be equal to 61 % when L/D = 1.5, and after that the trend of reduction decreased. Hence, according to the dimensions of the proposed flow diversion structure and the pier, the optimum clear distance between them to achieve the maximum yield, was near to 1.5 times of the pier diameter. In this situation, the maximum scour depth and the volume of scour hole around the pier were reduced 32 % and 61 %, respectively.

3.2 Velocity Components

In order to find out the velocity components changes at upstream side of the pier by installing the flow diversion structure, the stream-wise velocity component (u) and the vertical velocity component (w) at 35 grid points (Figure 2) in Tests 1 and 4 were measured by a micro ADV and compared to each other. Figure 6 shows a comparison of stream-wise velocity component (u) in Test 1 and 4. According to this figure, the stream-wise velocities at all grid points in Test 4 were less than those of Test 1. The averages of stream-wise velocity components at these 35 grid points in Test 1 and 4 were 0.23 and 0.07 m/s, respectively. It can be noted that the flow diversion structure reduced the average of stream-wise velocity component at the upstream side of the pier up to 70 %. The intensity of down-flow and horseshoe vortex are dependent on the magnitude of stream-wise velocity (u) at upstream face of the pier, therefore, it can be concluded that these parameters may be reduced by installing the flow diversion structure at a specific distance from the upstream of the pier.

Similarly, Figure 7 plots the vertical velocity component (w) in Test 1 and Test 4. The positive value of w indicates that the down-flow was reduced by installing the flow diversion structure. The averages of vertical velocity component in Test 1 and 4 were -0.015 and -0.006 m/s, respectively, and could be resulted that the intensity of down-flow in Test 4 reduced up to 60 % in comparison to Test 1.

Accordingly, it can be concluded that the proposed flow diversion structure may reduce the magnitudes of velocity components and diverts the streamline at the upstream of the pier and consequently, reduces the local scour around the pier.

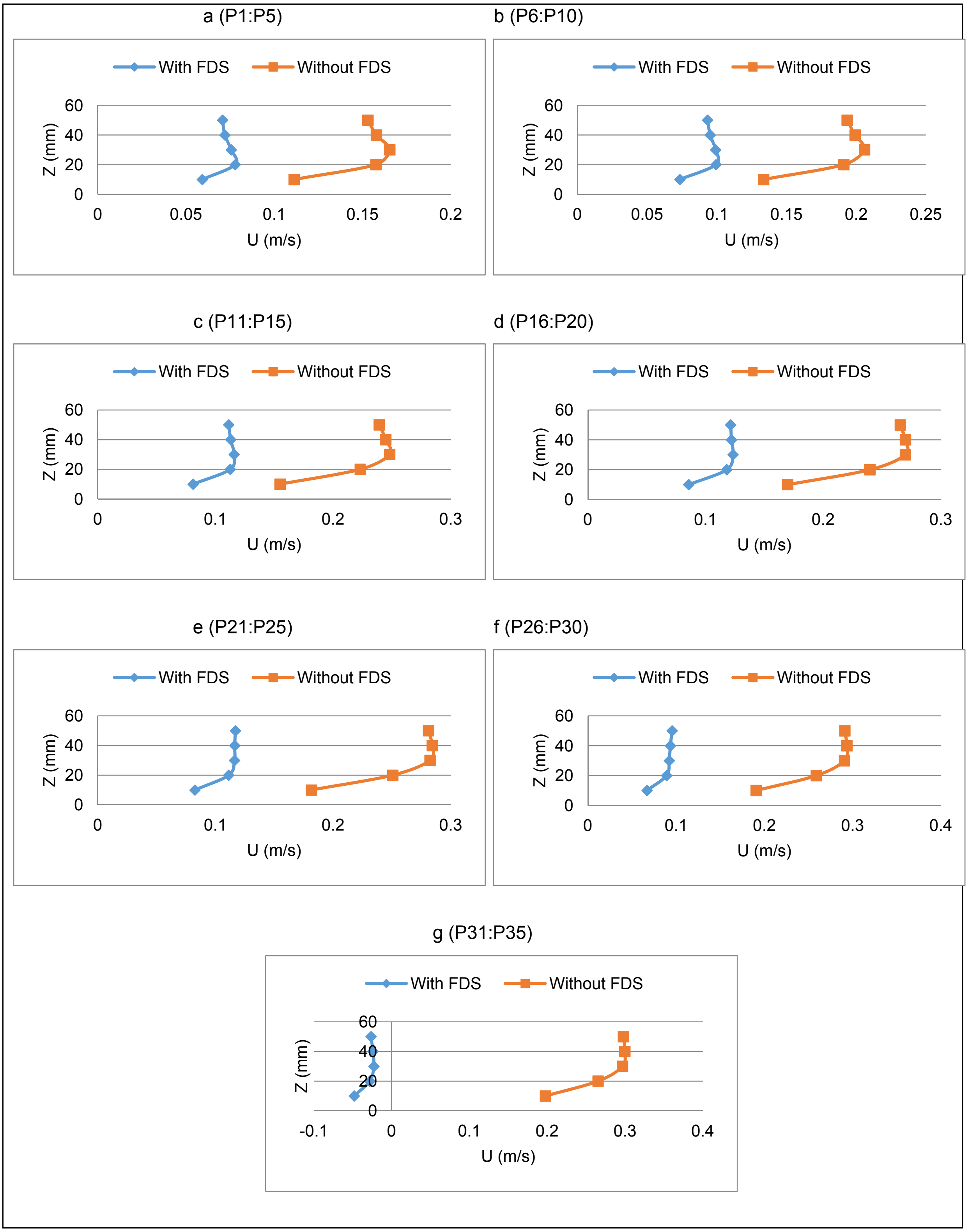

Figure 6. Comparison plot of stream-wise velocity component (u) in Test 1 (without flow diversion structure) and Test 4 (with flow diversion structure).

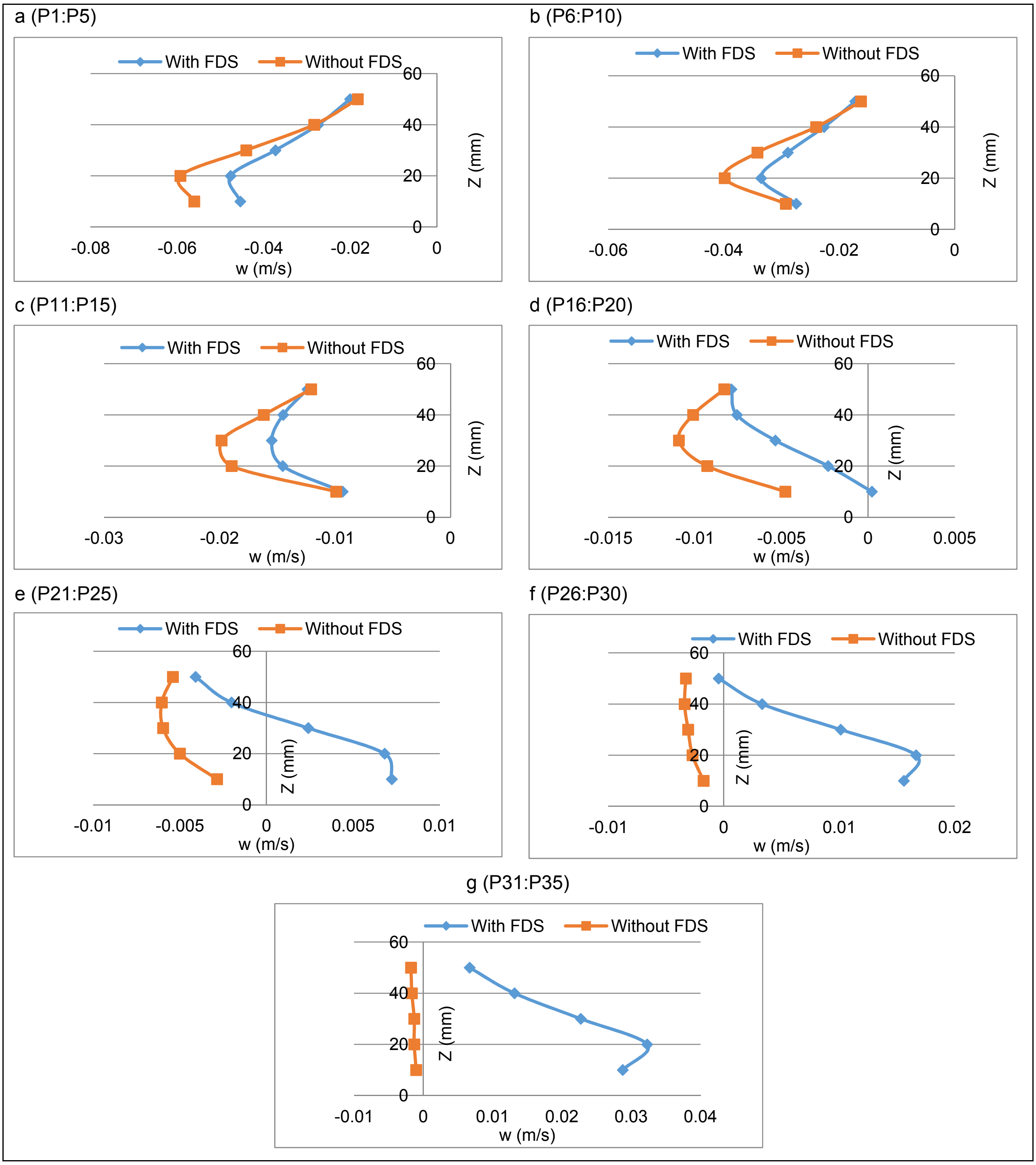

Figure 7. Comparison plot of vertical velocity component (w) in Test 1 (without flow diversion structure) and Test 4 (with flow diversion structure).

4 CONCLUSIONS

A flow diversion structure in the shape of a triangular prismatic structure has been introduced and employed as a countermeasure against local scour around the bridge pier. The findings of this experimental study clearly demonstrate the proposed structure affects the streamlines direction and diverts them from the upstream of the pier. In addition, the magnitudes of velocity components at the upstream of the pier reduce as a result of using the flow diversion structure. The clear distance between this structure and the pier significantly affects the reduction percentage of the local scour depth and the scour hole volume. According to the dimension of the flow diversion structure and the pier in this study, the optimum distance between them to achieve the maximum yield was found to be approximately 1.5 times of the pier diameter. In this situation, the scour depth and the volume of scour hole around the pier were reduced 38 % and 61 %, respectively.

REFERENCES

Chiew, Y. M. (1984). Local Scour at Bridge Piers, *PhD Thesis*. Department of Civil Engineering, Auckland University.

Chiew, Y. M. (1992). Scour Protection at Bridge Piers. *Journal of Hydraulic Engineering, ASCE*, 118(9), 1260 - 1269.

Chiew, Y. M. (2004). Local Scour and Riprap Stability at Bridge Piers in a Degrading Channel. *Journal of Hydraulic Engineering ASCE,* 130(3) 218 - 226.

Clopper, P. E., Lagasse, P. F. & Zevenbergen, L. W. (2007). Bridge Pier Scour Countermeasures. *World Environmental and Water Resources Congress*.

Dey, S., Sumer, B. M. & Fredsoe, J. (2006). Control of Scour at Vertical Circular Piles under Waves and Current. *Journal of Hydraulic Engineering, ASCE,* 132(3), 270 - 279.

Ettema, R. (1980). Scour at Bridge Piers, *PhD Thesis*. Department of Civil Engineering, University of Aucland.

FODT 2010. Bridge Scour Manual. Florida Department of Transportation.

Gogus, M. & Dogan, A. E. (2010). Effects of Collars on Scour Reduction at Bridge Abutments. *International Conference on Scour and Erosion*.

Grimaldi, C., Gaudio, R., Calomino, F. & Cardoso, A. H. (2009). Control of Scour at Bridge Piers by a Downstream Bed Sill. *Journal of Hydraulic Engineering, ASCE,* 135(1), 13 - 21.

Grimaldi, C., Gaudio, R., Calomino, F. & Cardoso, A. H. (2009). Countermeasures against Local Scouring at Bridge Piers: Slot and Combined System of Slot and Bed Sill. *Journal of Hydraulic Engineering, ASCE*, 135(5), 425 - 431.

Gris, R. (2010). Sheath for Reducing Local Scour in Bridge Piers. *Scour and Erosion*, 987-996.

Hamill, L. (1999). *Bridge Hydraulics*, USA and Canada, Routledge 29 West 35th Street, New York, NY 10001.

Imamzadehei, A.N., Heidarpour, M., Imamzadehei, M. N., Ghorbani, B. & Haghiabi, A. (2016). Control of the Local Scouring Around the Cylindrical Bridge Pier Using Armed Soil by Geotextile. *Journal of Geosynthetics and Ground Eng*ineering, 2(5).

Kirkegaard, L., Hebsgaard, M. & Jensen, O. (1998). Design of Scour Protection for the Bridge Piers of the Øresund Link. *Coastal Engineering*, 3634-3642.

Lauchlan, C.S. & Melville, B. W. (2001). Riprap Protection at Bridge Piers. *Journal of Hydraulic Engineering ASCE*, 127(5), 412–418.

Lauchlan, C.S. & Melville, B. W. (2002). Effects of Bed Degradation on Riprap Protection at Bridge Piers. *Journal of Water & Maritime Engineering* 154(1), 19–27.

Melville, B. W. (1975). Local Scour at Bridge Sites. Auckland, New Zealand, *Doctoral Dissertation,* School of Engineering, University of Auckland.

Melville, B. W. & Hadfield, A. C. (1999). Use of Sacrificial Piles as Pier Scour Countermeasures. *Journal of Hydraulic Engineering, ASCE,* 125(11) 1221–1224.

Melville, B. W. & Coleman, S. E. (2000). *Bridge Scour.* Water Resource Publications, LLC, Colorado, USA.

Park, S., Julien, P., Ji, U., Chang, T. & Park, B. (2007). Retrofitting Design and Physical Modeling for Pier-Scour Protection. *World Environmental and Water Resources Congress*, 1-14.

Qadar, A. (1981). The Vortex Scour Mechanism at Bridge Piers. *ICE Proceedings* of *Thomas Telford*, 71, 3.

Richardson, E. V. & Davis, S. R. (2001). *Evaluating Scour at Bridges.* Fourth Edition. FHWA NHI 01-001, HEC-18.

Sheppard, D. M. (2004). Overlooked Local Sediment Scour Mechanism. Transportation Research Record: *Journal of the Transportation Research Board*, 1890, 107-111.

Yanmaz, A. & Ozdemir, C. (2004). A Feasibility Study on Bridge Scour Countermeasures. *Critical Transitions in Water and Environmental Resources Management*, 1-8.

Yoon, T. H. & Kim, D. H. (2001). Bridge Pier Scour Protection by Sack Gabions. *World Water Congress 2001*.

LARGE-SCALE MODELLING OF DOUBLE-STILLING BASIN ARRANGEMENT, PAKISTAN – CASE STUDY

UBAID ULLAH[1], MUHAMMAD IQBAL[2], ERIC J LESLEIGHTER[3], BRONSON MCPHERSON[4], & UMAIR MANNAN[5]

[1]Principal Hydraulics Engineer, Engineering General Consultants (Pvt. Ltd.), Pakistan, ubaid006@gmail.com
[2]Principal Hydraulics Engineer, Associated Consulting Engineers (Pvt. Ltd.), Pakistan, iqbalg63@yahoo.com
[3]Private Hydraulics Consultant, Lesleighter Consulting Pty Ltd, Sydney, Australia, lesleighter@yahoo.com
[4]Director of Engineering, Manly Hydraulics Laboratory, Sydney, Australia, Bronson.mcpherson@mhl.nsw.gov.au
[5]Senior Engineer, Associated Consulting Engineers (Pvt. Ltd.), Pakistan, umair_mannan@hotmail.com

ABSTRACT

The Mohmand Dam is a 213 m tall concrete-faced rockfill dam (CFRD) under the design by a consortium of foreign and Pakistani consultants. The dam is constructed on the Swat River in Pakistan. The hydraulics detailing of the project has included large diversion tunnels, one to be converted to a permanent low level outlet works and sediment flushing outlet, and a seven-gated headworks with discharge into a 100 m wide spillway. A strategic component of the hydraulics studies has been large-scale physical model studies carried out by the Irrigation Research Institute, Nandipur, Pakistan. The paper presents the details of the model arrangements, particularly the final arrangement, and describes the hydraulic behaviour of a double hydraulic jump stilling basin facility as a means of breaking down the high heads for better energy dissipation control. While a ski-jump type spillway was considered, the large discharges into rock of relatively modest erosion resistance, with consequent deep and laterally extensive scour, made the selection of the hydraulic jump basins more attractive. The upper basin was designed to operate with a maximum head of about 100 m, and the lower basin was designed to operate with a maximum head of approximately 120 m. The studies considered the discharges up to 25,500 m^3/s. Detailed pressure transducer measurements of transients were made as part of the design of the basins. The chutes utilize a number of aerator steps for aeration of the flows along the chutes and into the stilling basins. The paper describes stilling basins and their effectiveness in handling such high discharges; basins which are generally based on the configuration of the USBR Type III stilling basin, utilizing a variation to the “normal” baffle blocks as a further hedge against cavitation potential.

Keywords: Hydraulic jump; stilling basins; cavitation; aeration; pressure transients.

1 INTRODUCTION

The planned Mohmand Dam Hydropower Project (MDHP) is one of several large power projects that has been studied and proposed to utilize the waters from the Himalayas, which flow in a number of large rivers. The Mohmand dam site is on the Swat River, approximately 200 km northwest of Islamabad. The location of the dam in relation to Peshawar is illustrated in Figure 1.

The dam site is a well-defined gorge, allowing the construction of a tall dam of modest length. The project has passed through a number of studies with a detailed feasibility study preceding the present lengthy study, which has derived the spillway arrangement – the subject of the present paper. The feasibility study was carried out under the auspices of the Japan International Cooperation Agency (JICA). The present work comprises site and dam selection, detailed hydrology, reservoir sedimentation aspects, power station sizing, diversion detailing, and hydraulics, which has progressed the earlier studies and has been carried out on behalf of the Water and Power Development Authority (WAPDA) by a consortium of consultant companies:

- SMEC International (Australia),
- Nippon Khoe (Japan),
- National Engineering Services (Pakistan),
- Associated Consulting Engineers (Pakistan),
- Engineering General Consultants (Pakistan), and
- BAK Consulting Engineers (Pakistan).

The diversion works comprise two 15 m diameter tunnels. One is to be developed into a permanent, low level outlet facility for necessary releases to the downstream and for drawdown purposes. The power intake will direct flows into a separate tunnel leading to a 800 MW power station on the right bank of the river a short distance away from the spillway discharge location. The low-level outlets, with a radial gate control structure is the subject of separate physical model studies.

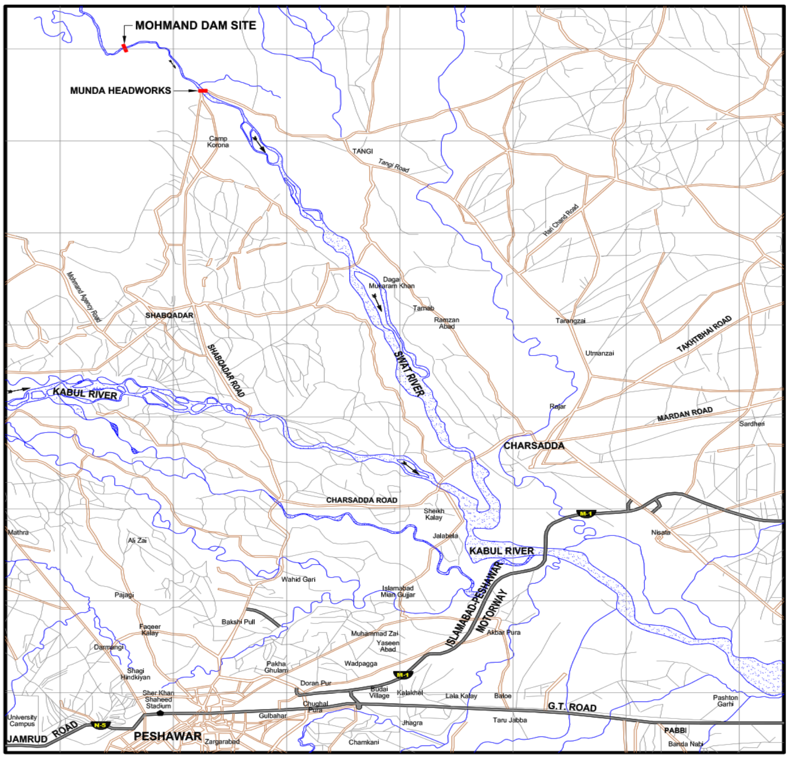

Figure 1. Location of the Mohmand Dam Project.

2 HYDROLOGY

The Swat River system was the subject of detailed hydrologic analysis. In July 2010, the river experienced extreme flooding with a discharge estimated as 9,909 m^3/s and was considered to have an Annual Exceedance Probability (AEP) of 1 in 1,000. The return periods for the Project went through a number of studies, updating and finally an accepted series of magnitudes. It was confirmed by WAPDA in January 2016 that the Project design team should adopt a panel of expert's recommendation for the Probable Maximum Flood (PMF) of 27,427 m^3/s inflow discharge. The computed peak value for AEP 1 in 1,000 and 1 in 10,000 are 10,669 m^3/s and 18,640 m^3/s, respectively. Figure 2 presents the inflow flood hydrographs at Mohmand Dam site.

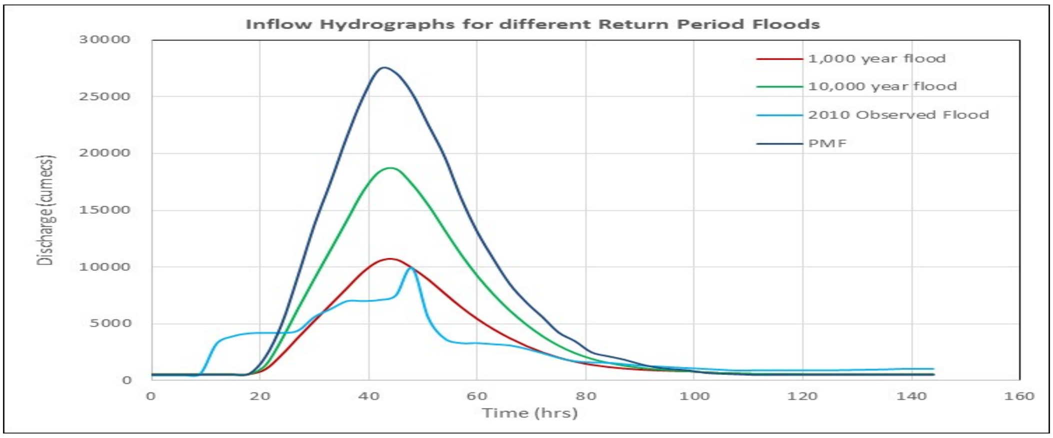

Figure 2. Inflow flood hydrographs.

As will be described later, the energy dissipation arrangement selected a two-stilling basin arrangement. The flood routing yielded a PMF outflow discharge from the reservoir of 25,362 m^3/s. For the spillway energy dissipation design, the design discharge was selected as 90 % of the PMF for the upper stilling basin and the AEP 1 in 10,000 discharge for the lower basin.

3 SPILLWAY TYPE AND KEY DIMENSIONS

The proposed spillway was to be located on the left abutment of the dam, following the dam-type selection of a concrete-faced rockfill dam (CFRD). This precluded placement of a spillway over the dam. The type of spillway received detailed consideration. Originally, the project commenced with the plan to use a flip bucket and plunge pool energy dissipation arrangement, for which the plunge pool pre-excavation would be a large-volume depression on the river's left and against a steep excavation of the hill on the spillway's left. Essential to the provision of an acceptable plunge pool dissipater was the consideration of rock scour and its longitudinal and lateral extent. Even the pre-excavation of the plunge pool would require a large slope excavation on the left side. The site investigations revealed rock largely classified as a foliated schist. Based on the Consultant's experience, it was considered very erodible under the action of velocities around 45 m/s.

The main issue with the plunge pool erosion, apart from a likely depth to 60 m below river bed level, was its lateral expansion and movement with the result that the entire left hill excavation would be undermined and be subject to collapse. This in turn would produce a large volume of scoured and collapsed material to form a huge blockage in the river, affecting the power station, and the spillway itself.

The flip bucket-plunge pool arrangement was abandoned and consideration moved to the application of a hydraulic jump stilling basin alternative as the means of dissipating the energy from the spillway.
Following are some design adopted parameters:

- Full Supply Level (FSL): EL555 m asl
- Spillway Ogee Crest Level: EL539 m asl
- Dam Crest Level: EL563 m asl
- Parapet Wall Top Level: EL564.5 m asl

The design team considered several chute and stilling basin arrangements. The headworks also passed through a number of alternatives for the number of gates, and whether part of the spillway would remain ungated with the crest at FSL. The result was seven gates, each 15 m wide, 5.3 m thick piers, all placed on a curved crest alignment on a 500 m radius. The chute was converged from the total crest width of approximately 137 m to a width of 100 m. This led to a unit discharge at PMF of approximately 255 m^2/s.

With a reservoir level in the region of EL 560 and the river bed in the dissipation area at EL360, clearly the 200 m head placed stringent conditions on the spillway design. Early considerations of a single stilling basin indicated the basin inflow velocities around 60 m/s, and in due course, it was decided to investigate the use of a double stilling basin configuration, somewhat similar to the arrangement used some decades earlier on the Mangla Dam spillway, also in Pakistan. It is the design of the double basin, which is the main purpose of this paper. Detailed physical model studies were carried out at the Irrigation Research Institute (IRI), Nandipur, Pakistan.

Figure 3 shows a plan view of the spillway and Figure 4 illustrates a profile, depicting the chute from the headworks into the upper basin with an end weir and discharge into the lower basin with an invert level at EL348.

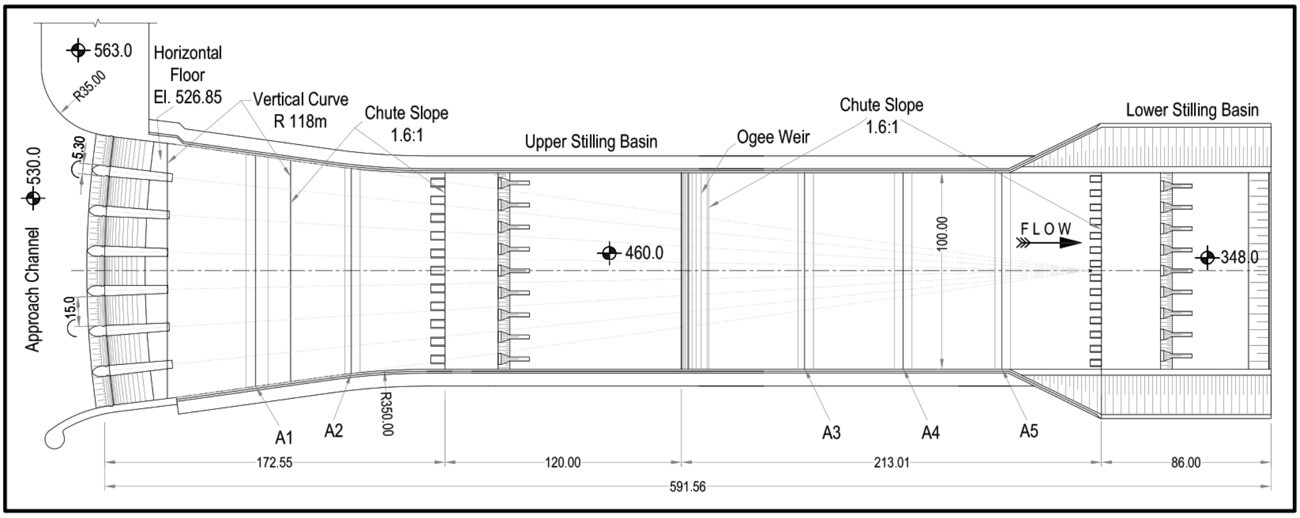

Figure 3. Plan of the double basin spillway.

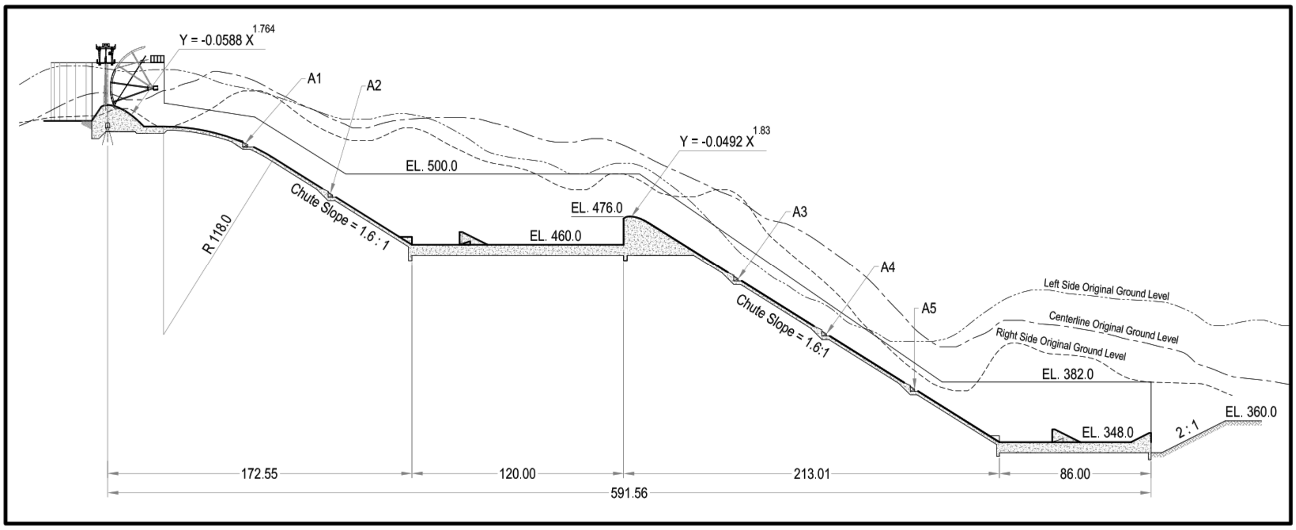

Figure 4. Profile of the spillway.

The upper basin was designed to operate with a maximum head of about 100 m, and the lower basin was designed to operate with a maximum head of approximately 120 m. The studies considered discharges up to 25,500 m^3/s. Detailed pressure transducer measurements of transients in the upper basin were made as part of the design of the basins, and the chutes incorporated several aerators along the length of the chutes, the geometry of which was studied and varied on the hydraulic model.

4 HYDRAULIC MODEL DESCRIPTION

The model was built and tested with a scale of 1:60. Figure 5 shows a general arrangement plan of the model boundary. It serves to show the dam, the left abutment spillway location, the power station on the river bank (located to avoid significant effects from the spillway discharges). Each stilling basin was designed initially with estimation of spillway losses, and basin length and depths based on the hydraulic jump characteristics, on the basis that a USBR Type III arrangement would be used. The basins were provided with conventional chute blocks, and baffle blocks were sized according to the jump characteristics and the USBR guidelines. The model was constructed in Perspex and instrumented with a large number of piezometers and several locations for pressure transducers. Figure 6 is a general view of the model in operation.

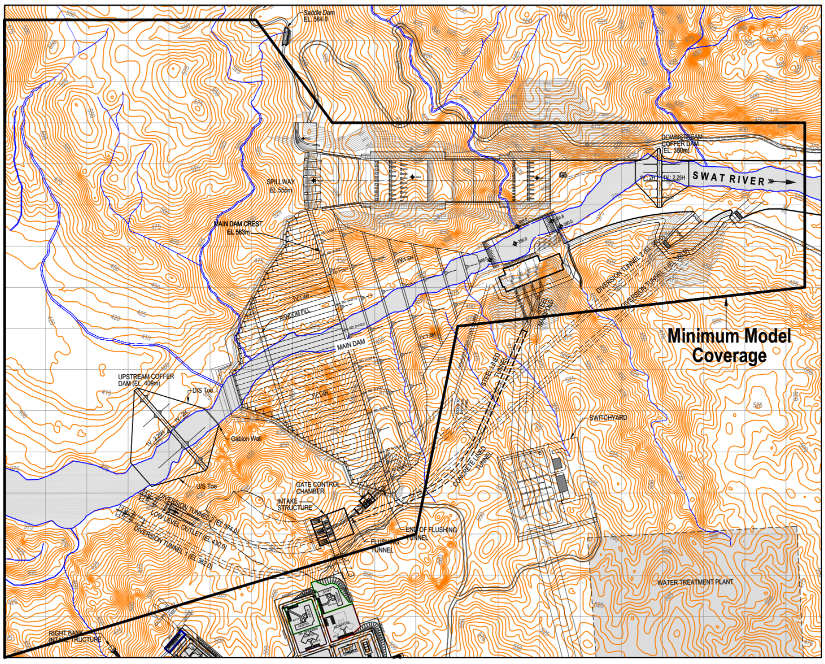

Figure 5. Coverage of the spillway model.

Figure 6. View of the model operation.

5 THE MODEL STUDIES

The paper focuses on the key and major aspects of the hydraulics, leading to a final design arrangement. In several ways, the estimates made and used as the basis for the early construction were found to be wanting, and the progressive changes not only showed the value of the model investigation but produced confidence that a workable and safe design could be achieved. As an indication, several aspects of the model dimensions and details were summarized in the following, which were subject to change:

- Length and end weir height for the upper basin, increased from 90 m to 12 0m and 14 m to 16 m, respectively.
- Number and location of the aerators, reduced from six to five – two on the upper chute and three on the lower chute.
- Variation in the height and slope of the aerator ramps.
- Height, location and number of the baffle blocks in the upper basin, and
- Invert level of the lower basin (lowered from EL 355 to EL348).

The baffle block dimensions were a departure from the conventional USBR shape, as it was decided to utilize the shape developed by USBR studies of a “supercavitating” block during testing for the Folsom Dam auxiliary spillway (USBR, 2009). The purpose was to “push the limits” for which baffle blocks could be used in a cavitation environment, meanwhile ensuring generous aeration of the lower flow layers in the chute and into the stilling basins.

While the prototype aerator performance will depart somewhat from the model indications, experience has shown that a sound representation of the nappe geometry and the induction behavior can be obtained from suitable modelling. The aerators on the Mohmand model showed that the nappe profiles well and the performance led to the lowering of ramp heights in some cases, to reduce the length of the aerated zone as well as relocating the aerators to command the chute length sufficiently to provide assurance that the full chute flow would have adequate aeration. There is sufficient experience, the model and prototype, to allow confidence in the designs, both in their location and in the air duct areas to meet the demands of the jets from the ramps. Figure 7 shows the dimensions of the five aerators.

As summarized above, the upper and lower basin geometry was changed. The estimated length of the upper basin was initially 90 m. This was found to be inadequate, with an incomplete jump length before flow passed over the end weir. Lengthening to 120 m and raising the end weir height provided good retention of the hydraulic jump. However, part of the success was attributed to the size and placement of the baffle blocks. Originally, with the shorter basin, they were 8.4 m tall. With the longer basin and end weir height increase, baffles with a height of 7.2 m were sufficient. The tailwater levels are dictated by the Munda Headworks barrage, some 5 km downstream of the dam site. With the variation in the spillway flows and the effects of the barrage, a tailwater curve was adopted. With its finalization and operation of the model at the basin design discharge, the basin floor was lowered by 7 m, which was found sufficient to provide jump retention even up to the PMF.

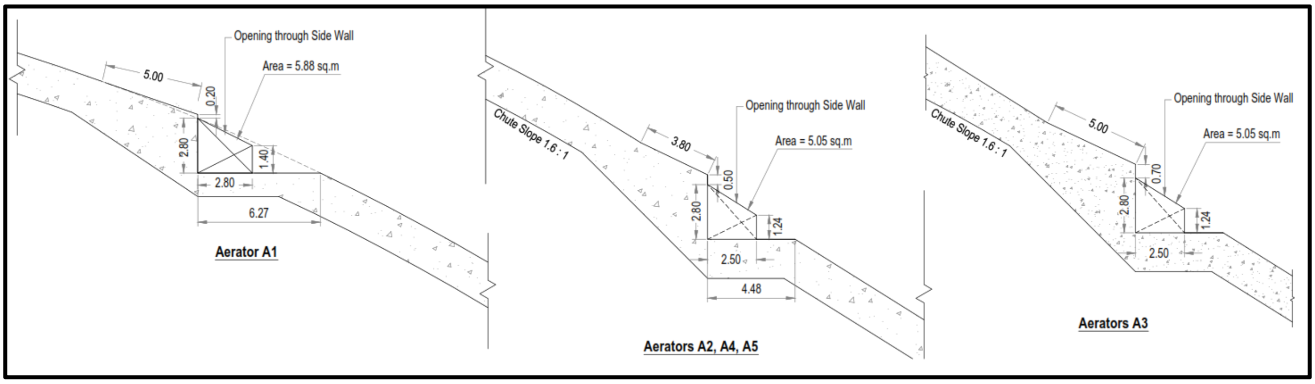

Figure 7. Final aerator geometry.

6 PRESSURE TRANSIENTS

The high-energy conditions in both stilling basins dictated close consideration of the pressure transients in the stilling basins for the purpose of the slab and anchoring design. The project team was able to introduce a capability to the laboratory to use multiple pressure transducers with associated analogue-digital capture of transients, as the basis of transients measurements, particularly in the highly turbulent conditions at the upstream end of the basins (upstream of the line of baffle blocks).

Figure 8 shows the deployment of eight transducers on the floor of the model upper basin, and simply by way of illustration, Figure 9 shows a small part-sample of the 2,300 s (prototype time) total capture of the transients at two of eight transducers in the upper basin. The information, together with cross correlation analysis of signals from pairs of transducers and spectra (from analysis by the Manly Hydraulics Laboratory, Australia), provided information for the design of the basin floor thickness as well as anchors.

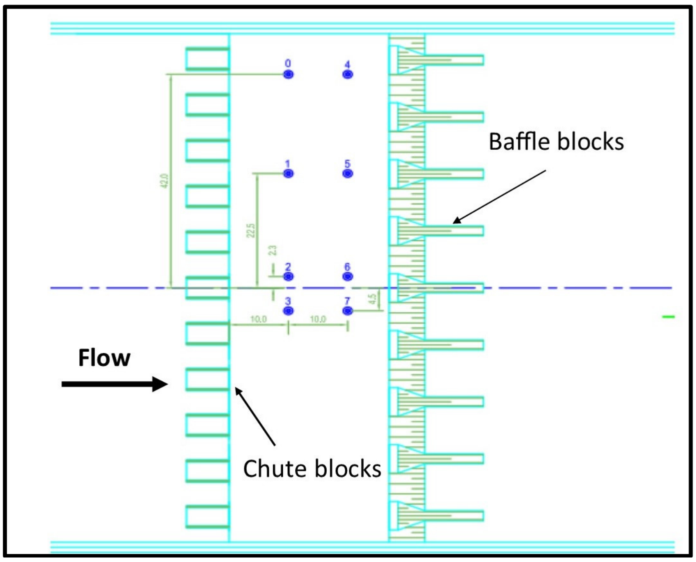

Figure 8. Placement of transducers in the upper basin for one test configuration.

A sample of the spectral density plots for one transducer for the PMF is shown in Figure 10. Clearly, the major fluctuations power is around 1 Hz or less, frequencies which are well within the "capability" of the structure floor slabs to respond and therefore, it is relevant for any dynamic analysis of the slab/anchor system.

7 CONCLUSIONS

The paper, describing detailed studies on a physical model, shows the value of the exercise in improving significantly on desk-type estimates. A number of aspects of the hydraulic structures should to be addressed by making significant modifications to the stilling basins, the aerators, and the stilling basin appurtenances. The spillway conditions are major by all comparisons, operating at high heads and with very large potential discharges. The use of the double stilling basin presented a workable and desirable option for the spillway to fit within a relatively narrow corridor with a high mountain (and appreciable excavation) on one side and the dam on the other side. The model results allowed confidence in the detailed design exercise which followed.

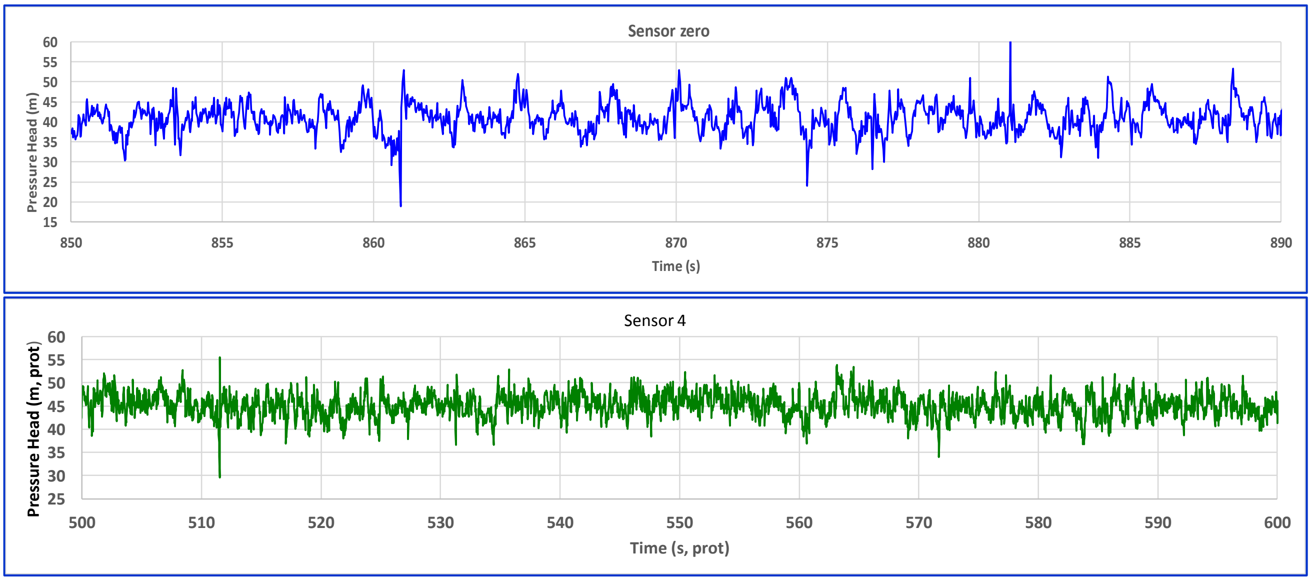

Figure 9. Sample transient pressures at two transducers, upper basin.

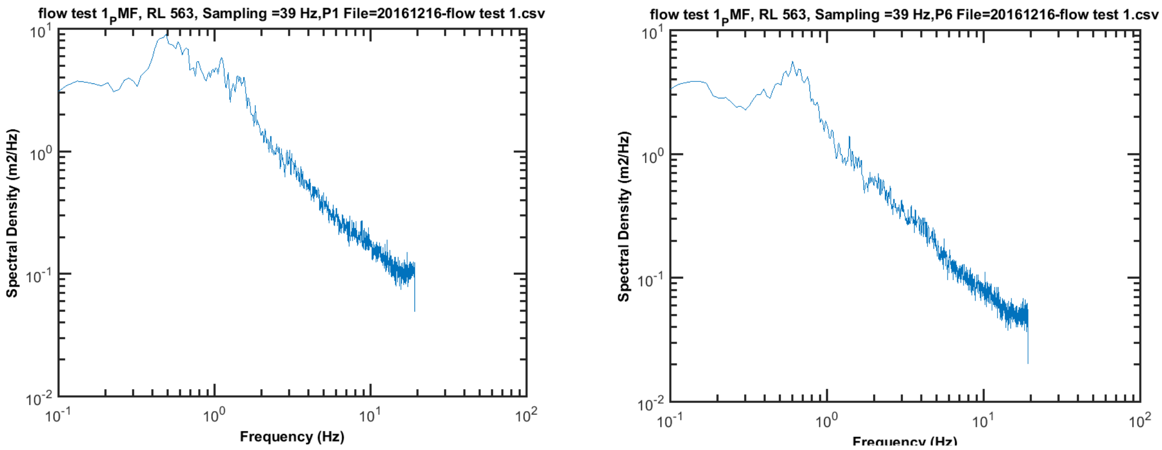

Figure 10. Sample spectral density plot for transducers 0 and 5 for the PMF.

ACKNOWLEDGMENTS

The authors express their appreciation to the Water and Power Development Authority (WAPDA) for permission to present the model study findings, to the IRI, Nandipur for its skill in building and testing the model, particularly research officers Tariq Anwar and Sana Ullah. Thanks also to Manly Hydraulics Laboratory's assistance in providing instrumentation and advice for the model transient work, and running the pressures analysis.

REFERENCES

USBR, Denver, Colorado, (2009). *Cavitation Potential of the Folsom Auxiliary Stepped Spillway.* Hydraulic Laboratory Report HL, 2009, 07.

SCOUR AND HYDRODYNAMIC EFFECTS OF DEBRIS BLOCKAGE AT MASONRY BRIDGES: INSIGHTS FROM EXPERIMENTAL AND NUMERICAL MODELLING

MOHSEN EBRAHIMI[1], RECEP KAHRAMAN[2], PRAKASH KRIPAKARAN[3], SLOBODAN DJORDJEVIĆ[4], GAVIN TABOR[5], DUŠAN M. PRODANOVIĆ[6], SCOTT ARTHUR[7] & MATTHEW RIELLA[8]

[1,2,3,4,5,8] Centre for Water Systems, University of Exeter, Exeter, United Kingdom
M.Ebrahimi@exeter.ac.uk; R.E.Kahraman@exeter.ac.uk; P.Kripakaran@exeter.ac.uk; S.Djordjevic@exeter.ac.uk; G.R.Tabor@exeter.ac.uk; mjr214@exeter.ac.uk
[6] Faculty of Civil Engineering, University of Belgrade, Belgrade, Serbia
dprodanovic@grf.bg.ac.rs
[7] Institute for Infrastructure and Environment, Heriot-Watt University, Edinburgh, United Kingdom
S.Arthur@hw.ac.uk

ABSTRACT

This paper describes preliminary results of a project investigating the scour and hydrodynamic effects of debris blockage at masonry bridges. Debris blockage, which is often cited as one of the primary causes of bridge failures in the UK and around the world, results in a larger obstruction to the flow leading to increased flow velocities, scour and hydrodynamic forces, compared to the conditions without debris. This, in turn, can affect the structural stability of bridges, for example, by undermining their foundations. Masonry bridges, many of which are valuable historical assets, are particularly vulnerable to debris blockage due to their short spans and low clearance. The reported study, being undertaken at the Centre for Water Systems at the University of Exeter, has two main phases: (i) laboratory experiments and (ii) CFD simulations. In the first phase, a 0.6m-wide and 10m-long flume is utilized to study the flow hydrodynamics and scour associated with pier/bridge models in several reference scenarios. The geometry of the pier/bridge and debris models are kept approximately similar to prototype conditions, with hydraulic conditions of the experiments designed to the degree that laboratory constraints allow to maintain Froude similarity. Velocities and scour are measured via an acoustic Doppler velocimeter and echo-sounding concept. Experimental results are used to calibrate and validate CFD models which can later enable simulation of more complicated scenarios. This paper will report these preliminary results from both experimental and CFD phases. Preliminary experimental results highlight the significance of debris existence in enhancing scour due to increasing flow downward velocities. Preliminary results from CFD modelling also show good agreement with experimental results.

Keywords: Debris blockage; masonry bridges; scour; laboratory experiments; CFD.

1 INTRODUCTION

Debris has been acknowledged for many years as a major factor affecting the risk of bridge failure during floods (Laursen and Torch, 1956; Chang and Shen, 1979; Diehl, 1997; Parola et al., 2000). It increases the effective width of a pier and constricts flow, thereby reducing conveyance and increasing water levels at the pier/bridge. These effects, in turn, enhance the hydraulic loading on structures such as culverts, bridge piers and abutments, and worsen scour (e.g. May et al., 2002; Bradley et al., 2005; McKibbins et al., 2006; Lagasse et al., 2010; Wallerstein et al., 2010; Arneson et al., 2012; Benn, 2013). Masonry bridges, which constitute 40% of the UK bridge stock (Bridle and Sim, 2009), are particularly vulnerable to debris blockage due to their special geometry that typically includes short spans and low clearances. The majority of masonry bridges, including a significant number classified as cultural and engineering heritage structures, were designed hundreds of years ago to withstand flood events less severe and less frequent than those happening today (RSSB, 2005). Consequently, during the flood events of the past decade such as those due to the storms (e.g. Storms Desmond and Frank) of winter 2015/16, hundreds of masonry bridges suffered significant damage with a few even taken to total collapse.

Despite recognising the role of debris in increasing the risk of bridge failure, the current UK guidance for assessment of bridge structures under hydraulic action (May et al., 2002; Highway Agency, 2012; Kirby et al. 2015) fails to provide a reliable approach for accounting for the scour and hydrodynamic effects of debris blockage. Presently the commonly adopted approach to predict scour due to debris blockage is by increasing pier width based on the original "effective pier width" concept of Melville and Dongol (1992). This concept substitutes debris and original pier with a pier with an increased width and does not explain the explicit effect of debris on flow hydrodynamics. However, while still recommended in the recently revised CIRIA manual for evaluating scour at bridges (Kirby et al., 2015), this approach is known to overestimate effective pier width (Lagasse et al., 2010). The current project is aimed at improving this approach at next stages.

  / ISSN 1562-6865 (Online) - ISSN 1063-7710 (Print)

Previous research on pier scour due to debris is limited to pier geometries or pier arrangements which are not representative of masonry bridges (e.g. Pagliara and Carnacina 2011, 2013). Also, available investigations have mainly focused on single pier and not the whole bridge (e.g. Lagasse et al. 2010). This is particularly important considering the significant number of failures of single span structures on small watercourses due to abutment scour (Benn, 2013). Therefore, there is a pressing need for scientific research to fill the knowledge gaps with respect to the hydrodynamic effects of debris blockage. Accordingly, a project was defined to investigate the effects of debris blockage on flow pattern, scour and hydrodynamic loads at masonry bridges under flood conditions. This project has three phases: (i) Flume experiments, (ii) CFD simulation, and (iii) Assessment guidance development. The goal of the first phase is to test reference scenarios of flow, debris and structure combinations to provide data for the development of numerical models and their validation in the second phase, i.e. CFD simulations. Scenarios at full-scale with real-life hydraulic conditions will then be simulated via developed CFD codes, and results from both phases will be used to develop an assessment guidance in the third phase of the project. Project outcomes will be built into the existing UK guidance (Kirby et al. 2015) for assessment of bridges under hydraulic action, and is expected to enable improved management of bridges at risk to debris blockage. A detailed review of the project background and methodology is presented in Ebrahimi et al. (2016). The present paper reports on preliminary results from flume experiments and CFD simulations.

2 FLUME EXPERIMENTS

Flume experiments were carried out in a sediment recirculating flume that is 0.6m-wide, 0.65m-deep and with a 10m-long working section. The flume is equipped with a 3-axis traverse system for positioning instruments at predefined (x, y, z) coordinates, with x, y and z being streamwise, cross stream and vertical directions. Flume experiments are designed to understand the effect of simple cylindrical debris on flow hydrodynamics and scour around a single pier. The flume's relatively small width does not allow for scaling down of all relevant hydraulic quantities such as pier geometry and sediment size proportionately. However experimental scenarios are still suitably representative of real conditions, and sufficiently varied to support CFD validation, which is the main purpose of the experiments.

2.1 Hydraulic conditions

The hydraulic conditions for the experiments discussed in this paper are summarized in Table 1. Experiments 1-2 were carried out to investigate only scour, while in experiments 3-4 both flow hydrodynamics and scour were measured (see subsections 2.3 and 2.4). In the table, B = flow width, d_{50} = average grain diameter of sediment, h = approach flow depth, Q = flow rate, R = flow Reynolds number (= Vh/v, with V = Q/(Bh) and v being the mean flow velocity and fluid kinematic viscosity, respectively), F = Froude number (= $V/(gh)^{1/2}$, where g stands for acceleration due to gravity), R_* = roughness Reynolds number (= $v_* k_s / v$, with v_* = $(gSR_h)^{1/2}$ as shear velocity, where S and R_h stand for longitudinal slope of the bed and hydraulic radius, respectively, and $k_s = 2d_{50}$ is granular roughness, Kamphuis, 1974), and V_{cr} = critical mean flow velocity for initiation of sediment motion (calculated as $V_{cr} = V/\eta_*^{1/2}$, where η_* is flow intensity calculated according to Yalin and da Silva, 2001). L_D and D_D are length and diameter of cylindrical debris.

Table 1. Hydraulic conditions of experiments at present paper (B = 60 cm, d_{50} = 1.37 mm).

Experiment	Approach flow depth ± 0.05 h (cm)	Discharge ± 0.1 Q (l/s)	R	F	R_*	V/V_{cr}	Debris Shape	Debris Length L_D (cm)	Debris Diameter D_D (cm)
1	7.9	19	31673	0.46	78.5	0.95	Cylindrical	30	1.9
2	7.9	19	31673	0.46	78.5	0.95	Cylindrical	30	3.2
3	13.1	35	58349	0.39	81.9	0.99	No debris	-	-
4	13.1	35	58349	0.39	81.9	0.99	Cylindrical	30	3.2

Reynolds number scaling is relaxed while keeping the flow turbulent (R > 2000-3000, Chanson, 2004). In addition, instead of having strict Froude similitude between model and prototype, flow is generally kept subcritical (F < 1). In all tests, the flow is uniform, and in fully rough regime of turbulent flow (R_* > 70, Yalin 1992; Yalin and da Silva, 2001). Experiments are carried out in clear-water scour conditions with V/V_{cr} being close to 1 in order to maximize scour depth.

Sediment in the current experiments is uniform silica sand with average grain diameter d_{50} = 1.37 mm and uniformity coefficient d_{60}/d_{10} = 1.37. d_{50} was identified based on

- Having a rough turbulent flow (R* > 70);
- Avoiding ripple forming sand (d50 < 0.6-0.7 mm, Raudkivi and Ettema, 1983; Ettema et al., 1998);
- Availability of the grain size on the market.

A compacted sand bed with sufficient thickness (based on the scour estimate, see Ebrahimi et al., 2016) was then installed in the flume. In order to maximize the number of experiments, duration of each experiment was

5 hours. While this is not sufficient for reaching equilibrium scour depth (Melville and Chiew, 1999), since all experiments with and without debris were run for the same duration, the results enable quantifying the effect of debris on scour, which is the central aim of this project.

2.2 Scaled models

As shown in the plan view schematic presented in Figure 1, the scaled single pier features two triangular cutwaters which are a typical feature of masonry bridges in the UK. Each cutwater is an isosceles triangle with base angle 45°. A pier width of 50 mm was chosen. This is much less than 1/6th of the flume width (B = 600 mm), the maximum pier size recommended for experiments to avoid adverse effects of side walls (Frostick et al., 2011). Pier streamwise length is 156 mm resulting in a width-to-length ratio of 0.32 that matches the average aspect ratio estimated for several masonry bridge piers mainly in Devon, UK (personal communication with Devon County Council, 2015).

Debris shapes, dimensions and types can vary from one stream to another in practice. However, to begin with, scaled debris in the experiments were represented with simple cylindrical elements representing a tree trunk without rootwads. Although strict scaling of debris was not required in the experiments, a sensible diameter/length ratio of cylindrical debris D_D/L_D was kept near 0.059 which is the average of the diameter/length ratios suggested by several field studies in US, Germany and Italy (Beechie and Sibley, 1997; Diehl, 1997; Kail, 2003; Comiti et al., 2006; Magilligan et al., 2008). The debris length, L_D , was 30 cm (covering half of the flow width) and diameter, D_D, was 1.9 cm. Also, an additional scenario with L_D = 30 cm and D_D = 3.2 cm was used to quantify the effect of cylindrical debris diameter on scour. Cylindrical debris was fixed to the pier cutwater nose just below the free surface of approach flow (Figure 1). Debris was fabricated by 3D printing using nylon powder. This is thought to be a useful technique to fabricate more complicated debris shapes in the next stages of the project.

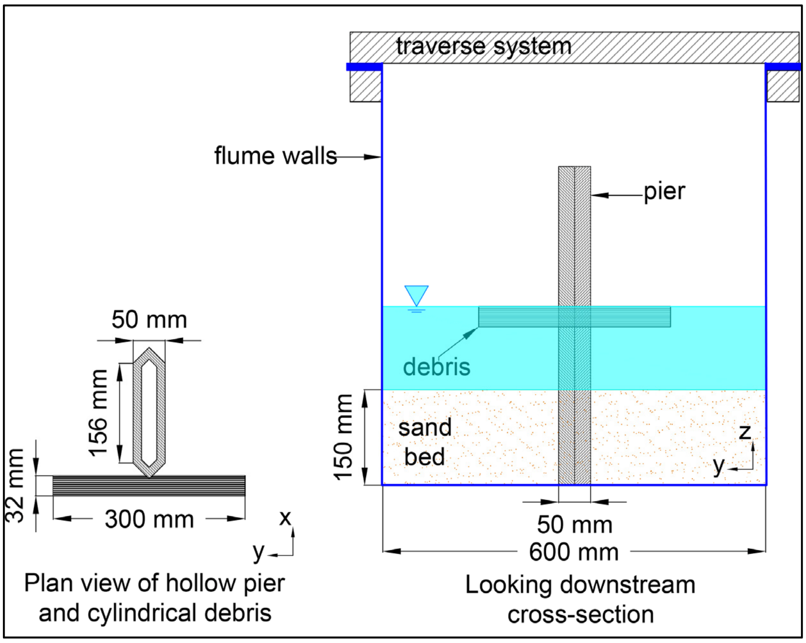

Figure 1. Schematics of experiment 5: Left. Plan view (x shows flow direction); Right. Cross-section.

2.3 Measurements

The flow rate was measured using an electromagnetic flowmeter (resolution ±0.1 l/s) installed in the suction pipe of the centrifugal pump. Approach flow depth was quantified using a digital point gauge (resolution 0.01 mm) mounted sufficiently upstream the pier to read undisturbed free surface elevation. During a 5-hour experiment, mean deviation of free surface elevation from its average was 0.5 mm (see Table 1).

Initial flow velocity field was measured only in experiments 3 and 4 and without any sediment in the flume. Therefore, bed roughness was different in flow experiments and the corresponding scour experiments. However, this was envisaged to be useful for investigating overall effect of debris on flow pattern and providing validation data for CFD modelling. Velocity measurements were carried out with the aid of a Vectrino Profiler ADV (accuracy 0.5% of measured velocity), installed on the 3-axis traverse system. Velocity measurements were performed on a grid of 20 predefined (x, y, z) coordinates. Velocity data collection duration at each point was between 3-20 minutes depending on the degree of turbulence and velocity fluctuations at that point.

Final scour geometry was measured after stopping the flow carefully to avoid any disturbance to the scour topography. Measurements were carried out using the distance measurement feature of ADV probe (accuracy of 0.5 mm) by moving the probe over a grid of ~ 240 predefined (x, y) points at one side of the flume (due to symmetry). Near the pier boundaries where ADV was unable to measure bed distance, additional points were measured manually using the point gauge. The scour topography, a sample of which is shown in Figure 2, was then produced by putting the measured distances together.

2.4 Results

In this section, scour results are presented first. Afterwards, velocity pattern, as the scour underlying process, is discussed.

2.4.1 Scour

Maps of scour final topography in experiments 1-4 are illustrated in Figure 2a-d. Maximum scour, $d_{s,max}$, was invariably located at the side edges of upstream cutwater marked by the yellow line. As can be seen, in high flow depth, i.e. tests 3 & 4, maximum scour increased from 95.7 mm to 112 mm, i.e. 17% increase. Also in low flow depth, maximum scour increased from 78.7 mm in test 1 to 87.8 mm in test 2, corresponding to 11.5%. In other words, for tested debris sizes, existence of debris has a higher effect on scour compared to that of debris dimensions. Role of debris in enhancing scour can be explained by analysing velocity pattern which is presented in Subsection 2.4.2.

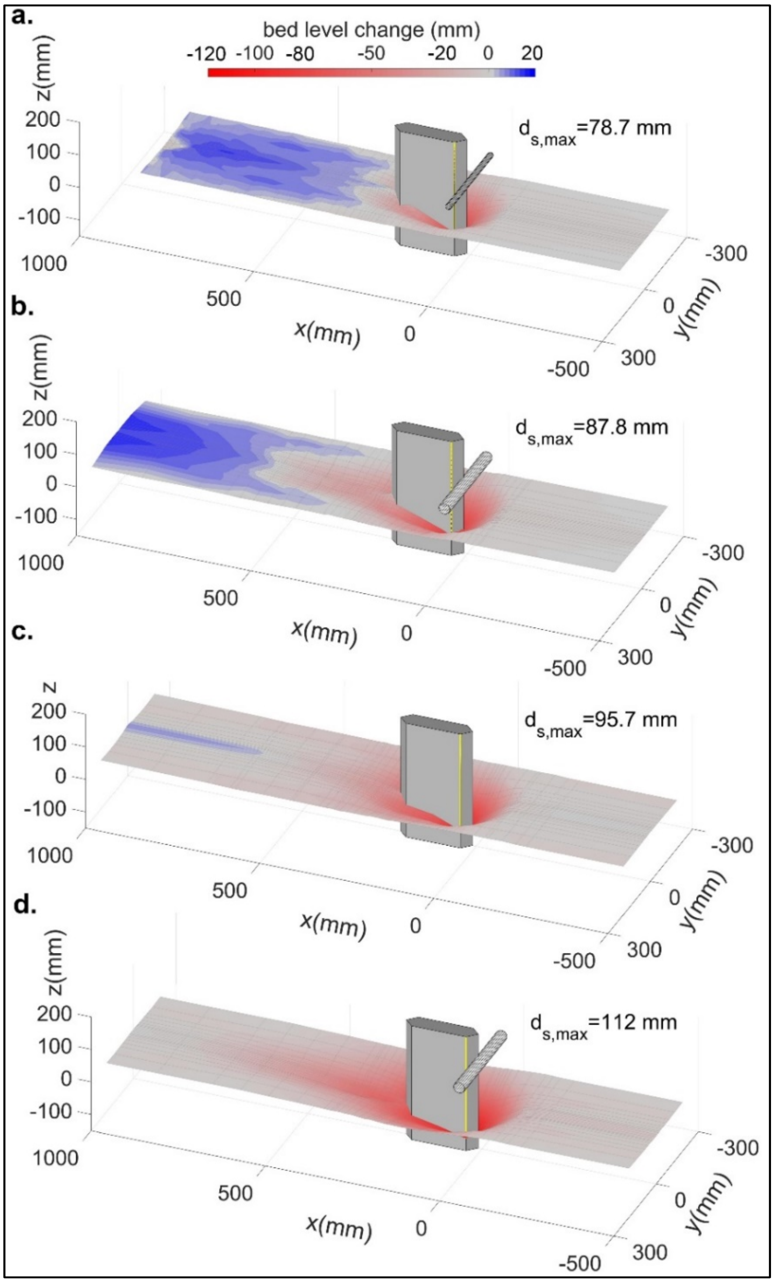

Figure 2. Maps of scour final topography: Experiments 1-5 (a-e). Yellow line marks location of maximum scour depth $d_{s,max}$.

2.4.2 Velocity

In order to have an overall picture of the flow pattern, initial velocity vector fields corresponding to experiments 3 and 4 are shown in Figure 3. It should be noted that velocity measurements were carried out without any sand in the flume and so with different roughness compared to scour experiments. Velocities were measured at twenty nodes in x-y plane numerated 1 to 20 by red colour (Figure 3a) and with resolution ~1 mm in vertical direction. Some of the nodes and vectors are removed for better visibility. Also velocities closer than ~4 cm to the free surface and ~1.5 cm to the bed were not measurable with the utilized instrument.

As can be seen overall velocity fields look similar in experiments 3 and 4. Velocity patterns upstream from the pier (e.g. node 1) are more or less similar in both cases. Downstream from the pier (e.g. nodes 14 and 16), velocities are significantly smaller due to the blocking effect of pier and, as expected, this effect is somewhat larger in the case with debris. Flow acceleration can be seen beside the pier (e.g. nodes 9 and 10) which is due to the narrowing effect of the pier on cross-section and this effect is somewhat larger in the case with debris.

A closer look at vertical velocity components reveals effect of debris in enhancing scour that was described in Subsection 2.4.1. As noted by many researchers (e.g. Hjulström, 1939; Yalin, 1992; van Rijn 1993 amongst others), vertical velocities can affect sediment movement significantly. Vertical component of velocity would loosen and lift sediment while horizontal velocity components remove sediment downstream. Here, this scour enhancing effect is demonstrated by analysing vertical velocities upstream the pier nose in experiments 3 and 4 as shown in Figure 4. In this figure, vertical velocities, i.e. w along z, are exaggerated five times for better visibility. According to the observation by the authors during the experiments, scour initiated at upstream cutwater of the pier. The closest nodes to the pier upstream being common in experiments 3 and 4 are nodes 3-5. In Figure 4, velocities at these nodes are compared between the two experiments. As shown, longitudinal velocities, i.e. u along x, are within the same order; but vertical velocities are substantially larger in experiment 4 with debris. Debris not only partially blocked the cross-section but also diverged the flow toward the bed and increased vertical velocities. Mean values of vertical velocity at all three nodes, calculated by averaging vertical velocities over the whole velocity profile, were similar and ~ -0.85 and -2.5 cm/s at experiments 3 and 4, respectively.

In other words, debris resulted in increased downward velocities ~ 2.9 times on average throughout the whole velocity profile. This enhancement was between 1.2 and 6.4 times with an increasing trend toward the upper border of the measured profile. It is expected that vertical velocities at higher elevations which are closer to debris are affected more than velocities at lower elevations. Consequently, it is expected that in shallower flow, near-bed elevations see higher effect of debris compared to a deeper flow, and so larger enhancement of scour. This will be investigated in the next stage of the current project.

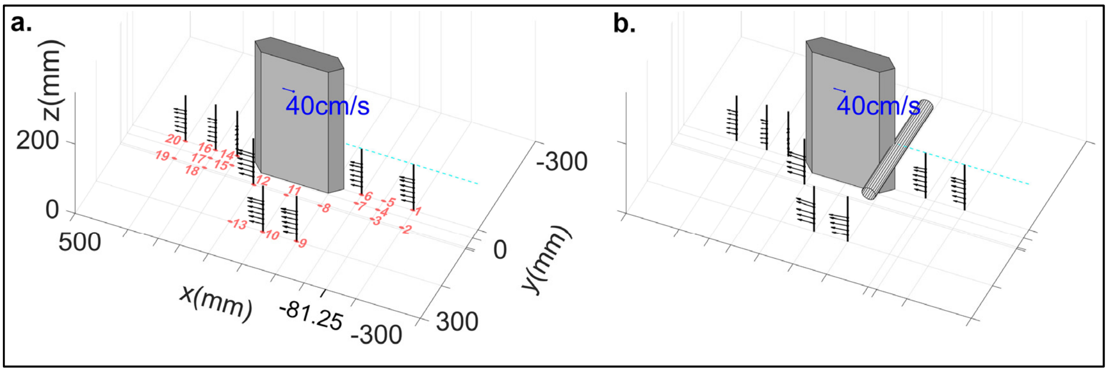

Figure 3. Initial velocity fields in tests 3 (a) & 4 (b). Velocities were measured at nodes numerated by red. Dash line represent free surface elevation & blue vector is reference.

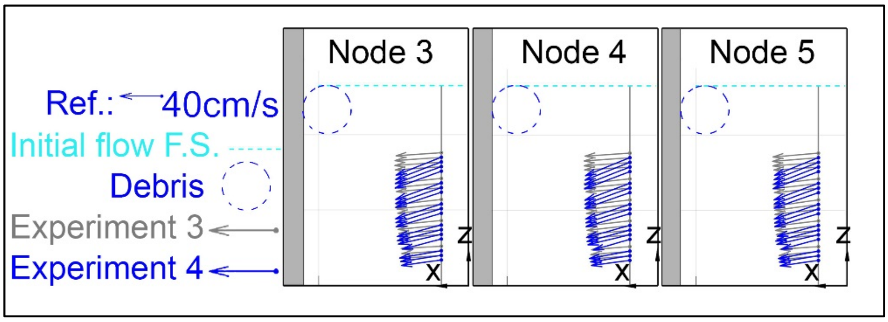

Figure 4. Velocity vectors in x-z plane in experiments 3 and 4 at nodes 3-5 (x = -81.25 mm). Velocity components along z are exaggerated five times for better visibility.

  / ISSN 1562-6865 (Online) - ISSN 1063-7710 (Print)

3 CFD SIMULATIONS

3.1 Model description

Throughout this work Computational Fluid Dynamics (CFD) is utilised to effectively model the experimental conditions found within the flume. The Unsteady Reynolds Averaged Navier-Stokes (URANS) equations governing fluid flow are solved numerically using the open-source CFD toolbox, OpenFOAM. OpenFOAM is developed based on the Finite Volume Method (FVM). The FVM is used for describing and evaluating the partial differential equation in form of algebraic linear equations. OpenFOAM includes various modelling capabilities, e.g. multiphase flow. There are several methods such as Mixture, Euler-Euler and Volume of Fluid (VOF) to simulate multiphase flows in OpenFOAM. The VOF method is one of the most widely used technique for tracking the interface between air and water and is often used for describing free surface flows. Therefore, the VOF method has been utilised in order to account for the free surface that is present within the flume. Turbulence modelling was achieved via the use of the k-ω SST model.

Two sets of simulations were conducted: a single phase simulation solved with the time dependent solver pimpleFoam and a multiphase simulation solved with interFoam. Both simulations use the flow conditions found in Experiment 3 in Table 1. The single phase simulations employ a slip boundary at the top of the domain in order to closely replicate experiment. The multiphase simulations account for both water and air phases with an interface separating them. The main motivation for this comparison was to investigate the Froude number effect on the flow field found around the pier and to deduce its potential effect on scouring at the piers base. The fluid domain is a complete replica of the experimental flume's geometry. This ensured continuity between both experiment and numerical modelling and facilitated direct comparisons. A fully structured mesh consisting of 8 million and 15 million cells, respectively, is used throughout both simulations.

3.2 Model validation

Four locations of interest around the pier were selected in order to investigate how the free surface affects the flow field. As an auxiliary effect the turbulence models effectiveness in capturing the shearing of the flow around the pier was also investigated. Point 1 denotes the upstream location, this was used to establish identical velocity profiles ensuring the inlet conditions were similar for both experiment and simulation. Point 2 is located 50 mm upstream of the pier. Point 3 and 4 are both located 35 mm from the pier, the location of which can be found in Figure 5.

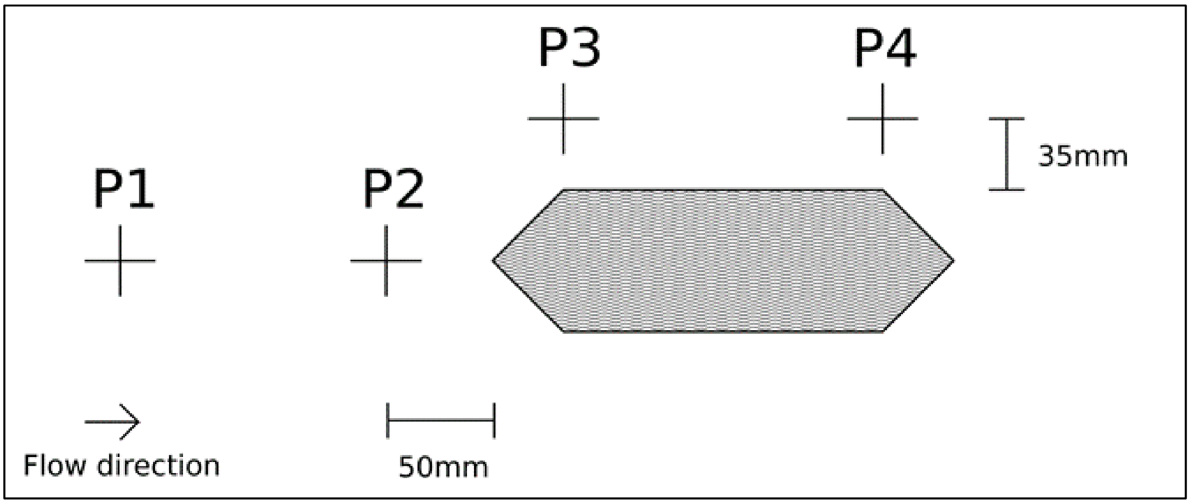

Figure 5. Location of sampling lines in CFD simulations.

The average streamwise velocities are sampled over the whole depth of the flow and are compared with those results recorded by the ADV, the results of which can be found in Figure 6. The y coordinate i.e. distance from the bed is normalised by the piers diameter and the streamwise velocities are normalised by the free stream velocity.

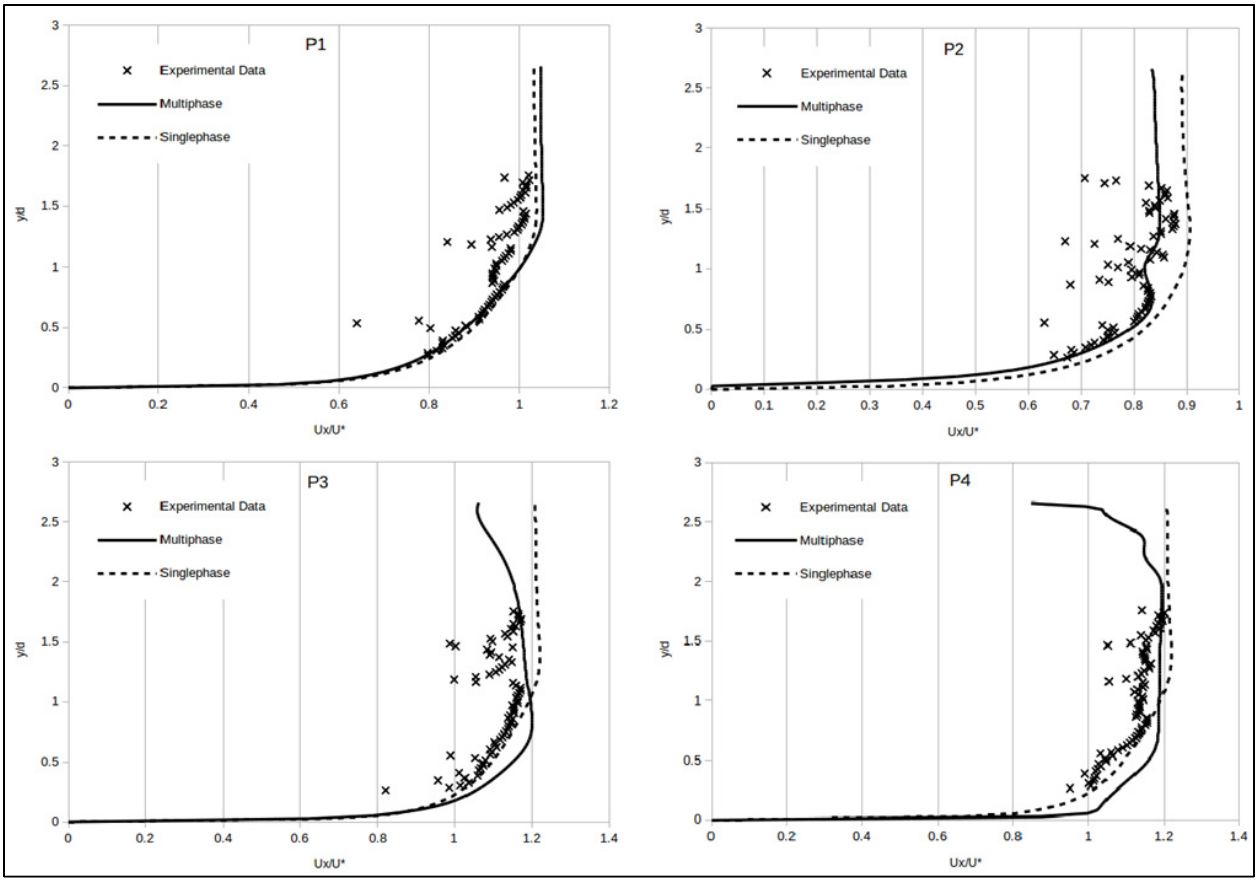

Figure 6. Normalised streamwise mean velocity profiles at four locations around the pier.

Looking at P1 it can be seen that the velocity profile is in good agreement for both simulations with the experimental data. There is a good match across the whole profile showing that the approach flow is accurately captured by the simulation. P2 highlights the effect the free surface has on the velocity profile, in contrast to the single phase simulation the velocities are noticeably retarded showing differences up to 12%. The boundary layer captured is in very good agreement with the experimental data. In this flow configuration a bulge is often present at the free surface often called a ‘surface roller’ this phenomenon is present within the model and is retarding the flow field across the depth of the flow.

P3’s location is of great interest as this is the area in which the Froude number has its greatest effect. Looking at Figure 7, the surface jump is shown as the gravity forces begin to dominate the approach flows velocity. This phenomenon is present solely due to the hydrodynamics caused by the pier’s geometry. There is a global increase in velocity as the flow is driven around the pier, the surface jump feeds into this process skewing the profile near the bed. Behaviour that isn’t present within the single phase simulation, although it can be seen that the single phase simulation is in better agreement in this area suggesting that the free surface effect is being overestimated.

Finally, P4 shows good qualitative agreement with experiment, especially in the multiphase simulation. The simulations overestimate the velocities shown in the experimental data but the overall behaviour is captured. It is evident from these results that the free surface effects have a large impact on the immediate flow field found around the pier.

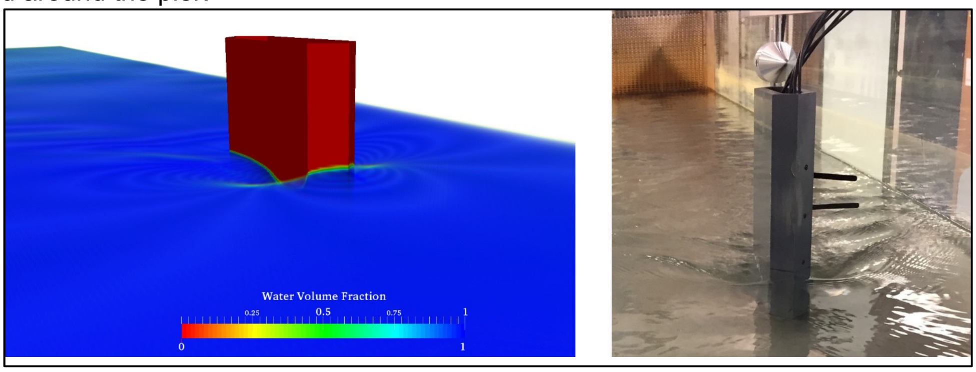

Figure 7. Free surface elevation around pier.

4 FUTURE RESEARCH

4.1 Flume experiments

Future experimental research will investigate scour at single span arch bridges due to debris blockage and the effects of various debris geometries such as a realistic tree trunk with rootwads. The project will also measure hydrodynamic pressures and forces using pressure sensors and load cells respectively. To the extent that time restrictions allow, effect of unsteady discharge and sediment grain diameter will also be investigated.

4.2 CFD simulations

Results from CFD simulations that for this geometry free surface effects are important even at relatively low Froude number. Although standard guidelines suggest a Froude number of less than 0.2 (Roulund et al. 2005) to omit the use of a free surface this facility is highly desirable. In an effort to predict real life conditions i.e. flooding this constraint is never going to be satisfied, also with the implementation of debris models the effect this has on the free surface is of great importance.

Building on these baseline simulations, the debris models will be implemented and solved with interFoam in order to account for the free surface. These will be compared directly with experimental results for further validation of the CFD models. Later the hydrodynamic effects of complex debris accumulations that are out of the scope of the experimental work such as block accumulations will be explored using CFD. The effect of Froude number on the free surface drop around the frontal corners of the pier will be explored to deduce how flooding conditions can exacerbate the scouring process.

A multiphase scour model will be developed which will run alongside interFoam. This will enable scour simulations in which the experimental data gathered in the flume can be directly compared and will enable validation.

5 CONCLUSIONS

Main findings of the present work are as following.

- Debris increased downward flow velocities and thereby scour at the base of the pier.
- The results between experiment and multiphase simulations show good overall agreement with an error estimated to be less than 10%.
- The Froude number of the flow has a large effect on the immediate flow field.
- From the baseline simulations the free surface has been effectively captured via the VOF method.

ACKNOWLEDGMENTS

The research presented in this paper was supported by funding from the UK's Engineering and Physical Sciences Research Council (EPSRC) under grant EP/M017354/1. For further information please refer to the project blog at http://blogs.exeter.ac.uk/ramb/ .

REFERENCES

Arneson, L.A., Zevenbergen, L.W., Lagasse, P.F. & Clopper, P.E. (2012). *Evaluating scour at bridges* (No. FHWA-HIF-12-003), Washington, DC.

Beechie, T.J. & Sibley, T.H. (1997). Relationships between Channel Characteristics, Woody Debris, and Fish Habitat in Northwestern Washington Streams. *Transactions of the American Fisheries Society*, 126(2), 217-229.

Benn, J. (2013). Railway Bridge Failure during Flooding in the UK and Ireland. *Proceedings of the Institution of Civil Engineers-Forensic Engineering*, 166(4), 163-170.

Bradley, J.B., Richards, D.L. & Bahner, C.C. (2005). *Debris Control Structures: Evaluation and Countermeasures*. US Department of Transportation, Federal Highway Administration.

Bridle, R.J. & Sims, F. (2009). The Effect of Bridge Failures on UK Technical Policy and Practice. *Proceedings of the Institution of Civil Engineers - Engineering History and Heritage,* 162(1), 39-49.

Chang, F.F. & Shen, H.W. (1979). *Debris Problems in the River Environment,* (No. FHWA-RD-79-62 Final Rpt.), Transportation Reasearch Board.

Chanson, H. (2004). *Hydraulics of open channel flow*. Butterworth-Heinemann, 1-650.

Comiti, F., Andreoli, A., Lenzi, M.A. & Mao, L. (2006). Spatial Density and Characteristics of Woody Debris in Five Mountain Rivers of the Dolomites (Italian Alps). *Geomorphology*, 78(1), 44-63.

Devon County Council (2015). *Meeting with Kevin Dentith on 25 August 2015,* Devon County Council, Exeter, UK.

Diehl, T.H. (1997). *Potential Drift Accumulation at Bridges*, US Department of Transportation, Federal Highway Administration, Research and Development, Turner-Fairbank Highway Research Center.

Ebrahimi, M., Kripakaran, P., Djordjević, S., Tabor, G., Kahraman, R., Prodanović, D. & Arthur, S. (2016). Hydrodynamic Effects of Debris Blockage and Scour on Masonry Bridges: Towards Experimental Modelling. *Proceedings of 8th International Conference on Scour and Erosion*. Oxford, UK, 743–750.

Ettema, R., Melville, B.W. & Barkdoll, B. (1998). Scale Effect in Pier-Scour Experiments. *Journal of Hydraulic Engineering*, 124(6), 639-642.
Frostick, L.E., McLelland, S.J. & Mercer, T.G. (2011). *Users Guide to Physical Modelling and Experimentation: Experience of the HYDRALAB Network*. CRC Press, 1-23.
Mercer, T.G. (2011). *Users Guide to Physical Modelling and Experimentation: Experience of the HYDRALAB Network*. CRC Press, 1-23.
Highways Agency. (2012). *The Assessment of Scour and other Hydraulic Actions at Highway Structures*. In Highways Agency, Design manual for roads and bridges, vol 3, section 4, Part 21, BD 97/12. London.
Hjulström, F. (1939). *Transportation of Detritus by Moving Water: Part 1*. Transportation, 5-31.
Kail, J. (2003). Influence of Large Woody Debris on the Morphology of Six Central European Streams. *Geomorphology*, 51(1), 207-223.
Kamphuis, J.W. (1974). Determination of Sand Roughness for Fixed Beds. *Journal of Hydraulic Research*, 12(2), 193-203.
Kirby, A.M., Roca, M., Kitchen, A., Escarameia, M. & Chesterton, O.J. (2015). *Manual on Scour at Bridges and other Hydraulic Structures,* second edition (Vol C742). London: CIRIA.
Lagasse, P.F., Clopper, P.E., Zevenbergen, L.W., Spitz, W.J. & Girard, L.G. (2010). *Effects of Debris on Bridge Pier Scour*, 653, Transportation Research Board.
Laursen, E.M. & Toch, A. (1956). *Scour around Bridge Piers and Abutments* (Vol 4). Ames, IA: Iowa Highway Research Board.
Magilligan, F.J., Nislow, K.H., Fisher, G.B., Wright, J., Mackey, G. & Laser, M. (2008). The Geomorphic Function and Characteristics of Large Woody Debris in Low Gradient Rivers, Coastal Maine, USA. *Geomorphology*, 97(3), 467-482.
May, R.W.P., Ackers, J.C. & Kirby, A.M. (2002). *Manual on Scour at Bridges and other Hydraulic Structures* (Vol. 551). London: CIRIA.
McKibbins, L.D., Melbourne, C., Sawar, N. & Gaillard, S.C. (2006). *Masonry Arch Bridges: Condition Appraisal and Remedial Treatment* (Vol. C656). London: CIRIA.
Melville, B.W. & Chiew, Y.M. (1999). Time Scale for Local Scour at Bridge Piers. *Journal of Hydraulic Engineering*, 125(1), 59-65.
Melville, B.W. & Dongol, D.M. (1992). Bridge Pier Scour with Debris Accumulation. *Journal of Hydraulic Engineering*, 118(9), 1306-1310.
Pagliara, S. & Carnacina, I. (2011). Influence of Large Woody Debris on Sediment Scour at Bridge Piers. *International Journal of Sediment Research*, 26(2), 121-136.
Pagliara, S. & Carnacina, I. (2013). Bridge Pier Flow Field in the Presence of Debris Accumulation. *Proceedings of the Institution of Civil Engineers-Water Management*, 166(4), 187-198.
Parola, A.C. Apeldt, C.J. & Jempson, M.A. (2000). *Debris Forces on Highway Bridges.* Transportation Research Board, 445.
Raudkivi, A.J. & Ettema, R. (1983). Clear-Water Scour at Cylindrical Piers. *Journal of Hydraulic Engineering*, 109(3), 338-350.
Roulund, A., Sumer, B.M., Fredsøe, J. & Michelsen, J. (2005). Numerical and Experimental Investigation of Flow and Scour around a Circular Pile. *Journal of Fluid Mechanics*, 534, 351-401.
RSSB. (2005). *Safe Management of Railway Structures, Phase 1: Flooding & Scour Risk*. London.
Van Rijn, L.C. (1993). *Principles of Sediment Transport in Rivers, Estuaries and Coastal Seas* (Vol. 1006). Amsterdam: Aqua publications, 1-17.
Wallerstein, N.P., Arthur, S. & Sisinnghi, D. (2010). Towards Predicting Flood Risk Associated with Debris at Structures. In *Proceedings of the IAHR APD conference 2010*, 1-10.
Yalin, M.S. 1992. River Mechanics, Pergamon Press, Oxford, 220.
Yalin, M.S. & da Silva, A.M.F. (2001). Fluvial Processes. *IAHR Monograph*, IAHR, Delft, 39(4),444.

COHERENT STRUCTURES IN A SHARPLY CURVED BEND WITH AND WITHOUT A SPUR DIKE

METE KOKEN[(1)] & EZGİ BUDAK[(2)]

[(1,2)] Civil Engineering Department
Orta Dogu Teknik Universitesi, Ankara, Turkey
mkoken@metu.edu.tr; ezbudak@metu.edu.tr

ABSTRACT

Results of three-dimensional (3D) Detached Eddy Simulation (DES) are used to investigate the changes in flow and large-scale coherent structures within a high-curvature open channel, with and without an isolated spur dike located on the outer bank of the channel. The flow of an 180^0 bend is simulated, in which the ratio between the bend curvature to the channel width is 1.25. The channel contained a flat bed, which represents the initiation of the scour process. The Reynolds number and Froude number are calculated using the channel depth at the inflow and the flume-averaged velocity were around 125,000 and 0.68, respectively. The cross-stream secondary flow and anisotropic effects play a crucial role in the redistribution of the streamwise momentum and influence significantly the distribution of the bed shear stress, which in turn, determines the capacity of the flow to entrain sediment. The presence of the isolated spur dike complicates the flow filed within the channel more, causing additional coherent structures to form around it. The eddy content is very rich within the flow field as compared to the case without the spur dike. It is shown that the secondary flow cell forming along the outer bank in the curved channel is not present once the spur dike is introduced. Moreover, there are differences in the bed shear stress distribution because of the inclusion of spur dike. In overall, the bed shear stress values get smaller within the curved reach whereas the patch of large shear stress values are shifted towards the inner bank once the spur dike is introduced.

Keywords: Open channels; coherent structures; detached Eddy Simulations; spur dike; secondary flow.

1 INTRODUCTION

Meanders observed in natural rivers considerably change the flow structure and increase the erosion capacity of a river along the bed and channel banks compared to the straight river reaches. Redistribution of the streamwise velocity, the secondary flow (cross-stream recirculation) and the coherent structures forming as a result of the curvature, causes a constantly evolving river morphodynmics with the continuous scour and erosion processes. In a strongly curved river, high core of streamwise velocity shifts towards the outer bank creating a pool as a result of scour along the outer bank. Meanwhile, the deposition of the sediment along the inner bank causes a bar formation.

The main cell of cross-stream circulation occupies most of the channel cross section during the initial stages of the scour (Blanckeart, 2010). After the development of pool and bar formations, the main cell occupies only the deeper part of the channel's cross section. Together with the main cell of cross-stream circulation, several other streamwise oriented vortical (SOV) cells are observed close to the inner and outer banks of the channel (Koken et. al. 2013). While the formation of a secondary cell at the outer wall was observed in curved reaches over a wide range of R/B ratios (R is the mean radius of curvature of the channel and B is the mean channel width), the formation of SOV cells at the inner bank is observed only for sharply curved channels (R/B < 2). As R/B decreases, the degree of non-linearity of the interactions between the cross-stream flow and the streamwise momentum increases. The same is true for turbulence anisotropy effects which are responsible for the formation of the secondary cell close to the outer bank, which rotates in the opposite direction as compared to the main cell of cross-stream circulation (Blanckaert and de Vriend, 2004; Blanckaert, 2011).

Spur dikes are constructed at the outer bank of a curved channel to protect it from scour. However, the intricate flow within the curved channel reach becomes even more complicated with the inclusion of the spur dike. Local flow features around isolated spur dikes within a straight channel (Koken and Constantinescu 2008, Paik et. al. 2010, Bressan et. al. 2011, Koken 2011) and flow in a curved channel (Constantinescu et. al. 2011, Kashyap et. al. 2012, Koken et. al. 2013) are investigated in the literature. However, there is no study that investigates the flow physics around a spur dike located in a curved channel. Because of the massively separated flow and the presence of the unsteady vortical structures within the flow domain, numerical eddy resolving techniques, such as LES (Large Eddy Simulation) or DES (Detached Eddy Simulation), are the most appropriate methods for investigating flow around spur dikes in a highly curved channel bend. Bed shear stress distribution along the bed and banks can be calculated and the unsteady dynamics of the coherent structures can be accurately predicted with these methods. It is shown that these methods provide a more accurate description of the mean flow and turbulence statistics in complex turbulent flows, such as flow in curved open channels (Keylock et al., 2012; Rodi et al., 2013). One of the main reasons for their better accuracy is that as the large-scale flow is resolved by these simulations, turbulence anisotropy effects associated with the large scales can be easily captured.

DES is used in the present study to show the changes in the coherent structures and the bed shear stress distribution in a sharply curved 180^0 bend with and without a spur dike attached at the outer bank of the channel.

2 NUMERICAL MODEL

Spalart Almaras type DES model is used in the current study where no wall functions are utilized close to the solid boundaries. The code uses fractional step method to integrate 3D incompressible Navier-Stokes equations on generalized curvilinear coordinates. Convective terms in the momentum equations are discretized using a blend of fifth-order accurate upwind biased scheme and second-order central scheme. All the other terms in the momentum and pressure Poisson equations are approximated using second-order central differences. More details regarding the code can be found in Koken and Gogus (2015).

Results of two simulations in a 180^o curved channel are presented here. One without a spur dike (case-NS) and one with a spur dike are attached on the outer bank of the channel (case-S). All the quantities used in the simulations are non-dimensionalized using the flow depth (D = 0.15 m) and the average flow velocity (U = 0.83 m/s). The dimensions of the numerical model are given in Figure 1. The channel has a straight incoming reach of 33D length, which is followed by a 180^o bend and continue with another straight reach of 45D length. Width of the channel, B, is 8D whereas the channel curvature, R, along the centerline is 10D. A spur dike with a length of 2D and a width of 0.33D is attached on the outer bank of the channel within the curved section at 30 degrees. The spur dikes make a right angle with the incoming flow. In both simulations, the computational mesh created for the simulations contained approximately 4.3 million grid points. Close to all the solid surfaces the first grid point was situated at one dimensionless wall unit away from the walls so that the viscous sublayer close to the solid boundaries are directly resolved without using any wall functions (Figure 1).

Free surface deformations in the channel is evaluated using Flow-3D software where identical models with and without a spur dike were run until steady state solutions were reached. Obtained free surface topographies are then imported into the corresponding models of the DES code for the next runs and assumed as rigid lids throughout these simulations. No slip boundary conditions are used for all the solid surfaces. A velocity profile, which contained realistic turbulent fluctuations, is fed at the inlet section in a time accurate fashion. These fluctuations are obtained from another LES simulation held in a periodic channel and stored in a file, which is then fed into the inlet section of the present simulations. They were run on a pc-cluster using 12 nodes with a time step of 0.02 D/U until a statistically steady state is reached; then data is collected approximately for a duration of 50 D/U to get statistics.

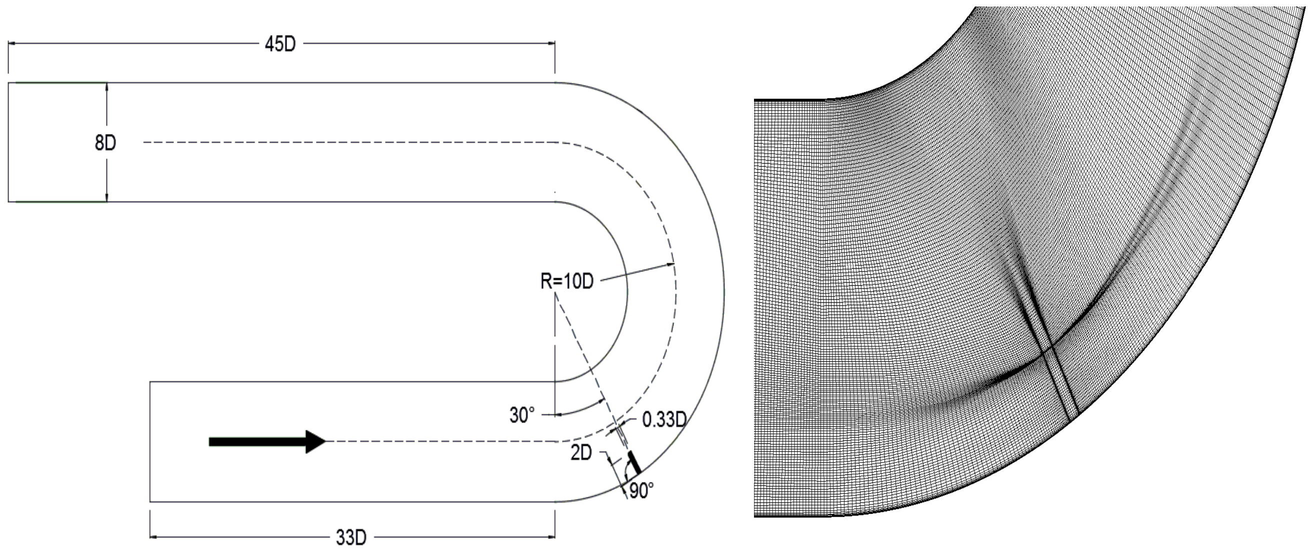

Figure 1. Descriptive sketch of the flow domain (left) and the computational mesh (right) close to the spur dike.

3 RESULTS

3.1 Shear layers

Distribution of the vertical vorticity contours on a horizontal plane at 0.9D above the channel bottom are shown together with the corresponding streamline patterns within the bend both for cases with and without spur dike in Figure 2. Vertical sections at different locations of the channel are labeled in this figure as well. Note that because of the excess lowering at the free surface level along the inner bank between sections D30 and D90 the horizontal plane does not cut through the fluid within this region in case-S. One energetic shear layer is observed in case-NS close to the inner bank, which is in fact an interface between the high speed flow in the mid-channel and the slower moving fluid close to the banks. This shear layer forms because of the movement of high speed fluid in the outward direction once it enters into the bend. Close to the outer bank between sections D30 and D60 high levels of vorticity magnitudes are observed. This is a consequence of the small separation region that forms just at the upstream of section D30 (see also Figure 4a). It should be noted that these high values of vorticity along the outer bank might contribute to the bank scour.

Inclusion of the spur dike considerably changes the flow patterns observed within the curved reach. Once the spur dike is introduced at section D30, because of the adverse pressure gradients introduced by the blockage, separation along the outer bank takes place around section D0, creating a shear layer penetrating towards the mid-channel. Two large recirculation regions are observed; one at the upstream and one at the downstream of the spur dike. The recirculation region at the upstream of the spur dike is larger compared to typical ones observed in front of a spur dike installed at the bank of a straight channel (Koken and Constantinescu 2008, Koken 2011). A second shear layer is initiated at the tip of the spur dike along the outer bank and these two shear layers start interfering with each other. Additional flow blockage created by the spur dike at channel section D30 causes larger flow acceleration here. Lowering of the flow depth along the inner bank further contributes to this flow acceleration. As a result, the shear layer along the inner bank becomes stronger as compared to Case-NS.

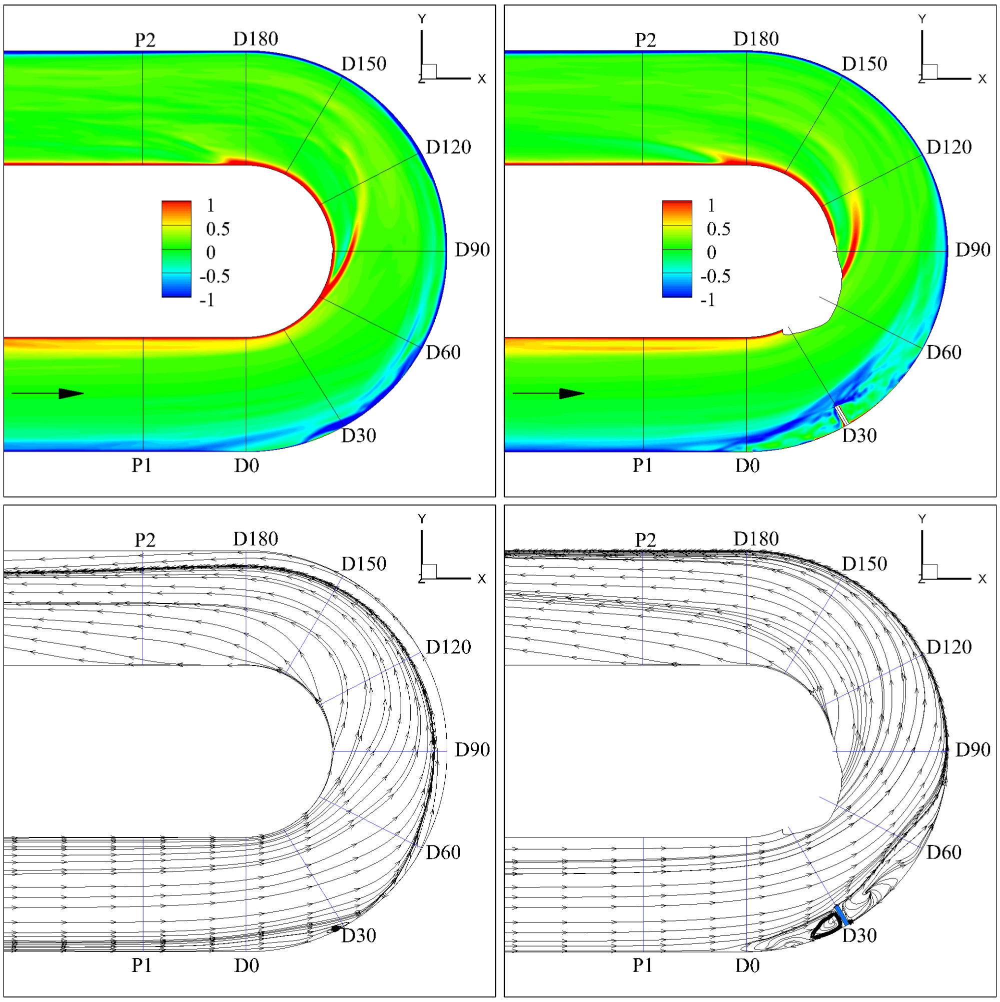

Figure 2. Non-dimensional mean out of plane vorticity contours, $\omega_z D/U$, and streamline patterns of the mean flow on a horizontal plane 0.9D above the channel bottom for case NS (left) and case S.

3.2 Coherent structures

Due to the high curvature, several streamwise oriented vortices (SOV's) form within the channel. Figure 3 shows the Q criterion iso-surfaces obtained for the mean flow in case-NS and case-S. In case-NS, three SOV cells are observed within the flow one close to the inner bank, VI, one close to the outer bank, VO, and one in the middle of the channel, VM. VI is initiated close to section D60 whereas VO is initiated at slightly upstream of section D60. Both of these vortices extend along the bank which they are initiated. Different from these two SOV's, VM is initiated close to the outer bank around section D30 which then moves towards the inner bank in the streamwise direction.

Once the spur dike is introduced at section D30 important changes takes place in terms of the coherent structures observed within the channel. Typically, a small horseshoe vortex forms around the tip of the spur dike, which is not very coherent, together with an additional shear layer that is initiated from the spur dike tip. As a result, VM is being shifted towards the inner bank. As discussed, two recirculation regions form one at the upstream and one at the downstream of the spur dike. The initiation point of VM shifts somewhat upstream closer to section D0 because of the recirculating flow forming at the upstream of the spur dike. Shear layer initiated at the tip of the spur dike creates a wake at the downstream and isolates the flow region confined in between the shear layer and the outer bank. As a result, VO which was observed here in case-NS cannot persist its existence once the spur dike is present (see also Figure 4e and 4f).

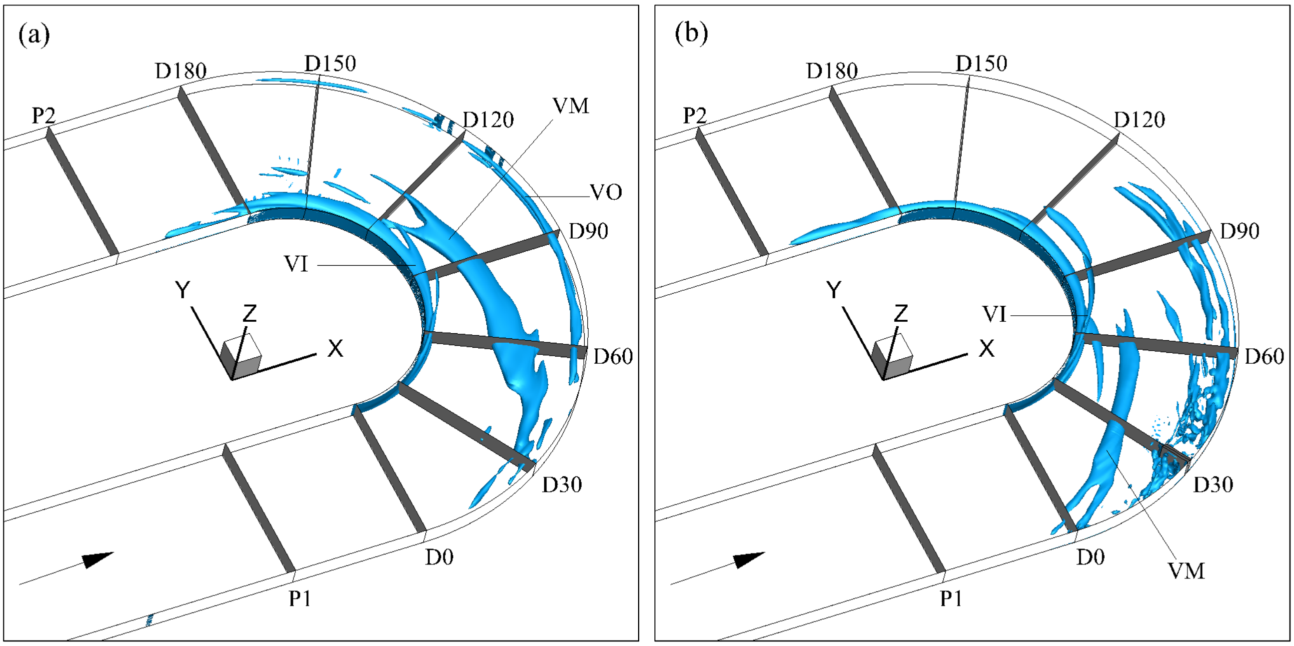

Figure 3. Coherent structures visualized using Q-criterion for: a) Case NS, b) Case S.

Figure 4 shows the streamline patterns and the non-dimensional streamwise velocity contours at sections D30, D90 and D120 for the mean flow in the curved channel for cases with and without the spur dike. As flow enters into the bend, the high core of streamwise velocity moves towards inner bank in both cases investigated. However, larger streamwise velocity magnitudes are observed at section D30 in case-S because of the additional blockage generated by the spur dike (compare Figure 4a and 4d). At the same section in case-NS, one can clearly identify the separation zone near the outer bank from the negative velocity contours (blue region in Figure 4a). Throughout the bend larger streamwise, velocity magnitudes are observed along the inner bank. This fact is also linked with the presence of VI along the inner bank of the channel. One can clearly see that the main cell of cross-stream circulation, VM is close to the outer bank at section D30 in case-NS (Figure 4a). On the other hand, at the same section, VM is approximately at the center of the channel in case-S (Figure 4d). At further downstream positions at sections D90 and D120, VM shifts towards the inner bank in both cases. In case-NS at section D120 even it is not possible to distinguish VI and VM as they merge with each other (Figure 4c). Although the outer streamwise oriented vortex, VO, is clearly visible in case-NS, with the inclusion of the spur dike, it disappears in case-S. One important difference between the two cases investigated is that the main cross-stream circulating flow is composed of two recirculating cells in case-Sat sections D90 and D120 (see Figure 4e and 4f). This might be linked with the reattachment of flow to the outer bank around section D90, which creates a relief within the flow as a result of the increase in the net flow area. This has an important consequence on the bed shear stress distribution, which will be discussed in the next subsection. One final thing to note here is that in both of the cases investigated at the downstream of the bend within the straight channel reach the core of high streamwise velocity shifts towards the outer bank (not shown here).

  / ISSN 1562-6865 (Online) - ISSN 1063-7710 (Print)

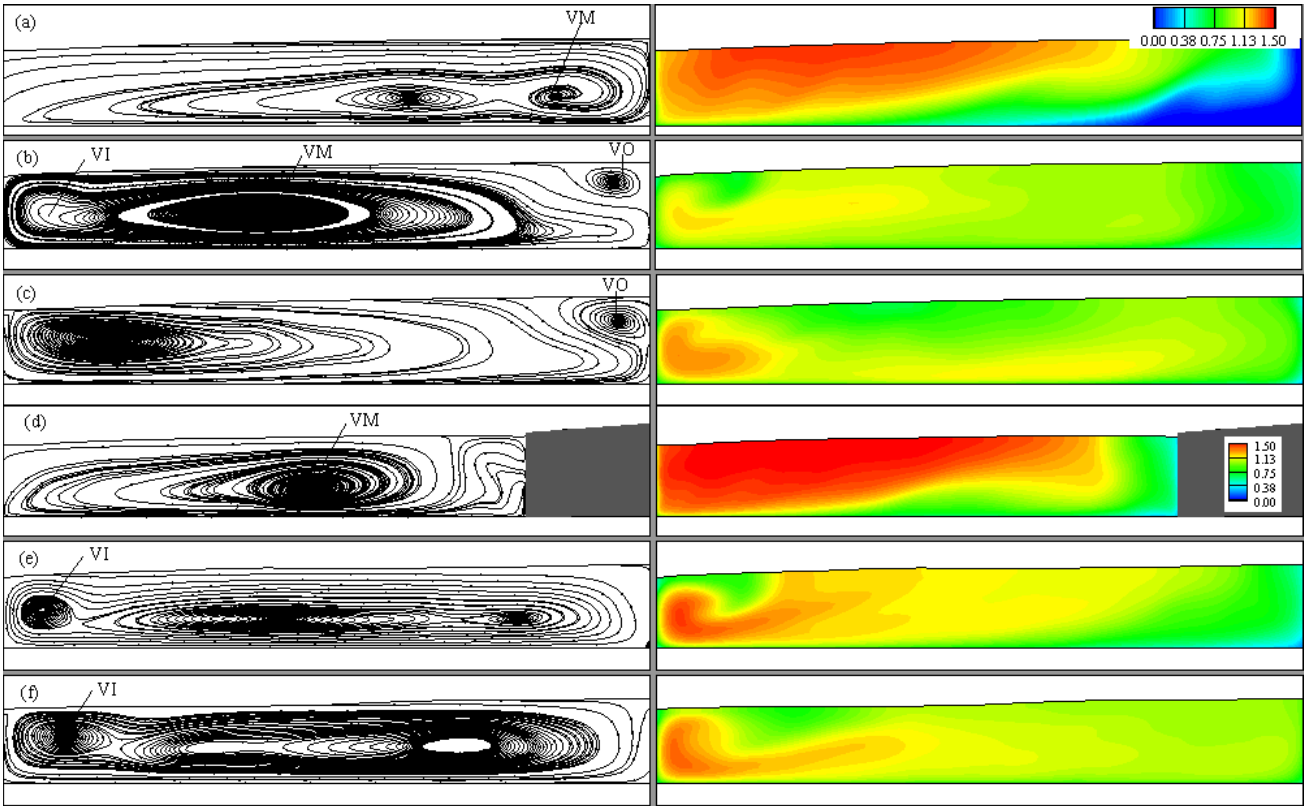

Figure 4. Streamline patterns (left) and non-dimensional streamwise velocity contours u_ξ/V (right) for the mean flow at: a) Case-NS section D30; b) Case-NS section D90; c) Case-NS section D120; d) Case-S section D30; e) Case-S section D90; f) Case-S section D120.

3.3 Bed shear stress distribution

Non-dimensional bed shear stress distribution on the channel bed is shown in Figure 4 for cases with and without spur dike. Bed shear stress is amplified within the curved reach along the inner bank and close to the outer bank in the straight channel section at the downstream of the bend. The magnitude of the maximum bed shear stress in both cases is comparable to each other, although there are important changes in the distribution of the bed shear stress. In overall, the bed shear stress values are approximately 30 % larger in between sections D60 and D120 in case-NS as compared to case-S. Even this difference by itself tells us that spur dike installed on the outer bank helps reducing the shear stress within the curved reach at the initiation of the scour process. In both cases, the region of high bed shear stress along the channel center mostly follows the trajectories of VM, VI and also the core of cross-stream circulation. In case-NS, this region is closer to the channel centerline whereas it is more shifted towards the inner bank in case-S. Since the main cross-stream circulation is composed of two cells in case-S, there is a second patch of high bed shear stress region along the mean path of the second cell close to the outer bank around section D120, which is absent in case-NS. Furthermore, at section D30, where the spur dike is located, as a result of the flow acceleration in case-S, larger bed shear stress values are observed close to the inner bank. On the other hand, because of the presence of the spur dike, in overall outer half of the channel is experiencing smaller magnitudes of bed shear stress up to section D90 in case-S.

4 CONCLUSIONS

It is shown that the flow field in a sharply curved channel is populated by several streamwise oriented vortices, which also contribute to the amplification of the bed shear stress. Yet, the characteristics of these vortices considerably change with the inclusion of a spur dike at the outer bank of the channel. Having a vertical spur dike at section D30, the initiation point of the mid-streamwise oriented vortex moves in the upstream direction. Moreover, it shifts towards the inner bank. The outer streamwise oriented vortex, which was observed along the outer bank, disappears with the inclusion of the spur dike. The horseshoe vortex, which forms around the spur dike, is not very coherent and do not make a considerable contribution to the bed shear stress amplification along its path.

There are important changes in the bed shear stress distribution when two cases are compared. Only at two locations bed shear stress increases when the spur dike is installed. The first location is close to the inner bank around section D30 across the spur dike. The second location is close to the outer bank around section D120. However, in overall, the magnitude of the bed shear stress within the curved reach is reduced by approximately 30 % with the introduction of the spur dike. Although spur dikes are mostly used for bank protection. It is shown that they might contribute on reducing the scour along the bed inside the bend of a sharply curved channel.

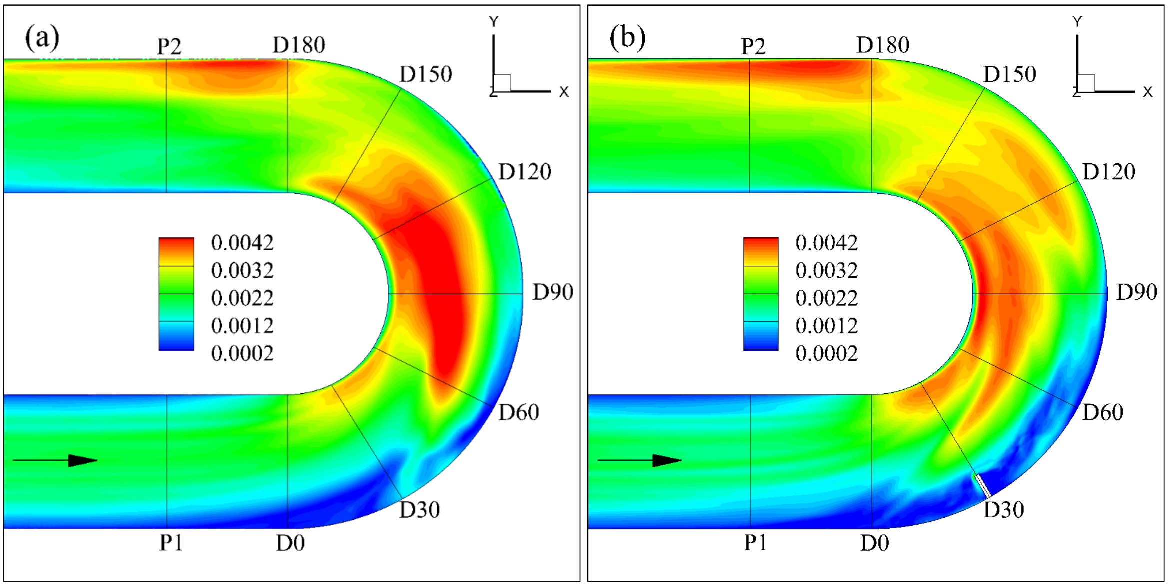

Figure 4. Non dimensional bed shear stress, $\tau_\omega/(\rho V^2)$, on the channel bed for: a) Case-NS; b)Case-S.

ACKNOWLEDGMENTS

The computational resources used in this study were partly provided by TUBITAK ULAKBIM High Performance Computing Center, and the Department of Computer Engineering at Orta Dogu Teknik Universitesi, which are gratefully acknowledged here.

REFERENCES

Blanckaert, K. 2010. Topographic Steering, Flow Recirculation, Velocity Redistribution and Bed Topography in Sharp Meander Bends. *Water Resources Research*, 46(9), 1-23.

Blanckaert, K. & de Vriend, H. J. (2004). Secondary Flow in Sharp Open-Channel Bends. *Journal of Fluid Mechanics,* 498, 353-380.

Blanckaert, K. (2011), Hydrodynamic Processes in Sharply Curved River Bends and their Morphological İmplications. *Journal of Geophysical Research,* 116, 1-22.

Bressan, F., Ballio, F. & Armenio, V. (2011). Turbulence around a Scoured Bridge Abutment. *Journal of Turbulence,* 12(3), 1–24.

Constantinescu, G., Koken, M. & Zeng, J. 2011. The Structure of Turbulent Flow in an Open Channel Bend of Strong Curvature with Deformed Bed: Insight Provided by an Eddy Resolving Numerical Simulation, *Water Resources Research,* 47(5), 1-17.

Kashyap, S., Constantinescu, G., Rennie, C., Post, G. & Townsend, R. (2012). Influence of Channel Aspect Ratio and Curvature on Flow, Secondary Circulation and Bed Shear Stress in a Bend. *ASCE Journal of Hydraulic Engineering,* 138(12), 1045-1059.

Keylock, C. J., Constantinescu, G. & Hardy, R. J. (2012). The Application of Computational Fluid Dynamics to Natural River Channels: Eddy Resolving Versus Mean Flow Approaches. *Geomorphology*, 179(4), 1–20.

Koken, M. & Constantinescu, S.G. (2008). An Investigation of the Flow and Scour Mechanisms around Isolated Spur Dikes in a Shallow Open Channel 1: Conditions Corresponding to the Initiation of the Erosion and Deposition Process. *Water Resources Research*, 44(8), 1-19.

Koken, M. (2011). Coherent Structures Around Isolated Spur Dikes at Various Approach Flow Angles. *Journal of Hydraulic Research*, 49, 736-743.

Koken, M. & Gogus, M. (2015). Effect of Spur Dike Length on the Horseshoe Vortex System and the Bed Shear Stress Distribution. *Journal of Hydraulic Research,* 53(2), 196-206.

Koken, M., Constantinescu G. & Blanckaert, K. (2013) Hydrodynamic Processes, Sediment Erosion Mechanisms, and Reynolds-Number-Induced Scale Effects in an Open Channel Bend of Strong Curvature with Flat Bathymetry. *Journal of Geophysical Research-Earth Surface,* 118, 2308-2324.

Paik,J., Escauriaza, C. & Sotiropoulos, F. (2010). Coherentstructure Dynamics in Turbulent flows Past In-Stream Structures: Some Insights Gained Via Numerical Simulation. *Journal of Hydraulic Engineering,* 136(12), 981–993.

Rodi, W, Constantinescu, G. & Stoesser, T. (2013). *Large Eddy Simulation in Hydraulics*. IAHR Monograph, CRC Press, Taylor & Francis Group.

COMPARISON OF SCOURING IN SHORT AND LONG CONTRACTIONS

SEPEHR KARIMI[1], AMIR REZA ZARRATI[2] & SADEGH ANVARI[3]

[1,2,3]Dept. of Civil and Environmental Engineering, Amirkabir University of Technology, Tehran, Iran. Sepehr.karimi@aut.ac.ir, zarrati@aut.ac.ir, Sadeghanvari92@aut.ac.ir

ABSTRACT

The contraction scour in a bridge crossing is evaluated by assuming a long contraction and employing sediment transport equations together with sediment and flow discharge continuity. This scour depth is then added to local and general scouring to find total scour depth at a bridge pier. In practice, the contraction length in a bridge crossing is not long. The present study is conducted to examine this assumption by comparing scouring in a short and long contraction with the same flow condition and geometry in a physical model. Experiments were carried out in a 12 m long and 0.7 5m wide horizontal bed flume. Results showed that the maximum scour depth at the edge and the scour depth at the center of a contraction entrance depend on the type of the contraction (short or long) and the flow rate. The experimental results showed that in a short contraction the local scour hole at the edges of the contraction extends at the contraction crossing and its depth even at the contraction center can be more than scouring in the long contraction. In another word, using long contraction formula for calculating the contraction scouring in a bridge crossing may lead to under estimation of scouring. Scour depth caused by the extension of the contraction edge scour hole at the center of the short contraction entrance in various flow rates was nearly 36 % more than the general scour depth in the long contraction. One experiment was also conducted with a pier located at the center of the short contraction to check the accuracy of adding up pier local scour hole and contraction scour.

Keywords: Scour; short contraction; long contraction; maximum scour depth; bridge pier.

1 INTRODUCTION

Structures built in rivers and estuaries are prone to scour around their foundations. Scour hole may undermine the foundations and endangers the stability of structures. There have been several cases of bridge failures, some causing loss of life and mostly resulting in significant transport disruption and economic loss, as a result of scour (Mey et al., 2002, Melville and Coleman, 2000, Briaud et al., 2005).

Three types of scouring are known at bridge piers: (1) degradation of the river bed due to long-term evolution in the river morphology (general scour), (2) erosion by flow contraction at the bridge section (contraction scour), and (3) local erosion around the piers (local scour) (Melville and Coleman, 2000). To calculate the total scour hole at a pier, these three scour depths are calculated and summed up (Raudkivi, 1998, Melville and Coleman, 2000). General scour occurs naturally in river reaches as a result of the changes in the hydraulic parameters governing the channel, such as changes in the flow rate or changes in the quantity of sediment (Forde et al., 1999). Contraction scour is the result of reduction in the channel's cross sectional area. At a channel contraction, flow velocity and bed shear stresses increase. The increasing of shear stresses increases sediment discharge and channel degradation at the contraction (Briaud et al., 1999). This process continues causes the increment in flow depth, as a result of scouring, reducing the flow velocity and bed shear stresses. Local scour occurs around individual bridge pier. Downward flow upstream of the pier and wake vortices downstream of it lead to localized erosion in the direct vicinity of the structure (Hamill, 1999) (see Figure 1.).

Figure 1. Failure of bridges due to scour. (a) Sava bridge, Zagreb and (b) Malahide viaduct, Dublin. Both bridges failed in 2009 (Prendergast and Gavin, 2014).

Based on our previous works, the contraction scour is evaluated by assuming a long contraction and employing sediment transport equations together with considering sediment and flow discharge continuity. Melville and Coleman (2000) suggested that the contraction scour is evaluated under live-bed or clear-water conditions by means of the Laursen's formulas (Fenocchi and Natale, 2015), which return a uniform scour value over the bridge cross section. As the sediment transport equations were derived under the hypothesis of long contraction, a uniform scour value over the bridge cross section is determined (Richardson and Richardson, 2008). In practice, the contraction length in a bridge crossing is not long.

The present study is conducted to examine this assumption by comparing scouring at a short and long contraction in a physical model.

2 EXPERIMENTS

Experiments were conducted in a horizontal flume with erodible bed of 14 m long, 0.75 m wide and 0.6 m deep. The flume had a working section in the form of a recess below its bed filled with sediment. The recess was 0.75 m wide, 2 m long and 0.3 m deep and was located 7 m downstream from the flume entrance. Median size of the sediment was 0.95 mm with a geometric standard deviation of sediment grading less than 1.2, which can be assumed as uniform.

Model of contractions was built from Perspex. The length of the short contractions (in flow direction) was 0.07 m and the length of the long contractions was 0.7 m. Both contractions' widths (transverse direction) were 0.11 m with rectangular sharp edged nose. Also, an experiment of short contraction in the presence of a pier was conducted to check the accuracy of adding up pier local scour hole and contraction scour. In this test, the pier diameter was 0.045 m. Figure 2 shows the plan view of the experiments.

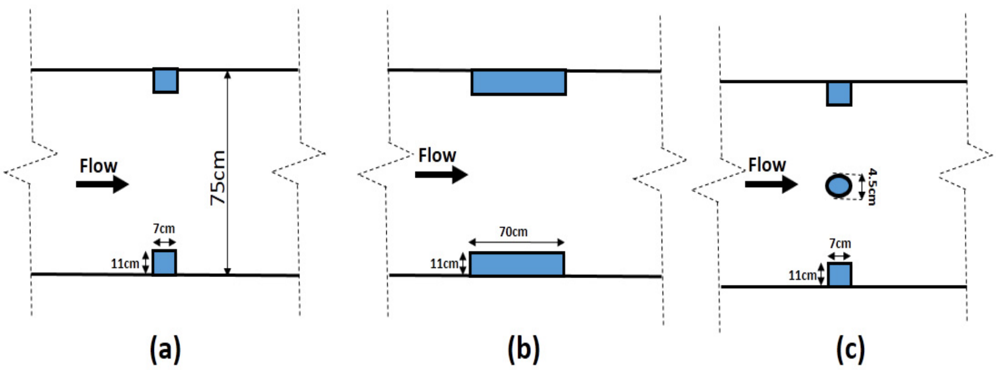

Figure2. Plan view of experimental setups: (a) short contraction, (b) long contraction, (c) short contraction with a pier.

Water was circulated in the flume by a centrifugal pump with maximum capacity of 100 (L/s). The flow rate in the flume was controlled and preset by a speed control unit attached to the pump system. An electrical flow meter was installed in the supply conduit to measure the discharge passing through the flume.

Tests were carried out with different bed shear stresses. The ratio of shear velocities (upstream of the contraction) tested in these experiments to the critical shear velocity calculated from Shields diagram, U_*/U_{*Cr} was from 0.53 to 0.85. Depth of the scour hole was measured by a laser point gauge. Details of the experiments are given in Table 1. In this table, 'V' is velocity and $\mathrm{Fr} = \sqrt{\mathrm{V}/(\mathrm{gy})}$ is the Froude number upstream of the contraction, where 'g' is the gravitational acceleration and 'y' is the flow depth.

Table 1. Details of experiments.

a. **No**	b. **Type of experiment**	c. **U*/U*Cr**	d. **V (cm/s)**	e. **Fr**
1		0.53	20.78	0.15
2	**Short contraction**	0.63	24.93	0.18
3		0.75	29.78	0.22
4		0.85	34.63	0.25
5		0.53	20.78	0.15
6	**Long contraction**	0.63	24.93	0.18
7		0.75	29.78	0.22
8		0.85	34.63	0.25
9	**Contraction with pier**	0.75	29.78	0.22

3 EXPERIMENTAL RESULTS

Figure 3 shows five points around a short and long contraction that are considered to study and compare the scouring around the contractions. Points 2 and 4 are at the nose of the contractions at which maximum scouring occurs. Points 1 and 3 are on the centerline of the channel at the entrance of the contractions. At these points the scour holes at two contractions' edge reach each other. Point 5 is considered in the middle of the long contraction centerline. At this point, scour depth due to long contraction is expected. This scour depth can also be calculated by considering conservation of sediment mass and using a sediment transport equation such as Laursen's formula (Laursen, 1960, Laursen, 1963).

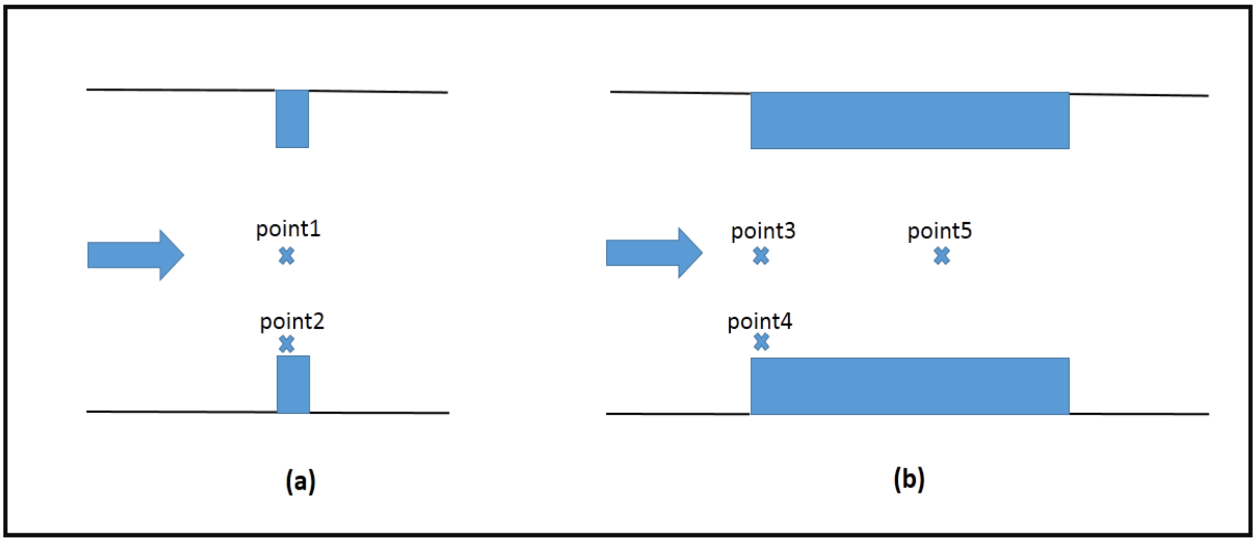

Figure 3. Plan of chosen points around the: (a) short contraction, (b) long contraction.

The measured scour depths at these five points (see Figure 3), are given in Table 2. The experimental data in Table 2 are made dimensionless with the scour depth at points 1 in U_*/U_{*Cr} = 0.75 (S1*).

Table 2. Non-dimensional scour depth at contraction points shown in Figure 3.

U*/U*Cr	Sc/ S1* at point1	Sc/ S1* at point2	Sc/ S1* at point3	Sc/ S1* at point4	Sc/ S1* at point5
0.53	0.61	2.54	0.53	1.87	0.40
0.63	0.76	2.88	0.65	2.28	0.49
0.75	1	3.46	0.83	2.90	0.63
0.85	1.13	3.82	0.95	3.31	0.71

Scour depth at points 1 and 3 are in fact a result of scour extension of points 2 and 4 that is the nose of the contraction. As shown in Table 2, the scour depth at point 3 is more than point 5 in all experiments. In other words, in any bed shear stress, the general scour in the long contraction is less than the local scour at the centerline of the contraction entrance. A sample scour contour lines in Experiment 7 is shown in Figure 4. In this figure, the scour depths are made dimensionless with S1* too.

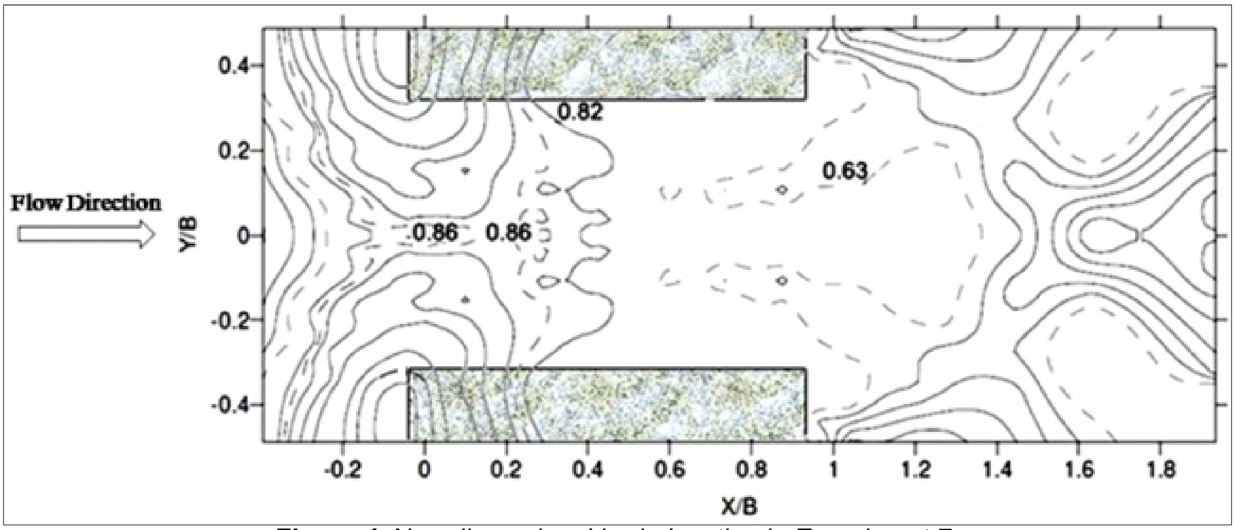

Figure 4. Non-dimensional bed elevation in Experiment 7.

The scour depth decreases along the long contraction till it is constant. The length from the entrance to the region at which scour hole becomes constant depends on the bed shear stress.

Moreover, based on experimental data in Table 2, scour depth at point 1 in the short contraction is more than points 3 and 5 in the long contraction. Higher turbulence at the entrance of the short contraction may be the reason for its higher scour hole depth.

From these results, it can be concluded that considering the contraction scour depth based on a long contraction assumption under predicts the scour depth.

One experiment was also conducted (Experiment 9) with a short contraction and a pier in the centerline of its entrance. The flow intensity in this experiment was U_*/U_{*Cr} = 0.75. In this experiment, the scour hole depth at the pier was measured and then compared with the sum of scour depth at the short contraction measured in Experiment 3 and a single pier without contraction (measured in another independent experiment). The results are shown in Table 3.

Table 3. Comparing short and long contraction in calculating pier scour.

Experiment	Scour Depth (cm)
single pier without contraction	9.5
short contraction without pier	4.3
Total scour depth	13.8

In the experiment with a short contraction and a pier (Experiment 9) the scour depth at the bridge pier was measured equal to 14.4 cm. As the total scour depth in Table 3 shows, adding the pier local scour hole to the scour depth in the contraction has an acceptable accuracy.

4 CONCLUSIONS

To calculate the total scour depth at a pier in a bridge crossing, a long contraction is assumed and its scour depth is added to local pier scour and general degradation. However, the contraction in a bridge crossing is not long. The present experimental work was conducted to compare the scouring at a long and short contraction with a similar flow condition.

It was observed that scouring in a short contraction is due to extension of the local scouring at its edges. Based on the measurements, the scour depth at the center of the short contraction can be more than general scouring at a long contraction. Therefore, using long contraction formula for calculating the contraction scouring in a bridge crossing may lead to under estimation of scouring. In the present work, the scour hole at the center of short contraction was about 36 % more than scouring in a long contraction. One experiment was also conducted with a pier located at the center of the short contraction to check the accuracy of adding up pier local scour hole and contraction scour, and it showed acceptable accuracy.

REFERENCES

Briaud, J.L., Ting, F.C., Chen, H.C., Gudavalli, R., Perugu, S. & Wei, G. (1999). SRICOS: Prediction of Scour Rate in Cohesive Soils at Bridge Piers. *Journal of Geotechnical and Geoenvironmental Engineering*, 125(4), 237-246.

Briaud, J.L., Chen, H.C., Li, Y., Nurtjahyo, P. & Wang, J. (2005). SRICOS-EFA Method for Contraction Scour in Fine-Grained Soils. *Journal of Geotechnical and Geoenvironmental Engineering*, 131(10),1283-1294.

Fenocchi, A. & Natale, L. (2015). Using Numerical and Physical Modeling to Evaluate Total Scour at Bridge Piers. *Journal of Hydraulic Engineering*, 142(3), 1-5.

Forde, M.C., McCann, D.M., Clark, M.R., Broughton, K.J., Fenning, P.J. & Brown, A. (1999). Radar Measurement of Bridge Scour. *Ndt & E International*, 32(8), 481-492.

Hamill, L. (1999). *Bridge Hydraulics*. London: E& FN Spon, 11 New Fetter Lane, London, EC4P 4EE, UK, 367.

Laursen, E.M. (1960). Scour at Bridge Crossings. *Journal of the Hydraulics Division*, 86(2), 39–54.

Laursen, E.M. (1963). An Analysis of Relief Bridge Scour. *Journal of the Hydraulics Division*, 89(3) 93-118.

May, R.W.P., Ackes, J.C. & Kirby, A.M. (2002). *Manual on Scour at Bridges and Other Hydraulic Structures*, Construction Industry Research and Information Association. London. 551.

Melville, B.W. & Coleman, S.E. (2000). *Bridge Scour*. Water Resources Publication.

Prendergast, L.J. & Gavin, K. (2014). A Review of Bridge Scour Monitoring Techniques. *Journal of Rock Mechanics and Geotechnical Engineering*, 6(2), 138-149.

Raudkivi, A.J. (1998). *Loose Boundary Hydraulics.* CRC Press.

Richardson, J.R. & Richardson, E.V. (2008). *Bridge Scour Evaluation*. Sedimentation Engineering: Processes, Measurements, Modeling and Practice, M.H. Garcia, Ed., ASCE, Reston, VA, 505–542.

UNDERSTANDING THE FORMATION OF WOODY DEBRIS JAMS AT BRIDGE PIERS

DIEGO PANICI[(1)] & GUSTAVO A. M. DE ALMEIDA[(2)]

[(1,2)] University of Southampton, Southampton, United Kingdom
D.Panici@soton.ac.uk, G.deAlmeida@soton.ac.uk

ABSTRACT

Woody debris accumulations at bridge piers can significantly increase the risk of flooding and bridge failure due to increased afflux upstream of bridges, additional structural loads and exacerbated scour. Despite the importance of this problem, limited research has been conducted on the topic. In this study, we experimentally analyse the process of accumulations of woody debris (modelled with twigs and natural sticks) at single piers exposed to flow and a continuous debris supply. Results show that these debris jams follow a three-phase growth: *unstable* (where growth occurs rapidly but debris are easily disengaged); *stable* (growth assumes a less pronounced trend and debris are less likely to be escaped); *critical* (the accumulation begins to oscillate about the pier and ultimately drifts away, i.e. fails). The dimensions of the accumulation at failure are observed to plot as well-defined functions of the flow and debris characteristics. In particular, while the cross-sectional and longitudinal dimensions of the accumulations are observed to decrease with increasing flow, the vertical component displayed an opposite trend. These results provide a worst-case scenario that can be useful for engineering bridge design and flood risk assessment.

Keywords: Bridge pier; flood risk; woody debris; debris jam; bridge clogging.

1 INTRODUCTION

The stability of fluvial bridges have long been a major concern for scientists and engineers. Bridge piers modify the flow field, inducing structural lateral loads and localised scour. The accumulation of woody debris at bridge piers significantly exacerbates these effects. Namely, woody debris jams cause important flow constrictions, affecting the neighbouring flow field (Daniels and Rohads, 2004; Pagliara and Carnacina, 2012), increasing the upstream water levels (Diehl, 1997; Lagasse et al., 2010) and intensifying pier scour (Lagasse et al., 2010). Diehl (1997) estimated that more than 30% of bridge failures in the United States is related to the accumulation of woody debris at piers.

Large Wood Debris (LWD) can be mobilised by several processes, especially bank erosion and buoying fallen trees on the floodplains (Diehl, 1997; Lyn et al., 2003; Lagasse et al., 2010), conveyed during flooding events. Obstacles within the LWD path, such as a bridge pier, are likely to entrap oncoming logs, possibly initiating a build-up process that leads to an LWD pile (Diehl, 1997). It has been reported that accumulations are generally begun by a key-element, i.e. a large and sturdy log (Diehl, 1997). This key-element becomes a source of recruitment for smaller debris, which allow the debris pile to expand (Manners et al., 2008, Lagasse et al., 2010). In-situ observations suggest that an inverted half-cone (Diehl, 1997; Lagasse et al., 2010) is the most typical jam shape.

In spite of the importance of debris to bridge stability and flooding, scientific studies aimed at understanding the potential size that might be reached by these debris jams are extremely limited. Most studies on LWD have been mainly based on field surveys (e.g. Diehl, 1997), where the actual evolution of the accumulation is rarely observed. Consequently, river bridge design and flood risk assessment guidelines either do not consider drift accumulations or suggest arbitrary design raft size (Diehl, 1997). Only a few and relatively recent experimental studies (e.g. Lyn et al., 2003; Bocchiola et al., 2008, Rusyda et al., 2014) have attempted to investigate the build-up phenomenon, although they have been limited in scope and have not analysed the fundamental relationship between LWD accumulation process and flow conditions.

The aforementioned issues associated with debris accumulations could be included in engineering design and flood risk assessment if the potential dimensions and coefficient of drag of the debris jam could be estimated. Developing predictive techniques for the dimensions of LWD accumulations would allow the estimation of debris-induced effect on the flow through momentum conservation principles by considering the drag force exerted on the debris jam:

$$F_D=\frac{1}{2}\rho C_D A v^2, \qquad [1]$$

where F_D is the drag force, ρ is the water density, C_D is the drag coefficient, A is the accumulation area normal to the flow and v is the approaching flow velocity.

The aim of this study is to analyse the growth and potential size of LWD accumulations at bridge piers. A total of 322 laboratory experiments were performed, in which natural sticks were introduced upstream of model piers in order to naturally form the debris accumulations. We first examined how debris accumulations grow over time, identifying clear patterns that were observed in all experiments. We then analysed the influence of debris length and pier size on the dimensions of formed jams for the idealised situation of uniform size debris supply. Finally, we compare accumulations obtained with uniform size debris against those that were formed by using a non-uniform length distribution of debris elements and assuming the accumulation was initialised by a key-element.

The results of these tests enabled a detailed analysis of the time evolution and critical dimensions of debris jams observed under a range of flow conditions and debris characteristics. Our findings help clarify the process by which debris accumulate at bridge piers and provide practical guidance for estimating the potential dimensions of debris accumulations.

2 DIMENSIONAL ANALYSIS

A dimensional analysis was carried out in order to derive a relationship among the variables that are relevant to the woody debris accumulation phenomenon. Assuming that all variables are interdependent (and assuming the channel boundaries are far enough to have negligible influence on the phenomenon) the following functional relation is proposed:

$$f\left(\rho,\mu,v,h,g,D,L,d,\rho_L,W,H,K\right)=0, \qquad [2]$$

where ρ=water density, μ=water dynamic viscosity, v=approaching flow velocity, h=water depth, g=gravity acceleration, D=pier width, L=single debris length, d=single debris diameter, ρ_L=debris density, W=accumulation width, H=accumulation height and K=accumulation length (W, H and K are indicatively sketched in Figure 1).

Applying Buckingham π-theorem to the functional relation [2] and using ρ, v and L as repeated variables yields

$$g\left(Fr_L,Re_L,\frac{h}{L},\frac{L}{D},\frac{d}{L},\frac{\rho_L}{\rho},\frac{W}{L},\frac{H}{L},\frac{K}{L}\right)=0, \qquad [3]$$

where Fr_L and Re_L are respectively the Froude and the Reynolds number with characteristic length L (the length of individual debris elements). Eq. [3] can be further simplified under certain assumptions. The flow is fully-developed turbulent and in this condition influence of the Reynolds number can be neglected (Wallerstein et al., 2001; Bocchiola et al., 2008). In addition, water depth h has been observed as non-influential if the debris accumulation is well above the river bed by Lyn et al. (2003). This was also observed in some of our preliminary experiments. Under these assumptions, the functional relation [3] can be simplified as

$$g\left(Fr_L,\frac{L}{D},\frac{d}{L},\frac{\rho_L}{\rho},\frac{W}{L},\frac{H}{L},\frac{K}{L}\right)=0. \qquad [4]$$

The dimensionless variables in [4] were then used in the design of the experiments and data analysis.

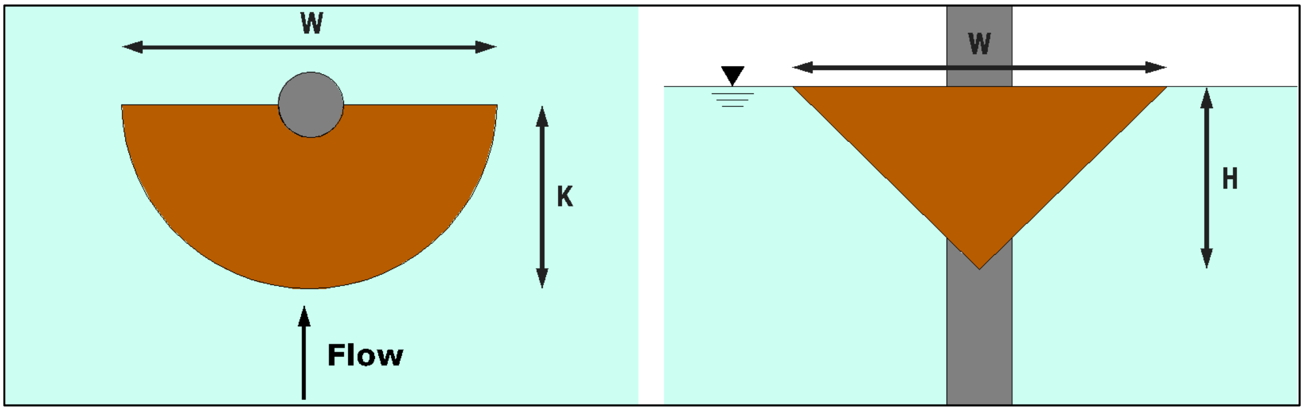

Figure 1. Sketch of an idealised woody debris jam indicating the main geometrical variables used in our analysis: width *W*, height *H* and length *K*. Left: plan view. Right: cross-section.

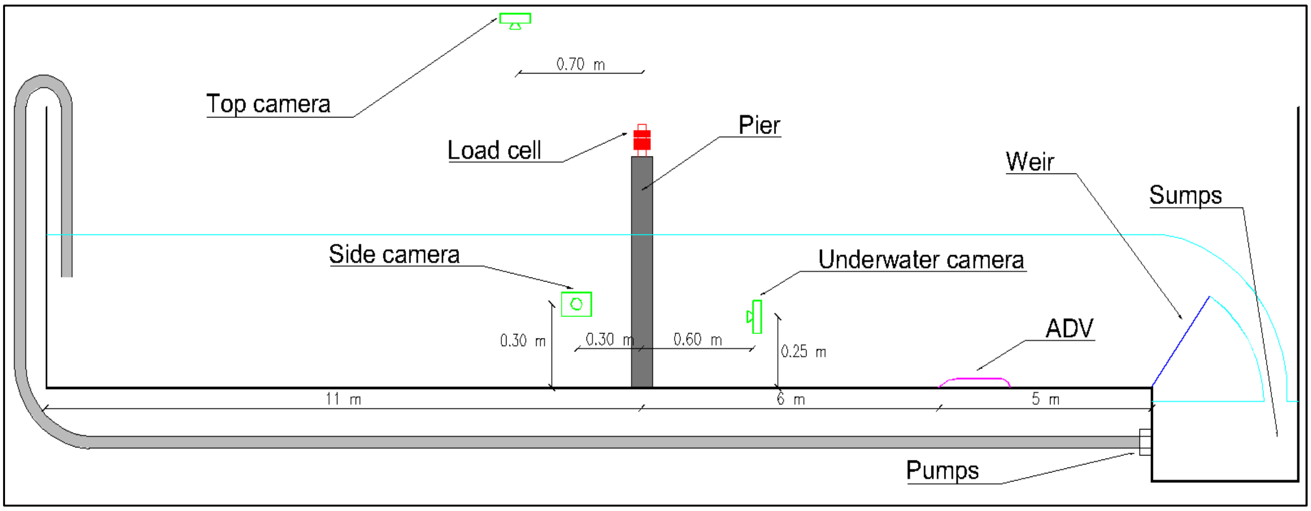

Figure 2. Sketch of the University of Southampton Hydraulics lab flume and the set-up used for woody debris experiments (not to scale).

3 EXPERIMENTS

Experiments were performed in a 22 m-long and 1.375 m-wide glassed-wall flume at University of Southampton. Figure 2 shows a sketch of the flume and the set-up adopted for the experiments. A circular pier was placed at the flume centreline, 11 m downstream the inlet. The pier was held from the top, at which point a load cell was connected to measure the force exerted on the pier over the course of the experiments. Flow conditions were constantly monitored by a multi-cell and multi-beam ADV placed 6 m downstream of the pier. The position of the ADV was selected in order to avoid debris-induced backwater effects on the measurements. Three cameras were installed in order to capture the time evolution of all the relevant geometric characteristics of the debris jam. The first camera was mounted on the top of the flume, the second on the side and the third was submerged 60 cm downstream of the pier.

The experiments consisted in dropping natural sticks individually (oriented parallel to the flow) at a constant frequency (approximately 20 sticks per minute) 7 m upstream of the pier. Debris were modelled using twigs and sticks collected from fallen branches or trees. Their density of debris elements was kept approximately constant by drying them after each experiment. Furthermore, debris diameter *d* was constant for each type of debris. We used two different types of debris, namely uniform and non-uniform size. Uniform size sticks had the same length *L* for all individual elements. Non-uniform sticks were used to mimic the supply of debris in natural channels, where a variety of debris dimensions is usually found (e.g. Sedell et al., 1988; Manners et al., 2008) and are typically non-normally distributed. We used a log-normal probability density function for relative lengths (relative to the highest length or key-element, as previously described):

$$p(\chi)=\frac{1}{\chi\sqrt{2\pi}\sigma}e^{-\left(\frac{\ln\chi-\mu}{\sqrt{2}\sigma}\right)^2}, \qquad [5]$$

where χ is the ratio between a debris length and the key-element length. Adopting for [5] mean and standard deviation respectively μ=-1.3039 and σ=0.7367, obtains a curve that is comparable to Sedell et al. (1988). Figure 3 shows a series of 100 sticks used for the non-uniform debris length experiments for one particular length *L* of the key-element.

We used three different piers, having diameters of 25, 50 and 100 mm. Five groups of experiments were conducted with 5 different combinations of *D* and uniform *L*, and 13 groups for the non-uniform debris length. For each group, a large number of experiments have been performed covering a range of flow discharges from 0.08 to 0.42 m^3/s. In total, 322 experiments were carried out. Table 1 indicates the variables adopted for each group.

4 RESULTS

4.1 Accumulation growth

The analysis of the accumulation temporal growth has shown a common behaviour for all jams. This growth can be conceptually classified into three different phases, hereafter referred to as *unstable*, *stable* and *critical*. These three stages are illustrated by the examples shown in Figure 4, where the dimensionless accumulation width *W/L*, height *H/L* and length *K/L* are plotted over the course of three uniform size debris experiments (having the same length *L* but different Fr_L).

Table 1. List of experiments. A1 to A5 are uniform size debris, B1 to B13 are non-uniform size debris.

Group	Debris length (mm)	Pier diameter (mm)	L/D	Number of flow conditions
A1	375.0	100	3.75	18
A2	250.0	50	5.00	21
A3	312.5	50	6.25	21
A4	375.0	50	7.50	19
A5	375.0	25	15.00	18
B1	500.0	100	5.00	17
B2	625.0	100	6.25	18
B3	375.0	50	7.25	15
B4	437.5	50	8.75	16
B5	500.0	50	10.00	18
B6	562.5	50	11.25	18
B7	625.0	50	12.50	18
B8	687.5	50	13.75	17
B9	750.0	50	15.00	18
B10	437.5	25	17.50	16
B11	500.0	25	20.00	18
B12	625.0	25	25.00	18
B13	750.0	25	30.00	18

The unstable phase occurs at the initial stage of the accumulation growth, when a few members (or the key-element) are entrapped by the pier and begin to recruit other oncoming debris. During this phase, the accumulation grows at a quick rate. In addition, debris elements can be easily mobilised and disengaged from the jam, resulting in frequent size variations.

After the accumulation has built a framework sufficient enough to entrap other members, the jam growth follows a less pronounced trend and becomes more stable. This slower pace of growth is likely to be the result of the cubic relation between volume and linear dimensions. During this phase, the accumulation size typically reaches its maximum dimensions, which can last for a longer time compared to the other phases. Moreover, at this stage the accumulation assumes the typical half-cone shape that has often been reported from field observations available in the literature.

Finally, at the critical phase the accumulation begins a rotational oscillatory movement about the pier. This pivoting eventually results in the accumulation being completely disengaged from the pier (hereafter referred to as *failure*). Figure 5 shows an example of the accumulation failure. All experiments were stopped after the failure of the debris accumulations.

4.2 Accumulation potential size

The maximum dimensions reached by woody debris jams at the beginning of the critical phase have shown a strong dependency on both flow conditions and debris length. Figures 6 and 7 show the maximum dimensionless width, height and length obtained for each experiment against Fr_L for respectively uniform and non-uniform debris. These figures show that when Fr_L is low, values of W/L and K/L are the highest, whereas H/L is smallest. With increasing Fr_L, width and length rapidly decrease, while height increases.

It is also clear that for the range of values tested in this study the ratio L/D seems to have no significant impact on the debris build-up. Although L/D values ranged from 3.5 to 15 (for uniform debris) and between 5 and 30 (for non-uniform debris), results shown in Figures 6 and 7 are all clustered within a narrow band irrespectively of L/D. A similar conclusion can be reached for the ratio d/L. The debris diameter d was kept constant and L was varied in all experimental groups, but the curves show no indications that this factor can have an influence within the range of values studied.

Figure 3. One particular set of 100 sticks used in the experiments with non-uniform debris.

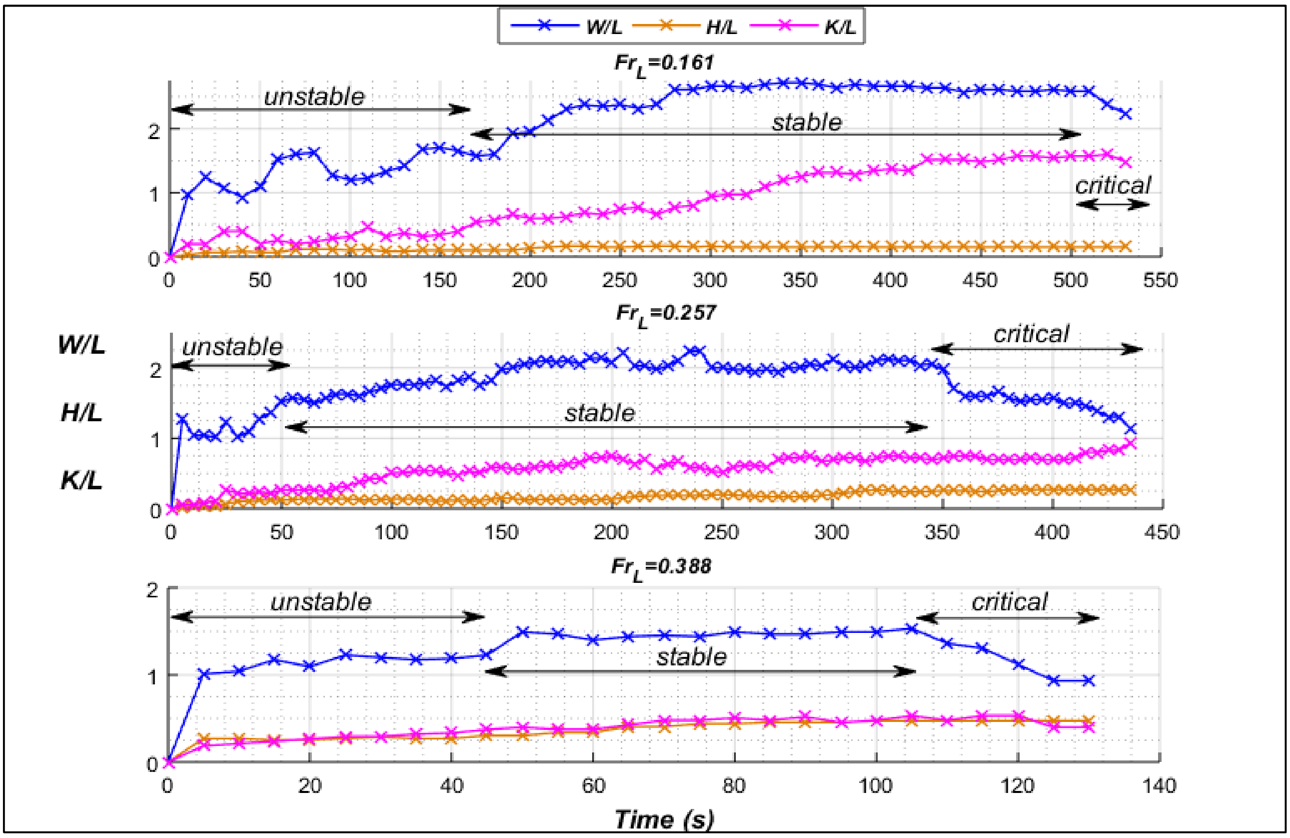

Figure 4. Time evolution for uniform size stick experiments (group A4) at three different values of Fr_L. On the vertical axis: dimensionless jam size variables *W/L*, *H/L* and *K/L*. Growth phases are indicatively reported. The last data point corresponds to the instant in which accumulation failure and dislodgement from the pier occur.

5 ANALYSIS AND DISCUSSION

Our results provide the first robust evidences of the formation, growth and failure of debris accumulations at bridge piers. While a few features observed in these experiments are consistent with the hypotheses suggested by Diehl, (1997), Manners et al. (2008) and Lagasse et al. (2010), the failure process (i.e. the *critical* phase which occurred for all jams) has not been previously reported in the literature. Only Lyn et al. (2007) observed that some debris piles were no longer in place between two site visits, and in one instance they supposed that a jam could have been dislodged from a pier and then re-accumulated at another downstream pier, although there was neither evidence of this nor a link to the failure mechanism. Our experiments unveiled

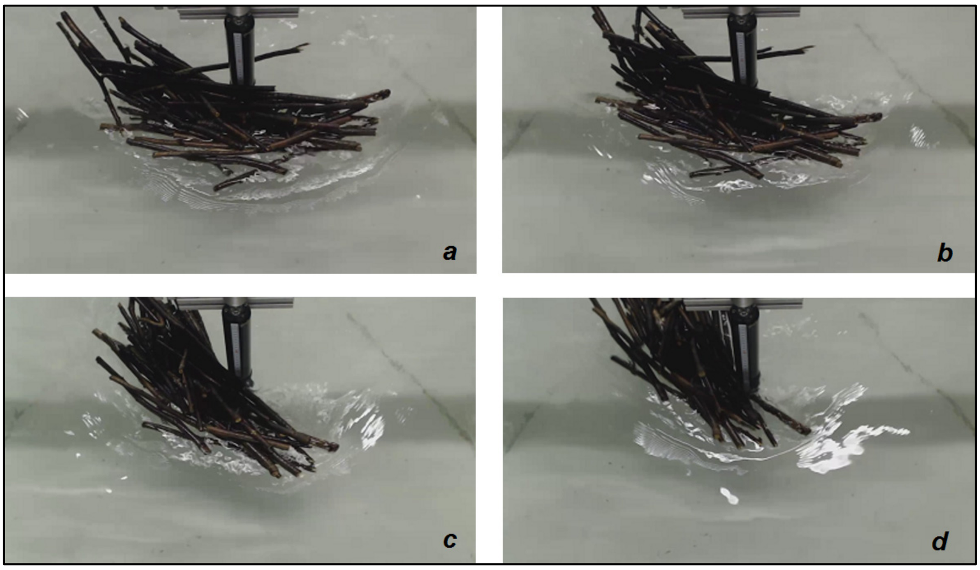

  / ISSN 1562-6865 (Online) - ISSN 1063-7710 (Print)

Figure 5. An example of accumulation failure for a non-uniform size debris jam from the beginning of the oscillation (a) to the final dislodgement (d).

that the lifetime and the size of a woody debris jam are limited by the critical condition after which the jam is completely removed from the pier. The critical condition provides an opportunity to define metrics representing the potential dimensions that can be reached by debris accumulations. The three dimensionless variables thus defined have shown a clear dependency the parameter Fr_L, indicating that any attempt to describe LWD accumulations must be linked to these variables. The results of our experiments with non-uniform debris and at low Fr_L show that an accumulation can reach a width up to 40~50% larger than the length of the key-element. This contradicts previous field-based observations that suggest a maximum width equal to the key-log. In addition, our results show that a jam is more likely to reach the river bed at high Fr_L.

Our experimental results unveiled substantial differences between the dimensions of debris jams formed by debris of uniform and non-uniform lengths. The former reach a size that is much larger than the latter at the same Fr_L. Consequently, idealised experiments adopting a constant size of debris will overestimate the actual size that a LWD pile can reach, as debris supply in natural environments is typically non-uniformly distributed. At low flow conditions, the width of formed accumulations was as high as 3 times the length of the uniform debris elements, but only 1.5 times the length of the key-element in the non-uniform experiments.

Data from our experiments can be used for engineering practice in flood risk analysis and bridge design as a first approximation for the potential size of accumulations that might be achieved at a bridge pier, for given flow and debris size characteristics.

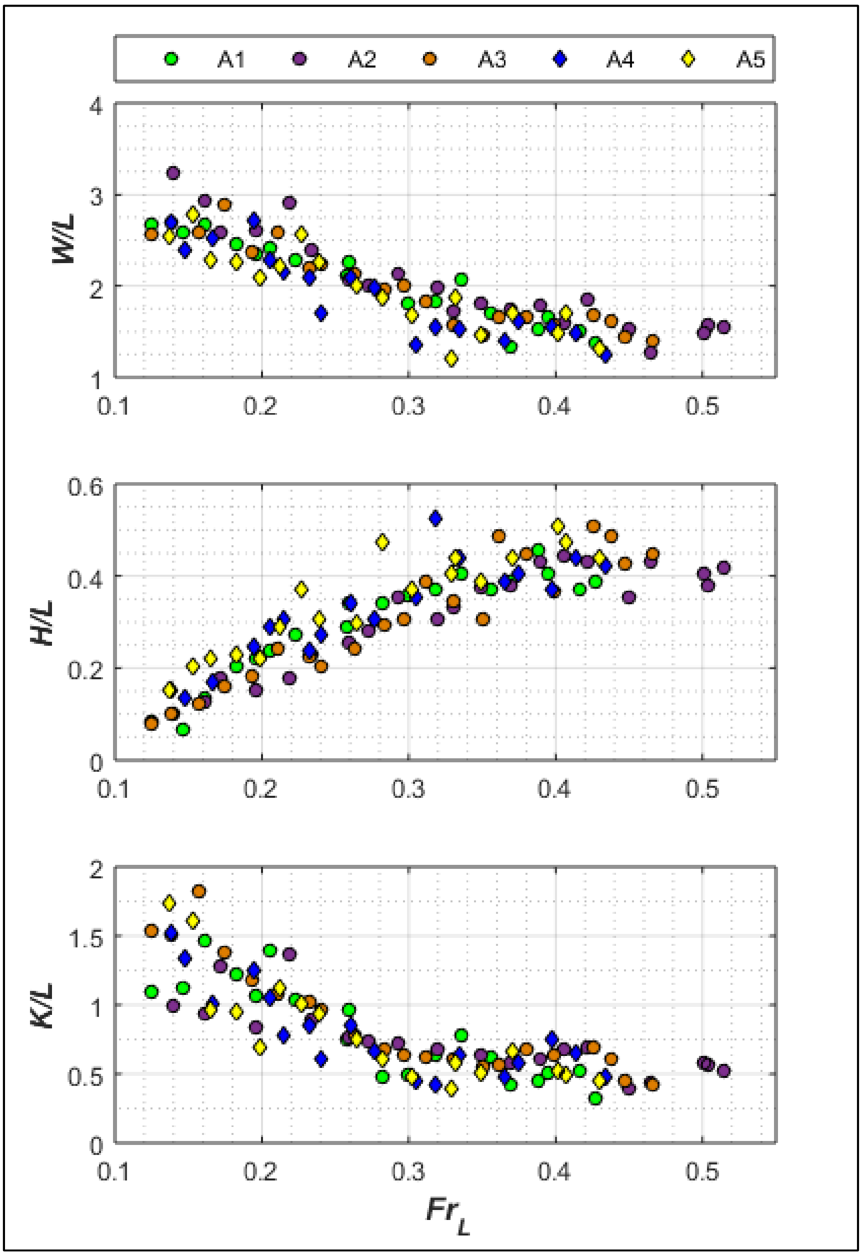

Figure 6. Dimensionless accumulation size variables against Fr_L for uniform size debris.

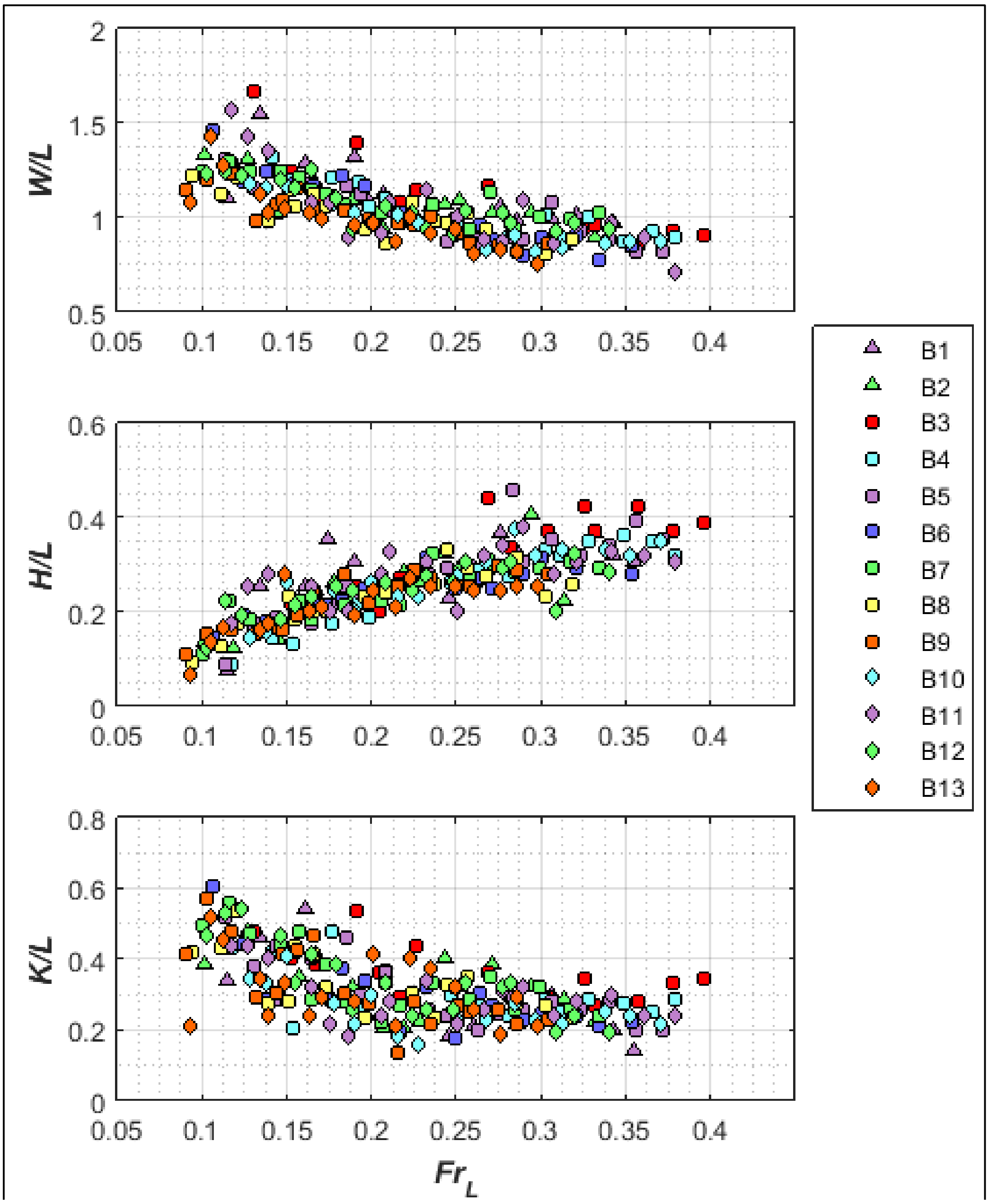

Figure 7. Dimensionless accumulation size variables against Fr_L for non-uniform size debris.

6 CONCLUSIONS

A set of experiments on woody debris accumulations at bridge piers has been carried out. Results have shown a three-phase behaviour that these jams assume during their lifetime. The critical phase is of a particular interest, since at the beginning of this stage accumulations typically reach their maximum size and begin to oscillate about the pier until they are disengaged and drifted away. This phase was found in all experiments we conducted.

Furthermore, debris jams were highly dependent on the variable Fr_L, which contains flow conditions and debris length. When Fr_L is low, debris pile width and length are highest, whereas height is minimal. When Fr_L is high, width and length are smallest and height is highest.

Experiments with idealised debris of uniform size formed accumulations that were much larger than those with a non-uniform distribution of lengths that tries to mimic the supply of debris in natural channels. Therefore, non-uniform debris would ensure a more accurate analysis, although uniform debris can still be used to provide important insights into the accumulation process.

These results are the first attempt to predict the expected accumulation size for given flow conditions and debris length. Also, these findings can be used to estimate the potential dimensions of debris accumulations at bridge piers, which can be particularly useful for bridge design and flood risk assessments purposes.

ACKNOWLEDGEMENTS

This research is funded by the Engineering and Physical Sciences Research Council (EPSRC). The authors would also like to thank the University of Southampton Hydraulics Lab officers Dr Toru Tsuzaki and Mr Karl Scammell for their technical help in setting up and carrying out the experiments.

REFERENCES

Bocchiola, D., Rulli, M. & Rosso, R. (2008). A Flume Experiment on the Formation of Wood Jams in Rivers. *Water Resources Research*, 44(2), 1-17.

Daniels, M. & Rohads, B. (2004). Effect of LWD Configuration on Spatial Pattern of Three-Dimensional Flow in Two Low-Energy Meander Bends at Varying Stages. *Water Resources Research*, 40(11), 1-14.

Diehl, T.H. (1997). *Potential Drift Accumulation at Bridges*, Federal Highway Administration, U.S. Department of Transportation, Washington D.C., USA.

Lagasse, P., Colopper, P., Zevenbergen, L., Spitz, W. & Girard, L. (2010). *Effects of Debris on Bridge Pier Scour*, National Cooperative Highway Research Program, Transportation Research Board, Washington D.C., USA.

Lyn, D., Cooper, T., Yi, Y., Sinha, R. & Rao, A. (2003). *Factors in Debris Accumulation at Bridge Piers*, Federal Highway Administration, U.S. Department of Transportation, Washington D.C., USA.

Lyn, D., Cooper, T., Condon, C. & Gan, G. (2007). *Debris Accumulation at Bridge Crossing: Laboratory and Field Studies*, Federal Highway Administration, U.S. Department of Transportation, Washington D.C., USA.

Manners, R.B. & Doyle, M.W. (2008). A Mechanistic Model of Woody Debris Jam Evolution and its Application to Wood-Based Restoration and Management. *River Research and Application*, 24, 1104-1123.

Pagliara, S. & Carnacina, I. (2012). Bridge Pier Flow Field in the Presence of Debris Accumulation. *Proceedings of the Institution of Civil Engineering*, 166(WM4), 187-198.

Rusyda, M., Hashimoto, H. & Ikematsu, S. (2014). Log Jam Formation by an Obstruction in a River. *Proceedings of the International Conference on Fluvial Hydraulics* (*River Flow 2014)*, Lausanne, Switzerland, 3-5 September 2014.

Sedell, J., Bisson, P. & Gregory, S. (1988). *From the Forest to the Sea: A Story of Fallen Trees. Chapter 3. What We Know about Large Trees that Fall into Streams and Rivers*, U.S. Department of Agriculture, Forest Service, Pacific Northwest Research Station; U.S. Department of the Interior, Bureau of Land Management, Portland, OR, USA.

Wallerstein, N.P., Alonso, C.V., Bennett, S.J. & Thorne, C.R. (2001). Distorted Froude-Scaled Flume Analysis of Large Woody Debris. *Earth Surface Processes and Landforms*, 26, 1265-1283.

Proceedings of the 37th IAHR World Congress
August 13 – 18, 2017, Kuala Lumpur, Malaysia

MODELING SYSTEM EMPLOYED FOR THE OPTIMIZATION OF THE DESIGN OF THE FILLING/EMPTYING SYSTEM OF THE THIRD SET OF LOCKS OF PANAMA CANAL

ANGEL N. MENÉNDEZ[(1)], EMILIO A. LECERTÚA[(2)] & NICOLÁS D. BADANO[(3)]

[(1,2,3)] INA (National Institute for Water), Hydraulics Laboratory, Ezeiza, Argentina anmenendez@gmail.com
[(1,2,3)] University of Buenos Aires, Eng. Dept., LaMM

ABSTRACT

The modeling system built to design the filling/emptying hydraulic system of the Third Set of Locks of Panama Canal, is described. This modeling system is constituted by a series of zero, one, two, and three-dimensional numerical models and a physical model. The main characteristics of the models and the concatenation of models among them are explained. Its application in order to select and optimize the design of non-standard hydraulic components, to determine opening and closing times for valves in order not to exceed design conditions, to calculate the mean vessel throughput and freshwater consumption, and to establish alternatives to minimize vorticity in the water intakes of the water saving basins, is discussed. It is shown that the numerical modeling was the key tool for design, and the mechanism to generate results at the prototype scale free of scale effects present in the physical model, while the main role of the latter one was to validate the numerical models.

Keywords: Panama canal; lock system; hydraulic design; modeling system; numerical modeling.

1 INTRODUCTION

The Panama Canal is a navigation route approximately 72 km long, which connects the Atlantic and Pacific Oceans (Figure 1). It includes two sets of locks. Between the Pacific lock system (Miraflores/Pedro Miguel) and the Atlantic one (Gatun), it develops Gatun Lake. The key component of the Expansion Project of Panama Canal (one of the world largest hydraulic works) is the Third Set of Locks, which introduced a third lane able to allow the passage of Post-Panamax vessels. Additional details on the project are presented in Panama Canal Authority (2011), Lara et al. (2014), and Re et al. (2010).

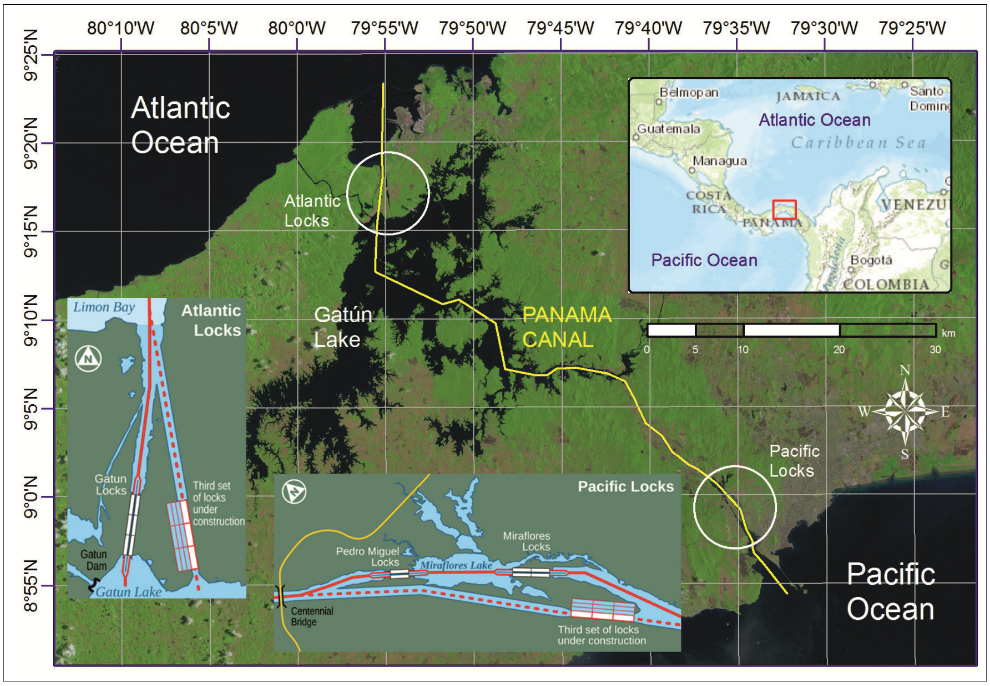

Figure 1. Location of Panama Canal and its third set of locks.

The hydraulic system for the filling/emptying of the lock chambers operates based on gravity. The objective of the study was to optimize the design of the hydraulic system in order to: (i) minimize the hydraulic times of operation, (ii) minimize the freshwater volumes flushed into the oceans during lock operations, (iii) minimize the hawser forces. Simultaneously, the following restrictions had to be fulfilled: (a) a maximum flow velocity of 8 m/s in the conduits and (b) maximum longitudinal and lateral free surface slopes of 0.14 ‰ and 0.10‰, respectively (as proxies for the hawser forces).

In order to study these problems, a modeling system was built, constituted by a variety of numerical models and a physical model, which operated in an interlinked way. In this paper, the main technical details of the modeling system are described, and the mains results obtained through its operation are shown and discussed. More details are presented elsewhere (Menendez et al., 2014).

2 FILLING/EMPTYING SYSTEM

The main components of the filling/emptying system are shown in Figure 2: (i) three chambers (Upper, Middle, and Lower) in series (each one 426.7 m long, 54.9 m wide, and 18.3 m deep), (ii) three Water Saving Basins, WSBs (Top, Middle, and Bottom) per chamber (each one 426.7 m long, 70 m wide, and 5.5 m deep), where some water is stored during chamber emptying operations, and from which some water is extracted during chamber filling operations, (iii) two main culverts (each one 8.3 m high, and 6.5 m wide) connecting the chambers, which end in water intakes from the lake, and outflow works to the oceans, (iv) four secondary culverts (square section 6.5 m side) fed by the main culverts through a Central Connection, (v) ten ports per secondary culvert (square section 2 m side) connecting with the corresponding chamber, (vi) conduits between the secondary culverts and the WSBs, including a connection to the secondary culvert, a Flow Divider, a Trifurcation and an a water intake, and (vii) valves in the main culverts and in the conduits between WSBs and secondary culverts.

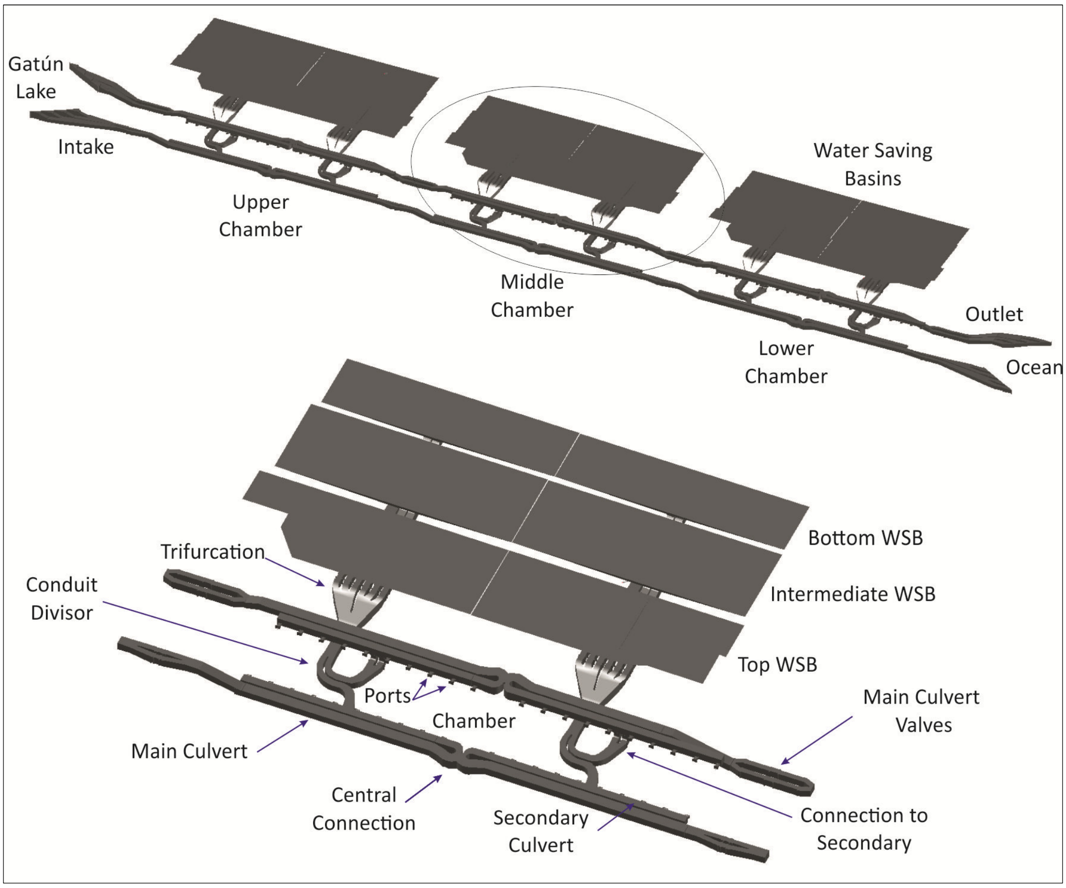

Figure 2. Components of the hydraulic system.

3 MODELING SYSTEM

3.1 General description

The modeling system is schematized in Figure 3. It is a combination of numerical models of different dimensions and a physical model. Each model type and their links are explained in the following.

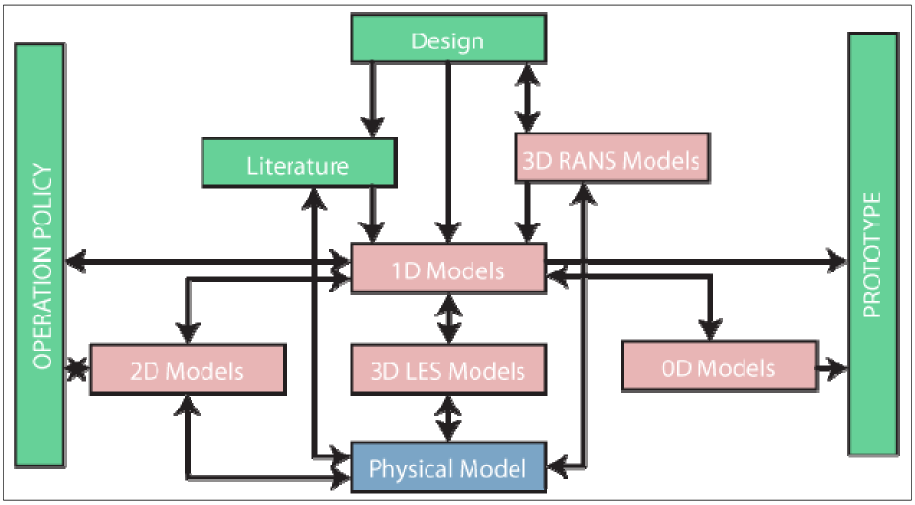

Figure 3. Modeling system.

3.2 1D models

The central component of the modeling system was a set of one-dimensional (1D) hydrodynamic models to simulate the flow along the different circuits between reservoirs (chambers, Lake, Ocean, WSBs) of the filling/emptying system, which the main objective was to determine filling/emptying times of the chambers for different operating conditions, and to verify the restriction on the maximum flow velocity (for which adjustments in the valve operation policies were performed). They simulated the transient flows produced during water levelling between reservoirs.

The 1D models were implemented based on commercial software Flowmaster V7 (http://www.flowmaster.com). Friction losses were expressed through Darcy-Weisbach formula, and the Darcy factor through Colebrook-White formula, which is parameterized in terms of the surface roughness and the Reynolds number (Miller, 1971). They were validated by comparing their predictions with measurements at the physical model, for both steady and unsteady flow, as illustrated in Figure 4 for the latter case. These comparisons were made using, for the numerical model, the actual dimensions of the physical model, as scale effects are relatively significant for the latter one (Menéndez and Badano, 2011).

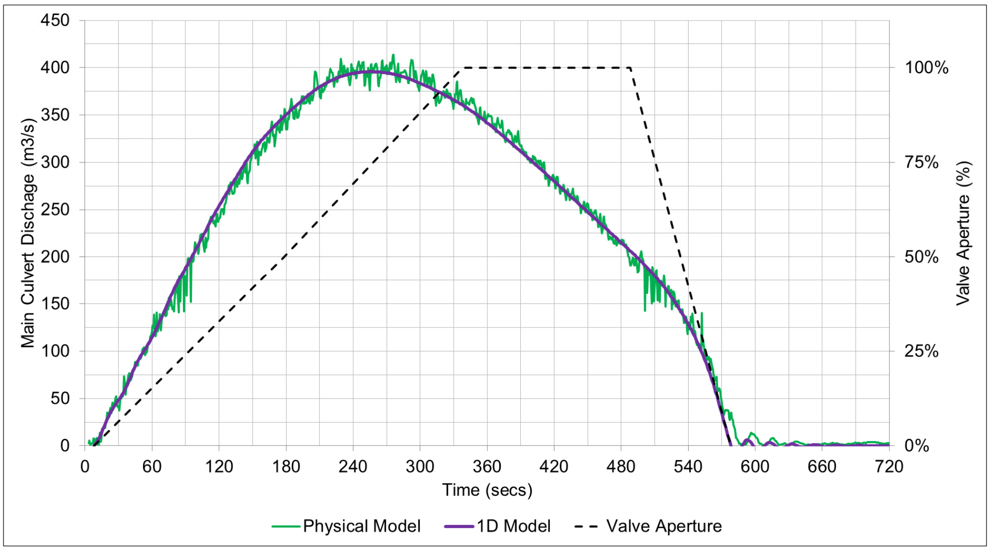

Figure 4. Comparison between 1D and physical models for a filling operation.

3.3 3D models

Three-dimensional (3D) RANS models of the non-standard hydraulic components were built in order to determine the associated energy losses, from which local energy loss coefficients were obtained to be used within the 1D models. These 3D models were employed to optimize the design of those hydraulic components, *i.e.* minimize the energy loss, though an iterative procedure. On the contrary, in the case of standard hydraulic components, the associated local energy loss coefficients were established based on literature (Miller, 1971; Idel'cick, 1979).

The 3D models were implemented based on open code OpenFOAM (Weller et al., 1998). Mesh generation was undertaken using open code Gmsh (http://geuz.org/gmsh), complemented with open code enGrid (http://www.ohloh.net/p/engrid) to build the grids adjacent to the walls, as boundary conditions were treated through wall functions, hence requiring that the first node should lie within the logarithmic zone of the velocity profile (Sagaut, 2001). The free surface was represented either as a rigid lid, or applying the volume of fluid method (Hirt and Nichols, 1981). A thorough previous validation of RANS modeling was undertaken, by comparing its predictions with empirical curves for energy loss coefficients.

Steady flow runs were made for the different hydraulic components and for combinations of them (in order to take into account their mutual influence). As an illustration, Figure 5 shows a 3D view of streamlines for the Central Connection under filling conditions.

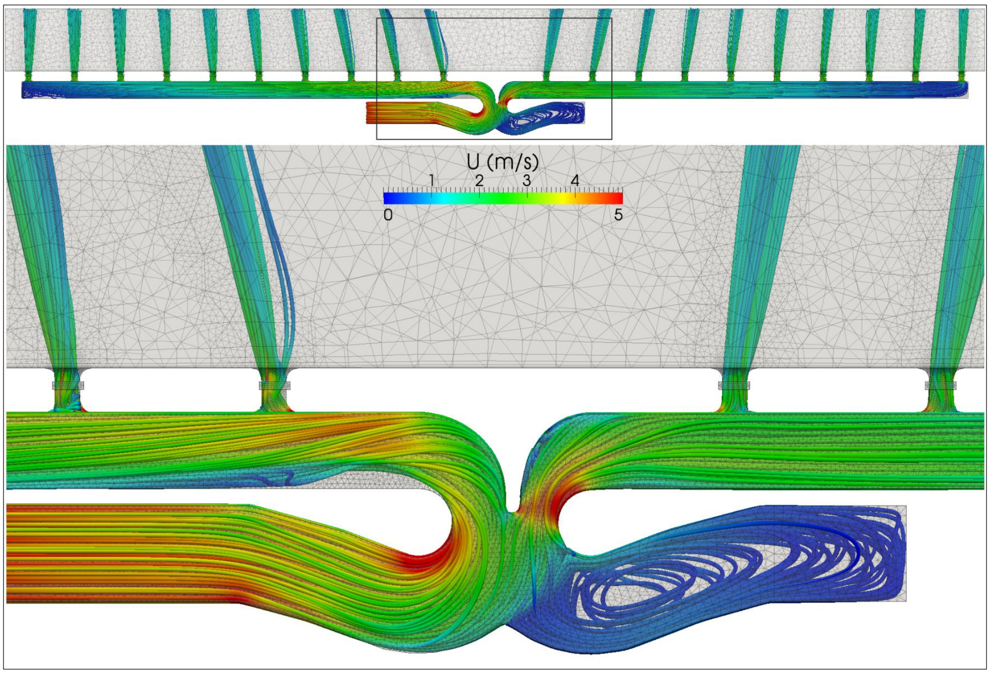

Figure 5. Streamlines for the Central Connection for a filling operation.

3D RANS models were also employed to study solutions, which minimize vorticity at water intakes for the WSBs, in order to avoid air entrainment. For this particular problem, surface tension was included in the numerical model, as this mechanism becomes significant in the physical model. Besides, an automatic and dynamic grid densification algorithm was developed and validated, in order to adequately represent the vortex flow.

In addition, a combination of 1D and 3D RANS models for the valves were implemented, in order to complement calculations undertaken to test the possibility of occurrence of cavitation and aeration.

3.4 2D models

Two-dimensional (2D) models were implemented to study free surface oscillations in the chamber arising from the filling and emptying operations. They were driven by the discharge hydrographs at the ports, provided by the corresponding 1D models. From their results, the maximum longitudinal and lateral slopes were obtained.

Numerical code HIDROBID II (Menéndez, 1990), developed at INA, was used to implement the 2D models. They were validated through comparisons with measurements from the physical model, as illustrated in Figure 6a. However, this methodology failed when the initial water level difference between chambers was very high, as illustrated in Figure 6b. This was not a limitation of the 2D model, but of its driving force; in fact, the 1D models are unable to represent turbulent oscillations produced at the Central Connection, which in this type of situation resonate with the longitudinal free surface oscillations in the chamber (Menéndez and Badano, 2011). In order to solve this restriction, a 3D LES model of the Central Connection was built, which successfully captured this phenomenon, as illustrated in Figure 7.

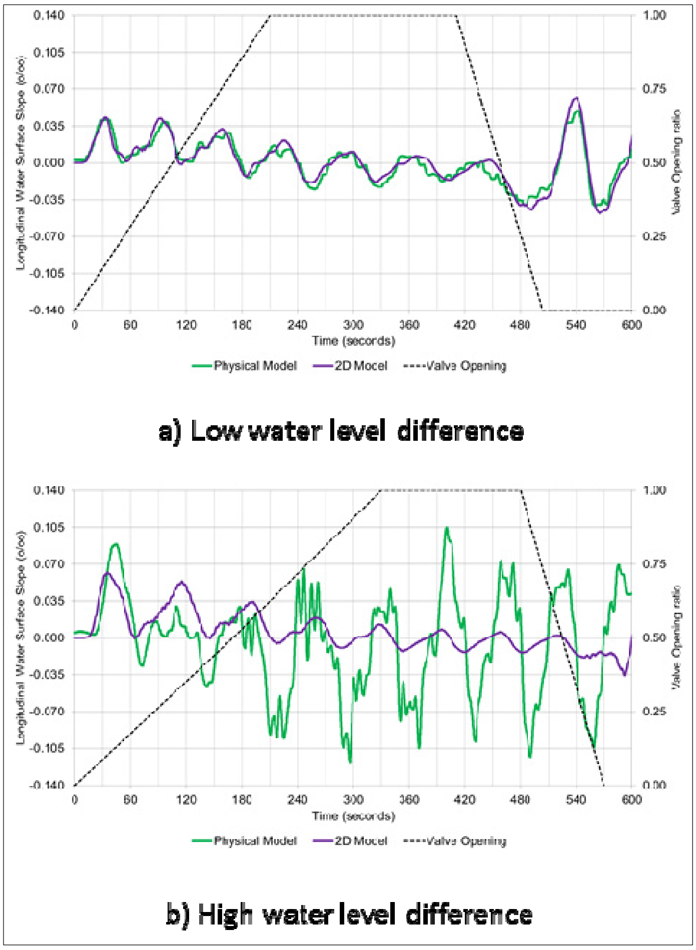

Figure 6. Comparison between longitudinal water slopes from 2D and physical model.

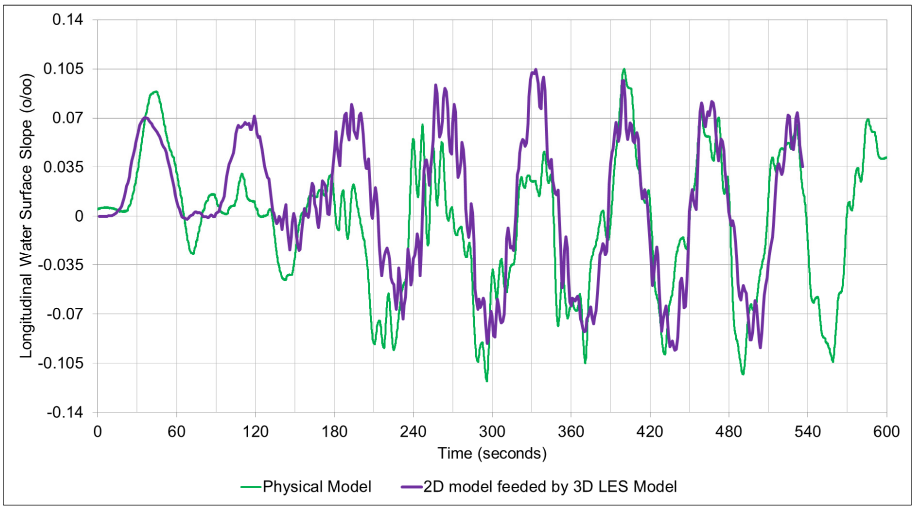

Figure 7. Comparison between longitudinal water slopes from 2D and physical model using 3D LES modeling.

3.5 0D Modeling

The zero-dimensional (0D) models of each one of the two lock systems simulate, for different Ocean and Gatun Lake water level conditions, the water interchange between Lake, Ocean, chambers and WSBs. They used as an input the relations between water level difference and filling/emptying times obtained from the 1D models, and provided the average vessel throughput, the consumed freshwater volume, and the statistics for water level differences between adjacent chambers (from which testing scenarios for the 1D model were defined).

The numerical code for the 0D models were developed ad-hoc, under the name ESCLUSA. The algorithm proceeds continuously in time, keeping track of the times and water volumes involved in the successive operations associated to the passage of a vessel since it enters till it leaves the lock system. It takes into account the simultaneous presence of more than one vessel. It also considers the inversion of vessel traffic each 12 hours, including the time and water volume necessaries to reinitialize the water levels at the chambers.

3.6 Physical Modeling

The physical model, at a 1/30 scale, was built at *Compagnie Nationale du Rhône* (CNR, Lyon, France), and represented two chambers and one set of WSBs. Regarding the hydraulic components design, the physical model operated, in general, as a validator of the results obtained with the numerical models.

4 RESULTS AND DISCUSSION

4.1 Strategies for selection and optimization

The critical elements which determine the performance of the filling/emptying system, in terms of the times needed to complete the locking operations, are the non-standard hydraulic components, where local energy losses are produced. Minimizing those losses was achieved through a design selection and optimization procedure for each component, though maintaining a compromise between low energy loss on one side, and structural and economic advantages on the other side. The optimization strategy was based on two criteria: (i) adjustment of the form to the streamlines in order to prevent flow separation and (ii) reduction of the approximation velocity, by introducing smooth expansions upstream. Figure 8 shows the evolution of the design for the connection to the secondary culvert stemming from the WSB.

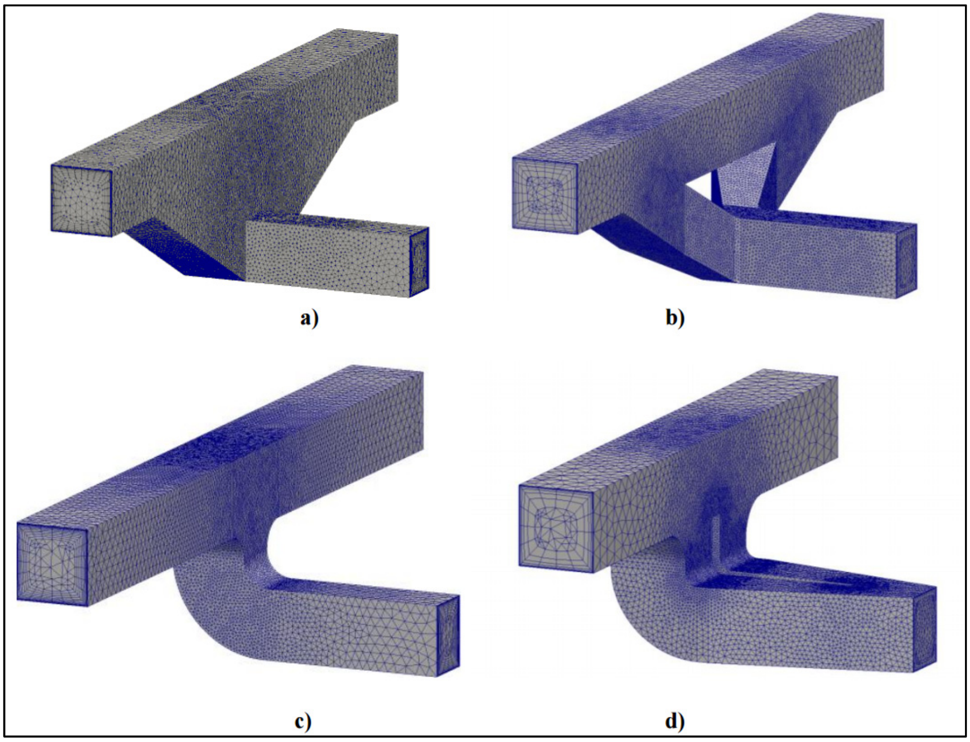

Figure 8. Successive designs for the conduit connection during the optimization procedure.

4.2 Filling/emptying times

By applying the 1D models with the prototype dimensions, the minimum times of aperture for the valves, which guaranteed non-exceedance of the maximum allowable flow velocity, were determined for different initial water level differences between reservoirs. Under those conditions, the filling/emptying times for the different operations were obtained, as illustrated in Figure 9a. Figure 9b presents a comparison between the filling/emptying times for the physical model and the prototype dimensions, as calculated with the 1D models, in order to illustrate scale effects. Note that, as expected, the filling/emptying times are larger for the physical model dimensions, hence providing an excessively conservative estimation, which in this case was corrected by using the prototype dimensions.

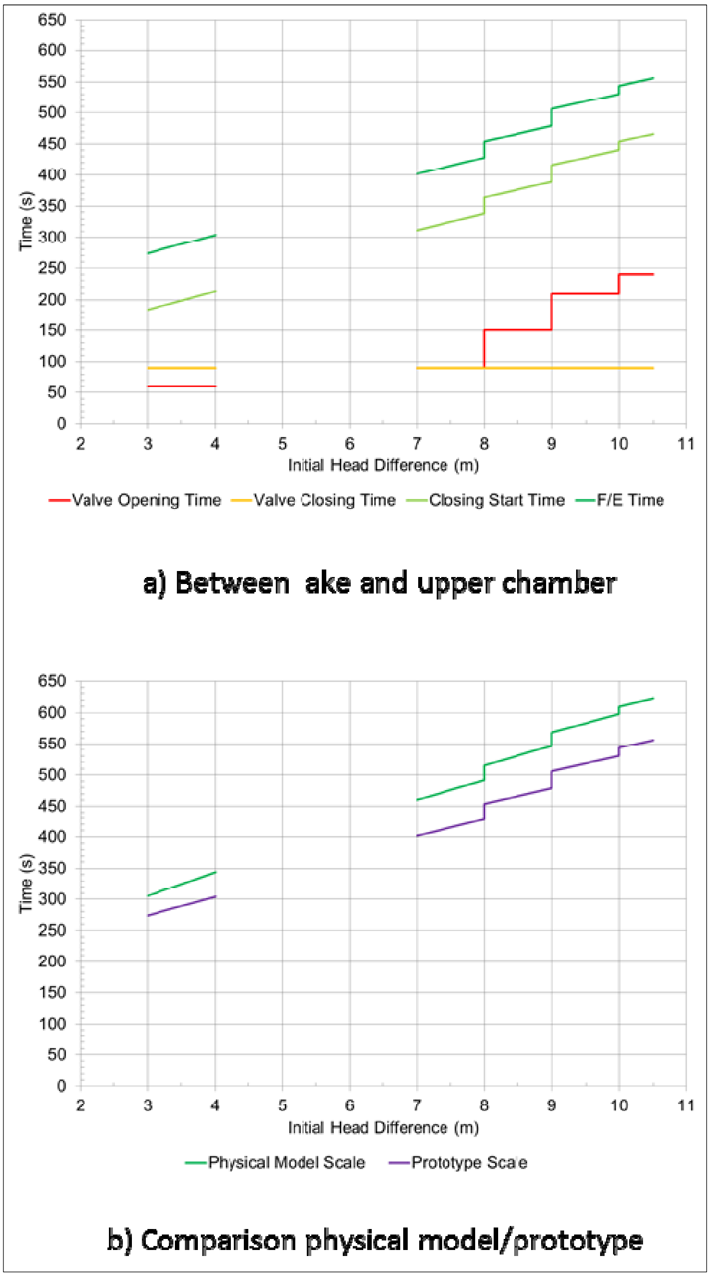

Figure 9. Filling/emptying times for different initial water level differences.

4.3 Maximum water surface slopes

By applying the 2D models with the prototype dimensions, times of closure for the valves were determined in order not to exceed the maximum allowable longitudinal and lateral water surface slopes at the chambers.

4.4 Vessel throughput and water saving

The 0D models were applied to determine the average rate of vessel throughput and freshwater consumption for each one of the two lock systems. The simulation was done for a one-year period, subdivided into four different scenarios (combining high and low water stages of Gatun Lake with maximum and minimum tide conditions). For both lock systems, an average daily throughput of 16 vessels was obtained; this would increase to about 20 if the WSBs were not operated. However, the operation of the WSBs produces, according to the model, an average rate of freshwater consumption of about 100,000 m^3/vessel, representing a freshwater saving rate of almost 60 %.

4.5 Vorticity in WSB intakes

It is well known that studying vorticity at intakes in a physical model provides non conservative results, due to the inability to represent surface tension effects at the proper scale. Hence, for this project a properly validated numerical model was applied in order to estimate conditions at the prototype scale. Figure 10 illustrates the comparison between the temporal evolution of the vertical component of vorticity at the physical model and the prototype scales, according to a 3D RANS model (Sabarots Gerbec et al., 2012). As expected, larger values are attained for the latter case. However, the increment is relatively low.

The physical model was used to establish the most efficient alternative in order to diminish vorticiy. It consisted in the incorporation of two spur dikes, so as to induce a flow pattern better oriented towards the intake.

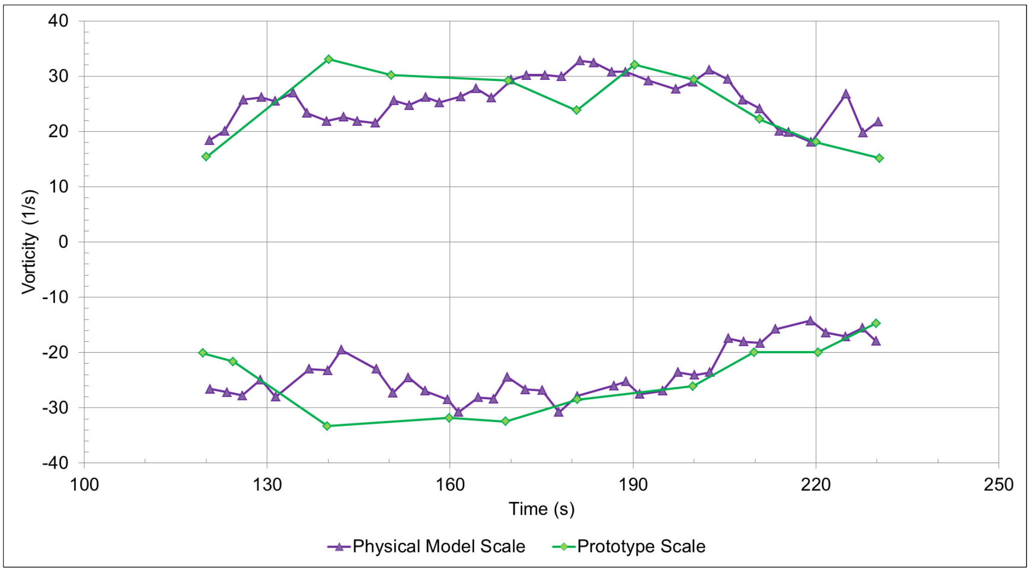

Figure 10. Evolution of maximum vorticity.

5 CONCLUSIONS

The design of the filling/emptying hydraulic system of the Third Set of Locks of Panama Canal constituted a paradigmatic case, regarding the use of an integrated modeling system, which involves a variety of numerical models and a physical model. Numerical modeling has been the fundamental base for design, and the mechanism to generate results at the prototype scale free of the scale effects present in the physical model. The key role of physical modeling was the validation of the numerical models.

The 1D models were the central components of the modeling system, providing filling/emptying times for the chambers, and verifying the restriction on the maximum allowable flow velocity. The 3D RANS models of non-standard hydraulic components determined with high precision energy losses between inflow and outflow, allowing an optimization of their design, and generating the local energy loss coefficients for the 1D models. 3D RANS models were also used to evaluate vorticity at intakes. The 2D horizontal models for the chambers adequately represented the free surface oscillations, driven by the hydrographs at the ports provided by the 1D models, allowing then the verification of the maximum allowable longitudinal and lateral free surface slopes (proxies for the maximum allowable hawser forces). For the cases with very high initial water level difference between chambers, resonance between these oscillations and the eddies generated at the Central Connection was detected in the physical model, leading to the necessity of using 3D LES models to generate the hydrographs at the ports instead of the 1D models, which are unable to represent turbulent oscillations. 0D models provided average vessel throughput and freshwater consumption rates, the main indicators of the system performance from a practical point of view.

As a synthesis, this paper describes an original combination of interlinked models to solve a very complex problem. In particular, a strategy to study lock systems has been established, which can be replicated with confidence in future studies.

The initial tests performed at the prototype of the lock systems, after inauguration, apparently showed a hydraulic performance in line with (or even better than) that estimated during the described studies.

ACKNOWLEDGMENTS

This work was part of the studies performed for consortium GUPC (Grupo Unidos por el Canal), through the consulting firm MWH (Montgomery-Watson-Harza). Nicolás Badano (MWH), Eng., was in charge of the supervision. The numerical modeling team was also constituted by Fernando Re, Martín Sabarots Gerbec and Mariano Re.

REFERENCES

Hirt, C.W. & Nichols, B.D. (1981). Volume of Fluid (VOF) Method for the Dynamics of Free Boundaries. *Journal of Computational Physics,* 39(1), 201–225.

Idel'cik, I.E. (1979). *Memento des Pertes de Charge*, Eyrolles Editor, Collection de la direction des études et recherches d'Electricité de France, Paris, France.

Lara, C.M., Lim Cárdenas, A.L. & Monroy, J.C. (2014). The Panama Canal Existing and New Locks: Same Goal, Different Scales, *Hydrolink* 1, 6-9.

Menéndez, A. N. (1990). Sistema HIDROBID II para simular corrientes en cuencos. *Revista internacional de métodos numéricos para cálculo y diseño en ingeniería*, 6(1), 25-36.

Menéndez, A.N. & Badano, N.D. (2011). *Interaction between Hydraulic and Numerical Models for the Design of Hydraulic Structures, Hydrodynamics – Optimizing Methods and Tools.* H.E. Schulz, A.L. Andrade Simoes, R. Jahara Lobosco (Eds.), InTech.

Menéndez, A. N., Lecertua, E. A., & Badano, N. D. (2014). Optimización del diseño del sistema de llenado/vaciado del Tercer Juego de Esclusas del Canal de Panamá. *RIBAGUA-Revista Iberoamericana del Agua*, 1(1), 4-13.

Miller, D.S. (1971). *Internal Flow Systems,* BHRA, The Fluid Engineering Center, Cranfield, Bedford, UK.

Panama Canal Authority (2011). *Proposal for the Expansion of the Panama Canal Third Set of Locks Project,* Panama Canal Authority.

Re, F., Badano, N.D., Menéndez, A.N., Sabarots Gerbec, M., Lecertúa, E.A. & Re, M. (2010). Modelación numérica del tercer juego de esclusas del Canal de Panamá para el estudio de alternativas de diseño. *Anales XXIV Congreso Latinoamericano de Hidráulica,* Punta del Este, Uruguay.

Sabarots Gerbec, M., Menéndez, A.N. & Badano, N.D. (2012). Cuantificación de efectos de escala de modelo físico durante el estudio de formación de vórtices en tomas de agua mediante modelación numérica. *Anales XXV Congreso Latinoamericano de Hidráulica*, San José, Costa Rica.

Sagaut, P. (2001). *Large Eddy Simulation for Incompressible Flows.* Springer-Verlag, New York, USA.

Weller, H.G., Tabor, G., Jasak, H. & Fureby, C. (1998). A Tensorial Approach to Computational Continuum Mechanics Using Object Orientated Techniques. *Computers in Physics*, 12(6), 620 - 631.

Proceedings of the 37th IAHR World Congress
August 13 – 18, 2017, Kuala Lumpur, Malaysia

EXPERIMENTAL AND NUMERICAL MODELLING OF AERATED FLOWS OVER STEPPED SPILLWAYS

JACOB VAN ALWON(1), DUNCAN BORMAN(2), ANDREW SLEIGH(3) & NIK KAPUR(4)

(1)EPSRC Centre for Doctoral Training in Fluid Dynamics, University of Leeds, Leeds, UK
scjva@leeds.ac.uk
(2,3) Institute for Public Health and Environmental Engineering (iPHEE), University of Leeds, Leeds, UK
d.j.borman@leeds.ac.uk; p.a.sleigh@leeds.ac.uk
(4)Institute of Thermofluids, University of Leeds, Leeds, UK
n.kapur@leeds.ac.uk
(01-04-0495)

ABSTRACT

Stepped spillways are a popular design choice for reservoir overflows due to the high rates of energy dissipation and air entrainment compared to smooth spillways. Air entrainment is important in spillway flows as it affects the pressures acting on the spillway surface, which in adverse conditions can damage the spillway. Air entrainment also causes flow bulking which increases the depth of flow. This study presents free surface and pressure data for aerated flows over an experimental stepped spillway, with pressures measured at different positions across the width of the channel. Within the step cavities, recirculating vortices are observed in both the stream-wise and cross-stream directions, with the direction of circulation alternating at each subsequent step. These 3D effects cause the pressures acting on the step edges to vary across the width of the channel. The Volume of Fluid (VOF) and Eulerian multiphase numerical models are used to predict flows over the spillway. The Eulerian multiphase model shows high levels of air entrainment and is able to predict the position of the free surface to reasonable accuracy. The VOF model, conversely, does not show any air entrainment and therefore under predicts the position of the free surface. The accuracy to which each numerical model predicts pressures on the step faces varies depending on the measurement location. Both of the numerical models accurately simulate the direction of circulation of the 3D vortices within the step cavities. Simulations with varying channel widths, conducted using the VOF model, show that the pattern of 3D vortices repeats as the channel width is increased.

Keywords: Stepped spillway; aeration; multiphase modelling

1 INTRODUCTION

Stepped spillways dissipate significantly more energy than smooth spillways (Rice and Kadavy (1996), Christodoulou (1993) & Rajaratnam (1990)) and are therefore a popular design choice for reservoir overflows. The development of roller compacted concrete in the 1980s led to step spillways becoming an increasingly popular design choice for concrete spillways which increased research into the performance of such spillways. Masonry stepped spillway at embankment dams, however, have been common since the 18th century. The average age of dams in the UK is over 110 years (British Dam Society, 2006) so the inspection and maintenance of dams and spillways is of high importance.

Modelling has an important role to play in both design of new spillways and the inspection of existing infrastructure. Computational Fluid Dynamics (CFD) has the potential to provide an invaluable tool to model flows over stepped spillways. Current industry standard is to model spillways experimentally; however, CFD has certain advantages over physical modelling. For example, CFD allows the full-scale spillway to be modelled so scale affects are not an issue. CFD models also allow any variable to be measured at any point in the domain, so vulnerable areas or specific flow conditions can be identified. CFD models, however, are less well understood than physical models. Before CFD can be used in isolation to model high risk structures, such as reservoir spillways, they must be proven to accurately predict the important features of the flows being considered. Some important phenomena that need to be accounted for to varying extents are briefly discussed below.

Skimming Flow Over Stepped Spillways: There are three flow regimes which occur over stepped spillways: nappe, transitional and skimming. For a given spillway geometry nappe flow occurs at low discharges, transitional flow occurs at moderate discharges and skimming flow occurs at high discharges (Chanson, 2002). This study focuses solely on the skimming flow regime. The characteristics of skimming flow have been described by many authors, including Chamani and Rajaratnam (1999), Chanson (1994), Rajaratnam (1990) and Sorensen (1985). During skimming flow, the bulk of the flow “skims” over the steps and recirculating vortices are formed in the step cavities (figure 1). The step edges form a pseudo-bottom which separates the recirculating vortices and the bulk of the flow. The interaction between the spillways surface and the flow creates turbulence and a boundary layer forms. Moving downstream, the boundary layer increases in depth until it meets the free surface at which point free surface aeration begins. This is known as the point of inception. Downstream of the inception point is a region of gradually varied flow. Air bubbles are transported to the pseudo-bottom and into the step cavities. The entrained air causes flow bulking, increasing the depth of flow. This is an important factor in the design of the spillway sidewalls as overtopping must be prevented. Further downstream, a uniform flow region is formed where the depth of flow, velocity profiles and air concentration remain relatively constant. Skimming flow is an efficient means of energy dissipation, with the primary dissipation mechanism being the transfer of shear stress from the bulk flow to maintain the recirculating vortices. Some energy is also dissipated through turbulence in the aerated region.

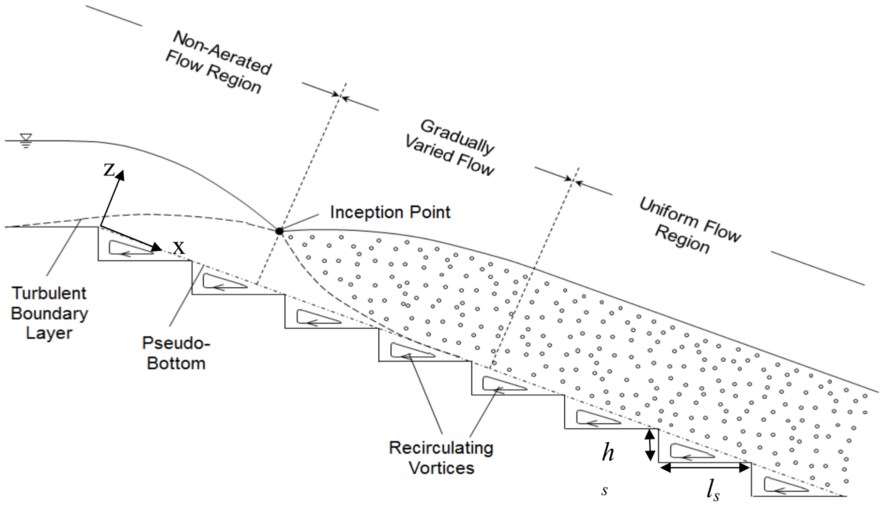

Figure 1. Skimming flow over a stepped spillway identifying key flow features such as the inception point, recirculating vortices and air entrainment.

Pressure effects: Under skimming flow conditions stepped spillways are subjected to large variations in pressure. Zhang et al. (2012), Sánchez-Juny et al. (2007) & Sánchez-Juny et al. (2000) show that high pressures occur at the downstream end of the horizontal step edge and the bottom of the vertical step edge, where the recirculating vortex impinges on the step. The upstream end of the horizontal step edge and the top of the vertical step edge are subject to lower pressures where flow separation occurs. These studies, and others, including Zhang and Chanson (2016), Xu (2015) and Matos et al. (1999), have all taken pressure measurements at the centreline of the spillway. This study investigates the variation in pressure across the width of the spillway channel.

Plucking: In masonry spillways, large pressure gradients can develop between the front of blocks, where flows cause low pressures, and the back of blocks, where backing material exerts a lateral earth pressure. This pressure gradient can cause blocks to be plucked from the spillway into the flow, leaving a gap in the spillway surface or sidewall. This gap allows water to ingress behind the spillway, causing erosion of backing material which can lead to failure of the spillway. This is particularly hazardous at earthen fill dams as the spillway often runs down the mitre of the dam, so ingress of water could cause erosion of the dam itself. Two high profile spillway failures in the UK occurred at the Boltby reservoir in 2005 and the Ulley reservoir in 2007 due to failure of the spillway sidewalls. It is thought that one of the failure mechanisms of the Ulley spillway was due to plucking of masonry blocks from the sidewall (Hinks et al., 2008). Missing blocks were also observed in the sidewall of the Boltby spillway (Mason and Hinks, 2008). Following these failures, the UK Environment Agency commissioned a detailed study into the safety of masonry stepped spillways which is described by Winter et al. (2010). Some key findings of the study are that small areas of damage to the spillway can further increase the risk of plucking and that localised variations in pressure are an important factor in the removal of masonry blocks.

Cavitation: Plucking does not occur on concrete spillways; however, consideration must be given to cavitation damage. Cavitation is the process by which the local pressure falls below the vapour pressure of the liquid causing the liquid to vaporise and form bubbles. When these bubbles are transported to an area of higher pressure, they collapse and produce extremely high localised pressures which can damage solid boundaries. There are no recorded cases of cavitation damage being observed on stepped spillways. Frizell et al. (2012) claimed that this is due to conservative designs preventing the conditions which could produce cavitation from occurring. Chanson (2002) claims, however, that there is no risk of cavitation damage to

  / ISSN 1562-6865 (Online) - ISSN 1063-7710 (Print)

stepped spillways due to slower flow velocities and greater water depths producing a cavitation index 10 to 100 greater than on smooth spillways with identical discharges.

Air Entrainment: Air entrainment is known to significantly reduce the risk of cavitation damage. Experiments conducted by Dong et al. (2010) and McGee (1988) show that air entrainment prevents the low pressures which cause cavitation from occurring. As both cavitation and plucking occur in low pressures regions, it follows that air entrainment would also reduce the risk of plucking in masonry spillways. This, however, leaves the non-aerated flow region at risk to plucking and possibly cavitation damage. One of the most challenging areas to model numerically is the air entrainment, and the resulting flow behaviour.

2 EXPERIMENTAL SETUP

Experiments were conducted in the spillway shown in figure 2 (a). The spillway channel was 150 mm wide and consisted of 15 steps with h_s = 80 mm and l_s = 80 mm. The spillway crest is curved to prevent the flow from jetting over the steps. Pressures were recorded at steps 2, 5 and 12 using an Omega PX409 pressure transducer with a measurement range of atmospheric pressure ± 6894.8 Pa. At each step, pressures were measured at four points on the horizontal step face and four points on the vertical step face. In each case, there were two measurement points along the centreline of the spillway and two points 20 mm from the wall of the spillway. This will allow any variation in pressure across the channel width to be identified.

To measure the position of the free surface, the side elevation of the spillway was digitally photographed using a 13–megapixel digital camera. The position of the free surface was then automatically calculated using image processing analysis of the images using the computation and visualization software MATLAB.

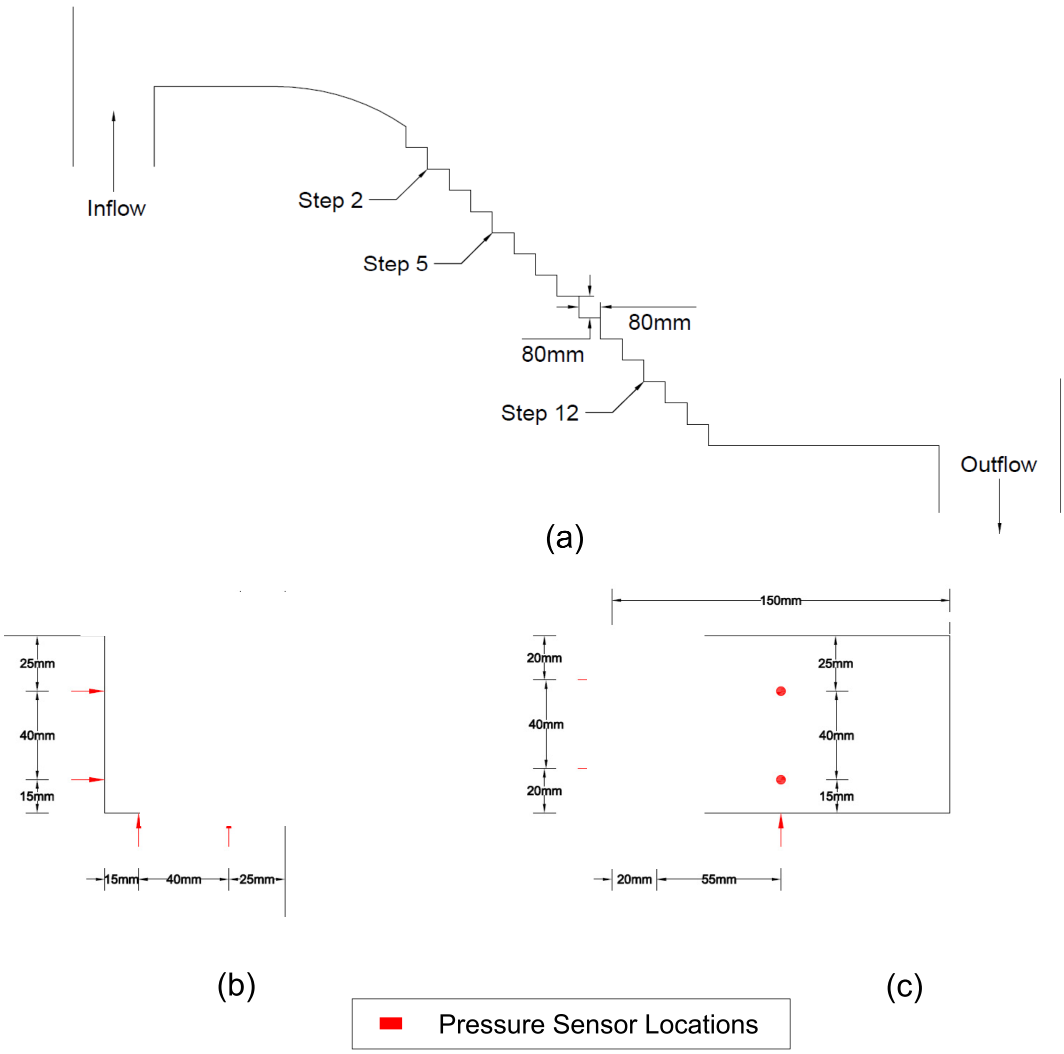

Figure 2. (a) Experimental spillway (b) Step profile (c) Vertical step face.

3 NUMERICAL MODELLING

3.1 Numerical models

Volume of Fluid (VOF) Model: The VOF model is a multiphase model first proposed by Hirt and Nichols (1981). The model assumes that all fluids are immiscible and is generally used where the interface between fluids is important. A single set of momentum equations are solved for all phases and the volume fraction of each fluid in a cell is tracked. The volume fraction of each secondary phase is calculated using a volume fraction equation based on the continuity equation:

$$\frac{\partial}{\partial t}(\alpha_k) + \nabla \cdot (\alpha_k \boldsymbol{u_k}) = \Gamma_k \quad [1]$$

where the subscript k denotes phase k, α is the volume fraction, $\boldsymbol{u}$ is the velocity and Γ is the mass generation. The volume fraction of the primary phase is calculated based on:

$$\sum_{k=1}^{n} \alpha_k = 1 \quad [2]$$

The following single momentum equation is then solved for all phases:

$$\rho \frac{D\boldsymbol{u}}{Dt} = -\nabla p + \nabla \cdot (\boldsymbol{\tau} + \boldsymbol{\tau}^T) + \rho \mathbf{g} + \boldsymbol{F}_s \quad [3]$$

where ρ is the average density of all phases, p is the pressure, $\boldsymbol{\tau}$ is the viscous stress tensor, $\boldsymbol{\tau}^T$ is the turbulent stress tensor and $\boldsymbol{F}_s$is the surface tension. The average density is calculated by:

$$\rho = \sum_{k=1}^{n} (\alpha_k \rho_k) \quad [4]$$

The average viscosity is calculated in the same manner.

The VOF model does not allow phases to interpenetrate, so therefore is limited to the extents that it can predict air entrainment. Despite this, several studies have been shown to be able to accurately predict certain characteristics of skimming flow over stepped spillways. Chen et al. (2002) used the VOF model to simulate skimming flow over a spillway with h_s = 60 mm and l_s = 45 mm. Reasonable predictions of velocity profiles and pressures acting on the step edges are made. Chakib (2013) used the VOF model to accurately predict velocity profiles at several locations. The numerical results show air entrainment along the chute. As the VOF model does not allow phases to interpenetrate, it is unclear how this result is achieved. Kositgittiwong et al. (2013) modelled a large scale experimental spillway with 25 steps of 1220 mm length and 610 mm height. Velocity profiles are accurately predicted in both the aerated and non-aerated regions. Bombardelli et al. (2011) used the TruVOF method, which is part of the commercial CFD package Flow-3D, to investigate the non-aerated region. In the TruVOF method, only the liquid phase is modelled. Good predictions of the velocity profiles, water depth and the depth of the turbulent boundary layer were made. Valero and Bung (2015) also used the one fluid approach in Flow-3D, this time with an air entrainment model included. Air entrainment and flow bulking were observed; however, the air entrainment, and therefore flow depth in the aerated region, was overestimated. This was attributed to calibration parameters used for smooth spillways not producing accurate results for stepped spillways. Borman et al. (2015) used the VOF model to accurately predict the location of the free surface of waves and hydraulic jumps in a full scale recreational white water course. In the study, the physical free surface was measured using laser scanning of white water, which is associated with air entrainment.

Eulerian Multiphase Model: The Eulerian multiphase model is described by Ishii and Hibiki (2010). In the model, phases interact with one another and one phase may become dispersed in another. Each phase is considered separately and therefore a set of conservation equations must be solved for each phase. For phase k the continuity equation is:

$$\frac{\partial}{\partial t}(\alpha_k \rho_k) + \nabla \cdot (\alpha_k \rho_k \boldsymbol{u_k}) = \Gamma_k \quad [5]$$

and the momentum equation is:

$$\alpha_k \rho_k \frac{D_k \boldsymbol{u}_k}{Dt} = -\alpha_k \nabla p + \nabla \cdot [\alpha_k(\boldsymbol{\tau}_k + \boldsymbol{\tau}_k^T)] + \alpha_k \rho_k \boldsymbol{g} + M_k \quad [6]$$

where M is the momentum transfer from the phase interface. The interaction between phases is controlled by the terms Γ and M and depends on the density of the dispersed phase, the diameter of the dispersed droplets or bubbles, the viscosity of the continuous phase, the interfacial area and the drag function.

Studies into free surface aeration modelling using the Eulerian multiphase model are relatively scarce. Cheng and Chen (2011) modelled a hydraulic jump using the Eulerian multiphase method. The air volume fraction, free surface position and velocity profiles were all accurately predicted. The use of the VOF model to model skimming flow over stepped spillways has been relatively well studied, however the model has limitations as it is unable to simulate air entrainment. The Eulerian multiphase model has the potential to predict free surface aeration over stepped spillways; however, the model's accuracy and reliability are not proven. This study investigates the Eulerian multiphase model's ability to predict air entrainment, and pressure profiles in skimming flow over stepped spillways and uses the VOF model as a benchmark for comparison.

3.2 Numerical modelling procedure

Numerical modelling was conducted using the CFD package ANSYS Fluent v16.2. All simulations were conducted in 3D using the Realizable $k-\varepsilon$ turbulence model and run transiently until a steady state solution was achieved. A symmetry boundary condition was used at the centreline of the spillway to reduce the size of the computational domain and still simulate the entire spillway. A structured quadrilateral mesh was used with each step containing 40 by 40 by 40 cells. Presented CFD results had been verified to be independent of the grid resolution.

4 RESULTS AND DISCUSSION

4.1 Flow characteristics

Experimental Model Results: The spillway was tested under a flow rate of 15 l/s. Figure 3(a) clearly shows the non-aerated region, inception point, gradually varied flow region and uniform flow region. Upstream of the uniform region the flow was unsteady. The location of the point of inception was not static in location over time, but fluctuated around a mean position by up to two steps in either direction. Figure 3(a) shows the inception point at approximately its average position. Strong free surface aeration was observed downstream of the inception point which increased the flow depth due to flow bulking. In the gradually varied flow region, there was intense splashing and the free surface position fluctuated almost constantly. The depth of flow perpendicular to the pseudo bottom was highest in the gradually varied flow region and settled to a slightly lower level in the uniform flow region.

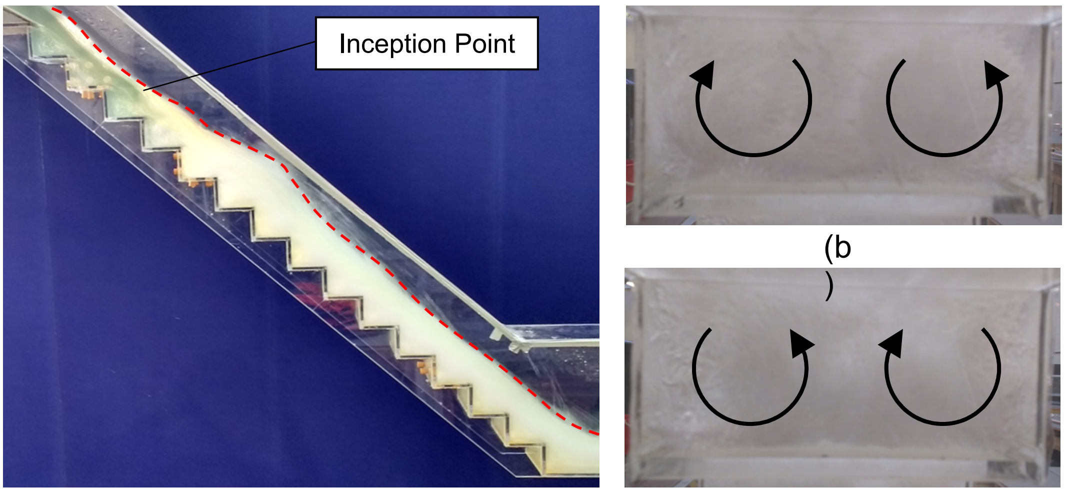

a) (b) (c)

Figure 3. (a) Experimental Spillway (b) & (c) Cross-stream Vortices.

As well as the stream-wise recirculating vortices shown in figure 1, further cross-stream vortices can be observed in the step cavities, recirculating perpendicular to the main flow direction. In each step, there were two vortices, circulating in opposite directions and interacting at the centreline of the spillway. The vortices circulated in one of two directions. Either the vortices flowed upwards at the wall and impinged on the horizontal step face at the centre (figure 3 (b)), or the vortices impinged at the wall and flowed upwards at the centreline (figure 3(c)). The direction of circulation changed at each step, with the odd numbered steps resembling figure 3(b) and the even numbered steps resembling figure 3(c). Matos et al. (1999) reports that

the recirculating vortices in the step cavities exhibit 3D behaviour; however, the detailed structure of the vortices is not described.
Numerical Model Results: Figure 4 shows contours of air volume fraction predicted at the centre plane of the spillway for the Eulerian and VOF models. The VOF model showed no air entrainment or inception point. The Eulerian model showed high levels of free surface aeration and resembled the experiments more closely. Defining the inception point as the location where air begins to be entrained into the flow, the Eulerian model showed the inception point at approximately the crest of the spillway. It can be seen from figure 3 (a) that this was not the case and the average position of the inception point was around step four. Air appears to be transported into the step cavities slightly further upstream in the experiments than in the Eulerian model. However, to accurately validate the volume of air entrained in the Eulerian model, measurements of air concentrations in the physical model are required.

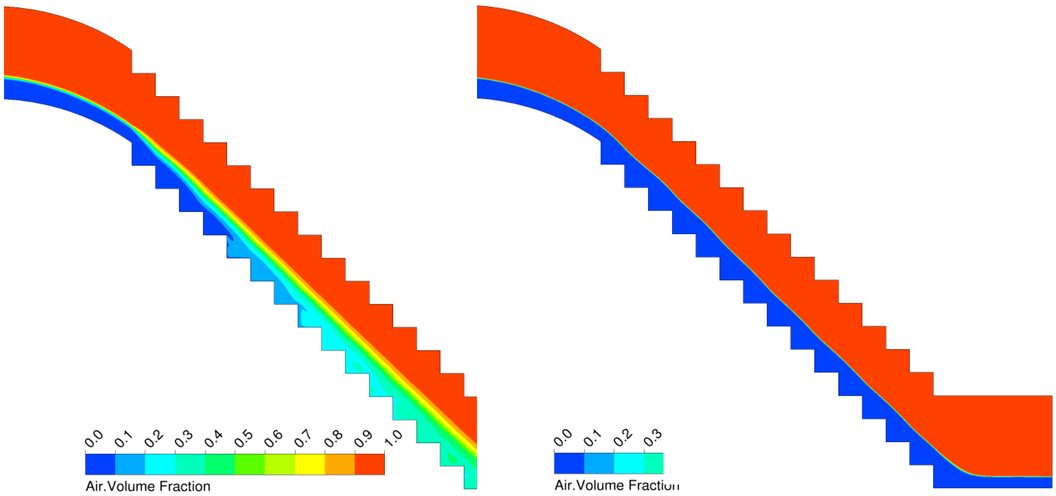

Figure 4. Air volume fraction for (a) Eulerian model (b) VOF model.

4.2 Free surface location

The red dashed lines in figure 3(a) shows the position of the free surface. This was calculated using image processing routines in MATLAB (based on the boundary between the darker coloured background and the lighter coloured water). In the numerical models, the free surface had been defined as the depth at which the air concentration = 90%. Figure 5 shows the experimental and numerical free surface levels perpendicular to the pseudo-bottom, where x is the distance along the pseudo-bottom from the spillway crest and z is the perpendicular distance from the pseudo-bottom. The inception point and subsequent increase in depth can be seen followed by the slight decrease in depth at the uniform flow region. The Eulerian model shows generally good agreement, with the free surface elevation being under predicted in the unsteady flow region and slightly over predicted in the uniform flow region. The Eulerian model shows a smooth free surface, whereas the experimental data shows that free surface is uneven. The VOF model under predicts the free surface at all locations. This is because in the VOF model no air is entrained into the flow so flow bulking is not predicted.

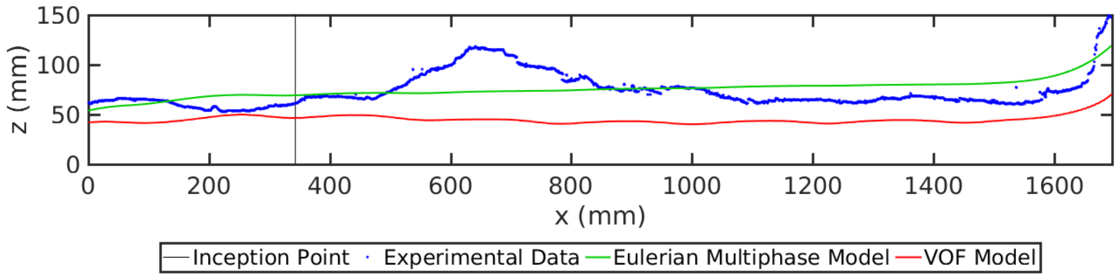

Figure 5. Experimental and numerical free surface depths perpendicular to the pseudo-bottom.

4.3 Pressure measurements

Pressures were measured in the experimental spillway at a sampling rate of 1 kHz for 30 seconds. All pressure data presented represents the mean pressure relative to atmospheric pressure. The locations of the

  / ISSN 1562-6865 (Online) - ISSN 1063-7710 (Print)

pressure data presented are detailed in figures 2(b) & (c). Figures 6 and 7 show the experimental and numerical pressures on the horizontal and vertical step faces, respectively. The left hand plots show the pressures at the centreline of the spillway and the right hand plots show the pressures 20 mm from the spillway wall. Figure 8 shows the contours of pressure on the horizontal and vertical step faces for both models. The experimental mean pressures were superimposed onto the contours in the corresponding locations.

On the horizontal step faces, the experimental data showed that the expected pressure profile, with the highest pressure at the downstream end of the step, can be seen close to the wall at steps two and twelve. At the centreline of these steps, however, the expected pressure profile was not seen and there was little variation in pressure between the upstream and downstream ends of the step face. This pressure pattern corresponded to the direction of circulation of the cross-stream vortices. At steps two and twelve, the cross-stream vortices impinged on the step face close to the wall of the spillway, where the expected pressure profile occurred. At the centreline of these steps, the cross-stream vortices flowed away from the horizontal step face and the expected pressure profile did not occur. At step five, the cross-stream vortices circulated in the opposite direction and the opposite pattern of pressure can be seen.

At the vertical step faces, there was much less variation in the pressure profiles across the width of the channel, and in all cases the expected pressure profile was observed, with the lowest pressures occurring at the top of the step. There was still, however, some variation in the pressures across the width of the channel which corresponded to the direction of circulation of the cross-stream vortices. At steps two and twelve, the pressures were slightly lower close to the wall and at step five the pressures were slightly lower at the centreline.

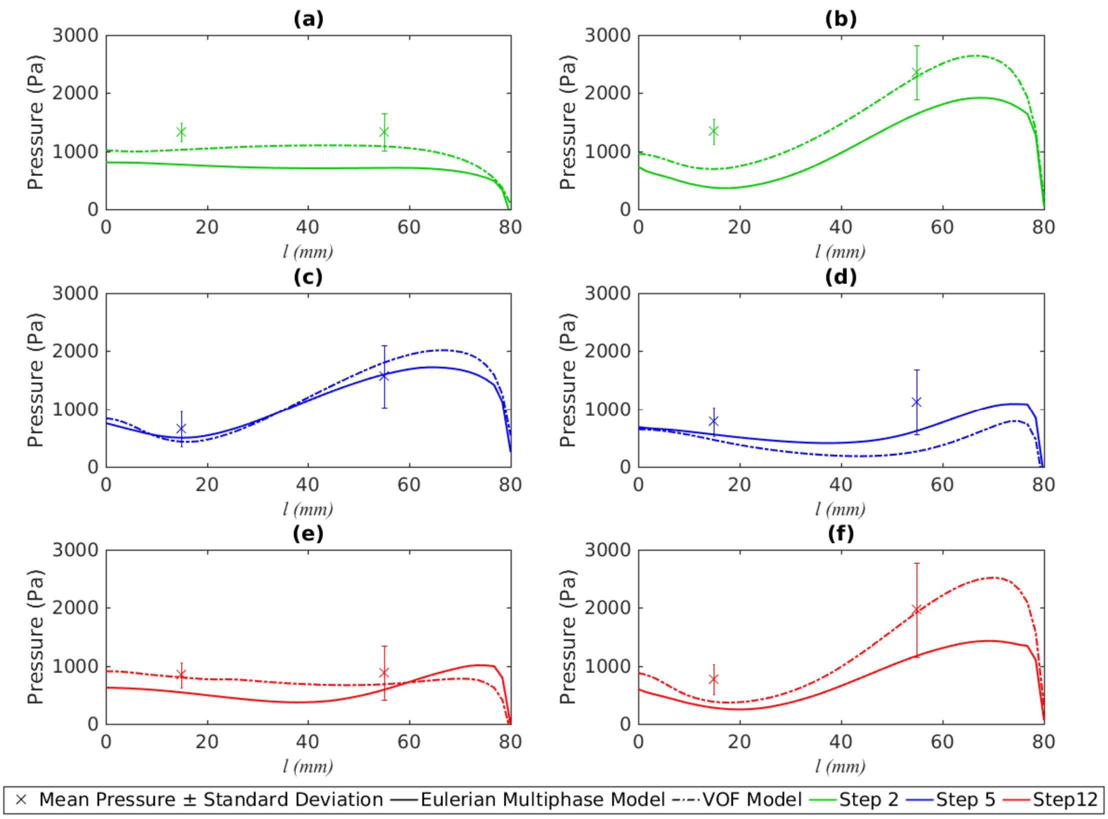

Figure 6. Experimental and numerical pressures acting on the horizontal step faces (a), (c) & (d) at the centreline of the spillway (b), (d) & (f) 20 mm from the spillway wall.

At the horizontal step faces, both the Eulerian and VOF models showed the same general profile as the experimental data, with the variations in pressure across the width of the channel corresponding to the direction of circulation of the cross-stream vortices. At step two, the VOF model performed better than the Eulerian model, with the Eulerian model underestimating the pressure at all positions. This is not surprising as step two lies within the unaerated region. The VOF model does not predict aeration; however, as can be seen in figure 4, some air entrainment occurs above step two in the Eulerian model. The VOF model was accurate at the downstream end of the step, however also underestimated the pressure at the upstream end of the step. At step five, both models performed well at the centreline of spillway; however, the Eulerian model predicted the pressures more accurately close to the wall. At step twelve, the Eulerian model predicted the pressures reasonably well at the downstream end of the step, however underestimated the pressures at the upstream end of the step. The VOF model performed more accurately than the Eulerian model; however underestimated the pressure at the upstream end of the step close to the wall.

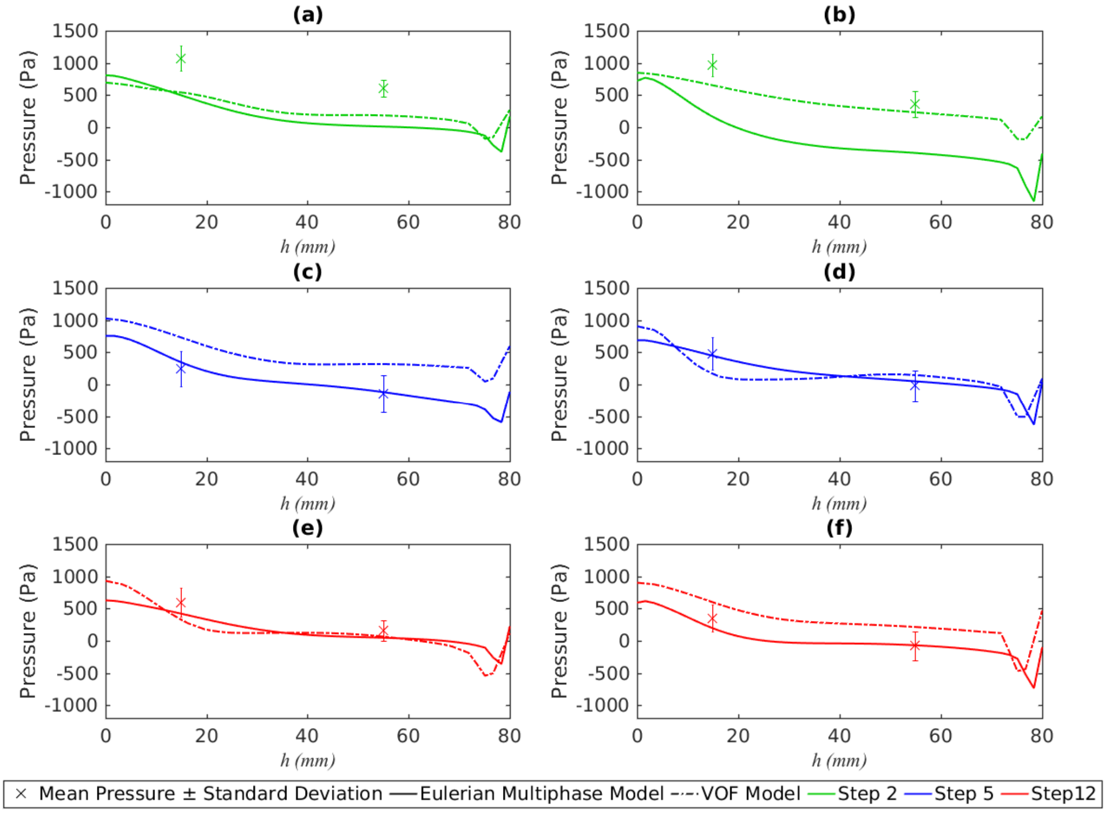

Figure 7. Experimental and numerical pressures acting on the vertical step faces (a), (c) & (d) at the centreline of the spillway (b), (d) & (f) 20 mm from the spillway wall.

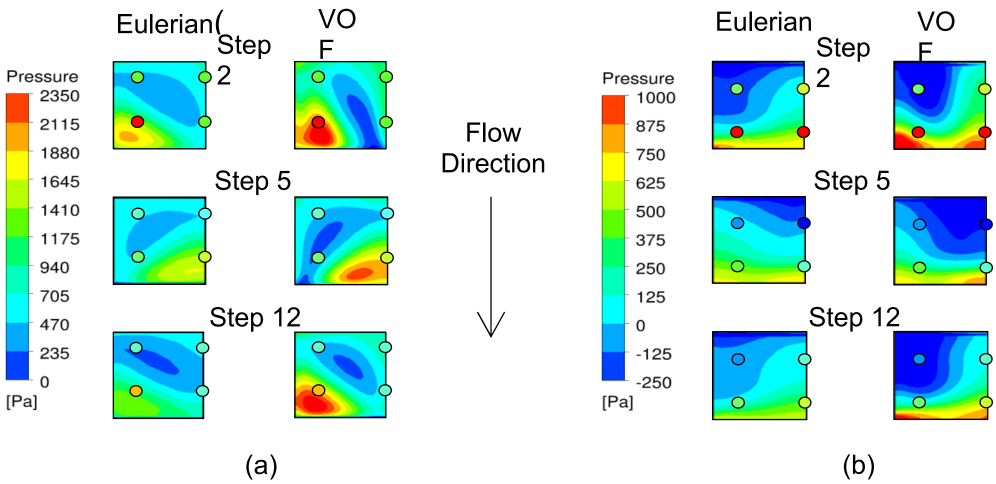

Figure 8. Numerical contours of pressure with experimental mean pressures superimposed in the corresponding locations. (a) Horizontal step faces. (b) Vertical step faces.

At the vertical step faces, the two numerical models also showed the same general pressure profiles as the experimental data. At step two, the Eulerian model underestimated the pressure at all positions. The VOF model performed slightly better than the Eulerian model, however, still underestimated the pressure at the centreline and at the bottom of the step face close to the wall. At steps five and twelve, the Eulerian model accurately predicted the pressure in all locations. The VOF model performed well at step five close to the wall and step twelve at the centreline. The largest variation between the Eulerian and VOF pressure profiles were at the centreline of step five and close to the walls of steps two and twelve. It is at these locations across the channel width, where the cross-stream vortices impinge on the horizontal step face. Increased turbulence in these regions may be the reason for the variation between the two numerical models.

4.4 3D vortex structures

Figure 9 shows the stream-lines over steps three and four and the pressure contours on the step faces for the Eulerian and VOF models. The streamlines had been seeded close to the step corner in each step cavity. In both the Eulerian and VOF models, two separate vortices which meet at the centre of the channel can be seen. The direction of circulation of these vortices changed at each subsequent step so that they impinged on the horizontal step face either at the centre of the spillway or close to the walls, matching the directions that were observed in the physical model.

It can be seen from figure 9 that there was no distinction between a cross-stream vortex and a stream-wise vortex and in fact there was only one three-dimensional vortex in each half of a step cavity. The axis of this vortex ran diagonally downstream from either the centre of the spillway to the wall, or the wall to the centre, depending on which step was being considered.

The variations in pressure across the width of the horizontal step faces matched the direction of these vortices closely, with the highest pressures occurring where the vortices impinged on the step face. On the vertical step faces, the lower pressure regions corresponded to the position where the axes of the vortices meet the step face.

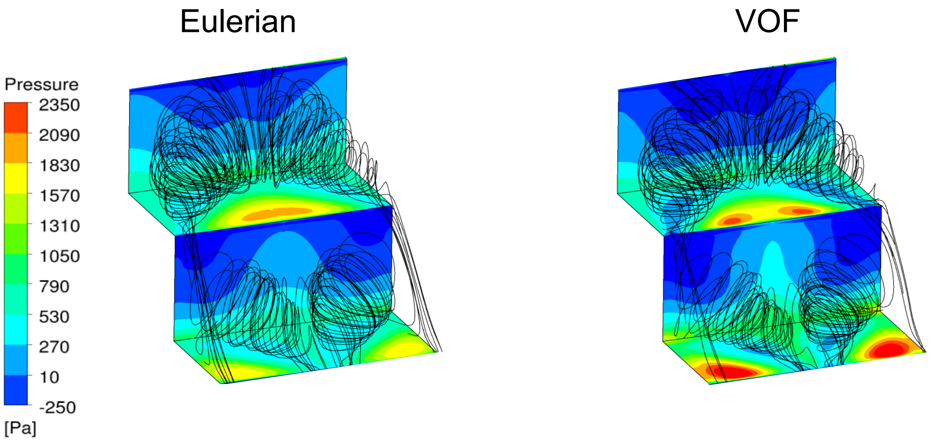

Figure 9. Pressure contours and streamlines at steps three and four.

The width of the experimental spillway was relatively narrow compared to prototype spillways and also provided a ratio of channel width to step height (or length) of 1.875:1. As this is almost 2:1 and two vortices occur across the step width, it was considered that the aspect ratio of channel width to step height or length may be the cause of the observed vortices. To determine whether the vortices occurred due to the narrow channel width, or the ratio of width to step height, simulations were conducted of spillways with varying channel widths. The simulations were conducted using the VOF model as the computational cost is significantly less than the Eulerian model, due to only a single momentum equation being solved. The VOF model had been shown to produce the same flow and pressure patterns that were observed in the experimental spillway so it can be used to simulate channels of varying width with reasonable confidence.

Figure 10(a) shows the stream-lines and pressure profiles at steps three and four of a channel of 300 mm width, double that of the experimental spillway. As with the previous cases, the simulation was conducted with a symmetry boundary condition at the centre of the spillway. The vortex structure observed in the simulations of the 150-mm wide spillway was repeated, so that there were 4 vortices rather than two. Again, the direction of the vortices changed at each subsequent step and the pressure profiles corresponded to the direction of circulation of the vortices. This pattern can also be seen for channel widths of 450 mm, producing six vortices, and 600 mm, producing eight vortices.

In figure 10 (b), a symmetry boundary condition had been used at both of the walls of the spillway, essentially giving the spillway an infinite width. Again, the repeating pattern of vortices and the corresponding pressure profiles can be seen. This shows that the vortex structures which are observed are not caused by the interaction between the fluid and the walls.

This pattern of repeating vortices, which change direction at each subsequent step, shows some resemblance to those described by Lopes et al. (2017). In this study, however, the repeating vortex structure only occurred with a channel width of 500 mm. With a channel width of 300 mm, the flow appeared to be relatively uniform across the width of the channel and at each subsequent step. The numerical data presented in this study shows that the occurrence of these vortices does not depend on the width of the channel. The work by Lopes et al. (2017) was conducted on a spillway with a ratio of *l* to *h* of 2:1 rather than 1:1 in this study. This difference may account for why different behaviours are observed for varying channel widths.

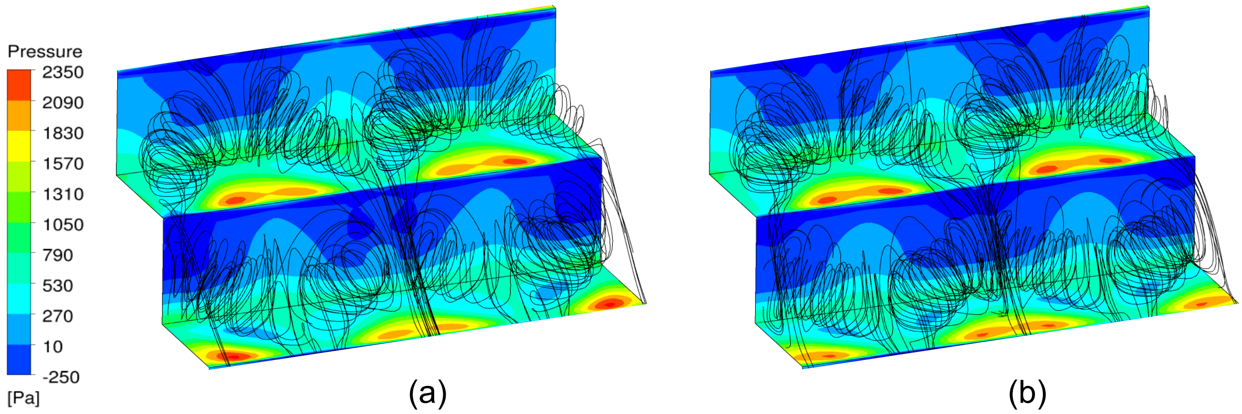

Figure 10. Pressure contours and streamlines at steps three and four for (a) a channel width of 300 mm and (b) infinite channel width.

5 CONCLUSIONS

This study presents free surface and pressure data for an experimental stepped spillway and the corresponding numerical data for two multiphase models. As well as the stream-wise recirculating vortices described by many authors, cross-stream vortices are also observed in the step cavities. The direction of circulation of these vortices changes at each step. These 3D flow patterns cause the pressures acting on the step faces to vary along the width of the chute.

The Eulerian multiphase model can reasonably predict the position of the free surface over the steps and shows aeration of the flow. The VOF model, however, does not show any air entrainment and therefore the free surface depth is under predicted. Both of the numerical models predict the correct general pattern of pressure as it varies across the channel width. The performance of each model varies depending on the measurement location. The Eulerian model generally predicts pressures accurately in the aerated region but underestimates the pressures in the non-aerated region, where the VOF model is more accurate. The VOF model predicts the pressures in the aerated region well in some locations, but less well in others.

Both of the numerical models accurately simulate the pattern of two 3D vortices in each step cavity, which change direction at each step. The VOF model is used to simulate spillways of increasing channel width, and this vortex pattern is found to repeat as the channel width increases. The vortex pattern is also found for a channel with symmetry boundary conditions at the two walls. This shows that the vortices are not caused by the interaction of the fluid and the walls.

ACKNOWLEDGEMENTS

This work is funded by EPSRC [grant number EP/L01615X/1]. The authors would also like to thank Hydrotec Consultants Ltd for constructing the spillway in which experiments are conducted.

REFERENCES

Bombardelli, F.A., Meireles, I., & Matos, J. (2011). Laboratory Measurements and Multi-Block Numerical Simulations of the Mean Flow and Turbulence in the Non-Aerated Skimming Flow Region of Steep Stepped Spillways. *Environmental Fluid Mechanics,* 11(3), 263-288.

Borman, D., Sleigh, P.A. & Coughtrie, A. (2015). Three Dimensional Free-Surface Modelling with a Novel Validation Approach. *E-proceedings of the 36th IAHR World Congress.* Leeds.

British Dam Society (2006). Improvements in Reservoir Construction, Operation and Maintenance. *Proceedings of the 14th Conference of the British Dam Society*, Thomas Telford.

Chakib, B. (2013). Numerical Computation of Inception Point Location for Flat-Sloped Stepped Spillway. *International Journal of Hydraulic Engineering*, 2(3), 47-52.

Chamani, M.R. & Rajaratnam, N. (1999). Characteristics of Skimming Flow over Stepped Spillways. *Journal of Hydraulic Engineering,* 125(4), 361-368.

Chanson, H. (1994). Hydraulics of Skimming Flows over Stepped Channels and Spillways*. Journal of Hydraulic Research,* 32(3), 445-460.

Chanson, H. (2002). *Hydraulics of stepped chutes and spillways*. CRC Press, 350.

Chen, Q., Dai, G. & Liu, H. (2002). Volume of Fluid Model for Turbulence Numerical Simulation of Stepped Spillway Overflow. *Journal of Hydraulic Engineering,* 128(7), 683-688.

Cheng, X.J. & Chen, X.W. (2011). Applying Improved Eulerian Model for Simulation of Air-Water Flow in a Hydraulic Jump. *World Environmental and Water Resources Congress 2011: Bearing Knowledge for Sustainability* 3882-3896.

Christodoulou, G.C. (1993). Energy Dissipation on Stepped Spillways. *Journal of Hydraulic Engineering,* 119(5), 644-650.

Dong, Z., Wu, Y. & Zhang, D. (2010). Cavitation Characteristics of Offset-into-Flow and Effect of Aeration. J*ournal of hydraulic research*, 48(1), 74-80.

Frizell, K.W., Renna, F.M. & Matos, J. (2012). Cavitation Potential of Flow on Stepped Spillways. *Journal of Hydraulic Engineering,* 139(6), 630-636.

Hinks, J.L., Mason, P.J. & Claydon, J.R. (2008). Ulley Reservoir and high Velocity Spillway Flows. Ensuring reservoir safety into the future: *Proceedings of the 15th Conference of the British Dam Society,* Thomas Telford Publishing, 227-237.

Hirt, C.W. & Nichols, B.D. (1981). Volume of Fluid (VOF) Method for the Dynamics of Free Boundaries. *Journal of Computational Physics,* 39(1), 201-225.

Ishii, M. & Hibiki, T. (2010). *Thermo-Fluid Dynamics of Two-Phase Flow.* Springer Science & Business Media, 518.

Kositgittiwong, D., Chinnarasri, C. & Julien, P.Y. (2013). Numerical Simulation of Flow Velocity Profiles along a Stepped Spillway. *Proceedings of the Institution of Mechanical Engineers, Part E: Journal of Process Mechanical Engineering*, 227(4), 327-335.

Lopes, P., Leandro, J., Carvalho, R.F. & Bung, D.B. (2017). *Alternating Skimming Flow over a Stepped Spillway.* Environmental Fluid Mechanics, 1-20.

Mason, P.J. & Hinks, J.L. (2008). Security of Stepped Masonry Spillways: Lessons from Ulley Dam. *Dams and Reservoirs,* 18(1), 5-8.

Matos, J., Sánchez, M., Quintela, A. & Dolz, J. (1999). Characteristic Depth and Pressure Profiles in Skimming Flow over Stepped Spillways. *Congress IAHR,* 28.

McGee, R.G. (1988). Prototype Evaluation of Libby Dam Sluiceway Aeration System. *Model-Prototype Correlation of Hydraulic Structures,* ASCE, 138–147.

Rajaratnam, N. (1990). Skimming Flow in Stepped Spillways. *Journal of Hydraulic Engineering,* 116(4), 587-591.

Rice, C.E. & Kadavy, K.C. (1996). Model Study of a Roller Compacted Concrete Stepped Spillway. *Journal of Hydraulic Engineering,* 122(6), 292-297.

Sánchez-Juny, M., Bladé, E. & Dolz, J. (2007). Pressures on a Stepped Spillway. *Journal of Hydraulic Research,* 45(4), 505-511.

Sánchez-Juny, M. S., Pomares, J. & Dolz, J. (2000, March). Pressure Field in Skimming Flow over a Stepped Spillway. *Proceedings of the International Workshop on Hydraulics of Stepped Spillways, Zurich.* AA Balkema, Rotterdam 137-146.

Sorensen, R.M. (1985). Stepped Spillway Hydraulic Model Investigation. *Journal of Hydraulic Engineering,* 111(12), 1461-1472.

Valero, D. & Bung, D.B. (2015, June). Hybrid Investigations of Air Transport Processes in Moderately Sloped Stepped Spillway Flows. *E-Proceedings of the 36th IAHR World Congress,* 28.

Winter, C., Mason, P., Baker, R. & Ferguson, A. (2010). *Guidance for the Design and Maintenance of Stepped Masonry Spillways,* Environment Agency, London, Report SC080015.

Xu, W., Luo, S., Zheng, Q. & Luo, J. (2015). *Experimental Study on Pressure and Aeration Characteristics in Stepped Chute Flows.* Science China Technological Sciences, 58(4), 720-726.

Zhang, G. & Chanson, H. (2016). Hydraulics of the Developing Flow Region of Stepped Spillways. II: Pressure and Velocity Fields. *Journal of Hydraulic Engineering,* 142(7), 04016016.

Zhang, J., Chen, J. & Wang, Y. (2012). Experimental Study on Time-Averaged Pressures in Stepped Spillway. *Journal of Hydraulic Research,* 50(2), 236-240.

THE STUDY ON HYDRAULICS CHARACTERISTICS OF TETRAHEDRON-LIKE PENETRATING FRAME DAM

HONGWEI KUANG [1], JINGTAO ZHENG [2], BO JIANG [3] & FANG YENN TEO [4]

[1,2,3] National Engineering Research Center for Inland Waterway Regulation, China,
[1,2,3] Changjiang Waterway Planning Design and Research Institute, Wuhan 430040, China,
springfly99@163.com
[4] Department of Irrigation and Drainage, Kuala Lumpur 50626, Malaysia

ABSTRACT

The tetrahedron-like penetrating frame dam is built up by the tetrahedron-like penetrating frames. Experiments on flow structures around both permeable and non-permeable dams were carried out in a flume. Through the tests of fixed bed, flow structure around the tetrahedron-like penetrating frame dam was measured. Comparison of that with the solid dam, it is realized that the tetrahedron-like penetrating frame dam could not only reduce flow velocity and promote sand deposition, but also have some ecological benefit. The new structure may provide the support of inland waterway regulation project.

Keywords: Tetrahedron-like penetrating frame dam; waterway; ecological benefit; speed reduction and deposition promotion.

1 INTRODUCTION

Permeable spur dike is a new river regulation building developed from 1970s, and it is used in river waterway regulation and channel revetment. Compared with traditional un-permeable spur dike, the flow structure around the permeable spur dike is very different because dike body has a certain number of permeable rate and water is guided and come from the dike body. Penetrating frame not only has effect of deceleration and deposition promotion, but also has effect of permeability and sand passing through, so it is widely used for beach protection, channel revetment. In 2013, tetrahedron-like penetrating frame dam was introduced into the phase II of the Dongliu waterway regulation project in the lower reach of Changjiang River (Tan. et al., 2012). In this project, tetrahedron-like penetrating frame dam was used for 100 m in the head of 1#, 2# thorn dam body to reduce the flow speed, maintain the dam stability and to promote deposition of the low beach, named tiger beach. It is the first time to use tetrahedron-like penetrating frame dam for regulation project in large river like Changjiang river. The result showed that this structure could reduce the flow velocity and had good regulation effect. But it was not recognized exactly how permeable dam would affect the flow structure, especially comparing with solid dam.

Li et al. (2013) built a penetrating dam by welding steel as dam framework, the dam surface was coated with diameter of 1.5 cm of barbed wire, and screen mesh with different layers, different diameter was filled in the dam to control the dam permeable performance, and permeable rate was tested at last. Li et al. (2013) got a conclusion that: compare with solid dam, penetrating frame dam could make flowing pass from its space in its body and that reduces the flow intensity over the dam, on the other hand, that mixes with the flowing over the dam and destroys all kind of vortex structures. This study carried out experiments on the penetrating frame dam in the flume, flow characteristic was learned and results provided theoretical basis and technical guidance for the penetrating frame dam projects. For analysis, experiments for the penetrating frame dam and solid dam were compared. Different test conditions were set, including small middle and large flow rate in submerged and non-submerged condition.

2 EXPERIMENTAL CONDITION

Experiments were carried out in the flume (34 m×3.2 m×0.5 m, length×width×height, maximum flow rate: 200 l/s). Flow rate in the upstream was controlled and measured by thin rectangular weir. The water supply system for flume is showed in Figure 1. Velocity was got by Acoustic Doppler flow meter. Water level was measured by automatic water level meter.

3 EXPERIMENT SETTING

3.1 Model design

The cross section of the spur dike was trapezoidal. The height of prototype dam was 9 m, top width was 5 m, the upstream slope of dam was 1:1.5, the downstream slope of dam was 1:2, the slope of dam head was 1:5, water depth of dam crest was 3 m. Considering of the section plane size and dam size, and according to the water supply ability and flume width, plane scale was: $\lambda_L = 60$ .The generalized model is designed as normal, plane scale was the same as vertical scale: $\lambda_L = \lambda_H = 60$ .So height of model dam was 15 cm, top width was 8 cm, Slope of dam was not changed. Dam direction was vertical to the flow direction, its length was 1.25 m. Details of dam was shown in Figure2. Solid dam was built by different blocks. For penetrating frame dam, firstly, steel was welded to form the skeleton structure, then tetrahedron-like penetrating frame were filled in the dam body, see Figure 3. The length of permeable frame was 1.7 cm.

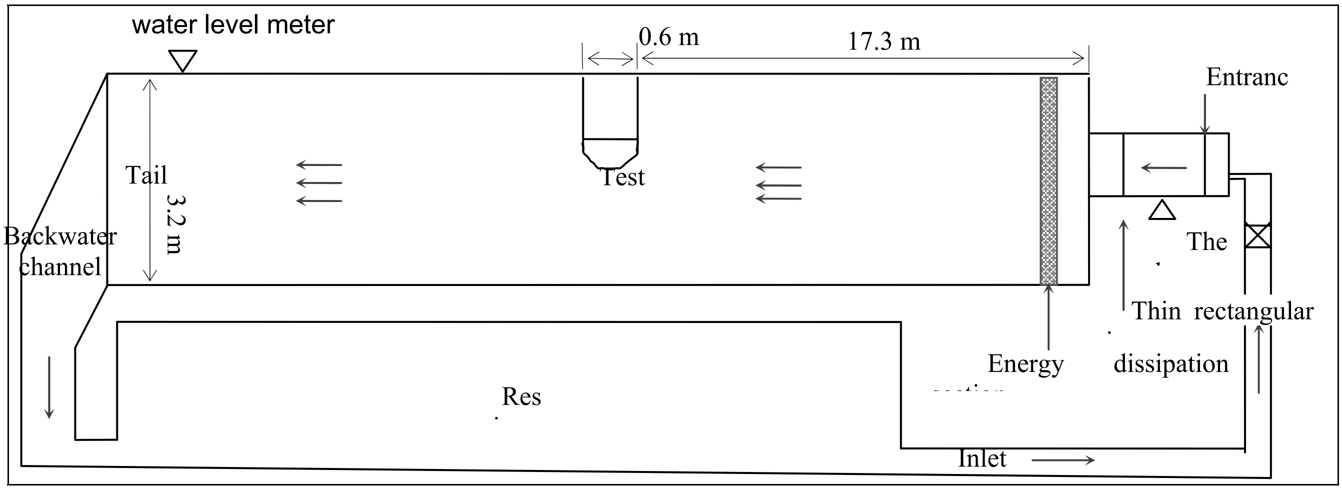

Figure 1. The map for water supply system and the ichnography of flume.

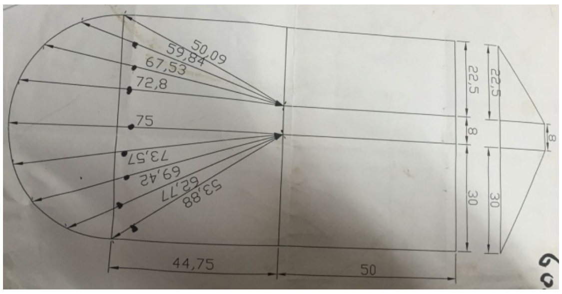

Figure 2. The design of dam.

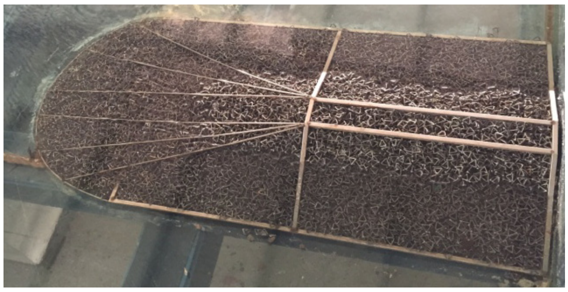

Figure 3. Tetrahedron-like penetrating frame dam.

3.2 Measuring section

The position for the dam in the flume was shown in Figure 4. There were 23 transverse sections for measuring velocity and topography (14.60 m～26.30 m). The details for transverse sections and distribution for measuring point were shown in below. There are also three measuring sections in longitudinal direction. The measuring sections for the flow velocity were 23 cross sections marked in Figure 4 below. Vertical lines were set interval 0.25 m in each cross section to obtain the velocity at depth of 0.6H. The measuring positions for water level were at points of intersections of the longitudinal sections and the cross sections.

3.3 Test conditions

Representative flow rates for the prototype river were 1.5 m/s, 2.0 m/s, 2.5 m/s, the corresponding flow rates for the model were 19.4 cm/s, 25.8 cm/s, 32.3 cm/s. The dam in the experiment was 15 cm, so the depth for submerged and non-submerged conditions were 10 cm and 20 cm corressponsibly. When experiment was carried out, firstly, the model dam was put in the flume, and then flow rate and water depth were set as planned, the different test conditions were shown in Table 1. After water flowing was stable, measuring could be started.

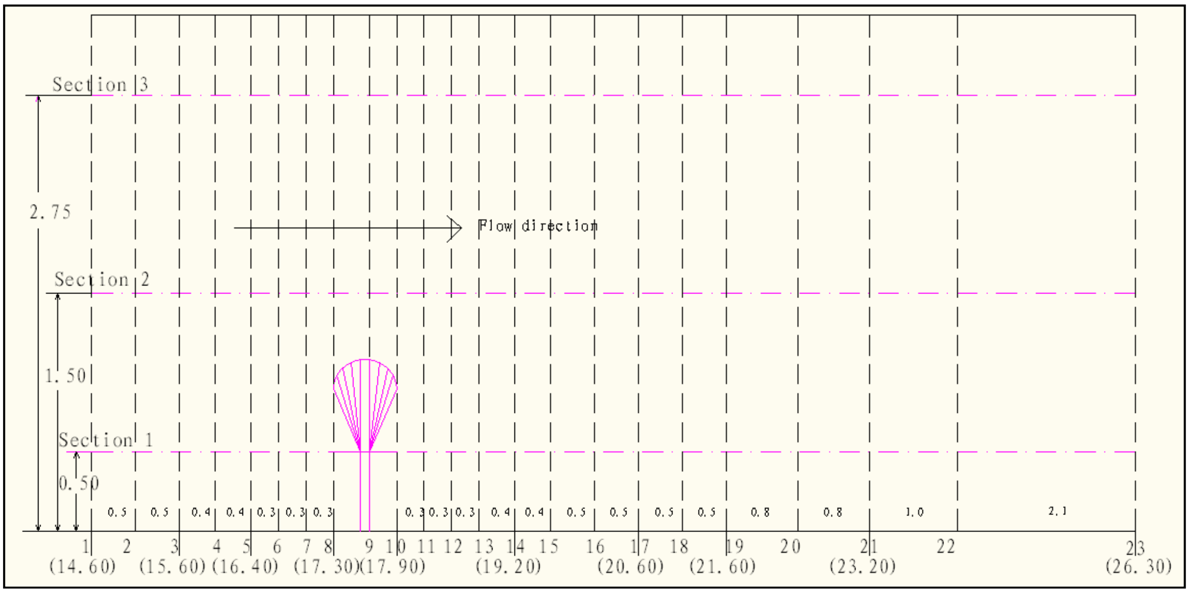

Figure 4. The position of dam and sections for measurement in the flume（m).

Table 1. Different test condition for fixed bed experiment.

Test NO for penetrating frame dam	Test NO for solid dam	Flow rate（l/s）	Average velocity（cm/s）	Depth（cm）
K1	S1	62	19.4	10
K2	S2	83	25.8	10
K3	S3	103	32.3	10
K4	S4	124	19.4	20
K5	S5	165	25.8	20
K6	S6	207	32.3	20

4 EXPERIMENTAL RESULTS

4.1 The water surface profile for penetrating frame dam

For penetrating frame dam, there were six test conditions (K1～K6) as shown in Table 1.Solid dam only had two conditions: S2 and S5. Measurement results of water surface profile for the penetrating frame dam could be seen from Figure 5. In general, in three non-submerged conditions, water level decreased significantly, especially in the area near the model dam head, penetrating frame dame project was the main reason. As water flew to the downstream, influence of model dam on flowing was gradually weakened, after 4 m downstream of the dam, water level tended to be gentle. Before 1 m upstream of the dam, water level was not affected by the model dam. Under submerged condition, water level fluctuation was large, in this way, measurement accuracy was not high and it was not discussed here.

For non-submerged conditions, the water level for three different flow rates (K1～K3) were different, the main performance was as follows: the greater the flow rate and velocity, the influence of penetrating frame dam on water level was more significant. In K1 condition, the water level difference between upstream and downstream on dam head was 3 mm, the influence distance was 4 m; In K2 condition, the water level difference on dam head was 6 mm, the influence distance was 5 m; in K3 condition, the water level difference was nearly 10 mm, the influence distance was 6 m. For three submerged conditions, the influence of penetrating frame dam on water level reduction was not obvious and with the increase of flow rate and velocity, influence of that on water level decrease was lower. In K4 condition, the water level difference on dam head was 4 mm; in K5 condition, the water level difference on dam head was 2 mm; in K6 condition, because of the water level fluctuation, water level difference was not obvious.


K1

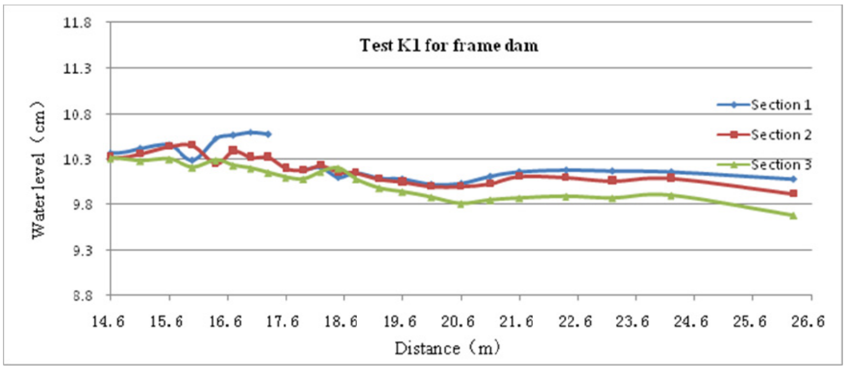
Test K1 for frame dam
Water level (cm)
11.8
11.3
10.8
10.3
9.8
9.3
8.8
14.6 15.6 16.6 17.6 18.6 19.6 20.6 21.6 22.6 23.6 24.6 25.6 26.6
Distance (m)
Section 1
Section 2
Section 3

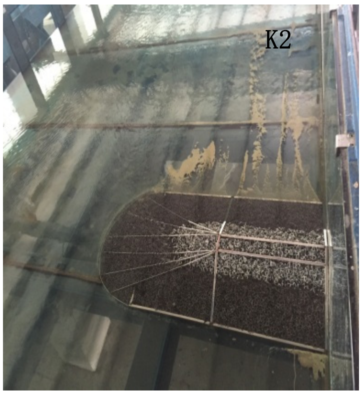
K2

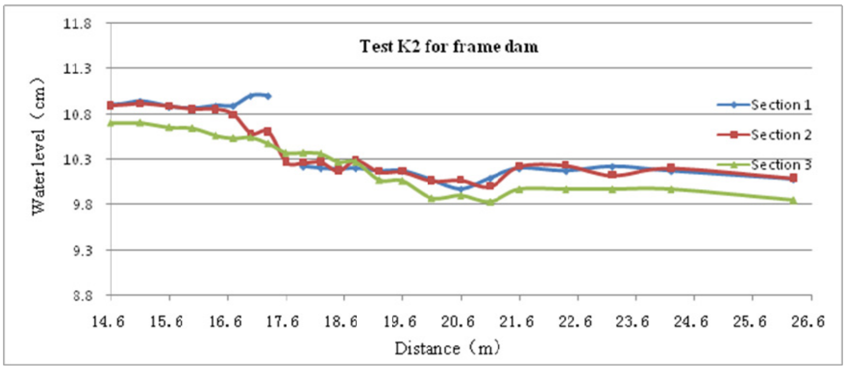
Test K2 for frame dam
Water level (cm)
11.8
11.3
10.8
10.3
9.8
9.3
8.8
14.6 15.6 16.6 17.6 18.6 19.6 20.6 21.6 22.6 23.6 24.6 25.6 26.6
Distance (m)
Section 1
Section 2
Section 3

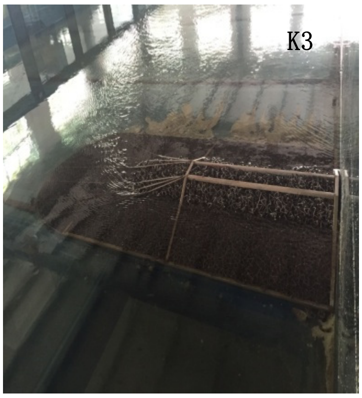
K3

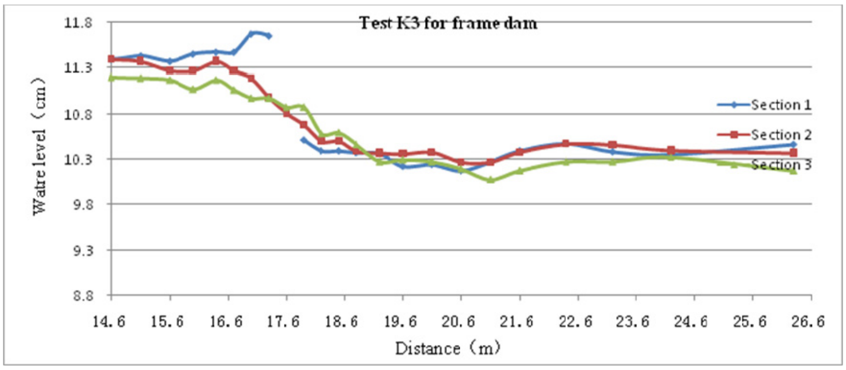
Test K3 for frame dam
Water level (cm)
11.8
11.3
10.8
10.3
9.8
9.3
8.8
14.6 15.6 16.6 17.6 18.6 19.6 20.6 21.6 22.6 23.6 24.6 25.6 26.6
Distance (m)
Section 1
Section 2
Section 3

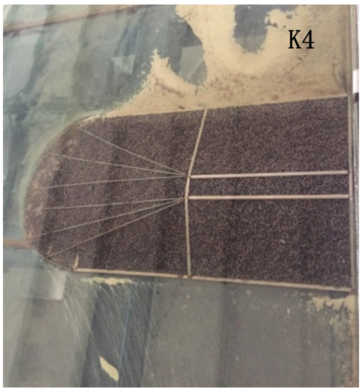
K4

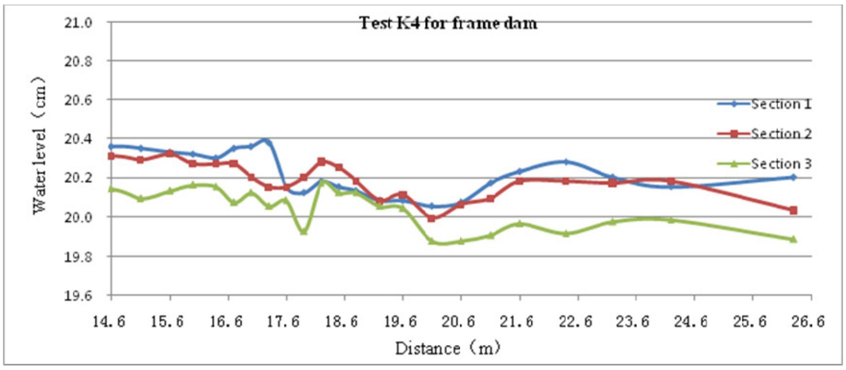
Test K4 for frame dam
Water level (cm)
21.0
20.8
20.6
20.4
20.2
20.0
19.8
19.6
14.6 15.6 16.6 17.6 18.6 19.6 20.6 21.6 22.6 23.6 24.6 25.6 26.6
Distance (m)
Section 1
Section 2
Section 3

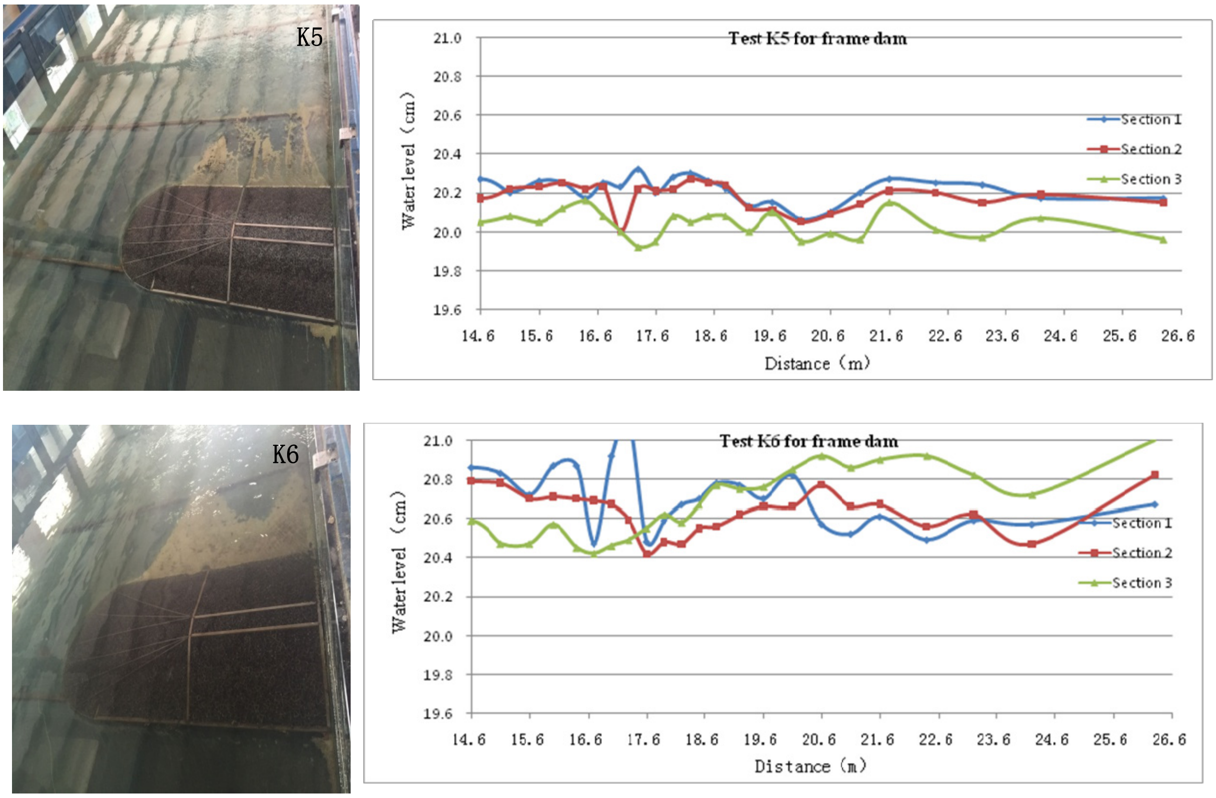

Figure 5. The water surface profile for penetrating frame dam (K1～K6).

4.2 Comparison of water surface profile

To compare the water resisting effect of penetrating frame dam, this study also carried out test with solid dam and had measurement. From the water profile measuring on solid dam (Figure 6), the water resisting effect by solid dam was more obvious. Under non-submerged conditions of S2 test, water level difference between upstream and downstream on dam head was 15 mm, the influence distance was 6 m. This effect on water level difference was far greater than that of K2 penetrating frame dam, S2 water level difference was 2 times K2 water level difference. It was proved that water resisting effect of penetrating frame dam was weaker than that of solid dam, main reason was water permeability of frame dam. Under submerged conditions of S5 test, water level data was fluctuated greatly by the point gauge measurement, which could not display the relevant law better. Compare with penetrating frame dam K5 in the same condition, water level fluctuation by K5 was small. And this showed that the interference of frame dam to water flow is less than that of solid dam. Pictures in K2 test also showed wave fluctuation produced by penetrating frame dam was less than that of solid dam in S2.

4.3 Comparison of flow

Because current meter was not set up in right position, there was about 5^0～7^0 difference between measurement and actual velocity direction, the direction turned to left. This deviation was preserved when processing the data. From the measurement of average velocity for two different types of dam (see K2 and S2 in Figure 7), decrease of velocity near the dam on the right side of flume was obvious, and velocity of area on the opposite side of dam increased, especially velocity near the dam head reached the maximum value in that cross section. Along with water flew to the downstream, influence of dike on flow gradually weakened, velocity gradually recovered from the area on the opposite side of dam to the cover of dam in the downstream. Because area influenced by dike was big, the influence range of velocity behind dike was much larger than that of affected area before dike. The flow velocity gradually became uniform behind dike, but it did not recover fully behind 0.60 m of dike. The change of flow velocity under non-submerged condition, penetrating frame dam and solid dam had some different features as below:

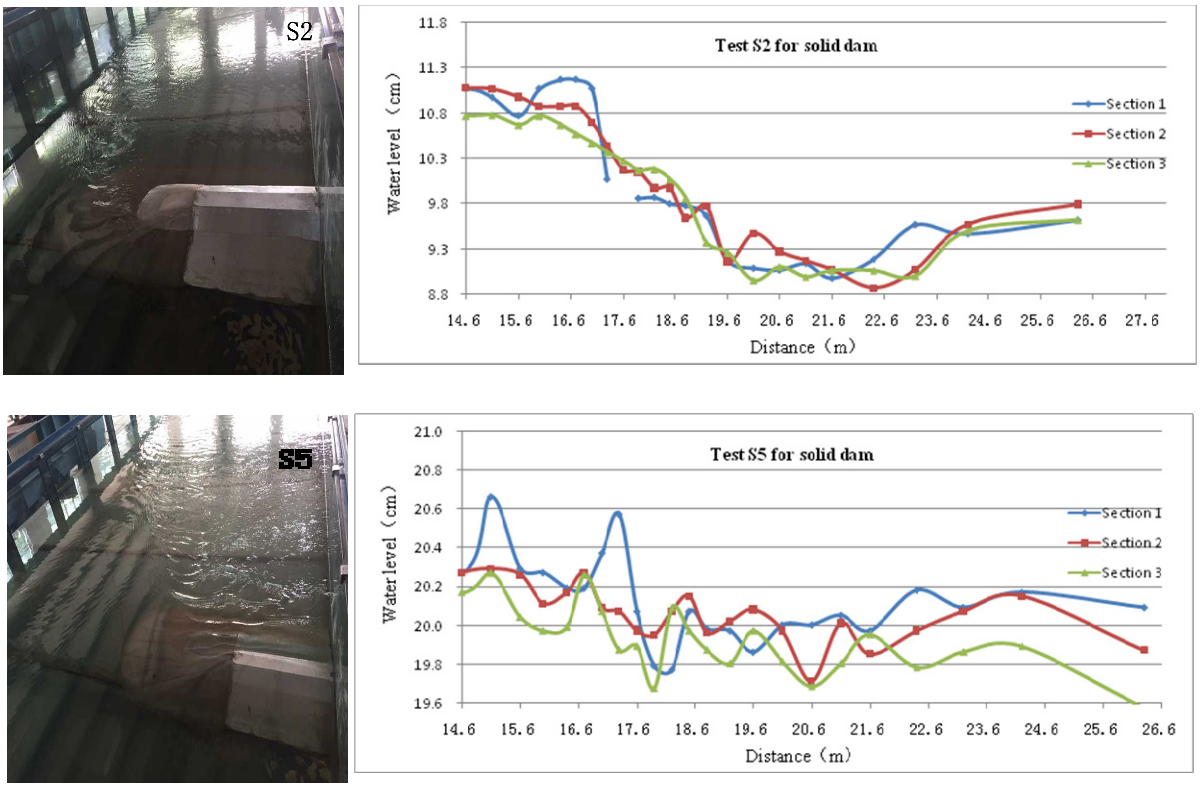

Figure 6. The water surface profile for solid dam (S2～S5).

The velocity behind penetrating frame dam reduced a lot, but its direction remained unchanged as normal; for solid dam, there was swirling flow near the dike head behind the dike (#12～#15), then down (#16～#22), flow velocity increased gradually with direction changing. Velocity behind penetrating frame dam remained unchanged in a certain range, and its distribution was uniform; velocity behind solid dam was smaller than that of frame dam. Then with distance increased, flow velocity increased gradually with direction changing. From section of #17, velocity for solid dam was larger than that of frame dam. Velocity distribution behind the frame dam was affected by the length of frame dam, and the length of section with small velocity was 0.95 m; velocity behind solid dam recovered gradually, that means that the length of section with small velocity reduced gradually, and velocity on the left of flume restored and extended to the right. On the left of flume without dike, velocity by solid dam was larger than that of frame dam. Take section behind dike of 0.60 m as example (#12), at 2.0 m in cross direction, velocity by solid dam was about 41.36 cm/s, it was bigger than that by frame dam, which was about 37.87 cm/s.

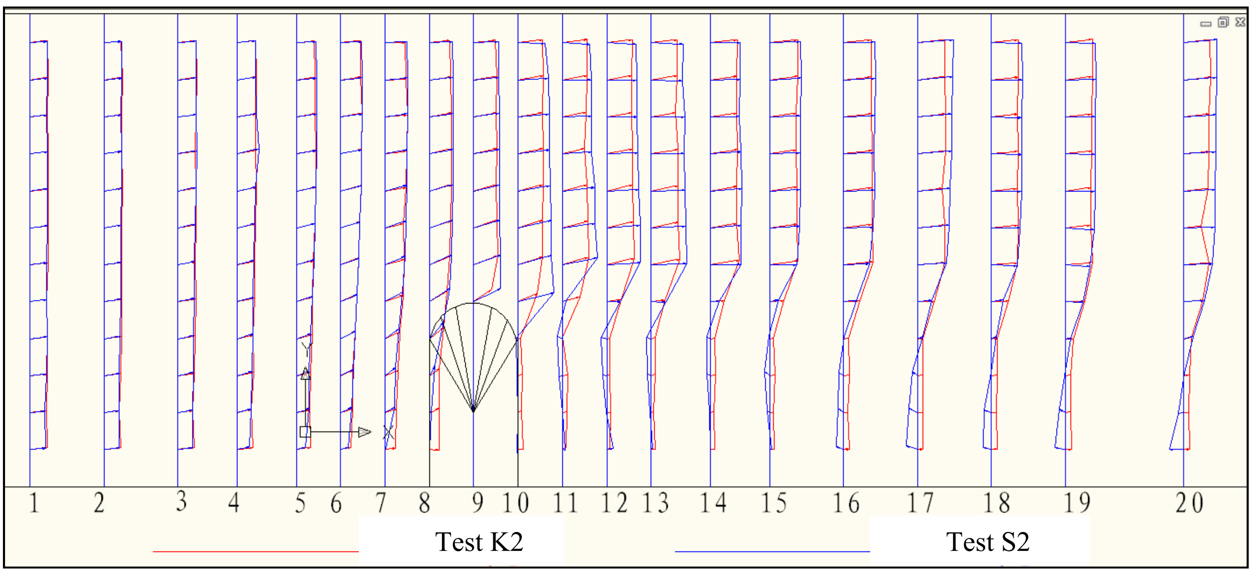

Figure 7. Flow field contrast diagram for K2 and S2 under non-submerged condition.

From the comparison of average velocity at 0.6H for penetrating frame dam (K5) and solid dam (S5) under submerged condition (see K5 and S5 in Figure 8): velocity near the dike on the right side of flume and in the upstream of dike did not change obviously, and there was no obvious change for the velocity in the downstream of dike. In the left side of flume, velocity increased a little, and reached maximum near the dike head. Frame dam and solid dam showed good consistency at velocity in the left side of flume. To the change of flow velocity under submerged condition, penetrating frame dam and solid dam had some different features as follow:

In the left of flume, the deflection effect of solid dam on water flow was greater than that of frame dam, the difference of deflection angle was about 7^0。On upstream section before the project (#8), velocity of solid dam was smaller than that of frame dam, especially at the dike position, permeability of frame dam was the main reason and flow did not meet obstruction. There was still swirling flow in a distance behind the solid dam (from #10 to #13), reason was flowing over the dam. Frame dam did not have swirling flow and velocity behind frame dike was greater than that of solid dam. The velocity recovering for the frame dam was showed that velocity increased with the flow extending downstream; for solid dam, the velocity on the right side of flume increased.

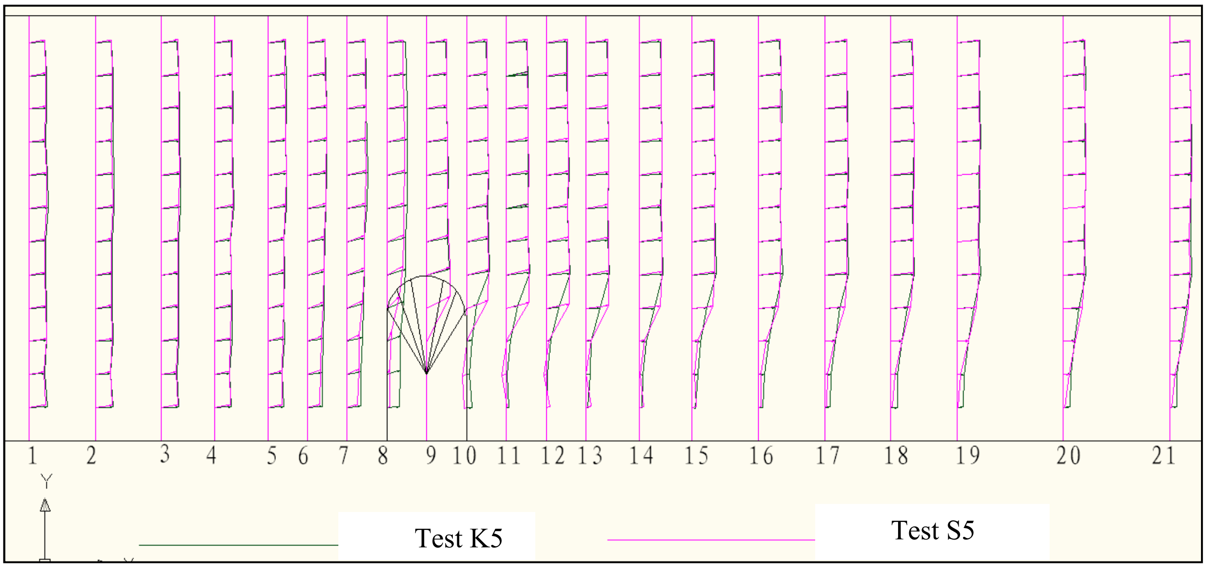

Figure 8. Flow field contrast diagram for K5 and S5 under submerged condition.

5 DISCUSSION

Tetrahedron-like penetrating frame is similar with trapezoidal artificial reef in material, structure, arrangement and combination, and it also has effect of ecological restoration and protection of fishery resources, just like artificial reef. Guo et al. (2015) made a study for beach protection project by permeable frame in the middle reach of Changjiang River. According to fixing-point acoustic monitoring and fish collection, it showed that tetrahedron-like penetrating frame group had aggregation effect on fish, especially when frames were under submerged condition, the number of fish was more than that under half submerged condition. Main reason was that habitat created by submerged condition was relatively stable. Most of penetrating frame dam was under water and could have stable habitat, it was benefit for aggregation of aquatic organisms, and the role of artificial reefs should be more obvious.

The artificial reef effect of the framework group is mainly caused by the flow field generated by the flow through the frame group. Wang et al. (2009) got a result that the various flow patterns formed by stacked reef model are the largest, followed by trapezoidal reef. And penetrating frame is similar with trapezoidal reef that is the reason for framework group having aggregation effect on fish. At the same time, the slow flow by penetrating frame was beneficial for plankton, benthos and algae staying or absorbing on the structure, then attracting fish and their predators (Lu et al., 2011). From these studies, penetrating frame dam could play a role as artificial reef, its space in the structure provided shelter for the aquatic organisms such as fish, and it had strong aggregation effect on fish.

Study showed that the average velocity for fish egg floating is about 0.25 m/s (Tang et al., 1989). The still water area by solid dam could make fish egg sink. Penetrating frame dam is permeable for water and sand. Fish egg would not sink but pass through its structure, so as to ensure the normal hatching eggs. At the same time, the flowing water can increase oxygen content (DO) of water that will be conductive to the incubation of fish eggs and fish growth.

6 CONCLUSIONS

From experiments, it is realized that the interference of penetrating frame dam to water surface profile and velocity was smaller than that of solid dam, and the effect of flowing concentrating for solid dam was greater than that of frame dam. At the same time, due to the frame dam body's permeability, swirling flow was weaker, it is better for the smooth of flow. Penetrating frame dam could play a role as artificial reef, its space in the structure provides shelter for the aquatic organisms such as fish, and it had strong aggregation effect on fish.

ACKNOWLEDGMENTS

The research reported herein is funded by Changjiang Waterway Planning Design, Research and Institute (2013-00-189).

REFERENCES

Guo, J., Wang, K., Duan, X.B., Chen, D.Q., Fang, D.M. & Liu, S.P. (2015). Water Acoustic Detection Study on the Influence of Channel Regulation Framework on Fish Cluster. *Journal of Hydro-ecology*, 36(5), 29-35.

Li, M., Huang, C.T. (2013). *The Study of Structure Type for Submerged Dike in Zhougongdi Waterway. Wuhan,* Changjiang Waterway Planning Design and Research Institute, 2013.

Lu, Y.J., Lu, Y. (2011). *A Report on the Process of Water and Sediment and the Ecological Effect of River by Waterway Regulation Projects*, Nanjing Hydraulic Research Institute.

Tang, M.Y., Huang, D.L., Huang, L.Z., Xiang, F. & Yin, W.Q. (1989). The Test of Hydraulic Characteristics for Eggs of Grass Carp, Black Carp, Silver Carp, Bighead, and their Egg Hatching Condition Preliminary Forecast in Three Gorges Reservoir Area. *Reservoir Fisheries*, 4, 26-30.

Tan, L.W. & Lei, G.P. (2012). The Preliminary Design for the Phase II of Dongliu Waterway Regulation Project in the Lower Reach of Changjiang River. Wuhan: Changjiang Waterway Planning Design and Research Institute.

Wang, L., Tang, Y.L., Huang, H.L., Jiang, S.Y. & Li, L.Z. (2009) Preliminary Analysis on the Selection of Artificial Reefs. *Marine Fisheries*, 31(3),308-315. (In Chinese)

Proceedings of the 37th IAHR World Congress
August 13 – 18, 2017, Kuala Lumpur, Malaysia

NUMERICAL SIMULATION OF DIKE DEFORMATION DUE TO SEEPAGE FLOWS

SHINICHIRO ONDA[(1)], YOSUKE HIGO[(2)] & TAKASHI HOSODA[(3)]

[(1,2,3)] Department of Urban Management, Kyoto University, Kyoto, Japan
onda.shinichiro.2e@kyoto-u.ac.jp; higo.yohsuke.5z@kyoto-u.ac.jp; hosoda.takashi.4w@kyoto-u.ac.jp

ABSTRACT

Dike failures, which occurred during floods, is due to seepage flows and soil deformation. In this study, a numerical model to predict a dike deformation process due to seepage flows was developed, by coupling a three-dimensional flow model and a soil deformation model based on elasto-plastic approach. The model was applied to a hydraulic experiment to validate the model performance. Soil deformation on the backside due to seepage flows is observed and this model can predict the dike deformation process due to seepage flows reasonably.

Keywords: Numerical simulation; dike deformation; seepage flows; three-dimensional open channel flow model; Generalized Interpolation Material Point Method.

1 INTRODUCTION

Dike failures could cause serious damages in landside area. Therefore, for risk management, it is of great importance to understand the mechanism of dike failure and predict its breaching process accurately. The mechanism of dike failures is mainly explained by the surface erosion of dike due to overtopping flows and soil deformation with reduction of effective stresses due to seepage flows. Therefore, in order to predict flow conditions and sediment transport around a dike accurately, the numerical model includes temporal change of water surface, seepage flow through the dike body and bed deformation process during the dike breaching.

In the previous studies, a number of hydraulic experiments have been carried out to elucidate the mechanism of dike failures. Coleman et al. (2002) carried out embankment breach tests and explained that erosion evolves from primarily vertical to predominantly lateral. Schmocker and Hager (2009) investigated dike-breaching processes under various geometrical and hydraulic conditions and discussed test repeatability, sidewall effect and scale effects.

Several computational models (Kakinuma and Shimizu, 2014; Mizutani et al., 2013; Onda et al., 2014, 2016; Pontillo et al., 2010; Volz et al., 2012) have been proposed to simulate dike erosion processes due to overtopping flows. Kakinuma and Shimizu (2014) used a two-dimensional shallow water equation and an equilibrium sediment transport model. Mizutani et al. (2013) applied a two-dimensional depth averaged flow model with effects of infiltration and a non-equilibrium sediment transport model. Onda et al. (2014; 2016) developed a three-dimensional flow model of simultaneous overflow and seepage through the embankment, and simulate dike breaching process due to overtopping flows, by incorporating a non-equilibrium sediment transport model. On the other hand, to simulate dike deformation due to seepage flows, finite element analysis is applied, using a elasto-viscoplastic theory (Oka et al., 2010), whereas it is not applicable to simulate large soil deformation.

In this study, to simulate dike failure due to seepage flows, a numerical model is developed by coupling a three-dimensional open channel flow model and a soil deformation model based on elasto-plastic approach. A basic equation is discretized by using Generalized Interpolation Material Point method (Bardenhagen and Kober, 2004), which is one of the particle in cell method. The developed model is applied to a hydraulic experiment of dike failure, and the applicability of the model is verified.

2 NUMERICAL METHOD

2.1 Flow model

To simulate dike deformation process due to seepage flows, a three-dimensional open channel flow model and a soil deformation model based on elasto-plastic approach are coupled. In the flow model, to consider calculating water surface variations in unsteady flows, a density function method is applied. In addition, by using the concept of volume fraction in the solid phase based on a porous media approach, overtopping and seepage flows around an embankment are simultaneously simulated. The basic equations (Onda et al., 2014) are described in the following:

  / ISSN 1562-6865 (Online) - ISSN 1063-7710 (Print)

$$\frac{\partial(1-c)\Phi}{\partial t}+\frac{\partial(1-c)u_j\Phi}{\partial x_j}=0 \qquad [1]$$

$$\begin{aligned}
&\frac{\partial}{\partial t}\{(1-c)u_i\}+\frac{\partial}{\partial x_j}\{(1-c)u_iu_j\}\\
&=(1-c)g_i-\frac{(1-c)}{\rho}\frac{\partial p}{\partial x_i}+\frac{\partial}{\partial x_j}\left\{-(1-c)\overline{u_i'u_j'}\right\}\\
&+\nu\frac{\partial}{\partial x_j}\left\{(1-c)\frac{\partial u_i}{\partial x_j}\right\}-\frac{\nu(1-c)^2u_i}{K_d}
\end{aligned} \qquad [2a]$$

$$\rho=\Phi\rho_{liq}+(1-\Phi)\rho_{gas} \qquad [2b]$$

$$\mu=\Phi\mu_{liq}+(1-\Phi)\mu_{gas} \qquad [2c]$$

Where, x_i = Cartesian coordinate; t = time; u_i = velocity vectors in the x_i directions; Φ = density function; c = volume fraction in the solid phase; p = pressure; ρ = density of fluid; ρ_{liq} = density of water; ρ_{gas} = density of gas; μ = viscosity of fluid; μ_{liq} = viscosity of water; μ_{gas} = viscosity of gas; ν = kinematic viscosity of fluid; g_i = gravitational acceleration vector; $-\overline{u_i'u_j'}$ = Reynolds stress; K_d = intrinsic permeability. The subscript indexes j and I denote the value of 1, 2 and 3 indicating the x, y and z directions, respectively. The last term in equation (2a) is resistance force and Darcy's law is applied for simplicity in this study.

The second order nonlinear *k*-ε model is used for turbulence model (Kimura and Hosoda, 2003) as

$$-\overline{u_i'u_j'}=\nu_tS_{ij}-\frac{2}{3}k\delta_{ij}-\frac{k}{\varepsilon}\nu_t\sum_{\beta=1}^{3}C_\beta\left(S_{\beta ij}-\frac{1}{3}S_{\beta\alpha\alpha}\delta_{ij}\right) \qquad [3]$$

$$\nu_t=C_\mu\frac{k^2}{\varepsilon} \qquad [4]$$

$$\begin{aligned}
&\frac{\partial(1-c)k}{\partial t}+\frac{\partial(1-c)ku_j}{\partial x_j}=-(1-c)\overline{u_i'u_j'}\frac{\partial u_i}{\partial x_j}\\
&-(1-c)\varepsilon+\frac{\partial}{\partial x_j}\left\{(1-c)\left(\frac{\nu_t}{\sigma_k}+\nu\right)\frac{\partial k}{\partial x_j}\right\}
\end{aligned} \qquad [5a]$$

$$\begin{aligned}
&\frac{\partial(1-c)\varepsilon}{\partial t}+\frac{\partial(1-c)\varepsilon u_j}{\partial x_j}=-(1-c)C_{\varepsilon1}\frac{\varepsilon}{k}\overline{u_i'u_j'}\frac{\partial u_i}{\partial x_j}\\
&-(1-c)C_{\varepsilon2}\frac{\varepsilon^2}{k}+\frac{\partial}{\partial x_j}\left\{(1-c)\left(\frac{\nu_t}{\sigma_\varepsilon}+\nu\right)\frac{\partial\varepsilon}{\partial x_j}\right\}
\end{aligned} \qquad [5b]$$

$$S_{ij}=\frac{\partial u_i}{\partial x_j}+\frac{\partial u_j}{\partial x_i} \qquad [6a]$$

$$S_{1ij}=\frac{\partial u_i}{\partial x_r}\frac{\partial u_j}{\partial x_r} \qquad [6b]$$

$$S_{2ij}=\frac{1}{2}\left(\frac{\partial u_r}{\partial x_i}\frac{\partial u_j}{\partial x_r}+\frac{\partial u_r}{\partial x_j}\frac{\partial u_i}{\partial x_r}\right) \qquad [6c]$$

$$S_{3ij}=\frac{\partial u_r}{\partial x_i}\frac{\partial u_r}{\partial x_j} \qquad [6d]$$

Where, k = turbulent kinetic energy, ε = dissipation rate, ν_t = eddy viscosity coefficient. The model coefficient C_μ is a function of strain and rotation parameters (S and Ω) and the details of model constants are described in Kimura and Hosoda (2003). The applicability of this model is already examined, by simulating the flow around a square cylinder (Kimura and Hosoda, 2003) and a spur dike (Nagata et al., 2005).

2.2 Soil deformation model

To simulate large deformation of soil, an elasto-plastic constitutive model (Oka et al., 1999) is used, and Generalized Interpolation Material Point (GIMP) method (Bardenhagen and Kober, 2004) is applied for discretization of basic equation. For formulating the constitutive model, the following assumption is used:

- A strain increment tensor is the sum of increments of elastic and plastic strain tensors;
- An increment of plastic strain tensor is calculated by generalized plastic flow rule;
- An over-consolidation boundary surface is introduced;
- A nonlinear kinematic hardening rule is used.

The details of the model are explained in the reference (Oka et al., 1999) and, the relation between skeleton stress increment tensor and strain increment tensor is derived by using the above constitutive model.

The equation of motion for whole mixture is described in Eq. [7a], and a u-p formulation is adopted in which a displacement of soil skeleton (u) and a pore water pressure (p) are used for unknown variables. Substituting the pore water pressure obtained from flow model, the displacement in the solid phase is solved.

$$\rho_m \dot{v}_i^s = \frac{\partial \sigma_{ij}}{\partial x_j} + \rho_m b_i \qquad [7a]$$

$$\sigma'_{ij} = \sigma_{ij} + P^F \delta_{ij} \qquad [7b]$$

$$P^F = S_r p^f + (1 - S_r) p^a \qquad [7c]$$

Where, ρ_m = density of whole mixture, v_i^s = velocity vector in solid phase, b_i = body force vector, σ'_{ij} = skeleton stress tensor, σ_{ij} = total stress tensor, P^F = averaged fluid pressure, p_f = pore water pressure, p_a = pore air pressure (p_a is assumed to be 0 in this study).

The equation of motion in Eq. [7a] is discretized, using the GIMP method. In this method, a continuum body is divided into a finite number of sub-regions consisting of material points. The variables in sub-regions for soil deformation are defined at each material point, whereas they are mapped to the computational grids for solving basic equations. Then, by using the weighting function (S_{IP}) and its gradient (∇S_{IP}) which means the relationship between a material point and a grid point, the governing equation yields

$$\dot{P}_I = \int_{\partial \Omega_r} \tau \cdot S_I(x) dS - \sum_p \sigma_p \nabla S_{Ip} V_p + m_I b \qquad [8]$$

$$m_I = \sum_p m_p S_{Ip} \qquad [9a]$$

$$P_I = \sum_p P_p S_{Ip} \qquad [9b]$$

$$S_{Ip} = \frac{1}{V_p} \int_{\Omega_p \cap \Omega} \chi_p(x) \cdot S_I(x) dx \qquad [10a]$$

$$\nabla S_{Ip} = \frac{1}{V_p} \int_{\Omega_p \cap \Omega} \chi_p(x) \cdot \nabla S_I(x) dx \qquad [10b]$$

$$S_I = \begin{cases} 0 & x_p - x_I \le -L - l_p \\ \frac{(L+l_p+(x_p-x_I))^2}{4Ll_p} & -L - l_p < x_p - x_I \le -L + l_p \\ 1+\frac{x_p - x_I}{L} & -L + l_p < x_p - x_I \le -l_p \\ 1+\frac{(x_p-x_I)^2+l_p^2}{2Ll_p} & -l_p < x_p - x_I \le l_p \\ 1-\frac{x_p - x_I}{L} & l_p < x_p - x_I \le L - l_p \\ \frac{(L+l_p-(x_p-x_I))^2}{4Ll_p} & L - l_p < x_p - x_I \le L + l_p \\ 0 & L + l_p < x_p - x_I \end{cases} \qquad [10c]$$

Where, m_I, P_I = mass and momentum of particle defined at a grid point, m_p, P_p = mass and momentum of each particle, V_p = volume of particle, □ = prescribed traction vector, L = grid size, $2l_p$ = control domain of particle, x_p = positon of particle, x_I = position of grid point.

Substituting Eq. [7b] into Eq. [8] leads to

$$\dot{P}_I = \tau_I - \sum_{p=1}^{N_p} \sigma'_p(x_p) \nabla S_{Ip} V_p + S_r \{K_v\}_I \, p_E^f + m_I b \qquad [11]$$

$$\{K_v\}_I = \int_\Omega \{B_v\}_I d\Omega \qquad [12a]$$

$$\{B_v\}_I^T = \left\{ \frac{\partial S_{1p}}{\partial x}, \frac{\partial S_{1p}}{\partial y}, \frac{\partial S_{2p}}{\partial x}, \frac{\partial S_{2p}}{\partial y}, \ldots, \frac{\partial S_{Ip}}{\partial x}, \frac{\partial S_{Ip}}{\partial y} \right\} \qquad [12b]$$

Where, N_p = number of particle.
Considering an initial state in Eq. [11], the momentum increment (□P_I) is derived in the following:

$$\begin{aligned} \Delta P_I = & -\sum_{p=1}^{N_p} V_p \left\{ \sigma'_p(x_p) - \sigma'_p(x_p)_{|t=0} \right\} \nabla S_{Ip} \Delta t + \tau_I \Delta t \\ & + S_r \{K_v\}_I \left\{ p_E^f - p^f_{E|t=0} \right\} \Delta t \end{aligned} \qquad [13]$$

2.3 Coupling of water flow and soil deformation models

Here, coupling algorism of water flow and soil deformation models is described. The values at (k+1) step are assumed to be solved, by using the known values at (k) step. The procedure is shown as follows:

i. A mass (m_I^k) and a momentum (P_I^k) of particles is calculated, using Eq. [9a] and [9b];
ii. A pore water pressure (p_E^f) is obtained from open channel flow model;
iii. Substituting pore water pressure into Eq. [13], a momentum increment (□P_I^L) is calculated;
iv. Using □P_I^L and P_I^L (= P_I^k +□P_I^L), a velocity of particles (V_p^{k+1}) and a position (X_p^{k+1}) are updated in Eq. [14a] and [14b];
v. Using a velocity of particle (V_p^{k+1}), a velocity defined at computational grid (v_I^{k+1}) and an increment of strain tensor (□□$_p^{k+1}$) is obtained in Eq. [15a] and [15b];
vi. Based on constitutive law, an increment of stress (□□$_p^{k+1}$) is calculated and updated in Eq. [16];
vii. A volumetric strain, void ratio and volume fraction in the solid phase is obtained;
viii. A process is going back to step i.

$$V_p^{k+1} = V_p^k + \sum_{I=1}^{N_n} \frac{1}{m_I^k} \Delta P_I^L S_{Ip}^k \qquad [14a]$$

$$X_p^{k+1} = X_p^k + \Delta t \sum_{I=1}^{N_n} \frac{1}{m_I^k} P_I^L S_{Ip}^k \qquad [14b]$$

$$m_I^k v_I^L = \sum_{I=1}^{N_n} M_p V_p^{k+1} S_{Ip}^k \qquad [15a]$$

$$\Delta \varepsilon_p^{k+1} = \frac{\Delta t}{2} \sum_{I=1}^{N_n} \left\{ \nabla S_{Ip} v_I^L + \left(\nabla S_{Ip} v_I^L \right)^T \right\} \qquad [15b]$$

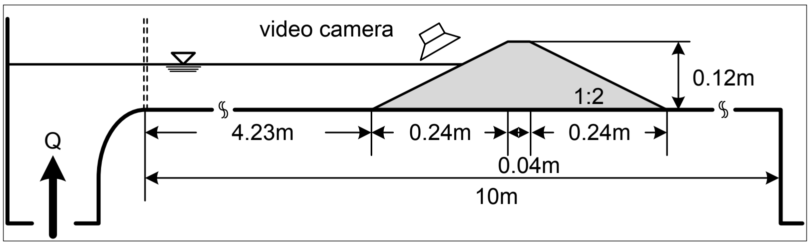

Figure 1. Schematic diagram of hydraulic experiment

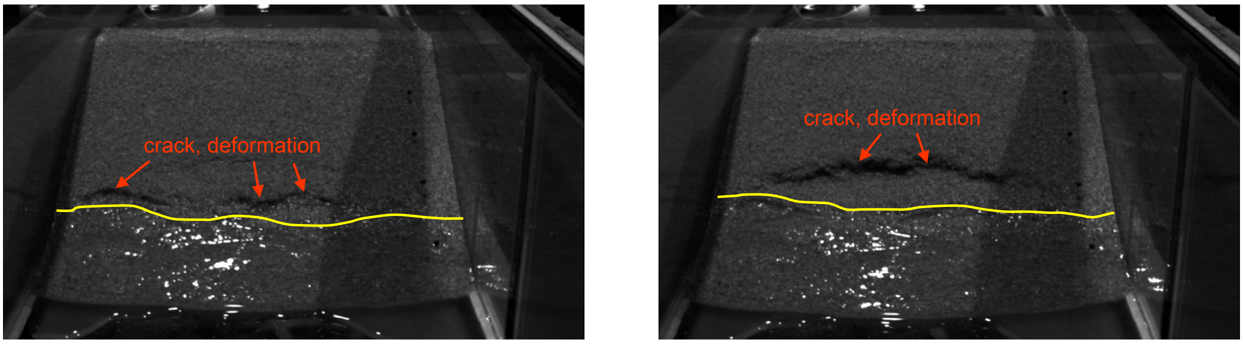

(a) t = 303 (s) (b) t = 305 (s)

Figure 2. Temporal change of dike failure process

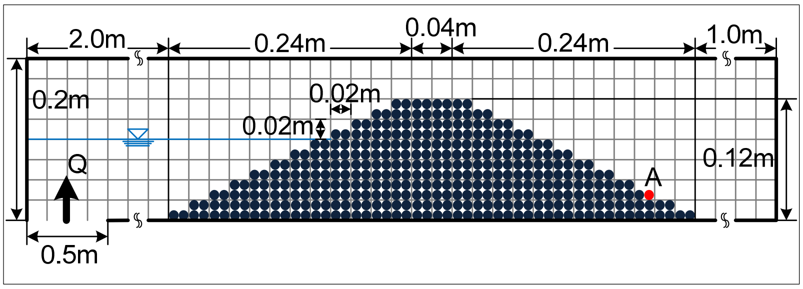

Figure 3. Computational flow domain

$$\sigma_p^{k+1} = \sigma_p^k + \Delta\sigma_p^{k+1} \qquad [16]$$

3 APPLICATION OF NUMERICAL MODEL

3.1 Hydraulic experiment

A hydraulic experiment of dike deformation due to seepage flows is carried out. The schematic diagram is shown in Figure 1 and the embankment is made of dry material without compaction, with crest height, width and slope gradient of 0.12 (m), 0.04 (m) and 1:2, respectively. The diameter of sand is 0.53 (mm) and the inflow discharge is 0.0008 (m^3/s). By using two high speed cameras, the dike failure process is recorded from the upper and lateral sides. The time that the water reaches the front toe of dike is assumed to be t = 0 (s).

From the movie, it is observed that the water reaches to the toe of backside at t = 287 (s) and the top of back slope at t = 304 (s). Figure 2 shows the dike failure process and the yellow line presents the water level. The back slope is cracked and deformed with rise of water level, as shown in Figure 2.

3.2 Results and discussion

The computational flow domain is presented in Figure 3, and the embankment is set at x = 2.0 (m) from the upstream end. The computational mesh in the streamwise, transversal and vertical direction consists of 178, 10 and 12 elements, respectively, with □x, □y and □z set to 0.02, 0.03 and 0.02 (m). The time step □t is adopted as 0.0002 (s). The water depth at upstream side is initially given for 0.02 (m), and hydraulic conductivity is assumed to be 0.02 (m/s). The initial stress in embankment is obtained by using LIQCA 2D, and a maximum of four particles are distributed in each cell based on the shape of dike, as seen in Figure 3. It should be noted that the effect of suction and the relationship between hydraulic conductivity and water saturation are not included in the numerical model. To reduce computational time, the spatial scale from water inlet to front toe of dike in computational flow domain is not same with the experiment, and consequently flow characteristics and its time scale is thought to be different between the experiment and the numerical simulation. In this study, the numerical results are qualitatively compared.

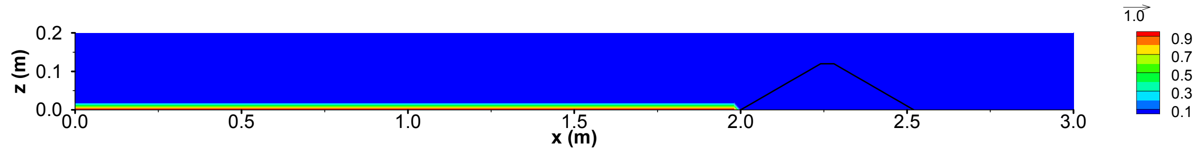

(a) t = 0 (s)

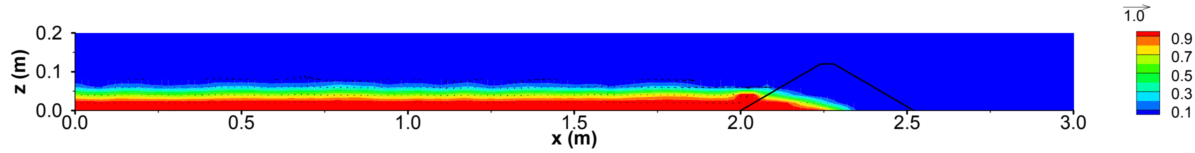

(b) t = 30 (s)

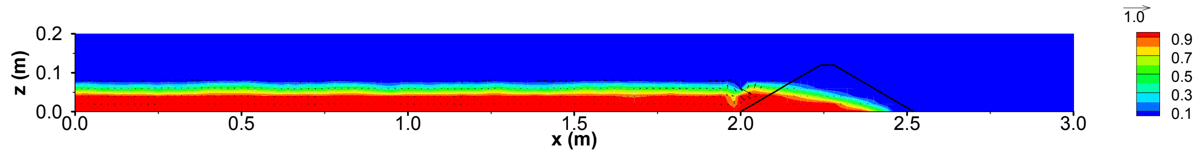

(c) t = 40 (s)

Figure 4. Temporal change of flow fields

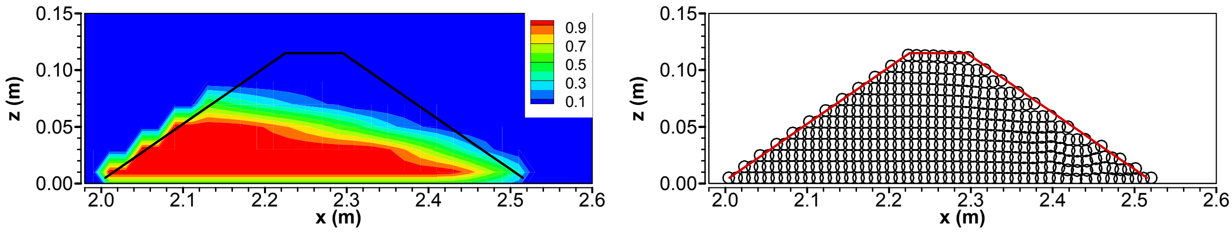

(a) t = 45 (s)

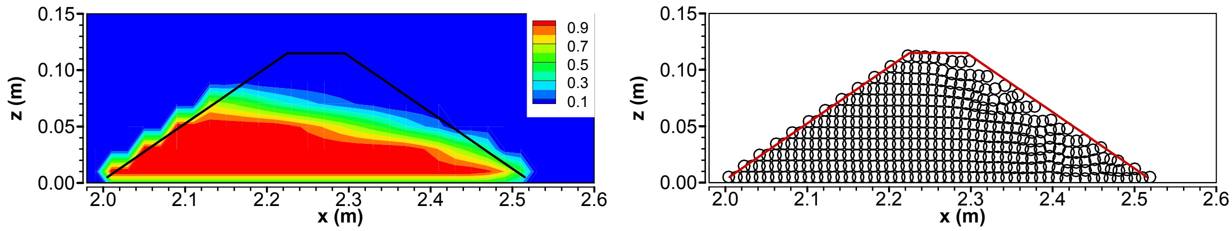

(b) t = 50 (s)

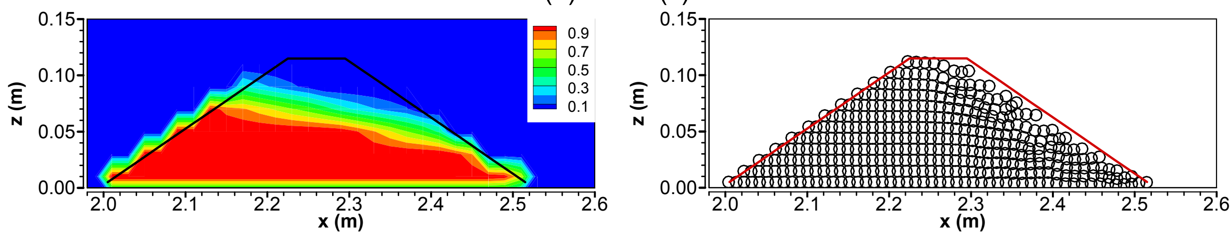

(c) t = 55 (s)

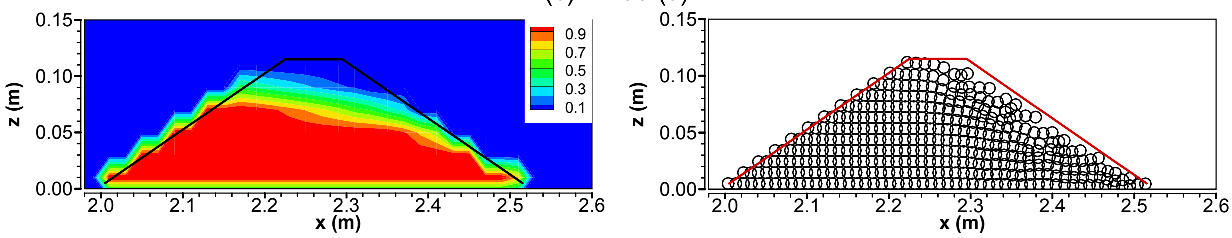

(d) t = 60 (s)

Figure 5. Temporal change of water saturation through a dike and soil deformation

Figure 4 presents the temporal change of flow fields, and the color contour represents the water saturation. It is observed that the overtopping and seepage flows are simultaneously simulated and water infiltrates to the toe of backside. Figure 5 shows the temporal change of water saturation through a dike and soil deformation, and the solid line represents the initial shape of embankment. As seepage flows approaches to the back toe, soil deformation on the backside is simulated well. However, the deformation of overall back slope is seen in the numerical simulation. The reason is that the effect of suction is not included in the flow model and then the restraining force for soil deformation is not considered. By including the effect of suction, the refinement of numerical model is required.

Figure 6 is the stress path at the particle A shown in Figure 3, and the initial state is presented by the plot. It is observed that the effective stress is decreased due to seepage flows.

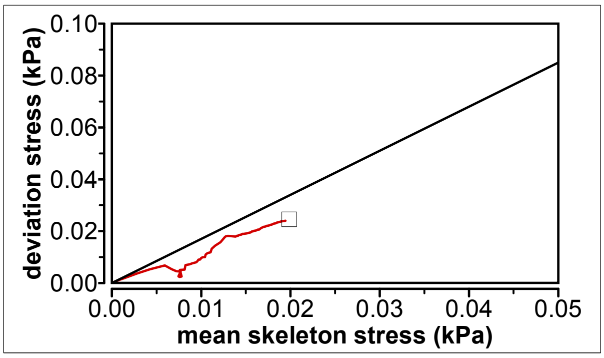

Figure 6. Stress path at particle A

4 CONCLUSIONS

In this study, a numerical model to simulate dike failure process due to seepage flows is developed, by coupling a three-dimensional flow model and a soil deformation model based on elasto-plastic approach. The model is applied to a hydraulic experiment, and it is concluded that soil deformation on the back side due to seepage flows is reasonably simulated in this model. In the next step, the numerical model is refined, by considering effect of suction.

ACKNOWLEDGEMENTS

This work was supported by JSPS KAKENHI Grant Number 15K18122. The authors extend their thanks to Mr. Motoya Kitabayashi, who was a master program student of Kyoto University, for his help in carrying out the hydraulic experiment.

REFERENCES

Bardenhagen, S.G. & Kober, E.M. (2004). The Generalized Interpolation Material Point Method. *Computer Modelling in Engineering and Science*, 5(6), 477-495.

Coleman, S.E., Andrews, D.P. & Webby, M.G. (2002). Overtopping Breaching of Noncohesive Homogeneous Embankments. *Journal of Hydraulic Engineering*, *ASCE*, 128(9), 829-838.

Kakinuma, T. & Shimizu, Y. (2014). Large-Scale Experiment and Numerical Modeling of a Riverine Levee Breach. *Journal of Hydraulic Engineering, ASCE*, 140(9), 04014039.

Kimura, I. & Hosoda, T. (2003). A Non-Linear K-□ Model with Realizability for Prediction of Flows around Bluff Bodies. *International Journal for Numerical Methods in Fluids*, Wiley, 42, 813-837.

Mizutani, H., Nakagawa, H., Yoden, T., Kawaike, K. & Zhang, H. (2013). Numerical Modelling of River Embankment Failure Due to Overtopping Flow Considering Infiltration Effects. *Journal of Hydraulic Research*, *IAHR*, 51(6), 681-695.

Nagata, N., Hosoda, T., Nakato, T. & Muramoto, Y. (2005). Three-Dimensional Numerical Model for Flow and Bed Deformation around River Hydraulic Structures. *Journal of Hydraulic Engineering*, *ASCE*, 131(12), 1074-1087.

Oka, F., Kimoto, S., Takada, N., Gotoh, H. & Higo, Y. (2010). A Seepage-Deformation Coupled Analysis of an Unsaturated River Embankment Using a Multiphase Elasto-Viscoplastic Theory. *Soils and Foundations*, 50(4), 483-494.

Oka, F., Yashima, A., Tateishi, A., Taguchi, Y. & Yamashita, S. (1999). A Cyclic Elasto-Plastic Constitutive Model for Sand Considering a Plastic-Strain Dependence of the Shear Modulus. *Geotechnique*, 49(5), 661-680.

Onda, S., Hosoda, T., Jacimovic, N. & Kimura, I. (2014). Numerical Simulation of Dike Erosion Process Due To Overtopping Flow. *Journal of JSCE*, 2, 168-175.

Onda, S., Hosoda, T., Jacimovic, N. & Kimura, I. (2016). 3D Numerical Simulation of Cross-Levee Breaching Process Due to Overtopping Flow. *River Flow 2016*, 1764-1771.

Pontillo, M., Schmocker, L., Greco, M. & Hager, W.H. (2010). 1D Numerical Evaluation of Dike Erosion Due to Overtopping. *Journal of Hydraulic Research*, *IAHR*, 48(5), 573-582.

Schmocker, L. & Hager, W.H. (2009). Modelling Dike Breaching Due to Overtopping. *Journal of Hydraulic Research, IAHR*, 47(5), 585-597.

Volz, C., Rousselot, P., Vetsch, D. & Faeh, R. (2012). Numerical Modelling Of Non-Cohesive Embankment Breach with the Dual-Mesh Approach. *Journal of Hydraulic Research, IAHR*, 50(6), 587-598.

TYPE OF DAMAGE AND THE PROPOSED SOLUTION TO THE IRRIGATION WEIRS IN MADURA ISLAND, INDONESIA

TATAS[1], MUHAMMAD HAFIIZH IMAADUDDIIN[2] & DIMAS P. DIBIANTARA[3]

[1,2,3] Institut Teknologi Sepuluh Nopember, Surabaya, Indonesia
tatas@ce.its.ac.id

ABSTRACT

Good irrigation system is an essential requirement of farmland. Agricultural infrastructure will be damaged if it is not maintained regularly. Weir as one of the agricultural infrastructures is part of the upstream irrigation systems to raise the water level and then distributing water to agricultural areas through the intake. As an agricultural island in Indonesia planted with tobacco and paddy, Madura is very dependent on good irrigation weir. The purposes of this paper are identification of dominant defects in the irrigation weirs and proposing a structural solution that can be applied to reduce the damage without replacing the irrigation weirs. Moreover, this paper writes about the proposal of repairing water structures, which is a topic with very limited reviews by other authors. The method used to identify the damage is to conduct a survey on several weirs in the Madura Island and to propose technical solutions to reduce further damage of the weir. To make repairs, the hydrological components are first calculated such as return period of rainfall with the Log Pearson III Method, time of concentration by Kirpich's Equation, Mononobe's Rain Intensity and Peak Discharge of Rational Method. To repair the weir structure design, the Lane's Equation and uplift pressure are used. For case study of the Grudjugan Weir, the remedy to the structural damage is proposed by cutting off the ruins of the stilling basin. Hydrologic analysis results show that the flood discharge is 56.2 m^3/s and water level on weir crest is 1.5 meter. A minimum length of weir structure is 9.25 meters, while the thickness of the stilling basin floor is at least 30 cm. Improvements recommended are by replacing the stilling basin floor with masonry and covered with 20 cm thick reinforced concrete, which is connected by anchor to the structure of masonry and old spillway.

Keywords: stilling basin, weirs remedy, weir structure damage.

1 INTRODUCTION

Good irrigation system is an essential requirement of farmland. Agricultural infrastructure will be damaged if regular maintenance is not carried out. Weir as one of the agricultural infrastructures is part of the upstream irrigation systems to raise the water level and then distributing water to agricultural areas through the intake. The function of the weir meets one reason for the need to build the weir, which consists of water level management, flow measurement, environmental enhancement or channel stabilization (Rickard et al., 2003). As an agricultural island which is planted with tobacco and paddy, Madura (see Figure 1) is very dependent on good irrigation weir. Unfortunately, the condition of irrigation infrastructure on the island is very alarming. Some of the weirs on Madura island suffered damage due to irregular maintenance.

Some of the existing irrigation weirs, in Madura Island - Indonesia, show similar type of damage. Based on identification on seven irrigation weirs, the damage typically occurred on the connection between ends of weirs with its stilling basin. Some of them are not broken laterally and the water flow is seen through gaps at the weir structure. These cases are as an indication that the damage is occurred because of piping process. From the seven weirs which were investigated in Pamekasan Regency in 2015 (see Figure 2), it was observed that Bulay Weir in Galis, Lancar Weir in Larangan, Klampar Weir in Proppo, Cenlecen Weir in Pakong and Grudjugan Weir in Larangan appeared to exhibit similar type of structural failure. The weight of the floor of stilling basins was insufficient to resist the uplift pressure. This uplift pressure caused the floor cracked and ruptured. This failure reduces the effective length of the impermeable floor and can cause failure of the weir structure. Nevertheless, even though the stilling basins are ruptured but the weirs do not collapse.

For these cases, the analysis of samples taken is based on problems that occurred in Grudjugan Weir. Sketch of Grudjugan Weir damage can be seen in Figure 3. These cases become complicated due to the unavailability of blueprint of the irrigation weirs that are recorded after the construction is done. This situation makes engineer clueless of the weir bottom design. They can only measure the dimensions of weir surface and reconstruct the ruins of stilling basin as a preliminary to design remedial structure. According to the background and problem, this paper proposes the handling of damage to the dam, without having to do a total demolition and rebuilding a new weir.

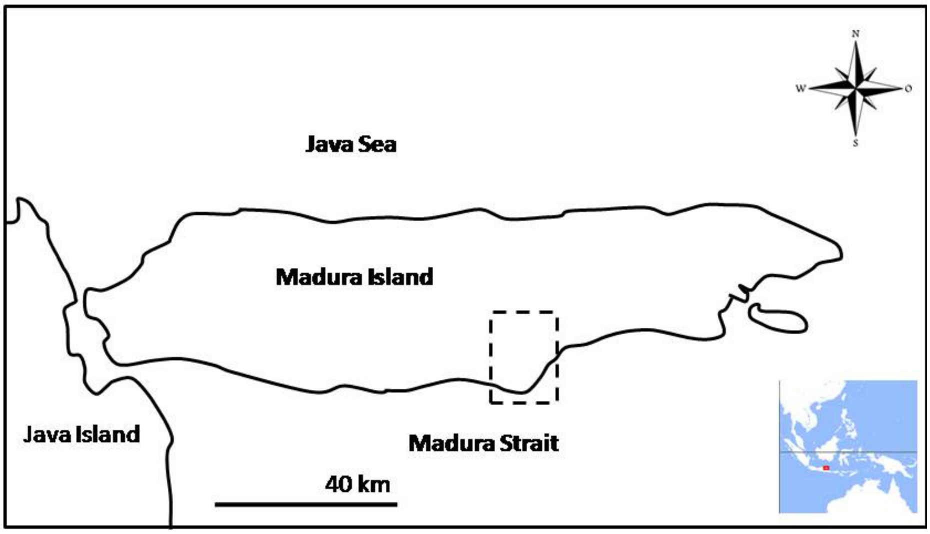

Figure 1. Map of Madura Island in Indonesia, and location of weir in the dotted line.

Figure 2. Bulay Weir, Lancar Weir, Klampar Weir, Cenlecen Weir and Grudjugan Weir exhibit similar failure at their stilling basin.

Stilling basin is used to reduce the energy of water and to prevent scouring that occurs when high-velocity water comes to the downstream of the weir. This scouring can damage the foundation of weir and also causes severe erosion at downstream. Figure 4 shows the basic component of weir structure.

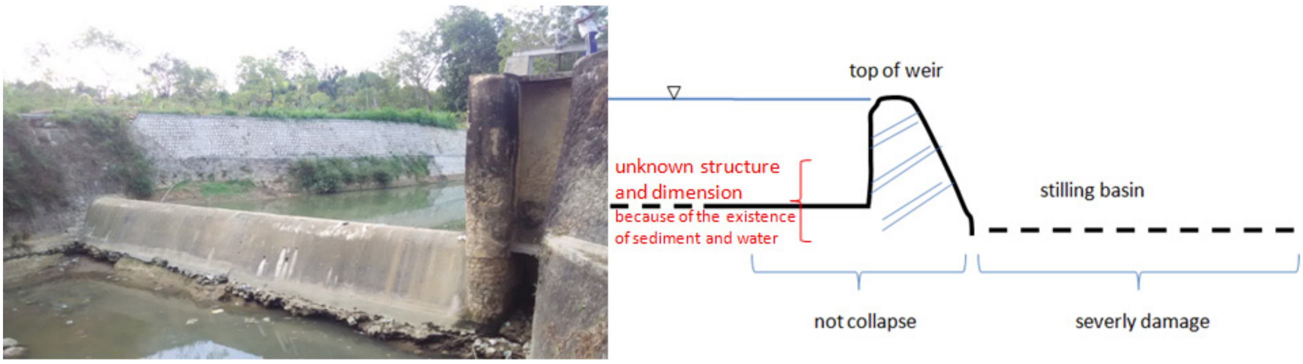

Figure 3. Damage in the stilling basin as a typical failure of weir in Madura Island and its sketch of cross section.

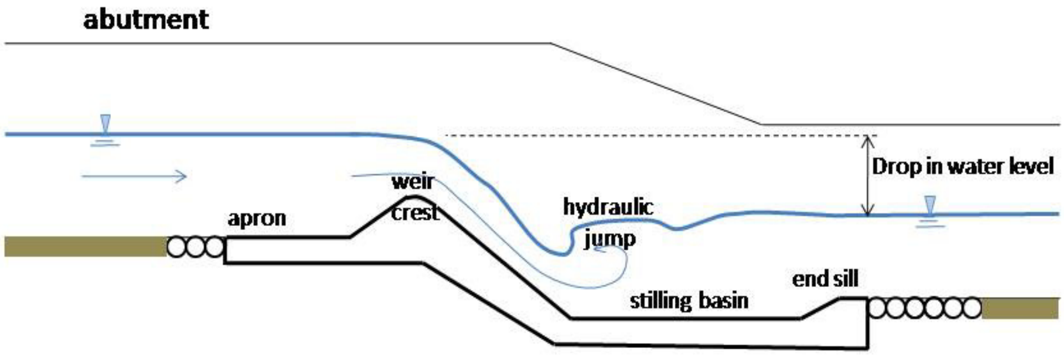

Figure 4. Basic component of weir structure (redrawn from Rickard et al., 2003).

2 METHOD

The methods used to fulfill the purpose of this paper was a field survey to measure dimensions of weirs and channels, conduct soil sampling, data collection of rainfall data and provision of topographic maps. Rainfall data was used to predict the depth of precipitation for various return periods using Log-Pearson Type III which is extensively used in USA (Subramanya, 1995) and in Indonesia (National Standar of Indonesia, 2016). For this distribution, the hydrologic dataset are firstly taken as logarithms, y = log y (Chow et al., 1988). From the logarithmic data, the mean, standard deviation and coefficient of skewness are calculated, which is the frequency factor that has been expressed by Kite (1977) and calculated by Chow et al. (1988).

Calculation of rain intensity (I in mm/hr) is defined by Mononobe's Equation (Hayashi et al., 2015; Iguchi et al., 1972):

$$\mathrm{I} = \frac{\mathrm{R}}{24} \cdot \left(\frac{24}{\mathrm{t}}\right)^{2/3} \qquad [1]$$

where R is rainfall depth (mm) from Log-Pearson Type III distribution and t is rainfall time (hours) which is corresponded with t_c as time of concentration.

In this paper, Kirpich's Equation was used to calculate time of concentration. The Kirpich's Equation was developed from catchment areas of 0.004-0.453 km2 (1-112 acres) and to the slope of 3% to 10%. Sharifi et al., (2011) have compared some formulas of time of concentration for some watersheds. The result is deduced from nine equations of concentration time and the Kirpich's Equation provided excellent value if applied elsewhere including for wider watershed. Time of concentration (minutes) was computed using Kirpich's Equation (Kirpich, 1940 in Subramanya, 1995). Kirpich's Equation is:

$$t_c = 0.01947 \cdot L^{0.77} \cdot S^{-0.385} \qquad [2]$$

where L is maximum length of travel of water (meters), S is slope of the catchment area = $\Delta H / L$ in which ΔH is difference in elevation between the most remote point and the outlet.

The peak discharge (Q) was calculated by rational method which was obtained by multiply rainfall intensity, catchment area and coefficient of run-off. The rational method is a simple technique developed by Kuichling (1889) for estimating a design discharge from a small watershed. This formula is adopted in Indonesia to be National Standard and applicable to watershed with area up to 50 km^2 (SNI, 2016; Subramanya, 1995.).

$$\mathrm{Q} = \frac{1}{3.6} \cdot \mathrm{C} \cdot \mathrm{I} \cdot \mathrm{A} \qquad [3]$$

where C is coefficient of run-off and A is area of catchment (km^2).

The general equation of discharge flows on weir was first proposed by Poleni (1717) in Guven, et al., (2013) and Saad, et al. (2016):

$$Q = C_d \cdot \frac{2}{3} \cdot B \cdot H^{3/2} \cdot \sqrt{2g} \qquad [4]$$

where Q is discharge over the weir (m^3/s), B is effective width of the weir in meters, H is head of water on the weir crest (meters), and g is acceleration due to gravity in m^2/s. This equation is used to calculate head of water on the weir crest using H as an input to determine one of some criteria in stability of weir.

Weir structure improvement due to the uplift pressures can be done by installing long impermeable floor with the right thickness and installing impermeable blanket in the upstream part to reduce uplift pressure at downstream (Shayan, et al., 2015). In this paper, a method was used to determine the length of the impermeable floor to resist uplift pressure that is calculated based on the thickness of the floor in the stilling basin. Length of impermeable floor can be calculated using creep distance in Lane's Equation (1934) in Hendrix, et al. (2009) with the Safe Weighted Creep Ratios shown in Table 1. Lane's Equation (1934) is:

$$C_w = \frac{L_w}{H} = \frac{[\text{vertical creep distance} + 1/_3 \text{horisontal creep distance}]}{H} \qquad [5]$$

where L_w is the weighted creep distance and H is the head of water in the reservoir.

Table 1. Safe Weighted Creep Ratios as recommended by Lane (Lane 1934 in Hendrix et al, 2009).

Material	Safe Weighted Creep Ratio
Very Fine Silt or Sand	8.5
Fine Sand	7
Medium Sand	6
Coarse Sand	5
Fine Gravel	4
Medium Gravel	3.5
Gravel and Sand	No Value
Coarse Gravel, Including Cobbles	3
Boulders with Some Cobbles and Gravel	2.5
Boulders, Gravel, and Sand	No value
Soft Clay	3
Medium Clay	2
Hard Clay	1.8
Very Hard Clay, or Hardpan	1.6

To determine the need of the floor thickness of the stilling basin, it can determined by the uplift pressure under weir structure (Lane, 1934) (Eq. 6) and the thickness of the stilling basin floor (d_x) by using Eq. 7. This formula was obtained from Book of Technical Manuals of Irrigation Design in Indonesia (Balitbang Depkimpraswil, 2002):

$$P_x = \left(H_x - \frac{L_x}{L} \cdot \Delta H\right) \cdot \gamma_w \qquad [6]$$

$$d_x \geq SF \cdot {}^{P_x}/_{\gamma_w} - w_x \qquad [7]$$

where P_x is uplift pressure in point x (tonnes/m2), H_x is head of water in the reservoir, L_x is creep distance from upstream to point x (meters), L is total distance under weir structure (meters), ΔH is head difference (meters), Y_w is specific gravity of water, SF is safety factor, and w_x is vertical distance from base of floor to end sill.

3 RESULTS

The Grudjugan weir is an irrigation weir in 760,243.6 mE and 9,212,254.5 mN on Tambakagung River. The elevation is 76.7 meter above mean sea level. Catchment area of this weir is 8.86 km^2 with slope of 0.0584. In this catchment area, the maximum flow distance is 5,192.85 meters and basin slope is 0.0584 m/m (Downer et al., 2002).

The annual maximum rainfall data can be seen in Table 2. The return period of rainfall was calculated by Log Pearson III. Rainfall for a return period of 5 years was 84 mm, with coefficient of skewness -0.7 and frequency factor of 0.857 (Chow et al, 1988). Furthermore, the values of maximum length of travel of water and slope were 5,192.85 meters and 0.0584, respectively. Using Eq. 2, the value of tc was 42.2 minutes. Based on the values of tc and R_5, from Equation 1 the value of rainfall intensity was 36.8 mm/hour.

Land use in Grudjugan Watershed consists of agricultural area and residential area. The agricultural area is wider than other areas which accounts for 80% of the watershed area. With the value of run off coefficient of agricultural area of 0.6 and settlements of 0.7 (Subramanya, 1995),the equivalent runoff coefficient was 0.62. Using Eq. 3 which is the discharge equation of rational method, results in Q_5=56.2 m^3/s. Using Eq. 4, with a width of spillway of 15.56 meters, the height of the water above the weir crest was 1.50 meters.

  / ISSN 1562-6865 (Online) - ISSN 1063-7710 (Print)

Table 2. The annual maximum rainfall.

Year	Rainfall Depth (mm)
2002	53.00
2003	47.00
2004	36.00
2005	33.00
2006	66.00
2007	82.00
2008	100.00
2009	77.00
2010	55.00
2011	87.00
2012	77.00
2013	64.00
2014	80.00

As the under weir structure condition was not known, it was assumed that its form was horizontal as the critical condition against uplift pressure. This was done to determine the minimum weir structure length from upstream to downstream (apron, spillway and stilling basin). Based on soil investigation, soil compositionwas sandy and gravelly clay with a hard consistency. Based on Table Lane, the value of c_w was then 1.6. The difference of water level in upstream and downstream was 1.93 meters. Thus, the minimum requirement of weir structure length was 9.25 meters (see Figure 5).

The final step was to determine the floor thickness of the stilling basin, using Eq. 7 for relationship between uplift pressures with weight of stilling basin. Stilling basin floor was made by replacing the broken floor with masonry (density 2.2 tonnes/m^3) and covered with reinforced concrete (density of 2.4 tonnes/m^3). Using a safety factor of 1.5, a minimum weir length of 9.25 meters, and reviewing the location of the thickness of the floor as far as 1 meter from the end sill, then by using Equation 7, the minimum thickness of stilling basin floor was 0.30 meters. Besides improvements with masonry, the floor coated with reinforced concrete was also proposed with a minimum thickness of 20 cm, which was connected to the old building (spillway) using the anchor (see Figure 5).

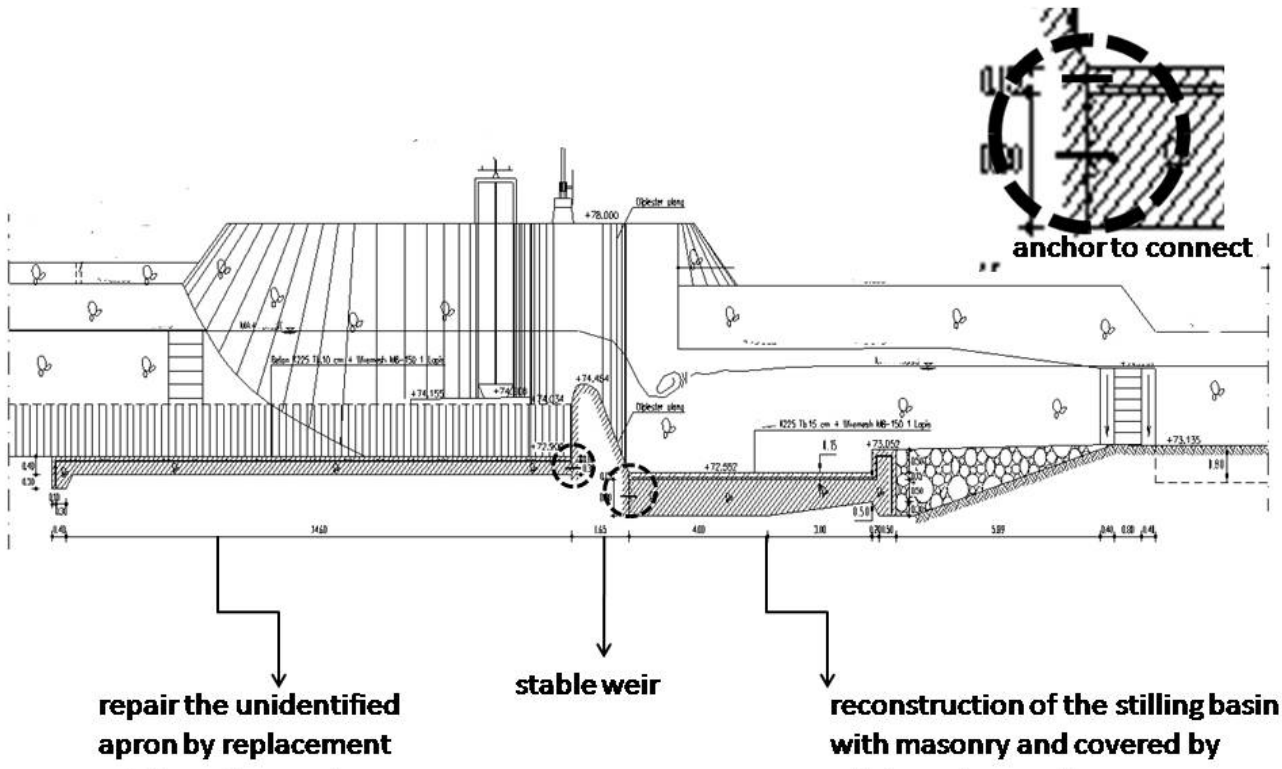

Figure 5. Sketch of remedy to the weir structure (modified from Brantas Basin Management, 2015).

4 CONCLUSIONS

The remedy of weir structural damage is proposed by cutting off the ruins of the stilling basin. From the hydrologic analysis results, the flood discharge is 56.2 m^3/s and water level on weir crest is 1.5 meter. Using Lane's Equation, the minimum length of the weir structure is 9.25 meters, while the thickness of the stilling basin floor is at least 30 cm. Improvements recommended are by replacing the stilling basin floor with masonry and also covered with 20 cm thick reinforced concrete which is connected by anchor to the masonry structure and old spillway.

ACKNOWLEDGEMENTS

Many thanks are due to BBWS Brantas in Surabaya-Indonesia and Mr. Taufik (the Director of SEIA Consultant) for giving the authors a chance to be an expert in some projects. We would also like to express our sincere gratitude to the Department of Civil Infrastructure Engineering, Vocational Faculty and LPPM ITS for supporting the seminar.

REFERENCES

Balitbang, D. (2002). *Pedoman/Petunjuk Teknik dan Manual Bagian 2 Irigasi.* Ed.1. Badan Penelitian dan Pengembangan Dep. Kimpraswil. Jakarta (In Bahasa Indonesia)

Brantas Basin Management. (2015). *Detail Design Engineering of Improvement of Irrigation Weir at Pamekasan,* Final Report, BBWS Brantas.

Chow, V.T., Maidment, D.R. & Mays, L.W. (1988). *Applied Hydrology.* McGraw-Hill International Edition, Singapore.

Downer, C.W. & Odgen, F.L. (2002). *GSSHA – User's Manual : Gridded Surface Subsurface Hydrologic Analysis,* Engineering Research Development Center, Vicksburg.

Guven, A., Hassan, M. & Sabir, S. (2013). Experimental Investigation on Discharge Coefficient for a Combined Broad Crested Weir-Box Culvert Structure. *Journal of Hydrology,* 500, 97–103.

Hayashi, S., Murakami, S. & Xu, K.Q. (2015). Watanabe M. Simulation of the Reduction of Runoff and Sediment Load Resulting from the Gain for Green Program in the Jialingjiang Catchment, Upper Region of the Yangtze River, China. *Journal of Environmental Management,* 149, 126–137.

Hendrix, J.M. & Stark, T.D. (2009). Predicting Underseepage of Masonry Dams. *Proceedings of 29th ASDSO Conference,* Hollywood, FL.

Iguchi, S. & Takahashi, H. (1972). *Stream Flow from Rainfall.* Mononobe Hydraulics Iwanami, Tokyo, Japan, 567–568. (In Japanese)

Kirpich, Z.P. (1940). *Time of Concentration of Small Agricultural Watersheds, Civil Engineering.* The Original Source for the Kirpich Equation, 10(6), 362.

Kite, G.W. (1977). *Frequency and Risk Analysis in Hydrology.* Water Resources Publications, Fort Collins, Colo, 230.

Kuichling, E. (1889). The Relation between the Rainfall and the Discharge of Sewers in Populous Districts. *Transactions of ASCE,* 20, 1-60.

Lane, E.W. (1934). Security from Under-Seepage: Masonry Dams on Earth Foundation. *Proceedings, ASCE,* 60,1235 –1272.

Poleni, J. (1717). De Motu aquae mixtto. *Patavii* (Padua).

Rickard, C., Day, R. & Purseglove J. (2003). *River Weirs – Good Practice Guide,* Guide - Section A. R&D Publication.

Saad, N.Y. & Fattouh, E.M. (2016). Hydraulic Characteristics of Flow over Weirs with Circular Openings. Ain Shams Eng Journal, 1-8.

Sharifi, S. & Hosseini, S.M. (2011). Methodology for Identifying the Best Equations for Estimating the Time of Concentration of Watersheds in a Particular Region. *Journal Of Irrigation And Drainage Engineering – ASCE,* 712-719.

Shayan, H.K. & Tokaldany, E.A. (2015). Effects of Blanket, Drains and Cutoff Wall on Reducing Uplift Pressure, Seepage and Exit Gradient under Hydraulic Structures. *International Journal of Civil Engineering,* 13, No. 4A, Transaction A: Civil Engineering, 486-500.

Subramanya, K. (1995). *Engineering Hydrology 2nd Ed.* Tata McGraw-Hill Publishing Company Ltd. Delhi 234-235.

EXPERIMENTAL RESULTS ON SEDIMENT ENTRAINMENT BY GRAVITY CURRENTS

JESSICA ZORDAN[(1)], CARMELO JUEZ[(2)], ANTON J. SCHLEISS[(3)] & MÁRIO J. FRANCA[(4)]

[(1,2,3,4)] Laboratoire de Constructions Hydrauliques, École Polytechnique Fédérale de Lausanne, Switzerland
jessica.zordan@epfl.ch

ABSTRACT

Gravity currents are geophysical flows responsible of the distal transport of high volumes of sediments. In particular, turbidity currents, a form of gravity currents where sediments in suspension confer the buoyancy that ignites the flow, are the main mechanism for distal sediment transport within lakes and reservoirs. In maritime environment, submarine clay-rich gravity currents can impact and may endanger human made infrastructures such as submarine cables and platforms. It is thus important to understand the dynamics of sediment transport associated to gravity currents. In the present research, it is intended to experimentally investigate the mechanisms of entrainment, transport and deposition of fine sediments caused by the passage of a saline gravity current. Conservative saline currents, with varied initial density, are let to flow over an erodible bed sector where fine sediments, with three different grain sizes, are at rest. A detailed description of the gravity current dynamics is reported using 3D instantaneous velocities measurements over a certain profile. Video records obtained synoptically and laterally through a transparent wall, provide a visualization of the entrainment and resuspension processes which is further related to the flow hydrodynamics. The critical threshold conditions for initiating sediment motion is frequently related to the balance of boundary shear stress and the submerged weight of the particle. However boundary shear stress is just one of several impelling forces and the particle submerged weight is just one of several inertial forces. Here the attention is first focused on the complete description of the flow velocity, in term of instantaneous and mean flow. A deep analysis of the hydrodynamic of one gravity current reproduced in laboratory is here presented and its role in sediments' entrainment discussed.

Keywords: Gravity currents; sediment entrainment; erodible bed; 3D instantaneous velocities profiles.

1 INTRODUCTION

In atmosphere and in water, examples of gravity currents are numerous. In most of the examples that we can find in nature this buoyancy driven flows interact with sediments. Considering the cases of lava flows, dust storms or snow avalanches: the presence of sediments increases the density of the fluid which getting in contact with the lighter ambient air forms gravity currents. In water, suspended sediments at relative high concentration cause the formation of turbidity currents. A common point for these flows is their high interaction with the material of the bed surface. Travelling on a surface that is generally composed of erodible sediments, entrainment and eventually deposition of material can take place at a rate that depends on the characteristics of both the current and of the bed. Furthermore, gravity currents in nature occurs over complex topographies and varied bed compositions.

In situ measurements of gravity current have been documented (Xu et al., 2004; Paull et al., 2002) among others) and in many cases such flows are major and often catastrophic agents of sediment transport, both on land and within the ocean (Kneller et al. 2000). Gravity currents have been widely studied through both numerical (Ooi et al., 2009; Adduce et al., 2011; Ottolenghi et al., 2013; Lombardi et al., 2015) and experimental (Britter and Linden, 1980; Huppert and Simpson, 1980; Altinakar et al., 1990; Garcia and Parker, 1993; Shin et al., 2004; Nogueira et al., 2013a; Nogueira et al., 2013b; Theiler and Franca, 2016) simulations. Despite the wide interest on the topic, the mechanisms behind the interaction between the highly turbulent gravity current and the bed over which it flows, at the bottom interface, are not yet completely understood. Few contributions focus on a detail description of current hydrodynamic at the lower boundary and even less on the ability of a gravity current to entrain material from the bed. In the present study, in order to analyze the contribution of sediments coming from the mobile bed, saline conservative currents experiments have been carried over erodible bed. Three initial current densities have been tested combined with three different sediment grain sizes conforming the erodible bed.

The set-up was specifically design to perform full-depth lock-exchange experiments. The standard configuration, previously used by many authors (Huppert and Simpson, 1980; Rottman and Simpson, 1983; Adduce et al., 2011; Nogueira et al., 2014), was here adjusted in order to form an extended slumping phase in which the front velocity is almost constant (Tokyay et al., 2011). The initial volume of denser fluid is here comparable to the volume of the ambient water in the second part of the channel (Shin et al., 2004). The bottom is horizontal and smooth. In these conditions, a quasi-steady regime is formed, similar to the steady state observed for constant feed gravity currents (Zordan et al., 2016).

This is particularly important since the dynamics of the near-bed region of such currents, which is characterized by high sediments concentration, is still poorly understood, as it is governed by intense particle-fluid and particle-particle interactions that give rise to mass and momentum exchanges between the current and the sediment bed. The coupling between the evolution of the gravity current and that of the underlying substrate is explored by analyzing the velocity profiles and the videos recorded from the side.

The present paper is structured as follows: first, the experimental set-up and the instrumentations are described. Subsequently, the results in term of streamwise and vertical velocity temporal evolutions and sediments entrainment from video analysis are presented. In the final section, the main findings are summarized and discussed looking at the possible further steps.

2 METHODS

2.1 Experimental set-up

The flume that was used to reproduce the gravity currents is 7.5 m long and 0.275 m wide and it is divided into two sections of comparable volumes by a vertically sliding gate (Figure 1). An upstream reach serves as head tank for the dense mixture (n.1 in Figure 1); a downstream reach is where the current propagates and where the main measurements are made. The bottom is horizontal and smooth along the whole channel apart for a section of 0.6 m of length, 2.5 m downstream the gate (n.2 in Figure 1). Here a mobile bed is localized and recreated by fulfilling a depression in the bed with sediments. The so called lock exchange technique is used: when the gate is removed, differences in the hydrostatic pressure cause the denser fluid to flow in one direction near the bottom boundary of the tank, while the lighter fluid flows in the opposite direction at the top (Shin et al., 2004). Downstream, the current is let to dissipate flowing down into a final large tank (n.3 in Figure 1).

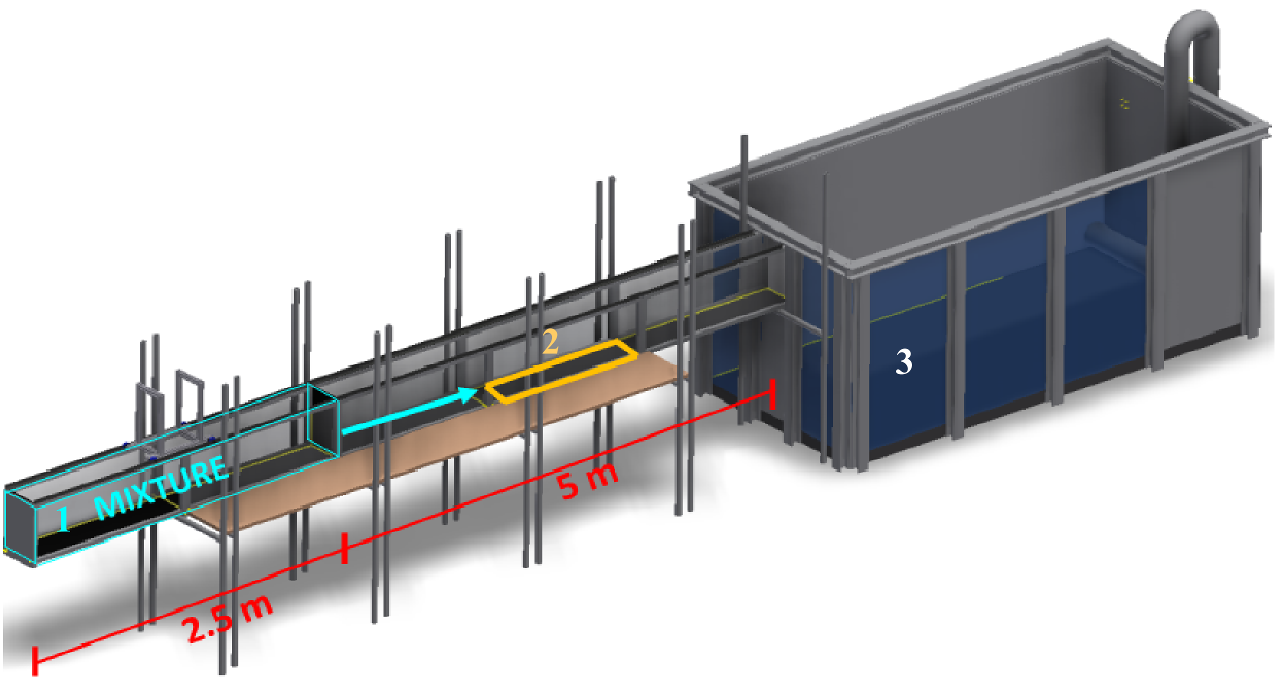

Figure 1. 3D view of the experimental set-up.

2.2 Measurements and instrumentation

The 3D Acoustic Doppler Velocity Profiler (ADVP) (Lemmin and Rolland, 1997, Franca and Lemmin, 2006) is a non-intrusive sonar instrument that measures the instantaneous velocity profiles using the Doppler effect without the need of calibration. It is placed right before the mobile bed and takes 3D instantaneous velocity measurements during the passage of the density current over a vertical, including the upper counter flow. For studies of turbulent flow, a high sampling frequency is desirable. The minimum number of pulse-pairs was here fixed at 32, in reason of our working conditions, which corresponds to a frequency of acquisition of 31.25 Hz (Lemmin and Rolland, 1997). The instrument consists of a central emitter surrounded by four receivers. The geometric configuration is the result of an optimization of the instrument that allows noise reduction by creating redundancy information for the velocity components (Blanckaert and Lemmin, 2006). This, together with the despiking procedure proposed by Goring and Nikora (2002), leads to a considerable reduction in the noise level of the data set. The analysis of the power spectra of the raw data collected with the ADVP allows the identification of the noisy frequencies that where furthermore cut off through a low-pass filter of the signal.

The high-speed camera SMX-160 records the evolution of the gravity current over the erodible bed laterally, from the transparent side. The acquisition frequency was 25 Hz and the area of interest had a resolution of 500 x 180 pixels. The images are converted to grey-scale matrices for being post-processed. The interface between the water and the density current is identified by the subtraction between the current image and the initial image (without the current). The current passing over the mobile bed takes in suspension the material from the bottom. More challenging was the detection of the limit between current and sediment in suspension. A threshold for the identification of the pixels needed to be estimated. At the beginning of the experiments the pixel value associated to the sediments is annotated. Then, this value is used as reference threshold to identify pixels characterized by the presence of sediments, considering an average value of a group of neighboring pixels.

2.3 Experimental parameters

The experimental parameters of the nine tests performed are shown in Table 1 where ρ_0 is the gravity current initial density (as measured with a densimeter in the upstream reach), ρ_a is the ambient water density (998 kg/m^3), g is gravity and g' is the initial reduced gravity of the dense fluid defined as:

$$g' = g\frac{\rho_0 - \rho_a}{\rho_a} \quad [1]$$

Fr is the bulk densimetric Froude number derived for each test as:

$$Fr_D = \frac{u_f}{\sqrt{g' h_c}} \quad [2]$$

with h_c the average height of the current (one third of the total height of the fluid in the channel H=0.2m) and u_f the velocity of propagation of the front. Re_0, the Reynolds number based on the initial quantities, is determined as:

$$Re_0 = \frac{U h_c}{\nu} \quad [3]$$

Where v is the kinematic viscosity and $U = \sqrt{g' h_c}$ the buoyancy velocity.

. **Table 1**. Experimental parameters for all experiments

Exp.	ρ_0 kg/m^3	g' m^2/s	u_f m/s	Re_0 x10^3	Fr_D -	D_{50} μm
R1.FINE	1028	0.29	0.101	48.2	0.593	80
R1.MEDIUM	1028	0.29	0.106	48.2	0.689	145
R1.COARSE	1028	0.29	0.126	48.2	0.771	91
R2.FINE	1038	0.39	0.117	55.7	0.595	80
R2.MEDIUM	1038	0.39	0.134	55.7	0.678	145
R2.COARSE	1038	0.39	0.127	55.7	0.646	191
R3.FINE	1048	0.49	0.131	62.4	0.595	80
R3.MEDIUM	1048	0.49	0.142	62.4	0.642	145
R3.COARSE	1048	0.49	0.155	62.4	0.704	191

The front velocity was computed through video analysis. The characteristic of the particle in terms of D_{50} (μm) is also given.

3 RESULTS

3.1 Flow velocity

The velocity data collected consists of instantaneous 3D velocity profiles along a vertical. Mean velocities where calculated by moving averaging the low-pass filtered instantaneous velocities following Baas et al. (2005). The time scale of the moving average was chosen by analyzing the power spectra of the instantaneous low-passed signals. The maximum time window which allowed to still recognize the characteristic frequencies of the signal was taken in order to apply the moving averaging. One characteristic test will be here deeply analyzed. In Figure 2 the mean streamwise and vertical velocities fields, together with the vector field, for test R2.medium is reported. The vertical length scale was normalized by the total water height (H=0.2m). The regions of the current can be identified. The head height is larger than the body of the current and it presents a three-dimensional velocity structure. High streamwise velocities are presented within the head and Kelvin-Helmholtz billows are generated on the front of the head. This turbulent structures are generally associated with high mixing (Britter and Simpson, 1978). While the current advances, a return flow forms on the upper ambient fluid layer. This counter-current shows a jet-flow configuration as displayed by the mean streamwise velocity field (Figure 2, first plot).

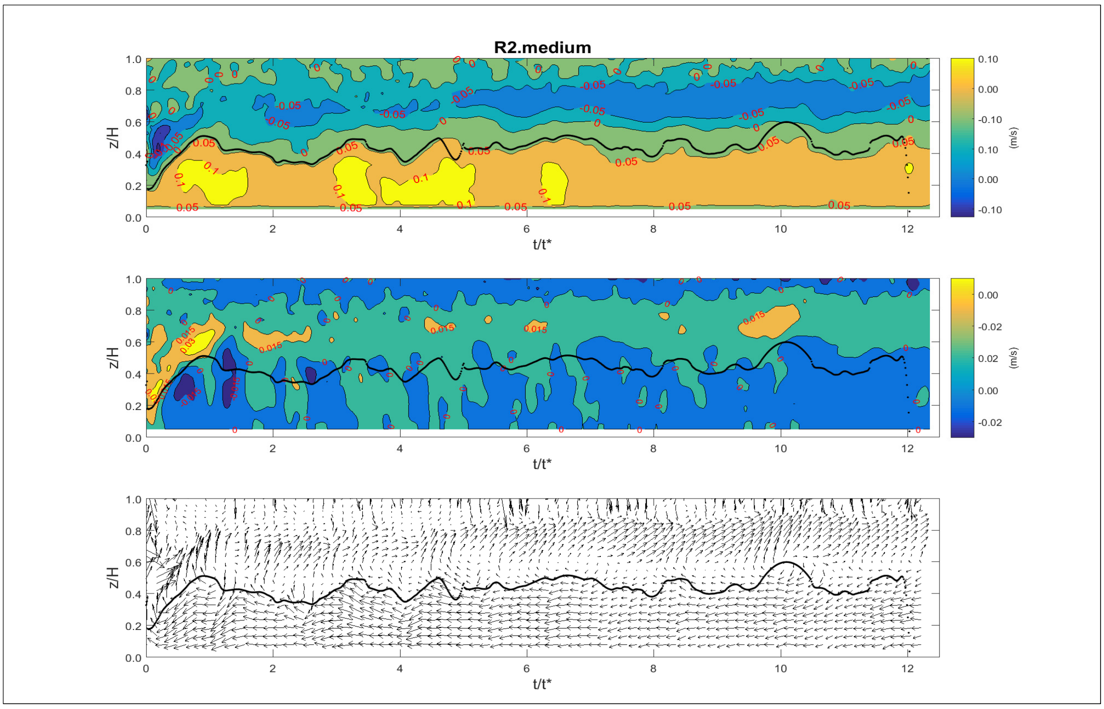

Figure 2. Mean streamwise (top) and vertical velocity field (middle) and vector field (bottom) for test R2.medium.

Peak of alternatively high positive and negative vertical velocities are present at the base of the current, near the bed. The advancing front causes a high-speed upward displacement of fluid that moves backward over the current's head.

The temporal evolution of the streamwise and vertical velocities are plotted for four different heights from the bed (Figure 3). The distances 18.8 mm, 31.3 mm, 52.1 mm and 72.9 mm have been considered as representative heights of the current. The highest streamwise velocities are detected at a distance of 18.8 mm from the bed. At 72.9 mm the streamwise velocities drop down and become negative: at this height the zone behind the head, characterized by a backward movement, is detected. The temporal evolution of the vertical velocities confirms the presence of upward and downward displacement of fluid, that are consistent along the whole vertical of the current. The highest values are recorded in the zone where the ambient water, pushed by the approaching front of the current, is displaced above and behind the head.

3.2 Sediments entrainment

Video analysis allows to track the sediments getting into suspension from the mobile bed. It was possible to compute the time evolution of the area occupied by the sediments by identifying the pixels occupied by the sediments in each picture taken. The same was done for the pixels belonging to the current. The areas of sediments and current are plotted in Figure 4 with the mean vertical velocities recorded at the closest recorded height from the bottom. It appears that the initiation of sediments entrainment begins in correspondence of the highest peak of vertical velocity. The time evolution of the current, as reported in Figure 4, shows that a peak is reached at around t/t^*=1, followed by a reduction. In fact the upper boundary of the current, at the interface with the ambient water, does not seem to be affected by the sediment's entrainment: the reduction of the height of the current, starting from around t/t^*=1, is rather related to the passage of the head which arises with respect to the body.

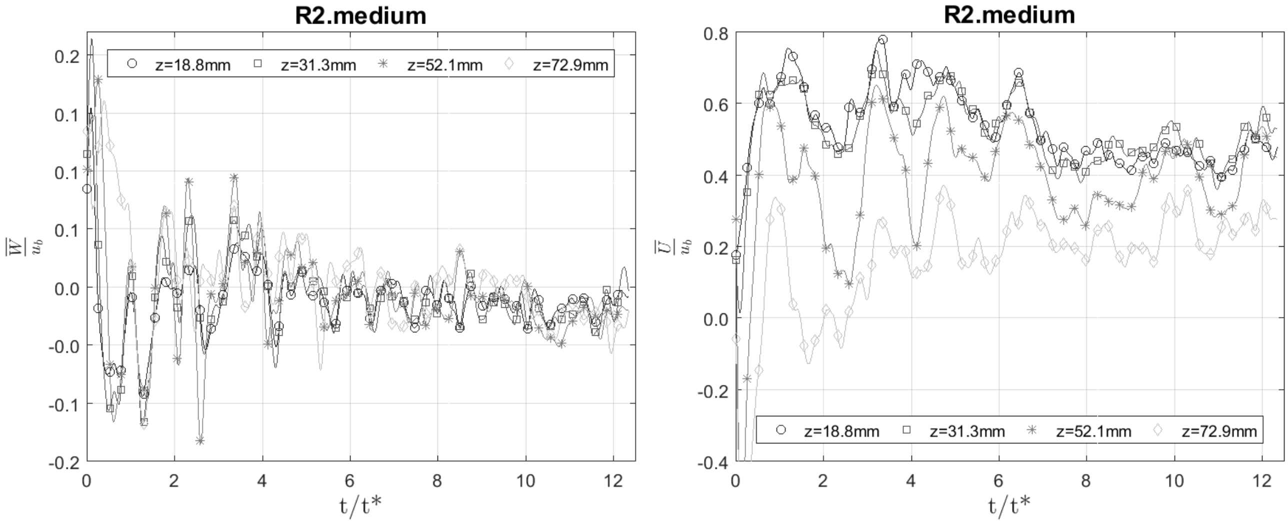

Figure 3. Streamwise (left) and vertical mean velocities (right) as a function of normalized time at four different elevations from the bed, for test *R2.medium*.

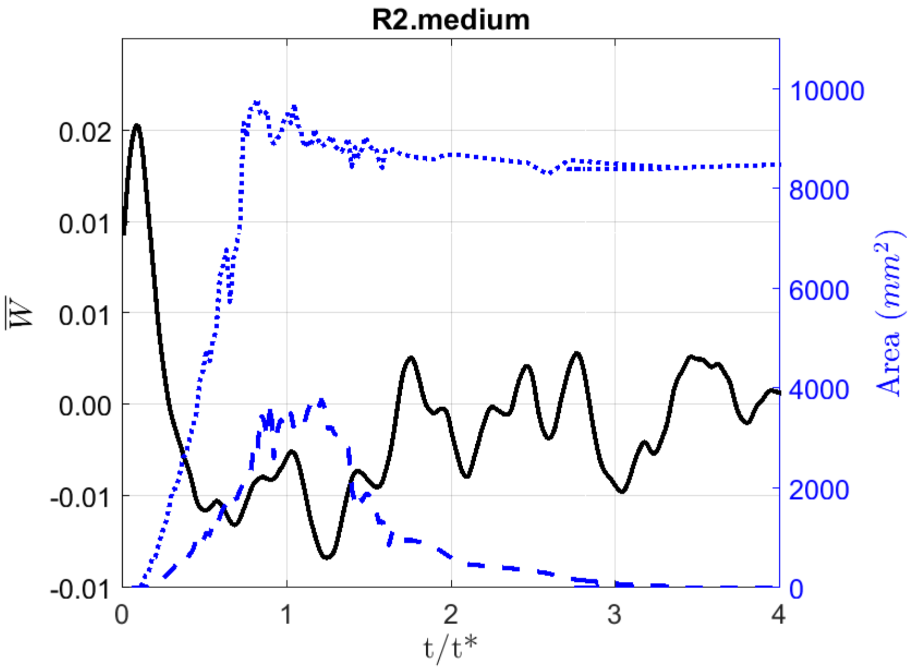

Figure 4. Time evolution of vertical velocity at the closest recorded height from the bottom (solid line), area of the current (dotted line) and of sediments (dashed line) from video processing.

4 CONCLUSION AND DISCUSSION

These preliminary results, allow to understand the mechanisms underlying the erosion and deposition processes. For this purpose, 3D-ADVP measurements have been performed, obtaining high resolution data for the velocities of the current before reaching the erodible bed. Velocity field provided useful information on the characteristics of the flow approaching the mobile bed. A peak in vertical upward velocity is present at the first instants of the front. The sediments entrainment was recorded with the high speed camera and the image processing allows to compute the time evolution of the area occupied by the sediments per each time frame. After synchronization of the measurements coming from the two instruments (ADVP and camera), the correspondence between mean vertical upward velocity and beginning of entrainment was highlighted. If the vertical velocity field can be related to the beginning of sediments motion, the author of sediments suspension subsistence needs to be identified. Moreover, a threshold at which the inertial forces overcome the impelling ones, implying sediments deposition, will be possibly determined. These are still open fields of study that will be addressed in the following of this research by investigating as well the role in the entrainment of sediments of bottom shear stress and of the turbulent quantities.

ACKNOWLEDGEMENTS

This research was funded by the European project SEDITRANS funded by Marie Curie Actions, FP7-PEOPLE-2013-ITN-607394 (Multi partner - Initial Training Networks).

REFERENCES

Adduce, C., Sciortino, G. & Proietti, S. (2011). Gravity Currents Produced by Lock Exchanges: Experiments and Simulations with a Two-Layer Shallow-Water Model with Entrainment. *Journal of Hydraulic Engineering*, 138(2), 111-121.

Altinakar, S., Graf, W.H. & Hopfinger, E.J. (1990). Weakly Depositing Turbidity Current on a Small Slope. *Journal of Hydraulic Research*, 28(1), 55-80.

Baas, J.H., McCaffrey, W.D., Haughton, P.D. & Choux, C. (2005). Coupling between Suspended Sediment Distribution and Turbulence Structure in a Laboratory Turbidity Current. *Journal of Geophysical Research: Oceans*, 110, 1-20.

Blanckaert, K. & Lemmin, U. (2006). Means of Noise Reduction in Acoustic Turbulence Measurements. *Journal of Hydraulic Research*, 44(1), 3–17.

Britter, R.E. & Simpson, J E. (1978). Experiments on the Dynamics of a Gravity Current Head. *Journal of Fluid Mechanics*, 88(02), 223-240.

Britter, R.E. & Linden, P. F. (1980). The Motion of the Front of a Gravity Current Travelling Down an Incline. *Journal of Fluid Mechanics*, 99(03), 531-543.

Garcia, M. & Parker, G. (1993). Experiments on the Entrainment of Sediment into Suspension by a Dense Bottom Current. *Journal of Geophysical Research*, 98, 4793-4793.

Goring, D.G. & Nikora, V.I. (2002). Despiking Acoustic Doppler Velocimeter Data. *Journal of Hydraulic Engineering*, 128(1), 117-126.

Franca, M.J. & Lemmin, U. (2006). Eliminating Velocity Aliasing in Acoustic Doppler Velocity Profiler Data. *Measurement Science and Technology*, 17(2), 313-322.

Huppert, H.E. & Simpson, J.E. (1980). The Slumping of Gravity Currents. *Journal of Fluid Mechanics*, 99(04), 785-799.

Kneller, B. & Buckee, C. (2000). The Structure and Fluid Mechanics of Turbidity Currents: A Review of Some Recent Studies and Their Geological Implications. *Sedimentology*, 47(1), 62-94.

Lemmin, U. & Rolland, T. (1997). Acoustic Velocity Profiler for Laboratory and Field Studies. *Journal of Hydraulic Engineering*, 12, 1089-1098.

Lombardi, V., Adduce, C., Sciortino, G. & La Rocca, M. (2015). Gravity Currents Flowing Upslope: Laboratory Experiments and Shallow-Water Simulations. *Physics of Fluids*, 27(1), 016602.

Nogueira, H.I., Adduce, C., Alves, E. & Franca, M.J. (2013). Analysis of Lock-Exchange Gravity Currents Over Smooth and Rough Beds. *Journal of Hydraulic Research*, 51(4), 417-431.

Nogueira, H.I., Adduce, C., Alves, E. & Franca, M.J. (2014). Dynamics of the Head of Gravity Currents. *Environmental Fluid Mechanics*, 14(2), 519-540.

Nogueira, H.I.S., Adduce, C., Alves, E. & Franca, M.J. (2014). Dynamics of the Head of Gravity Currents. *Environmental Fluid Mechanics*, 14(2), 519-540.

Ooi, S.K., Constantinescu, G. & Weber, L. (2009). Numerical Simulations of Lock-Exchange Compositional Gravity Current. *Journal of Fluid Mechanics*, 635, 361-388.

Ottolenghi, L., Adduce, C., Armenio, V., Inghilesi, R. & Roman, F. (2013). Gravity Currents Moving on Up-Sloping Boundaries. *Journal of Hydraulic Engineering,* 139(6), 593-601

Paull, C.K., Ussler, W., Greene, H.G., Keaten, R., Mitts, P. & Barry, J. (2002). Caught in the Act: The 20 December 2001 Gravity Flow Event in Monterey Canyon. *Geo-Marine Letters*, 22(4), 227-232.

Rottman, J.W. & Simpson, J.E. (1983). Gravity Currents Produced By Instantaneous Releases of a Heavy Fluid in a Rectangular Channel. *Journal of Fluid Mechanics*, 135, 95-110.

Shin, J.O., Dalziel, S.B. & Linden, P.F. (2004). Gravity Currents Produced By Lock Exchange. *Journal of Fluid Mechanics*, 521, 1-34.

Theiler, Q. & Franca, M.J. (2016). Contained Density Currents With High Volume Of Release. *Sedimentology*, 63(6), 1820-1842.

Tokyay, T., Constantinescu, G. & Meiburg, E. (2011). Lock-Exchange Gravity Currents with a High Volume of Release Propagating Over a Periodic Array of Obstacles. *Journal of Fluid Mechanics*, 672, 570-605.

Xu, J.P., Noble, M.A. & Rosenfeld, L.K. (2004). In-Situ Measurements of Velocity Structure within Turbidity Currents. *Geophysical Research Letters*, 31(9), 1-4.

Zordan, J., Schleiss, A.J. & Franca, M.J. (2016). *Bed Shear Stress Estimation for Gravity Currents Performed in Laboratory*, *River Flow 2016*. Taylor & Francis Group, London, 855-861 pp.

SCALE MODEL MEASUREMENTS OF IMPACT FORCES ON OBSTACLES INDUCED BY BED-LOAD TRANSPORT PROCESSES

MICHAEL STURM[1], BERNHARD GEMS[2], MARKUS AUFLEGER[3], BRUNO MAZZORANA[4], MARIA PAPATHOMA-KÖHLE[5] & SVEN FUCHS[6]

[1, 2, 3] Unit of Hydraulic Engineering, University of Innsbruck, Innsbruck, Austria,
michael.sturm@uibk.ac.at; bernhard.gems@uibk.ac.at; markus.aufleger@uibk.ac.at
[4] Institute of Earth Sciences, Universidad Austral de Chile, Valdivia, Chile,
bruno.mazzorana@uach.cl
[5, 6] Institute of Mountain Risk Engineering, University of Natural Resources and Life Sciences, Vienna, Austria,
maria.papathoma-koehle@boku.ac.at; sven.fuchs@boku.ac.at

ABSTRACT

Flood events in mountain streams mobilize and transport large amounts of sediment and often lead to sediment depositions on densely populated alluvial fans. The impacts of these fluviatile hazard processes potentially lead to a substantial damage of buildings, infrastructure facilities, etc. The work presented deals with experimental measurements and calculations of impact forces on obstacles induced by fluviatile sediment transport processes. A physical scale model, consisting of a force plate in a homogeneous flume to measure the fluviatile impacts, was set up at the scale 1:30. Influence of different parameters on the impact forces, such as channel gradient, flow discharge, grain size distribution of the supplied sediment, concentration of bed-load within the flow mixture, the incident flow angle to the object and different dimensions of the object were tested. Correlations of measured flow depths and velocities with the impact forces were further analysed. A 3d-numerical model (FLOW-3D) of the experimental flume was built up and numerical analyses were executed to validate the measured data under clear water conditions. Thereby the suitability of Froude similarity to scale the measurement data into prototype dimensions was verified. The results show that in the majority of experimental scenarios, the sediment input leads to a decrease of the impact forces due to the lateral deflection of the flow mixture in front of the plate, induced by the sediment deposition. However, the applicability of a 3d-numerical modelling approach to calculate impact forces of fluviatile hazards on obstacles is verified for clear water conditions. The study provides valuable information for further and more complex experiments on the fluviatile hazard impacts on buildings, associated analysis of consequences for buildings stability and serviceability, and vulnerability analysis of buildings exposed to fluviatile hazard events.

Keywords: Bed-load transport; physical scale model; impact force; fluviatile hazards; vulnerability.

1 INTRODUCTION

The detailed analysis and simulation of complex hydrodynamic flow processes is a very challenging task in hydraulic engineering. Besides the use of numerical modelling techniques, the application of physical scale model tests is a reliable tool when dealing with different hydraulic problems. Complex three-dimensional hydrodynamic flow processes featuring also sediment transport, can hardly be described with currently available numerical models (Gems et al., 2016). These processes require large calculation effort and the knowledge of several model parameters and accurate measurement data. Since appropriate real-scale data for model calibration and validation is often very limited, experimental modelling enables the extension of available databases for the application of numerical models. However, laboratory experiments are subjected to model-related simplifications and assumptions. Scaling effects, which inevitably emerges when representing complex flow processes at small model scales, and the transformation of modelling results to real-scale conditions according specific scaling-laws, have to be carefully considered.

Dynamic flow processes and the influence of sediments during fluviatile hazard events, debris floods and flows substantially influence damaging impacts on buildings located on alluvial fans (Fuchs et al., 2007; Mazzorana et al., 2014). Characteristics and impacts of fluviatile hazards depend on the properties of the triggering rainfall, the topography, the sediments and soil characteristics of the catchment, and of the quality and geometry of the elements at risk. Large amounts of mobilized sediments have a considerable high impact on the damages of buildings, infrastructure facilities and etc.. Available approaches for the calculation of dynamic flow processes are typically based on the determination of the static and dynamic forces in undisturbed conditions (Bergmeister et al., 2009). Any influences of obstacles on the characteristics of the flow field or, vice versa, fluid impacts on objects in the flow are not considered. Disturbed flow conditions in close vicinity to obstacles are very complex due to the three-dimensional expansion of the flow process. Several studies focused on the analysis of the flow process (e.g. Spinewine et al., 2003; Armanini et al., 2010) or the experimental modelling of debris flow (Scheidl et al., 2013). Nevertheless, information on the interaction between the process and the buildings is still scarce.

The work presented in this paper illustrates results from a physical scale model test dealing with the analysis of forces impacting a vertical plate under clear water conditions and with fluviatile bed-load transport. The main influencing parameters on the impacts are illustrated. The application of a 3d-numerical model, which is firstly aimed at the reconstruction of the experimentally analysed scenarios, and the corresponding simulation results are further presented. Secondly, the scalability of the measurement data from the physical model to real-scale dimensions is verified by the use of the calibrated numerical modelling. Moreover, a brief overview on current experiments on a larger scale model, focusing on the alluvial fan of the Schnannerbach torrent in Austria (Gems et al., 2014), is provided. The results of the presented study are further used for vulnerability analysis of buildings against torrential hazards (Fuchs et al. 2007; Papathoma-Köhle et al., 2012; Totschnig and Fuchs, 2013). The findings deliver a valuable contribution to the planning of local protection structures on flood-prone, steep alluvial fans as well as for any organizational and spatial planning action strategies.

2 MODELLING

2.1 Physical scale model (1:30)

The physical scale model consisted of a homogeneous flume with 0.5 m width, in which a vertical plate and a pressure sensor was mounted (Figure 1). In view of further investigations, the geometric scale of the model was set to 1:30. Essentially, the model consists of a homogeneous channel with an adjustable ramp to enable specific channel gradients between 4 % and 15 %. The model was built mostly with wooden and Plexiglas panels. As a consequence of the model construction and in order to simplify the measurement conditions and the calibration procedure of the numerical model, the roughness in the channel was very low. A highly sensitive sensor which allows for the three-axial measurement of impact forces was arranged in the flume (Figure 1). A vertical plate was mounted on the sensor in a way that impacts of the flow field on the plate can be measured at a high temporal resolution up to 200 Hz. The force plate can be mounted at different angles to the flow direction and also features different dimensions. Figure 1 shows a sketch of the scale model. Flow field measurements (flow velocities and depths) were executed during the experiments in order to analyse correlations between these data and the impact forces. The flow depths in the unaffected flow are rather low. Therefore, measurements were also accomplished in the impounded flow field in close vicinity to the vertical plate and further considered within the data analyses. PIV (Particle Image Velocimetry) measurements (Thieleke and Stamhuis, 2014) are identified as a valuable method to measure the flow velocities in the channel. Therefore, small swimming tracer elements are added to the flow and their flow velocities are tracked with a camera. The records are subsequently evaluated with PIV analysis methods (Thieleke and Stamhuis, 2014). Experiments were carried out under steady-state conditions and for a set of specific discharges in the flume.

The sediment load was added manually during the experiments. Therefore, the influence of different sediment concentrations and grain sizes on the impact forces was analysed. The physical model delivers results for basic research.

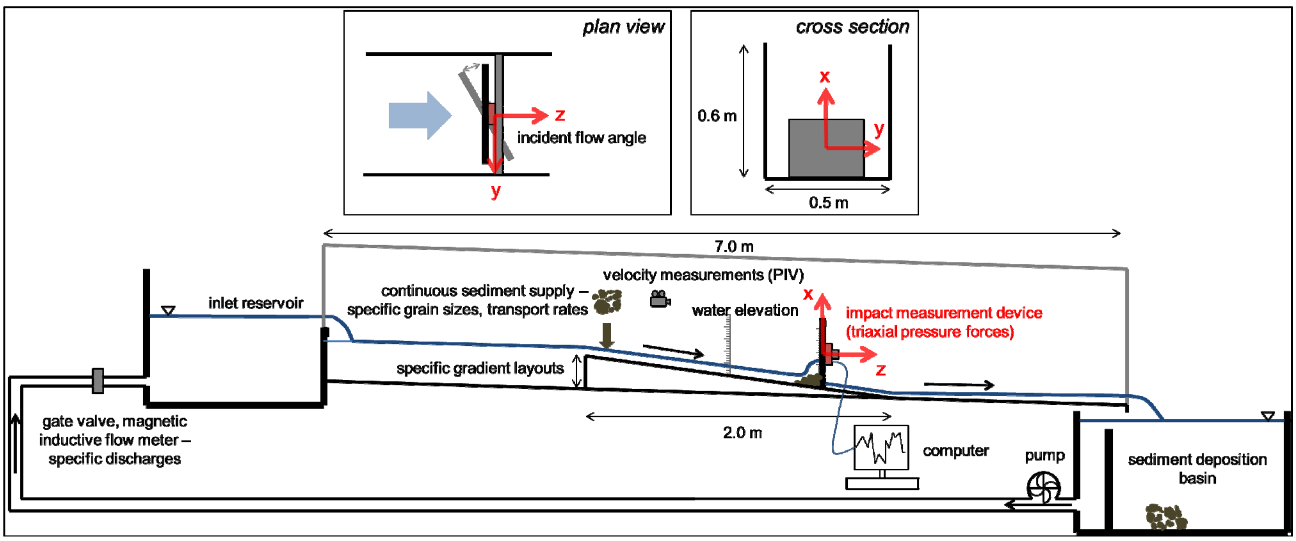

Figure 1. Sketch of the physical scale model.

Further analysis on a larger scale model, covering a torrent channel with the adjacent settlement area on an alluvial fan (Schnannerbach torrent, Austria) and building structures, which are analogously equipped with measurement devices, is currently under progress.

2.2 3D-numerical model (FLOW-3D)

For the numerical simulation of the laboratory experiments with the software FLOW-3D (Flow Science Inc., 2012), two models are set up. The first numerical model exactly reflects the dimensions of the experimental flume. In order to provide simulation results with a high spatial resolution in close vicinity to the vertical plate and the impounded flow field, the grid size of the computational mesh was set to 0,0025 m in close vicinity of the obstacle, whereas elsewhere it was set to 0,01 m in all three dimensions. The computational mesh of this model features a total number 3.17 million cells which constitutes a reasonable compromise between calculation accuracy and computational effort. At first, a calibration procedure was accomplished by adjusting the roughness parameter of the flume. Measured flow depths, inflow heights at the vertical plate and the flow velocities in the undisturbed flow field further upstream are considered as indicating parameters for the calibration.

The second numerical model was used to calculate the real-scale impacts on objects and to verify the transferability of the measurement data (scale 1:30 according Froude similarity) to real-scale dimensions. The model corresponds exactly to the scaled original model. The geometric dimensions of the computational grid were also scaled accordingly. Scaling of the roughness parameter was the main challenge associated with the calibration of the model. However, a corresponding roughness coefficient for the numerical model could also be determined in real-scale dimensions since the measured flow depths and velocities being scaled with Froude similarity are considered. Finally, the calculated impact forces of the first model, accordingly scaled by Froude similarity, were compared to the calculated impact forces of the second model.

As a part of the computational analysis, the influence of a changing structural roughness due to the processing of the terrain model with computational grids of different resolution (spatial discretization) was identified. Independence of modelling results from the computational mesh was not entirely provided, since there were marginal differences in the calculation of the impact forces. However, these differences were very small and thus not relevant for any further data analysis.

2.3 Investigation procedure

The investigations presented within this paper were divided in three main sections. Firstly, the results of the clear water experiments at the physical scale model are described (i). Secondly, the results of the numerical clear water simulations (FLOW-3D) are illustrated for both numerical models (ii) and, thirdly, the main findings of the experiments with sediment supply are introduced (iii). The boundary conditions of the physical scale model (discharges, concentrations of supplied sediment, grain sizes) as well as the tested channel gradients were chosen with regard to further investigations at the larger model of the Schnannerbach torrent. The mentioned input parameters and the channel gradient were derived from information related to the Schnannerbach flood event in 2005 (Rudolf-Miklau et al., 2006). Corresponding experimental analyses for the event reconstruction at the Schnannerbach torrent and the definition of sufficient structural protection measures in close range to the confluence with the receiving water course (Gems et al., 2014) deliver further valuable data for the experiments.

i. Clear water experiments

First of all, the laboratory flume was tested under steady-state, clear water conditions. Scale model experiments commonly feature specific challenging tasks. In this case, the appropriate use of the very sensitive sensor device to measure the impact forces was challenging but essential for the further procedures of the study. Simple clear water experiments provide first insights to be considered in further, complex experiments with sediment supply. Another task of these experiments was to show the possibilities of measuring forces in the flow to collect a sufficient data set under clear water conditions and to use them for the correlation of impact forces and flow depths (velocities). The measurement data was the basis for the numerical model calibration, embraced in the following section. Therefore, different discharges from 1 l/s to 10 l/s were analysed. These discharges were combined with different channel gradients within the range 4 % - 15 %. For the gradient of 13 %, the angle of the vertical plate related to the flow direction was also varied between 90° and 45°.

ii. 3d-numerical simulations

Based on the geometry of the experimental flume, numerical calculations were executed. Model calibration mainly focused on the measured flow depths and velocities. The calculated impact forces were then compared to the measurements. Further, the scalability of the impact forces according Froude similarity was verified. Stability of the calculations and mesh independence was further analysed. By the use of the calibrated numerical model, a larger set of model parameters and boundary conditions could be considered in terms of resulting impact forces on the vertical plate related to the experiments. Exemplary results from numerical modelling were presented herein.

iii. Experiments with sediment supply

Additional scenarios were analysed considering the supply of sediment. Further boundary conditions, such as the sediment concentration to the clear water discharge and the grain sizes were considered. The sediment concentration was limited to the transport capacity of the flume and ranges between 0 % and 15 % of the clear water discharge, depending on the channel gradient, the discharge and the grain sizes. Three different grain sizes (0.5 mm - 1.0 mm, 3.2 mm - 5.0 mm, 5.0 mm - 8.0 mm) were tested. Combinations of these input parameters with the different boundary conditions mentioned in the previous section deliver a large number of experiments and, accordingly, a large data set. The total sediment load of 50 kg was the same for each experiment. Depending on the different sediment concentrations, the experiment durations range between 50 s and 9.5 min.

3 RESULTS

3.1 Clear water experiments

There are always certain fluctuations in the water circulation system in the hydraulic laboratory, even at steady-state discharges. For this reason the results from the clear water experiments as shown in Figure 2 were illustrated in terms of boxplots. The minimum and maximum measured normal forces as well as the corresponding 25/75-percentiles and mean values were illustrated for every configuration of input and model parameters.

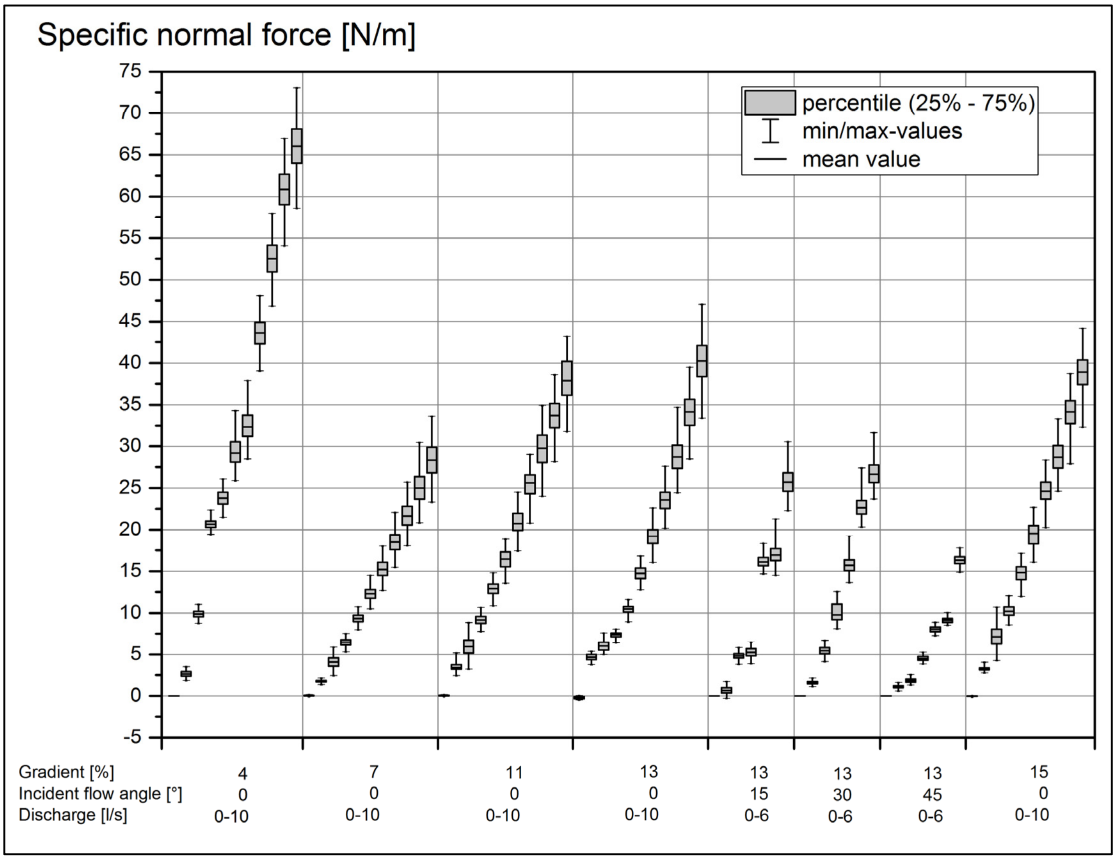

Figure 2. Resulting impacts (specific normal forces) on the vertical plate from the clear water experiments as a function of channel gradient, incident flow angle and discharge (laboratory dimensions, scale 1:30).

The results in Figure 2 were mainly divided into different gradient conditions and incidental flow angles. For every gradient, the measured (specific) normal forces are sorted according to the ascending impacting discharge. The clear water experiments show a clear relation of the measured normal forces with the impacting discharges. Fluctuations of the measured forces substantially increase with increasing discharge. Accordingly, an increase of fluctuations of the flow heights at the vertical plate could be observed with increasing discharge. Nevertheless, the measured data set was robust, both, in terms of accuracy and precision. The fluctuations induced by the construction of the plate and the sensor device itself can be assessed by analysing the measured forces at the discharge of 0 l/s in Figure 2. Further, the impact forces increase with increasing channel gradient, but the differences between the results for the gradients of 13 % and 15 % were marginal. The apparently higher impact forces at the gradient of 4 % result from a substantially pronounced backwater effect at the vertical plate. Furthermore, the width of the force plate in these experiments (gradient of 4 %) was set to 0.3 m, which was in contrast to the width of 0.2 m for all other experiments. However, the measurement results illustrated in Figure 2 were provided in terms of specific normal forces, characterizing the relation of the total impacts to the width of the plate. They are thus not instantly depending on the width of the plate. Incident flow angles reduce the normal forces due to the smaller projected area in flow direction. The higher the incident flow angle, the higher was the fraction of the total impact force which was deviated to the force in parallel direction to the plate. The shear forces in general were low. They marginally increase with increasing incident in flow angle.

In general, the static component of the total impact force was higher at lower channel gradients. The same holds for the dynamic component of the impacts, which is correlated with the flow velocity in the channel, at higher channel gradients. A relation of the measured flow depths in the undisturbed flow field and the flow velocities with the measured forces was shown in Figure 3. For the flow velocities, the numerical calculation results were also considered in the diagram. Thereby, post-processing was accomplished at different heights in the flow field. The calculated velocities showed good accordance with the measured data at flow depths close to the water surface.

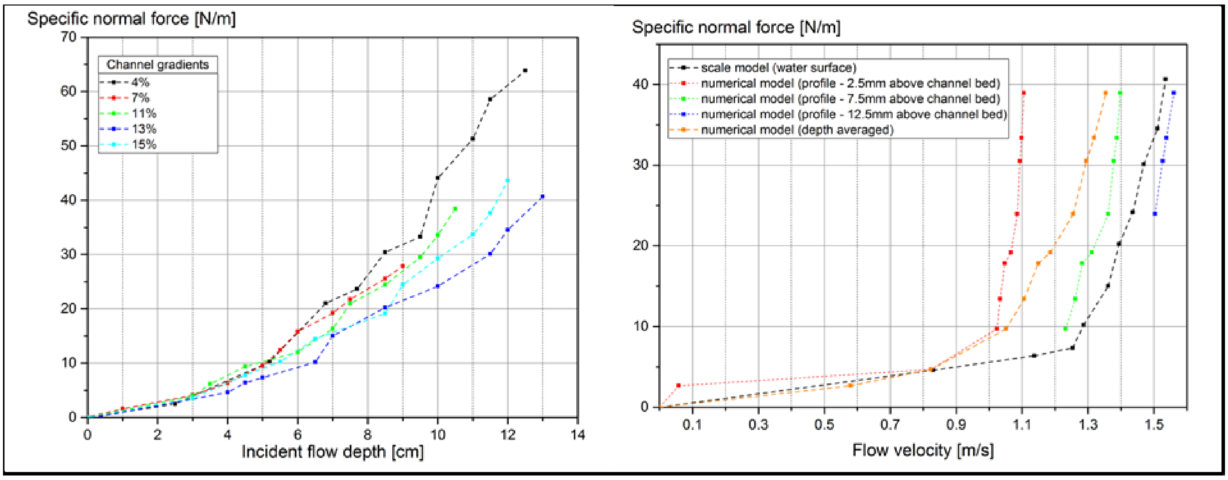

Figure 3. Specific normal forces under clear water conditions in relation to the flow depths in the undisturbed flow field (left) and the flow velocities (right) (laboratory dimensions, scale 1:30).

3.2 3d-numerical simulations

The 3d-numerical model in laboratory dimensions was calibrated on the measured flow depths and velocities. Therefore, the roughness parameters were considered as an important calibration parameter. The final results of the calibration show a good accordance with the flow depths and velocities. Figure 4 shows the comparison of selected results from experimental modelling and numerical simulation. First, the quantitative comparison of flow depths at the plate firstly considers values from experimental modelling. They were delivered from the video documentation, analysed in terms of mean flow depths along the entire plate width and, due to the marginal fluctuations in the water circulation system, within a short duration of steady-state flow conditions. Secondly, results from numerical modelling contain spatially variable flow depths from the steady-state condition in the flume. The flow velocities in the experimental setup could only be measured at spots where tracers were in the moment of detection. Those spots were used for calibration (see also Figure 3).

After model calibration, the accomplished experiments were simulated numerically and the impact forces on the plate are compared. The comparison of the calculated and the measured impact forces shows a good accordance (Figure 5). Obviously, the fluctuation of the measured data was more significant but the calculated forces mostly range clearly within the fluctuation range of the experimental setting. Further detailed numerical calculations were executed to prove the suitability of Froude similarity to scale the dynamic impact forces to real-scale dimensions. Simple calculation approaches for flow pressures use a static and a dynamic component (Bergmeister et al., 2009), mostly depending on the flow depths and flow velocities. Froude similarity uses different conversion factors for these parameters. For this analysis, the results of the numerical calculations were scaled to prototype dimensions (1:30). They were further compared to those from the calculations with the second, calibrated numerical model at real-scale dimensions. The comparison of these results shows a very close accordance. Small differences were evidentially induced by the grid resolution of the computational mesh. So the calculation results clearly show the suitability of Froude similarity to convert the experimentally measured data to real-scale dimensions (for further details see Sturm et al., in press).

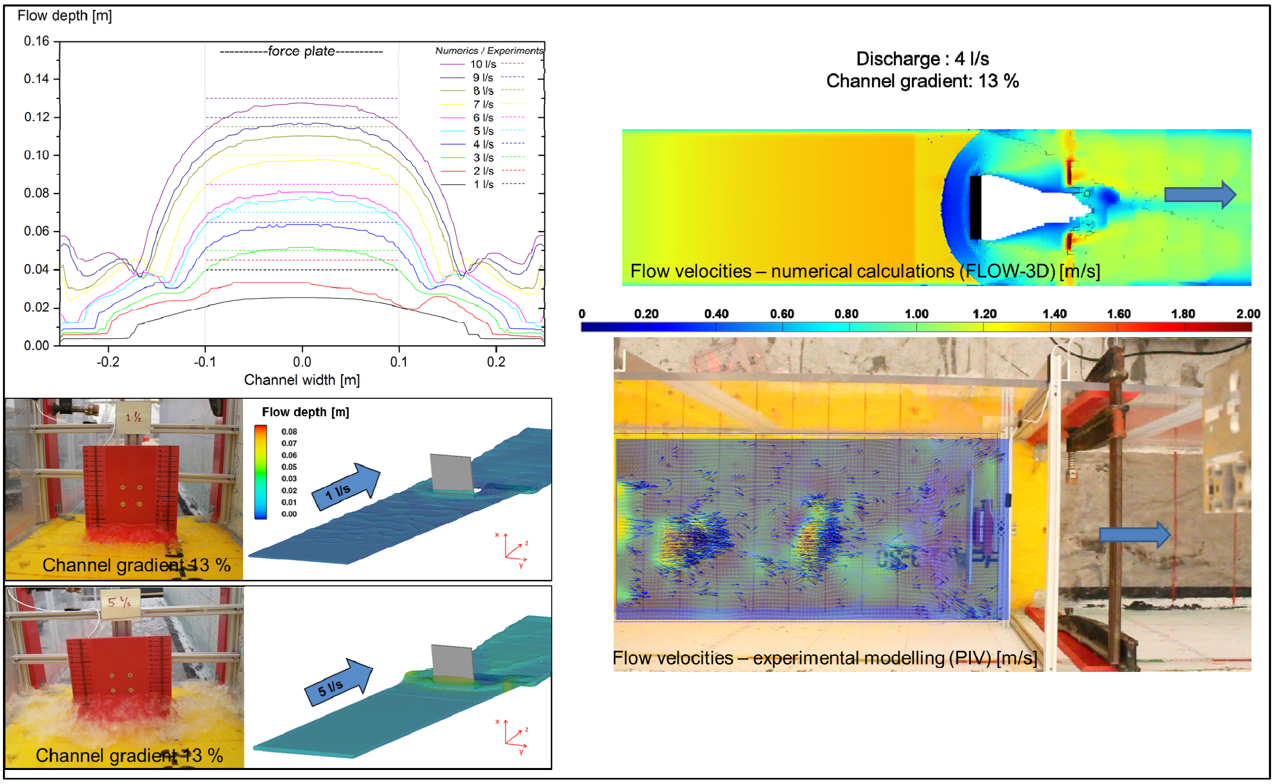

Figure 4. Results from numerical model calibration using the experimentally measured flow depths (left) and velocities (right) (laboratory dimensions, scale 1:30).

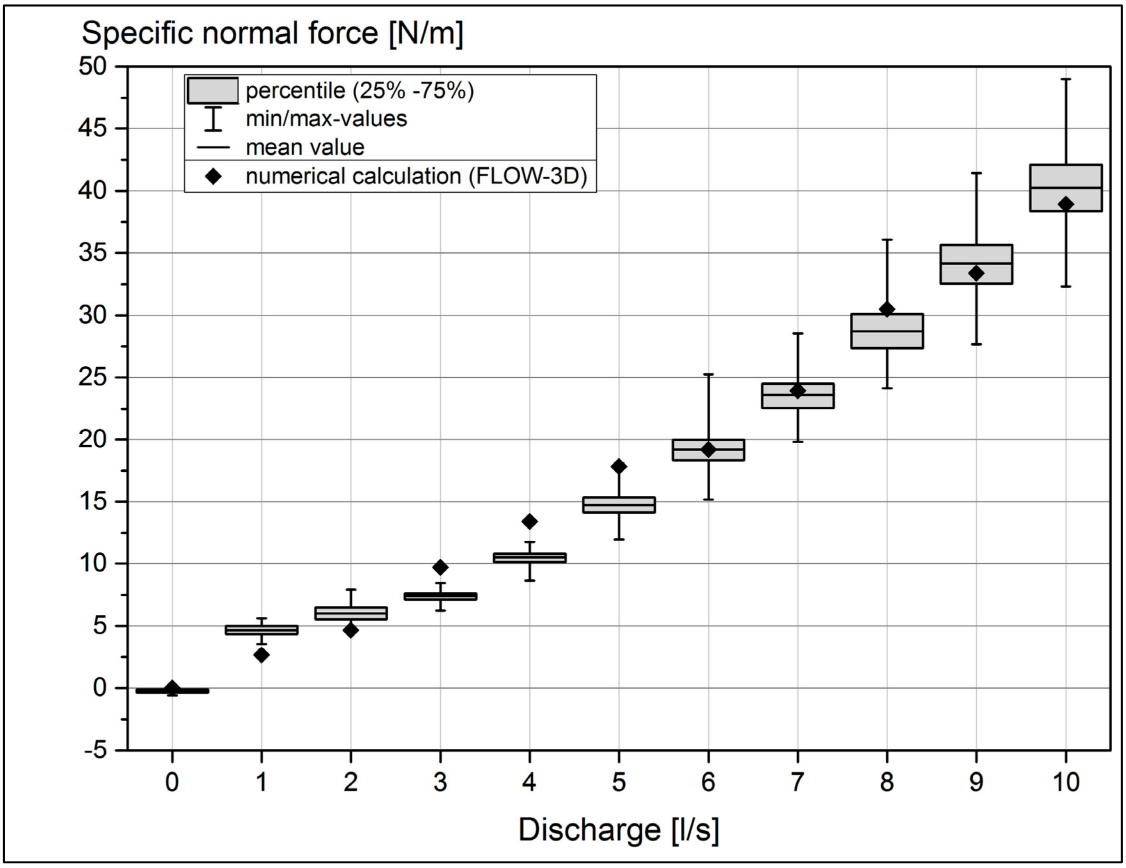

Figure 5. Comparison of the measured specific normal forces under clear water conditions from the physical scale model test and the numerical calculations at a gradient of 13 % (laboratory dimensions, scale 1:30).

3.3 Experiments with sediment supply

The observed processes under sediment-loaded conditions were much more complex and lead to a variety of resulting impacts on the vertical plate. An example of the recorded impact forces for a specific experiment is shown in Figure 6. This experiment was considered to be representative for one typically observed process phenomenon. Every experiment was divided in three parts. Firstly, steady-state clear water conditions in the flume were set. Subsequently, sediment was manually and constantly supplied to the steady-state discharge at the upstream model boundary (roughly 2 meter upstream the vertical plate). After a sufficient duration of sediment supply, which ensured a robust analysis of the impact forces and its fluctuation margins, sediment supply was stopped and the steady-state conditions were continued until the flume was in its original condition as before the sediment supply.

The three-dimensional impact forces on the plate and screenshots of the plate and the incidental flow field at three specific time steps, as well as the boundary conditions and input parameters for this experiment were illustrated in Figure 6. With regard to the three different conditions in the flume during the experiments with sediment supply, the three pictures clearly show different deposition states in front of the plate during an experiment. Sediment deposition in front of the plate leads to a deflection of the flow and a reduction of the incidental flow heights. As a consequence, the impact forces decrease. This behaviour could be observed in many of the experimental results, especially at conditions with low channel gradients and discharges. For higher discharges, the reduction of the impact forces due to the sediment supply was smaller. Fluctuations of the force measurements increase with increasing discharge. After stopping sediment supply the deposited sediment was flushed and the impact forces stabilize at the level of the clear water impacts.

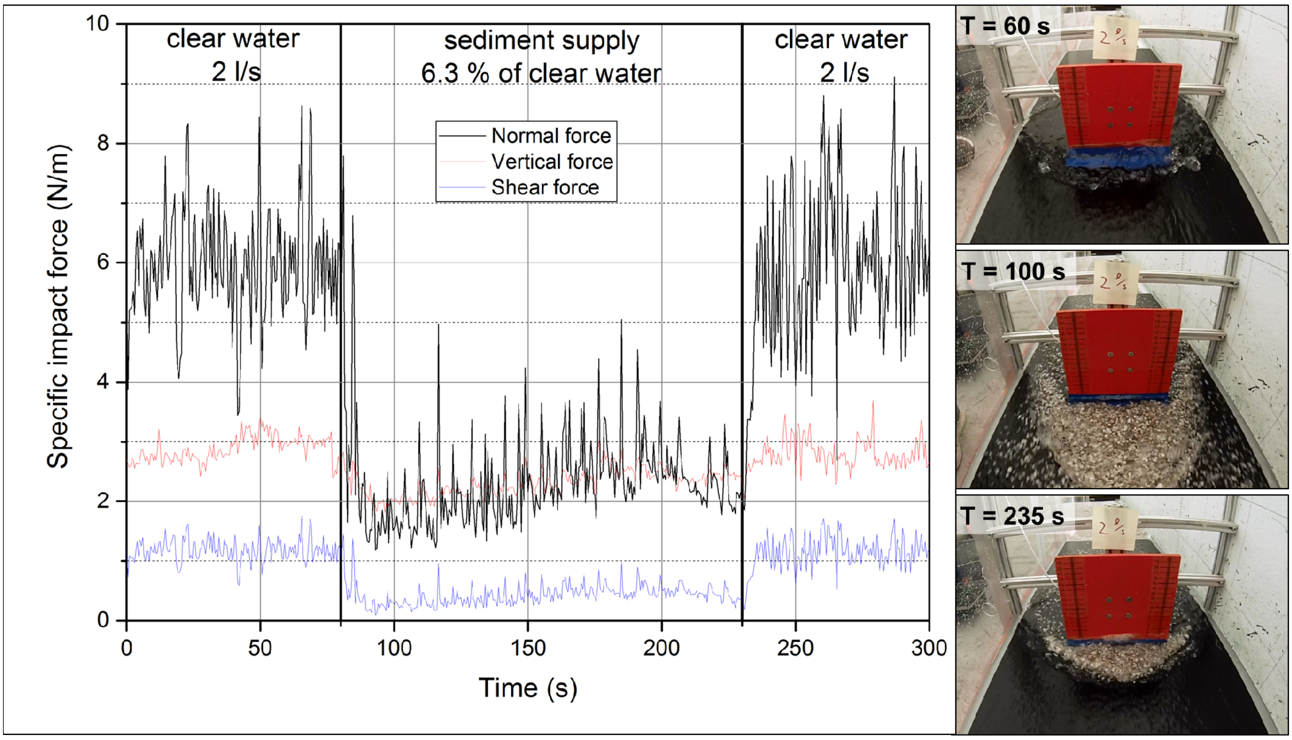

Figure 6. Specific impact forces in relation to the duration of the experiment and under the influence of sediment supply (channel gradient: 11 %; grain size of supplied sediment: 3.2 - 5.0 mm) (laboratory dimensions, scale 1:30).

Figure 7 shows the summary of a large amount of experimental results for four specific channel gradients. All four box plot diagrams show the specific normal forces on the plate, which were categorized according to the prevailing channel discharge. For a certain discharge, the results were further sorted in ascending order according the concentration of the supplied sediment. A small note was added in the box-plots, indicating which grain sizes were considered for the supplied sediment. For the gradient of 13 %, only one grain sizes were used and a larger set of sediment concentrations and discharges was analysed. The results show, that for a large amount of data sets, the impact forces under sediment loaded conditions were lower than the impact forces under clear water conditions. The reason is that the deposition of the sediment in front of the plate leads to a deflection of the flow and a reduction of the impact forces (compare Figure 6). As observed, the sediment velocities were substantially reduced in vicinity to the vertical plate. In some cases, sediment deposition in the backwater occurs without even touching the vertical plate. This effect was more pronounced with lower channel gradients. Beside the mentioned effect of deflecting flow and decreasing impact forces enables us could observe increased impact forces due to the influence of sediment transport.

This was because the deposition in the channel leads to higher impacts due to the canalization of the flow in the direction of the plate. It is clear that the fluctuations of the measurements were more pronounced in the sediment experiments rather than in the clear water experiments.

The influence of different sediment parameters, such as the sediment concentration and the grain size distribution on the impact forces seems to be rather small. The impact forces were highly influenced by the deposition in the channel which affects the flow and the specific flow in different areas. The deposition patterns vary for different grain sizes, but no clear influence on the impact forces could be detected. Depositions of finer sediments lead to a faster deflection of the flow, because these depositions seem to be more compact and stable than the ones of coarser sediments. After sediment supply was stopped, finer sediments got mobilized much faster. The duration of the experiments plays a minor role on the impact forces in the steady-state conditions as Figure 6 clearly demonstrates. A longer duration of sediment supply does not relevantly influence the measured impact forces.

Fluviatile transport processes differ fundamentally from debris flow, in particular with respect to the sediment concentration in the fluid-sediment bulk and flow behaviour. The presented experimental modelling results were clearly restricted to fluviatile processes. The sediment transport capacity of the channel is limited, mainly depending on the channel gradient, the impacting discharge (shear stress) and the grain sizes. In some of the experiments, the transport capacity of the flume was reached. Experiments with higher sediment concentrations lead to depositions in the channel section upstream the vertical plate, so they were not further considered for the analysis of the impact forces on the plate.

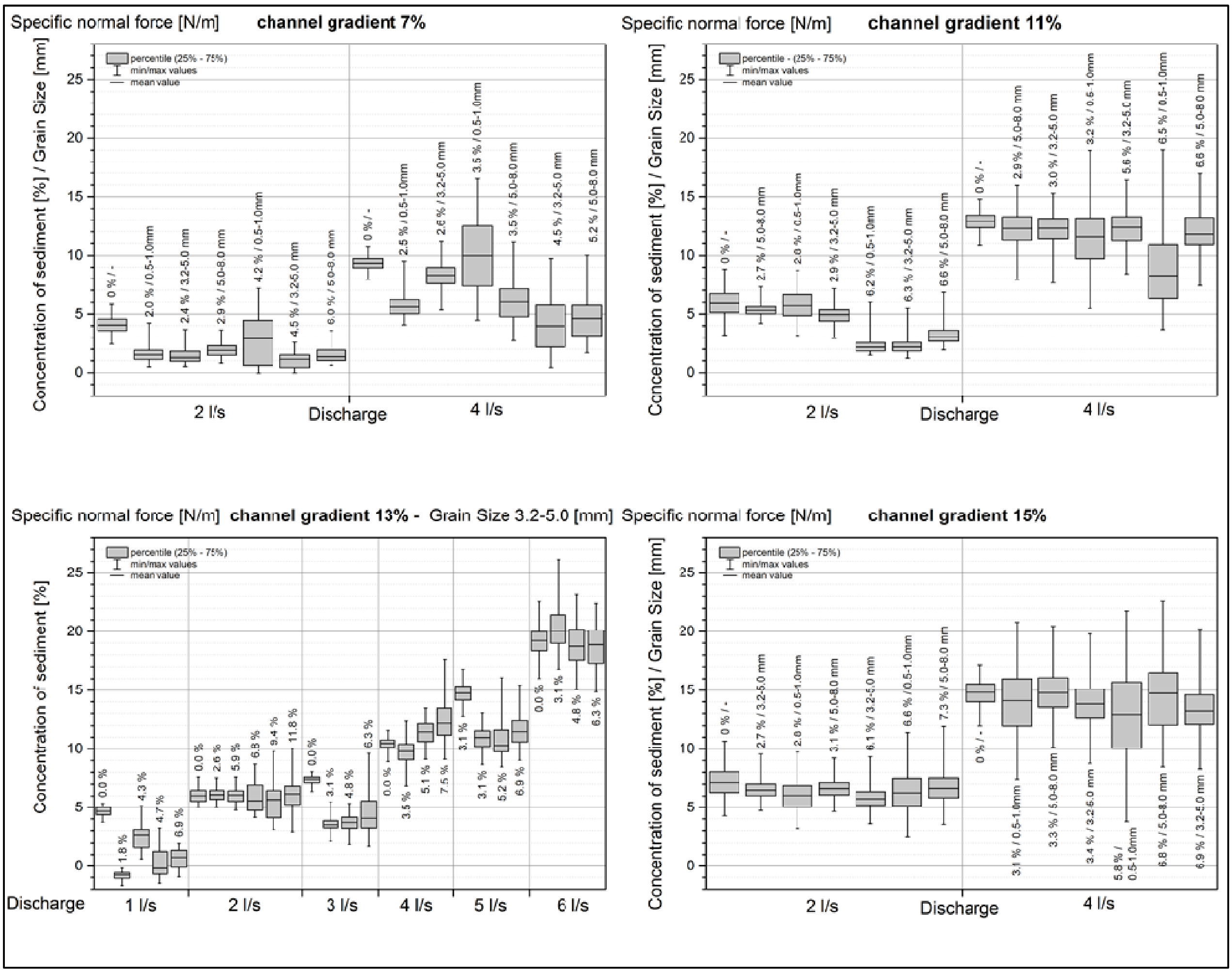

Figure 7. Compilation of specific normal impact forces due to fluviatile transport processes with different parameters: channel gradient, discharge, concentration of sediment, and grain size.

4 CONCLUSIONS AND OVERVIEW OF CURRENT EXPERIMENTS

The conducted investigations showed the possibilities of measuring complex impact forces on objects in the flow under clear water and sediment transport conditions. Further, the applicability of three dimensional, numerical calculations (FLOW-3D) to calculate impact forces is verified.

Clear water experiments show an evident relation between flow height and velocity in the undisturbed flow field and the impact forces on the plate (Figure 3). The discharge and the channel gradient are identified as the most influential parameters on the impact forces (Figure 2). However, the influence of the channel gradient on the impact forces decreases with increasing gradient. Impact forces at real-scale dimensions are in general difficult to measure. Moreover, limited information on the impacts of fluviatile hazard events on objects is currently available. The scale model itself proves to be a useful method to determine impact forces on objects under different boundary conditions. Flow depths and velocities can be captured. For that purpose, relations between these process indicators and the impact forces could help to estimate forces in nature.

The numerical modelling results are in accordance with the scale model results with high accuracy under appropriate model calibration (Figures 4 and 5). Even though 3d-numerical modelling deals with complex mathematics and numerical methods, the model setup in FLOW-3D is rather simple and less costly compared to experimental modelling. Numerical modelling, however, requires data for calibration. To determine the complex flow processes in the backwater of the plate the use of a three-dimensional numerical model is mandatory. For clear water conditions, the applicability of the model to calculate the impact forces and the flow behaviour in close range to the obstacle is verified. With the numerical model, Froude similarity to transfer the measurements to other scales is proven (for further details see Sturm et al. in press).

The impacting sediment processes increase the forces on the plate only in a few experiments, where the flow paths in the channel are essential. A large number of experiments show that the sediment leads to a decrease of the impact forces due to the deflection of the flow through the sediment deposition in front of the obstacle (Figure 7). The influence of sediment concentrations and grain sizes on the impact forces is low and there is no clear relation between those two input parameters and the measurement results. Different discharges and channel gradients influence the flow and deposition processes in the channel and in front of the plate and further the forces on the plate (Figure 6). By means of these findings, the shaped flow paths are identified as the most influential factor on the forces. Besides simple calculation approaches, the introduced investigations deliver information about impact forces depending on several indicators and support the estimations of impact forces during flood hazard scenarios on steep alluvial fans. In this context, it should be mentioned, that all of the executed experiments with sediment transport represent fluviatile transport processes. Debris flows feature entirely different flow behaviour and are thus not comparable with the introduced experiments. Several investigations about debris flows describe influential parameters at debris flow impacts (e.g. Scheidl et al., 2013). The introduced investigations aim at the determination of impact forces of fluviatile processes. Other damaging effects like the abrasion of wall elements caused by sediment impact, the stability of walls due to undermining or the damages caused by sediment deposition are not considered. For that reason a more general statement on the influence of sediments, e.g. that sediment supply reduces impact forces and consequently also reduces the expected damages, is not the case.

The investigations described in this paper intentionally feature a rather simple model setup with simple boundary conditions. To draw more accurate and substantiated conclusions about impacting sediment transport processes on obstacles, further research on models with more complexity and variability in geometry, etc. has to be executed. A more complex experimental model, featuring the alluvial fan of the Schnannerbach torrent (Gems et al., 2014) and building structures is set up, and the corresponding experiments are currently under progress. The models of selected buildings, which were damaged in the 2005-flood event, are equipped with measurement devices to analyse the impact forces on the wall elements of these buildings. Further, the material intrusion processes will be investigated, which is evaluated as another influential factor on damage causing mechanisms (Mazzorana et al., 2014; Gems et al., 2016). Different objects on the experimental alluvial fan, such as other buildings and single protection measures will be installed, to analyse the most influential parameters identified in this research such as the channelization and the deflection of the flow.

Using the knowledge on the impact forces on buildings caused by fluviatile flood events, the calculations of structural mechanics are executed to verify the serviceability and the sustainability of a building. The results are essential for physical vulnerability analysis. The latter is commonly based on the development of curves that express the relationship between the degree of loss and the height of the debris or fluid (Fuchs et al. 2007; Papathoma-Köhle et al., 2012; Totschnig and Fuchs, 2013). The present study provides information on additional characteristics of the process such as the impact force. The modelling results constitute a valuable input for any planning tasks in flood risk management. Additionally, the presented results may support hazard zone planning and analysis on the design of local structural protection measures as well as the design of disaster risk reduction strategies on local level.

ACKNOWLEDGEMENTS

The study is part of the project “Vulnerability analysis of buildings exposed to torrent hazards – small-scale experimental modelling of impacts on buildings and derivation of physics-based vulnerability functions”, funded by the Austrian Science Fund (FWF; P27400-NBL).

REFERENCES

Armanini, A., Larcher, M. & Odorizzi, M. (2010). Dynamic Impact of Steep Waves against a Vertical Wall. *Proceedings of First European IAHR Congress*, Edinburgh, 4-6.

Bergmeister, K., Suda, J., Hübl, J. & Rudolf-Miklau, F. (2009). Schutzbauwerke gegen Wildbachgefahren: Grundlagen, Entwurf und Bemessung, Beispiele, John Wiley & Sons. (in German)

Flow Science Inc. (2012). *FLOW-3D, v10.0, user manual*.

Fuchs, S., Heiss, K. & Hübl, J. (2007). Towards an Empirical Vulnerability Function for use in Debris Flow Risk Assessment. *Natural Hazards Earth System Sciences,* 7, 495-506.

Gems, B., Mazzorana, B., Hofer, T., Sturm, M., Gabl, R. & Aufleger, M. (2016). 3-D Hydrodynamic Modelling of Flood Impacts on a Building and Indoor Flooding Processes. *Natural Hazard Earth System Sciences,* 16, 1351-1368.

Gems, B., Sturm, M., Vogl, A., Weber, C. & Aufleger, M. (2014). Analysis of Damage Causing Hazard Processes on a Torrent Fan – Scale Model Tests of the Schnannerbach Torrent Channel and its Entry to the Receiving Water. *Conference Proceedings of Interpraevent 2014 in the Pacific Rim,* Nara.

Mazzorana, B., Simoni, S., Scherer, C., Gems, B., Fuchs, S. & Keiler, M. (2014). A Physical Approach on Flood Risk Vulnerability of Buildings. *Natural Hazards Earth System Sciences,* 18, 3817-3836.

Papathoma-Köhle, M., Zischg, A., Fuchs, S., Glade, T. & Keiler, M. (2015). Loss Estimation for Landslides in Mountain Areas – An Integrated Toolbox for Vulnerability Assessment and Damage Documentation. *Environment Modeling and Software,* 63, 156-169.

Rudolf-Miklau F., Ellmer, A., Gruber, H., Hübl, J., Kleemayr, K., Lang, E., Markart, G., Scheuringer, E., Schmid, F., Schnetzer, I., Weber, C. & Wöhrer-Alge, M. (2006). Hochwasser 2005 – Ereignisdokumentation, Teilbericht der Wildbach- und Lawinenverbauung, Vienna (in German)

Scheidl, C., Chiari, M., Kaitna, R., Müllegger, M., Krawtschuk, A., Zimmermann, T. & Proske, D. (2013). Analysing Debris-Flow Impact Models, Based on a Small Scale Modelling Approach. *Surveys in Geophysics,* 34, 121-140.

Spinewine, B., Capart, H., Larcher, M. & Zech, Y. (2003). Three-Dimensional Voronoi Imaging Methods for the Measurement of near-Wall Particulate Flows. *Experiments in Fluids,* 34, 227-241.

Sturm, M., Gems, B., Mazzorana, B., Gabl, R. & Aufleger, M. (2017). Validierung experimenteller und 3-D-numerischer Untersuchungen zur Einwirkung hydrodynamischer Fließprozesse auf Objekte (Validation of Physical and 3-D-Numerical Modelling of Hydrodynamic Flow Impacts on Objects), *WasserWirschaft* (in German).

Thieleke, W. & Stamhuis, E.J. (2014). PIVlab – Towards User-friendly, Affordable and Accurate Digital Particle Image Velocimetry in MATLAB. *Journal of Open Research Software,* 2(1), 1-30.

Totschnig, R. & Fuchs, S. (2013). Mountain Torrents: Quantifying Vulnerability and Assessing Uncertainties. *Engineering Geology*, 155, 31-44.

CHARACTERISTICS OF HYDRAULIC JUMPS BELOW DROP STRUCTURES

YOUICHI YASUDA[1]

[1]Nihon University, College of Science and Technology, Dept. of Civil Engineering, Tokyo, Japan,
yasuda.youichi@nihon-u.ac.jp

ABSTRACT

The free hydraulic jump in a rectangular channel has been investigated experimentally. Most of jumps are formed by using either sluice gate or gate nozzle (e.g., jet box). If the jump is formed at the immediate downstream of drop structure, the effect of curvature of stream-line at the toe of jump on velocity field in the jump might not be neglected. In this case, a high velocity turbulent flow continues near the bottom far downstream. Also, the velocity at the center line of the channel might not be represented as characteristics of the jump below the drop. From practical view point of hydraulic design, the jump formation at the downstream of drop structure should be studied precisely. This paper presents velocity fields in jumps at downstream of drop structures on the basis of velocity profiles, time averaged on maximum velocity decays, and the development of main flow in hydraulic jumps. Six different kinds of drop structures are utilized. In the jump region, three dimensional velocity profiles have been distributed by the formation of shock wave downstream of impingement point and also velocity profile like a wall jet has been continued until about 90 % of jump length. When the approaching supercritical flow is disturbed by the curvature of streamline, time averaged maximum velocity of main flow at each vertical section decays in a short distance is later compared with the case of a classical hydraulic jump. And, the main flow in the jump region does not lift to water surface, even if the turbulent boundary layer at the toe of the jump is developed. If the relative drop height becomes lower, the main flow continues along the bottom far downstream. In this case, the velocity profile is distributed as a wall jet in the jump region.

Keywords: Hydraulic jump; energy dissipater; hydraulic structures; drop structure; velocity profile.

1 INTRODUCTION

Free hydraulic jump in a horizontal rectangular channel has been investigated by many researchers (Hager, 1992; Liu and Rajaratnam, 2004; Novak et al., 2007; Ohtsu, 1976; Rajaratnam, 1967). In order to clarify jump characteristics, most of jumps were formed by using either sluice gate or gate nozzle (e.g., jet box) (Hager, 1992, Ohtsu et al., 1990; Vischer and Hager, 1995). From practical point of view, the jump has been utilized to dissipate a high velocity flow at downstream of drop structure (Bradley and Peterka, 1957; Peterka, 1978; The US Army Corps of Engineers, 1995). According to experimental investigations on free jump below sluice gate, if the turbulent boundary layer at the toe of jump was fully developed, the main flow in the jump lifts to the water surface from 60 % of jump length (Ohtsu, 1976; Ohtsu et al., 1990). In this case, the effect of curvature of stream line at the toe of jump on velocity field in the jump might not be neglected. As the precise information on characteristics of jump just below drop structures might be scarce, the development of main flow in the jump downstream of drop structures cannot be predicted. As a result, local scour of stilling basin might be developed during flood stages (see Photo 1), and the river bed downstream of drop structures could not be protected. For hydraulic design of energy dissipater below drop structure, it is important to understand jump characteristics below drop structures.

This paper presents velocity profiles, time averaged maximum velocity decays, development of main flow in hydraulic jumps downstream of six different kinds of drop structures on the basis of experimental works. By using physical models of abrupt drops (see Photo 2 b), experiments on free hydraulic jumps below drop structures were conducted under a wide range of slopes at the downstream face of drop (θ = 26.6º, 45º, 90º; θ is angle of slope), relative drop heights (H/d_c = 1.20, 2.79, 5.58; H is drop height, and d_c is critical depth) and jump locations (ℓ/d_c = 1.4, 3.5, 6.3; ℓ is the length from the impingement point to the toe of jump). The velocity profiles in the jump have been shown on the basis of systematical investigation. When the approaching supercritical flow was disturbed by the curvature of streamline, the experiments reveals that the decay of the time averaged maximum velocity of main flow at each vertical section decays differs from the case of a classical hydraulic jump. This is defined as the jump without the curvature of stream-line at the toe of jump. Also, it has been shown that the location of the main flow in the jump region was lower than that in the case of classical hydraulic jump, even if the turbulent boundary layer at the toe of the jump was developed. For low drop height, the location of the main flow and the velocity profile in the jump are compared with the case of a wall jet.

2 EXPERIMETAL SET UP

The experiments were conducted in a horizontal rectangular channel with channel width B = 80 cm, 60 cm height, and 15 m long. The physical drop models with 1.00 m long and three different heights (H = 0.10m, 0.20 m, and 0.40 m) were installed in the rectangular channel. In order to investigate the effect of the curvature of stream-line due to the impingement on velocity fields in the jump, the toe location of jump was changed on the basis of the experimental conditions shown in Table 1. Also, the velocity fields were measured at the downstream from the position of 60 % in the jump region for the comparison of classical hydraulic jump without the curvature of stream-line at the toe of the jump. Figure 1 shows the measurement position of the velocity. As shown in Figure 1, velocity profiles at y/(B/2) = 0, 0.25, 0.50, and 0.75 in transverse direction were recorded for each section of x = $0.65L_j$, $0.86L_j$, $1.08L_j$, and $1.46L_j$. In addition, a two-dimensional electro-magnetic current meter with I type probe (4 mm diameter) of KENEK CO. LTD was utilized to measure the velocities with both x and y components (sampling time of 120 seconds and sampling frequency of 20 Hz).

a) Flow condition immediately after reconstruction b) Flow condition after four years later

Photo 1. Change of sand bank at downstream of weir during four years.

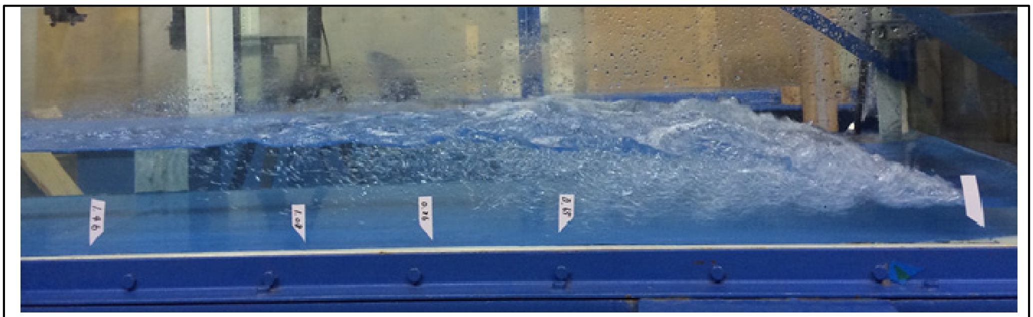

(a) Flow condition of jump below sluice gate

(b) Flow condition of jump downstream of drop

Photo 2. Comparison of flow condition of hydraulic jumps under F_1 = 2.87 and Re = 7.32 x 10^4.

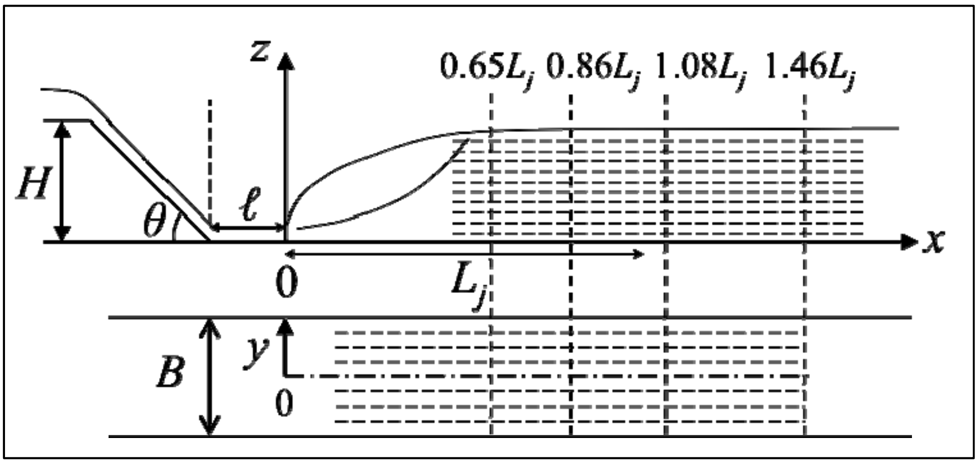

Figure 1. Definition sketch for hydraulic jump below drop.

Table 1. Experimental conditions.

θ = 45º, 90º	H = 0.10 m, (H/dc = 1.20)		
	ℓ/d_c = 1.4	ℓ/d_c = 3.5	ℓ/d_c = 6.3
Q (m^3/s)	6.03×10^{-2}	6.03×10^{-2}	6.03×10^{-2}
Re (-)	$7.32\text{x}10^4$	7.32×10^4	7.32×10^4
F_1 (-)	2.87	2.91	2.89
h_1 (m)	0.0413	0.0410	0.0411
h_2 (m)	0.147	0.146	0.146
L_j (m)	0.81	0.80	0.80

θ = 26.6º, 45º, 90º	H = 0.20 m, (H/dc = 1.20)		
	ℓ/d_c = 1.4	ℓ/d_c = 3.5	ℓ/d_c = 6.3
Q (m^3/s)	4.80×10^{-2}	4.80×10^{-2}	4.80×10^{-2}
Re (-)	5.69×10^4	5.69×10^4	5.69×10^4
F_1 (-)	4.50	4.37	4.30
h_1 (m)	0.0263	0.0269	0.0274
h_2 (m)	0.152	0.149	0.147
L_j (m)	0.83	0.82	0.81

θ = 26.6º, 45º, 90º	H = 0.40 m, (H/dc = 5.58)		
	ℓ/d_c = 1.4	ℓ/d_c = 3.5	ℓ/d_c = 6.3
Q (m^3/s)	4.80×10^{-2}	4.80×10^{-2}	4.80×10^{-2}
Re (-)	5.95×10^4	5.95×10^4	5.95×10^4
F_1 (-)	6.27	6.17	6.14
h_1 (m)	0.0211	0.0213	0.0214
h_2 (m)	0.173	0.171	0.171
L_j (m)	0.95	0.94	0.94

3 VELOCITY PROFILES AT TOE OF JUMPS

Figure 2 shows velocity profiles of supercritical flow at toe of jump. In this figure, V_1 is the averaged velocity at the toe of jump. If the toe of jump is located at the immediately downstream of the drop, as shown in Figure 2, the velocity profile can never be approximated by 7^{th} power law (Ohtsu and Yasuda, 1994), and the change of velocity is small in vertical direction. This might be caused by the acceleration of the velocity in which the pressure recovered during movements of increased pressure to static pressure.

In the comparison of velocity between trapezoidal and vertical drops, a three-dimensional nappe passing over the drop might be formed for a vertical drop. As shown in Figure 2 a) and b), the velocity profile changes transversely in the case of vertical drop.

In the comparison of velocity in different relative drop heights under given trapezoidal slope of drop, as in Figures 2 b) and c), the velocity profile changes transversely in the case of high drop. This might be caused by the degree of the impingement. If the relative drop height becomes higher, the leaping up of the nappe becomes large at the connection between side wall, channel bottom, and the supercritical flow is disturbed at the downstream of the impingement.

Accordingly, the velocity profile at the toe of jump affects both the relative drop height and the slope of downstream face of drop. At the same time effect of the inflow condition on velocity fields in the jump might not be neglected as well.

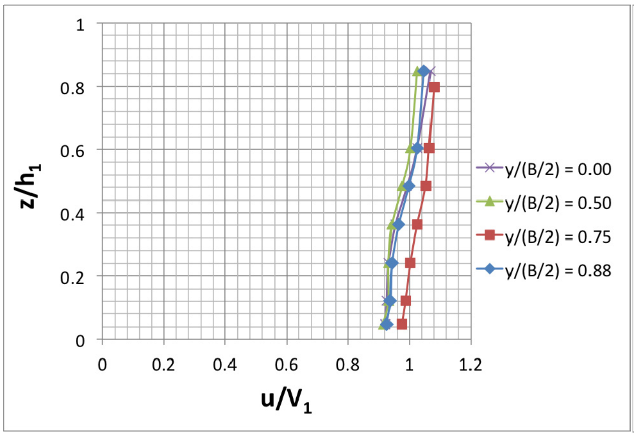

a) θ = 90º, H/d_c = 1.20, ℓ/d_c = 1.4, F_1 =2.87

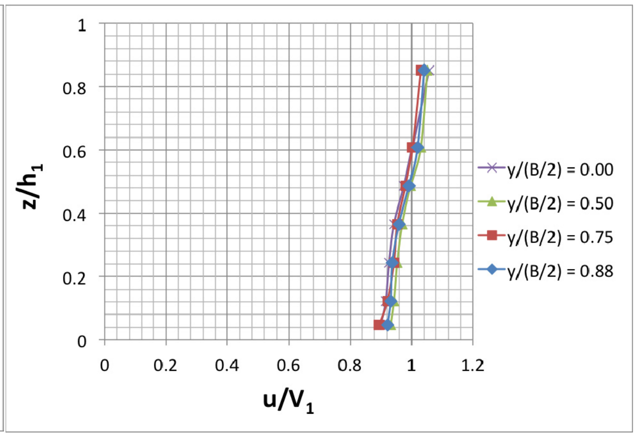

b) θ = 45º, H/d_c = 1.20, ℓ/d_c = 1.4, F_1 =2.89

Figure 2. Velocity profiles at toe of jump.

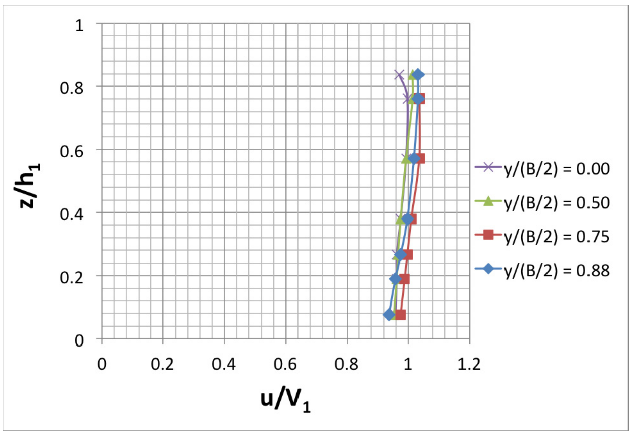

c) θ = 45º, H/d_c = 2.79, ℓ/d_c = 1.4, F_1 =4.50

Figure 2. Velocity profiles at toe of jump (continued).

4 VELOCITY CHARACTERISTICS OF HYDRAULIC JUMPS AT DOWNSTREAM OF DROP

4.1 Velocity profiles in Hydraulic jumps

In order to characterize velocity profiles at each section of x = $0.65L_j$, $0.86L_j$, $1.08L_j$, and $1.46L_J$, the data of the velocity were arranged in accordance with the relation of equation [1]. Table 2 shows the range of y/(B/2) arranged by the relation of [1] for each H/d_c and ℓ/d_c.

$$u/U_{max} = (z/Z,\ y/(B/2),\ H/d_c,\ \ell/d_c,\ x/Lj,\ \theta) = 0 \qquad [1]$$

Then, U_{max} is the maximum velocity at each measurement section, Z is the value of z in which the velocity is equal to / U_{max} 2 under du/dz < 0, and θ is the angle of slope at downstream face of drop.

Table 2. Range of y/(B/2) arranged by the relation of [1] for each H/d_c and ℓ/d_c.

	H/d_c = 1.20			**H/d_c = 1.20**	
ℓ/d_c = 1.40	x/Lj = 0.65	-0.75≤y/(B/2)≤0.75	ℓ/d_c = 6.30	x/Lj = 0.65	-0.75≤y/(B/2)≤0.75
	x/Lj = 0.86	-0.75≤y/(B/2)≤0.75		x/Lj = 0.86	No existence of Z
	x/Lj = 1.08	No existence of Z		x/Lj = 1.08	No existence of Z
	x/Lj = 1.46	No existence of Z		x/Lj = 1.46	No existence of Z
ℓ/d_c = 3.50	x/Lj = 0.65	-0.75≤y/(B/2)≤0.75			
	x/Lj = 0.86	-0.75≤y/(B/2)≤0.75			
	x/Lj = 1.08	No existence of Z			
	x/Lj = 1.46	No existence of Z			

  ISSN 1562-6865 (Online) - ISSN 1063-7710 (Print)

Table 2. Range of y/(B/2) arranged by the relation of [1] for each H/d_c and ℓ/d_c. (Continue)

	H/d_c = 2.79			**H/d_c = 2.79**	
ℓ/d_c = 1.40	x/Lj = 0.65	-0.75≤y/(B/2)≤0.75	ℓ/d_c = 6.30	x/Lj = 0.65	-0.50≤y/(B/2)≤0.50
	x/Lj = 0.86	-0.50≤y/(B/2)≤0.50		x/Lj = 0.86	No existence of Z
	x/Lj = 1.08	No existence of Z		x/Lj = 1.08	No existence of Z
	x/Lj = 1.46	No existence of Z		x/Lj = 1.46	No existence of Z
ℓ/d_c = 3.50	x/Lj = 0.65	-0.75≤y/(B/2)≤0.75			
	x/Lj = 0.86	No existence of Z			
	x/Lj = 1.08	No existence of Z			
	x/Lj = 1.46	No existence of Z			

	H/d_c = 5.58			**H/d_c = 5.58**	
ℓ/d_c = 1.40	x/Lj = 0.65	-0.75≤y/(B/2)≤0.75	ℓ/d_c = 6.30	x/Lj = 0.65	-0.50≤y/(B/2)≤0.50
	x/Lj = 0.86	-0.50≤y/(B/2)≤0.50		x/Lj = 0.86	No existence of Z
	x/Lj = 1.08	No existence of Z		x/Lj = 1.08	No existence of Z
	x/Lj = 1.46	No existence of Z		x/Lj = 1.46	No existence of Z
ℓ/d_c = 3.50	x/Lj = 0.65	-0.50≤y/(B/2)≤0.50			
	x/Lj = 0.86	No existence of Z			
	x/Lj = 1.08	No existence of Z			
	x/Lj = 1.46	No existence of Z			

As shown in Table 2, if the relative drop height becomes larger, the disturbance at the toe of the jump becomes higher, and the upper limit of x/L_j in which the velocity profile was arranged by the relation of [1] can be obtained becomes smaller. The relative length ℓ/d_c also becomes smaller under a given relative drop of height and the effect of the curvature of stream-line on the velocity profile becomes larger where the upper limit of x/L_j in which the velocity profile arranged by the relation of [1] can be obtained becomes larger. In addition, the effect of the angle of slope θ on the velocity profile is smaller.

Figure 3 shows velocity profiles arranged by the relation of [1] for θ = 90º, ℓ/d_c = 1.4, and x/L_j = 0.86. In this figure, the broken lines show the velocity profile for the classical hydraulic jump without the curvature of stream-line (Ohtsu, 1976; Ohtsu, 1976; Ohtsu et al., 1990).

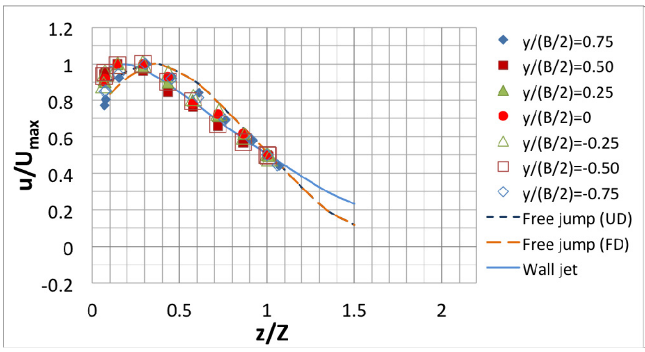

a) H/d_c = 1.20, ℓ/d_c = 1.4, x/L_j = 0.86

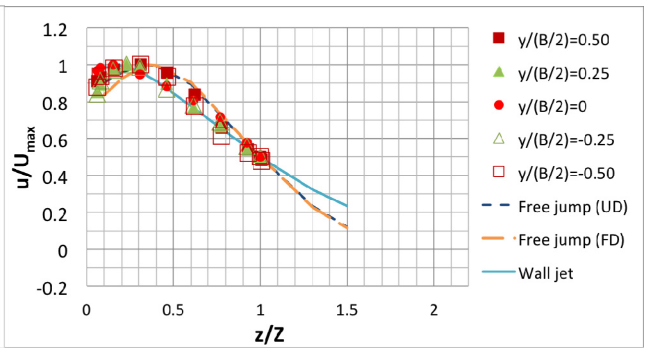

b) H/d_c = 2.79, ℓ/d_c = 1.4, x/L_j = 0.86

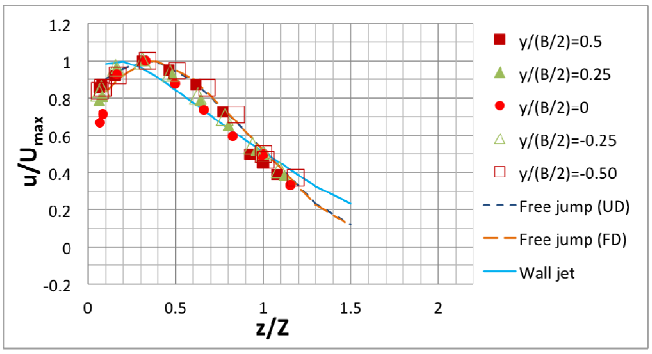

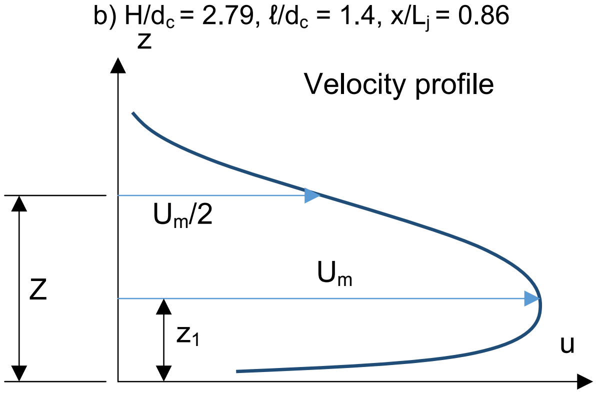

c) H/d_c = 5.58, ℓ/d_c = 1.4, x/L_j = 0.86

Figure 3. Velocity profiles arranged by the relation of [1] for θ = 90º, ℓ/d_c = 1.4, x/L_j = 0.86.

In broken lines, UD means undeveloped inflow in which the turbulent boundary layer was not developed at the toe of jump, and FD means fully developed inflow in which the turbulent boundary layer was fully developed at the toe of jump (Ohtsu and Yasuda, 1994). The solid line shows the velocity profile for the classical plane wall jet (Verhoff, 1963; Rajaratnam, 1976).

In the case of $\ell/d_c = 1.4$, the pressure at the toe of jump was larger than the static pressure, because the effect of the curvature of stream-line on the velocity field in the jump might not be neglected. As shown in Figure 3, the velocity profile can be arranged by the relation of [1] until the range of $x/L_j = 0.86$. If the relative drop height H/d_c becomes smaller, the disturbance at the toe of jump becomes smaller and the velocity profile was the same as in the case of the wall jet (Verhoff, 1963; Rajaratnam, 1976), even if the measurement section is located at $x/L_j = 0.86$. In addition, for $x/L_j = 0.65$, the velocity profile affects the formation of surface roller in the jump.

4.2 Longitudinal development of maximum velocity at each measurement section

In order to investigate the development of the maximum velocity at each measurement section, the data of the location of the maximum velocity z1 were arranged in accordance with the relation of equation [2]. Figure 4 shows the development of the maximum velocity at each measurement section under given ℓ/d_c.

$$z_1/h_1 = (x/L_j,\ y/(B/2),\ \theta,\ H/d_c,\ \ell/d_c) = 0 \qquad [2]$$

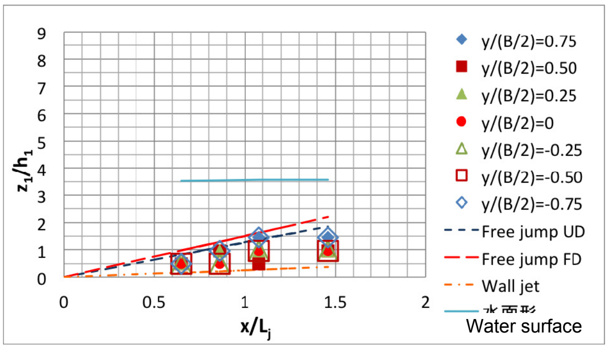

a) θ = 90°, $H/d_c = 1.20$, $\ell/d_c = 1.4$, $F_1 = 2.87$

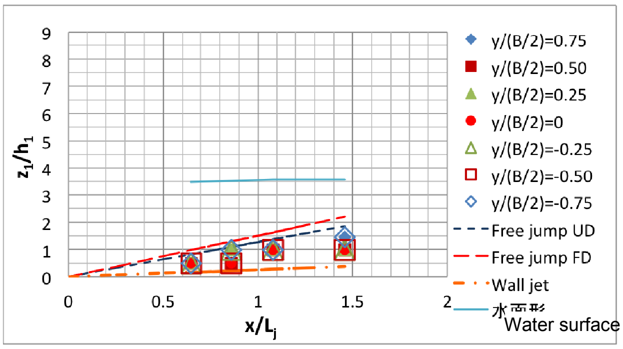

b) θ = 45°, $H/d_c = 1.20$, $\ell/d_c = 1.4$, $F_1 = 2.89$

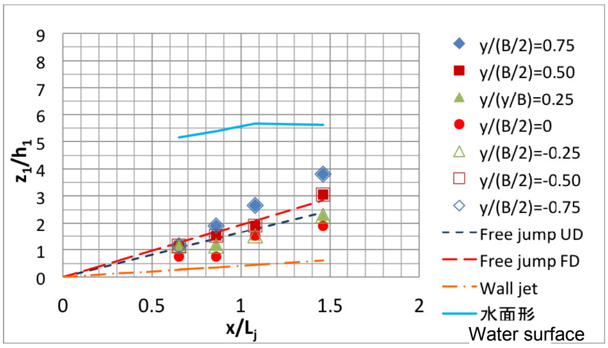

c) θ = 90°, $H/d_c = 2.79$, $\ell/d_c = 1.4$, $F_1 = 4.51$

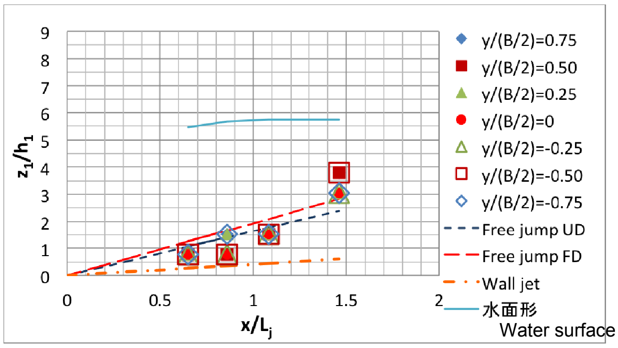

d) θ = 45°, $H/d_c = 2.79$, $\ell/d_c = 1.4$, $F_1 = 4.50$

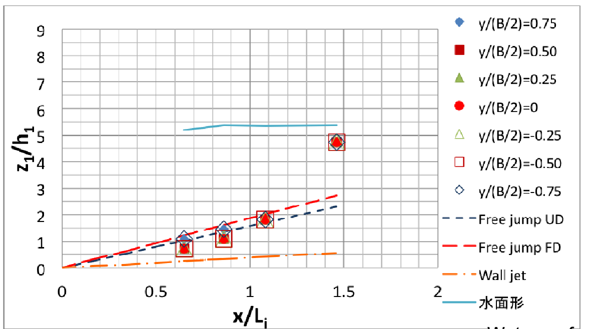

e) θ = 26.6°, $H/d_c = 2.79$, $\ell/d_c = 1.4$, $F_1 = 4.22$

Figure 4. Development for location of maximum velocity at each section.

In this figure, the broken lines showed the development of the maximum velocity at each section for the classical hydraulic jump without the curvature of stream-line. In this case, these lines applied for the range of 0.1 < x/Lj < 0.7 (Ohtsu, 1976; Ohtsu et al., 1990) were extended to the range of 0.1 < x/Lj <1.5. The dotted and chained line shows the development of the maximum velocity at each section for the wall jet (Verhoff, 1963; Rajaratnam, 1976).

The comparison of the development shown in Figures 4 a) and b) or Figures 4 c), d), and e) represents the effect the angle of slope on the development of the maximum velocity under given H/d_c and ℓ/d_c.

For H/d_c = 1.20, the inflow Froude number is smaller than 3 as shown in Figures 4 a) and b) and the main flow continues along the bottom far downstream. Also, the transverse change for the development of the maximum velocity is not negligible for a vertical drop. The maximum velocity at x/L_j = 1.46 was located between broken line and dotted and chained line. Accordingly, even if the velocity profile was not expressed by the relation of [1], the formation of the hydraulic jump below the low drop should be considered as a wall jet.

If the relative drop height becomes larger, as shown in Figures 4 c), d), and e), the effect of the angle of slope on the development of the maximum velocity becomes larger with the understanding if the angle of slope becomes larger. This might be caused by the degree of the disturbance at the inflow condition.

4.3 Maximum velocity decay in hydraulic jumps below drop

In order to investigate the maximum velocity decay in the range of $0.65 \le x/L_j \le 1.46$, the data of the maximum velocity at each section were arranged in accordance with the relation of equation [3]. Figure 5 shows the maximum velocity decay at each measurement section under given ℓ/d_c.

$$(U_{max} - V_2)/V_1 = f(x/L_j,\ y/(B/2),\ \theta,\ \ H/d_c,\ \ \ell/d_c \qquad [3]$$

Here, V_2 was the averaged velocity at the end of jump. The solid line in Figure 5 shows the maximum velocity decay for the classical hydraulic jump without the curvature of stream-line (Ohtsu, 1976; Ohtsu et al., 1990).

As in Figure 5, the maximum velocity at each section decays was compared with that for the classical hydraulic jump.

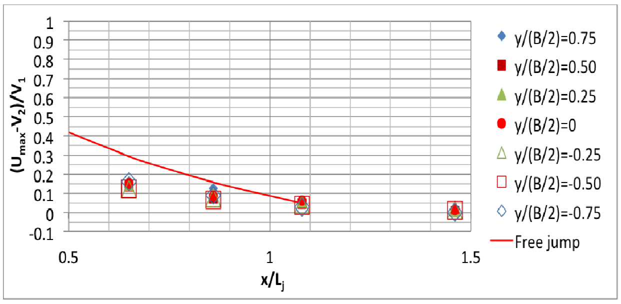

a) θ = 90°, H/d_c = 1.20, ℓ/d_c = 1.40, F_1 = 2.87

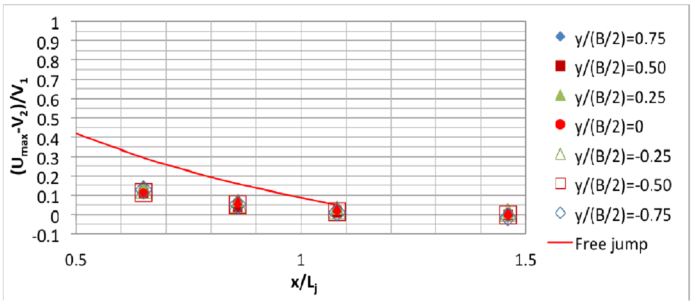

b) θ = 45°, H/d_c = 1.20, ℓ/d_c = 1.40, F_1 = 2.89

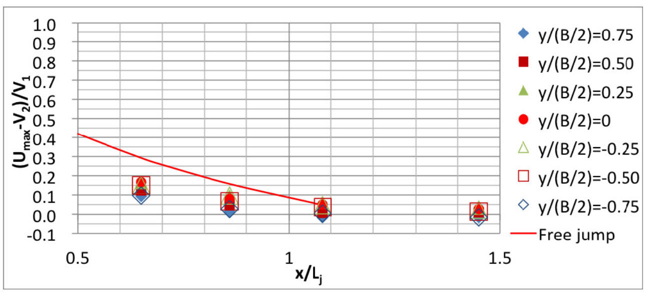

c) θ = 90°, H/d_c = 2.79, ℓ/d_c = 1.40, F_1 = 4.51

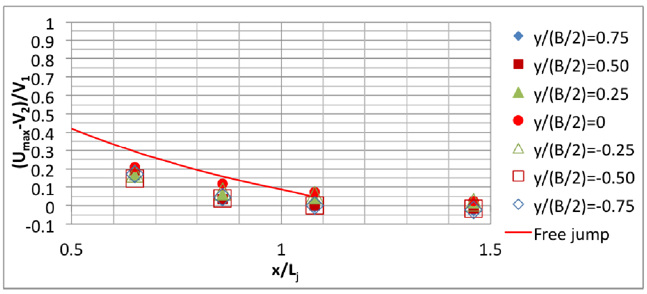

d) θ = 45°, H/d_c = 2.79, ℓ/d_c = 1.40, F_1 = 4.50

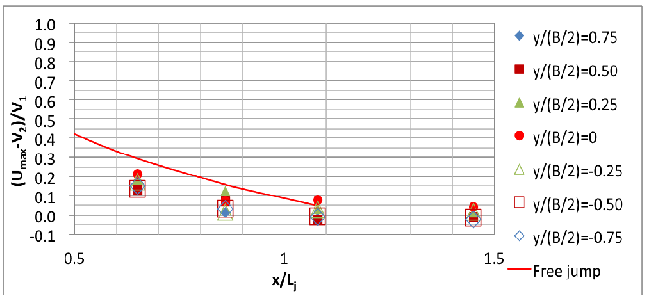

d) θ = 26.6°, H/d_c = 2.79, ℓ/d_c = 1.40, F_1 = 4.22

Figure 5. Maximum velocity decay in jump at downstream drop.

This might be caused by the effect of the curvature of stream-line on the velocity decay. As shown in Photo 2, different air-entrainment in the jump can be confirmed, even if the inflow Froude number, Reynolds number, and the velocity profile at the toe of jump (see Figures 2 a) and b)) are almost the same as in the case of the classical hydraulic jump without the curvature of stream-line.

The comparison of the velocity decays shown in Figures 5 a) and b) or Figures 5 c), d), and e) represents the effect of the angle of slope on the maximum velocity decay under given H/d_c and ℓ/d_c.

For H/d_c = 1.20, the degree for the disturbance at the inflow condition was small, and as shown in Figures 5 a) and b), the transverse change for the maximum velocity decay was negligible.

For H/d_c = 2.79, as shown in Figures 5 c), d), and e), the effect of angle of slope on the maximum velocity decay was small. Also, the transverse change for the maximum velocity decay was small.

5 CONCLUSIONS

The hydraulic jump below drop was investigated experimentally under the experimental conditions shown in Table 1. The effect of the curvature of stream-line due to the impingement on the velocity fields in the jump is clarified by comparing with those for the classical hydraulic jump without the curvature of stream-line at toe of the jump, and the experimental results are summarized as follows:

(1) The velocity profile at the toe of jump affects the relative drop height and the slope of downstream face of drop with reliance to the effect of the inflow condition on velocity fields in the jump is not to be negligible. If the relative drop height becomes larger, the leaping up of the nappe becomes larger at the connection between the side wall and channel bottom, and the supercritical flow is disturbed at the downstream of the impingement.

(2) If the pressure at the toe of jump is larger than the static pressure, the effect of the curvature of stream-line on the velocity field in the jump is not be neglected and the velocity profile can be arranged by the relation of [1] until the range of $x/L_j \leq 0.86$. If the relative drop height becomes smaller, the disturbance at the toe of jump becomes smaller and the velocity profile is the same as in the case of the wall jet, even if the measurement section is located at $x/L_j = 0.86$.

(3) For H/d_c = 1.20, the inflow Froude number is smaller than 3 and the main flow continues along the bottom far downstream. The transverse change for the development of the maximum velocity is not negligible for a vertical drop as well. The formation of the hydraulic jump below the low drop should be considered as a wall jet, even if the velocity profile is not expressed by the relation of equation [1].

(4) The maximum velocity at each section decays compared with that for the classical hydraulic jump without the curvature of stream-line occurs due to the impingement. This might be caused by the effect of the curvature of stream-line on the velocity decay.

REFERENCES

Bradley, J.N. & Peterka, A.J. (1957). Hydraulic Design of Stilling Basins: Stilling Basin with Sloping Apron (Basin V). *Journal of Hydraulic Division*, 83(5), 1-32.

Hager, W.H. (1992). *Energy Dissipators and Hydraulic Jump*. Water Science and Technology Library, Kluwer, 8.

Liu, M., Rajaratnam, N. & Zhu, D.Z. (2004). Turbulence Structure of Hydraulic Jumps of Low Froude Numbers. *Journal of Hydraulic Engineering*, 130, 511-520.

Novak, P., Moffat, A.I.B., Nalluri, C. & Narayanan, R. (2007). *Hydraulic Structures*, Fourth edition. E&FN SPON, UK, 249-252.

Ohtsu, I. (1976). Free Hydraulic Jump and Submerged Hydraulic Jump in Trapezoidal and Rectangular Channels. *Transactions of Japan Society of Civil Engineers*, 8, 122-125.

Ohtsu, I., Yasuda, Y. & Awazu, S. (1990). *Free and Submerged Jumps in Rectangular Channels*. Report of the Research Institute of Science and Technology, Nihon University, 35, 1-50.

Ohtsu, I. & Yasuda, Y. (1994). Characteristics of Supercritical Flow below Sluice Gate. *Journal of Hydraulic Engineering*, 120(3), 332-346.

Peterka, A.J. (1978). *Hydraulic Design of Stilling Basins and Energy Dissipators*. United States Department of The interior Bureau of Reclamation, Engineering Monograph, a Water Resources Technical Publication, 25.

Rajaratnam, N. (1967). Hydraulic Jumps. *Advances in Hydroscience*, 4(1), 197-280.

Rajaratnam, N. (1976). *Turbulent Jets, Development in Water Science*. 5, *Elsevier*, 218-219.

The US Army Corps of Engineers (1995). *Hydraulic Design of Spillways,* Technical Engineering and Design Guides as Adapted from the US Army Corps of Engineers, 12.

Visher, D.L. & Hager, W.H. (1995). Energy Disspators. *Hydraulic Structures Design Manual*, IAHR, A. A. Balkema, 9.

Verhoff, A. (1963). *Two-Dimensional Turbulent Wall Jet with and without an External Stream*, Report 626, Princeton Univeristy, May.

DESTRUCTION MECHANISM OF THE STEP BEHIND THE X-SHAPED FLARING GATE PIERS

ZONGSHI DONG (1), JUNXING WANG (2), JUNRONG DA (3), ZIYI LIAN (4) & WENCHUAN ZHANG (5)

(1,2,3,4,5)State Key Laboratory of Water Resources and Hydropower Engineering Science, Wuhan University, Wuhan, China
sdxy@whu.edu.cn

ABSTRACT

The combined energy dissipater of the X-shaped flaring gate pier and stepped spillway was invented under the specific condition of flood discharge and energy dissipation in Suofengying hydro-plant of China using this mechanism of which has been deeply studied by model testing. However, varying degrees of erosion destruction occurs on the step surface in the later popularization and application process in Dachaoshan Hydro-plant and Ludila Hydro-plant. In order to study the destruction mechanism of the step behind the X-shaped flaring gate piers, a hydro-plant on Jinsha River was investigated as an example. The parameters of water nearby the step surface, such as fluctuating pressure, impact pressure, fluid velocity and air concentration were analyzed by model test and numerical simulation. The simulated results are in good agreement with the model test results. The results show that the impact pressure on step surface is not enough to cause breakage on the step structure, while the low aeration region on the step surface is basically in coincidence with the destruction region, which means the lack of aeration is the reason that results in the erosion destruction on the step surface. The investigated results in the paper can provide reference for similar projects.

Keywords: Destruction mechanism; stepped spillway; X-shaped flaring gate pier; air concentration; impact pressure.

1 INTRODUCTION

Due to the special topography and geological conditions, the unit width discharge of lots of hydropower projects in China are larger than $100m^3 \cdot s^{-1} \cdot m$, and the problem of energy dissipation for them become very difficult.

A variety of combined energy dissipators have been developed to achieve the goal of energy dissipation, the combination of flaring gate pier (FGP) and stepped spillway is an advanced form of them. It was invented through model test under the specific conditions of flood discharge and energy dissipation in Ankang Hydropower Station of China. Subsequently, in the designing process of Suofengying Hydro-plant, the shape of FGP was further optimized, and a X-shaped FGP was put forward. The combined energy dissipation of the X-shaped FGP and stepped spillway can make full use of the steps by forming rolling flow for energy dissipation in a small flow discharge; while in a large flow discharge, it can significantly increase the energy dissipation through the contracted jet of FGP. Many hydro-plants in China, such as Shuidong, Suofengyin, Dachaoshan, adopt this kind of combined energy dissipator. These hydro-plants have different dam heights, shapes of FGP and have experienced different unit width discharge of flood. As expected, most of them work well but still a few stations underwent serious destruction in the stepped spillway at the beginning of operation. (as shown in Figure 1)

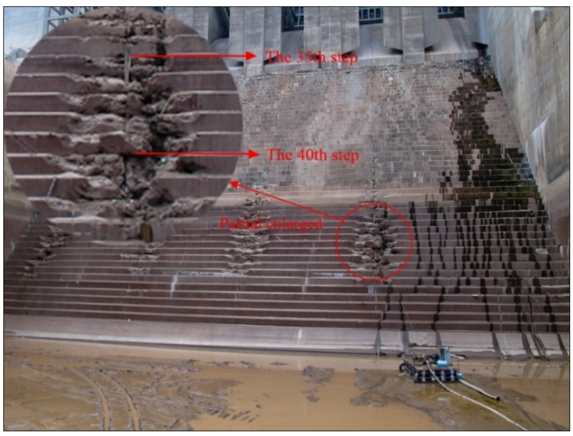

Figure 1. Erosion destruction of a certain dam

In recent years, many scholars around the word have carried out lots of research on the combined energy dissipator of the X-shaped FGP and steps spillway. Nan et al. (2003) had an early analysis on the pressure and velocity of water near the steps of Suofengying hydro-plant through the method of model test and illustrated the feasibility and superiority of this combined energy dissipator. Li et al. (2005) carried on the detailed research to the time-average pressure and fluctuating pressure of water near the step surface through the method of model test, and got the general rule of pressure distribution on the steps. Zhang et al. (2005) performed a 3D numerical simulation on water and air two-phase flows of the steps and FGP, obtaining the pressure and velocity characteristics. Wang et al. (2007) numerically studied the relationship of first step height, step slop and cavity in X-shaped FGP where a theoretical equation to calculate the size of cavity was put forward and its accuracy were verified. Jin et al. (2009) numerically simulated aeration and analyzed the pressure and velocity distribution at the step surface. The obtained results are almost consistent with that of Li's works. Li et al. (2012) carried on a theoretical and experimental research of the FGP on the surface spillway in a high-arch dam. Li et al. (2016) conducted a preliminary study on destruction mechanism of the steps behind FGP by means of model test and simplifying the load of material mechanics.

In this paper, a hydro-plant on Jinsha River of China that suffered erosion destruction was investigated using the software Flow 3D. The Tru-VOF technology to track the free surface and the independent aeration model to simulate the aeration was used. The parameters on the steps, such as pressure, fluctuating pressure and fluid veclocity, ware analyzed. The mechanism of erosion destruction on the step surface was revealed.

2 RESEARCH OBJECT

There are 5 overflow surface holes in this project. The size of the surface holes is 15m×19m (wide×height) ，the thickness of side pier is 4m, while the thickness of intermediate piers is 5m and the elevation of weir crest is 1204m. The upstream section of the weir surface curve is three circular arc curves and the downstream uses power-curve profile, whose equation is $y=0.0425x^{1.85}$. This connects a slope with a proportion of 1：0.854 and the elevation of slope end is 1179m. There are totally 50 steps and the width of each step is 0.9m where the first step height is 2.22m and the others are 1.2m. Behind the steps is a roller bucket whose bottom elevation is 1114m, the front half radius 10m and its central angle 53.13º, back half radius 15m and its central angle 21.06º. The stilling basin's bottom elevation is 1115m. The tail of the stilling basin connects a slope with the proportion of 1：4. The longitudinal plan of overflow section is shown in figure 2.

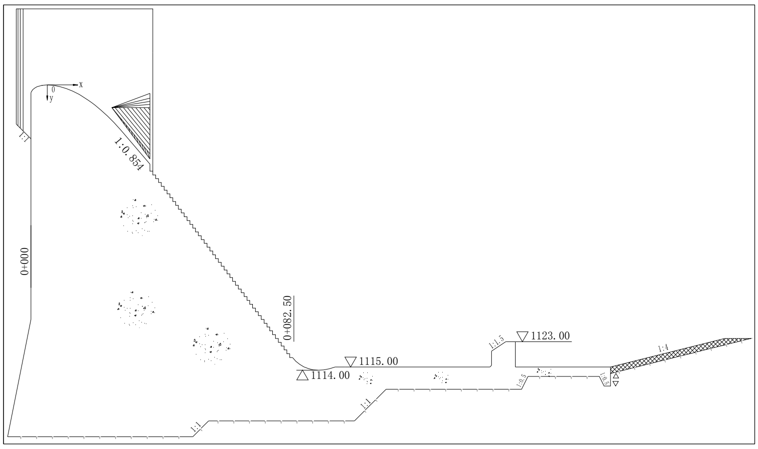

Figure 2. Longitudinal plan of overflow section.

3 MATHEMATICAL MODEL

3.1 Numerical scheme

Flow 3D was selected as the CFD software in the numeric simulation. Flow 3D tracks the position of the fluid surface in a special numerical way and has all the functions of VOF techniques, which can give a complete description about the free surface. The RNG *k-ε*model was chosen for turbulent model, and the FEM method was applied for equation discrete. GMRES iterative algorithm was used as the algebraic equation solution method. VOF was applied to proceed the track of free surface and Air Entrained model was used to calculate the air concentration.

3.2 Computational model and grid

Since the main focus area was the FGP and steps section, so only the surface holes, steps, and stilling basin were modeled in the simulation. The upstream boundary reaches 60m above the dam, and the downstream boundary reaches 350m below. To make a comparison with the model test results, the upstream, downstream and top boundary were all set as pressure inlet (at standard atmospheric pressure), plus water surface elevation was attached to the upstream and downstream at the same time. Left, right bank, and the bottom of the stilling basin are set as the wall boundary, and the roughness is set to 0.014. Nested grids were used. The size of containing mesh block was 1.5m, and the size of nested mesh was 0.3×0.4×0.67m（X×Y×Z). The FAVOR（Fractional Area Volume Obstacle Representation）grid technology of Flow 3D was used to describe complex geometry in a structured grid. The terminal time was controlled by the standard so that the fluid volume exchange rate within the grid area was less than 0.5%. The total number of the fluid grid reaches 1.47 million, as shown in Figure 3.

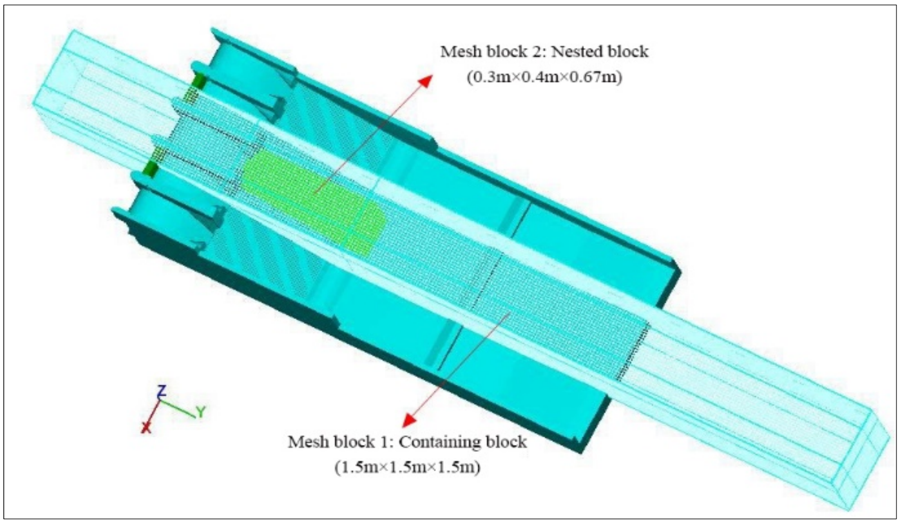

Figure 3. Computational domain and grid.

3.3 Calculation condition

According to operation data, the project mainly runs at normal water level of 1223m before the steps being destructed, and downstream water level is 1135m. Therefore, the upstream and downstream water level were set to 1223m and 1135m in the numerical calculation. Meanwhile, simplified plate gates were used for 2# and 4# surface hole to prevent water flow through the two holes stated.

4 CALCULATION RESULTS

4.1 Accuracy analysis of the calculation

3# hole gate was fully opened and upstream water level at 1223m were taken as the typical working condition for the calculation. The results in figure 4 indicate that the length of air cavity is about 10 steps. Meanwhile, the state of water near the steps is in of skimming flow, which is tangent to the envelope of the step convex corner. Its flow velocity is about 22 m/s, while the flow around concave corner is within 10m/s.

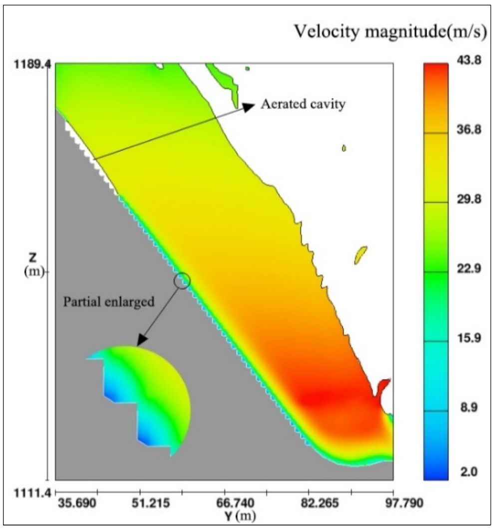

Figure 4. The velocity distribution at central axis of 3# gate hole

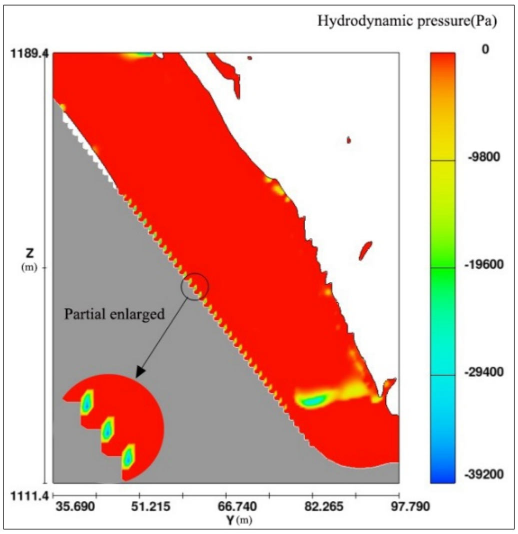

Figure 5. The pressure distribution at central axis of 3# gate hole

Figure 5 shows the pressure distribution of section in central axis of 3# gate hole. In order to highlight the range of negative pressure, the area with the pressure above 0 was set in red. The negative pressure with the value of -40 KPa occurs at the vertical face of the step, which is about 1/4 to 1/3 step height from the convex corner. Therefore, the calculation result was in accordance with the result in model experiment and references.

4.2 Analysis of the impact pressure

The impact pressure on the surface of steps around central axis of the 3# gate hole can be calculated by Baffles in Flow- 3D. Baffle was equivalent to zero-thickness pressure sensor attached to the step surface and it cannot be moved and deformed. Since step destruction mainly occurs within step No.35 to No. 45, the impact pressure from step No. 21 to No. 50 was taken as the calculating object. Baffles are set on the horizontal plane of relevant step along the central axis of 3# gate hole, with the size of 1m in length and 0.9m in width. Details are shown in Figure 6.

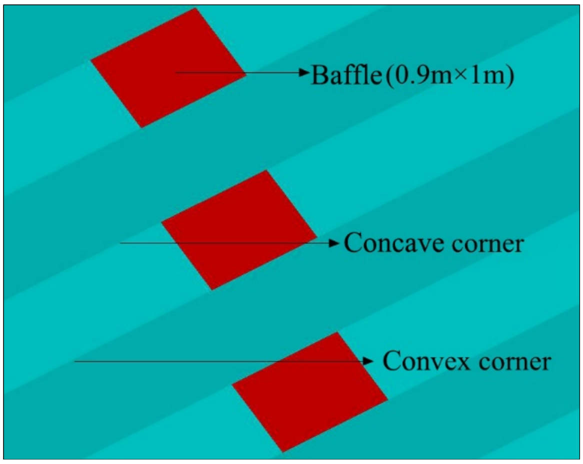

Figure 6. Layout of baffles

The total calculating time is 150 seconds, and the pressure sampling frequency of every baffle is at 50Hz. Through the statistical analysis done on about 10000 impact pressure values of each baffle in last 20 seconds, the average and peak value of every step can be summarized as in Figure 7.

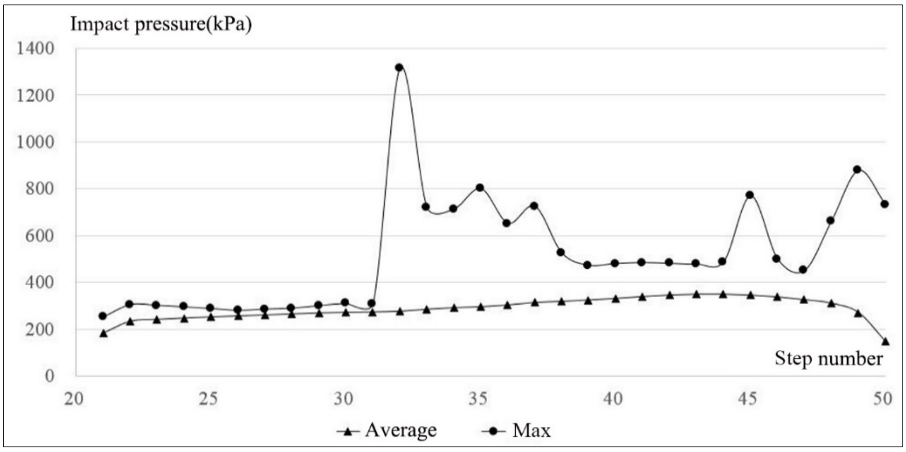

Figure 7. Impact pressure distribution of step surface

As shown in Figure 7, average pressure in step No.43 is the highest when compared from step No. 21 to step No.50, with the value of 349KPa. While at the pressure of 1314 KPa, peak pressure in step No. 32 is the highest among all steps. However, the design strength of RCC steps is generally over 25000 KPa, which is much greater than the impact pressure of step surface. Therefore, the impact pressure is not considered as the arch-criminal of step destructions.

4.3 Analysis on fluctuating pressure

Since destruction happens at steps from No.35 to No.45, steps No.21 to No.50 are taken as the calculating object for fluctuating research. Probes were set at the convex corner, concave corner and the highest negative pressure area along the central axis of 3# gate hole. Details are shown in Figure 8.

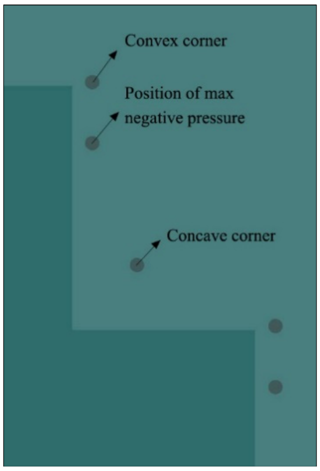

Figure 8. Layout of hydrodynamic pressure probe

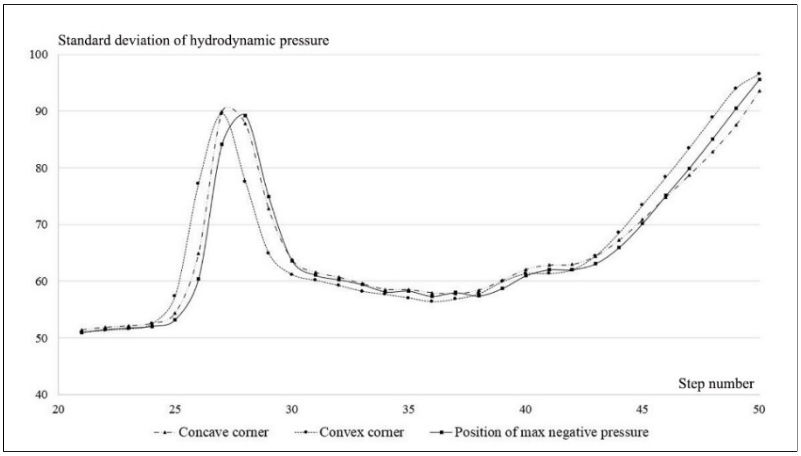

Figure 9. Standard deviation of hydrodynamic pressure at step surface

The standard deviation of hydrodynamic pressure of all measuring points from step No.21 to step No. 50 is shown in Figure 9 and the average of hydrodynamic pressure of all measuring points from step No.21 to step No. 50 is shown in Figure 10. There are two areas with relatively high fluctuating pressure in Figure 9. The first area is step No. 25 to step No. 50, with the highest fluctuating pressure valued at 90KPa. The second area is step No. 38 to step No. 50, where at first it slowly increases until step 43 and at after step 43 there is sharp increase in the results as shown in Figure 10. The highest fluctuating pressure is 95KPa, appearing on step No. 50. The mean of hydrodynamic pressure was about -60kPa near the convex of step No.21 to step NO.43.

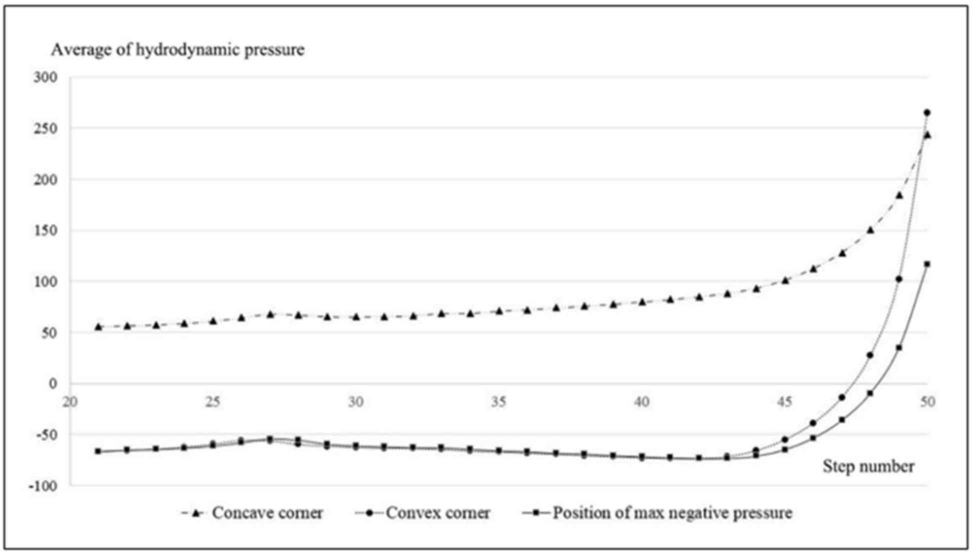

Figure 10. Average of hydrodynamic pressure at step surface

Through the analysis, it indicates that the larger standard deviation of hydrodynamic pressure off steps No. 25 to No. 30 comes from the adaption and deflection upon steps after the flow was longitudinally stretched by FGP. The larger standard deviation of hydrodynamic pressure from step No. 43 to No. 50 was derived from the strong turbulent motion in all directions due to flow out of bucket type stilling pool. The calculating result was matched with what of model experiment. The standard deviation of hydrodynamic pressure of main destruction area (step No. 35 to No. 45) is relatively small. Thus it can be concluded that fluctuating pressure is not the main reason of the step destruction.

4.4 Air concentration

The step has an obvious structure of pointedness, therefore, cavitation erosion is more likely to occur at a stepped spillway dam surface than a smooth overflow surface. Air can be entrained to the step surface from the non-water area behind the FGP, which is useful for avoiding cavitation erosion. Therefore, Air concentration near the stepped surface along the spillway can reflect the possibility of the step destruction to some extent.

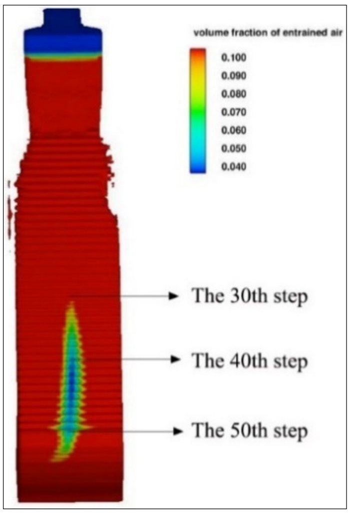

Figure 11. Air concentration contours

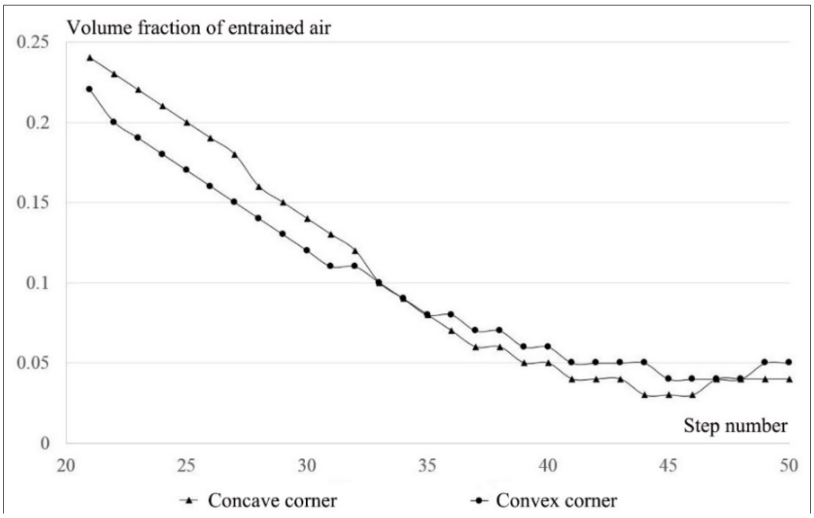

Figure 12. Air concentration at step surface

Figure 11 shows the 3D distribution of air concentration near the step surface (upward view). Figure 12 shows the distribution of air concentration near the concave corner and convex corner along the step at the central profile of the 3# gate hole. From figure 11 and 12, we can know that the air concentration of the main destruction area are all less than 10%, and the areas of low air concentration are highly overlapped with the main destruction area such as at steps 41~50 where the air concentration was lower than 5%. Due to these findings, cavitations erosion is likely to occur among these steps under certain pressure and velocity.

5 THE ANALYSIS OF THE REASONS FOR STEPS DESTRUCTED

The main destruction areas are from steps 35 ~ 45, near the central axis of the gate hole in this project which is rightly where the dam body crevices is located. The calculation results show that the maximum value of the peak impact pressure at the step surface is 1314kPa, while the max value of the mean impact pressure is 349kPa, which is far from causing destruction to the steps. The velocity near the step is about 10~15m/s, and there are areas of negative pressure at the step façade which is about 1/4 step height from the convex corner. Since the value of negative pressure reached -50~-60kpa, the pressure near convex corner is likely to reach the cavitation pressure (about 2400Pa) in consideration of the standard deviation of hydrodynamic pressure which is about 60kPa. Sufficient entrained air is needed to reduce the possibility of cavitation. While the air concentration at the steps of 35~45 are all less than 10% with the minimum value being only 5%. From this result we can see that the low entrained air area are highly overlapping with the main destruction area from 3D perspective and all the results above show that the most likely cause for steps destruction is Erosion destruction caused by cavitation. According to investigation, similar steps destruction has occurred in Dachaoshan hydro-plant in Yunnan province, and the destruction has been avoided effectively after aeration engineering measures were taken, which further verified that cavitation is the most likey cause of the steps destruction.

6 CONCLUSION

In order to study the destruction mechanism of the step behind the X-shaped flaring gate piers, a hydro-plant on Jinsha River is investigated as an example. The calculation results such as flow pattern, velocity, pressure are in good agreement with the model test results. The calculation results show that the impact pressure at the steps are far from causing destruction to the steps. The standard deviation of hydrodynamic pressure at step surface is about 50~90kPa and the area where standard deviation of hydrodynamic pressure is larger do not overlap with the main destruction area. While the air concentration near the main destruction area are only 4%~ 10%, and this is coupled with negative pressure near the convex corner of most the steps in the main destruction areas. Thus, insufficient aeration is the most likely cause of steps destruction. Only some key hydraulics parameters on the step surface were analyzed and some constructive achievements are obtained in this article. However, the destruction mechanism of the step is very complicated and many other factors like dam body crevices, RCC layers, construction quality and sealing structure are all very important to the destruction of the steps. Relevant experts can carry out further researches on other factors according to the results in this paper where the results can serve for better construction and operation.

REFERENCES

Jin, J. (2009). The Numerical Simulation of Stepped Spillways' Hydraulic Characteristics, *Doctoral Dissertation.* Xi'an University of Technology.

Li, B.L. (2005). Experimental Research of Pressure Characteristic on Stepped Overflow Dam, *Doctoral Dissertation.* Xi'an University Of Technology.

Li, N.W., Liu, C., Deng, J. & Zhang, X.Z. (2012). Theoretical and Experimental Studies of the Flaring Gate Pier on the Surface Spillway in a High-Arch Dam. *Journal of Hydrodynamics, Ser.B,* 24(4), 496-505.

Li, X.Y. & Yin, J.B. (2016). Study on The Damage of Stepped Spillways Combined with Flaring Gate Piers. *Journal of Yangtze River Scientific Research Institute*, 33(1), 61-64.

Nan, X.H. Liang, Z.X. & Liu, H.S. (2003). New Type of Flaring Pier for Improving Energy Dissipation of Stepped Surface Overflow Dam. *Journal of Hydraulic Engineering*, 2003(8), 49-57.

Wang, B., Wu, C., Hu, Y.H. & Mo, Z.Y. (2007). Relationship of First Height, Step Slope and Cavity in X-Shaped Flaring Gate Piers. *Journal of Hydrodynamics, Ser.B*, 19(3), 349-355.

Zhang, T., Wu, C., Liao, H.S. & Hu, Y.H. (2005). 3D Numerical Simulation on Water and Air Two-Phase Flows of the Steps and Flaring Gate Pier. *Journal of Hydrodynamics, Ser.B*, 17(3), 338-343.

Proceedings of the 37th IAHR World Congress
August 13 – 18, 2017, Kuala Lumpur, Malaysia

STUDY ON THE FLOW AND MORPHOLOGICAL CHANGES UTILIZES VEGETATED GROYNE

PRATIWI AZIZ [1] & AKIHIRO KADOTA [2]

[1,2] Ehime University, Matsuyama, Japan,
pratiwi_aziz@yahoo.com; akado@cee.ehime-u.ac.jp

ABSTRACT

In Japanese rivers, many groynes have been constructed to protect the riverbanks. This study focuses on clarifying the function of the existing groyne in the Shigenobu river, verify that vegetated groyne is more effective for stabilizing the flow of the river from the existing groyne and has an effect or not. In this study, field investigation is conducted located approximately 6.4 km section from Shigenobu River mouth. Survey of sand particle measurement is conducted to acquire the detailed analysis for the particle size distribution and the vegetation growth situation in the river. Based on reviews these results, analysis of the river bed variation is done by using simulation software river iRIC. The influence and flow control of the river when the water is calm, the flow rate at the time of the flood and the planning high water level is reviewed. Therefore, the vegetated groyne is believed to provide the same effect with the existing groyne when the water is calm. In addition, vegetated groyne is more effective for reducing polarization promotion of river channels as compared to the existing groyne. The higher a density of vegetation, vegetated groyne is also more effective.

Keywords: Morphological changes; vegetated groynes; Shigenobu river; iRIC.

1 INTRODUCTION

Groynes are hydraulic structures constructed from the riverbank some distance to the river for riverbank erosion protection and maintaining navigation canals. There are two types of groynes, emerged groynes and submerged groynes, and are generally placed in groups. The areas between the groups of groynes are groyne field.

In Japanese rivers, many groynes have been constructed to protect the riverbanks from two centuries ago after transferring technical knowledge of Netherlands design. In recent years, polarization proceeded has always occurred such as local sediment deposited by the development of vegetation in the river channel, local scouring on the other side from the low-flow channel, so the control on the river has become difficult. Even in Shigenobu River which flows through Matsuyama, Ehime Prefecture, the phenomenon of polarization of the river has occurred, outflow significant sediment and riverbank erosion.

Studies about groynes and the effect on the flow have been widely developed both experimentally and with numerical simulations. Asayama and Kadota (2014) conducted experiment with particle tracking velocimetry (PTV), numerical analysis of 3D flow and bed variation around the groynes. Groyne studied is permeable groyne with stone-gabion. It shows the significant effects of different groyne arrangement on flow and bed variation. The flow pattern such as mean velocity and bed variation around the successive groynes changed due to arrangement groynes. Ali (2013) conducted the experiment in a variety of models utilizes vegetation as an obstacle. The shape of the vegetation is important, small difference between the head loss due to vegetation shape. In case set the top of 5mm mesh of the weir was found lead to resistance than other shapes, such as cylindrical or conical shape. The effect was revealed that within 10 percent of the total energy head loss. Muraoka et al. (2009) have studied effects of permeability and the scales of the groyne and stone gabion for condition submerged or emerged flow over the groyne. The morphological, for example, sand waves have changed large due to the permeability, groyne length and flow conditions. Yossef and Uijttewaal (2003) has investigated the dynamics of the flow near groynes with two conditions, emerged and submerged. Ibrahim (2013) has performed an experimental study of groynes used combination the physical and numerical models in straight channels. Sukhodolov et al. (2002) examines a variety of recirculation flow patterns that develop in the groyne fields on rivers. Observations in flume experiments and field measurements. They revealed that the sequence of groyne fields affects the mixing layer between the river and the groyne field. Also show the distribution of deposited fine sediments in the groyne field with one-gyre circulating system and two-gyre circulating system. Przedwojski (1995) measured bed topography bend scour and local scour caused by impermeable groynes at concave banks. The width of scour holes and the local scour depth changes depend significantly on flow and bed topography in a given bend. They found a new equation for predicting the maximum depth of local scour around impermeable groynes.

In addition, studies about computation of flow with numerical modelling have been done for comparison experimental research. Suharjoko et al. (2013) analyzed simulation modelling groyne placement on the river bend using mathematical modeling approach by finite different method. Fischer-Antze et al. (2008) performed the morphological bed changes in a section of the Danube River using a 3D computational fluid dynamics model (CFD). Hooke et al. (2005) simulated the effects of floods upon the morphology by erosion and sedimentation and the interactions with vegetation in Ephemeral River channel using a computer model CHANGISM. Ouillon and Dartus (1997) presented the porosity method to track the free surface for flow computations and its application with a 3D Reynolds solver using the SIMPLE algorithm.

In this study, on-site survey in Shigenobu river, a rapid-flowing river was conducted and two-dimensional flow condition analysis using iRIC software. The case has a review is the existing groyne and modification the existing being vegetated groyne with variation density. It is clarified whether there is an effect of correcting the river way. In addition, we aim to make proposals for maintaining falling abilities of groyne and stabilizing river channels by proposing new vegetated groyne.

2 METHODOLOGY

2.1 Investigations around the groynes are overgrown vegetation

Shigenobu River during the calm water, sees sand and gravel riverbed and almost no running water. At the time of the flood, the gravel movement is becoming weaker and deposition sandbar encourage expansion areas of vegetation. In addition, the flow through the flow channel is low, which is a concentrated zone of water passing and scours occurs with a displacement of gravel resulting in polarization of the river.

At the present, there are 43 groynes that exist in Shigenobu river. The target groynes in this study are located in 6.2-6.6 km section from the estuary as seen in Figure 1. Summary of the groynes that reviewed are shown in Table 1. There are two impermeable groynes. In this place, where the groyne is located, the soil and sand will move greatly each time the flood, and local deep scouring may occur.

In this research, decrease in high the two of the concrete block impermeable groyne type by eliminating the top half of the existing groyne and set up a vegetation in the head becomes the permeable groyne type as seen in Figure 2. It's considered and proposed for preventing the progress of polarization of river channels by raising the water flow capacity at the time of flooding and moving the soil and sand to lubrication.

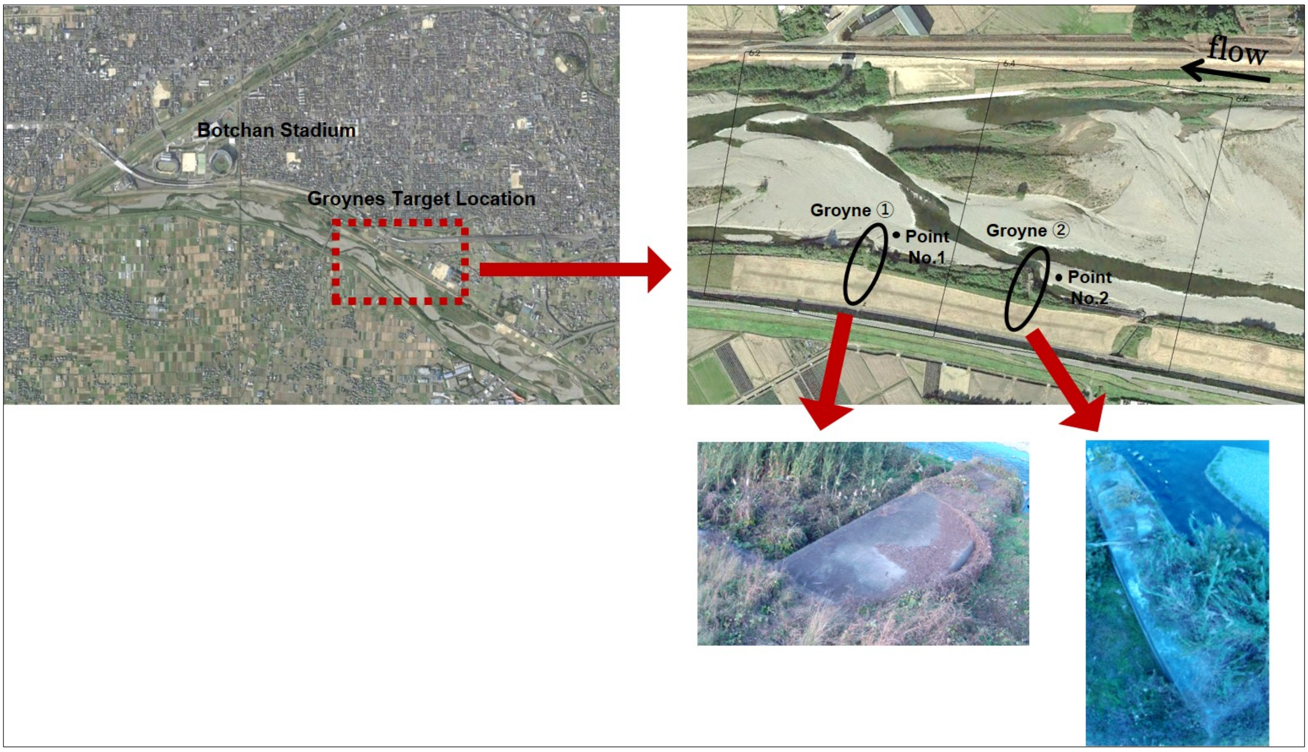

Figure 1. The target groynes of the study and existing groynes condition.

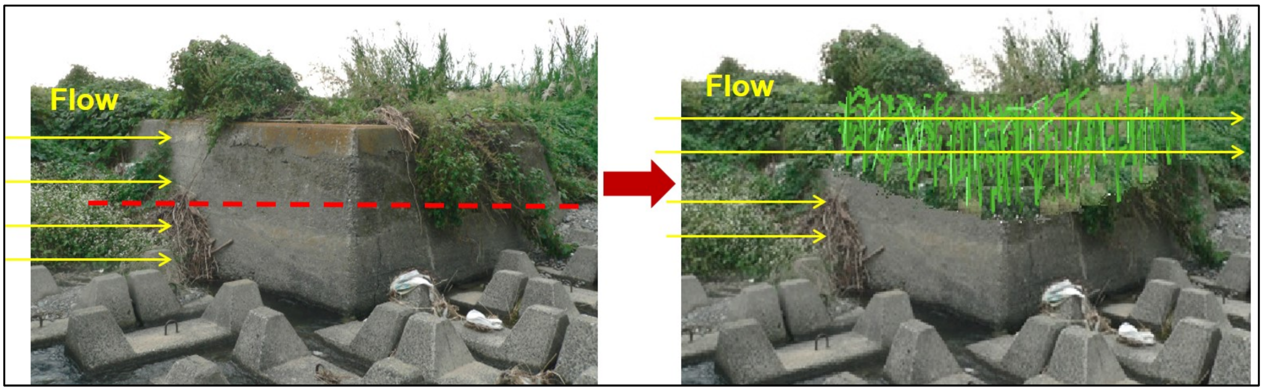

Figure 2. Simulation eliminating the top half of the existing groyne becomes vegetated groyne.

Table 1. Summary of the groynes that reviewed.

Installation groyne	Distance from estuary (km)	Construction		Size		
		Shape	Material	Height (m)	Width (m)	Length (m)
Groyne ①	6.322	I	concrete	1.20	4.20	18.00
Groyne ②	6.479	I	concrete	1.40	4.40	24.70

2.2 The particle size analysis using drone (BASEGRAIN)

In field measurements, surface riverbed images were taken by drone to estimate the optimal particle size distribution around the groyne. The images were analyzed by Matlab based software (BASEGRAIN) for particle size distribution of the riverbed gravel surface layer. The bed surface images were taken in two points around the groyne as seen in Figure 1. The riverbed particle size was found within the range 10 ~ 110 mm at the point no.1, and at the point no.2 the bed particle size was found up to 10 ~ 220 mm. So, a larger diameter bed particle located in the Point No.2 compared to at the Point No.1. The particle size for Point No.2 is 28 mm and particle size Point No.1 is 27 mm. Figure 3 shows the granules situation in field measurements. The bed particle size is set to 27. 5 mm and the averages passing mass percentage are 0.5. The result of the analysis at the two points by BASEGRAIN is shown in Figure 4.

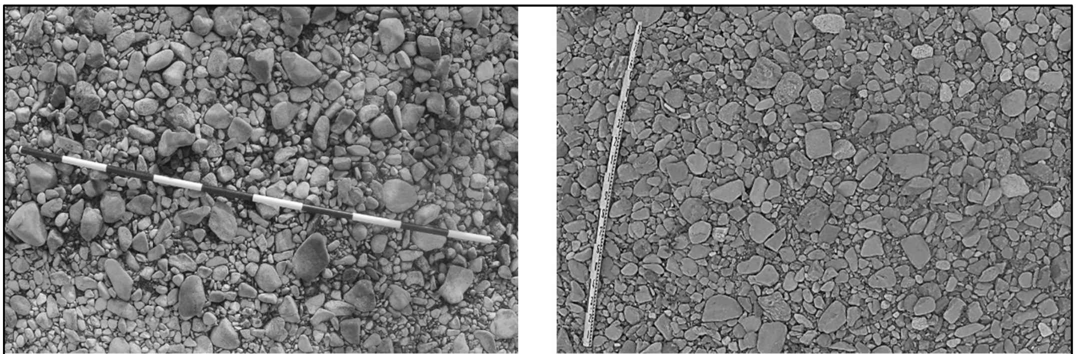

Granules situation (around point No. 1) Granules situation (around point No. 2)

Figure 3. Granules Situation.

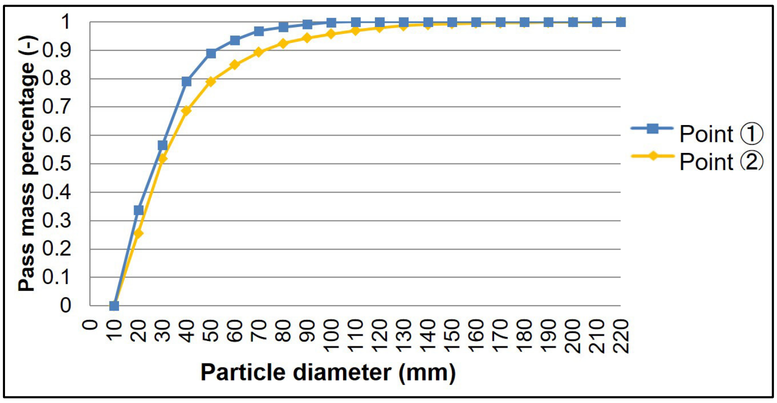

Figure 4. Particle size distribution (comparison at two sites).

3 ANALYSIS

3.1 Numerical simulations

In this study, we focused analysis on the result of field investigation with numerical simulations. Analysis for riverbed changes and flow velocity in around the groynes was conducted with river simulation software iRIC. Conventionally, iRIC included Nays 2D, Morpho 2D, FaSTMECH, etc. as a planar two-dimensional solver with the increased. Nays2D includes several options for simulating river flows such as an unsteady vortex generation in open channel flows and river morpho dynamics. Solver is developed in more multi-function is Nays2DH with the aim of broadly corresponding to the request of the user. Nays 2DH is a planar two-dimensional solver developed to calculate flow in the river, river bed change and river bank erosion. This function is for visualization and analysis of calculation results. Visualization of calculation results can be used for purposes such as creation of vector, contour, and other diagrams, as well as creation of graphs. Furthermore, visualization results can be output to file in graphic formats such as JPG, or output to Google Earth. Generally, the numerical simulations step is: create a grid for calculation using river survey data and/or Digital Elevation Model (DEM) data; set simulation discharge, boundary conditions, roughness and other items and run the simulation. After that, visualize the simulation results, such as flow velocity, water depth and riverbed elevation, by using a contour map and/or vector map.

3.2 Set of conditions in the analysis

Mesh was created from river bed data using numerical data of cross-section survey results according to the regular longitudinal cross-section survey guidelines set by the Ministry of Land, Infrastructure and Transport River Bureau. The transverse direction was 100; the main flow direction was 100 and divided the meshes into pieces. The number of gratings is 20301.

In this study, we analyze using flow rate of three patterns of water level: calm water, flood time and planning high water level. The flow rate in normal water is 24 hours from 15:00 on October 21, 2013 until 14:00 on October 22. The average flow rate is about 3.8 m^3/ s. The flow rate at the time of flooding is 24 hours from October 24, 2013 to October 25, 18:00, which recorded the peak flow value of the latest year among the existing data of the Ministry of Land, Infrastructure and Transport. The average flow rate is about 800 m^3/s. The planning high water level flow rate at the target position is set to 2520 m^3/s. Analysis time is 24 hours as in the case of flat water and flooding.

The roughness coefficient of Manning of the low waterway is 0.035, the value set by Matsuyama River National Highway Office. As there are many cultivated land and bushes, there are 0.05 for the high aqueduct as a value to adapt to either, vegetation is placed only in the part where trees are conspicuous and the value is 0.08. Figure 5 shows the layout of low water channel, flood channel and vegetation and the degree of vegetation group denseness. Since these values are based on the values prescribed by Matsuyama River National Highway Office, it can be said that the relevance is high.

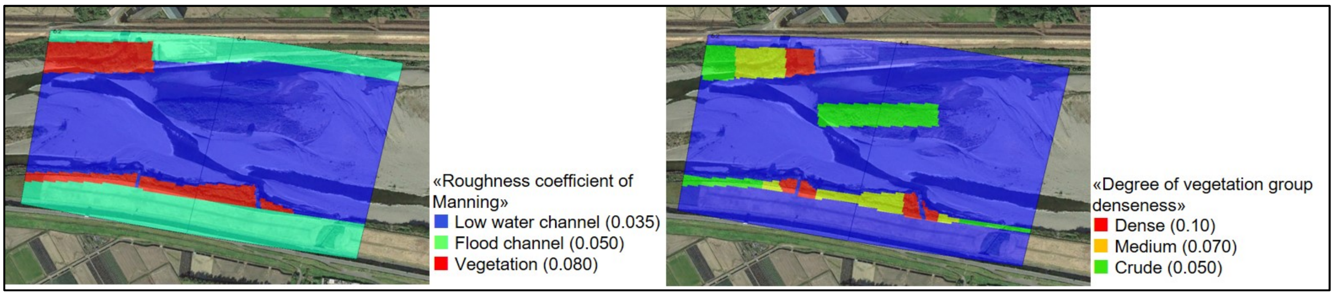

Figure 5. Roughness coefficient of Manning and degree of vegetation group denseness from Matsuyama River National Highway Office.

4 RESULTS AND DISCUSSION

4.1 Analysis of results for the plane two-dimensional flow-bed variation.

As a result of analyzing the plane two-dimensional flow and the bed fluctuation analysis, the magnitude of the flow velocity vector and the river bed variation after 24 hours are shown in Figure 6 and Figure 7 when the flow rate is normal, Figure 8 and Figure 9 in the case of flooding, Figure 10 and Figure 11 show the case of planning high water level. These figures also show the results of analysis of the vegetation part dense degree of existing groynes and vegetated groynes in order to grasp the function of each groynes more accurately. The length of the flow velocity vector indicates the velocity of the flow, and the direction of the arrow indicates the flow direction.

Figure 6 shows the flow velocity in case of calm water (about 3.8 m^3/s) around the two groynes in existing groynes condition and vegetated groynes condition with vegetation density variation. The variation of vegetation density consists of dense degree 0,1; 0,3; 0,5 and 0,9. Figure 7 shows the riverbed change in case of calm water with the same condition above. These figures seen no significant differences between existing groynes and vegetated groynes. Since the flow rate is low during calm water, it does not pass through the vegetation section of the vegetated groynes. So, it can be confirmed that there is no big difference to the river bed fluctuation compared to the existing groynes. Therefore, it can be expected that the vegetated groynes will exert the same effect as the existing groynes at the time of normal water (calm water).

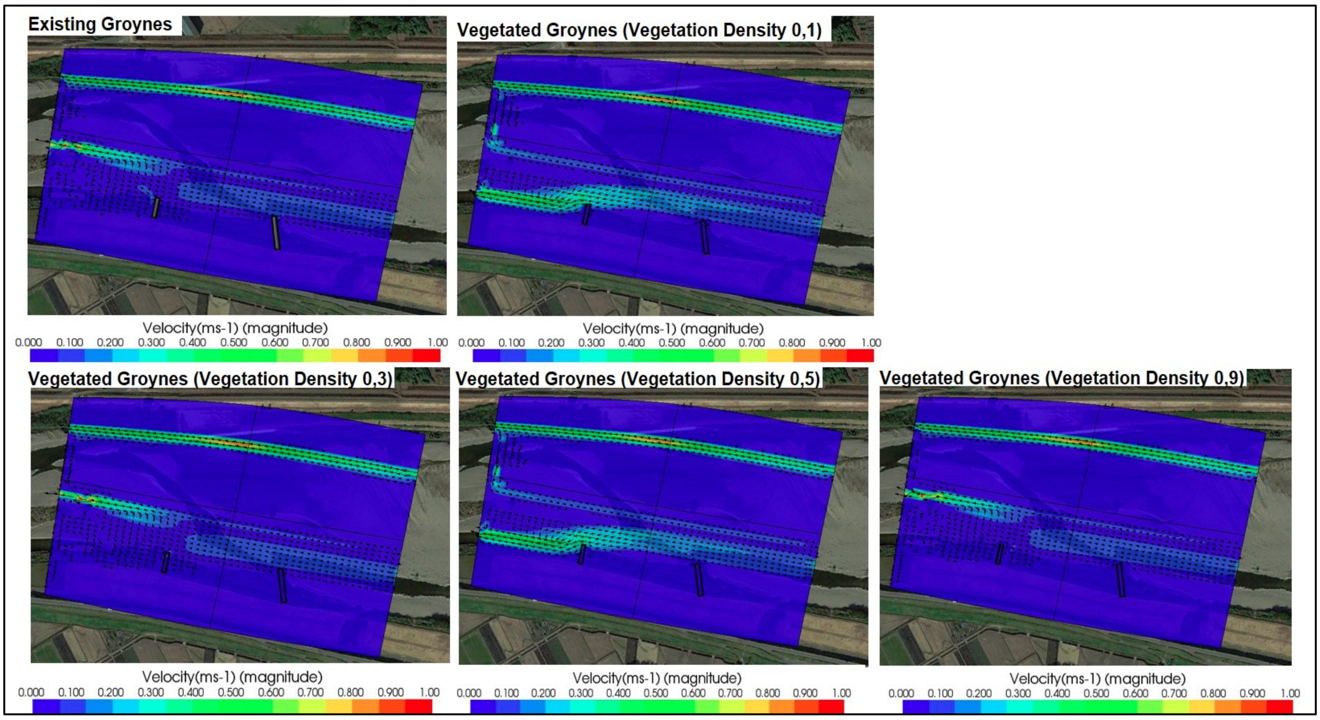

Figure 6. Flow velocity in case of calm water.

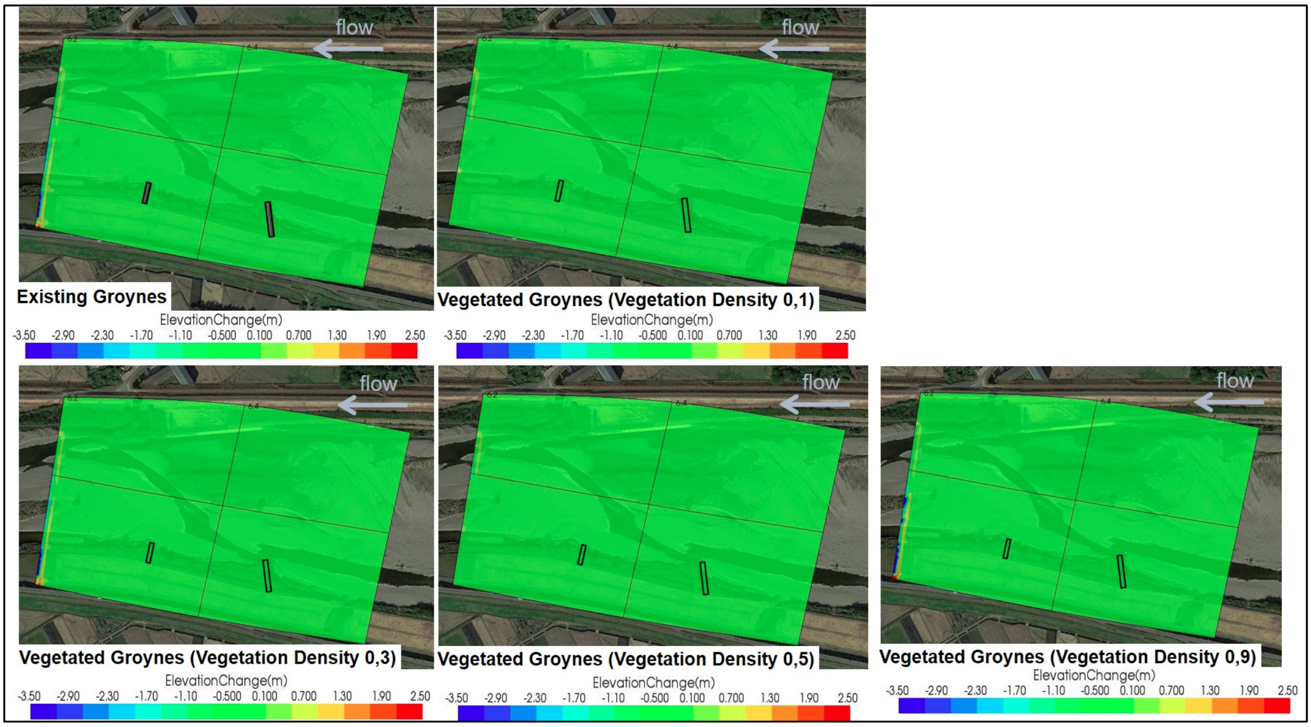

Figure 7. Riverbed change in case of calm water.

Figure 8 and Figure 9 shows the flow velocity and riverbed change in case of flooding (about 800m^3/s). At impermeable groyne (existing groyne), the flow not transmitted through the groyne. Furthermore, the speed on

  / ISSN 1562-6865 (Online) - ISSN 1063-7710 (Print)

the downstream side of the groyne is slowing down. Local deep scouring is seen near the tip of the groyne and sediment deposition is remarkable on the downstream side of the groyne. Permeating flow is seen on the downstream side of vegetated groyne and the speed difference from the flow velocity on the center side of the river. Moreover, local scouring and sediment deposition also visible near the vegetated groyne. Nevertheless, in comparison, deep scouring and sedimentation is reduced at vegetated groyne. River's bed fluctuations occur not only around the groyne but also widely in the section area, but the local scouring on the left bank side is decreasing.

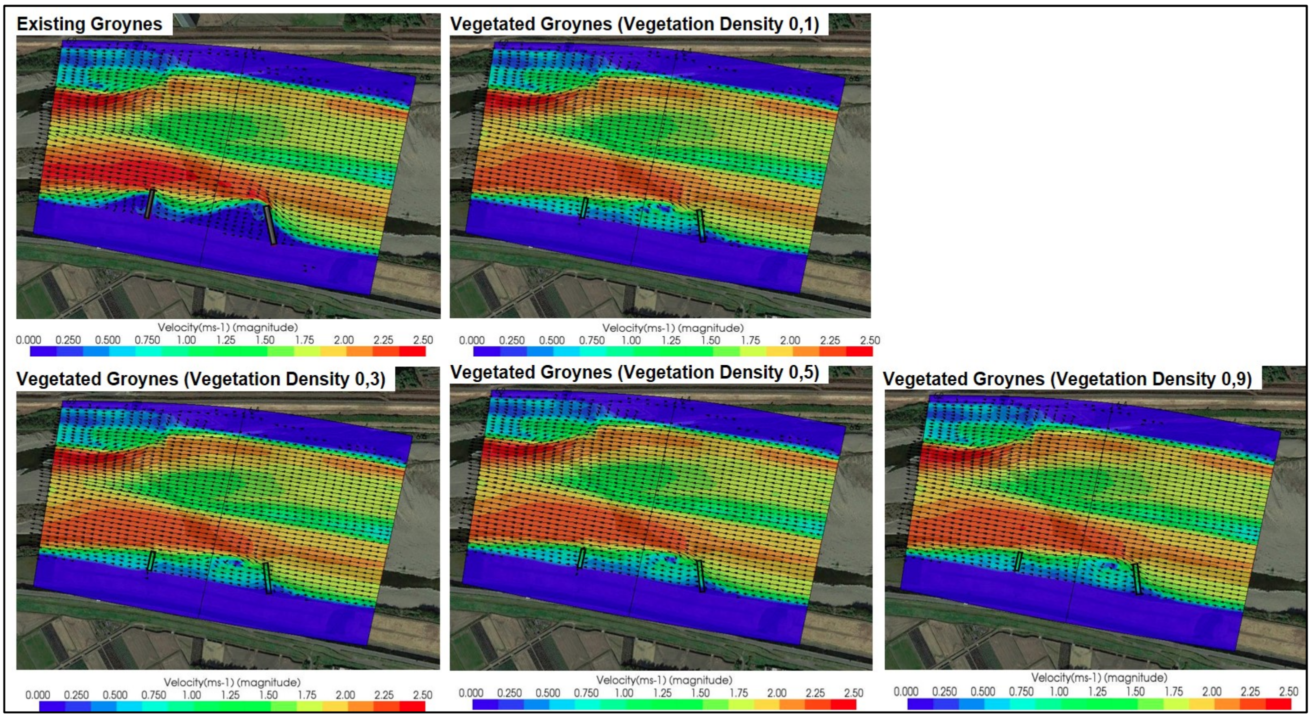

Figure 8. Flow velocity in case of flooding.

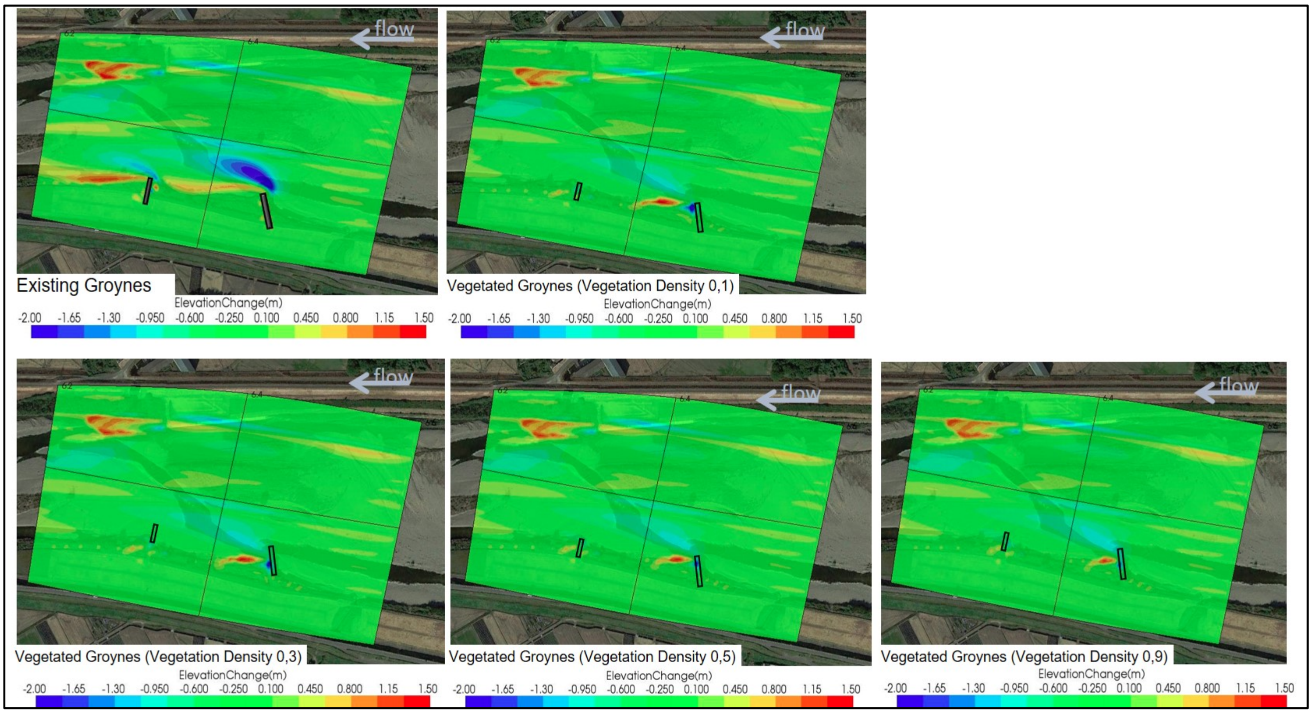

Figure 9. Riverbed change in case of flooding.

Figure 10 and Figure 11 shows the flow velocity and riverbed change in case planning high water level (about 2520m^3/s). At the time of flooding and planning high water level, the influence of the flow can reduce the flow velocity behind the groyne. However, the flow velocity difference with the center side of the river road becomes large. Soil and sand accumulate on the downstream side of the groyne, and generate the local deep scouring. On the other hand, the sediment accumulated on the downstream side of the groyne and the local deep scouring was confirmed also in vegetated groyne. It's same occurrence to the existing groyne. Moreover, the flow passed through the groyne. Thus, there is an effect of suppressing promotion of polarization of river way by alleviating flow velocity difference, reducing sediment deposition and deep scouring. This effect was remarkable when vegetated groynes have relatively high densities of vegetation.

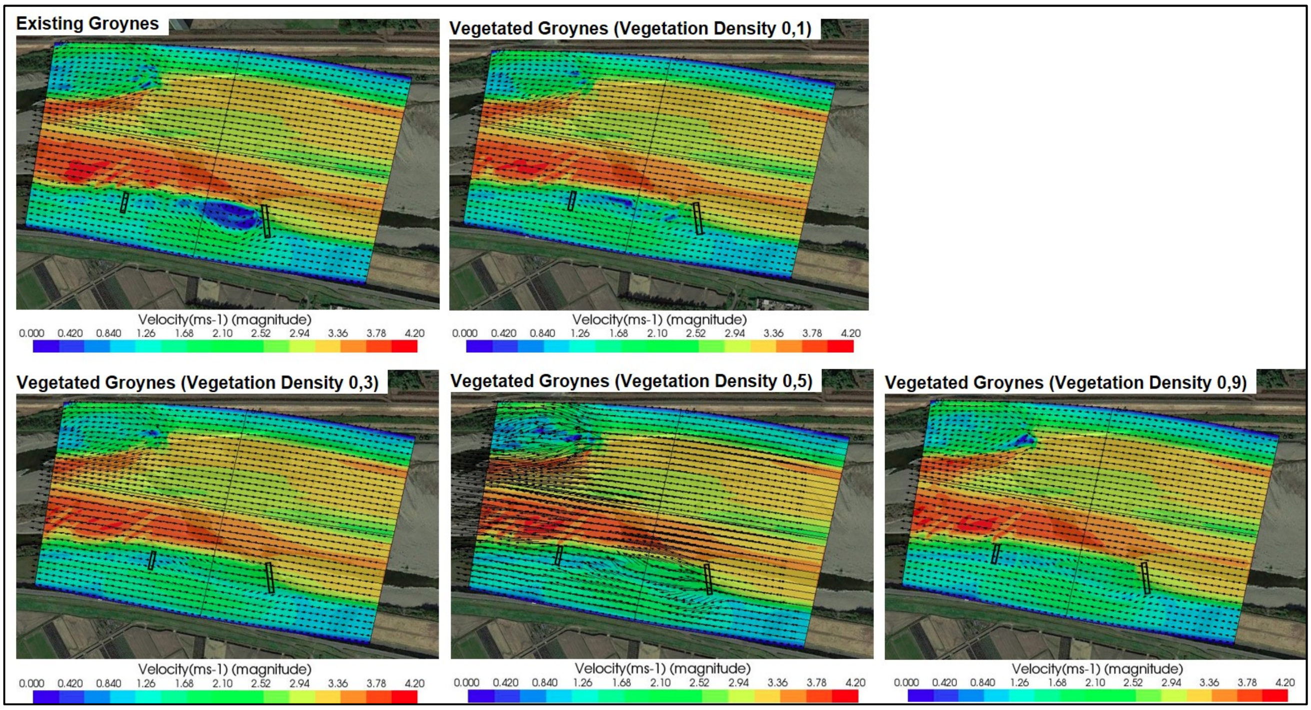

Figure 10. Flow velocity in case planning high water level.

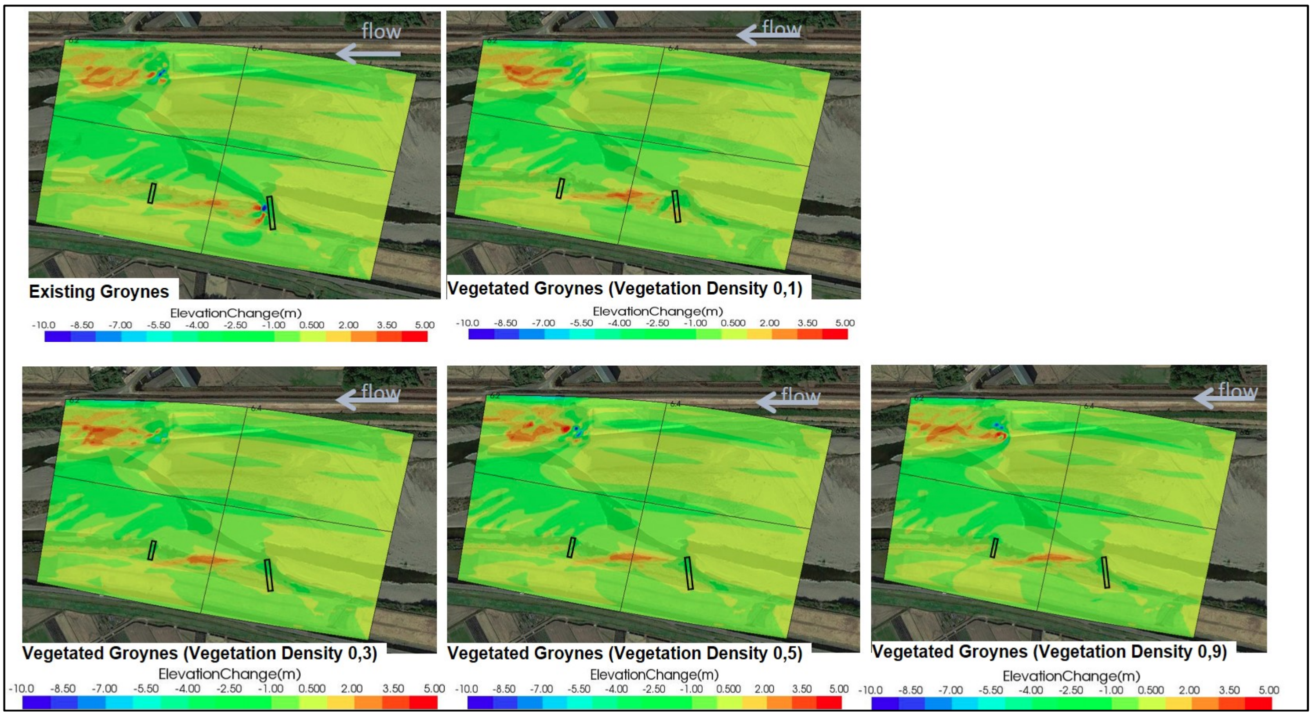

Figure 11. Riverbed change in case planning high water.

Based on the above results, the vegetated groyne exerts the same effect as the existing groyne at the time of calm water. The risk of polarizing the river channel due to sediment accumulation and deep scouring at the time of flood and planning high water level is visible. However, it is judged that it can be relaxed. In addition, from the viewpoint of suppressing polarization of river channels, the objective of this research is also to consider that the dense degree of vegetation, which is considered to be more effective at vegetated groyne is about 0.9.

5 CONCLUSIONS

The present study focuses to clarify the functions of the existing groynes and analyzing the morphological changes around vegetated groynes. As a result, the existing groynes and vegetated groynes during the calm water have the same effects in the river bed fluctuations. However, at the time flooding and planning high water level, vegetated groyne with high denseness of vegetation have an effect of suppressing promotion of polarization river way by alleviating flow velocity difference, reducing sediment deposition and deep scouring. In the future, along with the improve the accuracy of the analysis performed in this study, should be to propose a real improvement of the groynes in existence that can be applied to the river. Concrete river management that influences vegetated groyne.

REFERENCES

Ali, S. (2013). Flow over Weir-like Obstacles, *Master thesis*. University of Engineering and Technology, Taxila, Pakistan geboren te Faisalabad – Pakistan, 216.

Asayama, C. & Kadota, A. (2014). Study on Control for Suitable Bed Morphology around Successive Groynes. *International Symposium Geohazards: Science, Engineering and Management*, Kathmandu, Nepal.

Fischer-Antze, T., Olsen, N.R.B. & Gutknecht, D. (2008). Three-Dimensional CFD Modeling of Morphological Bed Changes in the Danube River. *Water Resources Research,* 44, 1-15.

Hooke, J.M, Brookes, C.J., Duane, W. & Mant, J.M. (2005). A Simulation Model of Morphological, Vegetation and Sediment Changes in Ephemeral Streams. *Earth Surface Processes and Landforms,* 30, 845–866.

Ibrahim, M.M. (2013). Local Bed Morphological Changes due to Oriented Groins in Straight Channels. *Ain Shams Engineering Journal,* 5, 333-341.

Muraoka, H., Fushimi, T., Kadota, A. & Suzuki, K. (2009). Experimental Study on Changes of Bed Configuration Caused by a Permeable Groyne of Stone Gabion. *Proceedings of 16th IAHR-APD Congress and 3rd Symposium of IAHR-ISHS,* 3, 1072-1077.

Ouillon, S. & Dartus, D. (1997). Three-Dimensional Computation of Flow Around Groyne. *Journal of Hydraulic Engineering,* 123(11), 962-970.

Przedwojski, B. (1995). Bed Topography and Local Scour in Rivers with Banks Protected by Groynes. *Journal of Hydraulic Research,* 33(2), 257-273.

Suharjoko, Bisri, M., Rispiningtati, Ruslin, M. & Anwar. (2013). Modelling of Groyne Placement on the River Bend Based on Sedimentation Analysis using Numerical Simulation Approach by Finite Difference Method. *International Journal of Engineering Research and Applications (IJERA)*, 3(1), 231-237.

Sukhodolov, A, Uijttewaal, W.S.J. & Engelhardt, C. (2002). On the Correspondence between Morphological and Hydrodynamical Patterns of Groyne Fields. *Earth Surface Processes and Landforms,* 27, 289-305.

Yossef, M.F.M. & Uijtewaal, W.S.J. (2003). On the Dynamics of the Flow Near Groynes in the Context of Morphological Modelling. *XXX IAHR Congress*. Thessaloniki, Greece, 102, 361-368.

Proceedings of the 37th IAHR World Congress
August 13 – 18, 2017, Kuala Lumpur, Malaysia

PRESSURE PROPERTIES AT THE BOTTOM OF A STILLING WELL

JINGJING ZHAI[(1)], QINGYUAN YANG[(2)] & TAO ZHU[(3)]

[(1,2)] Department of hydraulics, Changjing River Scientific Research Institute, Wuhan, China.
topzhaijingjing@163.com
[(3)] Administration of Gaoguan Reservior, Jingmen, China

ABSTRACT

Stilling well is usually used for the energy dissipation of pipe flows with high head and low discharge. Many studies focus on the empirical formula of the well scale and flow rate, and few are about the flow field and pressure properties in the well. Without the pressure distribution, it is hard to analyze the safety of the well when it is functioning. In this paper, a physical model is proposed to investigate the properties of pressure acting on the bottom of the stilling well. The runs of the experiment were with different flow rates and outlet distances. Quantitative relationships among pressure parameters, flow rate and outlet distance were established. The study show that the pressure acting on the bottom decreases nonlinearly as the distance L rise at same flow rate. When the △ equals to 0.5D (D, diameter of the pipe), the pressure is much larger than that with 1.0D. When the distance changes to 1.5D (and above), the pressure decreases a little compared to that with 1.0D.

Keywords: Stilling well; impact pressure; distance between pipe outlet; well bottom.

1 INTRODUCTION

In dam engineering, there are two types of energy dissipation (Guo, 1982): one is called the basic way of energy dissipation, such as hydraulic jump, ski-jump energy dissipation, bucket and submerged bucket energy dissipation, etc. The other type is called special energy dissipater, such as impact-type energy dissipater, jet energy dissipater, and stilling well dissipation, etc.

Jet flow stilling well dissipates the energy by the jet flow impacting on the well bottom. The high speed water gets into the well through the jet pipe, run against the well bottom, and mixes with other water in the well. The flow fluctuates strongly, and plenty of energy is dissipated in the well. The jet flow stilling well is good for energy dissipation of water with high head and low discharge. Guo (1982) proposed an experiment to investigate the energy dissipation in stilling well. In his study, the energy dissipation efficiency was analyzed, while the flow structure in the well was not presented. Liu (2002) also carried out a physical model to study the jet flow stilling well, and the study showed that for pipe flow with high head and low discharge, the valve near the outlet is useful for the energy dissipation while the fluid is flowing from the pipe. Wang (2005) came up with a function describing the major impact factors on stilling well based on experiment data.

For those vertical jet flows, the pressure is huge at the center of the bottom, and is small at the brim. The maximum impact pressure occurs at the center of the bottom, and it may generate erosion when the water head is high and the discharge is large. The maximum pressure is very important for the safety of stilling well, and few studies have been working on this area. The purpose of this paper is to investigate the impact pressure on bottom of stilling well.

2 PHYSICAL MODEL AND INSTRUMENT

The model was based on gravity similarity with a scale of 1/10, and model range covered patical jet pipe, stilling well and downstream channel. The jet pipe (diameter 0.1m), stilling well and downstream channel were all made of perspex, and the arrangement of the model and test points are shown in Figure 1. The main purpose of this study is to investigate the connection of distance (△) between jet pipe outlet and stilling well bottom on the bottom impact pressure. The impact pressure was measured by Pitot tube.

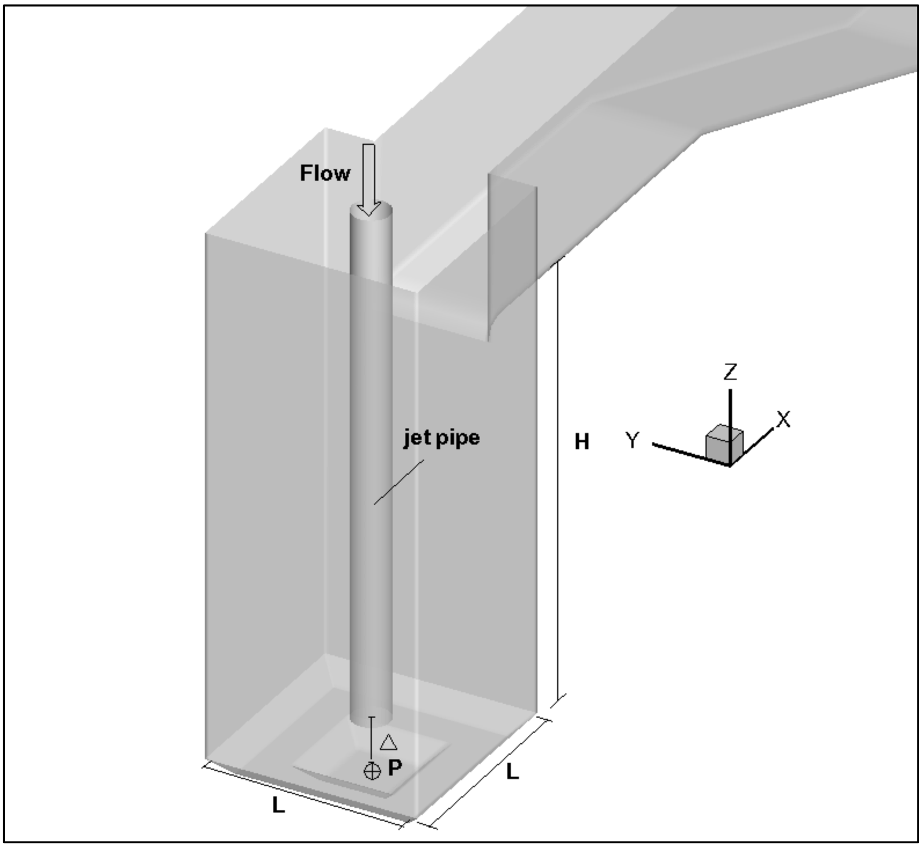

Figure 1. Sketches of physical model and test point of pressure

3 RESULTS AND DISCUSSION

Bottom impact pressures under different △(distance between jet pipe outlet and stilling well bottom) and H (depth of stilling well) are shown in Table.1. When the △ and H are both equal, the impact pressure (P) keeps rising as the discharge (Q) increase. Meanwhile, when the H and Q are both equal, the pressure is bigger as the △ get smaller.

Table 1 Table of bottom impact pressures of jet flow (unit: ×9.81KPa).

H (M)	Q (M^3/S)	△=0.5M	△=1.5M	△=2.5M	△=3.5M	△=4.5M	△=5.5M	△=6.5M
10	10.3	10.9	8.86	8.7	6.8	6.48	5.9	-
	6.8	5.3	3.6	3.7	2.9	2.39	2.55	-
	3.8	1.42	1.02	0.92	0.32	0.23	0.35	-
8.5	10.3	10.9	9.1	8.76	8.68	7.15	6.00	-
	6.8	4.52	3.83	3.31	3.63	2.92	1.75	-
	3.8	1.4	1.11	0.9	0.92	0.6	0.21	-
6.5	13.6	19.97	17.96	17.30	16.12	14.34	11.10	8.60
	10.3	11.66	10.13	9.95	9.80	7.77	6.12	4.73
	6.8	5.35	4.65	4.35	4.10	3.33	2.42	2.05
	3.8	2.02	1.72	1.50	1.53	0.85	0.73	0.71

According to the dimension analysis, the maximum pressure P_{max} at the bottom of stilling well may depend on:

$$P_{max} = f(Q, D, \Delta, g) \qquad [1]$$

where, Q is the discharge(m^3/s), D (m)is the diamerter of the jet pipe, and g($9.81 m/s^2$) is the acceleration of gravity.

In order to construct the formula connecting P_{max} and Q, D, Δ, g, the test data were converted to $\frac{P_{max}}{\Delta}$, $\frac{\Delta}{D}$, 、 $\frac{Q^2}{gD^5}$, and then analyzed in Figure 2.

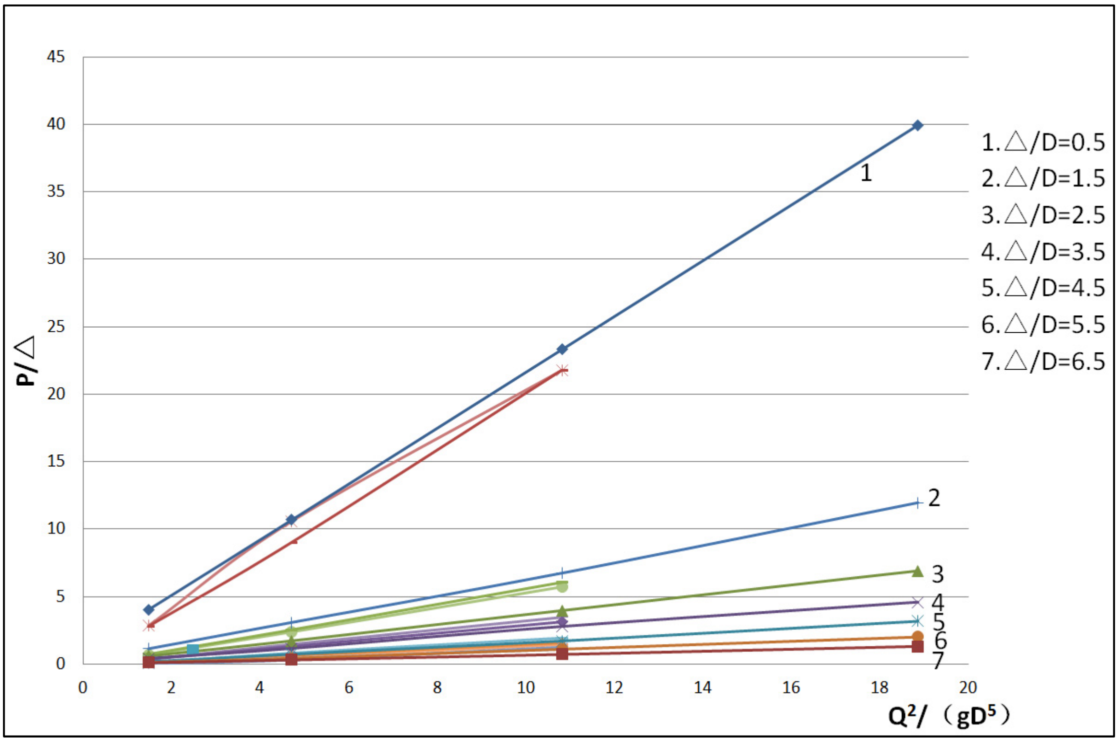

Fig.2 Curves **about P_{max}, Q, D, Δ, g**

The figure shows that under different Δ/D, $\frac{Q^2}{gD^5}$ and $\frac{P_{max}}{\Delta}$ have a linear connection. When Δ/D equals to 0.5, the slope of the curve is bigger than 2. When Δ/D≥1.5, the slopes of the curves are all less than 1. The larger the Δ/D, the smaller the slope.

Based on dimension analysis, the following was given:

$$\frac{P_{max}}{\Delta} = f\left(\frac{\Delta}{D}, \frac{Q}{\sqrt{gD^5}}\right) \qquad [2]$$

And further to：

$$\frac{P_{max}}{\Delta} = k_0\left(\frac{\Delta}{D}\right)^{k_1}\left(\frac{Q}{\sqrt{gD^5}}\right)^{k_2} \qquad [3]$$

where k_0, k_1, k_2 are constants. k is the slope of the curves of $\frac{P_{max}}{\Delta}$ and $\frac{Q^2}{gD^5}$ under different $\frac{\Delta}{D}$. The curve of k and Δ is shown in Figure 3.

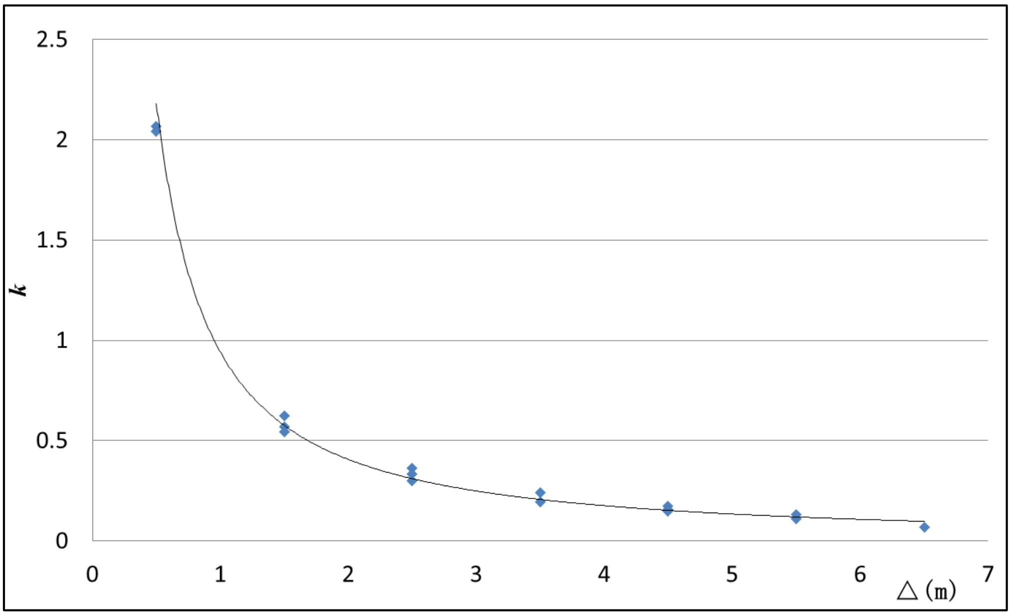

Figure 3 Fitted curve of factor k and △.

Then, it can be derived that $k_0 = 0.9415$, $k_1 = -1.212$, k_2 =2. Hence, the formula of P_{max} with Q, △ and D is:

$$P_{max} = 0.9415\left(\frac{\triangle}{D}\right)^{-1.212} \triangle\frac{Q^2}{gD^5} = 0.9415\left(\frac{\triangle}{D}\right)^{-0.212}\frac{Q^2}{gD^4} \quad [4]$$

4 CONCLUSIONS

(1) The bottom impact pressure decreases as the △ increases, and the pressure has a sharp drop when △ is smaller than 1.5m and slowly decreasing when △ is larger than 1.5m.

(2) Based on experiment data and dimension analysis, an empirical formula is constructed. Due the complexity of the flow in stilling well, the formula may not be applicable to other types of stilling well.

Future works need to be done for other stilling wells of jet flow.

ACKNOWLEDGEMENT

The work was partially supported by the central level scientific research institutes fund project of China (Grant No. CKSF2014046/SL, CKSF2014045/SL, CKSF2016042/SL, CKSD2016309/SL), National Natural Science Foundation of China (Grant No. 51609014).

REFERENCES

Guo, Z.Z. (1982). *Principle of Energy Dissipation & Erosion Prevention and Hydraulic Design*. Beijing, Science Press of China, Vol. 57, 396. (In Chinese)

Liu, H.F., Sun, P. & Li, Q. (2002). Experimental Research on Hydraulics Characteristics of Energy Dissipation in Vertical Stilling Well. *Advances in water science*, 13(5), 639-642. (In Chinese)

Wang, Y. (2005). Experimental Study on Energy Dissipation Mechanism of Circular Stilling Wells, *MSc Thesis*. Xinjiang Agricultural University. (In Chinese)

Proceedings of the 37th IAHR World Congress
August 13 – 18, 2017, Kuala Lumpur, Malaysia

NUMERICAL AND EXPERIMENTAL OPTIMIZATION OF FLOW PATTERN THROUGH PIERS OF DAM SPILLLWAYS

JAHANI MATIN[(1)], JABBARI EBRAHIM [(2)], SARKARDEH HAMED [(3)] & MAROSI MORTEZA [(4)]

[(1)]School of Civil Engineering, Iran University of Science and Technology, Tehran, Iran.
[(2)]Department of Civil Engineering, Faculty of Engineering, Iran University of Science and Technology, Tehran, Iran, Jabbari@iust.ac.ir
[(3)] Department of Civil Engineering, Faculty of Engineering, Hakim Sabzevari University, Sabzevar, Iran.
[(4)] Hydraulic Structures Division, Water Research Institute, Tehran, Iran.

ABSTRACT

In this study, the effect of vertical inclination of the piers on the flow pattern and rating curve of dam spillways was studied using numerical and physical models. Experiments on the flow pattern through vertical piers were conducted to produce measurement data of the discharge, flow depths and velocities over the spillway. Then sensitivity analysis of grid resolutions in the CFD simulations was performed for the vertical piers model. The performance of the CFD simulations with the selected grid resolution was examined and validated by comparing the results of the simulation with the measured data for vertical piers model. Generally, the simulation results were found to be in good agreement with the measured values, with an average relative deviation of less than 10%. Finally, the effect of vertical inclination of the piers on the flow pattern and rating curve was investigated using CFD simulations. Flow conditions between a vertical pier and two inclined piers (81° and 64° inclination from horizontal) were evaluated. Results showed that a longitudinal inclination of nose of the pier leads to improve the approach flow conditions. Assessing the performance of the 64° inclination shows that this scenario was suitable to pass smoothly flow through the piers and omitting the cross waves and caused the minimum separation along the piers and approach channel. To illustrate the performance of the 64° inclination, flow cross section was plotted which implies uniformity and no cross waves through the approach channel. Comparison between three inclination modes showed that with increasing 28% of vertical inclination of piers, depth averaged velocity in approach channel decreased to 16% and discharge coefficient of spillway increased approximately to 10% and as flow depth in approach channel decreases, discharge coefficient increases. To conclude, as the inclination increases, shock waves reduced and horizontal vortices eliminated.

Keywords: High dam; pier; vortex; spillway; numerical; physical modeling.

1 INTRODUCTION

A spillway is a hydraulic structure that is usually provided at storage and Diversion dam to release surplus or flood water that cannot be safely stored in the reservoir in order to prevent damage to the dam. Inlet flow condition to spillways has significant impact on its performance. In high velocities, vortices can also be appeared in the front of the inlet, which should be prevented because they lead to form unfavorable approach flow conditions, reducing the discharge capacity, and may compromise the dam safety. Therefore, a proper inlet channel design is very important for the spillway and must be hydraulically and structurally adequate in order to provide sufficient capacity (Wang et al., 2010). Study on the flow through the hydraulic structures usually is conducted using physical modeling. Physical modeling is based on the basic fluid mechanic equations. Physical modeling of hydraulic structures means that a scaled laboratory model from the prototype is constructed. This approach is a safe way to analyze the flow through or over the hydraulic structures (Kazemi et al., 2017; Khanarmuei et al., 2016; Azarpira et al., 2015; Nazari et al., 2015; Mardani et al., 2015; Marosi et al., 2015; Sarkardeh et al., 2015; Khanarmuei et al., 2014; Sarkardeh et al., 2014; Suprapto, 2013; Taghvaei et al., 2012; Amiri et al., 2011; Hager et al., 2010; Khodashenas et al., 2010; Roshan et al., 2010; Sarkardeh et al., 2010; Roshan et al., 2009; Safavi et al., 2009; Ettema, 2000; Tokmadzhyan et al., 1988; Aliev et al., 1987). Due to high cost of laboratory experiments, researchers have attempted to use numerical simulation along the physical modeling. In the field of numerical simulation, the governing equations of the flow which are usually Navier–Stokes equations together with turbulence models are solved with numerical methods (Khadem Rabe et al., 2016; Sajjadi et al., 2016; Sarkardeh et al., 2014; Maghsoodi et al., 2012; Rahimzadeh et al., 2012; Jorabloo et al., 2011; Yazdi et al., 2010; Versteeg et al., 2007; Bates et al., 2005; Nakayama et al., 1998; Patankar, 1980). Some researches were performed on guide wall structure. Jian (2005) compared flow conditions with varying curves of the guide wall. Based on the physical model experiment, Hua and Nan (2003) analyzed the optimal layout for a bank spillway. Wang and Chen (2010) studied the spillway of Yutang dam to remove vortex flow and separation on the guide wall. They proposed that the guide wall should be redesigned and present a new shape for the guide wall to elimination remove vortex front the gate. Parsaie et al. (2015) numerically studied the effect of geometry of guide walls of Kamal-Saleh dam on the flow pattern passing through the approach channel and over the ogee weir. They stated that the geometry of the right side wall causes cross wave creation through the spillway specifically at the entrance of approach channel.

Regarding the previous studies, there are few researches on design of guide wall structures at dam spillways. In the present study, the effect of vertical inclination of the piers on the flow pattern and rating curve of dam spillways was studied using numerical and physical models. Experiments on the flow pattern through vertical piers were conducted to produce measurement data of the discharge, flow depths and velocities over the spillway. Using the experimental data the numerical model was verified and the effect of pier inclination was investigated numerically.

2 MATERIAL AND METHOD

To verify the employed numerical model, experimental data of Jareh dam which is an earth fill dam located at the west south of Iran (Khuzestan Province) were used. Figure 1 shows the scaled laboratory model which was constructed to study the flow properties through the spillway. To assess the geometry of piers on the flow pattern, three cases were proposed for the piers spillway. Figure 2 shows different cases and their geometrical properties which were proposed for piers. In these figures the vertical inclination of piers are also shown. By considering the available criteria to avoid the scale effects in the physical model, the scale of the laboratory model was equal to 1:50 and the plexiglass was used as material for constructing the flume.

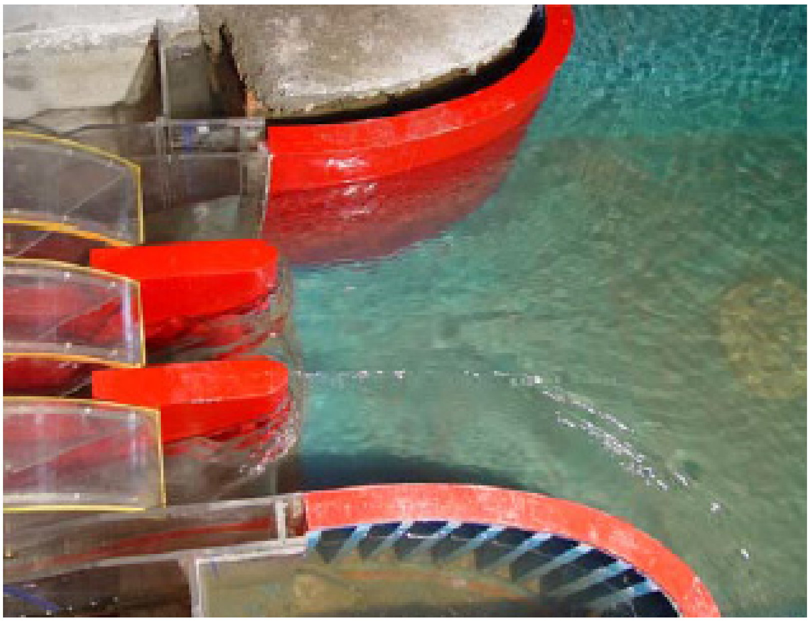

Figure 1. Sketch of the scaled laboratory model of the Jareh dam spillway.

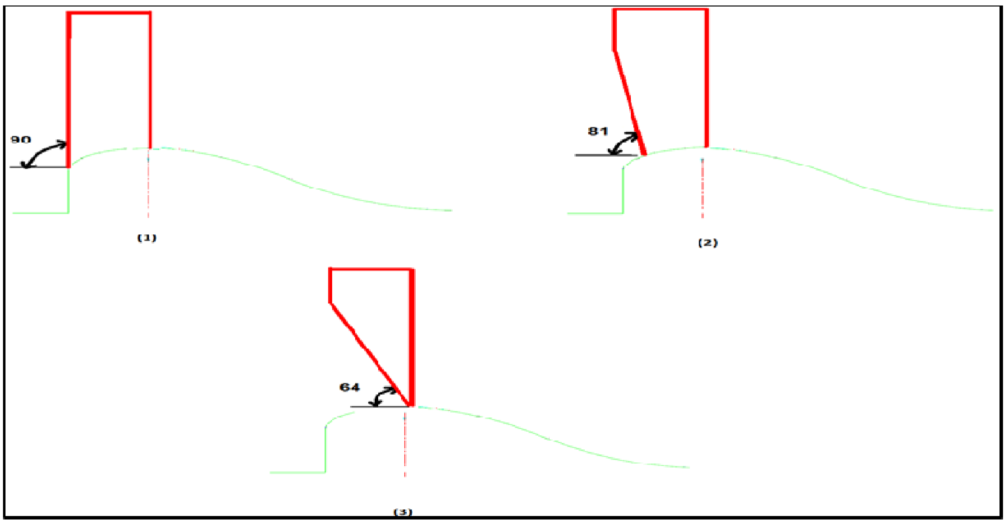

Figure 2. Different designed cases of piers over the spillway.

2.1 Numerical model

Numerical solution of the mean flow field requires resolving the Reynolds averaged Naviere-Stokes equations. These equations for incompressible and continuity flow in Cartesian tensor form can be written as given below, mass continuity:

$$v_f \frac{\partial \rho}{\partial t} + \frac{\partial}{\partial x}(uA_x) + \frac{\partial}{\partial x}(vA_y) + \frac{\partial}{\partial x}(wA_z) = \frac{PSOR}{\rho} \quad [1]$$

where u, v, z are velocity components in the x, y, z directions. A_x, A_y, A_z are cross-sectional area of the flow, q is the fluid density, PSOR is the source term, v_f is the volume fraction of the fluid and three-dimensional momentum equations are given in the Eq. [2].

$$\begin{aligned}
&\frac{\partial u}{\partial t} + \frac{1}{v_f}(uA_x \frac{\partial u}{\partial x} + vA_y \frac{\partial u}{\partial y} + wA_z \frac{\partial u}{\partial z}) = -\frac{1}{\rho}\frac{\partial p}{\partial x} + G_X + \\
&\frac{\partial v}{\partial t} + \frac{1}{v_f}(uA_x \frac{\partial u}{\partial x} + vA_y \frac{\partial u}{\partial y} + wA_z \frac{\partial u}{\partial z}) = -\frac{1}{\rho}\frac{\partial p}{\partial x} + G_y + . \\
&\frac{\partial w}{\partial t} + \frac{1}{v_f}(uA_x \frac{\partial u}{\partial x} + vA_y \frac{\partial u}{\partial y} + wA_z \frac{\partial u}{\partial z}) = -\frac{1}{\rho}\frac{\partial p}{\partial x} + G_z +
\end{aligned} \quad [2]$$

where P is the fluid pressure, G_x, G_y, G_z are the acceleration created by the body fluids, f_x, f_y, f_z are viscosity acceleration in three dimensions and v_f is related to the volume of fluid, defined by Eq. [3]. For modeling of free surface profile, the VOF Technique based on the volume fraction of the computational cells was used. Since the volume fraction F represents the amount of fluid in each cell, take value between 0 and 1.

$$\frac{\partial F}{\partial t} + \frac{1}{v_f}\left[\frac{\partial}{\partial x}(FA_x u) + \frac{\partial}{\partial y}(FA_y v) + \frac{\partial}{\partial z}(FA_z w)\right] : \quad [3]$$

Most popular turbulence models for hydraulic structures are K-epsilon, RNG-K-epsilon and large eddy simulation (LES). Modeling turbulent flow requires defining suitable turbulence model, which creates close form with Navier–Stokes equation. Re-Normalization Group (RNG) model is a powerful turbulence model which has suitable performance for modeling the fine vortices; therefore, this model is very useful for modeling flow pattern. Most equations used in RNG turbulence model are given in Eqs. [4] and [5].

$$\frac{\partial}{\partial t}(\rho k) + \frac{\partial}{\partial x}(\rho u_i k) = \frac{\partial}{\partial x_i}(\alpha_k \mu_{eff} \frac{\partial k}{\partial x_i}) + G_k + G_b - \quad [4]$$

$$\frac{\partial}{\partial t}(\rho \varepsilon) + \frac{\partial}{\partial x}(\rho u_i \varepsilon) = \frac{\partial}{\partial x_i}(\alpha_k \mu_{eff} \frac{\partial \varepsilon}{\partial x_i}) + C_{1\varepsilon}\frac{\varepsilon}{k}(G_k + C_{3\varepsilon}G_b) - C_{2\varepsilon}\rho\frac{\varepsilon^2}{k} - \quad [5]$$

In which Gk is the rate kinetic energy creation, and R is the density of turbulence which defined as below:

$$R = \frac{C_\mu \rho \eta^3 (1 - \eta/\eta_0)}{1 + \beta\eta^3}\frac{\varepsilon^2}{k}, \mu_t = \rho C_\mu \frac{k^2}{\varepsilon} \quad [6]$$

In these equations, $\beta = 0.012, \eta_0 = 1.38$. As Figure 3 showed, the entire geometrical domain in (x, y, z) had the dimensions of 145 x 120 x 110.5 m (1). The mesh grid was composed by three different mesh blocks with cubic cells (2). The boundary conditions were specified pressure at the entrance of channel through the definition of the corresponding water levels, outflow downstream of the chute and continuative between mesh blocks (3). In Figure 3, W = the wall, P = the specified pressure, S = symmetry, O = outflow and C = continuative boundary conditions.

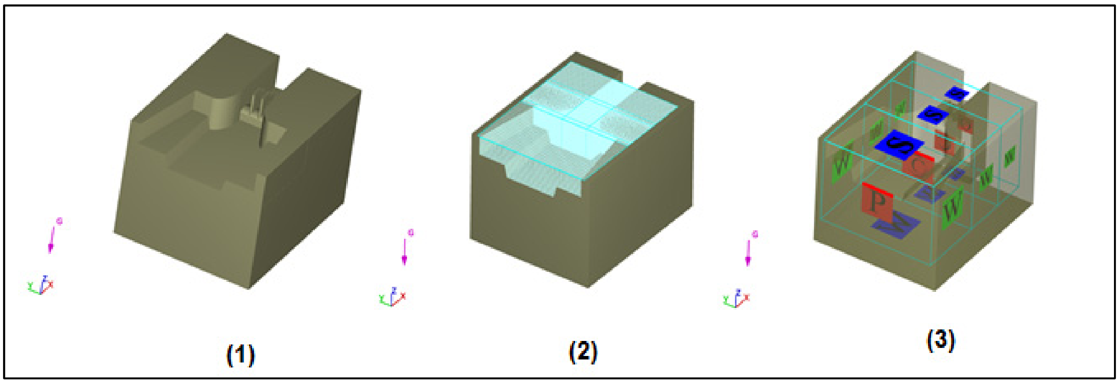

Figure 3. Sketch of 3D model of spillway of Jareh dam (1), Computational domain of model (2), Bindery condition of model (3).

3 RESULTS AND DISCUSSIONS

3.1 Grid- sensitivity analysis

To specify the mesh independency in this study, four numerical simulations were performed with different mesh sizes. Table 1 Indicates cell sizes for each mesh block. In each simulation, flow depth was recorded in the middle of symmetric part of the channel and was compared with the experimental data. The total deviations versus sizes of cubic cells were plotted in Figure 4. As shown in Figure 4, changes of deviation in mesh sizes of simulation 3 and 4 were negligible. Consequently simulation 3, with cell size 1.5m for mesh block 1, 0.6m for mesh block 2 and 0.75m for mesh block 3 is the best grid size. As the Figure 4 Shows, the numerical results were found to be in good agreement with the measured values, with an average relative deviation of less than 10%.

Table 1. Cell sizes for each simulation.

simulation	**block 1**	**block 2**	**block 3**
1	2	1	1.2
2	1.75	0.75	1
3	1.5	0.6	0.75
4	1.25	0.5	0.6

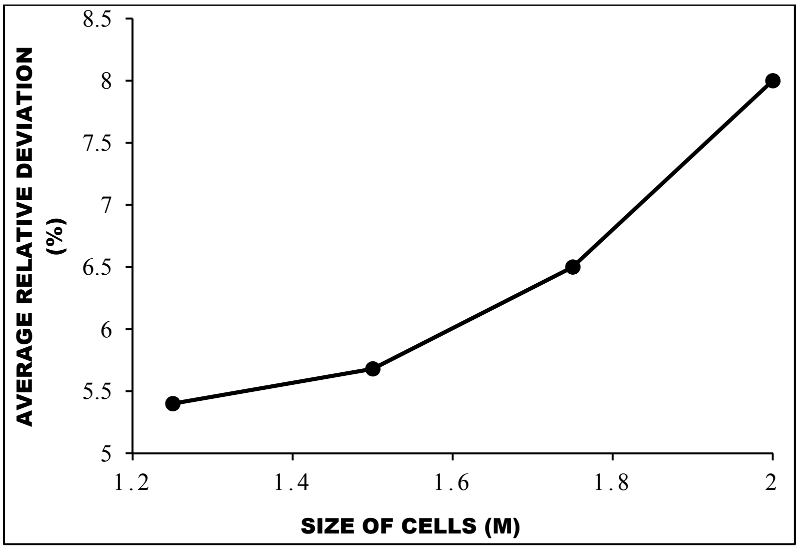

Figure 4. Deviation of simulations versus sizes of cubic cell in mesh block 1.

3.2 Prediction accuracy of flow depth

Figure 5 compares the flow depth obtained by CFD (the RNG with the simulation 3 grid) with the measured values obtained. The agreement between the results for the CFD analyses and those obtained by experiment are generally good. Generally, the average deviation between the results of the simulation and the measured results was approximately around 5%. In this figures P = height of spillway and z = flow depth and X = distance from ogee spillway and L_S = the length of spillway.

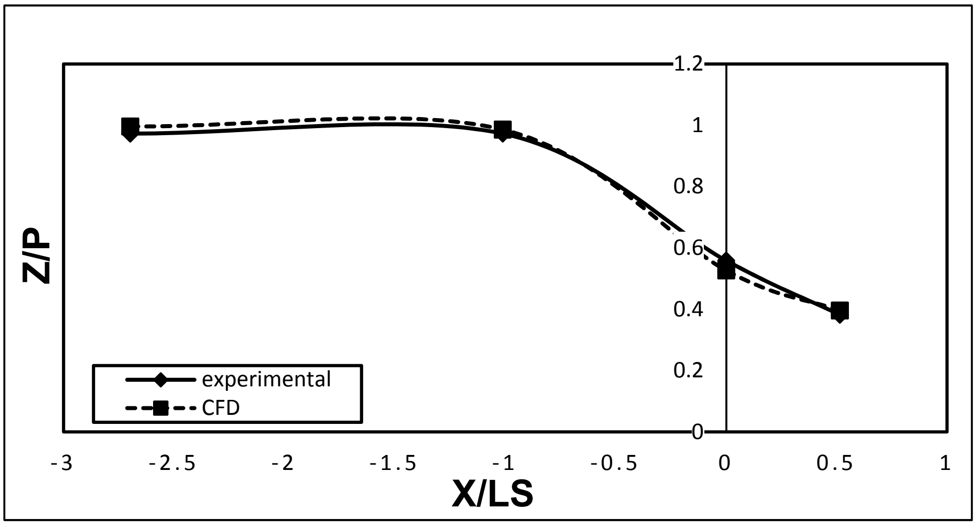

Figure 5. Comparison of flow depth as obtained by CFD analysis and experiment.

The flow was strongly disturbed close to the spillway and in the entire bays. Consequently, the flow over the chute was also perturbed and non-uniform (Figure 1). Considering the approach flow perturbations described and the disturbances generated on the chute, alternative solutions were proposed and tested on the model (Figure 2). Using movable and flexible elements, the research for a good shape showed that a longitudinal inclination of the nose of the piers allows improving the approach flow condition. The nose inclination of the piers like the prow of a ship contributes to a better flow distribution. Consequently, the separation zone was no more concentrated on one vertical line. Cross waves on spillway were reduced and the horizontal vortices were eliminated. As shown in Figures 6 and 7, with using Case 3 of the pier geometry caused passing flow smoothly with minimum cross waves creation. As shown in Figure 7, with increasing 28% of vertical inclination of piers, depth averaged velocity in approach cha nnel decreased to 16%. In this figures H_0 = the flow depth and V_0 = input velocity at entrance of the approach channel.

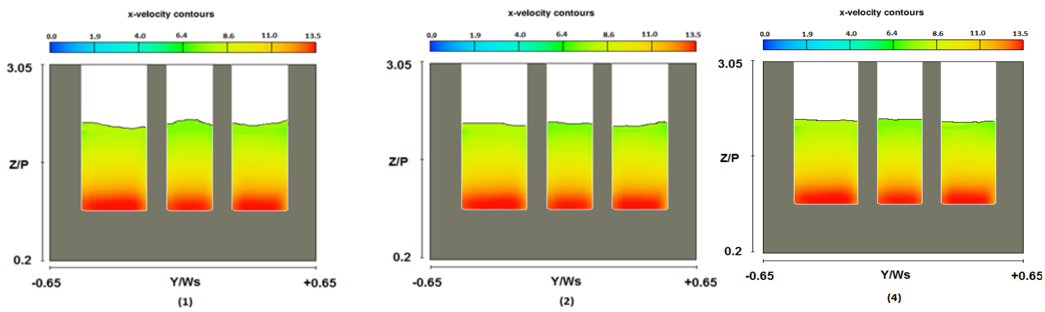

Figure 6. Cross section of the flow through the piers and cross waves on the spillway Cases 1, 2 and 3 of piers at H_0/P=2.56.

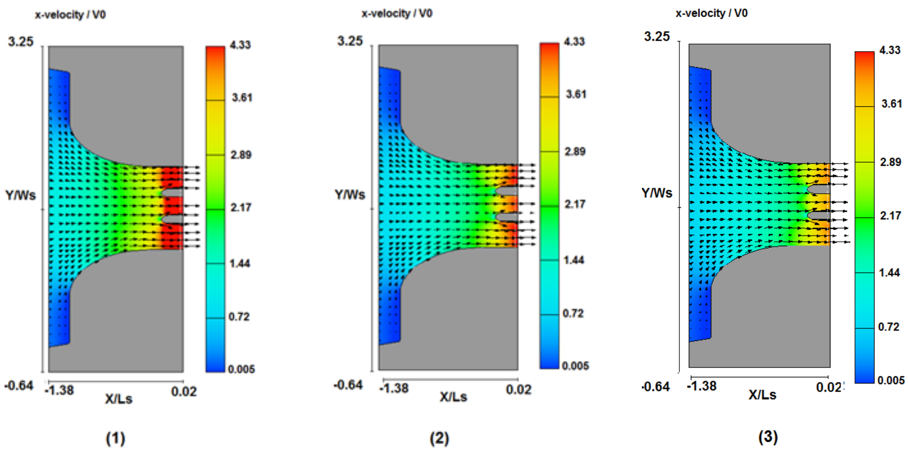

Figure 7. Flow pattern through the Cases 1, 2 and 3 of piers at H_0/P=2.56.

Optimization of the piers geometry allowed improving the flow behavior at the entrance of the bays. Consequently, this improves the flow along the chute down to the flip bucket. Furthermore, it permits to increase the gated spillway capacity. The hydraulic capacity Q of a free crest spillway is classically computed as:

$$Q = C_d \, b_e . \sqrt{2g} . H^{\frac{3}{2}} \qquad [7]$$

where Cd = the discharge coefficient, be = the effective width (m), g = the gravitational acceleration (m/s^2) and H = the upstream hydraulic head (m).

The effective width allows taking into account the lateral flow contraction due to the side walls and the piers. It can be expressed as:

$$b_e = b - (2.n.k_p + k_a).H \qquad [8]$$

where *b* (m) = the total width of the three bays, *n* = the piers number and k_p and k_a = the contraction factors for the piers, respectively. Contraction factors for the piers and the walls were determined experimentally as constant values of 0.05 and 0.2 (WES, 1952).

Compared to the vertical geometry, at different water level in the reservoir, the inclined wall allows increasing the evacuated discharge. Figure 8 shows the discharge coefficient versus vertical inclination for three different described geometries. The results showed that the vertical inclination of piers is the main effective factor of approach flow to spillways. In this study with increasing 28% of vertical inclination of piers, discharge coefficient of spillway increased approximately to 10%. As shown Figure 8, with decreasing flow depth in approach channel, discharge coefficient increased.

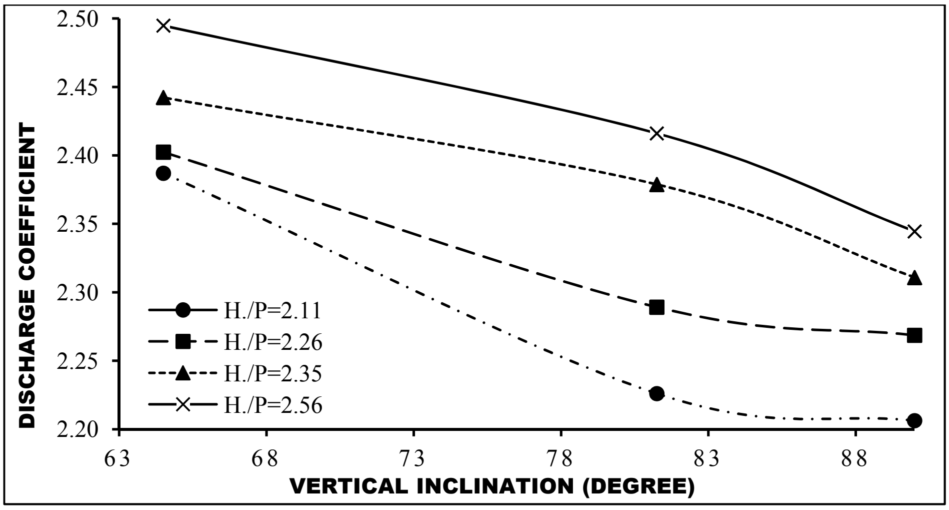

Figure 8. Discharge coefficient versus vertical inclination for Cases 1, 2 and 3 of the piers at H_0/P=2.56, 2.35, 2.26 and 2.11.

4 CONCLUSIONS

Present numerical study was performed to illustrate the hydraulic behavior of flow over a spillway during floods. A hydraulic model was employed to check the good behavior and the efficiency of the significant elements. A special focus was oriented towards the improvement of the piers geometry. Performance of the CFD simulations with the selected grid resolution was examined and validated by comparing the results of the simulation with the experimental data for the different vertical piers inclination cases. Generally, the numerical results were found to be in good agreement with the measured values, with an average relative deviation of less than 10%. Flow conditions between a vertical pier and two inclined piers (81° and 64° inclination from horizontal) were evaluated. Results showed that a longitudinal inclination of nose of the pier leads to improving the approach flow conditions. Assessing the performance of the 64° inclination case showed that this scenario was passed flow smoothly through the piers by omitting the cross waves and causes the minimum separation along the piers and approach channel. To illustrate the performance of the case (64°), flow cross section was plotted which implies uniformity and no cross waves through the approach channel. This comparison between three inclination cases showed that the higher inclination, allows increasing the hydraulic capacity for high water levels. To conclude, as the inclination increases, cross waves will be reduced and horizontal vortices can be eliminated. Comparison between three inclination modes showed that with increasing 28% of vertical inclination of piers, depth averaged velocity in approach channel decreased to 16%

and discharge coefficient of spillway increased approximately to 10% and as flow depth in approach channel decreases, discharge coefficient increases. To conclude, as the inclination increases, shock waves reduced and horizontal vortices eliminated.

REFERENCES

Aliev, É.V., Gamidov, R.A. & Seidov, A.G. (1987). Introduction of New Technology on the Construction of the Shamkhor Hydroelectric Station. *Hydrotechnical Construction*, 21(7), 414-417.

Amiri, S.M., Zarrati, A.R., Roshan, R. & Sarkardeh H. (2011). Surface Vortex Prevention at Power Intakes by Horizontal Plates. *ICE Journal of Water Management*, 164(4), 193-200.

Azarpira, M., Sarkardeh, H., Tavakkol, S., Roshan, R. & Bakhshi H. (2015). Vortices in Dam Reservoir: A Case Study of Karun III dam. *Sadhana*, 39(5), 1201-1209.

Bates, P.D., Lane, S.N. & Ferguson, R.I. (2005). *Computational Fluid Dynamics: Applications in Environmental Hydraulics*. John Wiley & Sons.

Ettema, R., Arndt, R., Roberts, P. & Wahl, T. (2000). *Hydraulic Modeling: Concepts and Practice*. ASCE Manuals and Reports on Engineering Practice, 97, 390.

Hager, W.H. & Pfister, M. (2010). Hydraulic Modelling–an Introduction: Principles, Methods and Applications. *Journal of Hydraulic Research,* 48(4), 557–558.

Hua, L.F. & Nan, X.H. (2003). Analysis of Pattern Layout and Research of Optimization for Chute Spillway. *Journal of Water Resources and Architectural Engineering*, 1(1), 21-24.

Jian, X.P. (2005). Research on the Experiments of Optimizing the Diversion Wall of the Spillway. *Journal of Hebei Institute of Architectural Science and Technology*, 22(3), 33-35.

Jorabloo, M., Maghsoodi, R. & Sarkardeh, H. (2011). 3D Simulation of Flow over Flip Buckets at Dams. *Journal of American Science*, 7(6), 931-936.

Kazemi, F., Khodashenas, S.R. & Sarkardeh H. (2016). Experimental Study of Pressure Fluctuation in Stilling Basins. *International Journal of Civil Engineering*, 14(1), 13-21.

Khadem Rabe, B., Ghoreishi Najafabadi, S.H. & Sarkardeh, H. (2016). Numerical Simulation of Anti-Vortex Devices at Water Intakes. *Proceedings of the Institution of Civil Engineers-Water Management*, 1-12.

Khanarmuei, M.R., Rahimzadeh, H. & Sarkardeh, H. (2014). Investigating the Effect of Intake Withdrawal Direction on Critical Submergence and Strength of Vortices. *Scientific information database,* 14(10), 35-42.

Khanarmuei, M.R., Rahimzadeh, H., Kakuei, A.R. & Sarkardeh, H. (2016). Effect of Vortex Formation on Sediment Transport at Dual Pipe Intakes. *Sādhanā,* 41(9), 1055-1061.

Khodashenas, S.R. & Paquier, A. (2010). A Geometrical Method for Computing the Distribution of Boundary Shear Stress across Irregular Straight Open Channels. *Journal of Hydraulic Research*, 37(3), 381-388.

Maghsoodi, R., Roozgar, M.S., Sarkardeh, H. & Azamathulla, H.M. (2012). 3D-Simulation of Flow over Submerged Weirs. *International Journal of Modelling and Simulation*, 32(4), 237-243.

Mardani, M., Rahimzadeh, H. & Sarkardeh, H. (2015) Analysis and Assessment of Installing Blocks on Performance of Stilling Basins. *Modares Mechanical Engineering*, 15(6), 31-41. (In Persian)

Marosi, M., Ghomeshi, M. & Sarkardeh, H. (2015). Sedimentation Control in the Reservoirs by using an Obstacle. *Sadhana*, 40(4), 1373-1383.

Nakayama, Y. & Boucher, R. (1998). *Introduction to Fluid Mechanics*. Butterworth-Heinemann, 344.

Nazari, O., Jabbari, E. & Sarkardeh, H. (2015). Dynamic Pressure Analysis at Chute Flip Buckets of Five Dam Model Studies. *International Journal of Civil Engineering, Transaction A: Civil Engineering*, 13(1), 45-54.

Parsaie, A., Haghiabi, A.H. & Moradinejad, A. (2015). CFD Modeling of Flow Pattern in Spillway's Approach Channel. *Sustainable Water Resources Management*, 1(3), 245-251.

Patankar, S. (1980). *Numerical Heat Transfer and Fluid Flow*. CRC press, 214.

Rahimzadeh, H., Maghsoodi, R., Sarkardeh, H. & Tavakkol, S. (2012). Simulating Flow over Circular Spillways by using Different Turbulence Models. *Engineering Applications of Computational Fluid Mechanics*, 6(1), 100-109.

Roshan, R., Sarkardeh, H. & Zarrati, A.R. (2009). Vortex Study on a Hydraulic Model of Godare- Landar Dam and Hydropower Plant. *WIT Transactions on Engineering Sciences (Computational Methods in Multiphase Flows V),* 63, 217-225.

Roshan, R., Karaminejad, A.R., Sarkardeh, H., Jabbari, E. & Zarrati, A.R. (2010). Design of Spillway Bucket for Kuhrang III Dam by Using a Physical Model. *International Symposium on Hydraulic Physical Modeling and Field Investigation*, China.

Safavi, K., Karaminejad, A.R., Jamali, H., Sarkardeh, H. & Zarrati, A.R. (2009). Hydraulic Design of a Multi-Level Intake Structure. Advances in Water Resources and Hydraulic Engineering, *Proceedings of 16th IAHR-APD Congress and 3rd Symposium of IAHR-ISHS,* 2064-2068.

Sajjadi, S.A.H., Sajjadi, S.H. & Sarkardeh, H. (2016). Accuracy of Numerical Simulation in a Symmetric Compound Channels. *International Journal of Civil Engineering*, 14-15, 1-13.

Sarkardeh, H., Jabbari, E., Zarrati, A. R. & Tavakkol, S. (2014). Velocity Field in a Reservoir in the Presence of an Air-Core Vortex. *Proceedings of the Institution of Civil Engineers*, 167(6), 356.

Sarkardeh, H., Marosi, M. & Roshan, R. (2015). Stepped Spillway Optimization through Numerical and Physical Modeling. *International Journal of Energy and Environment*, 6(6), 597.

Sarkardeh, H., Reza Zarrati, A., Jabbari, E. & Marosi, M. (2014). Numerical Simulation and Analysis of Flow in a Reservoir in the Presence of Vortex. *Engineering Applications of Computational Fluid Mechanics*, 8(4), 598-608.

Sarkardeh, H., Zarrati, A.R. & Roshan, R. (2010). Effect of Intake Head Wall and Trash Rack on Vortices. *Journal of Hydraulic Research*, 48(1), 108-112.

Suprapto, M. (2013). Increase Spillway Capacity using Labyrinth Weir. *Procedia Engineering*, 54, 440-446.

Taghvaei, S.M., Roshan, R., Safavi, K. & Sarkardeh, H. (2012). Anti-Vortex Structures at Hydropower Dams. *International Journal of Physical Sciences*, 7(28), 5069-5077.

Tokmadzhyan, O.V., Martirosyan, R.G., Petrosyan, V.U. & Vartanyan, P.A. (1988). Hydraulic Calculation of the Trench Intake of the Spillway of the Kapsk Reservoir. *Hydrotechnical Construction*, 22(10), 583-586.

US Army Engineer, (WES). (1952). Waterways Experiment Station, Hydraulic Design Criteria and subsequent editions. CRC Press, 680.

Versteeg, H.K. & Malalasekera, W. (2007). *An Introduction to Computational Fluid Dynamics: The Finite Volume Method*. Pearson Education.

Wang, J.B. & Chen, H.C. (2010). Improved Design of Guide Wall of Bank Spillway at Yutang Hydropower Station. *Water Science and Engineering*, 3(1), 67-74.

FLOW PROPERTIES AND SHEAR STRESS ON A FLAT-SLOPED SPILLWAY

ARMAGHAN SEVERI(1) & STEFAN FELDER(2)

(1,2) Water Research Laboratory, School of Civil and Environmental Engineering, UNSW Sydney, Australia,
a.severi@wrl.unsw.edu.au; s.felder@unsw.edu.au

ABSTRACT

Spillways are often associated with air entrainment attributed to turbulent velocity fluctuations close to the free-surface. At the upstream end of the spillway, a turbulent boundary layer is generated due to bed friction developing in downstream direction. In small dams, the boundary layer may not reach the free-surface at the downstream end of the spillway. In order to efficiently design an energy dissipator at the downstream end of the spillway, it is required to determine the flow resistance over the spillway. Detailed laboratory experiments were conducted on a large scale uncontrolled flat sloped ($\theta = 11°$) spillway with smooth bed. The present study aimed to investigate the developing turbulent boundary layer properties and shear stresses over the spillway. The non-aerated flow properties were measured with a Pitot tube, identifying the growth rate of the boundary layer, displacement and momentum thicknesses as $\delta \sim x^{0.86}$, $\delta_1 \sim x^{0.57}$ and $\delta_2 \sim x^{0.70}$, respectively. Despite reaching fully developed flow conditions, no free-surface aeration was observed and the surface remained rough with fast fluctuations and entrapped air at the air-water interface. The shear stresses were calculated using the logarithmic law of the wall, the outer flow region as well as the direct step method. The dimensionless shear stresses were in a range between $0.029 < \tau_o/(\rho \times g \times d_c) < 0.065$ corresponding to Darcy friction factors $0.024 < f < 0.027$. The present study results provided new insights into the turbulent boundary layer properties in high-velocity flows over a flat-sloped spillway which may be useful for a hydraulic design of spillway and downstream energy dissipator.

Keywords: Boundary layer; flat-sloped spillway; flow properties; flow resistance; shear stress.

1 INTRODUCTION

Spillways convey flows safely and efficiently to lower elevations. Spillways are commonly classified based upon geometrical parameters such as slope, length, intake conditions as well as bed roughness ranging from smooth invert to macro-roughness elements. At the upstream end of the spillway, a turbulent boundary layer is generated close to the bottom due to bed friction developing in streamwise direction. Spillways are often associated with air entrainment attributed to turbulent velocity fluctuations close to the free-surface (Lane, 1939; Bauer, 1954; Straub and Anderson, 1958; Lai et al., 1968; Keller et al., 1974). Downstream of the inception point of free-surface aeration the flow is aerated. While the self-aeration and the air-water flow properties on spillways have been researched in some detail (Straub and Anderson, 1958; Lai et al., 1968; Keller et al., 1974; Wood, 1991; Chanson, 1993b), a second phenomenon has also been observed in high-velocity flows at the interface between air and water (Straub and Anderson, 1958; Killen, 1968; Lai et al., 1968; Anwar 1994). When small amplitude free-surface waves including Kelvin Helmholtz instabilities and capillary waves start to collapse, the free-surface of the water becomes rough and unstable at the inception point of free-surface roughness (Young and Wolfe, 2014; Felder and Severi, 2016). Downstream of the inception point of free-surface roughness the free-surface is continuously rough and air is entrapped within a small layer at the air-water interface.

In small dams, the boundary layer may not reach fully developed flow conditions at the downstream end of the spillway and no flow aeration may be observed. In order to design an energy dissipator at the toe of the spillway, it is useful to determine the energy loss and the flow resistance over the spillway. Several studies focused on flow properties and flow resistance in non-aerated and aerated flows over spillways with macro-roughness elements such as step or block ramps which attributed to the from losses (i.e. Rouse, 1965; Pagliara et al., 2010; Felder and Chanson, 2016) for a wide range of slopes as well as spillways with smooth invert for steep slopes (Chanson, 1993a; Castro-Orgaz, 2010). Wood (1991) and Chanson (1993a) observed drag reduction in high velocity supercritical flows with air entrainment over steep slope spillway with smooth invert attributed to skin friction. To determine the flow resistance, several approaches are commonly applied including the backwater equations in gradually varied flows in conjunction with Darcy-Weisbach and Chezy concepts (Falvey, 1990; Hager and Blaser, 1998; Castro-Orgaz, 2010). Castro-Orgaz (2009; 2010) developed an analytical approach for boundary layer development by integrating the von Karman momentum equations using a power law velocity profile inside the boundary layer which yielded accurate equations for the free surface, the turbulent boundary layer profiles and flow resistance of an uncontrolled spillway with steep slope. However, limited research has been conducted on the flow resistance within developing and fully developed

  / ISSN 1562-6865 (Online) - ISSN 1063-7710 (Print)

flow region over flat sloped spillways (θ < 15˚) with smooth invert despite some studies focused on drag reduction in aerated flows (Wood, 1983; Chanson, 1996). A better understanding of the non-aerated flows is important for the hydraulic design of spillways, particularly on small dams where the turbulent boundary layer may not reach the free-surface and self-aeration may not occur. Herein, the present study investigated the flow properties including flow depth, velocity distributions, as well as boundary layer parameters and compared different methods to estimate the flow resistance on a flat sloped uncontrolled spillway with smooth invert. The results shed light on boundary layer properties and flow resistance to hydraulic designs of spillway and downstream energy dissipation structure.

2 EXPERIMENTAL FACILITY AND INSTRUMENTATION

New experiments were conducted on a spillway model at UNSW's Water Research Laboratory (WRL) with a rectangular cross section of width W = 0.8 m, length L = 9 m, and slope θ = 11˚ (Figure 1). Spillway bed and side walls were made of transparent Perspex with an estimated equivalent sand roughness of k_s = 0.1 mm. Any joints in Perspex were thoroughly sealed providing smooth flow conditions. At the upstream end, a header tank equipped with honeycomb screens allowed for calm inflows into the spillway section through an uncontrolled crest with upstream rounded corner. Water was supplied from Manly Dam to the header tank providing constant flow rates checked by a Venturi flow meter in the supply line. The experiments were carried out with flow rates per unit width between $0.019 < q_w < 0.125$ m^2/s corresponding to Reynolds numbers defined in terms of the hydraulic diameter of $7.3\times10^4 < Re < 4.5\times10^5$.

Figure 1. Large scale flume at Water Research Laboratory with L= 9 m, θ = 11˚ and k_s = 0.1 mm.

Non-aerated flow properties were measured with a Prandtl-Pitot tube with a diameter of Ø = 3 mm which was connected to an inclined 30˚ water manometer. The Pitot tube was used to measure the time-averaged velocity distributions of non-aerated flows in channel centerline at various cross-sections along the spillway. Also, the velocity data were used for the estimation of the boundary layer development along the spillway and for calculation of the flow resistance.

In the present study, the free-surface was rough and characterized by fast fluctuations (see Section 3; Felder and Severi, 2016). The Prandtl-Pitot tube was not able to measure the flow velocities immediately next to the free-surface and air-water flow instrumentation was applied to measure the flow properties in the thin layer of entrapped air at the air-water interface. The measurements were conducted with a dual-tip conductivity probe with two identical tips with inner electrode of Ø = 0.125 mm separated in transverse and longitudinal direction by Δz = 1.1 mm and Δx = 4.85 mm, respectively. For all flow conditions, the sampling duration was 45 s and the sampling rate was 20 kHz as recommended by Felder and Chanson (2015). The raw Voltage signals of the conductivity probe were post-processed based on typical air-water flow processing methods using the Fortran code of Felder (2013), providing a range of entrapped air flow properties including the local time averaged void fraction C.

Along the spillway, the flow depths were measured with a pointer gauge in spillway centerline. In the flow region characterized by entrapped air, the measurements of flow depths were difficult due to free-surface roughness and fast fluctuations of the free-surface. Therefore, the flow depth was also indirectly estimated with the conductivity probe based upon the equivalent clear water flow depth d:

$$d = \int_{y=0}^{y=Y_{98}} (1-C)\times dy \qquad [1]$$

where Y_{98} was the characteristic flow depth where C = 0.98 and y was the distance measured normal to the bed. In a detailed sensitivity analysis, the characteristic depth was Y_{98}, selected as the depth where the standard deviation of the free-surface fluctuations was smallest following the approach by Wilhelms and Gulliver (1994).

The transparency of the spillway boundaries provided an opportunity to observe the flow features from all angles. A Mikrotron™ MC4082 high-speed camera was used to record high-quality videos of the water motions with a frame rate of 457 Hz and resolution of 2336×1728 pixels. Detailed recordings were conducted through the sidewall towards the downstream end of the spillway providing information about the free-surface patterns and free-surface elevation. All experiments were documented with a Canon™ EOS 1000D camera.

3 FLOW PATTERNS ON THE FLAT SLOPED SPILLWAY

For all tested flow conditions, detailed visual observations of flow patterns revealed that the flow passed through critical depth over the crest at the upstream end of the spillway and that the flow depth decreased gradually in streamwise direction. Visual observations showed a smooth and clear surface at the upstream end of the spillway. At some distance from the spillway crest, due to the development of Kelvin Helmholtz instabilities and collapse of small amplitude free-surface waves, the water surface became wavy and rough (Figure 2). For all tested flow conditions, the longitudinal distance from spillway crest to the inception point of free-surface roughness L_{FR} was visually observed at a distance $1.7 < L_{FR} < 3.7$ m from the spillway crest (Felder and Severi, 2016). With increasing discharge, the inception point of free-surface roughness shifted downstream. These findings were consistent with recordings by Lai et al. (1968) who reported comparable values of L_{FR} on a smooth invert spillway with slope of $\theta = 18^\circ$. Downstream of the inception point of free-surface roughness, the free-surface remained agitated and air was continuously entrapped in a small layer at the air-water interface (Figure 2).

Detailed high-speed videos were recorded in a fully developed flow region towards the downstream end of the spillway ($6.3 \le x \le 6.8$ m). Figure 2 illustrates a typical image extracted from one of the side-looking high-speed videos. The flow was characterized by three flow regions. The first flow region was a clear water flow close to the spillway bed. The second region was defined as an entrapped air region characterized by rapid fluctuations of the free-surface and waviness. The third region was a region of clear air without any droplet ejections above the flow. The clear water flow region was maintained along the spillway for all tested discharges and occasionally single air bubbles were observed within this flow region. For $q_w \ge 0.075$ m^2/s, occasionally free-surface instabilities led to the release of single air bubbles into the upper area of the clear water flow region. These bubbles were advected in streamwise direction just below the entrapped air region indicating that turbulence forces within this flow region were stronger than buoyancy effects of the air bubbles.

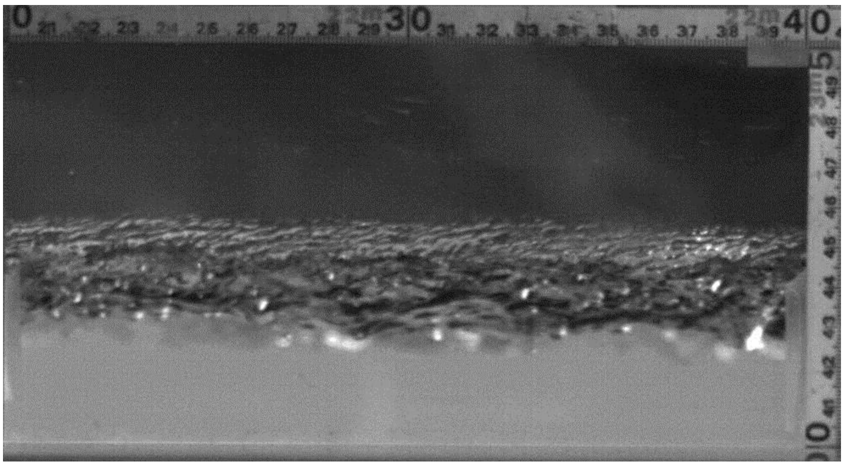

Figure 2. Free-surface roughness in fully developed flow region at $55.59 < x/d_c < 57.49$: $q_w = 0.125$ m^2/s, $L_{FR} = 3.7$ m, Re = 4.5×10^5; flow from right to left.

Figure 3 shows a typical dimensionless free-surface profile h/d_c in the present study as a function of the dimensionless distance along the spillway x/d_c. The experimental data were compared with gradually varied flow calculations and with a theoretical prediction of the decline of the free-surface (Castro-Orgaz, 2010). The present data were in good agreement with the theory (Figure 3). In addition, in Figure (3), the dimensionless equivalent clear water flow depth d_{98}/d_c and characteristic flow depth Y_{98}/d_c were presented in the flow region with entrapped air. Figure 3 reveals a good agreement between flow depth recorded with pointer gauge and characteristic flow depth Y_{98}. It appears that a conductivity probe is a suitable alternative for flow depth measurements within flow region characterized by entrapped air, but further research is needed.

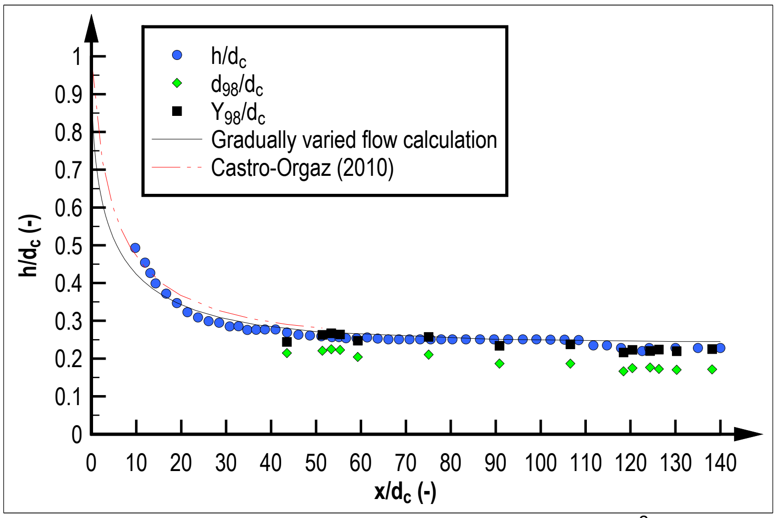

Figure 3. Dimensionless flow depth profile along the spillway: q_w = 0.05 m^2/s, L_{FR} = 2.7 m, Re = 1.90×10^5.

4 VOID FRACTION DISTRIBUTIONS

Measurements of the flow properties within the entrapped air region were performed with the double-tip conductivity probe at several locations downstream of the inception point of free-surface roughness. In Figure 4, typical void fraction distributions are plotted as a function of the dimensionless perpendicular elevation from the spillway bed y/Y_{98}. For all flow conditions, the void fraction distributions exhibited typical S-shape profiles (Figure 4). In the clear water flow region beneath the entrapped air region $y/Y_{98} < 0.6$, void fraction was $C \approx 0$ which was consistent with the visual observations presented in Figure 2. In the air flow region $y/Y_{98} > 1.05$, the void fraction was $C \approx 1$. In the flow region characterized by air entrapment ($0.6 < y/Y_{98} < 1.05$), the void fraction increased abruptly over a small section of the flow depth. A downward shift of void fraction distributions in streamwise direction indicated an increase in depth averaged void fraction towards the toe of the spillway. This gradual increase in depth averaged void fraction highlighted that no uniform flow conditions were attained at the downstream end of the spillway despite reaching fully developed flow conditions (Section 5). The depth-averaged mean void fraction C_{mean} was computed in each cross-section as:

$$C_{mean} = \frac{1}{Y_{98}} \int_{y=0}^{y=Y_{98}} (1-C) \times dy \qquad [2]$$

For all flow conditions, the mean void fraction increased from about C_{mean} = 0.17 just downstream of the inception point of free-surface roughness to C_{mean} = 0.28 at the toe of the spillway. This gradual increase was best correlated by:

$$C_{mean} = 0.153 + 6.179 \times 10^{-4} \times \frac{x}{d_c} \qquad [3]$$

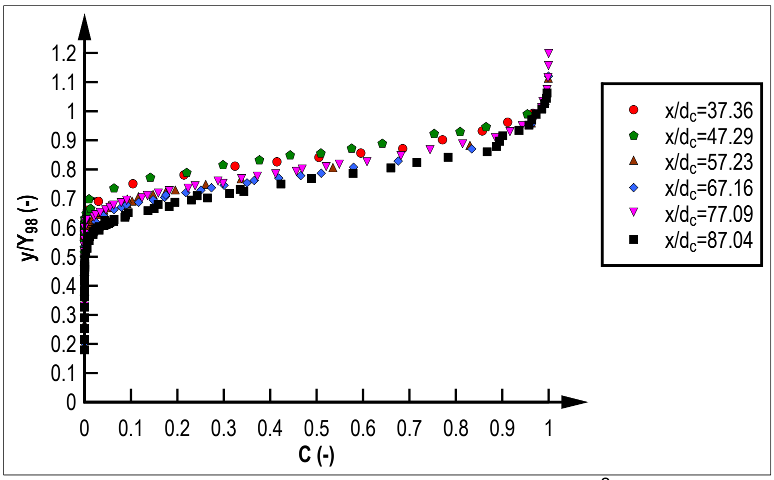

Figure 4. Void fraction distributions along the spillway: q_w = 0.10 m^2/s, L_{FR} = 3.5 m, Re = 1.9×10^5.

5 VELOCITY DISTRIBUTIONS AND BOUNDARY LAYER DEVELOPMENT

Velocity measurements were performed with the Pitot tube in channel centerline at several cross-sections between $0.42 \le x \le 8.76$ m for all flow conditions. At each cross-section, time-averaged local velocities V were measured between spillway bed and as close as possible to the free-surface. Typical velocity distributions and the corresponding boundary layer development are presented in Figure 5. In Figure 5, data for three different regions are shown comprising the flow region upstream of the inception point of free-surface roughness (hollow symbols), the flow region downstream of the inception point of free-surface roughness before the flow became fully developed (black bold symbol) and the fully-developed flow region downstream of the intersection point of turbulent boundary layer and free-surface (colored bold symbols). Figure 5 illustrates that the velocities increased along the spillway and that the flow became fully developed. Detailed analyses of the velocity data yielded the boundary layer characteristics such as turbulent boundary layer, boundary displacement and momentum thickness respectively (Campbell et al., 1965):

$$\delta = y_{0.99V_o} \quad [4]$$

$$\delta_1 = \int_0^{\delta_w} \left(1 - \frac{V}{V_o}\right) \times dy \quad [5]$$

$$\delta_2 = \int_0^{\delta_w} \frac{V}{V_o} \times \left(1 - \frac{V}{V_o}\right) \times dy \quad [6]$$

where the boundary layer thickness δ was defined as the distance from the spillway bed to the position where the velocity was 0.99 times the freestream velocity V_o (Bauer, 1954); δ_1 was the displacement thickness and δ_2 was the momentum thickness. The distance from the spillway crest to the intersection of turbulent boundary layer and free-surface L_{BL} was determined following the graphical approach by Bauer (1954) (Figure 5). The flow reached fully developed condition at a distance $1.76 < L_{BL} < 5.60$ m from the spillway crest and with increasing flow rate, L_{BL} increased. The flow was fully developed downstream of L_{BL}, but no free-surface aeration of the flow was observed (Figure 2). For all flow conditions in the present study, L_{BL} was larger than L_{FR} highlighting that the initiation of free-surface roughness was not triggered by turbulence fluctuations close to the free-surface, but by instabilities at the air-water interface. Furthermore, time-averaged interfacial velocities were measured with the conductivity probe in the entrapped air region and the results confirmed good agreement between measurements with the Pitot tube, revealing that a double-tip conductivity probe is suitable for the velocity measurement within entrapped air flows.

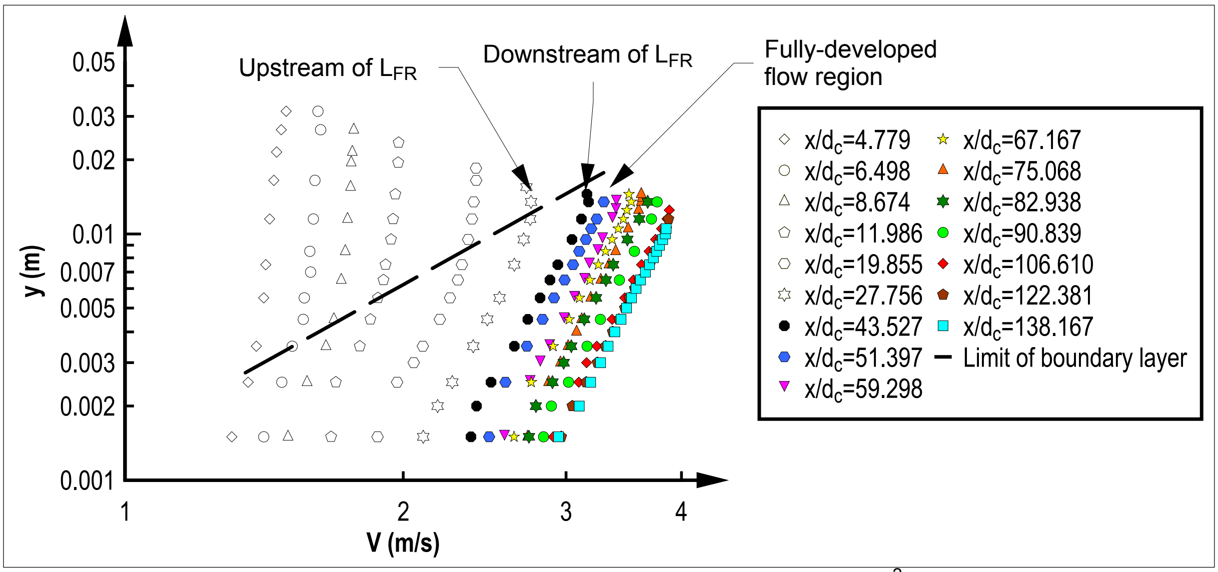

Figure 5. Velocity distributions and boundary layer development: $q_w = 0.05$ m^2/s, $L_{FR} = 2.7$ m, $L_{BL} = 2.85$ m and Re = 1.90×10^5 (Hollow, black bold and colored bold symbols illustrated velocity distributions upstream of L_{FR}, downstream of L_{FR} and in fully developed flow region).

For all data in the present study, Figure 6 presents the boundary layer thickness, displacement thickness, momentum thickness and their best fitted correlations:

$$\frac{\delta}{x} = 0.0235 \times \left(\frac{x}{k_s}\right)^{-0.135} \quad [7]$$

$$\frac{\delta_1}{x} = 0.068 \times \left(\frac{x}{k_s}\right)^{-0.431} \quad [8]$$

$$\frac{\delta_2}{x} = 0.011 \times \left(\frac{x}{k_s}\right)^{-0.296} \quad [9]$$

Figure 6 shows the dimensionless boundary layer properties as a function of a dimensionless streamwise position x/k_s within the developing region from the spillway crest to the point where the flow became fully developed. Results showed that the proposed boundary layer growth rate was about $\delta \sim x^{0.86}$ (Eq. [7]). These results were in reasonable agreement with previous observations of Bauer (1954) and Wood et al. (1983) who reported that boundary layer growth rate increased as $x^{0.8}$ to $x^{1.0}$ on smooth invert spillways with slopes ranging between $7.5^{\circ} \leq \theta \leq 75^{\circ}$. The present results were also similar to the turbulent boundary layer growth rate on smooth flat plates $\delta \sim x^{0.8}$ (Schlichting, 1979).

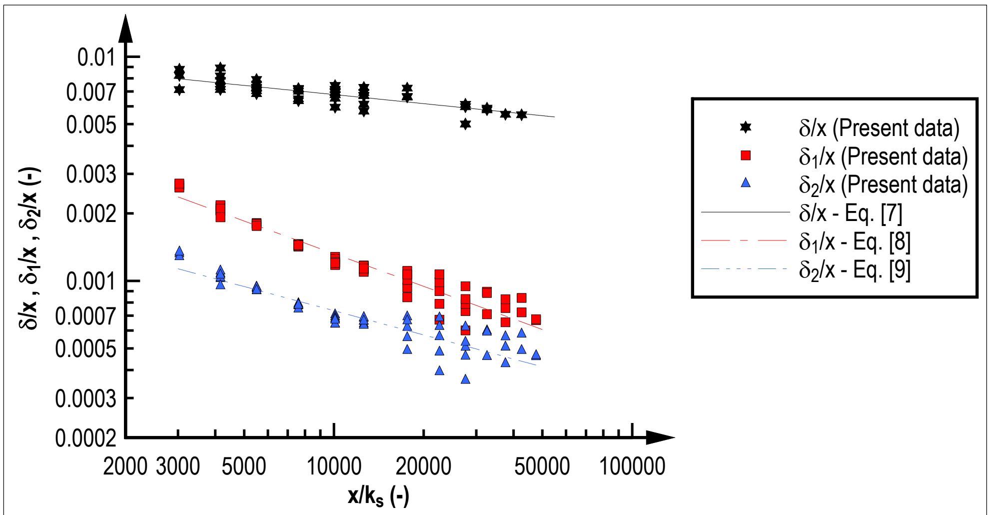

Figure 6. Dimensionless boundary layer thickness δ/x, displacement thickness δ_1/x, momentum thickness δ_2/x in developing flow region over flat sloped spillway.

The relationship between growth rate of boundary layer properties and Reynolds number $Re_x = \rho \times V_o \times x/\mu$, with ρ the water density, and μ the water dynamic viscosity yielded:

$$\frac{\delta}{x} = 0.063 \times \left(\frac{\rho \times V_o \times x}{\mu}\right)^{-0.156} \quad [10]$$

$$\frac{\delta_1}{x} = 0.102 \times \left(\frac{\rho \times V_o \times x}{\mu}\right)^{-0.30} \quad [11]$$

$$\frac{\delta_2}{x} = 0.014 \times \left(\frac{\rho \times V_o \times x}{\mu}\right)^{-0.203} \quad [12]$$

The comparison of current boundary layer and momentum thickness ratio with the data on smooth flat plates by Schlichting (1979) was in reasonable agreement, i.e. δ/x and $\delta_2/x \sim Re^{-0.2}$. The ratio of boundary displacement thickness was slightly higher than the reported value by Schlichting (1979) ($\delta_2/x \sim Re^{-0.2}$).

Figure 7 illustrated all dimensionless velocity distributions V/V_o of the present study as a function of the dimensionless depth y/δ showing self-similarity in the velocity profiles. The present velocity data were well correlated by a 1/6.4th power law (Figure 7).

$$\frac{V}{V_o} = \left(\frac{y}{\delta}\right)^{\frac{1}{6.4}} \quad [13]$$

Equation [13] was in close agreement with observations of Chanson (1997) on a smooth spillway (θ = 4˚) who reported a correlation of velocity data with a 1/6th power law.

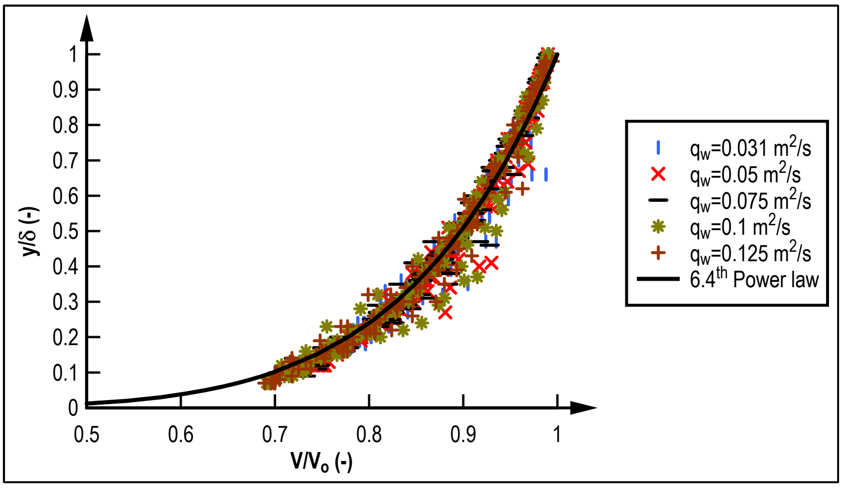

Figure 7. Velocity distributions in the developing flow region for all flow conditions; Comparison with 6.4th power law (Eq. [13]).

For all experimental data, the average values of δ_1/δ, δ_2/δ and δ_1/δ_2 were compared with the outcomes of proposed relations by Campbell et al. (1965) and Schlichting (1979) (Eqs. [14] to [16]) for a velocity power law with an exponent of N.

$$\frac{\delta_1}{\delta} = \frac{1}{1+N} \quad [14]$$

$$\frac{\delta_2}{\delta} = \frac{N}{(1+N)\times(2+N)} \quad [15]$$

$$\frac{\delta_1}{\delta_2} = \frac{N+2}{N} \quad [16]$$

where δ_1/δ_2 is the shape factor. In the developing flow region of the present study, the average values were $\delta_1/\delta = 0.170$, $\delta_2/\delta = 0.105$ and $\delta_1/\delta_2 = 1.70$. These values were compared with the results of the analytical solution for a power law with N = 6.4 corresponding to Eq. [14] to [16] as $\delta_1/\delta = 0.135$, $\delta_2/\delta = 0.103$ and $\delta_1/\delta_2 = 1.313$. The results revealed a slight difference between present study data and values calculated using Eqs. [14], [15] and [16]. These slight differences can be attributed to some subjectivity in defining the free-stream flow velocity and the turbulent boundary layer thickness.

6 SHEAR STRESS

The shear stress along the flat-sloped spillway was calculated based upon the detailed velocity measurements. Three different approaches were applied to compute the boundary shear stress comprising the logarithmic law within the inner flow region, the velocity defect law in the outer flow region, as well as the direct step method. In the inner flow region, the best fit of the velocity distributions with the logarithmic law provided the shear velocity V_*. For a smooth turbulent bed, the shear velocity was obtained by fitting the velocity data to (Liggett, 1994; Montes, 1998):

$$\frac{V}{V_*} = \frac{1}{K} \times Ln\left(\frac{V_* \times y}{\upsilon}\right) + 5 \qquad [17]$$

where υ is the dynamic viscosity of water, K is Von Karman constant (K = 0.4). Figure 8(a) illustrates a comparison of typical velocity distributions V/V_* with the logarithmic law (Eq. [17]) in terms of dimensionless elevation $V_* \times y/\upsilon$ for $y/\delta < 0.1$ to 0.15. The boundary shear stress was computed as $\tau_o = \rho \times V_*^2$ (Schlichting, 1979; Montes, 1998). The experimental results of the non-dimensional shear stress $\tau_o/(\rho \times g \times d_c)$ are illustrated in Figure 8(b) as a function of x/d_c. The present data revealed that the shear stress increased along the spillway varying between $0.029 < \tau_o/(\rho \times g \times d_c) < 0.043$. The flow resistance is commonly expressed by a Darcy-Weisbach friction factor f (Wood, 1985):

$$\tau_o = \frac{1}{8} f \times \rho \times V^2 \qquad [18]$$

and the friction factor for the log-law estimate was found to be on average f= 0.024.

The second approach to calculate the shear velocity V_* and the local shear stresses τ_o was based upon the best fit of velocity data to the velocity defect law in the outer flow region expressed as (Montes, 1998):

$$\frac{V_o - V}{V^*} = 5.5 \times \left(1 - \left(\frac{y}{\delta}\right)\right)^{1.5} \qquad [19]$$

Figure 9(a) shows a comparison of typical velocity distributions with the velocity defect law (Eq. [19]) as V_o-V/V_* versus dimensionless elevation y/δ for $y/\delta > 0.1$ to 0.15. Figure 9(b) presents the experimental results of non-dimensional shear stresses, $\tau_o/(\rho \times g \times d_c)$ for the velocity defect law in the outer flow region versus x/d_c. For all flow conditions, the local boundary shear stress increased gradually in streamwise direction varying between $0.048 < \tau_o/(\rho \times g \times d_c) < 0.065$. The corresponding friction factor was f = 0.039. The shear stress estimated based upon the velocity defect law were consistently larger compared to the log law estimate.

In the third approach, a direct step method combined with Darcy-Weisbach friction factor was applied to calculate the flow resistance. In the present study, the flow condition was not uniform equilibrium along the spillway. Therefore, Darcy-Weisbach friction factor was calculated for gradually varied flows (Henderson, 1966; Chanson, 1993a) using:

$$f = \frac{8 \times g \times S_f \times \left(\int_{y=0}^{y=Y_{98}} (1-C) \times dy\right)^2 \times \left(\frac{D_H}{4}\right)}{q_w^2} \qquad [20]$$

where f was the Darcy-Weisbach friction factor and D_H was the hydraulic diameter. $S_f = -\partial H/\partial x$ was the friction slope (Henderson, 1966) where H was the total head and x was the longitudinal distance in flow propagation direction. The direct step method applied to calculate the shear stress using both pointer gauge and conductivity probe data. Due to the free-surface roughness, the equivalent clear water flow depth derived from the double tip conductivity probe data was used to calculate the friction factor. The friction factor obtained from pointer gauge data and conductivity probe data were 0.024 and 0.027, respectively, which were in close consistency with the log law observations (Figure 8) and with the friction factor of 0.02 reported by Bung (2010) on a smooth invert spillway with 26.6° slope. Similarly, the dimensionless shear stress for the pointer gauge and conductivity probe data were in close agreement $\tau_o/(\rho \times g \times d_c) = 0.045$ and 0.040 respectively. This confirms that the double-tip conductivity probe data were suitable for estimating the shear stresses within entrapped air flows.

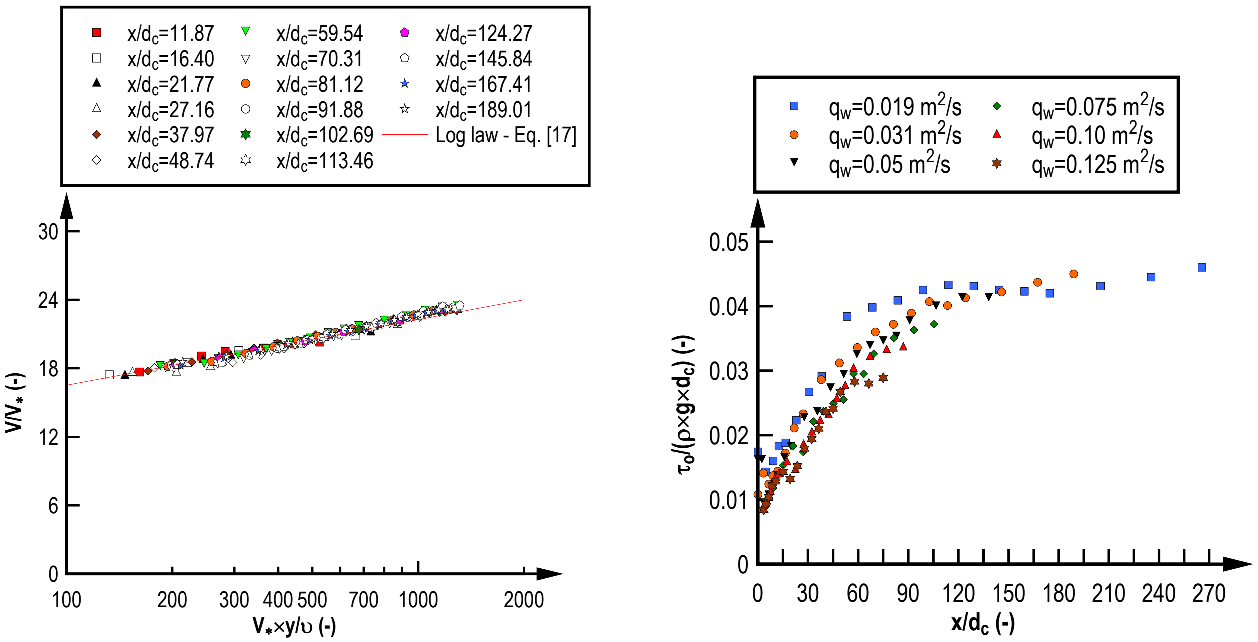

(a) Comparison of velocities with Eq. [17]: q_w = 0.031 m^2/s, L_{FR} = 2.3 m, L_{BL} = 2.51 m and Re = 1.2×10^5.

(b) Summary of experimental wall shear stress based upon log-law (Eq. [17])

Figure 8. Velocity distributions and summary of wall shear stress using log-law within inner flow region.

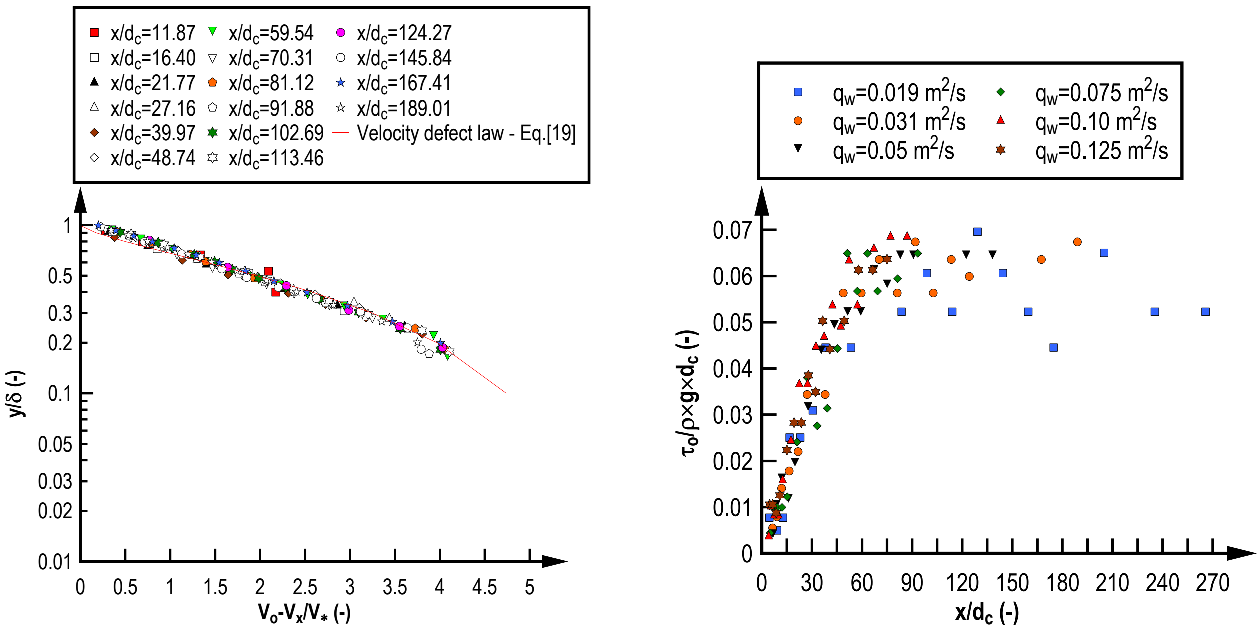

(a) Comparison of velocities with Eq. [19]: q_w = 0.031 m^2/s, L_{FR} = 2.3 m, L_{BL} = 2.51 m and Re = 1.21×10^5.

(b) Summary of experimental wall shear stress based upon velocity defect law Eq. [19]

Figure 9. Velocity distributions and wall shear stress using velocity defect law within outer region.

7 CONCLUSIONS

New experiments of velocity profiles, turbulent boundary layer properties and flow resistance were conducted on an uncontrolled flat-sloped spillway (θ = 11°) with smooth invert for a range of flow conditions (0.019 < q_w < 0.125 m^2/s). Visual observations of the flow patterns revealed a flow region with rapid free-surface fluctuations and strong free-surface roughness downstream of the inception point of free-surface roughness. Despite reaching fully developed flow conditions downstream of the intersection between boundary layer and free-surface, no free-surface aeration was observed. The surface remained rough and air was continuously entrapped within a small layer at the air-water interface. Time averaged velocity distributions within the turbulent boundary layer were well correlated with a 6.4th power law. Velocity measurements yielded the estimation of the growth rate of the turbulent boundary layer, displacement and momentum thicknesses of about $\delta \sim x^{0.86}$, $\delta_1 \sim x^{0.57}$ and $\delta_2 \sim x^{0.70}$ respectively.

Based upon the velocity data, the shear stress was calculated using different approaches comprising the law of the wall, the velocity defect law in the outer layer and direct step method. For both law of the wall in the inner flow region and velocity defect law in the outer region, the shear stress increased gradually and varied in a range between $0.029 < \tau_o/(\rho \times g \times d_c) < 0.065$. The median values of $\tau_o/(\rho \times g \times d_c)$, using the direct step method, were found to be 0.040 and 0.045 for pointer gauge and conductively probe data, respectively. The present study provided new insights into the turbulent boundary layer properties in high-velocity flows over a flat-sloped spillway which may be useful for the hydraulic design of spillway and downstream energy dissipator. Further research is needed to identify the effects of spillway bed roughness and inflow conditions upon the boundary layer properties and flow resistance.

ACKNOWLEDGEMENTS

The authors thank Robert Jenkins (UNSW, WRL) for his technical assistance.

REFERENCES

Anwar, H. (1994). Discussion of “Self-Aerated Flows on Chutes and Spillways”. *Journal of Hydraulic Engineering*, 120(6), 778-779.

Bauer, W.J. (1954). Turbulent Boundary Layer on Steep Slopes. *Transactions of the American Society of Civil Engineers*, 119(1), 1212-1233.

Bung, D.B. (2010). A Comparative Study of Self-Aerated Stepped Spillway and Smooth Invert Chute Flow: the Effect of Step-Induced Macro-Roughness. *Chinese-German joint symposium on hydraulic and ocean engineering*, 451-456.

Campbell, F.B., Cox, R.G. & Boyd, M.B. (1965). Boundary Layer Development and Spillway Energy Loss. *Journal of the Hydraulics Division*, 91(3), 149-163.

Castro-Orgaz, O. (2009). Hydraulics of Developing Chute Flow. *Journal of Hydraulic Research*, 47(2), 185-194.

Castro-Orgaz, O. (2010). Velocity Profile and Flow Resistance Models for Developing Chute Flow. *Journal of Hydraulic Engineering*, 136(7), 447-452.

Chanson, H. (1993a). Flow Resistance in High Velocity Supercritical Flows. *Transactions-Institution of Engineers Australia Civil Engineering*, 35, 141-141.

Chanson, H. (1993b). Self-Aerated Flows on Chutes and Spillways. *Journal of Hydraulic Engineering*, 119(2), 220-243.

Chanson, H. (1996). *Air Bubble Entrainment in Free-Surface Turbulent Shear Flows*. Academic Press, London, UK, 401.

Chanson, H. (1997). Air Bubble Entrainment in Open Channels: Flow Structure and Bubble Size Distributions. *International Journal of Multiphase Flow*, 23(1), 193-203.

Falvey, H.T. (1990). *Cavitation in Chutes and Spillways*. Water Resources Technical Publication, Engineering monograph 42, U.S. Dept. of Interior, U.S. Printing Office, Denver CO.

Felder, S. (2013). Air-Water Flow Properties on Stepped Spillways for Embankment Dams: Aeration, Energy Dissipation and Turbulence on Uniform, Non-Uniform and Pooled Stepped Chutes, *PhD thesis*. The University of Queensland.

Felder, S. & Chanson, H. (2015). Phase-Detection Probe Measurements in High-Velocity Free-Surface Flows Including a Discussion of Key Sampling Parameters. *Experimental Thermal and Fluid Science*, 61, 66-78.

Felder, S. & Chanson, H. (2016). Simple Design Criterion for Residual Energy on Embankment Dam Stepped Spillways. *Journal of Hydraulic Engineering*, 142(4), 1-11.

Felder, S. & Severi, A. (2016). Entrapped Air in High-velocity Free-surface Flows on a Flat-sloped Spillway. *20th Australasian Fluid Mechanics Conference*, Perth, Australia.

Hager, W.H. & Blaser, F. (1998). Drawdown Curve and Incipient Aeration for Chute Flow. *Canadian Journal of Civil Engineering*, 25(3), 467-473.

Henderson, F.M. (1966). *Open channel flow.* MacMillan, New York, 522.

Keller, R.J., Lai, K.K. & Wood, I.R. (1974). Developing Region in Self-Aerated Flows. *Journal of the Hydraulics Division*, (ASCE) 100(HY4), 553-568.

Killen, J.M. (1968). The Surface Characteristics of Self-Aerated Flow in Steep Channels, *PhD thesis*. University of Minnesota, Minneapolis, USA.

Lai, K.K., & BE, M. (1968). A Study of Air Entrainment in Steep Open Channels. *In Proceedings: Conference on Hydraulics and Fluid Mechanics*, Sydney.

Lane, E.W. (1939). Entrainment of Air in the Swiftly Flowing Water. *Civil Engineering*, 9, 89-91.

Liggett, J.A. (1994). *Fluid Mechanics*. McGraw-Hill, New York, USA, 495.

Montes, J.S. (1998). *Hydraulics of Open Channel Flow*. ASCE Press, New York, USA, 697 pages.

Pagliara, S., Carnacina, I. & Roshni, T. (2010). Self-Aeration and Friction over Rock Chutes in Uniform Flow Conditions. *Journal of Hydraulic Engineering,* 136(11), 959-964.

Rouse, H. (1965). Critical Analysis of Open-Channel Resistance. *Journal of the Hydraulics Division*, 91(HY4), 1-25. -Hill, New York.

Schlichting, H. (1979). *Boundary-Layer Theory*. 7th edn McGraw-Hill. New York, 66-67.

Straub, L.G. & Anderson, A.G. (1958). Experiments on Self-Aerated Flow in Open Channels. *Journal of the Hydraulics Division*, 84(7), 1-35.

Wilhelms, S.C. & Gulliver, J.S. (1994). *Self-aerated flow on corps of engineers spillways*, 112.

Wood, I.R. (1983). Uniform Region of Self-Aerated Flow. *Journal of Hydraulic Engineering*, 109(3), 447-461.

Wood, I.R. (1985). Air Water Flows. *21st IAHR Congress*, Melbourne, Australia, 18-29.

Wood, I.R. (1991). Air Entrainment in Free-Surface Flows. *IAHR Hydraulic Structures Design Manual* No. 4, Balkema Publ., Rotterdam.

Wood, I.R., Ackers, P. & Loveless, J. (1983). General Method for Critical Point on Spillways. *Journal of Hydraulic Engineering,* 109(2), 308–312.

Young, W.R. & Wolfe, C.L. (2014). Generation of Surface Waves by Shear-Flow Instability. *Journal of Fluid Mechanics*, 739, 276-307.

A NEW APPROACH TO HYDRAULICS BASED ON THE MOMENTUM BALANCE: SHARP EDGED OUTFOWS AND SLUICES

ANDREAS MALCHEREK[(1)]

[(1)] Institute of Water Sciences, University of the German Armed Forces Munich,
Andreas.malcherek@unibw.de

ABSTRACT

Most of the fundamental theories for the basic hydraulic structures use the continuity and Bernoulli equation to derive basic laws for the relation between flow and hydraulic head. When the results of such a theory do not agree well with measurements, an outflow coefficient is inserted to close the gap between theory and experiment. The momentum balance is only taken into account when losses have to be specified like in the sudden expansion case. In this paper, it will be shown that the hydraulic theory can also be based on momentum balance instead of Bernoulli's equation. The resulting formulas for the outflow through a sharp-edged orifice and through a sharp-edged sluice show a much better agreement to measurements than the formulas obtained from the Bernoulli equation.

Keywords: Torricelli principle; Bernoulli equation; outflow problem; sluice formulas weir formulas; fundamental principles of hydraulics.

1 INTRODUCTION

Since Torricelli's famous Opera Geometrica (Torricelli, 1644), the outflow velocity of a vessel is related to the filling height within the vessel. Torricelli stated that an efflux stream forced upwards rises to the filling height because it would also rise up to that height in communicating vessels. This explanation actually is wrong (Malcherek, 2016) and the fact that an efflux stream rises up to the filling height was doubted by Newton in his Principia (Newton, 1687) and after that quite often in the history of hydraulics. With the appearance of the Bernoulli equation it was also possible to prove that Torricelli's formula is correct. Since that time, the Bernoulli equation in combination with the continuity equation is applied to different kinds of hydraulic structures to obtain a basic relation between outflow and hydraulic head. In that way, the outflow from a vessel and under a sluice gate leads to the Torricelli formula, the overflow above a weir to the Poleni formula.

But this basic application of the Bernoulli equation to outflow problems out of vessels or under sluices is not able to distinguish neither between sharp crested and rounded orifices nor between vertical openings and sluice gates. In all cases, the outflow velocity is $v^2=2gh$ and an outflow coefficient has to be included to distinguish between the different cases, i.e. sharp or rounded or opening or sluice gate. When the orifice is sharp crested, the outflow coefficients are far away from unity (for the vertical outflow 0.7 and for the sluice 0.61) which means that the theory based on the Bernoulli equation has an error of about 30 % or 39 %, respectively.

Usually the discrepancy between theory and experiment is explained by assuming that the Bernoulli equation has to be applied at the vena contracta (Bernoulli, 1738, Weisbach, 1855). And later, potential theory is used to predict the contraction coefficient. But potential theory is only based on mass conservation and does not take into account momentum balance or energy conservation.

Therefore, a new theory will be set up based only on mass and momentum balance. In two preceding papers (Malcherek, 2016a and b), this theory was applied to the vertical outflow from vessels when the orifice is sharp edged. It was shown by the author that the momentum balance gives:

$$v=\sqrt{\frac{gh}{\beta-\frac{A_A}{A}}} \qquad [1]$$

for the outflow velocity, where A_A is the cross section of the orifice, A the vessel's cross section, h is the filling level in the vessel and $\beta \sim 1$ the momentum coefficient. This formula is in excellent agreement with measurements and can be regarded as a revolution because it contradicts Torricelli's principle (Torricelli, 1644).

When the same formalism is applied using standard simplifications to a sharp-edged sluice gate, the outflow velocity under the sluice is:

$$v=\sqrt{\frac{3}{4}gh}=0.6124\sqrt{2gh} \qquad [2]$$

Here h is the free surface elevation before the sluice gate. When looking in more detail on the sluice gate problem, the outflow coefficient is a function of the ratio of the opening height a to the free surface elevation h, a/h. In this paper, it will be shown that the new theory is able to reproduce also this dependency of the outflow coefficient when realistic pressure distributions on the gate and the bottom are taken into account.

It can be concluded that the hydraulic theory can be based on mass and momentum conservation without any usage of the Bernoulli equation. This is an extremely important conclusion because the Bernoulli equation gives wrong results, when applied to discontinuous problems like sudden pipe expansions, sharp edged outflow and sharp edged sluice gates.

2 HYDRAULICS BASED ON MOMENTUM BALANCE

The following hydraulic derivations are based on the mass and the momentum balance on a control volume Ω which must be chosen depending on the problem to be solved. The mass balance is only affected by the mass fluxes going in and out of the system:

$$\frac{dM}{dt}=\sum_i \dot{m}_i \qquad [3]$$

Here the sum is taken over I different openings where mass can enter or leave the system. The momentum balance is affected by the gravitation force acting on the mass of the system, the pressure forces on the boundary of the system and the fluxes of momentum going in and out of the system:

$$\frac{d\vec{I}}{dt}=M\vec{g}+\sum_i \dot{m}_i\vec{v}_i-\int_{\partial\Omega} p\vec{n}dA \qquad [4]$$

Viscous friction can also easily be taken into account but it is omitted here because it does not play any important role in outflow as well as in sluice underflow. These two balances are sufficient to describe the fundamental hydraulic behavior of any ideal, i.e. friction free hydraulic system.

Energy conservation in the shape of the Bernoulli equation can be derived from the momentum equation under certain circumstances as it is done in classical mechanics. Let us assume a certain volume of fluid M and let us follow this volume on a Lagrangean pathway. Then, the mass M does not change on the pathway and the momentum balance can be written as:

$$M\frac{d\vec{v}}{dt}=M\vec{g}-\int_{\partial\Omega} p\vec{n}dA \qquad [5]$$

Scalar multiplication with the velocity and integration over time yields:

$$\frac{1}{2}M\vec{v}_1^2+Mgz_1=\frac{1}{2}M\vec{v}_2^2+Mgz_2+\int_{\vec{x}_1}^{\vec{x}_2}\int_{\partial\Omega} p\vec{n}dA\,dx \qquad [6]$$

Applying Gaussian integral theorem to the pressure term yields:

$$\int_{\vec{x}_1}^{\vec{x}_2}\int_{\partial\Omega}\vec{n}pdAd\vec{x}=\int_{\vec{x}_1}^{\vec{x}_2}\int_{\Omega}\ \mathrm{grad}pd\Omega d\vec{x} \qquad [7]$$

If the control volume Ω is so small that the pressure gradient is constant on that volume, the integration is transformed to a multiplication with the volume itself:

$$\int_{\vec{x}_1}^{\vec{x}_2}\int_{\Omega}\ \mathrm{grad}pd\Omega d\vec{x}=\int_{\vec{x}_1}^{\vec{x}_2}\mathrm{grad}\ p\ V\ d\vec{x}=V\left(p_2-p_1\right) \qquad [8]$$

All together gives, after division by the fluid mass M, which introduces the density ϱ in our equation, the Bernoulli equation on a pathway:

$$\frac{\vec{v}_1^2}{2g}+z_1+\frac{p_1}{\varrho g}=\frac{\vec{v}_2^2}{2g}+z_2+\frac{p_2}{\varrho g} \qquad [9$$

  / ISSN 1562-6865 (Online) - ISSN 1063-7710 (Print)

This well-known derivation shows:
1. The Bernoulli equation is a special form of the momentum balance.
2. It is valid on the Lagrangean pathway.
3. Momentum balance and Bernoulli equation should not be applied together to a hydraulic problem because they are physically dependent from each other

3 OUTFLOW THROUGH A SHARP-EDGED ORIFICE

A new theory for the outflow through a bottom opening was presented in (Malcherek, 2016a; 2016b). It will be repeated here to show the general applicability of mass and momentum balance to every kind of hydraulic structure. The mass balance can be written as:

$$vA=v_A A_A \tag{10}$$

Here v is the settling velocity of the water column in the vessel and v_A is the outflow velocity in the opening, while A_0 is the vessels cross section and A is the opening cross section, respectively.

A turnaround in the hydraulic theory of the outflow problem can be achieved by looking at the momentum balance in a vessel. Here, the momentum change of the liquid in the vessel is due to

- gravitation acceleration
- efflux of momentum with the outflowing liquid
- forces of the bottom holding the liquid in the vessel.

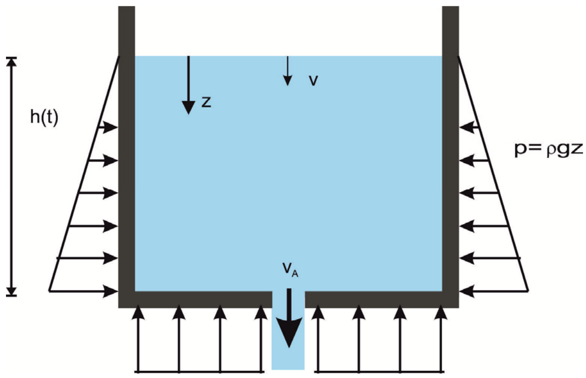

Figure 1. Pressure plan for the outflow problem: At the lateral walls of the vessel, a hydrostatic pressure distribution can be assumed. In total, the horizontal pressure forces cancel out from opposite points. At the free surface, atmospheric pressure is taken as the reference value. At the closed bottom of the vessel also hydrostatic pressure is assumed, while in the opening again atmospheric pressure is assumed, respectively.

Therefore, the momentum equation in the vertical direction is:

$$\frac{dI}{dt} = Mg - \beta\rho A_A v_A^2 - p(A - A_A) \tag{11}$$

Here the momentum coefficient β is taken into account because the efflux velocity is not constant over the cross section of the orifice. For homogeneous velocity distribution over the outflow cross section, the momentum coefficient is one, β=1.

The last term assumes a pressure force acting from the closed bottom ($A-A_A$) of the vessel against the moving liquid. Because the liquid above the closed parts of the bottom can be regarded as resting, the pressure can be approximated by the hydrostatic pressure ρgh:

$$\frac{dI}{dt} = Mg - \beta\rho A_A v_A^2 - \rho g h(A - A_A) \tag{12}$$

All the other pressure forces have no influence on the momentum balance: the atmospheric pressure at the free surface is canceled out by the atmospheric pressure at the bottom of the vessel. At the lateral walls, pressure forces are also canceling out due to opposite directions.

Replacing the fluid's momentum in the vessel as I=ρAhv and assuming an incompressible fluid, we obtain:

$$\frac{dhv}{dt}=hg-\beta\frac{A_A}{A}v_A^2-gh\left(1-\frac{A_A}{A}\right) \tag{13}$$

Applying product rule and the mass balance equation on the left-hand side leads to:

$$h\frac{dv}{dt}-v^2=-\beta\frac{A_A}{A}v_A^2+gh\frac{A_A}{A} \quad [14]$$

which can be transformed to an ordinary differential equation for the velocity in the vessel:

$$\frac{dv}{dt}=\frac{v^2}{h}\left(\beta-\frac{A}{A_A}\right)+g\frac{A_A}{A} \quad [15]$$

or for the outflow velocity

$$\frac{dv_A}{dt}=g-\frac{v_A^2}{h}\left(\beta-\frac{A_A}{A}\right) \quad [16]$$

, respectively. Three cases need special attention because they show the outstanding abilities of this new outflow theory:

1. For a fully closed bottom (A_A=0, β=1), the liquid does not move, because the momentum equation becomes:

$$\frac{dI}{dt}=\rho Ahg-\rho ghA=0 \quad [17]$$

   In this case, the pressure at the bottom is actually the hydrostatic pressure.
2. For a fully opened bottom (A_A=A, β=1), the outflow differential equation reads:

$$\frac{dv_A}{dt}=g \quad [18]$$

   The liquid actually is free falling out of the vessel.
3. In the stationary situation, the outflow velocity is:

$$v_A=\sqrt{\frac{gh}{\beta-\frac{A_A}{A}}} \quad [19]$$

This new outflow formula is different from the original Torricelli formula because it does not have the factor 2 under the square root. It is also different from the one derived from Bernoulli's energy and continuity equation because it varies with A_A/A instead of $(A_A/A)^2$.

The comparison to experimental results

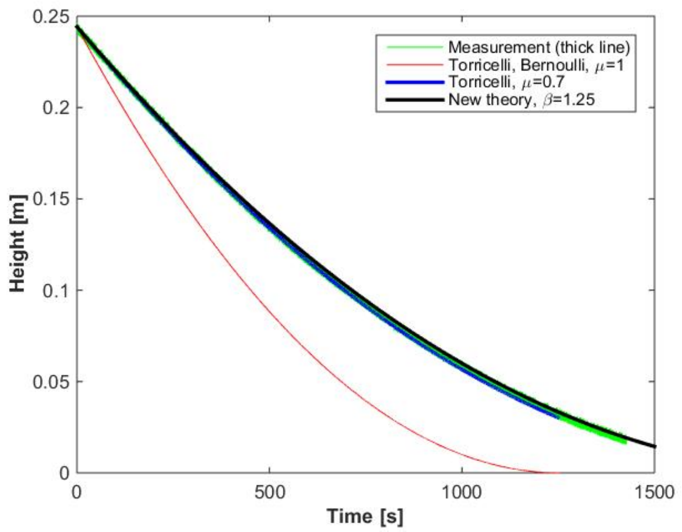

Figure 2. The filling height in the vessel: Comparison of a measurement with the theoretical results for the Torricelli formula, the Bernoulli equation and the new theory for β=1.25.

4 UNDERFLOW UNDER A SHARP CRESTED SLUICE

The underflow problem through a sharp crested sluice gate is a little bit different to the vertical outflow problem: First of all, we have an inflow and an outflow and we can assume stationary conditions. Assuming a constant width B of the channel and a sluice over the whole width, the mass balance reads:

$$h_0 = v_A a \qquad [20]$$

where h_0 and v_0 are the water depth and the depth averaged flow velocity upstream from the sluice and a is the gate opening height and v_A is the depth averaged flow velocity directly under the sluice gate, respectively. For the horizontal momentum balance, the control volume is taken as indicated in Figure 3. It starts somewhere upstream of the sluice gate and reaches directly to the gates plate. Then, the stationary momentum balance has to take into account.

- the momentum flux related to the inflow
- the momentum flux related to the outflow and
- the integral over the pressure going over the whole boundary of the control volume.

The horizontal momentum balance is obtained by scalar multiplication of the vector momentum balance with a horizontal unit vector $\vec{n}_H$:

$$0 = \rho B h_0 v_0^2 - \rho B\, a v_a^2 - \int_{\partial\Omega} p\vec{n}\vec{n}_H dA \qquad [21]$$

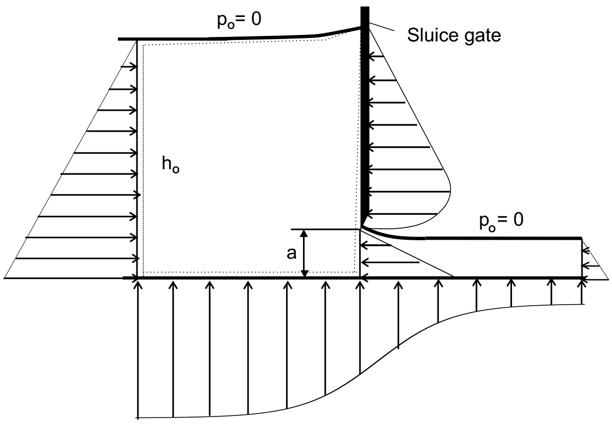

Figure 3. The pressure plan for the sluice gate: Hydrostatic conditions are assumed at the in- and outflow. At the sluice gate, the pressure starts to behave hydrostatic at the free surface. At the opening, it falls down to atmospheric pressure. The bottom pressure falls continuously from the hydrostatic bottom pressure before to the value behind the gate.

When every pressure is related to atmospheric pressure, then p = 0 can be assumed at the free surface. The pressure distribution is assumed to be hydrostatic in the entrance cross section as well as on the sluice gate canvas. In a certain distance, downstream of the sluice gate also hydrostatic pressure can be assumed in the channel. The most important assumption has to be made for the bottom pressure: It decreases continuously from its upstream to its downstream hydrostatic value. This is verified by Roth and Hager (1999).

For sake of simplicity, we assumed here, that the bottom pressure is in the middle between its upstream and its downstream hydrostatic value. Therefore, the whole horizontal projection of the pressure boundary integral reads:

$$\int_{\partial\Omega} p\vec{n}\vec{n}_H dA = \frac{1}{2}\rho g B h_0^2 - \frac{1}{2}\rho g B \left(h_0 - a\right)^2 - \frac{1}{2}\rho g B a \left(\frac{h_0}{2} + \frac{a}{2}\right) = \frac{3}{4}\rho g B a \left(h_0 - a\right) \qquad [22]$$

Introducing this into the momentum balance gives a new formula for the underflow velocity under a sluice gate:

$$v_A = \sqrt{\frac{3}{4} g h_0} \qquad [23]$$

This new formula can easily be compared to the Torricelli formula normally used as the basic expression for sluice gate formulas:

$$v_A = \sqrt{\frac{3}{8}}\sqrt{2gh_0} = 0.6124\sqrt{2gh_0} \qquad [24]$$

The resulting outflow coefficient is very close to values cited in literature. Therefore, this new hydraulic theory based on the momentum balance is outmatching the classical Bernoulli theory.

4.1 Improvement of the basic sluice gate theory

The Roth and Hager measurements showed that the pressure under the gate is not exactly the mean value of the bottom pressure values before and behind the gate. The measured bottom pressure directly under the gate can be written as a weighted interpolation between the two bottom pressures mentioned above:

$$p_B = \rho g(p^* h_0 + (1 - p^*)a) \quad with\ p^* \sim 0.618 \qquad [25]$$

Also, the pressure distribution on the gate's plate is not everywhere hydrostatic, especially when reaching the lower edge of the plate. Therefore, the pressure force on the gate can be corrected by a factor Π:

$$F_S = -\frac{1}{2}\Pi\rho g B(h_0 - a)^2 \qquad [26]$$

which was also determined in the experiments of Roth and Hager. When taking the mentioned effects into account, the following sluice gate formula is obtained:

$$v_A = \sqrt{2gh_0}\sqrt{\frac{\frac{h_0}{a} - (1 + \Pi - p^*)\frac{a}{h_0} - p^* - \Pi\left(\frac{h_0}{a} - 2\right)\frac{h_0}{a}}{4\left(1 - \frac{a}{h_0}\right)}} \qquad [27]$$

The second square root displays the dependency of the outflow coefficient from the opening ratio $\frac{a}{h_0}$ quite well. In (Malcherek, 2016c), further improvements of the theory can be found.

4.2 The submerged sluice gate

When the downstream hydraulic conditions require a higher water height in the channel than the opening height a of the sluice gate, the gate will be submerged. The pressure plan for this situation is shown in figure 4.

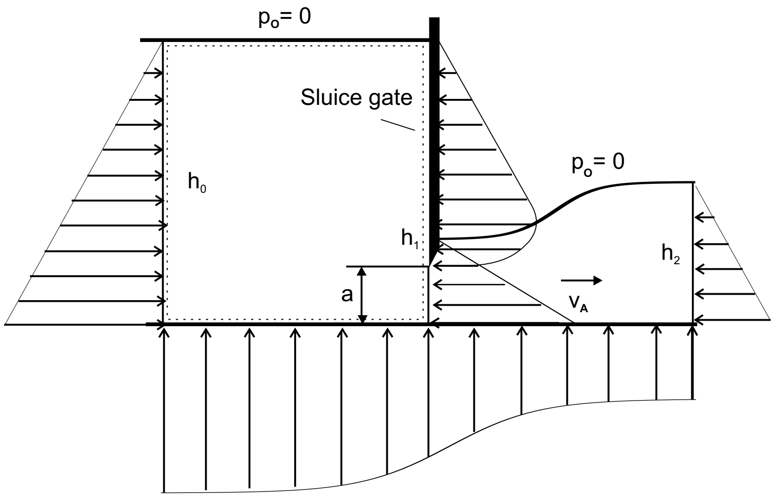

Figure 4. The pressure plan for the submerged sluice gate: Hydrostatic conditions are assumed at the in- and outflow. At the sluice gate, the pressure starts to behave hydrostatic at the free surface. At the opening, it falls down to atmospheric pressure. The bottom pressure falls continuously from the hydrostatic bottom pressure before to the value behind the gate.

The most important difference to the non-submerged case is the pressure in the opening. If we assumed the bottom pressure to be the mean value of the hydraulic heads h_0 and h_1, and the pressure at the lower edge of the plate to be rg(h_1-a), then the average pressure in the gate opening is:

$$p_A = \frac{1}{2}\rho g\left(h_1 - a + \frac{h_1+h_0}{2}\right) \qquad [28]$$

Then, the outflow velocity changes to:

$$\mathrm{v_A} = \sqrt{2\mathrm{gh_0}}\sqrt{\frac{3\left(1-\frac{h_1\, a}{a\, h_0}\right)}{8\left(1-\frac{a}{\mathrm{h_0}}\right)}} := \mu\sqrt{2\mathrm{gh_0}} \qquad [29]$$

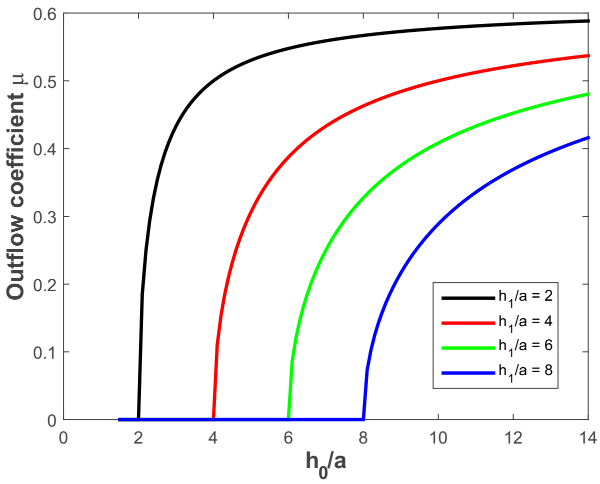

Figure 5. The outflow coefficient μ for a submerged sluice gate for different downstream water heights.

The resulting outflow coefficient is shown in Figure 5. Its principal behavior is comparable to the measurements.

5 CONCLUSIONS

When applying the Bernoulli equation to the outflow through sharp edged orifices or to sharp edged sluice gates, artificial coefficients are needed to close the gap between measurements and theoretical results. Here, a new fundamental hydraulic theory is presented which only needs the mass and the momentum balance for a control volume characterizing the hydraulic structure to be described. The Bernoulli theorem is not needed because it cannot be applied in many situations.

ACKNOWLEDGEMENTS

The research leading to this paper is not funded by any research agency. The author would never apply for a funding on a new theory improving the Torricelli formula because every scientific reviewer would reject such a proposal. The only but extremely important funding is my full professorship at the University of the German Armed forces giving me the freedom to do any kind of research in Hydraulic engineering.

REFERENCES

Malcherek, A. (2016). History of the Torricelli Principle and a New Outflow Theory. *Journal of Hydraulic Engineering,* 142(11), 1-7.

Malcherek, A. (2016b). Die irrtümlicheHerleitung der Torricelli-Formel aus der Bernoulli-Gleichung (The Erroneous Derivation of Torricelli's Formula from Bernoulli's Equation). *WasserWirtschaft,* 2(3), 73-78.

Malcherek, A. (2016c). Gerinnehydraulik und Flusswasserbau, Amazon-Kindle. (In German)

Newton, I. (1687). *Philosophiae Naturalis Principia Mathematica,* London.

Roth, A. & Hager, W.H. (1999). Underflow of Standard Sluice Gate. *Experiments in Fluids,* 27, 339-350.

Torricelli, E. (1644). *Opera Geometrica,* Amatoris Masse &Laurentij de Landis, Florenz.

Weisbach, J. (1855). *Die Experimental-Hydraulik,* Verlag von J.G. Engelhardt, Freiberg.

Proceedings of the 37th IAHR World Congress
August 13 – 18, 2017, Kuala Lumpur, Malaysia

EXPERIMENTAL STUDY ON FLOW CHARACTERISTICS IN ADJUSTMENT AND WAKE REGION AROUND A MODEL PATCH OF VEGETATION

DAN WANG[(1)], FENG LI[(2)], ZHI JIE LI[(3)], WEN QI LI[(4)] & KE JUN YANG[(5)]

[(1,3,5)] State Key Laboratory of Hydraulics and Mountain River Engineering, Sichuan University, Chengdu, China,
wangdan_cherry@126.com
[(2)] Chongqing Southwestern Hydraulic Institute for Water Way, Chongqing, China,
sculifeng@163.com

ABSTRACT

The interaction between vegetation and water flow is very common in the actual channel. This experimental study described how vegetation community density and bed form influence the velocity, upstream adjustment length and wake region around a non-submerged patch of model vegetation. Instantaneous measurements of longitudinal velocity, lateral velocity and vertical velocity were measured by a Nortek Vectrino. Based on the test data, the trend of longitudinal distribution of depth average velocity does not depend on bed form and vegetation community density, even if the values of flow velocity in all cases are not exactly the same. Moreover, bed form and vegetation community density have effects on upstream adjustment length and steady wake length. For high flow blockage, upstream adjustment length is greater than that of the low, and the variation of steady wake length is contrary. The bed form has little effects on the upstream adjustment length. L_0 is similar in packed, movable and feeding sediment cases. The presence of sediment leads to the decrease of steady wake length. By adding sediments to the flow upstream of the flume, we can find that the value of L_1 becomes smaller.

Keywords: Vegetation; density; velocity; adjustment length; wake region.

1 INTRODUCTION

The aquatic vegetation is common in natural rivers and plays an important role in the river corridor system. Owing to the competition of the survival environment, in wetlands and tidal rivers, the vegetation often exhibits a patch with finite width and length, and circular vegetation patch is the most familiar initial patch form. They contribute to totally different distributions of velocity and turbulent dynamic intensity around and within the patch (Ricardo, et al., 2014). This is worth to be further discussed because different flow patterns may result in different distributions of flow adjustment region and wake region (Zong and Nepf, 2012). Moreover, the variational sediment deposition may cause that the vegetation community is further developed into other shapes, and then the flow structure is impacted (Meire et al., 2014; Vargas-Luna, et al., 2016). In recent years, there are respectable studies regarding the vegetation community but they are incomplete, so the research on flow in vegetation community open-channel has important academic significance in mechanics of sediment transport and river dynamics.

Zong and Nepf (2010) researched on the flow and deposition observed in and around a finite patch of vegetation located at the wall of a channel, and indicated that the velocity field which was measured in and around the patch by acoustic Doppler velocimetry revealed three distinct zones. Rominger and Nepf (2011) showed that the flow adjustment region was associated with the canopy flow-blockage. Follett and Nepf (2012) described the sediment patterns formed in a sand bed around circular patches of rigid vertical cylinders, representing a patch of reedy emergent vegetation. Chen et al. (2013) studied the mean and turbulent flow structure in the wake of a circular array of cylinders, and proposed a method for estimating the wake length behind sparse and dense patches. Ortiz et al. (2013) examined how the spatial distribution of flow is connected to the spatial distribution of suspended sediment deposition, and linked the wake sediment deposition to both velocity and TKE, then found that TKE is the dominant factor that contributes to the depressed deposition in the wake. Within the model patch, Liu and Nepf (2016) experimentally determined the threshold of stem turbulence that is expressed using the stem Reynolds number, i.e. Red = 120, and presented two criteria for determining enhanced deposition inside a vegetation patch in laboratory experiments as well as in a field study. Shi et al. (2016) examined the influence of particle size and density, and channel velocity on the spatial deposition pattern around an emergent, circular patch of model vegetation located at the center of a channel. These research results broaden our understanding for the interaction of vegetation patches and flow structure.

In these studies, the conditions of vegetation patch and bed form were not comprehensive. They may not be applicable for some natural rivers where the density of vegetation patch and bed form is different in different seasons. For the appropriate management and restoration of rivers, isolated vegetation is often a practical means for improving stream habitat and ecology (Kim, et al., 2015). Meanwhile, in a natural scenario, the upstream sediment input is sufficient, which may affect the flow velocity. Thus, we are interested in the scenario of sparse and dense vegetation, and fixed bed and movable bed. Combining the distributions of velocity and turbulent dynamic intensity in upstream and downstream, this experimental study describes the flow adjustment region and wake region in different situations.

2 EXPERIMENT METHODS

Experiments were conducted in a 16 m long, 0.3 m wide and 0.4 m high straight Plexiglas flume with a 1.62 m long test section. A plate gate was arranged at the tag end of the flume, and the water surface slope can be controlled by adjusting it, which was used to keep the water flow to be uniform. In addition, a funnel was equipped upstream of the plate gate, and a filter screen connected with a valve at the bottom of it, which can be used to collect sands. Cylindrical bamboo sticks were used to simulate the rigid and non-submerged vegetation unit. The vegetation of a single plant was arranged into a circular vegetation community in the staggered pattern, then they were arranged into the punched plexiglass base plate.

The model patch (D = 6 cm) blocked 20% of channel width (30 cm), and patch density (a) was varied. The density of vegetation community was estimated using the following equations,

$$a = nd \tag{1}$$

where n is the plant number in the unit vegetation area and d is the diameter of the single plant . The plane graph of vegetation community are depicted in Figure 1. There were 7 test cross sections upstream of model patch and 25 test cross sections downstream of model patch.

(a) D= 6 cm, a= 0.254 cm^{-1}

(b) D= 6 cm, a= 0.523 cm^{-1}

Figure 1. Vegetation community arrangement pattern. The diameter of model patch is 6 cm. The density of sparse patch is 0.254 cm^{-1}, and the density of dense patch is 0.523 cm^{-1}. Model patch was arranged in the center of the flume.

To study the flow characteristics in adjustment and wake region in different vegetation community density and runoff-sediment conditions, fixed, movable and feeding sediment bed cases were designed in this experiment. There are all the test conditions in Table 1. While, in movable bed case, the bed was paved with uniform sediment, which is 0.08 m thick and 12 m long. The diameter of sediment is 1-2 mm which was estimated by the Sharmov formula. In feeding sediment case, in order to add sands to the flow continuously, a conveyor was arranged in the front of the flume.

Table 1. Test conditions.

Condition	$Q(m^3 \cdot s^{-1})$	h(m)	$U_0(m \cdot s^{-1})$	D(cm)	$a(cm^{-1})$	Bed Form
A1	0.018	0.125	0.48	6	0.254	fixed
A2	0.018	0.125	0.48	6	0.523	fixed
A3	0.018	0.125	0.48	Non-vegetated		movable
A4	0.018	0.125	0.48	Non-vegetated		feeding sediment
A5	0.018	0.125	0.48	6	0.254	movable
A6	0.018	0.125	0.48	6	0.254	feeding sediment
A7	0.018	0.125	0.48	6	0.523	movable
A8	0.018	0.125	0.48	6	0.523	feeding sediment

The slope of the flume was measured by spirit level and it was 1‰, which was measured and calculated repeatedly. There was a delivery mechanism in the head-end of the flume, which was used to add sands to the flow. The rate of this machine can be adjusted manually. Sands were added into the flume every 10 minutes, and the weight of the sands was determined by the sediment transport rates of different cases. Velocities were measured along the x-axis upstream and downstream of the patch and using a 3D Nortek Vectrino acoustic Doppler velocimeter (ADV). The sampling volume of the ADV was located from bottom to mid-depth in the flow. At each point, the three velocity components (u, v, w) were recorded at 50 Hz for 60 s. The upstream velocity (U_0 =48cm/s) was constant, and the water depth was 0.125 m. There were 7 sections upstream of the model patch and 25 sections downstream of it in the measurement of velocity, and the measuring position was from -4D to 23D. The velocity variation was violent when it was close to the model patch, so that the intervals were smaller and smaller when it approached the vegetation community. There were 7 vertical measuring lines in each section as well as 8 testing points, which were all evenly distributed according to the width and depth.

3 RESULTS AND DISCUSSION

3.1 Longitudinal distribution of average vertical velocity

Based on the recorded velocity data, longitudinal velocity profiles in fixed, movable and feeding sediment bed cases are depicted in Figure 2. In dense case (a = 0.523 cm^{-1}), longitudinal distributions of depth average velocity in channel center line in fixed, movable and feeding sediment bed conditions were similar. In the upstream of the model patch, the distribution curves began to decline, until a certain section which is in the downstream of the model patch, they touched the bottom. Then, the distribution curves increased gradually and finally tended to be steady in a cross section. Nevertheless, the cross section where the depth average velocity in center line reached its minimum values in different bed cases was disparate. Besides, the minimum values of the velocity in different cases were not exactly the same. In conclusion, the result shows that bed condition has little effects on the longitudinal profile of normalized average velocity.

To study the effects of vegetation community density results in depth average velocity distribution, sparse case (Case A5) and dense case (Case A7) were tested in this experiment. The graph (Figure 3) shows that in sparse case, depth average velocity in the channel center line began to decrease in x/D = -1.5 section, and reached the minimum value in x/D = 2.5 section, where the velocity was $0.4U_0$. Then, the velocity increased until x/D = 21 section, after which the velocity distribution stabilized gradually and U/U_0 = 0.7. While, in dense case, the velocity began to decrease in x/D = -2 section, and the velocity in the wake of the model patch decreased rapidly. This distribution trend continued until x/D = 2 section, and U/U_0 was about 0.3. Then, the velocity increased gradually until x/D=21 section, in which the velocity reached 0.9 U_0.

Comparing the two distribution curves, we can find that from upstream of the patch to the x/D = 3 section, the velocity of sparse vegetation was significantly greater than that of dense vegetation. After that section, the velocity value was greater in dense case. The result illustrated that vegetation community density has a significant impact on longitudinal distribution of depth average velocity. In the wake of the model patch, the velocity value of dense case was smaller than that of the sparse case. Moreover, the section of minimum value was different in different cases, and this section was near by the patch in dense case. It was because that when the vegetation community was denser, the disturbance to the flow was greater. Obviously, it caused that the energy consumptions by the water flow to be higher, and the flow velocity was smaller behind the model patch.

  / ISSN 1562-6865 (Online) - ISSN 1063-7710 (Print)

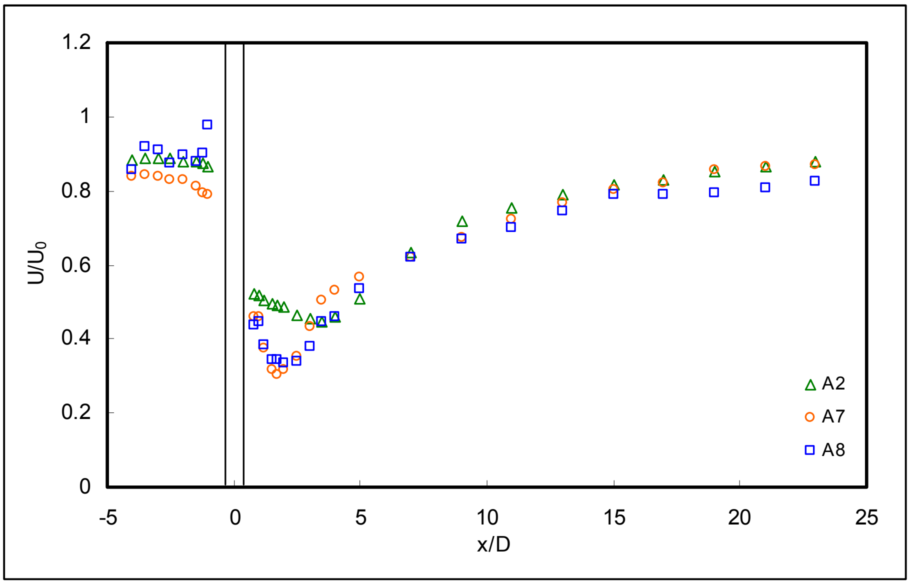

Figure 2. Longitudinal profiles of normalized depth average velocity in channel center line in different bed conditions. Velocity was normalized by the upstream value U_0. Three lines indicate the model patch with density of 0.523 cm^{-1} and diameter of 6 cm. The bed forms were fixed bed (Case A2), movable bed (Case A7) and feeding sediment bed (Case A8). The columnar represents the location of the model patch. The velocity in the wake of the patch decreased sharply, and then gradually recovered.

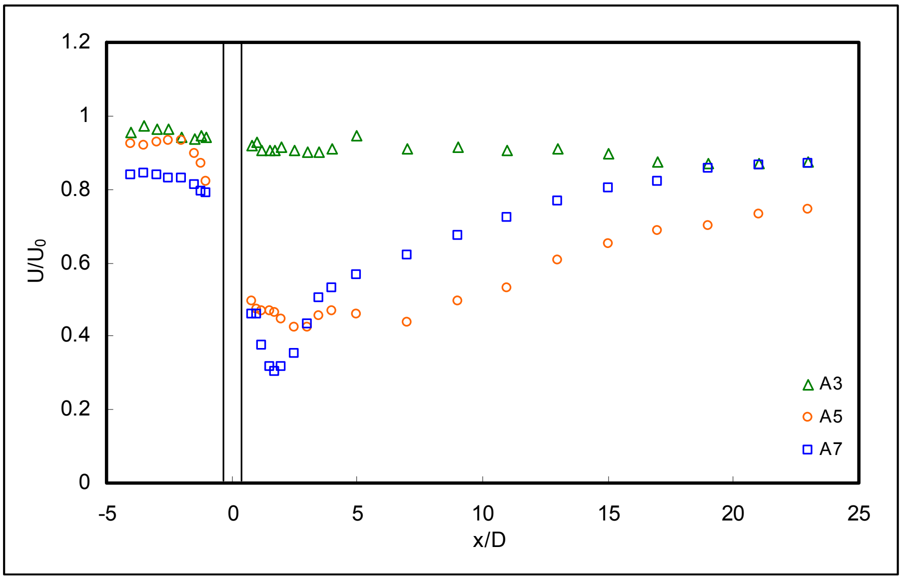

Figure 3. Longitudinal profiles of normalized depth average velocity in channel center line in non-vegetated, sparse and dense cases. The bed surface was movable in all three cases. Case A3 was the non-vegetated condition, which was the control group. In sparse case, the vegetation community density was 0.254 cm^{-1} (Case A5). While the vegetation community density was 0.523 cm^{-1} in dense case (Case A7).

3.2 Upstream adjustment length

The depth average velocity in upstream section of fixed bed case is depicted in Figure 4. In the cross section of upper of the model patch, the velocity began to decrease obviously, and the distance which from that starting section to the leading edge of the model patch was defined as upstream adjustment length L_0. For the limited width vegetation community, Romiginger and Nepf indicated that L_0 was related to the half width of the patch, and for the circular vegetation community L_0 was related to the patch diameter.

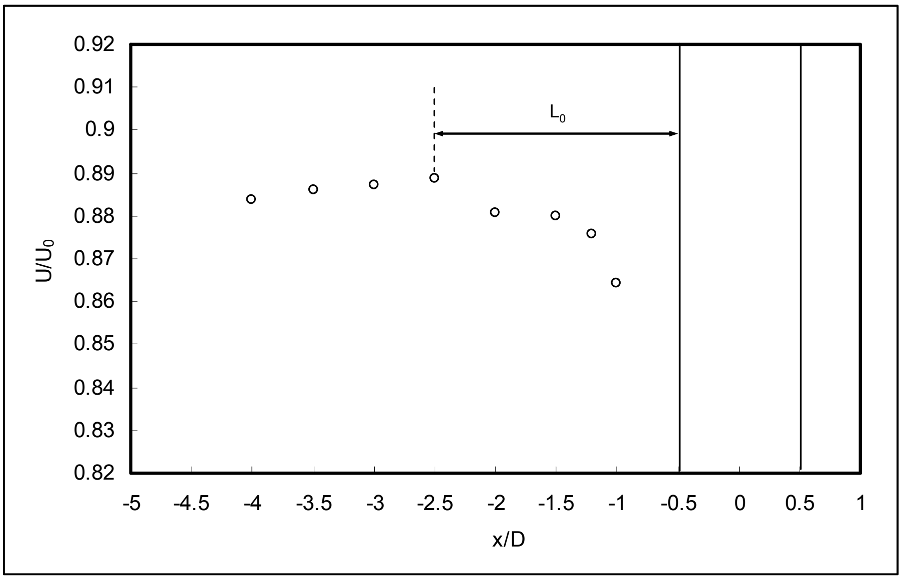

Figure 4. Upstream adjustment length of the patch. The columnar represents the location of the model patch. L_0 is upstream adjustment length, which is the distance that from the velocity decreasing section to the leading edge of the patch.

In this experiment, different bed condition cases and vegetation community density cases were tested. The results of all operating conditions are summarized in Table 2 (according to Figure 5). Based on the test data of movable bed case, the upstream adjustment length (L_0) was about 0.8D~1.2D for sparse vegetation, which was about 1.3D~1.7D for dense vegetation. When the vegetation community density increased, the flow disturbance was more violent, so that the effects of the model patch for velocity was more obvious. In fixed, movable and feeding sediment cases, the value of L_0 was approximated. Therefore, the bed condition has little effects on upstream adjustment length.

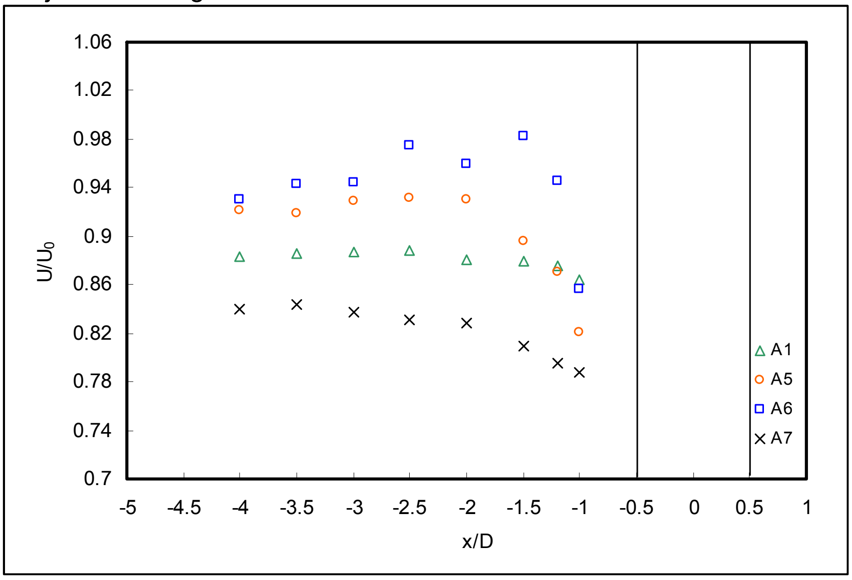

Figure 5. Upstream longitudinal profiles of normalized depth average velocity distributions in different conditions. In this figure, the bed surface and vegetation community density are all varying. The vegetation community density was 0.254 cm^{-1} in Case A1, A5 and A6, in which the bed conditions were fixed, movable and feeding sediment bed. In Case A7, the vegetation community density was 0.523cm^{-1}, and the bed condition was movable bed.

Table 2. Upstream adjustment length in different conditions.

Test condition	**Fixed Bed**	**Movable Bed**		**Feeding Sediment Bed**
	a= 0.254 cm^{-1}	a= 0.254 cm^{-1}	a= 0.523 cm^{-1}	a= 0.254 cm^{-1}
L_0	0.7D±0.3D	1D±0.2D	1.5D±0.2D	0.7D±0.3D

3.3Flow wake region

It would form a wake structure when water flows through porous media. In this experiment, there was also a wake shape downstream of the model patch. The distance between the end edge of the patch and the section that flow velocity resumes to normal is defined as the wake length L, which can be determined according to the velocity distribution. In some cases, there would be a section that the velocity fluctuated slightly in the wake region. Through the model patch, the flow velocity decreased suddenly and then to be minimum in one section, and the distance between these sections is called the steady wake length L_1. L and L_1 are depicted in Figure 6. The steady wake length is related to the diameter, density and drag coefficient of vegetation community. Chen et al. (2012) found that the steady wake length is constant (L_1 = 2.5D) for $C_DaD > 4$. While for $C_DaD < 4$, the steady wake length can be calculated by the following formula,

$$L_1 = 2.5\left[\frac{8-C_DaD}{C_DaD}\right]D \qquad (2)$$

where C_D is the cylinder drag coefficient.

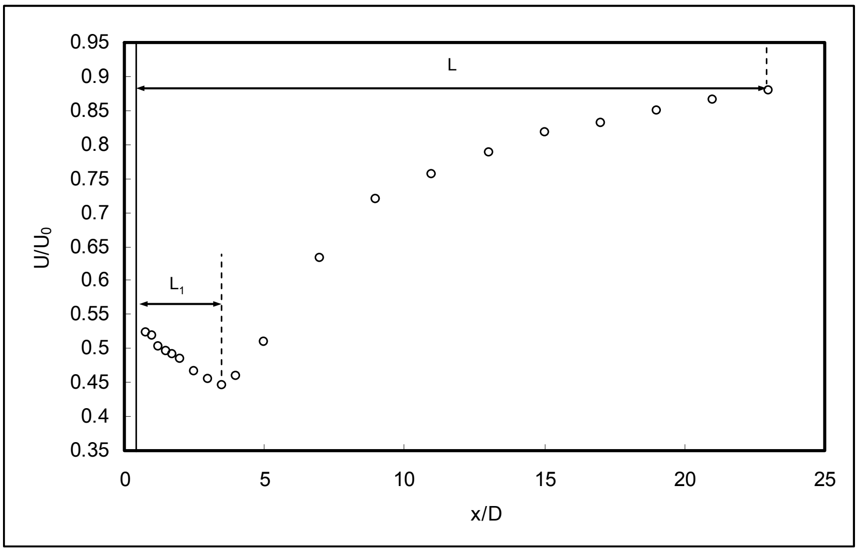

Figure 6. Wake length and steady wake length downstream of the patch. In this figure, the curve is the longitudinal distribution of the profile of normalized depth average velocity downstream of the model patch. L is called as wake length, and L_1 is the steady wake length of the flow. The vertical moulding in the figure represents the location of the model patch.

Using equation (2), the steady wake length can be calculated. Based on the test data, distributions of longitudinal profiles of normalized depth average velocity downstream of the model patch are depicted in Figure 7. Thus, we can obtain the values of steady wake length in different cases from this graph easily. To analyze the influences of bed condition and vegetation community density succinctly, the calculated values and measured values are collected in Table 3. Comparing the measured value with the calculated one, it can be found that for all the test conditions, the former was smaller than the latter. For the flow with dense vegetation, no matter in movable bed case or in feeding sediment case, the measured value was less than the calculated one. It shows that the presence of sediment accelerates the resuming of the flow velocity in the wake region, which leads to the gradual recovery of the flow velocity in a short distance, so that the steady wake length is shortened. Due to the effects of flow around the vegetation community, the velocity of flow through the model patch was smaller than that of the both sides. Therefore, in movable bed case, there were two deep longitudinal scour marks in both sides of the patch, and sediment deposition appeared behind the model patch. Then, after a certain distance, the bed form was restored, which resulted in the flow condition and the steady wake length was reduced. When sediment was added upstream of the flume, the sediment deposition was marching continuously, thus the longitudinal scour marks behind the patch were covered and this bed surface was restored. It resulted that the influence of bed form on flow condition decreased obviously, and the steady wake length was resumed.

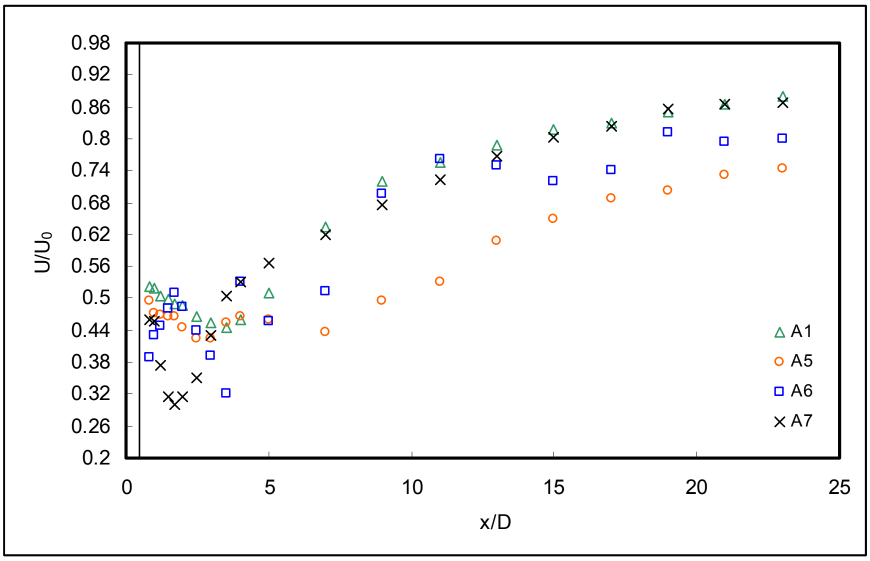

Figure 7. Downstream longitudinal profiles of normalized depth average velocity distributions in different conditions. In this figure, the bed conditions were fixed, movable and feeding sediment bed, and the vegetation community densities were 0.254 cm^{-1} and 0.523cm^{-1}.

Table 3. Steady wake length in different conditions.

Test condition	**Fixed Bed**	**Movable Bed**		**Feeding Sediment Bed**
	a= 0.254 cm^{-1}	a= 0.254 cm^{-1}	a= 0.523 cm^{-1}	a= 0.254 cm^{-1}
Measured Value L_1	2.5D±0.5D	2D±0.5D	1.5D±0.5D	1.2D±0.5D
Calculated Value L_1	3.2D	2.9D	2.5D	2.6D

Associating the distribution of depth average velocity with turbulent kinetic energy, the measured data turned out that there were two peaks and a trough in the turbulence intensity distribution in figure 8. The first peak appeared at the end edge of the model patch, and the second one appeared near by the Karman vortex street. Obviously, the steady wake region was also generated in this interval. Since the effects of the Karman vortex street on the flow were limited, the velocity eventually restored which led to the generation of the steady wake length. Besides, the position and values of the peak and though were different for various vegetation densities. From the viewpoint of energy, we found that the water energy exchange process of sparse and dense vegetation was distinguishing, which resulted in the wake length. The development of the transverse shear layer is the main factor that affects the steady wake length.

4 CONCLUSIONS

Flume experiments are presented for the flow of a model patch and how vegetation community density and bed form influenced the longitudinal distribution of average vertical velocity, upstream adjustment length and wake region has been explored. In different bed form case and patch density cases, the trend of longitudinal distributions of depth average velocity was close. The velocity began to decrease slightly upstream of model patch, and at the end edge of model patch the flow velocity decreased sharply and then to be minimum. After that, the flow velocity increased gradually and finally tended to be steady. However, the cross sections of the maximum values and minimum values of each distribution were different, and the corresponding velocity values were also different. The bed form has little effects on the upstream adjustment length. L_0 is similar in packed, movable and sediment load cases. In the dense case, the upstream adjustment length was greater than that in sparse case. Both bed form and vegetation community density have some influences on steady wake length. The presence of sediment leads to the decreasing of steady wake length. By adding sediment to the flow upstream of the flume, we can find that the value of L_1 becomes smaller. Besides, in the dense case, the steady wake length is smaller than the sparse one. In all test conditions, the calculated values of L_1 are approximately equal to the measured ones.

ACKNOWLEDGEMENTS

This study was financially supported by the National Natural Science Foundation of China (No. 51539007) at the State Key Laboratory of Hydraulics and Mountain River Engineering, Sichuan University.

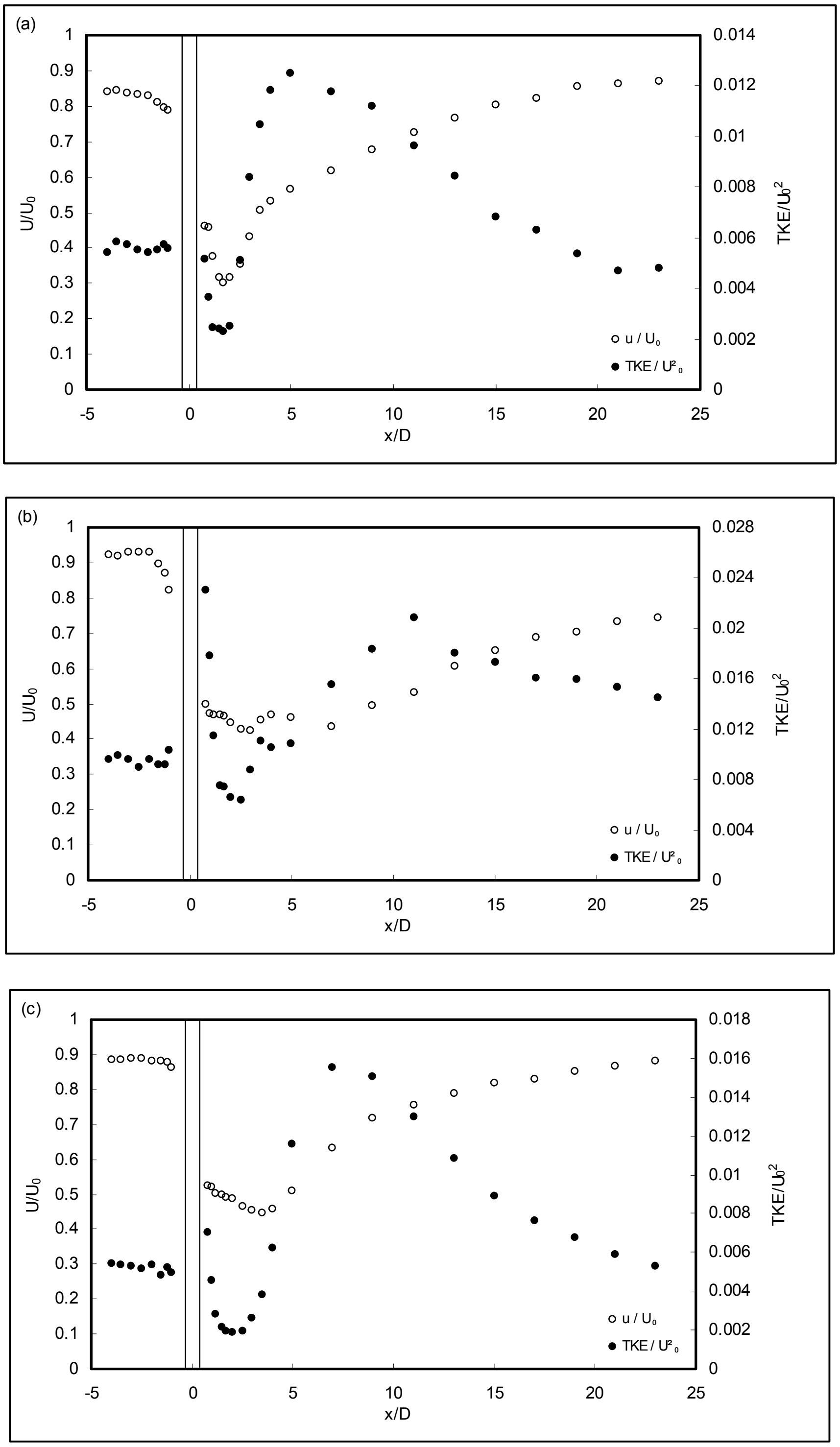

Figure 8. Distributions of longitudinal profiles of normalized velocity and turbulence kinetic energy. Turbulence kinetic energy (TKE) is normalized by U^2_0. (a) The bed form was fixed bed and the vegetation community density was 0.523cm^{-1} (Case A2). (b) The bed form was movable bed and the vegetation community density was 0.523cm^{-1} (Case A7). (c) The bed form was feeding sediment bed and the vegetation community density was 0.523cm^{-1} (Case A8).

REFERENCES

Chen, Z., Ortiz, A., Zong, L. & Nepf, H.M. (2012). The Wake Structure behind a Porous Obstruction and its Implications for Deposition near a Finite Patch of Emergent Vegetation. *Water Resources Research*, 48(9), 1-12.

Chen, Z., Jiang, C. & Nepf, H.M. (2013). Flow Adjustment at the Leading Edge of a Submerged Aquatic Canopy. *Water Resources Research*, 49(9): 5537-5551.

Follett, E.M. & Nepf, H.M. (2012). Sediment Patterns near a Model Patch of Reedy Emergent Vegetation. *Geomorphology*, 179, 141-151.
Kim, H.S., Kimura, I. & Shimizu, Y. (2015). Bed Morphological Changes around a Finite Patch of Vegetation. *Earth Surface Processes and Landforms*, 40(3), 375-388.
Liu, C. & Nepf, H.M. (2016). Sediment Deposition within and around a Finite Patch of Model Vegetation over a Range of Channel Velocity. *Water Resources Research*, 52(1), 600-612.
Meire, D.W.S.A., Kondziolka, J.M. & Nepf, H.M. (2014). Interaction between Neighboring Vegetation Patches: Impact on Flow and Deposition. *Water Resources Research*, 50(5), 3809-3825.
Ortiz, A.C., Ashton, A. & Nepf, H.M. (2013). Mean and Turbulent Velocity Fields near Rigid and Flexible Plants and the Implications for Deposition. *Journal of Geophysical Research*, Earth Surface, 118(4), 2585-2599.
Ricardo, A.M., Koll, K., Franca, M.J., Schleiss, A.J. & Ferreira, R.M. (2014). The Terms of Turbulent Kinetic Energy Budget within Random Arrays of Emergent Cylinders. *Water Resources Research*, 50(5), 4131-4148.
Rominger, J.T. & Nepf, H.M. (2011). Flow Adjustment and Interior Flow Associated with a Rectangular Porous Obstruction. *Journal of Fluid Mechanics*, 680, 636-659.
Shi, Y., Jiang, B. & Nepf, H.M. (2016). Influence of Particle Size and Density, and Channel Velocity on the Deposition Patterns around a Circular Patch of Model Emergent Vegetation. *Water Resources Research*, 52(2), 1044-1055.
Vargas-Luna, A., Crosato, A., Calvani, G. & Uijttewaal, W.S.J. (2016). Representing Plants as Rigid Cylinders in Experiments and Models. *Advances in Water Resources*, 93, 205-222.
Zong, L. & Nepf, H.M. (2010). Flow and Deposition in and around a Finite Patch of Vegetation. Geomorphology, 116(3), 363-372.
Zong, L. & Nepf, H.M. (2012). Vortex Development behind a Finite Porous Obstruction in a Channel. *Journal of Fluid Mechanics*, 691, 368-391.

Proceedings of the 37th IAHR World Congress
August 13 – 18, 2017, Kuala Lumpur, Malaysia

PHYSICAL MODELLING OF SCOUR AROUND BRIDGE PIERS CAUSED BY FLOOD WAVES

OSCAR LINK[1], SEBASTIÁN HENRÍQUEZ[2] & BERND ETTMER[3]

[1,2] Civil Engineering Department, University of Concepción, Concepción, Chile
olink@udec.cl; shenriquezp@udec.cl
[3] Civil Engineering Department, Magdeburg University of Applied Sciences, Germany
Bernd.Ettmer@hs-magdeburg.de

ABSTRACT

Scour around bridge piers of complex geometry and around pier groups cannnot be estimated following standard procedures, except for ideal conditions. Moreover, during flood waves, parameters typically involved in scour estimation, such as the flow intensity (U / U_{cr} with U the average flow velocity and U_{cr} the critical velocity for initiation of sediment motion), vary widely in time and cannnot be used in a straight forward manner for estimation of scour with existent scour formulas. Under such circumstances, the local scour problem should be studied in a physical model at reduced scale, less than 1:25 ratio. Typically in physical models of river flows, Froude similitude is required. For models with sediment transport geometric scaling of the sediment particles is however an issue when the model sediment achieve sizes as small as to present cohesive forces, typically in cases with sand in nature. Thus, the scalability of the scour process is by far not trivial, and has not been resolved yet. Thus, we present a dimensional analysis of the problem, identifying a consistent scaling criterion for the flow and for the sediment. This criterion is tested through carefully designed laboratory experiments, conducted at the Laboratories for Hydraulic Engineering of the University of Concepción, Chile, and at the Leichtweiß-Institut für Wasserbau, Technische Universität Braunschweig, Germany. Test was conducted in three different flumes having different sizes and piers of different diameters, with five sediments of different sizes and densities. Our results show that the dimensionless effective flow work, W* is a suitable criteria for scaling the effect of river flows on the local scour process around a pier in a given sediment. The dimensionless sediment diameter D* is also a suitable criteria for scaling sediments in order to achieve similar scour depths under similar flow conditions.

Keywords: Bridge pier scour; physical modelling; dimensional analysis; unsteady hydraulics; loose boundary hydraulics.

1 INTRODUCTION

Bridge pier scour occur mainly during flood waves (Hager & Unger 2010, López et al. 2014, Link et al. 2016) and is the main cause of bridge collapses worldwide (Briaud, 2006; Lu et al., 2010; Prendergast and Gavin, 2014). Moreover, climate change is expected to increase storm intensities and river floods magnitudes (Pachauri et al., 2015), thus increasing the risk of bridge failure due to scour (Wright et al., 2012).

Scour formulas provide results significantly different from each other (Sheppard et al., 2014) and their application is restricted to few pier geometries (Coleman, 2005; Kothyari and Kumar, 2012; Moreno et al., 2016) and configurations of pier groups (Ataie-Ashtiani and Beheshti, 2006; Amini and Melville, 2011). This therefore introduces important uncertainties in the hydraulic design of bridges (Briaud et al., 2013; Johnsons et al., 2015; Barbeta et al., 2016).

Alternatively, scaled movable bed river models provide valuable information on prototype fluvial processes that can be difficult to obtain in the field or with mathematical techniques (Thélusmond et al., 2013; Gorrick and Rodríguez 2014). Similitude between the prototype and model relies on equating dimensionless parameters for the flow and sediment transport, thus preserving consistent ratios of the dominant forces (Yalin and Kamphuis, 1971). However, maintaining similitude between movable bed laboratory models and the larger rivers they represent is difficult to do, and due to this the scale effects arise. The estimation of how scale effects qualitatively and quantitatively affect the model results and whether or not they can be neglected is a challenge for physical modelers (Heller, 2011). The design of scour tests should be improved so that more quantitative results can be obtained from model tests (Shen 1990).

The bridge pier scour involved complex interactions between the three-dimensional unsteady flow and the riverbed sediment around the pier (Link et al., 2012; Link et al., 2016). Raudkivi (1986) presented the functional trends of scour and Melville and Chiew (1999) studied the temporal scale in bridge pier scour showing that the scour depth after 10% of the time to equilibrium is between 50% and 80% of the equilibrium of scour depth, depending on flow intensity. Lee and Sturm (2009) showed that scour strongly depends on the relative size of the pier to sediment, attaining a maximum for D/d =25, and reducing D/d up to a 150% when D/d = 400. Moreover, using scaling arguments, Cheng et al. (2016) showed that parameters in scour formulas that consider Z* as an exponential function of time strongly depends on D/d. Furthermore, Ettema et al. (1998, 2006) analyzed the scale effects on scour and concluded that the use of laboratory flumes in developing accurate predictors of scour depth at full-scale piers was limited due to scale effects that may produce greater scour depths, Z* at the laboratory than at actual piers in rivers.

In this work, we analyze the bridge pier scour problem caused by flood waves. We identify the controlling dimensionless parameters, and present carefully designed laboratory experiments to test the validity of the theoretically derived controlling parameters.

2 MATERIALS AND METHOD

2.1 Dimensional analysis

Scour depth at a cylindrical bridge pier in a homogeneous sediment bed depends on variables characterizing the fluid, flow, sediment, and pier. In functional form:

$$f(\mu, \rho, u_{ef}, h, g, d_s, \rho_s, D, t, z) = 0 \qquad [1]$$

where *f* is a function, μ the fluid dynamic viscosity; ρ the fluid density; u_{ef} the effective flow velocity; *h* the flow depth at the undisturbed flow region; *g* the gravitational acceleration; d_s the representative sediment particle diameter; ρ_s the density of a sediment particle; *D* the pier diameter; *t* the time, and *z* is the scour depth. For the particular case of scour around a cylinder the effective flow velocity, u_{ef} corresponded to the excess velocity above the incipient scour condition $u_{ef} = u - u_{cs}$, with *u* the section averaged flow velocity, and u_{cs} the critical velocity for the incipient scour. According to the π-Buckingham theorem, the set of ten independent variables could be reduced to seven non-dimensional parameters. Taking ρ, u_{ef} and d_s as repeating variables:

$$f\left(\mathrm{Re}', Fr', \rho', \frac{h}{d_s}, \frac{D}{d_s}, \frac{u_{ef}t}{d_s}, \frac{z}{d_s}\right) = 0 \qquad [2]$$

where $\mathrm{Re}' = u_{ef} d_s / \nu$ is the effective particle Reynolds number; $Fr' = u_{ef} / \sqrt{g d_s}$ is the effective, particle Froude number; $\rho' = (\rho_s - \rho)/\rho$ is the relative density; h/d_s is the relative flow depth; and D/d_s, the relative size of the pier to sediment. Proper combination of dimensionless parameters in Eq. (2) leads to

$$f\left(D^*, Fr_d, \rho', \hat{h}, \frac{D}{d_s}, U^*, Z^*\right) = 0 \qquad [3]$$

Where $D^* = \left(\mathrm{Re}'^2 / \left(Fr'^2/\rho'\right)\right)^{1/3} = \left((\rho' g)/\nu^2\right)^{1/3} d_s$ is the dimensionless grain diameter; $Fr_d = Fr'(\rho')^{-0.5} = u_{ef} / \sqrt{\rho' g d_s}$ is the effective, densimetric Froude number; $U^* = 2(u_{ef}t/d_s)(D/d_s)^{-2} = u_{ef}t / (D^2/2d_s) = u_{ef}t / z_R$ is a flow unsteadiness parameter with z_R a reference length, $\hat{h} = (h/d_s)(D/d_s)^{-1} = h/D$ is the relative flow depth; and $Z^* = (z/d_s)(D/d_s)^{-1} = z/D$ is the normalized scour depth.

2.2 Similitude

Perfect similitude between model and nature was achieved if all parameters in Eq. [3] are identic. Difficulties arise, for finding model sediments that satisfy this restriction. Typically the desired model of sediments were lighter and coarser than nature sediments. However, according Link et al. (2016) scour around a pier, in a given sediment scale with effective dimensionless will work by the flow on the sediment bed around the pier $Z^* = f(W^*)$. This is where the flow work will be a function of the effective, densimetric Froude number and the unsteady parameter, $W^* = f(Fr_d, U^*)$. Restricting the analysis to cases where Z^* is independent of the relative flow depth, i.e. for $\hat{h} > 1.5$ (Raudkivi 1986, Melville 1997), and neglecting the effects of D/d_s and ρ' is where we hypothesize that self-similarity of the pier scour is achieved when the two controlling parameters D* and W* are identic in nature and model. This hypothesis was tested experimentally.

2.3 Experimental facilities

Experiments were conducted within three different flumes:

i. An in-floor rectangular flume of 26 m long, 1.4 m wide and 0.74 m deep with a plexiglass cylinder of diameter D = 0.15 m was mounted in the middle of a 2 m long sediment-recess. It was located 20 m downstream of the flume entrance. Scour was measured with a laser distance sensor as documented by Link et al. (2016).
ii. A tilting rectangular flume of 6.0 m long, 0.4 m wide and 0.4 m deep having a PVC cylinder of diameter 0.046 m was mounted in the middle of a 0.6 m long sediment-recess. This flume was located 4 m downstream of the flume entrance. Scour was monitored with a snake video camera having 7 mm in diameter that penetrated the free surface less than 1 cm, and recorded the sediment bed position on a graduation at the pier front.

Flumes (i) and (ii) are located at the Hydraulic Engineering Laboratory of the University of Concepción, Chile.

iii. A horizontal flume with smooth side walls in the Leichtweiß-Institut für Wasserbau at Technische Universität Braunschweig with 8 m in length, 0.3 m in width and 0.6 m in depth was used. A cylinder of 0.03 m diameter was mounted in the middle of a 1.2 m long and 12 cm deep sediment recess was placed 4.5 m downstream of the flume entrance. Scour was measured with a point gauge as described by Meyering & Ettmer (2010).

2.3.1 Sediment material

Sediments of different sizes and densities were used in the experiments. Table 1 shows the important properties of the sediment material.

Table 1. Properties of the sediment material.

	d_s [mm]	σ_g [-]	ρ [kg/m^3]	FF [-]	D* [-]
Sand 1	0,36	1,45	2650	0,70	9
Sand 2	0,74	1,18	2650	0,70	18
Sand 3	0,80	1,30	2650	0,70	21
Sand 4	1,60	1,29	2650	0,70	40
Acetal	2,60	1,00	1390	0,71	41
Polystyrene	2,74	1,05	1040	0,75	20

2.4 Experimental Series

Two series of experiments were conducted to test the hypothesis. The first series S1 includes experiments with variable discharge for testing the reliability of the dimensionless flow work, W* as a predictor of Z* in a given material. The second series S2 includes experiments with similar values of W* on different sediments having similar D*, in order to test the feasibility of D* in representing the sediment bed in the pier scour problem (Table 2).

Table 2. Experimental series.

Series	Experiment	Flume	Sediment	u_B [m/s]	h_B [cm]	u_p [m/s]	t_p [min]	t_{end} [min]	u_p/u_c	D/d_s	W* total	z/D final
S1	1	i	Sand 1	0,12	21	0,29	100	120	0,91	417	42,1	0,48
S1	2	i	Sand 1	0,12	21	0,29	20	120	0,91	417	40,1	0,47
S1	3	i	Sand 1	0,12	21	0,25	16-100	175	0,78	417	44,3	0,48
S2	1	ii	Sand 2	0,15	9,2	0,27	190	390	0,82	62	602	1,25
S2	2	i	Polystyrene	0,038	30	0,11	190	390	0,84	56	613	1,24
S2	3	ii	Sand 2	0,15	9,2	0,42	25	50	1,27	62	2446	1,67
S2	4	i	Polystyrene	0,038	30	0,17	25	50	1,39	56	2271	1,6
S2	5	ii	Sand 2	0,26	9,2	-	-	1368	0,8	62	4422	1,53
S2	6	i	Polystyrene	0,10	30	-	-	1351	0,8	56	3907	1,52
S2	7	iii	Sand 3	0,32	10	-	-	1440	1,0	19	52946	1,67
S2	8	iii	Acetal	0,21	10	-	-	1440	1,04	12	72780	1,67

Note that flume (ii) with Sand 2 corresponds to a scale model of flume (i) with Polystyrene, achieving perfect similitude.

3 RESULTS

3.1 Scaling the flow

Figure 1 shows the discharge Q, dimensionless, effective flow work W*, and relative scour depth z/D over time t, as well as the relative scour depth z/D over W* for experiments of series S1.

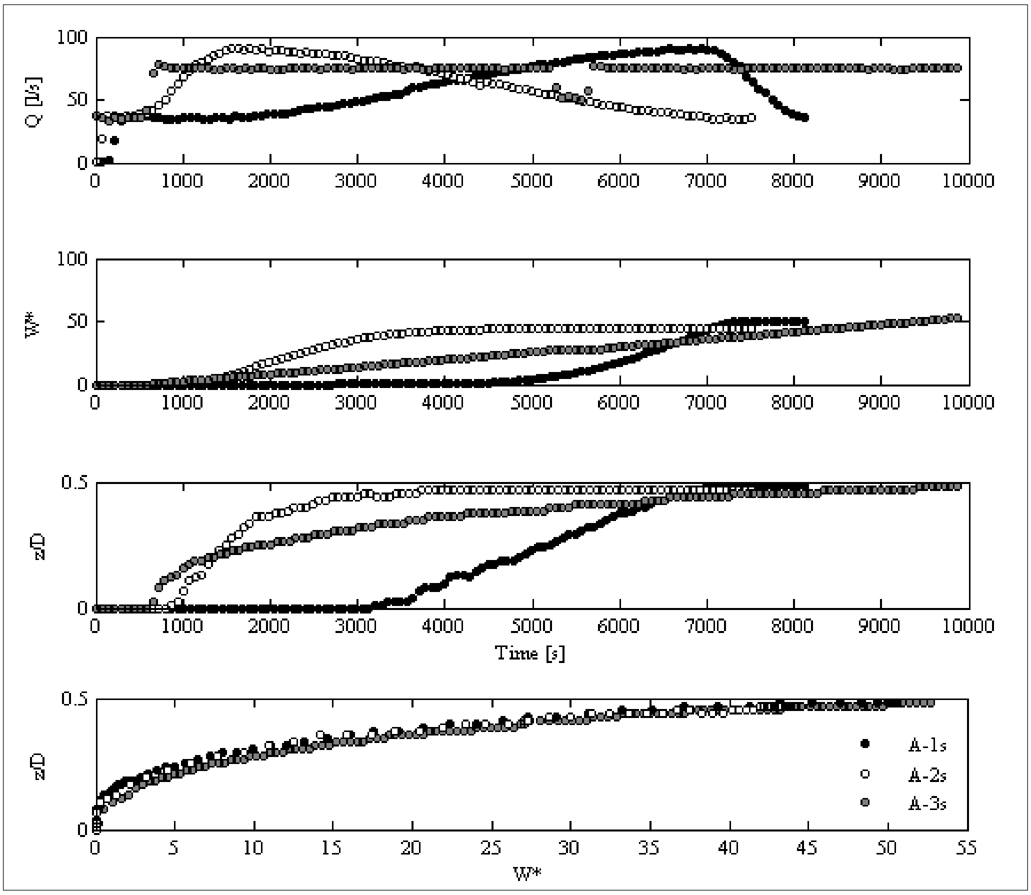

Figure 1. Discharge Q, dimensionless, effective flow work W*, and relative scour depth z/D over time t, as well as the relative scour depth z/D over W* for experiments of series S1.

Different hydrographs produced the same relative scour depth in the Sand 1. Moreover, for a given amount of W* the same value of z/D was obtained which partially confirms the hypothesis in the sense that the flow was well represented by W* for scaling purposes.

3.2 Scaling the sediment

The sediment scale was tested with experiments of series S2. Experiments S2-1 and S2-2 were conducted with Sand 2 and Polystyrene, respectively under the clear water condition. Both sediments have a similar dimensionless grain diameter of D*=18 and 20. Figure 2 shows that the discharge Q, dimensionless, effective flow work W*, and relative scour depth z/D over time t, as well as the relative scour depth z/D over W* for experiments S2-1 and S2-2.

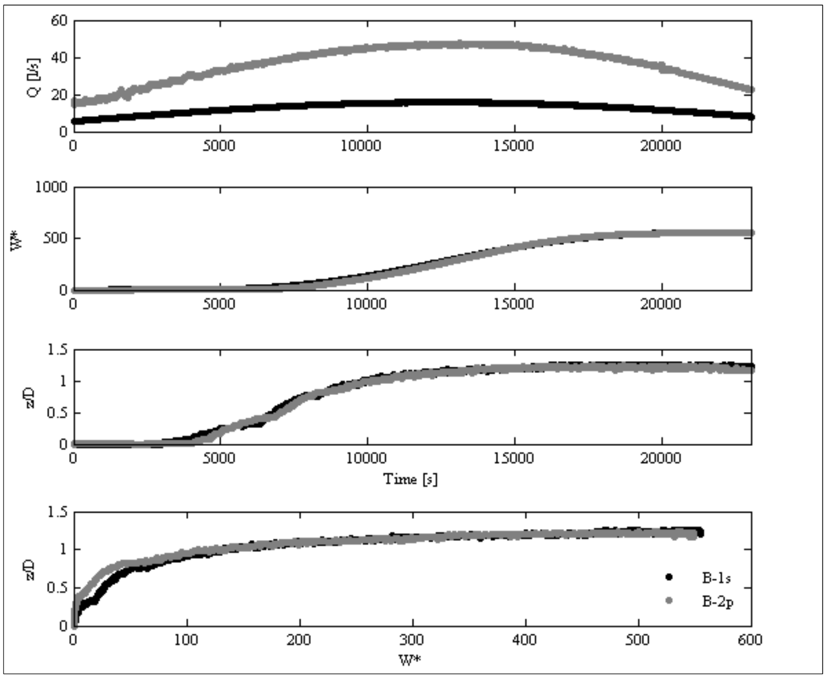

Figure 2. Discharge Q, dimensionless, effective flow work W*, and relative scour depth z/D over time t, as well as the relative scour depth z/D over W* for experiments S2-1 and S2-2.

Hydrographs with different discharges were designed for experiment S2-1 and S2-2, in order to produce the same value of W* on the sediment beds. Remarkably, in this case, we obtained a perfect self-similarity of the scour process. The curve of relative scour depth z/D on time coincides in both experiments, confirming our hypothesis.

Experiments S2-3 and S2-4 were conducted under the live-bed condition, with Sand 2 and Polystyrene, respectively. Figure 3 shows the discharge Q, dimensionless, effective flow work W*, and relative scour depth z/D over time t, as well as the relative scour depth z/D over W* for experiments S2-3 and S2-4.

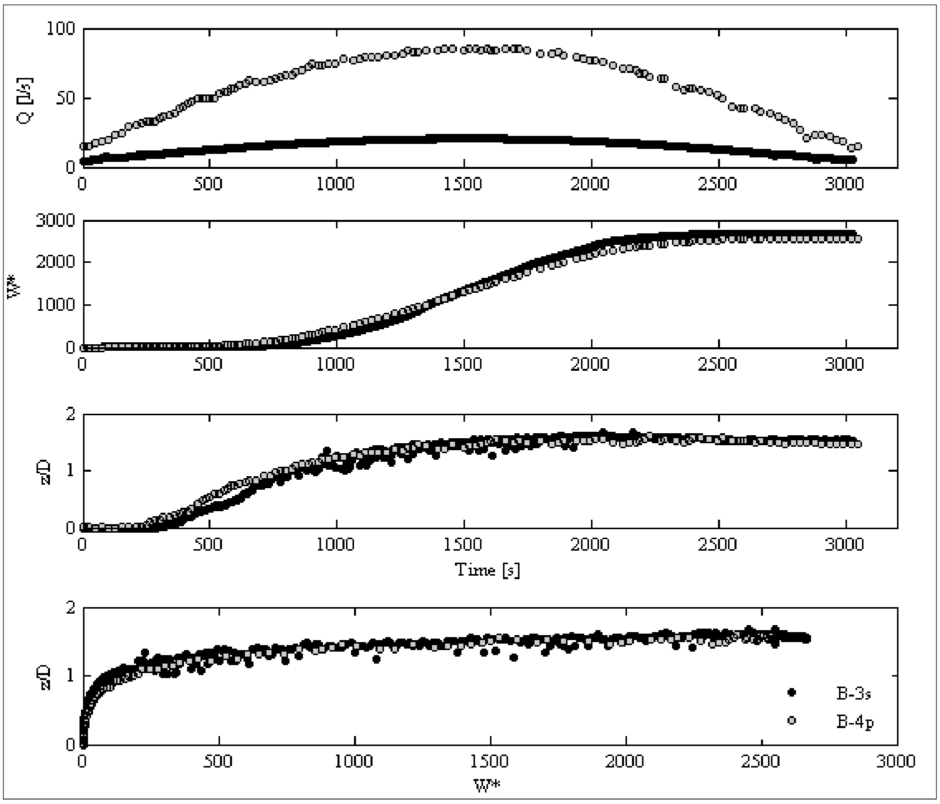

Figure 3. Discharge Q, dimensionless, effective flow work W*, and relative scour depth z/D over time t, as well as the relative scour depth z/D over W* for experiments S2-3 and S2-4.

Again, hydrographs with different discharges were designed for experiment S2-3 and S2-4, in order to produce the same value of W* on the sediment beds in time. Remarkably, in this case, we obtained a perfect self-similarity of the scour process even under the live bed condition. The curve of relative scour depth z/D on time coincides in both experiments, confirming our hypothesis.

Finally, Figure 4 shows the relative scour depth over the dimensionless, effective flow work for experiments S2-5 to S2-8. These experiments were conducted in Flume (iii) under constant discharge until advanced stages of scour. In particular, experiments S2-5 and S2-6 were conducted with Sand 3 and Polystyrene having D* of 16 and 18 , respectively, while experiments S2-7 and S2-8 were conducted with Sand 4 and Acetal having identical D*=40.

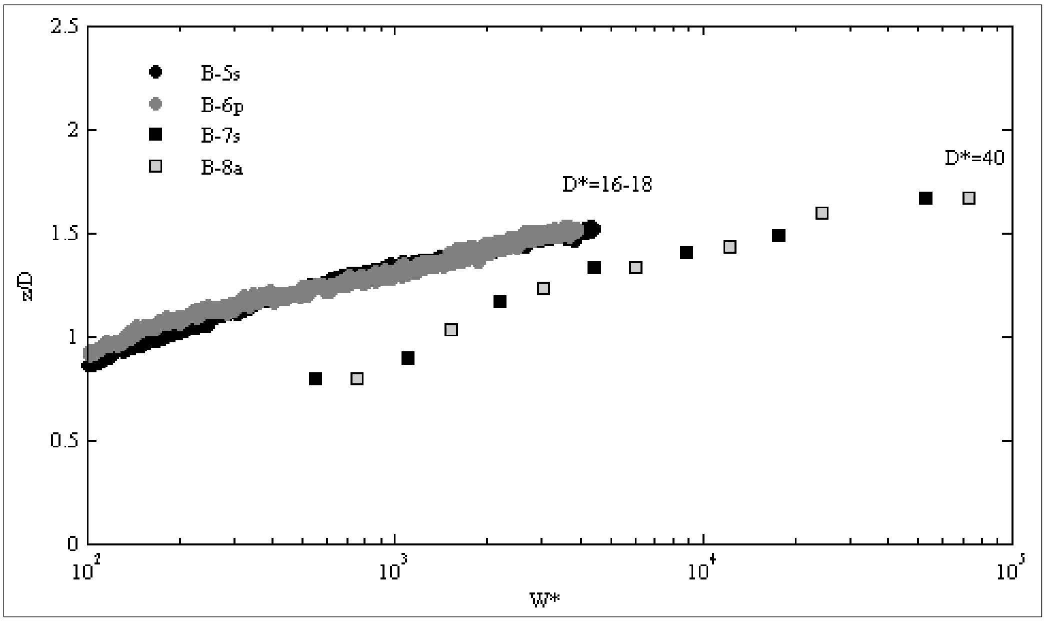

Figure 4. Relative scour depth over dimensionless, effective flow work W* for experiments S2-5 to S2-8.

Interestingly, our experimental results in Fig. 4 clearly confirm our hypothesis. Similar relative scour depth was achieved in a sediment bed of a given D* for a given value of the flow work, W*. Thus, the proposed scales for the flow and sediment in the pier scour problem are actually D* and W*.

4 CONCLUSIONS

The physical modeling of the bridge pier scour problem is analyzed through dimensional analysis and similitude theory. A hypothesis for the scalability of the flow and the sediment bed during scour is confirmed through carefully designed scour experiments that are conducted at three different experimental installations, using 5 different sediment materials. All this experiments covered steady and unsteady discharges, as well as clear-water and live-bed conditions.

The obtained results clearly confirmed the hypothesis stated theoretically. In the scour problem, the dimensionless, effective flow work is the controlling scale of the flow, while the dimensionless grain diameter D* is the controlling scale of the sediment bed. If both parameters are kept constant in model and nature, the scouring process is identically reproduced.

Further experimentation is needed in order to confirm our results at different scales, such as investigating bridges in nature.

ACKNOWLEDGMENTS

The financial support of the Chilean Research Council CONICYT through grant Fondecyt 1150997: “Bridge pier scour under flood waves” is greatly acknowledged.

REFERENCES

Amini, A., Melville, B.W., Ali, T.M. & Ghazali, A.H. (2011). Clear-Water Local Scour around Pile Groups in Shallow-Water Flow. *Journal of Hydraulic Engineering*, 138(2), 177-185.

Ataie-Ashtiani, B. & Beheshti, A.A. (2006). Experimental Investigation of Clear-Water Local Scour at Pile Groups. *Journal of Hydraulic Engineering*, 132(10), 1100-1104.

Briaud, J.L., Brandimarte, L., Wang, J. & D'Odorico, P. (2007). Probability of Scour Depth Exceedance Owing to Hydrologic Uncertainty. Georisk, 1(2), 77-88.

Briaud, J.L., Gardoni, P. & Yao, C. (2013). Statistical, Risk, and Reliability Analyses of Bridge Scour. *Journal of Geotechnical and Geoenvironmental Engineering*, 140(2), 04013011.

Cheng, N.S., Chiew, Y.M. & Chen, X. (2016). Scaling Analysis of Pier-Scouring Processes. *Journal of Engineering Mechanics*, 142(8), 06016005.

Coleman, S.E. (2005). Clearwater Local Scour at Complex Piers. *Journal of Hydraulic Engineering*, 131(4), 330-334.

Ettema, R., Melville, B. & Barkdoll, B. (1998). Scale Effect in Pier-Scour Experiments. *Journal of Hydraulic Engineering*, 124(6), 639–642.

Ettema, R., Kirkil, G. & Muste, M., (2006). Similitude of Large-Scale Turbulence in Experiments on Local Scour at Cylinders. *Journal of Hydraulic Engineering*, 132(1), 33–40.

Gorrick, S. & Rodríguez, J.F. (2014). Scaling Of Sediment Dynamics in a Laboratory Model of a Sand-Bed Stream. *Journal of Hydro-Environment Research*, 8(2), 77-87.

Hager, W. & Unger, J. (2010). Bridge Pier Scour under Flood Waves. *Journal of Hydraulic Engineering*, 136(10), 842–847.

Heller, V. (2011) Scale Effects in Physical Hydraulic Engineering Models. *Journal of Hydraulic Research*, 49(3), 293-306.

Pachauri, R. K., Meyer, L., Plattner, G. K. & Stocker, T. (2015). IPCC, 2014: Climate Change 2014: Synthesis Report. Contribution of Working Groups I, II and III to the Fifth Assessment Report of the Intergovernmental Panel on Climate Change. IPCC.

Johnson, P.A., Clopper, P.E., Zevenbergen, L.W. & Lagasse, P. F. (2015). Quantifying Uncertainty and Reliability in Bridge Scour Estimations. *Journal of Hydraulic Engineering*, 141(7), 04015013.

Kothyari, U. C. & Kumar, A. (2012). Temporal Variation of Scour around Circular Compound Piers. *Journal of Hydraulic Engineering*, 138(11), 945-957.

Lee, S. O. & Sturm, T. W. (2009) Effect of Sediment Size Scaling on Physical Modeling of Bridge Pier Scour. *Journal of Hydraulic Engineering*, 135(10), 793–802.

Link, O., González, C., Maldonado, M. & Escauriaza, C. (2012). Coherent Structure Dynamics and Sediment Particle Motion around a Cylindrical Pier in Developing Scour Holes. *Acta Geophysica*, 60(6), 1689–1719.

Link, O., Castillo, C., Pizarro, A., Rojas, A., Ettmer, B., Escauriaza, C. & Manfreda, S. (2016). A Model of Bridge Pier Scour during Flood Waves. *Journal of Hydraulic Research*, 55(3), 310-323.

López, G., Teixeira, L., Ortega-Sánchez, M. & Simarro, G. (2014). Estimating Final Scour Depth under Clear-Water Flood Waves. *Journal of Hydraulic Engineering*, 140(3), 328–332.

Lu, J. Y., Shi, Z. Z., Hong, J. H., Lee, J. J. & Raikar, R. V. (2010). Temporal Variation of Scour Depth at Non-Uniform Cylindrical Piers. *Journal of Hydraulic Engineering*, 137(1), 45-56.

Melville, B. & Chiew, Y. (1999) Time Scale for Local Scour at Bridge Piers. *Journal of Hydraulic Engineering*, 125(1), 59-65.

Moreno, M., Maia, R. & Couto, L. (2016). Prediction of Equilibrium Local Scour Depth at Complex Bridge Piers. *Journal of Hydraulic Engineering*, 142(11), 04016045.

Prendergast, L. J. & Gavin, K. (2014). A Review of Bridge Scour Monitoring Techniques. *Journal of Rock Mechanics and Geotechnical Engineering*, 6(2), 138-149.

Raudkivi, A. (1986). Functional Trends of Scour at Bridge Piers**.** *Journal of Hydraulic Engineering*, 112(1), 1-13.

Shen, H.W. (1990). *Movable Bed Physical Models.*312, Springer Science & Business Media.

Sheppard, M., Melville, B. & Demir, H. (2014) Evaluation of Existing Equations for Local Scour at Bridge Piers. *Journal of Hydraulic Engineering*, 140(1), 14-23.

Thélusmond, J. R., Chevalier, L. R., & DeVantier, B. A. (2013). The use of plastic media in a movable bed model to study sedimentary processes in rivers. *International Journal of Hydrology Science and Technology*, 3(2), 93-110.

Wright, L., Chinowsky, P., Strzepek, K., Jones, R., Streeter, R., Smith, J.B., Mayotte, J.-M., Powell, A., Jantarasami, L. & Perkins, W. (2012). Estimated Effects of Climate Change on Flood Vulnerability of US Bridges. *Mitigation and Adaptation Strategies for Global Change*, 17(8), 939-955.

Yalin M.S. & Kamphuis J.W. (1971). Theory of Dimensions and Spurious Correlation. *Journal of Hydraulic Research*, 9(2), 249-265.

Proceedings of the 37th IAHR World Congress
August 13 – 18, 2017, Kuala Lumpur, Malaysia

CFD STUDY OF A SPATIAL SUBMERGED HYDRAULIC JUMP

VIMALDOSS JESUDHAS[(1)], RAM BALACHANDAR[(2)] & TIRUPATI BOLISETTI[(3)]

[(1,2,3)] Department of Civil and Environmental Engineering, University of Windsor, Windsor, Canada
rambala@uwindsor.ca

ABSTRACT

Hydraulic jumps have been extensively studied due to their practical relevance as energy dissipators below hydraulic structures. When a high-velocity conduit drains into an expanding open channel a spatial hydraulic jump is formed. Despite their common occurrence in hydraulic engineering, they have not received enough attention from researchers. Three dimensional, unsteady Detached Eddy Simulation (DES) of a symmetric spatial submerged hydraulic jump (SSHJ) is carried out at Department of Civil and Environmental Engineering, University of Windsor, Canada. In the present paper, the validation of the simulation results with experimental data is presented with pertinent discussions. A three-dimensional nature of the flow field of SSHJ captured by the present simulations is also discussed. The evolution of shear layer is studied by examining the vorticity magnitude. The paper also showcases the capabilities of DES along with volume of fluid (VOF) multiphase model to capture the flow characteristics of a spatial submerged hydraulic jump.

Keywords: open-channel flow; hydraulic jump; detached eddy simulation; volume of fluid.

1 INTRODUCTION

Hydraulic jumps occur when a supercritical flow transitions into a subcritical flow. This transition is characterized by strong turbulence, free-surface fluctuations, air entrainment and energy dissipation. Since, hydraulic jumps are used extensively as energy dissipators below hydraulic structures they have been a subject of several studies. While these studies have generated improved empirical relationships for calculating the design parameters of hydraulic jumps, their internal structure is still not fully understood. A spatial hydraulic jump happens when a high-velocity flow conduit drains into an expanding open channel. Even though these types of spatial hydraulic jumps are often encountered in hydraulic engineering, they have not received sufficient attention as classical hydraulic jumps. Ohtsu et al. (1999) conducted an experimental study on spatial hydraulic jumps. His studies revealed that the type of hydraulic jump occurring in the open channel is dependent on the tail water depth in the open channel. Fig. 1 depicts the different types of hydraulic jumps that can happen below an abrupt expansion based on the tail water depth.

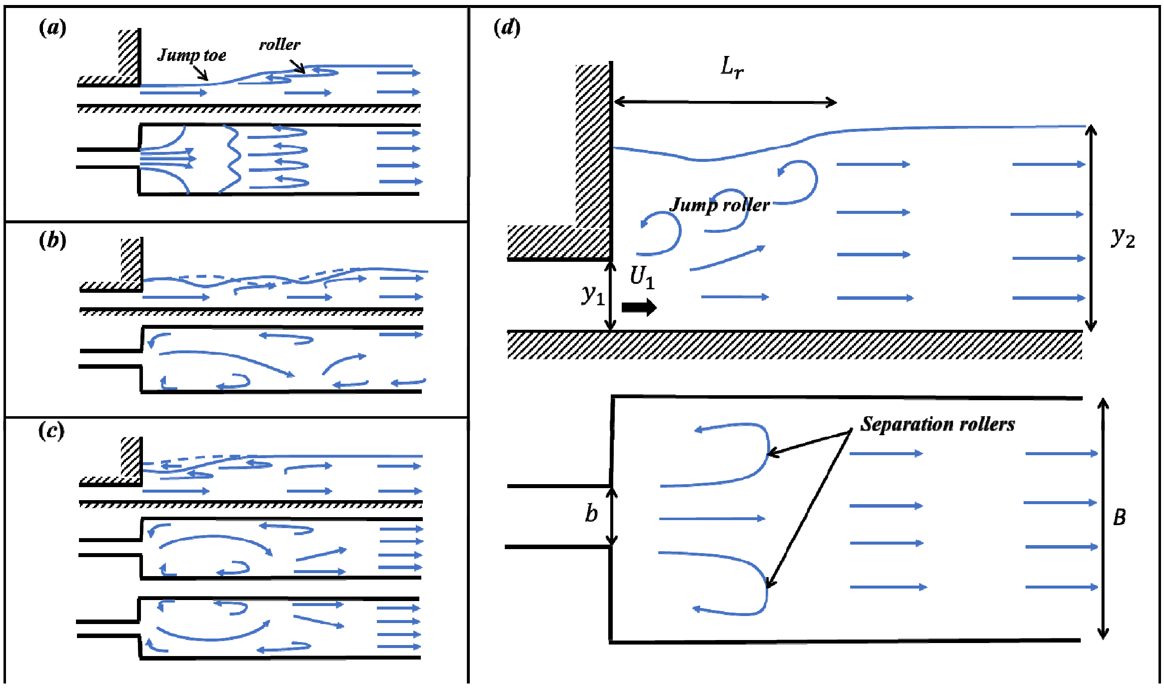

Figure 1. Schematic representation of different types of hydraulic jumps below abrupt expansions.

If the tail water depth y_2 in the open channel is less than the subcritical sequent depth $y_2^*$of a classical hydraulic jump for the given Froude number $F_1 = U_1/\sqrt{gy_1}$, where U_1 and y_1 are the velocity and flow depth at the outlet of the conduit, a classical hydraulic jump is formed in the open channel as shown in Fig. 1(a). As the tail water depth increases the toe of the hydraulic jump moves towards the conduit outlet and gets submerged. The high-velocity flow occurs on one side of the channel and a reverse flow occurs on the opposite side of the open channel as shown in Fig. 1(b). Further increase in tail water depth results in an asymmetric oscillatory flow pattern where the flow periodically shifts from one side of the channel to the other as shown in Fig. 1(c). A further increase in tail water depth results in a symmetric flow pattern as depicted in Fig. 1(d). The jump roller (reverse flow region near the free surface) of the hydraulic jump gets completely submerged. Also present are two counter rotating separation rollers near the conduit outlet (Fig. 1(d)). This flow pattern is called as the symmetric spatial hydraulic jump (SSHJ). For effective dissipation of energy, this symmetric flow pattern is targeted by designers of stilling basins (Vischer and Hager,1995).

Zare and Baddour (2007) conducted an experimental investigation of SSHJ using an acoustic Doppler velocimeter (ADV). Since ADV is a point measuring device, they were only partially successful in describing the complex three-dimensional flow field of SSHJ. Also, they did not study the turbulence parameters of the SSHJ, which are important to understand energy dissipation characteristics. In order to address these shortcomings and to generate new information on the internal structure of SSHJ, a three-dimensional unsteady, detached eddy simulation was carried out at the Department of Civil and Environmental Engineering, University of Windsor, Canada. The results of this simulation are validated with the available experimental data in the forthcoming sections of the paper. Also, the three-dimensional flow field of SSHJ captured by the simulations is presented with detailed discussions. The evolution of shear layer is analyzed by examining the vorticity field.

2 THE MODEL

The volume of fluid (VOF) multiphase model was used in conjunction with a version of the detached eddy simulation (DES) method for modeling turbulence in the present study. The DES method uses Reynolds-Averaged Navier-Stokes (RANS) models close to the walls and large-eddy simulation (LES) in the outer regions of the flow. Improved delayed detached eddy simulation (IDDES) model present in STAR-CCM+ commercial solver was also used in the present study. IDDES was selected because it had proven to be successful in simulating a submerged hydraulic jump (Jesudhas et al. 2016) and a classical hydraulic jump (Jesudhas et al. 2017). The present simulations use the k-ω detached eddy model as it is known to perform well in adverse pressure gradient flows such as the hydraulic jump. The complete formulation of IDDES was provided in Jesudhas (2016) and was ignored here for brevity. Fig. 2(a) and (b) provide the schematic representation of the simulation domain.

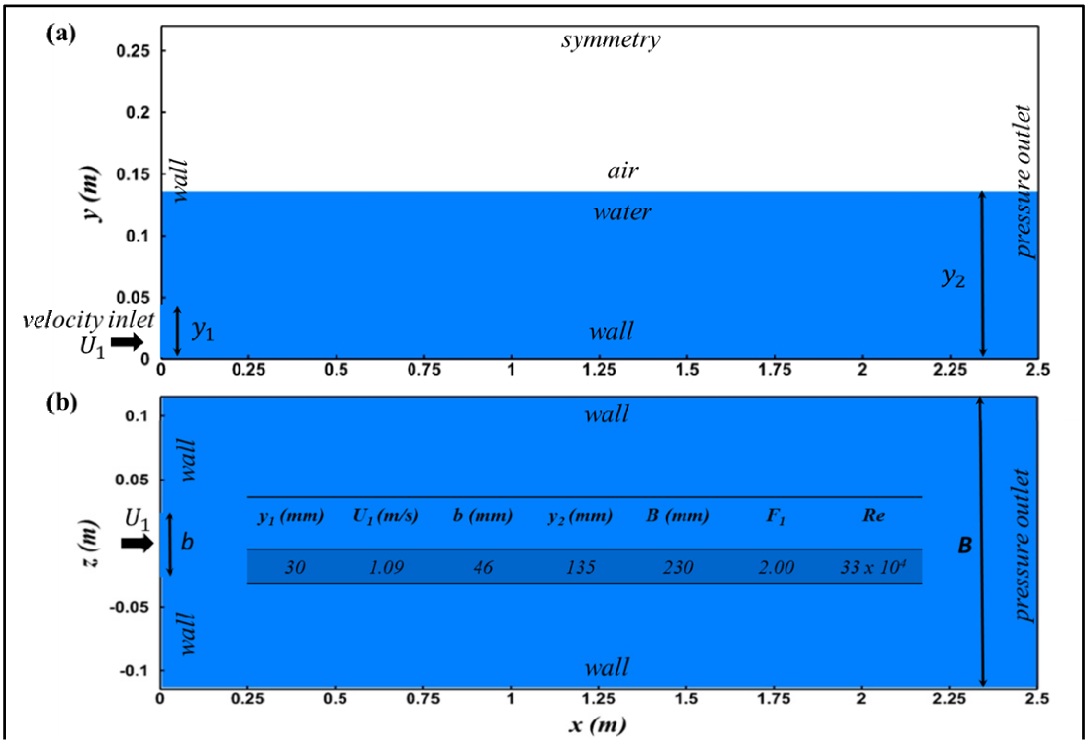

y_1 (mm)	U_1 (m/s)	b (mm)	y_2 (mm)	B (mm)	F_1	Re
30	1.09	46	135	230	2.00	33×10^4

Figure 2. Schematic representation of the simulation domain.

The simulation domain was selected based on the experiments of Zare and Baddour (2007) to enable comparison. The size of the simulation domain is 2.5m x 0.23m x 0.27m. The Cartesian coordinates x, y and z are adopted as streamwise, vertical (wall normal) and transverse directions, respectively. The origin of the coordinate system was located on the central plane of the flume at the bottom wall and below the outlet of the conduit, as depicted in Fig. 2. The boundary conditions used in the simulation are also shown in Fig. 2. The grid used in the present simulation consisted of about 3.5 million cells. Sufficient refinement was provided in the regions of interest and near the free surface. Prism layers were also used near the walls to capture the wall effects. The unsteady simulations were run with a time step of 0.001s. The convective Courant number, which was monitored at each time step, was found to be less than one. The solution was considered to be converged when the residuals of continuity and momentum fell below 10^{-6}. The velocity statistics of the present simulation have been calculated by averaging the data for 10 s following convergence.

3 VALIDATION

The results of the present simulations were compared with the experiments of Zare and Baddour (2007) as shown in Fig. 3. The present study uses high resolution interface capture (HRIC) technique for capturing the free surface. The mean free-surface profile captured by the present simulation in the central plane was compared with the experimental results in Fig. 3(a). It can be seen that the reduction in the depth near the outlet of the conduit is accurately captured by the present simulation. This reduction in depth was caused by the high-velocity flow coming out of the conduit. The free-surface height increases and reaches the tail-water depth after about $x/y_2 = 6$ in both experiments and the simulations. Fig. 3(b) shows the comparison of mean streamwise velocity at different streamwise locations along the central plane. The results of the present simulations agree well with the experimental results. Roller length L_r was defined as the distance from the conduit outlet to the end of the reverse flow region in the flow. The non-dimensional roller length reported by Zare and Baddour (2007) in the central plane was $x/y_2 = 6$. It is apparent from Fig. 3, that the simulation also predicts similar values of L_r in the central plane. Fig. 3(c) shows the comparison of streamwise velocity at different streamwise locations in a x-z plane located at $x/y_2 = 0.30$. Since, the results are symmetrical only one half of the flow domain is presented. The simulations results agree well with the experimental results, with a difference of less than 8% at all locations. In this type of flow field a difference of less than 10% is considered as reasonable (Witt et al., 2015). It was clear from Fig. 3 that the results of the present simulations agree well with the experimental results of Zare and Baddour (2007).

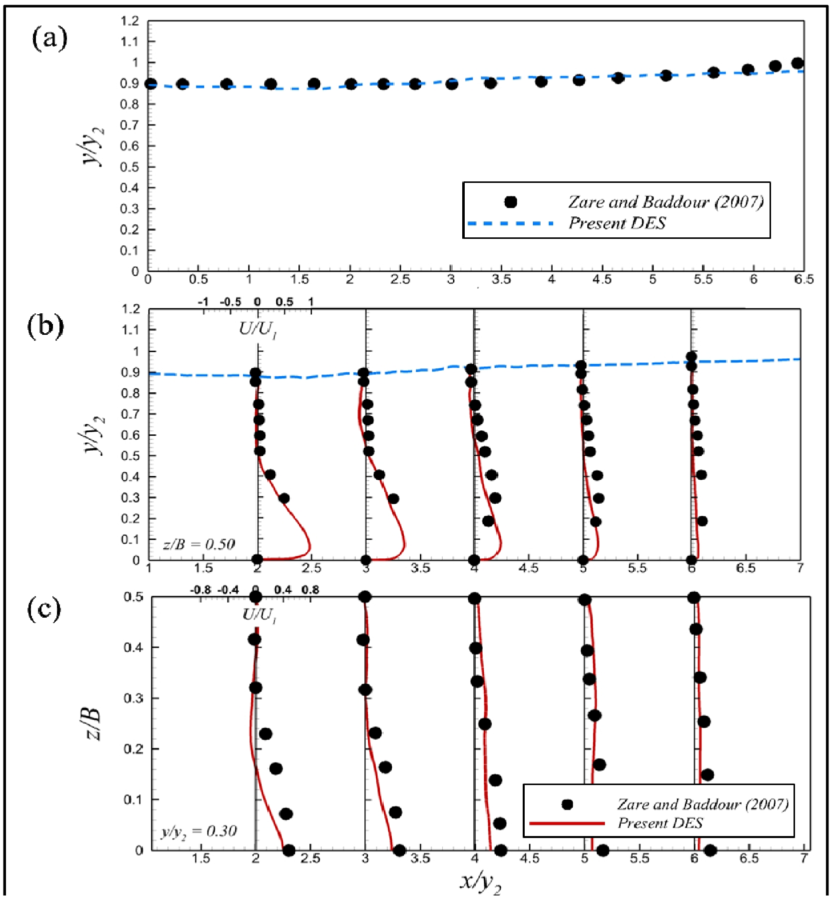

Figure 3. Comparison of experimental and simulation results.

4 RESULTS AND DISCUSSIONS

The three-dimensional mean free surface captured by the present simulations is shown in Fig. 4. The contours of mean streamwise velocity superimposed on the mean free surface clearly show the submerged jump roller reaching the free surface. This region of negative velocity was also the region with most free surface undulations as marked in Fig. 4. The free surface appears relatively flat both upstream and downstream of this region. In a symmetric submerged hydraulic jump where the expansion ratio was equal to one, the roller region was confined to the center with positive velocities near the wall (Jesudhas et al., 2016, Long et al., 1990). This phenomenon is termed as 'climb of the wall jet' (Long et al., 1990 and George, 1959). From Fig. 4, it is apparent that this is notably absent in a SSHJ, with the roller region extending throughout the width of the flume.

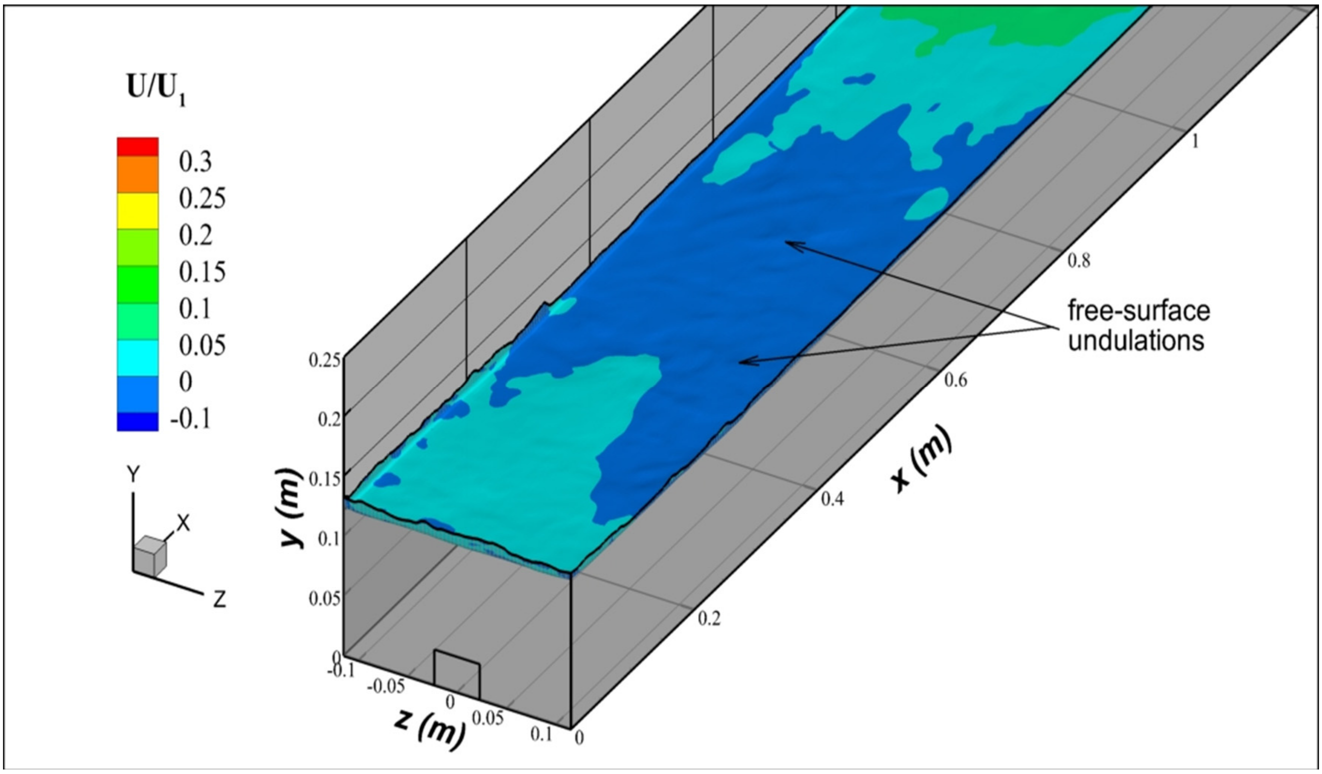

Figure 4. 3-D mean free surface captured by the simulation.

Fig. 5 presents the contours of mean streamwise velocity at three x-y planes located at z/B = 0, 0.25 and 0.35. The plane at z/B = 0 is the central plane while the plane at z/B = 0.35 was closest to the side wall. Fig. 5(a) clearly shows a region resembling the potential core of a jet between $0 < x/y_2 < 1.5$. After this, the wall jet expands in the vertical direction and the velocity decays in the streamwise direction. Above the wall-jet region there was a region of negative streamwise velocity. This region is called as the jump roller. The Froude number of the present simulation is 2, hence this is classified as a weak jump. Therefore, the intensity of roller was lower compared to hydraulic jumps at high Froude numbers (Vischer and Hager, 1995). From examining the three z/B planes one can conclude that the roller region was smallest in the central plane and increases in size as we move towards the wall. Also, the depth at which the roller region starts was higher in the central plane and lower (almost near the bed) as we move towards the wall. This was due to the absence of wall-jet flow in these planes near the bed. This feature is also in direct contradiction to the symmetric submerged hydraulic jump of expansion ratio equal to one, where the roller region were more confined to the center of the flume (Jesudhas et al., 2016, Long et al., 1990. Also, plotted in Fig. 5 were the free-surface profile at the different z/B planes. It can be noted that there were not any significant changes in the free-surface profiles at different z/B locations.

The contours of mean streamwise velocity at different x-z planes located at y/y_2 = 0.10, 0.30, 0.50 and 0.85 is plotted in Fig. 6. The plane located at y/y_2 = 0.10 was at a height of $0.5y_1$ from the bed. This plane clearly shows the expansion of the jet in the horizontal direction. Also, plotted in Fig. 6 are the mean velocity vectors. Notably absent in this plane were the separation rollers.

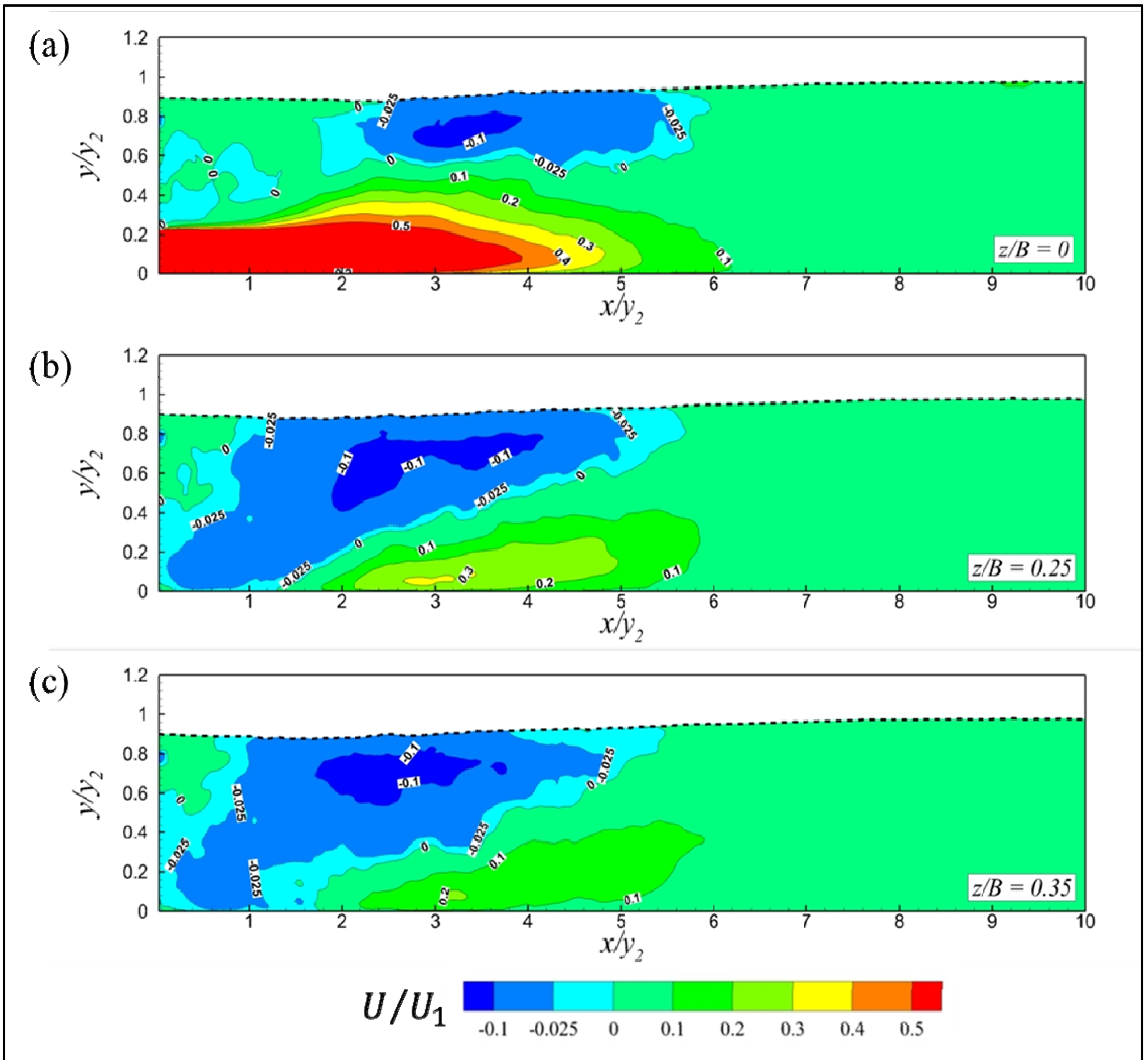

Figure 5. Contours of mean streamwise velocity in x-y planes located at z/B = 0.5, 0.25 and 0.35.

The x-z plane at y/y_2 = 0.3 is located at a depth higher than y_1 and cuts the vertically expanding wall jet as seen from Fig. 6(b). The separation rollers are starting to form in this plane as marked by the dotted ellipse in Fig. 6(b). The plane at mid-depth is depicted in Fig. 6(c), the separation rollers are clearly visible in this plane as marked by the dashed circle in Fig. 6(c). It can be observed that the separation rollers were formed once the jet starts to expand and decay. As we move towards the free surface the separation rollers were clearly visible in the plane located at y/y_2 = 0.85. It must be noted that the size and intensity of these separation rollers increase as we move towards the free surface.

Fig. 7 depicts the vorticity magnitude in different y-z planes along the streamwise directions. Also plotted are the mean velocity vectors. It can be seen at x/y_2 = 0.5, which was closest to the conduit outlet. There is a well-defined shear layer between the wall jet flow and the surrounding fluid. The shape of the shear layer was the same as the shape of the conduit i.e., rectangular. At location x/y_2 = 1.0, the shear layer expands resulting in an increase in thickness. The shear layer does not seem to stretch in the vertical direction as much as in the lateral direction. This is clearly observed at the locations x/y_2 = 1.5 and 2.0. This was due to the impact of the jump roller on the shear layer in the central plane as indicated by the arrows in x/y_2 = 1.5 and 2.0. This impact of the roller causes a collapse and dissipation of the shear layer as we move further downstream (x/y_2 = 3.0). It must be noted that significant amount of vorticity from the shear layer do not reach the free surface. This is important because the turbulence generated at the shear layer can break-up the free surface and result in air entrainment. Since, the present study is on a weak hydraulic jump, the air entrainment was negligible. The vorticity plots validate this conjuncture.

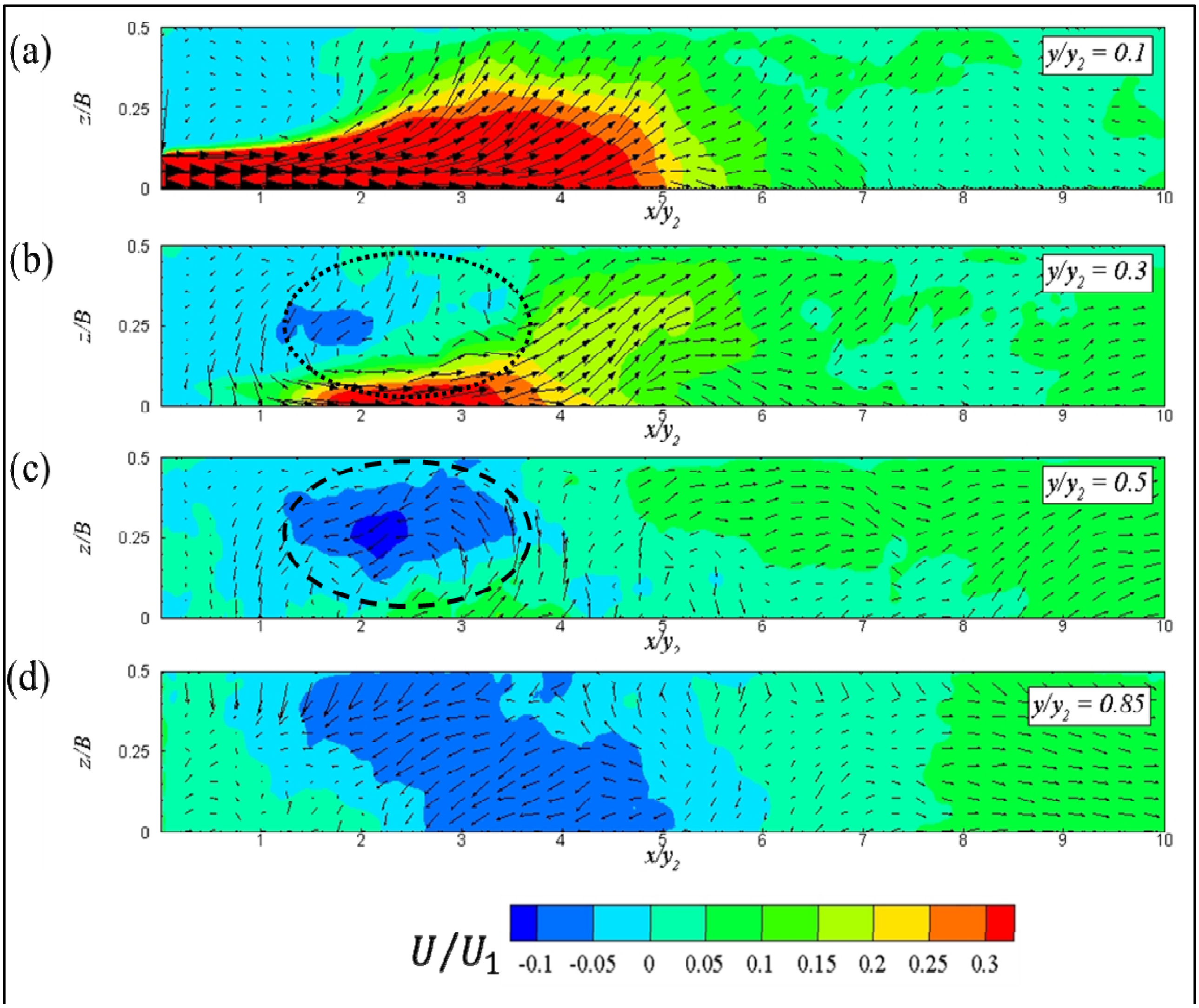

Figure 6. Contours of mean streamwise velocity in x-z planes located at y/y_2 = 0.11, 0.30, 0.50 and 0.85.

5 CONCLUSIONS

The results of three-dimensional unsteady detached eddy simulations of a spatial submerged hydraulic jump (SSHJ) are presented in the present paper. Based on the results of the simulations, the following conclusions can be drawn,

- The VOF model along with the HRIC is adequate to capture the free surface of the SSHJ accurately
- The results of the present simulations agreed well with the experimental results
- The mean velocity field shows the presence of a jump roller and two separation rollers in the flow field
- The jump roller increased in intensity as we moved from the central plane towards the wall; the separation rollers increased in intensity as we move away from the bed towards the free surface
- The 'climb of the wall jet' phenomenon was noticeably absent in SSHJ

From, the results of the present simulations it can be concluded that numerical simulations can be used as a viable alternative in flow fields were conventional experimental techniques are often not adequate.

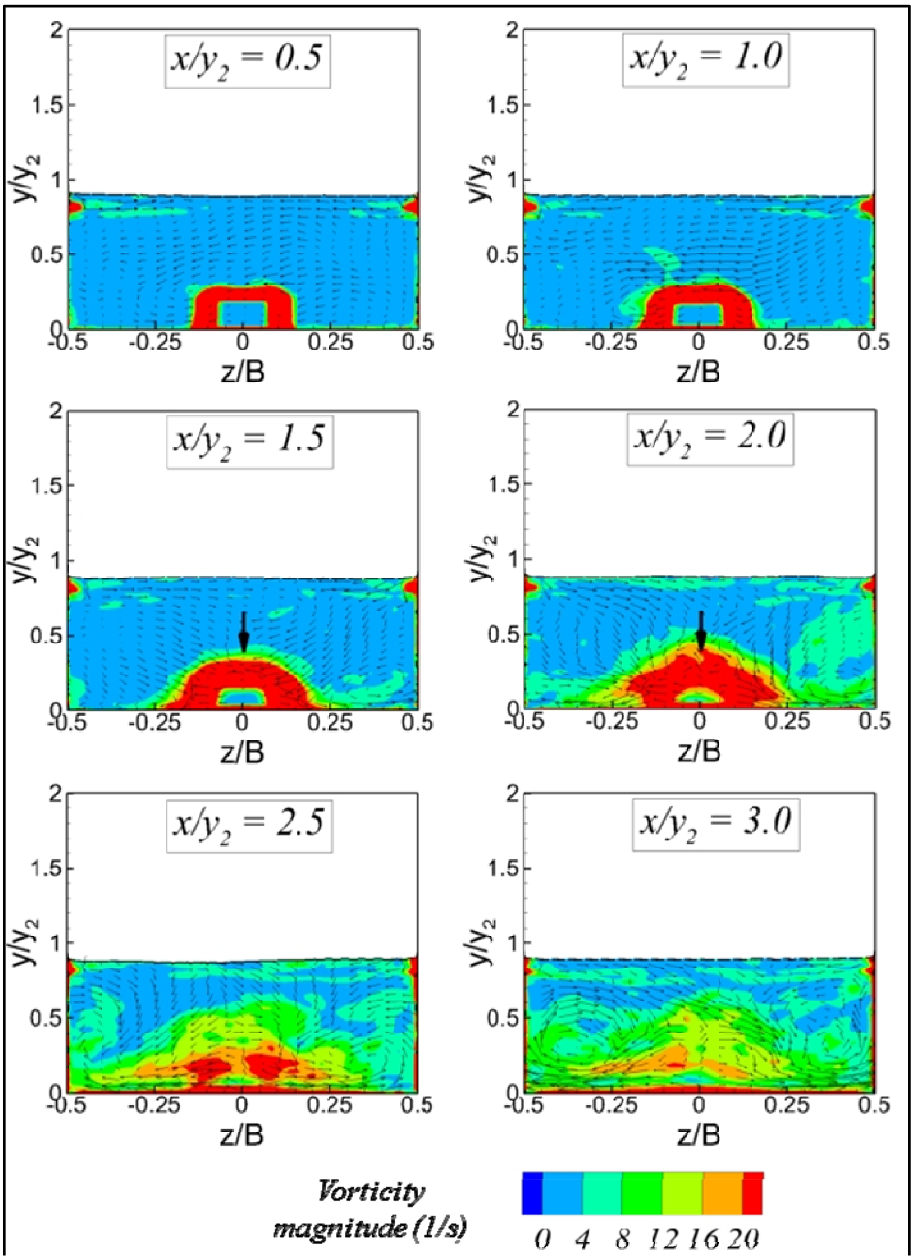

Figure 7. Evolution of shear layer in the streamwise direction.

REFERENCES

George, A.R. (1959). *An Investigation of a Wall Jet in a Free Stream.* DTIC Document, 479, Princeton Univ Nj.

Jesudhas, V., Roussinova, V., Balachandar, R. & Barron, R. (2017). Study of Classical Hydraulic Jump using DES. *Journal of Hydraulic Engineering* – under review.

Jesudhas, V. (2016). Modeling of Free-Surface Flows with Air Entrainment. *Electronic Theses and Dissertations*. University of Windsor, Canada.

Jesudhas, V., Roussinova, V., Balachandar, R., & Barron, R. (2016). Submerged Hydraulic Jump Study using DES. *Journal of Hydraulic Engineering*, 143(3), 1-11.

Long, D., Steffler, P. M. & Rajaratnam, N. (1990). LDA Study of Flow Structure in Submerged Hydraulic Jump. *Journal of Hydraulic Research*, 28(4), 437–460.

Ohtsu, I., Yasuda, Y. & Ishikawa, M. (1999). Submerged Hydraulic Jumps Below Abrupt Expansions. *Journal of Hydraulic Engineering*, 125(5), 492–499.

Vischer, D.L. & Hager, W. H. (1995). *Energy Dissipators, Hydraulic Structures Design Manual. IAHR, AA Balkema. Rotterdam. Netherlands*.

Witt, A., Gulliver, J. & Shen, L. (2015). Simulating Air Entrainment and Vortex Dynamics in a Hydraulic Jump. *International Journal of Multiphase Flow*, 72, 165–180.

Zare, H.K. & Baddour, R.E. (2007). Three-Dimensional Study of Spatial Submerged Hydraulic Jump. *Canadian Journal of Civil Engineering*, 34(9), 1140–1148.

LARGE-SCALE FLUME TESTS ON FLOW DISLODGMENT OF ROCKS FORMING BENDWAY-WEIRS

ROBERT ETTEMA[1], JONATHAN AUBUCHON[2], NATHAN HOLSTE[3], DAVID VARYU[4], DREW BAIRD[5], ROBERT PADILLA[6] & CHRISTOPHER THORNTON[7]

[1,7] Colorado State University, Fort Collins, United States of America
Robert.Ettema@colostate.edu; Christopher.Thornton@colostate.edu
[2,6] U.S. Bureau of Reclamation, Albuquerque, New Mexico, United States of America
jaubuchon@usbr.gov; rpadilla@usbr.gov
[3,4,5] U.S. Bureau of Reclamation, Technical Service Center, Denver, Colorado, United States of America
nholste@usbr.gov; dvaryu@usbr.gov; dbaird@usbr.gov

ABSTRACT

This paper discusses the findings from a series of large-scale flume tests conducted to determine the velocity magnitudes at which river flow may dislodge rocks assembled to form bendway-weirs. These bendway-weirs are low-elevation rock dikes angled upstream to the river flow and are intended to be submerged at flows above the base flow of a channel reach. Bendway-weirs are possible means of river channel control, especially for large channels used for navigation and may augment bank-protection methods in smaller channels. The flume tests are involved replicating the stream wise portion (or head) of a bendway-weir formed from reasonably uniform diameter rocks. Three diameters of rock were tested: 0.10m, 0.15m and 0.23m. Rates of water flow used ranged up to 5.7m^3/s. The findings are presented using a non-dimensional parameter expressing the ratio of flow inertia versus rock weight (density typical of quartz-based rock), and are of use in sizing rock used for constructing bendway-weirs.

Keywords: Rivers; hydraulic structures; channel control; armor rock.

1 INTRODUCTION

Bendway-weirs are a type of transverse, channel-stabilization structure used to maintain or shift the channel-thalweg alignment along alluvial channel bends. They comprise of linear piles of rock assembled on the bed of a bend and are oriented out from the bend's outer bank. Figure 1 illustrates a hydraulic model of bendway-weirs in a channel bend. The concept for bendway-weirs was initially proposed by Derrick et al. (1994), and the performance of bendway weirs as a means of alluvial-channel stabilization has been investigated in fairly numerous subsequent studies; e.g., Abt et al. (2016), Scurlock et al. (2015), Abad et al. (2008) and Derrick (1997).

However, very few studies have examined the stability of the rock used to form bendway-weirs. This point can also be associated regarding the stability of rock used to form other transverse, channel-control structures such as spur dikes and vanes (barbs); e.g., Baird et al. (2015) and Bressan and Papanicolaou (2012). Moreover, comparatively few studies have examined the flow field at an individual bendway-weir.

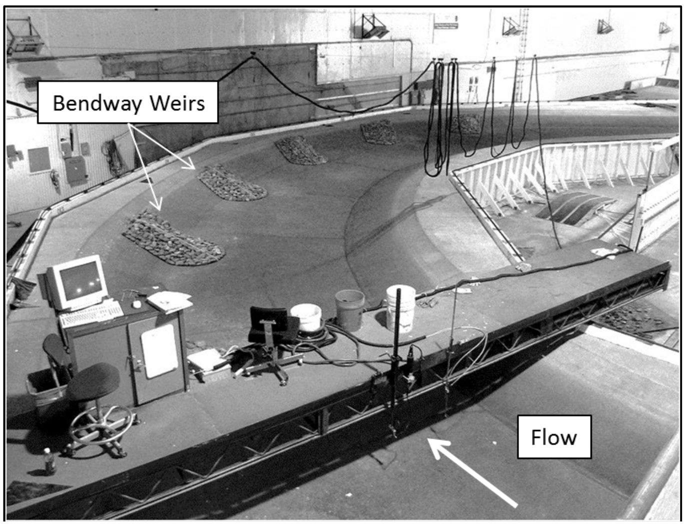

Figure 1. A hydraulic model of bendway-weirs placed in a channel bend (Scurlock et al., 2015).

The present tests is conducted with a large flume and discharges up to 5.7m^3/s show, that several flow fields may occur, depending on the approach-flow depth relative to bendway-weir height. The flow fields range from that when a bendway-weir is deeply submerged, to when a bendway-weir is not submerged. There are studies of the flow over a well-submerged linear structure, such as submerged spur dike (Kuhnle et al., 2008) and of flow around a structure, such as a bridge abutment, extending above the flow surface (Koken and Constantinescu, 2008). However, there is a lack of information regarding the weir-like flow field at a bendway-weir when the approach flow slightly exceeds bendway-weir height. The present study investigated the stability of rock forming bendway-weirs positioned on a flat, fixed base, and shows the flow conditions that may occur at bendway-weirs. Moreover, it indicates how changes in flow field may affect rock stability.

2 TEST DESIGN

The test design is documented by Ettema and Thornton (2017). A concise summary ensues.

2.1 Similitude

For rock of a given rock diameter, *D*, forming a bendway-weir, the variable of principal interest is the velocity, *V*, associated with the following two levels of failure or design concern:

a) Dislodgment of a few individual rock pieces. Several rock positions were considered (see Figures 2a&b, which show the end portion or tip of a bendway weir):
   i. At the toe of the end-face (position P-1);
   ii. At the crest and sloped end-face (position P-2);
   iii. On the downstream face (position P-3); and,
   iv. On the upstream face (position P-4).

b) Failure of many rocks and the washout collapse of the bendway-weir or a substantial portion thereof.

The dislodgment of a few individual rocks indicates incipient failure of a bendway-weir and then, at a larger velocity, the dislodgment of many rocks indicates the complete failure of a bendway-weir. Figures 2a&b indicate variables associated with a single bendway-weir, built of uniform-size rock, situated in a straight, fixed-bed channel. The velocity values associated with rock dislodgment in this situation also apply to bendway weirs in a curved channel with importance of the magnitude of velocity impinging on stone in the four locations mentioned above and indicated in Figures 2a&b. These figures are plan and elevation views, respectively, of the layout and pertinent variables of a test bendway-weirs set at $\beta = 30^o$. Bendway weirs set at $\beta = 90^o$ were also tested.

It can be assumed that a rock on a bendway-weir behaves as an isolated obstacle and shed wake vortices, because the surface of a bendway-weir is hydraulically rough, with roughness height approximating rock diameter. Further, if the rock is viewed as an isolated obstacle, the hydrodynamic force can be assumed to be predominantly a drag force. There may be a lift component to the hydrodynamic force, but is small compared to the drag component (Apperley and Raudkivi, 1989).

The program of flume experiments investigates the following relationship,

$$\frac{V}{(gD)^{0.5}} \propto f\left(\frac{Y}{H}, \frac{H}{D}, \beta, e\right) \quad (1)$$

Eq. (1) was developed for rocks at positions P-1, P-2, P-3, and P-4. Here, as indicated in Figures 2a&b, *H* = crest height; *D* = rock diameter; *Y* = depth of flow a short distance upstream of the bendway-weir; *V* = a representative velocity of flow (velocity near the end-portion (tip) and crest of the bendway-weir); β = crest angle to approach flow; *g* = gravity acceleration; and, *e* = void ratio of placed rock forming a bendway-weir. The parameters *Y/H* and *H/D* are respectively the relative submergence of the bendway-weirs, and bendway-weir height relative to rock diameter. Values of *Y/H* were varied over the target range 1.0 to 2.5, and *H/D* varied from 6.0 to 2.6. Practical considerations associated with changing water discharge yet aiming for a prescribed *Y/H* inevitably incurred giving rise to some variation in the actual values of *Y/H*.

Estimation of the stability of full-scale rock (nominally two to five times the 0.23m-diameter rock) can be made using Eq. (1) developed empirically using the test results that the writers present subsequently.

2.2 Flume

The tests were conducted using a flume test section that was 33.3m long, 2.4m wide and 2.4m deep. The flume itself was 60.0m long and 6.0m wide. The slope of the flume's concrete invert was zero. Water discharge into the flume was controlled by means of a 0.9m-diameter valve fitted with an ultrasonic flow meter. Water temperature was 8.3 ^oC for all the tests. The maximum discharge available to the flume was 5.7m^3/s. Flow entered the flume via a manifold pipe at the flume's upstream end, and passed from the flume's outlet to a small lake downstream. Four sluice gates at the downstream end of the flume were used to control the water level in the test section. Iterative adjustments of the flume's gates were needed to attain the target water level and flow rate. Though the flow was comparatively narrow, the experiments worked with actual magnitudes of flow velocity in the flume.

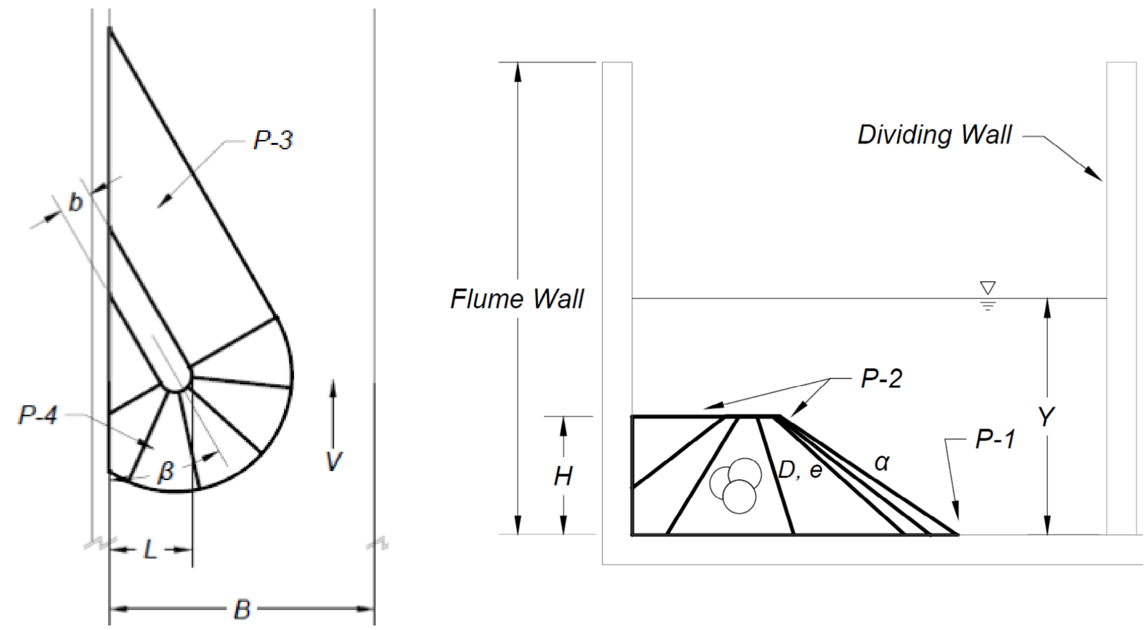

(a) (b)

Figure 2. The variables associated with rock stability on a bendway-weir set at an angle $\beta = 30^{o}$ to the approach flow in the flume test section: (a) plan view; and, (b) front elevation view. The test section of the flume is shown in light-grey outline.

2.3 Test bendway-weirs

For the layout shown in Figure 2a&b (plan and elevation views), the bendway-weirs extended a constant crest length distance of L = 0.75m into the test section; i.e., the bendway-weirs set at 30^{o} and 90^{o} had the same value of L. The crest length, L, occupied 31.3% of the section's width; and, the length to bendway-weir toe extended 68.8% of the width of the test section. The crest height was taken to be 0.60m, and the sideslope was 1 vertical to 1.5 horizontal. Figures 3a&b show a test bendway-weir in the flume before and during a test.

(a) (b)

Figure 3. A view (looking downstream) of a test bendway-weir in the test section of the flume; D = 0.23m, H = 0.60m and $\beta = 90^{o}$: (a) before the test: and, (b) during a test. The arrows in (a) indicate is the main location for velocity measurement. The location was just off the tip of the bendway weir.

The bendway-weirs were formed of rock hand-selected from rock sourced to meet the standard specifications for road and bridge construction required by the state of Colorado (CDOT 2011). Rock diameter, D, was 0.23m, 0.15m and 0.10m. The coefficient of uniformity of the rock was less than 2 for each test size of rock, and so the rock may be considered uniform (e.g., Bell, 1992). Rock density was assessed as 2.64 x 10^{3}kg/m^{3}. The range of values for void ratio (volume of voids/volume of solids), e, associated with rock placed to form the bendway-weirs was evaluated approximately by using two packing arrangements for rock placed in a known volume comparable to a segment of the bendway-weirs used in the tests. The resulting estimated range was $0.73 \leq e \leq 0.44$.

2.4 Velocity measurements

The prime location for velocity measurement was near the tip of the bendway-weir, as indicated in Figure 3a, and at 0.40 of the flow depth above the flume's invert. Velocities were found to be spatially uniform over the opening at the end of the bendway-weir and over the crest of the fully submerged bendway-weirs. The measurements were made using an ADV probe, as shown in Figure 3b. For the present tests, the velocity at the main measurement location, near the tip of the test bendway-weirs, was 1.47 and 1.25 times the mean velocity of the approach flow when Y/H = 1.5 and 2.5, respectively.

3 RESULTS

The results are presented first in terms of dimensional variable, and then using the non-dimensional parameters in Eq. (1) so as to indicate general trends.

3.1 Velocity for Rock Dislodgment

Figure 4 presents an example of the velocity magnitudes associated with flow dislodgment of rock from the test bendway-weirs and, in some cases leading to substantial failure of a test bendway-weir. This figure is accompanied by Figure 5, showing the bendway-weirs before and after a test. In Figure 4 –

- The hollow data points indicate no observed dislodgment of rock
- The solid data points indicate dislodgment of rock
- The numbers 1 and 2 relate to positions P-1 and P-2, and indicate when rock was observed to move from these positions
- Typically, rock in position P-1 was dislodged first
- The first indication of rock movement from position P-2 was taken to indicate incipient dislodgement of rock forming a bendway-weir
- Subsequent indication (at slightly higher velocities) of rock movement from position P-2 indicates extensive dislodgment of rock from the bendway-weir. Such indication of rock movement is shown as "BW failure"

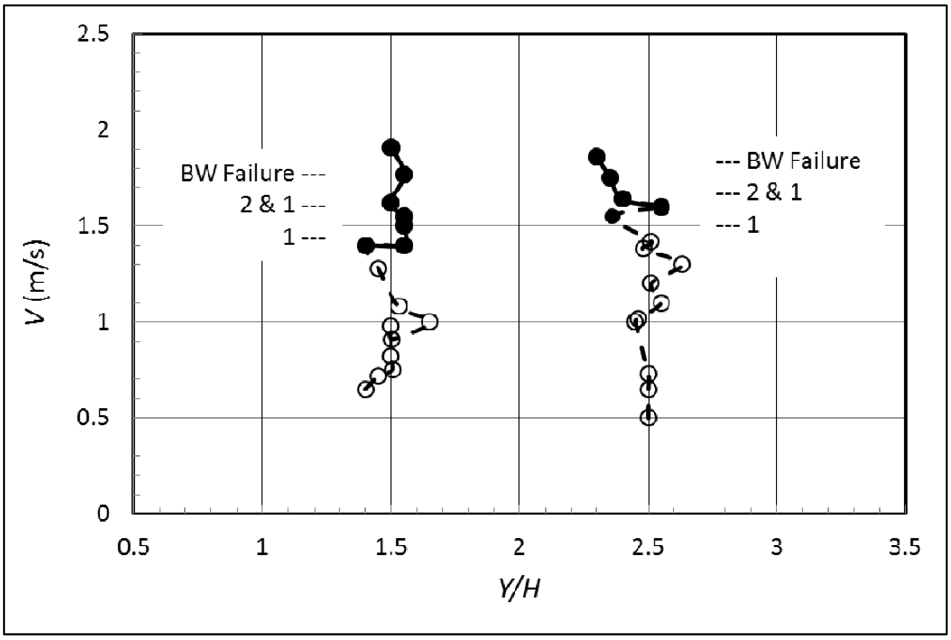

Figure 4. Velocity for rock dislodgment and bendway-weir (BW) failure: D = 0.10m, $\beta = 90^{\circ}$. The black dots indicate dislodgment, whereas the hollow dots indicate no observed dislodgment. Rock dislodgment from positions P-1 and P-2 are denoted as 1 and 2, respectively. Bendway-weir failure is denoted as BW failure.

Rock was observed to dislodge first from position P-1 at the toe of the end-face of a bendway-weir. The rocks in this position rested directly on the flat, concrete floor of the flume, and therefore were not seated fully amidst other rocks providing side restraint. Rocks seated in position P-2 (on the crest or on the end-face slope) were observed to dislodge next, as they were exposed to velocity magnitudes comparable to those measured at the location as indicated in Figure 3a. Rock dislodgement from position P-2 occurred over a

  / ISSN 1562-6865 (Online) - ISSN 1063-7710 (Print)

velocity range between first observed dislodgment (indicated as "2 & 1" in Figure 4) until extensive dislodgments began occurring, resulting in the failure of the bendway weir (indicated in Figure 4 as "BW failure"). As evident in Figure 4, it is explained:

- The velocity first indicated for dislodgment of rock from position P-2 (black dot at "2 &1") and this should be considered the incipient dislodgment condition. For this lower limit of the range, flow dislodged a few rocks whose seating was more exposed to the flow field.
- The higher velocity indicated for substantial dislodgment of rock from position P-2 (and dislodgment from position P-3) which was indicated as "BW failure". This should be considered as the velocity for major dislodgment. For this upper limit of the velocity range, flow dislodged rock seated with an average, or typical, exposure to the flow at positions P-2.

When the flow field over a bendway-weir occurred as weir flow (i.e., when $1.0 < Y/H \leq 1.5$), a portion of the flow accelerated down the downslope, impacting rock seated in position P-3 on the downslope. Consequently, rock seated in positions P-2 and P-3 often dislodged at practically the same instance. The dislodgment of rock from position P-3, especially along the lower portion of the downslope initiated a failure sequence akin to the upstream progression of a head-cut, thereby destabilizing rock higher up the downslope.

For the Y/H = 2.5 flow condition, flow over the bendway weir developed a relatively sheltered wake zone. Rocks seated in position P-3 (on the downstream slope) were dislodged only after a substantial number of rocks on the crest (P-2 position) were dislodged, disrupting the wake region and allowing rock failure at P-3.

In most of the tests, no rock was observed to be dislodged from position P-4, along the upstream slope of a test bendway-weir. The only time rock was dislodged from this position occurred when flow swept away the entire end segment of the test bendway-weir; i.e., for tests with the 0.10m-diameter rock (Figure 5b). Rock in this position experienced smaller velocity magnitudes than rock at the crest (similarly to the approach flow over a weir) and flow passed up the upstream slope such that a weight component of the rock exerted a larger restoring force than for rock on a flat or downward slope. Additionally, rock in position P-4 along the upstream face was pressed against the bendway weir, thereby causing the rock to be more stable.

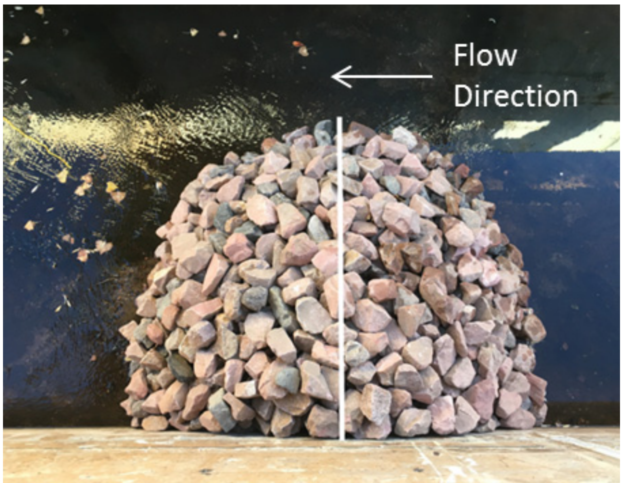

(a)

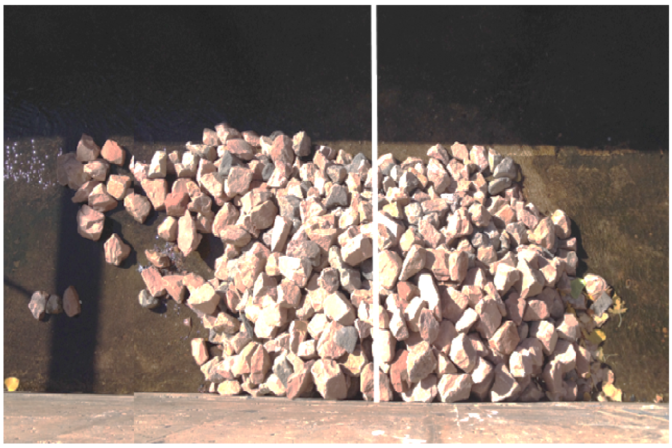

(b)

Figure 5. Before and after views of the test bendway-weir: $\beta = 90^{o}$, D = 0.10m and Y/H = 2.5: (a) before test; and, (b) after test.

3.2 General trends

Developing design relationships for sizing rock to be used in forming bendway-weirs requires the necessity to express the trends shown by the velocity data in figures like Figure 4 in terms of general, non-dimensional parameters. Figures 6 and 7 recast the velocity data in terms of the non-dimensional parameters $V/(gD)^{0.5}$ and Y/H, for bendway-weir orientations $\alpha = 90^{o}$ and 30^{o}, respectively; i.e., using the parameters identified in Eq. (7). The parameter $V/(gD)^{0.5}$ essentially expresses the ratio of flow inertia force to the weight of a rock. The data in Figures 6 and 7 pertain only to instances when rock dislodgment was observed (e.g., the solid dots in Figure 4).

Three limits or levels of rock dislodgment are indicated in Figures 6 and 7 as:

- A base limit pertaining to rock movement from position P-1
- A lower limit indicating dislodgment of a few rocks placed in positions P-2. At this limit, the flow dislodged rock is seated to be more exposed to the flow field

- An upper limit indicating major dislodgment of rocks in positions P-2. This limit is designated as a failure limit, because the flow dislodged a relatively large number of rocks, altered bendway-weir shape and, therefore, substantially weakened the bendway-weir's effect on the flow field

The relationship between $V/(gD)^{0.5}$ and *Y/H* indicates the following main trends:

(a) The bounds (dashed lines) are essentially the same for α = 90^{o} and 30^{o}. This finding indicates that the range of orientations used for bendway weirs, of platform orientation of bendway weir does not affect the stability of individual rocks.

(b) A base limit for $V/(gD)^{0.5}$ exists regarding rock dislodgment from position *P-1*. This limit for *P-1* stays essentially flat for all *Y/H*, because the same dislodgment mechanism for P-1 occurs for all *Y/H*.

(c) Rock dislodgment from position *P-2* starts at the lower limit (dislodgment of one or two rocks) and increases to the higher limit (substantial failure of the bendway-weir).

(d) The limits for rock dislodgment from position *P-2* are relatively insensitive to *Y/H* when *Y/H* ≥ 1.5, but drop when *Y/H* < 1.5. When Y/H < 1.0, flow passes around the bendway-weir. The drop is attributed to the significant change in the flow field that occurs over this range of *Y/H*, as Figures 6 and 7 imply. For *Y/H* < 1.5, flow over the bendway-weir increasingly becomes akin to flow over a weir (until *Y/H* = 1.0, whereupon flow goes entirely around the bendway weir), and flow was more able to dislodge rock from the crest and downstream slope.

(e) The higher limit for rock dislodgment from position *P-2* was elevated for the rock placed with the lesser void ratio, *e*; i.e., for the 0.10m diameter rock (*H/D* = 6.1). A smaller void ratio enables rock to sit more securely amidst adjacent rocks. This finding indicates that more compact placement of rock increases rock stability.

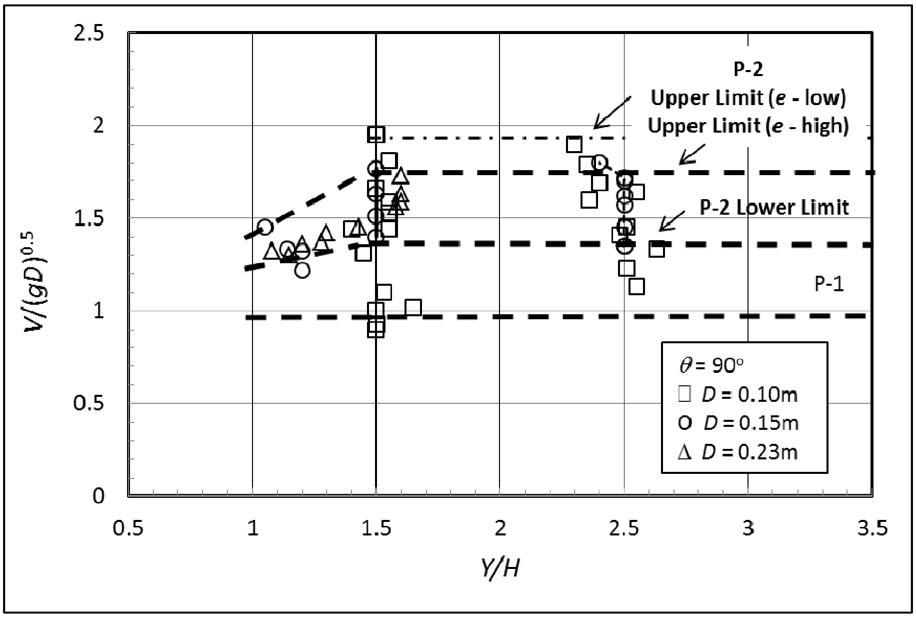

Figure 6. The data presented as $V/(gD)^{0.5}$ versus *Y/H*, with rock diameter (or *H/D*) as the third parameter. Here β = 90^{o}. All the data indicate rock dislodgment.

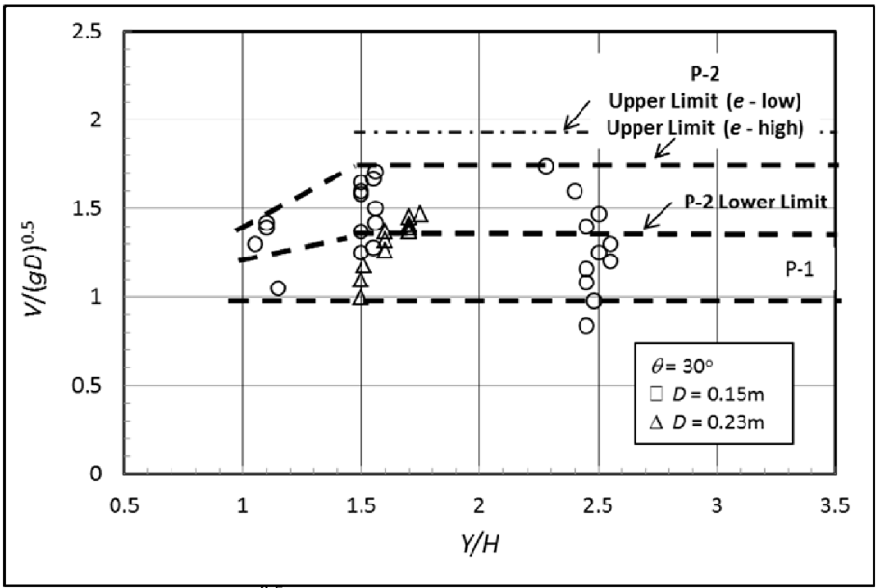

Figure 7. The data presented as $V/(gD)^{0.5}$ versus Y/H, with rock diameter (or H/D) as the third parameter. Here $\beta = 30^{o}$. No experiment was done with D = 0.10m for this orientation. All the data indicate rock dislodgment.

3.3 Flow field variation

An important outcome of the tests was the identification of several flow fields that can develop when the parameter Y/H varies from $Y/H \leq 1.0$ to $Y/H > 1.5$; these limits are approximate because other variables must be considered, such as those in Eq. (2). Figures 8a, 8b and 8c were sketches of the three flow fields associated with varying Y/H. The sketches, simplified as flow at cross-sections of the bendway weirs, indicate how the flow field changes substantially in accordance with value of Y/H. When $Y/H \leq 1.0$ little flow goes over a bendway weir and water was deflected around it where the rock stability on the end-face becomes critical (Figure 8a). When the value was $1.0 \leq Y/H \leq 1.5$, the bendway weir acts as form of weir with approach flow contracting and accelerating and it then passes over the crest which later further accelerates down the downslope (Figure 8b). This condition can create major hydrodynamic loads on rock forming the downslope, and be especially critical for rock stability. When $Y/H > 1.5$ and a bendway weir was fully submerged, the flow over it develops a wake region enveloping the downslope (Figure 8c). Rock on the downslope is somewhat sheltered by the wake region. The present tests did not extensively investigate the varying regimes of flow field over a bendway weir, but a recommendation stemming from the tests is that the regimes be further investigated.

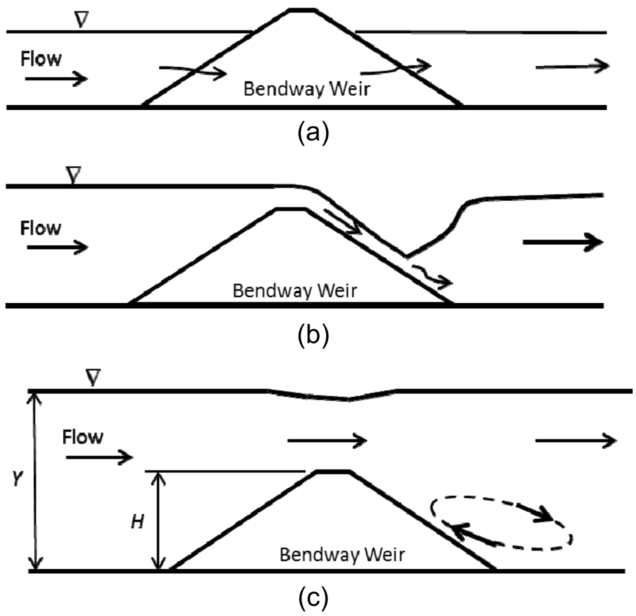

Figure 8. Sketches of cross-sectional views of bendway weirs indicating three flow-field conditions associated with varying Y/H: (a) $Y/H \leq 1.0$; (b) $1.0 < Y/H < 1.5$; and, (c) $Y/H \geq 1.5$.

4 CONCLUSIONS

The general trends regarding the velocity magnitude associated with rock dislodgement lead to the following main conclusions:

(a) The parameter $V/(gD)^{0.5}$ usefully characterizes rock stability in terms of velocity magnitude near the bendway-weir tip, *V*, and rock-diameter, *D*. By relating *V* to the mean approach velocity, it is possible to further adjust this parameter accordingly.
(b) A range of limit relationships for rock dislodgment can be set for rocks located in positions P-1 and P-2, and for characterizing bendway-weir failure.
(c) Three limits of rock stability can be identified. The lowest limit is associated with the dislodgment of rock at P-1, the toe at the end of bendway-weir. The next, and most important limit, refers to the dislodgment of a few exposed rocks seated in position P-2. The upper limit refers the substantial dislodgment of rock and, in effect, the failure of the bendway-weir.
(d) The void ratio, *e*, of placed rock forming the bendway-weir, influences the upper limit for rock stability and the overall failure of a bendway-weir. Smaller void ratio (greater compaction) of place rock raises the upper limit. The present tests suggest an upper velocity limit is elevated almost 10%.
(e) The limits did not vary for the two values of bendway-weir orientation investigated ($\beta = 90^o$ and 30^o);
(f) The limits vary with *Y/H* when $Y/H < 1.5$, because the flow field at a bend way weirs substantially changed with *Y/H*.
(g) The stability of rock on bendway-weirs when $Y/H < 1.5$ should be further investigated, because the flow field at this *Y/H* condition becomes similar to flow over a weir, such that flow directly impinges against rock seated on the downslope of a bendway-weir. In comparison when $Y/H > 1.5$, rock sits in the fairly sheltered region of the wake formed by flow passing over a bendway-weir. If the flow velocities are sufficiently large, when $Y/H < 1.5$, they may dislodge rock vulnerably seated on a downward slope.

ACKNOWLEDGEMENT

The research reported herein was funded by the U.S. Bureau of Reclamation's Albuquerque Office, New Mexico.

REFERENCES

Abad, J.D., Rhoads, B.L., Guneralp, I. & Garcia, M.H. (2008). Flow Structure at Different Stages in a Meander-bend with Bendway-weirs. *Journal of Hydraulic Engineering*, 134(8), 1052–1063.

Abt, S., Scurlock, M.S., Thornton, C., Cox, A. & Holste, N. (2016). Bendway-weir Riprap Sizing Criteria. *Journal of Hydraulic Eng*ineering, 142(12), 1943-7900.

Apperly, L.W. & Raudkivi, A.J. (1989). The Entrainment of Sediments by the Turbulent Flow of Water. *Hydrobiologia*, 176(1), 39-49.

Baird, D.C., Fotherby, L., Klumpp, C.C. & Scurlock, S.M. (2015). Bank Stabilization Design Guidelines. SRH-2015-25, U.S. Department of the Interior, Bureau of Reclamation, Technical Service Center, Sedimentation and River Hydraulics Group, Denver, CO.

Bell, F.G. (1992). *Engineering Properties of Soils and Rocks*. Third Edition, Butterworth-Heinemann, Oxford, UK.

Bressan, F. & Papanicolaou, T.N. (2012). Scour around a Variably Submerged Barb in a Gravel Bed Stream. Proc. *River Flow 2006*, Taylor & Francis, London, UK, 333-339.

CDOT (2011). *Standard Specifications for Road and Bridge Construction for the State of Colorado*, Colorado Dept. of Transportation, Denver, CO.

Derrick, D.L., Pokrefke, T.J., Boyd, M.B., Crutchfield, J.P. & Henderson R.R. (1994). *Design and Development of Bendway Weirs for the Dogtooth Bend Reach, Mississippi River*, Report HL-94-10. U.S. Army Corps of Engineers, Waterways Experiment Station, Vicksburg, MS.

Derrick, D.L. (1997). *Bendway-weirs Redirect Rivers to Protect Highway Bank Abutments*. U. S. Army Corps of Engineers, Waterways Experiment Station, Vicksburg, MS.

Ettema, R. & Thornton, C. (2017). *Flume Tests to Assess Rock Size for Bendway-weirs on Fixed Beds*, Report Submitted by Colorado State University to the U.S. Bureau of Reclamation, Denver, CO.

Koken, M. & Constantinescu, G. (2008). A Detached Eddy Simulation Study of the Horseshoe Vortex System in the Flow past a Bridge Abutment with Scour Hole at a High Reynolds Number. *Proceeding of Fourth International Conference on Scour and Erosion*, Tokyo, Japan, 169-173.

Kuhnle, R.A., Jia, Y. & Alonso, C.V. (2008). Measured and Simulated Flow near a Submerged Spur Dike. *Journal of Hydraulic Engineering*, 134(7), 916-924.

Scurlock, S.M., Thornton, C.I., Abt, S.R. & Baird, D.C. (2015). Convective Acceleration Effects from Transverse In-stream Structure Installations. Proc., *10th Federal Interagency Sedimentation and 5th Federal Interagency Hydrologic Modeling Conf*erence (SEDHYD 2005), Reno, NV, 468–480.

AN EXPERIMENTAL STUDY OF THE HYDRAULIC PERFORMANCE OF A BUOYANCY-AUTOMATED TIDAL GATE

JAMES SIMPSON[1], WILLIAM GLAMORE[2] & STEFAN FELDER[3]

[1,2,3] Water Research Laboratory, School of Civil and Environmental Engineering, UNSW Sydney, Australia,
s.felder@unsw.edu.au

ABSTRACT

Around the world, many low-lying estuaries has been converted into agricultural and commercial land via the installation of floodgates. These floodgates prevent natural tidal flushing upstream, causing the estuaries to degrade and acidify. The purpose of the study is to design and develop an improved buoyancy-automated tidal gate, allowing tidal flushing to resume upstream, improving water quality and aiding fish migration. The conceptual design was based upon hydrostatic pressure and buoyancy considerations while identifying optimal dimensions of buoyancy floats, pivot arm and counter weight. For a range of upstream and downstream flow depths, the hydraulic performances of the tidal gate is tested in a laboratory flume. The experiments confirmed that the gate met the design and operation objectives. This finding is in close agreement between observed closing profiles in the laboratory tests and the design calculations based upon hydrostatic considerations. The flow patterns of the gate exposed different flow regimes with variations in upstream and downstream flow depths including unsubmerged weir flows, submerged weir flows and submerged orifice flows. Head discharge curves and best fit equations were determined for each flow regime allowing the numerical modelling of tidal flows through the structure. The present study introduced a new tidal gate design, and the successful test of its hydraulic performance confirming its suitability for estuary remediation projects.

Keywords: Buoyancy-automated tidal gate; head discharge relationship; hydraulic design; physical modelling; self-regulating tidal gate.

1 INTRODUCTION

Tidal waters in estuaries have profound effects on the coast line and surrounding land shaping the landscape and providing habitats for a range of aquatic species. Throughout the world many estuaries have been degraded and converted to commercial land by the installation of tidal impeding floodgates. The gates prevent tidal flows into the estuary, causing a range of detrimental environmental effects such as acidifying waterways (e.g. Anisfeld and Benoit 1997; Indraratna et al., 2005) and preventing ecological passage (Pollard and Hannan, 1994; Streever and Genders, 1997; Lucas et al., 2009; Wright et al., 2015, 2016). While it would be best to remove these floodgates completely (Boys et al., 2012), coastal land is some of the most desirable land and landowners are reluctant to allow their lands to be flooded. The best option is often to modify the existing floodgates to allow partial tidal flushing to commence and at the same time disallowing flooding upstream.

Many types of floodgates exist including manually operated floodgates such as sluice gates as well as horizontally and vertically winched gates (Bos 1989; Rampano, 2009). While these manually operated floodgates are simple, durable and relatively inexpensive, they have to be monitored and closed / opened manually at different times in the tidal period (Glamore, 2012; Rampano, 2009). This shortcoming can be improved with self-regulating tidal gates which are designed to mimic natural tide variability in the upstream estuary. Whilst there is variation in the design of self-regulating tidal gates most designs tend to have a faceplate that opens and closes the orifice by an adjustable float. When the incoming tide reaches a particular level, the gate is closed automatically by buoyancy forces of the float (Adnitt et al., 2007; Belaud et al. 2008; Glamore, 2012). As the tidal water level rises, buoyancy forces increase applying a closing moment to the gate structure until complete closure. When the tidal water level recedes, buoyancy forces reduce and this decreases the closing moment of the structure until the gate opens automatically. The main benefit of these self-regulating tidal gates is that they allow the commencement of a muted regulated tidal exchange in an estuary. Around the world different designs of self-regulating tidal gates are used including swing gates (Figure 1) (Glamore, 2012), the Waterman gate (Waterman Industries, 2002), and the Seaton Gate (Ridgway and Williams, 2011). These designs are operated with floats as can be seen in Figure 1 for the swing gates at Tomago in Australia. Self-regulating tidal gates have been confirmed to improve estuary health and are recommended in estuary remediation projects (Rampano, 2009; Ridgway and Williams, 2011; Russel et al., 2012).

While self-regulating tidal gates provide environmental improvement to wetland systems, the permanent installation in saltwater systems and the mechanical parts enabling the self-regulation of the gate can lead to a degradation of the system (Figure 1). In the present study, a detailed assessment of existing gate designs is performed to identify the most important parameters for self-regulating tidal gates. Based upon this assessment an optimised self-regulating tidal gate was designed based upon hydrostatic considerations. To test the gates functionality and to provide design guidelines for a range of flow conditions, the performances of the gate were tested at laboratory scale. The hydraulic assessment comprised of gate functionality, flow patterns and discharge performances providing simple design guidelines for the gate. The gate design and the basic results of the hydraulic assessment are presented in this manuscript.

Figure 1. Self-regulating tidal gates at Tomago Wetland, Australia (in December 2015); Note the white floats on the gate structure and the attachment of the swing gates to the existing flap gate.

2 DESIGN OF TIDAL GATE AND EXPERIMENTAL TESTING

2.1 Gate design

For the new tidal gate design, it was critical to optimise the functionality of the structure. The focus was on developing a gate that was practical, reliable, durable and most importantly useful for a wide range of flow conditions. During the design process the following aspects were of primary importance:

- The gate structure had to be placed as far as possible above the water to limit the exposure of the gate towards flows reducing unsteady velocities and turbulences behind the gate members.
- The gate had to allow the retrofitting of existing tidal gates such as flap gates.
- The closing time of the gate had to be minimised to reduce periods of small gate openings associated with large flow velocities. This was important to allow fish passage and prevent potential scouring of the stream bed.
- The opening and closing profile of the gate had to be adjustable to a desired maximum upstream water level.
- The materials of the gate structure had to be durable, reliable and relatively inexpensive.
- The weight of the structure had to be small by maintaining the strength of the overall structure.
- Design of gate had to include an understanding of the hydraulics of the gate operations to allow an implementation in numerical models and a scaling of the gate to required size.

Based upon these aspects, the gate is designed in an iterative approach optimising the gate's functionality with a hydrostatic analysis of each member of the gate structure. The main gate members were the faceplate of the gate, the counter weight to allow an automatic opening in a receding tide, the floats to allow an automatic closing of the gate in a rising tide and the support structure of the gate (Figure 2). Figure 2a illustrates the finale gate design including all relevant members of the structure.

In the design process, the resultant force of each gate member was calculated depending on the water level and opening angle of the gate. The forces taken into account included both buoyancy forces related to the submergence of the gate member and the weight for each member. By calculating the individual moment of arms to the centroid of the members, the total moment on the pivot structure was found. As the gate was free to rotate, the gate positioned itself in a balance position where the resultant moment was 0. The acting forces and the moment arms of each member were adjusted in the design optimisation process by changes of dimensions, choice of materials, position of the pivot and any structural additions to the gate. The closing profile was recorded while changing the water elevation H_1 and calculating the corresponding opening angle of the gate α (Figure 2b). An Excel spreadsheet was developed to automate the optimisation process (Simpson, 2016). Note that the hydrostatic analysis assumed an equal water level for all gate members and that no hydrodynamic forces from the flow through the gate are taken into account. As shown in the experimental testing of the gate, the dynamic forces acted favourably to the gate's operation (Section 4).

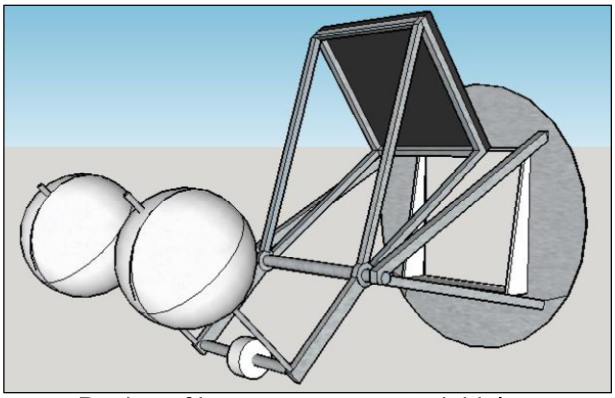

a. Design of buoyancy-automated tidal gate

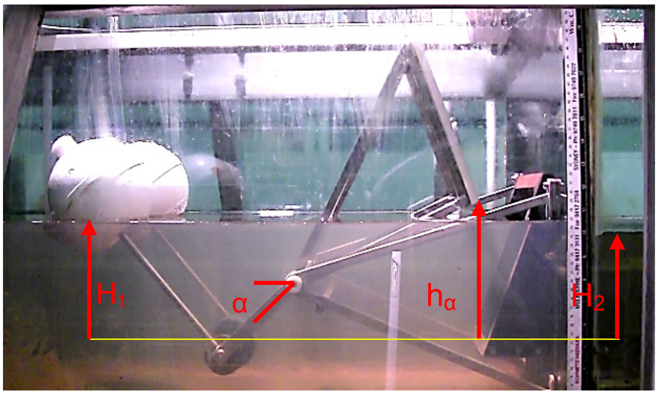

b. Definition of relevant parameters

Figure 2. Buoyancy-automated tidal gate in the present study.
(Note the attachment of the gate to an existing flap gate)

The final gate design is illustrated in Figure 2. The main benefit of the gate design was the simplicity of the structure providing several benefits:

- The small number of gate members reduced the risk of operational failure.
- The height of the floats was easily adjustable. A duplicate float was installed for contingency, but provided also an additional buoyancy force to the system.
- The arm holding the floats was shorter than the distance to the faceplate reducing the closing time of the gate.
- The faceplate was angled to utilise hydrostatic pressures to open and close the gate at small angles.
- The counter weight allowed for an automatic opening of the gate in a receding tide. The weight was centred to prevent torsion in the pivot structure.
- The structural supports of faceplate and the pivot structure were made of hollow square steel sections improving the stability of the structure.

The materials for all gate members were selected to achieve a durable and relatively inexpensive design. Delrin was used for the faceplate and the pivot member due to its relatively low density (ρ = 1450 kg/m^3), its high strength and stiffness as well as its corrosion resistance which is an important characteristic for waters of estuaries with low pH and sulphurous chemicals. For the floats, polystyrene was selected due to its low density (ρ = 45 kg/m^3). For the supporting members and the counter weight, stainless steel (ρ = 8000 kg/m^3) was selected due to its stability and durability under extreme conditions. The counter weight was made out of a solid steel block and the support structure out of hollow steel sections to reduce the overall weight of the structure. Note that the orifice opening was expanded inwards to optimise the closing of the gate (Figure 2).

2.2 Experimental setup

To confirm the gates hydraulic performance, a detailed experimental testing of the gate was conducted at laboratory scale (Figure 2b). The opening of the gate was square with a width and height of B = 0.2 m (Figure 2b). The gate was constructed using the dimensions and materials from the hydrostatic optimisation (see above). The gate was installed in an open channel flume at UNSW's Water Research Laboratory of 0.6 m length, 0.6 m height and 40 m length with glass sidewalls. Water was supplied directly from Manly Dam and a constant flow rate was controlled with an ABB Water Master FET100 electromagnetic flow meter with ± 0.4% accuracy. At the downstream end of the flume, the tail water was controlled with a sharp-crested weir with a winch. The gate was installed towards the downstream end of the flume where the flow was calm and uniform. The gate was attached to a 20 mm thick plywood partition with orifice opening simulating the attachment of the gate to an existing flap gate structure (Figure 2b).

The water elevation upstream and downstream of the structure H_1 and H_2 respectively were measured with pointer gauges. The upstream pointer gauge was located approximately 3 m from the structure and the downstream gauge at a position 1.5 m downstream of the gate (Bos, 1989). In these positions, the flows were calm and steady. Both pointer gauges were zeroes at the invert of the gate (Figure 2b). The opening angle of the gate was measured with a ruler and the height of the bottom of the faceplate above the invert h_α was calculated as:

$$h_\alpha = L \times [\sin(18) - \sin(18 - \alpha)] \quad \text{(mm)} \qquad [1]$$

where L is the length of the support beam between pivot and bottom of the gate. The gate height h_α was important for the calculation of the orifice areas contributing to the flow through the gate (Litrico et al., 2005). Depending upon the gate opening angle and the water elevations, the area below the gate, the areas on the side of the gate and/or the area above the gate contributed to the flow through the gate (see Section 5).

Detailed experiments were conducted for a range of flow rates 3 ≤ Q ≤ 40 l/s (Table 1). Table 1 summarises the flow conditions in the present study including the range of gate openings, the flow depths upstream and downstream of the structure and the float height H_{float}. The experiments tested the functionality of the design, the flow patterns around the structure and provided discharge coefficients for a range of flow conditions and opening angles. For some tests, the gate was unrestrained for a constant flow rate while for other tests the gate angle was fixed for a range of flow conditions. Note that experiments were conducted for two different flow directions to assess the hydraulic performances for both rising tides and receding water levels. The present manuscript focusses on the case with rising tidal water levels and the receding tidal case is only discussed secondary. Further details about the full range of tests can be found in Simpson (2016).

Table 1. Flow conditions for the experimental testing of the buoyancy-automated tidal gate; Zero elevation at invert of gate opening.

Testing	Q (l/s)	α (-)	H_1 (mm)	H_2 (mm)	H_{float} (mm)	Comment
Functionality	3-11	0-60º	0 - 310	-80 - 268	175-275	Unrestrained gate
Flow patterns	3-40	5-45º	0 - 310	-80 - 268	275	Unrestrained gate Fixed angle
Discharge coefficients	3-40	5-45º	0 - 310	-80 - 268	275	Fixed angle

3 FUNCTIONALITY TESTING OF THE TIDAL GATE

To confirm the functionality of the gate and to confirm the hydrostatic design approach of the closing profile, detailed experiments of a rising tide case were conducted. In these tests, the gate was unrestrained, being able to rotate freely as its submergence changed. Experiments were conducted for relatively small flow rates (3 < Q < 11 l/s) to prevent overtopping of the flume when the water level was high enough to shut the gate completely. The functionality tests included measurements of upstream and downstream flow depth H_1 and H_2 with the pointer gauges and the gate angle α with a ruler. All functionality tests were recorded with a site looking video camera as an additional observation of flow depths and closing angle. All tests were conducted for different float heights H_{float} to test the closing of the gate for a range of flow configurations.

For the rising tide case, the flow rate was kept constant and the downstream weir was raised fully allowing the flume to slowly fill (Figure 3). The flow depths H_1 and H_2 rose at a relatively constant rate. With increasing flow depth, the buoyancy force increased and the opening angle decreased closing the gate gradually. Initially the closing of the gate was slow, but accelerated for smaller gate angles. The closing of the gate was driven by the changing moment arm of the floats remaining at large gate angles most of the time. When the gate angle α < 15°, the gate closed rapidly, reducing the time with largest flow velocities and turbulences. For all tested float heights and flow rates, the same closing pattern was observed confirming the functionality of the gate under rising tide conditions. Figure 3 illustrates an example of the closing of buoyancy-automated tidal gate. Additional tests were conducted for the opening of the gate in a receding tide and for a flood case with large flows from the inland site. For both cases the functionality of the gate was confirmed including the automatic opening of the gate with receding water level and the flood case where the gate remained open for large flow rates and submerged floats due the dynamic force of the flow.

The relationship between closing angle and upstream water level was tested to confirm the design calculation of the closing of the gate which was conducted based upon hydrostatic conditions only (Figure 4). Figure 4 shows the relationship between α and H_1 for a range of flow conditions with different flow rates and float heights. All data collapsed reasonably well and resembled a linear relationship:

$$H_{float} - H_1 = 4.526 \times \alpha - 90.52 \quad \text{(mm)} \qquad [2]$$

Equation [2] can be used to calculate the gate position for any upstream flow depth H_1 and for any selected float height. The experimentally observed closing of the gate was very similar to the calculated profiles (not shown in this manuscript). For α < 35°, the calculated water height was slightly underestimated and for α < 35°, slightly overestimated due to a small hydrodynamic component. Overall the observations of the relationship between α and H_1 confirmed that the hydrostatic assumption was a valid initial assumption for the gate design.

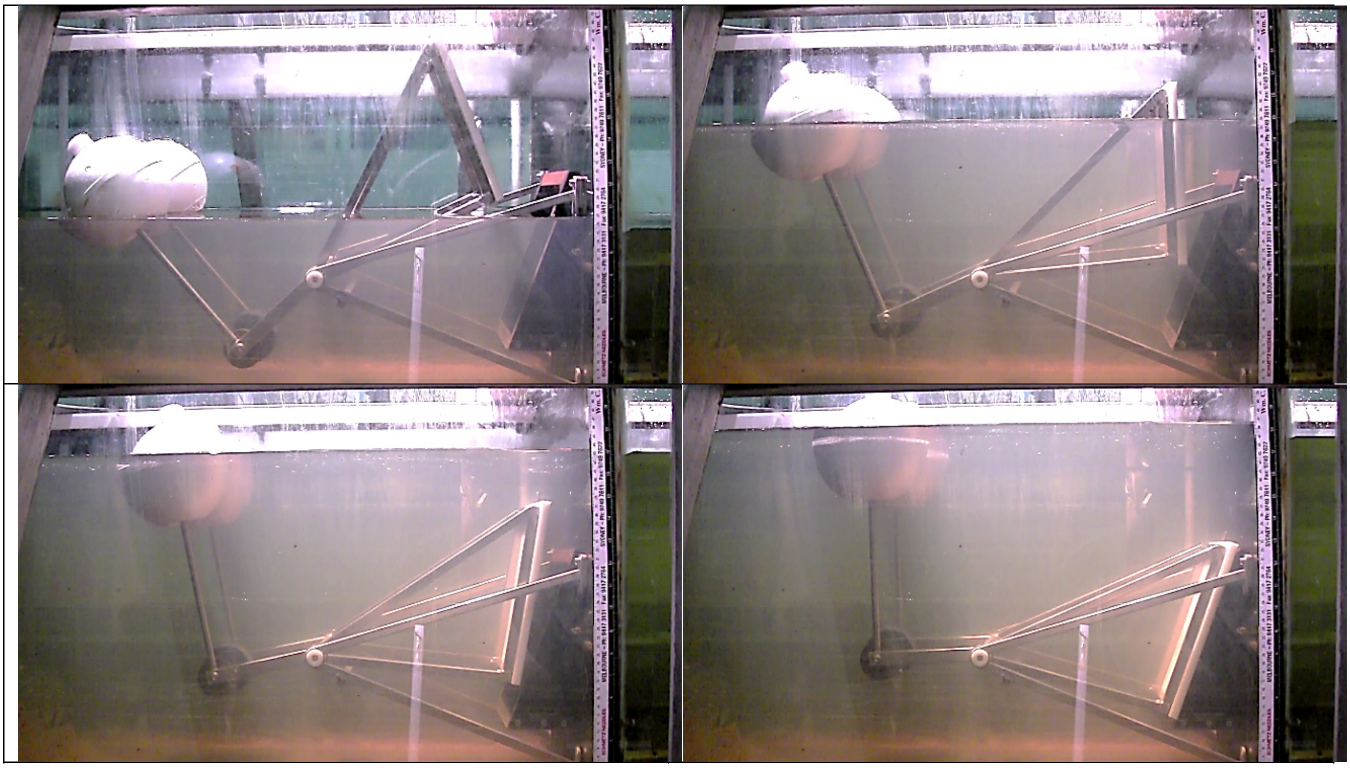

Figure 3. Closing of buoyancy-automated tidal gate; Q = 6 l/s, H_{float} = 275 mm; Flow from left to right. (Photo order from top left to bottom right)

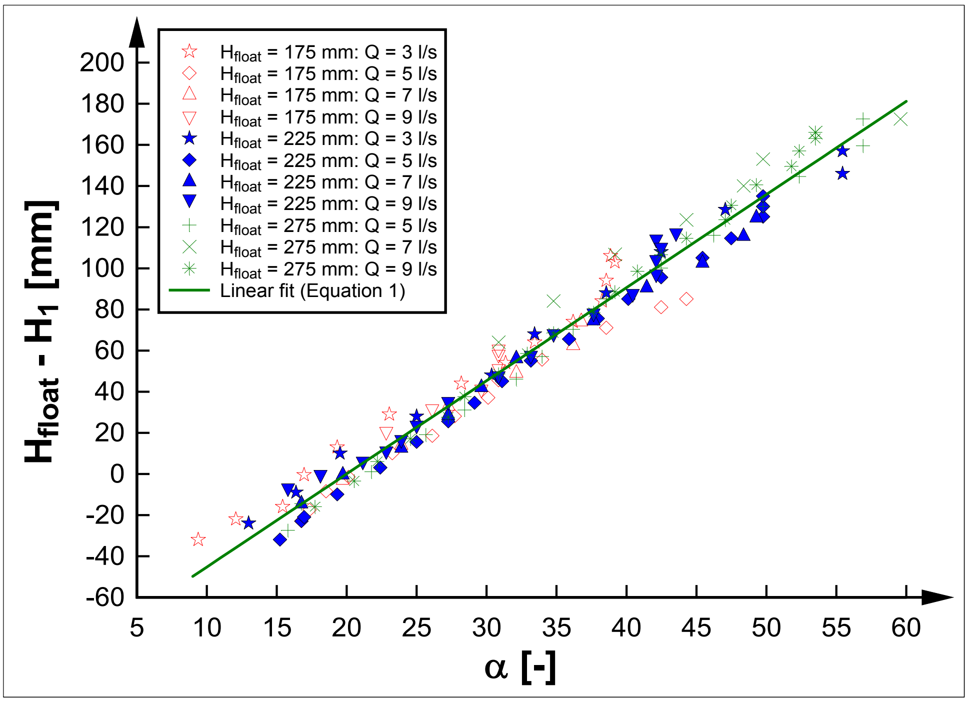

Figure 4. Observed relationship between opening angle of gate and upstream water level for various float heights; Comparison with best-fit equation (Eq. [2]).

4 FLOW PATTERNS OF THE TIDAL GATE

Detailed observations of the flow patterns were conducted comprising tests with both restrained and fixed gate. The main purpose of the unrestrained case was to test the gate's functionality including increasing, residing tides and upstream flooding (see previous section). While the flow patterns in the unrestricted case were observed for constant flow rates and changing gate openings, the restricted case allowed for detailed observations at a fixed gate position and for changing flow rates. Overall the flow patterns showed strong differences in flow behaviour reflecting various flow regimes depending upon the gate angle, as well as upstream and downstream flow depths. Overall three different flow regimes were classified comprising unsubmerged weir flows, submerged weir flow and submerged orifice flow. The flow regimes were differentiated similarly to culvert definitions using the ratio of upstream head to gate opening height H_1/B (Chow, 1959; Hager and Giudice, 1998). While the differentiation of flow regimes for the gates was sometimes difficult due to the complex flow behaviours for certain flow conditions (e.g. small opening angles, flow depths with large differences between upstream and downstream), the classification of flow regimes appeared to be suitable for all flow conditions in the present study. Typical flow patterns are shown in Figure 5 and further details can be found in Simpson (2016).

For $H_1 < 1.2$ B and $H_2 \leq 0$, the flow was classified as unsubmerged weir flow. In the experiments, H_2 was kept below the invert of the gate opening to allow a flow without tail water influences. When the gate opening was large ($\alpha > 25°$), the flow patterns was similar to a sharp crested weir (Figure 5a). For Q < 25 l/s the flow was calm but for Q ≥ 25 l/s, the bottom of the faceplate impacted on the flow leading to some flow disturbances due to the large head differential across the gate. For small gate opening angles ($\alpha \leq 25°$), the faceplate reduced the area of the gate opening and both the area under the gate and the side sections contributed to the flow through the gate. With increasing flow rate the flow velocities and turbulences increased. With decreasing gate opening, the head differentials across the gate increased for a given flow rate indicating both larger head losses and discharge coefficients. When $\alpha < 15°$, the gate would close rapidly as observed in the functionality tests (Figure 2) reducing the occurrence of flow events with strong flow disturbances for small opening angles.

For all flow conditions, the flow patterns upstream of the gate were undisturbed and calm and only for the largest flow rates and the smallest gate opening angles, a few surface ripples were observed upstream of the faceplate. At the downstream side, the low tail water level and the large differential head across the gate resulted in large flow velocities which would prevent fish passage across the gate for such flow conditions. The impact of the large flow velocities in an estuarine environment could also result in scour of the natural river bed. Therefore the unsubmerged weir conditions with large differential head across the structure should be avoided.

For $H_1 < 1.2$ B and $0 < H_2 \leq B$, the flow regime was classified as submerged weir flow. In this flow regime, the flows were much calmer compared to the unsubmerged weir flow regime allowing both fish migration and tidal buffering (Figure 5b). For large opening angles ($\alpha > 25°$), the flow conditions were relatively stable with a few surface ripples for upstream and downstream of the orifice. With increasing flow rates (Q > 18 l/s), these ripples became larger leading to some flow disturbances at the downstream side due to the interference of the flow with the lower edge of the faceplate. Interferences of the faceplate were also observed for large water levels which increases flow disturbances and turbulences at downstream of the gate opening.

For small gate openings ($\alpha \leq 25°$), flows upstream of the gate were more turbulent compared to flows with larger opening angles. The surface ripples increased in particular around the floats leading to some large scale vortex patterns. Downstream of the gate, the flow was significantly more disturbed including air entrainment and splashing. This was caused by the reduced orifice area for small gate openings, leading to flow acceleration through the orifice. Flow conditions with small opening angle would impact negatively upon fish passage and such conditions should be minimised.

For $H_1 > 1.2$ B and $H_2 > B$, the flow regime was classified as submerged orifice flow which appeared most favourable for fish migration (Figure 5c). Compared to the submerged weir flow regime, flows were calmer and flow disturbances were only observed for small gate opening angles and large flows. For $\alpha > 25°$, the flow was mostly calm with small surface ripples and eddies forming around the floats upstream of the gate. With increasing flow rate, the intensity and magnitude of these flow disturbances increased. Downstream of the gate, the ripples were larger due to the acceleration of the flows through the orifice. Occasionally a surface vortex formed entraining air through the gate leading to some flow aeration and stronger turbulences downstream. These vortices were not observed for the smaller gate openings ($\alpha \leq 25°$). For the smaller gate openings ($\alpha \leq 25°$), the reduced orifice area resulted in an increase in flow velocities through the gate and increased turbulences and air entrainment downstream of the gate. This case is not recommended for fish passage. The flow patterns upstream of the gate were similar to large gate openings with surface ripples and large eddies downstream of the floats.

Overall the observations of the flow patterns revealed relatively stable flow processes for large gate openings ($\alpha > 25°$) for all flow regimes. These large gate openings are associated with low flow velocities favouring fish passage through the structure. Smaller gate angles ($\alpha \leq 25°$) resulted in stronger flow velocities leading to flow disturbances and turbulence in particular downstream of the gate. It is recommended to design the gate to limit flow conditions with such small angles. This can be achieved through an increase in the gate opening, through the employment of a number of gates in parallel or through the adjustment of the float height. In the functionality tests it was shown that the gate would only be in a position with small opening angle for a short period of time, and to close rapidly for $\alpha = 15°$.

  / ISSN 1562-6865 (Online) - ISSN 1063-7710 (Print)

a. Unsubmerged weir flow

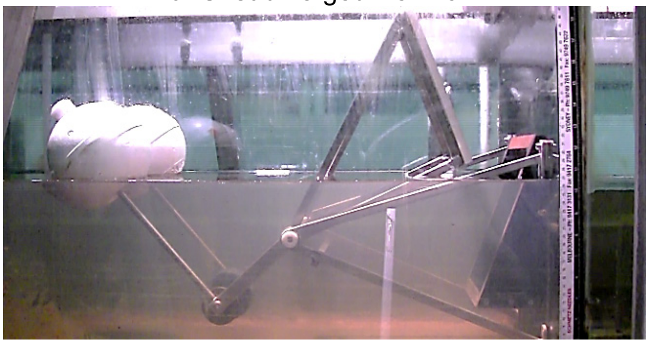

b. Submerged weir flow

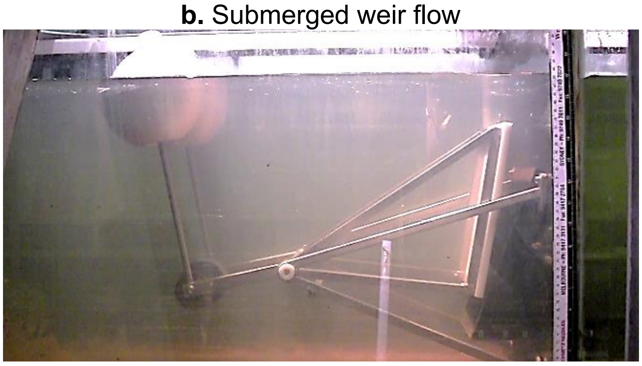

c. Submerged orifice flow

Figure 5. Flow regimes observed for the buoyancy-automated tidal gate (Flow from left to right).

5 DISCHARGE COEFFICIENTS

The purpose of quantifying the discharge coefficients C_D of the gate was to provide accurate gate flow estimates through a tidal cycle which is characterised by different water levels resulting in different gate openings (Equation 2). Therefore detailed experiments were conducted to find the discharge coefficients for a range of flow conditions (Table 1). While this manuscript only presents data for the rising tidal case (i.e. closing gate) the observations for the receding case (i.e. opening gate) showed similar results. Overall 340 data points for the rising tidal case were recorded.

Following the visual observations of three different flow regimes, all experimental data were separated into the respective flow regime and discharge relationships were found for each regime. The separation into the three flow regimes was simply done via determination of H_1/B consistent with the flow observations (Section 4). The major difficulty however was in the definition of the correct discharge area contributing to the weir and/or orifice flows. Depending upon water levels and gate opening positions, the gate could directly impact the opening area of the orifice and for certain flow conditions the actual orifice area could be smaller than the total gate opening. In these cases the flow was separated into three areas comprising the bottom area underneath the faceplate, the two side areas which is left and right of the faceplate and the top area above the faceplate. Depending upon the flow regime and the flow conditions, only parts of an area may contribute to the discharge. A similar approach was used by Litrico et al (2005), in their experiments on a Vluter Gate for small angles. In the present study, the contributing areas were calculated based upon geometrical observations depending upon the flow depth H_1, the gate opening angle α and the height of the bottom of the gate above the invert of the orifice H_α (Equation 1). When the faceplate of the gate was above the orifice (i.e. for large gate opening angles) the faceplate did not impact upon the flow for $H_1 \leq 1.5\ h_\alpha$. For $H_1 > 1.5h_\alpha$, the faceplate impacted upon the flow through the gate and the individual areas above, besides and above (only for the submerged orifice case) were calculated. Note that these areas were typically smaller than the area perpendicular to the flow ($B \times H_1$ for submerged and unsubmerged weir and $B \times B$ for the submerged orifice). In cases were the combined area A_{comb} below, besides and above the faceplate were larger than the area perpendicular to the flow, the smaller area was considered in the calculations. The calculation procedure of individual areas was based upon geometrical considerations and the equations can be found in Simpson (2016). It was assumed that the discharge coefficients below, besides and above the faceplate were the same following Litrico et al (2005).

For all flow cases, the flow rate through the floodgate can then be calculated using the typical orifice equation adopting the area A for the particular gate opening angle:

$$Q = C_D \times A \times \sqrt{2 \times g \times H_1 \times (1\text{-}s)} \qquad [3]$$

where A is the area contributing to the discharge through the orifice, i.e. $B \times H_1$ for submerged and unsubmerged weir flow with $H_1 \leq 1.5\ h_\alpha$, A_{comb} for submerged and unsubmerged weir flow with $H_1 > 1.5\ h_\alpha$ $B \times B$ for a submerged orifice flow with $H_1 \leq 1.5\ h_\alpha$, and A_{comb} for submerged orifice flow with $H_1 > 1.5\ h_\alpha$. The ratio of upstream to downstream flow depths $s = H_2/H_1$ was only relevant for submerged weir and orifice flows. Equation 3 was used to estimate the discharge coefficients through the gate for the full range of flow conditions. The discharge coefficients for the three flow regimes are illustrated in Figure 6.

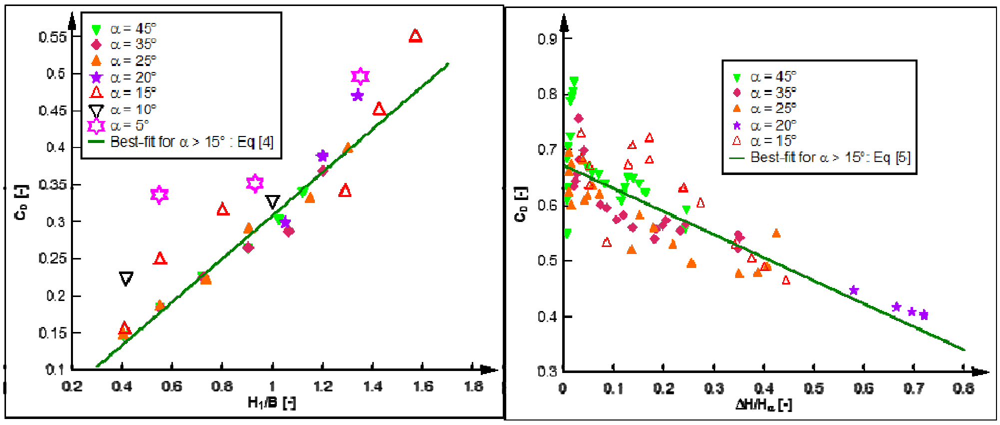

a. Unsubmerged-weir flow data; Comparison with Equation [4]

b. Submerged weir flow data; Comparison with Equation [5]

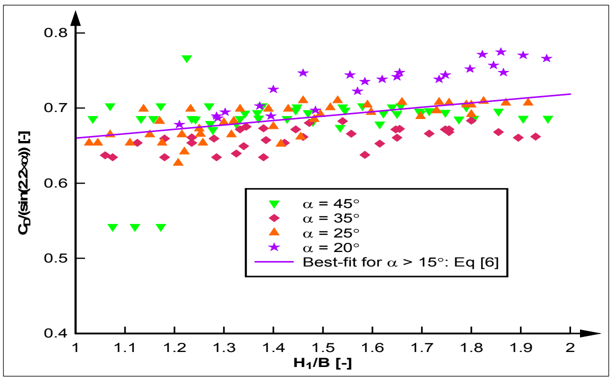

c. Submerged orifice flow data Comparison with Equation [6]

Figure 6. Experimental data of discharge coefficients for the three flow regimes; comparison with best fit equations

For the unsubmerged weir flow case, the experimental results are illustrated in Figure 6a where the discharge coefficients are illustrated as a function of the dimensionless upstream water elevation H_1/B for a range of gate opening angles ($5° \leq \alpha \leq 45°$). The results showed a linear trend between C_D and H_1/B which was best correlated with ($R^2 = 0.97$):

$$C_D = 0.016767 + 0.29177 \times \frac{H_1}{B} \quad ; \text{for } \alpha > 15° \qquad [4]$$

Note that the linear relationship was only established for $\alpha > 15°$ since the gate closed rapidly for $\alpha < 15°$ (Section 3). It is also unlikely that the gate opening will be small for the unsubmerged weir case with relatively low H_1. In Figure 6a, data for smaller gate openings are also added showing a larger data scatter linked with stronger flow disturbances for the smallest angles (Section 4).

Similar results were observed for the unsubmerged weir case where the experimental discharge coefficients are illustrated as a function of the dimensionless head differential across the gate $\Delta H/H_\alpha$, where $\Delta H = (H_1 - H_2)$ (Figure 6b). While the data exhibited some scatter, the data were reasonably well correlated with a linear relationship ($R^2 = 0.83$):

$$C_D = 0.67159 + 0.41528 \times \frac{\Delta H}{H_\alpha} \quad ; \text{for } \alpha > 15° \qquad [5]$$

For the largest gate opening ($\alpha = 45°$), the data scatter was largest due to small head differentials across the gate for small flow rates. The data for the unsubmerged orifice regime are shown in Figure 6c where a dimensionless expression of the discharge coefficient ($C_D/\sin(2.2 \times \alpha)$) is illustrated as a function of the dimensionless upstream water elevation H_1/B. A linear correlation provided reasonable results despite some data scatter ($R^2 = 0.47$):

$$C_D \big/ (\sin(2.2 \times \alpha)) = 0.60127 + 0.058689 \times \frac{H_1}{B} \quad ; \text{for } \alpha > 15° \qquad [6]$$

For the implementation of the buoyancy-automated tidal gate into real world applications, the present study provided the required design guidelines. Based upon geometrical considerations (Equation 1), the gate opening angle and the contributing orifice areas can be calculated depending upon the upstream flow elevation H_1, i.e. the height of the tide (Equation 2). The separation of the flow patterns into three different flow regimes based upon the ratio of H_1/B and the finding of simple linear relationships between flow depth and discharge coefficients (Equations 4 - 6) provided design equations for the calculation of the flow rate through the gate (Equation 3). Depending upon the flow conditions in the estuarine environment, the float height, the orifice opening and the number of gates can be optimised to allow sufficient flow movement through the flood gate.

6 CONCLUSION

A new buoyancy-automated tidal gate was designed to enable tidal flushing in estuarine environments. The gate is optimised based upon a detailed assessment of exiting self-regulating gates and hydrostatic force calculations. The optimised gate provided a simple and durable gate design. To test the gate's hydraulic performances, detailed laboratory experiments are conducted testing the gate's functionality, assessing the flow patterns and providing discharge curves. The functionality testing confoirmed the gate operation in reciding and rising tides as well as in flood events. A simple relationship was found between flow elevation and gate opening angle providing the required positionfor the buoyancy float. The visual observations of flow patterns highlighted three flow regimes depending upon the upsteram elevation, including unsubmerged and submerged weir flows and submerged orifice flows. The flow patterns showed calm and steady flows for large gate opening angles allowing fish migration through the orifice. For small opening angles, flow disturbances and turbulences increased. While these flow conditions were unwanted, the observations of the gate closing and opening indicated that small gate angles occurred only for a small period of time due to a rapid closing of the gate for $\alpha < 15°$. A detailed assessment of the discharge coefficients provided simple design guidelines for the three flow regimes. The discharge relationships are useful to calculate the flow through the gate for various flow elevations and gate opening positions. The hydraulic design guidelines can be incorporated in numerical simulations of estuarine remediation projects to optimise the gate design and to achieve maximum environmental benefits.

ACKNOWLEDGMENTS

The authors acknowledge the technical support of Rob Jenkins (WRL, UNSW Sydney).

REFERENCES

Anisfeld, S.C. & Benoit, G. (1997). Impacts of Flow Restrictions on Salt Marshes: An Instance of Acidification. *Environmental Science and Technology,* 31(6), 1650–1657.

Adnitt, C., Brew, D., Cottle, R., Hardwick, M., John, S., Leggett, D., Mcnulty, S., Meakins, N. & Staniland, R. (2007). *Saltmarsh Management Manual*. Bristol: Environment Agency, UK.

Belaud, G., Litrico, X., Graaff, B.D. & Baume, J.-P. (2008). Hydraulic Modelling of an Automatic Upstream Water Level Control Gate for Submerged Flow Conditions. *Journal of Irrigation and Drainage Engineering*, 134(3), 315-326.

Bos, M.G. (1989). *Discharge Measurement Structures*. 3rd Ed., Publication 20, International Institute for Land Reclamation and Improvement/ILRI, Wageningen, Netherlands.

Boys, C.A., Kroon, F.J., Glasby, T.M. & Wilkinson, K. (2012). Improved Fish and Crustacean Passage in Tidal Creeks following Floodgate Remediation. *Journal of Applied Ecology*, 49(1), 223-233.

Chow, V.T. (1969). *Open Channel Hydraulics*. Mcgraw-Hill, New York, N.Y.

Glamore, W. (2012). *Incorporating Innovative Engineering Solutions into Tidal Restoration Studies, In Tidal Marsh Restoration.* A Synthesis of Science and Management, Island Press, Washington, DC.

Hager, W.H. & Giudice, G.D. (1998). Generalized Culvert Design Diagram. *Journal of Irrigation and Drainage Engineering*, 124(5), 271-274.

Indraratna, B., Golab, A., Glamore, W. & Blunden, B. (2005). Acid Sulphate Soil Remediation Techniques on the Shoalhaven River Floodplain, Australia. *Quarterly Journal of Engineering Geology & Hydrogeology*, 38(2), 129-142.

Litrico, X., Belaud, G., Baume, J.-P. & Ribot-Bruno, J. (2005). Hydraulic Modelling of an Automatic Upstream Water-Level Control Gate. *Journal of Irrigation and Drainage Engineering*, 131(2), 176-189.

Lucas, M.C., Bubb, D.H., Jang, M.-H., Ha, K. & Masters, J.E.G. (2009). Availability of and Access to Critical Habitats in Regulated Rivers: Effects of Low-Head Barriers on Threatened Lampreys. *Freshwater Biology*, 54(3), 621-634.

Rampano, B. (2009). *Water Control Structures: Design Suitability for Natural Resource Management on Coastal Floodplains*, Department Of Industry and Investment (Aquatic Habitat Rehabilitation), Port Stephens.

Pollard, D.A. & Hannan, J.C. (1994). The Ecological Effects of Structural Flood Mitigation Works on Fish Habitats and Fish Communities and the Lower Clarence River System of South-Eastern Australia. *Estuaries*, 17(2), 427-461.

Ridgway, G. & Williams, M. (2011). *Self-Regulating Tide Gate, A New Design for Habitat Creation*, Horizon House, Deanery Road, Bristol, BS1 5AH: Environment Agency.

Russel, K., Erskine, J. & Glamore, W. (2012). Tomago Wetland Rehabilitation Project: Integrated, Innovative Approaches. *21st NSW Coastal Conference*, Kiama, Australia.

Simpson, J. (2016). The Hydraulics of a Buoyancy Automated Tidal Gate, *Honours Thesis*, UNSW Australia, 164.

Streever, W.J. & Genders, A.J. (1997). Effect of Improved Tidal Flushing and Competitive Interactions at the Boundary between Salt Marsh and Pasture. *Estuaries*, 20(4), 807-818.

Waterman Industries (2002). *SRT (Self-Regulating Tidegate) for Tidal Wetlands Preservation & Restoration*. In I. Waterman Industries, Ed, 19-24.

Wright, G.V., Wright, R.M. & Kemp, P.S. (2015). Impact of Tide Gates on the Migration of Adult European Eels, Anguilla. *Estuaries and Coasts*, 38(6), 2031-2043.

Wright, R.M., Wright, G.V., Bendall, B. & Kemp, P.S. (2016). Impact of Tide Gates on the Upstream Movement of Adult Brown Trout. *Ecological Engineering*, 91, 495-505.

AIR-WATER FLOW PROPERTIES IN HYDRAULIC JUMPS ON A POSITIVE SLOPE

LAURA MONTANO[(1)] & STEFAN FELDER [(2)]

[(1,2)] Water Research Laboratory, School of Civil and Environmental Engineering, UNSW Sydney, Australia,
l.montano@wrl.unsw.edu.au; *s.felder@unsw.edu.au*

ABSTRACT

Hydraulic jumps occur at the transition from supercritical to subcritical flows. They are characterised by generation of vortices, three-dimensional motions, high turbulence, air entrainment and strong energy dissipation. While there has been considerable research on air-water flows in classical hydraulic jumps in horizontal flat bed, little research has been conducted on air-water flows in hydraulic jumps on slopes. Herein the present study investigated the air-water flow processes and energy dissipation performances of hydraulic jumps on slopes comprising Type B and D jumps. The observations on the jumps on slope are compared with classical hydraulic jumps on horizontal bed with identical Froude and Reynolds numbers providing novel insights into the effects of bed slope upon the flow aeration and energy dissipation processes in hydraulic jumps. The comparison between hydraulic jumps on flat and sloped bed showed distinctive differences in flow patterns and distributions of air-water flow properties providing a better understanding of the connection between flow aeration and energy dissipation. Overall, Type D jumps represented the scenario with lowest energy dissipation and lowest flow aeration among the three jump types, while the classical hydraulic jump was the most efficient.

Keywords: Air-water flow properties; energy dissipation; flow patterns; hydraulic jump; positive slope.

1 INTRODUCTION

Hydraulic jumps occur at the sudden transition from supercritical to subcritical flow involving a complexity which has made this phenomenon fascinating for more than two centuries. Hydraulic jumps are characterized by strong turbulence, flow aeration and energy dissipation. The first systematic experiments of hydraulic jumps were conducted in a horizontal rectangular channel by Bidone (1820), followed by the well-known momentum analysis conducted by Bélanger (1841) to calculate the conjugate depth ratio (Ferriday, 1895; Bakhmeteff, 1932; Hager, 1990):

$$\frac{d_2}{d_1}=\frac{1}{2}\left(\sqrt{1+8\ Fr_1^2}\right)-1 \qquad [1]$$

where d_1 and d_2 are the upstream and downstream conjugate depths respectively and Fr_1 is the inflow Froude number. Equation [1] is widely accepted and has been confirmed in multiple experimental studies of hydraulic jumps in horizontal channels, named in this paper as classical hydraulic jumps (CHJ).

For hydraulic jumps on sloped channels, the conjugate depths ratio depends on the position of the jump on the slope and the steepness of the slope (Hager, 1989; Ohtsu and Yasuda, 1991; Beirami and Chamani, 2006). For positive slopes, hydraulic jumps are classified as Type A, B, C, D and E (Kindsvater, 1944; Rajaratnam, 1967; Peterka, 1978). Hydraulic jumps occurring at the downstream end of the spillway are classified as Type A. If the hydraulic jump occurs partially on both sloped and horizontal sections, the jump is classified as Type B. A Type C jump occurs when the downstream end of the jump coincides with the start of the horizontal section and Type D jumps are observed if the entire jump is on the sloped section. Type E jumps occur for flat and long sloped channels where the water surface of the jump is parallel to the channel bed (Rajaratnam, 1967).

Even though several authors has analyzed conjugate depths, energy dissipation and roller length for hydraulic jump Types A, B and D (Table 1), the analysis of internal flow features have predominantly focused on CHJ. Extensive research has been conducted to understand the air-water flow properties in CHJ including void fraction, bubble count rate, interfacial velocities and flow turbulence (e.g. Resch and Leutheusser, 1972; Chanson and Brattberg, 2000; Murzyn et. al., 2005; Wang et al., 2014; Zhang et. al., 2014). In hydraulic jumps on a positive slope, the air-water flow properties are widely unknown despite a study by Yasuda and Ohtsu (2008) highlighting the effect of pre-entrained supercritical inflow conditions on the roller length and the velocity distribution in Type B jumps. Measurements of mono-phase flow velocities for CHJ (Rajaratnam, 1965; Narayanan, 1975; Wu and Rajaratnam, 1995) and for hydraulic jumps on slopes (Rajaratnam and Murahari, 1974; Ohtsu and Yasuda, 1991; Gunal and Narayanan, 1996) suggested close similarity between velocity distributions for hydraulic jumps in horizontal and sloped channels. Despite research of the nonaerated flow properties on hydraulic jumps on slopes are being done, information about the air-water flow properties is limited.

Herein, new experiments of hydraulic jumps on a positive slope were conducted and a comparative analysis between hydraulic jumps in sloped and horizontal sections provided novel information about the effects of slope on hydraulic jumps. The analysis comprised detailed observations of flow patterns, conjugate depth relationships and air-water flow properties including void fraction, bubble count rate and interfacial velocity distributions. The experimental results suggested significant differences in air-water flow properties and energy dissipation efficiency between Type D jumps and CHJ.

Table 1. Relevant experimental research on hydraulic jumps in sloped channels.

Reference	Slope (°)	Hydraulic jump type			Fr_1 (−)	Re (−)	Measured Parameters			
Bakhmeteff and Matzke, (1938)	0 – 4			x	2 – 6.2	$5x10^4$ – $8.5x10^4$	x			
Kindsvater, (1944)	9.5			x	2 – 7.5	-	x			
Rajaratnam and Murahari, (1974)	1.1 – 14			x	5.1 – 8.1	$2.2x10^4$ – $3.2x10^4$				x
Peterka, (1978)	Type B: 2.9 - 16 Type D: 3.8 - 15.6	x	x	x	Type B: 8.8 -14 Type D: 2.9-19.2	Type B: $1.1x10^5$ – $2.7x10^5$ Type D: $4.6x10^4$ – $2.3x10^5$	x			
Hager, (1989)	45		x		3.6 – 17.5	$2x10^4$ – $3.9x10^5$	x	x		
Kawagoshi and Hager, (1990)	30		x		2.8 – 20	$1x10^4$ – $4x10^5$	x			x
Ohtsu and Yasuda, (1991)	8 – 60		x	x	4 – 12	-	x			x
Gunal and Narayanan, (1996)	0.05 – 0.1			x	4.5 – 7	-	x			x
Beirami and Chamani, (2006; 2010)	59	x	x	x	5 – 10	-	x	x		
Present Study	2.5	x	x	x	3 - 3.6	$9.8x10^4$ – $1.1x10^5$	x	x	x	x

2 EXPERIMENTAL FACILITY AND INSTRUMENTATION

Experiments were performed in a smooth, glass-walled flume located in UNSW's Water Research Laboratory for discharges between $0.01 < Q < 0.07$ m^3/s. The channel was rectangular, 40 m long, 0.6 m wide and 0.6 m high. Figure 1 shows a sketch of the experimental setup including the positioning of the hydraulic jumps in the present study and the instrumentation. A section with a positive slope of θ = 2.5° provided supercritical inflow conditions and the subcritical tail water was controlled by a weir at the downstream end of the flume. Constant flow rates were supplied directly from Manly Dam measured with an ABB WaterMaster FET100 electromagnetic flowmeter with $\pm$ 0.4% accuracy. The conjugate depths of the jump were measured with a point gauge upstream near the jump toe and downstream of the hydraulic jump where the flow depth was stable with an accuracy of $\pm$ 0.5 mm. A comparative analysis was conducted for classical hydraulic jumps and jumps on a slope (Type B and D) in the same channel (Figure 1). A Type C Jump was not tested because hydraulic characteristics of Type C and Type D jumps are similar if the beginning of a horizontal section of the channel and it occurs at the end of a Type D jump (Peterka, 1978; Ohtsu and Yasuda, 1991).

Detailed measurements of air-water properties were conducted for a selected range of flow conditions (Table 2). Table 2 summarises the flow conditions including the jump type, the inflow conditions, the longitudinal distance from the beginning of the slope, x_1 and the Reynolds number, Re. All experiments were conducted for comparable Froude and Reynolds numbers. A classical hydraulic jump was selected as the reference jump denoted as "A" in Table 2. Experiments "B.1" and "D.1" corresponded to jump Types B and D respectively for the same Froude number while experiments "B.2" and "D.2" corresponded to the same Reynolds number. The inflow conditions upstream of the jump toe were assessed with a Pitot tube (Ø=3mm) at several cross-sections on the sloped section. Partially developed inflow conditions occurred for hydraulic jump Type D (x_1 = 2.60 m) while Type B (x_1 = 5.40 m) and CHJ (x_1 = 6.20 m) were characterised by fully developed inflow conditions. The flow became developed at about x_1 = 4 m.

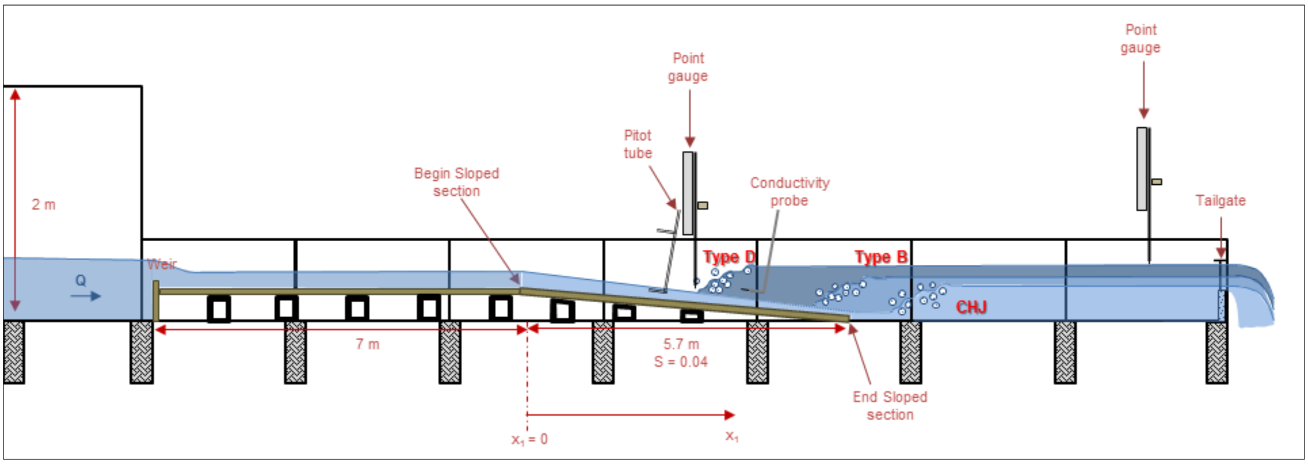

Figure 1. Experimental setup and positioning of the hydraulic jumps in the present study (not to scale).

Table 2. Experimental flow conditions for measurements of air-water flow properties on hydraulic jumps with horizontal and sloped channel bed.

Experiment	Hydraulic Jump Type	x_1 (m)	Q (m^3/s)	d_1 (m)	Fr_1 (−)	Re (−)	*Inflow condition*
A	**CHJ**	6.20	0.068	0.046	3.6	1.13×10^5	Fully Developed Flow
B.1	**B**	5.40	0.058	0.042	3.6	9.6×10^4	Fully Developed Flow
D.1	**D**	2.60	0.059	0.042	3.6	9.8×10^4	Partially Developed Flow
B.2	**B**	5.40	0.068	0.049	3.3	1.13×10^5	Fully Developed Flow
D.2	**D**	2.60	0.068	0.052	3.0	1.13×10^5	Partially Developed Flow

The air-water flow measurements were conducted with a double-tip conductivity probe (∅ = 0.125 mm inner electrode) in the center line of channnel at five cross-sections for each hydraulic jump (Table 2). The two tips of the conductivity probe were sampled simultaneously at 20 kHz and for 45 s. The longitudinal and transverse separations between leading and trailing probe tips were Δx = 5.01 mm and Δz = 1.17 mm respectively. The conductivity probe and the acquisition system has been self-developed at WRL and successfully benchmarked recently against well-established phase-detection intrusive probe systems (Felder and Chanson, 2016; Felder and Pfister, 2017).

The double-tip conductivity probe recorded instantaneous Voltage signals which corresponded to air or water phases (Nagash, 1994; Chanson, 2002). The raw signals were post-processed with a single threshold technique with a 50% threshold (Felder and Chanson, 2015). When the raw voltage signal was below the threshold, an air phase was recorded and when the signal was above the threshold, a water phase was recorded. This provided typical air-water flow properties including the time-averaged void fraction C and the bubble count rate F, i.e.the number of bubbles detected by a sensor per second. Cross-correlation analysis between the probe tips provided the average travel time of air and water entities between the two probe tips and the interfacial velocity. The signal processing was automated by a Fortran code developed by Felder (2013).

To increase the accuracy of the air-water flow measurements, the phase-detection probe should face the stream of incoming bubbles and droplets. In a CHJ, the conductivity probe was therefore placed parallel to the horizontal channel bed. In hydraulic jump Types B and D, a sensitivity analysis was conducted comparing the air-water properties measured with the conductivity probe placed parallel to the horizontal channel bed or parallel to the sloped channel bed. The sensitivity analysis showed that the position of the conductivity probe did not affect the detection of air-water flow properties and that the void fraction, bubble count rate and interfacial velocity distributions were unaffected. In the present experiments, the conductivity probe was therefore positioned parallel to the slope for Type B and D jumps (Figure 1).

3 FLOW PATTERNS

Detailed flow observations were undertaken for inflow Froude numbers between $3 < Fr_1 < 4.6$ corresponding to discharges $0.01 < Q < 0.07$ m^3/s for hydraulic jumps Type B and D and $0.05 < Q < 0.07$ m^3/s for classical hydraulic jumps. Classical hydraulic jumps with Froude numbers between $2.5 < Fr_1 < 4.5$ were known as transitional jumps and were characterised by pulsating and irregular flow behaviour (Peterka, 1978; Hager, 1992). All hydraulic jumps in the present study showed a defined roller with turbulence and air entrainment at the jump toe which increased with increasing discharge. Air entrainment was observed for $Q > 0.01$ m^3/s and $Fr_1 > 3$ for hydraulic jumps Type B and D although the Type D jump was more stable and had a more defined air entrainment region (Figure 2). A clear water layer underneath the jump can be identified for both jumps on the slope meaning low interaction between the shear region and the region underneath the jump toe.

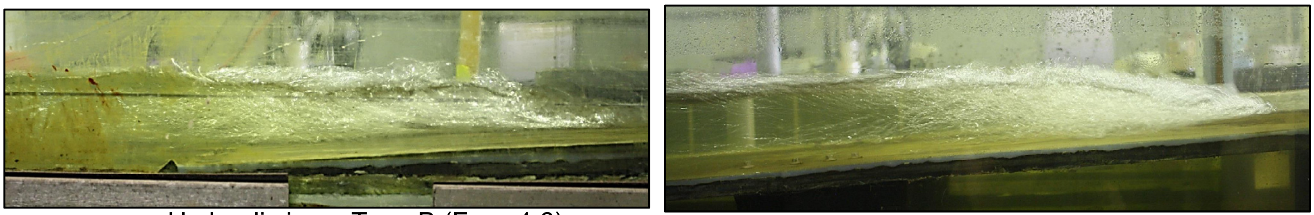

a. Hydraulic jump Type B (Fr_1 = 4.6) **b.** Hydraulic jump Type D (Fr_1 = 4.5)

Figure 2. Air-water flow patterns of hydraulic jumps on a positive slope (θ = 2.5º) ; Q = 0.012 m^3/s; Re = 2 x 10^4 (Flow from right to left).

The experiments showed that hydraulic jumps in the sloped section of the channel were significantly more stable than jumps occurring in the horizontal section. Visual observations indicated jump toe fluctuations of up to 40 cm for the hydraulic jumps on the horizontal channel while the fluctuations for jumps in the sloped section had a maximum of 15 cm. Higher jump toe oscillations resulted in larger irregular wave pattern and water surface fluctuations (Hager, 1990). Classical hydraulic jumps showed steeper increase of flow depth, rougher water surface and irregular wave patterns which was consistent with previous studies (Peterka, 1978; Hager, 1992) (Figure 3a). On the contrary, hydraulic jumps Type B and D (Figure 3b and 3c) were more stable as a result of the lower influence of tailwater waves in the jump and a more defined water surface along the roller. Flow visualizations suggested that Type D jump had the flattest free-surface profile.

Visual observations also suggested higher turbulence and stronger three-dimensional motions for CHJ resulting in stronger roller generation and more frequent splashes. For hydraulic jumps located on the slope, the roller formation in the recirculation region did not have significant impact on the water surface of the jump while CHJ were characterised by frequent flow fluctuations along the tranversal and longitudinal axes. Near the jump toe, air entrained at the impingement point was dispersed faster for CHJ. Figures 3b and 3c show a clear water layer underneath the jumps on the slope which was larger compared with hydraulic jumps on horizontal channels (Figure 3). These results indicated a lower vertical momentum transfer for Type B and D jumps associated with smaller interactions between air and water entities in the shear region.

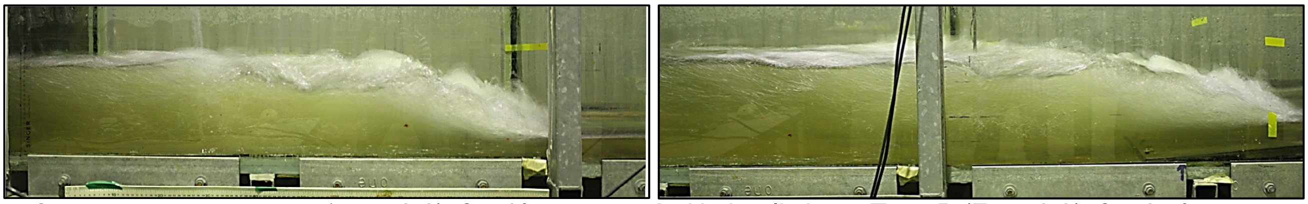

a. Classical hydraulic jump (Fr_1 = 3.6), θ = 0º **b.** Hydraulic jump Type B (Fr_1 = 3.3), θ = 2.5º

b. Hydraulic jump Type D (Fr_1 = 3), θ = 2.5º

Figure 3. Comparison between hydraulic jumps on a positive slope and in horizontal channel with same Reynolds number: Q=0.068 m^3/s, Re = 1.13 x 10^5.

For all hydraulic jumps in the present study, the flow depths were measured with the point gauge and the conjugate depth relationship, while the energy dissipation efficiencies were also recorded (Figure 4). The present data were compared with previous data on sloped and horizontal channels with similar Froude number and slope. Figure 4a shows the relationship between inflow Froude number $\mathrm{Fr1}$ and the conjugate depth ratio $\mathrm{TW/d1}$ where TW is the tailwater depth. While the tailwater depths for CHJ and Type B jump were located in the horizontal section of the channel (Figure 3a & b) (Ohtsu and Yasuda, 1990; 1991), the tailwater of Type D jumps occured on the slope (Figure 3c) (Peterka, 1978; Ohtsu and Yasuda, 1991). Previous experimental data showed that the differences in conjugate depth ratio between CHJ, Type B and Type D jumps decreased with increasing Froude number (Peterka, 1978; Beirami and Chamani, 2006) and the Froude numbers in the present study were in a range of Fr_1 which only showed small differences in the

  / ISSN 1562-6865 (Online) - ISSN 1063-7710 (Print)

conjugate depth relationship (Figure 4a). Despite the small range of present Froude numbers, differences in the conjugate depth ratio could be identified between the hydraulic jumps in the present study. Hydraulic jumps in the sloped section showed a higher conjugate depth ratio compared with CHJs (Figure 4a). The present data were consistent with previous experimental observations.

The abrupt transition from supercritical to subcritical flow in hydraulic jumps generated high turbulence and strong energy dissipation which was estimated as the ratio between upstream and downstream head difference, where the upstream total head (Hager, 1989), provides the energy efficiency η:

$$\eta=\frac{H_1-H_2}{H_1}=\left(\frac{(TW-d_1)^3}{4\ TW\times d_1}\right)/H_1 \qquad [2]$$

Figure 4b shows the energy dissipation efficiency for CHJ and Type B and D jumps as a function of Fr_1. The experimental results were also compared with the observations of Hager (1990) on a horizontal channel with similar Froude number with the Bélanger equation (Eq. [1]). The present results indicated that the energy dissipation efficiency increased with increasing Froude number for all hydraulic jumps (Figure 4b). This observation was consistent with previous studies (e.g. Peterka, 1978; Hager, 1989; 1990; Beirami and Chamani, 2010). Classical hydraulic jumps and Type B jump had similar efficiency rates. This similarity appeared to be associated with the flat slope (θ = 2.5º) and the low inflow Froude numbers which affected the conjugate depth ratio (Peterka, 1978; Beirami and Chamani, 2006). In contrast, hydraulic jump Type D dissipated lower energy for all Froude numbers. This was associated with the lower aeration and higher stability compared with the other jumps. Overall, the experimental datawere was in agreement with previous studies although there was limited information for small slopes and small Froude numbers. For the present experiments, hydraulic jump Type D had the lowest energy dissipation efficiency.

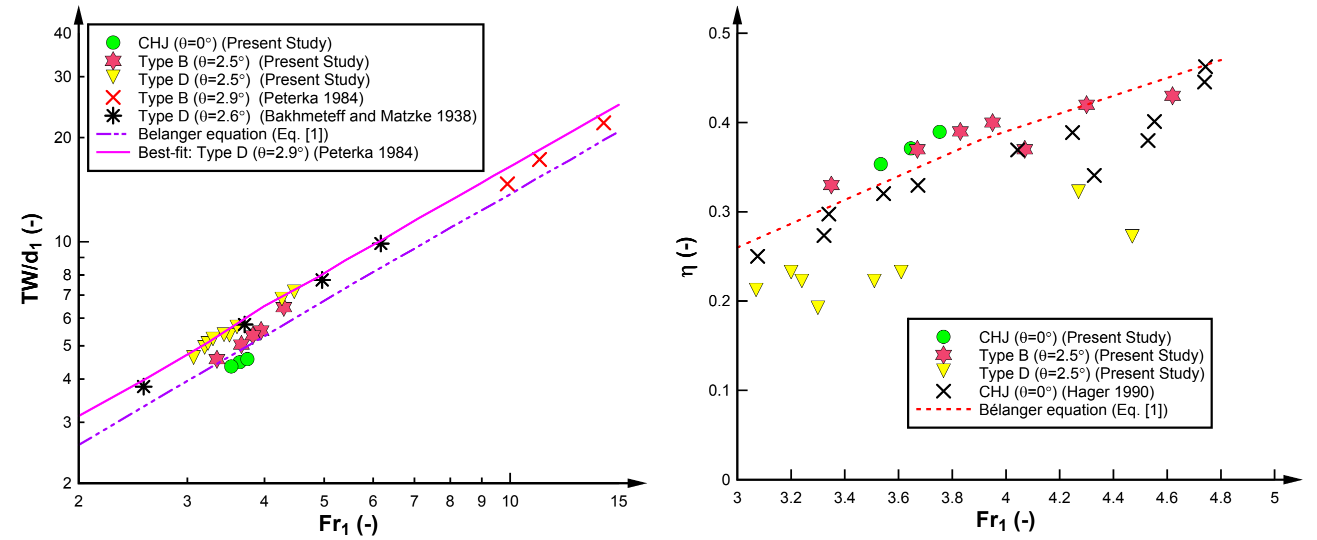

a. Conjugate depth relationship

b. Energy dissipation efficiency.

Figure 4. Comparison of conjugate depth and energy efficiency of present CHJ and Type B and D jumps with previous experimental data on similar slope and empirical equation by Peterka (1984) and Equation [1].

4 AIR-WATER PROPERTIES

4.1 Void fraction

Figure 5 shows the void fraction distributions for the three hydraulic jump types in the present study as a function of the dimensionless flow depth y/d_1. The void fractions are compared for the same Froude number Fr_1 = 3.6 and for the same dimensionless cross-sections along the jump $(x-x_1)/d_1$. For all hydraulic jumps, the void fraction distributions showed typical shapes exhibiting two distinctive regions in the jumps. In the shear region, the void fractions were characterised by a local peak associated with the entry of air at the impingement point, the advective and convective transport of air bubbles and the breaking up of bubbles due to shear stress (Chanson, 1996; Chanson and Brattberg, 2000; Murzyn et. al., 2005). In the recirculation region, in the upper part of the jump, the air exchange with the free-surface was affected by buoyancy effects and the void fraction increased monotonically up to the free-surface (Chanson, 1996; Chanson and Brattberg, 2000; Murzyn et. al., 2005; Zhang et. al. 2014). Overall, the shapes of the void fraction distributions were similar between CHJ and Type B jump although the void fraction data for CHJ showed a stronger data scatter related to the stronger jump toe fluctuations. The strongest effect of the slope was observed in the void fraction distributions for the Type D jump with a reduction in the advective peak in the shear region compared to CHJ (Figure 5). The increased void fractions for CHJ and Type B jumps indicated a lower aeration for hydraulic jumps occurring entirely in sloped channels, i.e. Type D jumps. The void fraction profiles in the recirculation region were almost the same for the three hydraulic jumps. This finding suggested that the most remarkable difference between Type D jump and CHJ was observed in the shear region (Figure 4b). Hence, low turbulence and higher stability in hydraulic jumps Type D was associated with lower air entrainment in the shear region. The void fraction distributions of Type B jumps were very similar to CHJ for cross-sections located near the jump toe where the flow depths of the jumps were similar (Figure 5a-c). For the last cross-section ($(x-x_1)/d_1 = 14$), the maximum local void fraction in the shear region was larger for the CHJ indicating an increase in air entrainment lengths compared with hydraulic jumps on the slope (Figure 5d).Experiments with the same Reynolds number showed smaller differences between void fraction distributions for CHJ and Type B and D jumps including similarities in void fractions in the recirculation region. This is further discussed in Section 5.

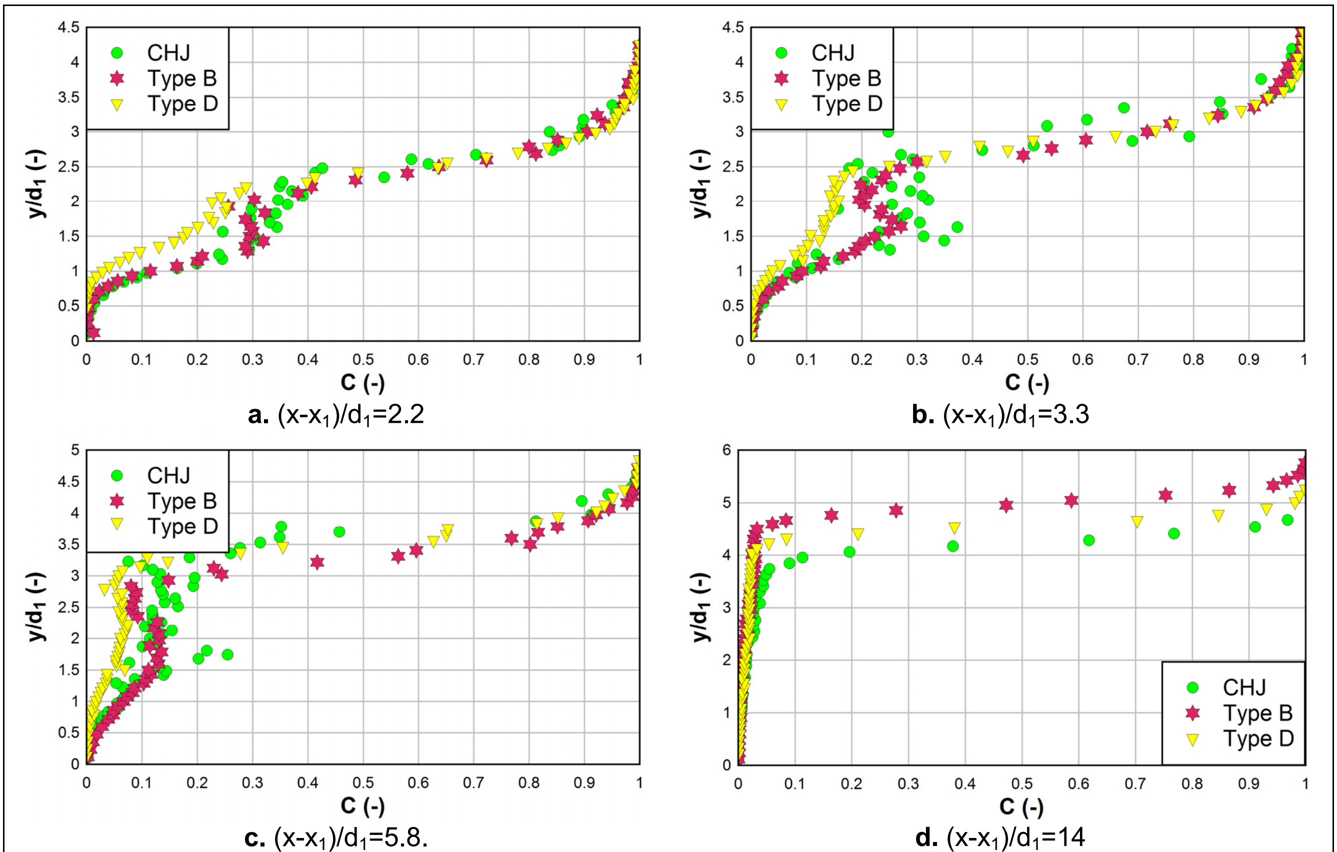

Figure 5. Time-averaged void fraction distribution with same Froude number ($Fr_1 = 3.6$); CHJ: Q = 0.068 m^3/s, Re = 1.13×10^5; Type B: Q = 0.058 m^3/s, Re = 9.6×10^4, Type D: Q = 0.059 m^3/s, Re = 9.8×10^4.

4.2 Bubble count rate

The bubble count rate provided information about the air-water interactions in the hydraulics jumps. Figure 6 shows the comparison of bubble count rate distributions for several dimensionless cross-sections along the jump for the same Froude number. Overall the bubble count rate distributions showed similar features independent of jump type with two distinct peaks in the shear and recirculation regions respectively. However differences were observed in terms of the Type D jump which showed a lower bubble count rate compared to CHJ and Type B jump in particular, especially in the roller just downstream of the jump toe (Figure 6a-c). The maximum bubble count rate distributions were similar between CHJ and Type B jumps for $(x – x_1)/d_1 \leq 9.4$. For $(x-x_1)/d_1 = 14$ whereelse the bubble count rate distributions for Type B and D jumps were close. Overall, the data showed a higher number of bubbles for CHJ when compared with jumps on a slope. Based upon the total number of measured bubbles, Type B and D jumps had a reduced number of detected bubbles compared to CHJ of approximately 75% and 55% respectively. The much lower bubble count rate for Type D jumps suggested a smaller interfacial area and smaller air-water interactions associated with lower energy dissipation. In contrast, in a comparative analysis for the same Reynolds number, the bubble count rate distributions were similar for all positions along the CHJ and the Type B jump while the bubble count rate for Type D jump was consistently smaller. Overall, the bubble count rate was higher for CHJ compared with jumps on the slope indicating a reduction in air-water flow interactions.

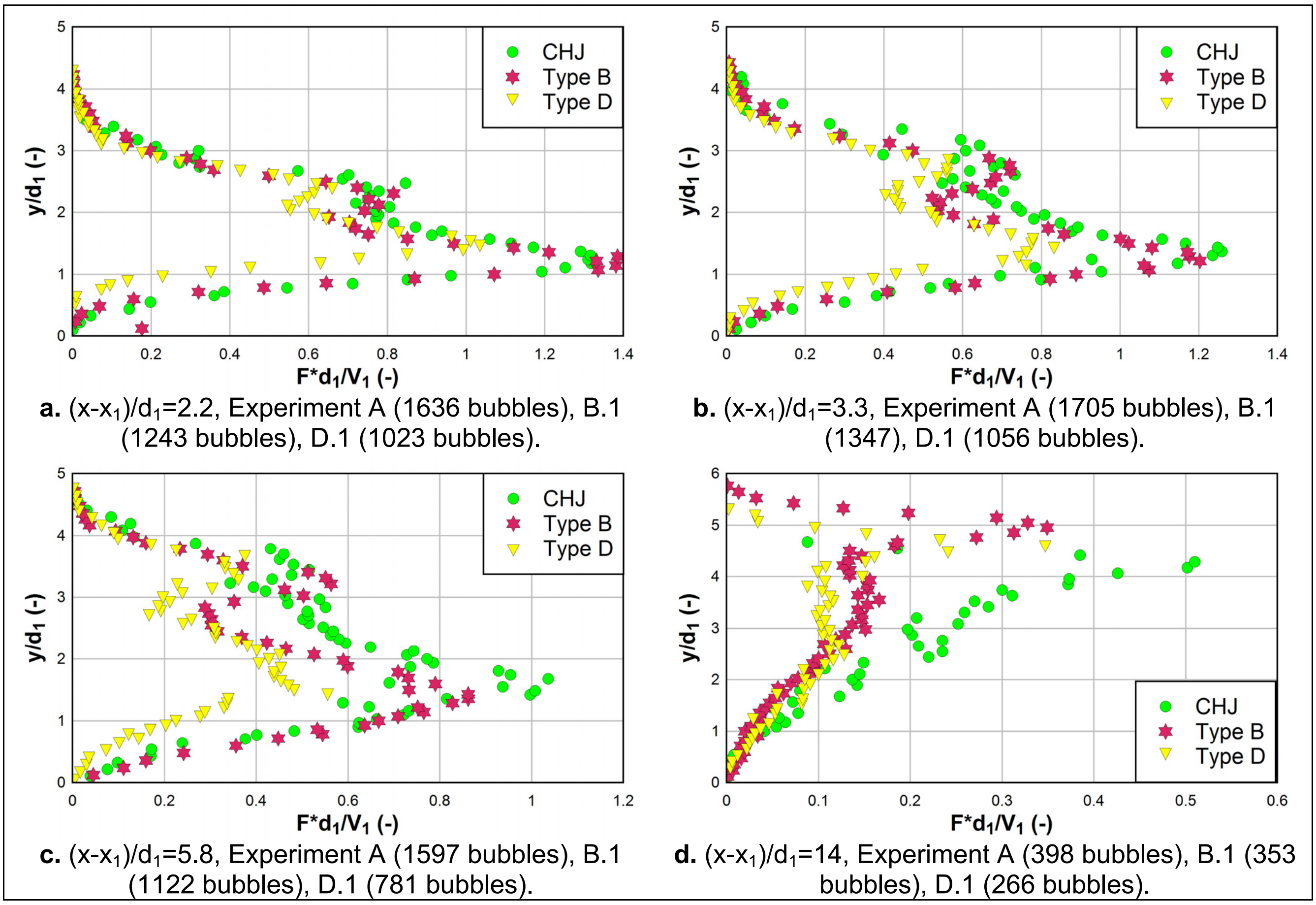

a. $(x-x_1)/d_1=2.2$, Experiment A (1636 bubbles), B.1 (1243 bubbles), D.1 (1023 bubbles).

b. $(x-x_1)/d_1=3.3$, Experiment A (1705 bubbles), B.1 (1347), D.1 (1056 bubbles).

c. $(x-x_1)/d_1=5.8$, Experiment A (1597 bubbles), B.1 (1122 bubbles), D.1 (781 bubbles).

d. $(x-x_1)/d_1=14$, Experiment A (398 bubbles), B.1 (353 bubbles), D.1 (266 bubbles).

Figure 6. Bubble count rate distributions for experiments with the same Froude number (Fr_1 = 3.6). CHJ: Q = 0.068 m^3/s, Re = 1.13×10^5; Type B: Q = 0.058 m^3/s, Re = 9.6×10^4, Type D: Q = 0.059 m^3/s, Re = 9.8×10^4.

4.3 Interfacial velocity

The time averaged in interfacial velocity distributions are compared in Figure 7 for CHJ and Type B and D jumps with same Froude number (Fr_1 = 3.6). For all hydraulic jumps, positive and negative velocities were measured in the recirculation region resulting in some data scatter. Similarly, the velocity profiles in the shear region were similar for all jumps although the Type D jump had slightly lower velocites compared to the velocity distribution of CHJ and Type B jumps (Figure 7a). In the recirculation region, despite strong similarity in the velocity distributions, lower scatter was found for the Type D jump (Figure 7a). Overall the hydraulic jumps in the present study had very similar velocity distributions independent of channel slope.

The dimensionless maximum velocity decay for the present data V_{max}/V_1 is illustrated in Figure 7b as a function of the dimensionless distance from the jump toe. The present data are compared with previous studies of CHJ and Type B and D jumps (Figure 7b). The velocity decay was overall similar for all jumps included in the analysis albeit some differences in magnitude. Figure 7b shows similar velocity decays values between the data of Rajaratnam (1965) and the present study with lower velocity decay values compared to experimental data from other researchers (Resch and Leutheusser, 1972; Babb and Aus, 1981; Ohtsu et al., 1991; Chanson and Brattberg, 2000). The difference may be associated with the inflow conditions because apart from Rajaratnam (1965) and Wu and Rajaratnam (1996), the experiments were conducted with partially developed inflow conditions. In general, the velocity distribution was independent of the jump type meaning there was no influence of the slope and the Froude number on the velocity decay in hydraulic jumps.

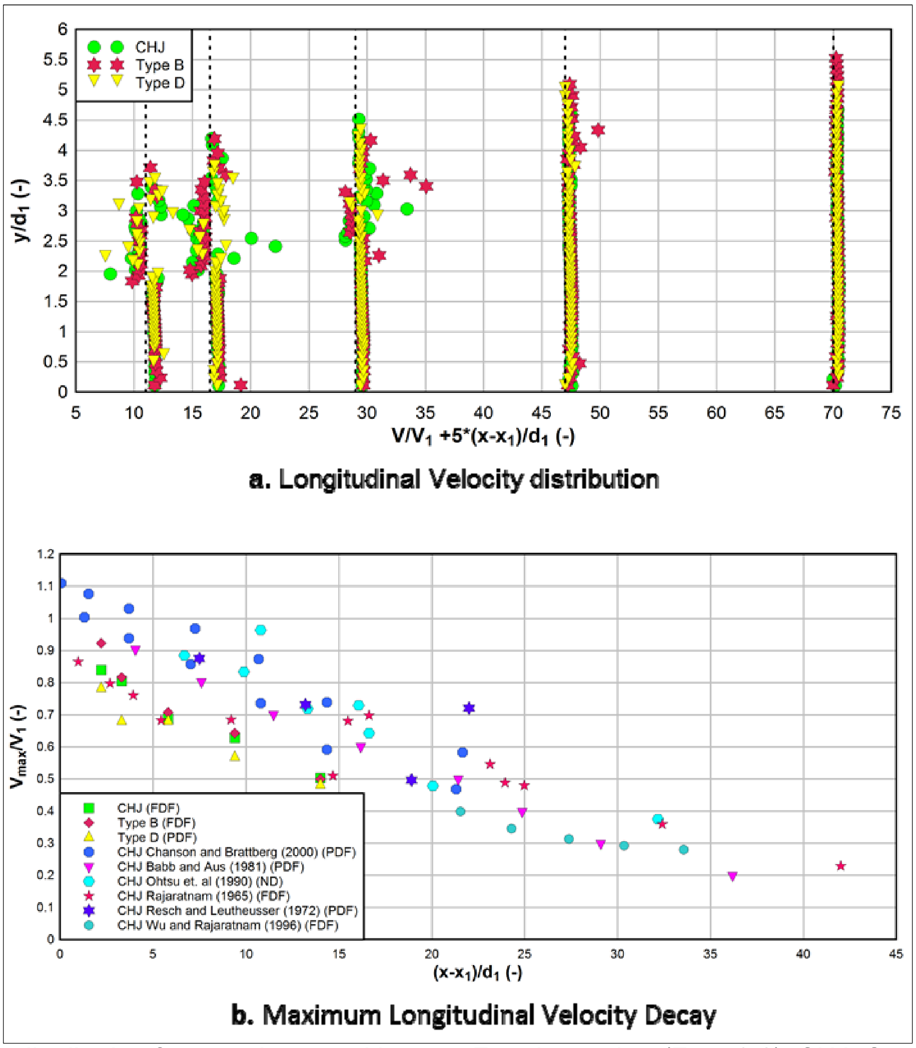

Figure 7. Velocity distribution for experiments with same Froude number (Fr_1 = 3.6); CHJ: Q = 0.068 m^3/s, Re = 1.13x10^5; Type B: Q = 0.058 m^3/s, Re = 9.6x10^4, Type D: Q = 0.059 m^3/s, Re = 9.8x10^4.

5 DISCUSSION

Differences in the void fraction profiles are identified for hydraulic jumps for the same Froude number (Figure 5). In contrast, the results obtained for hydraulic jumps with the same Reynolds number shows a closer agreement (Figure 8a). For these experiments, the void fraction profile exhibited similar distributions in the shear region and larger differences in the recirculation region while experiments conducted with the same Froude number show the opposite behaviour. For (x-x1)/d_1≥ 5.8, the differences between the hydraulic jump types increased. This result suggested that in the first half of the jump, the void fraction distributions are more susceptible to changes in Reynolds numbers for hydraulic jumps on slope.

The comparison of bubble count rate distributions with the same Reynolds number showed a close agreement in distributions for the three hydraulic jump types. CHJ had the lowest peak in the shear region while Type B jump exhibited the largest peak. Although CHJ presented the lowest peak, the differences are small compared to the differences identified for hydraulic jumps with the same inflow Froude number. Along the first half of the jump, the Type D jump showed the minimum bubble count rate distribution while CHJ and the Type B jump had similar distributions. In the second part of the jump, CHJ had the largest bubble count rates while the Type D jump showed the lowest values. Despite higher similarities in air-water flow properties between jumps with same Reynolds number, small differences were identified in the shear region for hydraulic jump Type D suggesting lower aeration for hydraulic jumps located entirely on the slope either for the same Froude or Reynolds numbers.

Overall, the comparative analysis of energy dissipation and air-water properties suggested optimum ennergy dissipation and air entrainment for CHJ. Type B jumps showed similar air-water properties and energy dissipation while Type D jumps presented the lowest energy efficiency. The results provided insights for the design of stilling basins although the experimental configuration was limited for a small range of Froude numbers. Further experiments are required to compare energy dissipation and air entrainment properties for a larger range of Froude numbers and steeper slopes. Future research should also include hydraulic jump fluctuations and further air-water flow properties.

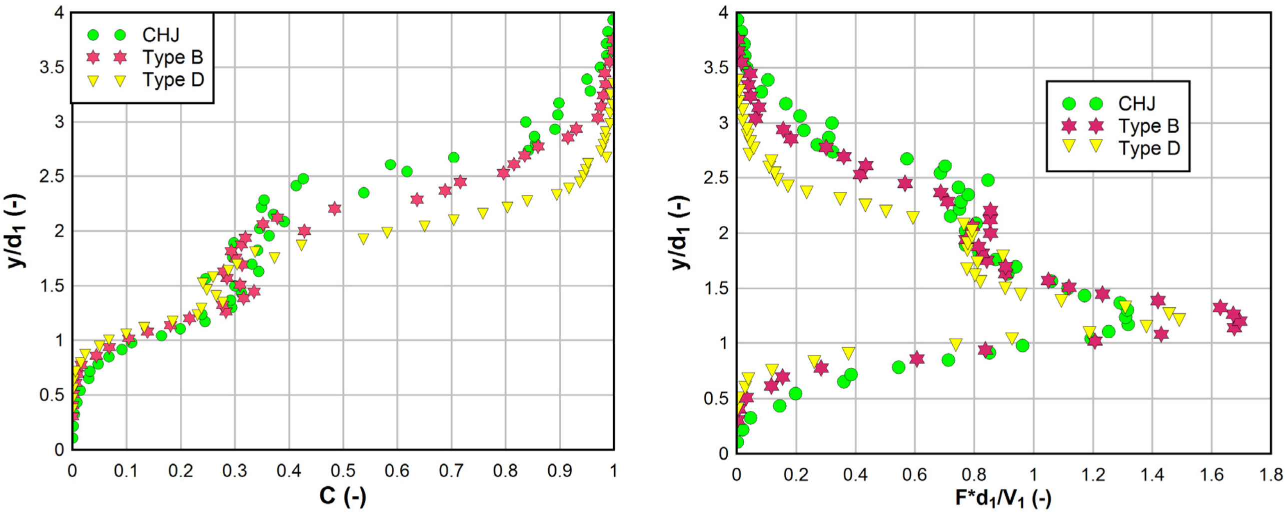

a. Void fraction distributions **b.** Bubble count rate distribution

Figure 8. Air-water flow properties for experiments with same Reynolds number (Re = 1.13×10^5, Q = 0.068 m^3/s) at $(x-x_1)/d_1=2.2$; CHJ: Fr_1 = 3.6; Type B: Fr_1 = 3.3, Type D: Fr_1 = 3.0.

6 CONCLUSION

New experiments are conducted in an open channel flume, researching the effects of channel slope upon the flow patterns and the air-water flow properties in hydraulic jumps. Three different types of hydraulic jumps were tested comprising classical hydraulic jumps on a horizontal channel as well as Type B and Type D jumps on a slope with θ = 2.5º. Visual observations of the flow patterns highlighted stronger jump toe fluctuations and higher water surface oscillations in hydraulic jumps on a horizontal channel. Energy dissipation analysis indicated that Type D jumps had the lowest energy dissipation efficiency. For the range of Froude numbers in the present study, the energy dissipation efficiency is similar between CHJ and the Type B jump. The comparative analyses of basic air-water flow properties highlighted strong effects of channel slope upon the flow aeration. For the same Froude number, lower flow aeration and lower number of air bubbles are measured for hydraulic jumps on a slope. The strongest differences in air-water flow properties are observed in the shear region which showed that the flow turbulence and air-water interactions are reduced for hydraulic jumps on the slope. Interfacial velocity distributions showed a similar profile for the three hydraulic jump types. A comparison between hydraulic jumps with similar Reynolds and Froude numbers respectively showed stronger differences for the Froude similitude and relatively close agreement for equal Reynolds numbers. Future experiments should be conducted for a larger range of Froude numbers and variations in bed slope to identify the effect of channel bed slope on the air-water flow properties for a wider range of flow conditions.

ACKNOWLEDGEMENTS

The authors acknowledge the technical support of Rob Jenkins (WRL, UNSW Sydney).

REFERENCES

Bakhmeteff, B.A. (1932). The Hydraulic Jump and Related Phenomena. *Trans. of the ASME*, 54, 1-12.
Bakhmeteff, B.A. & Matzke, A.E. (1938). The Hydraulic Jump in Sloped Channels. *Trans. of the ASME*, 60, 111-118.
Beirami, M.K. & Chamani, M.R. (2006). Hydraulic Jumps in Sloping Channels: Sequent Depth Ratio. *Journal of Hydraulic Engineering*, 132(10), 1061-1068.
Beirami, M.K. & Chamani., M.R. (2010). Hydraulic Jumps in Sloping Channels: Roller Length and Energy Loss. *Canadian Journal of Civil Engineering*, 37(4), 535-543.
Bidone, G. (1820). *Expériences sur le remou et sur la propagation des ondes*. (*Experiences about the Eddies and Waves Propagation*) Turin: De L'Imprimerie Royale. (In French)
Chanson, H. (1996). *Air Bubble Entrainment in Free-Surface Turbulent Shear Flows.* Academic Press, London, UK, 73–92.
Chanson, H. (2002). Air-Water Flow Measurements With Intrusive, Phase-Detection Probes: Can We Improve Their Interpretation?. *Journal of Hydraulic Engineering*, 128(3), 252-255.
Chanson, H. (2009). *Applied Hydrodynamics: An Introduction to Ideal and Real Fluid Flows*, CRC, Taylor and Francis Group, Leiden, Netherlands.
Chanson, H. & Brattberg, T. (2000). Experimental Study of the Air-Water Shear Flow in a Hydraulic Jump. *International Journal of Multiphase Flow*, 26(4), 583-607.
Ferriday, R. (1895). The Hydraulic Jump. *Engineering News*, 34(2), 28.

Felder, S. (2013). “Air-Water Flow Properties on Stepped Spillways for Embankment Dams: Aeration, Energy Dissipation and Turbulence on Uniform, Non-Uniform and Pooled Stepped Chutes”, *Ph.D. Thesis*. Department of Civil Engineering, University of Queensland, Australia.

Felder, S. & Chanson, H. (2015). "Phase-Detection Probe Measurements in High-Velocity Free-Surface Flows Including a Discussion of Key Sampling Parameters." *Experimental Thermal and Fluid Science*, 61, 66-78.

Felder, S. & Chanson, H. (2016). *An Experimental Study of Air-water Flows in Hydraulic Jumps with Channel Bed Roughness*. WRL Research Report WRL, 259, 1-166.

Felder, S. & Pfister, M. (2017). Comparative Analyses of Phase-Detective Intrusive Probes in High-Velocity Air-Water Flows. *International Journal of Multiphase Flow*; 90, 88-101.

Hager, W.H. (1989). B-Jump in Sloping Channel. *Journal of Hydraulic Research,* 27(1), 539-558.

Hager, W.H. (1990). Geschichte des Wassersprungs (History of Hydraulic Jumps). *Schweizer Ingenieur und Architekt*, 108(25), 728-735. (In German)

Hager, W.H., Bremen, R. & Kawagoshi, N. (1990). Classical Hydraulic Jump: Length of the Roller. *Journal of Hydraulic Research*, 25(5), 591-608.

Hager, W.H. (1992). *Energy Dissipators and Hydraulic Jump*. Netherlands: Kluwer Academic Publishers.

Kawagoshi, N. & Hager, W.H. (1990). B-Jump in Sloping Channel, II. *Journal of Hydraulic Research,* 28(4), 461-480.

Kindsvater, C.E. (1944). The Hydraulic Jump in Sloping Channels. *Trans. of the ASCE,* 109, 1107-1120.

Murzyn, F., Mouaze, D. & Chaplin, J.R. (2005). Optical Fibre Probe Measurements of Bubbly Flow in Hydraulic Jumps. *International Journal of Multiphase Flow,* 31, 141-154.

Naghash, M. (1994, August). Void Fraction Measurement Techniques for Gas-Liquid Bubbly Flows in Closed Conduits: A Literature Review. In *Fundamentals and Advancements in Hydraulic Measurements and Experimentation* 278-288, New York: American Society of Civil Engineers.

Narayanan, R. (1975). Wall Jet Analogy to Hydraulic Jump. *Journal of Hydraulic Division,* 101(3), 347-359.

Ohtsu, I. & Yasuda, Y. (1990). Discussion of ‘B-Jump in Sloping Channel’ by Hager WH. *Journal of Hydraulic Research,* 28(1), 105-119.

Ohtsu, I. & Yasuda, Y. (1991). Hydraulic Jump in Sloping Channels. *Journal of Hydraulic Engineering,* 117(7), 905-921.

Peterka, A.J. (1978). *Hydraulic Design of Stilling Basins and Energy Dissipators.* Department of the Interior, Bureau of Reclamation.

Rajaratnam, N. (1965). The Hydraulic Jump as a Wall Jet. *Journal of Hydraulic Division,* 91(5), 107-132.

Rajaratnam, N. (1967). Hydraulic Jumps. *Advances in Hydroscience,* 4, 197-280.

Rajaratnam, N. & Murahari, V. (1974). Flow Characteristics of Sloping Channel Jumps. *Journal of the Hydraulics Division,* 100(6), 731-740.

Resch, F.J. & Leutheusser, H.J. (1972). Le ressaut hydraulique: mesures de turbulence dans la région diphasique (The Hydraulic Jump : Turbulence Measurements in the Diphasic Region). *La Houille Blanche,* (4), 279-293. (In French)

Resch, F.J., Leutheusser, H.J. & Alemu, S. (1974). Bubbly Two-Phase Flow in Hydraulic Jumps. *Journal of Hydraulic Division,* 100(1), 137-149.

Wang, H., Felder, S. & Chanson, H. (2014). "An Experimental Study of Turbulent Two-Phase Flow in Hydraulic Jumps and Application of a Triple Decomposition Technique." *Experiments in Fluids*, 55(7), 1775-18.

Wu, S. & Rajaratnam N. (1995). Free Jumps, Submerged Jumps and Wall Jets. *Journal of Hydraulic Research,* 33(2), 197-212.

Yasuda, Y. & Ohtsu, I. (2008). Flow Characteristics of Plunging Flows in Steep Sloping Channels with Horizontal Channel Portion. *Acta Mechanica,* 201, 95-104.

Zhang, W., Liu M., Zhu, D.Z. & Rajaratnam, N. (2014). Mean and Turbulent Bubble Velocities in Free Jumps for Small to Intermediate Froude Numbers. *Journal of Hydraulic Engineering,* 140(11), 1-9.

PHYSICAL MODELING OF OVERTOPPING INDUCED FLUVIAL DIKE FAILURE: EFFECTS OF MAIN CHANNEL FLOW AND FLOODPLAIN INNUNDATION

ISMAIL RIFAI[1], SEBASTIEN ERPICUM[2], PIERRE ARCHAMBEAU[3], DAMIEN VIOLEAU[4], MICHEL PIROTTON[5], BENJAMIN DEWALS[6] & KAMAL EL KADI ABDERREZZAK[7]

[1] EDF R&D, National Laboratory for Hydraulics and Environment, Saint Venant Laboratory for Hydraulics, Chatou, France, and ArGEnCo Department, Research Group Hydraulics in Environmental and Civil Engineering (HECE), University of Liège, Liège, Belgium
i.rifai@doct.ulg.ac.be
[2,3,5,6] ArGEnCo Department, University of Liege (ULg), Research Group of Hydraulics in Environmental and Civil Engineering (HECE), Liège, Belgium
s.erpicum@ulg.ac.be; pierre.archambeau@ulg.ac.be; michel.pirotton@ulg.ac.be; b.dewals@ulg.ac.be
[4,7] EDF R&D and National Laboratory for Hydraulics and Environment, and Saint Venant Laboratory for Hydraulics, Chatou, France
damien.violeau@edf.fr; kamal.el-kadi-abderrezzak@edf.fr

ABSTRACT

Fluvial dikes have been constructed as flood defense structures, but their failure may lead to casualties and major damages in protected areas. Flow overtopping is listed as the main cause of dike failure. An accurate assessment of the breach evolution is a prerequisite to a sound flood risk assessment and management. In contrast, the current knowledge of physical processes involved in fluvial dike failure by overtopping remains highly fragmented. This paper presents experimental tests on the breaching of homogenous sand-dikes in a fluvial configuration, i.e. the upstream flow is parallel to the longitudinal dike axis. Overtopping is initiated over a pilot notch at the dike crest. Experiments are performed for different inflow discharges in the main channel and under different levels of floodplain confinement. The transient evolution of the dike geometry is monitored using laser profilometry technique. The detailed reconstruction of the breach formation and expansion provides key insights into the mechanisms involved in the failure of fluvial dikes. Results show that the breach development differs highly from experiments disregarding the flow parallel to the dike axis (i.e. frontal configuration) as in the fluvial configuration where the breach develops mainly in the flow direction and the floodplain water level, strongly conditions the breach horizontal and vertical extents.

Keywords: Breach; floodplain plain confinement; fluvial dike; overtopping; subaqueous reconstruction.

1 INTRODUCTION

Dikes along river banks are built to channelize the flow and limit lateral riverbed migration, or as defense structures against floods. Deterioration of these structures due to lack of maintenance, poor management of the protective cover, animal burrows (Orlandini et al., 2015) and exposure to frequent extreme events increase dike vulnerability. Overtopping is identified as the main cause of failure (Vorogushyn et al., 2010, Fry et al., 2012), occuring typically if the river discharge exceeds the design value of the dike during a flood event or typically when the water level exceeds the dike crest or the flow overtops a weak dike segment. However, the current knowledge on the physical processes underpinning fluvial dike failure due to overtopping remains limited, although an accurate prediction of the breach geometry and outflow hydrograph are paramount to estimate the inundation risks and to plan emergency operations. The available knowledge relies generally on statistical analyses of historical data (e.g. Froehlich et al., 2008; Jandora and Říha, 2008), numerical modeling (e.g. Wu et al., 2012; Kakinuma and Shimizu, 2014), and on laboratory experiments. Characterization of real-world dike failure events remain limited as their monitoring is hardly feasible for safety reasons.

The breach process has been often assessed using standard models, mostly developed empirically from frontal dike (i.e. dam) configurations. These models disregard the specific boundary conditions and flow features related to the fluvial configuration (Roger et al., 2009), though their application to field cases remains questionable.

Abundant and extensive experimental studies on frontal configurations exist (Rifai et al., 2015), covering breach development and shape, effects of upstream water level (e.g. falling or constant), dike material (e.g. cohesion, grain size diameter, compaction, water content) as well as dike reinforcements. However, those on fluvial dike configurations remain fragmented with differences in the outcomes (Rifai et al., 2016a). In addition, crucial aspects, such as the effect of the main channel flow momentum and the feedback of the floodplain inundation on the breach development and the breach hydrograph, remain unanswered.

The present study tackles overtopping induced fluvial dike breaching via experimental modeling. The presented tests simulate the effect of various flow conditions in the main channel and different floodplain confinement levels. The experiments are part of a broader research work including additional tests with different channel and dike dimensions as well as dike material and reinforcement. The paper is organized as follows: Section 2 presents the experimental setup, instrumentation, and test program. Results are presented in Section 3 and discussed in Section 4, followed by conclusion in Section 5.

2 EXPERIMENTS

2.1 Experimental setup

A series of tests (Table 1) were conducted at the Engineering Hydraulics Laboratory of the University of Liège, Belgium. The main channel consisted of a 10 m long and 1 m wide, straight flume opened over 3 m on one side toward a 4.3 m × 2.5 m floodplain (Figure 1). The flume and floodplain were at the same level and the side opening was closed with a sand dike. The flume and floodplain were covered with impermeable whitewash coatings to ensure roughness's continuity between the flume, floodplain and sand dike. The floodplain edges were either free or confined. In the former case, the water across the breach was freely discharged with no tail water effects. In the latter case, a wood panel (i.e. confinement) was added to simulate floodplain inundation inducing tail water effects. The seepage flow was limited by installing a drainage system at the bottom of the dike (Figure 1). The drained water was collected in a reservoir located below the dike.

A perforated plane was used to regulate the flow in the main channel. For a given inflow discharge Q_i, the number of holes and their arrangement were selected to ensure that the water level in the main channel was at the dike crest level. Evenly distributed holes in the perforated plane allow for a quasi-uniform velocity distribution over the cross-section.

The dike was 3 m long, 0.3 m high and trapezoidal in shape with 1:2 (V:H)of inner and outer slopes. The crest was 0.1 m wide. The dike was composed of non-cohesive, uniform sand of median diameter d_{50} = 1 mm and sorting coefficient $\sigma = (d_{84}/d_{50}+d_{50}/d_{16})/2 = 1.22$, with d_{16} = 0.84 mm and d_{84} = 1.24 mm. The sand had a density of 2500 kg/m^3, a bulk density of 1600 kg/m^3 and a porosity of 0.36. To control the location of the initial overtopping, a 0.02 m deep and 0.1 m wide initial notch was cut in the dike crest (Figure 1).

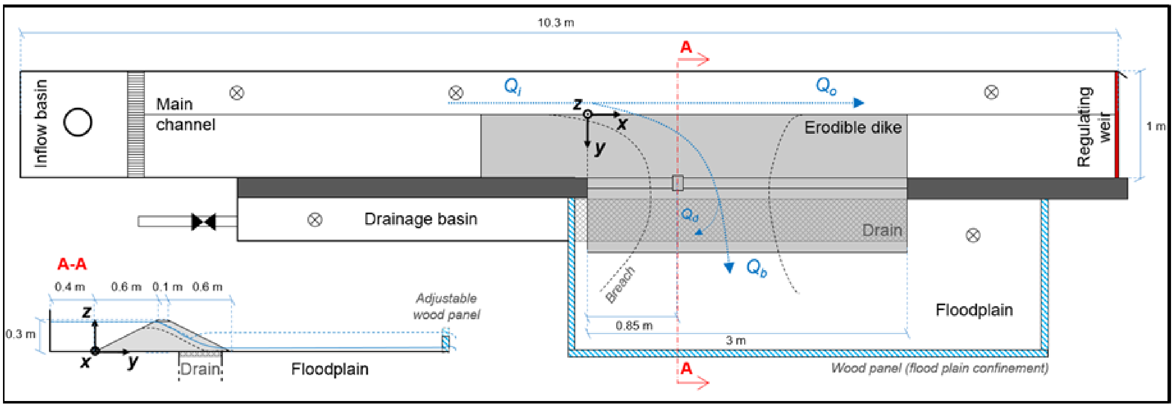

Figure 1. Setup plan view and dike cross-section (⊗ designate the location of ultrasound probes).

2.2 Test program

Table 1 summarizes the considered configurations for 11 tests presented in this paper. The inflow discharge Q_i was constant during each test. The inlet Froude number $\mathbf{F}_i$ was in the range between 0.066 and 0.189. Tests 1 to 5 was conducted with different inflow discharges, Q_i and a free floodplain. Tests 3a, b, and c investigated repeatability of dike breaching experiments. Tests from 6 to 9 investigate the effect of floodplain confinement defined by the ratio $C_F = Z_c/Z_d$ with Z_c the water level fixed in the floodplain and Z_d the dike height.

For each test, the dike was placed by staking and compacting manually the sand so as to avoid any structural defect. The main channel was filled progressively with a discharge equal to about 75% of the test inflow discharge Q_i. The dike and drainage system were inspected and the inflow discharge was then increased up to Q_i. The water level in the main channel increased and overtopped the dike over the initial notch, resulting in the dike breaching. Tests were stopped when the breach stabilized or when one of the breach sides met the rigid wall of the flume.

Table 1. Test configurations.

Test n°	1	2	3a	3b	3c	4	5	6	7	8	9
Q_i (m^3/s)	0.02	0.03	0.04	0.04	0.04	0.05	0.057	0.04	0.04	0.04	0.04
$\mathbf{F}_i$	0.066	0.100	0.133	0.133	0.133	0.166	0.189	0.133	0.133	0.133	0.133
C_F	0 % (No floodplain confinement)							16.7 %	33.3 %	50 %	66.7 %

The confinement of the floodplain (Tests 6 to 9) was achieved by contouring the floodplain perimeter with a wood panel. This simulates the case of the breaching of a dike with a floodplain already flooded or a confined floodplain with a rising water level as the breach is still evolving. In those tests, prior to overtopping, water was pumped into the floodplain until the water level reached the wood panel level. The water level in the floodplain was continuously monitored during each test and remained roughly at the desired level.

2.3 Measurements

Water levels in the main channel (and confined floodplain) were measured using ultrasonic sensors of ± 1 % accuracy (mic+35/IU/TC by Microsonic). The drainage discharge Q_d was deduced from the water level evolution in the drainage basin. The drainage discharge was limited at 2 l/s at the test start and at 1.2 l/s for the remaining test duration. The inflow discharge Q_i was recorded using an electromagnetic flowmeter of ± 0.4 % accuracy (Siemens MAG 5000W). The channel outflow discharge Q_o was determined by measuring the water level downstream of the regulating weir and upstream of a rated V-notch weir. The breach discharge Q_b was deduced from the mass balance in the main channel.

The breach geometry development was monitored continuously using a non-intrusive laser profilometry technique. The method consists of the swiping of a laser sheet (Z-Laser Z30M18S3-F-640-LP75) over the breaching dike. The acquisition was set to Full-HD resolution (1920×1080 pixels) and a recording speed of 60 frames/s. One complete swiping lasted about 1.5 second resulting in roughly 90 profiles for each reconstruction. Subaqueous parts of the dike that was subjected, was equally affected by refraction. This causes a biased image of the dike and consequently a distorted 3D reconstructed geometry that was addressed by adding a refraction correction module to the laser profilometry algorithm. This module relies on the Snell-Descartes law assimilating the water surface in the channel and floodplain to a horizontal plane and the flow across the breach is approximated as an inclined plane. Details of the breach geometry reconstruction are given by Rifai et al. (2016b).

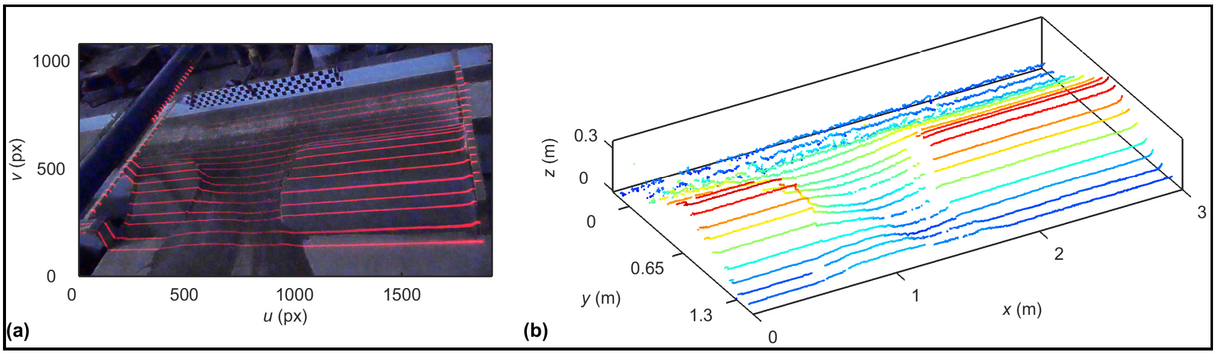

Figure 2. Three-Dimensional (3D) Dike geometry reconstruction. (a) raw images and (b) 3D reconstruction.

3 RESULTS

3.1 General observation on fluvial breaching

Tests 3a, 3b, and 3c were conducted under the same boundary conditions and were aimed to assess the repeatability of the dike failure experiments. Figure 3a to d shows the longitudinal profiles of the dike and a good overall agreement between the three experiments is obtained. However, during the breach widening, effects of apparent cohesion appear on the emerged sides of the breach, and the breach expansion becomes less gradual, which can explain some gaps in the reconstructions regarding these parts of the breach. The evolution of the main channel water level and the breach hydrograph (Figure 3e and f) confirms the repeatability of the experiments as well.

The qualitative description of the breaching process presented hereafter is valid for all laboratory tests without floodplain confinement. For the sake of brevity, results are shown for Test 3a only.

By increasing the inflow discharge to Q_i, the water level in the main channel increases and overtops the initial notch. Local erosion of the dike crest was triggered. During this very first phase, the erosion rate was relatively slow as the overtopping flow height was still very low. Gradually, as the breach deepens, overtopping heights increase and the erosion process was accelerated. Deepening and widening of the breach was observed with the breach centerline being shifted toward the downstream end of the channel. The hour glass shape of the breach, as reported for dam breaching experiments (Frank & Hager 2016; Rozov 2003), forms but loses it symmetry as the breach expands. Upstream of the initial notch (x < 0.85 m), erosion of the channel side of the dike is observed. It was caused by the acceleration of the flow upstream of the breach (from 0.19 m/s to 0.97 m/s) increasing the shear stress applied on the channel-side of the dike. The breach widening continues exclusively toward the downstream of the channel by successive slope failures of the breach downstream side and transport of the collapsed material by the breach flow.

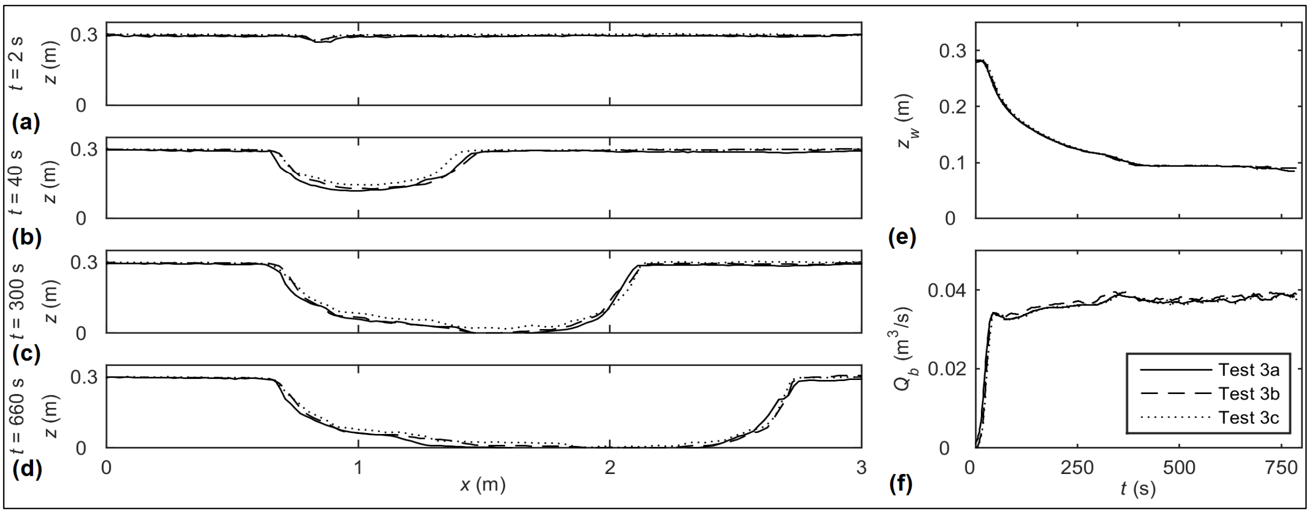

Figure 3. (a) to (d) Longitudinal profiles of the dike at different times, (e) water level evolution in the main channel, and (f) breach flow hydrograph for tests 3a, 3b, and 3c.

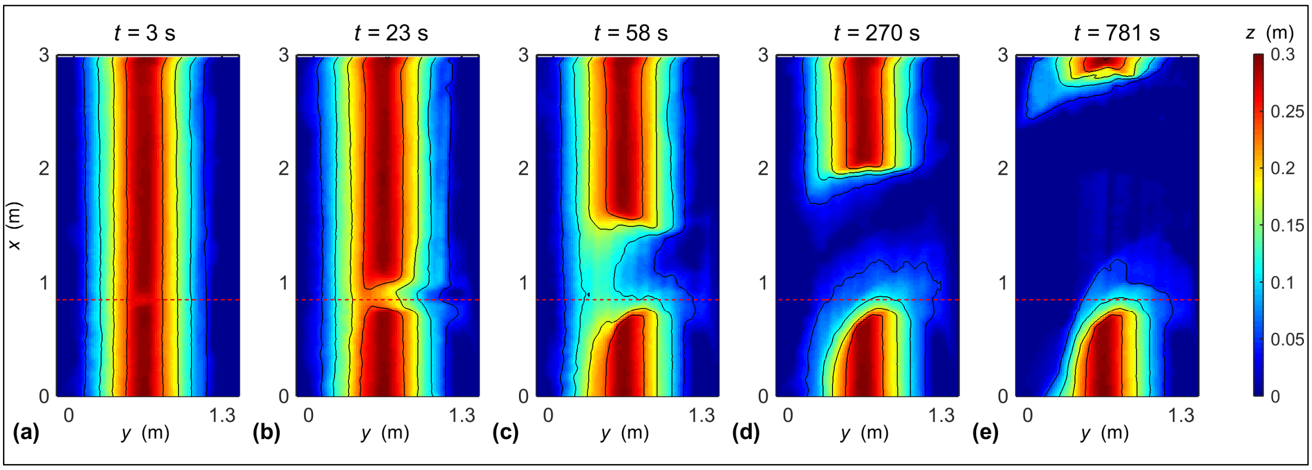

Figure 4. Reconstructed breach topography for Test 3a. (--) indicates the position of the initial notch.

3.2 Effect of inflow discharge

Tests f1 to 5 were conducted with different inflow discharges (Table 2). Figure 5 shows the breach profiles for tests with Q_i ranging from 0.02 to 0.05 m^3/s. The dynamics of the breach evolution was strongly affected by the inflow discharge Q_i. The breach deepens and widens faster for tests with a higher inflow discharge. Therefore, the duration of the breaching process was influenced by the flow velocity in the main channel. The breach shapes reveal also a higher erosion of the downstream side of the breach as the inflow discharge increases, as shown in Figure 5b and c. For all tests, the breach discharge Q_b quickly rises during the first minute. For tests 1 and 2, the peak discharge exceeds the inflow discharge Q_i. The breach discharge then tends to stabilize toward its final value that ranges from about 90 to 98 % of the inflow discharge. The gap between Q_i and the final Q_b increases as Qi increases.

3.3 Effect of the floodplain confinement

Tests 3a and 6 to 9 were conducted with different levels of the floodplain confinement. Figure 6 shows the variation of the channel water level and the breach discharge. Tests 3a and 6 were stopped because the breach reached the limits of the erodible dike (Figure 1). In contrast, tests 7, 8, and 9 were stopped as the breach stabilized.

Figure 6b shows that a small floodplain confinement (16,7 %) had no effect during the first phase of fast increase in the breach discharge. Once the breach invert reaches the floodplain water level, the breach evolution was slowed down and the breach discharge Q_b stabilize at a lower value compared to the test without floodplain confinement (Test 3a). Tests with higher C_F show the same feature with an earlier deviation of the breach hydrograph from the reference test (3a). The water level in the main channel decreases as expected values close to the water level was fixed at the floodplain. The difference between the stabilized channel water level and the floodplain water level decreases as C_F increases. This observation agrees with low values of Q_b of the corresponding tests and to the decelerated breach evolution rate (Figure 7).

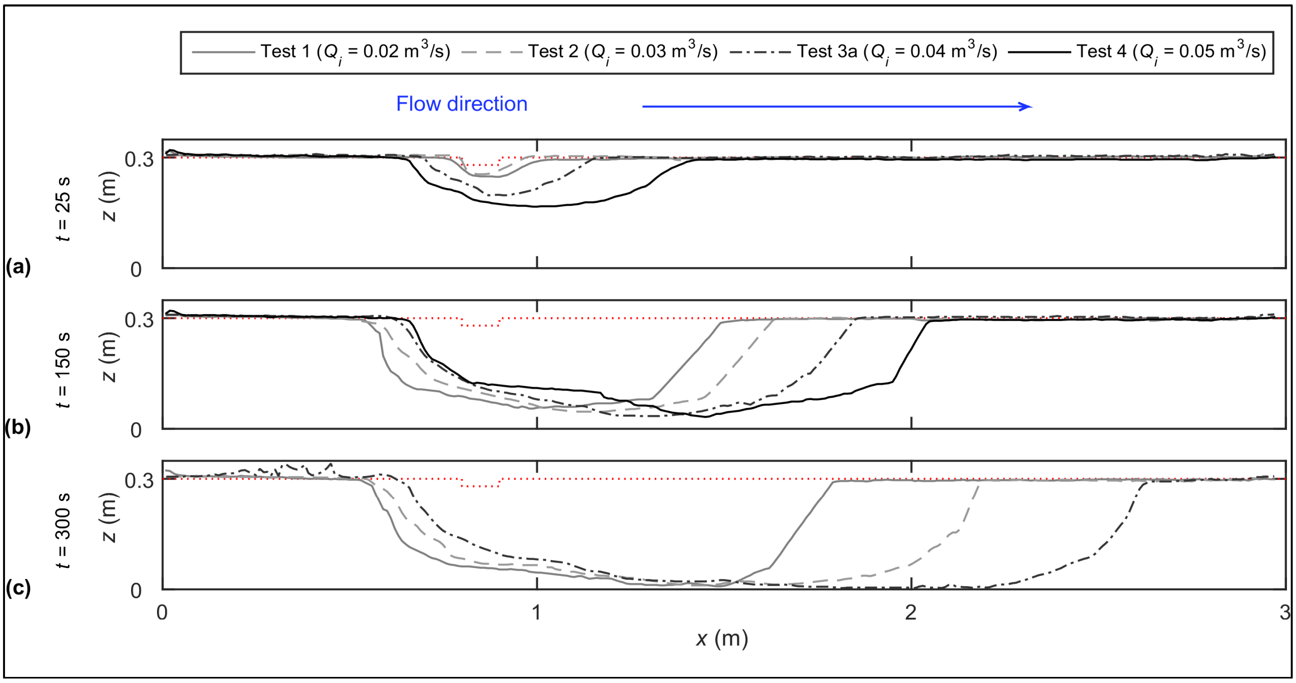

Figure 5. Longitudinal breach profiles at different times (Test 4 ended at t = 481 s). (····) indicates initial dike profile shape.

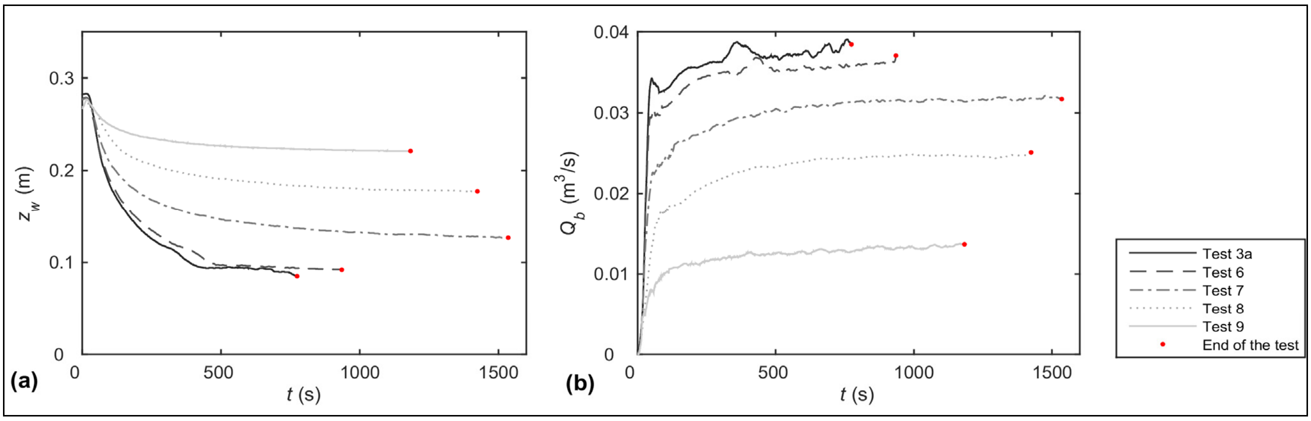

Figure 6. (a) Water level evolution in main channel, (b) breach flow hydrograph.

Overall, the breach evolution was highly influenced by the floodplain confinement (Figure 7). Increasing the floodplain confinement level leads to the erosion of the channel side of the dike and the upward breach widening decrease. The breach deepening and downward widening were also reduced and the overall breach extent was limited. On the other hand, the breach geometry shows a clear preferential pattern of the breach flow, with the *breach channel* contracted toward the downstream of the channel. The breach channel deviation angle to the channel axis was lower for higher floodplain confinement levels.

4 DISCUSSION

4.1 Breach widening

In the case of a frontal configuration (*i.e.* dam configuration without any downstream confinement), the evolution of the breach is a function of the water level upstream of the dike and the intrinsic characteristics of the dike material (Coleman et al. 2002; Froehlich 2008). The breach geometry displays a symmetrical evolution as the breach flow remains symmetrical as well. The present experiments conducted with a flow parallel to the dike axis strongly differ from analogous frontal experiments where the breach develops almost exclusively in the channel flow direction and the channel flow momentum has a strong impact on the breach widening. As presented in section 3.1 and illustrated in Figure. 4 for the test 3a, in all tests, the breach starts developing almost symmetrically with an *hour glass* shape, in agreement with dam configuration observations. However, the channel flow momentum causes the breach flow distribution to be uneven and more concentrated toward the downstream of the channel, and thus, the breach gradual erosion moves to be more concentrated toward the same side. As the breach expands and the upstream channel flow velocity increases, the channel flow momentum increases and erosion intensifies at the downstream channel side of the breach toe. The breach expansion is less gradual and marked by consecutive slope collapses exclusively on the channel downstream side.

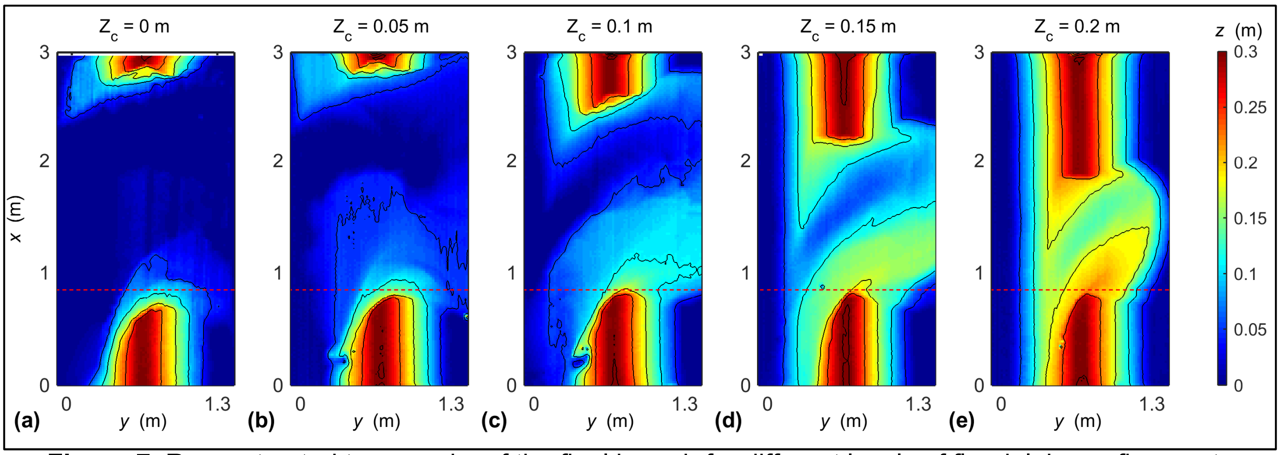

Figure 7. Reconstructed topography of the final breach for different levels of floodplain confinement: 3a (a), 6 (b), 7 (c), 8 (d), and 9 (e). (--) indicates the position of the initial notch.

Experiments conducted with different inflow discharges highlight this aspect. An increase in the channel inflow discharge results in faster breach widening, increasingly shifted toward downstream, and a more profiled breach shape (Figure. 5). The increase in the channel inflow discharge also affects the orientation of the breach channel. For a given breach width, the breach deviation angle increases with increasing inflow discharge, which underlines the impact of the channel flow momentum on the breach widening.

4.2 Breach deepening

In the presented tests, the breach evolution is mainly governed by bed load caused by the flow shear stress over the breach invert. Thus, the breach evolution is a result of; firstly, a deepening of the breach caused by the erosion of its invert and a simultaneous adjustment of the breach sides to satisfy the friction angle of the dike material. This is reflected by the almost parabolic breach invert during the gradual breach evolution phase (Figure 5a). The reduction of the difference of the water level between the upstream and downstream sides of the breach due to floodplain confinement reduces the breach flow velocities and therefore the subsequent bed load. The breach evolution (both the widening and deepening) becomes slower. In addition, the “fan opening” of the breach flow at the floodplain induces a reduction of the sediment transport capacity of the flow and the deposition of the eroded material at the breach toe (Figure 7d and e). At the final recorded states, the breach invert levels at the crest section are 0, 0, 0.01, 0.06, and 0.14 m for tests with Z_c = 0, 0.05, 0.1, 0.15, and 0.2 m respectively. For tests in which the non-erodible bottom of the model was not reached (i.e. Tests 7 to 9), the maximum breach flow depth is about 0.09, 0.09, and 0.06 m (for Z_c = 0.1, 0.15, and 0.2 m respectively), denoting to a decrease in the erosion capacity of the flow.

5 CONCLUSION

Laboratory experiments are conducted to better understand overtopping induced fluvial dike breaching. The breach geometry is continuously monitored with a non-intrusive high resolution technique. Two series of tests have been presented, investigating: (1) variations of the inflow discharge and (2) modifications of the floodplain confinement level. Tests show that erosion occurs preferentially in the direction of the flow in the main channel and the breach widening is intensified by the increase in the inflow discharge. The breach evolution rate is also found to be highly dependent on the floodplain confinement because previous or ongoing flooding of the floodplain hampers the erosion rate and induces shallower breaches.

Undoubtedly, fluvial dike breaching differs from dam breaching as the channel flow momentum has a strong impact on the breach evolution process. The breach evolution and formation time cannot be expressed only as a function of the water level upstream of the dike and of the intrinsic dike characteristics; a characterization of the flow momentum must be included. In addition, flooding downstream of the breach is often observed during dike breaching events and its feedback on the breach development or stabilization should be considered. Such peculiarities of the fluvial configuration are to be accounted for in the prediction of breach evolution because usual dam breach models do overlook these effects.

The present study is an addition to existing literature on dam breach configurations and is part of ongoing work aiming to study overtopping induced fluvial dike breaching, covering a broader range of main channel, floodplain and dike configurations as well as dike material.

REFERENCES

Coleman, S.E., Andrews, D.P. & Webby, M.G. (2002). Overtopping Breaching of Noncohesive Homogeneous Embankments, *Journal of Hydraulic Engineering*, 128(9), 829–838.

Froehlich, D.C. (2008). Embankment Dam Breach Parameters and their Uncertainties. *Journal of Hydraulic Engineering*, 134(12), 1708–1721.

Fry, J., Vogel, A., Royet, P. & Courivaud, J. (2012). Dam Failures by Erosion: Lessons from ERINOH Data Bases. *6th International Conference on Scour and Erosion (ICSE),* Paris, 273-280.

Jandora, J. & Říha, J. (2008). *The failure of embankment dams due to overtopping*, Brno University of Technology, Brno, Czech Republic.

Kakinuma, T. & Shimizu, Y. (2014). Large-Scale Experiment and Numerical Modeling of a Riverine Levee Breach, *Journal of Hydraulic Engineering*, 140(9), 1–9.

Orlandini, S., Moretti, G. & Albertson, J.D. (2015). Evidence of an Emerging Levee Failure Mechanism causing Disastrous Floods in Italy. *Water Resources Research*, 51, 7995–8011.

Rifai, I., Erpicum, S., Archambeau, P. Benoit, M., Pirotton, M., Dewals, B. & El kadi Abderrezzak, K. (2015). Physical Modeling of Lateral Dike Breaching due to Overtopping. *9th symposium of River Coastal and Estuarine Morphodynamics (RCEM),* Iquitos.

Rifai, I., Erpicum, S., Archambeau, P., Violeau, D., Pirotton, M., Dewal, B. & El kadi Abderrezzak, K. (2016a). Sensitivity of the Breaching Process in the Case of Overtopping Induced Fluvial Dike Failure. *8th International Conference on Fluvial Hydraulics (River Flow)*, Saint Louis, Missouri.

Rifai, I., S. Erpicum, P. Archambeau, D. Violeau, M. Pirotton, K. El kadi Abderrezzak, & B. Dewals (2016b). Monitoring topography of laboratory fluvial dike models subjected to breaching based on a laser profilometry technique. 13th International Symposium on River Sedimentation (ISRS), Stuttgart.

Roger, S., Dewals, B.J., Erpicum, S., Schwanenberg, D., Schuttrumpf, H., Kongeter, J. & Pirotton, M. (2009). Experimental and Numerical Investigations of Dike-Break Induced Flows. *Journal of Hydraulic Research*, 47(3), 349–359.

Rozov, A.L. (2003). Modeling a Washout of Dams. *Journal of Hydraulic Research*, 41(6), 565–577.

Vorogushyn, S., Merz, B., Lindenschmidt, K.E. & Apel, H. (2010). A New Methodology for Flood Hazard Assessment Considering Dike Breaches. *Water Resources Research*, 46(8), 1–17.

Wu, W., Marsooli, R. & He, Z. (2012). Depth-Averaged Two-Dimensional Model of Unsteady Flow and Sediment Transport due to Noncohesive Embankment Break/Breaching. *Journal of Hydraulic Engineering*, 138(6), 503–516.

Proceedings of the 37th IAHR World Congress
August 13 – 18, 2017, Kuala Lumpur, Malaysia

MULTI-INDEX EVALUATION ON RIVER HEALTH ASSESSMENT: IWE METHOD

HUIDONG SU [(1)], TIANTIAN JIN [(2)], SHI FENG [(3)] & JUNQIANG LIN [(4)]

[(1,2,3,4)] State Key Laboratory of Simulation and Regulation of Water Cycle in River Basin, China Institute of Water Resources and Hydropower Research, Beijing, China;
694702713@qq.com; jtt_05@163.com; fengshi@iwhr.com; linjq@iwhr.com
[(1)] College of Earth Environmental Science, Lanzhou University, Lanzhou, China

ABSTRACT

The current river health assessment is mainly done by multi-index evaluation method, and the decisive factors are index, weight and index assignment. Due to the variation of rivers, the construction of index system and assignment of weight and index are ambiguous, complex and subjective. Based on these facts, this paper puts forward a new method of river health assessment based on the summary of previous studies which is the IWE method. In the IWE method, the weights of different rivers are relatively fixed and widely applicable, but the threshold values which determine the index assignment are variable and changeable with different rivers. The steps of river health assessment by IWE method are as follows: firstly, construct a Widely applicable index system; secondly, assign the weight of each index to be a fixed value which is appropriate for all kinds of rivers; thirdly, show the index quantification method and threshold index assignment principle variable to adapt to different rivers, namely the index key threshold variable to reflect the different types of rivers and lastly,assess the river health by comprehensive health index of each index and the weight assignment. Here, it should be noted that the river health assessment should focus on the valuation of different indicators, and carry out river ecological restoration plus management accordingly.

Keywords: IWE method; river health assessment; weight; assignment; critical threshold.

1 INTRODUCTION

With the development of ecosystem health, the healths of rivers are being paid more and more attention, and the research on river health in China has a long history of more than 20 years. However, until now, the connotation of river health is not unified, and the principles, methods, indicators and standards of river health assessment vary from one and another,

What is a healthy river? At present, domestic and foreign scholars has given many definitions. Simpson et al. (1999) and Karr (1999) respectively regarded the undisturbed rivers and the ones which are disturbed but their value are not degraded now and in the future as healthy rivers. Fairweather (1999) introduced the social value of river system and the political and economic factors into the river health assessment. Rogers and Biggs (1999) set the goal of river health management as the basis of social expectations. According to the situation of our country, most scholars believe that the river health evaluation is the foundation of river protection and management and sustainable utilization (Wu et al., 2005; Gao, 2006; Wang et al., 2014). Based on this understanding, the river health assessment highlights the guidance of river management. In order to survive and develop, the necessity and rationality of development of water resources should be taken into account in the river health (Meyer, 1997; Vugteveen et al., 2006).In the process of China's rapid economic development, the contradicting problems between human and river are increasingly serious based on the current social and economic structure and the level of science and technology. In addition to the needs of the theoretical research, river health assessment should also be the guiding role of river management in future.

At present, the main method of river health assessment is multi-index method. The three decisive factors in multi-index river health assessment are: index, weight and index assignment respectively. Domestic and foreign scholars do a lot of research on the factors (Boulton, 1999; Wang et al., 2014). However, the calculation of the comprehensive index of river health is often subjective and is often difficult to compare and thus it becomes a difficulty in river health assessment. In order to promote river ecological protection and restoration work, plus be convenient for the river health assessment and management work, it is in urgent need of a set of simple and objective methods which are suitable for the national conditions. This can be used to achieve horizontal contrast and for decision making. Based on this, summing up the previous research and study, this paper puts forward a new method: IWE method, which the three factors are effectively combined with simple, scientific and feasible method of river health assessment.

2 SUMMARY OF RIVER HEALTH ASSESSMENT

Multi-index evaluation of river health is the main method to evaluate river health at home and abroad. Among the multi-index evaluation of river health cases, the representative ones are mainly in the United States, Australia, Britain, South Africa and the European Union and others (see Table 1).

Table 1. Multi-index for main river health assessment.

Australia	ISC	Evaluation content: Based on the 5 evaluation factors, such as river hydrology, water quality, aquatic life, morphological characteristics and riparian zone, the evaluation index system of the 22 indexes was constructed Main principle: The index assignment was to compare the current situation of the river and the reference system, and to evaluate the health status of the river on the basis of scoring (Parsons, 2002)
America	RBPs	Evaluation content: The index including algae, macroinvertebrates, aquatic organisms, fish and habitat Main principle: Standardization for monitoring and evaluation methods (Barbour et al., 1999)
The UN		Evaluation content: Background information, river data, river bank erosion, riparian zone characteristics, sediment characteristics, vegetation types, land use and other indicators Main principle: Evaluation of river ecological environment by investigating the difference between the current situation and the state of human disturbance (Raven et al., 1998)
The EU	EU Water Framework Directive	Evaluation content: Evaluation elements including biological, hydrological, chemical and physical (Chave, 2001; Wang et al., 2014)
China	MWR V1.0	Evaluation content: The index system was constructed from five factors: hydrology, water quality, biology, physical structure and social economy Main principle: It can provide reference for the construction of index system, the quantification of index and the determination of index threshold (The Ministry of Water Resources Water Conservancy Department of River Lake National Health Technology Group, 2010)

There are two main differences between domestic and foreign methods of river health assessment. One is the foreign assessment emphasis on river ecosystem health where the service function of the rivers is regarded as an important part in domestic research. The other is foreign evaluation criteria for each indicator by comparing between the the current state and the state without interference, which is constantly changing. In order to construct a universally applicable method for most rivers in China, the China Yangtze River, the Yellow River and the Pearl River system in accordance to health assessment experience and the domestic evaluation criteria for each indicator is trying to be established at a relatively consistent evaluation standard.

The three decisive factors of river health assessment are index, weight and index assignment, respectively. The index system, despite that the name may be different and it's connotation and the significance may be variable, it involves five elements including river hydrology, water quality, biological, physical form and service function (or social economy).So far, it is widely believed that the index weight of each river varies with river types and plus the methods of assigning weight are plenty, such as AHP (Deng et al., 2014), fuzzy evaluation method (Wang, 2007), multi level grey correlation method (Luo, 2008) the combination-weight method (Shan et al., 2012) and expert-evaluation method. As for index assignment, however, current research focuses on index system scoliosis surgery and little research focus on standardization of index assignment (The Ministry of Water Resources Water Conservancy Department of River Lake National Health Technology Group, 2010; Wang et al., 2014; Wu et al., 2005).

The previous three factors: index, weight, the index assignment varies at various rivers. This means, even for the same river, scholars will get different conclusions because of different professional knowledge and research purposes with great subjectivity of index type, index weight and index assignment at different points. The weight given by different scholars will be different and the evaluation results are not the same as well. For different rivers, the difference will be greater. So these methods are unable to avoid the influence of subjective factors on the distribution of the weight.. For example, at the same river, experts in different fields of river health assessment's results can be never be compared due to variety of datsat the same point of river,and because of this the evaluation results can never be a good guide for use of management and recovery of the river. The index system and weights that is constructed by such a set of methods that it is applied only to a river health assessment will not be applicable for others and will not be suitable for the promotion of the subjective data. This is the reason why it is difficult to compare between different river health assessment results. There is also a great deal of doubt about the allocation of weights, and many scholars begin to doubt the reliability of multi index evaluation of river health. Some scholars prefer to show the results of the radar map for each element of the river evaluation rather than give a comprehensive assessment index of the health of the river (Wu et al., 2005). Therefore, it is urgent to find a standardized method of river health assessment, which is applicable to a wide range of rivers and at the same time is simple and feasible where the results are credible.

3 PRINCIPLE OF THE IWE METHOD

IWE method (Index-Weigh-Eigenvalue method, namely Index-Weigh-Index assignment method) was use to solve the problem of weight assignment. First of all, we will discuss the problem of allocation of index weight. Here we discuss whether it is possible for only one kind of weight allocation method to be used which will be suitable for all types of river health assessment. IWE method means that the weight of the index is subjective but objective existence will not vary with the various rivers. Weight is the main understanding point related to the importance of various evaluation factors (hydrology, water quality, biological, physical structure, habitat conditions, service function) of river health assessment. These factors are the response of people's attention on importance of river health under certain social and economic conditions. So in a certain historical period, the weight is relatively fixed. However the assignment of the index changes, where the valuation criteria of the index changes with different types of rivers. River health is a relative concept, which is subjective and fuzzy in the scientific sense, including the public expectation of the river and the value orientation of different social backgrounds (Sun and Hu, 2008). Therefore, the valuation of each index should be a reasonable valuation after the consideration of the public health of each river with minimum acceptable value, the best state value and the worst state value (unacceptable value). It should not be a unified standard. Such as the city river, the public expectation on river water quality standard is class III. If the water quality reached class III,, people will think it as the health of rivers in the city where the assignment points should be 60 points and above (out of 100 points). For rivers in the ecological protected area, the public's expectations of the river water quality should be class II, or even better if class I. This is a comparison of two distinct cases, where although the standards of water quality index assignment changes, but the awareness of the importance water quality has not changed especially the weight of importance does not change. For another example, the importance of the rivers function to human being which in the urban river has a high degree of concern. The function of rivers to human beings in ecological point of view for rivers in protected areas has a higher degree of concern. However, in order to maintain a healthy river, it requires rivers in city areas to make the best out of the human activities while the rivers in the ecological protected areas should control human activities to be within a certain range. In other words, in two different situations, people's attention to the index will never change. This is where, the index assignment criteria have changed, which is decided by critical threshold. For another example, in urban rivers, people do not need a lot of fish in the river and the low fish diversity index is high enough to meet people's health requirements. However, the fish diversity index must be protected at high value in the rivers with the ecological function. Therefore, from another perspective, the weight is unchanged, but the index assignment standard (by different critical threshold can be realized) is constantly changing where the critical threshold of each river index is not the same.

At fixed weight, the index assignment of each river is different. The evaluation of each index, must be considered for each specific circumstances of the river. Based on the specific geographical location, climate, human activities, social and economy growth and science and technology level, several critical thresholds values of rivers are delineated. Thus, they must include four thresholds as follow: (1) the maximum value of index that the river can reach in a particular geographical and climatic conditions without human disturbance. (2) The historical value of index which the river is in a healthy state in history. (3) The lowest acceptable value that the public can accept in current human social, economic, scientific and technological conditions and (4) is the index value of serious interference and destruction. While doing the river health evaluation, only the current situation of each index was compared with a critical threshold. According to the comparison results, the index assignment can be calculated.

The key idea of IWE method is based on the principle of constant weight: firstly, construct a Widely applicable index system; secondly, assign the weight of each index at a fixed value which is appropriate for all kinds of rivers; thirdly, show the index quantification method and threshold index assignment principle variable to adapt to different rivers, namely the index critical threshold variable to reflect the different types of rivers and lastly, assess the river health by comprehensive health index of each index and the weight assignment. In a changing world, IWE method is a method that use fixed index, weight and variable index assignment standardization to assess specific rivers.

4 METHOD APPILICATION

The purpose of the IWE method was to find a simple and feasible method, which was applicable to all the multi-objective river health assessment and is fast and feasible. The core idea is to fix the two factors of the river health evaluation of the three factors where indicators and weights are unchanged. The method was divided into the following four steps:

- **Step 1** Construct the index system
  Since the construction of index system and the quantification of indicators were well-documented elsewhere, we would not describe it in this article. Here are some reference of research on the construction of index system (The Ministry of Water Resources Water Conservancy Department of

River Lake National Health Technology Group, 2010; Gao et al., 2007; Wu et al., 2005; Feng et al., 2014).

What needs to be emphasized here is the index system constructed by IWE method are the description of the river condition, where the indicators are reflected in the current situation of various elements of the river. The index cannot be directly assigned according to the size of the quantitative indicators, but need to be compared with the reference point or the desired value that can be assigned.

The 6 elements of river health assessment (hydrology, water quality, biological, physical structure, habitat, service function) must be involved in the index system. Each evaluation element must choose at least one index (if it is not within the scope of the service function of river health assessment, it can be omitted.). According to the different rivers, a few key indicators were selected to characterize the elements of the river situation. The choice of each element in the evaluation of 1~4 indicators was appropriate (other indicators can be added depending on the specific circumstances). Available indicators are shown in Table 2.

- **Step 2** Assign the fixed weight
  IWE method considers the importance of each element weight and index weight were fixed values. In order to get the objective weight values, this paper adopts the method of statistics. In this paper, the distribution of the weights were averaged for the representative multi-index river health evaluation in the multi-objective method calculated in our country, which may be the closest to the public expectation. Combined with some expert opinions, we amend error as close as possible to the current social concern for each index value. This article refers to the weight assignment examples (Gao et al., 2007; Shan et al., 2012; Deng et al., 2014;). The statistical results of weight are shown in Table 2.

Table 2. The index and weight of IWE method.

Elements and weight	Index and weight
hydrology (0.08)	Runoff fluctuation index (1)
Water quality (0.12)	dissolved oxygen index (0.15) Water temperature variation (0.1) Sediment index (0.3) Organic-pollutant index (0.15) Heavy-metal index (0.3)
Hydrobios (0.15)	Fish index (0.3) Plankton index (0.3) BIB index (0.2)
Physical structure (0.15)	Riverbank stability (0.4) River connectivity (0.4) Riparian human disturbance index (0.2)
Habitat (0.1)	Wetland index (0.3) Vegetation Coverage index (0.4) Ecological water guarantee rate (0.3)
service function (0.4)	Flood control index (0.1) Landscape suitability (0.35) Natural vegetation coverage (0.3) Water utilization (0.25)

Note: the weight is in the brackets. The weight of specific indicators can be added or deleted accordingly.

- **Step 3** Select the critical thresholds
  According to IWE, because the rivers are situated at a specific geographic location, climate and environment, social and economic conditions, can be considered as the best expected index value and it will not the same from one place to another. Due to the public demand at th river basin, expected index was not the same. Therefore, the valuation of each river is not the same and each index needs to be assigned according to the specific conditions. The variation of the standard value of the assignment was reflected by the change of the critical threshold:

Table 3: Selection and assignment of critical thresholds

Critical threshold	Description and acquisition of critical threshold	Eigen value
Best expected value	It is the prediction that the maximum value of this index can be achieved without human activity, which needs to be combined with the actual situation of the river.	100
Historical value	The actual value of the index in the case of historical human activities. It is necessary to select the historical data of the river with less interference and related data.	80
Minimum acceptable value	It is the critical value of the river health or not. In the current social, economic and technical conditions, under the condition of not destroying the sustainable development, the public can accept the minimum value of the index of the river. This can refer to the specific requirements of the government indicators of the river, or consult the relevant experts.	60
Serious threaten value	The public thinks the river health has been seriously threatened. Not only the production and living of human beings have been seriously threatened, but also the ecological environment has been destroyed. Urgent need for river management.	30
Completely destroyed value	Ecology has been destroyed by the destruction of human beings and the river has been unable to maintain the production and life.	0

- **Step 4** Calculation and evaluation
  The weight of each index multiplied by its' eigen value,is the index assignment, and then add the results of all the index and get the river health Synthetic index. The formula is as follows:

$$\mathrm{R_h} = \sum_{\mathrm{i=1}}^{\mathrm{N}} W_i \times E_i \quad [1]$$

Where the R_h is river health Synthetic index, N is the number of the index, Wi is the index weight, E_i is eigen value of the index or the index assignment.

5 DISSCUSSION

Is it appropriate for us to assess river health in fixed index and weight or various index assignment criterions? At present, the multi-objective river health evaluation of our country thinks that the index weight of river health assessment must be variable with rivers. Because if the index weight of the river was fixed, there would be many contradictions. For example, in rivers ecological protection zone, the area of the sources of the river water quality index and the biological index are so important that the rivers health could only depended on them. If these two indicators were in good health, the public would regard these rivers are healthy. If these two indicators were unhealthy, the rivers would be unhealthy. So the public think the weight of these two indicators must be very large, while the function of the river for human services must be very small or negligible. For urban rivers, water and service functions of the river are very important, the weight of both must be very large". First of all, we do not deny that there is a certain sense of rationality. But in the case of fixed weight, it can also be a scientific evaluation of two different types of river health, which is conflicting or contradictory with the former method. As a matter of fact, the service function of rivers in ecological function protection area is as important as that of City Rivers. However, the public subjectively ignore a fact that the service function in the river at ecological protection zone must be kept at a very low state to be considered as a healthy river, while the service function in the city river needs to be relatively at high status to meet the public requirements. In other words, what has changed is the index assignment criterion and not weight in two distinguished cases.

Due to limitation in academic level and professional knowledge, the weight distribution in this paper may be biased and assert. If it is agreed that the weight is fixed and invariable, the next step is to explore the distribution of the weight. A way to unify the critical threshold criterion is another important research. The future work must focus on the identification criteria of critical thresholds to be a guide to the national river health assessment

6 CONCLUSIONS

The weight of the index is fixed, and the evaluation criterion of the index (the determination of the critical threshold) is changed by the river. Therefore to construct a universal index system, each index system should be given a constant objective weight status, index quantification method and a set of standardized description of the river according to the specific circumstances of each river. The critical threshold of each river must be compared with the critical threshold for the index value according to the status quo of the rivers. Finally, the index assignment, the index weight and index value of river health must be obtained from the compared data. Finally a simple standardization of weights and indicators, with the changing evaluation criteria (that is, the threshold of change) can be used to reflect the different rivers health.

ACKNOWLEDGMENTS
This study is supported by National Key Research and Development Program 2016YFC0502103.

REFERENCES
Barbour, M.T., Gerritsen, J., Snyder, B.D. & Stribling, J.B. (1999). *Rapid Bioassessment Protocols for use in Streams and Wadeable Rivers: Periphyton, Benthic Macro Invertebrates and Fish*. US Environmental Protection Agency, Office of Water. 1-340.
Boulton, A.J. (1999). An Overview of River Health Assessment: Philosophies, Practice, Problems and Prognosis. *Freshwater Biology*, 41(2), 469-479.
Chave, P. (2001). *The EU Water Framework Directive*. IWA publishing.
Deng, X.J., Xu, Y.P., Zhai, X.L., Liu, Y. & Li, Y. (2014). Establishment and Application of the index System for Urban River Health Assessment. *Acta Ecologica Sinica*, 34(4), 993-1001.
Fairweather, P.G. (1999). State of Environment Indicators of “River Health” Exploring the Metaphor. *Freshwater Biology*, 41(2), 211-220.
Feng, Y., He, D.M. & Yang, L.P. (2012). Selection of Major Evaluation Indicators on River Health Evaluation. *Geographical Research*, 31(3), 389-398.
Gao, Y.S. (2006). *Study on River Health Life Assessment and Restoration Technology*, China Institute of Water Resources and Hydropower Research, Beijing.
Gao, Y.S., Wang, H. & Wang, F. (2007). Construction of Evaluation Index System for River’s Healthy Life. *Advance in Water Science*, 18(2), 252-257.
James, R.K. (1981). Assessment of Biotic Integrity using Fish Communities. *Fisheries*, 6(6), 21-27.
Karr, J.R. (1999). Defining and Measuring River Health. *Freshwater Biology*, 41(2), 221–234.
Luo, B.Y. (2008). *Study on AHP-Grey Relation Analysis Evaluation Modeling River Health Assessment based on GIS*, Guangzhou Industrial University.
Meyer, J.L. (1997). Stream Health: Incorporating the Human Dimension to Advance Stream Ecology. *Journal of the North American Benthological Society*, 16(2), 439-447.
Parsons, M. (2002). *Australian River Assessment System: Review of Physical River Assessment Methods-A Biological Perspective*. Department of the Environment Australia.
Raven, P.J., Holmes, H.T.H., Dawson, F.H., Fox, P.J.A., Everard, M., Fozzard, I.R. & Rouen, K.J. (1998). *River Habitat Quality the Physical Character of Rivers and Stream in the UK and Isle of Man*, River Habitat Survey Report No. 2.
Rogers K. & Biggs H. (1999). Integrating Indicators, Endpoints and Value Systems in Strategic Management of the Rivers of the Kruger National Park. *Freshwater Biology,* 41(2), 439–451.
Shan, C.J., Dong Z.C., Fan, K.M. & Yang, J.H. (2012). Application of Combination Weighting Method to Weight Calculation in River Health Evaluation. *Journal of Hohai University*, 6, 622-628.
Simpson, J., Norris, R. & Barmuta, L. (1999). *AusRivAS-national river health program*, User Manual Website Version.
Sun, X.L. & Hu, C.H. (2008). River Health Evaluation Index System. *Journal of Sediment Research*, 4, 21-27
The Ministry of Water Resources Water Conservancy Department of River Lake National Health Technology Group. (2010). *The National Assessment of Health Technology Assessment and File: River Health Indicators, Standards and Methods of V1.0.Z assessment*, Beijing: Ministry of water resources.
Vugteveen, P., Leuven R.S.E.W., Huijbregts, M.A.J. & Lenders, H.J.R. (2006). Redefinition and Elaboration of River Ecosystem Health: Perspective for River Management. *Hydrobiologia,* 565(1), 289-308.
Wang, C., Xia, J. & Li, L.C. (2014). Research and Progress on River Health Assessment. *Journal of Water Resources Research*, 03, 189-197.
Wang, G.S. (2007). *Study on Index System and AHP-Fuzzy Comprehensive Evaluation Model in River Health Assessment*, Guangzhou Industrial University.
Wu, E.N., Yang, K., Che, Y. & Yuan, W. (2005). Characterization of Rivers Health Status and its Assessment. *Advance in Water Science*, 16(4), 602-608.

Proceedings of the 37th IAHR World Congress
August 13 – 18, 2017, Kuala Lumpur, Malaysia

PERFORMANCE EVALUATION OF NUMERICAL SIMULATION FOR TURBULENCE CHARACTERISTICS AROUND CIRCULAR BRIDGE PIER

PRAVEEN RATHOD[(1)] & VIVEK L.MANEKAR[(2)]

[(1)]S.V. National Institute of Technology, Surat, India
praeenrathodsh03@gmail.com
[(2)]Civil Engineering Department, S.V. National Institute of Technology, Surat, India
vlm@ced.svnit.ac.in

ABSTRACT

Experimental and numerical simulations were carried out to study the suitability of widely used numerical models for the flow structure interaction problem in context of turbulence characteristics around cylindrical bridge pier. Present study mainly concentrates on the comparative study between the results obtained from experimental and numerical determination of turbulence characteristics. To capture the continuous point velocity data during the experimentation, Acoustic Doppler Velocity meter (ADV) was used. Pre and post processing treatment was done for the Acoustic Doppler Velocity meter (ADV) data used in the determination of turbulence characteristics around the bridge piers by phase thresholding Method. The obtained results were compared with the numerical simulations carried out using the ANSYS FLUENT computing tool. The turbulence characteristics across the depth of the flow were quantified by measuring the vertical distribution of time averaged velocity and Turbulence kinetic energy. The same experimental setup and flow conditions were simulated in the ANSYS FLUENT with k-ε model and same turbulence characteristics were commutated after extracting the velocity magnitude in XY plane. It has been concluded that the results obtained from k-ε model are in good agreement with the experimental results.

Keywords: Flow structure interaction; phase thresholding; ANSYS FLUENT; turbulence characteristics; acoustic doppler velocity meter (ADV).

1 INTRODUCTION

Water flows in an open channel under the gravity. When it comes in contact with an obstacle, flow pattern changes around the obstacle. In the present study, circular pier is being considered as the obstacle. When flowing water passes by pier, it generates a lot of turbulence. For a better insight into the turbulence and flow field around the circular pier in clear water equilibrium scour condition, many researchers such as Melville and Raudkivi (1977), Melville (1975), Dargahi (1989), Muzzammil and Gangadhariah (2003), Dey and Raikar (2007), Graf and Yulistiyanto (1998), Kirkil et al. (2009) and Ettema et al. (2006), have greatly contributed in this area. In the Subhasish Das (2015) experimental study for two identical circular piers, it was shown that the eccentric pier arrangement and the interference between the piers play an important role in the creation and formation of the greater scour depth at the eccentric rear pier. Vortex strength of the eccentric rear pier was found to be higher than the front pier.

Roulund et al. (2005) experimentally showed that the horseshoe vortex around single circular pier is greatly influenced by the pier Reynolds number, boundary-layer thickness, and bed roughness. Application of experimental study to the real world problems may be less reliable. Cost in restoring the damaged structure may be large but the cost associated due to interruption in the traffic is five times greater (Rhodes, 1999). However, most of the studies have been done in flumes under idealized conditions, such as uniform sediment, steady flow, simplified geometry, etc. Therefore, their applications to field situations may still be problematic and may produce questionable results. Collecting large data related to flow properties and scouring process may not be feasible. Therefore, there is a more satisfactory alternative which is to simulate the flow field and scouring processes accurately using a 3D numerical model (Esmaeili 2009). From the literature, it has been observed that model results obtained using the RNG (Re-Normalisation Group) and k- ε models show some inconsistency with the measured bed shear stress. For the flat bed condition Reynolds stress model performed well in simulating shear stress distribution and velocity distribution around circular pier. As compared to field observed scour depth, available scour equations commonly overpredict (Bhesti, 2010). Johnson (1995) compared seven of the commonly equations using a large set of observed field data, for both clear-water scour and live-bed, and concluded that there is still a need for additional research on the scour process.

Turbulent flow around a bridge pier is a classic case of a complex flow that has been studied both computationally and experimentally by Melville and Raudkivi (1977), Dargahi (1990), Ettema et al. (2006), Dey and Raikar (2007). A computational fluid dynamics (CFD)-based simulation methodology using a

  / ISSN 1562-6865 (Online) - ISSN 1063-7710 (Print)

dynamic mesh updating technique is proposed. This method can numerically describe the complicated 3D scour behavior around the piers of bridges. By redeveloping a commercial CFD computer program, the transient shear stress in a k- ε turbulence model was first calculated, where the shear stress was regarded as a key parameter to judge the sediment incipient motion in scour process. Then, the dynamic mesh updating technique was implemented to assure a practical and accurate scour simulation by individually updating the finite element (FE) model nodes of the riverbed in each time step. In the present study, ADV (Acoustic Doppler velocity meter) was used for the measurement of the flow velocity across the depth.

From the literature, it has been found that RNG approach, which is a mathematical technique to derive turbulence, similar to K-ε model, results in a modified form of the epsilon equation which attempts to account for the different scales of motion through changes to the production term. RNG has shown improved results for modelling rotating cavities, but show no improvements over the standard model for predicting vortex evolution (Yakhot, 1992). Since the vortex plays very important role in the scour phenomenon and RNG has no significant improvement in the results at the higher cost of computation, K-e model is being used for the study to simulate turbulence and its effect on the scour. In the present study, ADV was used for the measurement of instantaneous point velocity. Then, experimental results were compared with the widely used k-ε model. Objective of this research is to compare the numerical and experimental results of turbulence quantification in uniform flow condition around the circular cylinder. There are many researches which have compared experimental and numerical results but all were in Cartesian coordinates systems. None of the studies have shown the comparative results in cylindrical coordinates. Present study mainly focused on extracting the experimental point velocity in cylindrical coordinates and at the same points, numerical results were compared.

2 EXPERIMENTAL SETUP AND DATA COLLECTION

The experimental set up, designed and developed as part of present study included recirculating tilting flume of size 15.0 m X 0.89 m X 0.6 m (L x B x H) with complete arrangements like centrifugal pumps, recirculation pipe, digital flow meter, tail gate, sediment traps, sediment feeder with conveyor belt, water level sensors, downstream water collection tank, instrument carriage, pointer gauge and stilling arrangement at the inlet of the flume. Besides, the line sketch of complete experimental set-up is shown in Figure 1.

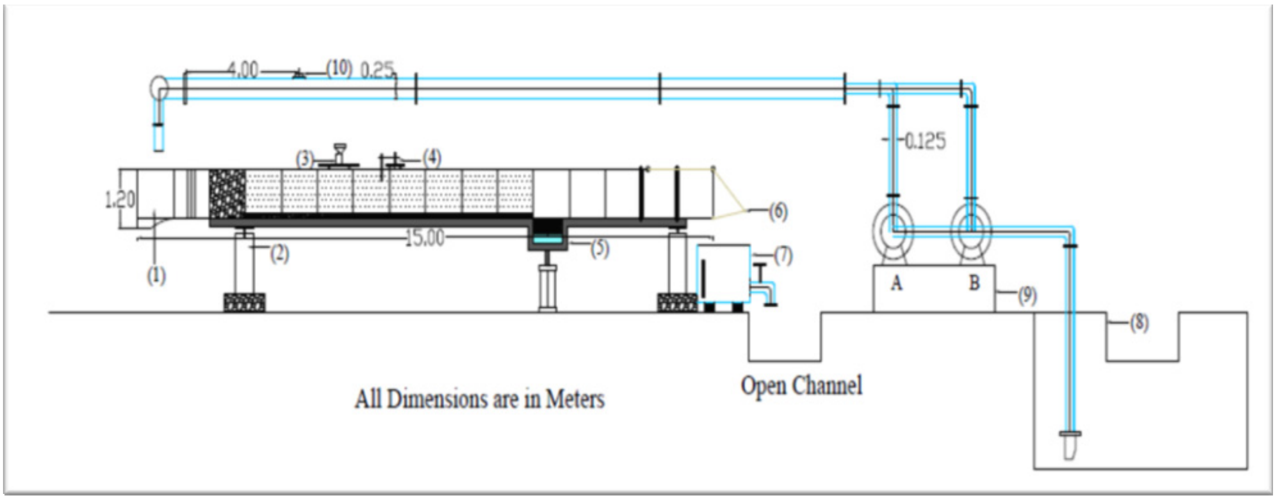

Figure 1. Side view of recirculating flume,flume parts: (1) up-stream tank (2) screw-jack (3)sediment feeder (4) instrument carriage (5) sediment trap (6) tail- gate (7) volumetric tank (8) down stream reservoir (9) pump unit (10) digital fow -meter.

3 DATA COLLECTION

The instantaneous three-dimensional (3D) velocity components were measured using a 16 MHz 3D Acoustic Doppler Velocimetry (MicroADV) of SonTek/YSI. Vertical distributions of the instantaneous flow velocities have been measured at every 2cm interval. The ADV sampling stations were located along the centre line of the flume. ADV measurements were taken above 0.5 cm from bed and up 6 cm below the water surface by using down-looking probes. The measurements for velocity components were made in vertical planes of symmetry, respectively, in radial planes at θ =0°-180° at every 30° interval. Here, angle α = 0° accord with the central line of the flume and the pier from the upstream side. Velocity distributions the vertical profiles at radial distance, i.e., r = 7cm,10cm,15cm, 20cm, 25cm and 30cm were observed in each of the radial planes. Data measurements points in radial planes and distances are as shown schematically in Figure 2.

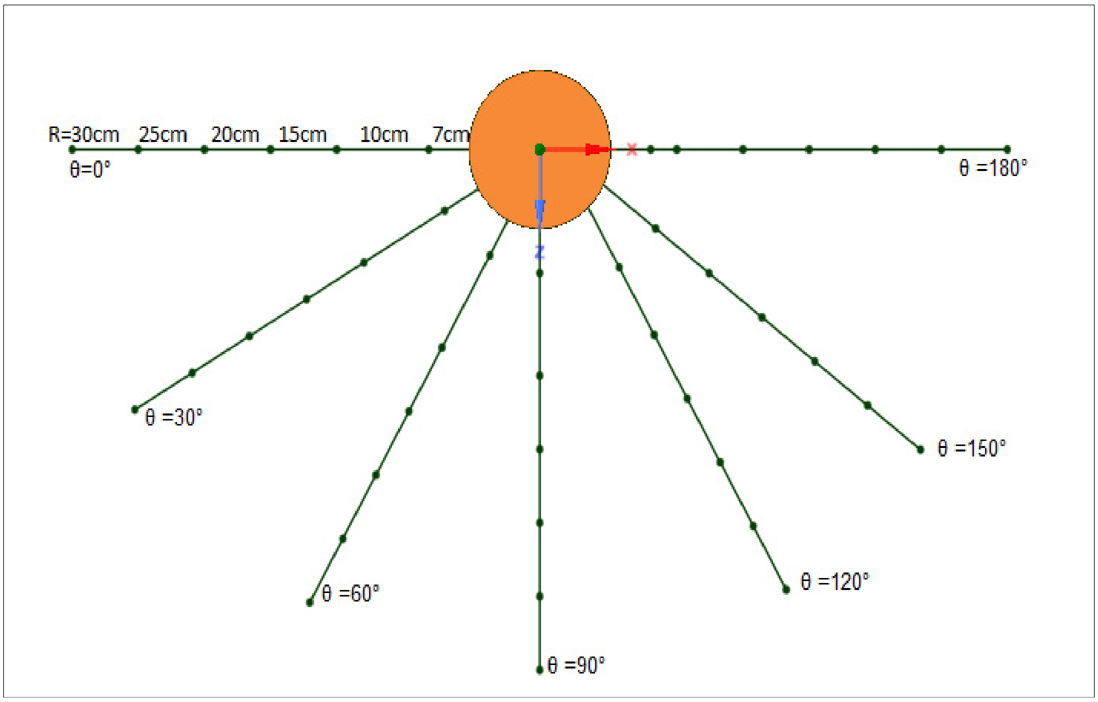

Figure 2. Schematic representation of data collection points.

4 FLUENT MODEL DESCRIPTION AND MODEL SETUP

K-ε turbulence two-equation models allow the estimation of both a time scale and turbulent length by solving two separate transport equations. Standard K- ε determines the turbulence kinetic energy, and its rate of dissipation, from the following transport equations, (Fluent Theory Guide, 2013)

$$\frac{\partial}{\partial t}(\rho k) + \frac{\partial}{\partial x_i}(\rho k u_i) = \frac{\partial}{\partial x_j}\left[\left(\mu + \frac{\mu_t}{\sigma_k}\right)\frac{\partial k}{\partial x_j}\right] + G_k + G_b - \rho\varepsilon - Y_M + S_k \qquad [1]$$

$$\frac{\partial}{\partial t}(\rho\varepsilon) + \frac{\partial}{\partial x_i}(\rho\varepsilon u_i) = \frac{\partial}{\partial x_j}\left[\left(\mu + \frac{\mu_t}{\sigma_\varepsilon}\right)\frac{\partial \varepsilon}{\partial x_j}\right] + C_{1\varepsilon}\frac{\varepsilon}{k} + (G_k + C_{3\varepsilon}G_b) - C_{2\varepsilon}\rho\frac{\varepsilon^2}{k} + S_\varepsilon \qquad [2]$$

where, Gk represents the generation of turbulence kinetic energy due to the mean velocity gradients, Gb is the generation of turbulence kinetic energy due to buoyancy, Ym represents the contribution of the fluctuating dilatation in compressible turbulence to the overall dissipation rate, $C_{1\varepsilon}$, $C_{2\varepsilon}$, $C_{3\varepsilon}$, are constants. σ_k , σ_k are the turbulent Prandtl numbers for k and ε respectively. Sk and Sε are the user defined source terms.

The turbulent (or eddy) viscosity, μt is computed by combining k and ε as follows

$$\mu_t = \rho C_\mu \frac{k^2}{\varepsilon} \qquad [3]$$

where C_μ is a constant

In the fluent modal constants such as C_1ε, C_2ε, C3ε, σ_k and σ_k uses the following default values (Fluent Theory Guide, 2013)

5 DOMAIN DESCRIPTION

A single phase model having only water as a flow domain was considered and the free surface of the flume was taken as the symmetry boundary condition. By doing this, simulation of multiphase problem having air at the top of the water can be avoided. User can also adopt multiphase problem considering air on the top of the free surface. Pier model and flow domain was developed using the space claim application of the ANSYS Fluent 18.10. Figure shows the pier model and the flow domain. Dimension of the pier was selected to be exactly the same as the experimental model and flow domain width and the depth were kept in conjunction to the flume size but the length was kept ten times the height of the pier. As per the literature, length of the flow domain can be kept 4-6 times of the model's largest size. Figure 3 shows the flow domain and pier model placed at the center.

6 MESHING

Result of CFD simulation mainly depends on how fine is the mesh but it costs high computational time. Meshing has to be made finer at the locations where turbulence has to be captured more precisely. Near the wall and vicinity of the pier requires fine meshing. Fine meshing is done using the inflation command in Fluent. Mesh sizing was kept to be 5mm. The meshing of flow domain and the pier model are shown in figure 4.

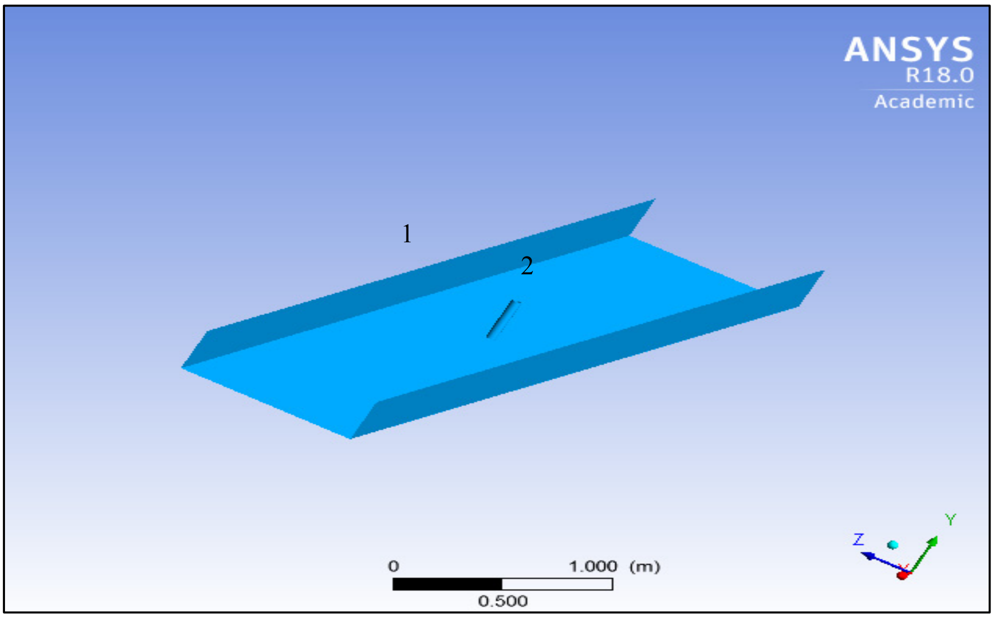

Figure 3. Flow domain and pier model placed at the center, 1 flow domain 2. pier model.

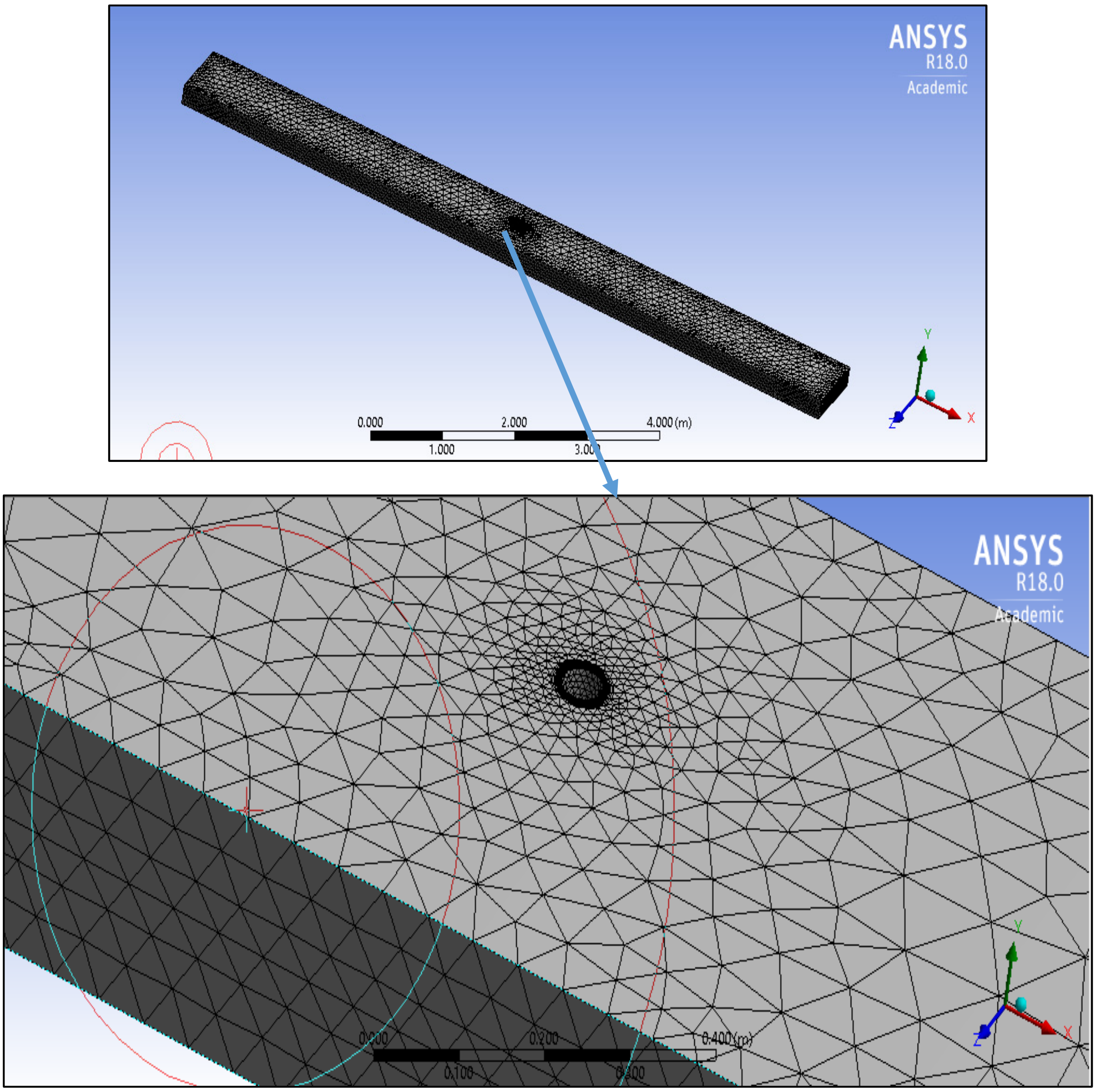

Figure 4. Meshing of flow domain and pier model.

7 BOUNDARY CONDITIONS

Proper boundary conditions similar to experimental setup were given into the FLUENT K-ε model. The inlet boundary condition was specified as velocity inlet with average velocity of 0.13m/s. The outlet condition was given as pressure outlet. The top surface of the flow was set to symmetry boundary. The pier, side walls and the bottom of the domain were set as no-slip wall condition.

8 MODEL APPLICATION

$k-\varepsilon$ model is widely used for the many applications such as flow structure interaction problem in medical field, aerodynamic applications and turbulence characterization in open channel. The aim of the study is to validate $k-\varepsilon$ model for pier flow interaction and this study can be further extended to study of scour around the bridge pier. Three dimensional $k-\varepsilon$ model under steady state and pressure based simulation were carried out. For pressure-velocity coupling, SIMPLE scheme was adopted. Second-order Upwinding Scheme was adopted for spatial discretization.

9 RESULT AND DISCUSSION

9.1 Vertical Distribution Of Time Averaged Velocity

The normalized profiles of mean flow velocities along flow direction (u+), perpendicular to flow direction (v+) and normal to flume bed (w+) . Hydraulic parameters for the experimental run are shown in Table 1.

Table 1. Hydraulic parameters.

Details	**Magnitude**
Flow Depth (cm) h	26
Aspect Ratio (B/D)	1.48
Water Surface Slope, So	0.0009
Flow Rate (Q) (Cumec)	0.03
Froude Number, Fr	0.04
Sediment Size (mm) (d50)	0.75

Figure 5-8 shows the velocity distribution at zero angle. From the figure 5-8, it can be seen that magnitude of velocity near the bed was higher for the K-ε model as compared to experimental results. As the depth increased, velocity became more uniform than the actual velocity distribution. Near the free surface, actual velocity was higher than that of the K-ε model. From figure 9, it can be seen that velocity distribution near the structure towards upstream direction was more uniform and at downstream of the structure, and there was a lot of vortices. Velocity in all the planes except $\theta=180^{o}$ was almost uniform, and there was a lot of turbulence in the downstream plane.

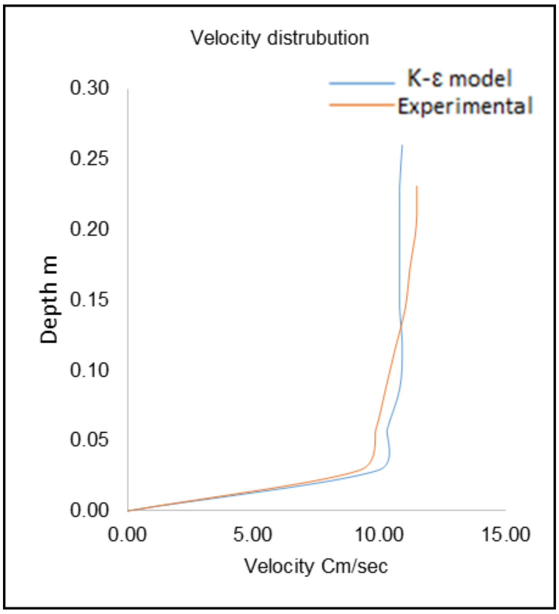

Figure 5. Velocity distribution at 7cm plane.

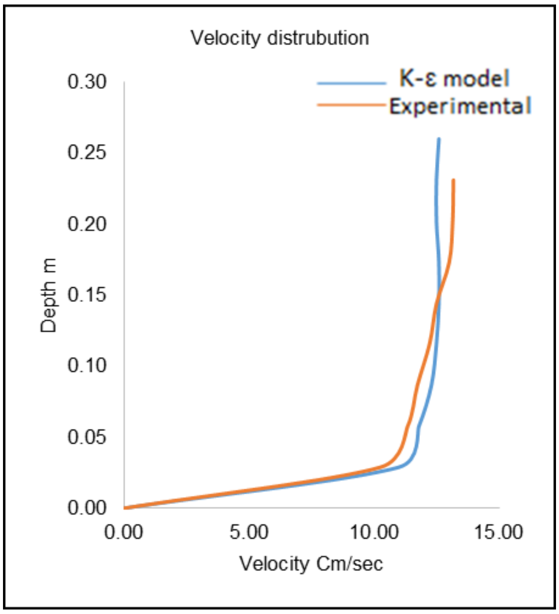

Figure 6. Velocity distribution at 10cm plane.

  ISSN 1562-6865 (Online) - ISSN 1063-7710 (Print)

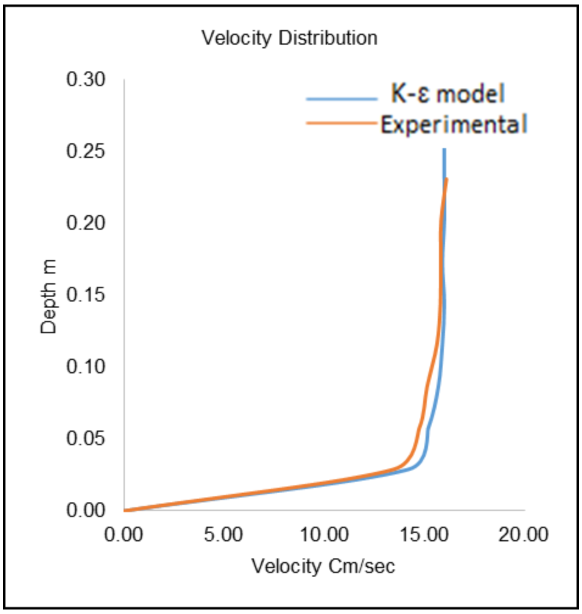

Figure 7. Velocity distribution at 15cm plane.

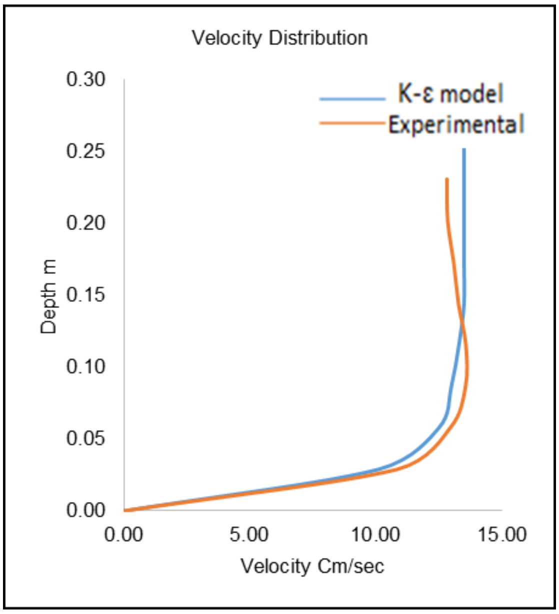

Figure 8. Velocity distribution at 20cm plane.

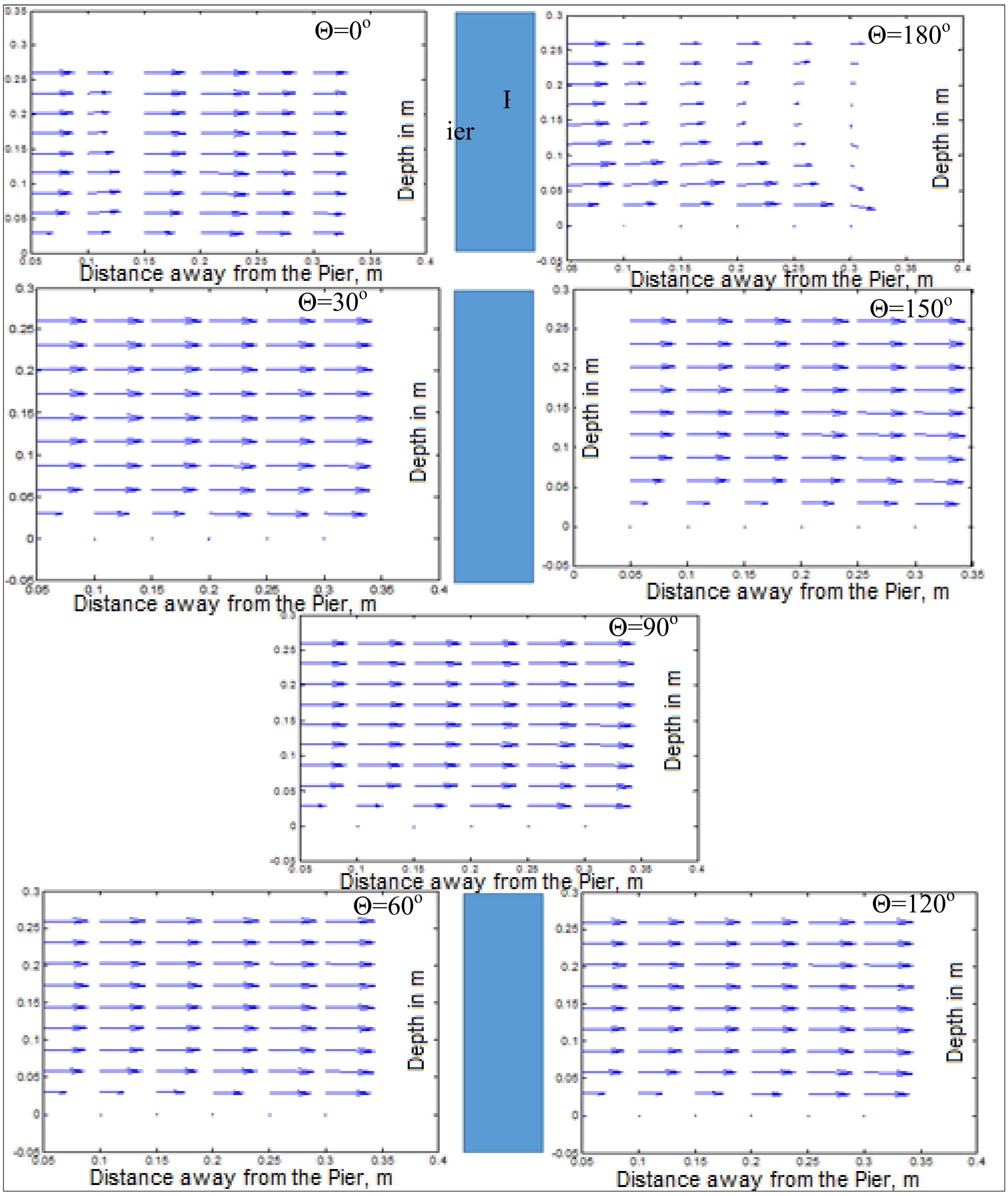

Figure 9. Velocity vectors at different planes in cylindrical co-ordinates.

In the present study, it is mainly focused on the performance of the model spatially as well as the error difference between the actual and predicted model.

9.2 Turbulence Kinetic Energy

The stream wise instantaneous velocities were decomposed into mean and fluctuations. Turbulence intensity is the “root mean square” of the fluctuating velocity components.

A turbulence intensity of 1% or less is commonly considered low and turbulence intensities larger than 10% are considered high. Turbulence kinetic energy (TKE) is the mean kinetic energy per unit mass connected with eddies in turbulent flow. Physically, the turbulence kinetic energy is considered by measured root-mean-square (RMS) velocity fluctuations. Figure 10-14 show the TKE at different planes across the depth. From the figure 10-14, it can be seen that TKE was always greater at 10^o or 15^o section in any planes. Another interesting thing observed is that TKE was always greater at the bottom of the channel but the same is not the case for the 180^0 plane. TKE is greater between 15cm to 20cm above the bed.

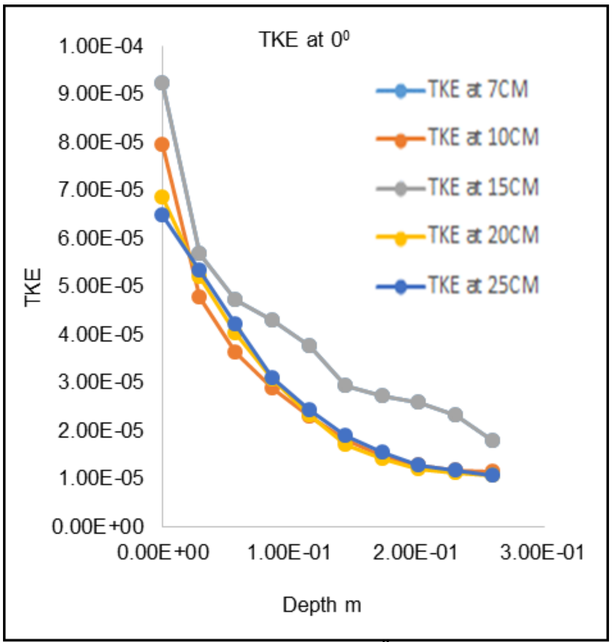

Figure 10. TKE at 0^0 plane.

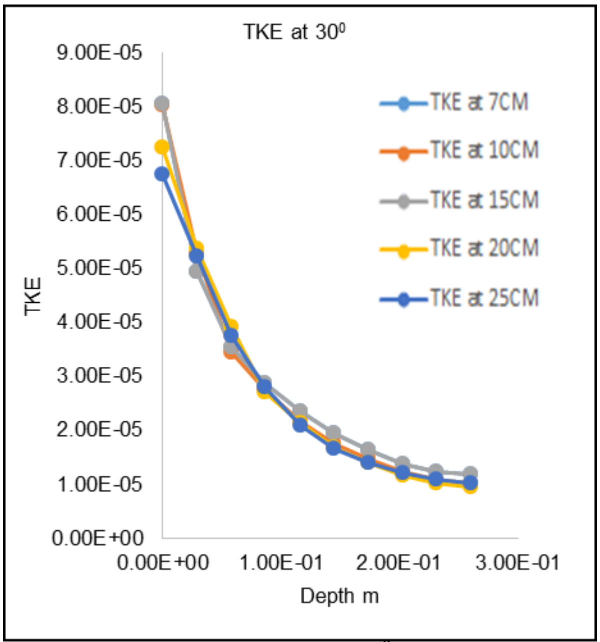

Figure 11. TKE at 30^0 plane.

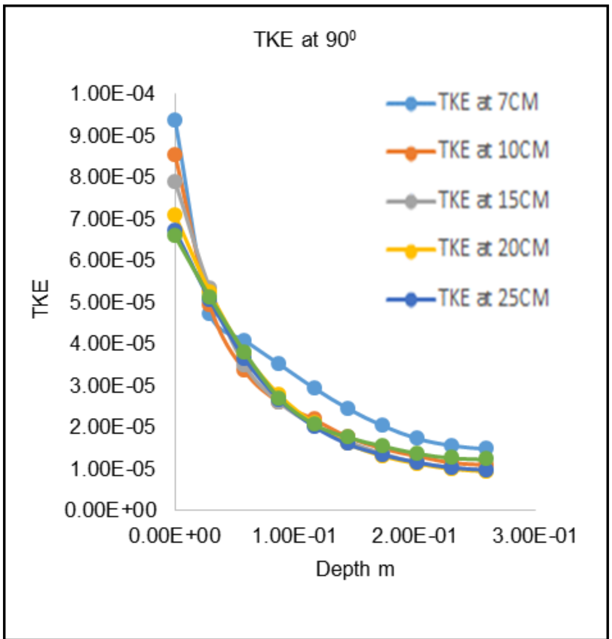

Figure 10. TKE at 90^0 plane.

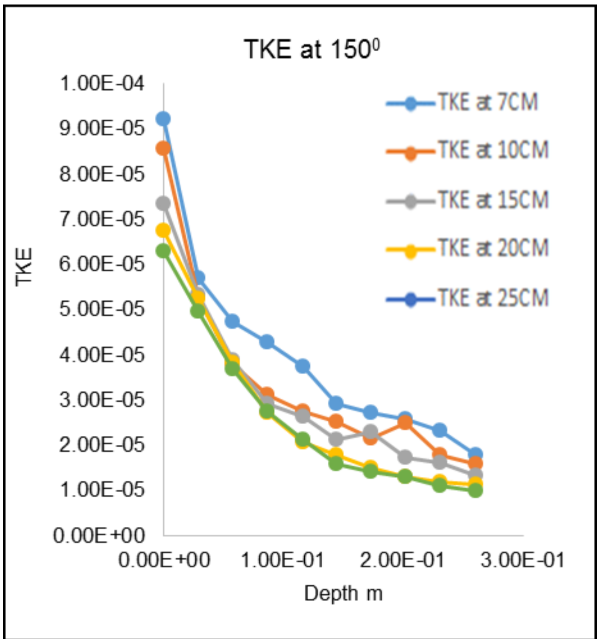

Figure 11. TKE at 150^0 plane.

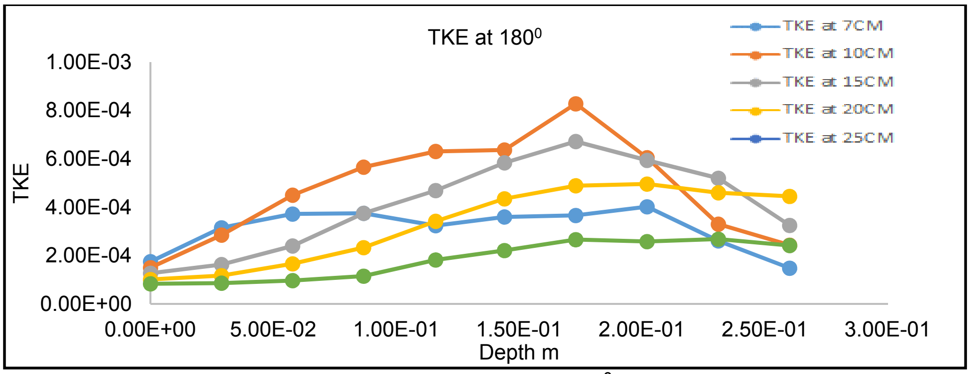

Figure 12. TKE at 180^0 plane.

10 CONCLUSIONS

For the present study, it has been attempted to compare widely used K-ε model with the experimental data. Boundary conditions which were maintained in the experimentation, was maintained in the same way in the CFD simulation with the K-ε model. From the study, the following points were observed. Velocity near the bed was greater for the K-ε model as compared to experimental results. As the depth increased, velocity became more uniform than the actual velocity distribution. Velocity in all the planes except θ=180^o was almost uniform, and there was a lot of turbulence in the downstream plane (θ=180^o). Velocity at the 0 ^{o} plane was more uniform than the velocity at the 180 ^{o} plane, this is the reason for more scour towards the downstream of the pier. K-omega model performs better in less turbulence zone. TKE was always greater at 10^o or 15 ^{o} section in any planes. Another interesting thing observed was that TKE was always greater at bottom the channel but the same was not the case for the 180^0 plane. TKE was greater between 15cm to 20cm above the bed.

REFERENCES

Beheshti, A.A. & Ataie-Ashtiani, B. (2010). Experimental Study of 3-Dimensional Flow Field around a Complex Bridge Pier. *Journal of Hydraulic Engineering*, 136, 143-154.

Dargahi, B. (1989). The Turbulent Flow Field around a Circular Cylinder. *Experiments in Fluids*, 8(1), 1–12.

Dey, S. & Raikar, R.V. (2007). Characteristics of Horseshoe Vortex in Developing Scour Holes at Piers. *Journal of Hydraulic Engineering*, 133(4), 399–413.

Esmaeili, T., Dehghani, A. A., Zahiri, A. R. & Suzuki, K. (2009). 3D Numerical Simulation of Scouring around Bridge Piers (Case Study: Bridge 524 Crosses The Tanana River). *World Academy of Science, Engineering and Technology,* 58, 1028-1032.

Ettema, R., Kirkil, G. & Muste, M. (2006). Similitude of Large Scale Turbulence in Experiments on Local Scour at Cylinders. *Journal of Hydraulic Engineering*, 132(1), 33–40.

Fluent Theory Guide. (2013). *ANSYS Fluent Theory Guide 15.0*. Inc, Canonsburg, PA.

Graf, W.H. & Yulistiyanto, B. (1998). Experiments on Flow around a Cylinder: The Velocity and Vorticity Fields. *Journal of Hydraulic Research*, 36(4), 637–654.

Kirkil, G., Constantinescu, S.G. & Ettema, R. (2009). Detached Eddy Simulation Investigation of Turbulence at a Circular Pier with Scour Hole. *Journal of Hydraulic Engineering*, 135(11), 888–901.

Melville, B.W. (1975). *Local Scour at Bridge Sites*, Auckland: School of Engineering, University of Auckland. Report no. 117.

Melville, B.W. & Raudkivi, A.J. (1977). Flow Characteristics in Local Scour at Bridge Piers. *Journal of Hydraulic Research*, 15(4), 373–380.

Muzzammil, M. & Gangadhariah, T. (2003). The Mean Characteristics of Horseshoe Vortex at a Cylindrical Pier. *Journal of Hydraulic Research*, 41(3), 285–297.

Rhodes, J. & Trent, R.E. (1999). Economics of Floods, Scour and Bridge Failures. *Journal of ASCE,* Reston, 1013-1018.

Roulund, A., Sumer, B. M., Fredsøe, J. & Michelsen, J. (2005). Numerical and Experimental Investigation of Flow and Scour around a Circular Pile. *Journal of Fluid Mechanics*, 534, 351-401.

Das, S. & Mazumdar, A. (2015). Turbulence Flow Field around Two Eccentric Circular Piers in Scour Hole. *International Journal of River Basin Management*, 13(3), 343-361.

Yakhot, V., Orszag, S.A., Thangam, S., Gatski, T.B. & Speziale, C.G. (1992). "Development of Turbulence Models for Shear Flows by a Double Expansion Technique". *Physics of Fluids A: Fluid Dynamics*, 4(7), 1510-1520.

Proceedings of the 37th IAHR World Congress
August 13 – 18, 2017, Kuala Lumpur, Malaysia

USING THE TELEMAC 3D MODEL FOR ESTIMATING THE IMPACT OF BRIDGE CONSTRUCTION TO RIVER HYDRODYNAMIC REGIME

NGOC DUONG VO[(1)], QUANG BINH NGUYEN[(2)] & PHILIPPE GOURBESVILLE[(3)]

[(1, 2)] Faculty of Water Resource Engineering,
University of Science and Technology, the University of Da Nang, Viet Nam
[(2, 3)] Innovative City lab URE 005
Polytech'Nice Sophia, Nice Sophia Antipolis University, France.
nqbinh@dut.udn.vn; vo.ngoc.duong@dut.udn.vn; Philippe.GOURBESVILLE@unice.fr

ABSTRACT

Tran Thi Ly is one of the large bridges on Han River, Danang, Vietnam. This bridge plays an important role in regional socio economic development. However, its construction is judged to affect particularly flow regime and morphology of Han River. It may cause serious consequences towards river bank and work stability. In order to reduce the negative impacts, there is a need to estimate the variation in hydrodynamic of Han River under the impact of Tran Thi Ly Bridge. For this purpose, one TELEMAC 3D is established to represent, in detail, Han River flow process before and after Tran Thi Ly construction. The study is expected to analyze reasonable level of Tran Thi Ly Bridge's hydraulic aspect as well as to provide basic scientific bases for mitigating any unexpected consequence. The paper also demonstrates TELEMAC 3D ability in simulating the river hydrodynamic regime and in determining the river's variation due to outside factors.

Keywords: River's morphological variation; river construction; computational modeling; TELEMAC-3D.

1 INTRODUCTION

Erosion (scour) around the piers or abutments is considered as one of main causes undermining the bridges (Hamill, 1998; Chaudhry, 2007; Sturm, 2010). Following the study of (Trần, 2008), there are different types of scour. However, local scour is the most popular in reality and this type is quite difficult to be predicted accurately in comparison with other ones.

Erosion is defined as a process of interacting between the hydrodynamic and sediment transport, which can remove the soil, rock, or dissolved material from one location then transport it away to another location. The erosion is expected to appear at location where there is significant changes in flow velocity, flow direction, river bed resistance, and topography characteristic as well (Van Rijn, 1993; Chien & Wan, 1999). These conditions are quite similar to the characteristics of the flow and river bed variation when constructing the bridge. The appearance of bridge piers or abutments will change the stream flow and rived bed locally in comparisons with origin. It makes the water to move more swiftly, causes the bridge scour phenomenon and compromises the work structure potentially (Melville & Coleman, 2000).

In order to reduce the impact of erosion to piers, abutments as well as river banks, many studies have been realized up to this day. They have contributed significantly to determine the bridge pier structure. Through an experiment on cylindrical pier in open channel flow condition, Melville, B.W. & Raudkivi, A.J. (1977) determined concretely the flow patterns, turbulence intensity distributions, boundary shear stress distribution in the scour zone and interaction of the vortices shed by the cylinder with the horseshoe vortex. However, these results were only for the case of the clear water scour condition and initial flat bed. The condition might be not appropriate in reality. Regarding to effects of geometry on bridge pier scour, Melville, B.W. & Raudkivi, A.J. (1996) believed that the scour depth depends highly on the shape of the piers and the depth of the bed. Similarly, the study of Melville, B.W. & Chiew, Y.-M. (1999) also analyzed the scour development, but concentrated much on time scale. Following that, they confirmed that scour depth increases depend on the approach flow velocity. It mostly happens in the beginning phase of the process. Recently, these issues were mentioned in the research of Parvin Eghbali et al. (2013).

Due to the application of empirical formula, semi empirical formula or experiment, these studies might not present the hydraulic processes and erosion near adding constructions accurately. Furthermore, the difficulties about the simulated condition have made that most of the above studies concentrate only in analyzing the flow regime around the works. The analysis at small area is judged to be not able to express the phenomena surrounding the piers completely. It might affect the unreasonableness in designing piers or abutment structures, then, causes the erosion situation become more complicated and more serious. By using high performance algorithms, the development of numerical models nowadays is expected to overcome the limitation of traditional approaches.

Computational Fluid Dynamics (CFD) is considered as a robust method for solving and analyzing problems that involve fluid flows. With the support of high performance computing systems, the CFD method presents the hydraulics as well as the sediment transport process in the river more and more accurately. Consequently, this method is hoped to simulate the fluid flow variation and scour phenomena effectively after constructing the bridge.

In this study, CFD method was applied to simulate the impact of Tran Thi Ly Bridge scours on Han River's flow regime and erosion process. A coupling model between TELEMAC-3D and SISYPHE, which has been developed based on CFD code, was built in an area of 27,500m^2 of the Han River. The simulated result demonstrates that with adding works, the fluid flow around Han River scours varies significantly. These variations make the erosion situation in the area surrounding scours become more serious and influence considerably on scour stability. The result is hoped to provide the basics for mitigating the impact of Tran Thi Ly Bridge on fluid flow, to look for reasonable solutions to protect river bank or to increase the scour stability. The simulation might be considered as a demonstration of the efficiency of numerical method (CFD method) in solving the problem of stream flow around adding works as well as erosion issues.

2 TRAN THI LY BRIDGE

Han River is the downstream part of Vu Gia Thu Bon river system, flowing through Danang city which is considered as the most dynamical economic city in Vietnam.

The Han River plays an important role in the social development of the region. Its flow regime separates into different seasons. The flood season lasts generally from September to December. In this season, the flow of Han River is affected hugely by two factors, flow from upstream and sea level at downstream. Conversely, during dry season in the remaining months, the flow running from the upstream section is low and stable. The water level and river flow direction are mainly affected by the tide. However, it is noted that in the period from May to June, the flow would be added by a significant volume due to the rain (Office, n.d.). In recent years, under the effect of urbanized process, this river section has been trained considerably. Many constructions such as bridge, training works or river bank protection have been constructed. The human intervention has made big variation in river bed, flow regime, and erosion as well.

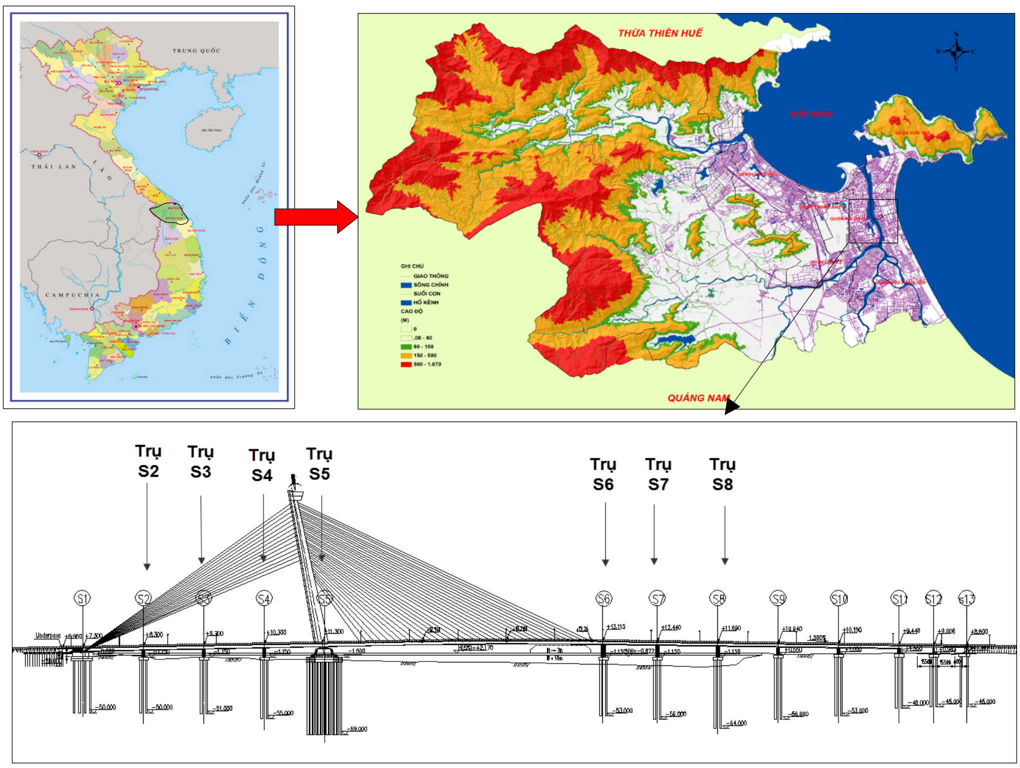

Figure 1. Study area.

Tran Thi Ly is one of the largest bridges connecting two sides of Han River. Besides the Han River and Rong Bridge, Tran Thi Ly Bridge is constructed for improving the circulation situation which augments more and more quickly in the central city. The Tran Thi Ly Bridge is constructed for a length of 731m with a concrete structure. Its design is demonstrated in Figure 1.

3 METHODOLOGY

The TELEMAC-MASCARET system is a famous product of the National Hydraulic and Environment Laboratory, Electricity of France (EDF). By developing the finite-element method and using unstructured grid of triangular elements to represent the space, this system is expected to be a powerful integrated modeling tool for use in the field of free-surface flows (Villaret, 2004; Kabir, 2005; Hervouet et al., 2011; Smolders et al., 2014; Langendoen et al., 2016).

TELEMAC-3D is a three-dimensional computational code describing the 3D velocity field (u, v, w) and the water depth h (and, from the bottom depth, the free surface S) at each time step. Besides, it solves the transport of several tracers which can be grouped into two categories, namely the so called “active” tracers (primarily temperature and salinity), which change the water density and act on flow through gravity), and the so-called “passive” tracers which do not affect the flow and are merely transported (DESOMBRE, 2013). TELEMAC-3D solves problems with two different approaches, the first is based on Navier-Stokes equation with assumption that the equation takes into account of the hydrostatic pressure and the second is with the assumption that the Navier-Stokes equation does not take into account of the hydrostatic.

The SISYPHE is also a module of TELEMAC-MASCARET which is developed for modelling the sediment transport and morphodynamic process in water environment (Villaret, 2004; Giardino & Monbaliu, 2005). By using different theories to solve the issue, such as classical sediment transport formula for sediment transport at bedload, additional transport equation for the depth-averaged suspended sediment concentration, bed evolution equation for morphological development, this module is hoped to represent the sediment transport process in the river most accurately and most truthfully.

In this study, TELEMAC-3D was used to simulate the hydrodynamic regime around bridge piers and neighboring area. The model variation was realized by comparing with the result of (Kabir, 2005). Then, the validated model was coupled with SISYPHE to represent the bed evolution phenomena.

4 APPLICATION FOR TRAN THI LY BRIDGE

In an attempt to estimate the impact of Tran Thi Ly Bridge piers on Han River bed evolution, a coupling model between TELEMAC-3D and SISYPHE was established. Two meshes were created, one for original bathymetry and another for adding bridge piers (Table 1, Figure 2, 3). They were built based on the altitude of 3310 points provided by project of Da Nang hydrology and urban development simulation model (Danang construction department, 2013) and on Tran Thi Ly design document provided by Transport engineering consulting joint stock company no. 533, n.d.

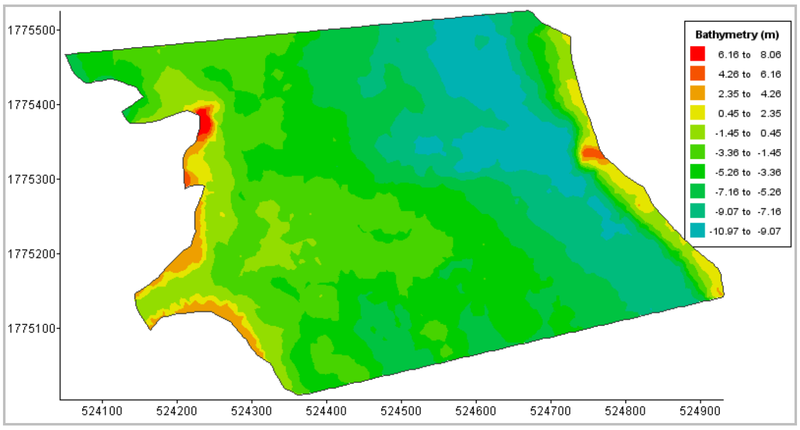

Figure 2. Bathymetry at Han river before constructing Tran Thi Ly bridge.

The boundary condition was set with discharge at upstream (Q) and water level (H) at downstream. From the observed data in 32 years (1976 – 2007) of Cam Le station and Nguyen Van Troi bridge, the above data were determined with Q = 7576,73m^3/s and H = 3,63m, respectively. These numbers were defined to answer the required frequency in Vietnamese standard (Ministry of transport, n.d.).

The sediment characteristics, which is presented in table 2, is referred to measured data of Transport engineering consulting joint stock company no. 533.

Table 1. Mesh setup.

Name	Origin	After bridge construction
Node	5247	97696
Element	9968	195128

Table 2. Sediment characteristics.

Characteristics	Value	Unit
Mean diameter of the sediment	0.01	m
D_{90}	0.0033	m
Sediment density	2650	Kg/m^3
Shields parameters	0.045	

  / ISSN 1562-6865 (Online) - ISSN 1063-7710 (Print)

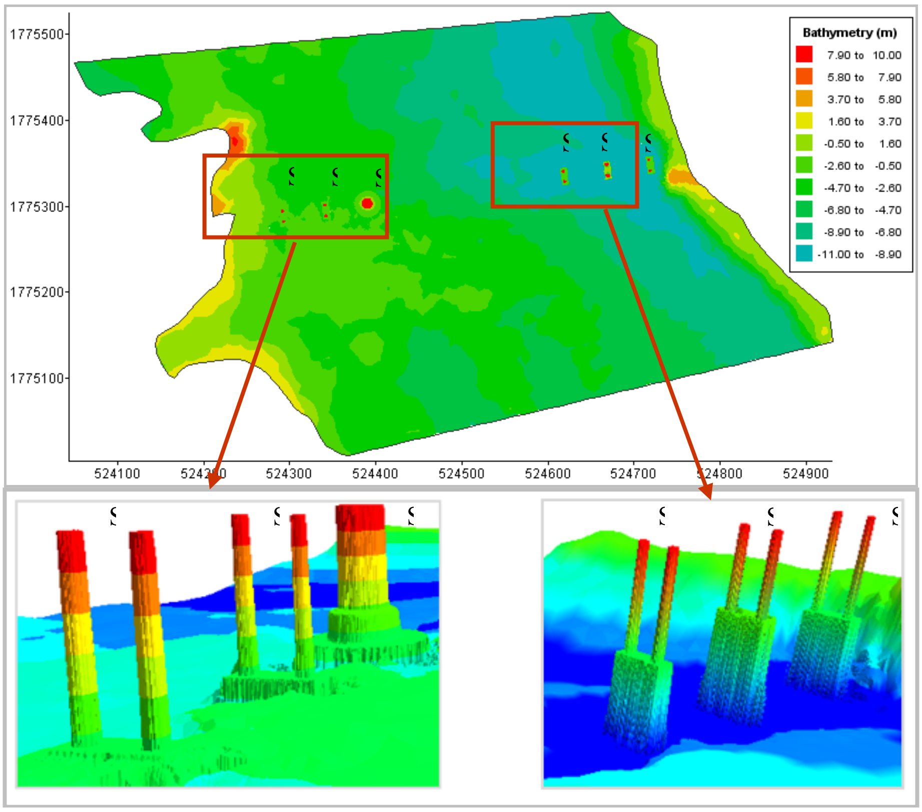

Figure 3. Bathymetry at Han river after constructing Tran Thi Ly bridge and piers.

5 RESULT AND DISCUSSION

5.1 Flow velocity change

The simulation shows that the Tran Thi Ly bridge construction influences significantly on the Han River flow, especially on velocity. The variation is demonstrated in Figure 4 and Figure 5.

In general aspect, after adding the bridge, the flow velocity increases at most of pier location. The largest increase is on the main flow when the value changes from 2.42m/s to 3.05m/s.

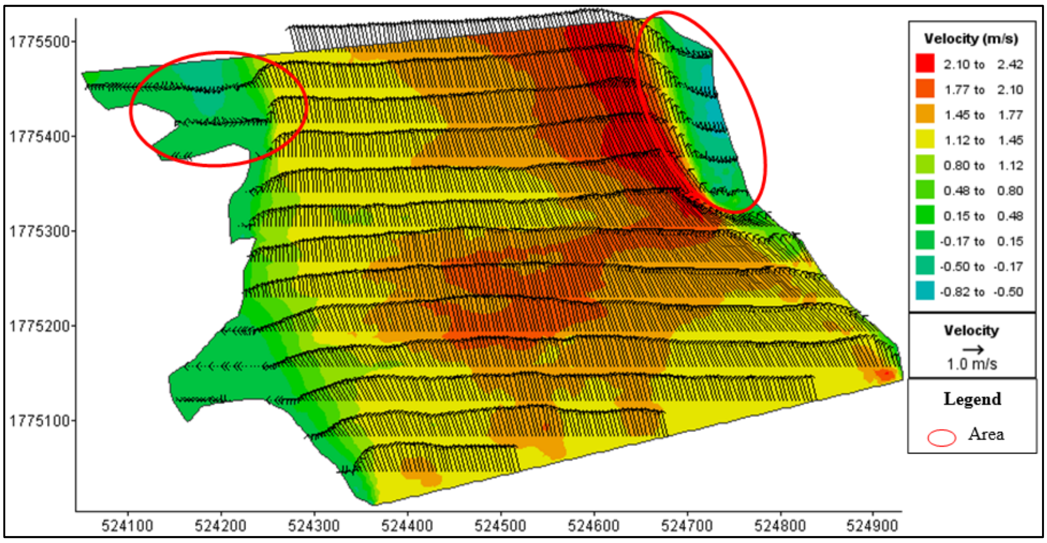

Figure 4. Flow velocity before Tran Thi Ly bridge construction.

However, comparing with the study result of (Đoàn Công Minh, 2014), which applied the RIVED 2D to also simulate the Han River flow after Tran Thi Ly Bridge construction, the TELEMAC-3D result is still lower. The difference between the two results is roughly 0.49m/s. The lower might be due to the difference in capacity of mesh production. The TELEMAC-3D possesses an outstanding capacity in creating the mesh, so it can represent the river bathymetry as well as geometry of adding structure better than other models, such as RIVED 2D (Hervouet 2000). This preeminence is expected to make its results become more accurate and more confident.

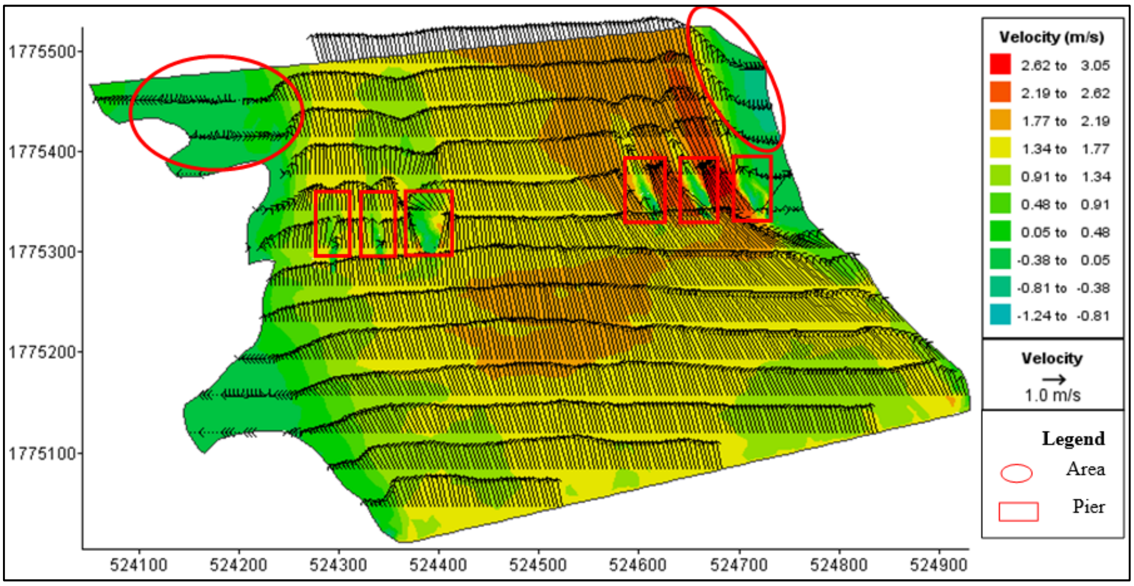

Figure 5. Flow velocity after Tran Thi Ly bridge construction.

On the contrary, the flow closed to river banks is virtually not changed. In both scenarios, with or without bridge, the flow separation appears in area along the banks, followed by small eddies. These can be understood that the piers do not impact much on flow near the banks. The flow separation is caused by the disparity in water depth and velocity between two areas, main stream versus along river.

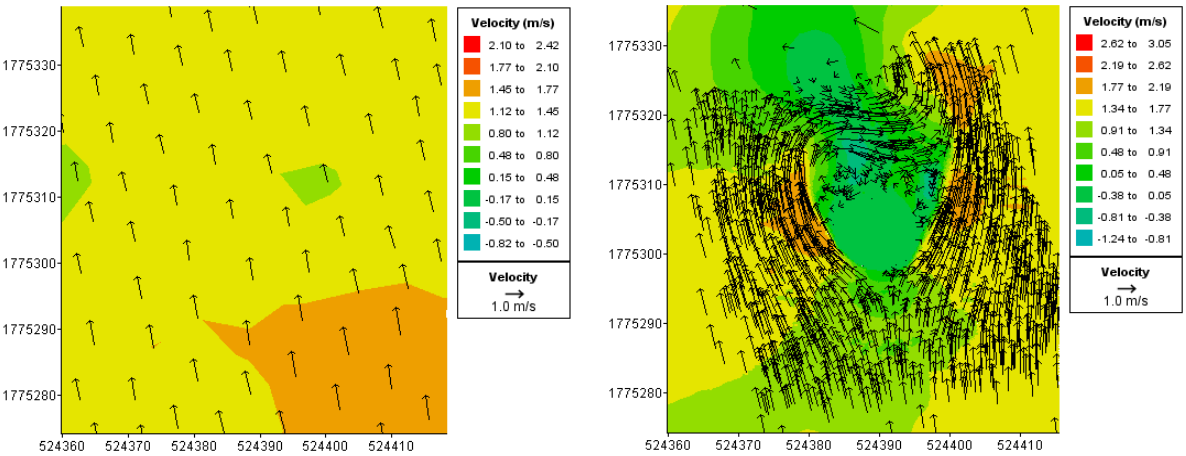

Figure 6. Detail flow velocity at pier S5 before and after Tran Thi Ly Bridge construction (without bridge: left, with bridge: right).

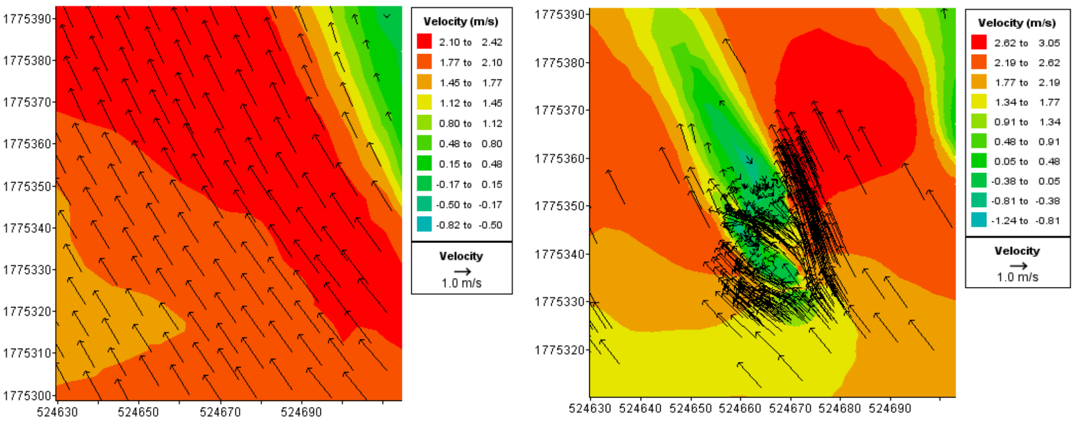

Figure 7. Detail flow velocity at pier S7 before and after Tran Thi Ly Bridge construction (without bridge: left, with bridge: right).

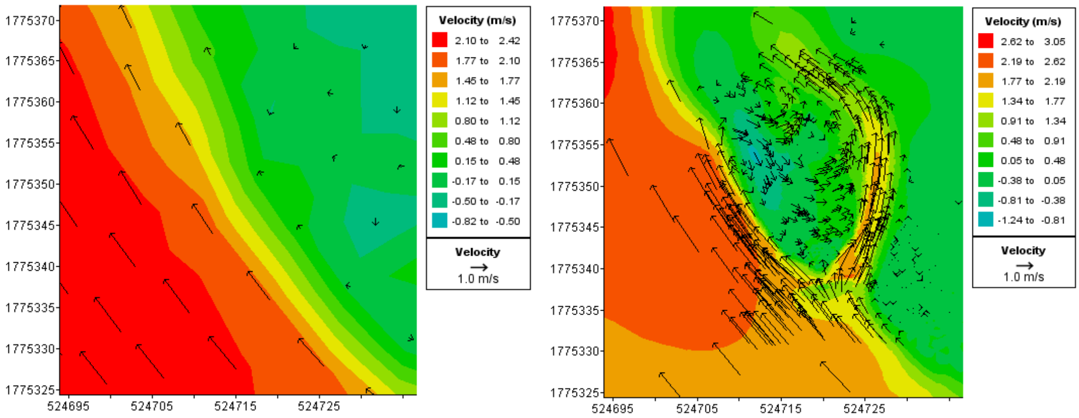

Figure 8. Detail flow velocity at pier S8 before and after Tran Thi Ly Bridge construction (without bridge: left, with bridge: right).

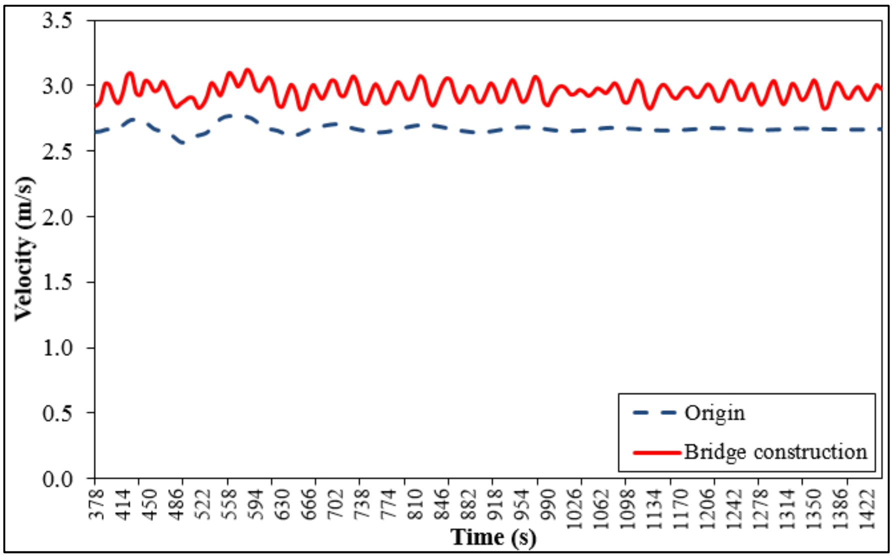

Figure 9. Velocity variation due to the time at main stream flow before and after bridge construction.

Regarding to local aspect, the results of piers S5, S7, S8 are presented from Figure 6 to Figure 8. After Tran Thi Ly Bridge construction, the velocity at pier location increase similarly to the general aspect (Figure 10). Therefore, the value fluctuates so significantly. The maximum change reaches to 0.52m/s, occurring at piers S7, S8 (Figure 7, 8). Besides that, the simulation also demonstrated that there are eddies appearing after piers. As the reality, the eddy geometry and location change causally due to the interaction between flow and works.

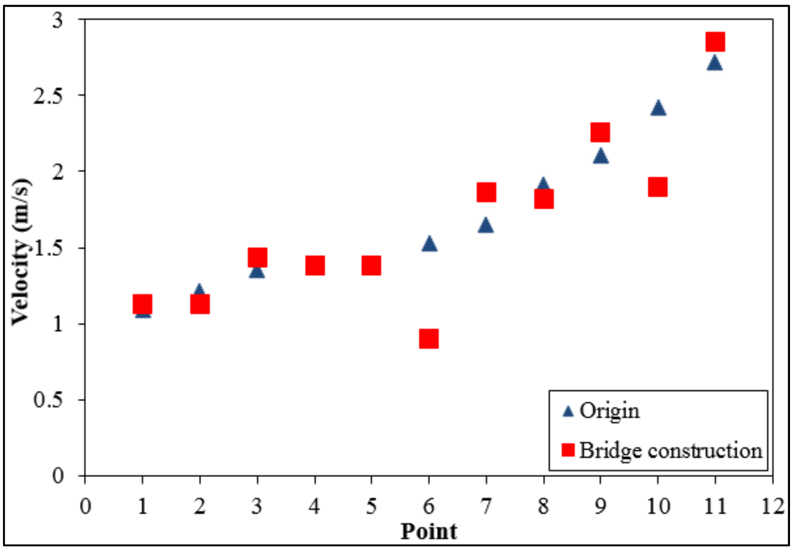

Figure 10. The difference of average velocity before and after Tran Thi Ly Bridge construction.

The flow velocity after adding the piers augments in overall and unequally between locations. The flow between the piers is seemingly faster. Inversely, the one in front of the tents to decrease (Figure 10).

5.2 Water level change

Tran Thi Ly Bridge construction is judged for causing the water level to change hugely. The modelling proves that water level after adding the construction will go up at upstream parts. The augmentation leads to a big disparity of water level between up and downstream parts. The maximum difference can reach to 0.17m (Figure 12).

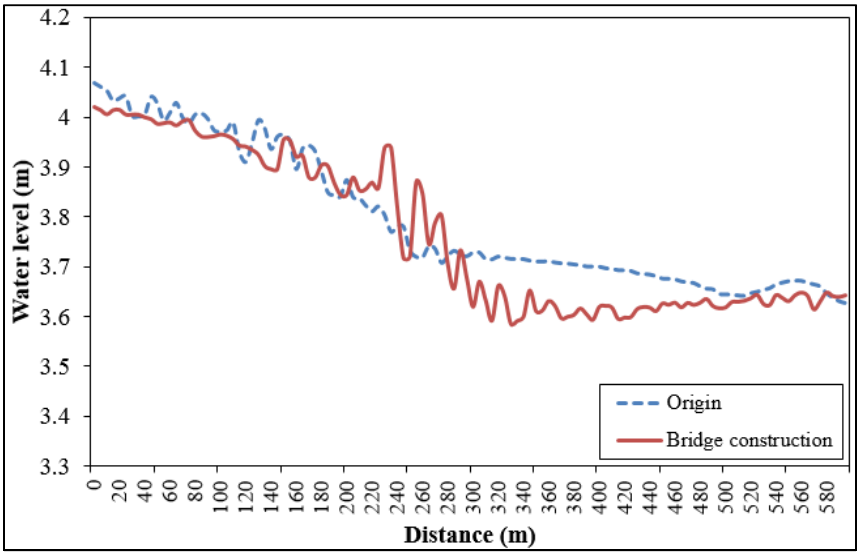

Figure 12. Water level along the river.

5.3 River bed variation

The impact of bridge construction on flow velocity has been demonstrated at section 5.1. As a result, these lead to the change in bed evolution process.

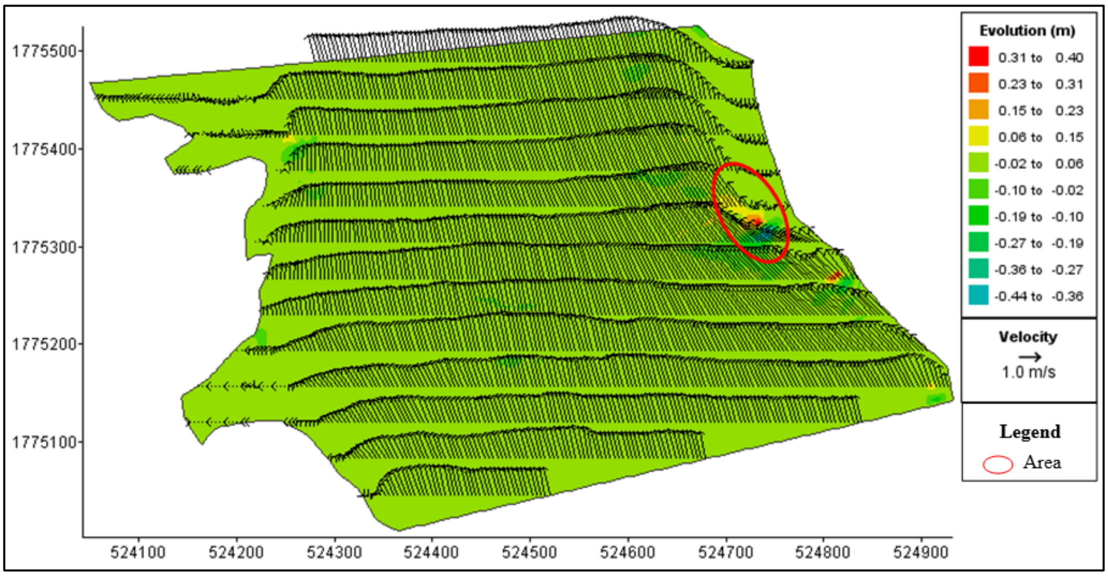

Figure 13. River bed evolution before Tran Thi Ly construction.

Following that, the erosion before building the bridge occurs apparently in right side of river where the bathymetry change significantly. However, the phenomenon appears locally and its depth is not very big. The sediment just moves and deposited around erosion area, so the varied depth of bathymetry fluctuates from -0.44m to +0.4m. Therefore, the evolution process is not big in original case (Figure 13). Otherwise, the erosion and deposition occur more seriously with the case of adding construction. The phenomenon in this scenario appears not only on the right side but also in the area surrounding piers. The erosion and deposition depth after adding the bridge fluctuate from -0.82m to 0.7m, higher than that of the original case of -0.27m to 0.3m, respectively. Due to the increase of velocity, the sediment around the piers might be removed and

  / ISSN 1562-6865 (Online) - ISSN 1063-7710 (Print)

transported easily. It happens considerably at location of pier S5, S7, S8 (Figure 15, 16, 17). The depth fluctuation of this phenomenon is from -1.0m to 0.95m. The sediment movement makes the bed evolution becomes more complicated. The big change concentrates at area around pier S5. This erosion process is showed in Figure 18. In the case of pier S5, 15.75 m from the piers is the length of erosion hole. Longer than this distance, the pier does not affect anymore on scour phenomenon.

The scour around the piers is expected to affect significantly on the stability of Tran Thi Ly Bridge.

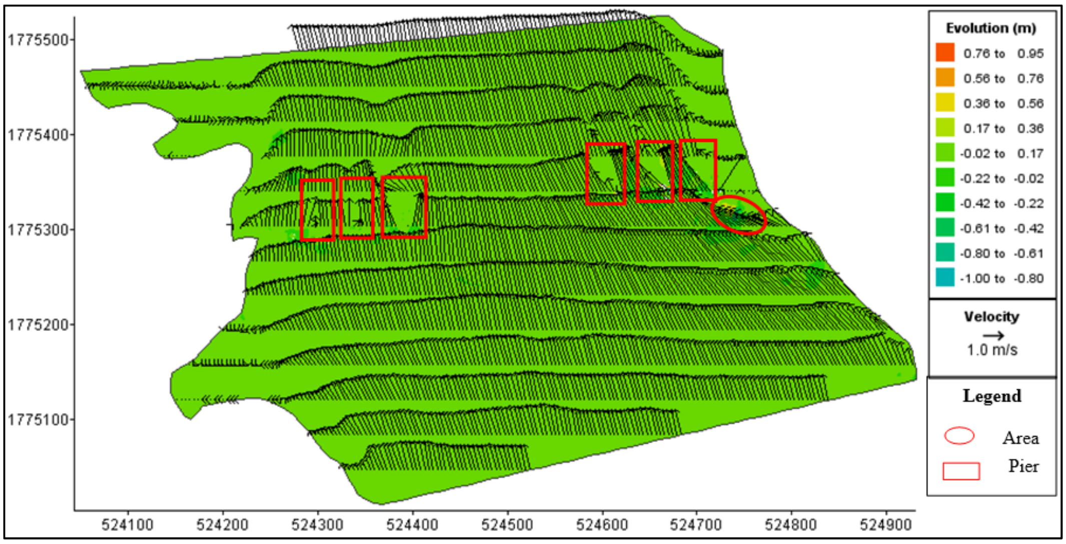

Figure 14. River bed evolution after Tran Thi Ly Bridge construction.

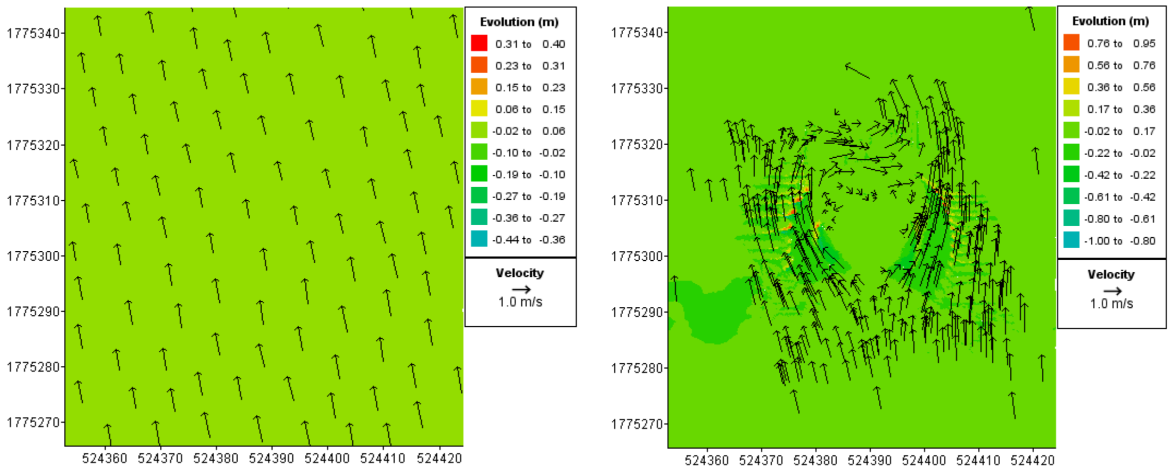

Figure 15. Comparing the bed evolution at pier S5 before and after Tran Thi Ly construction (without bridge: left, with bridge: right).

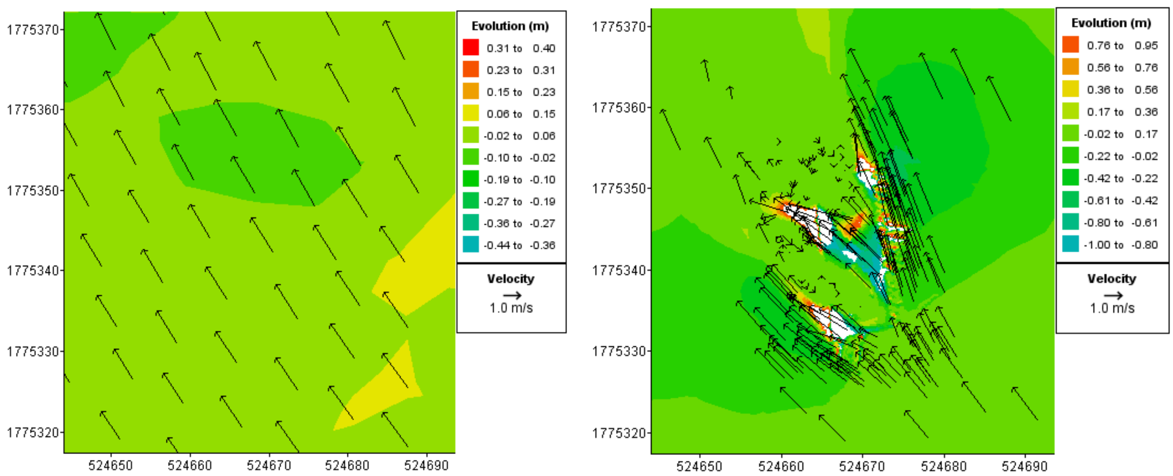

Figure 16. Comparing the bed evolution at pier S7 before and after Tran Thi Ly construction (without bridge: left, with bridge: right).

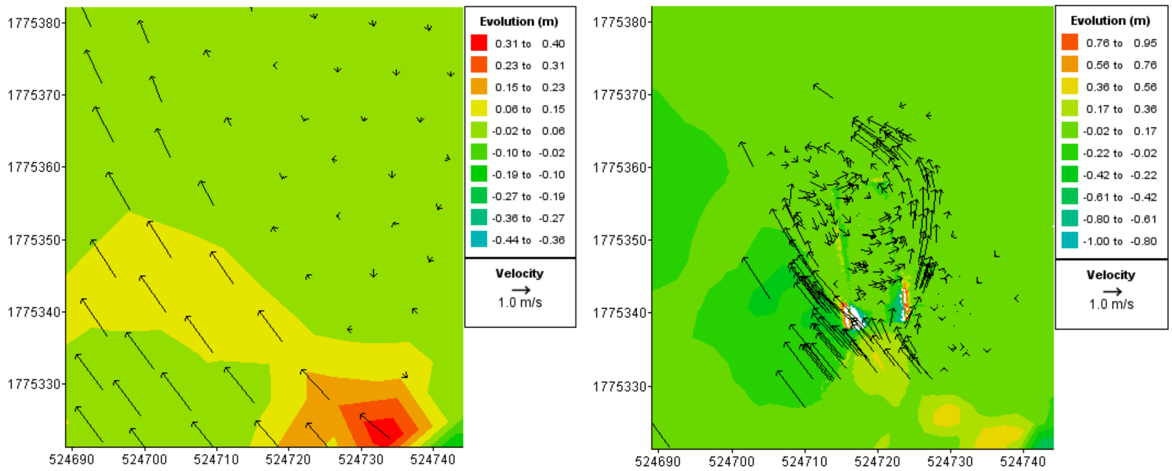

Figure 17. Comparing the bed evolution at pier S8 before and after Tran Thi Ly construction (without bridge: left, with bridge: right).

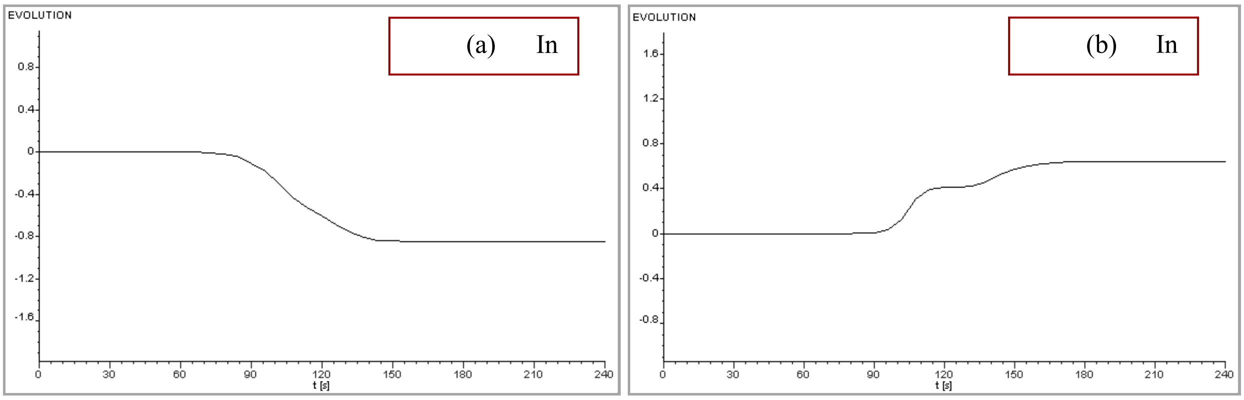

Figure 18. Erosion process at pier S5 after constructing bridge.

6 CONCLUSIONS

In this study, a coupling model TELEMAC-3D/ SISYPHE was used to simulate the bed evolution at the Han River under the impact of Tran Thi Ly Bridge. The study shows that after adding the bridge, the hydraulic flow regime at the area around the piers fluctuates considerably. The velocity increases generally. In particular, the maximum augmentation concentrates roughly around piers S5, S7, S8. The biggest change reaches to 0.52m/s in comparison with the original case. Furthermore, flow direction surrounding the piers varies locally and unstably due the obstruction of additional works. It leads to the appearance of eddies at the side as well as the downstream part. Subsequently, the erosion and deposition activity happen more seriously after constructing Tran Thi Ly Bridge.

The study is expected to provide an overview about the impact of Tran Thi Ly Bridge construction to enable authorities to mitigate its impact, and also for river bank protection. Additionally, the study demonstrates the high performance capacity of the TELEMAC-3D/ SISYPHE model in modelling river hydraulic regime, sediment transport, and bed evolution as well.

REFERENCES

Chaudhry, M.H. (2007). *Open-Channel Flow*. Springer Science & Business Media, 523.

Chien, N. & Wan, Z. (1999). *Mechanics of Sediment Transport*, United States: American Society of Civil Engineers, Reston, VA (US),

Danang construction department (2013). *Da Nang Hydrology and Urban Development Simulation Model*. Retrieved from: <http://www.sxd.danang.gov.vn/>

DESOMBRE, J. (2013). *TELEMAC Modelling System - TELEMAC-3D Software, Operating manual*, 4 Canadian Hydraulics Centre, National Research Council.

Giardino, A. & Monbaliu, J. (2005). *Morphodynamic Evolution of a Sand Bank*, Technical report, Catholic University of Leuven, Civil Engineering Department, Hydraulics Laboratory.

Hamill, L. (1998). *Bridge Hydraulics*. CRC Press, 384.

Hervouet, J. (2000). TELEMAC Modelling System: An Overview. *Hydrological Processes*, 14(13), 2209–2210.

Hervouet, J. M., Razafindrakoto, E., & Villaret, C. (2011). Dealing with Dry Zones in Free Surface Flows: A

New Class of Advection Schemes. *In Proceedings of the 34th World Congress of the International Association for Hydro-Environment Research and Engineering*, *33rd Hydrology and Water Resources Symposium and 10th Conference on Hydraulics in Water Engineering*, 4103, Engineers Australia.

Kabir, A. (2005). Modelling Local Scour around Bridge Piers using TELEMAC*, Doctoral dissertation*, University of Cape Town.

Langendoen, E.J., Mendoza, A., Abad, J.D., Tassi, P., Wang, D., Ata, R., Abderrezzak, K.E.K. & Hervouet, J.-M. (2016). Improved Numerical Modeling of Morphodynamics of Rivers With Steep Banks. *Advances in Water Resources*, 93, 4–14.

Melville, B. W. & Coleman, S. E. (2000). *Bridge Scour*. Water Resources Publication, 550.

Minh, Đ. C. (2014). *Nghiên cứu đề xuất phương pháp tính xói cục bộ tại trụ cầu Trần Thị Lý, thành phố Đà Nẵng*. Đại học Đà Nẵng.

Ministry of transport. (n.d.)., Bridge Design Standard 22TCN 272-05. Retrieved from: <http://mt.gov.vn/vn/Pages/Trangchu.aspx>

Office, D.N.C.C.C. (n.d.). No Title. Retrieved from: <http://ccco.danang.gov.vn/>

Smolders, S., Maximova, T., Vanlede, J., & Teles, M. J. (2014). Implementation of Controlled Reduced Tide and Flooding Areas in the TELEMAC 3D Model Of The Scheldt Estuary. *Proceedings of the 21st TELEMAC-MASCARET User Conference*,15th-17th October 2014, Grenoble – France, 11-118.

Sturm, T.W. (2010). *Open Channel Hydraulics*. McGraw-Hill New York.

Trần, Đ. N. (2008). *Xói lở ở công trình cầu: Phần 2*. NXB Xây Dựng.

Transport engineering consulting joint stock company no. 533. (n.d.). No Title. Retrieved from: http://www.tecco533.com.vn/ on January 2017

Van Rijn, L. C. (1993). *Principles of Sediment Transport in Rivers, Estuaries and Coastal Seas*. Aqua publications Amsterdam 1006, 1-17.

Villaret, C. (2004). *SISYPHE Release 5.4. User Manual*, Report P75G17, EDF/LNHE, Chatou, France, 1–69.

Proceedings of the 37th IAHR World Congress
August 13 – 18, 2017, Kuala Lumpur, Malaysia

FLOW NEAR GROYNES: EXPERIMENTAL OR COMPUTATIONAL APPROACHES

QUANG BINH NGUYEN [1], NGOC DUONG VO[2] & PHILIPPE GOURBESVILLE [3]

[1, 2] Faculty of Water Resource Engineering,
University of Science and Technology, the University of Da Nang, Viet Nam
[2, 3] Innovative City lab URE 005
Polytech'Nice Sophia, Nice Sophia Antipolis University, France.
nqbinh@dut.udn.vn; vo.ngoc.duong@dut.udn.vn; Philippe.GOURBESVILLE@unice.fr

ABSTRACT

The research of Mohamed F.M Yossef and Huid J. de Vriend published in the Journal of Hydraulic Engineering (2011) presented the dynamics of the flow near groynes in detail. By physical experiment, in a fixed bed flume, the authors found out the differences in nature of turbulence between submerged and emerged groyne stage. They provided insight into the flow pattern in vicinity of groynes, the shape and extent of the mixing layer at different flow stages, and the dynamic behavior of velocity along the mixing layer of the main channel and the groyne fields. With the aim of modeling, with a numerical tool, the observed results, this paper presents the work developed on the TELEMAC 3D modeling system and the hypothesis used by Yossef and De Vriend (2010). The simulation is very impressive. It could represent almost all characteristics existing in the experiment. The performance of the simulation demonstrates the strong capacity of computational modeling systems like TELEMAC 3D in representing the flow stage in different cases. The result also confirms the preeminence of computational program about flexibility, simulated time and result expression in comparison with experiment. The paper is expected to provide an insight about using computational model for hydraulic research and to be useful for studying the dynamics of flow near groynes by hydrodynamics simulation.

Keywords: Flow near groyne; dynamic behavior of velocity; hydrodynamic; modeling; TELEMAC 3D.

1 INTRODUCTION

River flow regime influences much on the socio economic development of a region. However, under the development pressure, humans are expected to impact the river increasingly. These impacts have been judged to change the stream flow regime which are the main causes of bank erosion and bedform movements. These processes bring many negative consequences back to human society. Hence, it is necessary to determine and have solutions to maintain the bedform stability. In many solutions, training works such as groynes or spur dikes are seemly the most satisfactory (Przedwojski et al., 1995; Uijttewaal, 2005; Yossef & de Vriend 2010). The groyne or spur – dike is often constructed at an angle to the flow and begins at the riverbank with a root, and ends at the desired regulation line with a head. Due to its capacity in maintaining a deep, straight channel for improved navigation, a range of groynes are used to restrict the flow in a narrow channel to keep it away from erodible banks (McCoy et al., 2008). Therefore, the adding structures will cause a local significant disorder in river flow. Flow around them, in particular flow near groyne, alters complicatedly in three dimensions with different levels. Process consequences are the appearance of multiple secondary flows and eddy area which are quite difficult for modeling out of our limited knowledge about the exchange process between groyne fields and main channel (Chrisohoides et al., 2003; Nagata et al., 2005; Haltigin et al., 2007; Raudkivi, 1986). Even if, these problems have been studied deeply in many aspects from theory, experiment or modeling, the comprehension on them is seemly still not enough to be able to represent accurately the phenomena at groyne area. For example, the famous study of Altunin (1962) supplied an theory about how to determine reasonable design of training work. Recently, due to the development of technology and equipment, many experiments have been realized to find out the effective structure and reasonable placement of groyne. In order to find efficient alternative designs, in the physical, economical, and ecological sense, for the standard groynes for large rivers in Europe, Uijttewaal (2005) released an experiment which concentrated to test the effects of various groyne shapes on the flow in a groyne field. 69 scenarios were run by the setup of Yeo et al. (2005) to get the knowledge for writing down the Korean designed standard of river training works. These experiments concentrated to analyse the arrangements, structure of groyne system in Korean river system. Similarly, Shahrokhi & Sarveram (2011) also published an experience on 3D simulation for researching the effect of groyne on flow regime.

Although developing on two different methodologies, numerical and experimental, they have given results which are rather similar (Constantinescu et al., 2009), (Zhang et al., 2009). They have been expected to contribute remarkably to the understanding of the characteristic of flow, the interaction between the flow and morphology at groyne fields and also in designing the training works. Nevertheless, experiment and modeling methodologies possess particularities which are believed as their advantages and disadvantages. The experiment which is realized via physical modeling is used to apply for designing large constructions (Przedwojski et al., 1995). Because of present technology, this method has been only able to demonstrate its performance in river segments having the simple shape where hydrodynamic regime is not complicated. In the case of complex locations such as junctions, high bathymetry variations or shallow areas, this approach seems inappropriate to simulate flow characteristics. Furthermore, the cost of physical modeling is also a big limitation, especially with medium and small works (Garde et al., 1961; Rajaratnam & Nwachukwu, 1983; Melville, 1992; Kuhnle et al., 1999). Inversely, nowadays with the developing of mathematics and computational system, numerical modeling is seen as a convenient, high performance, flexible and low cost tool for analyzing the hydrodynamic characteristics at groyne fields (Ge & Sotiropoulos, 2005). Lots of models have been developed such as TELEMAC 3D, Delft 3D, FLOW 3D. They have demonstrated their conveniences in comparison with experiment. However, the problem is that the experiment has to be carried out in advance to supply fundamental knowledge for developing the numerical model and also test their capacity. With these reasons, Mohamed F.M Yossef and Huid J. de Vriend realized a famous experiment which aims to study the dynamics of the flow near groynes. The process was executed on a fixed bed flume which was constructed based on the geometry of Dutch River Vaal, and model size is scale of 1:40 of the typical real dimension. By testing with different flow depth inputs, these authors observed and analyzed quite concretely, the flow stage in two dimensions (2D) at groyne fields, tips of groyne as well. Their achievement has been appreciated and contributed importantly for designing the training works and for developing numerical modeling. With the aim of modeling with a numerical tool the observed results, this paper presents the work developed with the TELEMAC 3D modeling system and the hypothesis used by Yossef and De Vriend (2010). The simulated results are quite similar with the experiment in many aspects. The performance of the simulation demonstrates the strong capacity of computational modeling systems like TELEMAC 3D in representing the flow stage in different cases. The result also confirms the preeminence of computational program about flexibility, simulated time and result expression in comparison with experiment. The paper is expected to provide an insight about using computational model for hydraulic research and to be useful for studying the dynamics of flow near groynes by hydrodynamics simulation.

2 METHODOLOGY

2.1 Study area

The Waal is the largest distributary of the Rhine River flowing through Netherlands (Figure 1). This river plays an important role in inland water transport in Europe where it is the major waterway connecting the port of Rotterdam to Germany. In order to protect river banks, guarantee a sufficient depth and width for waterway, a major hydraulic engineering work system has been constructed since long time ago. Until now, this system reaches to more than 500 groynes with a quite reasonable design (Hoffmans, 2012).

Figure 1. Study area.

2.2 TELEMAC 3D

The TELEMAC-MASCARET system is a famous product of the National Hydraulic and Environment Laboratory, Electricity of France (EDF). By developing on the finite-element method and using unstructured grid of triangular elements to represent the space, this systems is expected to be a powerful integrated modeling tool for use in the field of free-surface flows (Villaret, 2004; Kabir, 2005; Hervouet et al., 2011; Smolders et al., 2014; Langendoen et al., 2016). TELEMAC-3D is a three-dimensional computational code describing the 3D velocity field (u, v, w) and the water depth h (and, from the bottom depth, the free surface S) at each time step. Besides, it solves the transport of several tracers which can be grouped into two categories, namely the so-called “active” tracers (primarily temperature and salinity1), which change the water density and act on flow through gravity), and the so-called “passive” tracers which do not affect the flow and are merely transported. (DESOMBRE, 2013). TELEMAC 3D solves problems with two different approaches, the first is based on Navier-Stokes equation with the assumption that the equation takes into account of the hydrostatic pressure and the second is with the assumption that the Navier-Stokes equation does not take into account of the hydrostatic.

The Mohamed F.M Yossef and Huid J. de Vriend’s experiment, which concentrates measuring the flow velocity in three dimensional ways, determine the effect of training works on flow regime, is seemingly appropriate with principle of second approach, non – hydrostatic equation. Relying on above reason, in this study, the non – hydrostatic Navier-Stokes equation was used.

2.3 Model setup

The model setup was almost similar to the experiment realized in the Laboratory of Fluid Mechanics at Delft University of Technology.

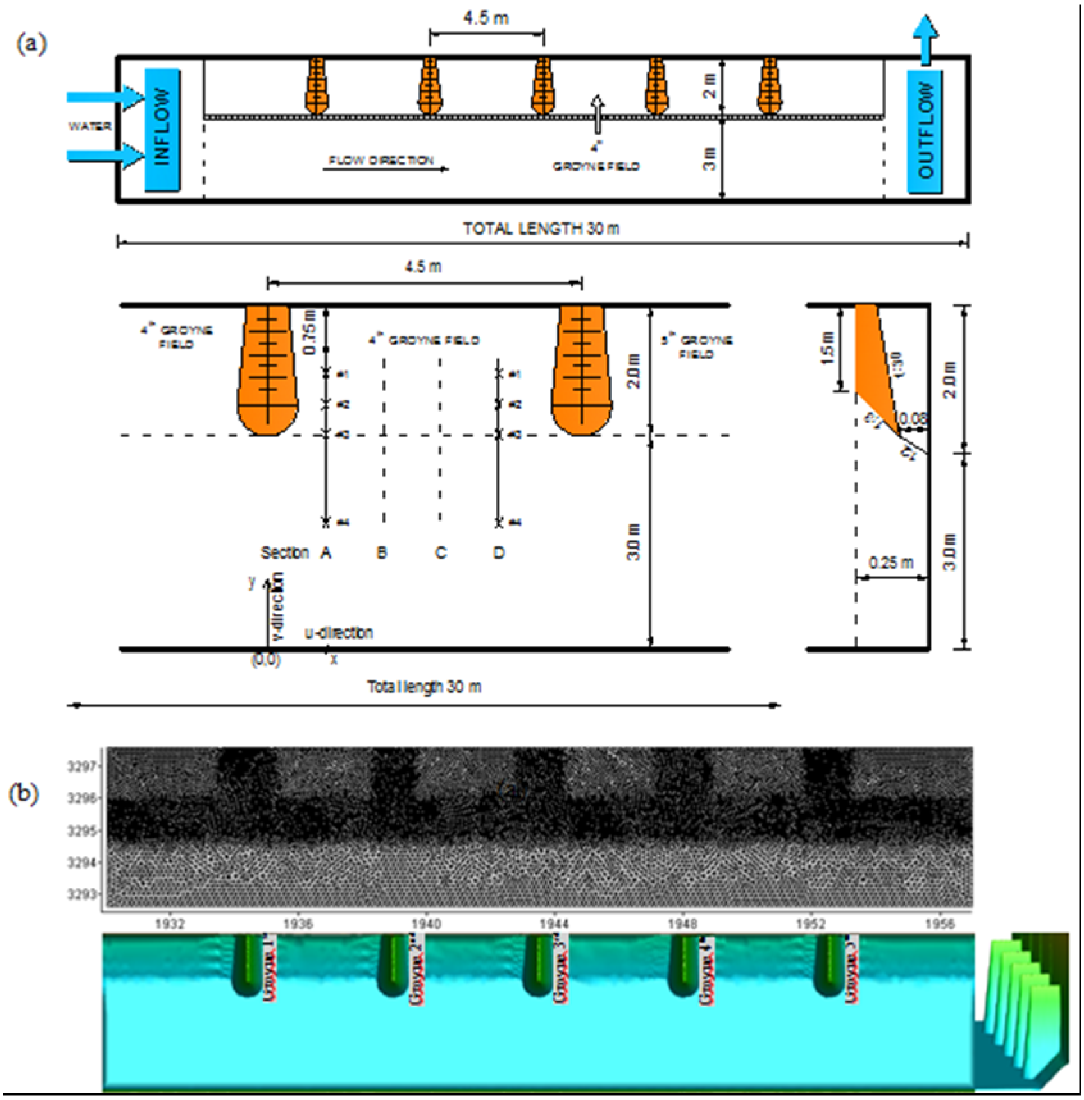

Figure 2. Model setup, (a) Experiment in Laboratory, (b) TELEMAC 3D modeling.

Accordingly, a Waal river straight typical segment was re-traced through a miniature copy at a scale of 1:40. The duplicate measured 5m in width, 30m in length, containing five groynes. Simulated groyne is the representative structure of this system which is straight, impermeable and perpendicular to river bank. This structure is expressed via Figure 2 with 0.25m in height, 1.5m in crest length, its slope on all sides is 1:3 and beach slope of groyne fields is 1:30. The bed of the model was fixed and flat in the main channel; and sloped towards the bank in the area between the groyne. All characteristics of experiment flume were represented in TELEMAC 3D via a mesh with 27,200 nodes and 53,824 elements. For simulating the flow characteristic accurately, the mesh structure was constructed varying due to bed topography, groyne location and flow regime. Relying on this principle, the mesh in this study was created with three different areas. The first was groyne, around groynes and transition area between groyne field and main channel. The second area is the space between groynes. The last area is the main channel. The mesh density factor was 0.05, 0.1 and 0.15 respectively (Figure 2b).

Experimental condition, which is key factor decided to the flow stage, is replaced by boundary condition in numerical model. In order to represent the emergent and submerged flow stages like in the experiment, the simulation was carried out with two different scenarios, described in boundary condition in table 1. Following that the mean velocity of main channel was maintained at a constant value about 0.3m/s, the flow dynamic variation was depended on water level inputs that were 0.248m and 0.31m corresponding with two flow stages.

The simulation time lasted more than 1800s to ensure the observation of a full coverage of the largest turbulence structure. In comparison with the experiment of Mohamed F.M Yossef and Huid J. de Vriend, the simulation time is longer than three times.

With the aims of obtaining subcritical flow as observe in the prototype, the Froude number (F) in experiment was around 0.2. Besides, the Reynolds number ® was maintained high enough to ensure turbulent flow in both channel region ($R \cong 6.10^6$) and groyne fields region ($R \cong 6.10^4$). In the TELEMAC 3D model, the Manning Coefficient was set up variously to agree with the above conditions. Depending on flume material, after model calibration, the manning number was defined for two regions as in table 2.

Table 1. Boundary condition for TELEMAC 3D simulation.

No	State	Velocity, V (m/s)	Discharge, Q (m^3/s)	Water level, h (m)
1	Emergence	0.3	0.248	0.248
2	Submergence	0.3	0.305	0.310

Table 2. Manning Coefficient.

Polygons	Manning, n
Groyne and groyne field	0.015
Main channel	0.025

3 RESULTS AND DISCUSSION

3.1 Horizontal velocity comparison

The simulation result showed that in case of emergent flow, high velocity field in u direction occurred at the entrance where it contained a lot of fluctuations in the main riverbed, then high velocity field tended to separate gradually from the region near the tip of groyne foot (Figure 3). Conversely, in submerged case, the velocity field was distributed quite uniformly, taking higher values in riverbed and appeared locally at the position of groyne 1; this field tended to move away from the top of groyne (Figure 4). The highest velocity (the maximum speed) belonged to the emergent case was higher than that of submerged case, corresponding to 0.45m/s, 0.43m/s respectively.

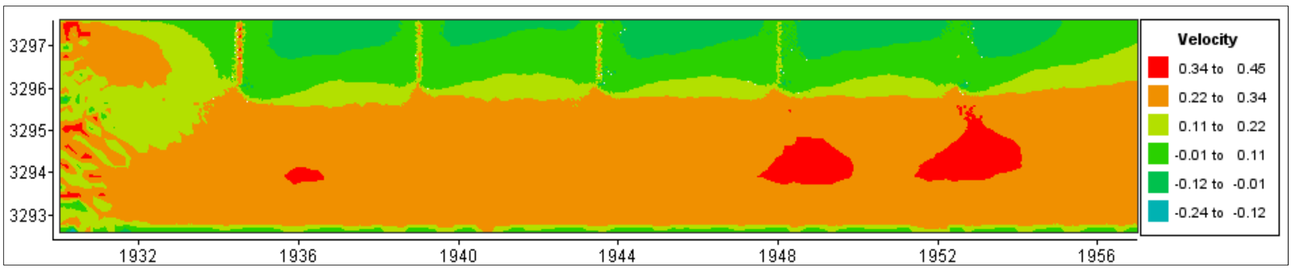

Figure 3. TELEMAC 3D result: Velocity U (m/s) in the case of emergent flow.

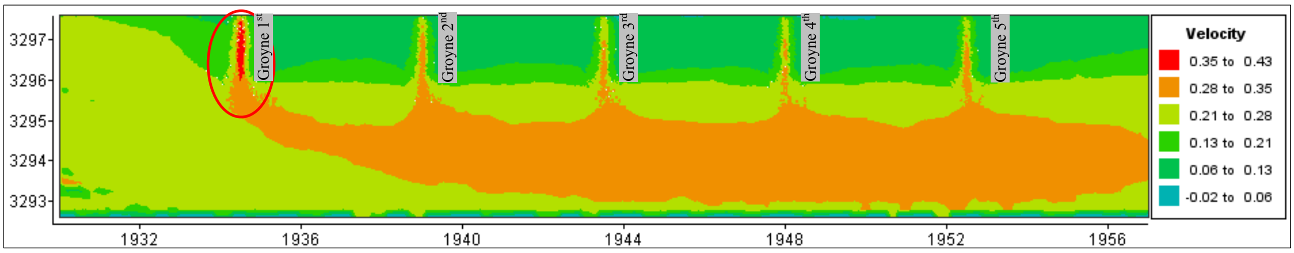

Figure 4. TELEMAC 3D result: Velocity U (m/s) in the case of submerge.

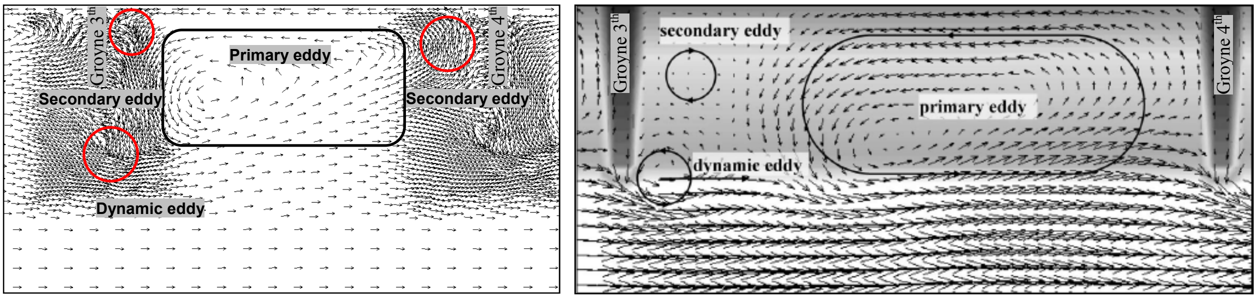

(a) (b)

Figure 5. The flow velocity distribution at groyne 4 in emergent case.
(a) TELEMAC 3D, (b) Experiment.

In considering the velocity field between two embankments, by comparing to the experimental result in submerged case, at the location of embankment 4, based on simulated results, the scale of turbulent region, which appeared near to the embankment 4, was larger than the distance from the top of this embankment nearly 1,24m and the main turbulent region fluctuated in a short scale of approximately 2,1m. Moreover, the turbulence also existed at the small scales which concentrates at the bottom of embankment 5. In contrast to the above experiment, the turbulence varied conveniently with the scale of 2.8m and further than embankment 4 (Figure 5).

3.2 Velocity in special points

Regarding to the simulated and experimental results at points 2 and 3 in two cases (Figure 6, 7), the simulated result of velocity amplitude was smaller than the experimental result, especially with velocity v. The highest velocity amplitudes belonged to emergent flow in the direction of u, v are 0.066m/s, 0.067m/s respectively. Otherwise, the results corresponding to submerged case were 0.099m/s, 0.044m/s respectively while the others of experimental results were 0.17m/s, 0.2m/s and 0.15m/s, 0.28m/s. However, the values of average velocity were nearly approximated (Figure 6, 7). Comparing the similarity between experiment and modeling, the value and amplitude of the velocity in the direction of vector u were more similar than these of the velocity in the direction of vector v.

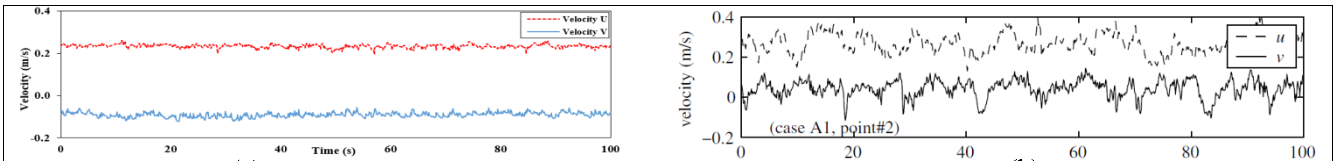

(a) (b)

Figure 6. U, V velocities at point 2 in the case of emergent flow.
(a) TELEMAC 3D, (b) Experiment.

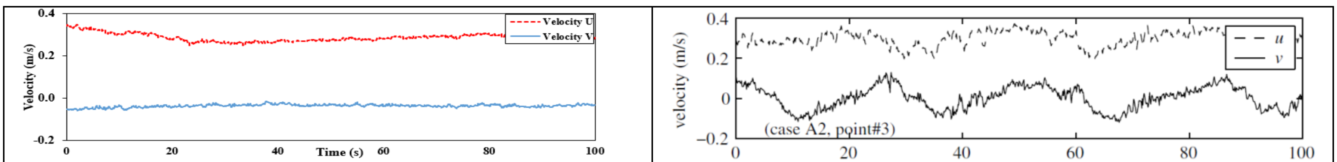

(a) (b)

Figure 7. U, V velocity at point 3 in the case of submerged flow.
(a) TELEMAC 3D, (b) Experiment.

 ©2017, IAHR. Used with permission / ISSN 1562-6865 (Online) - ISSN 1063-7710 (Print)

3.3 Velocity at cross sections

In considering the velocity distribution in horizontal direction of all four cross sections at four different positions, the velocity at river banks in modeling and experimental was nearly approximated while the modeling result at area changing between embankment and river bed was smaller (Figure 8).

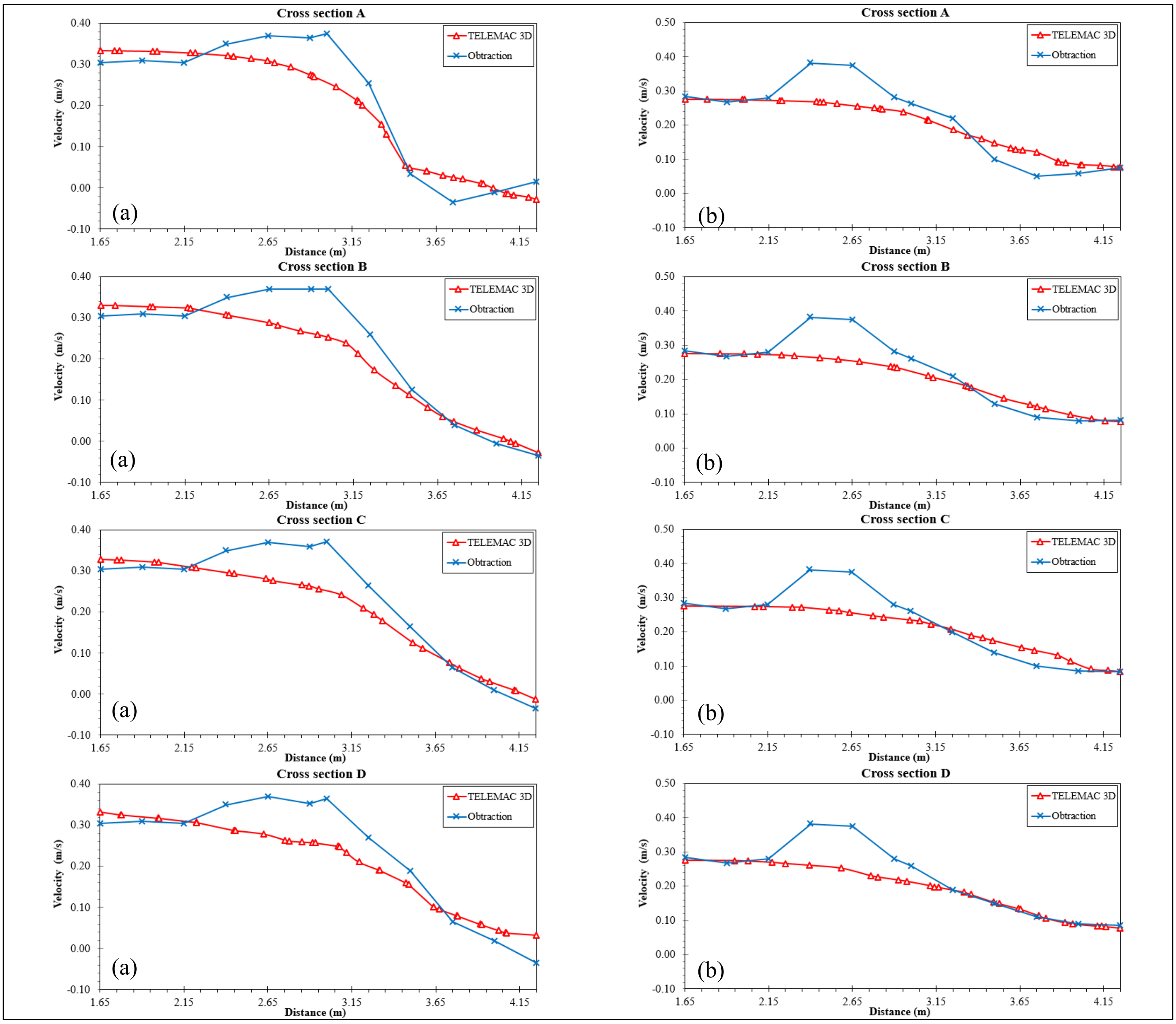

Figure 8. Experimental and modeling velocity at groyne field 4.
(a) Emergent, (b) Submerge.

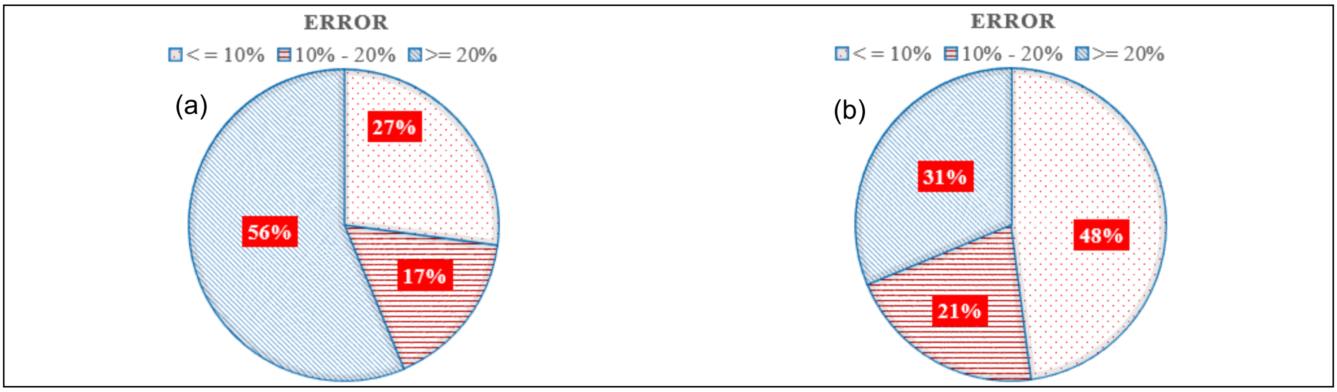

Figure 9. Comparison of similar level between experimental and computational modeling.
(a) Emergent flow, (b) Submerged flow.

In particular, the bias in velocity between simulation and experiment at groyne foot, where there was an area changing between groyne and the main river bed (3 metres calculated from the right side) in four cross sections A, B, C, D in case of emergent flow were 0.13m/s, 0.117m/s, 0.13m/s, 0.116m/s respectively. The result corresponding to submerged flow case were: 0.047m/s, 0.051m/s, 0.026m/s, 0.045m/s respectively. In order to illustrate the similarity between experiment and modeling concretely, the results at 48 points were compared point by point. After comparison, the difference was divided into three groups: smaller than 10%, 10% to 20%, and more than 20%. Comparing the average values of the above groups, the error result in the case of submerged flow was smaller than the one of emergent flow (Figure 9). The main reason to explain for this result is that k-ε turbulence model has not yet caught completely the velocity fluctuation at the groyne foot and the region which contains sudden variation in bathymetry.

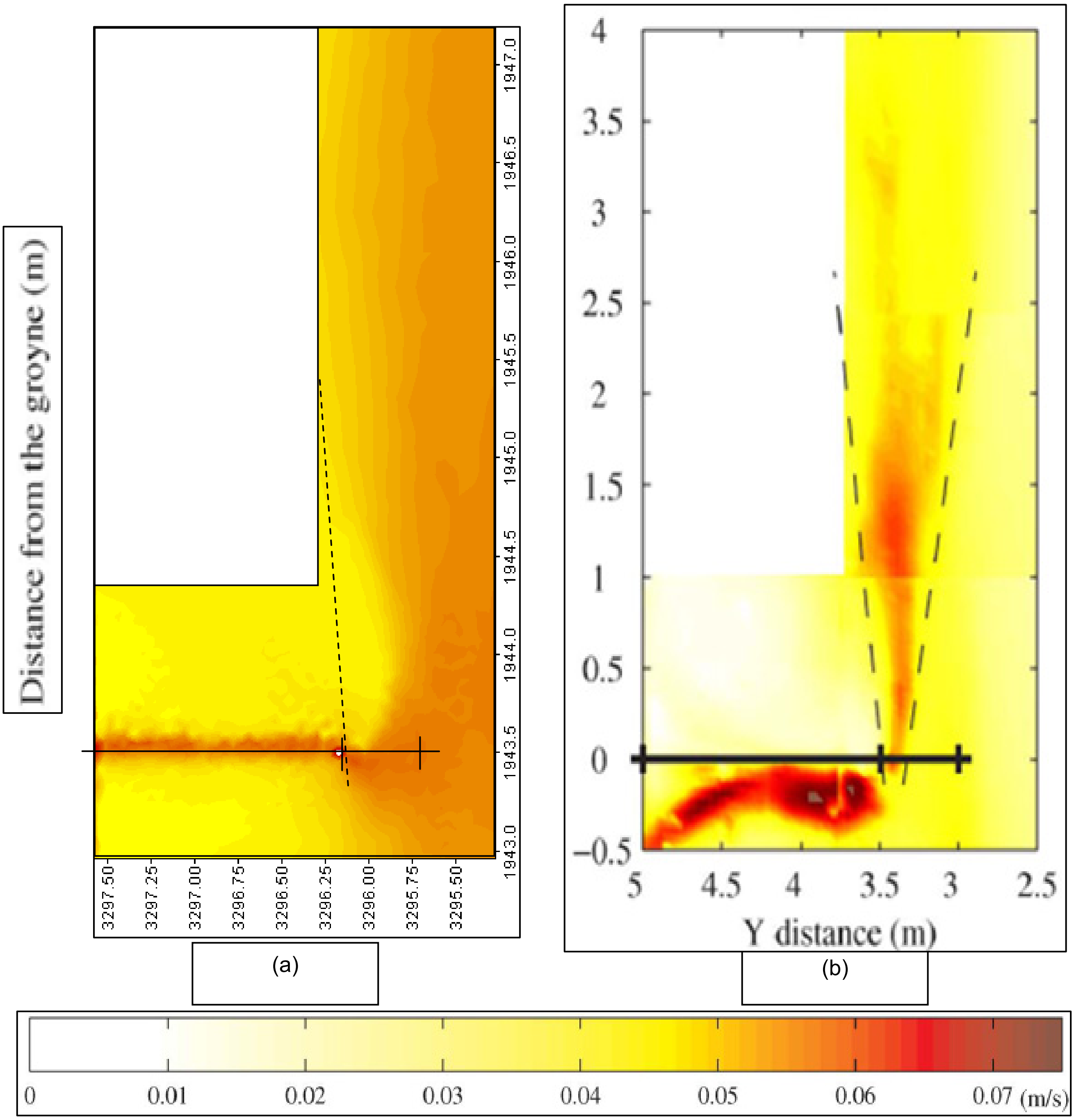

Figure 10. Total turbulence intensity in the case of emergent flow (Continuous line presents for of groyne, break line presents fluctuated area of layers from bottom to top) (a) TELEMAC 3D, (b) Experiment.

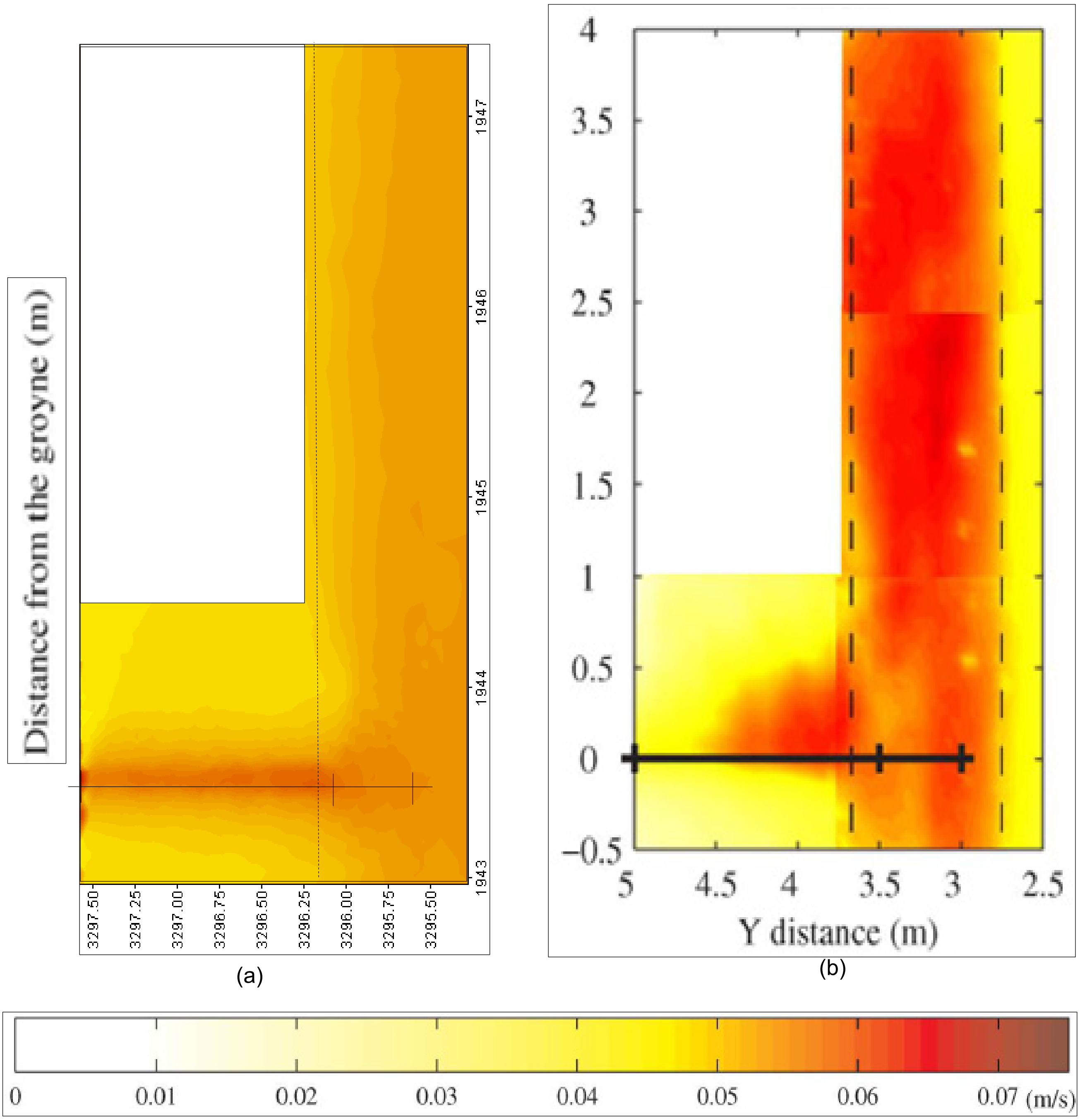

Figure 11. Total turbulence intensity in the case of submerged flow (Continuous line presents for top of groyne, break line presents fluctuated area of layers from bottom to top) (a) TELEMAC 3D, (b) Experiment.

Corresponding to this experiment, turbulent intensity in TELEMAC 3D began varying dramatically at the top of the groyne and increased the width in the direction of the downstream. The maximum turbulent intensity in the case of submerged flow and emergent flow were 0.055m/s, 0.051m/s respectively, calculated from the closer top of the groyne was 1,25m as compared to the downstream. Corresponding to the result in the experiment were 0,065m/s to 0.063m/s, calculated from the closer top of the groyne was 1,5m (Figure 10, 11). The uniformity of turbulent intensity in downstream region results in the no significant variation in the pressure of 4 cross sections A, B, C, D and maximum pressure was smaller than experiment. This problem will be discussed with more detail in the next section.

3.4 Pressure

In two cases, the simulated pressure was always smaller than experimental one except cross section D in emergent flow case. There was no significant change in pressure value at four cross sections so their graphics were quite similar (Figure 12). In both cases, simulated results in case of emergent flow is more appropriate as compared to experiment. The large differences appeared at area where the bathymetry varied significantly - the area between main river bed and groyne fields.

The maximum bias, corresponding to cross section C, was located between two groynes where it contained the maximum turbulent intensity. Specifically, the TELEMAC values in case of submerged and emergent flow were 1.03N/m^2, -0.76N/m^2 respectively and the corresponding values in experiment were -1.8N/m^2, -1.9N/m^2.

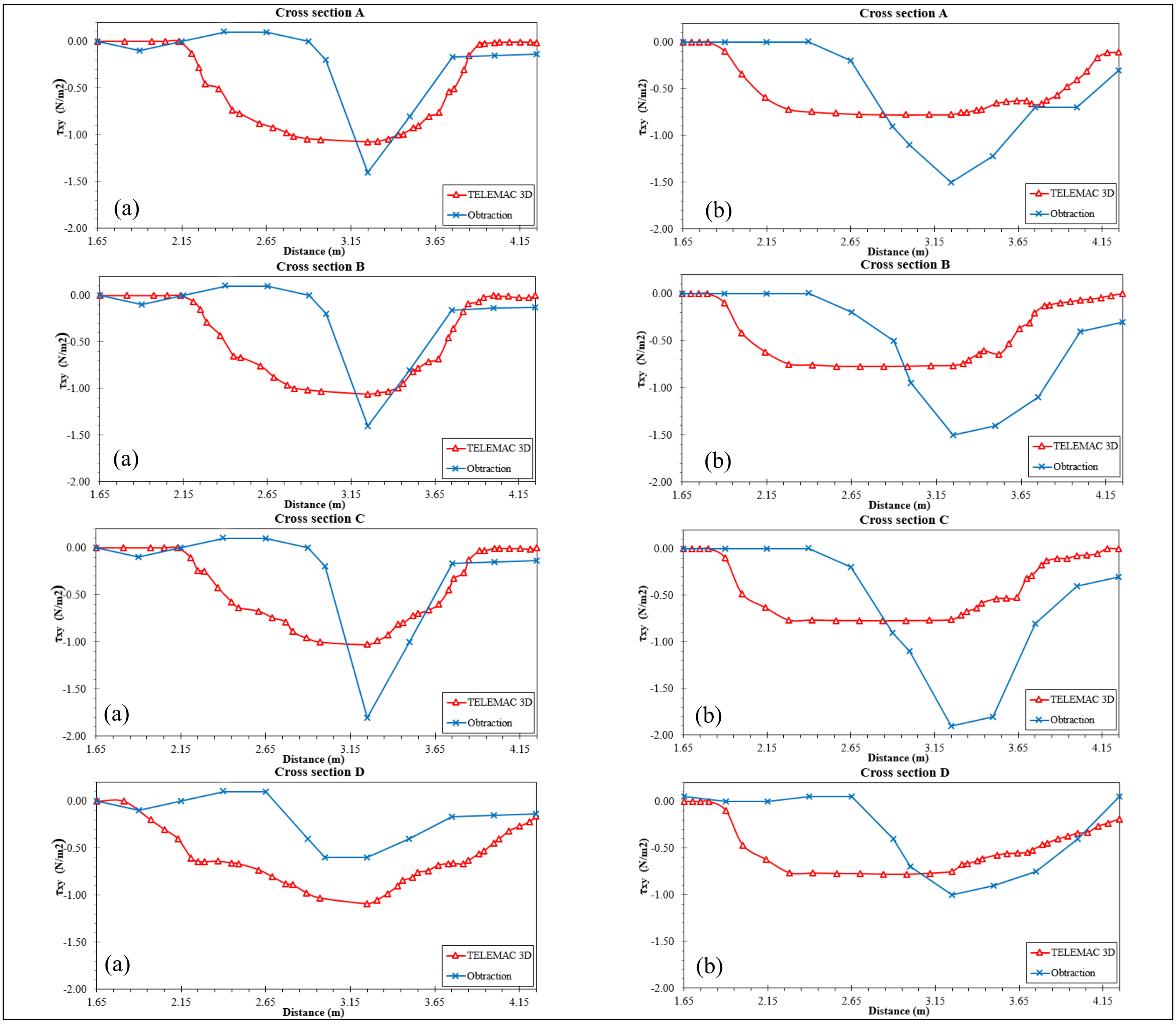

Figure 12. Comparisons of transverse shear stress between experiment and modeling at cross section 4 of groyne field 4. (a) Emergent, (b) Submerge.

4 CONCLUSIONS

The comparison between 3D simulation and experiment for flow around groyne helps to clarify the complexity of flow not only in front of and behind the groyne but also in the middle of main stream and groyne area. The modeling result presents a high coincidence with experimental result in many aspects. The maximum bias of result occurred at groyne foot, along the area, suffering a sudden variation in height between riverbed and groyne.

The amplitude of velocity fluctuation in simulated case was smaller than experimental case, especially with velocity v. The amplitude of velocity fluctuation reached the maximum in the case of emergent flow in the direction of u, v but the values of average velocity were nearly approximated. Velocity in the direction of u had value and amplitude fluctuation was more exact than the one of direction of v.

Turbulence intensity in TELEMAC began changing dramatically behind the crest of groyne and increasing the width along the downstream. The maximum turbulence intensity appeared near to the downstream. The uniformity of turbulent intensity in downstream region results in the no significant variation in the pressure of 4 cross sections A, B, C, D and maximum pressure was smaller than experiment.

In all 4 cross sections, the velocity along to river bank of modeling and experiment was almost similar. However, at the bathymetry variation, the modeling velocity was smaller than the experimental one. Regarding

  / ISSN 1562-6865 (Online) - ISSN 1063-7710 (Print)

to pressure, the value of transverse shear stress and the shape of diagram were quite similar between TELEMAC 3D and experiment.

REFERENCES

Altunin, S. T. (1962). *Channel Regulation*. Sel'khozizdat, Moscow.

Chrisohoides, A., Sotiropoulos, F. & Sturm, T. W. (2003). Coherent Structures in Flat-Bed Abutment Flow: Computational Fluid Dynamics Simulations and Experiments. *Journal of Hydraulic Engineering*, 129(3), 177–186.

Constantinescu, G., Sukhodolov, A. & McCoy, A. (2009). Mass Exchange in a Shallow Channel Flow with a Series of Groynes: LES Study and Comparison with Laboratory and Field Experiments. *Environmental Fluid Mechanics*, 9(6), 587–615.

DESOMBRE, J. (2013). *Telemac Modelling System - Telemac-3D Software,* Operating Manual.

Garde, Rj., Subramanya, K. & Nambudripad, K. D. (1961). Study of Scour Around Spur-Dikes. *Journal of the Hydraulics Division*, 87(6), 23–37.

Ge, L. & Sotiropoulos, F. (2005). 3D Unsteady RANS Modeling of Complex Hydraulic Engineering Flows. I: Numerical Model. *Journal of Hydraulic Engineering*, 131(9), 800–808.

Haltigin, T. W., Biron, P. M. & Lapointe, M. F. (2007). Predicting Equilibrium Scour-Hole Geometry Near Angled Stream Deflectors using a Three-Dimensional Numerical Flow Model. *Journal of Hydraulic Engineering*, 133(8), 983–988.

Hervouet, J. M., Razafindrakoto, E. & Villaret, C. (2011). Dealing with Dry Zones in Free Surface Flows: A New Class of Advection Schemes. *In Proceedings of the 34th World Congress of the International Association for Hydro-Environment Research and Engineering: 33rd Hydrology and Water Resources Symposium and 10th Conference on Hydraulics in Water Engineering*, 4103. Engineers Australia.

Hoffmans, G. J. C. M. (2012). *The Influence of Turbulence on Soil Erosion,* Vol. 10. Eburon Uitgeverij BV.

Kabir, A. (2005). *Modelling Local Scour Around Bridge Piers using TELEMAC*. DISS, University of Cape Town.

Kuhnle, R. A., Alonso, C. V. & Shields, F. D. (1999). Geometry of Scour Holes Associated with 90 Spur Dikes. *Journal of Hydraulic Engineerin*g, 125(9), 972–978.

Langendoen, E. J., Mendoza, A., Abad, J. D., Tassi, P., Wang, D., Ata, R., Hervouet, J.-M. (2016). Improved Numerical Modeling of Morphodynamics of Rivers with Steep Banks. *Advances in Water Resources*, 93, 4–14.

McCoy, A., Constantinescu, G. & Weber, L. J. (2008). Numerical Investigation of Flow Hydrodynamics in a Channel with a Series of Groynes. *Journal of Hydraulic Engineering*, 134(2), 157–172.

Melville, B. W. (1992). Local Scour at Bridge Abutments. *Journal of Hydraulic Engineering*, 118(4), 615–631.

Nagata, N., Hosoda, T., Nakato, T., & Muramoto, Y. (2005). Three-Dimensional Numerical Model for Flow and Bed Deformation around River Hydraulic Structures. *Journal of Hydraulic Engineering*, 131(12), 1074–1087.

Przedwojski, B., Błazejewski, R. & Pilarczyk, K. W. (1995). *River Training Techniques: Fundamentals, Design and Applications*. BOOK, AA Balkema, 1-686.

Rajaratnam, N. & Nwachukwu, B. A. (1983). Flow Near Groin-Like Structures. *Journal of Hydraulic Engineering*, 109(3), 463–480.

Raudkivi, A. J. (1986). Functional Trends of Scour at Bridge Piers. *Journal of Hydraulic Engineering*, 112(1), 1–13.

Shahrokhi, M. & Sarveram, H. (2011). Three-Dimensional Simulation of Flow Around a Groyne with Large-Eddy Turbulence Model. *Journal of Food, Agriculture & Environment*, 9(3&4), 677–681.

Smolders, S., Maximova, T., Vanlede, J. & Teles, M. J. (2014). Implementation of Controlled Reduced Tide and Flooding Areas in the TELEMAC 3D Model of the Scheldt Estuary. *Proceedings of the 21st TELEMAC-MASCARET User Conference,15th-17th October 2014, Grenoble – France,* 111-118.

Uijttewaal, W. S. (2005). Effects of Groyne Layout on the Flow in Groyne Fields: Laboratory Experiments. *Journal of Hydraulic Engineering*, 131(9), 782–791. JOUR.

Villaret, C. (2004). SISYPHE release 5.4. *User Manual. Report P75G17*, EDF/LNHE, Chatou, France, 1–69.

Yeo, H. K., Kang, J. G. & Kim, S. J. (2005). An Experimental Study on Tip Velocity and Downstream Recirculation Zone of Single Groynes of Permeability Change. *KSCE Journal of Civil Engineering*, 9(1), 29–38.

Yossef, M. F. M. & de Vriend, H. J. (2010). Flow Details Near River Groynes: Experimental Investigation. *Journal of Hydraulic Engineering*, 137(5), 504–516.

Zhang, H., Nakagawa, H., Kawaike, K. & Yasuyuki, B. (2009). Experiment and Simulation of Turbulent Flow in Local Scour around a Spur Dyke. *International Journal of Sediment Research*, 24(1), 33–45.

FURTHER STUDIES ON OPTIMAL HYDRAULIC SECTION OF STEADY UNIFORM FLOW IN RECTANGULAR OPEN CHANNELS

MIN FAN [1], YUANLE ZHU[2], YAOZU JIANG[3] & BOLE JIAO[4]

[1,3,4] Changjiang River Scientific Research Institute, WuHan, HuBei, China,
[1] Key Laboratory of Inland Waterway Regulation Engineering Ministry of Con-nun cations, Chongqing,China
[2] State Key Laboratory of Safety Technology of Metal Mines, Changsha Institute of Mining Research Co.Ltd, ChangSha,China
hmfanmin@163.com

ABSTRACT

Optimal hydraulic section determines the maximum capacity of open channel, which plays a vital role in practical engineering. Based on our existing research, this paper focuses on the optimal hydraulic section of steady uniform flow in rectangular open channels. The results are as follow: (1) the optimal hydraulic section of steady uniform flow in rectangular open channels is concerned with Reynolds number and the width-depth ration. (2) For the laminar steady uniform flow in rectangular open channels, the optimal hydraulic section is the one when the width-depth ration is 5.8. (3) For the turbulent steady uniform flow in rectangular open channels, the optimal hydraulic section is influenced by Reynolds number and width-depth ration and the optimal hydraulic section of the flow with large Reynolds number is the one when the width-depth ration is 2.

Keywords: Rectangular open channel; optimal hydraulic section; laminar flow; turbulent flow.

1 INTRODUCTION

Optimal hydraulic section is an important research topic, which is of great importance in channel design in theoretical reach and practical engineering. The optimal hydraulic section is selected as the section of which the area is the smallest under the fixed design capacity or the section of which the flow capacity is the largest under the fixed area. At present, researches (Huang et al., 2005; Liu et al., 2006; Zhang et al., 1998) on the optimal hydraulic section generally focus on selecting the section with the maximum flow capacity under the fixed section area, canal bottom slope and roughness. In this process, the roughness has to be kept constant to ensure the above results are correct. However, the factors affecting the roughness are not a single one that it cannot be regarded as a fixed parameter while studying the optimal hydraulic section. Therefore, based on the mechanical energy loss which is inferred from the mathematical model of the viscous fluid in fluid mechanics, this paper redefines the optimal hydraulic section as the section with the maximum flow capacity under the fixed section form, fixed section area and fixed canal bottom slope. And further analysis of the influencing factors of optimal hydraulic section, and through the calculation of the channel flow under the same area and bottom slope conditions, the optimal section under the above computing conditions can be obtained.

2 THEORETICAL ANALYSIS OF OPTIMAL HYDRAULIC SECTION

In terms of hydraulics, the optimal hydraulic section is the section with the maximum flow capacity under certain conditions. According to the formula of flow capacity i.e. the discharge in hydraulics:

$$Q = AC\sqrt{Ri_b} = A\sqrt{8gi_b}\sqrt{\frac{R}{\lambda}} = A^{\frac{3}{2}}\frac{\sqrt{8gi_b}}{\sqrt{\lambda\chi}} \qquad [1]$$

where, Q is the discharge in the section, C is the Chezy coefficient, R is the hydraulic radius, λ is the mechanical energy loss coefficient, i_b is the open channel bottom slope.

Equation [1] can be rewritten as

$$Q^2\lambda\chi = 8gi_bA^3 \qquad [2]$$

Equation [2] shows that the flow capacity is mainly composed of mechanical energy loss coefficients λ, wetted perimeter χ, the cross-sectional area A and the open channel bottom slope i_b. Under the same cross-sectional area and the same bottom slope, the flow capacity is mainly determined by the mechanical energy

loss coefficient λ and wetted perimeter χ . Existing results (Liu et al., 2014) show that the mechanical energy loss coefficient is affected by Reynolds number and the section shape of open channels. Above all, flow capacity Q is affected by Reynolds number, wide depth ratio and the mechanical energy loss coefficient. Define $\xi = H/R$ as the shape parameter.
Derivate *H* in equation [2] on both side, then:

$$2Q\frac{dQ}{dH}\lambda\chi + Q^2\chi\left[\frac{\partial\lambda}{\partial \mathrm{Re}_R}\frac{1}{\upsilon}\frac{\chi\frac{dQ}{dH} - Q\frac{d\chi}{dH}}{\chi^2} + \frac{\partial\lambda}{\partial\xi}\frac{1}{A}(\chi + H\frac{d\chi}{dH})\right] + Q^2\lambda\frac{d\chi}{dH} = 0 \quad [3]$$

When flow capacity is maximum, which requires $\frac{dQ}{dH} = 0$, then equation [2] can be simplified as:

$$-\frac{Q^3\chi}{\upsilon\chi^2}\frac{\partial\lambda}{\partial \mathrm{Re}_R}\frac{d\chi}{dH} + \frac{Q^2\chi}{A}\frac{\partial\lambda}{\partial\xi}(\chi + H\frac{d\chi}{dH}) + Q^2\lambda\frac{d\chi}{dH} \quad [4]$$

Further reduces to equation:

$$(\lambda + \frac{\chi H}{A}\frac{\partial\lambda}{\partial\xi} - \mathrm{Re}_R\frac{\partial\lambda}{\partial \mathrm{Re}_R})\frac{d\chi}{dH} + \frac{\chi^2}{A}\frac{\partial\lambda}{\partial\xi} = \quad [5]$$

When $Q = Q_{\max}$, then:

$$\frac{d\chi}{dH} = \frac{\frac{\chi^2}{A}}{(\mathrm{Re}_R\frac{\partial\lambda}{\partial \mathrm{Re}_R} - \lambda - \frac{\chi H}{A}\frac{\partial\lambda}{\partial\xi})}\frac{\partial\lambda}{\partial\xi} \quad [6]$$

2.1 Laminar open channel flow

According to existing results (Liu et al., 2014), the mechanical energy loss coefficient is affected by Reynolds number and wide depth ratio under laminar flow condition. Define $\eta = \frac{B}{H}$, $\xi = \frac{H}{R}$, the formula of mechanical energy loss coefficient in laminar flow is:

$$\lambda = \frac{24}{\mathrm{Re}_R}\frac{1}{\xi^2}\frac{1}{1 - K(\eta)} \quad [7]$$

where,

$$K(\eta) = \frac{384}{\pi^5}\frac{1}{\eta}\sum_{m=0}^{\infty}\frac{1}{(2m+1)^5}\tanh\left[\frac{\pi}{2}\left(m + \frac{1}{2}\right)\eta\right] \quad [8]$$

From equation [7], the following equations are obtained:

$$\frac{\partial\lambda}{\partial \mathrm{Re}_R} = -\frac{24}{\mathrm{Re}_R{}^2}\frac{1}{\xi^2}\frac{1}{1 - K(\eta)} \quad [9]$$

$$\frac{\partial \lambda}{\partial \xi} = -\frac{24}{\mathrm{Re}_R}\frac{1}{\xi^2\left(1-K(\eta)\right)}\left[\frac{2}{\xi}+\frac{1}{2}\frac{\eta^2}{1-K(\eta)}\frac{\partial K(\eta)}{\partial \eta}\right] \quad [10]$$

where,

$$\frac{\partial K(\eta)}{\partial \eta} = \frac{384}{\pi^5}\left[\frac{\pi}{4}\frac{T_2(\eta)}{\eta} - \frac{1}{\eta^2}T_1(\eta)\right] \quad [11]$$

$$T_1(\eta) = \sum_{m=0}^{\infty}\frac{1}{(2m+1)^5}\tanh^2\left[\frac{\pi}{2}\left(m+\frac{1}{2}\right)\eta\right] \quad [12]$$

$$T_2(\eta) = \sum_{m=0}^{\infty}\frac{1}{(2m+1)^4}\mathrm{sech}^2\left[\frac{\pi}{2}\left(m+\frac{1}{2}\right)\eta\right] \quad [13]$$

Combining equations (9), (10) and (6), the following equation is obtained:

$$\frac{2-\eta}{4+\eta+\frac{4}{\eta}} = \frac{\frac{2\eta}{2+\eta}+\frac{1}{2}\frac{\eta^2}{K(\eta)}\frac{\partial K}{\partial \eta}}{2-\left(1+\frac{2}{\eta}\right)\left(\frac{2\eta}{2+\eta}+\frac{1}{2}\frac{\eta^2}{1-K(\eta)}\frac{\partial K}{\partial \eta}\right)} \quad [14]$$

Equation [10] is a function of the wide depth ratio and ultimately, we get $\eta = B/H = 5.8$. Thus, for the laminar steady uniform flow in rectangular open channels, the optimal hydraulic section is the one of which the width-depth ration is 5.8.

2.2 Turbulent open channel flow

Based on our existing results, the mechanical energy loss coefficient changed with the varied Reynolds number and wide depth ratio. Mechanical energy loss coefficient is affected by Reynolds number and wide depth ratio under moderate Reynolds number conditions, while mechanical energy loss coefficient is only affected by Reynolds number in high Reynolds number conditions. The optimal hydraulic section was analyzed in moderate Reynolds number and high Reynolds number respectively as follows.

2.2.1 Moderate Reynolds number flow

In moderate Reynolds number, the mechanical energy loss coefficient is related to Reynolds number and wide depth ratio, thus $\lambda = f(\mathrm{Re}_R, B/H)$. The optimal hydraulic section satisfies equation [6], then from equation [6], $\frac{\partial \lambda}{\partial \mathrm{Re}_R}$ and $\frac{\partial \lambda}{\partial \xi}$ vary relatively complicated. The changes still need to be further explored.

2.2.2 High Reynolds number flow

In high Reynolds number, the mechanical energy loss coefficient is only related to Reynolds number, thus $\lambda = f(\mathrm{Re}_R)$. According to $\frac{\partial \lambda}{\partial \xi} = 0$, equation [6] can be simplified as:

$$\frac{d\chi}{dH} = 0 \quad [15]$$

Equation [11] shows that $\frac{d\chi}{dH}$ equals 0 when Reynolds number is increased gradually.

In Rectangular open channels, $\chi = B + 2H = \frac{A}{H} + 2H$, then $\frac{d\chi}{dH} = -\frac{B}{H} + 2 = 0$, ultimately $\frac{B}{H} = 2$. That is, the optimal hydraulic section is the one when the width-depth ration is 2 in large Reynolds number which is consistent with the results in hydraulics (Rong, 2003).

3 CALCULATION OF OPTIMAL HYDRAULIC SECTION FOR LAMINAR OPEN CHANNEL FLOW

According to equation [1], the calculation of optimal hydraulic section should fully considerate the impact of width-depth ration in rectangular open channel. The Reynolds number should be taken into account to meet the requirements of laminar flow in open channels i.e. the Reynolds number is between 0 and 500. The formula of Reynolds number is $\mathrm{Re}_R = \frac{UR}{\nu}$, where U is the mean velocity in the section and it is based on the reference (Liu et al., 2014).

$$U_1 = \frac{gH^2 \sin\theta}{2\nu}\left\{\frac{2}{3} - \frac{256}{\pi^5}\frac{H}{B}\sum_{m=0}^{\infty}\frac{1}{(2m+1)^5}\tanh\left[\frac{\pi}{2}\left(m+\frac{1}{2}\right)\frac{B}{H}\right]\right\} \quad [16]$$

Flow capacity of rectangular open channel with different wide depth ratios was calculated under the condition of laminar flow and the results are shown in Figure 1. From Figure 1, the discharge in rectangular open channel was related to the Reynolds number and the width-depth ratio and the maximum discharge appeared in the area of which the width-depth ratio approximately equaled 6 and in large Reynolds number.

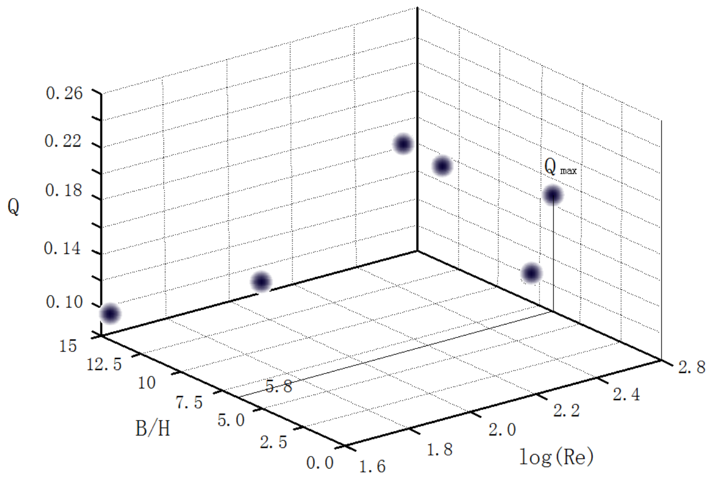

Figure 1. Variations of Q against Re and B/H for laminar flow in rectangular open channel.

4 CALCULATION OF OPTIMAL HYDRAULIC SECTION FOR TURBULENT OPEN CHANNEL FLOW

The rectangular open channels with the same area and bottom slope were calculated by a three-dimensional mathematical model based on Reynolds stress model to simulate the flow characteristics under these different conditions.

4.1 Mathematical model and numerical calculation method

4.1.1 Governing equations

The governing equations for 3D flow with RSM are as follows:

$$\frac{\partial \bar{u}_i}{\partial x_i} = 0 \quad [17]$$

$$\frac{\partial \bar{u}_i}{\partial t} + \frac{\partial \bar{u}_i \bar{u}_j}{\partial x_j} = -\frac{1}{\rho}\frac{\partial \bar{p}}{\partial x_i} + \frac{\partial}{\partial x_j}\left(\nu \frac{\partial \bar{u}_i}{\partial x_j} - \overline{u_i u_j}\right) + g_i \quad [18]$$

$$\frac{\partial \overline{u_i u_j}}{\partial t} + \bar{u}_l \frac{\partial \overline{u_i u_j}}{\partial x_l} = G_{ij} + \Phi_{ij} + D_{ij} - \varepsilon \delta_{ij} \quad [19]$$

$$\frac{\partial k}{\partial t}+\bar{u}_l\frac{\partial k}{\partial x_l}=2\nu_t\bar{S}_{ij}\frac{\partial \bar{u}_i}{\partial x_j}-\frac{\partial}{\partial x_j}\left[(\nu+\frac{\nu_t}{\sigma_k})\frac{\partial k}{\partial x_j}\right]-\varepsilon \quad [20]$$

$$\frac{\partial \varepsilon}{\partial t}+\bar{u}_l\frac{\partial \varepsilon}{\partial x_l}=C_{\varepsilon 1}\frac{\varepsilon}{k}\left[2\nu_t\bar{S}_{ij}\frac{\partial \bar{u}_i}{\partial x_j}\right]-\frac{\partial}{\partial x_l}\left[\left(\nu+\frac{\nu_t}{\sigma_\varepsilon}\right)\frac{\partial \varepsilon}{\partial x_l}\right]-C_{\varepsilon 2}\frac{\varepsilon^2}{k} \quad [21]$$

where $\bar{u}_i$ and $\bar{p}$ refer to the mean velocity and mean pressure; ν and ν_t refer to the kinematical viscosity coefficient and turbulent eddy viscosity coefficient; ρ and $\overline{u_i u_j}$ refer to the density of water and Reynolds stress tensor; G_{ij}, Φ_{ij} and D_{ij} refer to Reynolds stress generation term, pressure dependent variable and diffusion term, respectively; $\bar{S}_{ij}$ refers to the strain-rate tensor of mean velocity field; k and ε refer to the turbulent kinetic energy and turbulent kinetic dissipation rate; σ_k, σ_ε, $C_{\varepsilon 1}$ and $C_{\varepsilon 2}$ are empirical parameters.

4.1.2 Boundary conditions

The solid boundary was handled with no-slip condition, i.e. $\overline{u_i}=0$. The boundary condition for the free surface was determined according to the Rigid-lid Hypothesis. At the inlet, $\overline{u_1}$ is given, while $\overline{u_2}=\overline{u_3}=0$. The open channels are long enough to ensure that the flow is fully developed at the outlet. So, at the outlet, the flow is considered as fully developed.

4.1.3 Numerical scheme

The 3D turbulent flow in the rectangular open channel with the same hydraulic radius and the different width-depth ratios were simulated. The governing equations were discretized by FVM (Finite Volume Method) over the control volume, a first-order accuracy SIMPLE scheme was used for the convection term, while central difference scheme for diffusion term. The variables were located in the center of the control volume and the collocated variables arrangement was employed to deal with the coupling relationship between pressure and velocity.

The algebraic equations were solved by the Gauss-Seidel iteration method in this paper. The converging criterion is that the unit mass flow residual should be less than 0.01% of the inflow and overall mass flow residual should be less than 0.5% of the inflow.

4.2 Calculation of optimal hydraulic section

The flow in rectangular open channels with different wide depth ratios of which the section area and bottom slope are stable (A=0.72m^2, i=0.0001) was calculated at different Reynolds numbers. The calculated cases are shown in Table 1.

Table 1. Rectangular open channel calculation condition.

B/H	B (m)	H(m)	H/R
1	0.85	0.85	3.00
2	1.20	0.60	2.00
5	1.90	0.38	1.40
10	2.68	0.27	1.20
15	3.29	0.22	1.13
20	3.79	0.19	1.10

In Figure 2, the variations of flow capacity against the shape parameter and the Reynolds number are given. It can be seen that (1) the discharge increased with shape parameter at first, then monotonously decreased for a given Reynolds number and the maximum discharge appeared when the width-depth ration equaled 2, (2) the discharge increased with Reynolds numbers for a given shape parameter. Figure 3 clearly shows the maximum discharge appeared in the area of which the width-depth ration equaled 2 and large Reynolds number which was consistent with the result in chapter 2.2 (the optimal hydraulic section is the one when the width-depth ration is 2 in large Reynolds number).

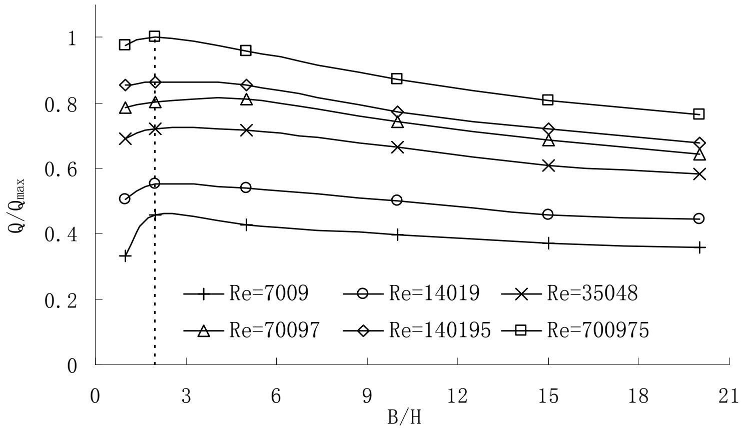

Figure 2. Variations of Q against B/H.

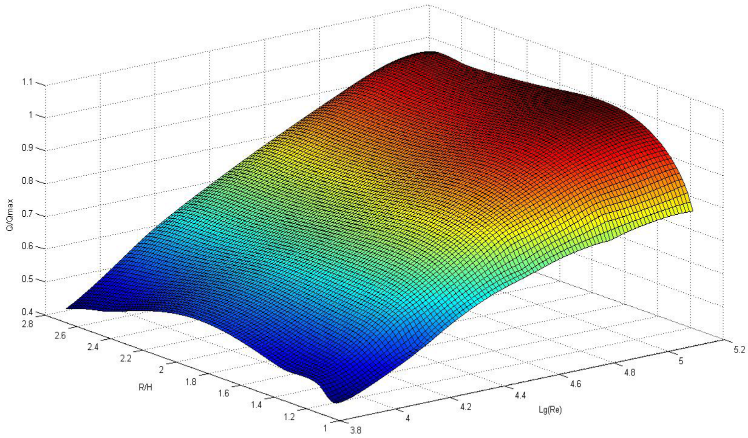

Figure 3. Variations of Q against Re and R/H.

5 CONCLUSIONS

Through theoretical analysis and numerical simulation, the results are as follow:

(a) Optimal hydraulic section of steady uniform flow in rectangular open channels is concerned with Reynolds number and the width-depth ratio.

(b) For the laminar steady uniform flow in rectangular open channels, the optimal hydraulic section is the one of which the width-depth ratio is 5.8.

(c) For turbulent steady uniform flow in rectangular open channels, the optimal hydraulic section is influenced by Reynolds number and width-depth ratio and the optimal hydraulic section is the one of which the width-depth ratio is 2 in large Reynolds number.

ACKNOWLEDGEMENTS

The authors would like to acknowledge the support given by the National Key R&D Program of China (Grant No. 2016YFC0402004), the Foundation Key Laboratory of Inland Waterway Regulation Engineering Ministry of Con-nun cation of ChongQing JiaoTong University (Grant No. NHHD-201507) and the National Natural Science Foundation of China (Grant No. 51379019).

REFERENCES

Huang, C.A., Gong, M.F. & Chen, Z.C. (2005). Stable Channel Shape based on the Principle of Minimum Stream Power. *Journal of Hydrodynamics*, Ser. A, 20(2), 189-195.

Liu, H.Y., Zhang, X.Y. & Sun, D.H. (2006). Design of Optimal Hydraulic Section and Economic Practical Section for Compound Canal. *Journal of Water Resources and Water Engineering,* 17(4), 90-93.

Zhang, X.P. & Wu, J. (1998). General Formulation of Best Hydraulic Channel Section. *Water Resources and Water Engineering,* 3(9), 22-26.

Liu, S.H., Fan, M. & Xue, J. (2014). The Mechanical Energy Equation for Total Flow in Open Channels. *Journal of Hydrodynamics*, Ser.B, 26(3), 416-423.

Rong, F.T. (2003). Derivation of Unified Equation for Best Hydraulic Section of Trapezoid-Typed Channel. *Shanxi Hydrotechnics*, 10(4), 5-7.

Proceedings of the 37th IAHR World Congress
August 13 – 18, 2017, Kuala Lumpur, Malaysia

EFFECT OF FLOW INTENSITY ON BRIDGE PIER SCOUR GEOMETRY FOR LOW BLOCKAGE RATIOS

PRISCILLA WILLIAMS[1], RAM BALACHANDAR[2] & TIRUPATI BOLISETTI[3]

[1]Department of Civil and Environmental Engineering, University of Windsor, Windsor, Canada
williamq@uwindsor.ca
[2,3]University of Windsor, Windsor, Canada
rambala@uwindsor.ca; tirupati@uwindsor.ca

ABSTRACT

Experiments are conducted to investigate the influence of flow intensity (U/U_c, where U is the mean flow velocity and U_c is the critical velocity to initiate sediment motion) on relative scour depth (d_{se}/D, where d_{se} is the maximum value of the equilibrium scour depth and D is the pier diameter). Two sets of 3 tests are carried out at three values of U/U_c for two low values of blockage ratio. It is determined that for the range of flow intensity observed, relative scour depth increased with flow intensity. For tests with values of $U/U_c < 1$ in both sets, the form of scour is very similar; however, for tests with values of $U/U_c = 1.00$, there are differences in scour form in both centerline and contour profiles.

Keywords: Bridge pier scour; scour prediction; blockage effects; flow intensity; bridge pier design.

1 INTRODUCTION

In North America, scour and erosion are responsible for a majority of bridge pier failures annually (Melville and Coleman, 2000; Wardhana and Hadipriono, 2003; Foti and Sabia, 2011. Hence, many design standards include provisions for design of bridge pier foundations with respect to scour. This design is frequently accomplished using code-specified empirical equations which have been developed using experimental results over the past several decades. Commonly used equations calculate relative scour depth, the depth relative to pier diameter below which bridge pier foundations should be placed to avoid the effects of scour and erosion, and functions of experimentally-defined scour-governing dimensionless parameters related to fluid, flow, time, pier and sediment characteristics.

Dimensional analysis has indicated that for fully turbulent subcritical flow surrounding normally aligned circular piers, three dimensionless parameters are most highly influential in the scouring process. Therefore, it is commonly used to predict the previously described relative scour depth (d_{se}/D, where d_{se} is equilibrium depth of scour and D is pier diameter), flow intensity (U/U_c), the ratio between mean flow velocity U and critical velocity of sediment U_c, flow shallowness (h/D), the ratio between mean flow depth h and pier diameter coupled with relative coarseness (D/d_{50}), the ratio between pier diameter and median sediment diameter d_{50}. The relationships between relative scour depth and each of these dimensionless parameters have been thoroughly explored and well documented (Ettema et al., 2011).

Detailed analysis has determined that such equations have a tendency to over-predict scour depth (Williams et al., 2013; Williams et al., 2017), yielding unnecessarily high construction costs (Ettema et al., 1998). Since design equations were primarily developed on the basis of experimental results from various investigations, the conditions under which these results were obtained require closer examination.

Scale effects are prevalent in hydraulic models, and are usually manifested in the form of disproportionately high outputs (Heller, 2011). In the case of scour modelling, scale effects can be attributed to a number of experimental conditions. For instance, flow is typically uniform in experiments, which is an improbable characteristic in river flow. Sediment is normally distributed in most laboratory experiments, which, again, is very unlikely in a natural flow environment. Finally, close sidewall proximity to the pier is frequently seen in scour experimentation but does not often occur in the field. Many experiments which exceed the recommended maximum value of channel blockage of 10 percent (Chiew, 1984) have been used for development of scour-predicting equations. Therefore, use of these equations and the conditions under which they were carried out require re-examination. This includes further exploration of the relationship between relative scour depth and flow intensity.

The present investigation explores the influence of flow intensity, U/U_c on scour geometry over a range of values in and just at the threshold of clear-water classification ($U/U_c < 1$, $U/U_c = 1$) at two low blockage ratios.

2 METHODOLOGY

Experiments were carried out at the University of Windsor in a 1.22 m wide flow recirculating flume with a length of 10 metres and a height of 0.84 metres. Two flow straighteners of decreasing diameter were placed upstream of the test section near the inlet tank of the flume in order to regulate incoming flow. A PVC ramp

  / ISSN 1562-6865 (Online) - ISSN 1063-7710 (Print)

was constructed just downstream of the second flow straightener, leading up to a PVC box which held the required sediment. A schematic of the general experimental set-up can be found in Figure 1.

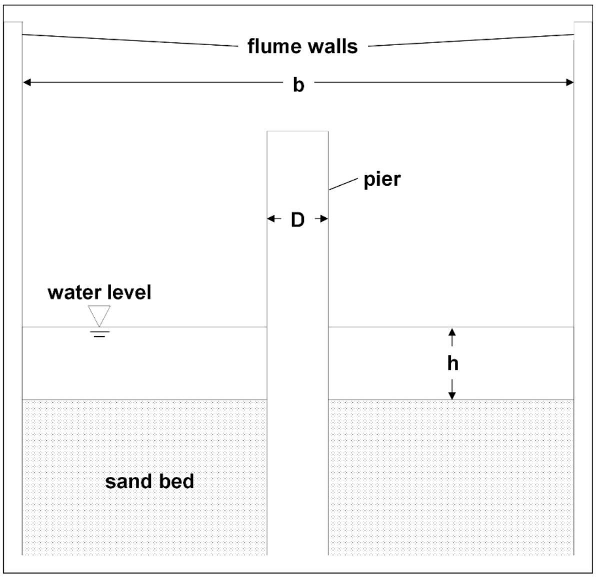

Figure 1. Experimental set-up.

A Nortek USA acoustic Doppler velocimeter (ADV) was used to determine the depth-averaged velocity of flow for each case in the absence of the pier. Prior to each experiment, the bed sediment was levelled using a flat trowel and a model pier of the required size was centered between the flume walls. The water level was slowly increased so as to not disturb the control surface of the channel bed, until the desired water depth was reached. The pump was then turned on and the flow controller was adjusted until the desired flow intensity had been reached. Each test was conducted for duration of 48 hours, after which the pump was turned off and the flume was slowly drained to preserve the generated bed forms. The scour geometry (centerline and contour) was then measured using a laser distance meter and photographed.

The sediment used for experiments in the current investigation was uniformly distributed and had a d_{50} of 0.77 mm and a standard deviation σ_g of 1.34. Two sets, each encompassing of three experiments were carried at each of two blockage ratios, 2.5 and 5.0 percent. Pier diameter was held at 0.03 m for set A and 0.06 m for set B, where the flow depth was 0.12 m in all tests in order to maintain constant flow shallowness h/D in each set. For each set, three tests under these conditions were carried out for flow intensity U/U_c of 0.77, 0.88 and 1.00. The parameters for each test can be found in Table 1.

Table 1. Experimental parameters.

	D/b	U/U_c	h/D	D/d_{50}	d_{se}/D
A1	0.025	0.77	4.0	39	1.31
A2	0.025	0.88	4.0	39	1.85
A3	0.025	1.00	4.0	39	2.39
B1	0.050	0.77	2.0	78	0.69
B2	0.050	0.88	2.0	78	1.42
B3	0.050	1.00	2.0	78	1.79

3 RESULTS AND DISCUSSION

Figure 2 shows the relationship between d_{se}/D and U/U_c for set A with D/b = 2.5% and set B with D/b = 5%. For the range of U/U_c in this study (0.77 – 1.00), it can be seen that relative scour depth increases linearly with increasing flow intensity, which is in agreement with literature. Closer examination of the scour geometry for each test demonstrates the greater influence of U/U_c, particularly in the wake region of the pier.

Figures 3 and 4 show the centerline profiles for set A and set B tests. For all figures, the x-direction is the stream-wise direction, the y-direction is transverse to the flow or span-wise and the z axis is normal to both the x and y axes. It can be seen that the form of the scour profiles upstream of the pier was very similar for all tests. Scour depth increases very nearly linearly from the start of the scour hole to the upstream face of the pier. However, greater differences can be seen downstream of the pier. In both centerline superimpositions, it can be seen that, as U/U_c increases, the length of the scour hole in the x-direction also increases. In effect, location of the primary deposit (defined as the point at which the scour profile first crosses the mean bed level line downstream of the pier) moves further downstream.

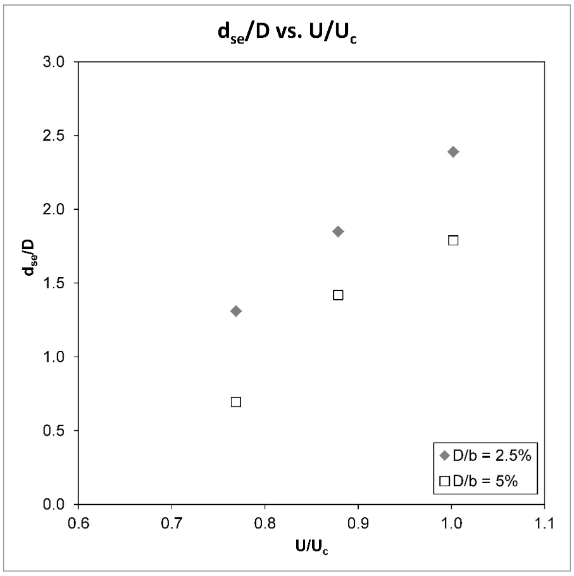

Figure 2. d_{se}/D vs. U/U_c for set A (D/b = 2.5 %) and set B (D/b = 5%).

This can be related to the nature of the large-scale turbulence structures surrounding the pier. As the flow intensity increases, so do the size and strength of the horseshoe vortex upstream of the pier, resulting in greater scour depth with greater flow intensity. Similarly, the strength of the vortices in the wake region increases with flow intensity, carrying and depositing sediment further downstream with increasing mean flow velocity (and subsequently, flow intensity). These observations are evident for both set A and set B centerline profiles. In addition, it is interesting to note that for each set A and set B test with U/U_c = 1.00 (A3 and B3), the length of the primary deposit was very long (in both cases, at least longer than 10D).

Figures 5 and 6 show the contour profiles for set A and B tests and Figures 7 and 8 show photographs of scour for set A tests. It can once more be seen that the size (in this case, the width in the y-direction, or span-wise, and length in the x-direction, or stream-wise) of the scour hole increases with increasing flow intensity. While the shape of the scour centerline on upstream of the hole is quite similar for all tests, the shape of the scour contour for tests A3 and B3 (U/U_c = 1.00) differs slightly. The shape of the scour hole contour upstream of the pier for tests A1 and B1 (U/U_c = 0.77) and A2 and B2 (U/U_c = 0.88) is rounded and very similar in form. However, for tests A3 and B3, the scour hole contour upstream of the pier is slightly less rounded and more pointed in the upstream direction.

The relative orientation of the scour hole around the pier is also dependent on the value of flow intensity. For set A, the centre of the scour hole relative to its stream-wise length was closer to the pier in test A1. The centre of the scour hole progresses further downstream of the pier in tests A2 and A3. Similarly, for set B, the centre of the scour hole was on upstream of the pier in test B1, close to the pier in test B2 and downstream of the pier in test B3.

Downstream of the pier, none of the scour contours for any of the six tests reach the sidewalls, which is to be expected for tests with lower blockage ratios. The photographs for the downstream view of all set A tests (Figure 8) show the propagation of the primary deposit towards downstream as flow intensity increases. It can also be seen that while the scour hole was relatively circular with a small divot downstream of the pier for all tests with U/U_c < 1, the scour holes for tests A3 and B3 with U/U_c = 1.00 are elongated with adjacent troughs developing downstream.

It is interesting to note that for centerline and contour profiles, the form of scour for all tests with U/U_c < 1 is quite similar. However, for all tests with U/U_c = 1.00, scour form demonstrates small but clearly visible differences.

In addition, it should be noted that it is not reasonable to compare tests between the two sets because, as shown in Table 1, all tests in set A have differing values of D/d_{50} and h/D as well as D/b from all tests in set B. Any differences noted in scour geometry between, for example, tests A1 and B1 could not be attributed to a change in any one of these parameters as more than one of the scour-governing parameters was changing. Analysis for this section had been restricted to each of the two sets separately with associated similarities.

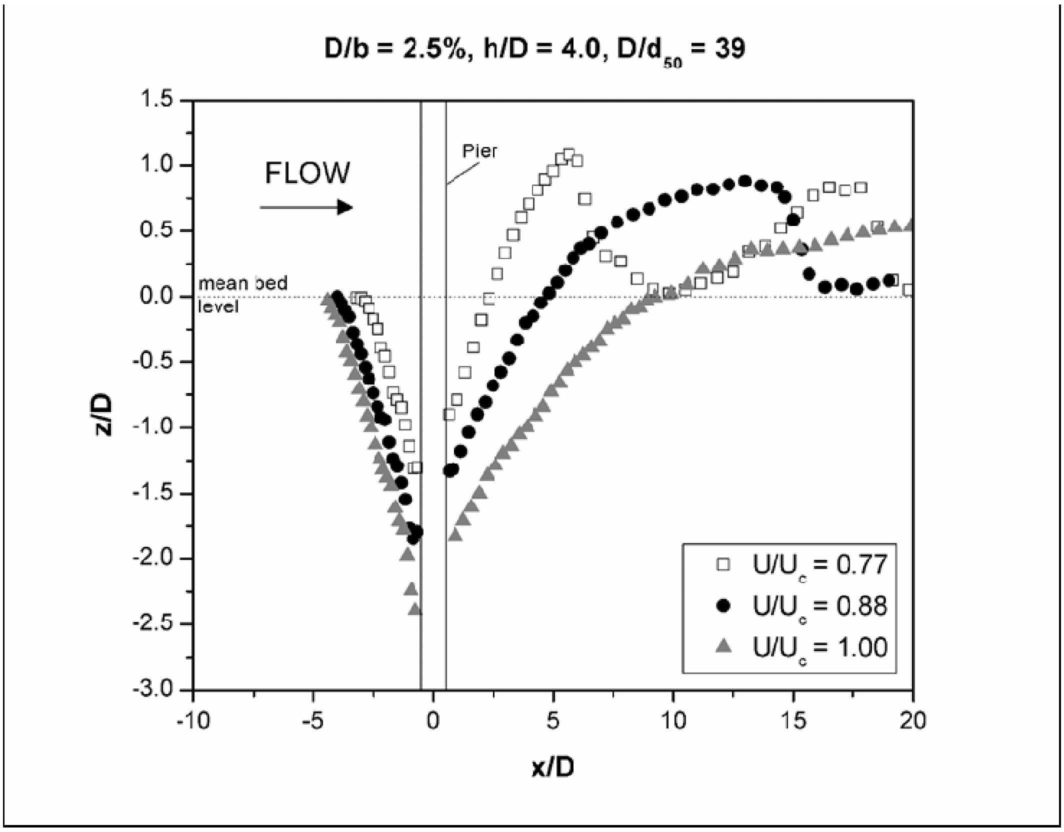

Figure 3. x/D vs. z/D for set A.

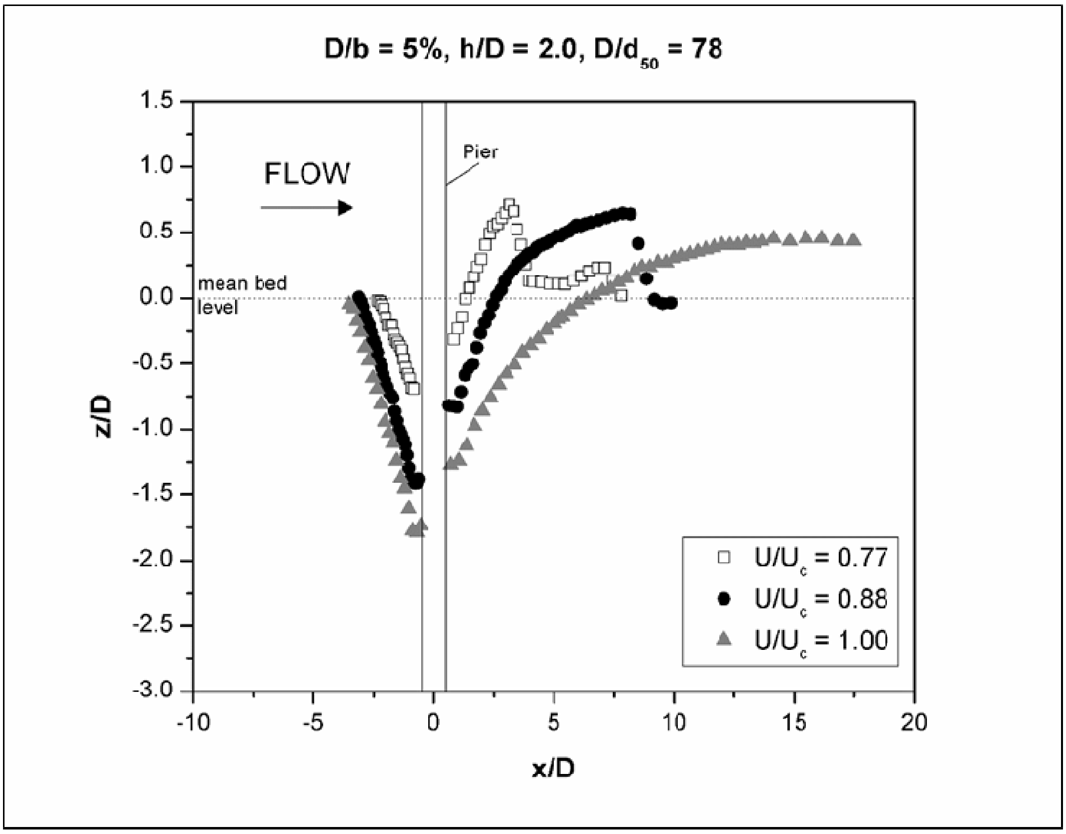

Figure 4. x/D vs. z/D for set B.

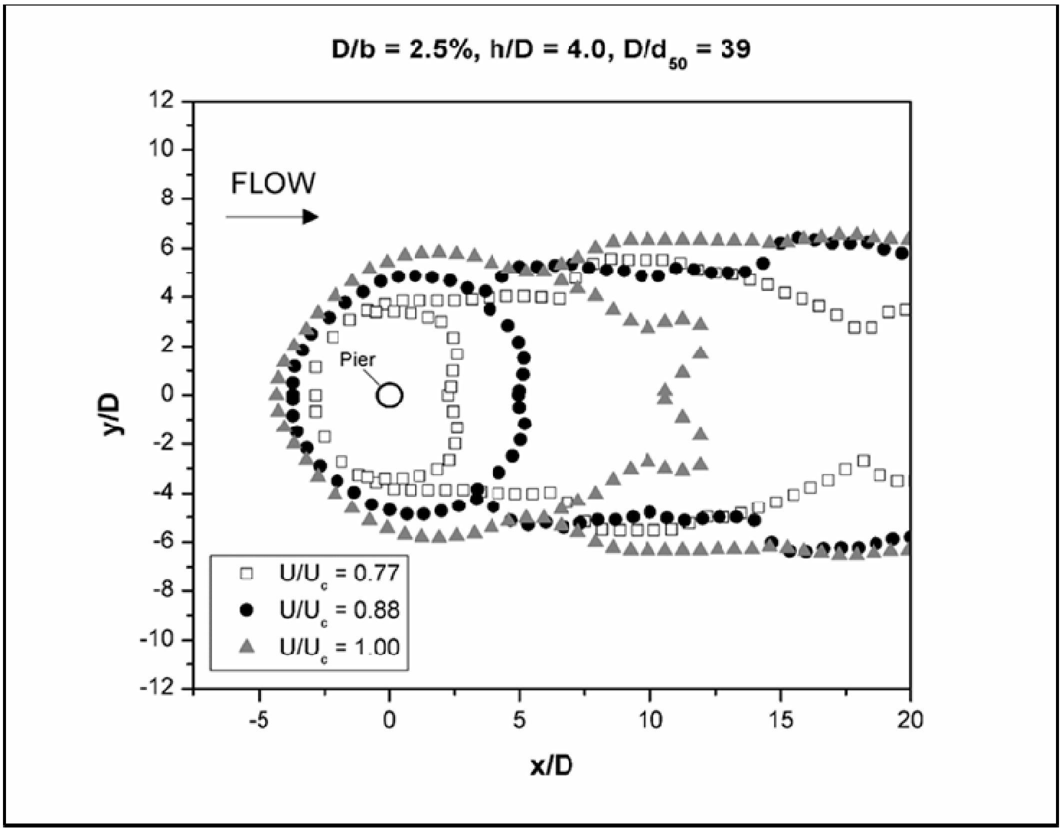

Figure 5. x/D vs. y/D for set A.

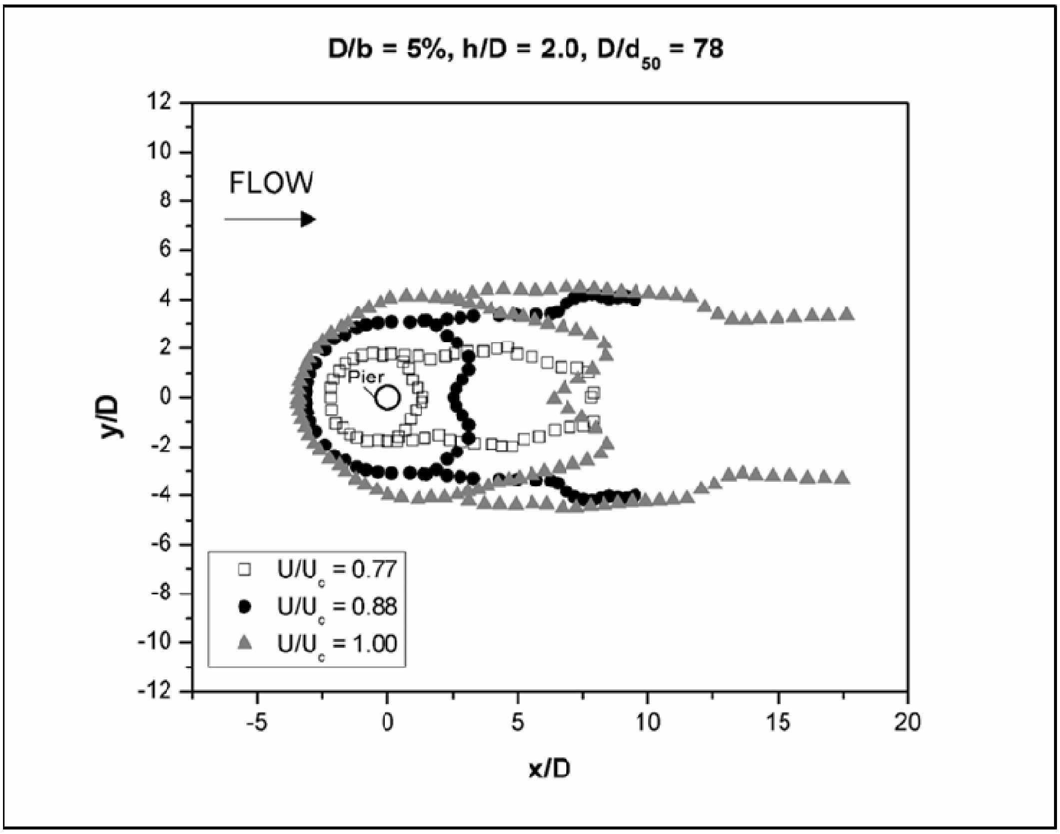

Figure 6. x/D vs. y/D for set B.

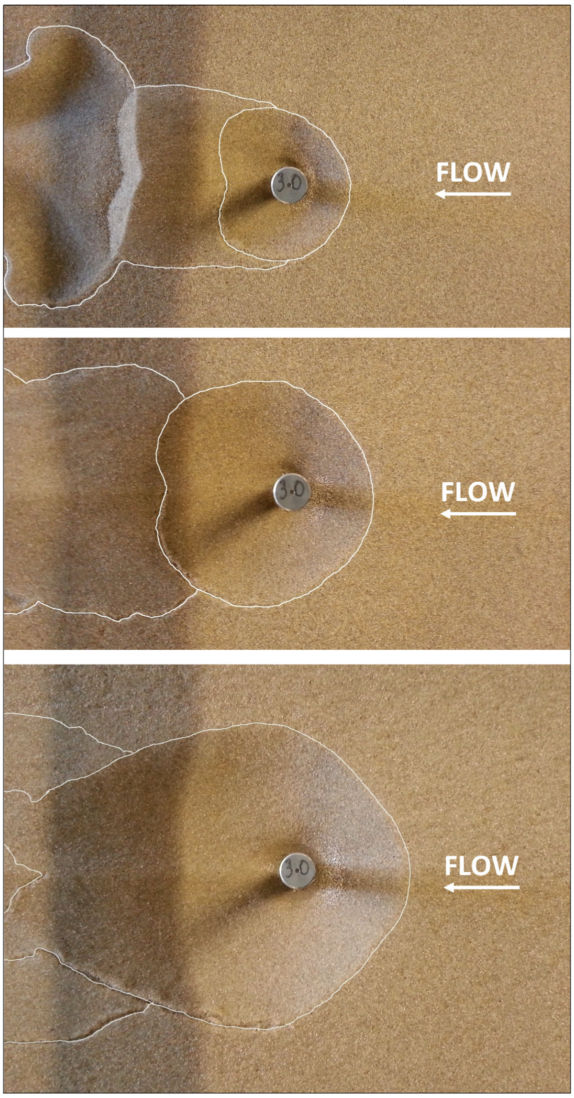

Figure 7. Contour view photographs of set A tests (top: A1, middle: A2, bottom: A3).

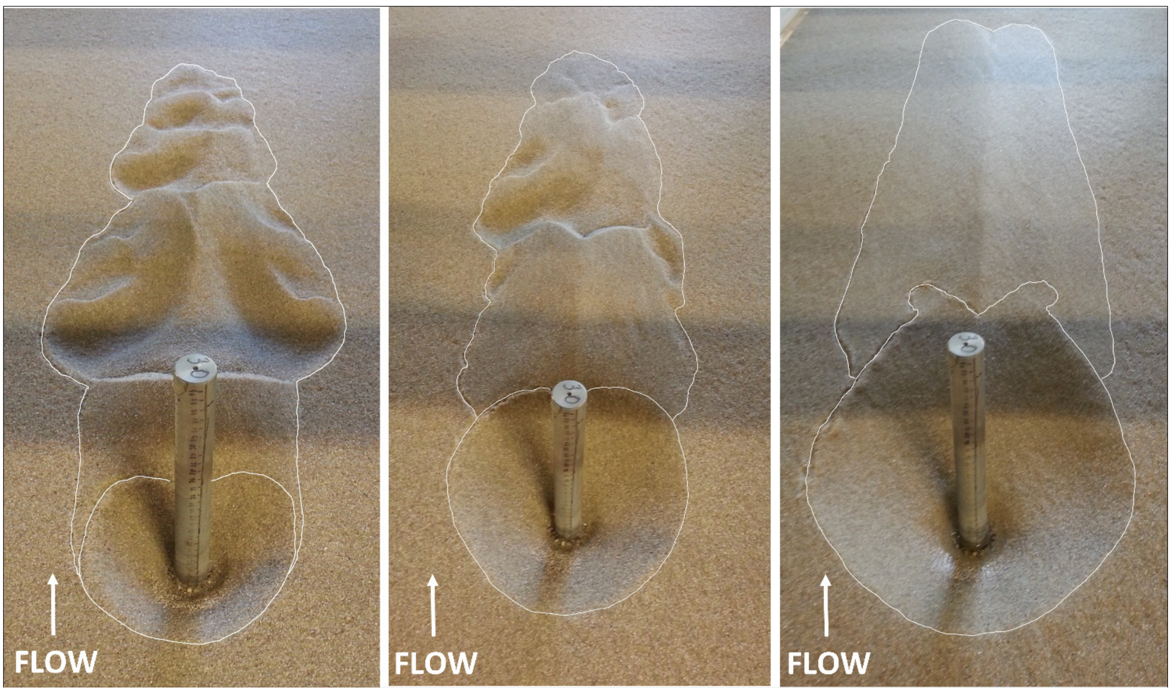

Figure 8. Upstream view photographs of set A tests (left: A1, middle: A2, right: A3).

4 CONCLUSIONS AND RECOMMENDATIONS

This investigation explores the role of U/U_c for low blockage ratios, as the parameters of many investigations used for analysis in this area has employed blockage ratios exceeding the minimum value described by Chiew (1984). Two sets of three tests each indicated that relative scour depth increases with flow intensity, and the shape of scour geometry for all tests with $U/U_c < 1$ is very similar. However, scour for tests with $U/U_c = 1.00$ differs slightly in form.

Although the role of blockage ratio is not explicitly explored in the current investigation, its role in the relationship between relative scour depth and flow intensity could be isolated by changing the proximity of test section sidewalls as opposed to pier diameter, allowing for constant h/D and D/d_{50}. Similarly, while the present study deals with scour within and just at the threshold for clear water conditions ($U/U_c < 1$, $U/U_c = 1$), further experimentation could be carried out in order to determine changes in scour form which may occur under live-bed conditions just beyond the threshold ($U/U_c > 1$), in order to gain a more detailed understanding of the role of U/U_c in clear-water and live-bed scour.

REFERENCES

Chiew, Y. (1984). Local Scour at Bridge Piers, *PhD Thesis*. Auckland: School of Engineering, University of Auckland, New Zealand.

Ettema, R., Melville, B. & Barkdoll, B. (1998). Scale Effects in Pier-Scour Experiments. *Journal of Hydraulic Engineering*, 124(6), 639–642.

Ettema, R., Constantinescu, G. & Melville, B. (2011). NCHRP Web-Only Document 175: Evaluation of Bridge Scour Research: Pier Scour Processes and Predictions. Retrieved from *http://onlinepubs.trb.org/onlinepubs/nchrp/nchrp_w175.pdf*

Foti, S. & Sabia, D. (2011). Influence of Foundation Scour on the Dynamic Response of an Existing Bridge. *Journal of Bridge Engineering*, 16(2), 295–304.

Heller, V. (2011). Scale Effects in Physical Hydraulic Engineering Models. *Journal of Hydraulic Research*, 49(3), 293-306.

Melville, B. & Coleman, S. (2000). *Bridge Scour.* Colorado: Water Resources Publications.

Wardhana, K. & Hadipriono, F. (2003). Analysis of Recent Bridge Failures in the United States. *Journal of Performance of Constructed Facilities*, 17(3), 144–150.

Williams, P., Balachandar, R. & Bolisetti, T. (2013). Evaluation of Local Bridge Pier Scour Depth Estimation Methods. *Proceedings of the 24th Canadian Congress of Applied Mechanics held in Saskatoon*, SK, Canada, 2-6 June 2013.

Williams, P., Balachandar, R. & Bolisetti, T. (2017). Evaluation of Governing Parameters on Pier Scour Geometry. *Canadian Journal of Civil Engineering*, 2017, 44(1), 48-58.

SEEPAGE SIMULATION ON PUTRAJAYA EARTH FILL DAM

MUHAMMAD RIZAL RAZALI[1], SAAD SH SAMMEN[2], AZZLIA MOHD UNAINI[3] & THAMER AHMED MOHAMMED ALI[4]

[1] Corporate Planning Division, National Hydraulic Institute of Malaysia (NAHRIM), Selangor, Malaysia,
mrizal@nahrim.gov.my
[2,3,4] Faculty of Engineering, University Putra Malaysia, Selangor, Malaysia

ABSTRACT

A seepage simulation is focused on clay core-rock fill dam all the time. In this study, Putrajaya dam is taken as a case study, the saturated stable seepage computation model was used to analyse Putrajaya dam seepage problem. Two-dimensional finite element model of the clay core-rock fill dam was established by the Geo-Slope/SEEPW Software. The numerical simulation computation was carried on dam seepage situation under different conditions. A proposed model is describing the flow pattern and seepage behaviour through the dam. The flow is assumed to be two-dimensional and under steady-state condition. The non-linear differential equation governing the flow is solved using an iterative finite element scheme. The finite element formulation is computer-implemented into a flexible computer program called SEEPW. The results show that the seepage amount through the dam was equal to 3.5620 x $10^{-8} m^3$/sec.

Keywords: Seepage; hydraulic conductivity; finite elements; modelling; SEEP/W.

1 INTRODUCTION

It was found (Hasan, 1999) that from 1000 of dams being built today, almost 10 of the dams are failed with the ratio of 1:100. From the records available, more than 200 dams that failed in the 20th century involved the dam's size of either more than 15 meters high or less than 15 meters high. Of the total failures, 30 incidents are recorded between 1950 and 1959 and 25 incidents are recorded between 1960 and 1965. Since 1998, the number of unsafe dams in United States has risen by 33% to more than 3500, while federally owned dams are in good condition and there have been modest gains in repair, the number of dams identified as unsafe is increasing at a faster rate than those being repaired. US$10.1 Billion is needed over the next 12 years to address all critical non-federal dams, which pose a direct risk to human life should they fail (ASCE, 2005).

There are many types of dam failures but the two common failure modes are hydraulic failure (overtopping) and piping or seepage. According to ICOLD, The International Commission on Large Dams, the most common cause of failure of earth fill and rock fill dams is seepage and piping (Fell, 1992), as shown in Table 1.

Table 1. Causes for dam (over 15m height) failure (Fell, 1992).

Causes Failure	Percentage (%)
Piping and Seepage	38
Overtopping	35
Foundation	21
Others	6

This survey was carried out in 1973. Hydraulic failure accounts for over 40% of earth dam failure and may be due to one or more of the following:

i. By overtopping: When free board of dam or capacity of spillway is insufficient, the flood water will pass over the dam and wash it downstream;
ii. Erosion of downstream toe: The toe of the dam at the downstream side may be eroded due to heavy cross-current from spillway buckets or tail water. When the toe of downstream is eroded, it will lead to failure of dam;
iii. Erosion of upstream surface: During winds, the waves developed near the top water surface may cut into the soil of upstream dam face which may cause slip of the upstream surface leading to failure;
iv. Erosion of downstream face by gully formation: During heavy rains, the flowing rain water over the downstream face can erode the surface, creating gullies, which could lead to failure.

Seepage always occurs in the dams. If the magnitude is within design limits, it may not harm the stability of the dam. However, if seepage is concentrated or uncontrolled beyond limits, it will lead to failure of the dam. Following are some of the various types of seepage failure:

i. Piping through dam body. When seepage starts through poor soils in the body of the dam, small channels are formed which transport material downstream. As more materials are transported downstream, the channels glow bigger and bigger which could lead to wash out of dam as shown in Figure 1;

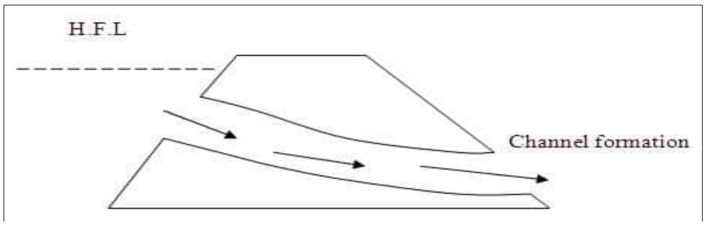

Figure 1. Failure of dam due to piping through dam body.

ii. Piping through foundation: When highly permeable cavities or fissures or strata of gravel or coarse sand are present in the dam foundation, it may lead to heavy seepage. The concentrated seepage at high rate will erode soil which will cause increase flow of water and soil, as shown in Figure 2. As a result, the dam will settle or sink leading to failure;

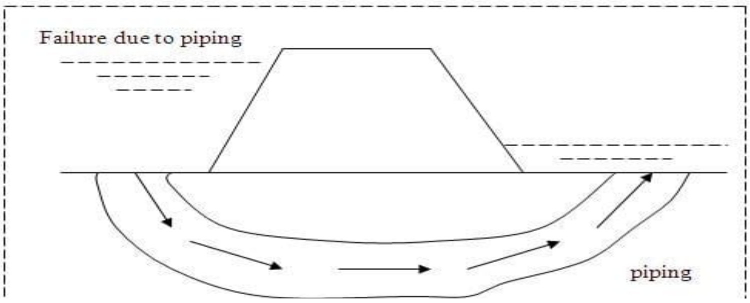

Figure 2. Failure of dam due to piping through foundation.

iii. Sloughing of downstream side of dam: The process of failure due to sloughing starts when the downstream toe of the dam becomes saturated and starts getting eroded, causing small slump or slide of the dam. The small slide leaves a relative steep face, which also becomes saturated due to seepage and also slumps again and forms more unstable surface. The process of saturation and slumping continues, leading to failure of dam.

2 PROBLEMS STATEMENT

Most of the past studies have involved seepage under the dam foundation (Ersayin, 2006). However, in embankment dams, there is seepage in the dam body following a phreatic line. An earth fill dam's body prevents the flow of water from dam's back to downstream. However, with the most impermeable materials used in the dam's body, some amount of water seeps into dam's body and goes out from downstream of body slope. Seepage through or under an embankment may occur at a high enough rate to cause a boil, usually called a sand boil. Presence of sand boils can play a major role in embankment failure. Seepage of floodwater through or under an embankment is a normal process. However, when seepage occurs at a high rate, the seepage water can carry soil material with it.

3 STUDY AREA AND BASIC DATA

Putrajaya Dam is owned by Perbadanan Putrajaya and was constructed in 2001 with a 400-hectare man-made lake created. It is a zoned earth filled embankment located upstream of the confluence of Sg. Chuau and Sg. Bisa in the state of Selangor. The dam embankment was raised to EL 21.0m. It has a crest length of about 735m and a maximum height of 18 – 30m with 145m length of embankment. The seepage chamber location is shown in Figure 3.

  / ISSN 1562-6865 (Online) - ISSN 1063-7710 (Print)

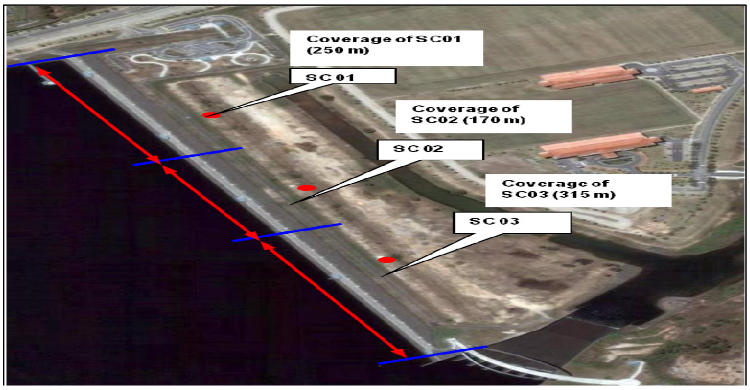

Figure 3. Seepage measurement chamber location – SC 02.

The type of spillway is labyrinth with a reservoir capacity of 24 million cubic meter and a maximum flood discharge at spillway is 904m^3/s. The main purpose of the dam is to provide recreational facilities to Putrajaya communities.

4 METHODOLOGY

In this study, the analysis computation was used for dam's seepage by GEO-SLOPE/SEEPW finite element software. This software's function includes process kinds of non-uniform nature soil layer distribution and complex dam situation; set assign head and current capacity, water-proof boundary, and so on many kinds of boundary conditions; compute saturation line automatically; output equipotential line, streamline, saturation line, kinds of computed result curve and seepage quantity, slope fall of seep export, etc.

The boundary conditions were hydraulic conductivity, pore water pressure, and reservoir levels. We can find pore water pressure at different point by multiplying the piezometric reading with unit weight of water, which is 9.81kN/m^3. SEEP/W divided the entire flow domain into a finite element mesh. Each element in the mesh must be associated with a soil type. At some points, it is needed to forecast the seepage fluxes across some sections. We can predict the critical section for the seepage rate and it is usually located at filter outlet of the dam. It has been noted several times earlier that in seepage analyses only the head (H) or flow (Q or q) can be specified as a boundary condition. There are, however, situations where neither 'H' nor 'Q' is known. A typical situation is the development of a downstream seepage face, as illustrated in Figure 4. Another common situation is the seepage face that develops on the upstream face after rapid drawdown of a reservoir.

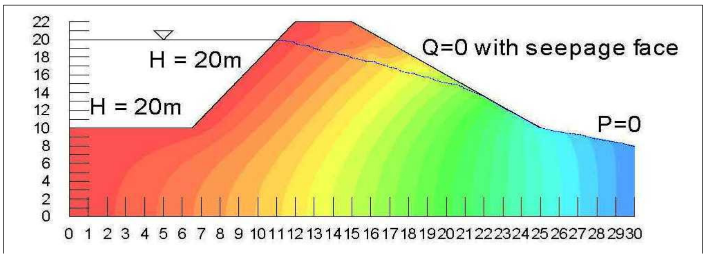

Figure 4. Seepage on down slope dam face (no toe under drain in this case).

A flow net is in map of contours of equal potential crossed with flow lines. For the flow net to represent a correct solution to the Laplacian equation, the equipotential lines and flow lines must follow certain rules. The flow lines must for example cross the equipotential lines at right angles. Also, the area between two adjacent flow lines is called a flow channel and the flow in each channel has to carry the same amount of flow. A correctly constructed flow net is a graphical solution to Laplacian equation. SEEP/W does not create a true flow net because flow nets can be created for a few special situations. SEEP/W, however, does compute and display many elements of a flow net, which are useful for interpreting results in the context of flow net principles. For example, flow lines must be approximately perpendicular to equipotential lines. Features like this provide a reference point for judging the SEEP/W results. SEEP/W is formulated in terms of total hydraulic head. Contours of total head are the equivalent of equipotential lines. So, equipotential lines can be drawn and displayed by creating a plot of total head contours. They are identical to equipotential lines in a flow net. In this example, there are eight equipotential drops from 20 to 12, one meter each. In SEEP/W, we can draw paths as illustrated in Figure 5 and flow net approximation as shown in Figure 6. These are lines that an imaginary droplet of water would follow from entrance to exit; they are not flow lines in the true context of a flow nets. In flow net terminology, the area between two flow paths is called a flow channel. In a flow net, the amount of the flow between each flow line must be the same; that is, the amount of flow is the same in each flow channel. It is possible for simple cases to compute flow lines so that they create exact true flow channels.

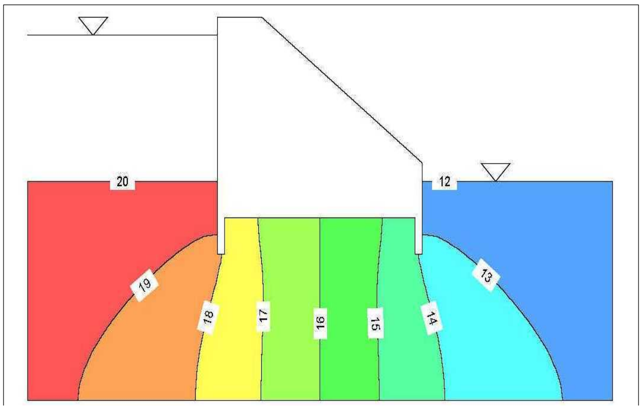

Figure 5. Plot of total head contours or equipotential lines.

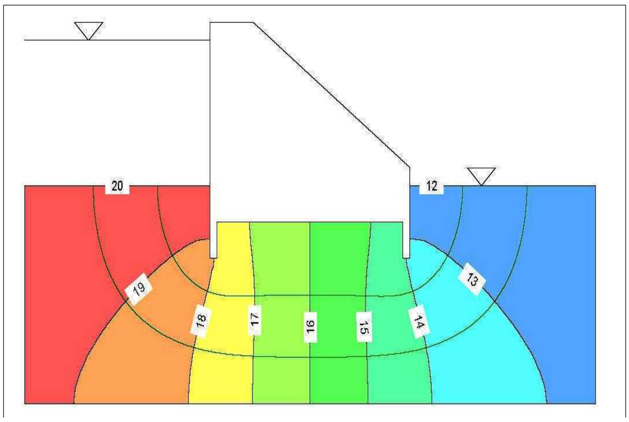

Figure 6. Flow net approximation.

The permeability of embankment and foundation materials adopted in the design based on Angkasa Consulting Services S/B Consulting Engineers are as in Table 2. Only two main parameters were adopted in this simulation study. Three seepage measurement weirs are installed to facilitate the measurement of the seepage water through the dam embankment, the foundation and ground water at the abutments draining into the dam toe area (which is not significant in the case of Putrajaya main dam considering the abutment elevation is low.

Table 2. Permeability of embankment and foundation materials.

Material	Coefficient of Permeability (m/sec)
Rock fill	1×10^{-2}
Clay core	2×10^{-9}
Shoulder Material	1×10^{-8}
Sand fill	1×10^{-3}
Organic soils and soft clay	1×10^{-8}
Alluvial silty sand	1×10^{-7}
Naturally occurring residual soils	1×10^{-8}

Based on suggestion by Angkasa Consulting Services S/B, the maximum allowable seepage value at each seepage chamber estimated is 0.5 litre/sec. This seepage measurement chambers comprise of a 900 V-notch weir, stick gauge (depth indicator) and basin. The objective of the V-notch weirs is to measure the amount of dam seepage water. Based on Angkasa Consulting Services S/B, the seepage quantity is estimated using the following equation:

$$Q = 1340 * H^{2.5} \qquad [1]$$

where Q is the flow, litres/sec.

'H' is the head of water upstream over the bottom of the V-notch, meter. The measured seepage rate will be compared against the permissible seepage rate by International Committee of Large Dam (ICOLD), which is 0.5l/s (as suggested by Angkasa Consulting Services S/B) for each seepage chamber set by the dam designer for dam safety evaluation. The Table shows the seepage V-notch weir Conversion Table 3 and the dam cross section is shown in Figure 7.

Table 3. The seepage V-notch weir Conversion Table.

Water depth above weir (mm)	Flow (l/sec)	Water depth above weir (mm)	Flow (l/sec)	Water depth above weir (mm)	Flow (l/sec)
0.00	0.00	28.00	0.19	56.00	1.05
2.00	0.00	30.00	0.22	58.00	1.15
4.00	0.00	32.00	0.26	60.00	1.25
6.00	0.00	34.00	0.31	62.00	1.36
8.00	0.01	36.00	0.36	64.00	1.47
10.00	0.01	38.00	0.40	66.00	1.58
12.00	0.02	40.00	0.46	68.00	1.71
14.00	0.03	42.00	0.52	70.00	1.83
16.00	0.05	44.00	0.58	72.00	1.96
18.00	0.06	46.00	0.65	74.00	2.10
20.00	0.08	48.00	0.72	76.00	2.25
22.00	0.10	50.00	0.80		
24.00	0.13	52.00	0.88		
26.00	0.16	54.00	0.96		

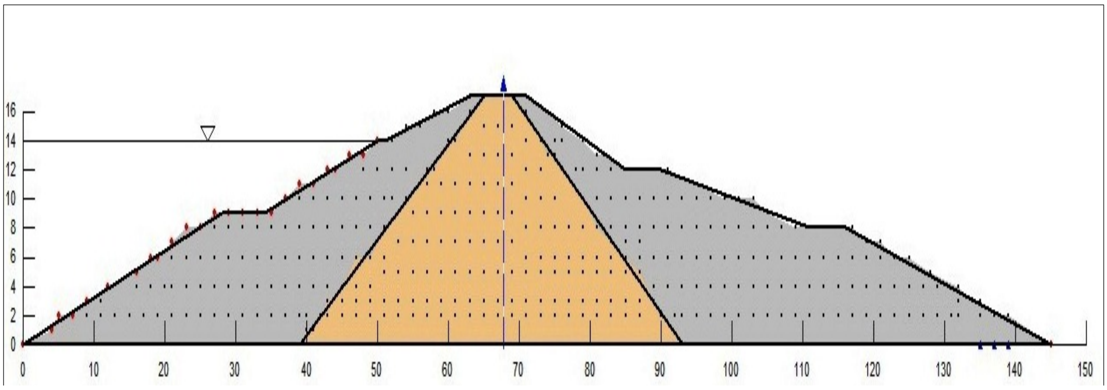

Figure 7. Dam cross-section.

5 RESULTS AND DISCUSSIONS

The seepage simulation values obtained from seepage analysis using SEEP/W is 3.5620 x $10^{-8}m^3$/s.m, as shown in Figure 8 and Figure 9. Based on field data collection and using equation 1, the result for seepage collecting data for one-year period time (in 2010) is shown in Table 4.

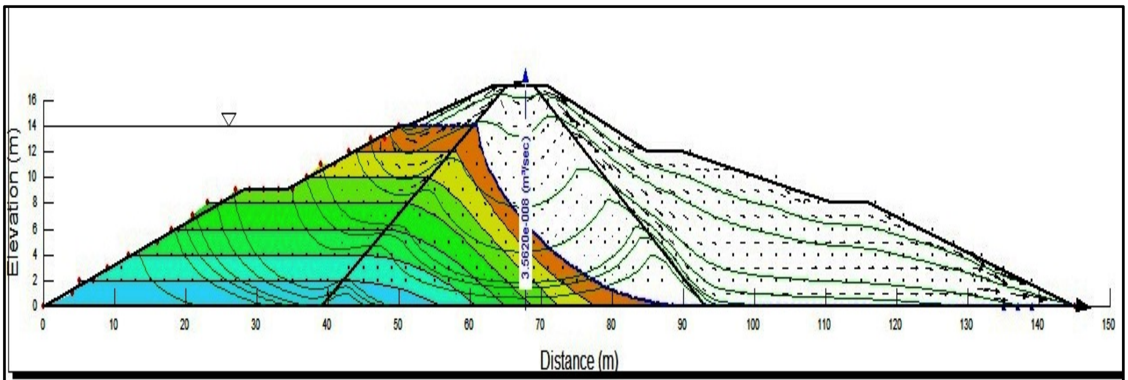

Figure 8. Contour and phreatic line (q = 3.5620 x $10^{-8}m^3$/sec).

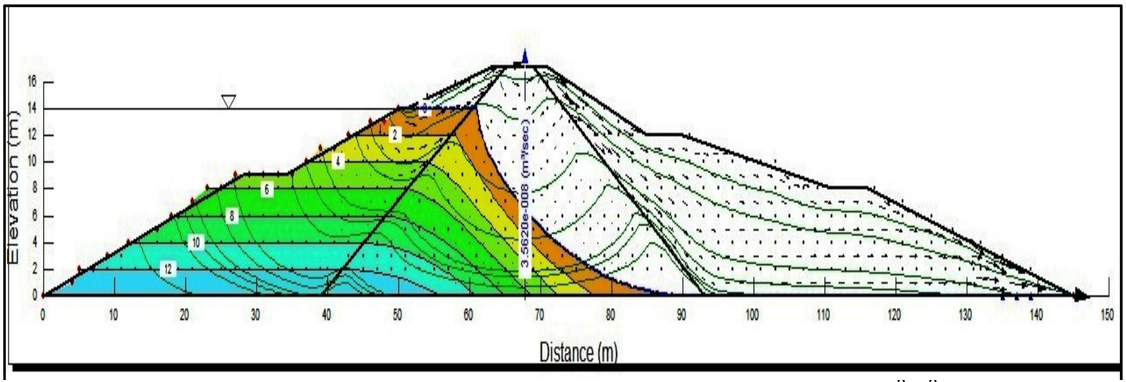

Figure 9. Phreatic line at 14.0m water head level (q = 3.5620 x $10^{-8}$$m^3$/sec).

Table 4. Seepage rate base on varies value.

Scenario	Hydraulic Conductivity			Seepage rate (m^3/s.m)
	Rock fills (m/s)	Clay core (m/s)	Reduce by	
1	5 x 10^{-3}	1 x 10^{-9}	2 times	1.73 x 10^{-8}
2	1 x 10^{-3}	2 x 10^{-10}	10 times	3.53 x 10^{-9}
3	1 x 10^{-4}	2 x 10^{-11}	100 times	3.56 x 10^{-10}

Based on the analysis carried out on the parameters and data of seepage flow on Putrajaya dam provided, it is found that the quantity is theoretically lower than the value set by the seepage of the International Committee of Large Dam (ICOLD) of 3.5620 x $10^{-8}$$m^3$/sec. The analysis and simulation of seepage on Putrajaya dam found the seepage rate decreases with the reduction of hydraulic conductivity, k. Based on the analysis done by simulating three different values of hydraulic conductivity, the seepage flow rate is found decreases with the decrease of hydraulic conductivity. All simulation of these analysis as shown in Figure 10, Figure 11 and Figure 12. The lower rate of seepage is better for stability of the dam. It is important for selecting material for filling the dam embankment with low permeability material. This is to ensure the minimum seepage through the dam embankment.

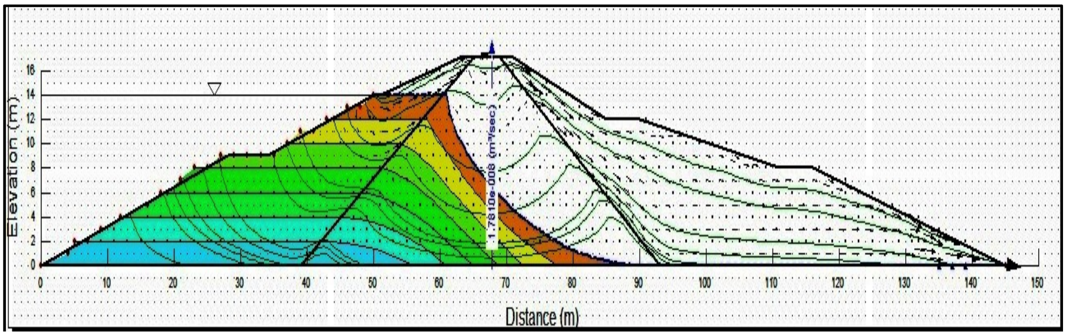

Figure 10. The seepage flow rate and phreatic line in reduce by 2 times.

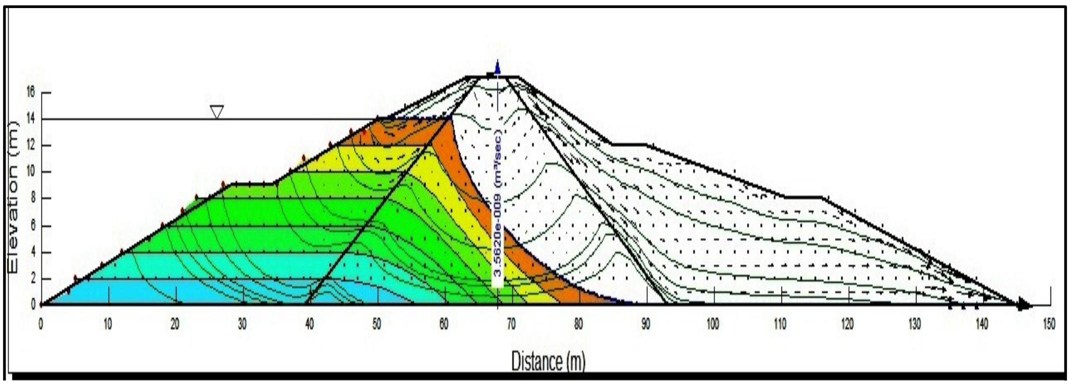

Figure 11. The seepage flow rate and phreatic line in reduce by 10 times.

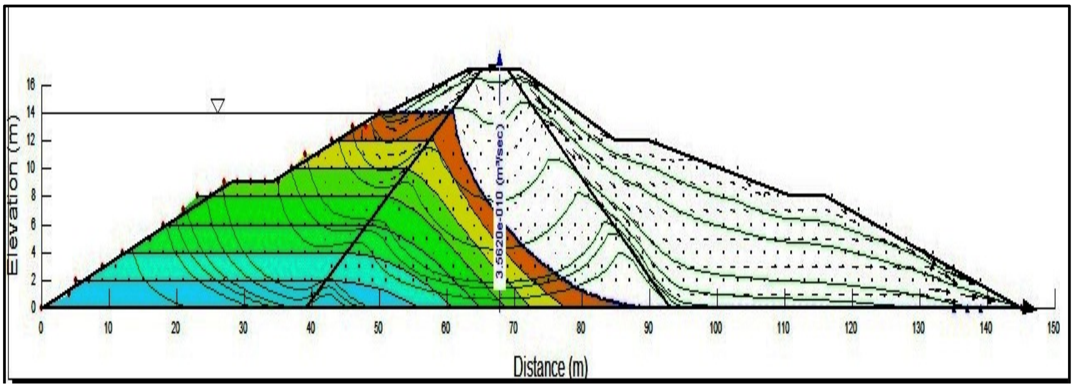

Figure 12. The seepage flow rate and phreatic line reduce by 100 times.

6 CONCLUSIONS

In this study, the seepage problem through Putrajaya dam was carried out:

i. A seepage flow rate value is not similar as compared with the actual seepage monitoring value done by Perbadanan Putrajaya. The simulation value is less than combination of three seepage chamber values at Hydraulic Conductivity, k value of 1 x 10^{-2}m/sec for rock fill and 2 x 10^{-9}m/sec for clay core, respectively. The seepage simulation value is 3.5620 x $10^{-8}$$m^3$/sec.m, where the total seepage is 0.0262l/s;

ii. The simulation values of total seepage through the Putrajaya Dam decrease when the value of Hydraulic Conductivity, k is reducing 2 times, 10 times and 100 times as compare with allowable combined seepage limit of 1.5l/sec, where the total seepage reduced to 0.0127l/sec, 0.0026l/sec and 0.0003l/s, respectively;

iii. The seepage amount is reducing when the Hydraulic Conductivity, k is reduced. It shows that the seepage is dependent on k;

iv. Finite element method can analyse the seepage problem faster and more accurate than the other method such the flow-net method;

v. The difference between the observed value of seepage and the predicted value of seepage is due to the limitation of two materials were considered as compared to the seven varies of materials zoning in the actual dam bodies.

REFERENCES

Ahmed, A.A. (2009). Stochastic Analysis of Free Surface Flow through Earth Dams. *Computers and Geotechnics,* 36(7), 1186-1190.

American Society of Civil Engineer (ASCE). (2005). Infrastructure Report Card, United States.

Department of Irrigation and Drainage (DID). (2009). *Dam Safety, Inspections and Monitoring*, DID Manual 9, 6.1-6.21.

Ersayin, D. (2006). Studying Seepage in a Body of Earth-Fill Dam by (Artificial Neural Networks) ANNs, *MSc Thesis.* Department of Civil Engineering, Izmir Institute of Technology.

Fu, L. (1994). *Neural Networks in Computer Intelligence*. McGraw-Hill, 24-78.

Geo-Slope International Ltd. (undefined). User Guide of SEEP/W, Canada.

Geo-Slope International Ltd. (2012). *Seepage Modelling with SEEP/W: An Engineering Methodology*, *July Edition*, Calgary, Alberta, Canada.

Geo-Slope International Ltd. (2007). *Seepage Modelling with SEEP/W: An Engineering Methodology, Fourth Edition*, Calgary, Alberta, Canada.

Hasan, M.K. (1999). Keselamatan Empangan di Malaysia: Pemantauan Risipan di Empangan Semenyih, *BSc Thesis*. Universiti Teknologi Malaysia.

Jansen, R.B. (1983). Dams and Public Safety. *In Water Resources Technical Publication*, United States Departmental of the Interior Bureau of Reclamation (UBSR).

Kasim, F. & Wong, S.F. (2002). Numerical Parametric Simulations for Seepage Flow Behaviour through an Earth Fill Dam, *MSc Thesis.* Universiti Teknologi Malaysia.

Krahn, J. (2004). *Seepage Modelling with SEEP/W: An Engineering Methodology*, GEO-SLOPE International Ltd., Calgary, Alberta, Canada.

Lam, L., Fredlund, D.G. & Barbour, S.L. (1987). Transient Seepage Model for Saturated-Unsaturated Soil Systems: A Geotechnical Engineering Approach. *Canada Geotechnical Engineering Journal,* 24(4), 565-580.

Liew, S.S., Kamaruzaman, M.H. & Darjad, O. (2010). Dam Safety Monitoring and Surveillance in Malaysia. Paper presented at the Asia Water 2010 Conference (ASIAWATER 2010), Kuala Lumpur Convention Centre, Kuala Lumpur.

Li, Q. & Liu, J. (2010). Numerical Analysis of the Seepage Field in Core-Dam. *School of Engineering and Architecture*, Southwest Petroleum University, Chengdu, China, 492-499.

Li, X. & Wang, L. (2009). Study on Seepage Stability of Jingyugou Tailing Dam. *School of Mechanics and Engineering*, Liaoning Technical University, Fuxin, China.

M. Subane, A.R. (2010). Simulation of Seepage Flow Behaviour Through Earth Fill Dams, *MSc Thesis.* Universiti Putra Malaysia.

Malaysian Inter-Departmental Committee on Dam Safety. (1989). *Guidelines for Operation, Maintenance and Surveillance of Dams*, 1-38.

Marino, M. & Luthin, J.N. (1982). *Seepage and Groundwater*. Elsevier Scientific Publishing Company, New York.

Mohamed, T.A. (2006). Seepage through Homogenous and Non-Homogenous Earth Dams: Comparison between Observation and Simulation. *Electronic Journal of Geotechnical Engineering*, 11.

Oklahoma Water Resources Board. (2010). Dam Inspection Guidelines-OWRB the Water Agency, 405, 530-8800, 1-12.

Othman, Z.A. (2006). Overview of Dam Safety in Malaysia. *Jurutera*, *Institution of Engineers Malaysia*, 22-23.

Peter, P. (1982). Canal and River Levees, Developments in Geotechnical Engineering. *Elsevier Scientific Publishing Company*, Amsterdam. 29.

Sherard, J.L., Woodward, R.J. & Gizienski, S.F. (1963). *Earth and Earth-Rock Dams*. John Wiley & Sons, New York.

Singh, A.K. (2008). Analysis of Flow in a Horizontal Toe Filter, *Proceedings of the 12th International Conference, International Association for Computer Methods and Advances in Geo-Mechanics* (IACMAG), Goa, India.

Szczesny, J. & Truty, A. (2004). Dam Surveillance and Maintenance – General Approach and Case Studies. *Cracow University of Technology*, Institute of Water Engineering and Water Management, Warszawska, Krakow, Poland, 151-166.

Uromeihy, A. & Barzegari, G. (2007). Evaluation and Treatment of Seepage Problems at Chapar-Abad Dam, Iran. *Engineering Geology*, 91(2-4), 219-228.

United States Cold Storage (USCOLD). (1998). Seepage can Take Place through and under Earth Fill of Dams.

Yu, H., Li, S., Liu, Y. & Chen, C. (2009). Evaluation and Rehabilitation of the Seepage Problems at the Fengman Dam. *Electronic Journal of Geotechnical Engineering*, 14, 1-14.

PREDICTION OF COMPLEX PIER SCOUR USING GENE EXPRESSION PROGRAMMING

REZA MOHAMMADPOUR [(1)] & AMINUDDIN AB GHANI [(2)]

[(1)] Department of civil engineering, Estahban Branch, Islamic Azad University, Estahban Iran
reza564@gmail.com
[(2)] River Engineering and Urban Drainage Research Centre (REDAC), Universiti Sains Malaysia, Engineering Campus, Nibong Tebal, Penang, Malaysia
Redac02@usm.my

ABSTRACT

Accurate estimation of scour depth at complex pier leads to an economic and correct design for level of foundation. Due to technical and economic reasons, complex piers (pier including foundation) are more general for bridge design. In this study, two robust techniques, artificial neural networks (ANNs) and Gene Expression Programming (GEP) were employed for prediction of scour depth at complex piers. A wide range of dataset was collected from present study as well as literature, the clear water condition was chosen for experimental tests. The result shows that the scour depth at complex piers is a function of pier diameter (b_c) and foundation level (Y). The RBF (Radial Base Function) network with R^2=0.945 and RMSE =0.031 provides better prediction in comparison with previous equations and the GEP techniques (R^2=0.811and RMSE=0.263). A formula was developed using GEP to predict local scour at complex piers. Although, accuracy of the RBF is higher than GEP, the GEP based formula is more useful for practical purposes and can be easily employed to predict the depth of scour at complex piers. This paper highlights that the mentioned techniques can be successfully used for accurate estimation of local scour and lead to the protection of bridge piers.

Keywords: Neural Network; GEP; Local scour; Complex piers scour; Erosion.

1 INTRODUCTION

Accurate estimation of scour depth at bridge pier is one of the major concerns during a flood hazard. Bridge piers are usually constructed on the foundation (pile cap) with or without the group of piles (complex piers). Due to technical and economic reasons, complex piers are more general for bridge design (Ataie-Ashtiani et al., 2010; Sheppard and Glasser, 2004). Generally, the foundation of complex piers can be found below the initial bed. Moreno et al. (2016) showed that scour around pile groups is caused by two types of mechanisms: (1) those causing local scour at individual piles, i.e., downflow, horseshoe vortex, wake vortices, and bow wave; and (2) those attributable to the interaction of the different piles, i.e., scour reinforcement, sheltering, wake vortex interaction, and compressed horseshoe vortices (Figure 1).

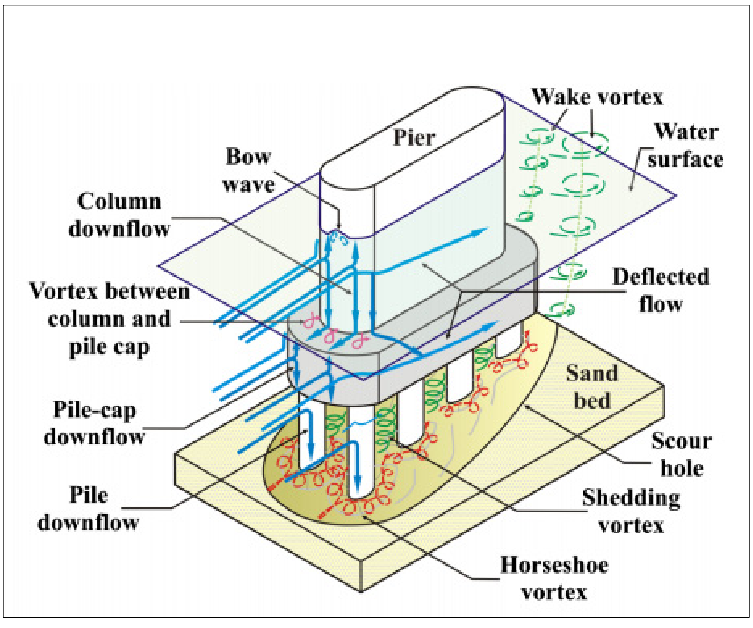

Figure 1. Flow structure around complex piers (Moreno et al., 2016).

During the flood hazard, the flow erodes sediments and the foundation will be exposed to flow and influences the scour depth (Melville and Coleman, 2000; Jones et al., 1992; Ferraro et al., 2013).

Different methods have been suggested for estimation of local scour around complex piers. The Federal Highway Administration (FHWA) suggested a superposition method to determine the scour depth at complex piers in HEC-18 (Richardson and Davis, 2001). Florida Department of Transportation (FDOT) proposed an alternative methodology, based on superposition method to estimate scour depth (Sheppard and Renna, 2005). In this methodology, complex pile is represented by a single pier with an effective diameter. Amini et al. (2014) indicated that superposition method which is used in HEC-18 and FDOT gives inadequate prediction of scour depth at complex piers. However, robust methods such as Artificial Neural Networks (ANNs) and Gene Expression Programming (GEP) can be used for accurate estimation of local scour at complex piers.

Several investigations have already been carried out to estimate local scour at uniform pier and abutment (Melville and Coleman, 2000; Mohammadpour et al., 2013a, 2015a,b; Kothyari and Raju, 2001; Ballio and Orsi, 2001). Only some studies are available in literature to predict the maximum scour depth at complex piers (Parola et al. 1996; Melville and Coleman 2000; Ferraro et al., 2013; Mohammadpour et al., 2014b; Ghani and Mohammadpour, 2015). Over the past two decades, soft computing techniques such as GEP and ANNs are successfully used in water resources field (Guven and Gunal 2008, Guven et al., 2012; Muzzammil, 2011; Muzzammil et al., 2015; Mohammadpour et al., 2014a, 2015b, 2016). Azamathulla et al. (2010) have applied GEP to predict the scour depth around piers. The GEP provides better prediction in comparison with other regression methods. The GEP gives satisfactory results compared to empirical equations and ANNs. Mohammadpour et al. (2013a) used GEP and ANNs to estimate variation of local scour around short abutment. Results indicated that although the accuracy of ANNs is better than the GEP, the GEP is a more practical technique.

In the present study, ANNs and GEP were used as robust techniques to predict the local scour around complex pier. Several experimental tests were conducted for different shape of complex piers under clear water condition. To evaluate the mentioned techniques, a wide range of dataset was collected from present study and literature. Finally, result of GEP and ANN is compared with conventional equations.

2 EXPERIMENTAL SETUP

The experimental investigations were conducted in a concrete flume with rectangular cross section and dimension of 30.0 m length, 1.0 m width and depth of 0.75 m. To make sure a fully developed boundary layer was obtained, the working section was selected at 21.0 m downstream of flume entrance. As shown in Table 1, cylindrical shape was chosen for foundation while three different shapes, circle, square and lozenge, were selected for piers. In all experiments, the foundation was located below the initial bed and level of foundation (Y) was measured from the initial bed (Figure 2). Four series of tests were performed and in each series, pier diameter (b_c) and foundation diameter (b_{pc}) were held constant while the Y was variable (Table 1). Melville (1992) indicated that the maximum scour depth around uniform piers is 2.4 times of pier diameter (dsmax= 2.4bc). However, for Y>2.4bc, the foundation level is below the maximum depth of scour and the scouring around complex pier is similar to uniform pier. In this study, the case of Y=12 cm has similar condition.

Table 1. Summary of tests for the present study.

Test	*Pier shape*	*Foundation Shape*	*Foundation elevation Y (cm)*	*Foundation Diameter b_{pc} (cm)*	*Pier Dimension b_c (cm)*
C-0	Circle	Cylinder	12.0	7.9	4.8
C-1	Circle	Cylinder	6.3	7.9	4.8
C-2	Circle	Cylinder	1.0	7.9	4.8
C-3	Circle	Cylinder	0.0	7.9	4.8
S-0	Square	Cylinder	12.0	7.9	4.8
S-1	Square	Cylinder	6.3	7.9	4.8
S-2	Square	Cylinder	1.0	7.9	4.8
S-3	Square	Cylinder	0.0	7.9	4.8
L-0	Lozenge	Cylinder	12.0	7.9	4.8
L-1	Lozenge	Cylinder	6.3	7.9	4.8
L-2	Lozenge	Cylinder	1.0	7.9	4.8
L-3	Lozenge	Cylinder	0.0	7.9	4.8

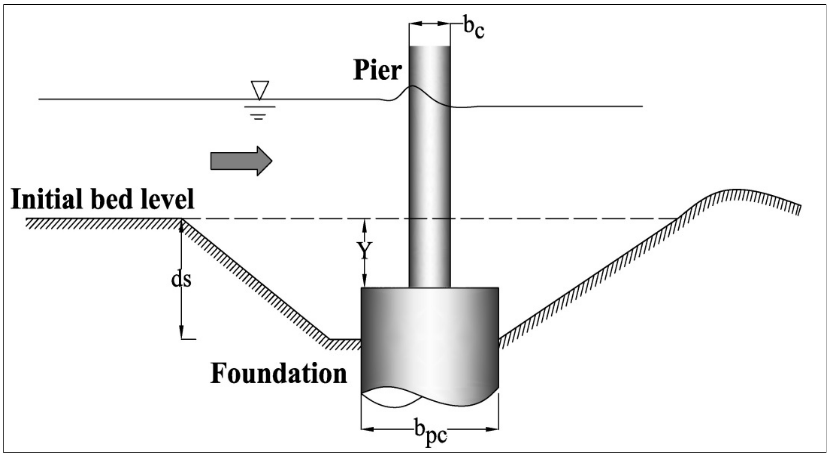

Figure 2. Foundation below the initial bed

The uniform sediment with d_{50} = 0.92 mm and geometric standard deviation, σ_D=1.20 was selected in all experiments. To avoid the effects of sediment on local scour, the ratio of b_c/d_{50} should be more than 50 (Melville and Chiew ,1999). Raudkivi and Ettema (1983) reported that for $d_{50} \geq 0.7$ mm, the experiments can be run successfully without ripple. To provide the clear water conditions and maximum depth of scour, the mean velocity of flow was set close to the critical sediment velocity. The expressions given by Melville and Coleman (2000) and Shields diagram were used to estimate the critical velocity of sediment (Uc). A gate was used to adjust the flow depth at the downstream end of the flume. At the end of each experiment, a point gauge with high accuracy was used to measure the topography of scour hole around the complex pier.

3 DIMENSIONAL ANALYSIS

In this study, the complex pier included pier and foundation. The effect of pier, foundation, fluid and sediments on scour depth (d_s) can be expressed functionally as (Ataie-Ashtiani et al., 2010):

$$d_s = f\left(b_c, b_{pc}, h, L_u, L_f, Y, d_{50}, U, U_c, K_{sc}, K_{spc}\right) \quad [1]$$

where, b_c=pier diameter/width; b_{pc}=foundation diameter/width; h= approach flow depth; L_U and L_f =extensions of the foundation at upstream and side of the pier, respectively; Y=foundation level; d_{50}=median size of sediments; U= flow velocity ; U_c = sediment critical velocity ; K_{spc} and K_{sc} = shape factors for foundation and pier, respectively. Melville and Sutherland (1988) indicated that for $h/b_c \geq 3.4$ and $b_c/d_{50} > 5$, the depth of flow and sediment size have no significant effect on the local scour. In present study, the collected data was chosen in such a way that the flow depth and sediment size have no effect on the scour depth. Therefore, a functional relationship based on the dimensional analysis may be written as:

$$\frac{d_s}{b_c} = f\left(\frac{b_c}{b_{pc}}, \frac{L_u}{L_f}, \frac{Y}{b_c}, \frac{U}{U_c}, K_{sc}, K_{spc}\right) \quad [2]$$

This equation was used to develop ANNs and GEP models.

4 EXPERIMENTAL RESULTS

Table 2 shows the maximum scour depth at complex pier. For Y=0 cm, the scour depth is 10.1 cm, 10.6 cm and 10.5 cm for circle, square and lozenge pier, respectively. It can be concluded that the shape of pier has no significant effect on scour depth when the foundation level is located at both initial bed (Y=0) and under scour hole (Y≥12). In this condition, extension of foundation in front of pier is similar to an obstacle and weakens the effect of pier horseshoe vortices (Figure 1). Over time, the scour hole in front of the pier is gradually enlarged and the foundation horseshoe vortices form at upstream of the foundation which increase the scour depth. However, in range of 0< Y<12, the effect of pier shape is considerable.

Table 2. Summary of tests in the present study.

Test	*Flow depth h (cm)*	*Foundation level Y (cm)*	*d_{50} (mm)*	*d_{smax} (cm)*
C-0	17.60	12.0	0.92	9.1
C-1	17.60	6.3	0.92	7
C-2	17.60	1.0	0.92	7.7
C-3	17.60	0.0	0.92	10.1
S-0	17.60	12.0	0.92	9.2
S-1	17.60	6.3	0.92	8.2
S-2	17.60	1.0	0.92	10
S-3	17.60	0.0	0.92	10.6
L-0	17.60	12.0	0.92	9.0
L-1	17.60	6.3	0.92	8.5
L-2	17.60	1.0	0.92	9.7
L-3	17.60	0.0	0.92	10.5

Figure 3 shows a comparison between present and previous studies at complex pier. The circle and square piers from this study were chosen for this comparison. Previous studies included the experiments conducted by Chabert and Engeldinger (1956), Melville and Raudkivi (1996), Parola et al. (1996), Coleman (2005) and Ataie-Ashtiani et al. (2010). As shown in Figure 3, three cases were observed regarding the foundation level ratio(Y/b_c). In Case I, level of foundation is under the base of the scour hole; therefore, scour depth depends on pier diameter (b_c), and the scour hole around the complex piers is similar to uniform piers. In this condition, maximum scour depth is $2.4b_c$. In Cases II and III, the top of foundation exposes into scour hole and the scour depth is usually smaller than maximum scour depth for uniform abutment. Starting from a Y/b_c approximately equal to 2.4 and subsequently decreasing, the foundation rises to the scour hole, and the scour depth decreases and reaches a minimum at Y/b_c =1.1~1.3. In Case II, the pier horseshoe vortices are weakened by the foundation and, the depth of scour is confined by the foundation. In the next step (Case III), scour depth ratio (d_s/b_c) increases when Y/b_c decreases again, it can be due to formation of foundation horseshoe vortices in front of complex pier.

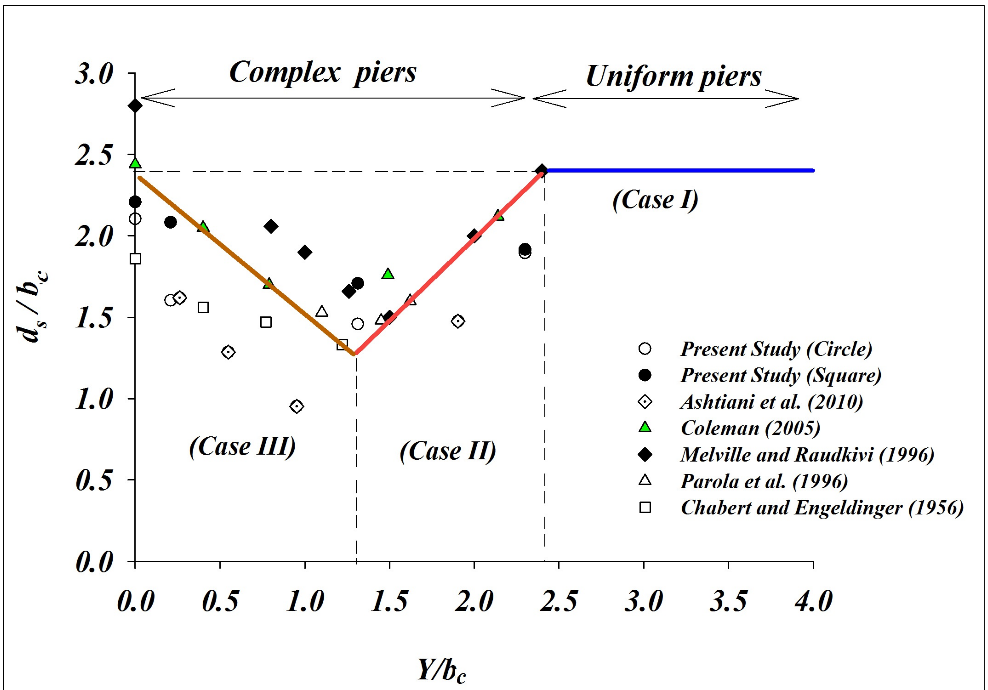

Figure 3. Variation of scour depth at complex pier in terms of foundation level.

5 DEVELOPMENT OF GENE EXPRESSION PROGRAMMING (GEP)

The GEP as a learning program has been developed using genetic programming (GP) and genetic algorithms (GA). In this technique, a fitness function was employed to evaluate the chromosomes which are randomly generated in each individual population. Several operators were used to modify chromosomes such as, cross-over transpositions, mutation and inversion.

Firstly, the optimum size of population was selected to be equal to 30 (Ferreira, 2001). In the next step, the Root Relative Squared Error (RRSE) was selected to evaluate the chromosomes. In the third step, in each gene, a basic mathematical function (power) and the operations of +, -, *, / (four basic arithmetic operators) were selected for generation of chromosomes. The architecture of chromosome was chosen based on the number of genes, length of head and tail. Mohammadpour et al. (2013b) showed that three genes per chromosome provide the best results. In the next step, the operators of multiplication and addition were assessed to determine the best GEP linking function. However, the addition function provides more accurate results and it was employed for linking between the chromosomes (sub-expression). In the last step, the mentioned operators were used to develop the GEP. A summary of the parameters is shown in Table 3.

Table 3. Parameters of the optimized GEP model.

Description of parameter	Setting of parameter
Function set	(+, -, *, /, power)
Population size	30
Head length	8
Number of genes	3
Mutation rate (%)	50
Linking function Addition	Addition
Inversion rate (%)	10
One-point recombination rate (%)	30
Two-point recombination rate (%)	30
Gene recombination rate	0.1
Gene transportation rate	0.1

In total, 128 datasets were used to estimate the scour depth at complex pier from present and earlier studies by Jones et al. (1992); Parola et al. (1996); Melville and Raudkivi(1996), Coleman (2005), Oliveto (2012), Umeda et al. (2010), Ataie-Ashtiani et al. (2010), Eghbali et al. (2013) and Amini et al. (2014). Out of the total dataset, approximately 80% (100 datasets) were selected randomly for training and remaining 20% (28 datasets) of dataset were employed for testing. The range of data is shown in Table 4.

Table 4. Range of data for training and testing.

Parameter	***Training***		***Testing***	
	Min	***Max***	***Min***	***Max***
L_u/L_f	0.00	3.48	0.00	3.48
L_f/b_c	0.00	3.55	0.11	1.50
b_c/b_{pc}	0.25	1.00	0.25	1.00
Y/b_c	0.00	20.00	0.00	5.10
U/U_c	0.55	1.00	0.64	1.00
K_{sc}	0.90	1.10	1.00	1.10
K_{spc}	1.00	1.10	1.00	1.10
d_s/b_c	0.08	3.28	0.13	2.93

As shown in Table 5, set of functions and terminals were chosen for each gene to create the chromosomes. In this work, the set of terminals included the six independent parameters in Equation 2, i.e *T*={ $\frac{b_c}{b_{pc}}, \frac{L_u}{L_f}, \frac{Y}{b_c}, \frac{U}{U_c}, K_{sc}, K_{spc}$ } and dependent variable of d_s/b_c. The simplified analytic form of the proposed GEP model may be expressed as:

$$\frac{d_s}{b_c} = \left(\frac{b_c}{b_{pc}}\right)^2 + \frac{\left(\frac{b_c}{b_{pc}}\right)^2}{K_{sc}^3 + 77.58\left(\frac{Y}{b_c}\right)} + K_{spc}\left(K_{sc}\right)^5\left(\frac{U}{U_c}\right)\left(\frac{b_c}{b_{pc}}\right) + \left(0.05\frac{Y}{b_c} - 0.16\right)\frac{L_u}{L_f} \qquad [3]$$

The expression trees of this model are indicated in Figure 4.

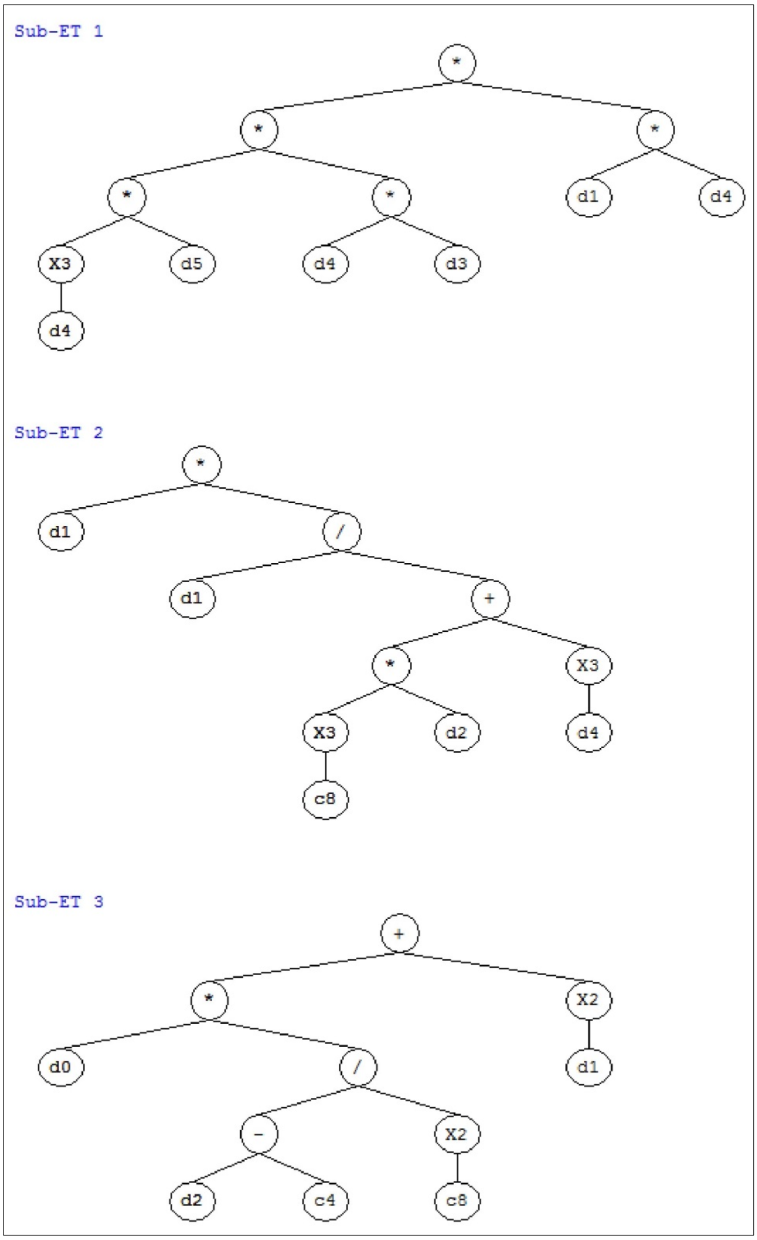

Figure 4. Expression trees for the GEP formulation.

6 DEVELOPMENT OF ARTIFICIAL NEURAL NETWORKS

The artificial neural networks (ANNs) attempt to represent the low-level intelligence of the human brain. An ANNs typically consists of input, hidden and output layers which shows a random mapping between the input and output dataset. The neuron is the main and smallest part of ANNs. In this research, the Softmax

  / ISSN 1562-6865 (Online) - ISSN 1063-7710 (Print)

transfer was employed as a function at each node. A radial basis function (RBF) is a network for function approximation and can be expressed as (Bateni and Jeng, 2007):

$$\phi_j(x) = \frac{\exp\left(-\frac{\|x-\mu_j\|^2}{2\sigma_j^2}\right)}{\Sigma\exp\left(-\frac{\|x-\mu_j\|^2}{2\sigma_j^2}\right)} \quad [4]$$

where: x= input dataset, μ_j= radial basis function centre for the J^{th} hidden node, σ_{j}= radius for the J^{th} hidden node and $\|x-\mu_j\|^2$ = the Euclidean norm.

To assess performance of the selected techniques, three statistical parameters, coefficient of determination (R^2), mean absolute error (MAE) and root mean square error (RMSE), were used in this research. Expression of these parameters are given in the following:

$$R^2 = 1 - \frac{\Sigma_{i=1}^{p}(O_i - P_i)^2}{\Sigma_{i=1}^{p}(O_i - \overline{O}_i)^2} \quad [5]$$

$$MAE = \frac{1}{n}\Sigma_{i=1}^{p}\left|O_i - P_i\right| \quad [6]$$

$$RMSE = \sqrt{\frac{\Sigma_{i=1}^{p}(O_i - P_i)^2}{n}} \quad [7]$$

where O_i= observed data, P_i=calculated data. $\overline{O}_i$ = average of observed value and n= the number of data. To find the best network of RBF-ANN method, the spread coefficient (α) should be found based on trial and error. However, a range of value between 0 and 1.2 was chosen for spread coefficient to train the RBF. As shown in Table 5, the best result for testing data was obtained for a network with 20 neurons in hidden layer and spread constant of 0.8 (R^2=0.945 and RMSE=0.031).

Table 5. Result of RBF based on statistical measures.

No. of Neurons	*Spread Constant*	*Training*			*Testing*		
		R^2	RMSE	MAE	R^2	RMSE	MAE
1	0.8	0.513	0.095	0.069	0.370	0.104	0.076
2	0.8	0.553	0.091	0.066	0.474	0.095	0.073
3	0.8	0.601	0.086	0.062	0.530	0.090	0.074
5	0.8	0.700	0.075	0.049	0.665	0.076	0.053
7	0.8	0.718	0.072	0.046	0.657	0.077	0.052
10	0.8	0.728	0.071	0.043	0.732	0.068	0.045
12	0.8	0.733	0.071	0.042	0.777	0.062	0.040
14	0.8	0.737	0.070	0.040	0.802	0.058	0.039
16	0.8	0.738	0.070	0.040	0.798	0.059	0.040
18	0.8	0.787	0.063	0.035	0.851	0.051	0.036
20	0.8	0.828	0.057	0.035	0.900	0.042	0.031
30	0.8	0.863	0.051	0.029	0.945	0.031	0.023
40	0.8	0.878	0.275	0.142	0.897	0.243	0.201
50	0.8	0.883	0.269	0.124	0.897	0.242	0.201

7 RESULT AND DISCUSSION

Table 6 compares the performance of the selected techniques with the equations recommended by Melville and Raudkivi (1996), Coleman (2005) and HEC-18. In overall, the ANNs-RBF with R^2=0.945, RMSE=0.031 and MAE=0.023 gives better predictions in comparison with GEP and other methods.

Table 6. Performance of various approaches to predict scour depth at compound piers.

Model	*Training*			*Testing*		
	R^2	*RMSE*	*MAE*	R^2	*RMSE*	*MAE*
ANNs-RBF	0.863	0.051	0.029	0.945	0.031	0.023
GEP	0.856	0.276	0.224	0.811	0.263	0.204
HEC-18	0.687	0.59	0.41	0.612	1.332	1.05
Coleman (2005)	0.505	1.303	0.916	0.550	1.582	1.25
Melville and Raudkivi(1996)	0.421	1.64	1.15	0.492	1.827	1.448

Figure 5 shows a comparison between the RBF and GEP methods. The RBF outperforms in best-value prediction, as reflected a high value of R^2=0.945 and a lower RMSE = 0.031. A comparative result was observed between RBF and GEP method with R^2=0.811, RMSE=0.263.

Although the RBF predicts the scour depth with high accuracy, it is not as easy to use as the empirical equations and do not give enough insight into the generated model. However, GEP based formula is more useful for practical purposes and can be easily employed to predict the depth of scour at complex piers.

It should be mentioned that prediction of HEC-18 (with R^2=0.811, RMSE=0.263) is better than the empirical equations suggested by Coleman (2005) and Melville and Raudkivi(1996). However, in comparison with HEC-18 method, the GEP approach can be recommended as rapid and direct methods to reduce substantial time and effort by minimizing the process and calculation. This study should encourage other researchers and managers to apply these techniques as highly reliable alternatives to predict scour depth and can be commonly used for accurate predication of aquatic system in the world.

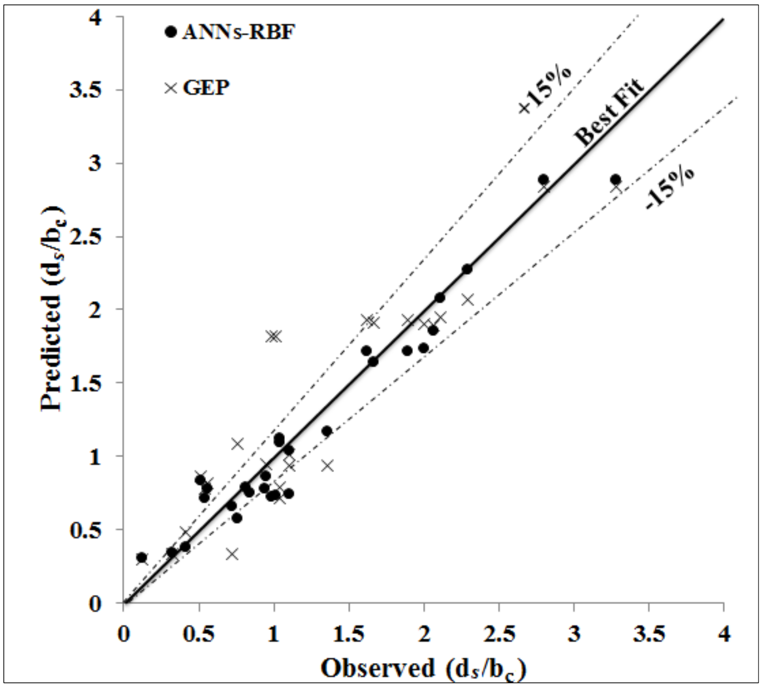

Figure 5. Comparison of ANNs-RBF and GEP.

8 CONCLUSIONS

In this study, ANNs-RBF and GEP techniques were employed to predict the scour depth at complex piers. The clear water condition was chosen for all experimental where the top of foundation was located below the initial bed level. The results indicated that the minimum scour depth occurs in range of Y/b_c=1.1~1.3. Furthermore, the shape of pier has no significant effect on scour depth when the foundation level (Y) was located at initial bed. A high value of the coefficient of correlation (R^2=0.945) and low error (RMSE =0.031) indicated that the ANNs-RBF provides better prediction in comparison with GEP technique (R^2=0.811and RMSE =0.263). Although the accuracy of ANNs-RBF is high, the GEP-based formula is more practical and can be easily used to estimate the scour depth at complex piers. This research highlights that the mentioned techniques can be commonly used for accurate predication of aquatic system in the world.

ACKNOWLEDGMENT

The author would like to thank Estahban Branch, Islamic Azad University, for the financial support.

REFERENCES

Amini, A., Melville, B. W. & Ali, T. M. (2014). Local Scour at Piled Bridge Piers Including an Examination of the Superposition Method. *Canadian Journal of Civil Engineering*, 41(5), 461-471.

Ataie-Ashtiani, B., Baratian-Ghorghi, Z. & Beheshti, A. A. (2010). Experimental Investigation of Clear-Water Local Scour of Compound Piers. *Journal of Hydraulic Engineering-ASCE*, 136(6), 343-351.

Azamathulla, H.M., Ab Ghani, A., Zakaria, N. A. & Guven, A.(2010). Genetic Programming to Predict Bridge Pier Scour. *Journal of Hydraulic Engineering-Asce*, 136(3), 165-169.

Ballio, F. & Orsi, E. (2001). Time Evolution of Scour around Bridge Abutments. *Water Engineering Research*, 2(4), 243-259.

Bateni, S.M. & Jeng, D.S (2007). Estimation of Pile Group Scour using Adaptive Neuro-Fuzzy Approach. *Ocean Engineering,* 34(8), 1344-1354.

Chabert, J. & Engeldinger, P. (1956). *Etude des affouillements autour des piles de ponts*. . Serie A, Laboratoire National d'Hydraulique. Chatou, France.

Coleman, S.E. (2005). *Clearwater* Local Scour at Complex Piers. *Journal of Hydraulic Engineering-Asce*, 131(4), 330-334.

Eghbali, P., Dehghani, A., Arvanaghi, H. & Menazadeh, M. (2013). The Effect of Geometric Parameters and Foundation Depth on Scour Pattern around Bridge Pier. *Journal of Civil Engineering and Urbanism*, 3(4), 156-163.

Ferreira, C. (2001). Gene Expression Programming: A New Adaptive Algorithm for Solving Problems. *Complex Systems*, 13(2), 87–129.

Ferraro, D., Tafarojnoruz, A., Gaudio, R. & Cardoso, A. (2013). Effects of Pile Cap Thickness on the Maximum Scour Depth at a Complex Pier. *Journal of Hydraulic Engineering*, 139(5), 482-491.

Ghani, A.A. & Mohammadpour, R.(2015). Temporal Variation of Clear-Water Scour at Compound Abutments. *Ain Shams Engineering Journal*, 7(4), 1045-1052.

Guven, A. & Gunal, M. (2008). Genetic Programming Approach for Prediction of Local Scour Downstream of Hydraulic Structures. *Journal of Irrigation and Drainage Engineering*, 134(2), 241-249.

Guven, A., Aytek, A. & Azamathulla, H. M. (2012). *A* Practical Approach to Formulate Stage–Discharge Relationship in Natural Rivers. *Neural Computing and Applications*, 23(3), 873-880.

Jones, J.S., Kilgore, R.T. & Mistichelli, P. (1992). Effects of Footing Location on Bridge Pier Scour. *Journal of Hydraulic Engineering*, 118(2), 280-289.

Kothyari, U.C. & Raju, K.G.R. (2001). Scour around Spur Dikes and Bridge Abutments. *Journal of Hydraulic Research*, 39(4), 367-374.

Melville, B.W. & Chiew, Y.M. (1999). Time Scale for Local Scour at Bridge Piers. *Journal of Hydraulic Engineering-Asce*, 125(1), 59-65.

Melville, B.W. & Coleman, S.E. (2000). *Bridge Scour.* Water Resources Publications, Highlands Ranch, Colo, 1-550.

Melville, B. W. (1992). Local Scour at Bridge Abutments. *Journal of Hydraulic Engineering-Asce*, 118(4), 615-631.

Melville, B.W. & Raudkivi, A.J. (1996). Effects of Foundation Geometry on Bridge Pier Scour. *Journal of Hydraulic Engineering-Asce*, 122(4), 203-209.

Melville, B.W. & Sutherland, A. J. (1988). Design Method for Local Scour at Bridge Piers. *Journal of Hydraulic Engineering*, 114(10), 1210-1226.

Mohammadpour R, Shaharuddin S, Chang C.K., Zakaria N.A. & Ghani A.A. (2014a). Spatial Pattern Analysis for Water Quality in Free Surface Constructed Wetland. *Water Science and Technology*, 70(7), 1161–1167.

Mohammadpour, R., Ghani, A.A., & Azamathulla, H. M. (2013b). Prediction of Equilibrium Scour Time around Long Abutments. *Proceedings of the Institution of Civil Engineers: Water Management*, 166(7), 394-401.

Mohammadpour, R., Ghani, A. A., & Azamathulla, H. M. (2013a). Estimation of Dimension and Time Variation of Local Scour at Short Abutment. *International Journal of River Basin Management*, 11(1), 121-135.

Mohammadpour, R., Ghani, A.A., Zakaria, N.A., & Ali, T.A.M. (2015a). Predicting Scour at River Bridge Abutments over Time. *Proceedings of the Institution of Civil Engineers - Water Management*, 1-16.

Mohammadpour, R., Ghani, A., and Zakaria, N. (2014b). Time Variation of Scour Depth around Complex Abutment. Paper Presented at the Scour And Erosion. *Proceedings of the 7th International Conference on Scour and Erosion,* Perth, Australia, 455-460.

Mohammadpour, R., Ghani, A., Vakili, M., & Sabzevari, T. (2015b). Prediction of Temporal Scour Hazard at Bridge Abutment. *Natural Hazards*, 80(3), 1891-1911.

Moreno, M., Maia, R. & Couto, L. (2016). Prediction of Equilibrium Local Scour Depth at Complex Bridge Piers. *Journal of Hydraulic Engineering*, 142(11).

Muzzammil, M. (2011). ANFIS-Base Approach to Scour Depth Preidiction at Abutment in Armored Bed. *Journal of Hydroinformatics*, 13(4), 669-713.

Muzzammil, M., Alama, J. & Danish, M. (2015). Scour Prediction at Bridge Piers in Cohesive Bed Using Gene Expression Programming. *Aquatic Procedia*, 4, 789-796.

Oliveto, G. (2012). Temporal Variation of Local Scour at Bridge Piers with Complex Geometries. *International Conference on Scour and Erosion*, ICSE6 Paris, 1-7.

Parola, A.C., Mahavadi, S.K., Brown, B.M. & Elkhoury, A. (1996). Effects of Rectangular Foundation Geometry on Local Pier Scour. *Journal of Hydraulic Engineering-Asce*, 122(1), 35-40.

Raudkivi, A.J. & Ettema, R. (1983). Clear-Water Scour at Cylindrical Piers. *Journal of Hydraulic Engineering*, 109(3), 338-350.

Richardson, E. V. & Davis, S.R. (2001). *Evaluating Scour at Bridges*. Hydraulic Engineering Circular No. 18 (HEC-18), 4th Ed., Rep. No.FHWA NHI 01-001, Federal Highway Administration, Washington,D.C.

Sheppard, D.M. & Glasser, T. (2004). Sediment Scour at Piers with Complex Geometries. *Proceeding of the 2nd International Conference on Scour and Erosion*, World Sceientific, Singapore, 1417.

Sheppard, D. M. & Renna, R. (2005). *Florida Bridge Scour Manual*, Florida DOT, Tallahassee,Fla.

Umeda, S., Yamazaki, T. and Yuhi, M., (2010). An Experimental Study of Scour Process and Sediment Transport around a Bridge Pier with Foundation. *In Scour and Erosion*, 66-75.

  / ISSN 1562-6865 (Online) - ISSN 1063-7710 (Print)

NEW EQUATIONS FOR FLOW DRAG FORCE AND ITS APPLICATION

SHU-QING YANG

School of Civil, MAining and Environmental Engineering, University of Wollongong, NSW 2530, Australia.
e-mail: shuqing@uow.edu.au

ABSTRACT

Determination of form drag by a blunt object in fluid flows is practically useful and an important topic for fundamental research. Flow resistance has been described by N-S equations, i.e., the boundary shear stress or the skin friction dominates the flow resistance. The skin friction has been well defined and understood, but the definition of form drag is not so successful even in the simplest case, i.e., the pipe flow with roughness like Nikuradse' experiment. To make attempt to understand those, this paper first defines form drag as $F_d = \rho g A_1 C_d U^2 / 2g = \rho g k V_w$, where ρ = fluid density, g = gravitational acceleration, k = coefficient, A_1 = projection area of an object and U = approaching velocity. Yang (2013) noticed that $U^2/2g$ has the length dimension, and the product of area A and a length yields a volume of V_w. He interpreted that the form drag is actually an alternative form of Archimedes' law, i.e., the drag force is proportional to the volume of wake behind an object. This paper verifies this interpretation by examining the measured volume of wake behind cylinders and spheres using the available data in the literature. It is found that in the existing expression of C_d, the skin friction on the front part is included. If the skin friction is excluded, the C_d should be a constant, not a variable dependent on the Reynolds number. This paper extends the basic idea of boundary layer flow (or the 1st type of boundary layer flow) formed by a flat plate to a blunt object, and "the 2nd type of boundary layer flow" is proposed to express the fluid zone of wake behind the object. The 1st type of boundary layer has been proposed by Prandtl to express the skin friction where the near boundary flow is parallel to the main flow direction, and the viscous effect generates the skin friction that is proportional to the contact area. The 2nd type is caused by the back flow, and its magnitude is proportional to a volume.

Keywords: Green's theorem; form drag; skin friction; boundary layer theory; wake volume.

1 INTRODUCTION

Determination of flow resistance is an important topic that has been studied by many researchers in the history of hydraulics and fluid mechanics, like Chezy, Manning, Darcy, Prandtl, Nikuradse, Schlichting, Colebrook & White, etc. It is widely agreed that the most important unresolved problem in fluids engineering is how to determine frictional force or energy loss (Flack and Schultz, 2010). The existing formulae available in the literature have been proven to be not sufficiently robust and applicable in practice (i.e., eco-hydraulics). Generally, the work done by Nikuradse has been widely extended from circular pipes to ship design, open channel flows and atmospheric boundary flows. He correlated the friction factor f with two parameters i.e., Reynolds number Re (=UR/ν) and relative roughness R/k_s, in which U = mean velocity, R = hydraulic radius, ν = kinematic viscosity, k_s = equivalent roughness height. Nikuradse observation has not been well understood and explained. For example, it is not clear on why roughened pipes behave like a smooth pipe when the grain Reynolds number (Re_* = $u_* k_s/\nu$) is less than 5; if the Reynolds number is high enough, the friction factor becomes a constant and is independent of Reynolds number (or fully rough). Between these two extremes, the measured friction factor depends on both Re and R/k_s and it is termed as the transition region. In other words, the friction factor is independent of other factors like roughness shape, roughness density and even when the Reynolds number is very high.

However, many researchers like Schlichting (1936) have found that the friction factor f depends on many factors including the shape of roughness elements and its distribution. These following experimental phenomena cannot be explained by any existing theory:

1) When sphere is used to roughen the surface and packed tightly, the result that k_s = 0.627d is different from Nikuradse's conclusion that k_s = d. When spherical segment is used to roughen the surface in a tightly packed tightly condition, the result is $k_s = 1.404k$ (where k = roughness height). As Nikuradse's conclusion of k_s = d cannot be repeated in many cases (e.g., for sediment transport k_s = 2.5d is widely used, Yang and Tan, 2008), many explanations have been proposed, and one of the widely accepted assumption is that the roughness height in Nikuradse experiments was less than d/2, because the lower part of the grains was immerged in the smoothened concrete and the roughness surface was also painted in order to stabilize the particles on the pipe wall.

2) The friction factor also depends on the density of roughness distribution λ and the roughness shape. In other words, Nikuradse's results of friction factor f = F_n(Re, R/k_s) is incomplete, and more parameters should be considered. Wooding et al. (1973) have collected extensive data describing the variation of k_s with concentration λ and the results are shown in Figure 1.

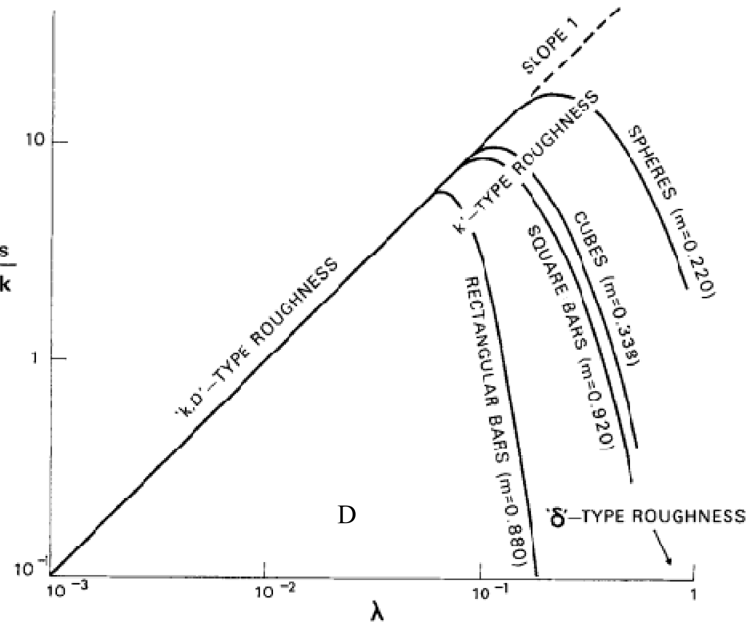

Figure 1. Variation of equivalent roughness with concentration of roughness elements after Wooding et al. (1973) where m is the coalescing factor introduced by Koloseus and Davidian (1966), the concept of K, D (pipe diameter or boundary layer thickness) type roughness was introduced by Perry et al. (1969).

For the dependence of k_s on λ, many useful investigations have been done and comprehensive reviews can be found in Raupach et al. (1991), Jimenez (2004) and others. An important conclusion by Raupach et al is that the roughness sublayer is the region directly above the roughness extending about 5k from the surface in which the turbulent motions are directly influenced by the roughness length scales whilst the important conclusion by Jimenez is that the D-type roughness suggested by Perry et al (1969) is inconclusive.

3) Nikuradse's experimental results show that in the laminar flow regime, the friction factor of roughened pipes is identical to the smooth pipes. At very high Reynolds number, the friction factor is independent of Re and f is a constant. However, the experiments in roughened pipes by cutting square threads on its internal surface show that large discrepancy exists in the laminar flow (small Reynolds number), at very high Reynolds number the measured friction factor never becomes a constant, but always depends on Re number. Based on some experimental data available in the literature, together with their own experimental data from a wind tunnel, Perry et al., (1969) proposed that there are two types of roughness, referred to K- and D- type roughness. The K-type roughness performs like Nikuradse roughness in the f and Re relationship. The D-type roughness is roughened by spanwise grooves, its k_s is not proportional to the roughness height k, but to the boundary layer thickness (D).

The discrepancy between Nikuradse's observation and other researchers' data has stimulated intensive experimental, theoretical and numerical investigations, and many important progresses have been made. Most of the researchers investigated the roughness effect by assessing the similarities of turbulence structures over smooth and rough surfaces, the parameters examined include: 1) the velocity distribution u, or the velocity retarded by the roughness elements Δu over the distance from the crests of the elements to a reference level, from which level the log-law can be obtained (e.g. Perry et al., 1969); 2) velocity fluctuations distribution u' or v' (e.g. Ligrani and Moffat, 1986); 3) two point correlations of the velocity and swirling (e.g. Volino et al., 2009); 4) Reynolds shear stress distribution (e.g., Roussinova and Balachandar, 2011), etc.

The Nikuradse data have been explained using the hypothesis of viscous sublayer in almost all text books in hydraulics and fluid mechanics: if the roughness elements are completely submerged in the viscous sublayer, then the flow resistance is entirely unaffected by roughness. If the sublayer is very small relative to the roughness height, k, then the flow resistance depends on k only. This hypothesis can explain many interesting phenomena (Yang and Dou, 2010), but obviously it cannot sufficiently explain the above-mentioned problems quantitatively.

Relative to the variation of sublayer thickness, the research community has paid less attention to the variations of vortex created by roughness elements, like its length, area and volume. Yang et al. (2011) attribute Nikuradse's observation of hydraulically smooth, transition and fully rough regimes to the horizontal variation of eddies induced by roughness elements as shown in Figure 2, in which the surface irregularities are represented by a dune. If there is no flow separation or backflow, then only skin friction exists, which is proportional to the contact liquid-solid area, the viscosity and the velocity gradient, or the hydraulically smooth regime termed by Nikuradse. If the trough is fully covered by a backflow, then the flow resistance is independent of viscosity, but depends on the eddy size that is proportional to the size of roughness elements. Between these two extremes, the friction factor varies with both Re and relative roughness R/ks as the backflow only occupies part of the trough. Mathematically, the energy loss over the dune can be written as:

$$h_L = h_L^{'} + h_L^{''} \tag{1}$$

where h_L = energy loss over L, h_L' = energy loss by skin friction over L' and h_L'' = energy loss by the large eddy over L''. The energy slope can be accordingly determined as:

$$S = \frac{h_L}{L} = S'\frac{L'}{L} + S''\frac{L''}{L} \tag{2}$$

where S = energy slope, S' energy slop associated with skin friction and S'' = energy slope related with form drag. Alternatively, Eq. 2 can be rewritten as:

$$\tau_0 = \tau'\frac{L'}{L} + \tau''\frac{L''}{L} \tag{3}$$

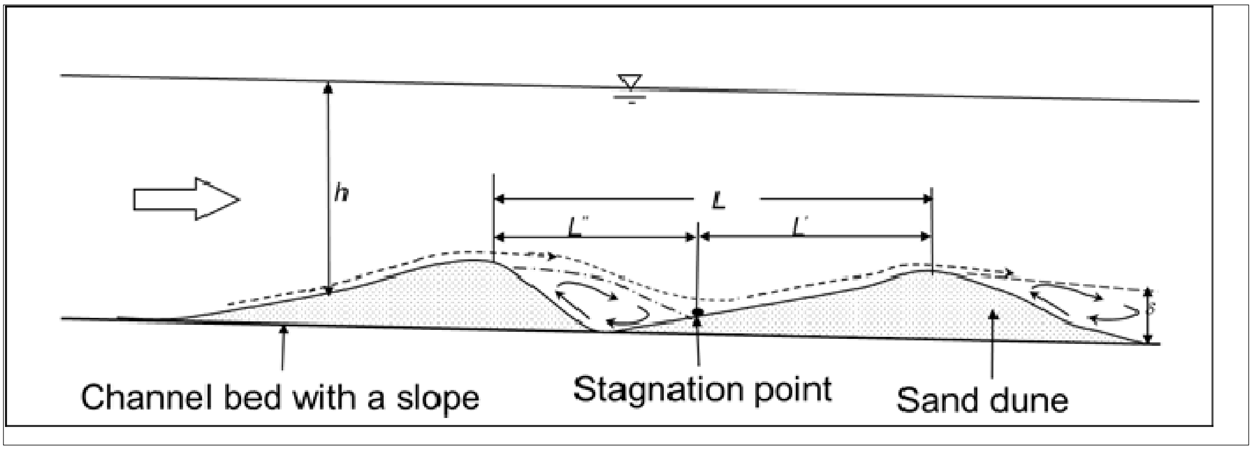

Figure 2. Combination of skin friction and form drag over a trough between roughness elements

Eq. 2 is different from those equations proposed by Engelund (1966) and Meyer-Peter and Muller (1948) with the following form

$$S = S' + S'' \tag{4}$$

Einstein and Bank (1950) used the following equation to study the flow resistance over composite roughness:

$$\tau_0 = \tau' + \tau'' \tag{5}$$

Yang et al. (2011) successfully used Eq. 3 to express the measured data by Nikuradse and good agreement has been achieved, and the horizontal variation of eddy zone can also explain Nikuradse' observation. As a continuous effort, this paper will investigate the flow resistance over 2-D roughness distribution by extending Eq. 3 from 1-D roughness in Figure 2. The research objectives of the paper are:

1) To interpret and redefine the hydraulic radius and roughness height, so that the influence of roughness on friction factor in laminar flows can be explained;
2) To develop a unified f versus Re theory, so that the observed discrepancy between Nikuradse's observation and other experimental data can be explained;
3) To explain why the measured friction factor in D-type roughness depends on the viscosity or Reynolds number in fully rough region.

2 NEW DEFINITIONS OF SKIN FRICTION AND FORM DRAG AND INTERACTIONS

Prandtl (1904) proposed a revolutionary theory to divide the flow domain into two zones, i.e., the boundary layer flow and the outer flow (Table 1). The boundary layer thickness is defined as the distance away from the surface to someplace where the velocity reaches 99% of the free-stream velocity. Beyond this layer, the flow is inviscid or ideal, without significant energy dissipation induced by the immersed object, while within the boundary layer the flow velocity is retarded by the object and this induces the friction force. The novel idea of Prandtl's boundary layer theory is not his mathematical treatment for Reynolds equations, but the flow region division, which suggests that for an external flow, a solid object only has its influence to a small region adjacent to it. Out of this small region, the fluid can be treated as undisturbed. Similar to this, this study also divides the flow field as shown in Figure 2 into the undisturbed region and the dead zone region by assuming that the energy dissipated in the undisturbed region is only small part (≈1%) of the energy dissipated in the dead zone, thus the former is negligible in practice. Thus, the very difficult form drag determination has been converted to the prediction of dead zone, a relatively simpler work. Direct determination of skin friction is very difficult, but this picture simplifies the calculation of friction.
Different from the skin friction, form drag is an integration of pressure around an object in a moving fluid, the former is the force tangent to a surface, but the latter, normal to the surface. Both integrations are also extremely difficult, if not impossible. Therefore, it is useful to seek its alternative expression. Similar to Prandtl's treatment, we can assume that the flow beyond the dead zone of a bluff object is inviscid or ideal, the energy dissipation in the "outer region" is negligible. The drag force can be assumed to be proportional to the dead zone volume, this is somewhat similar to Archimedes' principle i.e., the force can be determined from a volume of the submerged object. This may greatly simplify the prediction of form drag. It also indicates that the resistance is minimum if $V_w = 0$, this explains why a streamlined object has very small flow resistance.

Table 1. Comparison the boundary layer flows of a flat plate and a bluff object

	A flat plate	A bluff object
Flow pattern Force caused by	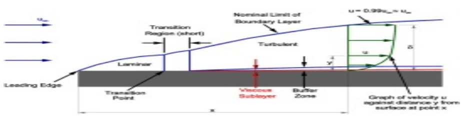	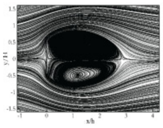 Pressure difference
Characteristics of boundary layer	By 99% of U, divergence, open,	By 99% of P, convergence, closed
Force is proportional to	Contact area (τA)	Wake volume V_w
Drag can be reduced by	Keeping laminar flow regime	Decreasing the wake volume
Turbulent energy is dissipated by	99% in the boundary region by small eddies	99% in the wake by large eddies
Location of boundary layer	Both sides of the an object	Rear of an object

In real flows, the flow resistance is always comprised of skin friction and the form drag, their difference can be seen from the flow direction near a solid boundary:

1) if the flow is opposite to the incoming flow, the boundary bears the form drag;
2) if the flow follows the direction of incoming flow, the boundary is governed by the skin friction that depends on the velocity gradient or u_*, viscosity, etc..

For the form drag, the velocity gradient and viscosity are no longer important, and the force depends on the separation zone (or dead zone). The coexistence of form drag and skin friction can be widely observed, and their difference can be defined as shown in Figure 3:
It is well known that the form drag F_d can be expressed as

$$F_d = C_d \rho A_p \frac{U^2}{2} \tag{6}$$

where A_p is projection area of the object in the flow direction, C_d is the drag coefficient, ρ is the density of fluid, U is the approaching velocity. The $U^2/2g$ has length dimension, or

$$L_{dz} = k_1 \frac{U^2}{2g} \tag{7}$$

Therefore Eq. 6 states that

$$F_D = k\rho g V_w \tag{8}$$

$$V_w = k_0 A_p L_w \tag{9}$$

where k and k_0 are coefficients. In Eq. 8, we argued that the volume V_w is actually the volume of the dead zone (see Figure 4) because the form drag disappears when the dead zone volume is zero. It implies that the form drag can be expressed by water volume.

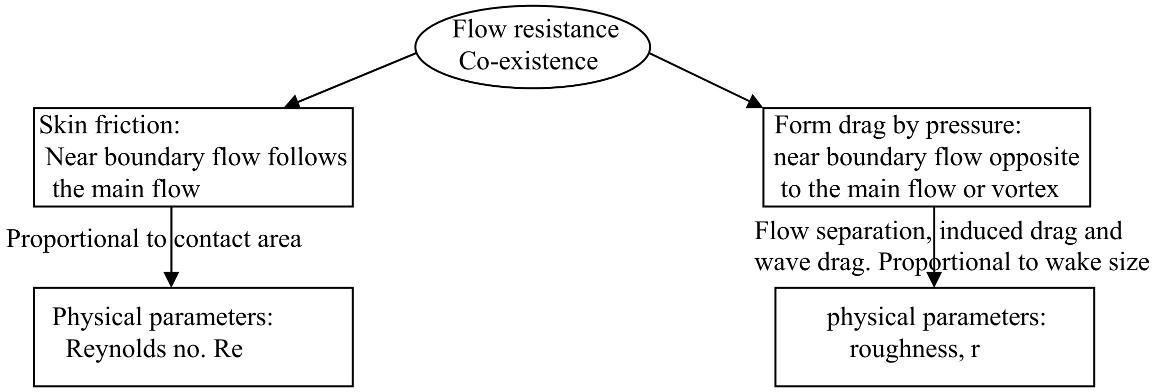

Figure 3. Flow resistance and parameters

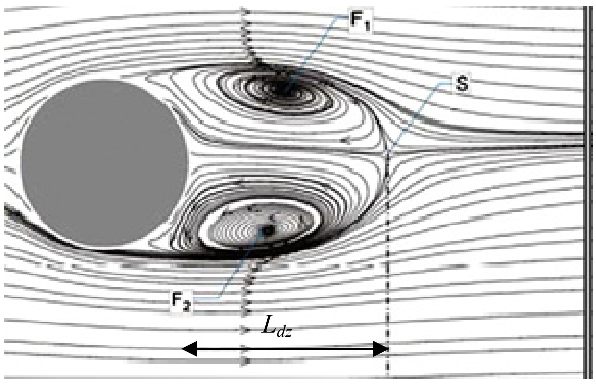

Figure 4. Dead zone after a sphere as a typical example after Ozgoren et al. (2011).

Eq. 8 reveals that similar to the buoyant force, the form drag is also proportional to fluid volume, also it extends the concept of boundary layer theory that tells an object's influence on its flow is constrained within a boundary region, majority of the energy to overcome the form drag is dissipated in the dead zone, the larger the zone is, the higher the drag force will be.

Eq. 8 states that the form drag is proportional to the stagnant fluid's volume. If the fluid's volume is replaced by a solid, no flow energy is dissipated by the turbulence, thus the drag force becomes very small and only the skin friction bears the flow resistance, in such case the object becomes streamlined.

Eq. 8 provides a very simple law to explain our daily observations, for example, an opening at bridge pier can significantly reduce the form drag. Eq. 8 shows that the reduction of form drag is caused by the reduction of dead zone volume. In a windy day, the trees tend to bend its branches and trucks in order to reduce the dead zones, and then the form drag.

Although the buoyant force is caused by the pressure distribution in static state, Archimedes principle avoids the complex measurement of pressure distribution around an object submerged in fluid, this makes the calculation of buoyance become very easy and simple. Similarly, the form drag is also caused by the uneven distribution of pressure in a flowing environment, it is almost impossible to measure the local pressure everywhere abound a submerged object, Eq. 8 greatly simplified the troublesome work as Archimedes principle achieves.

Alternatively, the skin friction and the form drag are shown in Figure 5 where an object is submerged in flowing fluid. When the Reynolds number is low, the drag on a streamlined body is dominated by the skin friction, but this dependence diminishes when the Reynolds number is sufficiently high. Let *F* be the drag force in the flow direction and ***n*** be the normal direction to the boundary. Let $\mathbf{n_x}$ be the component of ***n***, in x (i.e. the flow) direction. The skin friction and form drag can thus be theoretically expressed as follows:

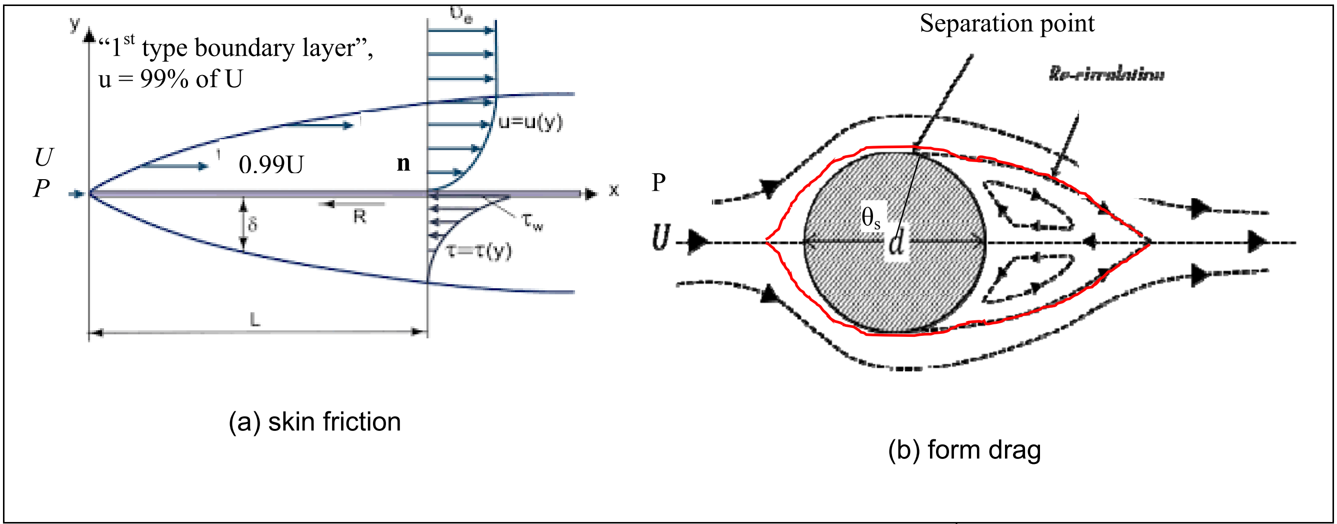

Figure 5. Two types of flow resistance on a solid surface. 0.99U forms the "1st type boundary layer line" for skin friction (a); 0.99P forms the "2nd type boundary layer" for form drag.

$$F_{sf} = \mu \iint \left.\frac{\partial u}{\partial n}\right|_{boundary} dA \qquad (10)$$

where the subscript *"sf"* denotes the skin friction, and d*A* is the surface area, μ = fluid dynamic viscosity, u = point velocity.

The form drag on a blunt body shown in Figure 6a has a dead zone behind it, in which a flow separation occurs and the form drag is induced. The pressure difference around the object yields the drag force, or it can be expressed as follows:

$$F_d \approx -\iint p|_{boundary} n_x dA \qquad (11)$$

where F_d is the form drag and p is the pressure.

For an object submerged in water, it is primarily the direction of near boundary flow which determines whether Eq. 10 or 11 should be used for its resistance. Eq. 10 is applicable if no reverse flow near the body is observed. Otherwise Eq. 11 should be applied. Actually, Eq. 11 is also valid for determining the buoyancy in a static fluid, but its integration is very difficult as it is necessary to know the pressure at every point. Archimedes linked the force to the volume, but his idea becomes invalid to determine the form drag as shown in Eq. 11.

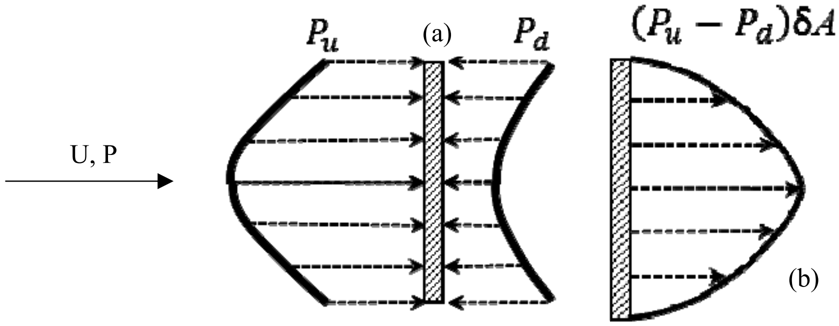

Figure 6, pressure distribution for a plate in a moving fluid (a); distribution of net pressure force per unit area around the plate (b).

The integration of Eq. 10 or 11 is extremely difficult, if not impossible. Therefore, it is useful to seek its alternative expression. Similar to Prandtl's treatment, it is assumed that the flow beyond the dead zone in Figure 5b is inviscid or ideal, the energy dissipation in the "external region" is negligible, and the pressure along the red solid line of Figure 5b is the same as the free stream pressure. Similarly, for a plate in Figure 6b, the integration of pressure along the "2nd type of boundary layer" yields

$$\iint_{redline} p n_x ds = 0 \qquad (12)$$

Alternatively, Eq. 12 can be written in the following form:

$$\iint_{redline} pn_x ds = \iint_{body} pn_x ds + \iint_{wake} pn_x ds = 0 \tag{13}$$

Substituting Eq. 13 into Eq. 12, one has

$$F_d \approx -\iint p\big|_{boundary} n_x ds = \iint_{wake} pn_x ds = \rho g k V_w \tag{14}$$

where ρ is the fluid density, k is a proportionality factor and V_{dz} denotes the volume of the dead zone. It can be seen from Figure 6 that the distribution of ΔpdA has the similar shape like the dead zone, or it is proportional to V_{dz}. Obviously, the skin friction plays a dominant role if V_{dz} = 0. Eq. 14 indicates that the form drag disappears if V_{dz} = 0 and this explains why a streamlined object has very small flow resistance.

3 EXPERIMENTAL VERIFICATION BY SHEPHE

Dye visualization has been used to reveal the wakes by Magarvey & Bishop (1961) to show drops of an immiscible liquid in water. The vortex size of the flow past a sphere has been studied by a number of researchers at varying Reynolds numbers. Taneda (1956) used flow visualization methods to study the wake of a sting-mounted sphere for 5<Re<300, where Re is based on the velocity U and sphere diameter D. He determined that at Re ≈ 24, vortexes were formed and separation from the rear of a sphere occurred and resulted in the generation of an axisymmetric vortex ring. The rings remained stable and axisymmetric up to Re = 210. In the range 210≤ Re ≤270, the flow became non-axisymmetric as the ring vortex shifted off-axis and dye was released from the wake in two parallel threads. When a Reynolds number is higher than 300, the vortices begin to be periodically shed. When a Reynolds number > 800, the hair-pin-shaped vortices begin to change from the laminar to turbulent vortices with alternate fluctuations, this pattern of vortex shedding continues as far as the region of Re = 3.7 x 10^5, which is called the upper critical Reynolds number. Tomboulides (1993) presented results for the flow over a sphere for 25<Re<10^3 and with large-eddy simulation at Re=2×10^4. Natarajan & Acrivos (1993) investigated the stability of the axisymmetric sphere flow.

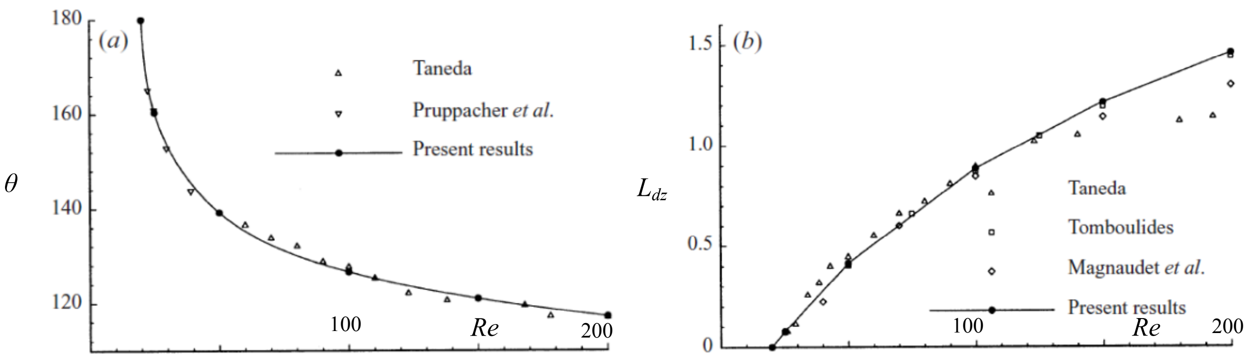

Figure 7**.** Measured separation angle (a) and wake length (b) for a sphere in flowing fluid by Taneda (1956).

From Figure 7, one can see that the higher Reynolds number generates the higher wake volume. Consequently, the drag force is increased.

For 2-D bluff objects shown in Figure 8, the flat plate has not any skin friction in the flow direction. One can easily ascertain that its drag coefficient is independent on the Re. This is verified by the measured C_d shown in Figure 8. From Eq. 6 and 8, one can find that

$$C_d = k\frac{V_w}{A_p\dfrac{U^2}{2g}} \approx \frac{kA}{A_p} = \frac{kD_{\max}}{D} = 2.0 \tag{15}$$

where D_{max} is shown in Figure8c where the Reynolds number is the same and Re = 10^5, and the maximum cross section of objects with different shapes is unchanged, i.e., diameter is D. If k = 1, visually one has D_{max}/D = 1.8, and it gives C_d = 1.8, and the measured C_d = 2.0, the predicted value is 10% less.

For the cylinder, Figure 8c gives D_{max}/D = 36mm/30mm = 1.2, and Eq. 15 predicts C_d = 1.2, and the measured C_d = 1.2, both are the same.

For the streamline body D_{max}/D = 5mm/26mm = 0.19, and the measured C_d = 0.12.

For the cylinder diameter of 1/10d, the D_{max}/D = 6mm/4mm = 1.5, and the measured C_d = 1.2.
For the last figure in Figure 8c, D_{max}/D = 18mm/27mm = 0.667, and the measured C_d = 0.6.

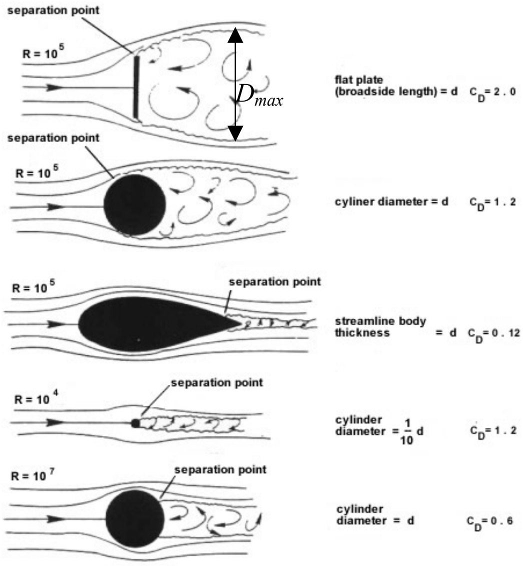

Figure 8. Measured drag coefficients C_d from different objects.

Similarly, for 3-D objects, Eq. 15 can be rewritten as its alternative form:

$$C_d = k\frac{V_w}{A_p\dfrac{U^2}{2g}} \approx \frac{kA}{A_p} = k\left(\frac{D_{\max}}{D}\right)^2 \tag{16}$$

Figure 9 shows the measured C_d for typical objects and these figures can be found in textbook of fluid mechanics. The table on the left lists 3-D shapes like disks, cones, and spheres. On the right of Figure 9 is for 2-D shapes like plates, wedges, and cylinders. On the 3D side, note the flat circular disk in shape No. 7. The drag coefficient for this shape is given as 1.17 which is different from the flat plate in Figure 8. If k = 1 is assumed, thus Eq. 16 gives D_{max}/D = 1.08, the estimated wake width is shown in Figure 9 by red lines. It can be seen that this is similar to the sketch of separation line (black line). However, the difference between the black lines and red lines is big for small C_d. For example, the sphere's drag coefficient is C_d = 0.47, and $D_{max}/D = 0.47^{0.5}$ = 0.686, but the black line gives $D_{max}/D \approx 1.0$. It is not clear on why the difference is large for cases 1-6. It seems that the agreement between red lines and black lines for case 7-11 is acceptable.
For 2-D objects list on the right of Figure 9, Eq. 15 can be used to estimate the width of separation zone, i.e.,

$$\frac{D_{\max}}{D} = \frac{C_d}{k} \approx C_d \tag{17}$$

The estimated width of separation line is shown in Figure 9 by red lines. For 2-D cylinder in shape No. 12, the cylinder is oriented with its axis perpendicular to the flow rather than into the flow. The measured drag coefficient is about 1.17, the estimated boundary line or the separation line matches the original sketch very well, same for shape No. 13, 14, 16, 17, and 22. The remaining shapes have large discrepancy and the reason is not clear, and more research is needed to understand the error source. This explanation shown in Eq. 15 has provided a simple way to estimate the drag coefficient. Understanding the drag characteristics of these simple shapes can often be very useful in predicting how more complicated objects behave. It also explains the similarities between these different shapes, such as how they all collapse into flat disks and produce the same drag. Simple rules of thumb like these are often very useful as a method of quickly evaluating the accuracy of experimental data compared to theoretical predictions.
Based on the above mentioned relationship, one can roughly estimate the drag coefficient of smooth ball and golf ball based on the flow wake zone shown in Figure 9c, which is downloaded from website. It can be seen that for a smooth ball $D_{max}/D \approx 1.35$, and Eq. 16 gives that C_d = 1.16. But at the same Reynolds number, for a golf ball $D_{max}/D \approx 0.70$, and Eq. 16 predicts that C_d = 0.84. This clearly shows that a golf ball has less flow resistance by observing its separation line. Similarly, by observing the wave volume shown in Figure 10, one

can easily find that the experimental observation supports Eq. 14, i.e., higher wake volume corresponds to higher drag force.

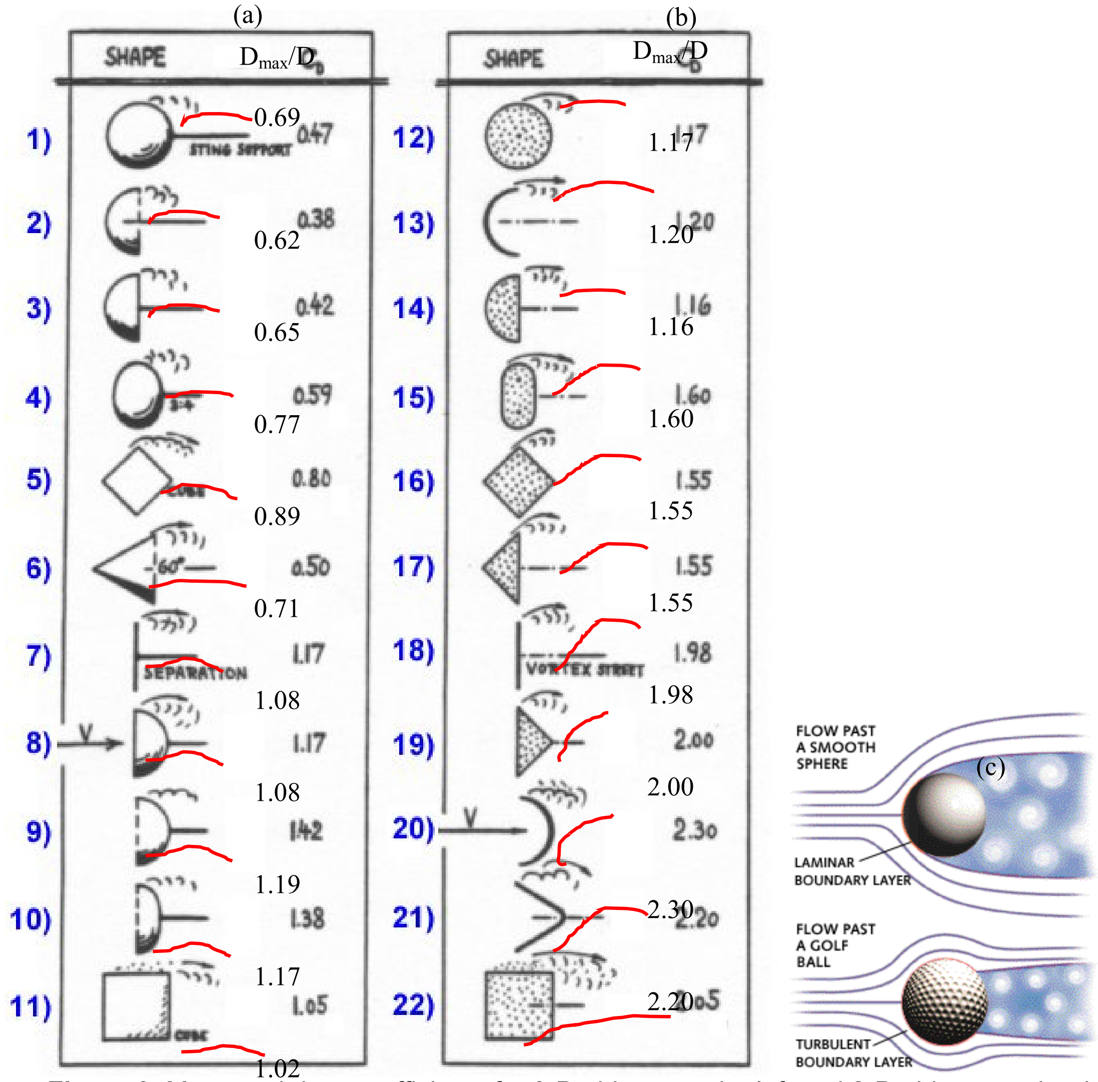

Figure 9. Measured drag coefficients for 3-D objects on the left and 2-D objects on the right and estimated wake width based on Eqs. 15 and 16.

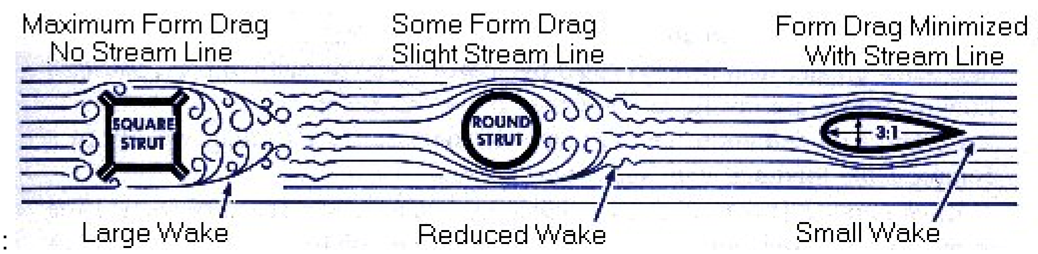

Figure 10. Relationship between wake volume and drag force

4 DEPENDENCE OF FRICTION FACTOR (C_d) ON Re AND SIZE OF K AND D TYPE ROUGHNESS

As shown in Figs. 3 and 4, the skin friction and the form drag are always coexisted for any object. If the Reynolds number is very small, no separation occurs, and only the skin friction exists, this is why the measured friction depends on the Reynolds number. When the separation occurs, the form drag is induced, if the wakes covers the whole surface, the viscous effect disappears, this is why Nikurads observed that the friction factor depends on roughness size.

Physically, his observation can be interpreted by Eq. 14, the roughness height is actually the index of wake volume as V_w/A_s = K (roughness height). Now, we link the observation of flow resistance with the skin friction and form drag in the following way:

$$F = F_{sk} + F_d = \tau_{sk} A + \rho g k V_w \quad (18)$$

As shown in Figure 2, the wake size V_w and the surface with skin friction A (contact area in flow direction) are interrelated. If V_w is very large and the wake can fully cover the surface, then A = 0, and the flow resistance is independent of skin friction or Reynolds number. This has been widely reported and summarized in Nikuradse' observation, later this is termed by K type of roughness by Perry. However, when the wake size V_w is confined within groove on a surface, the skin friction will always exist, i.e., A ≠ 0 and this can be observed that on the top surface, the flow direction follows the main flow direction without reversing flows. As τ_{sk} depends on Reynolds number, so it is certain that Perry cannot repeat Nikuradse' experiment, i.e., the friction factor is independent of Reynolds number, even Re is very high.The above argument can even be seen from Figure 11 for sphere or disk's C_d. For a disk, it can be seen that when the separation is full, A = 0, thus C_d is constant (=1.17), giving D_{max}/D = 1.08. However, for a sphere, the front part of Figure 4 always has the skin friction. This implies that the C_d in Figure 11 has two components, i.e.,

$$C_d \rho g A_p \frac{U^2}{2g} = \tau_{sk} A + \rho g k V_w \quad (19)$$

Eq. 19 explains why in Figure 11a, the measured C_d depends on Re even Re is as high as 10^6-10^7. The reason is similar to Perry's observation in pipes, i.e., the wake volume (or separation keeps changing). Figure 11b shows flow separation at Re = 1.5×10^4. The measured Cd = 0.40, using Eq. 16, one has k = 0.4/(28mm/26mm) = 0.345. Figure 11c shows that D_{max}/D = 15/20 = 0.75, using Eq. 16, one can estimated C_d = $k(D_{max}/D)^2 = 0.345*0.75^2$ = 0.194. Figure 11a shows that at Re = 3×10^5, the measured C_d = 0.2, and the error is 3%. This shows that if k in Eq. 16 is calibrated, very accurate C_d can be obtained.

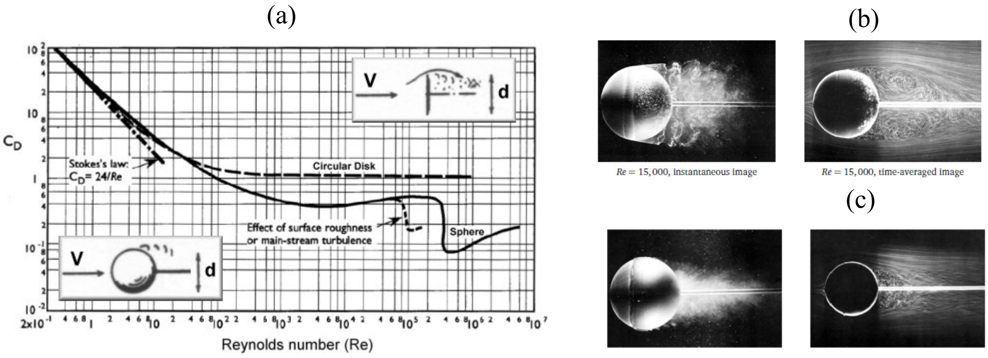

Figure 11. Measured drag coefficient for a sphere and disk (a), and flow separation at Re = 3×10^5 (b).

5 CONCLUSIONS

This paper investigates the mechanism of form drag. It clarifies that the flow resistance can be divided into skin friction and form drag, and they are proportional the contact area and dead zone volume, respectively. It shows the idea of boundary layer theory developed by Prandtl can be extended to a bluff object placed in a flow, and the mechanism of flow resistance is the same for both internal and external flows. Reynolds number is the measurement of skin friction. The relative roughness defined by Nikuradse lacks very clear physical interpretation. This paper redefines the parameter as the ratio of potential energy carried by volume V to the dead zone volume, i.e., the energy from the main flow is dissipated by the eddies in a dead zone.

REFERENCES

Yang S.Q. & S.K. Tan (2008). Flow Resistance over Mobile Bed in an Open-Channel Flow. *Journal of Hydraulic Engineering*, 134(7), 937-947.

Yang S.Q. & G-R Dou (2010). Turbulent Drag Reduction with Polymer Additive in Rough Pipes. *Journal of Fluid Mechanics*, 642, 279-294.

Yang S.Q., Nadeesha D. & Han Y. (2011). Flow Resistance over Fixed Roughness Elements. *Journal of Hydraulic Research*, 49(2), 257–262.

Yang, S.Q. (2013). A Simple Model to Extend 1-D Hydraulics to 3-D Hydraulics. *Proc. of IAHR World Congress*, Chengdu, China.

OPTIMIZING DISCHARGE COEFFICIENTS OF SPILLWAYS LABYRINTH IMPLEMENTING TWO HYDRODINAMIC FORMS DEVICES IN THE UPSTREAM APEX

DELGADO GUSTAVO(1), MONTENEGRO JULIO(2) & ERICES FABIAN(3)

(1) Geda instituto, Universidad Central de Venezuela. Caracas, Venezuela
guszzz@hotmail.com
(2) Universidad Nacional de Ingenieria de Perú. Lima, Perú
Montenegro.julio@gmail.com
(3) Universidad Austral de Chile. Valdivia, Chile
F.erices@hotmail.com

ABSTRACT

Today hydrology´s change affects the performance of original water structures; as a consequence, their design results are insufficient. The implementation of labyrinth weirs has been proven to be beneficial elements in water reservoir or water conducts because they increase the discharge in high events. This characteristic is an advantage because it can increase the body´s normal level of water to replace losses, while maintaining the same level of "high water". This structure can also be applied to a new design too, so that some developing projects can bear this situation in the future. The first important characteristic of labyrinth weirs is the position of weirs segments in alternative position, looking in plant like teeth. It increases the effective length of discharge for the same channel width. However, various aspects in regard to the functions of these structures have not been investigated. .In simple cases, it is still advisable to carry out the study of the hydraulic operation in reduced physical models. The labyrinth weirs can present some problems because the hydrodynamic adaptation to the water flow depends on the construction requirements. In previous structures that use these elements, it has been found that nape interference occurs over the crest and disturbance flow zones happen along the weir. For these reasons, it is necessary to incorporate several characteristics like specific shapes and long apex. The purpose of this research is to implement a hydraulic device to reduce the nape interference effects and increase the discharge. For this reason, this study investigates this device as an equivalent to the physical geometric scale of a labyrinth weir. It is necessary to test various designs and optimizing the configuration. The values obtained from measurements of hydraulic head and flow transited, are processed to obtain the coefficients of discharge. This coefficient is a dimensionless value related to the characteristics of the weir and the flow rate.

Keywords: Labyrinth; weirs; hydrodynamic; coefficient; upstream.

1 INTRODUCTION

Recently, dam's designers have started to use labyrinth weirs in spillways. Today's climate change affects the performance of original dams; as a consequence, their design results are insufficient. The implementation of labyrinth has been indicated as a beneficial element in water reservoir because it increases the discharge in high events. This weir design is an advantage because it can increase the body´s normal level of water to replace losses of dam volume, while maintaining the same level of "high water" in case of rehabilitation reservoir. Climate change has contributed to a different basin hydrologic regime, which can increase the input water over the dam and as a consequence in the spillway. This structure can be used in a new design too, so that some developing projects can bear this situation in the future.

The first most important characteristic of labyrinth weirs is the position of discharge segments in alternative position, looking in plant like teeth. It increases the effective length of spillway discharge for the same channel width. There is extensive literature that provides the design of a labyrinth weir (Tullis, et al., 1995).

However, many aspects of the functioning of these structures have not been investigated. In simple cases, it is still advisable to carry out the study of the hydraulic operation in reduced physical models.

The labyrinth weirs can present some problems because the hydrodynamic adaptation to the water flow depends on the construction requirements. In previous spillways that use these elements, it has been found that nape interference occurs over the crest and disturbance flow zones along the weir. For this reason, it is necessary to implement several characteristics to the design like specific shapes and long apex. The main purpose of this research is to implement a hydraulic device to lower the nape interference effects and increase the discharge.

For this reason, it is important that we have resorted to the study of this device as an equivalent to physical geometric scale of a labyrinth weir spillway. The values obtained from measurements of hydraulic head and flow transited, are processed to obtain the coefficients of discharge. This coefficient is a dimensionless value related to the characteristics of the weir and the flow rate. Stands primarily when low hydraulic load values are used in all the configurations, is that almost similar behavior is observed in magnitude and in the curves describing the relationship with the discharge coefficient.

It is necessary to know the real performance of the apex upstream hydraulic devices by the discharge coefficient, and build a research model to test several flow conditions and other characteristics. Also, it is necessary to obtain several numerical performances to several devices design. Finally, it is necessary to obtain graphics that show the discharge coefficient related to the implementation of upstream devices. Usually, the discharge coefficients can present a numerical graphic to give a better idea about the weir performance and understand its best implementation in a real project.

2 PROCEDURE

This research will determine the hydrodynamic device influences of the apices labyrinth spillways, where discharge coefficient provides qualitative and quantitative information to be used by Engineers and Planners in rehabilitation and design of new dams.

To conduct this research, a model was built in industrial acrylic. The model used generic scale labyrinth spillway with three straight crest cycles with 0.5 chutes slope and circular sides approach. As for the three hydrodynamic devices on the apexes of the spillway, they had a pyramidal geometry with variable length (6, 12 and 18 cm).

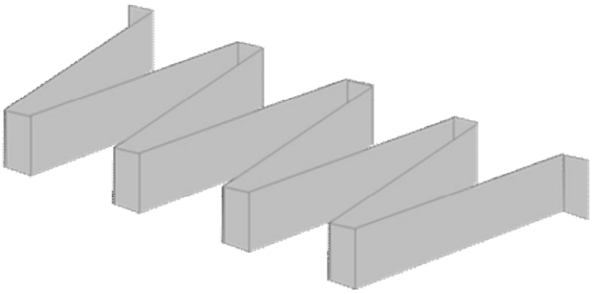

Figure 1. The Labyrinth model configuration to be used in several cycles.

Once the model was made, it was installed in a channel hydraulic test water flow by changing level of volume, with rectangular section of 38 cm width and variable height, which had a “V” weir that will gradually change the flow spillway discharges in the study. Subsequently, readings will take hydraulic head by a meter edge upstream and over the spillway, and 150 measurements will be taken for each of the three characteristics studied. One calibration comparative analysis was made. Therefore, all precautions to decrease the frictional energy losses and allow a laminar flow in the test channel were taken.

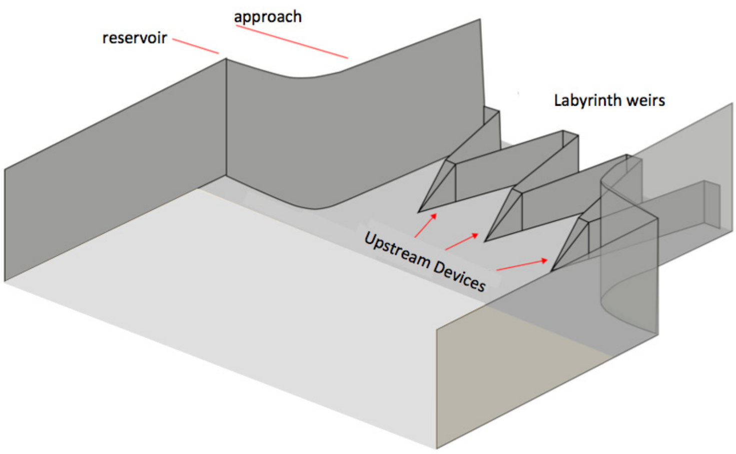

Figure 2. The complete model configuration.

Finally, the research will be oriented to show, observe and measure the different heights of hydraulic load on a model of a generic labyrinth spillway level and report their status according to the indicators and the selected work. To obtain the discharge coefficient, it will use the equation given by Tullis et al. (1995), without making any intervention in the variables.

3 CHARACTERISTIC OF THE MODEL

The model required several characteristics in order to develop a discharge of high performance, so it referred to previous studies to simulate the high conditions of the coefficients. These previous studies were about the physical characteristics and design.

  / ISSN 1562-6865 (Online) - ISSN 1063-7710 (Print)

3.1 Configuring a trapezoidal labyrinth weir

Numerous weirs were designed using this type of structure for discharge, in which the number and the direction of cycles were varied. Varying the direction of cycles was performed in order to be able to extend the effective length or adding more cycles. Orientation can project cycle in a linear way, being located next to each other was also considered including an axis perpendicular to the flow.

Previous studies[2] showed that according to empirical tests on the structure geometry with three cycles (N = 3), it was possible to observe the highest rates of discharge based on the options studied. This fact can be attributed to the low interference suffered by the nape effluent to pass through the weir crest because ground geometry provides increased effective length straight discharge.

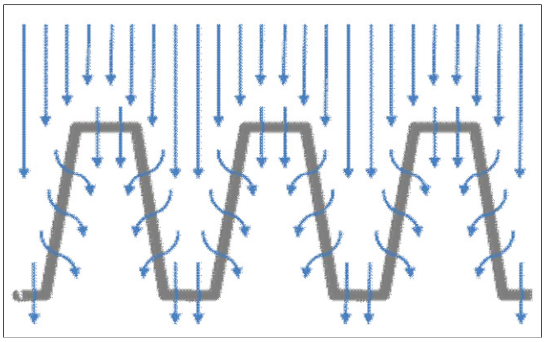

Figure 3. View plant. Flow over three labyrinth weirs cycles.

3.2 Crest length

The trapezoidal labyrinth weir type crest length for a cycle is given by the equation:

$$Lt = 2b + 4a \qquad [1]$$

where "b" is the measured weir wall and "a" is the value of half the apex.
But in another study (Taylor et al., 1970), a methodology of calculation was developed that resulted in a graph where the weir discharge length with respect to a length of spillway crest was drawn straight.

3.3 Angle between walls weirs (α)

In another study (Tullis, 1994), a series of assemblies was developed to determine the angle that occurred between the cycle´s walls in a trapezoidal weir, where the author presented graphics results for different values subjected to experimentation. It expressed values for angles from 6° to 90°, which was equivalent to a weir crest rect. The value of 8º was the best discharge coefficient value obtained.

3.4 Apex A

The complete equation for calculating the apex was deduced previously (Falvey, 2003) that in his research indicated that the lowest value, by which the interference of a trapezoidal weir discharge occurs, is given by:

$$A = \sin((w-4\alpha) / (\alpha L-4)) \qquad [2]$$

The complete equation for calculating the apex indicates that the lowest value in which the interference of a trapezoidal weir discharge happens.

3.5 Approach conditions

As for other authors (Tullis, 1994), they highlighted the need to develop experimental models using symmetrical lateral approach. It was further based on the chess-river dam studies for the structure design approach channel. They conducted important studies regarding variants of the approach flow and breaking schemes to locate the weir structure entirely within the reservoir.

The labyrinth cycles extension within the reservoir for observations in discharge was his initiative, but it did not express graphics about his results (Houston, 1983).

Using a linear model of a generic type scale concluded that if the weir was introduced into the water reservoir, it influenced the discharge (Delgado, 2009).

3.6 The channel output

According to this author, his previous studies determined that the best conditions to the output pieces between the weirs segments was 0, 5 inclinations (Delgado, 2009).

3.7 Dimensionless scaling factors

The dimensionless parameters included in this relationship were typical fluid mechanics problems and special names associated with those who had made significant contributions to related aspects, or that had been proposed for specific problems, among them were: R, Reynolds number; F, Froude Number; M, Mach number; W, Weber number; E, Euler number.

3.8 Crest form

The crest used in the weir top was Quarter Round type, because it has the best performance opposite to the nape interference.

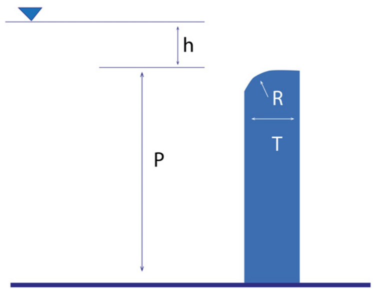

Figure 4. The Quarter round Profile.

Finally, the model characteristic is as follows:

Table 1. Dimensions used in the model.

Dim	Lon
W	30 cm
Wc	10 cm
Lc	41,5 cm
B	18,25 cm
A	1,25cm
α	8º
P	8 cm
N	3
Lt	124,5

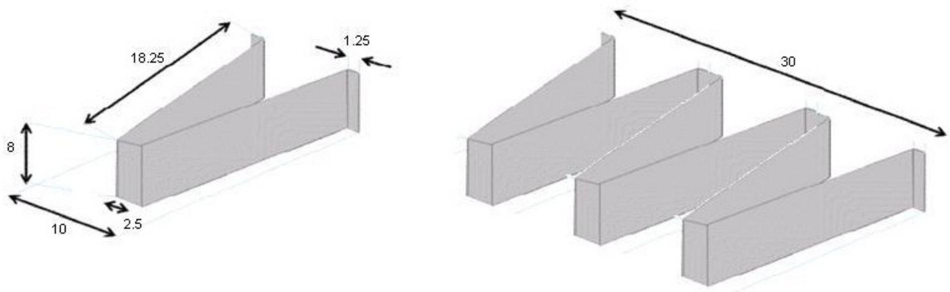

Figure 5. Model`s dimensions.

4 DISCHARGE COEFFICIENT

It is a dimensionless coefficient which implies the weirs characteristics and the flow increase. Many authors have attempted developing their own discharge coefficient equations, but in the same way have pointed out shortcomings in the results, especially when making comparisons between obtained experimental setups and measured on the prototype. Tullis[1] used a discharge coefficient equation widely cited by some researchers similar as Falvey (2003). The equation is based on weir elements and the discharged flow (the hydraulic head height H). The discharge coefficient can be determined by several formulas, but the most relevant, directed from previous studies was that developed by Tullis et al. (1995). This equation states that the discharge coefficient is a function of the weir and the values of Ho extent discharge.

$$Q_L = C_d * L * \frac{2}{3} * \sqrt{2g} * H^{\frac{2}{3}} \quad [3]$$

5 THREE-DIMENSIONAL VIEW OF THE DIFFERENT CONFIGURATIONS OF APPROACH TO BE TESTED

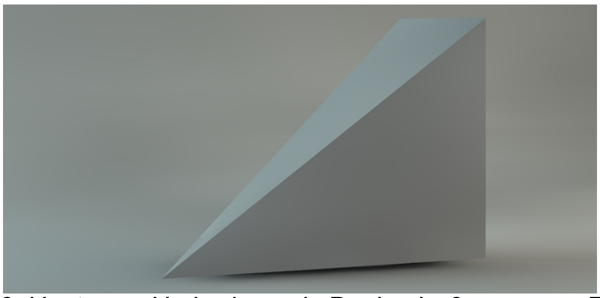

Figure 6. Upstream Hydrodynamic Device L=6 cm.

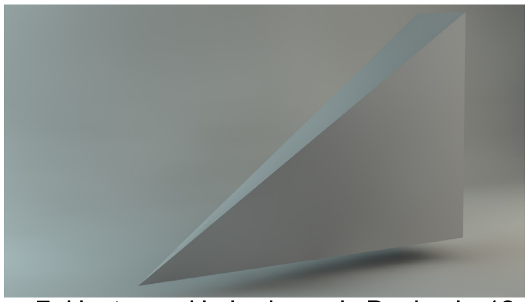

Figure 7. Upstream Hydrodynamic Device L=12 cm.

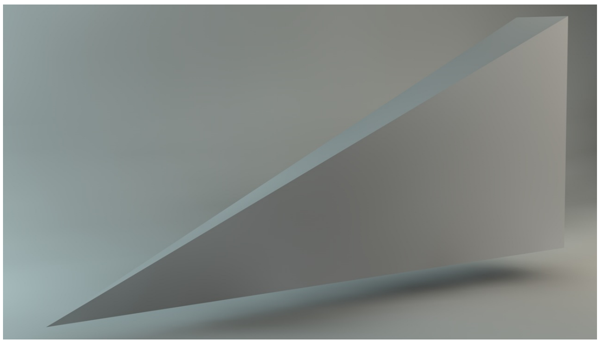

Figure 8. Upstream Hydrodynamic Device L= 18cm.

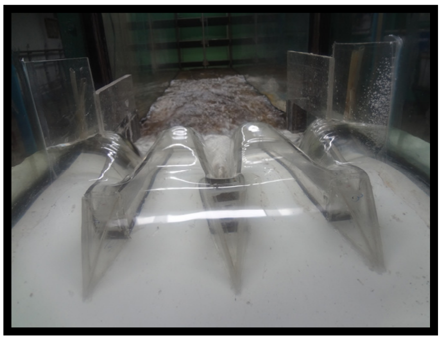

Figure 9. The model during testing.

6 RESULTS

Finally, after testing, the flow rate values were obtained, and these were computed, to obtain the coefficients of discharge. These values were plotted in graphs that were nominated according to the terms Cd and Ho/P. “Cd” was obtained from the equation, “Ho” is the flow level over the crest weir and “P” is the weir height. The results were relevant to the hydrodynamics devices 6, 12 and 18 cm.

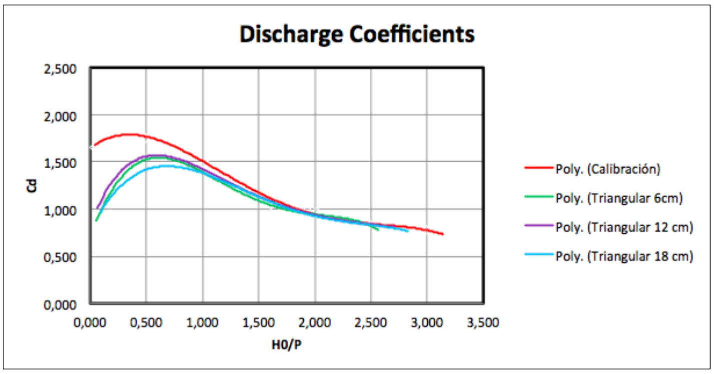

Figure 10. The graphics of the discharge coefficients for 6 cm, 12 cm and 18 cm devices.

Considering the three tested devices, it is necessary to build a length for evaluation by analyzing the indicated average discharge coefficient. It is considered as finding the best performance in the discharge event.

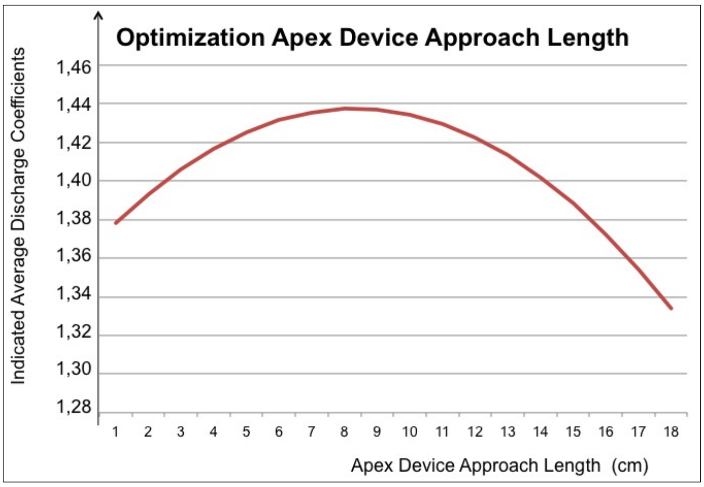

Figure 11. The graphics for the Optimization Apex Device Approach Length.

7 RESULTS ANALYSIS

As shown in the graph of discharge coefficients, the influence of the hydrodynamic approach favored the tested weir discharge coefficient. The device significantly increased the discharge flow of the system tested. In turn, it should be noted that among the tested configurations, the length equaled to 8 cm could be the most efficient hydraulically. Further, this configuration (8 cm) was not tested. However, the approach leads to a more expensive construction which is a factor to consider when designing and implementing.

REFERENCES

Bolinaga, J.J. (2005). Mecánica Elemental de los Fluidos. ucab. Caracas, 93-234.
Bolinaga, J.J. (2002). Proyectos de Ingenieria Hidraulica. Fundaciòn Polar Editions. Caracas, 34-56.
Chow, V. (2003). *Canals Flow.* McGraw-Hill, Mexico, 78-236.
Falvey, H. (2003). *Hydraulic Design of Labyrinth Weirs,* American Society of Civil Engineers, USA, 56-316.
Fuentes, R. (1977). *Curso de aforadores en canales,* Laboratorio nacional de hidráulica, Caracas, 25-28.
Fuentes, R. (1985). Modelos hidraulicos, teoria y diseño. *Lilian salinas ayala ediciones, Chile,* 34-53
Delgado G. (2009). *Modelaciones para la rehabilitación de Pao-La Balsa,* Laboratorio Nacional de Hidraulica, Venezuela
Sartor L. (2011). Estudo sobre o comportamento hidráulico du vertedouros labirinto. Universidade Federal do Paraná, Brasil, 67-69.
Streeter, V. (2000). *Mecánica de Fluidos.* Editorial Mc Graw Hill, Colombia, 67-103.
Suarez Villar, L.M. (2002). Incidentes en las Presas de Venezuela. Editorial Arte. Caracas
Tullis, J.P., Amanian, N. & Waldron, D. (1995). Design of Labyrinth Spillways. *Journal of Hydraulic Engineering, ASCE,* 121(3), 247-255.
Tullis, J.P. & Steven I.B. (1995). *Model Study of Wirtz Dam,* Conducted for Freese and Nichols.
Tullis, J.P. & Standley, K. (1993). *Lake Dam Model Study,* Conducted for the City of Westminster.
Tullis, J.P., Rahmeyer J. (1981). *Stacy Dam Service Spillway Model Study,* Conducted for the Colorado River Municipal Water District.
Tullis, J.P. & Barfuss, S.I. (1993). *Model Study of the Hubbard Creek Spillway,* Conducted for Freese and Nichols, Inc.
Tullis, J.P. & Barfuss, S.I. (1993). *Model Study of the Buchanan Dam 7-gate Spillway,* Conducted for Freese and Nichols, Inc. and Lower Colorado River authority (lcra),
Tullis, J.P. & Barfuss, S.I. (1989). *Model Study of Applewhite Dam Service Spillway,* Conducted for Freese and Nichols, Inc.
Tullis, J.P. & Swatara, T. (1985). *Dam Spillway Model Study,* Conducted for Incorporated,
Tullis, J.P. (1984). *Applewhite Dam Service Spillway Model Study,* Conducted for the San Antonio City Water Board and Freese and Nichols, Inc.,
Tullis, J.P. Rahmeyer, W.R. & South W.D. (1980). *Labyrinth Weir Service Spillway Model Study,* Conducted for Tarrant County Water Control and Improvement District Number 1, and Freese and Nichols, Inc.
Tullis, J.P. (1989). *Eagle Mountain Dam Spillway Model Study - Revised Design.* Colorado State University, Department of Civil Engineering. Prepared for Freese, Nichols and Endress, 69-70.
Tullis, J.P. & Albertson, M.I. (1986). *Proposed Modifications to the Labyrinth Weirs Outlet Works.* Prepared for Denver Board of Water Commissioners, Denver, Colorado,
Tullis, J.P. & Karaki, S. (1988). *Eagle Mountain Dam Spillway Model Study.* Colorado State University Department of Civil Engineering, Prepared for Freese, Nichols and endress, 68.

REDUCTION PULSATING WAVES WITH CASCADE ON THE DOWNSTREAM OF POSO I HYDROPOWER STATION'S ENERGY DISSIPATOR)

LINDA PRASETYORINI[(1)], DWI PRIYANTORO[(2)] & NADJADJI ANWAR[(3)]

[(1,3)]Civil Departement, Institute of Teknologi Sepuluh Nopember, Surabaya, Indonesia
linda.wre03@gmail.com; nadjadji@ce.its.ac.id
[(1,2)]Water Resources Departement, University of Brawijaya, Malang, Indonesia
dwiprie@ub.ac.id

ABSTRACT

The PosoI Hydropower Station is located on the Poso River, at the downstream section of the Poso Lake in Central Sulawesi Province. The weir site is about 14 km away from Poso Lake outlet. At the weir site, the catchment area is 1906.30 km^2, and the structures are designed for a 50 year return period and flood discharge of 1456,50 m^3/s. According to the hydraulic calculation results, stilling basin of 45,0m length is arranged in the downstream of the weir bay. The aim of the model test is to evaluate and achieve the perfect, safe and optimum hydraulic design of the Hydropower Station. The model is using an undistorted model with scales of 1 to 60. Based on the research results, it can be concluded that the hydraulic performance of the original design is good and high speed in the escape gate is more than 15 m/s. In order to improve the hydraulic design, it is recommended to modify the stilling basin and make cascade on the downstream to reduce pulsating flow that happens by considering 25% sloping river on downstream.

Keywords: Physical hydraulic model test; stilling basin; cascade.

1 INTRODUCTION

The PosoI Hydropower Station is about 45km from the Poso Harbor and about 235km from Palu, the capital of Central Sulawesi Province. The PosoI Hydropower Station takes advantage of Poso Lake to form the reservoir. The weir site is about 14km away from Poso Lake outlet. At the weir site, the catchment area is 1906.30 km^2, the mean annual discharge is 127.85m^3/s, the full supply water level is 510.50m, and minimum operating level is 506.00m. The power plant is developed in two phases, with an installed capacity of 2 ×35MW for Phase I, additional 2 ×35MW for Phase II, and a total installed capacity of 140MW. The PosoI Hydropower Station applies low-gate diversion type development. The main structures include the weir, the water intake on the right bank, water diversion culvert pipes, surge chamber, steel penstocks, surface powerhouses, and tail water structures.

Hydropower Station design refers to design of dams with barrage type that has important problems in the downstream area, where there is a steep slope of the river bottom. Stilling basins are any device designs to protect downstream areas from erosion by reducing the velocity.

Stilling basin below hydraulic structures has attracted the attention of many researches. A.J. Peterka (1958) conducted experiments with six test flumes and classified the different types of stilling basin for high dam, canal structure ,and outlet works. Hanger (1992) investigated the performance of free jets hydraulic jump with Bremen stilling basin, while Chanson (1999) classified the stilling basin type, plunge pool type, and flip bucket type for stilling basins.

The studies about stilling basin are of great importance for the construction, maintenance and safety of the large hydraulic structures. The increase of the efficiency of the energy dissipation has shortened the risk of the downstream area. The main purpose of this study is the development of design criteria for estimating the stilling basin length located at the downstream end of the gate. Since tailwater depth is variable and completely dependent on downstream conditions, the advantage of the present work is the elimination of the tailwater depth from the analysis.

2 MATERIAL AND DATA COLLECTIONS

The aim of the model test was to evaluate and to achieve the perfect, safe and optimum hydraulic design of the Hydropower Station. The model was based on undistorted model with scales of 1 to 60. Experiments were conducted at the Hydraulics Model Laboratory of Water Resources Department, University of Brawijaya. Some characteristic operation conditions from radial gate to stilling basin were analyzed in the physical model. The water levels, mean velocities and instantaneous pressures, in various points of the flow were measured with point gauge, pitot tube, and current meter. The capacity of diesel pump laboratory is approximately 150 lt/dt.

 / ISSN 1562-6865 (Online) - ISSN 1063-7710 (Print)

2.1 Hydrology Design

According to the calculation results of hydrology, the design results with different flood frequencies at the weir site of Poso-I Hydropower Station are shown in Table 1.

Table 1. Results of design floods for PosoI Hydropower Station.

S/N	Return period (year)	Design flood discharge (m^3/s)
1	2	758.1
2	25	1319.9
3	50	1456.5
4	100	1591.7
5	1000	2039.5

The models were simulated by various discharge at 2, 25, 50, 100, and 1000 return period year which were previously estimated to be 42.89, 74.67, 82.39, 90.00, and 115.37lt/s, respectively in scale model.

2.2 Water retaining structures, water release structures

Gravity dams were arranged respectively on both banks of the gate bay for water retaining. The left-bank gravity dam was arranged on the left side of the 1# release sluice with a total length of 45.0m. It was divided into 3 dam sections. 1# and, 2# dam monoliths were ordinary dam sections, with dam crest of 6.0m wide and maximum dam height of 14.0m; 3# dam monolith was dam section for store gate slot, with dam crest of 12.0m wide and dam height of 19.0 m-22.0m.The right-bank gravity dam was arranged on the right side of the 2# water intake, with a total length of 32.0m.

According to the calculation results of the discharge capacity, the layout scheme of the water release structure was designed as one scouring sluice and three release sluices. The riverbed elevation in the gate line was about 494.00m. According to the terrain and geological conditions of gate site, as well as comprehensive consideration of reservoir operation method and requirements on full scale sand sluicing for watercourses, the bottom slab elevations of the scouring sluice and release sluice were selected as 494.00m. The bottom slab was 3.0m thick and basically built in the silty sand with boulder and gravels.

There were three release sluices, with an average gate outlet dimension of 8.0m×7.0m (width × height). The elevations of the bottom slab and gate crest were 494.00m and 513.00m, respectively. One arc service gate was arranged for each outlet for water retaining, and a flat steel gate was added as bulkhead gate. The bottom slab of the flood discharge gate was 3.0m thick, with maximum gate height of 24.0m. Deep gullet in 2.0m was respectively arranged for upstream and downstream to improve the anti-sliding stability of the gate bay.

There was one scouring sluice, with an average gate outlet dimension of 3.0m×4.0m (width × height). The elevations of the bottom slab and gate crest were 494.00m and 513.00m, respectively. An arc service gate was arranged for outlet for water retaining, and a flat steel gate was added as bulkhead gate. The bottom slab of the sand sluicing gate was 3.0m thick, with maximum gate height of 4224.0m. Deep gullet in 2.0m was respectively arranged for upstream and downstream to improve the anti-sliding stability of the gate bay.

Weirs of the project were built in soft foundation. Joints set in the center of the weir pier were employed in the design to avoid impact on the gate operation due to the settlement and deflection of the gate bay. The detailed scheme is as follows: 1# and 2# release sluices were poured as a whole (the total width was 24.5m). 3# release sluice and scouring sluice were poured as a whole (the total width was 19.5m). Side pier was 2.5m wide, middle pier with joint was 5.0m wide, and middle pier without joint was 3.0m wide.

According to the calculation results of stable stress of weir bay, as well as the consideration of foundation bearing capacity and requirements on the gate layout, the length of the gate bay was selected as 35m.
Concrete blanket, which was 15m in length and 1.5m in thickness, was arranged in the upstream of the gate bay. The upstream and downstream sides of the blanket bottom were all equipped with gullets.

2.3 Layout of water intake structure

Since sands from the upstream can be deposited in the Poso Lake, so sediments of the PosoI Hydropower Station are mainly originated from the section sediments of the 14km watercourse from the Poso lake outlet to the PosoI weir site. According to the materials provided by the owner, average annual discharge at PosoI Hydropower Station is about 30,400t, and the average annual sediment concentration is 7.7g/m^3. The sediment concentration is relatively small, which indicates that sediment prevention and discharge are not control elements in the PosoI water intake layout.

Therefore, according to the terrain and geological condition of gate site, as well as the comprehensive consideration of the layout of primary buildings and cut-off walls of PosoI Hydropower Station, the layout of water intake was designed as forward direction intake. 1# and 2# water intakes were all arranged at the right bank of the riverbed, and connected to the scouring sluice. The crest elevation was 513.00m. The water intake can be divided as trash racks and gates, transition sections and intake gates along the axial direction of the water intake. The crest elevation of the bottom slab of trash rack section was 496.00m, and the length along the flow was 10.0m. 1# and 2# water intakes were respectively divided into two holes, and the width of each hole was 8.0m. The top slab elevation was 509.00m, and the bottom slab was 5.5m to 5.0m thick. The middle pier was 1.5m thick, and the side pier was 2.0m thick. A working trash rack and a maintenance trash rack were arranged in each hole, with breast wall arranged on the top. The orifice dimension was of 8.0m×11.0m. The transition section was 17m long. The width of the transition section was gradually changed from the 21.5m of the top to about 12.5m, while the crest elevation of the bottom slab was also gradually changed accordingly. The layouts of the weir are shown in Figure 1.

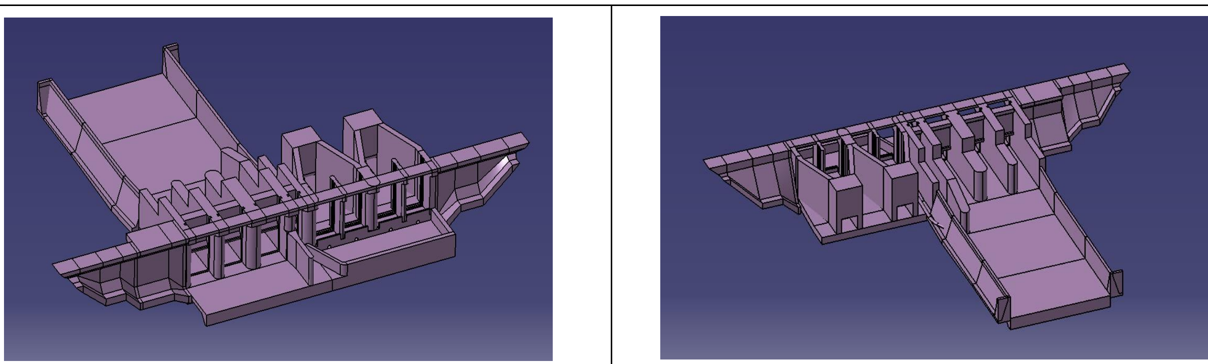

(a)From the upstream (b)From the downstream

Figure 1. 3D display of weir and intake layout

2.4 Discharge capacity calculation of scouring sluice and release sluice

The dam crest elevation is mainly controlled by the full supply level, and at this point, the calculated minimum dam crest elevation was 512.47m. With the consideration of the uncertainty of the flood data, for the dam crest elevation, apart from the free board, a certain margin shall be considered. Therefore, the proposed dam crest elevation of the gate dam of the Posol Hydropower Station was 513.00m.

The design flood discharge with 100 year return period was 1591.70 m^3/s, and the check flood discharge was 2039.50 m^3/s. The discharge capacity of the scouring sluice and the release sluice can be calculated as per the weir flow formula (Equation 1) and orifice outflow formula (Equation 2):

$$B_0 = \frac{Q}{\sigma \varepsilon m \sqrt{2g}\, H_0^{\frac{3}{2}}} \tag{1}$$

$$B_0 = \frac{Q}{\sigma' \mu h_e \sqrt{2gH_0}} \tag{2}$$

where:

σ—submergence coefficient of weir flow;
m—discharge coefficient of weir flow;
ε—side-contracta coefficient of weir flow;
B_0—orifice clear width, (m);
H_0—weir head included in the water head of the approach velocity, (m);
σ´—submergence coefficient of orifice flow;
μ—discharge coefficient of orifice flow;
he—Height of orifice, (m).

The calculation results of discharge capacity of scouring sluice and release sluice are shown in Table 2.

2.5 Calculation of Energy Dissipation Structure

According to the hydraulic calculation results, stilling basin of 45.0m length was arranged in the downstream of the weir bay. In which, the former 15.0m was the transition section with a slope of 1:10, and the latter 30.0m was the flat section. The elevation of bottom slab of stilling basin was 492.50m, and gullets were respectively arranged in upstream and downstream. In which, the upstream gullet was 2.0m deep, and the downstream gullet was 34.0m deep. In order to reduce the uplift pressure of the bottom slab of the stilling basin, filtration gutter, which was connected to the downstream watercourse through drainage hole, was arranged on the bottom of the bottom slab.

50-year flood data was used for the design flood of the dissipation. The corresponding flood discharge was 1456.5m^3/s. Calculation of stilling basin consisted of depth calculation, length calculation and calculation of thickness of bottom slab.

Table 2 Calculation results of discharge capacity of scouring sluice and release sluice of Posol Hydropower Station

Upstream water level (m)	Upstream depth, H_0 (m)	Discharge of 1 scouring sluice, Q_1 (m^3/s)	Discharge of 3 release sluices, Q_2 (m^3/s)	Total discharge, Q_3 (m^3/s)	Remarks
494.50	0.50	1.69	13.54	15.24	
495.00	1.00	4.79	38.31	43.09	
496.00	2.00	13.54	108.34	121.89	
497.00	3.00	24.88	199.04	223.92	
498.00	4.00	38.31	306.44	344.75	
499.00	5.00	53.53	428.26	481.80	
500.00	6.00	70.37	562.97	633.34	
501.00	7.00	85.22	709.42	794.64	
502.00	8.00	97.21	866.75	963.96	
503.00	9.00	107.82	1034.24	1142.05	
504.00	10.00	117.44	1211.31	1328.75	
505.00	11.00	126.32	1360.03	1486.35	
505.78	**11.78**	**132.82**	**1459.45**	**1592.28**	Design flood discharge of 1591.70 m^3/s
506.00	12.00	134.60	1486.06	1620.66	
507.00	13.00	142.40	1600.59	1742.99	
508.00	14.00	149.80	1706.53	1856.32	
509.00	15.00	156.84	1805.70	1962.54	
509.76	**15.76**	**162.79**	**1877.33**	**2040.12**	Check flood discharge of 2039.50 m^3/s
510.00	16.00	163.58	1899.36	2062.94	
511.00	17.00	170.05	1988.39	2158.44	
512.00	18.00	176.29	2073.46	2249.75	

(1) Depth calculation formula

$$d=\sigma_0 h_c'' - h_s' - \Delta Z \tag{3}$$

$$h_c'' = \frac{h}{2}\left(\sqrt{1+\frac{8aq^2}{gh_c^3}}-1\right)\left(\frac{b}{b_2}\right)^{0.25} \tag{4}$$

$$h_c^3 - T_0 h_c^2 + \frac{aq^2}{2g\varphi^2} = 0 \tag{5}$$

$$\Delta Z = \frac{aq^2}{2g\varphi^2 h_s'^2} - \frac{aq^2}{2gh_c''^2} \tag{6}$$

Where:

- d—depth of stilling basin, (m);
- σ_0—submergence coefficient of hydraulic jump, 1.05-1.10;
- hc'' —water depth after hydraulic jump, (m);
- hc—contracted depth, (m);
- a—correction coefficient of flow kinetic energy, 1.00-1.05;
- q—discharge per unit width at the gate, (m^3/s);
- b1—width of head end of stilling basin, (m);
- b2—width of terminal of stilling basin, (m);
- T0—Total potential energy calculated from top of bottom slab of stilling basin, (m);
- ΔZ—water drop of stilling basin outlet, (m);
- hs'—downstream depth of stilling basin outlet, (m);
- φ —velocity coefficient of flow out of stilling basin outlet.

(2) Calculation of stilling basin length

$$L_{sj} = L_s + \beta L_j \tag{7}$$

$$L_j = 6.9(h_c'' - h_c) \tag{8}$$

Where:

- Lsj—length of stilling basin, (m);
- Ls—horizontal projection length of slope section of stilling basin, (m);
- β— correction coefficient of hydraulic jump length, 0.7-0.8;
- Lj—length of free hydraulic jump, (m);
- hc'' —water depth after hydraulic jump, (m);
- hc—contracted depth, (m).
- T0—Total potential energy calculated from top of bottom slab of stilling basin, (m);
- ΔZ—water drop of stilling basin outlet, (m);
- hs'—downstream depth of stilling basin outlet, (m);
- φ —velocity coefficient of flow out of stilling basin outlet.

According to the calculation results and relevant engineering layout achievements, the scheme of stilling basin behind the gate bay of Posol Hydropower Station was selected, in which the depth was 1.5m, length along the flow direction was 45.0m, bottom slab elevation was 492.50m and bottom slab thickness was 2.0m. Flexible concrete apron with length of 25.0m was arranged at the back of the stilling basin.

3 RESULT AND DISCUSSION

The perfect flow condition was obtained by the original design running test with 2 until 1000 years return period discharge. Experimental data was obtained from measurement in the laboratory. Those results of barrage capacity are shown in Figure 2.

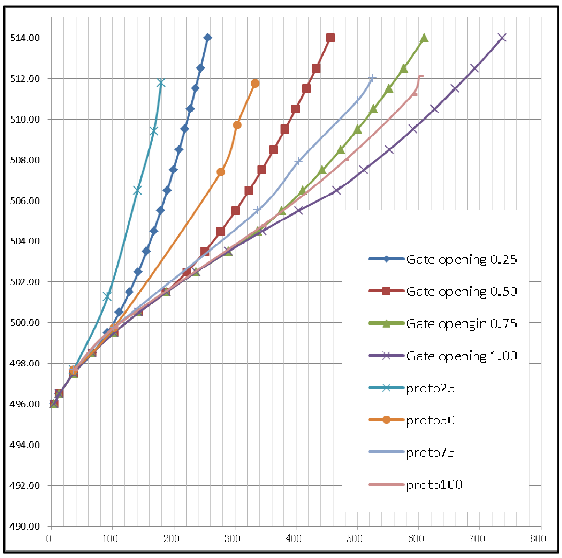

Figure 2. Graph of Barrage Capacity

The main purpose of this study was the development of design criteria for estimating the stilling basin length where it was located at the downstream end of the gate. Since tailwater depth is variable and completely dependent on downstream conditions, the advantage of the present work is elimination of the tailwater depth from the analysis.

Based on the research results, it can be concluded that the hydraulic performance of the original design was relatively good, but the stilling basin problems were still present. From the experiment, flow occurred rotating on stilling basin that happened from 2 return period years. The condition of stilling basin is shown in Figure 3.

The upstream flow condition | The upstream gate condition
The downstream gate condition | The stilling basin flow condition

Figure 3. The flow condition of the model

According to the experiment with various flood discharge, the average velocity from the gate more than 15 m/s, and 25% sloping on the downstream river resulted in the turbulence waves over the flow. To reduce these effects, the height of the riverbed should be made as cascade, in addition to modifying the stilling basin. Peterka recommended that the tail water depth should be 10% greater than the conjugate depth. Based on model tests, detanted end sill was added with 3,5m height, 2,4m width, and the distance between detanted sills of 1,8m. The final design condition is shown in Figure 5.

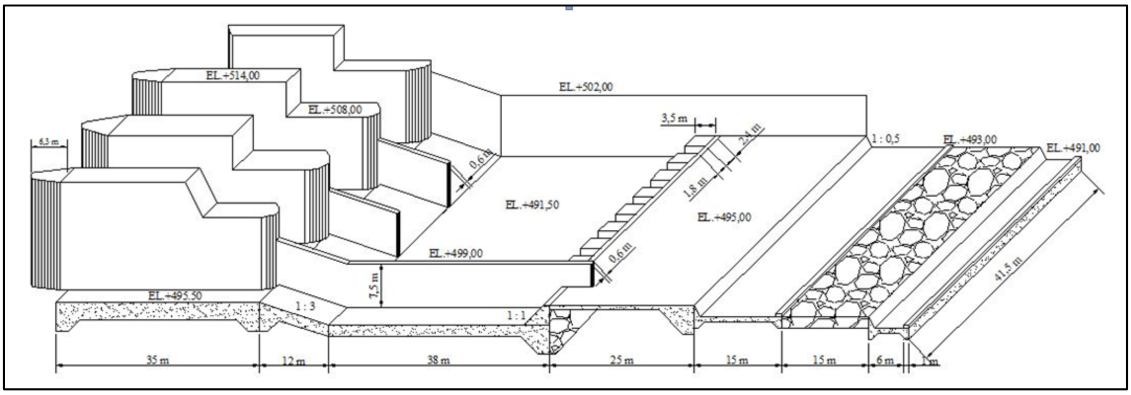

Figure 4. The model's change condition

The upstream flow condition

The stilling basin flow condition

The stilling basin flow condition

The cascade flow condition

Figure 5. Final Design's Flow condition

4 CONCLUSIONS

The studies about stilling basin are great of importance for the construction, maintenance and safety of the large hydraulic structures. The increase of the efficiency of the energy dissipation has shortened the risk of the downstream area. The modification of stilling basin is its simplicity in practice to increase end sill height and make a cascade structure for controlling the velocity of the stilling basin downstream.

ACKNOWLEDGEMENTS

The research reported herein is the collaboration result between Water Resources Department University of Brawijaya and funded by Bukaka Teknik Utama in 2015.

REFERENCES

Chanson, H. (1999).*The Hydraulics of Open Channel Flow: Basic Principles, Sediment Motion, Hydraulic Modelling, Design of Hydraulic Structures*. Elsevier's Science & Technology Rights Department in Oxford, UK.1999.

Hager W.H. (1992). *Energy Dissipators And Hydraulic Jump*, Kluwer Academic Publications, Dordrecht, The Netherlands

Tiwari, H. (2013). Analysis of Baffle Wall Gap in the Design of Stilling Basin Model. *International Journal of Civil Engineering*, 4(4), 66-71.

Jose Charls C., Renata, C.R. & Marcelo, G.M. (2009). A Numerical and Experimental Study of Hydraulic Jump Stilling Basin".in *Journal of Advanced in Hydro Science and Engineering Vol.VI*.

Peterka.(1958). *Hydraulic Design of Stilling Basin and Stilling Basins*, Berau of Reclamation, Washington

Proceedings of the 37th IAHR World Congress
August 13 – 18, 2017, Kuala Lumpur, Malaysia

PLANNING OF LOWER MALWATHU OYA RESERVOIR PROJECT-COST BENEFIT ANALYSIS

DON AJITH ROHANA DOLAGE[(1)] & KITHSIRI WELIGEPOLAGE[(2)]

[(1)]Department of Civil Engineering, The Open University of Sri Lanka, Colombo Sri Lanka, dadol@ou.ac.lk
[(2)]Director of Irrigation, Department of Irrigation, Colombo Sri Lanka,
diwrp@irrigation.gov.lk

ABSTRACT

The Malwathu Oya (called Aruvi Aru in the lower reaches), the second largest river basin in Sri Lanka, is flowing through the Anuradhapura city which is its ancient capital. This paper describes the cost benefit analysis of this project. The total project cost is Rs. 12,500 million, which consists of irrigation infrastructure development cost of Rs. 11,000 million and the other infrastructure development cost of Rs. 1,500 million. The main benefit of the project is the cropping intensity of the combined command areas of the two reservoirs Giant's Tank and Akitamuruppu Tank, a total of 30,680 acres of lands, will be increased from around 1.0 to 1.7. In addition, the project entails a number of benefits which include generation of 4.0 gWh hydropower and provision of 2 MCM of raw water for drinking purposes.

Keywords: Water resources management; cost benefit analysis; irrigation; cropping intensity.

1 INTRODUCTION

The implementation of large-scale dams for irrigation is in the political agenda of several developing countries for the purpose of increasing their local food production and promoting food security. These countries seek the assistance of funding agencies and governments that could support the required investments in new irrigation projects worldwide. The funding agencies invariably seek a comprehensive but simple cost-benefit analysis before granting any funds for a water resource development project.

Most of the research studies conducted in this subject domain are concerned with various advanced quantitative methods for evaluating and comparing alternative water resources projects. Loucks et. al. (1981) and Major (1977) deal with a number of advanced quantitative methods for evaluating water resource projects which involves multi objective modeling, simulation and optimization models.

Water resource planning decisions are typically based on multiple objectives measured in a range of financial and non-financial units (Gough and Ward, 1996). The expectations of water resources projects are varying and numerous due to the different types of beneficiaries. According to Hajkowicz and Higgins (2008), often the outcomes are highly intangible and may include items such as biodiversity, recreation, scenery and human health. These characteristics of water planning decisions make multiple criteria analysis (MCA) a versatile approach. A lot of research work has been carried out studying different aspects of MCA (Hajkowicz and Higgins, 2008; Hajkowicz and Collins, 2007; Theodor J. S. and Scott L., 1995). Although, MCA has a widespread and growing usage in the field of water resource management, the application of it is extremely tedious. There is a tendency that more and more research work are undertaken in order to fine tune MCA. As a result, less and less research studies are undertaken to improve the simple cost benefit analysis. This situation has created a dearth of research articles which simply present the conduct of cost-benefit analysis using case studies showing how and what various factors are considered. Therefore, the purpose of this study is to demonstrate how and what factors are considered in a cost benefit analysis of a multipurpose water resource project.

Under 'Uthuru Wasanthaya Program' the Ministry of Irrigation and Water Resources Management decided to carry out a fresh feasibility study on Malwathu Oya Reservoir Project in 2012 in response to the urgent need for the project shown by the people of Mannar District and to consider the changes taking place in this region over the last 50 years. Malwathu Oya has a catchment area of 3246 sq.km, average annual rainfall of 1226 mm and discharge volume of 192 MCM (Sri Lanka Water Development project, 2006). The lower Malwathu Oya Reservoir proposed in 1960 had a capacity of 282,000 ac.ft (348 MCM) with full supply level (FSL) of 57.1 m msl. However, with the currently proposed reservoir while FSL is lowered to 54.1 m, the capacity is lowered to 169,000 ac.ft (209 MCM) in order to minimize the requirement to clear forest in upper catchment for reservoir inundation; will be reduced from 16,652 acres to 10,720 acres. The extent of land required to be developed under Giant's Tank and Akitamuruppu Tank in 1960, was 20,000 acres and it was suggested to develop further 12,000 acres of new lands just downstream of proposed Malwathu Oya Reservoir. At present, 30,680 acres have been developed under Giant's Tank and Akatimuruppu Tank and only 2,000 acres of new lands will be developed (just downstream of reservoir) mainly to cater to the needs of the people who will be displaced due to the construction of the new reservoir. Figure 1 shows the catchment of Malwathu Oya.

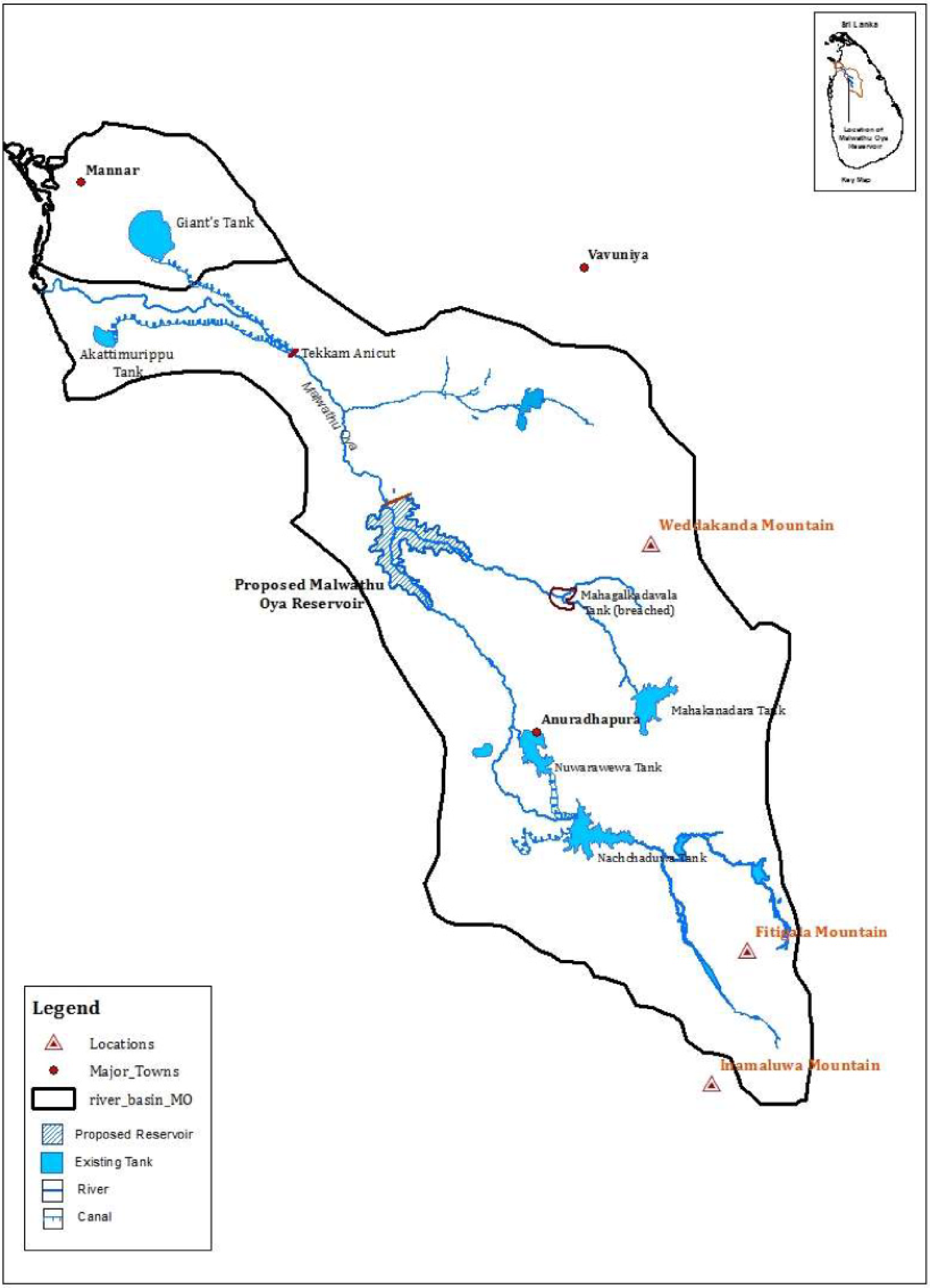

Figure 1. Catchment of the Malwathu Oya

The lower Malwathu Oya Reservoir project includes the following:

(i) Construction of 3,590 m long dam across Malwathu Oya at Kappachchi
(ii) Construction of 7.62 m wide and 7.01 m high, 10 Nos radial gated spillway, incorporated with 1 mW power house, river release structure and LB sluice with 1 cumec capacity
(iii) Construction of RB sluice with 1 cumec capacity
(iv) Construction of 3.89 km long LB main canal
(v) Construction of 87.17 m long RB main canal
(vi) Construction of secondary and tertiary irrigation infrastructure for 700 acres of land just downstream of proposed reservoir on both banks
(vii) 1,300 acres of new lands with drip irrigation facilities just downstream of proposed reservoir on both banks for fruit cultivation (under commercial agriculture)
(viii) Improvements to existing irrigation infrastructure D/S of Tekkam Diversion weir and
(ix) Construction of social infrastructure for the relocation of displaced people due to the new reservoir

Malwathu Oya cascade is one of the largest and intensively cultivated small tank cascade systems in Anuradhapura district of Sri Lanka (Kumari *et al*., 2013). Under the new irrigation infrastructure development, it is proposed to provide 700 acres of lands for paddy and other food crop cultivation, and 1,300 acres of lands for fruit cultivation under commercial agriculture supported with drip irrigation facilities. As a result, the cropping intensity of the existing area of 30,680 acres of lands (under Giant's Tank and Akitamuruppu Tank) will increase from around 1.0 to 1.7. Hence, together 2,000 acres of new area and 30,680 acres of existing area shall produce 24,450 metric tons of paddy, 16,750 metric tons of maize, 360 metric tons of green gram and 2,340 metric tons of soya beans and 25,263 metric tons of fruits per year over and above the present production level in the region. In addition to agricultural benefits, 2 MCM of raw water will be available from the reservoir to provide domestic water to Cheddikulam and Thantrimale townships, and to new settlement areas. Under the project it is planned to generate 4.0 gWh of hydro power annually through a 1 mW power plant by using irrigation water released to Tekkam anicut from the lower Malwathu Oya reservoir. While a unit of raw water is priced at Rs. 5.00, a unit of energy is priced at Rs. 17.00. Standard conversion factor of 0.85 has been used in economic benefit calculations.

In addition to direct benefits, other infrastructure development shall provide a lot of indirect benefits, which will enhance the quality of life and farm income due to investments on agriculture and livestock development in the project area. The implementation of the project especially investments on other infrastructure shall provide safe water and sanitation, improve accessibility to better markets, improve transport, improve agricultural technology and availability of better quality seeds and planting material leading to increased agricultural production in the region. Investments on irrigation infrastructure development shall produce net present value of 26,998 million Rupees, while achieving 32% internal rate of return with 4.48 benefit-cost ratio on the investment.

2 ESTIMATION COSTS AND BENEFITS

2.1 Project Cost

2.1.1 Basis of Cost Estimate

The following assumptions were made in the estimation of project costs:

i) Costs are based on January 2016 price levels
ii) Construction unit rates are based on the 'Approved Rates for 2016' applicable for Irrigation and Drainage Works carried out in Anuradhapura District of Sri Lanka
iii) Quantities in the estimates are obtained from the Engineering Surveys available for the area and the preliminary designs of works
iv) iv) Engineering and administration overhead costs are 6% of the total costs of civil and mechanical works
v) Physical contingencies are 10% of the total costs of civil and mechanical work
vi) Overheads and price contingencies are calculated as 10% of the total civil and mechanical works
vii) Profit factor of 1.26 was used in headwork while a profit factor of 1.21 was used for Irrigation facilities

Project cost estimate based on the above criteria is considered as the financial cost estimate of the project, which is used in the financial and economic analysis.

2.1.2 Cost of Civil Works

Most of the unit costs used in the estimates are based on quantities taken off from preliminary designs and unit rates approved by the Regional Director's Office of Department of Irrigation for the year 2016.

2.1.3 Cost of Mechanical Works

Cost of hydro-mechanical equipment such as spillway gates, stoplogs, intake gates, trash racks etc, are based on prices of similar items used for ongoing construction works. The costs of radial gates are incorporated in the spillway structure.

2.1.4 Cost of Canal System

The LB and RB main canal costs are based on quantities taken off from drawings, canal sections on ground levels available on 8 chains to 1 inch engineering survey sheets. Cross drainage structures have also been provided wherever necessary according to the ground conditions and designed bed levels of the main canals. The cost of the other conveyance and control structures are also included in the respective canal estimates. In the tertiary canal system to be provided in the proposed irrigable area (of 700 Acres) for the benefit of the farmers who would be relocated due to inundation, a pro rata cost of Rs. 125,000/- per acre was assigned.

2.1.5 Project Cost Estimation

The breakdown of project cost estimation is as follows:

i) Cost of head works
ii) Cost of conveyance system for new irrigation area
iii) Cost of rehabilitation of existing irrigation area
iv) Cost for the establishment of Operation and Maintenance (O and M) units
v) Cost of social infrastructure development for the resettlement area
vi) Cost of construction of a fence for elephants
vii) Cost of land acquisition
viii) Cost of general items
ix) Cost of VAT

The cost of rehabilitation of existing irrigation area is identified as Rs. 750 million. In order for the establishment of the O and M unit Rs. 375 million has been set aside. For the construction of Elephant Fence Rs. 75 million is set apart while for Land acquisition Rs. 1300 million is allocated. For general items, standard percentages were used as per the available departmental guidelines.

2.2 Project Benefits

2.2.1 Agricultural Benefits

The total command area under the proposed project is about 32,680 acres, of this while 2,000 acres are new lands, the balance area of 30,680 acres is existing lands. At present, of the existing land area that comes under Giant's Tank Scheme and Akitamuruppu Scheme, the entire extent is cultivated during *Maha* season and only 2,000 acres are cultivated during *Yala* season. Cropping pattern and crop areas for different crops of Giant's Tank system, Akitamuruppu Tank Scheme and proposed area for relocated farmers are shown in tables 1.1, 1.2 and 1.3 respectively.

Table 1.1. Giant's Tank system –Cropping pattern and Crop Area (in acres)

System	FWOP/FWP	Season	CI	Paddy	Maize	Green Gram	Soya Beans
Giant's tank	FWOP	Maha	1.0	24,450			
system		Yala	0.08	2,000			
(24,450	FWP	Maha	1.0	24,450			
acres)		Yala	0.7	8,800	6,300	840	1,000

Table1.2. Akitamuruppu's Tank system –Cropping pattern and Crop Area (in acres)

System	FWOP/FWP	Season	CI	Paddy	Maize	Soya Beans
Akitamuruppu	FWOP	Maha	1.0	6,230		
tank system		Yala	0.0			
(6,230 acres)	FWP	Maha	1.0	6,230		
		Yala	0.7	2,200	1,100	980

Table 1.3. Proposed area for relocated farmers–Cropping pattern and Crop Area (in acres)

System	FWOP/FWP	Season	CI	Paddy	Maize	Green Gram	Soya Beans
Proposed area for relocated farmers (700 acres)	FWOP	Maha	0.0				
		Yala	0.0				
	FWP	Maha	1.0	700			
		Yala	0.7		100	100	290

2.2.2 Expected Benefits of the Proposed Agricultural Crops

A new irrigable area of 1,300 acres is proposed under the project for commercial agriculture where only the fruit crops will be considered. Cropping patterns and crop areas are indicated in Table 1.4.

Table 1.4. Proposed area for commercial agriculture–Cropping pattern and Crop Area (in acres)

System	FWOP/FWP	Perennial Crops				
		Mango	Pomegranate	Guava	Dragon fruit	Papaya
Proposed area of commercial agriculture (1300 acres)	FWOP					
	FWP	300	250	300	150	300

2.2.3 Yields and Farm Gate Prices of Seasonal Crops and Fruit Crops

With proper irrigation facilities and other inputs, the following seasonal yields are assumed for paddy, maize, soya bean and green gram in existing and new irrigation areas. In the area identified for commercial agricultural area, it is intended to grow fruits such as mango, pomegranate, guava, dragon fruit and papaya. The estimated yields and farm gate prices used in benefit calculations for seasonal crops and fruit crops are shown in tables 1.5 and 1.6 respectively. The average production of fruit cultivation is shown in Table 1.7.

Table 1.5. Yields of Seasonal Crops and Farm gate prices

Crop	Yield in District wise (kg/ha)				Farm gate prices in District wise in (Rs/kg)			
	Mannar		Anuradhapura		Mannar		Anuradhapura	
	Yala	Maha	Yala	Maha	Yala	Maha	Yala	Maha
Paddy		3,615	6,430	5,733	29.78	30.16		27.92
Maize	5,523		5,523		31.98		31.98	
Soya Bean	2,548		2,548		70.00		70.00	
Green Gram	951		951		164.00		164.00	

Table 1.6. Yields of Fruit Crops and Farm gate prices

Crop	**Yield kg / ha**							**Farm gate Prices Rs/kg**
Mango	5th year		6th to 9th year			10th year onwards		105.00
	6,429		30,714			100,714		
Guava	2nd year	3rd year	4th year	5th year		6th year		25.00
	6,400	19,200	48,000	80,000		80,000		
Pomegranate	2nd year	3rd year	4th year	5th year	6th year	7th year		125.00
	300	880	4,400	13,200	22,000	66,000		
Dragon Fruit	2nd year	3rd year	4th year	5th year	6th year	7th year	8th year	175.00
	5,500	11,000	16,500	22,000	27,500	27,500	49,500	
Papaya	2nd year	3rd year	4th year	5th year	7th year	8th year	10th year	20.00
	38,500	42,778	37,250	38,500	42,778	37,250	38,500	

Table 1.7. Average Production of Fruit Cultivation

Crop	Area (ha)	Average Yield (kg/ha)	Average Yield (Mts/ha)	Average Annual Production (Mts)
Mango	121	67,150	67.2	8,152
Guava	121	46,720	46.7	5,672
Pomegranate	101	50,642	50.6	5,124
Dragon Fruit	61	25,000	25.0	1,518
Papaya	121	39,509	39.5	4,797

2.2.4 Other Indirect Benefits

(a) Inland fisheries Development

The proposed reservoir can be used for inland fisheries development as a fairly large fishing community is living around the major reservoirs in the region. According to information from the Fisheries Ministry, a minimum yield of 200kg/ha can be expected from the proposed reservoir and a minimum price of Rs.50.00 per kilogram will be guaranteed. At the full supply level, the proposed reservoir has a water spread area of about 4600 ha.

(b) Creation of employment during construction

It is estimated that skilled and unskilled labour force of about 1500 will be directly employed under the irrigation infrastructure development and another 500 people will be employed for other infrastructure development. In addition, a labour force of 1000 will be required for other services, indirectly connected with the construction work.

(c) Development of other Infrastructure

The implementation of this project will substantially contribute to the improvement of the infrastructure such as roads, telecommunication facility, power distribution system etc. in the area. With the introduction of large water body to the area, local and foreign tourist arrivals will be greatly improved. This will bring increased incomes to the people of the area as there are a lot of important archeological sites in the area.

2.2.5 Benefits of Other Infrastructural Development

These infrastructural improvements in addition will provide lots of social benefits that could be gained by investing in these sectors though quantification could be difficult. Pipe borne water supply will improve the access to safe water and sanitation, which will lead to better health standards in the project area. This will improve the productivity of the labour force of the project area and reduces the health sector expenses drastically. Improvements to road network in the area will improve the accessibility to better markets for the farmers and improve their incomes and consequently poverty levels in the region will drop. By regularizing lands, people will get the ownership of the lands and this will motivate the farmers to cultivate their lands in a more systematic manner resulting in higher yields per unit area. Similarly agricultural and livestock investments will improve crop yields and milk production in the area contributing to enhanced farmer incomes. This will improve the quality of life in the area and reduction of poverty in the region largely.

3 ECONOMIC ANALYSIS

3.1 General

The Lower Malwathu Oya reservoir project will generate benefits to the Sri Lankan economy by way of agricultural production, hydro power generation, domestic water supply and employment generation through irrigation infrastructure development. Investment in other infrastructural development will certainly improve the living standards of the people of project area although quantifiable direct benefits of these investments cannot be easily determined. Therefore, costs and benefits of other infrastructure development were excluded from the economic analysis.

Quantifiable benefits of the irrigation infrastructure development could be computed and so economic analysis was carried out for the irrigation infrastructure development component of the investment. Economic viability of this component was established by evaluating economic internal rate of return (EIRR), benefit/cost ratio (B/C) and net present value (NPV) on the investment. The evaluation is based on the estimated costs and benefits of the irrigation infrastructure development component of the project. The works cost includes the civil, mechanical and electrical works while benefits include increased agricultural production, raw water production and hydro-power generation. In the determination of costs and benefits, the economic life of all project works and equipment were taken as 25 years from the completion of the project.

3.2 Construction Period

It is programmed to complete the construction of the irrigation works in two years and 'other infrastructure' by the end of the third year. As the construction is to start at the beginning of the 2017 all project works should be completed by the end of 2019.

3.3 Economic Benefits

The benefits due to irrigation infrastructure were estimated by computing the incremental benefit from 'without' project conditions to 'with' project conditions. The farm budgets were prepared after having worked out the rates in a similar done in the feasibility study of *Kubukkan Oya* reservoir project. While the market prices were multiplied by the standard conversion factor (SCF) of 0.85 to obtain economic prices, the production costs were too multiplied by SCF of 0.85 to obtain the economic value of the production costs. Net benefits are obtained by deducting the economic input cost from economic prices of outputs (per hectare) for each crop. The total net benefit is calculated by multiplying the net benefit with crop area with respect to each crop.

The annual incremental agricultural benefits are calculated by deducting operation and maintenance cost from annual benefits. The Operation and Maintenance cost for gravity irrigation is taken as Rs.450/ha/season and to obtain economic cost this is multiplied with the SCF of 0.85. For raw water and hydro power, the financial benefit is calculated by multiplying unit price for raw water at Rs. 5.00 and that for hydro power at Rs. 13.00 respectively. The economic benefit is calculated by multiplying net benefit with the SCF of 0.85.

3.4 Economic Comparison

The results of economic comparison are as displayed in Table 1.8.

Table 1.8. Results of Economic Analysis

EIRR %	**Net present Value at 10% Discount Rate (million Rs.)**	**Benefit/Cost Ratio at 10% Discount Rate**
15.98%	3,375	1.49

3.5 Sensitivity Analysis

Sensitivity of the economic indicators of the project to the following changes has been investigated.
Case I: Construction cost is increased by 10%
Case II: The net benefit is reduced by 10%
Case III: The project is extended by 1 year
Case IV: The combination of Cases I, II and Case III
The results of economic and sensitivity analysis are shown in Table 1.9.

Table 1.9. Results of Economic and Sensitivity Analysis

Economic Indicator	Economic Analysis	Sensitivity Analysis			
		Case I	Case II	Case III	Case IV
NPV at 10% (Rs. million) discount rate	3,375	2,702	2,350	2,796	1,250
B/C ratio at 10% discount rate	1.49	1.36	1.34	1.44	1.18
Internal rate of return (%)	15.98	14.43	14.25	15.24	12.23

From the results of sensitivity analysis it could be observed that at 10% discount rate the benefit-cost ratio is greater than unity for all adverse conditions. However, it could be observed the net present value reduces from 3,375 million Rupees to 1,250 million Rupees in Case IV.

4. CONCLUSIONS

In this study, the cost-benefits analysis has been supplemented with an economic analysis. All costs such as headworks cost, canal construction cost and mechanical works cost have been considered in the computation of total cost. In working out the benefits, the agricultural benefit has been worked out in addition to numerous other benefits such as inland fisheries, employment creation during construction and development of other infrastructure facilities. Economic viability of the irrigation infrastructure development component was established by evaluating economic internal rate of return (EIRR), benefit/cost ratio (B/C) and net present value (NPV) on the investment. Sensitivity of the economic indicators of the project to the following changes has been investigated for four cases when; construction cost is increased by 10%, net benefit is reduced by 10%, project is extended by 1 year and combination of Cases I, II and Case III.

The project implementation would take place within the period 2017-2019, while irrigation infrastructure shall be implemented during 2017-2018 period by the Department of Irrigation. Other infrastructure development shall be implemented by the respective line agencies either at provincial level or national level. With the full development by the start of 2019, the irrigation infrastructure will be completed and the project will be in readiness to produce 24,450 metric tons of paddy, 16,750 metric tons of maize, 360 metric tons of green gram and 2,340 metric tons of soya beans over and above the present production levels in the area.

REFERENCES

Gough, J.D. & Ward, J.C. (1996). Environmental Decision Making and Lake Management. *Journal of Environmental Management*, 48(1), 1–15.

Gunarathna, M. H. J., & Kumari, M. K. N. (2014) Sustainable Management of Malwathu Oya Cascade – Present Status and Future Needs, *GSTF Journal of Agricultural Engineering*, 1(1).

Hajkowicz, S. & Higgins, A. (2008). A Comparison of Multiple Criteria Analysis Techniques for Water Resource Management, *European Journal of Operational Research*, 184, 255–265.

Hajkowicz, S & Collins, K. (2007). A Review of Multiple Criteria Analysis for Water Resource Planning and Management, *Water Resources Management*. 21,1553–1566.

Kumari, M. K. N., Pathmarajah, S. & Dayawansa, N.D.K. (2013). Characterization of Agro-Well Water in Malwathu Oya Cascade- In Anuradhapura District of Sri Lanka. *Tropical Agricultural Research*, Vol. 25 (1), 46-55.

Loucks, D. P, Stedinger, J. R. & Haith, D. A. (1981). *Water Resource Systems Planning and Analysis*. Prentice-Hall. New Jersey.

Major, D.C. (1977). *Multi Objective Water Resource Planning*, Water Resource Monograph Series, American Geophysical Union. USA.

Sri Lanka Water Development project (2006), *World Water Assessment programme*, UNESCO.

Theodor J. S. & Scott L. (1995) A Scenario-Based Framework for Multicriteria Decision Analysis in Water Resources Planning. *Water Resources Research*, 31(11).

Proceedings of the 37th IAHR World Congress
August 13 – 18, 2017, Kuala Lumpur, Malaysia

ESTIMATION OF FAILURE TIME FOR EMBANKMENT DAMS

SAAD SHAUKET SAMMEN[1], THAMER AHMEED MOHAMED[2], ABD ALHALIM GHAZALI[3], LARIYAH MOHD SIDEK[4] & AZLAN ABDUL AZIZ[5]

[1, 2, 3, 5]Department of Civil Engineering, Faculty of Engineering, University Putra Malaysia, Serdang, Selangor, Malaysia
[1]Department of Civil Engineering, College of Engineering, Diyala University, Diyala Governorate, Iraq
[4]Sustainable Technology & Environment Group, Institute for Energy Infrastructure, University Tenaga Nasional, Selangor, Malaysia
SAAD123engineer@yahoo.com

ABSTRACT

Several approaches have been used for estimation of failure time when dam failure occurs. Generalized Regression Neural Network (GRNN) model has been proposed in this present study as a novel method to estimate the dam failure time. It has also made a comparison of the results of the GRNN models with the results obtained from the existing approaches. Various reservoir and dam characteristics have been used in the development of the GRNN models in order to estimate the dam failure time. To obtain the optimum results from the GRNN models, all models are optimized to smooth factor values. The values are found to range from 0.001 to 0.03. Furthermore, training the network takes up 85% of the total data and testing the network takes up 15% of the total data. Three statistical indices are used to assess the results of GRNN models. They are the Root Mean Square Error (RMSE), Mean Relative Error (MRE), and Coefficient of Correlation (R^2). The results show that the value of the MRE could be decreased more than 50% by using the GRNN models as compared to the values of the existing empirical techniques.

Keywords: Dam safety; dam failure; failure time; generalized regression neural network.

1 INTRODUCTION

Dams are built to improve human life. They are constructed as multipurpose structures and are used to produce hydroelectric power, provide water for irrigation and water supply, for improvement of economics, and for the control of flooding (Hooshyaripor et al., 2014). Thus, they have become a vital component of any country's infrastructure (Wahl, 2010). However, the huge volume of water that is stored in the reservoir behind the dam wall can lead to a damaging flood to the population and their properties located downstream from the dam if the stored water is suddenly released (Razad et al., 2013). Therefore, an analysis of the dam break is considered as tremendously important so that the peak outflow and its associated Emergency Action Plan (EAP) can be determined (Wahl, 2010). There are three main stages in a dam break analysis; they are the geometric breach parameter estimations (height, width, and side slope), hydrologic breach parameter estimations (failure time and peak outflow), and downstream routing of the flood. A physical model and numerical modeling methods can be employed to study the analysis of the dam break. As the physical model is quite expensive, numerical modeling is thought to be a better and less expensive approach (Wahl, 2010).

To carry out an analysis of the failure of the embankment dam, the parameters of the breach are considered to be the most important key parameters that must be estimated with accuracy because of their effect on the degree of the failure risk as well as the consequence of the peak outflow. As a result, many of the contributions to the literature in the past few decades have been focused on the development of precise and simple methods to handle these kinds of problems (Bentaher, 2013; Xu and Zhang, 2010; Wahl, 1998; 2004; 2010; Froehlich, 1995; 2008).

Over the past few decades, research has been carried out on noncohesive and cohesive embankment dams by employing experimental research works which have been able to explain how breaches develop. In addition, these experimental research works have contributed to the provision of data which is necessary for both statistical and numerical studies (Gaucher et al., 2010; Coleman et al., 2002). Moreover, some numerical and analytical tools have been utilized to solve the Sainte Venant equations for the study and analysis of flood waves which result from the dam failure (Xia et al., 2010; Tsai, 2005; and Ponce et al., 2003). Besides that, numerical techniques which solve the shallow water equation have been employed to estimate the hydrograph of the peak outflow, and to determine the velocity along the distance, time, and inundation area (Gallegos, 2009; Liang et al., 2007). The eroding capacity of the flow can be determined by using a more reasonable methodology which takes the mean velocity of the flow and the mean shear stress as independent variables (Macchione, 2008). However, the fields as well as the experimental research works have given evidence that this methodology could possibly be suitable for only a few stages in the development of the breach, but cannot be applied for all the stages of the development breach (Wahl, 1998).

The statistical analysis method is thought of as a traditional technique which can be employed to predict the characteristics of the flow and the breach in the dam. In this technique, the characteristics of the reservoir,

  / ISSN 1562-6865 (Online) - ISSN 1063-7710 (Print)

such as the water volume and the depth were used as the dependent variables for determining the characteristics of the flow as well as the parameters of the breach (Xu and Zhang, 2009; Froehlich, 1995a, 2004, 2008; Von Yhun and Gillette, 1990; and USBR, 1988). When the database of dam failure cases is highly documented, preferred equations can result from a case study analysis (Xu and Zhang, 2009). After the 1970s, as shown in Table 1, various observational equations have been developed using the regression analysis. These relations, which are not very complex, are still needed, especially in situations where the intention is not to have detailed simulations or they are impossible to be applied easily or conveniently (Froehlich, 2008). However, these relations need to be represented with the relevant uncertainty such as confidence limit. For instance, on the other hand, relations such as these must be represented with the relevant uncertainty like when confidence is limited. For instance, Wahl (2004) has given a description of an uncertainty analysis technique and has compared the uncertainty estimates for the equations of the peak outflow prediction and breach parameters. Following the work by Wahl (2004), Pierce et al. (2010) also gave a description of the uncertainty analysis of the parameters of a breach. Limited data sets and their low adaptability to data varieties cause the uncertainty of these equations. Furthermore, the databases do not cover a wide scope of included

Table **1.** Previous studies for breach width prediction.

Investigator	Number of case studies	Equation
Von Thun and Gillette (1990)	36	$T_f = 0.15Hw$ (for high erodible)
Von Thun and Gillette (1990)	36	$T_f = 0.15Hw +0.25$ (for erosion resistance)
Froehlich (1995a)	34	$T_f = 0.00254(V_w)^{0.53}(H_b)^{-0.9}$
Froehlich (2008)	unknown	$T_f = 0.0176[(V_w/(gH_b^2)]^{0.5}$
Xu and Zhang (2009)-1	unknown	$T_f = C_1T_r(H_d/H_r)^{0.654}(V_w^{1/3}/H_w)^{1.246}$
Xu and Zhang (2009)-1	unknown	$T_f = 0.304\ e^BT_r(H_d/H_r)^{0.654}(V_w^{1/3}/H_w)^{1.246}$

where:

H_d : Height of dam (m), H_b : Height of breach (m), V_w : Volume of water in reservoir at failure time (m^3), H_w : Height of water in reservoir at failure time (m), C_1 : Factor related to dam erodibility , H_r : Dam height reference = 15m., T_r : Time failure reference = 1hr.

variables as they do not incorporate various cases of failures involving large dams (Nourani, 2012). Because of this, the mathematical statements made by employing such restricted databases are not very dependable for most cases.

Estimating these parameters is considered to be a very complex task as the relationships of the parameters of the dam breaches are highly nonlinear and because of their time variations. Thus, if an appropriate database is available, the black-box models can be employed as an alternative method. With the black-box method, the targets inside the model and the inputs are mapped directly with no need to consider the details of the structure inside the physical process (Hakimzadeh et al., 2014). An Artificial Neural Network (ANN) is known as a black-box model that has usefulness that exceeds the normally used statistical models like the free-pattern of forecasting model, a data-driven nature, and a toleration to data inaccuracy (Azmatullah et al., 2005). Besides its capability and simplicity, ANN has been employed in several common areas. These include hydraulics (Karunanithi et al., 1994), (Avarideh et al., 2001), (Liriano and Day, 2001), (Bateni and Jeng, 2006), (El-Shafie et al., 2007), (Zounemat-Kermani et al., 2009), and (Azamathulla and Gani, 2011); flood prediction (Chang et al., 2007); groundwater flow remediation (Ranjithan et al., 1993); rainfall forecasting (Ramirez et al., 2005); the design of reservoir operating policies (Raman and Chandramouli, 1996), (Chandramouli and Raman, 2001), (Cancelliere et al., 2002), (Liu et al., 2006); water resources management (Li and Huang, 2012); and the prediction of the peak outflow from a dam breach (Babaeyan et al., 2011; Nourani 2012; Hooshyaripor et al., 2012; Hooshyaripor et al., 2014;). In an ANN model that was developed recently, Nourani (2012) gathered data from laboratories, historical cases, and a numerical model that was physically-based, and then a simulation of an outflow hydrograph from the earth dam breach was created using the ANN model. The sensitivity analysis of his work verified that, when dealing with the breach process, not only is the depth of the water in the reservoir when the failure occurs a very important physical parameter but also the volume of the reservoir as compared to others. According to the review of the literature, Artificial Neural Networks are not employed to predict the width of a dam breach although they have the capability of estimating the nonlinearity of the relationship for any kind of data and although the already available techniques, which are employed to estimate the width of a beach in a dam, have a degree of uncertainty. As a result, this present study has been proposed to interduce the Generalized Regression Neural Network (GRNN) which is usually adopted for the function of approximating in order to improve the accuracy of the dam failure time estimation. This proposed GRNN has been trained and tested by applying real data so that its performance accuracy could be demonstrated.

2 DATA COLLECTION AND EXISTING APPROACHES

The magnitude of the peak outflow is the main attribute of the hydrograph of the breach outflow which affects the losses of property and life in a dam break phenomena. This attribute is affected by the various parameters of the breach, such as the dam failure time (Costa, 1985). There are a few models available in the literature which are physically-based and used to simulate how breaches in dams develop (Hanson, 2005; Froehlich, 2004; Visser, 1998; Fread, 1984, 1993; Ponce and Tsivoglou, 1981; and Cristofano, 1965). These models have a poor understanding of the development of the breach although they are dependent on water discharge and sediment erosion equations (Wahl, 2004). The database applied in this work included data from the failures of more than 140 real dams, which were gathered from a variety of sources. The results from various related research works (Froehlich, 1995; Singh, 1988; Wahl, 1998; Taher Shamsi et al., 2003; Xu and Zhang, 2009; and Pierce et al., 2010) were used in this present work.

A large number of the currently available methods employ the regression analysis to depict the value of the breach width as a function of the volume of water in the reservoir as well as the water depth behind the wall of the dam. The reported outcomes of the abundant regression analyses are illustrated for the incorporation of the prediction equation as well as the number of case study investigations employed as an element in the analysis, and can be seen in Table 1. Wahl (2004, 1998) introduced the case study data that were employed by previous researchers to determine the equations which can be utilized for the prediction of the peak outflow of the breach in a dam.

3 ARTIFICIAL NEURAL NETWORK

Neural Networks are normally thought of as black boxes which have been trained on a substantial number of data sets for a specific function. They are the worldview of data handling, which is motivated by the manner in which the natural biological nervous system processes information. Each network consists of numerous interconnected handling elements (neurons) working with each other as a single unit to deal with various problems. Neural systems have an impressive ability to determine the significance in loose or confounding information. In addition, they can be employed to focus on designs and identify patterns which are too complex to be noticed in any manner, either by people or even other computer strategies (Datt, 2012). The general structure of the neural network consists of three layers of neurons, which are the hidden layer and the output and input layers. An abundance of laboratory and hypothetical research works have explained that a complex nonlinearity function can be adequately approximated with an ANN having only one hidden layer. Similarly, it has been proposed that the furthest point for any number of the neurons in the layer that is hidden be less than 2n + 1, where n is the number of the input neurons (Hecht-Nielsen, 1987).

GRNN is a kind of new neural system which was introduced by Specht. GRNNs have a design that is similar to the Multilayer Perceptron Neural Networks (MLNNs); however, there is an important distinction between them. GRNNs carry out regression where there is a consistent objective variable, whilst MLNNs carry out characterization where there is a categorical objective variable. GRNNs are set up to evaluate any approximate function of data which has been previously recorded. The GRNN is a modification of the Radial Basis Function Neural Network (RBFNN), which is dependent on kernel regression networks (Cigizoglu, 2005; Celikoglu, 2006). No iterative preparation methodology as back propagation networks is needed by GRNNs. Any discretionary function that has two or more variable vectors is approximated by the GRNN, drawing the function which has been evaluated in a straightforward manner from the data used for training. Moreover, it is consistent enough that, when a large data set has been used for training, the error of the estimation will approach zero and only slight limitations will be put on the function (Celikoglu, 2005). GRNNs are consisted of four layers. These layers are the input and output layers, the design layer, and the summation layer. The general structure of the GRNN which was employed in this present study is illustrated in Figure 1. GRNNs are thought of as standardized RBFNNs where there is a unit centered during each training stage.

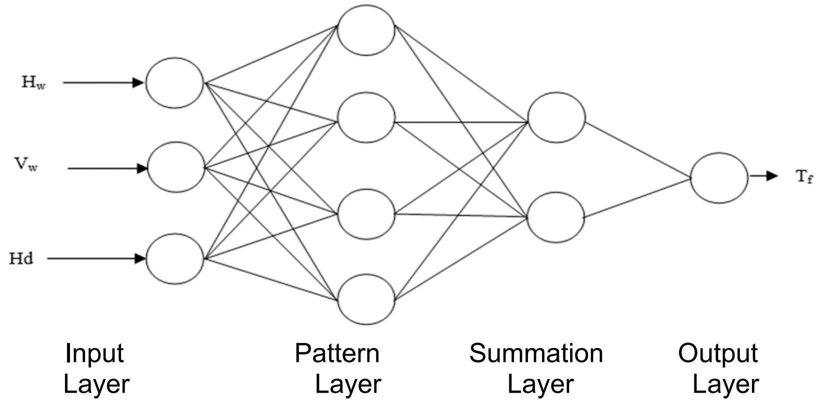

Figure 1. The general structure of GRNN.

  / ISSN 1562-6865 (Online) - ISSN 1063-7710 (Print)

The network is designed as a one-pass learning algorithm with a structure that is very parallel. Remarkably, the calculation provides smooth moves starting from one target value and moving to another even if using a poor data set in an estimation space which is multi-dimensional. An algorithmic structure can be employed with any problem of regression as a part of which there is no confirmation of a supposition of linearity. GRNNs are comprehensive approximations for a smooth function. As such, they are able to solve any problem of smooth function estimation (Disorntetiwat, 2001). Initial weight values cannot be arbitrarily appointed as the feed forward back propagation method's execution is tremendously sensitive. However, this problem was not encountered in the GRNN simulation in any case (Celikoglu, 2005). It was explained by Specht that GRNNs do not require any iterative preparation process as is needed in the back-proliferation method. There was no problem of a local minima being encountered when the GRNN model was used. As a result, the preference was given to the GRNN model instead of the feed forward back propagation. The total number of data units present in the input layer is dependent upon the total number of parameters which have been employed. The pattern layer and the input layer are connected to each other; and in the pattern layer, each neuron represents a training pattern and the pattern's output. The pattern layer is also joined to the summation layer. There are two distinct kinds of summation in the summation layer; they are the summation units and the division unit. The summation layer along with the output layer carries out the standardization of the output data. During the training of the network, the radial basis is employed in the hidden layer. At the same time, in the output layer, the function of linear activation is employed. In the summation layer, every two neurons (S and D) are joined to one of the units located in the pattern layer. All of the weighted output of the pattern layer is processed by the S summation neuron, whilst the unweighted output is computed by the D summation neuron (Kim 2004). The following equation is used to determine the output value from the GRNN model.

$$\mathrm{Output} = \frac{\sum_{j=1}^{n} y_i \cdot \exp\left(\frac{-\sum_{i=1}^{m}\left(x_i - x_{ij}\right)^2}{2\sigma^2}\right)}{\sum_{j=1}^{n} \exp\left(\frac{-\sum_{i=1}^{m}\left(x_i - x_{ij}\right)^2}{2\sigma^2}\right)} \qquad [1]$$

where:n: No. of training cases,

m: No. of output data.

The term of (xi – xij) is equal to the difference between the training data xij and the point of estimation xi of the ith data.

The accuracy of the function resulting from the training stage of the GRNN was influenced by the factor for smoothing (spread), which was found to be equal to the standard deviation σ. The nature of the data is the key factor influencing the selection of the smoothing factor's value. For example, a small value of the smoothing factor has to be chosen for regular data; whereas, a large value is appropriate for irregular data so that a good performance can be achieved from a GRNN. The GRNN was selected for this study because it learns quickly and has the capability of converging to the optimum regression surface. Simply put, the GRNN is a method employed to assess any function when presented with only the data used for training. As there is a probability of the density function coming from the training stage without any biases in regards to its shape, the framework is completely general. There is no problem if the functions are created out of multiple disjointed non-Gaussian locals, in a variety of measurements, and in addition to those of easier dispersions (Wasserman, 1993).

4 METHODOLOGY

Figure 2 below shows the proposed methodology that was utilized to build the GRNN models so that the dam failure time could be estimated and a comparison of the results with the results that were achieved by employing existing approach could be made. A database of 140 breached dams was employed to create the ANN models. The first stage in the building of the ANN model was to divide the data of the dam failures into a training and a testing set. To achieve this, the training set used 85% of the data and the testing set used the remaining 15%.

For better accuracy of the results and to create a more efficient neural network, a preprocessing step had to be performed on the variables of the network. It is often helpful, to scale the targets and inputs so that they will, generally, fall inside a limit that is predetermined before beginning to train a network. In this present research work, the targets and inputs had been scaled so that they would fall in the range of -1 and +1. The preprocessing step was performed by applying the equation that follows:

$$X = \frac{2(X_i - X_{min})}{X_{max} - X_{min}} - 1 \qquad [2]$$

where: X is the standardized value of Xi, X_{min} is the minimum value of data and X_{max} is the maximum value of data.

The main explanation behind needing to standardize the data is that measurement of the variables is usually made in different units. By taking this step, the variance in the levels amongst the data could be avoided (Romesburg, 1984; Sudheer et al., 2002).

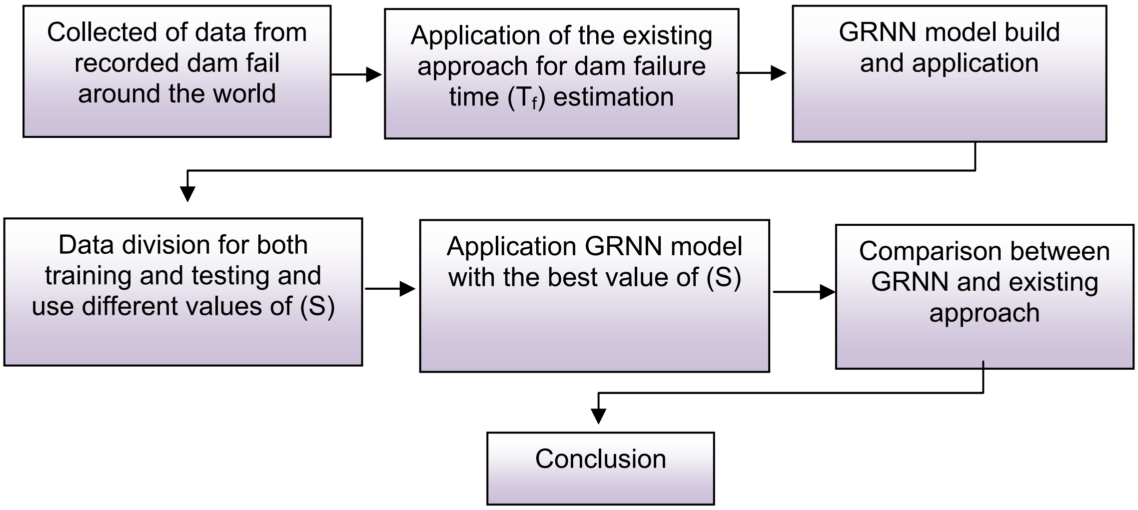

Figure 2. Flowchart of proposed GRNN model for dam failure time estimation.

After the simulation was completed, all of the output values were de-standardized by multiplying them by the respective factor of standardization to get the actual values of the peak outflow. This preprocessing step was made for a more efficient stage of training by enhancing the process of learning (Demuth, 2001). A variety of standard statistical performance evaluation measures was employed to evaluate how the developed GRNN models performed. The three statistical performance indices employed in this study have been presented below:-

1- Mean Relative Error (MAE): measures the mean absolute error between the observed and the predicted values.

$$\mathrm{MRE} = \frac{1}{n}\sum_{1}^{n}\frac{(x_o - x_p)}{x_o} \qquad [3]$$

2- Root Mean Square Error (RMSE): measures the root square of the

$$\mathrm{RMSE} = \sqrt{\sum_{1}^{n}\frac{(x_o - x_p)^2}{n}} \qquad [4]$$

3- Coefficient of Determination (R^2) : this coefficient of efficiency is calculated as:

$$R^2 = \frac{\left[\sum_1^n (x_o - x_{m1})(x_p - x_{m2})\right]^2}{\sum_1^n (x_o - x_{m1})^2 \left(x_p - x_{m2}\right)^2} \qquad [5]$$

where: x_o is the observed values, x_p is the predicated values, x_{m1} is the average of the observed values and x_{m2} is the average of the predicated values.

The statistical parameters were calculated by employing the data of the dam failure time which were estimated with the GRNN model and other existing approaches. Use of the optimum value of the factor for smoothing (spread) is necessary if more accurate results are to be obtained with the GRNN model. Thus, to obtain a more efficient GRNN model, the researcher carried out a sensitivity analysis for various values of the factor for smoothing.

5 RESULTS AND DISCUSSION

Two scenarios were performed to predict the dam failure time; each scenario employed different variables as the input. In addition, a comparison was made between the already available techniques for the linear regression analysis of width estimation of dam breaches and these proposed models. The details and results of each model are presented below.

5.1 First scenario

The water depth upstream (Hw) of the dam was used in this model to predict the dam failure time when dam break happens. Von Thun and Gillette employed a linear regression analysis in order to create a relationship between T_f and H_w. For the smoothing factor (spread) value, the range from 0.0001 to 1 was utilized to obtain the optimum value to achieve results with better accuracy. In Figure 3, it can be seen that, the optimum value for the smoothing factor (spread) with this model was equaled to 0.001.

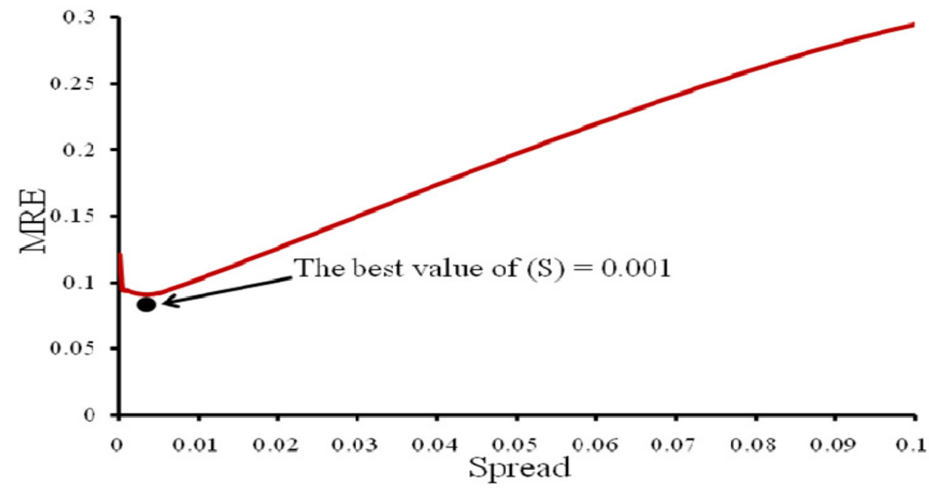

Figure 3. MRE variation with different smoothing factors values for first scenario.

The performance of the GRNN model for each of the stages (training and testing) is presented in Figure 4. For further analysis, the statistical analysis results for the GRNN model as well as the other empirical equations which were used for the estimation of the dam failure time depending on the depth of the water (Hw) are presented in Table 2. As can be seen from the results in Table 2, when comparing with the regression equation, the GRNN model had a high value of NSE and low value of RMSE. Furthermore, the MRE value was decreased by more than 90% when employing the GRNN model as compared to employing the Von Thun and Gillette equation.

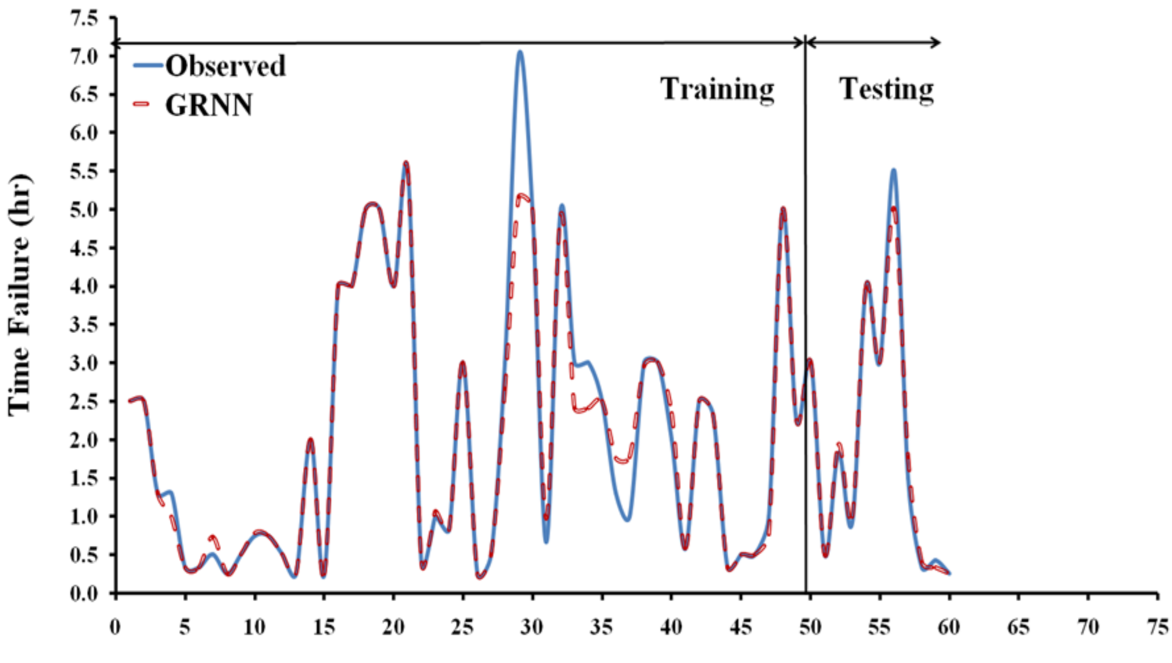

Figure 4. GRNN performance for Tf estimation for first scenario.

Table 2. Results of GRNN model and empirical method for first scenario.

Method	RMSE	R^2	MRE
GRNN	0.20	0.995	0.09
Von Thun and Gillette	2.093	0.614	0.57

5.2 Second scenario

In this scenario, an estimation was made of the dam failure time depending on the volume, depth of the water in the reservoir and the dam height. According to the literature, Xu and Zhang (2009) found the most well-known equations for the relationship between (V_w, H_b) and (T_f). Thus, a comparison was made between the results of the GRNN model and the results of that technique. The optimum spread value was found to be equal to 0.028 as can be seen in Figure 5.

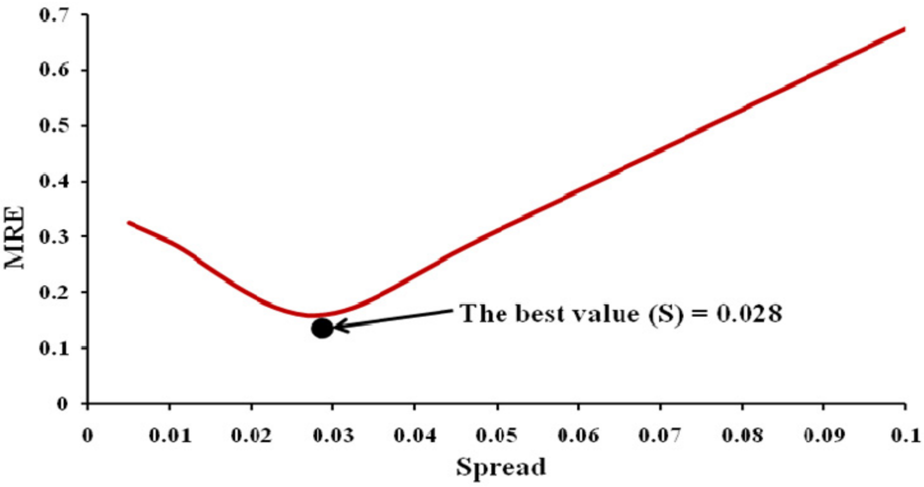

Figure 5. MRE variation with different smoothing factors values for second scenario.

Figure 6 shows the performance of the GRNN model for both the training stage and the testing stage. It was obvious from the figure that the GRNN model was able to predict the value of T_f close to the value that was actually observed.

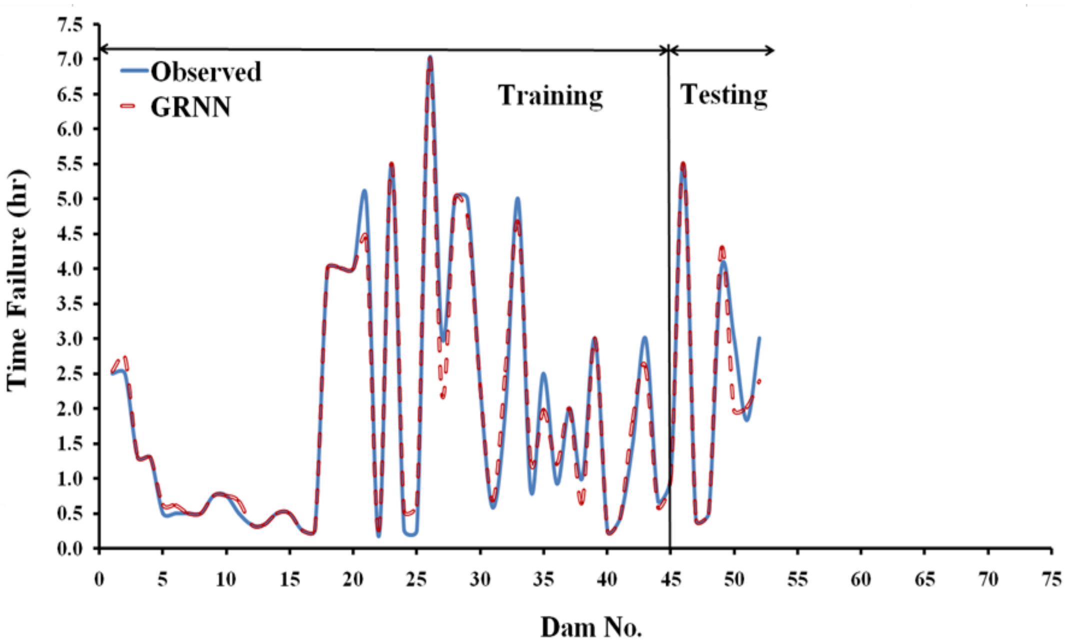

Figure 6. GRNN performance for T_f estimation for second scenario.

Table 3 tabulated the statistical evaluation of the GRNN model and Xu and Zhang (2009) for dam failure time estimation. As can be seen from the results in Table 3, the GRNN model can estimate the dam failure time with good accuracy in comparison to the regression equation. It was very clear from the high values of the NSE and the low values of the RMSE and the MRE. In addition, when the GRNN model was used, the value of the MRE was reduced by about 50%.

Table 3. Results of GRNN model and empirical method for second scenario.

Method	RMSE	NSE	MRE
GRNN	0.569	0.955	0.16
Xu and Zhang	1.038	0.836	0.34

6 CONCLUSION

In recent decades, the development of precise and simple models for the prediction of dam breach parameters have been quite a challenging task because of the importance of the preparation of emergency action plans as well as the assessment of risk when the failure of the dam occurs. A generalized regression artificial neural network model is used in this present study for the estimation of the dam failure time. The results are later compared with the results of the existing empirical approaches. A study of the problem of the prediction of the dam failure time is carried out and the analysis is performed by employing data from more than 140 recorded dam failures worldwide, which are gathered from the related literature. Network training has made use 85% of the total data, and network testing has made use of the remaining 15%. The values of the RMSE, R2, and MRE, which resulted from the analysis, demonstrate the potential of employing the GRNN as a predictive tool for estimation of the breach width. Additionally, the results show that the MRE values of the breach width prediction estimated using the common regression analysis techniques can be decreased about 50%.

REFERENCES

Avarideh, F., Banyhabib, M.A. & Tahershamsi, A. (2001). Application of Artificial Neural Networks in River Sediment Estimation. *3th Iran Hydraulic Conference,* Kerman, Iran, 269-275.
Azmathullah, H.Md., Deo, M.C. & Deolalikar, P.B. (2005). Neural Networks for Estimation of Scour Downstream of a Ski-Jump Bucket. *Journal of Hydraulics Engineering,* 131(10), 898–908.
Azamathulla, H.Md. & Ghani, A. (2011). ANFIS-based approach for Predicting the Scour Depth at Culvert Outlets. *Journal of Pipeline Systems Engineering and Practice,* 2(1), 35-40.
Bateni, S.M. & Jeng, D.S. (2006). Estimation of Pile Group Scour using Adaptive Neuro Fuzzy Approach. *Ocean Engineering,* 4(8-9),1344–1354.
Babaeyan, A.A., Nourani, V., Hakimzadeh, H. (2011). Application of Artificial Intelligence Tools to Estimate Peak Outflow from Earth Dam Breach. *International Journal of Earth Science Engineering,* 4(6), 243 – 246.
Bentaher, L.S. & Elmazoghi, H.G. (2013). Estimation of Dam Breach Width using a Neuro-Fuzzy Computing Technique. *Seventeenth International Water Technology Conference,* IWTC17, Istanbul.
Cristofano, E. (1965). *Method of Computing Erosion Rate for Failure of Earthfill Dams,* US Department of the Interior, Bureau of Reclamation, Denver.
Costa, J.E., (1985). *Floods from Dam Failures,* Open File Report 85-560, Secretary, 59.
Chandramouli, V. & Raman, H. (2001). Multireservoir Modeling with Dynamic Programming and Neural Networks. *Water Resources Planning Management ASCE,* 127(2), 89-98.
Cancelliere, A., Giuliano, G., Ancarani, A. & Rossi, G. (2002). A Neural Networks Approach for Deriving Irrigation Reservoir Operating Rules. *Water Resources Management,* 16(1), 71–88.
Cigizoglu, H.K. (2004). Estimation and Forecasting of Daily Suspended Sediment Data by Multilayer Perceptrons. Advanced Water Resources, 27, 185 – 195.
Cigizoglu, H.K. & Alp, M. (2005). Generalized Regression Neural Network in Modelling River Sediment Yield. Advanced Engineering Software, 37, 63 – 80.
Celikoglu, H.B. (2006). Application of Radial Basis Function and Generalized Regression Neural Networks in Non-Linear Utility Function Specification for Travel Mode Choice Modelling. *Mathematical and Computer Modelling,* 44, 640–58.
Chang, F.J., Chiang, Y.M. & Chang, L.C. (2007). Multi-Step-Ahead Neural Networks for Flood Forecasting. *Hydrology Science Journal,* 52(1), 114–130.
Demuth, H. & Beale, M. (2001). *Neural Network Toolbox for use with MATLAB,* Guide, V. 4.0, MathWorks, Inc., MA., www.mathworks.com.
Disorntetiwat, P. (2001). Global Stock Index Forecasting using Multiple Generalized Regression Neural Networks with a Gating Network, *PhD Thesis,* University of Missouri-Rolla, USA.
El-Shafie, A., Taha, M.R. & Noureldin, A. (2007). A Neuro-Fuzzy Model for Inflow Forecasting of the Nile River at Aswan High Dam. Water Resources Management, 21(3), 533–556.
Froehlich, & David, C. (1987). Embankment-Dam Breach parameters, Hydraulic Engineering. *Proceedings of the 1987 ASCE, National conference on Hydraulic Engineering,* Williamsburg Virginia, August 3-7,1987, 570-575.

Froehlich, D. (1995a). Embankment Dam Breach Parameters Revisited. Water Resources Engineering. *Proceedings of the ASCE Conference on Water Resources Engineering,* New York, 887–891.
Froehlich, D.C. (1995). Peak Outflow from Breached Empankment Dams. *Journal of Water Resources Planning Management,* 121, 90 – 97.
Froehlich, D. (2004). Two-Dimensional Model For Embankment Dam Breach Formation and Flood Wave Generation. *Proceedings of the 21st Annual conference of the Association of State Dam Safety Officials,* Lexington, Ky.
Froehlich, D.C. (2008). Embankment Dam Breach Parameters and Their Uncertainties. *Journal of Hydraulics Engineering, ASCE,* 134(12), 1708–1721.
Gallegos, H.S. (2009). Two-Dimensional, High- Resolution Modeling of Urban Dam-Break Flooding: A Case Study of Bald- Win Hills, California. Advanced Water Resources, 32(8), 1323-1335.
Gaucher, J., Marche, C. & Mahdi, T. (2010). Experimental Investigation of the Hydraulic Erosion of Noncohesive Compacted Soils. Journal of Hydraulics Engineering, 136(11), 901 – 913.
Hecht-Nielsen, R. (1987). Kolmogorov's Mapping Neural Network Existence Theorem. *Proceeding of 1st IEEE International Conference on Neural Networks,* San Diego, 3, 11 – 14.
Hanson, G., Cook, K. & Hunt, S. (2005). Physical Modeling Of Over -Topping Erosion and Breach Formation of Cohesive Embankments. *Transactions ASAE,* 48(5), 1783 – 1794.
Hooshyaripor, F. & Tahershamsi, A. (2012). Comparing the Performance of Neural Networks for Predicting Peak Outflow from Breached Embankments when Back Propagation Algorithms meet Evolutionary Algrithms. *International Journal of Hydraulics Engineering,* 1(6), 55 – 67.
Hooshyaripor, F., Tahershamsi, A. & Golian, S. (2014). Application of Copula Method and Nueral Networks for Predicting Peak Outflow from Breached Embankments. *Journal of Hydrology Environment Research,* 8(3), 292– 303.
Hakimzadeh, H., Nourani, V., Babaeyan, A.A. (2014). Genetic Programming Simulation of Dam Breach Hydrograph and Peak Outflow Discharge. *Journal of Hydrology Engineering,* 19(4), 757 – 768.
Johnson, F.A. & Illes, (1976). A Classification of Dams Failures. *International Water Power and Dam Construction,* December, 43-45.
Karunanithi, N., William, J.G., Darrell, W. & Ken, B. (1994). Neural Networks for River Flow Prediction. *Computing in Civil Engineering,* 8(2), 201–220.
Kim, B., Lee, D.W., Parka, K.Y., Choi, S.R. & Choi, S. (2004) Prediction of Plasma Etching using a Randomized Generalized Regression Neural Network. *Vacuum,* 76, 37–43.
Liriano, S.L. & Day, R.A. (2001). Prediction of Scour Depth at Culvert Outlets using Neural Networks. *Journal of Hydroinformatics,* 3(4), 231-238.
Liu, P., Guo, S.L., Xiong, L.H., Wei, L. & Honggang, Z. (2006). Deriving Reservoir Refill Operating Rules by using the Proposed DPNS Model. *Water Resources Management,* 20(3), 337–357.
Liang, D.F., Lin, B.L. & Falconer, R.A. (2007). A Boundary-Fitted Numerical Model for Flood Routing with Shock-Capturing Capability. *Journal of Hydrology,* 332(3-4), 477-486.
Li, Y.P. & Huang, G.H. (2012). Risk Analysis and Management for Water Resources Systems. *Stochastic Environmental Research and Risk Assessment,* 27(3), 593-597.
Macchione, F. (2008). Model for Predicting Floods due to Earthen Dam Breaching. I: Formulation and Evaluation. *Journal of Hydraulics Engineering,* 134(12), 1688 – 1696.
Nourani, V., Hakimzadeh, H. & Alireza, B.A. (2012). Implementation of Artificial Neural Network Technique in the Simulation of Dam Breach Hydrograph. Journal of Hydroinformatics, 14(2), 478 – 496.
Ranjithan, S., Eheart, J.W. & Garrett, J.H. (1993). Neural Network based Screening for Groundwater Reclamation under Uncertainty. *Water Resources Research,* 29(3), 563–574.
Raman, H. & Chandramouli, V. (1996). Deriving a General Operating Policy for Reservoirs using Neural Network. *Water Resources Planning Management, ASCE,* 122(5), 342–347.
Ramirez, M.C.V., Ferreira, N.J. & Velho, H.F. (2005). Artificial Neural Network Technique for Rainfall Forecasting Applied to the Sa˜o Paulo Region. *Journal of Hydrology,* 301(1-4),146 – 162.
Razad, A.Z.A., Muda, R.S., Sidek, L.M., Azia, S.A., Mansor, F.H. & Yalit, R. (2013). Simulation of Breach Outflow for Earthfill Dam. IOP Conference Series Earth Environmental Science, 16(1), 1-5.
Tsai, C.W. (2005). Flood Routing in Mild-Sloped Rivers Wave Characteristics and Downstream Backwater Effect. Journal of Hydrology, 308, 151–167.
Von Thun, J. & Gillette, D. (1990). *Guidance on Breach Parameters,* Internal Memorandum, U.S. Dept. of the Interior, Bureau of Reclamation, Denver, 17.
Wasserman, P.D. (1993). *Advanced Methods in Neural Computing,* Van Nostrand Reinhold, New York, USA, 155–161.
Wahl, T.L. (1998). *Prediction of Embankment Dam Breach Parameters: A Literature Review and Needs Assessment,* U.S. Bureau of Reclamation Dam Safety Rep. No. DSO-98-004, Denver.
Wahl, T.L. (2004). Uncertainty of Predictions of Embankment Dam Breach Parameters. *Journal of Hydraulics Engineering,* 130(5), 389 – 397.

Wahl, T.L. (2010). Dam Breach Modeling – An Overview of Analysis Methods. *Joint Federal Interagency Conference on Sedimentation Hydrologic Modeling,* 27.

Xia, J., Lin, B., Falconer, R.A. & Wang, G. (2010). Modelling Dam-Break Flows over Mobile Beds using a 2D Coupled Approach*. Advances Water Resources,* 33(2), 171–183.

Xu, Y. & Zhang, L.M. (2010). Breaching Parameters for Earth and Rockfill Dams. *Journal of Geotechnical Geoenvironmental Engineering,* 135, 1957-1970.

Zounemat-Kermani, M., Beheshti, A., Ataie-Ashtiani, B. & Sabbagh-Yazdi, S. (2009). Estimation of Current-Induced Scour Depth around Pile Groups using Neural Network and Adaptive Neuro Fuzzy Inference System. Applied Soft Computing, 9(2), 746–755.